SCMAM'19

30th November ~ 2nd December; 2019

INTERNATIONAL CONFERENCE
ON
Synthesis, Characterization and Modelling Study of Advance Material

Conference Proceeding

AIET Bhubaneswar

Aryan Institute of Engineering and Technology Bhubaneswar

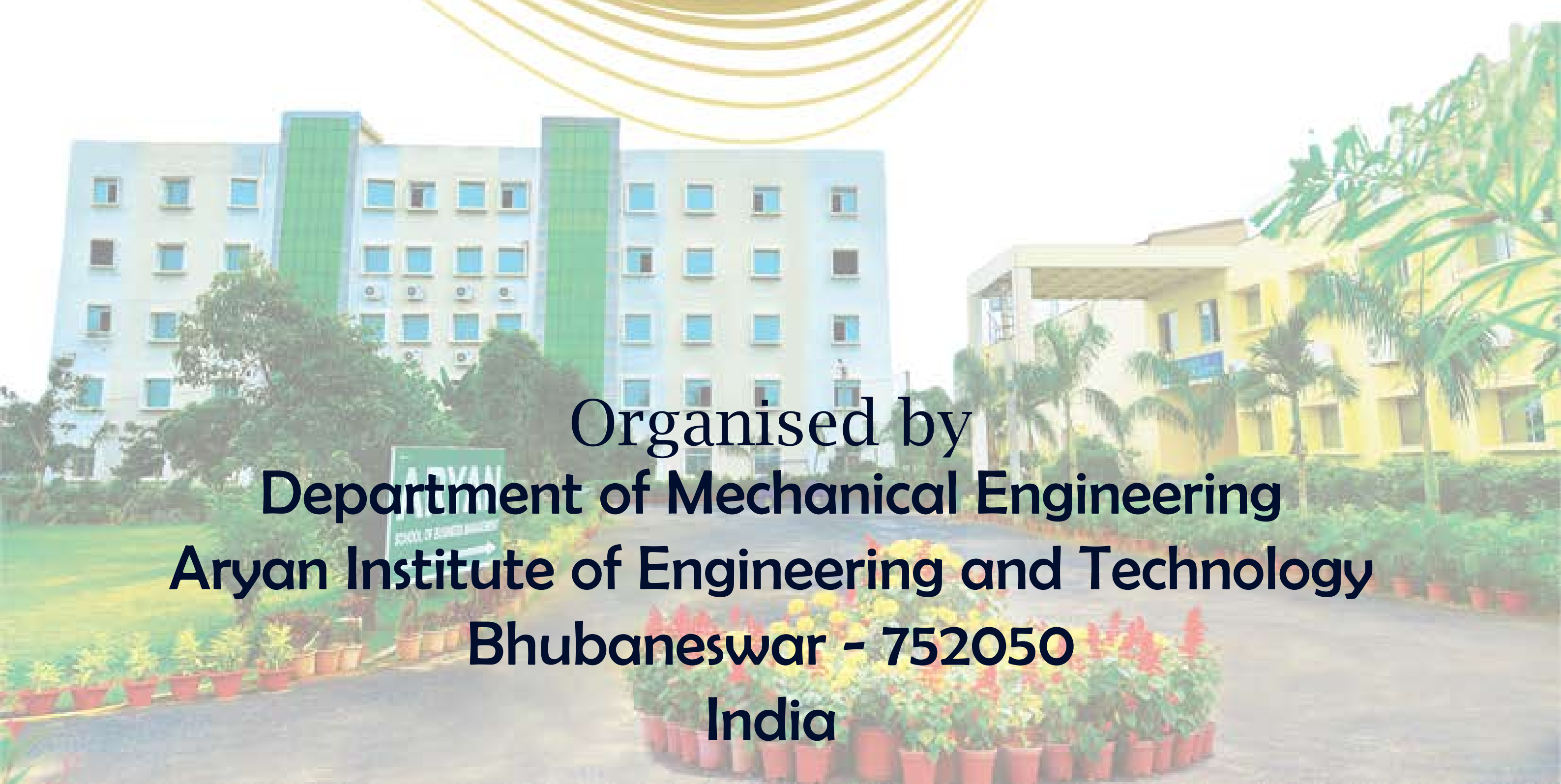

Organised by

Department of Mechanical Engineering

Aryan Institute of Engineering and Technology

Bhubaneswar - 752050

India

Few research facilities of the Department of Mechanical Engineering

Synthesis, Characterization and Modelling Study of Advance Material

30th Nov. - 2nd Dec. 2019

Conference Proceeding

Organized by

Department of Mechanical Engineering
Aryan Institute of Engineering and Technology
Bhubaneswar – 752050

List of Sponsors

Star Testing Systems

ICON Analytical Equipments Pvt. Ltd

JEOL India Pvt. Ltd

Odisha Hydro Power Corporation Ltd

Citicon Engineers Pvt. Ltd

Punjab National Bank Ltd

Mahanadi Coal Field Ltd

Utkal Alumina International Limited

Hindalco Industries Ltd

ABOUT THE CONFERENCE

Science and materials has continuously evolved through decades. SCMAM 2019 was organized in Nov-2019 and was successful in capturing the development of materials and processing. Department of Mechanical Engineering, AIET, Bhubaneswar is organizing SCMAM-2019 to showcase recent advances in materials processing and applications. In keeping up with the research interest of the materials community, SCMAM-2019 will provide an update on scientific and technical aspects covering broad areas of interests in engineering materials, processing and applications.

ABOUT THE DEPARTMENT

The Department of Mechanical Engineering has been in existence since 2009 with the inception of the college with an initial intake capacity of 60 and is producing high quality technical manpower needed by industry, R&D organizations, and academic institutions. The intake capacity was enhanced to 120 in the year 2011.The Department has full fledged faculty members who are specialized in the fields of design, thermal, production and CAD/CAM. Laboratories are fully equipped to enhance the knowledge of the student, periodic industry trips and visits to various project sites are arranged. Special lectures and seminars are held on a frequent basis to assist them tailor in their particular areas of interest and trying hard to transform students of even mild talent to professionals in the mechanical and mechatronics field. Already more than750nos of alumni have been produced so far, placed in different Government, private, Public & other sectors and some of them have pursued higher studies. However, with the progress of time, many more frontier areas of mechanical engineering have been taken up for active research.

ABOUT THE INSTITUTE

Established in the year 2009 , Aryan Institute of Engineering and Technology(AIET) is one of the premier engineering colleges in the self-financing category of Engineering education in eastern India. It is situated at temple city Bhubaneswar, Odisha and is a constituent member of Aryan Educational Trust. This reputed engineering college is accredited by NAAC, UGC and is affiliated to BPUT, Odisha. AIET aims to create disciplined and trained young citizens in the field of engineering and technology for holistic and national growth.

The college is committed towards enabling secure employment for its students at the end of their four year engineering degree course. (The NAAC accreditation in the year 2018 vouches for the college's determination and dedication for a sustainable learning environment). The academic fraternity of AIET is a unique blend of faculty with industry and academic experience. This group of facilitators work with a purpose of importing quality education in the field of technical education to the aspiring students. Affordable fee structure along with approachable location in the smart city of Bhubaneswar, makes it a preferred destination for aspiring students and parents.

The Institute works with a mission to expand human knowledge beneficial to society through inclusive education, integrated with application and research. It strives to investigate on the challenging basic problems faced by Science and Technology in an Inter disciplinary atmosphere and urges to educate its students to reach their destination, making them come up qualitatively and creatively and to contribute fruitfully. This is not only its objective but also the ultimate path to move on with truth and brilliance towards success.

Organizing Committee Members

PATRON:

Dr. Madhumita Parida
Chairperson
Aryan Institute of Engineering and Technology

Director
Prof. Sasmita Parida

Convener
Prof. (Dr.) P. K. Swain

Co- Convener
Prof. Biswaranjan Biswal

Organizing Secy.
Prof. Shaik Mozammil

Jt. Organizing Secy.
Prof. A. K. Sahoo

Treasurer
Prof. Nirmal Charan Mallik

Jt. Treasurer
Prof. Nilgrib Mohanty

INTERNATIONAL ADVISORY COMMITTEE

Dr. S. V. Kamat
Director
Defense Metallurgical Research Laboratory,
(DMRL)
Hyderabad, India

Prof. Raj N. Singh
School of Materials and Engineering,
Oklahoma State University
USA

Dr. P. M. Ajayan
Professor and Founding Chair
Department of Material Science and
Nanoengineering, Rice University
Houston, USA

Dr. Mitjan Kalin
University of Ljubljana
Slovenia

Dr. Eric Jaegle
Chinese University of Hong Kong
Hong Kong

Dr. Abidul Hassan
Professor and Founding Chair
Department of Material Science and
Nanoengineering
King Saud University, Saudi Arabia

NATIONAL ADVISORY COMMITTEE

Dr. Anil Kumar Bhargava
Professor and Head
Department of Metallurgical and Material Engineering
Malaviya National Institute of Technology Jaipur

Dr. N. Venkataramani
Professor and Head
Department of Metallurgical Engineering and Material Science
National Institute of Technology, Jamshedpur

Dr. Arvind Bharti
DRDO Headquarters
New Delhi

Dr. Prakash Gopalan
Director
Thapar University, Thapar

Dr. Dipak Mazumdar
Professor
Department of Materials and Metallurgical Engineering
National Institute of Technology, Patna

Dr. R. K. Mandal
Professor and Head
Department of Metallurgical Engineering
Indian Institute of Technology (BHU), Varanasi

Dr. Gour Gopal Roy
Professor and Head
Department of Metallurgical and Materials Engineering
National Institute of Technology, Silcher

Dr. S. K. Ray
Distinguished Visiting Professor
Indian Institute of Technology, Mandi

Prof. K. K. Raina
Distinguished Professor and Vice Chancellor
DIT University,
Dehradun

Dr. Vikas Kumar
Director
Defense Metallurgical Research Laboratory
Hyderabad

LOCAL COMMITTEE MEMBERS

Prof. N. C. Mallik
Department of Mechanical Engineering

Prof. Babita Meher
Department of Mechanical Engineering

Prof. R. B. Rao
Department of Civil Engineering

Prof. A. P. Das
Department of Civil Engineering

Assist. Prof. Prakash Dehury
Department of Computer Science Engineering

Prof. P. K. Rautray
Department of Computer Science Engineering

Prof. D. K. Sahoo
Department of Electrical Engineering

Prof. Subashish Mohanty
Department of Electrical Engineering

Prof. Ajit Kumar Panda
Department of Electrical Engineering

Prof. Sambit Parida
Department of Civil Engineering

Prof. Sagarika Patro
Department of Electrical and Electronics Engineering

Prof. Abhishek Mohanty
Department of Electrical and Electronics Engineering

Prof. Ipsita Pahi
Department of Electrical and Electronics Engineering

Prof. S. K. Panda
Department of Electronics and Communications Engineering

Prof. P. C. Satpathy
Department of Electronics and Communications Engineering

Prof. Biswajit Mishra
Department of Electronics and Communications Engineering

Prof. A. K. Jena
Department of Basic Science and Humanities

Prof. Deepak Sahoo
Department of Basic Science and Humanities

Conference Committee Management

1. Reception Management

- Rasmi Rekha Mahato
- Rajkumari Lopamudra
- Bidyabati Samal
- Urmila Sahoo
- Smita Digal
- Sunita Priyadarsini

2. Transit/Accommodation Management

- Krishna Naidu
- Biswanath Majhi
- Kishore Chandra Pradhan
- Duga Prasad Padhy
- Jyoti Prakash Khunti
- Deepen Kumar Jena
- Manoranjan Mahunta

3. Seminar Hall Management

- Prasannjeet Pattanaik
- Pravat Ranjan Mishra
- Priti Ranjan Jena
- Samrat Kharabela Senapati
- Bidyadhar Jena
- Chinmaya Mohapatra

4. Catering Management

- Pradyumna Badajena
- Pravat Kumar Sahoo
- Hara Prasad Mishra
- Asutosh Bal

5. Printing/Stationary Management

- Sumit Ghosh
- Akhilesh Singh
- Vikas Meher
- Vishal Gupta

6. Design Team

- Sridhar Jena
- Mahesh Nayak
- Nitesh Samal

7. Anchoring In Inauguration Ceremony

- Rudra Prasad Nanda
- Nilimashree Niharika

Conference Sub-Committee Management

- Dillip Kumar Pradhan
- Junaid Mohammad
- Chinmaya Mohapatra
- Naresh Sharma
- Pradeep Ghadei
- Dinesh Shah
- Narendra Mallick

<table>
<tr><th colspan="2">ORAL</th><th>Session 1</th><th rowspan="12">Lunch</th><th>Session 2</th><th rowspan="12">Tea Break</th><th>Session 3</th><th colspan="2">Poster(18:00 - 19:00)</th></tr>
<tr><td rowspan="4">30-Nov</td><td>Room 1</td><td>Nanomaterials</td><td>Nanomaterials</td><td>Nanomaterials</td><td rowspan="6">30-Nov</td><td>Advanced Structural Steels</td></tr>
<tr><td>Room 2</td><td>Surface Engineering</td><td>Surface Engineering</td><td></td><td>Ceramics and Polymer Materials</td></tr>
<tr><td>Room 3</td><td>Advanced Structural Steels</td><td>Advanced Structural Steels</td><td>Advanced Structural Steels</td><td>High Temprature Materials</td></tr>
<tr><td>Room 4</td><td>High Temprature Materials</td><td>High Temprature Materials</td><td>Ceramics and Polymer Materials</td><td>Material Processing</td></tr>
<tr><td rowspan="4">1-Dec</td><td>Room 1</td><td>Advanced Materials for Energy Conversion and storage</td><td>Extractive Metallurgy</td><td>Extractive Metallurgy</td><td>Nanomaterials</td></tr>
<tr><td>Room 2</td><td>Material Processing</td><td>Material Processing</td><td>Material Processing</td><td>Surface Engineering</td></tr>
<tr><td>Room 3</td><td>Joining of Materials</td><td>Joining of Materials</td><td>Biomaterials and Tissue Engineering</td><td rowspan="5">1-Dec</td><td>Advanced Materials for Energy Conversion and storage</td></tr>
<tr><td>Room 4</td><td>Composite Materials</td><td>Composite Material</td><td>Composite Material</td><td>Biomaterials and Tissue Engineering</td></tr>
<tr><td rowspan="3">2-Dec</td><td>Room 1</td><td>Material Processing</td><td rowspan="3"></td><td rowspan="3"></td><td>Composite Material</td></tr>
<tr><td>Room 2</td><td>Composite Materials</td><td>Extractive Metallurgy</td></tr>
<tr><td>Room 3</td><td>Biomaterials and Tissue Engineering</td><td>Joining of Materials</td></tr>
</table>

CHAIRPERSON'S MESSAGE

I am delighted in acknowledging the International Conference **SCMAM 2019** organized by the Mechanical Engineering Department of Aryan Institute of Engineering & Technology on **"Synthesis, Characterization and Modelling Study of Advance Material".**

Aryan Institute of Engineering and Technology (AIET) was established in the year 2009 and it is one of the self-financing premier institutes in eastern Odisha. The Institute is accredited by NAAC, UGC, and is affiliated to BPUT, Odisha.

I ensure that this International Conference will motivate a large number of our B.Tech students and encourage them to actively participate in the program and gain some adequate knowledge. I congratulate the convener and members of the local, National and International organizing committees of this program.

I welcome on behalf of AIET to all the delegates and speakers for their participation in this International Conference. I am sure that this proceeding will be highly useful to researchers in their field.

I wish all the success to the conference.

Dr. Madhumita Parida

With regards,
Dr. Madhumita Parida
Chairperson
Aryan Institute of Engineering & Technology
Arya Vihar, Bhubaneswar, Odisha

DIRECTOR'S MESSAGE

I am glad to note that the Department of Mechanical Engineering is organizing an International Conference on "**Synthesis, Characterization and Modelling Study of Advance Material**" (SCMAM-2019) from 30th November to 2nd December 2019. I am sure that this conference deliberation will be highly stimulating embracing advancement in simulation, optimization and Mechanical Engineering.

I am sure that this conference will help in understanding the ever-changing corporate world and the corresponding reforms in India.

I congratulate the organizers of the Institute for their sincere effort to organize this conference.

I wish all the success to the conference.

Sasmita Parida

With regards,
Prof. Sasmita Parida
Director
Aryan Institute of Engineering & Technology
Arya Vihar, Bhubaneswar, Odisha

PRINCIPAL'S MESSAGE

I am immensely happy that the Mechanical Engineering department of our Institute is organizing an International Conference on **"Synthesis, Characterization and Modelling Study of Advance Material"** (SCMAM'19) on 30th November 2019 and is going to present a collection of various technical papers in the proceeding.

With the proper guidance of our management, the Aryan Institute of Engineering & Technology continues to march on the way to success with confidence.

I also congratulate Convener, staff members, students of our institute for their efforts in organizing this conference.

I wish the conference a grand success.

With regards,
Prof. (Dr.) Shart Chandra Mishra
Principal
Aryan Institute of Engineering & Technology
Arya Vihar, Bhubaneswar, Odisha

CONVENER'S MESSAGE

As the Convener of the of Conference SCMAM'2019, I would like to cordially invite all academicians, researchers, and engineers in the broad disciplines of Mechanical & Civil Engineering to attend/present their papers at this conference. This conference is intended to boost the publication of research papers of Mechanical & Civil Engineering faculty members as well as be a platform for newcomers to present their technical papers. However, this conference is also open to all researchers throughout India to share their research findings.

The conference will be held from 30th November to 2nd December 2019 at AIET, Bhubaneswar. Kindly mark your calendar, prepare your submissions, visit our website and keep in touch with me for updates. I hope you all will have a good deliberation during the conference and wish you all success in your research work. Looking forward to your participation in SCMAM'2019.

With regards,
Prof. (Dr.) P. K. Swain

Dean of Academics, Professor and HOD of Mechanical Engineering
Aryan Institute of Engineering & Technology
Arya Vihar, Bhubaneswar, India

Contents

Part II Poster Presentation

CONFERENCE PROCEEDING

ORAL PRESENTATION

Effect of Rotary-Klin Pyrolyse in Transient Modelling

P K Swain, *Department of Mechanical Engineering, Aryan Institute of Engineering & Technology, Bhubaneswar, pkswain25@gmail.com*
Nalinikanta Swain, *Department of Mechanical Engineering, Capital Engineering College, Bhubaneswar, nalini_526@yahoo.co.in*
Kalpana Mallick, *Department of Mechanical Engineering, Raajdhani Engineering College, Bhubaneswar, kalpanam11@outlook.com*

Abstract: The increasing interest in small-scale renewable-energy plants for distributed power generation has led to a demand for best software tools to analyse and build control systems to manage suitable integrated systems. Biomass, as a renewable energy resource, should be processed if it is to be exploited in small CHP units and pyrolysis is one of the best options for transforming solid biomass into needful liquid and gaseous fuels. This research is focus on the innovation of a time-dependent model of a rotary-kiln pyrolyser for biomass: the model is tends for the improvement of control systems and the modelling of the integrated energy systems, where the pyrolyser is equipped with power generation package. The simulation model was developed with TRANSEO based environment and on a quasi 2-D numerical discretisation of the rotary kiln. Results are shown for actual case that is currently under construction: the simulation based model is capable to predict the impact of various suitable operating environment on fuel yields along with capturing the main transient phenomena during modification in the pyrolyser operating environment.

Kewords: Biomass, pyrolysis, distributed generation, transient modelling.

INTRODUCTION

Due to the increasing price of oil, the Kyoto commitment of European countries and favourable political and social conditions, there is currently a large demand for biomass energy conversion systems of relatively small size (below 20MW of thermal input) in Europe. Northern European countries have been successfully operating thermal or cogenerative biomass-fuelled plants for several years, while Southern European countries, such as Italy, where the average annual demand for heat is low, are struggling to promote this type of system because of its poor economic sustainability [1], despite economic incentives.

However, there are already opportunities for niche applications for full-electric or cogenerative energy plants below 1MW electric power thanks to the availability of unexploited residual biomasses (wood industry residues, furniture industry residues, meat and bone meal, etc.) or biomass waste (waste water treatment residuals, organic urban waste fraction, etc.): in such cases, the zero or negative cost of biomass fuel is often counterbalanced by the relatively small quantities available over the course of an entire year without facing the costs of long-distance transportation. The use of biomass in microturbines or internal combustion engines necessarily requires thermochemical pre-treatment (such as gasification and pyrolysis) to produce a low LHV gaseous fraction that can be used as primary fuel and there is renewed interest, especially in Italy, in the slow pyrolysis of waste and biomass by means of semi-conventional rotary kilns (Fig. (**2**) – main dimensions in Table **4**), as an effective and robust way to process solid biomass [2-4].

The advantages envisaged for this type of technology are:

- simple design and proven technology,
- capability of processing almost untreated biomass with characteristic dimensions up to 50mm (larger particles may be processed at lower throughputs),
- fuel flexibility, i.e. capability of switching from one type of biomass to another during normal operation in a quite straightforward way.

From the perspective of energy use, the main disadvantage is the presence of tars in the gaseous products, which need to be abated to acceptable levels for the prime-movers considered: nevertheless, gas cleaning is a problem of all biomass thermochemical processes.

The development of pyrolyser and prime-mover integrated systems requires simulation tools for developing and testing suitable control strategies. Existing detailed models of particle pyrolytic decomposition, such as in [5], focus on capturing biomass particle behaviour and pyrolysis product distribution, rather than describing a particular pyrolysis process. Other models, such as [4], show the off-design behaviour of the system without describing the time-dependent characteristics.

This work aims to develop a transient model of the entire biomass rotary kiln pyrolyser process for control system analysis. The model was developed within the TRANSEO environment, which exploits the MATLAB-Simulink visual interface: since TRANSEO already has the capability of simulating microturbines and microturbine-based advanced cycles [6-8], the next step in this work is the transient study of the integrated system to gain information on the overall plant dynamics. Nevertheless, this paper is focused on the first part of this programme, which is the transient analysis of the pyrolyser itself.

THE TRANSEO TOOL

TRANSEO is an original tool for the transient and dynamic simulations of energy systems. The tool is specifically designed for managing microturbine-based cycles, but, in principle, any cycle layout and size could be modelled.

TRANSEO is based on the MATLAB-Simulink environment, but it merely exploits the visual interface and time machine, retaining the management of several fundamental calculations outside, in original dynamic-link libraries.

The focus of the analysis is on the transient behaviour of the system, which is mainly related to the mass and energy balances; momentum balance related effects, such as pressure-wave propagation, are normally neglected. Nevertheless, TRANSEO is already provided with dynamic models of a number of components (i.e.: pipe and ejector components), which can be employed for the full dynamic analysis of their behaviour. Unfortunately this approach is very time-consuming and it is seldom worth extending the full dynamic analysis to the whole cycle. Most cycles can be effectively simulated on a transient basis, which already provides sufficient accuracy, as demonstrated by the validation results.

Fig. (**1**) presents a conceptual sketch of TRANSEO's position within MATLAB-Simulink, together with its own objects. At the MATLAB level a complete set of thermo-physical functions was developed to equip the tool with the properties required by the component models. At the Simulink level, each component model, which is incorporated in the TPG (Thermochemical Power Group) library, interacts with the C MEX function to provide the necessary thermo-physical properties. All gases are considered to be semi-ideal: they are supposed to follow the ideal gas law and to have cp variable with temperature. Water/steam has a different treatment since its properties are calculated according to steam tables.

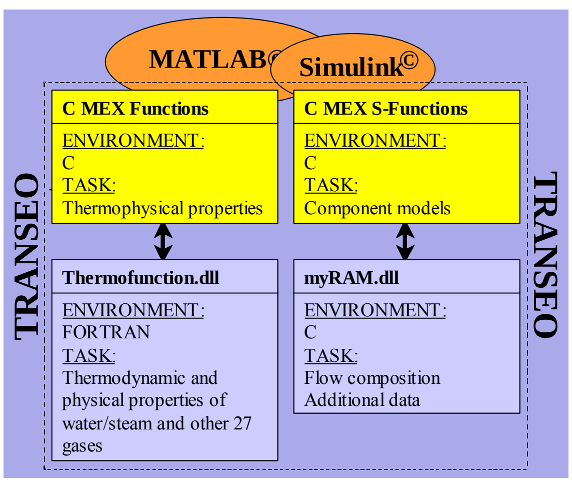

Fig. (1). Conceptual organisation of TRANSEO, and interaction with MATLAB-Simulink.

The TPG library is organised like any other Simulink library, and contains some sub-libraries (e.g.: component, control, interface, etc.) with complete sets of components. Each component is provided with more than one model, which can be flexibly chosen and changed by the user. The main models available are:

- on-design model (static response)
- off-design model (static response)
- lumped-volume model
- dynamic model

Depending on the component, single or multiple models are available. The main difference between lumped-volume and dynamic models lies in the different form of the momentum equation, either in the steady-state form (lumped-volume) or in the unsteady-state form (dynamic): both models, however, fully describe the thermal transient of the component. In the case of the rotary kiln pyrolyser described here, a transient lumped-volume model has been developed.

PYROLYSER FOR BIOMASS

In general terms biomass pyrolysis can be divided into three main categories, based on residence time in the reactor: carbonisation, slow pyrolysis and fast/flash pyrolysis. Each category provides different distribution products, which may be generally defined as fuel syngas, liquid tars, and solid char. Several technological options are available, and they may perform the pyrolysis at low, atmospheric or high total pressure: a comprehensive description may be found in [9].

The rotary-kiln pyrolyser studied in this work performs a "slow" atmospheric pyrolysis of biomass, as the residence time may vary from a few tens of minutes to one hour. A schematic picture is presented in Fig. (**2**).

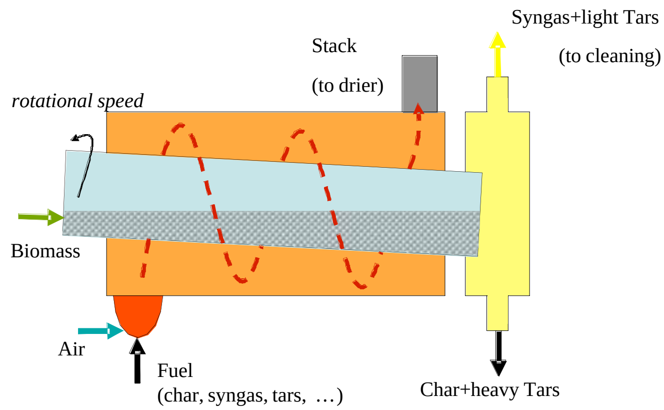

Fig. (2). Scheme of the rotary-kiln pyrolyser.

The biomass enters from one side of the rotating kiln, which leans a few degrees off the horizontal: this is necessary to allow the biomass to flow from the inlet to the outlet of the kiln. Usually inlet and outlet kiln diameter restrictions (not reported in the figure) allow a part of the biomass to remain permanently within the kiln, thus undergoing slow pyrolysis reactions. The kiln can be provided with internal fins which help to mix and rotate the biomass, thus ensuring its uniform state (temperature and chemical composition) in the radial direction, with the secondary effect of contributing to the transfer of heat from the hot wall to the biomass. From the outside, the kiln looks like a normal pipe without any fins, as they would be quickly damaged by the high external temperatures. The processed biomass exits at the opposite side of the kiln, where, due to gravity, char and heavy tars are separated from the syngas and light tars (which remain in a gaseous state). Char may be recycled to provide the necessary heat to process [10], while the syngas is sent to the cleaning section to reduce the dust and tar content to levels acceptable for the prime-mover (microturbine or internal combustion engine). Gas cleaning is a major world-wide area of research because of the problems associated with output-gas purity levels and associated costs. However, gas cleaning is outside the scope of this work: for the real applications under consideration wet scrubbing is the preferred technical solution.

Heat for the process is indirectly supplied by an external combustor: hot exhausts circle around the external wall of the kiln in a helicoidal manner to the stack exit. The overall hot exhaust heat exchange with the biomass can be either co-flow or counter-flow. The former ensures a larger thermal gradient at the biomass inlet, which reaches the reaction temperature (>350°C) more rapidly, but at the same time the overall heat exchange is less efficient and the exhausts exit the stack at a higher temperature. The situation is reversed in the second case, which provides a more efficient heat exchange between the hot exhausts and rotary kiln but takes more pipe length to bring the biomass to the reaction temperature. In this work the co-flow configuration was considered, as shown in Fig. (**2**).

A sealing must be placed between the rotating kiln and the exhaust chamber: in fact, this does not represent a particular technical challenge as the kiln rotates at slow speeds (order of magnitude of 10-100 rpm). The rotational speed and angle of inclination of the kiln must be adjusted according to the feeding biomass flow [3].

The main factor which limits the throughput of rotary kilns is the heat transfer from the hot external exhaust chamber to the internal biomass. In fact, at least three thermal resistances in series are present: convection/radiation between the hot exhausts and the outer kiln wall, conduction between the outer and inner walls, conduction/radiation between the inner wall and the biomass particles. The first and the last heat exchange mechanisms mostly limit the overall heat transfer to the reacting biomass, and they affect the overall dimensions required for the rotary kiln: in practice, the more effective the heat exchange, the smaller the surface required to perform the overall process. Another important parameter which affects the reactor throughput is the biomass inlet humidity: in the case of untreated biomass, it may exceed 50% of the overall input weight, hence requiring a large quantity of heat just to dry it. Therefore, it would be advantageous to pre-treat the biomass in an upstream drier that exploits the hot exhausts from the pyrolyser to bring the biomass to standard humidity conditions (e.g. 10% of the weight): this would allow better operation and constant throughput for the pyrolysing reactor.

Finally, although outside the scope of this work, it is worthwhile mentioning the performance achievable by an integrated pyrolyser energy system. The work presented in [11] shows that different levels of integration may lead to very different net performances in terms of electrical efficiency: the results are reported in Table **1**. The differences in electrical efficiency are, of course, counter-balanced by different capital costs (not reported), which may drive the final decision away from the best thermodynamic option. Nevertheless Table **1** shows that rotary-kiln pyrolysers have remarkable potential for energy applications, which justifies the interest in this type of technology.

In this work, char has been assumed to be recirculated to the external combustor, providing the heat for the rotary kiln.

Table 1. Electrical Efficiency for Rotary-Kiln Pyrolysis Gas Turbine Integrated Plants as Reported in [11] (Biomass Thermal Input = 1000 kg/h, LHV = 14600 kJ/kg)

External Fuel to Pyrolyser	Gas Turbine	Char Steam Boiler	HRSG	Electrical Efficiency
Char	X			8%
Char	X		X	12.50%
Gas	X	X	X	28%
Gas		X		15%

TRANSIENT MODEL

In this work a quasi-2D time-dependent model of the rotary-kiln biomass pyrolyser, including pyrolysis kinetics, has been developed and described. The computational mesh is presented in Fig. (**3**).

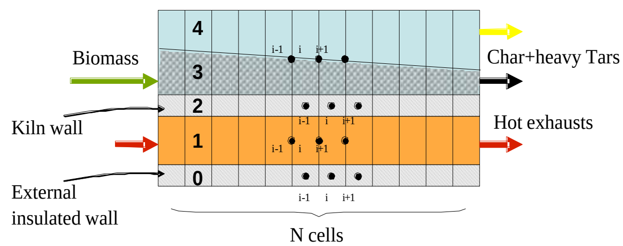

Fig. (3). Computational discretisation of the quasi 2-D rotary-kiln pyrolyser model.

The model may be divided into three main parts:

1. Geometrical parameters
2. Pyrolysis reactions
3. Energy balance

Geometrical Parameters

The first geometrical parameter is the available surfaces for heat exchange.

With reference to Fig. (**3**), hot exhausts and biomass are considered to pass through two concentrical cylinders, where the external section is occupied by the hot exhausts and the internal section by biomass and gas&tars. There are six main geometrical parameters that influence the reactor dimensions, from the model perspective: the inner diameters of the two cylinders (D_0, D_2), their thicknesses (s_0, s_2), their total length (L) and the filling factor of the inner cylinder section (FF): the last is defined as the fraction of D_2 occupied by the biomass (the rest is occupied by the gaseous phase). FF can be considered practically constant for the entire kiln length, due to the restrictions of the inlet and outlet diameters which keep an almost constant volume of biomass within the rotary kiln.

It should be noted that the calculation mesh divides the total length into N cells and N+1 sections (just for fluids), so the available heat transfer surface must refer to the single cell. Thus, the heat exchange surfaces in equations (1)-(6) can be obtained: S_0 is the outer surface of the external cylinder, S_1 is the inner surface of the external cylinder, S_2 is the outer surface of the internal cylinder (rotary kiln), S_3 is the inner surface of the internal cylinder in contact with the biomass, S_4 is the inner surface of the internal cylinder in contact with the gaseous phase, S_5 is the contact surface of the biomass and the gaseous phase.

$$S_{0,i} = \pi\left(D_0 + 2\cdot s_0\right)\cdot\left(\frac{L}{N}\right) \tag{1}$$

$$S_{1,i} = \pi\cdot D_0\cdot\left(\frac{L}{N}\right) \tag{2}$$

$$S_{2,i} = \pi\left(D_2 + 2\cdot s_2\right)\cdot\left(\frac{L}{N}\right) \tag{3}$$

$$S_{3,i} = \arctan\left[\frac{\sqrt{FF\cdot(1-FF)}}{0.5-FF}\right]D_2\cdot\left(\frac{L}{N}\right) \tag{4}$$

$$S_{4,i} = \pi\cdot D_2\cdot\left(\frac{L}{N}\right) - S_{3,i} \tag{5}$$

$$S_{5,i} = 2\cdot\sqrt{FF\cdot(1-FF)}\cdot D_2\cdot\left(\frac{L}{N}\right) \tag{6}$$

In (4) the denominator of the arctan object becomes negative when FF exceeds 0.5, which means that the solid biomass occupies more than half the section (more than half D_2). In fact, this is practically impossible, because for FF=0.5 would require the inlet and outlet diameters of the rotary kiln, usually smaller than the diameter in the "active" length L, to be equal to zero, which is clearly unfeasible. Since such a diameter would be non-zero, the biomass cannot surpass FF=0.5 at either the inlet or the outlet. So, such an angle will always be positive.

The rotary kiln has been assumed to be un-finned from the heat exchange point of view, which means neglecting the contribution of the inner fins to the internal heat exchange.

The second geometrical parameter is the sections for the exhaust, biomass and syngas flows. Equations (7)-(11) can be derived from simple geometrical considerations: A_0 is the section of the external cylinder (wall thickness), A_1 is the section available for the hot exhaust flows, A_2 is the section of the internal cylinder (wall thickness), A_3 is the section available for the biomass flow, A_4 is the section available for the syngas flow.

$$A_0 = \pi\left[\left(\frac{D_0}{2}+s_0\right)^2 - \left(\frac{D_0}{2}\right)^2\right] \tag{7}$$

$$A_1 = \pi\left[\left(\frac{D_0}{2}\right)^2 - \left(\frac{D_2}{2}+s_2\right)^2\right] \tag{8}$$

$$A_2 = \pi\left[\left(\frac{D_2}{2}+s_2\right)^2 - \left(\frac{D_2}{2}\right)^2\right] \tag{9}$$

$$A_3 = \arctan\left[\frac{\sqrt{FF\cdot(1-FF)}}{0.5-FF}\right]\cdot\left(\frac{D_2}{2}\right)^2 \tag{10}$$

$$A_4 = \pi\cdot\left(\frac{D_2}{2}\right)^2 - A_3 \tag{11}$$

Mass Flows and Source Terms

Mass balances are performed for each calculation cell, so it is sufficient to describe the mass balance for just one cell as it is repeated N-times for the kiln length.

It should be noted that while the model aims to fully represent the transient thermal behaviour of the pyrolyser, the hot-exhaust and pyrolysis vapour (gas&tar) mass flow rates are calculated at the steady state because of their negligible time to regime compared to the overall transient system behaviour: this is in accordance with the previously outlined lumped-volume approach of TRANSEO.

Hot exhausts clearly do not change composition or mass flow rate in the reactor, unless there are undesired leakages through the rotary kiln sealing.

The total biomass mass flow rate is reduced by the drying process in the initial part of the kiln, and the pyrolysis reactions, which convert virgin biomass into char, tar and gas, in the last part of the kiln. Such changes in the mass flow cause the absorption or release of energy, which must be taken into account in the energy source terms.

The first phenomenon that changes the total biomass mass flow is the drying process. It is assumed that the biomass reaches the saturation temperature of water at the process pressure (i.e.: Tsat=100°C at 1.013·105 Pa), and it stays approximately at such a temperature until all the water evaporates. Therefore, the energy source terms can be calculated as reported in (12). So q_{eva} corresponds to the heat available at the i-th cell, which is absorbed by the biomass for evaporating humidity: the amount of evaporated water can be calculated by dividing q_{eva} by the latent heat of vaporisation. In the cell where humidity reaches zero, q_{eva}=0 and the temperature of the biomass starts to increase again.

$$q_{eva,i} = -\frac{\lambda_{bio}\cdot S_{3,i}}{d_{eff}}\left(T_{2,i}-T_{sat}\right) - h_4 S_{5,i}\left(\frac{T_{4,i}+T_{4,i+1}}{2}-T_{sat}\right) \tag{12}$$

The second phenomenon that changes the total biomass mass flow is the pyrolysis decomposition. The pyrolysis reactions have been modelled with the kinetic correlations reported in [12], and presented in Table **2**: such data were used for the present pyrolyser model because, as stated in [12], particle size (in the 75-425μm range) and the heating rate (in the 10-100°C/min range) had only a limited influence on the kinetic parameters. In fact, the heating rate is the operating condition which mostly influences the process yields: therefore, considering the type of technology modelled in this work, 10°C/min can be a good approximation of the real heating rate of the biomass (slow pyrolysis). Therefore, such kinetic laws are assumed to be suitable for our application.

The biomass was assumed to be composed of three main constituents, hemicellulose (actually subdivided into two types: hemicellulose 1 and 2), cellulose and lignin: each of these thermally decomposes independently of the others, following first order kinetic mechanisms. No information was provided on the gas and tar produced, thus the model prediction only referred to the weight loss of the virgin bio-mass: the solid mass flow at the kiln exit was considered to be char, while the gaseous phase included both syngas and tars.

Table 2. Kinetic Parameters for the Slow Pyrolysis (10K/Min) of Forest Residues of 425µm Size [12]

	AA (1/Min)	E (kJ/Mol)	C (%)
hemicellulose 1	$4.6*10^{10}$	112.2	5.2
hemicellulose 2	$3.7*10^{10}$	124.8	23.9
cellulose	$1.1*10^{19}$	235.9	35.9
lignin	$4.9*10^{1}$	34.5	19.7

The rate of conversion for the n-th constituent can be expressed as in (13), where k represents the reaction rate, expressed, as usual, by the first order Arrenius formulation (14). $m_{n\infty}$ is the mass (or mass flow) obtainable after infinite residence time, and it is expressed by (15) where the new parameter C must be determined from experiments, as along with AA and E.

$$-\frac{dm_n}{dt} = k_n\left(m_n - m_{n\infty}\right) = k_n \cdot m\left(\tilde{x}_n - \tilde{x}_{n\infty}\right) \tag{13}$$

$$k_n = AA_n e^{-\left(\frac{E_n}{RT}\right)} \tag{14}$$

$$m_{n\infty} = m_{biodry_{in}}\left(\tilde{x}_n - C_n\right) \tag{15}$$

$$\dot{m}_{pyro,i} = \sum_n -\frac{dm_{n,i}}{dt} = \sum_n k_n \cdot m\left(\tilde{x}_{n,i-1} - \tilde{x}_{n\infty}\right) \tag{16}$$

Equation (13) provides the mass flow which decomposes in each cell of mass “m”, which is simply a function of the filling factor. Such a mass flow loss is equal to the gaseous phase produced (syngas+tar).

The properties of the biomass (water, cellulose, hemicellulose, lignin) are continuously transported through the kiln using a standard transport approach based on the residence time of the biomass in each cell.

Open literature offers a wide range of values for the reaction energy associated with biomass decomposition, mainly due to the uncertainties associated with the measurement of a small quantity of energy compared to the heat required for heating the biomass up to pyrolysis temperatures. In this work, the value of θ_{pyro}=-255 kJ/kg (endothermic reaction) was assumed from [5]. Thus, for every cell, the endothermic heat flux required can be calculated as reported in (17).

$$q_{pyro,i} = \dot{m}_{pyro,i}\theta \tag{17}$$

No secondary reactions were considered in the gaseous phase.

Energy Balance

Once the mass flows in each cell are known, as well as the source terms to be applied in the energy equation, the overall system energy balance can be solved. Such an energy balance is written according to the mesh in Fig. (**3**). General energy balances, which distinguish between “fluid” and “still” fields, are reported in (18) and (19).

$$\frac{\partial\left(\rho c_v TA\right)}{\partial t} = -\frac{\partial\left(\dot{m} c_p T\right)}{\partial x} + \bar{q} \quad j=1,3,4,5 \tag{18}$$

$$\frac{\partial\left(m c_v T\right)}{\partial t} = q \quad j=0,2 \tag{19}$$

Every field, identified by the “j” subscript, is discretised in N cells where the properties are considered uniform. The “fluid” fields are characterised by N+1 temperatures and the “solid” fields by N temperatures. Overall, the discretisation results in a quasi-2D description of the thermal behaviour of the rotary-kiln pyrolyser.

- j=0

$$\begin{aligned} &\frac{m_{0,i} c_{v_0}\left(T_{0,i}^{n+1} - T_{0,i}^{n}\right)}{\Delta t} = \\ &h_0 S_{1,i}\left(\frac{T_{1,i}^{n+1} + T_{1,i+1}^{n+1}}{2} - T_{0,i}^{n+1}\right) - h_{amb} S_{0,i}\left(T_{0,i}^{n+1} - T_{amb}\right) + \\ &\frac{\lambda_0 A_0\left(T_{0,i-1}^{n+1} - 2T_{0,i}^{n+1} + T_{0,i+1}^{n+1}\right)}{\Delta x} \end{aligned} \tag{20}$$

- j=1

$$\begin{aligned} &\frac{\rho_{1,i} c_{v_1} A_1}{\Delta t}\left(T_{1,i}^{n+1} - T_{1,i}^{n}\right) = \\ &-\frac{h_0 S_{1,i}}{\Delta x}\left(\frac{T_{1,i+1}^{n+1} + T_{1,i}^{n+1}}{2} - T_{0,i}^{n+1}\right) - \frac{h_1 S_{2,i}}{\Delta x}\left(\frac{T_{1,i+1}^{n+1} + T_{1,i}^{n+1}}{2} - T_{2,i}^{n+1}\right) - \\ &\frac{\dot{m}_1 c_{p_1}}{\Delta x}\left(T_{1,i}^{n+1} - T_{1,i-1}^{n+1}\right) \end{aligned} \tag{21}$$

- j=2

$$\begin{aligned} &\frac{m_{2,i} c_{v_2}\left(T_{2,i}^{n+1} - T_{2,i}^{n}\right)}{\Delta t} = h_1 S_{2,i}\left(\frac{T_{1,i} + T_{1,i+1}}{2} - T_{2,i}\right) + \\ &\frac{\lambda_2 A_2\left(T_{2,i-1} - 2T_{2,i} + T_{2,i+1}\right)}{\Delta x} + \\ &+\frac{\lambda_{bio} S_{3,i}}{d_{eff}}\left(T_{2,i} - \frac{T_{3,i} + T_{3,i+1}}{2}\right) - \\ &h_2 S_{4,i}\left(T_{2,i} - \frac{T_{4,i} + T_{4,i+1}}{2}\right) \end{aligned} \tag{22}$$

- j=3

$$\begin{aligned} &\frac{\rho_{3,i} c_{v_3} A_3}{\Delta t}\left(T_{3,i}^{n+1} - T_{3,i}^{n}\right) = \\ &-\frac{h_4 S_{5,i}}{\Delta x}\left(\frac{T_{3,i-1}^{n+1} + T_{3,i}^{n+1}}{2} - \frac{T_{4,i-1}^{n+1} + T_{4,i}^{n+1}}{2}\right) + \\ &+\frac{\lambda_{bio} S_{3,i}}{d_{eff}\Delta x}\left(T_{2,i-1}^{n+1} - \frac{T_{3,i-1}^{n+1} + T_{3,i}^{n+1}}{2}\right) - \\ &\frac{\dot{m}_{3,i} c_{p_3}}{\Delta x}\left(T_{3,i}^{n+1} - T_{3,i-1}^{n+1}\right) + \frac{q_{eva,i}}{\Delta x} + \frac{q_{piro,i}}{\Delta x} \end{aligned} \tag{23}$$

- j=4

$$\frac{\rho_{4,i} c_{v_4} A_4}{\Delta t}\left(T_{4,i}^{n+1} - T_{4,i}^{n}\right) = \frac{h_4 S_{5,i}}{\Delta x}\left(\frac{T_{3,i-1}^{n+1} + T_{3,i}^{n+1}}{2} - \frac{T_{4,i-1}^{n+1} + T_{4,i}^{n+1}}{2}\right) + \frac{h_2 S_{4,i}}{\Delta x}\left(T_{2,i-1}^{n+1} - \frac{T_{4,i-1}^{n+1} + T_{4,i}^{n+1}}{2}\right) - \frac{\dot{m}_{4,i} c_{p_4}}{\Delta x}\left(T_{4,i}^{n+1} - T_{4,i-1}^{n+1}\right) \tag{24}$$

They are specified in the equations (20-24), which report, for each domain field, the discretised general forms of the aforementioned energy balances.

Equations (20)-(24) can be reduced to a linear system with unknown temperatures, which can be solved straight-away, obtaining the temperatures of the entire domain in the next time step.

Equations (20)-(24) contain several assumed constant parameters, presented in Table **3**. The parameters related to the exhausts were calculated using their composition and assuming semi-ideal behaviour.

The convective heat exchange parameters need to be estimated and vary according to the operating conditions. All equivalent convective coefficients (h_0, h_1, h_2, h_4) included both parallel convective and radiative heat transfers (the equivalent convective coefficient is the sum of the two). With regard to h_{amb}, an average value representative of a well insulated furnace was been assumed.

Table 3. Constant Parameters of Energy Balance and Heat Transfer

c_{v0}	753 [J/kgK]	λ_0	19 [W/mK]
c_{v2}	753 [J/kgK]	λ_2	19 [W/mK]
$c_{v3}= c_{p3}$	2.0 [J/kgK]	λ_{bio}	0.13 [W/mK]
c_{v4}	1100 [J/kgK]	ε of walls	0.9
c_{p4}	1300 [J/kgK]	ε of biomass	0.75
h_{amb}	1 [W/m^{2}K]	ε of exhausts (with particles)	0.2

The linearised form of the equivalent convective heat transfer coefficient in (25) was used for the radiation. The F factor was always approximated with one: this is acceptable for both the heat exchanges between the hot exhausts and the rotating pipe, considering the distribution of the exhausts around the rotating pipe to be uniform, and the heat exchanges between the rotating pipe and biomass, which actually have F=1 at the contact surface S3. The emissivities are reported in Table **3**. Radiation was neglected for the heat exchanges with the inner gaseous phase (j=4).

$$h_{rad} = \left(\frac{1}{\varepsilon_1} + \frac{1}{\varepsilon_2} - 1\right)^{-1} F_{1\to 2}\sigma\left(T_1 + T_2\right)\left(T_1^2 + T_2^2\right) \tag{25}$$

The convection heat regime varied: the hot exhausts exchanged heat with the walls in a turbulent regime, while the inner pyrolysis gases were considered to be in laminar motion. This was due to the considerable difference in their mass flows (about 10 to 1). The correlations (26) and (27) were taken from [13] and used for the hot exhausts (flow over immersed body) and the inner gaseous phase (circular horizontal tubes with constant wall temperature and laminar flow), respectively.

The heat exchange between the biomass and rotating pipe was considered to occur at the contact surface S_3, where it was composed of radiation and contact conductance, and between S_4 and S_5, where it only consisted of radiation. The pyrolysis vapours were considered transparent to radiation.

The equivalent convective coefficient for the contact conductance and the effective biomass particle diameter are defined in (28).

$$h = 0.0266 * \left(\frac{\lambda}{D_{eq}}\right) * Re^{0.8} * Pr^{0.33} \tag{26}$$

$$h = 3.66 + \left(\frac{0.19Gz^{0.8}}{1 + 0.117Gz^{0.467}}\right) \text{ with } Gz = Re\,Pr\left(\frac{D_{eq}}{L}\right) \tag{27}$$

$$\frac{\lambda_{bio}}{d_{eff}} = h_{bio} = \frac{\lambda_{bio}}{d}\cdot(1-\nu) + h_{rad}\cdot\nu \tag{28}$$

Fig. (**4**) illustrates the final appearance of the pyrolyser model: thanks to the Simulink visual interface, its integration with energy generation modules will be straightforward at the simulation level.

The results were obtained with 20 longitudinal cells and 0.1s time step. Mesh does not affect the results down to 6-8 nodes. Time independence was checked.

STEADY-STATE ANALYSIS

The geometry of the rotary-kiln pyrolyser and its nominal operating conditions were fixed according to Table **4**. The data were similar to those of a rotary-kiln which is currently under construction at a biomass residue collection site.

Under such operating conditions, as shown in Fig. (**5**), the biomass exits the kiln in the form of char at about 470°C, with a total mass loss of about 62% with respect to the inlet. Since 20% of the mass flow of gaseous products consisted of original biomass humidity, the dry inlet biomass was converted to syngas and tars with a (0.62-0.2)/0.8 = 0.52 conversion factor.

Fig. (**5**) shows the behaviour of the main properties along the length of the rotary-kiln. It was interesting to observe a relatively small temperature floor during the drying process that shifted forward the following increase in the biomass temperature: after drying, the biomass temperature curve shows a decreasing slope, which is due to the co-current heat exchange configuration, as the difference in temperature between the biomass and hot exhausts is reduced between the kiln entry and exit. The biomass mass flow initially decreased because of the drying process, and then, after achieving temperatures of the order of 350-400°C, rapidly decreased while being transformed into char: the high negative slope at the end of the pyrolyser suggests that additional length may help to increase the overall conversion of solid biomass. Of course, the increase in length cannot be massive,

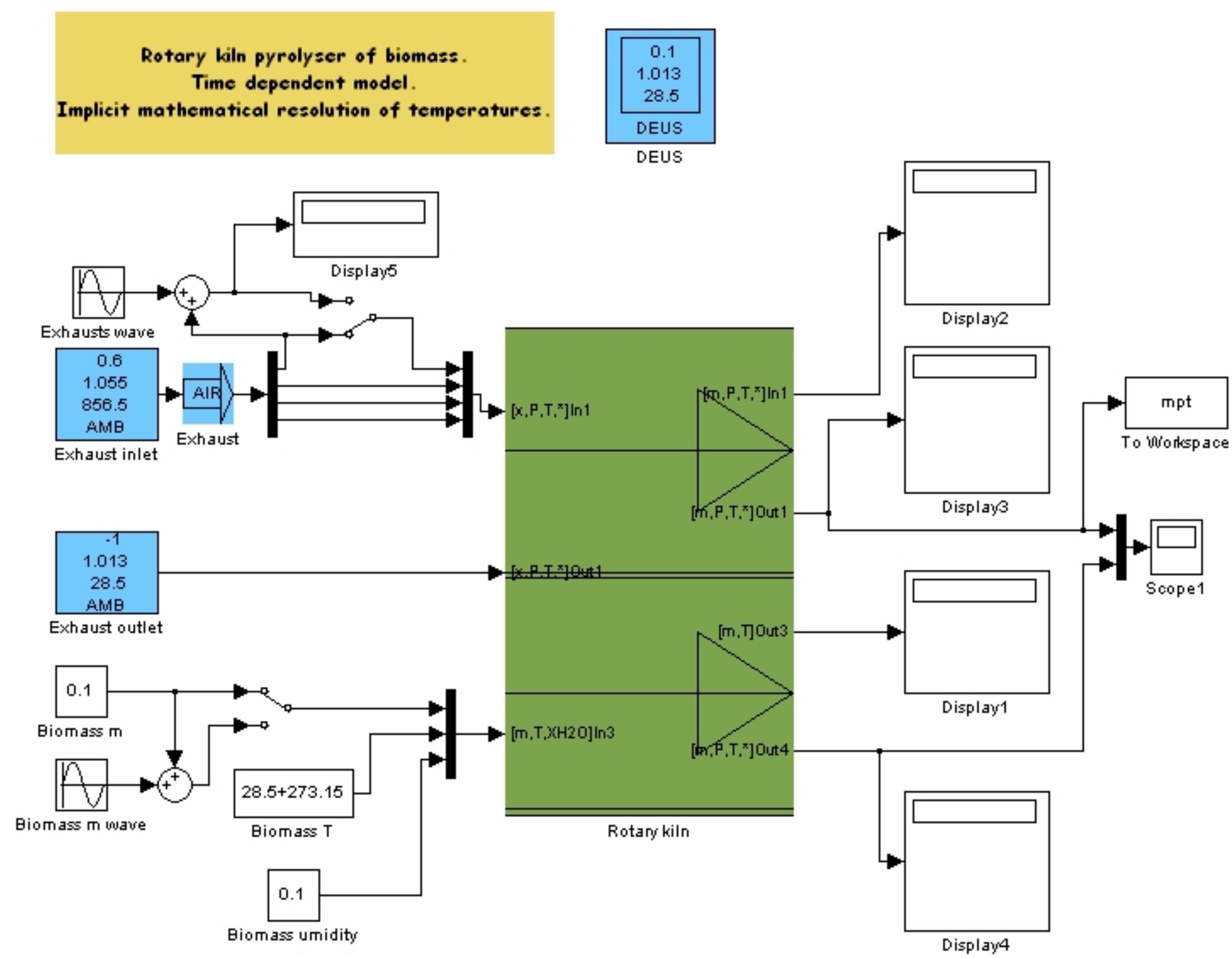

Fig. (4). Graphical interface of rotary-kiln pyrolyser model.

as the rotary kiln wall temperature could rise, reducing the mechanical resistance of its walls. An upper threshold of 650°C was assumed for the rotary-kiln wall temperature: therefore, the assumed geometry might represent a good compromise between design, economic feasibility and biomass conversion. The decrease in the biomass mass flow was clearly counter-balanced by an increase in the syngas mass flow.

Finally, it was demonstrated that the nominal operating condition was thermally self-sustaining, i.e. the output char was slightly in excess of the quantity necessary to provide the temperature and the flow of hot inlet exhausts.

The off-design analysis, which was performed at the steady-state by varying the biomass input operating conditions, was useful for characterising the behaviour of the system as well as obtaining information for adapting the design to different feedstock.

This analysis was concerned with the assessment of the impact of biomass feedstock on pyrolyser performance, i.e. the representative diameter of the biomass particles (d) and the biomass humidity. The hot-gas inlet temperature (i.e. the

Table 4. Geometry of Rotary-Kiln Pyrolyser, Nominal Operating Conditions and Yields

Total humid biomass flow rate	0.1 [kg/s]
Representative diameter of biomass particles	10 [mm]
Biomass humidity (water weight over total weight)	20%
Biomass density	600 kg/m^3
Biomass void fraction	0.3
Filling Factor FF	0.5
Dry biomass composition [% of hemicellulose 1, hemicellulose 2, cellulose, lignin]	[7%, 28%, 42%, 23%]
Rotary kiln length	3 [m]
Inner diameter of rotary kiln, wall thickness, outer diameter of combustion chamber	0.7, 0.03, 1.2 [m]
Inclination of kiln with respect to horizon	5°
Rotary kiln wall mass, insulation mass	1600.0, 1000.0 [kg]
Mass flow of hot exhausts	0.625 kg/s
Temperature of hot exhaust inlet	900°C

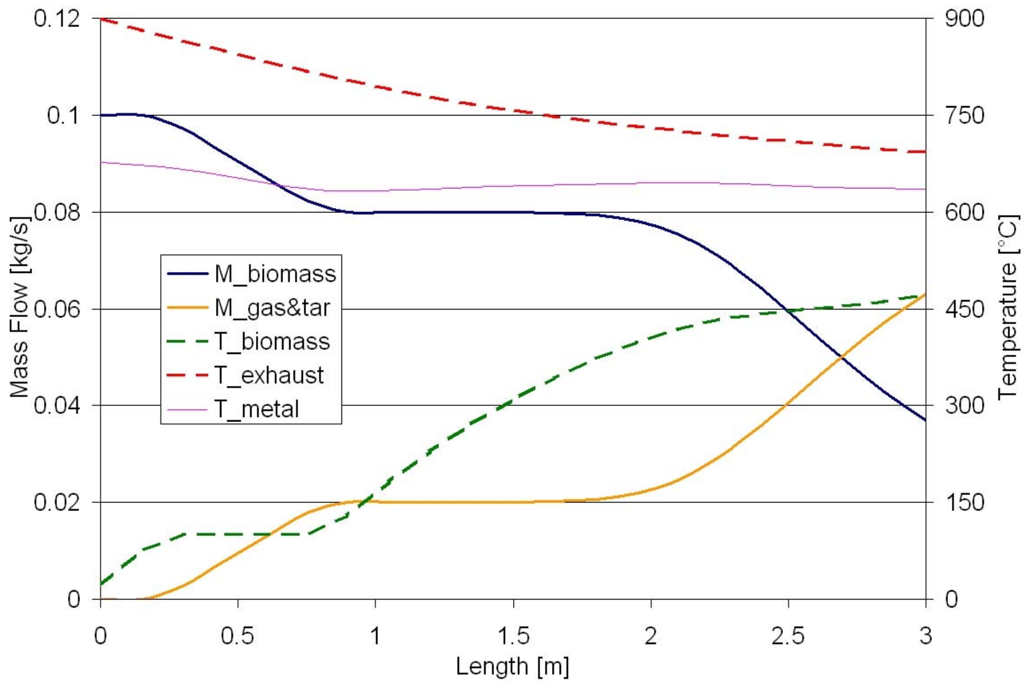

Fig. (5). Biomass temperature and mass flow profiles within the rotary kiln at the design point.

adiabatic flame temperature) and mass flow were always kept constant at the maximum nominal level, as the objective was to maximise the reactor throughput.

The representative biomass diameter affected the heat exchange with the rotating wall, because it increased the overall resistance, as shown in (28). Nevertheless, this effect might be partially counterbalanced by an increase in the void fraction (not considered here), which increased the radiation contribution.

Fig. (**6**) shows the impact of the biomass diameter on the char temperature. This result clearly shows a reduction in biomass size is beneficial to its conversion in this type of pyrolyser, unless a higher unconverted char output yield is acceptable, offering lower conversion into gaseous products. The biomass diameter is clearly an important design parameter because an increase in biomass size leads to an increase in rotary-kiln length, assuming that the desired conversion factor is constant.

Humidity is one of the major variables in the case of untreated biomass, which strongly influences the pyrolyser throughput because of the different heat requirements for drying the biomass. The humidity was varied in the 15-25% range, which is representative of biomass pre-treated in an external dryer: higher inlet humidity was not considered for the pyrolyser geometry under study because it would bring the conversion of biomass to gaseous products to less than 40% mass on a dry basis, which is not considered attractive for this application: in such a case, either reduced throughput or increased length would be necessary. It is important to outline that in this humidity analysis the total inlet biomass mass flow rate was kept constant, so that different humidities mean different dry biomass inlet flow rates (the sum of the inlet biomass water and inlet dry biomass is constant).

Fig. (**7**) shows that the inlet humidity significantly decreased the final char temperature and thus the conversion of biomass into gaseous products. This is explained by the

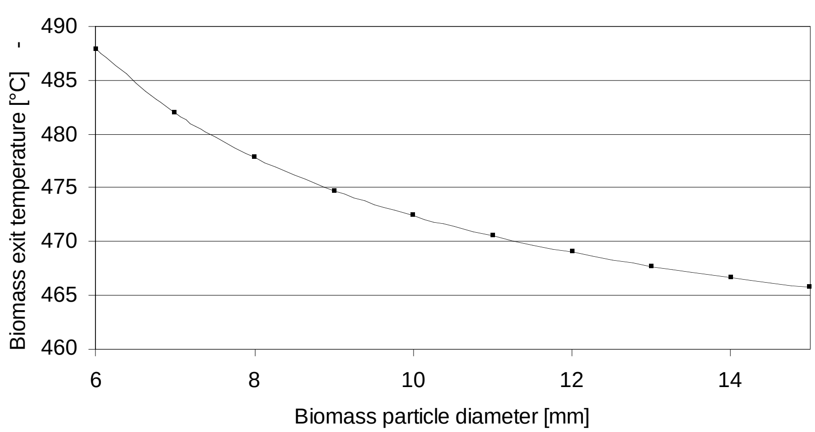

Fig. (6). Biomass exit temperature *vs* representative biomass diameter.

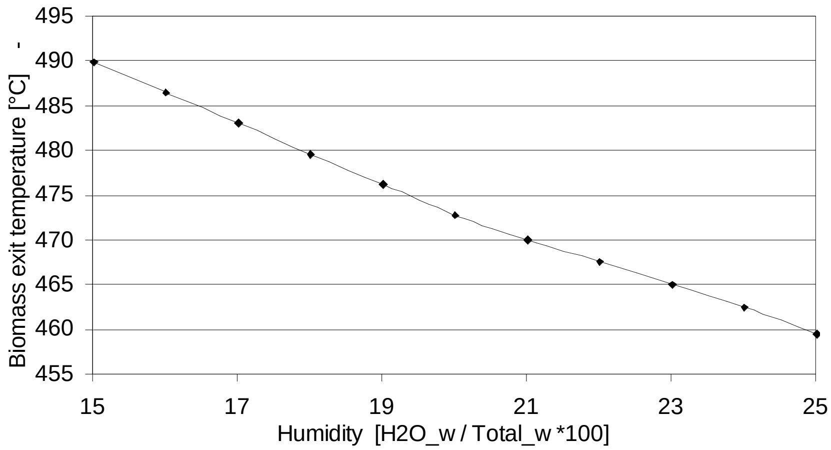

Fig. (7). Biomass exit temperature *vs* biomass humidity.

higher heat absorbed during the internal drying process, which occupied an increasing portion of the kiln length.

TRANSIENT ANALYSIS

The model was tested to assess the behaviour of the rotary-kiln pyrolyser during transient operating conditions, an essential step for developing suitable control strategies. This study is expected to be reviewed as soon as field data measurements are available, but it will be used in the design phase of the control system. Three type of transients were studied: the system start-up, the step change in the inlet biomass humidity, the step change in the biomass mass flow.

System Start-Up

The start-up of high-temperature chemical reactors is usually a very delicate procedure because thermal time-gradients must be controlled to avoid damage to refractory or moving parts, and because external energy resources may be required for non-negligible periods of time: the latter is one of the reasons why the start-up time should usually be minimised. Therefore, instead of focusing on the limitations and constraints which might push system operators to opt for small temperature ramps (i.e.: extended start-up time), the aim of this work was the simulation of the fastest possible start-up: this was done by feeding the pyrolyser, starting at ambient conditions, with nominal hot exhaust flows and a nominal biomass flow. The pyrolyser was initially considered to be filled with biomass at the nominal filling factor FF. The results obtained gave the time threshold below which it would be impossible to start up the system because of its thermal capacitances.

Fig. (**8**) shows the pyrolyser yields during the start-up. Apart from the steam of the drying process, pyrolysis decomposition substances were produced after about 1800s, when the final section reached about 300°C. From then on there was a rapid increase in the gaseous products due to an increase in the temperature in all the previous sections. The positive slope started to decrease significantly after about 1400s, when the final section passed 450°C, causing the almost total pyrolysis of the biomass. In this respect, the time to regime of the pyrolysis was a bit lower than the time to regime of the heating process.

Fig. (**9**) shows that the biomass thermal capacitance had a strong influence on the time to regime of the reactor: in fact,

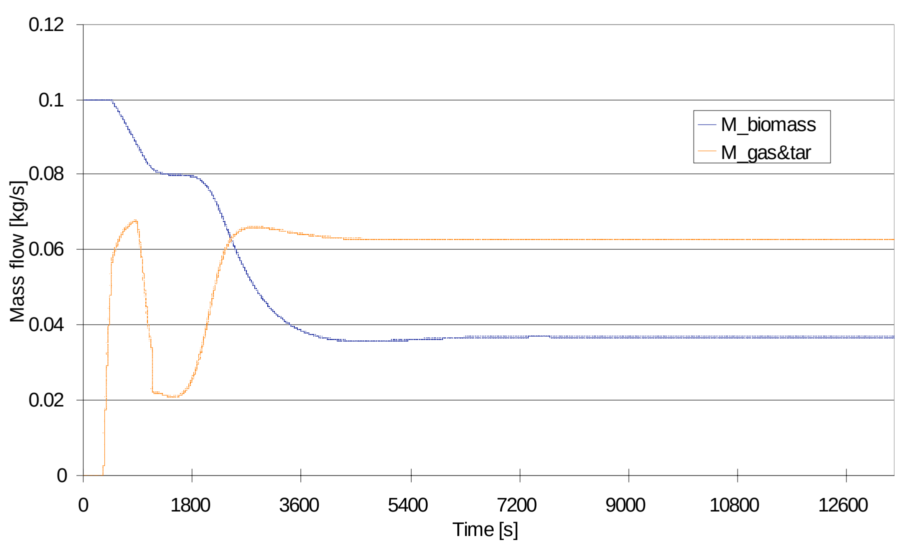

Fig. (8). Pyrolyser biomass (char) and vapour (gas&tar) yields during the start-up.

the last section reached the steady-state only after about 3600s, which was of the same order of magnitude as the estimated residence time of about 3000s. Actually, earlier sections reached the steady-state before the latter sections, which is a direct consequence of the biomass flow direction. It is interesting to observe that the temperature curve for each section presented a horizontal phase during the first 500-700s. When the temperature reached about 100°C it stayed constant for some time, waiting for the full vaporisation of the biomass humidity.

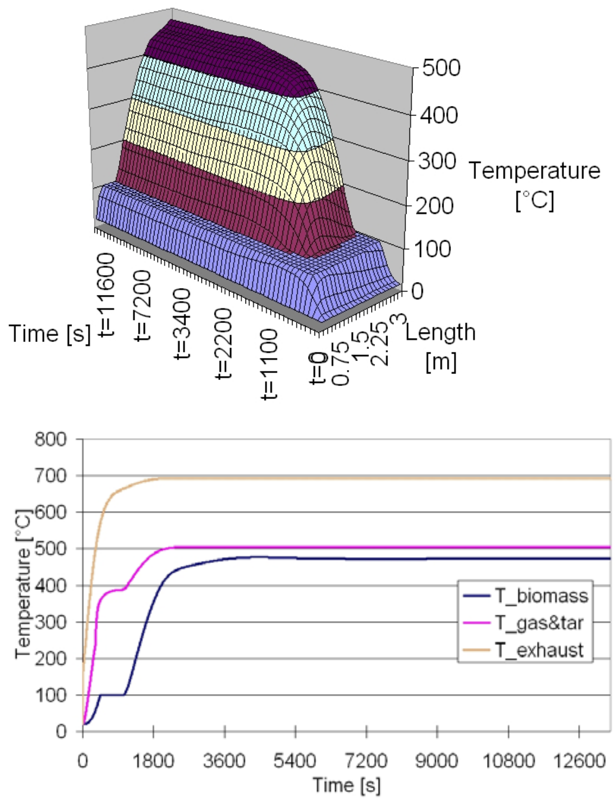

Fig. (9). Top: evolution of the biomass temperature in the kiln during the start-up. Bottom: biomass, gas&tar and exhaust exit temperatures during the start-up.

This was why the gas mass flow peaked about 800s after the start-up. The drying of the biomass started at the pyrolyser inlet and then propagated to the latter sections until they also reached the steady-state conditions.

Step Change in the Inlet Biomass Humidity

Changes may be expected in the inlet biomass humidity during normal operation because of the variability of feedstock. So, the analysis of this transient behaviour was particularly interesting for understanding the capability of this type of technology to handle a rapidly varying inlet biomass.

Initially, the pyrolyser was at steady-state conditions. Then a step was applied to the inlet biomass humidity: in the first case, the inlet humidity was changed from 10% to 20% (+10% step), in the second case the inlet humidity was changed from 20% to 10% (-10% step).

Fig. (**10**) shows the process yields during the entire transient. Firstly, an overall time to regime of about 2500s was observed, which means that the system is characterised by significant thermal capacitance that limited its fast response capability to new operating conditions: at the same time, this feature should help to smooth out rapid oscillations in the biomass humidity at the inlet, which should not affect the overall behaviour of the reactor output. In both cases, it is interesting to observe a fast decrease or increase in the gas output, followed by an opposite trend with over-elongation beyond the new regime. This can be explained by the system's thermal capacitance, which initially evaporated a part of the water in the biomass, releasing or absorbing heat, and then needed to counterbalance such a heat exchange before reaching the regime.

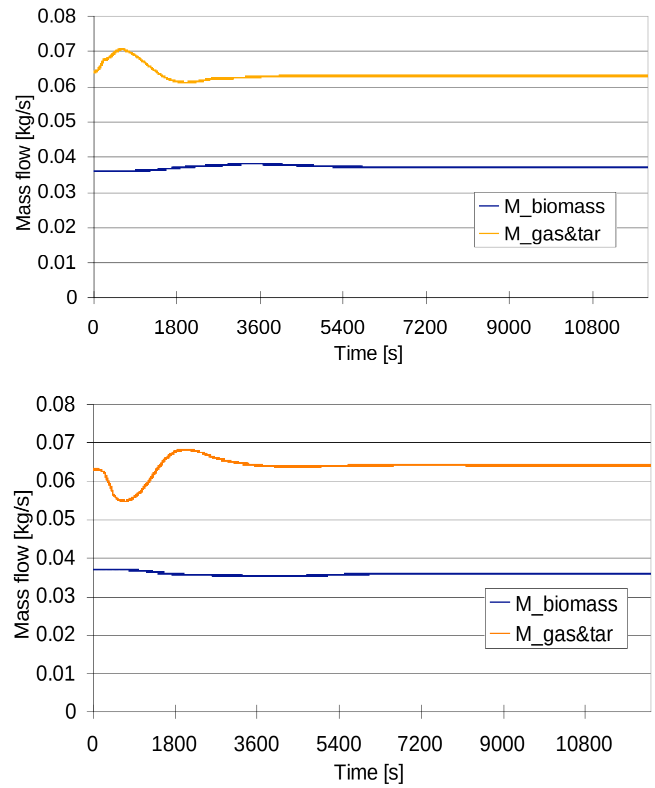

Fig. (10). Pyrolyser biomass (char) and vapour (gas&tar) yields after the humidity step change (Top: + 10%; Bottom: -10%).

The sudden increase or decrease in the inlet humidity reduced or increased the mass flow of dry biomass (the inlet total mass flow was constant), which changed the outlet char flow rate only after a period approximately equal to the residence time: this happened with almost unchanged temperature profiles. The output temperature curves in Fig. (**11**) show that they move much slower than the gaseous output did, mainly following the behaviour of the char yield. This was expected, but it represents a detrimental feature for the controllability of this system, which mainly exploits the gaseous output as a useful product for power generation.

Step Change in the Biomass Mass Flow

Changes in the biomass inlet mass flow could be necessitated by a scarcity of feedstock or a reduced production requirement. Thus, it is interesting to characterise the response of the pyrolyser to this type of disturbance.

Initially, the pyrolyser was at steady-state conditions. Then a step was applied to the inlet biomass flow rate: in the first case, the mass flow was changed from 80% to 100% of the nominal flow rate (+20% step), in the second case the mass flow was changed from 100% to 80% (-20%step).

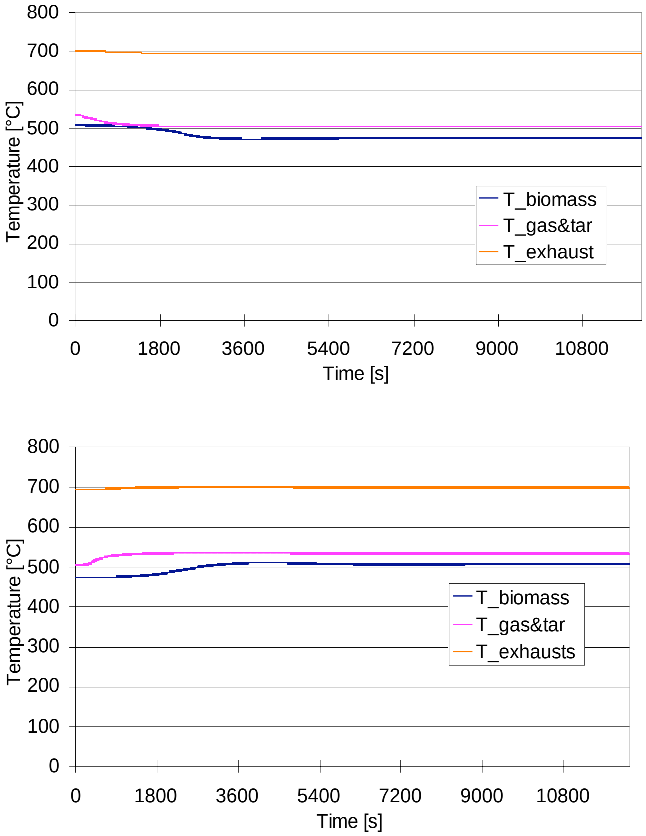

Fig. (11). Biomass, gas&tar and exhaust exit temperatures after the humidity step change (Top: + 10%; Bottom: -10%).

Fig. (**12**) shows the outlet mass flow behaviour during the transient, while Fig. (**13**) reports the corresponding exit temperatures. It showed a quicker response than the gaseous phase, which was mainly due to the change in the biomass humidity evaporation rates. In terms of its impact on the char mass flow rate, the inlet biomass flow rate step became apparent at the kiln exit only after more than 3000s had elapsed, which was the approximate residence time of the biomass. Thus, the char mass flow behaved as a lag-dominated parameter, while the gaseous mass flow had a more disturbed behaviour. In fact, the char behaviour can be well understood by monitoring the char exit temperature, while gaseous yields may show variations which can hardly be correlated with the input disturbances (when they are not known).

CONCLUSIONS

A quasi 2-D time-dependent model of a rotary-kiln biomass pyrolyser showing first-order low pyrolysis biomass kinetics from literature. The model was developed for providing necessary information on the transient response of the system and incorporate with other source of energy devices.

A steady-state shows that, the performance of the pyrolyser shows great effect and it shows great time saving unit.

was strongly affected by such inlet biomass conditions as diameter and humidity.

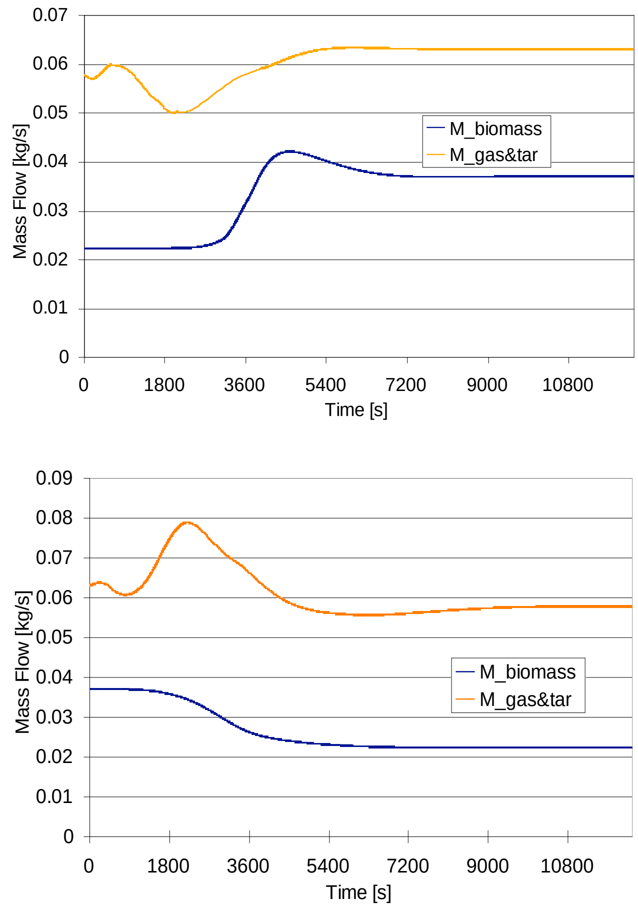

Fig. (12). Pyrolyser biomass (char) and vapour (gas&tar) yields after the inlet biomass mass flow rate change (Top: + 20%; Bottom: -20%).

Transient analyses were demonstrated for three operating cases: the start-up, variation of step in the entry biomass midity and the step variation in the inlet of biomass mass flow rate. The higher possible starts without affecting constraints on the temperature ramp was modeled to assess the lower threshold for bringing the pyrolyser to normal conditions : a lower time to regime of about 3600s was analysed. . In the form of the humidity change, the pyrolyser needs about 2500s to reach the new regime, with characterstic sovra-elongation behavior in the gaseous yield, which may form control issues. The step changes analyses of the biomass flow rate confirmed the affinity between the exit char temperature and the char yield, while the gaseous flow rate may be change significantly quicker with oscillation : for this purpose the control of such yields may different in actual applications.

Above all , it was found that the rotary-kiln biomass pyrolyser is a relatively not faster response system which is actually driven by its vast thermal capacitance. Output gaseous yields may be subject to rapid changes in response to inlet variation in the biomass humidity and flow. Moreover, these can be regulated by the accurate management of the biomass feedstock: such a duty is expected to facilitate integration with a prime-mover, because it would dismiss the variation trends in the yield that were found in the case-studies taken in this work.

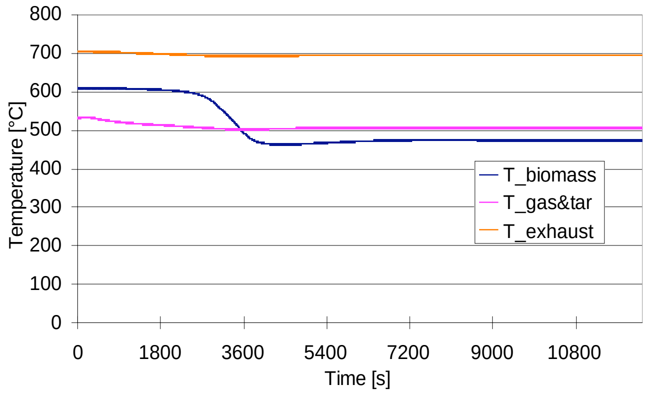

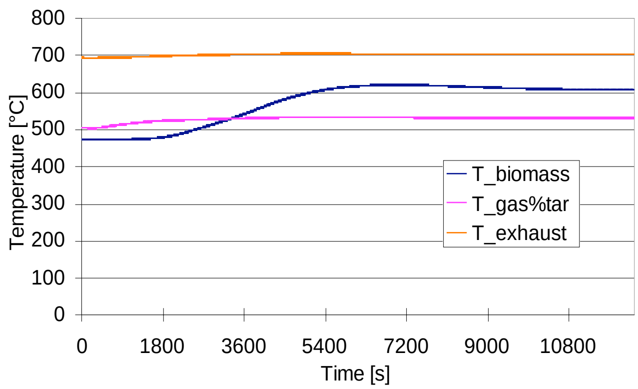

Fig. (13). Biomass, gas&tar and exhaust exit temperatures after the inlet biomass mass flow rate change (Top: + 20%; Bottom: -20%).

ACKNOWLEDGEMENTS

This research was partially supported by the European Commission (project Dev-BIOSOFC, FP6-042436, MTKD-CT-2006-042436).

NOMENCLATURE

A = Section [m^2]

AA = Frequency factor [s^{-1}]

c_p = Constant pressure specific heat [J/kg K]

c_v = Constant volume specific heat [J/kg K]

C = Fractional contribution to overall mass loss

CHP = Combined Heat and Power

d = Representative diameter of biomass particles [m]

D = Diameter [m]. Equivalent diameter of a section A is (4A/perimeter)

E = Activation energy [kJ/mol]

F = View factor for radiation [kJ/mol]

FF = Filling factor

Gz = Graetz number (defined in eq.27)

h = Convective coefficient [W/m^2K]

HRSG = Heat Recovery Steam Generator

L = Active length of rotary kiln [m]

LHV = Low Heating Value [J/kg]

k = Reaction rate [s^{-1}]

N = Number of horizontal cells

m = Mass [kg]

$\dot{m}$ = Mass flow rate [kg/s]

n = n-th Type of biomass constituent (hemicellulose, cellulose, lignin)

Pr = Prandtl number ($= c_p\mu/\lambda$)

q = Heat flux [W]

$\bar{q}$ = Heat flux per unit length [W/m]

R = Gas constant [kJ/mol·K]

Re = Reynolds number ($= \rho v D/\mu$)

s = Thickness [m]

S = Surface [m^2]

t = Time [s]

T = Temperature [K]

$\tilde{x}$ = Mass fraction of biomass constituent

Δx = Single cell length [m] (= L/N)

v = Velocity [m/s]

Greek Letters

ε = Emissivity

λ = Thermal conductivity [W/mK]

μ = Dynamic viscosity [Pa·s]

ν = Void fraction

θ = Heat of pyrolysis [J/kg]

ρ = Density [kg/m^3]

σ = $5.670 \cdot 10^{-8}$ Stephan-Boltzmann constant [W/m^2K^4]

Subscripts

0 = Insulated external wall

1 = Hot exhausts

2 = Kiln wall

3 = Outer wall of kiln

4 = Insulated external wall

amb = Ambient

bio = Biomass

char = Char

dry = Dry

eff = Effective

eq = Equivalent

eva = Evaporation

i = i-th Cell in the 1-N range

in = Inlet

n = Temporal instant

pyro = Pyrolysis

rad = Radiation

sat = Saturation

REFERENCES

[1] M. Porta, A. Traverso, L. Marigo, "Thermoeconomic Analysis of a Small-Size Biomass Gasification Plant for Combined Heat and Distributed Power Generation", ASME paper GT2006-90918, 2006.

[2] F. Berti, A. F. Massardo, "Micro Gas Turbines for Electricity Generation from Waste Water Treatment Plants", Proceedings of Pow_Gen Europe 2006, Cologne.

[3] F. Fantozzi, U. Desideri, P. Bartocci, S. Colantoni, "Rotary Kiln Slow Pyrolysis for Syngas and Char Production from Biomass and Waste – Part 1: Working Envelope of the Reactor", ASME Paper GT-2006-90818, 2006.

[4] F. Fantozzi, U. Desideri, P. Bartocci, S. Colantoni, "Rotary Kiln Slow Pyrolysis for Syngas and Char Production from Biomass and Waste – Part 2: Introducing Products Yields in the Energy Balance", ASME Paper GT-2006-90818, 2006.

[5] C. Di Blasi, "Heat, Momentum and Mass Transport through a shrinking biomass particle exposed to thermal radiation", Chemical Engineering Science, Vol. 51, No. 7, pp.1121-1132, 1995.

[6] M. Ferrari, A. Traverso, A. F. Massardo, "Control System For Solid Oxide Fuel Cell Hybrid Systems", ASME Paper 2005-GT-68102, 2005.

[7] A. Traverso, "TRANSEO Code For The Dynamic Simulation Of Micro Gas Turbine Cycles", ASME Paper 2005-GT-68101, 2005.

[8] A. Traverso, R. Scarpellini, A. F. Massardo, "Experimental Results And Dynamic Model Validation Of An Externally Fired Micro Gas Turbine", ASME Paper 2005-GT-68100, 2005.

[9] A. V. Bridgwater, G. V. C. Peacocke, "Fast pyrolysis processes for biomass", Renewable and Sustainable Energy Reviews, Vol. 4, pp.1-73, 2000.

[10] Ing. Francesco Berti, Bmach Srl, Personal communication.

[11] R. Tenti, P. Camiciola, "Termovalorizzazione dei rifiuti tramite pirolisi e impianto combinato per la produzione di energia elettrica e calore", Proceedings of ECOMONDO exhibition, Rimini, 2004 (in Italian).

[12] D. Vamvuka, E. Kakaras, E. Kastanaki, P. Grammelis, "Pyrolysis characteristics and kinetics of biomass residuals mixtures with lignite", Fuel, Vol. 82, pp.1949–1960, 2003.

[13] Perry's Chemical Engineer's Handbook (Perry R. H., Green D. – editors), 7th edition, McGraw-Hill, New York, 1997.

A Review on Cryogenic Treatment

Babita Meher, *Department of Mechanical Engineering, Aryan Institute of Engineering & Technology, Bhubaneswar, baitamh784@gmail.com*
Deepikarani Swain, *Department of Mechanical Engineering, NM Institute of Engineering & Technology, Bhubaneswar, depika_r19@yahoo.co.in*
Sikendar Sharma, *Department of Civil Engineering, Raajdhani Engineering College, Bhubaneswar, sikendarsharma92@gmail.com*

Abstract: The use of cryogenic treatment (CT) to improve mechanical properties of materials has been developed from end Sixties. In the recent time, the starting mistrust about CT has been cleared and many research about different materials are reporting the testing laboratory results, microstructural analysis and hypothesis on CT strengthening mechanisim reported in various journals. The diminishes of retained austenite grouped with fine dispersed -carbides precipitation have largely observed and their influence on mechanical properties have been mapping. Beside this, some latest articles figure out separate mechanisim for fatigue strengthening of stainless steels, which associated with nano-martensite formation during the CT. Present research analyses the state of art about CT, keep focus on various methods, parameters, results and assumed microstructural mechanisim to find out a beginning point for new researches to come.

INTRODUCTION

The use of thermal treatments to improve mechanical properties of metal components is an ancient art expanded down the ages until today. Many of the developed processes apply treatments in a range of temperature higher than room temperature. The first attempts to perform subzero treatments were investigated at the beginning of the 20th century, but the actual interest on cryogenic treatment (or cryo-treatment, CT) was developed during the last years of the century.

The basic CT consists in a gradual cooling of the component until the defined temperature, holding it for a given time (freezing time) and then progressively leading it back to the room temperature. The aim is to obtain an improvement of mechanical properties, typically hardness and wear resistance, but in recent tests fatigue limit too, and to achieve an optimal ratio between conflicting properties, like hardness and toughness.

The research about CT has been validated by the first results on machinery tools, which have shown remarkably enhancement in hardness and durability. From the Nineties, the interest in CT effects has also been applied to many different components: i.e. motor racing parts [1], in particular gears and bearings [2-6], oil drills, gun barrels, knives, surgical and dental instruments [7] and even brass musical instruments [8], piano and guitar strings (Dean Markley Blue Steel™), baseball bats and golf clubs too. Nowadays, many companies offer CT services, especially in the USA and in Canada, and in some cases if no improvement in component life has been obtained they promise a refund.

Even though the mechanism behind improvement has not been totally clarified, different hypotheses coherently with microstructural observations have been suggested in literature.

The aim of the present review is to summarize the most significant works of the last thirty years, focusing on methods, parameters, results and assumed microstructural mechanisms, in order to give to the reader a starting point to approach the CT topic.

The work represents the first step of a research project carried out during the last three years by the authors in the context of a Ph.D. thesis, which will be discussed in early 2008. Due to some Italian law restrictions, all the results from the above research project will be available for publication only after Ph.D. thesis discussion; for this reason they are not included in the present paper.

TREATMENT PARAMETERS

A fundamental distinction among different CT is given by the parameters of the cooling-warming cycle. In [9] two families depending on the minimum temperature reached during the cycle are categorized:

- Shallow Cryogenic Treatment (SCT) or Subzero Treatment: the samples are placed in a freezer at 193 K and then they are exposed to room temperature;
- Deep Cryogenic Treatment (DCT): the samples are slowly cooled to 77 K, held-down for many hours and gradually warmed to room temperature.

Fig. (**1**) shows an example of a common DCT temperature profile. The typical process parameters are: minimum temperature ($T_{\min}$), hold time, cooling and warming rate. In literature, different values of these parameters used by authors during SCT and DCT on different materials can be found (see Table **1**), but anyway it is possible to infer some general indications:

- In some cases, the actual $T_{\min}$ could be higher than the nominal one because of thermal insulation limits, especially after a significant exploitation of the system and the consequent ageing of the chamber seals.
- Each new material needs to be treated and tested at different temperature levels, in order to identify optimum conditions. In most cases, two or three temperature levels (i.e. 88 K, 143 K and 193 K) are enough to obtain a quick indication in the selection of a specific temperature by means of microstructural changes investigation (i.e. calorimetry or acoustic emission);

Table 1. Literature Parameters of SCT and DCT on Different Materials

First Author, [#]	Material	T_{min} [K]	Ramp Down [K/min]	Hold Time [h]	Ramp Up [K/min]
Huang, [19]	AISI M2 tool steel	77	-	168	-
da Silva, [15]	AISI M2 tool steel	77	1.0	20	1.0
Leskovšek, [13]	AISI M2 tool steel	77	immersion	1	-
Mohan, [39]	AISI M2, T1, D3 tool steel	from 163 to 93	-	6 and 24	-
Molinari, [17, 18]	AISI M2, H13 tool steel	77	from 0.3 to 0.5	35	0.07
Yun, [16]	AISI M2, T1 tool steel	77	-	24 and 48	-
Gordo, [20]	M3/2 HSS matrix with Nb and Ta carbides	77	0.36	35	0.07
Meng, [3]	Fe-12Cr-Mo-V-1.4C tool steel	223 and 93	-	-	-
Meng, [4]	Fe-1.4Cr-1C bearing steel	223 and 93	-	1	-
Bensely, [9, 22, 41]	En 353 carburized steel	193 and 77	immersion and 1.24	5 and 24	0.64
Preciado, [21]	Carburized steel	83	1.0	22	-
Kollmer, [40]	AISI 4140 cold rolled steel	89	1.13	6-10	1.13
Zhirafar, [12]	AISI 4340 low alloy steel	77	1.8	24	1.8
Yong, [24]	ASSAB 760 medium carbon steel	89	0.57	18	0.57
Yang, [46]	13Cr2Mn2V high Cr white iron	77	immersion	3	-
Liu, [45]	3Cr13Mo1V1.5 high Cr cast iron	77	immersion	3	-
Darwin, [10]	SR34 18% Cr martensitic stainless steel	from 193 to 89	from 0.5 to 3.5	from 6 to 36	1.0
Ianamura, [28]	Fe-18Cr-8Ni austenitic stainless steel	195	-	-	-
Myeong, [27]	Fe-18Cr-8Ni austenitic stainless steel	197	-	3	-
Singh, [25, 26]	AISI 304L welded joints	88	from 0.34 to 0.85	30	from 0.17 to 0.34
Zhisheng, [47]	Cr-Zr-Cu alloy electrodes	123 and 103	6.0	2 and 4	-
Chen, [32]	Al alloy	89	-	24	-
Lulay, [33]	7075-T651 Al alloy	77	-	2 and 48	-
Trieu, [31]	UHMWPE	89	0.5	14	-

- Hold time over 36 hours does not bring significant improvements and in most cases 24 hours are enough to obtain results;
- Cooling rate values range is restricted in order to prevent thermal-shock cracking. Commonly, the applied values vary from 0.3 K/min to 1.2 K/min;
- In many cryogenic systems warming rate is not closely controllable and little importance to this parameter is given in literature despite of some suggested hypothesis about carbides precipitation during the warming phase.

In [10], the Taguchi Design of Experiment (DOE) method is applied to identify and to optimize the critical parameters of DCT on a 18% Cr martensitic stainless steel used for piston rings. The Analysis of Variance (ANOVA) of wear test results has pointed out that the most significant factor has been the soaking temperature (72% in contribution), followed by the soaking time (24%) and the cooling

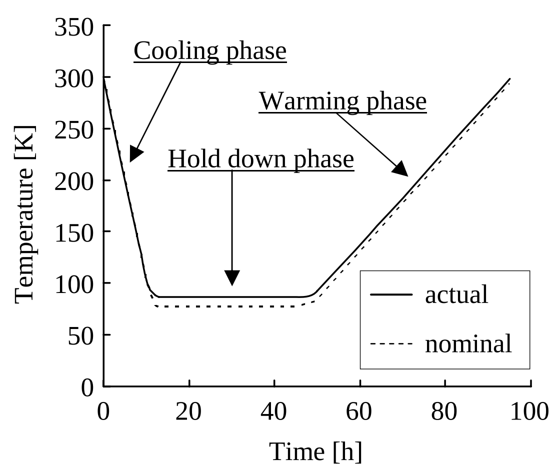

Fig. (1). Example of DCT temperature profile.

rate (10%). Little importance (2%) for the temperature of the tempering process performed after DCT has been observed, while the tempering time is emerged as an irrelevant parameter. Little or no significance for parameters interactions has been calculated and in the end the authors have obtained an optimal combination of 89 K soaking temperature, 36 hours soaking time, 1 K/min cooling rate and 1 hour tempering at 523 K, predicting a wear loss of 2.26 mg (95% in confidence). A test performed on samples treated with these parameters has confirmed the result.

CRYOGENIC SYSTEMS

A cryogenic system is an equipment which allows to control temperature in the cryogenic range into a chamber, using liquid nitrogen or helium.

Until the end of the Sixties, any attempt to perform CT had been done by direct immersion into liquid nitrogen, with the catastrophic result of cracking the components. The cryogenic treatment system developed by Ed Busch (CryoTech, Detroit, MI) in the late 1960s and later improved by Peter Paulin (300 Below Inc., Decatur, IL) with a temperature feedback control on cooling and heating rate, allows to perform effective and crackless CT. As a result, many companies have developed systems to perform CT, mainly in the USA and in Canada, but also in China, India and Japan.

The three most important cooling systems are described in [11]:

- Heat Exchanger: the liquid nitrogen flows through a heat exchanger and the output cooled gas is diffused inside the chamber by a fan. There is no contact between nitrogen and samples;
- Direct Nebulization: the liquid nitrogen is nebulized directly in the chamber or in a cavity around the chamber. A fan allows to obtain a homogeneous temperature distribution; the liquid nitrogen is dispersed around the samples;
- Gradual Immersion: the samples are immersed into the liquid nitrogen for a specific time, then they are extracted and gradually led back to the room temperature by means of a flow of temperature controlled air.

Another type of cooling system is the so-called "Hybrid System", which combines direct nebulization and gradual immersion during different phases of the cooling process, in order to reduce liquid nitrogen consumption (i.e. Vari-Cold™ from Cryotron, Canada).

Fig. (**2**) shows the layout of a direct nebulization cryogenic system. The Control Unit (CU) receives the temperature information from the sensor (S) placed in the chamber (C). The CU operates on the electrovalve (EV) by the regulation of the liquid nitrogen flow through the injectors (I). The fan (F), which is controlled by an electric engine (E), helps to diffuse the nitrogen homogeneously. The CU allows to control the cycle parameters and it provides a print of time-temperature diagram. In a direct nebulization system with a chamber of about 0.25 m^3, an ordinary cycle, requires from 1000 l to 2000 l of liquid nitrogen usually stored in a tank (T), depending on cycle parameters and on the treating material quantity.

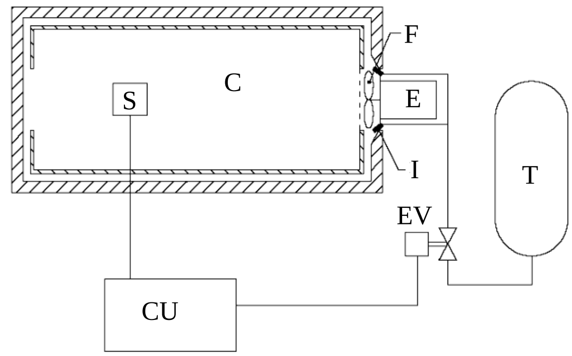

Fig. (2). Sketch of a direct nebulization cryo-system.

EFFECTS ON THE MATERIAL MICROSTRUCTURE

Ferrous Alloys

According to the literature about cryo-treated tool steels, the improvement of mechanical properties can be ascribed to different phenomena:

- Complete transformation of the retained austenite into martensite;
- Fine dispersed carbides precipitation;
- Removal of residual stresses.

It is known that almost all steels at 193 K transform the austenite into martensite. The use of cold treatment has been initially developed on martensitic tool steels in order to remove retained austenite with benefits on hardness.

A reduction from 5.7% to 4.2% in retained austenite volume has been measured after DCT by the use of neutron diffraction on AISI 4340 steel [12]. The temperature reached in SCT is enough to obtain this result, therefore the use of a lower temperature by DCT can only be justified if it activates some different phenomena which lead to a further improvement of the mechanical properties. In [13], a reduction in retained austenite fraction and a rod-like carbides precipitation during tempering after DCT have been observed, pointing out a correlation between the carbide dimension and the tempering temperature. Moreover the authors have obtained a greater dimensional stability of DCT components after each subsequent tempering, which is a result strictly related to the retained austenite elimination, thanks to the lower volume compared to the martensite. The dimensional stability is a desired property for some accurate applications as worn plug gages [14]. The X-ray diffractometric observations carried-out in [15] have confirmed both phenomena: 25% of the retained austenite observed before DCT treatment has been transformed into martensite and fine carbides precipitation has been promoted. Most of the authors, especially in recent papers, have agreed on ascribing to the fine carbides precipitation the improvement of the wear behavior.

Precipitation of fine dispersed carbides has also been previously observed in AISI T1 and M2 high-speed tool steels [16] and in AISI H13 tool steel [17, 18] where, after DCT, the disappearing of twinned submicrostructures present in tempered martensite has been noted. The authors have called this phenomenon "tempered martensite detwinning" but no information is available in literature about something similar. Fine η-carbides in cryo-treated Fe-12Cr-Mo-V-1.4C tool steel has been observed with TEM [3, 4]; the authors have proposed a precipitation mechanism based on the contraction and the expansion of the martensitic lattice in different directions, with a slightly shifting of carbon atoms, in order to segregate η-carbides along the carbon-rich bands. The effect is an improved wear resistance ascribed by the authors to the strength and the toughness enhancement of the martensite matrix.

An interesting analysis of possible phenomena inside the material during the CT is proposed in [19]. By measuring the presence of spherical Fe4M2C (where M = W, Mo, Cr, V) carbides in M2 steel before and after DCT, the authors have found that particles size-range and size-distribution are similar in treated and non-treated samples, but the population and the volume fraction are different and the carbides distribution is more homogeneous in treated samples. Moreover, the carbides volume fraction is increased from 5% to 11% after DCT. The authors suggest that, during the cooling, microscopic internal stresses are generated by different thermal contractions due to the composition and to the microstructure spatial variation; as a consequence, there is a generation of dislocations and of twins, where carbon and alloying atoms subsequently segregate. The hypothesis of this localized diffusion process is in the agreement with the long holding time normally required in CT. Furthermore in the same article the hypothesis for which also the reduction in residual stresses, reported by other authors, could be a consequence of carbides precipitation has been proposed. Quoting a private communication with M.A. Bourke, the authors suggest that the precipitation mechanism could be related to different behaviors of lattice parameters *c* and *a* during the cooling and the warming-up processes observed through an *in-situ* neutron diffraction study.

An interesting result on tools built with different classical AISI steels has been obtained in [20], using DCT on HSS base composites reinforced with Nb and Ta carbides with a high level of retained austenite. The authors have achieved the transformation of retained austenite into martensite, with the consequent increase in hardness and a fine carbides precipitation in the matrix.

Concerning the carburized steels commonly used for gears [9], with the help of an optical microscope it has been observed that both retained austenite elimination and fine carbides precipitation are effective DCT mechanisms, whereas in SCT only the first mechanism acts in the material. Fine carbides precipitation has been observed in a carburized steel in [21] too, but no decrease of retained austenite fraction has been detected.

An important role for the improvement of the mechanical performance of materials and components is played by the residual stress distribution. This aspect of CT has been well analyzed in [22] on a carburized EN 353 steel. The authors have measured the residual stress distribution using X-ray diffraction on conventionally heat treated, SCT and DCT samples in both tempered and untempered condition. They have observed that residual stress distribution is strictly related to both retained austenite reduction and fine carbides precipitation mechanisms. On the one hand, untempered DCT specimens have shown an increase (from −125 MPa to −235 MPa) in surface compressive residual stress, as a consequence of DCT retained austenite reduction from 28.1% to 14.9%. On the other hand, after a necessary tempering (otherwise the following grinding would have led to crack formation in all specimens, independently of treatment), the surface residual stress in DCT specimens has dropped to −80 MPa, while in a conventionally heat treated it has risen to −150 MPa. This overturning has been attributed by the authors to the stress relieving loss of martensite tetragonality, which is caused by the carbides precipitation and which in its turn has been promoted during tempering just by previous DCT-enhanced compressive stress state. From these results it is possible to infer that compressive residual stress and fine carbides precipitation, which are both mechanical performance enhancing mechanisms, move into opposite directions during tempering. As a consequence, understanding and controlling the optimal ratio between them could be the key for achieving best results.

With the aim of understanding microstructural changes and phases evolution during DCT and the subsequent tempering, an important role can be played by the recent development of numerical heat treating modeling techniques. An approach to DCT numerical simulation is proposed in [23]. The authors have implemented an optimization algorithm in a commercial heat treatment simulation software package (DANTE®), in order to calculate phase transformation kinetic parameters, starting from dilatometry experimental results. The simulation involves the whole thermal treatment process including heating, carburizing, quenching, DCT and tempering for a bar model with a notch on the top surface. The model predicts a reduction in retained austenite content and subsequent additional compressive stress in the top surface after DCT and tempering, compared to as-quenched condition. On the contrary, experimental results used for model validation have indicated a lower superficial compressive stress after DCT and tempering. The authors have attributed this difference to a wrong assumption of balanced biaxial stress in the case of measured stress calculations, but the similarity with the results reported in [22] legitimizes to suspect that the reason of the gap could be the unpredicted carbides precipitation during the final tempering simulation.

It is interesting to observe that a recent work [24] states that cryo-treated tools can lose their wear resistance when they are subjected to prolonged periods of high temperature at the cutting edge. Hence, the authors have concluded that the state of the material after CT is metastable, but in the light of what is stated in [22] and reported above, this loss can be explained as an overtempering effect due to a prolonged high temperature working, with the consequent relief of beneficial compressive residual stress.

According to the literature, a totally different mechanism occurs during CT of austenitic stainless steels. The effect of DCT on welded cruciform joints of AISI 304L austenitic stainless steel has been investigated in [23, 24]: the crack initiation life has been extended by strain-induced martensite formed during CT. In addition, the authors have observed a different residual stress configuration near the welded metal after DCT: the tensile residual stresses have been relieved and a compressive stress field has been induced as a consequence of expansion of the weld metal during this transformation. While in [25] the authors have found a slight decrease of *m* and *C* Paris constants after DCT, indicating a reduction in crack growth rate, the result has not been confirmed in [26] by the same authors. In the discussion about crack initiation life extension, the authors have suggested a dislocation-pinning mechanism in agreement with the TEM observation and with the diffractometric analysis performed in [27-29], which have revealed the presence of nano-martensitic particles in pre-strained austenitic stainless steels after an SCT performed with a few hours hold-time at 3 K above Ms (martensite start temperature).

Non-Ferrous Alloys

Despite of the advertisement on cryo-companies web sites, which promises enhancement on a wide range of materials, there are few papers in literature about CT of non-ferrous materials. In [30], the DCT effects on a wide range of polymers and composites have been tested, pointing out interesting results for some of them. Using X-ray diffraction the authors have found a marginal increase in cristallinity after the DCT on Polyetherimide (PEI) and on Polyimide (PI), while no changes have been detected on Polytetrafluoroethylene (PTFE). The change in cristallinity of PEI has been confirmed by Differential Scanning Calorimetry (DCS), which has shown an increase of the glass transition temperature (T_g) from 488 K to 526 K. The authors have related the increase in wear resistance of PEI and of PI to the change in cristallinity. Moreover, Scanning Electron Microscopy (SEM) has pointed out a rougher topography for the surface of the cryotreated PEI. In order to explain these observations, the authors have suggested the development of residual stresses in the polymer as a consequence of the contraction at cryogenic temperatures and subsequent uneven expansion during the warming phase. In the case of the PTFE, the improvement in wear behavior after the DCT has been attributed to the hardness enhancement. In addition, the SEM observations of PTFE powder have shown agglomeration and fibrillation phenomena after DCT, which the authors have related to the ductile behavior, at low temperature too, of PTFE.

Any significant or detectable changes in dimension, cristallinity, tensile strength and elongation on Ultra-High Molecular Weight Polyethylene (UHMWPE) samples after DCT has been found in [31].

The heat affected zone of an unspecified aluminum alloy, which has been welded with Variable Polarity Plasma Arc (VPPA) technique, has been investigated before and after DCT in [32]. Using X-ray diffractometry, the authors have detected a reduction in residual stresses, but no microstructural analysis has been performed.

DCT has also been performed on 7075 aluminum alloy samples [33], but the authors did not find any enhancement in tensile, impact and hardness properties and no further analysis about the material structure has been carried out.

EFFECTS ON THE MECHANICAL PROPERTIES

An extensive collection of CT test results is reported in [34-38] concerning hardness and wear resistance of a wide range of steel grades. This series of papers represents a milestone in the CT field. The papers [37, 38] show wear and hardness results for respectively twelve tool steels, three stainless steels and four other steels. By comparing the results obtained with 189 K SCT and 77 K DCT, the authors have observed a significant abrasive resistance increase for the tool steels subjected to the colder treatment, whereas the stainless steels have shown a difference of less than 10% and the plan carbon and the cast iron did not improve with either SCT and DCT.

After the investigations carried out in papers [34-38] many works reporting test results on CT materials have been published, but each one has focused on one or on few materials instead of collecting data from many of them. As a consequence, it can be helpful to summarize the published results in order to have an overall picture of the measured effects. Table **2** gives some general indications about CT effects on mechanical properties reported by the literature on five steel types and on aluminum alloys. A brief discussion about effects on each property is proposed in the following paragraphs.

Wear Resistance

Wear resistance represents an important property of a material when it is used in applications that lead to reciprocal moving of in-contact components, such as machining tools, bearings, gears, brake rotors, piston seals, etc. Among the listed above microstructural changes related to CT, both retained austenite reduction and carbide precipitation can lead to an improvement in wear resistance by the increase of the steel hardness.

It is almost impossible to carry out a complete comparison between the results obtained in literature, because of different test conditions (such as sliding velocity, distance or

Table 2. Literature Effects of SCT and DCT on Different Materials

	Tool Steels		Carburized Steels		Austenitic Stainless Steels		Martensitic Stainless Steels		High Cr Cast Iron		Aluminum Alloy	
	SCT	DCT	SCT	DCT	SCT	DCT	SCT	DCT	SCT	DCT	SCT	DCT
Hardness	na	+	+	+	na	+	na	+	na	+	na	=
Wear resistance	+	+	+	+	na	na	na	+	na	+	na	na
Tensile/Bending strength	na	+	na	–	=	na	na	na	na	na	na	=
Yield strength	na	na	na	na	=	na	na	na	na	na	na	=
Fatigue life	na	na	na	na	+	+	na	+	na	na	na	=
Toughness	na	+	na	na	na	na	=	–	na	na	na	+

+: improvement, -: worsening, =: invariant, na: not available.

applied load) used by the authors and different wear indicators reported as results (i.e. wear rate or wear resistance).

The most experimented effect of CT is the enhancement of the wear resistance, especially on tool steels. Table **3** shows the wear resistance improvement reported in literature, after the publications [34-38] about different materials and test configuration. Different setup are reported in literature for wear test, but the most used configuration is the pin-on-disk, according to the ASTM standards and the results are usually reported in terms of wear resistance or of wear rate. Some authors have also performed tests directly on cryo-treated tools, by measuring the tool life in number of worked pieces, in the so-called "flank-wear test" or in the "twist drill test".

As it is shown in Table **3**, one of the most cryo-tested materials is AISI M2 high speed tool steel, which is widely used for drills, milling cutters and other tools. Wear resistance is an important property not only for tools, but also for many components subjected to rolling or sliding contact, in different industrial fields like automotive, mining, oil-drilling, etc. Some studies about effects of CT on bearing-steels and carburized steels used in automotive industries are available in literature (i.e. En353 has a significant application for crown wheel, crown pinion, bevel pinion, bevel wheel, timing gears, king pinion, pinion shaft).

Many authors agree with [3] about the reason of the wear resistance improvement: it is the fine carbides precipitation that enhances strength and toughness of the martensite matrix, rather than the reduction or the elimination of the retained austenite fraction. In [17, 18], the wear rates of an AISI M2 tool steel have been compared after four different treatment combinations and sequences:

- Quenching then double tempering (A);
- Quenching, double tempering then DCT (B);
- Quenching, DCT then tempering (C);
- Quenching, DCT then double tempering (D).

The (B) samples have shown a reduction of 51% in wear rate compared with the (A) samples, against 40% and 35% for (C) and (D) specimens respectively. The authors have concluded that greater benefits are obtained when DCT is carried out after tempering process.

Another interesting comparison has been proposed in [39] between cryo-treated and TiN coated samples, which has shown that CT for 24 hours at 93 K is more effective on wear resistance than TiN coating. Through the comparison of the results of CT specimens treated with different parameters, the authors have also concluded that the mechanism responsible for the wear resistance improvement is essentially an isothermal process and the soaking time is more

Table 3. DCT Improvement of Wear Resistance in Literature

First Author, [#]	Material	Test Configuration	Maximum Wear Improvement
da Silva, [15]	AISI M2 tool steel	Pin-on-disk	No significant changes
		Brandsma rapid facing tests	+44% tool life
		Twist drills	+343% tool life (catastrophic failure end-life criterion)
		Shop floor test (special shaper milling cutter)	–22.8% produced parts (appearance of burrs end-life criterion)
Mohan, [39]	AISI M2, T1, D3 tool steel	Pin-on-disk (M2, D3)	+135% wear resistance for M2 +174% wear resistance for D3
		Flank wear (T1, M2, D3)	+110.2% wear resistance for T1 +86.6% wear resistance for M2 +48% wear resistance for D3
Molinari, [17, 18]	AISI M2, H13 tool steel	Pin-on-disk	–51% wear rate for M2 –29% wear rate for H13
Pellizzari, [43]	X155CrMoV12 X110CrMoV8 cold work tool steels	Block-on-disk dry sliding	–42.4% wear rate for X155 –25.3% wear rate for X110
Meng, [3]	Fe-12Cr-Mo-V-1.4C tool steel	Sample-on-wheel	"110% to 600% improvement", p. 206
Meng, [4]	Fe-1.4Cr-1C bearing steel	Sample-on-wheel	–50% wear rate (*)
Bensely, [9]	En 353 carburized steel	Pin-on-disk	+85% wear resistance for SCT +372% wear resistance for DCT
Preciado, [21]	Carburized steel	Pin-on-disk	–20% wear rate (*)
Yong, [24]	ASSAB 760 medium carbon steel	Flank wear	–33% flank wear (*) after 300 s of continuous cutting
Yang, [46]	13Cr2Mn2V high Cr white iron	M-200 Abrasion Experimental Aircraft	+8% relative wear ratio (*)
Liu, [45]	3Cr13Mo1V1.5 high Cr cast iron	M-200 Abrasion Experimental Aircraft	+5% relative wear ratio (*)
Darwin, [10]	SR34 18% Cr martensitic stainless steel	Reciprocatory Friction Test	–43,8% wear loss

(*) Approximate results obtained from graphs.

important than the minimum temperature reached during the treatment. In addition, they have found CT to be more beneficial on untempered than on tempered samples.

The influence of the soaking temperature on DCT wear improvement has been confirmed in [10].

According to [30], the wear resistance of some engineering polymers and composites can be improved by DCT. The authors have obtained an increase up to 60% in abrasive wear resistance of cryotreated PTFE, while PEI and PI have shown improvements up to 35% and 58% respectively. In particular, the paper focus on the different responses to DCT, which have been obtained for the same polymeric matrix combined with different amouts and qualities of fibers or fillers. As an example, a +30% in wear resistance have been reported for cryotreated PEI without fiber reinforcement, while the same material 40% glass fibers reinforced have shown a –35% in wear performance after DCT. Some interesting results have been reported, in the same paper, for Polyetherimide Copolymer, for Polyurethane (PU) and for Polycarbonate.

Hardness

Many hardness tests about CT are reported in literature because this property is related to the wear resistance. Hardness properties are usually measured through indentation tests and they are espressed in different scales depending on the penetrator shape. The most used methods are the Rockwell and the Vickers ones. While the first method is a macro-indentation test, the second one can be performed both as macro or micro-indentation, depending on the applied load, as performed in [25, 26]. The hardness of a tool steel is mainly influenced by retained (soft) austenite and in this way CT can play an important role. However, when compared to wear results, hardness test results (see Table **4**), indicate that the mechanisms can be different for different materials. For instance, in [17] a little increase (+0.13%) in hardness has induced a –51% in wear rate for AISI M2 and the authors have concluded that AISI M2 wear resistance improvement can be attributed to hardness increase. The same test on AISI H13 tool steel has shown an improvement of 6.9% in hardness related to a decrease of 29% in wear rate and, according to the authors, the wear resistance improvement has been correlated to the enhanced toughness of the CT material.

The paper [13] suggests that playing on carbides fraction and dimension and on retained austenite allows to achieve an optimized ratio between hardness and toughness in high speed steels. Interesting results on HSS base composites reinforced with Nb and Ta carbides have been obtained, with about 10% increased hardness [20].

Concerning non-ferrous materials, no significant changes in hardness of aluminum alloys [32, 33] and of Ultra-high Molecular Weight Polyethylene [31] have been detected, while PTFE, PEI, PI, PU and PC have shown important changes in Shore D hardness [30].

Tensile and Bending Strength

A few tensile and bending test results have been published comparing properties before and after CT. This is

Table 4. DCT Improvement of Hardness in Literature

First Author, [#]	Material	Maximum Hardness Improvement
da Silva, [15]	AISI M2 tool steel	No significant changes
Leskovšek, [13]	AISI M2 tool steel	+5.26% Rockwell-C hardness
Molinari, [17, 18]	AISI M2, H13 tool steels	+8.3% Vickers hardness on M2 +6.9% Rockwell-C hardness on H13
Yun, [16]	AISI M2, T1 tool steels	+2.6% Rockwell-C hardness on M2 +2.8% Rockwell-C hardness on T1
Pellizzari, [43]	AISI H13 tool steel	+6.9% Rockwell-C hardness
Pellizzari, [44]	X155CrMoV12 X110CrMoV8 cold work tool steels	No significant changes on both steels
Gordo, [20]	M3/2 HSS matrix composite with Nb and Ta carbides	+12.35% Rockwell-C hardness
Bensely, [9]	En 353 Carburized steel	+3.48% Vickers hardness
Jordine, [5]	En36A carburized steel	+17% Vickers hardness (*)
Preciado, [21]	Carburized steel	+17% Vickers microhardness (*)
Kollmer, [40]	AISI 4140 cold rolled steel	No significant changes
Zhirafar, [12]	AISI 4340 low alloy steel	+2.4% Rockwell-C hardness
Yang, [46]	13Cr2Mn2V high chromium white iron	+3.2% Rockwell-C hardness (*)
Liu, [45]	3Cr13Mo1V1.5 high chromium cast iron	+5.5% Rockwell-C hardness (*)
Singh, [25, 26]	AISI 304L welded joints	No changes in macrohardness (10 kg) +18.8% in Vickers microhardness (50 g)
Zhisheng, [47]	Cr-Zr-Cu alloy electrodes	+3.13% Brinell hardness
Lulay, [33]	7075-T651 Al alloy	No significant changes (–0.5%)

(*) Approximate result obtained from graphs.

mainly due to the fact that tensile properties are less relevant than hardness and wear resistance in tool steels, which are the most studied materials in the CT literature. Furthermore, static properties are expected to be not strongly affected by retained austenite fraction, while concerning precipitation strengthening it is supposed that very small precipitates can be easily bypassed at high stress levels by the dislocation climbing mechanism. However, the only published results about tool steel refer to AISI M2 and T1 and indicate a remarkable improvement of about 20% and of 25% respectively in bending strength [16]. In [40], an increase from 7% to 16% in tensile strength of 4140 cold rolled steel specimens has been detected after CT.

In [41], a slight reduction in tensile strength has been measured for a carburized steel-815M17 subjected to CT, compared to the same material conventionally treated. In particular the authors have observed a decrease of 1.5% for SCT and of 9.34% for DCT.

The cryogenic treatment does not seem to be effective on tensile properties of AISI 304 and 316 stainless steels [27-29].

No significant changes in tensile properties have been detected on aluminum alloys [32, 33] and on UHMWPE [31].

Fatigue Resistance

Fatigue of materials has been one of the most important research topics from the beginning of the 20th century until today in the area of materials and mechanical engineering. All the above listed CT microstructural changes are related to the fatigue behavior, someone with beneficial effects and other ones with detrimental effects. A field of fine hard carbides or the presence of nano-sized martensite in an austenitic matrix can be the effective mechanisms in delaying or blocking dislocations motion at low stress amplitude, when dislocation climbing is unlikely to appear. From this point of view, on the one hand the observed DCT fine carbides precipitation can lead to a prolonged crack nucleation phase. On the other hand, the retained fraction of ductile austenite can act as a crack arrestor in the propagation phase and then its reduction could have a detrimental effect on the final stage of fatigue. In addition, the residual stresses too play an important role in crack nucleation mechanism, in particular during the bending fatigue. Therefore it is necessary to weigh up all these effects, in order to understand the fatigue results.

Despite of their great importance in many mechanical applications, fatigue properties of CT steels have not been investigated by many authors [42] is the oldest paper found in literature about low temperature treatment and fatigue strength. The authors have subjected a cold rolled steel to two different DCT: a rapid treatment by direct immersion in liquid nitrogen for 1 hour, a slow treatment by controlled cooling and 30 minutes holding time. Bending fatigue test results on treated and non-treated specimens have shown no differences in mean values of fatigue limit, but a smaller dispersion for DCT samples has been found. In addition, the authors have carried out an acoustic spectra analysis finding clear differences in the amplitude of harmonics of DCT specimens, but no microstructural changes have been detected in metallographic and fractographic inspections. For this reason the authors have suggested a residual stresses effect, supposing a connection with the redistribution of the lattice defects.

Some studies about CT and fatigue have been conducted at the Precision and Intelligence Laboratory of the Tokyo Institute of Technology [27-29]. During these researches the authors have measured the Ms (martensite start temperature) of a stainless steel with the acoustic emission technique, then they have cooled the samples just 3 K above Ms and they have returned the samples to the room temperature. In [27] the test has been conducted on an austenitic Fe-18Cr-8Ni stainless steel pre-strained by 2% in order to increase the dislocation density. The result, as reported in Fig. (**3**), have shown that the CT does not increase the fatigue life in the low-cycle regime (< 10^4 cycles). However, CT samples have shown longer life in high-cycle regime (> 10^4 cycles). Considering a maximum stress of 350 MPa, the number of cycles to failure is about four and five times larger in CT specimens than in non-treated ones. In addition, the authors have found that at a maximum stress of 310 MPa (just above the fatigue limit), the number of cycles to failure has been $2.8{\cdot}10^5$ for non-treated samples whereas subzero treated specimen did not fail at $1.7{\cdot}10^7$ cycles, (> 60 times longer). In [28], the same material has been pre-strained by 10% and subjected to the same subzero treatment, obtaining an extension of fatigue life of more than 10 times. Similar results have been found on AISI 304 (2% and 10% pre-strained) and on AISI 316 samples [29]. The authors have stated that by controlling dislocation density and temperature it is possible to control the size of martensite in the material; they have also suggested that the nano-sized martensite formed at intersection of two partial dislocations is effective in pinning dislocation, with the result of extending fatigue life by prolonging the nucleation phase.

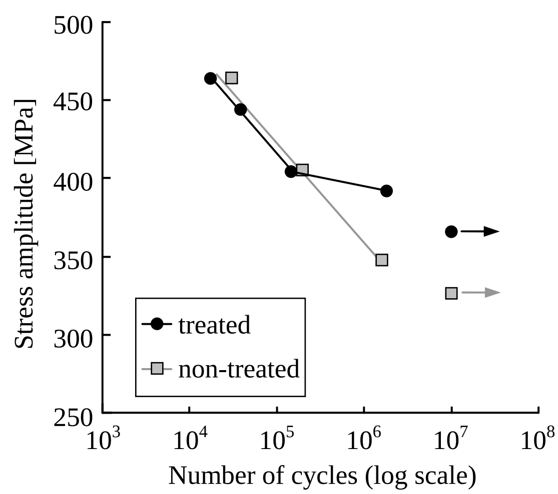

Fig. (3). Fatigue life extension of Fe-18Cr-8Ni austenitic stainless steel (from [28]).

A slight increase (25-30 MPa on about 600 MPa) in fatigue limit has been also measured in [12] for the rotating fatigue test on AISI 4340 steel. The authors have attributed this result to the slight increase in hardness, but they did not propose any microstructural mechanism for the explanation of the phenomenon.

Concerning non-ferrous materials, a high-cycle fatigue test has been performed at room temperature on an unspecified aluminum alloy as-welded and cryo-treated, which has not shown a noticeable improvement [32].

Thermal Fatigue Resistance

In many engineering applications, in particular for internal combustion engines, the combination of thermal and mechanical cycles is a normal operational requirement and therefore it could be interesting to perform an analysis of CT effects on the thermomechanical fatigue behavior of materials. Nevertheless, the only study which has been published until now is a preliminary test about effect of DCT on pure-thermal fatigue properties, without mechanical loads [43]. By subjecting a rotating disk to a cyclic induction-warming and water-cooling (from 353 K to 973 K) a crack network has been generated on its surface. After measuring the thermal crack density ρ, the mean crack length l_m and the maximum crack length $P_{\max}$, the authors have calculated the pyrocracking factor C as the product of these values. The DCT disk has shown a pyrocracking factor of 0.6 µm against 1.18 µm of the untreated one. The parameter responsible for this decrease has been the crack density, which has reduced from 3.49 mm^{-1} to 1.53 mm^{-1}. The mean crack length and the maximum crack length have remained almost the same for DCT and non-DCT samples, leading the authors to conclude that DCT can delay the crack nucleation process without increasing the propagation.

Fracture Toughness

Fracture toughness is a measure of the breaking resistance of a material which contains a crack. Together with the fatigue behavior, fracture toughness is one of the keys of the design applications of the last century. As mentioned in the Fatigue Resistance paragraph, retained ductile austenite fraction can play the role of crack arrestor in martensitic steels, enhancing the toughness.

In [13], the authors have suggested that carbides fraction and dimension and retained austenite fraction play an important role in the optimization of the ratio between hardness and toughness of high speed steels. The authors did not performed any test to measure fracture toughness K_{IC}, but they have used a semi-empirical equation proposed by themselves to calculate it, pointing out a decrease in toughness after CT:

$$K_{IC} = \frac{1.363 \cdot HRc}{HRc - 53} f_{carb}^{-1/6} \left(1 + f_{aust}\right) \sqrt{Ed_p} \ ,$$

where HRc is the Rockwell-C hardness, f_{carb} and f_{aust} the volume fractions of undissolved eutectic carbides and retained austenite, E the Young elastic modulus expressed in MPa, and d_p is the mean distance between undissolved eutectic carbides in the matrix. The value of d_p has been estimated by the authors by measuring the mean diameter of undissolved carbides D_p from a 1000× magnification image obtained with a Scanning Electron Microscope (SEM) and using:

$$d_p = D_p \left(1 - f_{carb}\right) \sqrt{\frac{2}{3 f_{carb}}} \ .$$

It is evident that an higher fraction of smaller carbides leads to lower values of d_p and K_{IC}. It is also evident the role played by d_p, f_{carb} and f_{aust} in controlling the ratio between HRc and K_{IC}.

In contrast with the results of [13], the Charpy impact tests reported in [17, 18, 44] have shown an increase of K_{IC} on AISI H13 tool steel after a double tempering and a DCT, without any effect on hardness and impact energy. The impact toughness before and after DCT on M2 and T1 tool steels has been measured in [16], obtaining an increase of about 43% and 58% respectively. No DCT effect on toughness has been found on 4140 cold rolled steel [40].

An evident toughness drop (14.3%) after DCT has been observed in [12] on AISI 4340 steel; the authors have attributed this decrease to the higher martensite content of the cryotreated samples.

A slight increase (+11.8%) of the impact toughness J after 48 hours DCT on a 7075 aluminum alloy has been measured in [33], with a confidence level of about 90-95%.

CONCLUSIONS

According to the literature, the first mistrust about CT effect on mechanical properties of materials seem to be now cleared up, particularly in the area of tool steels. The significant conclusions are come out through a literature are:

- Cryogenic systems regulate the important cycle process parameters such as cooling rate, lower reached temperature and soaking time. The choice of optimal treatment parameters needs specific analysis on each material, but as in case of steels some needful indications can be taken out from published works;
- Wear resistance and hardness influence have been mostly confirmed by published papers, particularly by the ones concerning tool steels. Advantages of CT on toughness and fatigue behavior have also been reported by authors. With low exceptions, no visible influence on tensile properties have been reported in literature.
- Fine dispersed -carbides precipitation seems to be effective on the wear resistance DCT improvement of tool steels.
- The only proposed microstructural mechanism for fine carbides precipitation in tool steels is the martensite contraction, due to thermal stresses during cooling, which leads carbon atoms to segregate near lattice defects;
- In case of fatigue strengthening, further research are necessary for example, on the nano-martensite evoluation mechanisim for austenitic steels, on the dislocation density effect produced by a field of fine hard carbides in martensitic steels and on the role of retained austenite and of residual stresses.
- CT influence on the thermal and thermo-mechanical fatigue behavior may be an quite emerge research field.
- For better improvements in wear and hardness of PTFE, PI and PEI, further research about the influence of CT on mechanical properties of polymers and composites could be a quite interesting research topic.

REFERENCES

[1] Schiradelly, R. and Diekman, F. J. "Cryogenics – The Racer's Edge", Heat Treating Progress, pp. 43-50, November 2001.

[2] P. Paulin, "Frozen gears", *The Journal of Gear Manufacturing,* pp. 26-29, Mars/April 1993.

[3] F. Meng, K. Tagashira, R. Azuma and H. Sohma, "Role of eta-carbide precipitations in the wear resistance improvements of Fe-12Cr-Mo-V-1.4C tool steel by cryogenic treatment", *ISIJ Int.*, vol. 34(2), pp. 205-210, 1994.

[4] F. Meng, K. Tagashira and H. Sohma, "Wear resistance and microstructure of cryogenic treated Fe-1.4Cr-1C bearing steel", *Scripta Metall. Mater.*, vol. 31(7), pp.865-868, 1994.

[5] A. Jordine, "Increased life of carburised race car gears by cryogenic treatment", *Int. J. Fatigue*, vol. 18(6), p. 418, 1996.

[6] R. N. Wurzbach and W. DeFelice, "Improving component wear performance through cryogenic treatment", in Lubrication Excellence 2004 Proceedings, 2004. [Online] Available: www.cryo plus.com [Accessed Nov. 11, 2007].

[7] J. W. Kim, J. A. Griggs, J. D. Regan, R. A. Ellis and Z. Cai, "Effect of cryogenic treatment on nickel-titanium endodontic instruments", *Int. Endod. J.*, vol. 38(6), pp. 364-371, 2005.

[8] J. N. Jones and C. B. Rogers, "Chilling trumpets: does it have an acoustic effect?", in 146th Acoustical Society of America Meeting, 2003. [Online] Available: http://www.acoustics.org/ [Accessed Nov. 30, 2007].

[9] A. Bensely, A. Prabhakaran, D. Mohan Lal and G. Nagarajan, "Enhancing the wear resistance of case carburized steel (En 353) by cryogenic treatment", *Cryogenics*, vol. 45, pp. 747-754, 2005.

[10] J. D. Darwin, D. Mohan Lal and G. Nagarajan, "Optimization of cryogenic treatment to maximize the wear resistance of 18% Cr martensitic stainless steel by Taguchi method", *J. Mater. Process. Technol.*, Article in press, Corrected Proof, doi:10.1016/j.jmatprotec.2007.05.005.

[11] D. M. Rusiñol, "Efecto del tratamento cryogénico en las propiedades mecànicas de los aceros de herramienta de trabajo en frio", M.S. tesi, Escola Tècnica Superior d'Engynieria Industrial de Barcelona, Spain, 2004.

[12] S. Zhirafar, A. Rezaeian and M. Pugh, "Effect of cryogenic treatment on the mechanical properties of 4340 steel", *J. Mater. Process. Technol.*, vol. 186, pp. 298-303, 2007.

[13] V. Leskovšek and B. Ule, "Influence of deep cryogenic treatment on microstructure, mechanical properties and dimensional changes of vacuum heat-treated high-speed steel", *Heat Treat. Met.*, vol. 3, pp. 72-76, 2002.

[14] I. A. Revis, A. M. Levinson, V. S. Naletov and S. A. Popov, "Use of cryogenic treatment to restore worn plug gages", *Chem. Petrol. Eng.*, vol. 10(5), p. 474, 1974.

[15] F. J. da Silva, S. D. Franco, E. O. Ezugwu, A and M. Souza Jr., "Performance of cryogenically treated HSS tools", *Wear*, vol. 261, pp. 674-685, 2006.

[16] D. Yun, L. Xiaoping and X. Hongshen, "Deep cryogenic treatment of high-speed steel and its mechanism", *Heat Treat. Met.*, vol. 3, pp. 55-59, 1998.

[17] A. Molinari, M. Pellizzari, S. Gialanella, G. Straffelini and K. H. Stiasny, "Effect of deep cryogenic treatment on the properties of tool steel", in Proceedings of Conference on Advances Materials Processes Technologies, 1999, pp. 1461-1469.

[18] A. Molinari, M. Pellizzari, S. Gialanella, G. Straffelini and K. H. Stiasny, "Effect of deep cryogenic treatment on the mechanical properties of tool steels", *J. Mater. Process. Technol.*, vol. 118, pp. 350-355, 2001.

[19] J. Y. Huang, Y. T. Zhu, X. Z. Liao, I. J. Beyerlein, M. A. Bourke and T. E. Mitchell, "Microstructure of cryogenic treated M2 tool steel", *Mater. Sci. Eng. A*, vol. 339, pp. 241-244, 2003.

[20] E. Gordo, F. Velasco, N. Candela, J. M. Torralba, M. Pellizzari and A. Molinari, "Cryogenic treatment on HSS base composites reinforced with Nb and Ta carbides", in Proceedings of EUROPM'99 Conference, 1999, pp. 75-82.

[21] M. Preciado, P. M. Bravo and J. M. Alegre, "Effect of low temperature tempering prior cryogenic treatment on carburized steels", *J. Mater. Process. Technol.*, vol. 176, pp. 41-44, 2006.

[22] A. Bensely, S. Venkatesh, D. Mohan Lal, G. Nagarajan, A. Rajadurai and K. Junik, "Effect of cryogenic treatment on distribution of residual stress in case carburized En 353 steel", *Mater. Sci. Eng. A*, Article in press, Corrected Proof, doi:10.1016/j.msea. 2007.07. 035.

[23] B. L. Farguson, Z. Li and A. M. Freborg, "Modeling heat treatment of steel parts", *Comp. Mater. Sci.*, vol. 34, pp. 274-281, 2005.

[24] A. Y. L. Yong, K. H. W. Seah and M. Rahman, "Performance evaluation of cryogenically treated tungsten carbide tools in turning", *Int. J. Mach. Tool. Manu.*, vol. 46, pp. 2051-2056, 2006.

[25] P. J. Singh, B. Guha and D. R. G. Achar, "Fatigue life improvement of AISI 304L cruciform welded joints by cryogenic treatment", *Eng. Fail. Anal.*, vol. 10, pp. 1-12, 2003.

[26] P. J. Singh, S. L. Mannan, T. Jayakumar and D. R. G. Achar, "Fatigue life extension of notches in AISI304L weldments using deep cryogenic treatment", *Eng. Fail. Anal.*, vol. 12, pp. 263-271, 2005.

[27] T. H. Myeong, Y. Yamabayashi, M. Shimojo and Y. Higo, "A new life extension method for high cycle fatigue using micro-martensitic transformation on an austenitic stainless steel", *Int. J. Fatigue*, vol. 19(1), pp. S69-S73, 1997.

[28] T. Ianamura, R. Abe, T. H. Myeong, M. Shimojo and Y. Higo, "Fatigue life extension by nano-sized martensite particles in steels", in Proceedings of the 7th International Fatigue Congress, 1999, pp. 633-638.

[29] M. Shimojo and Y. Higo, "Formation of nanosized martensite and its application to fatigue strengthening", *in Amorphous and Nanocristalline Materials - Preparation, Properties and Applications*, eds. A. Inoue and K. Hashimoto, Berlin: Springer 2001, pp. 186-204.

[30] J. Indumathi, J. Bijwe, A. K. Ghosh, M. Fahim and N. Krishnaraj, "Wear of cryo-treated engineering polymers and composites", *Wear*, vol. 225-229, pp. 343-353, 1999.

[31] H. H. Trieu, L. H. Morris, M. E. Kaufman, R. Hood and L. S. Jenkins, "Investigation of cryogenic treatment of UHMWPE", in Proceedings of the Sixteenth Southern Biomedical Engineering Conference, 1997, pp. 90-91.

[32] P. Chen, T. Malone, R. Bond and P. Torres, "Effects of cryogenic treatment on the residual stress and mechanical properties of an aerospace aluminum alloy", in Proceedings of the 4th Conference on Aerospace Materials, Processes, and Environmental Technology, 2001.

[33] K. E. Lulay, K. Khan and D. Chaaya, "The effect of cryogenic treatments on 7075 aluminum alloy", *J. Mater. Eng. Perform.*, vol. 11(5), pp. 479-480, 2002.

[34] R. F. Barron, "Effect of cryogenic treatment on lathe tool wear", in Proceedings of the 13th International Congress of Refrigeration, vol. 1, 1973, pp. 529-534.

[35] R. F. Barron, "Do treatments at temperature below –120 °F help increase the wear resistance of tool steels? Here are some research findings that they do", *Heat Treating*, pp. 14-17, June 1974.

[36] R. F. Barron and C. R. Mulhern, "Cryogenic treatment of AISI-T8 and C1045 steels", *Adv. Cryog. Eng. Materi.*, vol. 26, pp. 171-178, 1980.

[37] R. F. Barron, "Cryogenic treatment of metals to improve wear resistance", *Cryogenics*, vol. 22(8), pp. 409-313, 1982.

[38] R. F. Barron, "Cryogenic treatment of tool steels", in Proceedings of Conference Manufacturing Strategies, vol. 6, 1996, pp. 535-548.

[39] D. Mohan Lal, S. Renganarayanan and A. Kalanidhi, "Cryogenic treatment to augment wear resistance of tool and die steels", *Cryogenics*, vol. 41, pp. 149-155, 2001.

[40] K. P. Kollmer, "Applications & Developments in the Cryogenic Processing of Materials", *The Technology Interface, Electronic Journal for Engineering Technology*, vol. 3(1), 1999. [Online] Available: http://et.nmsu.edu/~etti/ [Accessed Nov. 30, 2007].

[41] A. Bensely, D. Senthilkumar, D. Mohan Lal, G. Nagarajan, and A. Rajadurai, "Effect of cryogenic treatment on tensile behavior of case carburized steel-815M17", *Mater. Charact.*, vol. 58, pp- 485-491, 2007.

[42] G. Belisario, F. Caproni and E. Marchetti, "Influence of low temperature treatment on fatigue life of strain hardened steel specimen", in Proceedings of the Eleventh International Cryogenic Engineering Conference – ICEC 11, vol. D, 1986, pp. 791-794.

[43] M. Pellizzari, A. Molinari, S. Gialanella and G. Straffelini, “Effetto del trattamento criogenico sulle proprietà microstrutturali dell’acciaio AISI H13”, *La Metallurgia Italiana*, vol. 1, pp. 21-27, 2001.

[44] M. Pellizzari and A. Molinari, “Deep Cryogenic treatment of cold work tool steel”, in Proceedings of 6th International Tooling Conference, vol. I, 2002, pp. 657-669.

[45] H. H. Liu, J. Wang, B. L. Shen, H. S. Yang, S. J. Gao SJ and S. J. Huang, “Effects of deep cryogenic treatment on property of 3Cr13Mo1V1.5 high chromium cast iron”, *Mater. Des.*, vol. 28, pp. 1059-1064, 2007.

[46] H. S. Yang, J. Wang, B. L. Shen, H. H. Liu, S. J. Gao and S. J. Huang, “Effect of cryogenic treatment on the matrix structure and abrasion resistance of white cast iron subjected to destabilization treatment”, *Wear*, vol. 261, pp. 1150-1154, 2006.

[47] W. Zhisheng, S. Ping, L. Jinrui and H. Shengsun, “Effect of deep cryogenic treatment on electrode life and microstructure for spot welding hot dip galvanized steel”, *Mater. Des.*, vol. 24, pp. 687-692, 2003.

Effect of Nucleophilic Attack on Hydrido-Bridged Copper Rings

Shaik Mozammil, *Department of Mechanical Engineering, Aryan Institute of Engineering & Technology, Bhubaneswar, smozammil157@gmail.com*
Biswa Ranjan Pradhan, *Department of Civil Engineering, Capital Engineering College, Bhubaneswar, biswaranjanpradhan78@gmail.com*
Debi Prasad Singh, *Department of Mechanical Engineering, Raajdhani Engineering College, Bhubaneswar, deboprasad_1159@gmail.com*

Abstract: Electronic structure calculations (B3LYP/6-311+G**) predict that nucleophilic attack of the aromatic *cyclo*-Cu (μ-) ring gains ligand-stabilized tetranuclear Cu trace calculate as cyclo-Cu (μ-) Nuc (n = 1-4; Nuc = N , CO, H O, NH and PH). Based on the number of addition of nucleophiles, the tetranuclear Cu traces in adopt planar, bent or 3D tetrahedral shapes. following molecules shows aromatic properties, which is caused due to 4s and 3d repeated electron dislocation on the Cu frame (s and d-orbital aromaticity). The aromaticity of the new ligand stabilized trtranuclear Cu traces was checked by a group of selected criteria of aromaticity. Particularly, the nucleus independent chemical shift, NICS(0) and NICS(1) and their out-of-plane components NICS (0), NICS (1) and the NICS scaned pictures are shows for the aromaticity of the planar, bent and tetrahedral Cu traces. The influence of the substitutes on the aromatic properties of the Cu traces is the crucial factor of the current research. It seems that rising the value attacking nucleophiles influence the diatropic response of the aromatic tetranuclear Cu traces. However, the aromaticity of 3D surface is larger than the aromaticity of the planar and bend orientations. The influence of oriented nucleophiles, on the stability, electronic structure and connecting mode of the cyclo-Cu (μ-) Nuc molecules is analysed is properly.

Keywords: Aromaticity, DFT calculations, Four-member copper rings, nucleophilic attack, metallaromaticity.

1. INTRODUCTION

Recently, we have communicated on a new class of cyclic copper(I) hydrides (hydrocoppers) formulated as $Cu_n(\mu\text{-}H)_n$ (n = 3-6) as the cyclic hydrocarbon analogues in the diverse tapestry of inorganic chemistry [1]. The choice of the copper(I) hydrides was based on the well known tendency of copper(I) centers to cluster together in a variety of organocopper(I) compounds involving even the alkyl groups as bridging ligands, a representative example being the cyclic Cu_4R_4 tetramer [2-11]. The cyclic hydrocoppers(I) and some of their substituted derivatives were predicted to be stable species with a perfectly planar configuration, thus expanding the borders of inorganic chemistry into the realm of organic chemistry by building molecules containing bonds that are characterized by a common ring-shaped electron density, more commonly seen in organic molecules, with new properties and chemical reactivity. Moreover, these findings may not only expand the aromaticity concept in all-metal systems with structures resembling those of the aromatic hydrocarbons, but may also indicate whole classes of new inorganic aromatic species (substituted derivatives) resulting upon substitution of the H atoms by other groups such as alkyls (R) and aryls (Ar), halides (X), amido (NR_2), hydroxide (OH) and alkoxides (OR) etc.

The structures of HCN-Cu_n (n = 1-3) clusters were determined through high resolution infrared spectroscopy [12]. All complexes were found to be bound to the nitrogen end of the HCN molecule and on the "atop site" of the copper cluster. The HCN-Cu interactions changes from a strong van der Waals bond in n = 1 to a partially covalent bond in HCN-Cu_3. Very recently [13] the important intermediate phenylcopper complexes $[C_6H_5Cu_m]^-$ (m = 1-3], which are produced from the reactions between copper metal clusters formed by laser ablation and the benzene molecules seeded in argon carrier gas, were studied by photoelectron spectroscopy (PES) and density functional theory (DFT).

Herein we address a number of important issues related to the response of the aromatic *cyclo*-$Cu_4(\mu\text{-}H)_4$ molecule towards successive nucleophilic attack by a series of nucleophiles, Nuc, yielding ligand-stabilized tetranuclear Cu_4 clusters formulated as *cyclo*-$Cu_4(\mu\text{-}H)_4Nuc_n$ (n = 1-4; Nuc = N_2, CO, H_2O, NH_3 and PH_3). The molecular and electronic structures, stabilities and bonding features of these novel ligand-stabilized tetranuclear Cu_4 clusters are thoroughly presented, using electronic structure calculation methods at the DFT level of theory.

2. THEORETICAL METHODS

In view of the good performance of density functional theory (DFT), we were instigated to perform DFT calculations at the B3LYP level of theory on all of the compounds we studied using the GAUSSIAN03 program suite [14]. The geometries of all species were fully optimized at the Becke's 3-Parameter hybrid functional [15,16] combined with the Lee-Yang-Parr [17] correlation functional abbreviated as B3LYP level of density functional theory, using the 6-311+G(d,p) basis set. Full geometry optimization was performed for each structure using Schlegel's analytical gradient method [18], and the attainment of the energy minimum was verified by calculating the vibrational frequencies that result in absence of imaginary eigenvalues. The vibrational modes and the corresponding frequencies are based on a harmonic force field. This was achieved with the SCF convergence on the density matrix of at least 10^{-9} and the rms force less than 10^{-4} au. All bond lengths and bond angles were optimized to better than 0.001 Å and 0.1°, respectively. The computed electronic energies were corrected to constant pressure and 298 K, for zero point energy (ZPE) differences and for the contributions of the translational, rotational and vibrational partition functions. Magnetic shielding tensors have been computed with the GIAO (gauge-including atomic orbitals) DFT method [19] as implemented in the GAUSSIAN03 series of programs [14] employing the B3LYP level of theory. Nucleus-Independent Chemical Shifts (NICS) values were computed at the B3LYP/6-311+G(d,p) level according to the procedure described by Schleyer *et al*. [20]. The magnetic shielding tensor elements was calculated for a ghost atom located at the center of the ring. Negative (diatropic) NICS values indicate aromaticity, while positive (paratropic) values imply antiaromaticity.

3. RESULTS AND DISCUSSION

3.1. Structures of the *cyclo*-$Cu_4(\mu\text{-}H)_4Nuc_n$ (n = 1-4; Nuc = N_2, CO, H_2O, NH_3 and PH_3) Molecules

Stationary point geometries of the *cyclo*-$Cu_4(\mu\text{-}H)_4Nuc_n$ (n = 1-4; Nuc = N_2, CO, H_2O, NH_3 and PH_3) molecules computed at the B3LYP/6-311+G(d,p) level of theory are presented in Figs. (**1**) and (**2**).

Perusal of Figs. (**1**) and (**2**) reveals that the addition of the nucleophiles, Nuc (Nuc = N_2, CO, H_2O, NH_3 and PH_3) to the Cu(I) metal centers of the parent *cyclo*-$Cu_4(\mu\text{-}H)_4$ (D_{4h}) molecule in some cases alters the planar *cyclo*-$Cu_4(\mu\text{-}H)_4$ stereochemistry affording three-dimensional (3D) structures with C_{2v}, C_{3v} and T_d symmetries. In the case of the addition of two carbonyl ligands in 1,2-positions of the ring, ring opening occurs by insertion of the hydride ligand between the two copper atoms bearing the carbonyl ligands, yielding complex **7**. The addition of one and two nucleophiles, Nuc, changes the rectangular Cu_4 core structure (D_{4h} point group) of the parent molecule to a rhombic core structure having C_{2v} and D_{2h} symmetry, respectively.

Nucleophilic attack of the *cyclo*-$Cu_4(\mu\text{-}H)_4$ species by one and two N_2 nucleophiles does not alter the planarity of the *cyclo*-$Cu_4(\mu\text{-}H)_4$ cluster, yielding the *cyclo*-$Cu_4(\mu_2\text{-}H)_4(\eta^1\text{-}N_2)$, **1** and *cyclo*-$Cu_4(\mu_2\text{-}H)_4(\eta^1\text{-}N_2)_2$, **2**, complexes, having C_{2v} and D_{2h} symmetry, respectively. Dinitrogen is coordinated to copper(I) centers in an end-on coordination mode (η^1-N_2). Moreover, in complex **2** the distance between the copper atoms, which have not attacked by the nucleophile, is 2.855 Å, indicating weak intermetallic interactions between these two copper atoms as well. On the other hand, nucleophilic attack of the *cyclo*-$Cu_4(\mu\text{-}H)_4$ species by three and four N_2 nucleophiles strongly alters the planarity of the $Cu_4(\mu\text{-}H)_4$ core structure, yielding the 3D structures $Cu_4(\mu_2\text{-}H)_4(\eta^1\text{-}N_2)_3$, **3** and $Cu_4(\mu_2\text{-}H)_4(\eta^1\text{-}N_2)_4$, **4**, with C_{3v} and T_d symmetry, respectively. It is important to be noticed that in the 3D structures the hydride ligands are triply-bridged face-capping the tetrahedral structure.

A variety of structures are obtained upon coordination of one to four CO ligands with the copper(I) metal centers of the parent *cyclo*-$Cu_4(\mu\text{-}H)_4$ cluster. Thus, coordination of one CO ligand yields the *cyclo*-$Cu_4(\mu_2\text{-}H)_4(\eta^1\text{-}CO)$, **5**, cluster belonging to C_{2v} point group. The addition of the first CO ligand to one of the Cu(I) metal centers results in the shortening of the Cu-Cu bond distance between the non attacked Cu(I) metal centers by 0.021 Å, while the adjacent Cu-Cu bonds are elongated by 0.143 Å with respect to the Cu-Cu bond distance of the parent *cyclo*-$Cu_4(\mu\text{-}H)_4$ molecule (2.440 Å).

Three minima were located on the potential energy surface (PES) of the $Cu_4H_4(CO)_2$ system. The global minimum corresponds to the planar structure **6 (D_{2h})**, with the two CO ligands in 1,3-positions. Noteworthy is the relatively short Cu···Cu distance of 2.689 Å between the non attacked Cu(I) centers in the rhombic "all-metal" ring indicating the existence of intermetallic interactions between these copper atoms as well. Conformer **7**, with the two CO ligands in 1,2-positions corresponds to a local minimum 6.9 kcal/mol higher in energy than the global minimum **6**. In conformer **7**, the Cu···Cu distance between the copper atoms bearing the CO ligands has dramatically increased to 3.036 Å, illustrating the ring opening at this point and the two copper atoms are only symmetrically bridged by a hydride ligand. The third isomer **8**, corresponding to a local minimum at 27.3 kcal/mol higher in energy than the global minimum, adopts a 3D configuration with C_{2v} symmetry. All bridging hydride ligands are triply bridging ligands face-capping the tetrahedral $Cu_4(\mu_3\text{-}H)_4(\eta^1\text{-}CO)_2$ structure. Three minima were also located on the PES of the $Cu_4H_4(CO)_3$ system. The global minimum, corresponding to conformer **9**, adopts a bent structure of C_s symmetry. The Cu-Cu-Cu-Cu dihedral angle is 147.9º, while the bent around the Cu···Cu hinge forms weakly bonding Cu···Cu interactions (Cu···Cu distance of 2.711 Å). Conformer **10**, adopting a 3D tetrahedral structure of C_{3v} symmetry, corresponds to a local minimum 9.6 kcal/mol higher in energy with respect to the global minimum **9**. The planar conformer **11** belonging to C_{2v} point group corresponds to a saddle point (ν = 35.5i cm^{-1}), 2.2 kcal/mol higher in energy with respect to the global minimum. Following the imaginary frequency and re-optimizing the structure the global minimum is achieved. Finally, for the $Cu_4H_4(CO)_4$ species we were able to locate three minima on the PES corresponding to conformers with tetrahedral, bent and planar structures. In the tetrahedral structure, **12**, with T_d symmetry, corresponding to the global minimum, the Cu-Cu bond distances are 2.536 Å, while all hydride ligands are triply bridging face-capping the tetrahedral structure. The bent structure, **13**, possessing D_{2d} symmetry is a local minimum 7.3 kcal/mol higher in energy. The Cu-Cu-Cu-Cu dihedral angle in **13** is 105.3º. The planar conformer, **14**, of D_{4h} symmetry corresponds to a saddle point (ν = 20.4i cm^{-1}) 14.4 kcal/mol higher in energy with respect to the global minimum. Following the imaginary frequency the local minimum, **13**, is obtained.

Analogous is the response of the *cyclo*-$Cu_4(\mu\text{-}H)_4$ species towards the nucleophilic attack by the H_2O, NH_3 and PH_3 nucleophiles (Fig. **2**). Coordination of one and two H_2O ligands does not alter the planar configuration of the clusters.

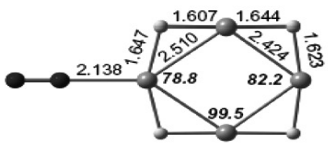

1 (C_{2v})
cyclo-$Cu_4(\mu_2$-H)4(η^1-N_2)

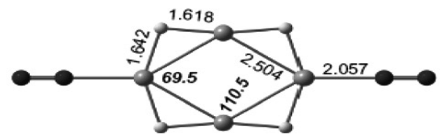

2 (D_{2h})
cyclo-$Cu_4(\mu_2$-H)4(η^1-$N_2)_2$

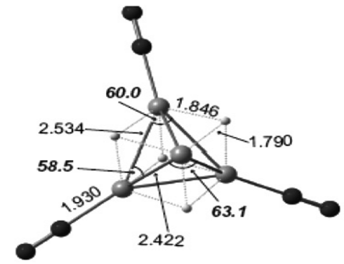

3 (C_{3v})
cyclo-$Cu_4(\mu_2$-H)4(η^1-$N_2)_3$

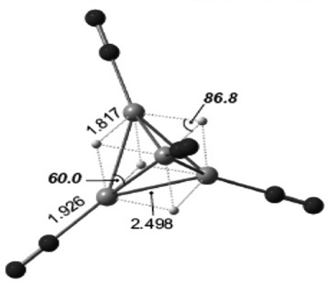

4 (T_d)
cyclo-$Cu_4(\mu_3$-H)4(η^1-$N_2)_4$

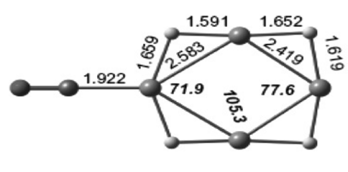

5 (C_{2v})
cyclo-$Cu_4(\mu_2$-H)4(η^1-CO)

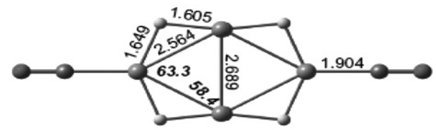

6 (D_{2h})
cyclo-$Cu_4(\mu_2$-H)4(η^1-CO$)_2$

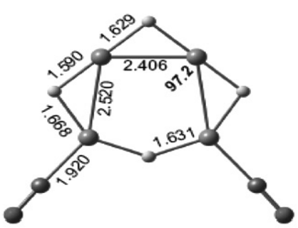

7 (C_{2v})
cyclo-$Cu_4(\mu_2$-H)4(η^1-CO$)_2$

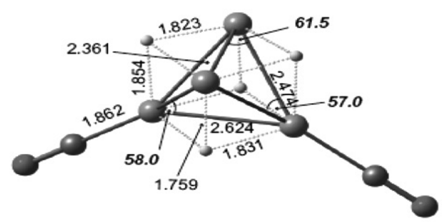

8 (C_{2v})
cyclo-$Cu_4(\mu_3$-H)4(η^1-CO$)_2$

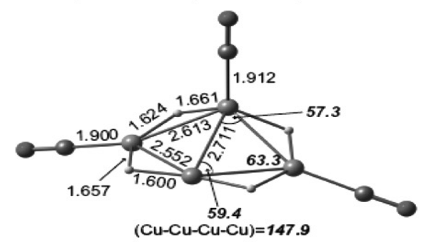

9 (C_s)
cyclo-$Cu_4(\mu_2$-H)4(η^1-CO$)_3$

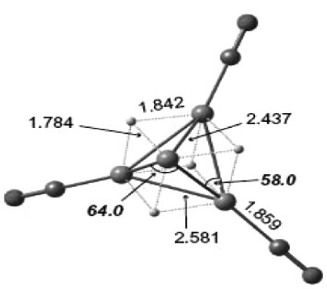

10 (C_{3v})
cyclo-$Cu_4(\mu_3$-H)4(η^1-CO$)_3$

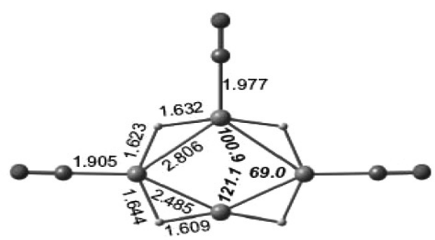

11 (C_{2v})
cyclo-$Cu_4(\mu_2$-H)4(η^1-CO$)_3$

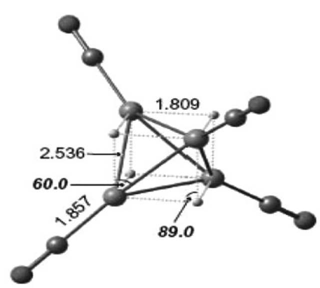

12 (T_d)
cyclo-$Cu_4(\mu_3$-H)4(η^1-CO$)_3$

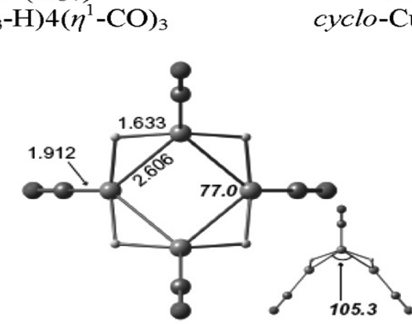

13 (D_{2d})
cyclo-$Cu_4(\mu_3$-H)4(η^1-CO$)_4$

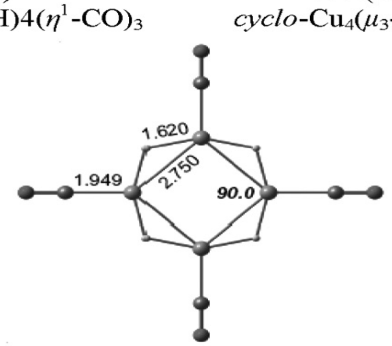

14 (D_{4h})
cyclo-$Cu_4(\mu_2$-H)4(η^1-CO$)_4$

Fig. (1). Equilibrium geometries (bond lengths in Angstroms, angles in deg) of the stationary points located on the PES of the Cu_4(Ï-H$)_4$Nucn (n = 1-4; Nuc = N_2, CO) molecules, computed at the B3LYP/6-311+G(d,p) level.

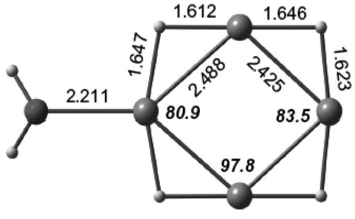

15 (C_s)

cyclo-$Cu_4(\mu_2\text{-}H)_4(OH_2)$

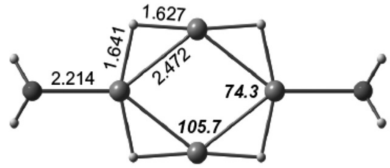

16 (C_{2h})

cyclo-$Cu_4(\mu_2\text{-}H)_4(OH_2)_2$

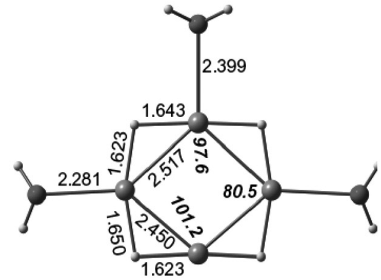

17 (C_s)

cyclo-$Cu_4(\mu_2\text{-}H)_4(OH_2)_3$

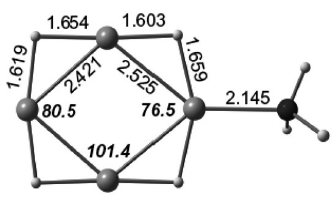

18 (C_s)

cyclo-$Cu_4(\mu_2\text{-}H)_2(\mu_3\text{-}H)_2(NH_3)$

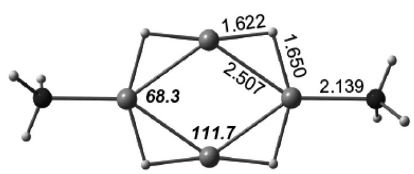

19 (C_{2h})

cyclo-$Cu_4(\mu_2\text{-}H)_4(NH_3)_2$

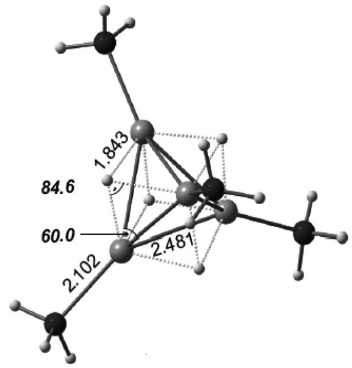

20 (T_d)

cyclo-$Cu_4(\mu_3\text{-}H)_4(NH_3)_4$

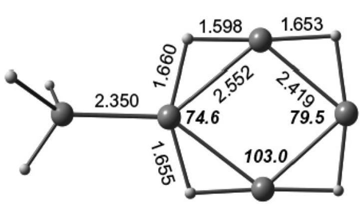

21 (C_s)

cyclo-$Cu_4(\mu_3\text{-}H)_4(PH_3)$

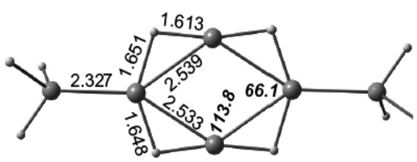

22 (C_{2h})

cyclo-$Cu_4(\mu_2\text{-}H)_4(PH_3)_2$

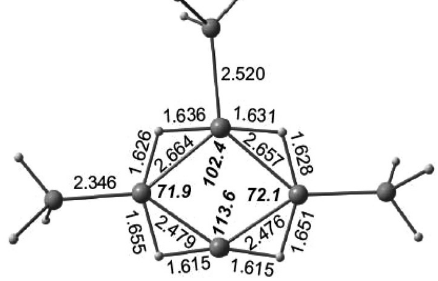

23 (C_s)

cyclo-$Cu_4(\mu_2\text{-}H)_4(PH_3)_2$

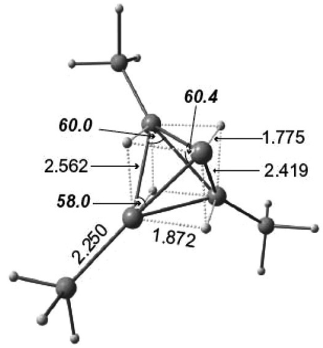

24 (C_{3v})

cyclo-$Cu_4(\mu_3\text{-}H)_4(PH_3)_3$

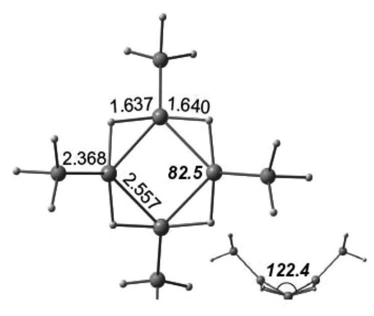

25 (D_{2d})

cyclo-$Cu_4(\mu_2\text{-}H)_4(PH_3)_4$

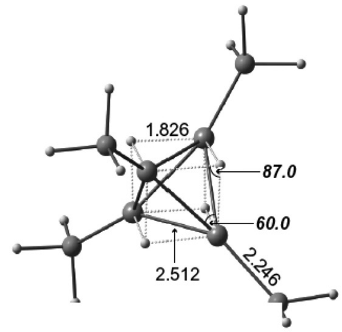

26 (T_d)

cyclo-$Cu_4(\mu_3\text{-}H)_4(PH_3)_4$

Fig. (2). Equilibrium geometries (bond lengths in Angstroms, angles in deg) of the stationary points located on the PES of the Cu_4(Ï-H)4Nuc_n (n = 1-4; Nuc = OH_2, NH_3, PH_3) molecules, computed at the B3LYP/6-311+G(d,p) level.

In the *cyclo*-$Cu_4(\mu\text{-}H)_4(OH_2)$, **15**, cluster the hydrogen atoms of the coordinated H_2O molecule are oriented out of the molecular plane, thereby the symmetry of the molecule is the C_s. The same holds also true for the *cyclo*-$Cu_4(\mu\text{-}H)_4(OH_2)_2$ species, **16** of C_{2h} symmetry where the hydrogen atoms of the coordinated H_2O molecules are oriented on both sides of the molecular plane. Another conformer of C_{2v} symmetry with the hydrogen atoms of the coordinated H_2O molecules oriented on one side of the molecular plane corresponds to a local minimum 0.04 kcal/mol higher in energy than the global minimum, **16**. Notice that only the *cyclo*-$Cu_4(\mu\text{-}H)_4(OH_2)_2$ conformers with the coordinated H_2O molecules in 1,3-positions were located in the PES. The global minimum of the $Cu_4H_4(OH_2)_3$ system corresponds to the planar structure **17** (**C_s**), while a 3D tetrahedral structure, **18** (C_3) is a local minimum at 26.4 kcal/mol higher in energy. Attempts to locate a minimum in the PES of the $Cu_4H_4(OH_2)_4$ system were unsuccessful.

Nucleophilic attack of the *cyclo*-$Cu_4(\mu\text{-}H)_4$ species by one molecule of the NH_3 nucleophile, affords the *cyclo*-$Cu_4(\mu\text{-}H)_4(NH_3)$, **19**, cluster, which keeps the planarity of the parent *cyclo*-$Cu_4(\mu\text{-}H)_4$ molecule. Notice that one of the hydrogen atoms of the coordinated NH_3 ligand is coplanar with the molecular plane. The second NH_3 ligand is coordinated to a Cu(I) center in 1,3-positions affording the *cyclo*-$Cu_4(\mu\text{-}H)_4(NH_3)_2$, **20**, cluster having C_{2h} symmetry. Attempts to locate a minimum in the PES of the $Cu_4H_4(NH_3)_3$ system were unsuccessful. The fully substituted $Cu_4(\mu\text{-}H)_4(NH_3)_4$, **21**, cluster adopts a 3D tetrahedral stereochemistry belonging to T_d point group. In the T_d structure all bridging hydride ligands are triply bridging face-capping the tetrahedron.

Finally, the successive nucleophilic attack of the aromatic parent *cyclo*-$Cu_4(\mu\text{-}H)_4$ molecule by the PH_3 nucleophile yields mono-, di-, tri- and tetra-substituted derivatives. The mono-substituted derivative, **22**, retains the planarity of the parent *cyclo*-$Cu_4(\mu\text{-}H)_4$ species, but the perfect square planar Cu_4 core of the parent molecule is transformed to a rhombic "all-metal" core. In the di-substituted derivative, **23**, of C_{2h} symmetry, the two PH_3 ligands occupy the 1,3-positions in the rhombic Cu_4 structural core. Two tri-substituted derivatives were located on the PES of the $Cu_4H_4(PH_3)_3$ system. The global minimum corresponds to a planar structure, **24**, having C_s symmetry, while a 3D structure, **25**, of C_{3v} symmetry is a local minimum 14.9 kcal/mol higher in energy. For the tetra-substituted *cyclo*-$Cu_4(\mu\text{-}H)_4(PH_3)_4$ derivative the global minimum corresponds to the bent structure, **26**, belonging to D_{2d} point group, while the 3D structure, **27**, with T_d symmetry is a local minimum only 1.7 kcal/mol higher in energy. Notice again the triply bridging hydride ligands face-capping the tetrahedron.

3.2. Stability of the *cyclo*-$Cu_4(\mu\text{-}H)_4L_n$ (n = 1-4; Nuc = N_2, CO, H_2O, NH_3 and PH_3) Molecules

The stability of the *cyclo*-$Cu_4(\mu\text{-}H)_4Nuc_n$ (n = 1-4; Nuc = N_2, CO, H_2O, NH_3 and PH_3) molecules are investigated using the following fragmentation pattern:

$$cyclo\text{-}Cu_4(\mu\text{-}H)_4Nuc_n \rightarrow cyclo\text{-}Cu_4(\mu\text{-}H)_4 + nNuc$$

The calculated binding energies are compiled in Table **1**.

Table 1. Total Electronic Energy *E* (in Hartrees) and Binding Energies ΔE_1, ΔE_2 and ΔE_3 (in kcal/mol) of the *cyclo*-$Cu_4(\mu\text{-}H)_4Nuc_n$ (n = 1-4; Nuc = N_2, CO, H_2O, NH_3 and PH_3) Molecules Computed at the B3LYP/6-311+G(d,p) Level

Cluster	Point Group	ΔE_1[a] [kcal/mol]	ΔE_1/n [kcal/mol]
cyclo-$Cu_4(\mu\text{-}H)_4(N_2)$, **1**	C_{2v}	-0.8	-0.8
cyclo-$Cu_4(\mu\text{-}H)_4(N_2)_2$, **2**	D_{2h}	-2.3	-1.2
$Cu_4(\mu\text{-}H)_4(N_2)_3$, **3**	C_{3v}	-25.1	-8.4
$Cu_4(\mu\text{-}H)_4(N_2)_4$, **4**	T_d	-33.7	-8.4
cyclo-$Cu_4(\mu\text{-}H)_4(CO)$, **5**	C_{2v}	-10.2	-10.2
cyclo-$Cu_4(\mu\text{-}H)_4(CO)_2$, **6**	D_{2h}	-23.6	-11.8
cyclo-$Cu_4(\mu\text{-}H)_4(CO)_2$, **7**	C_{2v}	-16.8	-8.4
$Cu_4(\mu\text{-}H)_4(CO)_2$, **8**	C_{2v}	-42.8	-21.4
cyclo-$Cu_4(\mu\text{-}H)_4(CO)_3$, **9**	C_s	-28.0	-9.3
$Cu_4(\mu\text{-}H)_4(CO)_3$, **10**	C_{3v}	-64.9	-21.6
cyclo-$Cu_4(\mu\text{-}H)_4(CO)_3$, **11**	C_{2v}	-25.8	-8.6
$Cu_4(\mu\text{-}H)_4(CO)_4$, **12**	T_d	-87.2	-21.8
cyclo-$Cu_4(\mu\text{-}H)_4(CO)_4$, **13**	D_{2d}	-33.4	-8.3
cyclo-$Cu_4(\mu\text{-}H)_4(CO)_4$, **14**	D_{2h}	-26.3	-6.6
cyclo-$Cu_4(\mu\text{-}H)_4(OH_2)$, **15**	C_s	-6.1	-6.1
cyclo-$Cu_4(\mu\text{-}H)_4(OH_2)_2$, **16**	C_{2h}	-11.5	-5.8
cyclo-$Cu_4(\mu\text{-}H)_4(OH_2)_3$, **17**	C_s	-12.4	-4.1
$Cu_4(\mu\text{-}H)_4(OH_2)_3$, **18**	C_3	-32.5	-10.8
cyclo-$Cu_4(\mu\text{-}H)_4(NH_3)$, **19**	C_s	-11.7	-11.7
cyclo-$Cu_4(\mu\text{-}H)_4(NH_3)_2$, **20**	C_{2h}	-22.8	-11.4
$Cu_4(\mu\text{-}H)_4(NH_3)_4$, **21**	T_d	-58.5	-14.6
cyclo-$Cu_4(\mu\text{-}H)_4(PH_3)$, **22**	C_s	-9.0	-9.0
cyclo-$Cu_4(\mu\text{-}H)_4(PH_3)_2$, **23**	C_{2h}	-19.1	-9.6
cyclo-$Cu_4(\mu\text{-}H)_4(PH_3)_3$, **24**	C_s	-19.7	-6.6
$Cu_4(\mu\text{-}H)_4(PH_3)_3$, **25**	C_{3v}	-51.2	-17.1
cyclo-$Cu_4(\mu\text{-}H)_4(PH_3)_4$, **26**	D_{2d}	-22.0	-5.5
$Cu_4(\mu\text{-}H)_4(PH_3)_4$, **27**	T_d	-66.8	-16.7

Footnotes: a). $\Delta E_1 = E(cyclo\text{-}Cu_4(\mu\text{-}H)_4Nuc_n) - \{E[cyclo\text{-}Cu_4(\mu\text{-}H)_4] + nE(Nuc)\}$.

It can be seen that all nucleophiles, Nuc, are loosely associated with the parent *cyclo*-$Cu_4(\mu\text{-}H)_4$ molecule, the estimated interaction energies were found in the range of -0.8 to -21.8 kcal/mol. In particular, dinitrogen, N_2, is the most loosely coordinated ligand with the Cu(I) centers, with interaction energies in the range of -0.8 to -8.4 kcal/mol. On the other hand, carbonyl, CO, forms stronger Cu-CO coordination bonds with bond energies in the range of -6.6 to -21.8 kcal/mol. The estimated Cu-OH_2, Cu-NH_3 and Cu-PH_3 bond energies were found in the ranges of -4.1 to -6.1, -11.4 to -14.6 and -5.5 to -17.1 kcal/mol, respectively. All nucleo-

Table 2. The Hardness, η, and the Electrophilicity Index, ω, of the *cyclo*-$Cu_4(\mu\text{-}H)_4Nuc_n$ (n = 1-4; Nuc = N_2, CO, H_2O, NH_3 and PH_3) Clusters Computed at the B3LYP/6-311+G(d,p) Level

Cluster	η [eV]	ω [eV]
cyclo-$Cu_4(\mu\text{-}H)_4(N_2)$, **1**	2.15	2.12
cyclo-$Cu_4(\mu\text{-}H)_4(N_2)_2$, **2**	1.98	2.16
$Cu_4(\mu\text{-}H)_4(N_2)_3$, **3**	1.93	1.95
$Cu_4(\mu\text{-}H)_4(N_2)_4$, **4**	1.96	2.00
cyclo-$Cu_4(\mu\text{-}H)_4(CO)$, **5**	1.98	2.47
cyclo-$Cu_4(\mu\text{-}H)_4(CO)_2$, **6**	1.85	2.52
cyclo-$Cu_4(\mu\text{-}H)_4(CO)_2$, **7**	1.92	2.52
$Cu_4(\mu\text{-}H)_4(CO)_2$, **8**	1.94	2.08
cyclo-$Cu_4(\mu\text{-}H)_4(CO)_3$, **9**	2.04	2.39
$Cu_4(\mu\text{-}H)_4(CO)_3$, **10**	1.96	2.19
cyclo-$Cu_4(\mu\text{-}H)_4(CO)_3$, **11**	1.72	2.59
$Cu_4(\mu\text{-}H)_4(CO)_4$, **12**	2.02	2.36
cyclo-$Cu_4(\mu\text{-}H)_4(CO)_4$, **13**	2.03	2.47
cyclo-$Cu_4(\mu\text{-}H)_4(CO)_4$, **14**	1.78	2.46
cyclo-$Cu_4(\mu\text{-}H)_4(OH_2)$, **15**	2.41	1.41
cyclo-$Cu_4(\mu\text{-}H)_4(OH_2)_2$, **16**	2.24	1.22
cyclo-$Cu_4(\mu\text{-}H)_4(OH_2)_3$, **17**	2.13	1.07
$Cu_4(\mu\text{-}H)_4(OH_2)_3$, **18**	1.73	1.19
cyclo-$Cu_4(\mu\text{-}H)_4(NH_3)$, **19**	2.36	1.29
cyclo-$Cu_4(\mu\text{-}H)_4(NH_3)_2$, **20**	2.15	1.04
$Cu_4(\mu\text{-}H)_4(NH_3)_4$, **21**	1.44	0.68
cyclo-$Cu_4(\mu\text{-}H)_4(PH_3)$, **22**	2.34	1.53
cyclo-$Cu_4(\mu\text{-}H)_4(PH_3)_2$, **23**	2.15	1.36
cyclo-$Cu_4(\mu\text{-}H)_4(PH_3)_3$, **24**	1.95	1.22
$Cu_4(\mu\text{-}H)_4(PH_3)_3$, **25**	2.11	0.92
cyclo-$Cu_4(\mu\text{-}H)_4(PH_3)_4$, **26**	2.09	1.04
$Cu_4(\mu\text{-}H)_4(PH_3)_4$, **27**	2.12	0.84

philes are more strongly bonded in the 3D than the planar or bent structures. Moreover, the bond energies increase upon increasing the number of the coordinated nucleophiles.

We have also computed the heat of formation of the *cyclo*-$Cu_4(\mu\text{-}H)_4Nuc_4$ molecules upon tetramerization of their HCuL monomeric species according to the chemical equation:

$$4HCuNuc \rightarrow cyclo\text{-}Cu_4(\mu\text{-}H)_4Nuc_4$$

It was found that all formation processes are exothermic indicating that these species could be isolated in their cyclic tetrameric form within a supersonic jet. The estimated formation energies were found to be -76.3, -85.9, -45.1 and -77.1 kcal/mol for the $Cu_4(\mu\text{-}H)_4(N_2)_4$, $Cu_4(\mu\text{-}H)_4(CO)_4$,

Table 3. The NICS Values (in ppm) Calculated at the Ring Center, NICS(0), 1.0 Å Above the Ring Center, NICS(1) and the Corresponding zz-Components $NICS_{zz}(0)$ and $NICS_{zz}(1)$ of the Shielding Tensor Element, for the *cyclo*-$Cu_4(\mu\text{-}H)_4Nuc_n$ (n = 1-4; Nuc = N_2, CO, H_2O, NH_3 and PH_3) Molecules Computed at the GIAO/ B3LYP/6-311+G(d,p) Level

Cluster	NICS(0)	NICS(1)	$NICS_{zz}(0)$	$NICS_{zz}(1)$
cyclo-$Cu_4(\mu\text{-}H)_4(N_2)$, **1**	-6.9	-3.1	12.5	-0.5
cyclo-$Cu_4(\mu\text{-}H)_4(N_2)_2$, **2**	-7.6	-5.5	14.9	-0.1
$Cu_4(\mu\text{-}H)_4(N_2)_3$, **3**	-22.7	-	-	-
$Cu_4(\mu\text{-}H)_4(N_2)_4$, **4**	-21.2	-	-	-
cyclo-$Cu_4(\mu\text{-}H)_4(CO)$, **5**	-9.3	-4.1	10.1	-2.2
cyclo-$Cu_4(\mu\text{-}H)_4(CO)_2$, **6**	-8.6	-3.3	15.5	-1.3
cyclo-$Cu_4(\mu\text{-}H)_4(CO)_2$, **7**	-8.6	-3.9	5.5	-2.3
$Cu_4(\mu\text{-}H)_4(CO)_2$, **8**	-22.4	-	-	-
cyclo-$Cu_4(\mu\text{-}H)_4(CO)_3$, **9**	-9.9	-	-	-
$Cu_4(\mu\text{-}H)_4(CO)_3$, **10**	-19.7	-	-	-
cyclo-$Cu_4(\mu\text{-}H)_4(CO)_3$, **11**	-	-	-	-
$Cu_4(\mu\text{-}H)_4(CO)_4$, **12**	-17.4	-	-	
cyclo-$Cu_4(\mu\text{-}H)_4(CO)_4$, **13**	-10.7	-	-	-
cyclo-$Cu_4(\mu\text{-}H)_4(CO)_4$, **14**	-	-	-	-
cyclo-$Cu_4(\mu\text{-}H)_4(OH_2)$, **15**	-6.9	-3.1	12.2	-0.7
cyclo-$Cu_4(\mu\text{-}H)_4(OH_2)_2$, **16**	-7.0	-2.9	14.3	-0.1
cyclo-$Cu_4(\mu\text{-}H)_4(OH_2)_3$, **17**	-6.9	-3.2	12.6	-0.3
$Cu_4(\mu\text{-}H)_4(OH_2)_3$, **18**	-16.0	-	-	-
cyclo-$Cu_4(\mu\text{-}H)_4(NH_3)$, **19**	-7.0	-3.1	12.3	-0.8
cyclo-$Cu_4(\mu\text{-}H)_4(NH_3)_2$, **20**	-7.2	-2.7	16.2	0.1
$Cu_4(\mu\text{-}H)_4(NH_3)_4$, **21**	-20.7	-	-	-
cyclo-$Cu_4(\mu\text{-}H)_4(PH_3)$, **22**	-6.8	-3.0	13.0	-0.5
cyclo-$Cu_4(\mu\text{-}H)_4(PH_3)_2$, **23**	-7.1	-2.7	16.9	0.2
cyclo-$Cu_4(\mu\text{-}H)_4(PH_3)_3$, **24**	-6.7	-3.0	13.2	-0.2
$Cu_4(\mu\text{-}H)_4(PH_3)_3$, **25**	-17.8	-	-	-
cyclo-$Cu_4(\mu\text{-}H)_4(PH_3)_4$, **26**	-8.0	-3.9	10.5	2.6
$Cu_4(\mu\text{-}H)_4(PH_3)_4$, **27**	-14.5	-	-	-

$Cu_4(\mu\text{-}H)_4(NH_3)_4$ and $Cu_4(\mu\text{-}H)_4(PH_3)_4$ complexes, respectively. It is worth to be noticed that fully substituted complexes involving the OH_2 nucleophile was not possible to be located on the PES either as local minima or saddle points.

3.3. The Hardness and Electrophilicity of the *cyclo*-$Cu_4(\mu\text{-}H)_4Nuc_n$ (n = 1-4; Nuc = N_2, CO, H_2O, NH_3 and PH_3) Molecules

The hardness and electrophilicity parameters of the *cyclo*-$Cu_4(\mu\text{-}H)_4Nuc_n$ (n = 1-4; L = N_2, CO, H_2O, NH_3 and PH_3) molecules are compiled in Table **2**.

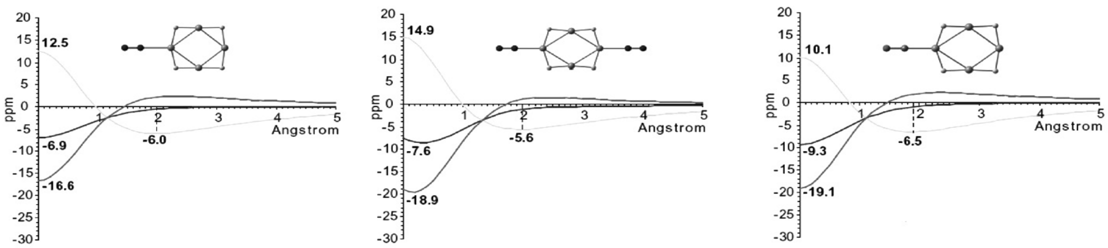

1 (C_{2v}) *cyclo*-$Cu_4(\mu_2$-H)4(η^1-N_2) **2** (D_{2h}) *cyclo*-$Cu_4(\mu_2$-H)4(η^1-$N_2)_2$ **5** (C_{2v}) *cyclo*-$Cu_4(\mu_2$-H)4(η^1-CO)

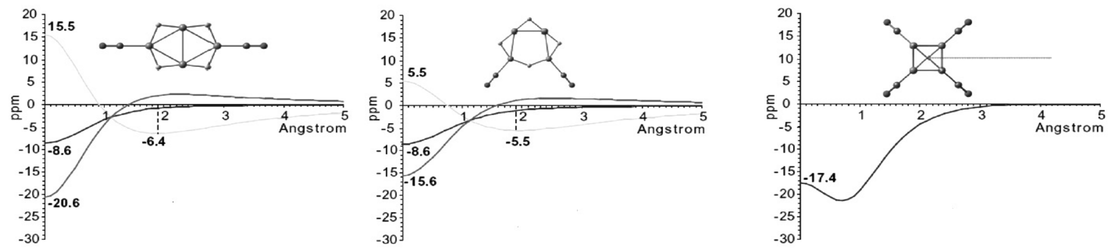

6 (D_{2h}) *cyclo*-$Cu_4(\mu_2$-H$)_4(\eta^1$-CO$)_2$ **7** (C_{2v}) *cyclo*-$Cu_4(\mu_2$-H$)_4(\eta^1$-CO$)_2$ **10** (C_{3v}) *cyclo*-$Cu_4(\mu_3$-H$)_4(\eta^1$-CO$)_3$

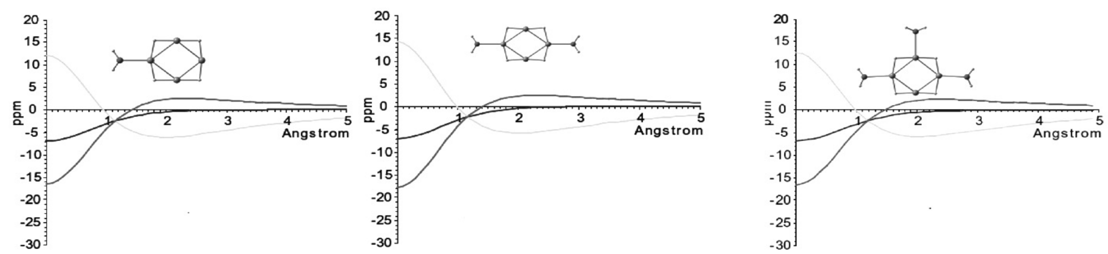

15 (C_s) *cyclo*-$Cu_4(\mu_2$-H$)_4(OH_2)$ **16** (C_{2h}) *cyclo*-$Cu_4(\mu_2$-H$)_4(OH_2)_2$ **17** (C_s) *cyclo*-$Cu_4(\mu_2$-H$)_4(OH_2)_3$

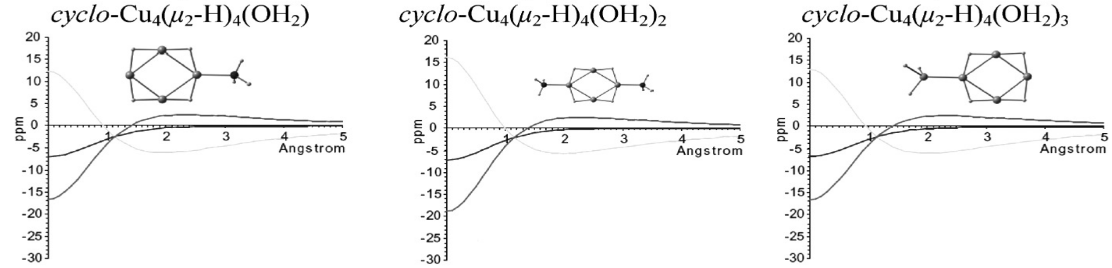

18 (C_s) *cyclo*-$Cu_4(\mu_2$-H$)_2(\mu_3$-H$)_2(NH_3)$ **19** (C_{2h}) *cyclo*-$Cu_4(\mu_2$-H$)_4(NH_3)_2$ **21** (C_s) *cyclo*-$Cu_4(\mu_3$-H$)_4(PH_3)$

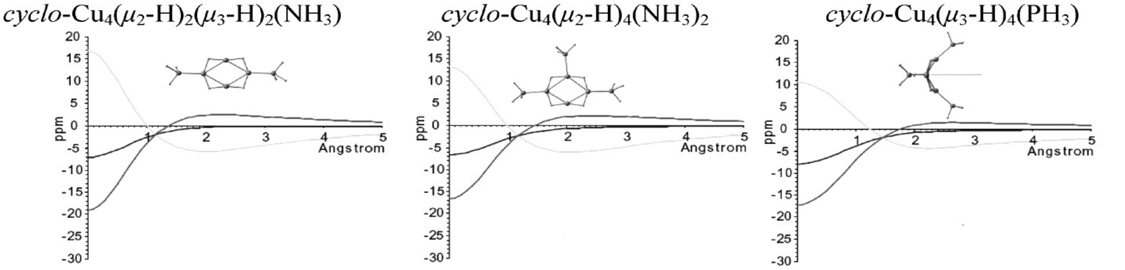

22 (C_{2h}) *cyclo*-$Cu_4(\mu_2$-H$)_4(PH_3)_2$ **23** (C_s) *cyclo*-$Cu_4(\mu_2$-H$)_4(PH_3)_2$ **25** (D_{2d}) *cyclo*-$Cu_4(\mu_2$-H$)_4(PH_3)_4$

Fig. (3). The NICS scan pictures for the isotropic σ^{iso}(bq) ——, σ^{zz}(bq_{out}) ——, and σ (bq_{in}) —— tensors of representative *cyclo*-$Cu_4(\mu$-H$)_4Nuc_n$ (n = 1-4; Nuc = N_2, CO, OH_2, NH_3, PH_3) molecules computed at the B3LYP/6-311+G(d,p) level.

The high stability of the *cyclo*-$Cu_4(\mu$-H$)_4L_n$ (n = 1-4; L = N_2, CO, H_2O, NH_3 and PH_3) molecules is also reflected on the estimated high values of hardness, η defined as $\eta = (\varepsilon_{LUMO} - \varepsilon_{HOMO})/2$ [21]. Generally, according to the computed η values the stability of the *cyclo*-$Cu_4(\mu$-H$)_4L_n$ molecules decreases upon increasing the degree of substitution. According to the hardness, the stability of the *cyclo*-$Cu_4(\mu$-

$H)_4L_n$ molecules follows the trend: $H_2O > NH_3 > PH_3 > N_2 >$ CO.

The electrophilicity index ω (Table **2**) computed [22] as $\omega = \mu^2/2\eta$, where μ and η are the chemical potential and hardness respectively, given approximately by the expressions $\mu = (\varepsilon_{LUMO} + \varepsilon_{HOMO})/2$ and $\eta = (\varepsilon_{LUMO} - \varepsilon_{HOMO})$ measures the electrophilic character of the four-member ring and consequently is a measure of the aromatic character of the ring. It can be seen that the electrophilicity decreases upon increasing substitution. The electrophilicity of the four-member ring core structure follows the trend: CO > N_2 >PH_3 > H_2O > NH_3. The lowering of the electrophilicity of the *cyclo*-$Cu_4(\mu\text{-}H)_4(OH_2)_{1\text{-}4}$ and *cyclo*-$Cu_4(\mu\text{-}H)_4(NH_3)_{1\text{-}4}$ species involving the pure σ-donor H_2O and NH_3 ligands could be attributed to the increase of the π-electron density on the four-membered Cu_4 ring.

3.4. Aromacity/Antiaromaticity of the *cyclo*-$Cu_4(\mu\text{-}H)_4$ Nuc_n (n = 1-4; Nuc = N_2, CO, H_2O, NH_3 and PH_3) Molecules

Planarity, high stability, bond length equalization and hardness are conventionally good indicators of aromaticity, but this is restrictive in many examples. In order to quantify the aromaticity/antiaromaticity of the clusters we applied the magnetic criterion, viz. nucleus-independent chemical shift (NICS), proposed by Schleyer *et al.* [20]. Negative (diatropic) NICS values indicate aromaticity, while positive (paratropic) values imply antiaromaticity. NICS(0) is usually computed at the ring centers, but also can be calculated at certain distance above or below the center of the ring; the NICS obtained at 1 Å above the ring centroid, NICS(1) as well as the $NICS_{zz}(1)$ tensor component are considered to be better aromaticity indices than NICS(0) [23,24]. The NICS(0), NICS(1), $NICS_{zz}(0)$ and $NICS_{zz}(1)$ are given in Table **3**.

To get a better insight into the origin of the aromaticity of the *cyclo*-$Cu_4(\mu\text{-}H)_4Nuc_n$ (n = 1-4; Nuc = N_2, CO, H_2O, NH_3 and PH_3) molecules we applied the recently proposed NICS scan procedure, which is based on scanning the NICS, σ(bq), values over a distance R and dissecting them into in-plane, $\sigma^{iso}(bq_{in})$ and out-of-plane, $\sigma^{zz}(bq_{out})$ components [25,26]. The NICS scan pictures for the isotropic $\sigma^{iso}(bq)$, $\sigma^{zz}(bq_{out})$, and $\sigma(bq_{in})$ tensors of representative molecules are given in Fig. (**3**).

It can be seen that all *cyclo*-$Cu_4(\mu\text{-}H)_4Nuc_n$ (n = 1-4; Nuc = N_2, CO, H_2O, NH_3 and PH_3) molecules exhibit negative NICS(0) values, only slightly affected by the degree of substitution. On the other hand, the aromaticity of the 3D tetrahedral Cu_4 core structures, the so-called spherical aromaticity, is higher than the aromaticity of the isomeric planar structures. Noteworthy is the antiaromaticity of all planar rings suggested by the positive $NICS_{zz}(0)$ values. The $NICS_{zz}(1)$ values become negative, but very small suggestive of non aromaticity for these systems. However, the $NICS_{zz}$ component acquires negative values (in the range of -5.6 to -10.5 ppm) in a distance of 1.6 – 1.8 Å above the ring plane. Considering that the $NICS_{zz}$ component is a better index of aromaticity [23,24] we could say that all planar structures keep the aromatic character of the parent *cyclo*-$Cu_4(\mu\text{-}H)_4$ molecule.

4. CONCLUSIONS

The results can be summarized as follows:

Repeated nucleophilic attack of the base aromatic *cyclo-Cu (μ-) molecule by a number of nucleophiles affords* novel *cyclo*-$Cu_4(\mu\text{-}H)_4Nuc_n$ (n = 1-4; Nuc = N_2, CO, H_2O, NH and PH) traces. Depend upon the nature of the nucleophile and the degree of substitution, the *cyclo*-$Cu_4(\mu\text{-}$H) Nuc traces contains planar, bend or 3D tetrahedral shapes. The 3D shapes are getting for the higher values of substitution, mainly is in the Cu (μ-) Nuc moleculs.

All *cyclo*-$Cu_4(\mu\text{-}H)_4Nuc_n$ (n = 1-4; Nuc = N_2, CO, H_2O, NH and PH) molecules are shows to be bound with their dissociation according to the respective dislocation pattern.

$$cyclo\text{-}Cu_4(\mu\text{-}H)_4Nuc_n \rightarrow cyclo\text{-}Cu_4(\mu\text{-}H)_4 + nNuc$$

The energy of the M-Nuc involvement follows the trend: NH > CO > PH > H O> N . The computed bond dilocation energies for the Cu-Nuc bonds are in the range of -0.8 to -21.8 kcal/mol.

The attachment of bond between the cyclo-Cu (μ-) Nuc molecules is characterized by a common ring shaped electron density, which is made by highly localized , - and -type MOs.

All cyclo-Cu (μ-) Nuc molecules in their planar, bend and 3D tetrahedral shapes shows negative NICS(0) values, and so keep the aromatic character of the parent cyclo-Cu (μ-) molecule.
.

ACKNOWLEDGEMENTS

This work was sponsored by the Greek Ministry of Education (EPEAK, PYTHAGORAS II, Project 77).

REFERENCES

[1] (a) A. C. Tsipis, and C. A. Tsipis, "Hydrometal Analogues of Aromatic Hydrocarbons: A New Class of Cyclic Hydrocoppers(I)", *J. Am. Chem. Soc.,* vol. 125, pp. 1136-1137, February 2003. (b) C. A. Tsipis, E. E. Karagiannis, P. F. Kladou, and A. C. Tsipis, "Aromatic Gold and Silver 'Rings': Hydrosilver(I) and Hydrogold(I) Analogues of Aromatic Hydrocarbons", *J. Am. Chem. Soc.,* vol. 126, pp. 12916-12929, October 2004. (c) A. C. Tsipis, and C. A. Tsipis, "Ligand-Stabilized Aromatic Three-Membered Gold Rings And Their Sandwichlike Complexes", *J. Am. Chem. Soc.,* vol. 127, pp. 10623-10638, August 2005. (d) C. A. Tsipis, "DFT study of 'all-metal' aromatic compounds", *Coord. Chem. Rev.*, vol. 249, pp. 2740-2762, December 2005.

[2] V. W. W. Yam, W. K.-M. Fung, and K.-K. Cheung, "Luminecence Behavior of Polynuclear Alkynylcopper(I) Phosphines", *J. Cluster Sci.*, vol. 10, pp. 37-69, March 1999.

[3] M. M. Olmstead, and P. P. Power, "Isolation and first structural characterization of dimethyl sulfide solvates of phenyllithium, phenylcopper, and lower and higher order lithium phenylcuprate reagents", *J. Am. Chem. Soc.*, vol. 112, pp. 8008-8014, October 1990.

[4] B. Lenders, D. M. Grove, W. J. J. Smeets, P. van der Sluis, A. L. Spek, and G. van Koten, "Use of dimethyl sulfide in organocopper chemistry: X-ray crystal structures of *cyclo*-tetrakis(μ-2-methylphenyl)bis(dimethy lsulfide)tetracopper(I) and of the Polymeric copper bromide adduct bromo(dimethyl sulfide)copper(I)", *Organometallics*, vol. 10, pp. 786-791, March 1991.

[5] E. M. Meyer, S. Gambarotta, C. Floriani, A. Chiesi-Villa, and C. Guastinit, "Polynuclear aryl derivatives of group 11 metals: synthesis solid state-solution structural relationship, and reactivity with phosphines", *Organometallics*, vol. 8, pp. 1067-1079, April 1989.

[6] B. Schiemenz, and P. P. Power, "Synthesis of sterically encumbered terphenyls and characterization of their metal derivatives

$Et_2OLiC_6H_3$-2,6-$Trip_2$ and $Me_2SCuC_6H_3$-2,6-$Trip_2$ (Trip = 2,4,6-i-$Pr_3C_6H_2^-$)", *Organometallics*, vol. 15, pp. 958-964, February 1996.

[7] H. Eriksson, and M. Håkansson, "Mesitylcopper: Tetrameric and Pen-tameric", *Organometallics*, vol. 16, pp. 4243-4244, September 1997.

[8] H. Eriksson, M. Örtendhal, and M. Håkansson, "Arylmagnesium to Arylcopper Conversion Monitored by Solid State Characterization of Halide Intermediates. Synthesis of Homoleptic (o-Vinylphenyl) copper", *Organometallics*, vol. 15, pp. 4823-4831, October 1996.

[9] M. Håkansson, H. Eriksson, and S. Jagner, "Pentamethylphenyl-copper(I): a square-planar tetranuclear cluster", *Inorg. Chim. Acta*, vol. 277, pp. 233-236, August 1998.

[10] M. Håkansson, H. Eriksson, B. A. Åhman, and S. Jagner, "Tetrameric trienylcopper and pentanuclear trienylcuprate", *J. Organomet. Chem.*, vol. 595, pp. 102-108, January 2000.

[11] M. Håkansson, H. Eriksson, and S. Jagner, "Tetranuclear Homoleptic copper and silver aryls: 2,4,6-Triethylphenylcopper and 2,4,6-triethylphenylsilver", *Inorg. Chim. Acta*, vol. 359, pp. 2519-2524, May 2006.

[12] P. L. Stiles, and R. E. Miller, "Structures and Bonding Nature of Small Monoligated Copper Clusters (HCN-Cu_n, n = 1-3) through High-Resolution Infrared Spectroscopy and Theory", *J. Phys. Chem. A*, vol. 110, pp. 10225-10235, August 2006.

[13] X.-J. Liu, X. Zhang, K.-L. Han, X.-P. Xing, S.-T. Sun, and Z.-C. Tang, "Experimental and Theoretical Study on the Structure and Formation Mechanism of $[C_6H_5Cu_m]^-$ (m = 1-3)", *J. Phys. Chem. A*, vol. 111, pp. 3248, May 2007.

[14] M. J. Frisch, G. W. Trucks, H. B. Schlegel, *et al., Gaussian 03*, revision A1; Gaussian, Inc.: Pittsburgh, PA, 2003.

[15] A. D. Becke, "Density-functional thermochemistry. I. The effect of the exchange-only gradient correction", *J. Chem. Phys.*, vol. 96, pp. 2155-2160, February 1992.

[16] A. D. Becke, "Density-functional thermochemistry. III. The role of exact exchange"*J. Chem. Phys.*, vol. 98, pp. 5648-5652, April 1993.

[17] C. Lee, W. Yang, and R. G. Parr, "Development of the Colle-Salvetti correlation-energy formula into a finctional of the electron density", *Phys. Rev. B*, vol. 37, pp. 785-789, January 1988.

[18] H. B. Schlegel, "Optimization of Equilibrium Geometries and Transition Structures", *J. Comput. Chem.*, vol. 3, pp. 214-218, Summer 1982.

[19] J. Gauss, "Effects of electron correlation in the calculation of nuclear magnetic resonance chemical shifts" *J. Chem. Phys.*, vol. 99, pp. 3629-3643, September 1993.

[20] P. V. R. Schleyer, C. Maerker, A. Dransfeld, H. Jiao, and N. J. R. v. R. Hommes, **"**Nucleus-Independent Chemical Shifts: A Simple and Efficient Aromaticity Probe", *J. Am. Chem. Soc.*, vol. 118, pp. 6317-6318, July 1996.

[21] R. G. Pearson, "Absolute Electronegativity and Hardness Correlated with Molecular Orbital Theory", *Proc. Natl. Acad. Sci. U.S.A.*, vol. 83, pp. 8440-8441, November 1986.

[22] R. G. Parr, L. v. Szentpaly, and S. Liu, **"**Electrophilicity Index", *J. Am. Chem. Soc.*, vol. 121, pp. 1922-1924, March 1999.

[23] P. v. R. Schleyer, M. Monoharan, H. J. Jiao, and F. Stahl, "The Acenes: Is There a Relationship between Aromatic Stabilization and Reactivity?", *Org. Lett.*, vol. 3, pp. 3643-3646, November 2001.

[24] C. Corminboeuf, T. Heine, G. Seifert, P. v. R. Schleyer, "Induced magnetic fields in aromatic [n]-annulenes-interpretation of NICS components", *Phys. Chem. Chem. Phys.*, vol. 6, pp. 273-276, January 2004.

[25] (a) A. Stanger, "Nucleus-Independent Chemical Shifts (NICS): Distance Dependence and Revised Criteria for Aromaticity and Antiaromaticity", *J. Org. Chem.*, vol. 71, pp. 883-893, February 2006. (b) A. Stanger, "Can Substituted Cyclopentadiene Become Aromatic or Antiaromatic?", *Chem. Eur. J.*, vol. 12, pp. 2745-2751, March 2006.

[26] (a) J. Poater, J. M. Bofill, P. Alemany, and M. Solà, "Role of Electron Density and Magnetic Couplings on the Nucleus-Independent Chemical Shift (NICS) Profiles of [2.2]paracyclophane and Related Species", *J. Org. Chem.*, vol. 71, pp. 1700-1702, February 2006. (b) J. O. C. Jiménez-Halla, E. Matito, J. Robles, and M. Solà, "Nucleus-independent chemical shift (NICS) profiles in a series of monocyclic planar inorganic compounds", *J. Organometal. Chem.*, vol. 691, pp. 4359-4366, October 2006.

Analysis of Fluid Flow in a Compact Phase Separator

Pili Kumari Sahoo, *Department of Mechanical Engineering, Aryan Institute of Engineering & Technology, Bhubaneswar, p.kumari4gmail.com*
Ranjan Kumar, *Department of Mechanical Engineering, NM Institute of Engineering & Technology, Bhubaneswar, kumarranjan75@gmail.com*
Saswati Nayak, *Department of Mechanical Engineering, Capital Engineering College, Bhubaneswar, saswatinayak2574@gmail.com*
Bipash Mohanty, *Department of Civil Engineering, Capital Engineering College, Bhubaneswar, bipashmohanty784@gmail.com*

Abstract: A compact separator consisting of two volutes (inlet and outlet) connected with a cylindrical chamber is pro-posed as a cost-effective alternative to conventional separators. The separator has a wide range of applications in the oil and gas industry. It has the advantages of being compact, free of the effect of motion on floating platforms, more tolerant to flow fluctuations and can be modularised in series to remove liquid or gas carry-over. In order to optimize the system performance a series of CFD simulations is programmed covering a wide range of inlet flows (phase mixing percentage). The starting point will be the CFD analysis of the liquid-gas flow, in various inlet flow patterns. The present paper pre-sents the results of the initial two-phase separation process simulation, carried out using the FLUENT commercial CFD code in terms of pressure, velocity and volume fraction distribution for both phases and all over the separator. The cross analysis of the results leads to a better understanding of the two-phase flow and separation inside each component and aids the research team to set up an experimental procedure up and proceed to the next step of the research programme.

INTRODUCTION

In the study of two-phase flow in pipes, discussion regarding entrainment, often refer to liquid droplets travelling in the gas or vapour core of annular two phase flow. The opposite case, that is, bubbles travelling in the liquid film, appears to be just as frequent and suitable for detailed characterization. In the case where separation of the phases is needed, separators are used to “separate” the flow from the secondary phase. A novel separator consisting of two involutes (inlet and outlet) connected with a cylindrical chamber is proposed as a cost-effective alternative to conventional separators.

An initial numerical approach has been performed by Ghiaus and Margaris [1] using PHOENICS code, submitting a qualitative insight in the flow field of the novel separator. Similar reports on centrifugal (conventional) separators operating at the same conditions have been reported by Oropeza-Vazquez *et al.* [2] (experimental and modelling) and Barbat *et al.* [3] (numerical) and give an insight of the capabilities of the devices the novel separator is supposed to replace.

The purpose of the present study is to perform a numerical investigation of the two-phase flow (water - air) inside a compact separator, using FLUENT code, submitting quantitative data, in order to analyze and to be able to better-design the separator for minimum pressure drop and maximum separation efficiency. In the two extreme cases, it is assumed that a primary liquid phase (water) is carrying a secondary gas phase (air - bubbles) or a primary gas phase (air) is carrying a secondary liquid phase (water – droplets). The first one is to be analysed in the present paper.

THEORY

CFD Methods for Two-Phase Flow: Modelling the two-phase flow (water – air) requires primarily to recognize and define the continuous primary phase and the dispersed secondary phase. The secondary phase forms bubbles (air) or droplets (water) which interact with the primary phase flow. The quantity describing the presence of a phase at any point in the flow domain is the volume fraction. It is defined as the ratio of the volume occupied by the phase under consideration in an arbitrary small control volume around the point.

$$vf = \lim_{\delta V \to 0} \frac{\delta V_{phase}}{\delta V} \tag{1}$$

Currently there are two approaches for the numerical calculation of multiphase flows: Euler-Lagrange approach and Euler-Euler approach.

Euler – Lagrange Approach: The method also referred as Lagrangian tracking method, treats the fluid as a continuum by solving the time-averaged Navier-Stokes equations while the dispersed phase is solved by tracking a large number of particles, droplets or bubbles through the calculated flow field. In order to capture the multiphase flow by using a Lagrange tracking method, the secondary (dispersed) phase should occupy a low volume fraction (although $\dot{m}_{particles} \geq \dot{m}_{fluid}$ is acceptable), the size of the particles should be small compared to the characteristic length of the flow and the surface effects should be considered of low importance. The Discrete Phase Model (DPM) implemented in FLUENT 6 [4] is an Euler-Lagrange approach model that tracks individual particles of the secondary phase in a continuous flow of the primary phase.

Euler – Euler Approach: In the Euler – Euler approach to a multiphase flow problem, the carrier phase and the dispersed phase(s) are considered as interpenetrating continua for which flow equations are solved. It is assumed that the volume of one phase cannot be occupied by another phase.

This assumption is expressed by the volume fraction of the phase. Three models of this kind are implemented in FLUENT 6, the Volume of Fluid model, the Eulerian model and the Mixture model.

Volume of Fluid (VOF) Model [4]**:** This is a surface-tracking technique applied to a fixed Eulerian mesh. It solves a single set of momentum equations for a mixture of two or more immiscible fluids. Applications of the model include stratified flows, free surface flows, filling, sloshing, motion of large bubbles in a fluid, motion of liquid after dam break, prediction of jet break-up and the steady or transient tracking of any liquid-gas interface. This model is not suitable for the present application.

Eulerian Multiphase Model [4]**:** The model solves sets of momentum equations for each phase of the flow. Coupling is achieved through the pressure and inter-phase exchange coefficients. Applications of the model include bubble columns, risers, particle suspension and fluidized beds The Eulerian Multiphase Model solves the following equations:

1. Continuity equations for each secondary phase. They will determine the phasic volume fraction field for the primary phase, coupled with the condition that all volume fractions sum to one.
2. Momentum equations for each phase. The pressure field is the only field variable shared by all the phases. Besides the traditional terms of a momentum transport equation, these equations contain terms to account for: interphase forces modeled through the interphase exchange coefficients K_{pq}, based on a selection of drag models for the particulate structures;
3. Turbulence model equations (k and ε). Since the Eulerian Multiphase Model accounts separately for the momentum of each phase, it will be able to capture most of the complex physics involved in the phase separator for the whole range of problem parameters. The computational expense though, is higher when using the Eulerian Multiphase model. Moreover, with the Eulerian model, solution behavior is more non-linear and convergence is achieved in a larger number of iterations for all the sets of momentum equations considered in the problem.

Multiphase Mixture Model [4, 5]**:** The model solves a single set of momentum equations for the mixture phase, coupled with a model for the slip velocity between the carrier and the dispersed phases. It applies to fluid or particulate phases and the phases can be interpenetrating. For homogenous multiphase flows, this model can be used without the relative velocities for the secondary phase(s). Applications of the model include particle-laden flows with low loading, bubbly flows sedimentation and flows in cyclone separators.

The mixture model uses a single-fluid approach. It allows the phases to be interpenetrating and move at different velocities. It solves the momentum equation for the mixture and the volume fraction equation for the secondary phases. If the phases are moving at different velocities it solves algebraic expressions for the relative velocities.

The Mixture model solves the following equations [4, 5]:

- Continuity equation: At any point in space a mixture fluid can be defined by weighting the properties and field quantities of phases with the local volume fraction values.

$$\frac{\vartheta}{\vartheta t}\left(\rho_m\right)+\nabla\cdot\left(\rho_m\,\vec{\upsilon}_m\right)=\dot{m} \tag{2}$$

- Momentum equation:

$$\frac{\vartheta}{\vartheta t}(\rho_m\vec{\upsilon}_m)+\nabla\cdot(\rho_m\vec{\upsilon}_m\vec{\upsilon}_m)=-\nabla p+$$

$$\nabla\cdot\left[\mu_m\left(\nabla\upsilon_m+\nabla\vec{\upsilon}_m^{T}\right)\right]+$$

$$+\rho_m\vec{g}+\vec{F}+\nabla\cdot\left(\sum_{k=1}^{n}\alpha_k\rho_k\,\vec{\upsilon}_{dr,k}\,\vec{\upsilon}_{dr,k}\right) \tag{3}$$

- Slip Velocity: The area of application for the Mixture Model is restricted to multiphase flows in which the secondary phase (index p - *particulate*) structures reach equilibrium with the surrounding primary phase (index q) in a small relaxation time interval τ_p. A simple algebraic relation between the slip(relative) velocity for each secondary phase is used to define different velocity fields for the phases:

$$\underbrace{\vec{\upsilon}_{qp}}_{\substack{slip\\velocity}}=\vec{\upsilon}_p-\vec{\upsilon}_q=\vec{\alpha}\cdot\tau_p\cdot\underbrace{\frac{\rho_p-\rho_m}{\rho_p}}_{\approx-\rho_m}\cdot\frac{1}{f_{drag}}=$$

$$\underbrace{\left[\vec{g}-(\vec{\upsilon}_m\cdot\nabla\vec{\upsilon}_m+\frac{\vartheta\vec{\upsilon}_m}{\vartheta t})\right]}_{\vec{a}=secondary\_phase\_acceleration}\cdot\underbrace{\left[\frac{\rho_p d_p^2}{18\mu_q}\right]}_{\tau_p=relaxation\_time}\cdot\frac{\rho_p-\rho_m}{\rho_p\cdot f_{drag}} \tag{4}$$

- Volume Fraction Equation for Secondary Phase:

$$\frac{\vartheta}{\vartheta t}(\alpha_p\rho_p)+\nabla\cdot(\alpha_p\rho_p\vec{\upsilon}_m)=-\nabla\cdot(\alpha_p\rho_p\vec{\upsilon}_{dr,p}) \tag{5}$$

- Turbulence model equations for the mixture. Three models can be used. Standard k-ε, Renormalization Group (RNG) k-ε and Realizable k-e. In the present study, since the flow in the separator features a swirling pattern, the RNG k-ε model will be used [4].

For small diameter droplets and / or small inlet velocities, the particulate relaxation time will be small compared to the characteristic flow time scale and the Mixture Model (computationally less expensive) can be used. However, for larger droplet sizes and / or for higher velocities at the inlet, the particulate relaxation time becomes comparable with the flow characteristic time scale, and the Eulerian Model must be used.

Model Criterion: A dimensionless criterion to decide if the Mixture Model can be used for a particular combination of parameters is based on the Stokes number *St*, defined as the ratio between the particulate relaxation time τ_p and the primary phase flow characteristic time scale $\tau_q=D/U$. Here, D and U are, respectively, the characteristic length scale and the characteristic velocity scale of the primary phase flow. Hence, Mixture Model has valid assumptions if *St<<1*.

Using estimation (4) for the particulate relaxation time, and considering that D=0.1 m, U=20 m/s, ρ_p=1.225 kg/m^3, μ_q=0.001003 kg/m.s, and d_p=10^{-4}, we conclude to the following:

$$St = \frac{\tau_p}{\tau_q} = \frac{\rho_p \cdot d_p^2}{18\mu_q \cdot (D/U)} \approx 13570 \times 10^{-8} << 1 \qquad (6)$$

Based on the above criteria, either Mixture or Eulerian multiphase model can be used for the phase separator cases. For the present study, the Mixture model is used because of the lower computational requirements.

Numerical Solutions – Control Volumes: Having produced the numerical analogue of the partial differential equations, a technique of numerical discretisation has to be adopted. Finding a unique model for the description of a multiphase flow remains a problem of fundamental research. Abbott and Basco [6] give a good survey of turbulence Modelling. Three numerical techniques, i.e. finite differences, finite elements and finite volumes, are generally used to calculate the solution of two phases flow equations. The later one is probably the most popular. This method is similar in some ways to the finite difference method. The method was developed specifically to solve equations of heat transfer and fluid flow and is described in detail by Patankar [7, 8].

Mesh Generation: A structured mesh was chosen for the geometry of the problem, consisting mainly of hexahedral cells. Excess time and effort were needed compared to the "unstructured mesh approach" but the results are considered as more accurate and reliable. The geometry was split in domains. Most of them were similar in geometry to a "skewed cube", and the structured meshing with hexahedra was straightforward. The cylindrical domains included in the geometry were meshed with hexahedra using the o-type technique, and the domains similar to a "bent" spine, were meshed with spine-cells. The later domains were the only containing cells with "low skewness". These were "refined" at the post-processing stage of the mesh-generation. Details about the geometry and the mesh are given in following paragraph.

NUMERICAL SIMULATION SET-UP

Modelling Assumptions for the Analysis of the Separator: As mentioned earlier, a computational method is proposed to analyze the flow inside a phase separator. The present analysis is based on the following assumptions:

(a). Air and water flows are incompressible within the separator.

(b). There is no inter-phase mass transfer between water and air.

(c). Air bubbles have an average diameter of 10^{-4} m (100 μ).

(d). The mixture flow is isothermal, i.e. water and air properties can be calculated at an average discharge pressure and temperature conditions. Gauge pressure is 1atm (101325 Pa) and Temperature 288.15 K.

(e). Steady state analysis is performed for the reported calculations.

(f). Gravity forces are acting downward along the vertical axis of the separator body (-z as seen in Fig. (**1**)), with a magnitude of 9.81 m/s^2.

(g). For the present study, primary phase is water and secondary phase is air with an inflow volume fraction of 10% (volume fraction=*vf*=0.1).

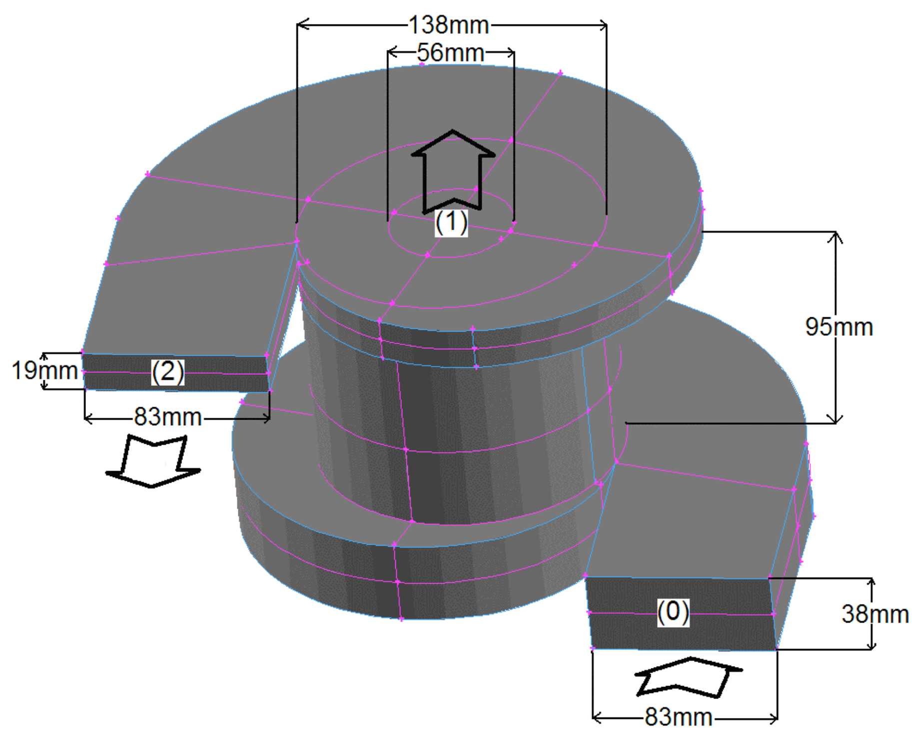

Fig. (1a). Outline of separator –Dimensions.

Fig. (1b). Picture of the separator.

Design Parameters: Fig. (**1a**) presents the schematic and dimensions of the separator. The novel separator consists of two volutes connected through a separation chamber. The inlet (bottom) volute has 38 mm thickness and a rectangular cross section entrance of 83X38 mm^2. The separation chamber has cylindrical shape with 95 mm height and 138 mm diameter. The outlet (top) volute has 19 mm thickness and two exits: one of rectangular cross section (83x19 mm^2) and the other of circular cross section (56 mm diameter). Both volutes have a "spiral arc" shape with dimensions shown in Fig. (**1a**). The mixture, on entry tangentially into the first volute, is spun around with high angular velocity creating low pressure in the core of the involute, which will practically suck-in the lighter phase of the mixture. Inside the separation chamber the lighter and denser phases are separated under the generated high "g" forces. The fluids then enter the second volute, where the dense phase is again spun around and exits tangentially through one exit, and the light phase is axially evacuated through the other.

Mesh Generation – Pre Processing: GAMBIT pre – processing CFD tool was used to produce the grid shown in Fig. (**2**). The geometry was split in domains and each domain was meshed separately. All domain meshes are structured consisting of tetrahedral components except for the two domains shown in circles in Fig. (**1a**), which consist of spines. The mesh produced with GAMBIT consisted of 36000 cells. The mesh quality considering skewness of cells (minimum skewness=0.8) is classified as good and sufficient for the present study.

Mesh Quality Assessment and Post Processing: The quality of the mesh plays a significant role in the accuracy and stability of the numerical computation. The attributes associated with mesh quality are node point distribution, smoothness, and skewness. In order to improve these attributes, the mesh created with GAMBIT was "inserted" in FLUENT for post processing. In order to avoid large truncation errors, the quality of the mesh should be high. As far as mesh quality is concerned, the refinement needed, concerned smoothness in order for the neighbouring cells to have similar volume and the aspect to be lower than 5:1. With a factor of 1.5 for the ratio of two neighbouring volumes and A<5:1 for the aspect, we resulted in a grid with 515628 cells, 1650616 faces and 620852 nodes. Having done that, the wall neighbouring cells complied with the criterion for the node point distribution [4]:

$$y_p = \sqrt{u_\infty / v \cdot x} \leq 1 \tag{7}$$

where:

y_p = distance to the wall from the adjacent cell centroid

u_∞ = free stream velocity (5-20 m/s)

v = kinematic viscosity [(0.001003 kg/m.s)/998 kg/m^3].

x= distance along the wall from the starting point of the boundary layer

Taking into consideration the geometry studied and the turbulent nature of the flow, a strong interaction of the mean flow and turbulence was expected. The numerical results for turbulent flows tend to be more susceptible to grid dependency than those for laminar flows. In the near-wall region, different mesh resolutions are required depending on the near-wall model being used. The non equilibrium wall function approach was implemented because of the phase separation phenomenon taking place. Because of the capability to partly account for the effects of pressure gradients and departure from equilibrium, the non-equilibrium wall functions are recommended for use in complex flows involving separation, where the mean flow and turbulence are subjected to severe pressure gradients and change rapidly. In such flows, improvements can be obtained, particularly in the prediction of wall shear (skin-friction coefficient) and heat transfer (Nusselt or Stanton number). Taking into account the above mentioned considerations, the resulting post processed grid meets all the "academic" requirements for producing grid independent numerical results. All the simulations for the present study were performed with that "post processed" Grid.

Flow Specification - Design parameters: The aim of the research program is to perform a series of CFD simulations with a "base case geometry" of the separator followed by laboratory experiments, in order to produce a "base-case database" of results concerning the separator performance. After having positive (experimental) feedback about the validity of the CFD approach followed during the present study, the optimal operating conditions of the separator based on the operating conditions will be chosen and we can then alter the design parameters improving the separator furthermore. Possible alterations can include a different height of the "connecting chamber", different ratios between all three surfaces of inflow(0), outflow(1) and outflow(2) and probably a cylinder attached to the air outflow(1) that extends inside the volume of the separator (as used in "centrifugal" separators). The Geometry of the Separator is fixed in the present study as presented in Fig. (**1**). Therefore the

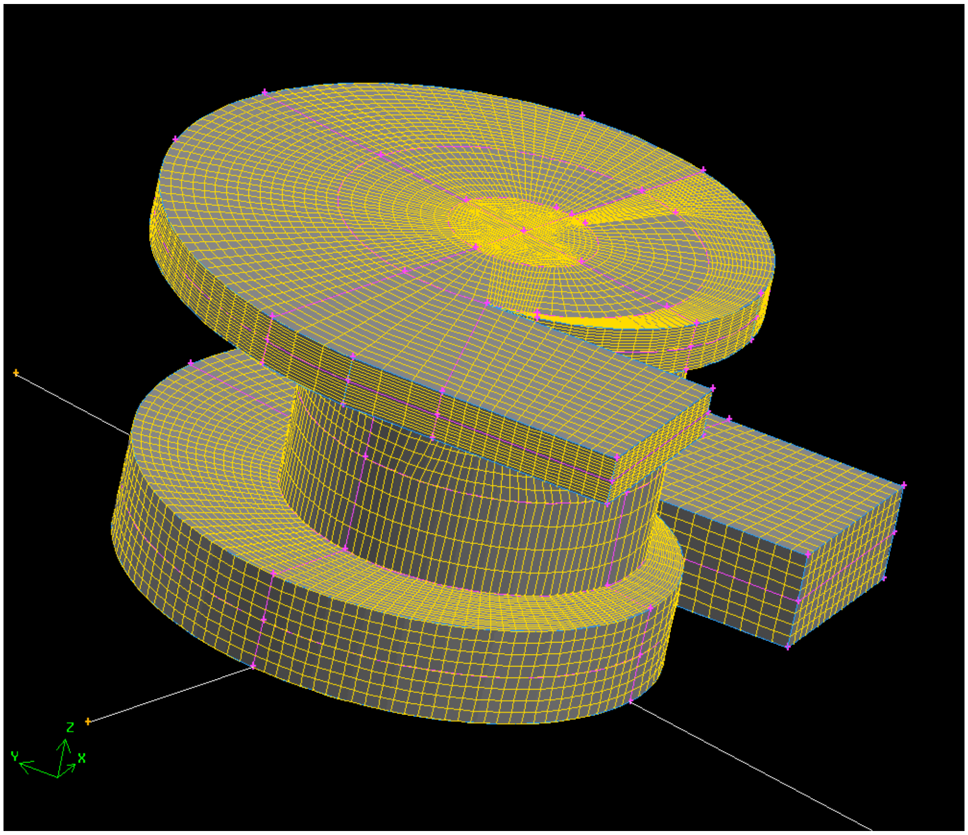

Fig. (2). Mesh created with GAMBIT.

design parameters do not have any influence to the separator performance.

Flow Specification - Operating Conditions: The basic aim of the present study is to identify the effects of the operating conditions on the performances of a certain design (base – case geometry) for the separator. This information is extracted from CFD runs with different values for velocity magnitude. CFD runs with different values for air volume fraction and bubble diameter at the mixture inlet will be performed only after the positive experimental verification of the present simulation approach.

Flow Specification - Separator Performance Quantities: The performance of the separator is described by the following quantities:

(1). Mass flow rate of air exiting through the "air-outlet" [outlet (1)].

(2) Mass flow rate of water exiting through the "water – outlet" [outlet (2)].

(3) Pressure drop along the water main flow route, between the "mixture – inlet" [inflow (0)] and the "water – outlet" [outlet (2)].

The above mentioned quantities are calculated based on the steady state CFD solution. In order to be able to compare different operating conditions, the following performance ratios are defined:

(1). Air separation efficiency ratio:

$$\alpha_{air} = \dot{m}_{1-air} / \dot{m}_{0-air} \tag{8}$$

(2). Water separation efficiency ratio:

$$\alpha_{water} = \dot{m}_{2-water} / \dot{m}_{0-water} \tag{9}$$

(3). Pressure drop ratio:

$$a_P = (P_2 - P_0) / P_0 \tag{10}$$

RESULTS AND DISCUSSION

Calculation of the numerical solution: The mesh used for the CFD runs and its "post-processing" characteristics were given in previous paragraph. The discretization of the momentum and continuity equations and their solution was performed by means of the segregated solver. The governing equations were linearised in the implicit form. All CFD data were calculated for the steady state solution. Pressure-velocity coupling is achieved by using the SIMPLE algorithm [4, 7, 8]. For Pressure discretization, the PRESTO! (PREssure STaggering Option) scheme was used [4]. Second order accuracy for Momentum, Turbulence Kinetic Energy and Turbulent Dissipation Rate was implemented where first order accuracy was implemented for the Volume Fraction. The convergence criterion was set at to 10^{-5} and more than 4000 iterations were held for each run. The reduced results are presented and analysed in the following paragraphs.

Design Parameters and Separator Performances: As mentioned in previous paragraph, only one separator design set-up was analysed in the present study. The alteration of the design parameters in order to examine the separator per-

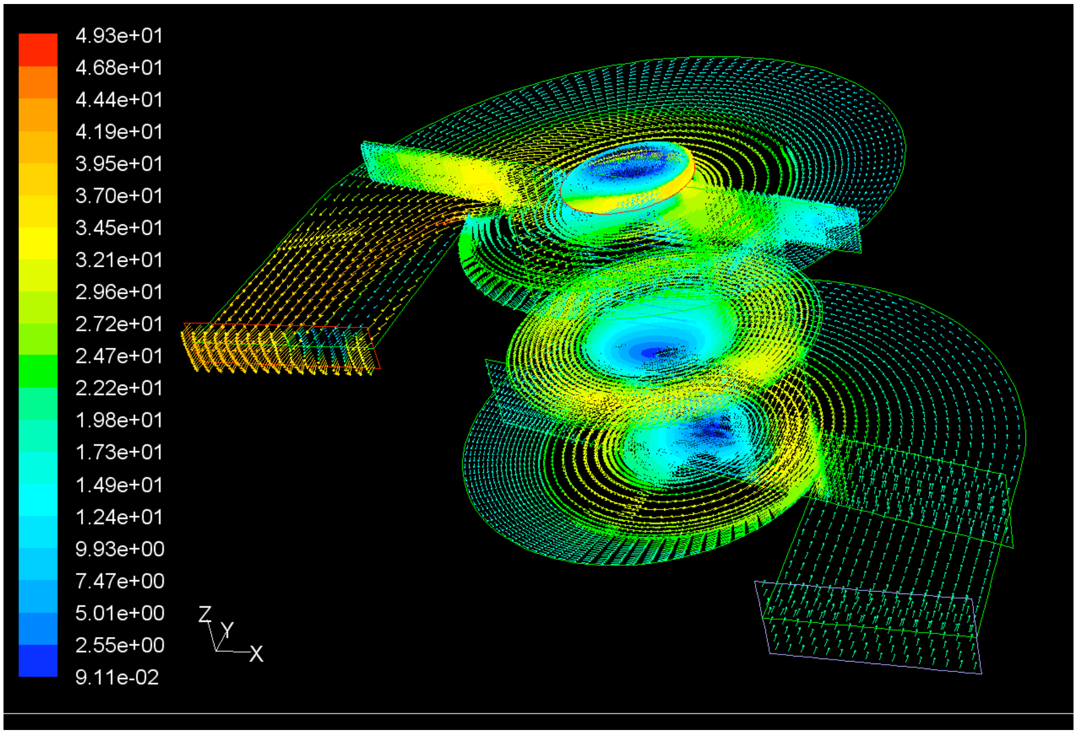

Fig. (3). Velocity vectors for $v_{(0)}$=20 m/s vf=0.1.

formance is programmed for the next stages of the research program and is not a factor for the present study.

Typical Flow Field Patterns Resulted From CFD Analysis: The goals of the following analysis are to highlight the separation process through qualitative results (pictures captured through the various CFD runs). Fig. (**3**) displays a "combined view" of the velocity vectors through the separator, coloured by velocity magnitude. The presence of some flow recirculating zones is obvious. These areas will be watched closely in order to avoid collecting air – bubbles (or water droplets) and hence affecting the separation efficiency and the pressure drop performance of the design. Fig. (**4**) shows the contours of velocity, coloured by velocity magnitude for the same combined view, where Fig. (**5**) shows the

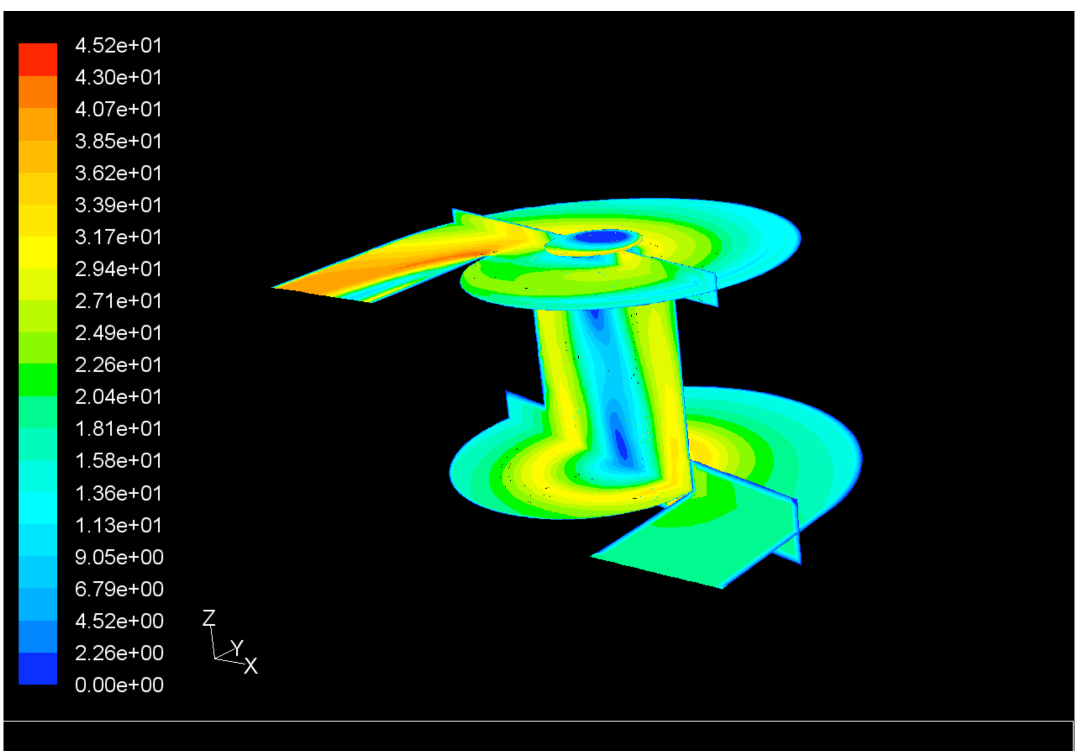

Fig. (4). Contours of velocity for $v_{(0)}$=20 m/s vf=0.1.

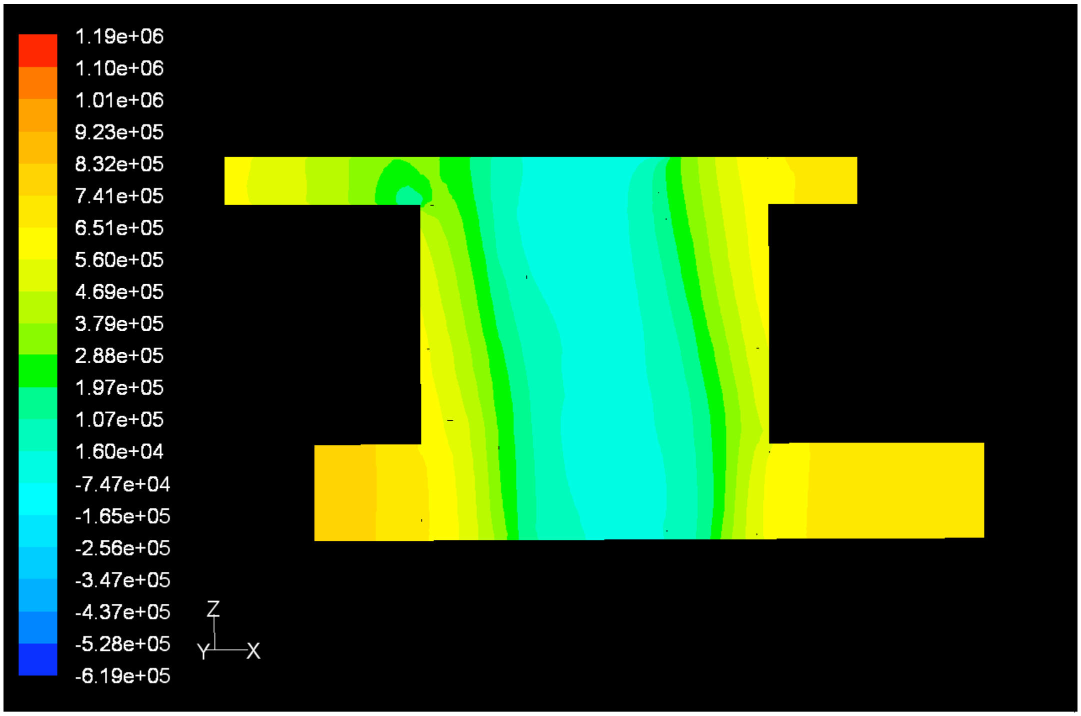

Fig. (5). Contours of pressure for $v_{(0)}$=20 m/s vf=0.1.

contours of pressure coloured by magnitude. Fig. (**6**) shows the distribution of air volume fraction (vf) in a combined view inside the separator and Fig. (**7**) in an axial plane cut (zx plane). The distribution shows (as expected) relative high air mass loading at the "air outlet"(1) of the separator and high water mass loading at the "water outlet"(2). The separation process is clearly visible and is more effective for higher mixture inflow velocities as will be shown in the next paragraph. However the apparent flow recirculating zones act as air – traps affecting negatively the separation process and the pressure drop efficiency of the device. Towards the elimination of these deficiencies, various alterations of the present design will be considered in the next stages of the research program.

Operating Conditions and Separator Performances: The simulations were performed for various operating conditions applied for the design defined as "base case geometry"

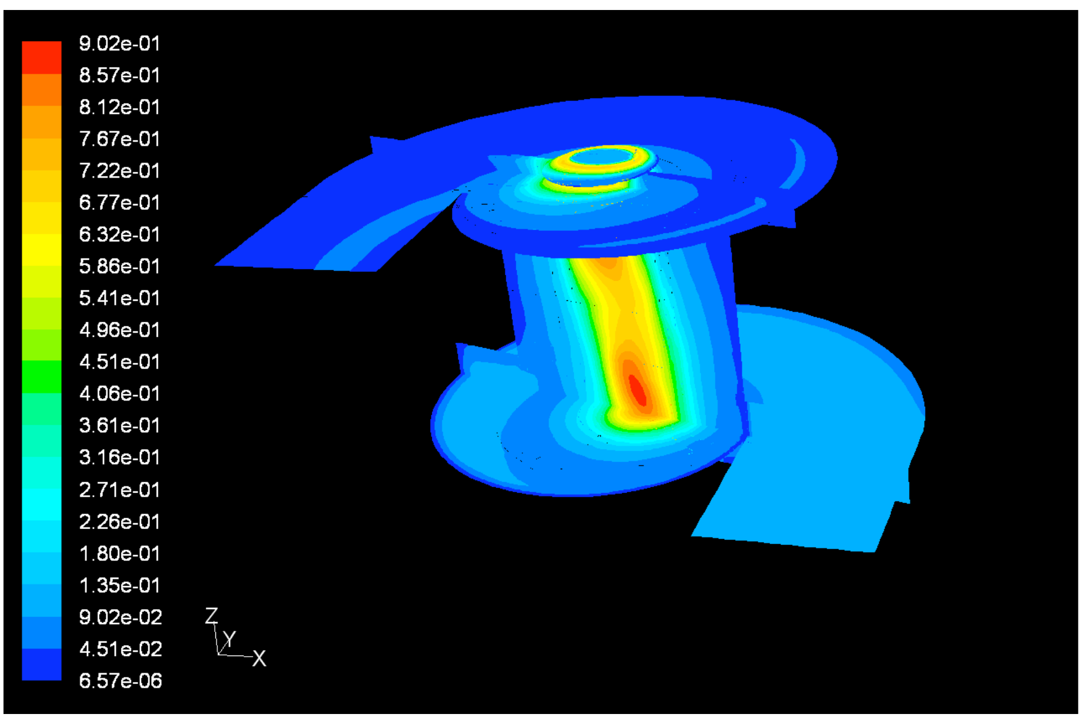

Fig. (6). Contours of air vf for $v_{(0)}$=20 m/s vf=0.1.

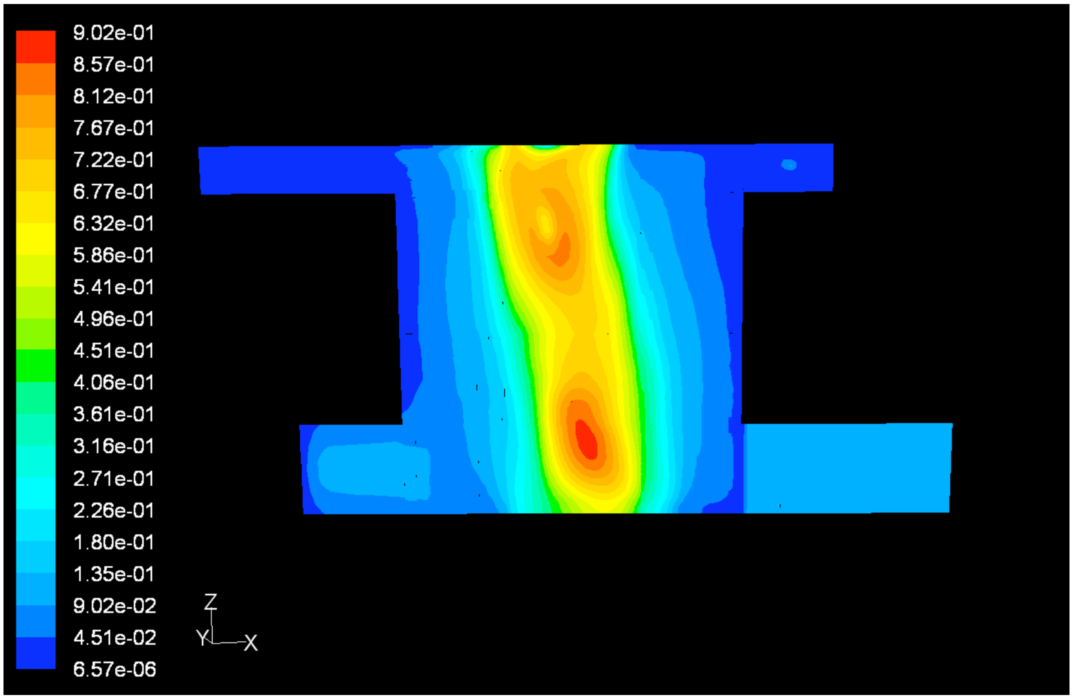

Fig. (7). Contours of air *vf* for $v_{(0)}$=20 m/s *vf*=0.1.

(Fig. **1a**) varying the inlet velocity between 5 m/s and 20 m/s. The separator performance ratios based on the separation efficiency and pressure drop ratios are computed and compared for these problems. The results are presented in Figs. (**8a-c**). The goals of the following analysis are to highlight the separation process through quantitative data gathered through various CFD runs and presented in graphs. This type of data presentation allows for comparisons between different flow conditions.

Fig. (**8a**) shows that the air separation efficiency ratio $\alpha_{(air)}$ (equation 8)of the separator increases in a linear manner *vs* mixture inflow velocity. For lower speeds (5-10 m/s), the separation efficiency is characterized as unacceptable (lower

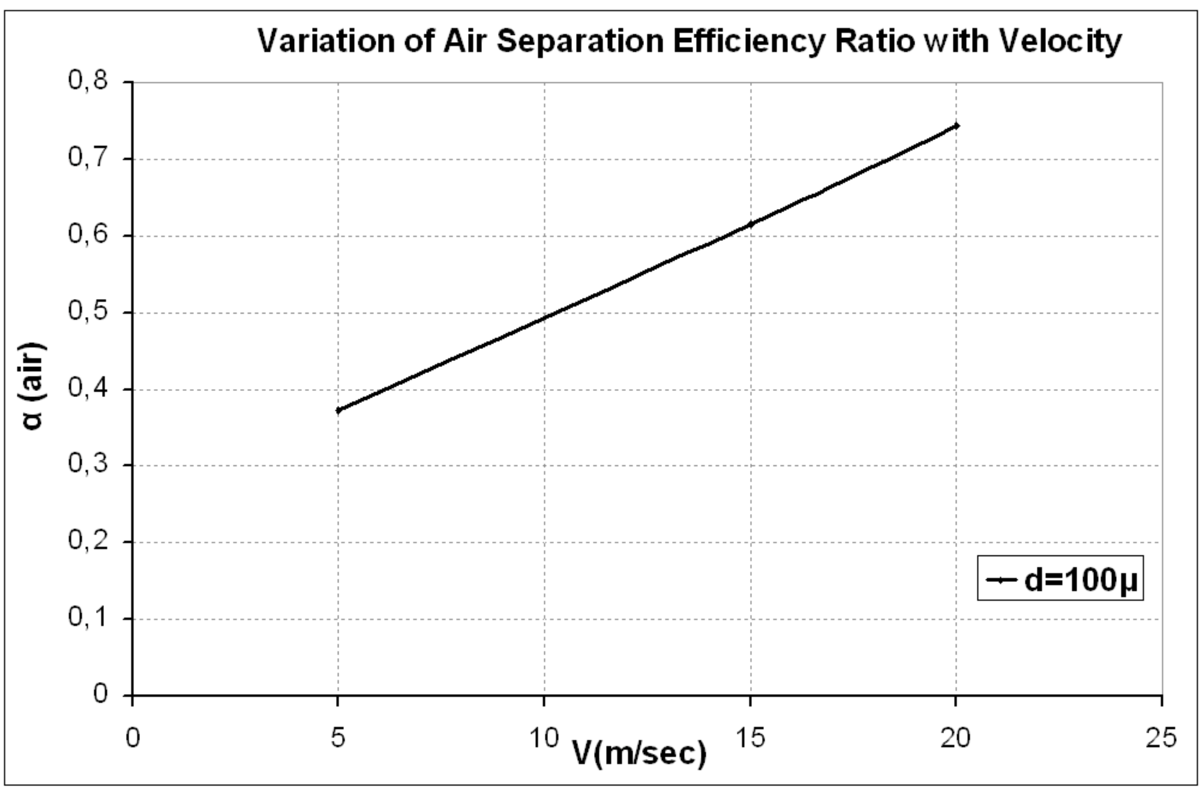

Fig. (8a). Variation of $\alpha_{(air)}$ *vs* $V_{(inflow)}$

than 50%). For speeds in the region of 20 m/s (high speeds) the separation is good (above 70%).

Fig. (**8b**) shows that the water separation efficiency ratio $\alpha_{(water)}$ (equation 9) is consistently increasing with the flow rate processed by the separator. This efficiency seems to reach an upper limit (stabilizes) at 0.85%.

Fig. (**8c**) shows that the pressure drop ratio $\alpha_{(p)}$ (equation 10) increases slightly with the flow rates. It remains for all cases tested in the region of 30% pressure drop.

At this point, the general performance of the separator is very close to that of a centrifugal separator [3], operating at the same (or close) conditions, concerning air and liquid separation efficiency.

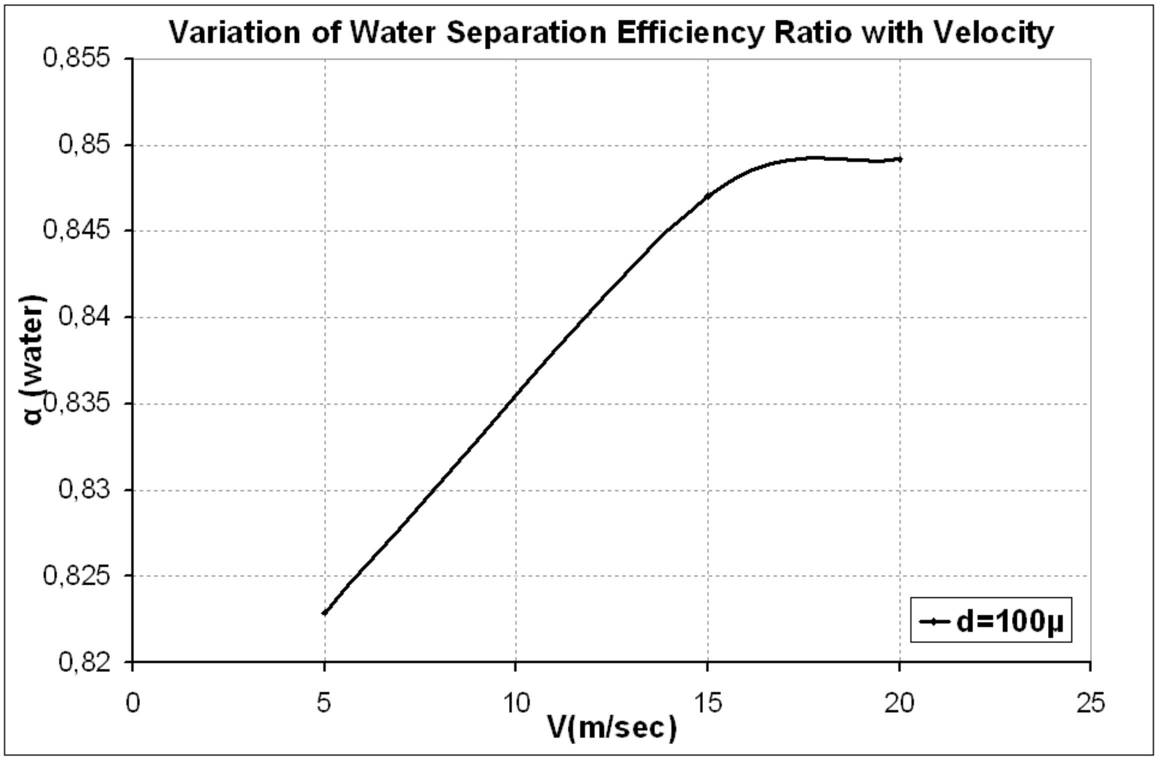

Fig. (8b). Variation of $\alpha_{(water)}$ *vs* $V_{(inflow)}$.

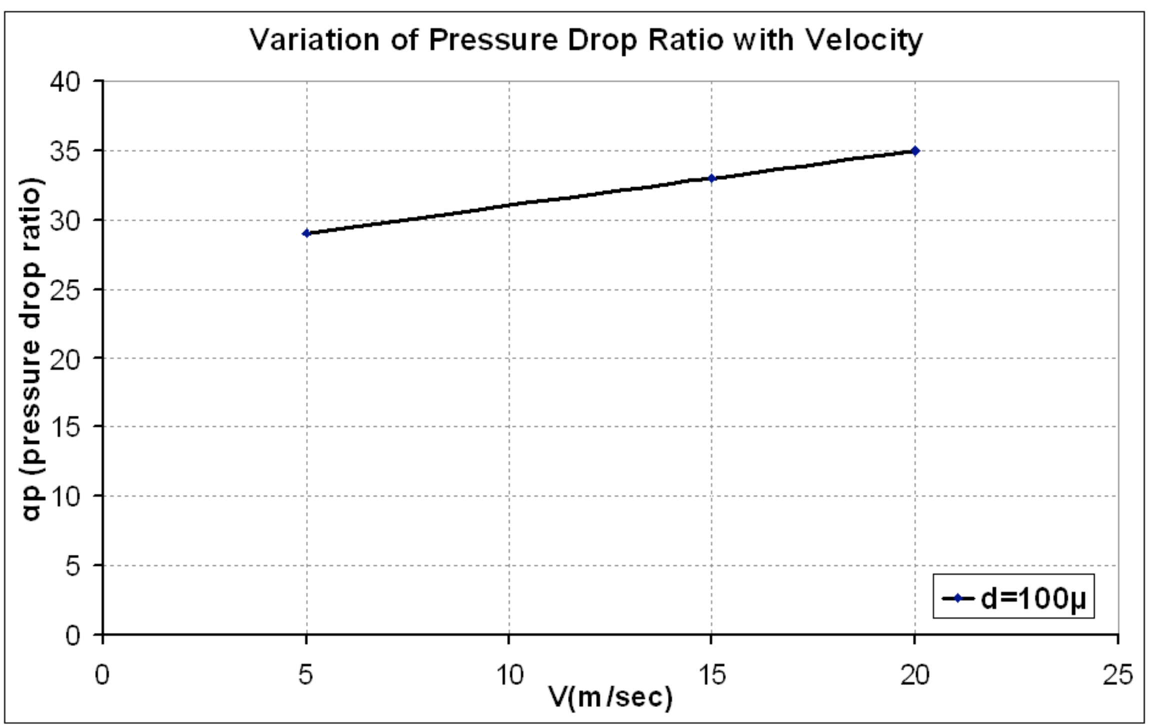

Fig. (8c). Variation of $\alpha_{(p)}$ *vs* $V_{(inflow)}$.

It is obvious that due to the limited CFD data available at this point no more analysis can be performed on the above presented data because the extracted comments and improvement recommendations will not be "confident enough". The above presented data give us a first insight of the behavior of the separator under various flow conditions. These data will have to be confirmed by experiments. Once this is achieved it is only a matter of "computational" time to produce graphs with more data and extract more detailed conclusions.

Experimental Test Results on the Centrifugal Separator: A phase separator with the dimensions given in Fig. (**1a**) has been constructed from Plexiglas and is presented in Fig. (**1b**). The experimental tests are the next step of the research program. The first tests have already been conducted with very good results. The experimental results will be presented and analysed in future report.

CONCLUSIONS

An investigation of air-water separation process has been conducted using numerical simulation. Separator performance has been analyzed in terms of separation efficiency and pressure drop along the water flow path. The goal of the present study was to evaluate the predictions of CFD methods for different operating conditions for a fixed geometry of the device. The Multiphase model used for this study is the Mixture Model – featured in the commercial code FLUENT6. Steady state analysis was performed for the reported calculations. All the geometrical models, meshes, and numerical models are built and run using parametric journal files. Numerical simulation results at different operating conditions, (CFD results) predict correctly that the separator efficiency will increase with the flow rate as well as the pressure drop. Analysis of contours of air volume fraction and flow field patterns showed that the geometry of the separator and specifically the two outlets and the "connecting cylinder", are to be considered also in improving the performance of the separator.

NOMENCLATURE

C	=	Constant or coefficient (-)
D	=	Characteristic length scale (m)
d	=	Diameter (m)
f	=	Function
f_{drag}	=	Drag function
g	=	Acceleration due to gravity (9.81 m/s^2)
$\dot{m}$	=	Mass flow rate (Kgr/s)
n	=	Exponent
P	=	Pressure (Pa)
Re	=	Reynolds number (-)
St	=	Stokes number (-)
t	=	Time (s)
U	=	Characteristic velocity scale (m/s)
u_∞	=	Free stream velocity (m/s)
υ	=	Velocity (m/s)
V	=	Volume (m^3)
vf	=	Volume fraction (-)
x	=	Horizontal distance (m)
y_p	=	Distance: wall from the adjacent cell centre
z	=	Vertical distance (m)

Greek Letters

α_{air}	=	Air separation efficiency ratio
α_{water}	=	Water separation efficiency ratio
a_P	=	Pressure drop ratio
$\vec{\alpha}$	=	Acceleration (m/s^2)
μ	=	Viscosity (Pa-s)
v	=	Kinematic viscosity (m^2/s)
ρ	=	Density (Kg/m^3)
τ	=	Relaxation time (s)

Subscripts

dr	=	Drift
in	=	Inlet - inflow
m	=	Mixture
max	=	Maximum
min	=	Minimum
p	=	Particulate
q	=	Primary phase
T	=	Total
w	=	Water phase

REFERENCES

[1] A.G. Ghiaus, and P.D. Margaris, "Numerical Investigation of a Novel Compact Separator", 4th GRACM Cs on Computational Mechanics, GRACM 2002, 27-29 June, Patras, Greece, 2002.

[2] C. Oropeza-Vazquez, E. Afanador, L. Gomez, S. Wang, R. Mohan, O. Shoham, and G. Kouba, "Oil – water Separation in a Novel Liquid – Liquid Cylindrical Cyclone (LLCC©) Compact Separator – Experiments and Modelling" *J. Fluids Eng.,* vol. 126, pp.553-64, 2004.

[3] T. Barbat, K. Bhatia, and S. Pitla, "CFD Study of Phase Separators in A/C Automotive Systems" *SAE Technical Paper Series*, 2003-01-0736, 2003.

[4] FLUENT V6 – *Fluent User's Guide*, Fluent, Inc; (2001).

[5] M. Manninen, T. Veikko, and K. Sirpa, *On the mixture model for multiphase flow*, VTT Publications, Technical Research Centre of Finland, 1996.

[6] M.B. Abbott, and D.R. Basco, *Computational Fluid Dynamics-An Introduction for Engineers*, Longman, 1989.

[7] S.V. Patankar, and D.B. Spalding, "A calculation procedure for heat, mass and momentum transfer in three dimensional parabolic flows", *Int J Heat Mass Transfer,* 15 1787, 1972.

[8] S.V. Patankar, *Numerical Heat Transfer and Fluid Flow*, McGraw Hill, 1980.

[9] G. Hetsroni, *Handbook of Multiphase Systems*, Hemisphere, 1982.

[10] H. Schlichting, *Boundary Layer Theory*, McGraw Hill, New York, 1979.

[11] J.O. Hintze, *Turbulence*, McGraw-Hill, New York, 1975.

Significance of Vibration and Magnetic bearing on Machine Tool Spindle

P. Paulpandian, *Department of Mechanical Engineering, Aryan Institute of Engineering & Technology, Bhubaneswar, p_pandian@gmail.com*
Chinmay Swain, *Department of Mechanical Engineering, Raajdhani Engineering College, Bhubaneswar, chinmayswain1972@gmail.com*
Barsa Priyadarshini Sahoo, *Department of Civil Engineering, Raajdhani Engineering College, Bhubaneswar, barsap_sahoo@gmail.com*
Binapani Mohapatra, *Department of Civil Engineering, Raajdhani Engineering College, Bhubaneswar, binapanimohapatra@yahoo.co.in*

Abstract: Due to manufacturing flaws or cyclic loading, cracks frequently appear in a rotating spindle system. These cracks adversely influence the dynamic characteristics in rising modes of the rotating machinery. For higher rotational speeds, particularly for super-high-speed cutting, a spindle with magnetic bearings is required. Moreover, a number of investigations on spindle system dynamic characteristics have been addressed particularly to ball-bearing-type spindles. The effect of rotating cracked spindle systems with magnetic bearings is checked in this investigation. A Euler-Bernoulli beam of circular cross section is adopted along with Hamilton principle to find out the equation of motion for the spindle system. The influence of crack thickness, rotational velocity and length of bearing on the dynamic response of a rotating magnetic bearing spindle system are analysed in this investigation.

INTRODUCTION

Cracks frequently appear in rotating machinery due to manufacturing flaws or cyclic fatigue during operation. Numerous cracks can be observed after severe operating conditions, especially in high speed spindles [1, 2]. Local structural irregularities caused by cracks in the spindle may significantly change the dynamic behavior of a rotating machinery system. The effects of cracks on the dynamic and static behaviors of structures have been studied by a number of researchers [3-5]. The effects of cracks on spindle dynamics, shaft and rotor systems, were also studied by researchers [6-9]. When a spindle rotates, the vibrational response is altered by the crack opening and closing in each cycle. Most investigations were motivated by the hypothesis that only opening cracks markedly change the spindle dynamics. This paper focuses on the dynamics of a spindle with a transverse crack.

High speed machining is one of the most modern manufacturing engineering technologies. In a machining system, the spindle is the most critical element that affects the dynamic performance and capabilities of the system in the machining process. However focusing exclusively on the spindle system is insufficient because the bearings can change the dynamics of a machining spindle system. Hence, the bearing effects on the spindle system must also be considered. Bearings are used in many rotating machines to brace the rotating spindles and rotors. In the past, the required rotor speed was low, allowing ball and roller bearings to be used in rotating machinery. High temperatures are generated with ball-bearing spindle systems operating at high speeds. The high temperatures often bring about machine failure. To attain greater complexity and accuracy, modern engineering technologies demand machinery that can be run at high speeds. To avoid the high temperatures generated by the contact between the spindles and bearings, non-contact magnetic bearings are used for the spindle and rotor in high speed rotating machinery.

Traditionally, ball bearings have been used to support the spindle systems when the rotational speed was not high. Previous investigations on bearing spindle systems were confined to spindles with ball bearings. In some studies, the focus was on the dynamic response of a spindle supported by bearings [10, 11]. At higher speeds, this bearing changes the stiffness of the entire spindle system and significantly alters the system properties [12-15]. Precise machining requires higher spindle speeds, making the magnetic-bearing spindle necessary. Investigations as [16-20] studied the performance and dynamic properties of magnetic bearings**.** Most studies deal with a magnetic ring for a radial magnetic bearing used as an unlimited one long magnetic bar for a permanent magnetic bearing. Investigation as [21] studied the bearing capacity and stiffness of radial magnetic bearings.

Thus far, most investigations as [22-24] on the dynamic characteristics of a cracked spindle system were limited to ball-bearing-type spindles. This study examines the crack effects on the dynamic response of a rotating spindle system with magnetic bearings. A Euler-Bernoulli beam of circular cross section was used to approximate the spindle model. The equations of motion for the bearing-spindle system were derived using the Galerkin method and Hamilton principle. A model the size of an actual spindle system was used. To simplify the calculations, massless springs were employed to model the stiffness of the magnetic bearings. The effects of crack depth, rotational speed and bearing length on the dynamic response of a spindle system were investigated.

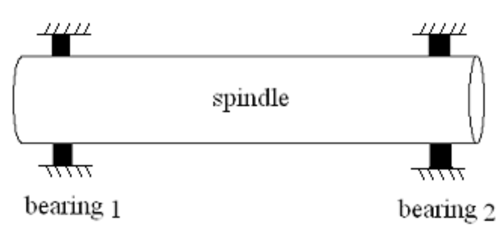

a spindle supported by bearings

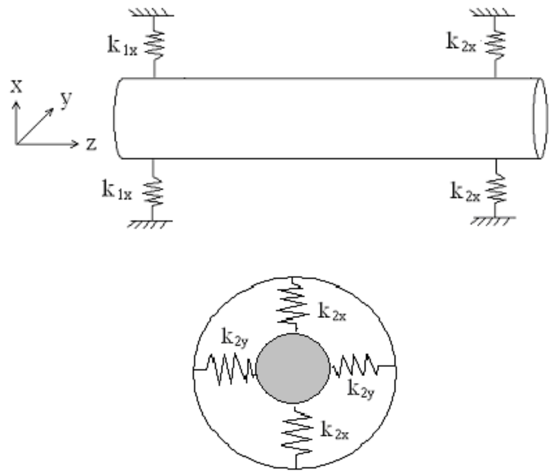

a simple model of bearing spindle system

Fig. (1). A rotating spindle with bearings scheme.

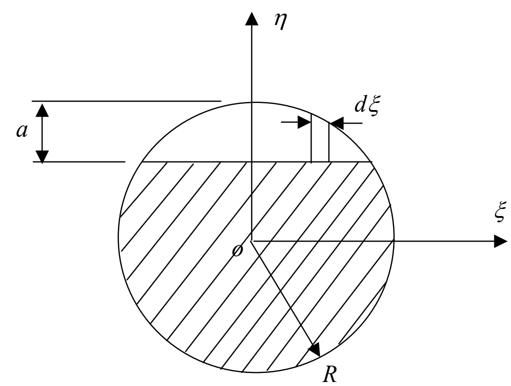

Fig. (2). Geometry of a cracked spindle.

Theory

This paper considers a spindle supported by magnetic bearings, as shown in Fig. (**1a**), to elucidate the dynamic response of a spindle system. Fig. (**1b**) presents a simple model for this bearing-spindle system. In this model, massless springs are employed to simulate the stiffness of the magnetic bearing and support the spindle. The rotational speed Ω of the spindle cannot be ignored in the rotating machinery bearing application. In this study, the deflection components $v(z,t)$, and $u(z,t)$ denote the two transverse flexible deflections of the spindle system. E and I represent the Young's Modulus and area inertia of the spindle, respectively. Only the transverse flexible deflections are studied in this article.

According to [25], the governing equations of the spindle system are displayed as:

$$\rho A\ddot{u} - 2\rho A\Omega\dot{v} - \rho A\Omega^2 u + EI\left(u''\right)'' + k_{x1}u\delta\left(z - z_1\right) + k_{x2}u\delta\left(z - z_2\right) = 0 \tag{1}$$

$$\rho A\ddot{v} + 2\rho A\Omega\dot{u} - \rho A\Omega^2 v + EI\left(v''\right)'' + k_{y1}v\delta\left(z - z_1\right) + k_{y2}v\delta\left(z - z_2\right) = 0 \tag{2}$$

where

k_{x1} : the bearing stiffness in u deflection at a position z_1,

k_{y1} : the bearing stiffness in v deflection at a position z_1,

k_{x2} : the bearing stiffness in u deflection at a position z_2,

k_{y2} : the bearing stiffness in v deflection at a position z_2,

ρ : density ,

A : cross section area,

Ω : rotating speed,

$\delta(\ )$: Dirac delta fuction,

z_1 : the first located position of bearings,

z_2 : the second located position of bearings.

For convenience, the dimensionless equations of motion for this spindle are:

$$\ddot{\bar{u}} - 2\sqrt{\frac{EI}{\rho AL^4}}\bar{\Omega}\dot{\bar{v}} + \frac{EI}{\rho AL^4}\Big\{-\bar{\Omega}^2\bar{u} + \left(\bar{u}''\right)'' + \bar{k}_{x1}\bar{u}\delta\left(\bar{z} - \bar{z}_1\right) + \bar{k}_{x2}\bar{u}\delta\left(\bar{z} - \bar{z}_2\right)\Big\} = 0 \tag{3}$$

$$\ddot{\bar{v}} + 2\sqrt{\frac{EI}{\rho AL^4}}\bar{\Omega}\dot{\bar{u}} + \frac{EI}{\rho AL^4}\Big\{-\bar{\Omega}^2\bar{v} + \left(\bar{v}''\right)'' + \bar{k}_{y1}\bar{v}\delta\left(\bar{z} - \bar{z}_1\right) + \bar{k}_{y2}\bar{v}\delta\left(\bar{z} - \bar{z}_2\right)\Big\} = 0 \tag{4}$$

where the dimensionless parameters are given using:

$$\bar{z} = \frac{z}{L},\ \bar{z}_1 = \frac{z_1}{L},\ \bar{z}_2 = \frac{z_2}{L},\ \bar{\Omega} = \Omega\Big/\sqrt{\frac{EI}{\rho AL^4}}, \tag{5}$$

$$\bar{u}\left(\bar{z}\right) = \frac{u\left(\bar{z}\right)}{L},\ \bar{v}\left(\bar{z}\right) = \frac{v\left(\bar{z}\right)}{L},\ \bar{k}_{x1} = \frac{k_{x1}L^3}{EI}, \tag{6}$$

$$\bar{k}_{x2} = \frac{k_{x2}L^3}{EI},\ \bar{k}_{y1} = \frac{k_{y1}L^3}{EI},\ \bar{k}_{y2} = \frac{k_{y2}L^3}{EI} \tag{7}$$

and the boundary conditions are:

$$\bar{u}'' = \bar{u}''' = \bar{v}'' = \bar{v}''' = 0 \text{, at } \bar{z} = 0 \tag{8}$$

$$\bar{u}'' = \bar{u}''' = \bar{v}'' = \bar{v}''' = 0 \text{, at } \bar{z} = 1 \tag{9}$$

The Galerkin method is employed to derive the spindle equations of motion in matrix form. Therefore, the solutions for Eqs. (3) and (4) can be assumed to be:

$$\bar{u}\left(\bar{z},t\right) = \sum_{i=1}^{m}\phi_i\left(\bar{z}\right)p_i\left(t\right) \tag{10}$$

$$\bar{v}\left(\bar{z},t\right) = \sum_{i=1}^{m}\varphi_i\left(\bar{z}\right)q_i\left(t\right) \tag{11}$$

where $\varphi_i\left(\bar{z}\right)$, $\phi_i\left(\bar{z}\right)$ are comparison functions for the spindle system, and $p_i\left(t\right)$, $q_i\left(t\right)$ are the time coefficients to be determined for the system. The exact solution for a beam with free-free boundary conditions is considered, and five comparison function modes are used.

$$\phi_i\left(\bar{z}\right) = \varphi_i\left(\bar{z}\right) = \left(\lambda_i\bar{z}\right)^2\left(\right) \qquad - \qquad -$$

$$\lambda_i = \left(i - \frac{3}{2}\right)\pi u^*\left(i-2\right),\ i = 1,\ 2,\ 3,\ \cdots \tag{13}$$

where $u^*\left(\ \right)$ is the unit step function. Substituting Eqs. (10) and (11) into Eqs. (3) and (4) respectively, the equations of motion in matrix form for the spindle system can be derived as:

$$\begin{aligned}&\begin{bmatrix}\left[M\right]_1 & 0\\ 0 & \left[M\right]_2\end{bmatrix}\begin{Bmatrix}\ddot{p}(t)\\ \ddot{q}(t)\end{Bmatrix} + 2\bar{\Omega}\gamma\begin{bmatrix}0 & \left[G\right]_1\\ \left[G\right]_2 & 0\end{bmatrix}\begin{Bmatrix}\dot{p}(t)\\ \dot{q}(t)\end{Bmatrix}\\ &+\gamma^2\begin{bmatrix}\left[K_e\right]_1 & 0\\ 0 & \left[K_e\right]_2\end{bmatrix}\begin{Bmatrix}p(t)\\ q(t)\end{Bmatrix} + \bar{\Omega}^2\gamma^2\begin{bmatrix}\left[K_\Omega\right]_1 & 0\\ 0 & \left[K_\Omega\right]_2\end{bmatrix}\begin{Bmatrix}p(t)\\ q(t)\end{Bmatrix}\\ &+\gamma^2\begin{bmatrix}\left[K_{s1}\right]_1 & 0\\ 0 & \left[K_{s1}\right]_2\end{bmatrix}\begin{Bmatrix}p(t)\\ q(t)\end{Bmatrix} + \gamma^2\begin{bmatrix}\left[K_{s2}\right]_1 & 0\\ 0 & \left[K_{s2}\right]_2\end{bmatrix}\begin{Bmatrix}p(t)\\ q(t)\end{Bmatrix} = 0\end{aligned} \tag{14}$$

where $\gamma = \sqrt{\dfrac{EI}{\rho A L^4}}$.

The elements of the matrices in the above equation are given as follows,

$$\left(m_{ij}\right)_1 = \int_0^1 \phi_i\phi_j d\bar{z} = -\left[\left(k_\Omega\right)_{ij}\right]_1 \tag{15}$$

$$\left(m_{ij}\right)_2 = \int_0^1 \varphi_i\varphi_j d\bar{z} = -\left[\left(k_\Omega\right)_{ij}\right]_2 \tag{16}$$

$$\left(g_{ij}\right)_1 = -\int_0^1 \phi_i\varphi_j d\bar{z} \tag{17}$$

$$\left(g_{ij}\right)_2 = \int_0^1 \varphi_i\phi_j d\bar{z} \tag{18}$$

$$\left[\left(k_e\right)_{ij}\right]_1 = \int_0^1 \phi_i''\phi_j'' d\bar{z} \tag{19}$$

$$\left[\left(k_e\right)_{ij}\right]_2 = \int_0^1 \varphi_i''\varphi_j'' d\bar{z} \tag{20}$$

$$\left[\left(k_{s1}\right)_{ij}\right]_1 = \bar{k}_{x1}\left\{\phi_i\left(\bar{z}_1\right)\right\}\left\{\phi_j\left(\bar{z}_1\right)\right\}^T \tag{21}$$

$$\left[\left(k_{s1}\right)_{ij}\right]_2 = \bar{k}_{y1}\left\{\varphi_i\left(\bar{z}_1\right)\right\}\left\{\varphi_j\left(\bar{z}_1\right)\right\}^T \tag{22}$$

$$\left[\left(k_{s2}\right)_{ij}\right]_1 = \bar{k}_{x2}\left\{\phi_i\left(\bar{z}_2\right)\right\}\left\{\phi_j\left(\bar{z}_2\right)\right\}^T \tag{23}$$

$$\left[\left(k_{s2}\right)_{ij}\right]_2 = \bar{k}_{y2}\left\{\varphi_i\left(\bar{z}_2\right)\right\}\left\{\varphi_j\left(\bar{z}_2\right)\right\}^T \tag{24}$$

For the sake of convenience, Eq. (14) can be rewritten as,

$$\left[M\right]\left\{\ddot{X}\right\} + \gamma\left[G\right]\left\{\dot{X}\right\} + \gamma^2\left[K\right]\left\{X\right\} = 0 \tag{25}$$

where

$$\left[M\right] = \begin{bmatrix}\left[M\right]_1 & 0\\ 0 & \left[M\right]_2\end{bmatrix} \tag{26}$$

$$\left[G\right] = 2\bar{\Omega}\begin{bmatrix}0 & \left[G\right]_1\\ \left[G\right]_2 & 0\end{bmatrix} \tag{27}$$

$$\begin{aligned}\left[K\right] = &\begin{bmatrix}\left[K_e\right]_1 & 0\\ 0 & \left[K_e\right]_2\end{bmatrix} + \bar{\Omega}^2\begin{bmatrix}\left[K_\Omega\right]_1 & 0\\ 0 & \left[K_\Omega\right]_2\end{bmatrix}\\ &+\begin{bmatrix}\left[K_{s1}\right]_1 & 0\\ 0 & \left[K_{s1}\right]_2\end{bmatrix} + \begin{bmatrix}\left[K_{s2}\right]_1 & 0\\ 0 & \left[K_{s2}\right]_2\end{bmatrix}\end{aligned} \tag{28}$$

A space vector is introduced in Eq. (25) to solve the eigenvalue problem for the system.

$$\left\{V\right\} = \begin{Bmatrix}\dot{X}\\ X\end{Bmatrix}. \tag{29}$$

Substituting Eq. (29) into Eq. (25), the equation can be rearranged as;

$$\begin{bmatrix}\left[M\right] & 0\\ 0 & \gamma^2\left[K\right]\end{bmatrix}\left\{\dot{V}\right\} + \begin{bmatrix}\gamma\left[G\right] & \gamma^2\left[K\right]\\ -\gamma^2\left[K\right] & 0\end{bmatrix}\left\{V\right\} = 0 \tag{30}$$

The non-dimensional frequency $\bar{\omega}_n$ in Eq. (30), i.e., the natural frequency of the spindle system, is defined as:

$$\bar{\omega}_n = \omega_n \Big/ \sqrt{\frac{EI}{\rho A L^4}} \quad \text{for } n = 1,2,\ldots.. \tag{31}$$

In industry, ball bearings are frequently used to support rotating spindles in rotating machinery. Recently, magnetic bearings have been employed increasingly to support spindles because they must rotate at higher speeds. Few investigations focused on the dynamic responses of defective spindle systems with magnetic bearings. Therefore, this investigation addresses the dynamic response of a cracked spindle supported by magnetic bearings.

Crack Effect

Considering a crack located at $\bar{z} = \bar{z}*$ on this spindle, the strain energy of the defective spindle will include the released energy caused by the crack. Fig. (**2**) shows the geometry of a cracked spindle. The released energy caused by a crack, as noted in [26], with a depth of a may be expressed as:

$$U^c = \int_{-b}^{b}\frac{\left(1-\mu^2\right)}{E}K_I^2\left(\xi\right)d\xi \tag{32}$$

where $b = \sqrt{R^2 - \left(R-a\right)^2}$

and μ is the Poisson's ratio of the spindle, K_I is the stress intensity factor under a mode I load and R is the radius of the spindle. In this case, the stress intensity factors K_I can be approximated as

$$K_I\left(\xi\right) = \frac{4M_b}{\pi R^4}\sqrt{R^2-\xi^2}\sqrt{\pi\alpha}\ F_2\left(\alpha\big/h\right) \tag{33}$$

where, M_b is the bending moment, and

$$h = 2\sqrt{R^2-\xi^2} \tag{34}$$

$$\alpha = a + \sqrt{R^2 - \xi^2} - R \tag{35}$$

$$F_2\left(\alpha/h\right) = \sqrt{\frac{2h}{\pi\alpha}\tan\left(\frac{\pi\alpha}{2h}\right)}\frac{0.923+0.199\left[1-\sin\left(\frac{\pi\alpha}{2h}\right)\right]^4}{\cos\left(\frac{\pi\alpha}{2h}\right)} \tag{36}$$

The notations a and R are the maximum crack depth and radius of the spindle, respectively. Based on the investigations in [26, 27], alterations of the elastic deformation energy caused by lateral bending moments are the only important changes in the case of slender beams with a crack. The released energy of the crack with respect to ξ due to the bending moment is obtained as:

$$U_\xi^c = E\left(1-\mu^2\right)\pi\int_0^L\int_0^a\int_{-b}^b\left[\frac{\partial^2 v}{\partial z^2}\delta\left(z-z^*\right)\right]^2 \left(R^2-\xi^2\right)\alpha F_2^2\left(\alpha/h\right)d\xi\, d\alpha\, dz \tag{37}$$

Similarly, the released energy of the crack with respect to η is derived as follows,

$$U_\eta^c = E\left(1-\mu^2\right)\pi\int_0^L\int_0^a\int_{-b}^b\left[\frac{\partial^2 u}{\partial z^2}\delta\left(z-z^*\right)\right]^2 \xi^2\alpha F_1^2\left(\alpha/h\right)d\xi\, d\alpha\, dz \tag{38}$$

where

$$F_1\left(\alpha/h\right) = \sqrt{\frac{2h}{\pi\alpha}\tan\left(\frac{\pi\alpha}{2h}\right)}\frac{0.752+2.02\left(\frac{\alpha}{h}\right)+0.37\left[1-\sin\left(\frac{\pi\alpha}{2h}\right)\right]^3}{\cos\left(\frac{\pi\alpha}{2h}\right)} \tag{39}$$

For simplification, the dimensionless equations are employed as:

$$U_\eta^c = \frac{4R}{L}\left(1-\mu^2\right)\pi\int_0^1\left[\frac{\partial^2\bar{u}}{\partial\bar{z}^2}\delta\left(\bar{z}-\bar{z}^*\right)\right]^2 Q_1\left(\frac{\xi}{R},\ \frac{\alpha}{R}\right)d\bar{z} \tag{40}$$

$$U_\xi^c = \frac{4R}{L}\left(1-\mu^2\right)\pi\int_0^1\left[\frac{\partial^2\bar{v}}{\partial\bar{z}^2}\delta\left(\bar{z}-\bar{z}^*\right)\right]^2 Q_2\left(\frac{\xi}{R},\ \frac{\alpha}{R}\right)d\bar{z} \tag{41}$$

where

$$Q_1\left(\frac{\xi}{R},\ \frac{\alpha}{R}\right) = \int_0^{a/R}\int_0^{b/R}\frac{\xi^2}{R^2}\frac{\alpha}{R}F_1^2\left(\alpha/h\right)d\frac{\xi}{R}d\frac{\alpha}{R} \tag{42}$$

$$Q_2\left(\frac{\xi}{R},\ \frac{\alpha}{R}\right) = \int_0^{a/R}\int_{-b/R}^{b/R}\left(1-\frac{\xi^2}{R^2}\right)\frac{\alpha}{R}F_2^2\left(\alpha/h\right)d\frac{\xi}{R}d\frac{\alpha}{R} \tag{43}$$

The bearing-spindle with a crack can be obtained as:

$$\ddot{\bar{u}} - 2\sqrt{\frac{EI}{\rho AL^4}}\bar{\Omega}\dot{\bar{v}} + \frac{EI}{\rho AL^4}\left\{-\bar{\Omega}^2\bar{u} + \left(\bar{u}''\right)'' - \frac{8R}{L}\left(1-\mu^2\right)Q_1\left(\frac{\xi}{R},\ \frac{\alpha}{R}\right)\left[\bar{u}''\delta\left(\bar{z}-\bar{z}^*\right)\right]'' + \bar{k}_{x1}\bar{u}\delta\left(\bar{z}-\bar{z}_1\right) + \bar{k}_{x2}\bar{u}\delta\left(\bar{z}-\bar{z}_2\right)\right\} = 0 \tag{44}$$

$$\ddot{\bar{v}} + 2\sqrt{\frac{EI}{\rho AL^4}}\bar{\Omega}\dot{\bar{u}} + \frac{EI}{\rho AL^4}\left\{-\bar{\Omega}^2\bar{v} + \left(\bar{v}''\right)'' - \frac{8R}{L}\left(1-\mu^2\right)Q_2\left(\frac{\xi}{R},\ \frac{\alpha}{R}\right)\left[\bar{v}''\delta\left(\bar{z}-\bar{z}^*\right)\right]'' + \bar{k}_{y1}\bar{v}\delta\left(\bar{z}-\bar{z}_1\right) + \bar{k}_{y2}\bar{v}\delta\left(\bar{z}-\bar{z}_2\right)\right\} = 0 \tag{45}$$

Similarly, the equations of motion for the defective spindle, i.e. Eq. 13, can be rearranged in matrix form using Galerkin's method as follows:

$$\begin{bmatrix}[M]_1 & 0\\ 0 & [M]_2\end{bmatrix}\begin{Bmatrix}\ddot{p}(t)\\ \ddot{q}(t)\end{Bmatrix} + 2\bar{\Omega}\gamma\begin{bmatrix}0 & [G]_1\\ [G]_2 & 0\end{bmatrix}\begin{Bmatrix}\dot{p}(t)\\ \dot{q}(t)\end{Bmatrix} + \gamma^2\begin{bmatrix}[K_e]_1 & 0\\ 0 & [K_e]_2\end{bmatrix}\begin{Bmatrix}p(t)\\ q(t)\end{Bmatrix} + \bar{\Omega}^2\gamma^2\begin{bmatrix}[K_\Omega]_1 & 0\\ 0 & [K_\Omega]_2\end{bmatrix}\begin{Bmatrix}p(t)\\ q(t)\end{Bmatrix} - \gamma^2\begin{bmatrix}[K_c]_1 & 0\\ 0 & [K_c]_2\end{bmatrix}\begin{Bmatrix}p(t)\\ q(t)\end{Bmatrix} + \gamma^2\begin{bmatrix}[K_{s1}]_1 & 0\\ 0 & [K_{s1}]_2\end{bmatrix}\begin{Bmatrix}p(t)\\ q(t)\end{Bmatrix} + \gamma^2\begin{bmatrix}[K_{s2}]_1 & 0\\ 0 & [K_{s2}]_2\end{bmatrix}\begin{Bmatrix}p(t)\\ q(t)\end{Bmatrix} = 0 \tag{46}$$

where

$$\left[\left(k_c\right)_{ij}\right]_1 = \frac{8R\left(1-\mu^2\right)}{L}Q_1\left(\frac{\xi}{R},\ \frac{\alpha}{R}\right)\left[\varphi_i''\left(\bar{z}\right)\varphi_j''\left(\bar{z}\right)\right]_{\bar{z}=\bar{z}^*} \tag{47}$$

$$\left[\left(k_c\right)_{ij}\right]_2 = \frac{8R\left(1-\mu^2\right)}{L}Q_2\left(\frac{\xi}{R},\ \frac{\alpha}{R}\right)\left[\varphi_i''\left(\bar{z}\right)\varphi_j''\left(\bar{z}\right)\right]_{\bar{z}=\bar{z}^*} \tag{48}$$

Supported by Magnetic Bearing

Few investigations on radial magnetic bearings were found, so these bearings were selected for this article. The rotor is kept in the desired position by a magnetic bearing stator using a magnetic field induced by permanent magnets. According to [21], the bearing force F_r is derived as follows,

$$F_r = \frac{B_{r1}B_{r2}}{4\pi\mu_0}S \tag{49}$$

Where B_{r1} : remanence of the external magnetic loop for the magnetic bearing; B_{r2} : remanence of the internal magnetic loop for the magnetic bearing; μ_0 : permanence in vacuum and,

$$S = \left(S_{23} + S_{14} - S_{13} - S_{24}\right) \tag{50}$$

$$Rx_1 = \left(x_1 + x_0 - x\right)^2 + \left(e + R_3\cos\alpha - R_2\cos\beta\right)^2 + \left(R_3\sin\alpha - R_2\sin\beta\right)^2 \tag{51}$$

$$Rx_2 = \left(x_1 + x_0 - x\right)^2 + \left(e + R_3 \cos\alpha - R_1 \cos\beta\right)^2 + \left(R_3 \sin\alpha - R_1 \sin\beta\right)^2 \quad (52)$$

$$Rx_3 = \left(x_1 + x_0 - x\right)^2 + \left(e + R_4 \cos\alpha - R_1 \cos\beta\right)^2 + \left(R_4 \sin\alpha - R_1 \sin\beta\right)^2 \quad (53)$$

$$Rx_4 = \left(x_1 + x_0 - x\right)^2 + \left(e + R_4 \cos\alpha - R_2 \cos\beta\right)^2 + \left(R_4 \sin\alpha - R_2 \sin\beta\right)^2 \quad (54)$$

$$S_{23} = \int_0^{2\pi}\int_0^{2\pi}\int_0^{l_m}\int_0^{l_m} \frac{R_2 R_3 \left(e + R_3 \cos\alpha - R_2 \cos\beta\right) d\alpha d\beta dx dx_1}{Rx_1^{3/2}} \quad (55)$$

$$S_{13} = \int_0^{2\pi}\int_0^{2\pi}\int_0^{l_m}\int_0^{l_m} \frac{R_1 R_3 \left(e + R_3 \cos\alpha - R_1 \cos\beta\right) d\alpha d\beta dx dx_1}{Rx_2^{3/2}} \quad (56)$$

$$S_{14} = \int_0^{2\pi}\int_0^{2\pi}\int_0^{l_m}\int_0^{l_m} \frac{R_1 R_4 \left(e + R_4 \cos\alpha - R_1 \cos\beta\right) d\alpha d\beta dx dx_1}{Rx_3^{3/2}} \quad (57)$$

$$S_{24} = \int_0^{2\pi}\int_0^{2\pi}\int_0^{l_m}\int_0^{l_m} \frac{R_2 R_4 \left(e + R_4 \cos\alpha - R_2 \cos\beta\right) d\alpha d\beta dx dx_1}{Rx_4^{3/2}} \quad (58)$$

where R_1: external radius of the external magnetic loop $R + 2h_g + L_{mg}$

R_2 : internal radius of the external magnetic loop $R + h_g + L_{mg}$

R_3 : external radius of the internal magnetic loop $R + h_g$

R_4 : internal radius of the internal magnetic loop R

l_m : length of the magnetic loop

L_{mg} : clearance between the internal and external magnetic loops

h_g: the thickness of the magnetic loop

e : is eccentric of the magnetic bearing

Consequently, the stiffness of a radial magnetic bearing can be derived as follows:

$$k_m = \frac{F_r}{e} = \frac{B_{r1} B_{r2}}{4\pi\mu_0} \frac{S}{e} \quad (59)$$

ANALYSIS AND DISCUSSION

In ultra-high-speed machining, using magnetic bearings to support the spindle is necessary [28]. The dynamic properties of a multi-mode spindle with bearings of the size actually used in engineering applications are addressed and a magnetic bearing is considered in this work. The dimensions $R=0.02m$ and $L=0.2m$ of a rotating spindle are assumed. The bearings positions are assumed to be $\bar{z}_1 = 0$ and $\bar{z}_2 = 1$.

A spindle system braced by a magnetic bearing is important in engineering applications, especially for high-speed rotational machinery. For the above-mentioned spindle dimensions, the important magnetic bearing parameters were selected as follows. *Nd-Fe-B* material was employed to model the elements of a permanent magnet in the radial magnetic bearings. For this material, the remanence $B_{r1} = B_{r2} = 1.13\, wb/m^2$ can be shown. Corresponding to the spindle imension, the length of the magnetic $l_m = 20mm$ and the clearance $L_{mg} = 0.001m$ were assumed.

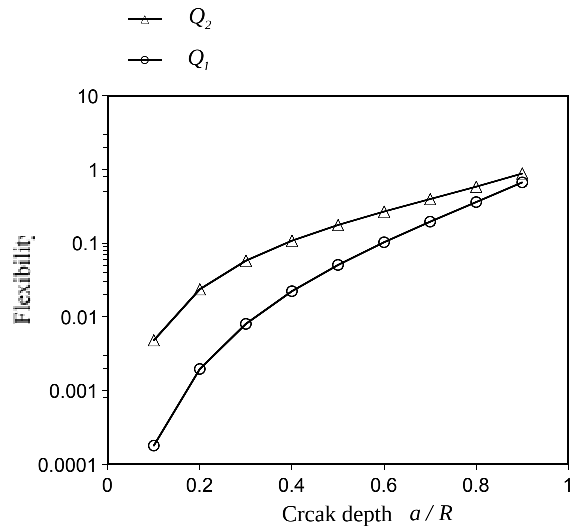

Fig. (3). The variations in the crack flexibility with the crack depth ratio.

The variation in the crack flexibility with the crack depth ratio is plotted in Fig. (**3**). The numerical analysis reveals that the crack flexibility increases as the crack depth is increased. From the results, the crack depth markedly affects the shaft stiffness. As a whole, these results and those from previous investigation [29] are identical. Fig. (**4**) presents the natural frequencies of a spindle bearing system with and without cracks. The logarithmic scale was employed to study higher modes in this figure. At lower modes, the natural frequencies of the spindle bearing system change slightly regardless of whether there is a crack or not in the system. However, at higher modes, the natural frequencies of a spindle bearing system decrease when there is a crack in this spindle system. With magnetic bearings, the crack effect on the dynamics of a spindle system has more influence at the higher modes than at the lower modes. The effect of the crack depth on the natural frequencies is considered in Fig. (**5**). In this figure, the lower and higher mode natural frequencies, the 1^{st} and 5^{th} modes, are studied together. Both the 1^{st} and 5^{th} natural frequencies decrease with increasing crack depth. If the crack depth were $\bar{\gamma} \le 0.1$, the crack size would have little influence on the natural frequencies of a rotating blade system. However, the natural frequencies are depressed significantly when the crack size is larger than 0.1.

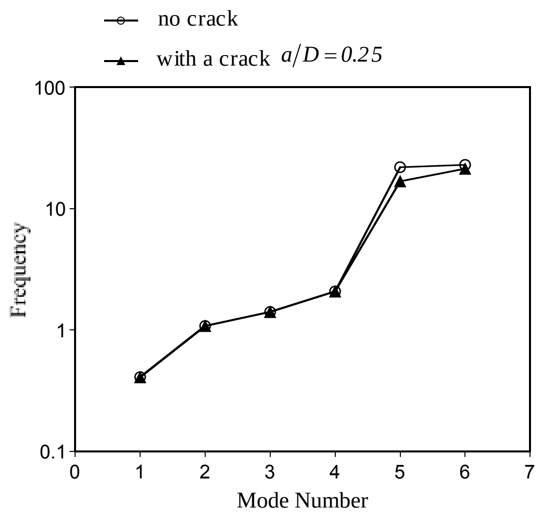

Fig. (4). The natural frequencies of a magnetic-bearing spindle with and without a crack, ($\bar{\Omega} = 0.5,\ a/D = 0.25,\ \bar{z}^* = 0.5$).

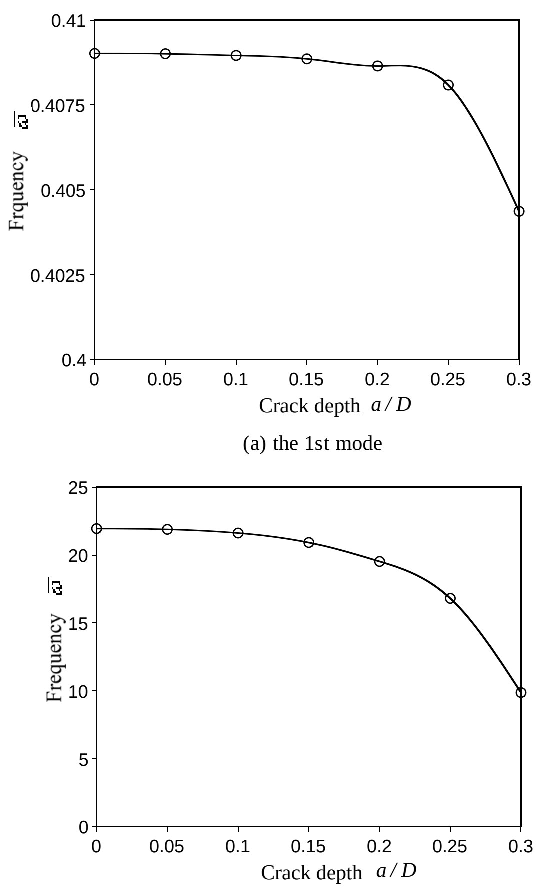

(a) the 1st mode

(b) the 5th mode

Fig. (5). The natural frequencies of a magnetic-bearing spindle with different crack depths, ($\bar{\Omega} = 0.5,\ \bar{z}^* = 0.5$).

Crack location dramatically changes the dynamics of a spindle with magnetic bearings. Fig. (**6**) shows the variation in the natural frequencies of a spindle with different crack locations. As mentioned above, only the *1*st and *5*th natural frequencies were examined. When the crack is located at both ends, the natural frequencies are almost the same as a system without a crack. The value of the natural frequencies of the system is the lowest when the crack is located at the middle of the spindle. The phenomena illustrated in Fig. (**6a**) and (**6b**) are similar. The effect of rotation speed on the dynamics of a cracked spindle with magnetic bearings is plotted in Fig. (**7**). Double roots for the natural frequencies of a cracked spindle with magnetic bearings are observed only if this system has no rotation speed. With rotation speed, the natural frequencies of this system are divided into two parts, the forward and backward frequencies. Only the *1*st and *2*nd natural frequencies are shown in this figure. The *1*st natural frequency of a cracked spindle with magnetic bearings increases as the rotational speed increases. However, it was found that if the rotational speed increases, the *2*nd natural frequency decreases.

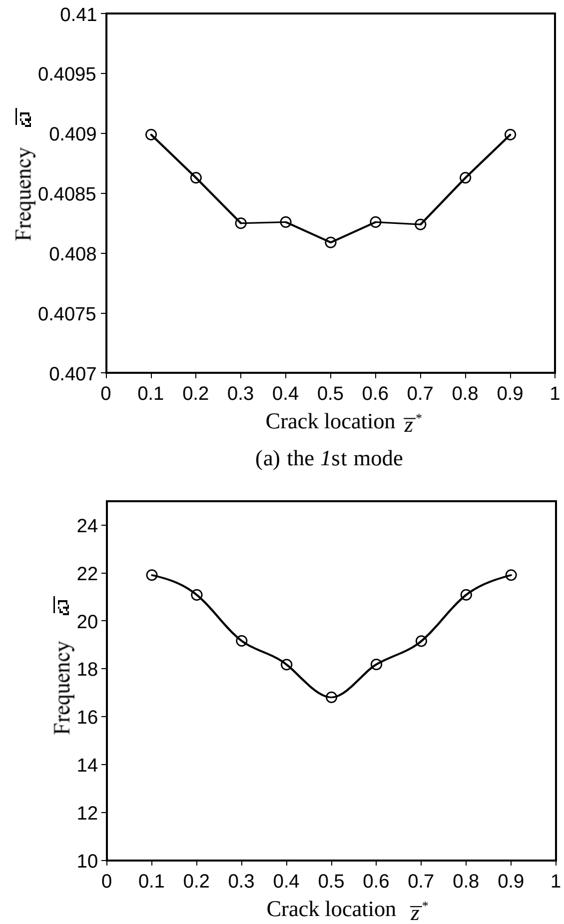

(a) the *1*st mode

(b) the *5*th mode

Fig. (6). The natural frequencies of a magnetic-bearing spindle with different crack locations, ($\bar{\Omega} = 0.5,\ \ a/D = 0.25$).

For radial magnetic bearings, the length of the bearings remarkably alters the system stiffness. Fig. (**8**) illustrates the variations in natural frequencies for a cracked spindle with different magnetic bearing lengths. The results indicate that the natural frequencies of a magnetic-bearing spindle increase as the magnetic bearing length increases. Finally, the frequency responses of a spindle system with and without cracks are illustrated in Fig. (**9**). Both the lower and higher frequency domains were examined. In the lower frequency domain, the figure shows that the frequency response of a bearing-spindle system without a crack is almost the same as one with a crack. The peak frequency response values for a spindle with magnetic bearings are depressed in the higher frequency domain if there is a crack in the spindle. As above, the effect of a crack may significantly influence the dynamics of a spindle system with magnetic bearings at higher modes.

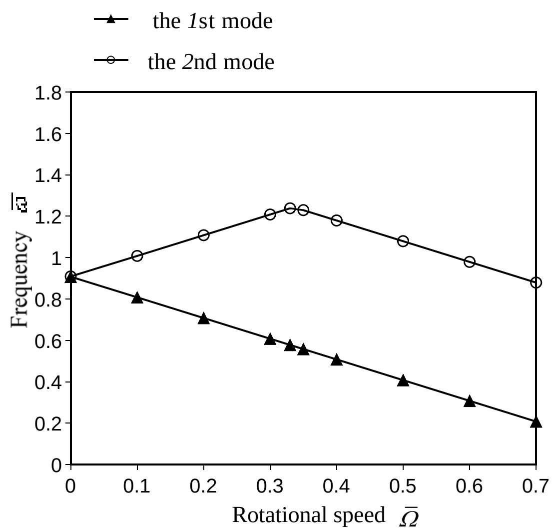

Fig. (7). The natural frequencies of a magnetic-bearing spindle with different rotational speeds, ($\bar{z}^* = 0.5, \quad a/D = 0.25$).

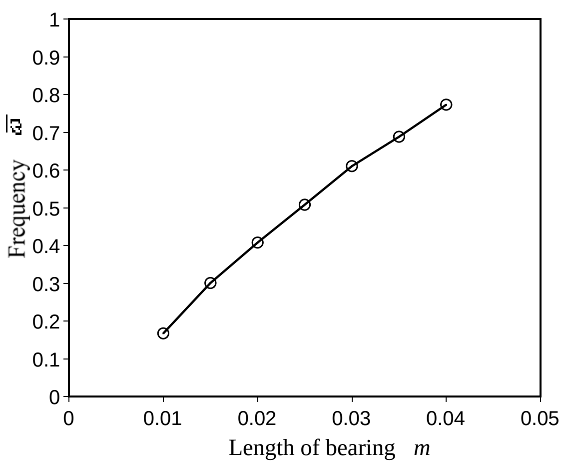

Fig. (8). The natural frequencies of a rotating cracked spindle with different lengths of magnetic bearing, ($\bar{z}^* = 0.5, \quad a/D = 0.25$).

CONCLUSIONS

The influence of cracks on the dynamics of a spindle supported by magnetic bearings was analysed. Most of the findout in this investigation are categorized as follows:

1. With magnetic bearings, the true frequencies of a spindle system lowered as the thickness of the crack rises.
2. At rising mode, a crack will adversely influence the dynamics of a spindle with magnetic bearings. Moreover, at decreasing modes, the true frequencies of the spindle bearing system change just marginally no matter whether there is a crack is present or not.
3. The circular velocity as well as magnetic bearing length will significantly affect the dynamics of a spindle with magnetic bearings.

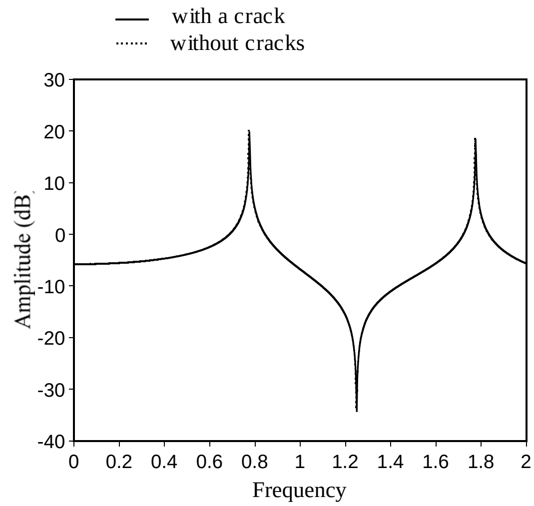

(a) a lower frequency domain

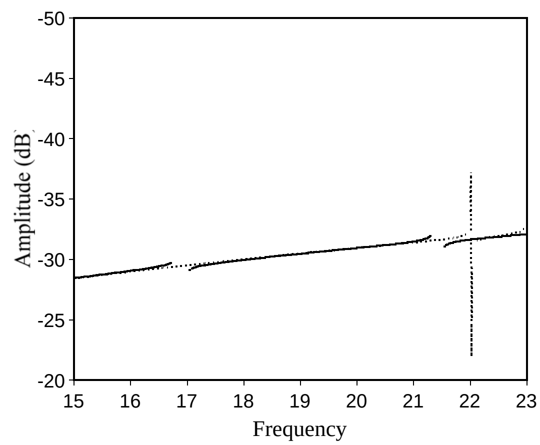

(b) a higher frequency domain

Fig. (9). The frequency response of a rotating spindle with and without a crack, ($\bar{\Omega} = 0.5, \ a/D = 0.25, \ \bar{z}^* = 0.5$)

4. The crack will drastically influence the dynamic characteristics of a spindle with magnetic bearings if the crack is present at the middle portion of the spindle.

REFERENCES

[1] S. C. Huang, Y. M. Huang and S. M.Shieh, "Vibration and Stability of a Rotating Shaft Containing a Transverse Crack", *Journal of Sound and Vibration*, vol.162, pp. 387-401, 1993.

[2] S. K. Bhaumik, R. Rangaraju, M. A. Venkataswamy, T. A. Bhaskaran and M. A. Parameswara, "Fatigue fracture of crankshaft of an aircraft engine", *Engineering Failure Analysis*, vol. 9(3), pp. 255-263, 2002.

[3] P. F. Rizos, N. Aspragathos, A. D. Dimarogonas, "Dimarogonas Identification of Crack Location and Magnitude in a Cantilever Beam from the Vibration Mode," *Journal of Sound and Vibration*, vol. 138, pp. 381-388, 1990.

[4] D. Broek, "*Elementary Engineering Fracture mechanics*", Martinus Nijhoff Publishers, 1986.

[5] H. Tada, P. Paris and G. Irwin, "*The Stress Analysis of Crack Handbook*", Hellertown, Pennsylvania: Del Research Corporation, 1973.

[6] B. Grabowski, "The Vibrational Behavior of a Turbine Rotor Containing a Transverse Crack", *ASME, Journal of Mechanic Design*, vol. 102, pp. 140-146, 1980.

[7] A. S. Sekhar, "Effects of cracks on rotor system instability", *Mechanism and Machine Theory*, vol. 35(12), pp. 1657-1674, 2000.

[8] N. Bachschmid, P. Pennacchi, E. Tanzi and A. Vania, "Identification of transverse crack position and depth in rotor systems", *Meccanica*, vol. 6, pp. 563-582, 2000.

[9] P. N. Savedra and L .A. Cuitino, "Vibration analysis of rotor for crack identification", *Journal of Vibration and Control*, vol. 8(1), pp.51-67, 2002.

[10] M. J. Goodwin, "Dynamics of Rotor-Bearing System", Unwin Hyman, London, 1989.

[11] J. A. Brandon and K. J. H. Al-Shareef, "On The Applicability of Modal and Response Representations in The Dynamic Analysis of Machine Tool Spindle Bearing Systems", *IMechE, Journal of Engineering Manufacture*, vol. 205, pp. 139-145, 1991.

[12] B.R. Jorgensen and Y. C. Shin, "Dynamics of Spindle-Bearing Systems at High Speeds Including Cutting Load Effects", *ASME, Journal of manufacturing Science and Engineering*, vol. 120, pp. 387-394, 1998.

[13] W. R. Wang and C. N. Chang, "Dynamic Analysis and Design of a Machine Tool Spindle-Bearing System", *ASME, Journal of Vibration and Acoustics*, vol. 116, pp. 280-285, 1994.

[14] R.G. Parker and C. j. Mote, "Vibration and Coupling Phenomena in Asymmetric Disk-Spindle Systems", *ASME, Journal of Applied Mechanics*, vol. 63, pp. 953-961, 1996.

[15] I.Y. Shen, "Closed-Form Forced Response of a Damped, Rotating, Multiple Disks/Spindle System", *ASME, Journal of Applied Mechanics*, vol. 64, pp. 343-352, 1997.

[16] F.T. Barwell, Bearing System, Principles and Practice, Oxford University Press, New York, 1979.

[17] M. Chinta and A. B. Palazzolo, "Stability and Bifurcation of Rotor Motion in a Magnetic Bearing", *Journal of sound and vibration*, vol. 214(5), pp. 793-803, 1998.

[18] C. Delprete, G. Genta and A. Repaci, "Numerical Simulation of the Dynamic Behavior of Rotors on Active Magnetic Bearings", In: Proceedings of the 7th International Symposium on Transport Phenomena and Dynamics of Rotating Machinery, Honolulu, Hawaii, USA, 1998.

[19] M. Komori and T. Hamasaki, "Improvement and Evaluation of Bearing Stiffness in High Tc Superconducting Magnetic Bearing", *IEEE Transactions on Applied Superconductivity*, vol. 11(1), pp. 1677-1680, 2001.

[20] H. Chang and S. C. Chung, "Integrated Design of Radial Active Magnetic Bearing Systems Using Genetic Algorithms", *Mechatronics*, vol. 12(1), pp.19-36, 2002.

[21] Q. Tan, M. Liu and H. Meng, "Study on Bearing Capacity and Stiffness of Radial Magnetic Bearing", *Journal of Tribology* (in China), vol. 14(4), pp. 337-344, 1994.

[22] Y. He, D. Guo and F. Chu, "Using genetic algorithms to detect and configure shaft crack for rotor-bearing system", *Computer Methods in Applied Mechanics and Engineering*, vol. 190(45), pp. 5895-5906, 2001.

[23] M. A. Mohiuddin and Y. A. Khulief, "Dynamic response analysis of rotor-bearing systems with cracked shaft", *ASME, Journal of Mechanical Design*, vol. 124(4), pp. 690-696, 2002.

[24] S. Prabhakar and A. S. Sekhar and A R. Mohanty, "Detection and monitoring of cracks in a rotor-bearing system using wavelet transforms", *Mechanical Systems and Signal Processing*, vol. 15(2), pp. 447-450, 2001.

[25] B. W. Huang and H. K. Kung, "A Variation of Instability in a Rotating Spindle System with Various Bearings", *International Journal of Mechanical Science*, vol. 45(1), pp. 57-72, 2003.

[26] A. D. Dimarogonas and S. A. Paipetis, "*Analytical Methods in Rotor Dynamics*", Applied Science Publishers, New York, 1983.

[27] M. Krawczuk and W. M. Ostachowicz, "Transverse Natural Vibrations of a Cracked Beam Loaded with a Constant Axial Force", *ASME, Journal of Vibration and Acoustics*, vol. 115, pp. 524-528, 1993.

[28] S. Herranz, F. J. Campa, L N López de Lacalle, *et al*., "The milling of airframe components with low rigidity: a general approach for the avoidance of static and dynamic problems", *Procc. Int. Mechanical Inst. Part B Journal of Engineering Manufacture*, vol. 219(B11), pp. 789-801, 2005.

[29] M. C. Wu and S. C. Huang, "Vibration and Crack Detection of a Rotor with Speed-Dependent Bearings", *International Journal of Mechanical Science*, vol. 40(6), pp. 545-555, 1998.

Ductile Tearing under Low-Constraint Conditions

Bhagyashree Panda, *Department of Mechanical Engineering, Aryan Institute of Engineering & Technology, Bhubaneswar, bhagyashree2561@gmail.com*
Subhasis Sarkar, *Department of Mechanical Engineering, NM Institute of Engineering & Technology, Bhubaneswar, subhasissarkar14@yahoo.co.in*
Sidharth Pradhan, *Department of Mechanical Engineering, Capital Engineering College, Bhubaneswar, sidharthpradhan265@gmail.com*

Abstract: This paper deals with several issues in the ductile tearing assessment relevant to the fracture criteria and test methods for find out resistance of crack growth under low-constraint conditions. Specially, the influence of specimen geometry and shape, type and length of the main stress raiser, boundary restraints, load biaxiality, history of loading and plastic were thoroughly analysed experimentally. With respect to the problem of transferring crack anisotropy, our results shows that underlying assumptions of the current concept of ductile tearing evoke a suspicion from different points of view. To find out the reason for space between the model descriptions and measurements we place forward a concept of innovative engineering through-life assessment of the fracture process in sheet metals.

Keywords: Plane stress fracture, crack parameters, load biaxiality, thin-sheet aluminium, steady state tearing.

INTRODUCTION

Thin-walled components find many applications in aerospace, mechanical, civil, and ocean engineering. The nucleation and propagation of crack-like flaws in such components of ductile materials is often accompanied by the development of low-constraint flow fields under the uniform distribution of tensile or compressive stresses. It is of scientific and practical interest to develop a general fracture criterion and a test method such that the nucleation and extension of a single tear crack in damage-tolerant components made from metallic, nonmetallic or composite materials could be assessed in a unified manner. This is the main reason behind the long-standing efforts of our research team towards the development of a general concept of Mode I fracture under biaxial loading in tension and/or compression.

To establish the basic principles of this concept, called the Unified Methodology (UM) of fracture investigation, we performed an extensive experimental study of stable crack growth in brittle and ductile materials [1-17]. Focus was on the fracture behaviour of a single through crack in plates and tubes subjected to monotonic loading in tension and compression. Specimens of different geometries and sizes were made from notionally homogeneous metallic and non-metallic materials with widely varying properties. The overall objective of the UM development is to formulate a Transferring Law (TL), i.e., a common function for experimental data on stable crack growth in simple specimens of a relatively small size and large-scale components of complicated geometry. This function can be seen as a key result of the coordinated research efforts towards developing an advanced, coherent, and harmonised Fitness-For-Service (FFS) procedure for a through-life assessment of tearing in thin-walled components made from sheet materials of any physical nature. Because of the breadth of this research programme, the UM concept remains at the development stage and the related exploratory studies are still in progress.

It should be emphasised that in the most practical applications of thin-walled components, the accumulation of structural damage, nucleation of a tear crack and its extension occur under biaxial loading. Presently, a well-known lack of consensus exists with respect to the magnitude and direction of the differences in the biaxial fracture behaviour as compared to the uniaxial tension. According to Eftis *et al.* [18] "…the theories of Griffith and Irwin are incapable of proper treatment of biaxial effect". What is more, they are also conceptually incapable to describe Mode I crack growth in brittle materials under uniform uniaxial compression, i.e., at an extremely low level of in-plane constraint.

Much literature evidence exists in support of both statements. For example, Mode I fracture was repeatedly observed in thin-walled tubes and plates of highly brittle (glassy) materials [5, 7-9, 11, 17] when they were tested under uniform compression. In these tests, through cracks were growing in a well-controlled manner under zero and negative values of the applied stress intensity factor K_I. Of course, sufficient knowledge in this area of fracture mechanics is not yet available and additional research endeavours are highly needed. This is true even for the simplest case where the fracture toughness (K_c) of brittle metallic and non-metallic materials should be determined on standard specimens of the same type under tensile loading. As regards tearing in ductile materials, it is incomprehensible how the residual strength of a large-scale component with globally elastic fracture behaviour could be predicted from the data obtained on laboratory-sized specimen fractured under general yielding. This explains why the problem of plane stress fracture under biaxial loading has not yet been covered by the European FFS procedure FITNET [19].

Further development of the UM is addressed in two parts. The first one consists in continuing our long-standing search for an inherently consistent model description of biaxial fracture in brittle and ductile materials with notionally homogeneous mechanical properties. And the second part is related to the development of a test method for a unified through-life assessment of crack growth in damage-tolerant components operated under low-constraint conditions.

Initially, we intend to compare current fracture criteria and test methods with those used in the UM concept of plane stress tearing. It will be done through conducting an in-depth study of stable crack growth in typical sheet metals widely differing in their mechanical behaviour. The object is to develop, using a minimum number of parameters, a basic TL, which would allow predicting the residual strength of thin-walled components fractured under uniaxial and proportional biaxial loading. Due to the complexity of the problem, the subject matter of these research efforts was reduced to the greatest possible simplicity. Ideally, we intend to deal with only two identical tips of the same internal crack extending within a single straight neck.

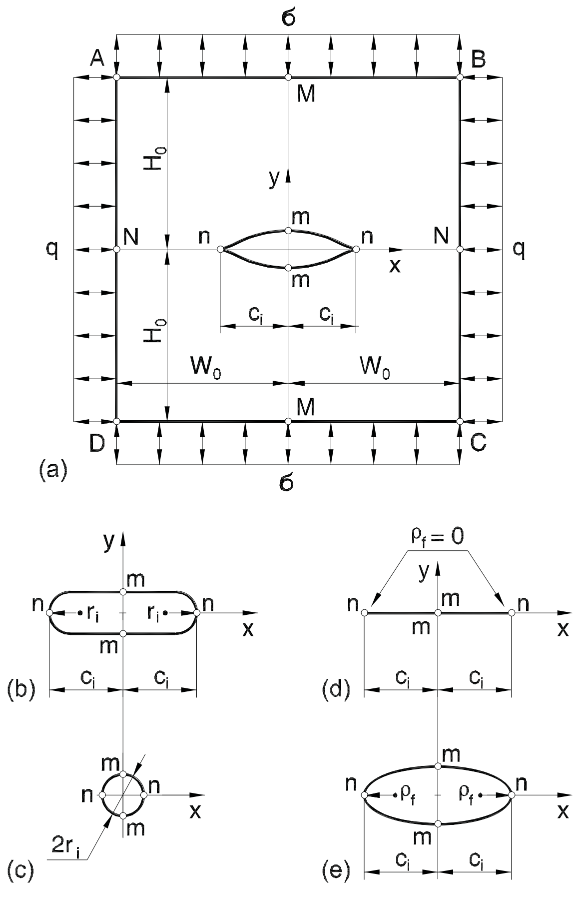

Fig. (1). The basic structural element ABCD with an original geometric imperfection of length $2c_i$ (**a**) and stress raisers having a well-defined geometry of their surfaces, which are often used in fracture mechanics testing (**b**), (**c**) and analysis (**d**), (**e**).

The problem in question is confined to Steady State Tearing (SST) in a square plate shown in Fig. (**1a**). Both in-plane geometry and stress state of this plate, called the Basic Structural Element (BSE), are symmetric with respect to the *x*- and *y*-axes. At the SST stage of the fracture process, the crack-tip stress-strain fields and localised necks, moving ahead the crack tips, can be considered fully developed and self-similar. The length $2c$ of the SST crack is taken as $2c > \kappa B_0$, where B_0 is the original thickness of the BSE and κ is some quotient much larger than 1.0. Thus, the problem under investigation can be readily approximated by a two-dimensional state of generalised plane stress. When the crack tips are advancing synchronously, the outer BSE boundaries move freely under a prescribed value of the remote stress biaxiality ratio $k = q/\sigma$. With regard to the future FFS procedure, the BSE can be treated as a square element removed from a component that is subjected to specific operating conditions.

Brief Outline of the State-of-the-Art

Over the years there has been an urgency to develop valid fracture criteria and standard test methods for a unified assessment of the residual strength of thin-walled components with through cracks growing under low-constraint conditions. As to this research field, the majority of up-to-date advancements are reflected in papers of the Special Issue on Fundamentals and Applications of the CTOA [20], International Standardisation Organisation working document ISO/TC 164/SC 4 N413.3 [21], and ASTM standard E2472-06 [22]. They all underline the worldwide interest in the Crack Tip Opening Angle (CTOA-ψ) and the Crack Tip Opening Displacement (CTOD-δ) as local fracture parameters for metallic materials. Previously, it was pointed out [23] that a single fracture parameter is sufficient to describe the crack-tip stress and strain fields under plane stress conditions. So, a wide consensus exists in the fracture mechanics community that a one-parameter characterisation of stable crack growth under uncontained yielding is conceptually possible and resistance to tearing, at least in sheet metals, can be quantified solely by a constant value ψ_c of the CTOA-ψ parameter.

In order to complete the existing flaw assessment procedure SINTAP, the CTOD-δ_5 parameter was proposed [24, 25] as a thin-wall option of the SINTAP. Thus, the general CTOD term should be replaced with the CTOD-δ_5 anticipating an implicit use of the stress intensity factor *K* and *J*-integral in the related FFS procedure. This way towards the development of a general engineering concept that would cover the whole range of industrial applications is not by far the best. There are an abundance of papers reflecting a long-standing controversy whether the R-curves expressed in terms of the *K*, *J*, CTOA-ψ and CTOD-δ, i.e., the local fracture parameters, are proper measures of the resistance to slow stable crack growth. A computational analysis of ductile crack growth [26] demonstrates convincingly that "no approach can be based on a single parameter resistance curve". Decisive experimental evidences of the validity of these statements are widely encountered in the literature. For instance, they are partly presented in our works [1-17, 27-29]. Taken together with a large body of related literature data, they support a common knowledge that the concepts of *K*- and *J*-controlled crack growth in thin-sheet metals are in most cases invalid.

Although fracture toughness testing and analysis are performed by numerous research organisations, there are no standardised methods for the through-life assessment of tearing in sheet materials. Here the term *through-life assessment* means that all measures of fracture resistance are determined continuously from the instant of nucleation of a Naturally Forming Crack (NFC) and up to the complete loss of load carrying capacity. This technique of collecting and analysing test data was first used in our tests of thin plates made from a ductile metallic material. A set of the relevant experimental results, treated as the displacement-based fracture parameters, are presented in what follows. The remaining test data and analyses will be considered in two forthcoming papers entitled: "Energy-Based Assessment of Ductile Tearing under Low-Constraint Conditions" and "Comprehensive Assessment of Ductile Tearing under Low-Constraint Conditions". The latter paper will combine the recent achievements in the field and in this way will foster overcoming a number of problems that prevent completion of the FFS procedure FITNET [19].

The contribution of these studies to advancing the state-of-the-art will concern identifying: (i) where current fracture criteria and test procedures are inadequate, (ii) how they could be modified to improve the transferability of data obtained under uncontained yielding and, finally, (iii) whether or not the local measure of fracture resistance (CTOA-ψ_c) can be coupled with the local and global measures of SST resistance used in the UM concept.

Original Stress Raisers

Any study on plane stress tearing in specimens or components made from thin sheets of ductile metallic materials deals with the interplay of elasticity, plasticity, necking, damage, and cracking. Generally, the life cycle of unnotched specimens tested under uniaxial or biaxial loading may be considered to comprise the following stages: (i) elastic behaviour with the initiation of plastic behaviour, (ii) diffused necking, (iii) localised necking, (iv) nucleation of an NFC and, finally, (v) its propagation up to the complete loss of load carrying capacity. For the conventional fracture mechanics analysis, the first three stages, being the precursor of the last two, usually are not related directly to the cracking behaviour. This undesirable gap impedes both improvement of fracture mechanics analyses and development of an effective FFS procedure.

In the UM, localised necking is treated as an integral part of ductile tearing both at the instant of NFC nucleation and during the whole process of crack extension. The exact location of the fracture initiation site is an ill-defined function of inevitable imperfections in the specimen geometry, loading conditions, and boundary restraints imposed by the grips, together with the variability of the material properties. To trigger the progressive process of single-site necking followed by single-site cracking in a predetermined location and direction, a variety of imperfections are employed in plane-stress fracture studies. According to the standard test methods, the specimen should contain initial fatigue precracks at the tips of the starting slot [21, 22]. However, it is common knowledge that the crack extension resistance of metallic materials may be influenced significantly by the preloading history. In particular, a strong influence of the fatigue crack growth history on the fracture toughness of thin-sheet aluminium alloy 2024-T3 was reported in [30] for a specific value of the ratio B_0 / c.

At present, there is no possibility to establish a one-to-one correspondence between the initial fatigue damages near the crack tips in different specimens whose geometry and boundary restraints vary over wide ranges. That is why in the specimen preparation, special care must be taken to prevent the introduction of uncontrollable initial damages and residual stresses into the material to be tested. The UM tests are carried out on specimens with original imperfections having relatively simple geometry and a well-defined form of their tips. By convention, the specified starting slots (Figs. **1b** and **1c**) are taken as damage-free defects. Their dimensions 2 c_i and 2 r_i are sufficiently small. It means that at the instant of fracture initiation the tensile stress σ or compressive stress q averaged across the BSE ligament depends only slightly on the variation of the notch size. At the same time, the imperfection should be sufficiently large to concentrate all thinning, hardening, plastic dissipation, and structural damage inside a single localised neck. Cracks initiated from such imperfections often raise the most concern when the residual strength of damage-tolerant components need to be assessed.

Generally, necks and cracks initiate inboard of an internal geometric imperfection with smooth surfaces [31], i.e., away from the points n in Figs. (**1b**) and (**1c**). This is due to the absence of lateral stresses on the traction-free surface of the imperfection, which reduces the hydrostatic component of the local stress field and also the normal stress. As compared to the tests of specimens with a fatigue precrack, the proper amount of slow stable crack extension in a notched specimen that correlates with the initial NFC state can be established in a relatively simple and reproducible manner. This has an important bearing on the practical implementation of the UM procedure for assessing ductile tearing in thin-sheet metals. Earlier we demonstrated by experimental examples [32, 33] that an open circular hole of a specific size is the preferable geometric imperfection to avoid the complicated analysis of the transition in fracture behaviour from the "flat" to "slant" mechanism of crack extension. In specimens with this stress raiser, both nucleation and extension of the NFC occur by shear localisation, i.e. by mixed Mode I and Mode III cracking in the plane inclined at 45° to the loading plane.

Through-Life Assessment of Plane Stress Tearing

The UM test method should provide an easy-to-use tool for through-life assessment of crack growth in laboratory-sized specimens showing purely elastic, elastic-plastic, and purely plastic fracture behaviour. For an engineering concept of such a wide scope, it is appropriate to operate with mechanical parameters that can be quantified using simple and well-defined procedures. Therefore, the TL we are searching for should be based mostly on the analysis of data that are collected by macroscopic measurements in the form of test records *loads vs. displacements vs. crack extensions*. Here, a special attention is given to the displacements of the so-called extreme points m, n on the inner and M, N on the outer BSE boundaries (Fig. **1a**). The displacements v(m), u(n), taken together with the displacements v(M), u(N), serve as the main geometric variables needed for linking changes in the geometry of a growing crack with those of the outer boundaries. When developing the UM, we realised from the outset that no parameter of near-crack-tip fields and no micromechanically-based description of the fracture process can be incorporated into a sufficiently general and practical computational procedure unless the above linkage is properly described.

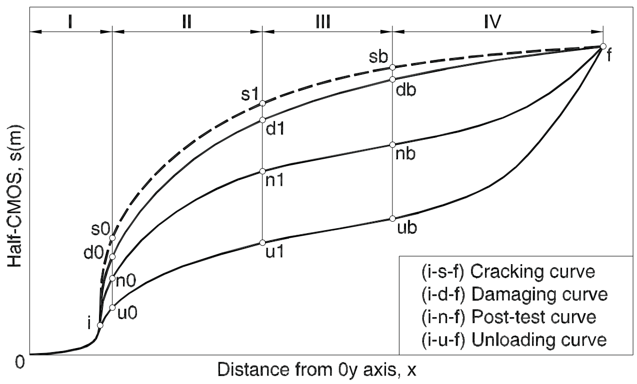

Fig. (2). Schematic presentation of through-life fracture curves relating to each other by imaginary (instantaneous) unloading – reloading cycles made at the moment "0" of the NFC nucleation (states s0-u0-d0), moment "1" of the onset of SST crack growth (states s1-u1-d1), and moment "b" of the transition to the TET stage of fracture process (states sb-ub-db).

The UM focuses on changes in the geometry of the whole crack border, instead of considering mainly the crack-tip displacements, which are given much attention in current fracture mechanics analyses. Ductile tearing is seen as an interplay of four concurrent processes represented by the through-life fracture curves (Fig. **2**), which characterise the step-wise crack growth (*i-s-f* curve), accumulation of localised damage ahead of the crack tips until the critical level is reached (*i-d-f*), attainment of the zero value of stresses in the immediate vicinity of the crack tips (*i-n-f*), and formation of specific stress-strain fields in the fully-unloaded specimen (*i-u-f*). These curves, excluding (*i-n-f*), can be readily plotted using the test records P *vs*. $2c$ and P *vs*. $2s$(m), where $2s$(m) is the Crack Mouth Opening Spacing (CMOS) measured between points m (Fig. **1**).

To construct the post-test fracture curve (*i-n-f*), the crack border distance $2s(\mathrm{m})_n$ and the corresponding crack length $2c$ should be measured in pairs using the upper and lower halves of the fully fractured specimen. A quarter of the upper crack border is sketched in Fig. (**3a**). The virtual crack extension is modelled by moving the upper specimen half towards its lower counterpart, as it was described by Lloyd [34] for an idealised fracture of a middle cracked specimen. Thus, the changes in the geometric parameters of the inner and outer boundaries should be assessed jointly for a loaded (moving crack), fully unloaded (arrested crack), and broken-down (fully developed crack) specimen.

Assume that an undeformed undamaged unstressed specimen of the BSE type contains a small stress raiser with the simplest geometry (Fig. **1c**). Shortly after the application of monotone tensile load σ, two localised necks start forming in the vicinity of the extreme points n. The necks concentrate plastic deformation and damage inside Active Damage Zones (ADZ). Each zone encompasses some volume of severely transformed material with specific damage morphology. The structural damage accumulated inside the ADZs reaches its critical level at the instant i (stage I in Fig. **2**). During further loading, both zones simultaneously become fully developed just before the moment where an NFC starts to grow (state $s0$ in Fig. **2**). The NFC comprises two tear cracks that freely nucleate inboard of the plate and then come to the surfaces of the original stress raiser by the mechanism of internal necking near the points n (Fig. **1c**).

Immediately after the nucleation, the NFC starts to propagate with an intermittent attainment of the local instabilities in a step-wise manner (stage II in Fig. **2**). The repeated cycles *loading-partial unloading-reloading* generate a cyclic variation in the crack profile geometry, which is bounded by the cracking and damaging curves shown in Fig. (**2**). Thus, tearing is thought of as the incubation of localised damage followed by the material separation in the ADZs. The SST regime of crack extension is attained at the instant $s1$ (stage III), when the alternating process of cracking and damaging occurs in a self-similar manner. Thereafter the SST crack growth enters stage IV, called the Tail-End Tearing (TET) fracture. As the crack tips continue to move, they are under the increasing influence of the BSE boundaries ($x = \pm W_0$ in Fig. **1a**). Finally, the fracture process comes to an end at the instant f of full separation. It should be underlined that the crack growth portion of each test record (*o-f* curves in Figs. **2** and **3**) cannot be treated as reflecting the real material properties without introducing essential restrictions on the geometries of the specimen and original stress raiser, testing system stiffness, boundary conditions imposed by the grips, loading rate, and fracture process as such.

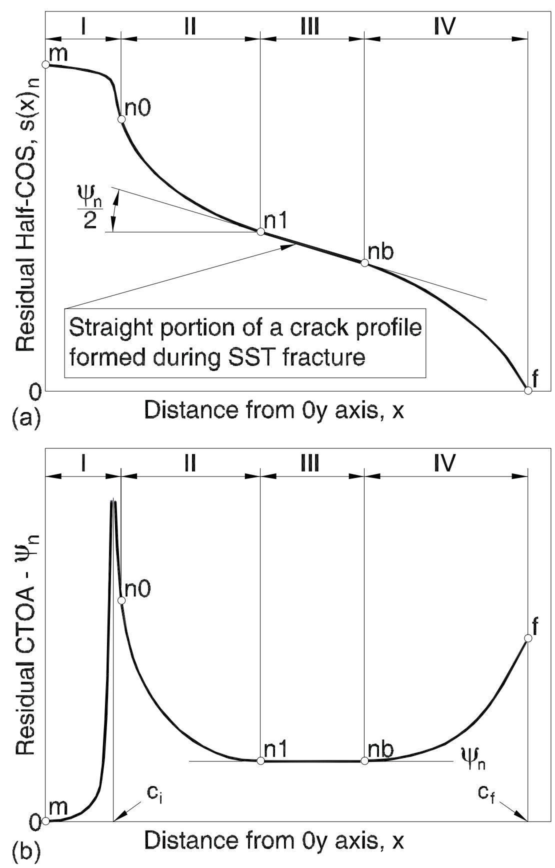

Fig. (3). Schematic presentation of through-life fracture curves expressed in terms of the residual crack opening spacing (**a**) and residual CTOA (**b**) determined by moving the upper half of a completely fractured BSE towards its lower one.

In the tests to separation failure, the displacements v(M) and u(N) of the outer boundaries should increase at a constant and extremely small strain rate, i.e., under the quasi-fixed grip condition. This is needed for providing the regime of displacement-controlled tearing from the very instant of NFC nucleation and also for making the SST range of crack extension as wide as possible. The SST portion of the post-test curves (n1-nb in Figs. **2** and **3**) denotes the quasi-static fracture process occurring nearly at constant levels of the net-section stresses σ_N and q_N (see Fig. **1a**), wherein the increments in the Crack Opening Spacing (COS), $2\Delta s(x, c)_n$, are in direct proportion to those in the distance between the virtual crack tips. To establish the SST portion of crack advancements unambiguously, one should consider the through-life fracture curve (Fig. **3a**) obtained on a specimen broken down in two identical pieces by a slow stable tear crack. To reduce unavoidable scatter in determining the CTOA angle ψ_n (Fig. **3**), two tear cracks of identical geometry must be initiated in a sufficiently large plate from an original stress raiser of a sufficiently small size.

Parameters of a Centre Crack and Fracture Criteria

The centre crack border provides the basis for much of the following discussion, so it is important to outline the main features of its characterisation. In the current concept of plane stress tearing, the original crack is represented by its planar dimensions irrespective of the spacing $2s(x, c)_u$ between its upper and lower boundaries in a fully unloaded specimen (compare Figs. **4a** and **4b**). The crack modelling procedure is specified by the equation $2a = 2c$, where $2a$ is the length of a mathematically sharp cut with coinciding surfaces (see straight lines in Figs. **1d** and **4a**). In the conventional analysis of tearing, the COS, $2s(x, c)$, and the Crack Opening Displacement (COD), $2v(x, c)$, both being caused by the same applied load, are undistinguishable. Consequently, the crack profile angle ψ_c measured near the crack tip (Fig. **4a**) is usually treated as the opening angle, i.e., as an increment in the angular displacement induced by external loading. However, the spacing-based and displacement-based parameters in a real specimen can differ widely, as seen from the scheme in Fig. (**4b**). It is common knowledge that such differences depend on the specimen geometry and size, type and length of the original stress raiser, boundary restraints, material properties, and loading history. It is pertinent to mention that in the immediate vicinity of the tear crack in a fully unloaded specimen, the material is highly damaged and its behaviour does not respond to the original constitutive relationships.

First, we outline the standard approach to the characterisation of a tear crack profile extending under low-constraint conditions [21, 22]. The commonly used fracture criterion states that crack growth occurs when the CTOA-ψ or, equivalently, the COS-δ at a fixed distance behind the crack-tip attains its critical value ψ_c or δ_c, respectively. Here we consider the determination of the ψ_c angle using optical microscopy to measure the crack contour near its tip (Fig. **4a**). Direct measurements of the COS-δ should be made behind the crack tip and then transformed into the CTOA-ψ values from the following expression:

$$\psi_c = \frac{1}{N}\sum_{i=1}^{N}\psi_i\,,\ \psi_i = 2\tan^{-1}\left(\frac{\delta_{ci}}{2d_i}\right) \qquad \text{... (1)}$$

Here, d_i is the distance measured behind the crack tip, which ranges from 0.5 to 1.5 mm, and δ_{ci} is the related value of the COS. The steady state (average) value of the ψ angle, denoted as ψ_c, is established after a minimum amount of crack

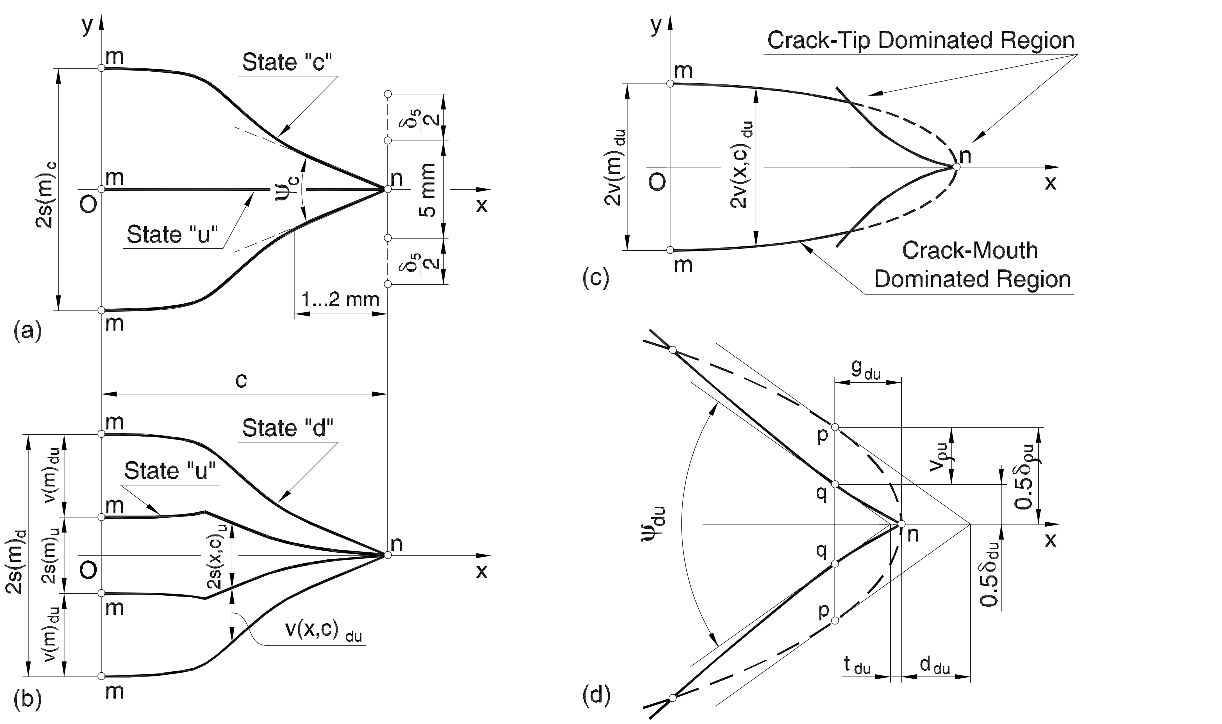

Fig. (4). Definition of the local (ψ_c, δ_5, ψ_{du}, δ_{du}, δ_{pu}, t_{du}, d_{du}) and global [c, $s(m)_c$, $v(m)_{du}$] parameters of the tear crack profile used in the current (**a**) and in the UM (**b**), (**c**), and (**d**) procedures for characterising the fracture resistance during the tear crack extension (all variables are not in scale).

extension Δc_{min}. The latter corresponds to the instant where the angle ψ attains a nearly constant level. If the size requirements of the standards [21, 22] are met, then ψ_c is deemed to characterise the material in the thickness of a specimen tested and to be independent of the in-plane geometry and loading scheme. The practicality and usefulness of this formulation of the fracture criterion for predictions of tearing in airframe materials was demonstrated in many experimental and numerical studies, e.g., those performed by Newman [35-37].

Alternatively, the δ_5-R curve concept developed by Schwalbe [38] can be used for an approximate determination of the CTOA. This concept has a global nature with respect to a growing crack and requires much less effort than the previous one to experimentally determine the ψ_c angle. It provides a relatively simple method because the measurement points should not migrate with the moving crack tip. The CTOD-δ_5 is given by the relative displacement δ_5 between a pair of points on either side of the initial fatigue crack, as shown in Fig. (**4a**). In the initial range of crack extension, the δ_5-R curve can be approximated by a power-law regression fit of the experimental measurements. In this way the CTOD-δ_5 values related to the values Δc of advancement of one crack tip are used to calculate the CTOA according to the relationships

$$\delta_5 = D\Delta c^p\,,\ \psi = \tan^{-1}\left(\frac{d\delta_5}{d\Delta c}\right) \approx \frac{d\delta_5}{d\Delta c} = Dp\Delta c^{p-1} \qquad \dots (2)$$

Our concept of plane stress tearing is based on presenting the profile of a central crack in terms of the COD-$v(x, c)_{du}$, i.e., distances between the mating points on the crack border for a loaded (state d) and fully unloaded (state u) specimen (Figs. **2** and **4b**). For a BSE of a ductile material, it may be described by simple model equations (well-defined curves). The first curve encompasses the so-called crack-mouth dominated region and the other the crack-tip dominated region, as indicated in Fig. (**4c**). Their intersection denotes an imaginary transition from the convex to concave portions of the crack profile. In an actual specimen, these portions are connected by a smooth curve of a transient behaviour. The length of the crack-tip dominated region in brittle materials is negligibly small, compared with the length of the crack-mouth dominated region for the same crack.

First, we consider the UM approach as applied to modelling a tear crack in the BSE of a homogeneous linear elastic material. For this simplest case, the following hypothesis was taken as a starting point. The physical essence of the fracture micro-mechanisms within the ADZ is independent of the sign and value of the stress biaxiality ratio k. This hypothesis suggests that the model descriptions of fracture in tension-dominant and compression-dominant crack geometries are conceptually identical. A simple and still physically relevant approach is to treat the SST as a two-directional extension of an ideal crack in the form of an open elliptic hole (Fig. **1e**). Both tips of this hole in a stress-free BSE made from a given material of a given thickness have identical curvature radii of the surface $\rho = b^2 / c$, where b and c are the minor and major semi-axes of this imaginary hole.

The radius ρ is not a directly measurable physical quantity, but a mathematical abstraction quantitatively characterised by the following equation:

$$\rho_{du} = \frac{v(m)^2_{du}}{c} = \rho \cdot \frac{\left\{1 + C_n\left(\sigma_{du}/E\right)\right\}^2}{\left\{1 + C_m\left(\sigma_{du}/E\right)\right\}} \qquad \dots (3)$$

where C_n and C_m are the stress concentration factors at the points $x = \pm\, c$, $y = 0$ and $x = 0$, $y = \pm\, b$, respectively. They take the form

$$C_n = F_v \cdot \left[1 + 2\sqrt{\frac{c}{\rho}} - k\right] \text{ and } C_m = F_u \cdot \left[k + 2k\sqrt{\frac{\rho}{c}} - 1\right].$$

In the case of a BSE with free-to-move boundaries, the dimensionless elastic compliances of the crack border along the transverse, $F_v = v\left(x = 0, k\right) \cdot E / \left\{b\left(1 - k\right) + 2c\right\} \cdot \sigma$, and longitudinal, $F_u = u\left(x = c, k\right) \cdot E / \left\{k\left(c + 2b\right) - c\right\} \cdot \sigma$ directions depend only upon the dimensionless parameters ρ/c, c/W_0, and H_0/W_0. Taking into account that the F_v/F_u ratio does not vary with the stress-biaxiality ratio k, one can define the ρ radius from equation (3) using the $v(m)_{du}$ values measured on a BSE-type specimen under uniaxial tension.

Due to the interplay between the moving crack tips and the outer specimen boundaries, the ρ value depends upon the aforementioned dimensionless parameters. The initial radius $\rho = \rho_f$ is treated as a characteristic of an SST crack of any length in a stress-free BSE of a given material, plate thickness, and loading scheme. The critical radius of an imaginary elliptic hole corresponds to the geometry of an actual crack extending in the SST regime, when $\rho_{du} = \rho_d$. Here, we assume that the radius ρ_d is an inherent length scale of an ideally brittle material characterising the resistance to SST crack growth in a BSE at a given level of in-plane constraint measured by the k ratio. Thus, the UM criterion of SST fracture at a fixed value of the stress biaxiality ratio k requires that the conditions $\rho = \rho_f$ and $\rho_{du} = \rho_d$ be met simultaneously.

In order to assess the ductile tearing resistance under plane stress conditions, a set of additional assumptions was incorporated in the UM fracture analysis. They can be formulated as follows: (i) There are no intrinsic differences between the micromechanical behaviour of a material during the accumulation of diffused damage, localisation of plastic deformation, nucleation of an NFC, and its stable propagation; (ii) Once the peak levels of strain hardening and diffused damage are attained, the incubation and accumulation of localised damage near the stress-free crack surfaces manifest themselves mainly as an increase in the crack-border spacing; and (iii) The behaviour of the SST crack under general yielding reflects a specific interplay between the inner and outer boundaries of a cracked plate.

The latest (updated) version of the multi-parameter characterisation of near crack-tip profiles is sketched in Fig. (**4d**). All geometric variables in question emerge from the joint consideration of two model equations:

$$v(x,c)_{du} = v(m)_{du}\sqrt{1 - x^2/c^2} \qquad \dots (4)$$

$$v(x,c)_{du} = G \cdot \left(c - x\right)^F \qquad \dots (5)$$

that describe geometries of the crack-mouth and crack-tip dominated regions, respectively. Taking the derivatives of these expressions with respect to the distance x from the $0y$ axis (Fig. **4c**) and upon equating them, one can define the characteristic points on the near crack-tip profile. These are two pairs of points p and q behind the crack tip where the CTOA-ψ and COD-δ both attain their critical values ψ_{du} and δ_{du}, respectively. When taken together with the global crack profile parameters (Fig. **2**), the crack-tip parameters shown in Fig. (**4d**) can be used in assessing the ductile tearing resistance. Despite the fact that the UM uses a large number of geometric parameters, all of them are directly related to each other and also to the data of macroscopic measurements.

To be in line with the standards [21, 22], the UM fracture criterion is formulated solely in terms of the CTOA-ψ parameter. We hope that the latter has a great deal of physical significance because the geometry of the crack-tip dominated region results from direct measurements. It is assumed that the critical state of an extending tear crack is reached at the instant when its tips enter the SST range of crack advancement (point $s1$ in Fig. **2**). This fracture event corresponds to the instant where the minimum value ψ_n of the residual angle ψ_{res} (point $n1$ in Fig. **3b**) and the maximum value of the active component of the CTOA- ψ_{du}, denoted ψ_d, are attained simultaneously. Finally, the UM criterion of ductile tearing is given by two conditions:

$$\psi_{res} = \psi_n \text{ and } \psi_{du} = \psi_d \qquad \ldots (6)$$

Scope of Study and Specimens

This paper deals with the characterisation of plane stress tearing under uncontained yielding in flat specimens (Fig. **5**) made from thin sheets of an aircraft-skin aluminium alloy. The principal obstacle to the development of an easy-to-use TL is placed by the need to correlate too many variables governing the plane-stress crack growth in ductile materials. These are the parameters of elasticity, including those of out-of-plane

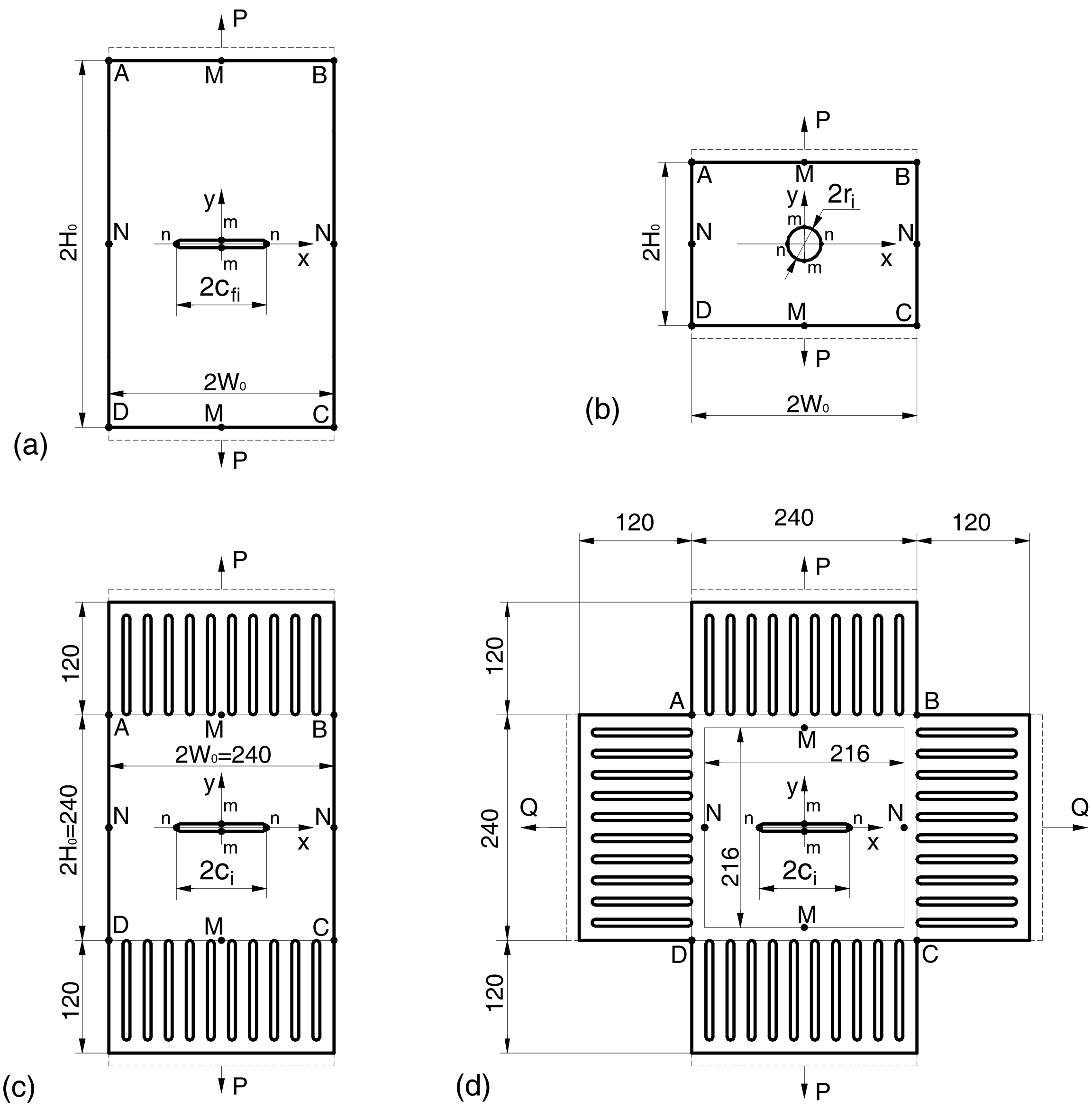

Fig. (5). Problem domains ABCD attached to different loading fixtures referred to as (**a**) – M(T), (**b**) –MR(T), (**c**) – MM(T), and (**d**) – MM(T-TC) specimens (the dimensions are indicated in millimetres).

deformation (buckling); plasticity, including those of residual stress effects and anisotropy; geometric and structural imperfections; diffused and localised necking; damage and cracking. So it seems highly improbable that the stable crack growth could be predicted using only the near crack-tip parameters in isolation from the global deformation pattern and localised necking.

The problem under consideration is addressed in two parts. We start with comparing the profiles of tear cracks in loaded and in fully-unloaded specimens of different geometries under different boundary conditions. The intent is to reveal the basic distinctions between the current and the UM approaches to analysing changes in the overall geometry of a stationary and an extending tear crack in the BSE. In the second part of this work, different characterisations of plane stress tearing are contrasted with each other. The objective is to determine whether they can or cannot assess the SST state of a crack growing under different in-plane constraint states. To obtain conclusive evidences, we tested specimens of widely different shapes, sizes, and loading scheme.

The need for a better understanding of the reason for the gap between the results of model descriptions and measurements dictates the breadth of experimental efforts. Therefore, the fracture tests in question are meant to give the "big picture" of structural behaviour of a middle-cracked plate under different constraint states (Fig. **5**). The uniaxial and biaxial crack extension tests were performed on flat specimens with Problem Domains (PD) of various shapes and sizes given in Table **1**. Each rectangular PD was attached to a specific loading fixture.

Table 1. Principal Dimensions of Specimens

Specimen code [a]	$2W_0$ mm	$2H_0$ mm	$2H_p(2W_q)$ mm	$2c_i$ mm
MM(T-TC) - 1.0 - 2.0	240	240	480(480)	30
MM(T) - 1.0 - 2.0	240	240	480	Variable
M(T) - 3.0 - 10.0	1200	3600	3600	60
M(T) - 1.0 - 10.0	1200	1200	1200	Variable
MR(T) - 1.0 - 1.0	120	120	120	2.0
MR(T) - 0.1 - 1.0	120	12	12	2.0

[a] The numerical values in the specimen code denote the shape ratio (H_0 / W_0) and scale ratio (W_0 / W_0^{BSE}), respectively. In this work we take $2W_0^{BSE}$ =120 mm.

It should be emphasised that providing a sufficiently high degree of uniformity of nominal stress fields in tension- and/or compression-dominant PDs is essential for collecting acceptable test data. In the case of tensile loading, this can be achieved through increasing the aspect ratio H_0 / W_0 for the M(T) specimen (Fig. **5a**). However when the PD geometry and size are fixed, some special modifications in the loading fixture design must be used [39, 40]. One of them is applying the external load through thin strips placed between the PD and the grips. These strips in specimens of thin-sheet materials are usually cut with saw, as shown in Figs. (**5c**) and (**5d**).

The larger is the number of slots in each side of the fixture and the thinner and longer they are, the larger the size of a uniformly stressed region. This region was defined for a crack-free PD with the use of the photoelastic and, in parallel, elastic finite element analyses [39]. The accepted number of the slots of length equal to 0.85 W_0 in each side of the MM(T-TC) specimen was 15. In this case, the width and height of the uniformly stressed region reach 0.9 of the PD dimensions $2W_0$ = $2H_0$ = 240 mm. The deviation of the peak values in the nominal stress distribution from the average values of the elastic stresses $\sigma(x) = P / 2W_0 B_0$ and $q(y) = Q / 2H_0 B_0$ does not exceed 2% within the uniformly stressed region. There are good reasons to suggest that in our specimens the uniformly stressed region is larger than that in typical specimens used in biaxial fracture tests. References [18, 41-44] show an example.

Consider unavoidable distinctions between the boundary conditions for the PDs of the cruciform specimen (Fig. **5d**) and the BSE (Fig. **1a**). The lack of restraints imposed by an actual loading fixture on the deformation of an actual PD is seldom if ever in occurrence. For typical combinations of the specimen and grips, exact stress and displacement conditions along the boundaries between the middle-cracked PD and the loading fixtures are usually nonuniform and unknown. Generally, both stress conditions and displacement conditions are present. Under mixed boundary conditions the applied stress is a function not only of position, but also of the crack aspect ratio c/W_0 and shape ratio H_0 / W_0. Mixed boundary conditions are part way towards the general compliant boundary conditions. Such is indeed the case for the elastic-plastic behaviour of the specimens shown in Figs (**5c**) and (**5d**).

When the restraints imposed on the outer boundaries are close to the case of displacement-controlled loading, the fracture response strongly depends on the crack length both in the quantitative and qualitative senses [45]. Earlier it was shown [15] that the asymptotic values of the energy dissipation rate R for the MM(T) and MM(T-TC) specimens (Fig. **5**) made of low-carbon steel are substantially different. On the other hand, the imposition of the "fixed-grip" and "dead-load" constraints on the outer BSE boundaries may have the effect of eliminating the presence of the remote load q in the energy rate calculations [18].

In our tests we used three types of loading fixtures. The first one provides rigid clamping along the horizontal boundaries of a PD (Figs. **5a** and **5b**). If the shape requirements $H_0 \geq 2\ W_0$ and $c \leq W_0 / 3$ are fulfilled and buckling is prevented, the geometry in Fig. (**5a**) is usually referred to as the standard M(T) specimen. The second loading fixture ensures a nearly uniform distribution of the nominal tensile stress $\sigma(x)$ on the horizontal boundaries of a PD with no initial crack. This geometry (Fig. **5c**) is referred to as the MM(T) specimen. It is rigidly clamped along the lines $y = \pm H_p$, where $H_p = (H_0 + 120)$mm. Finally, the third fixture in combination with a square PD represents a cruciform specimen (Fig. **5d**) designated as MM(T-TC). When $2c_0 = 0$, nearly uniform stresses $\sigma(x)$ and $q(y)$ prevail on the horizontal and vertical boundaries of the given PD, respectively. The specimen is rigidly clamped along the lines $x = \pm W_q$ and $y = \pm H_p$. The MM(T-TC) geometry is treated as the physical counterpart of the BSE geometry.

A centred starting slot of length $2c_i$ was made in each specimen of the M(T), MM(T) and MM(T-TC) geometry by manual cutting. The depth of cut was kept to the practical minimum for a jeweller's saw. All slots had nominally straight and parallel flanks with the root radii r_i less than 0.06 mm. A single circular hole of diameter $2r_i$ = 2mm was introduced in each MR(T) specimen (Fig. **5b**). This hole is treated as a small geometric imperfection ensuring that the fracture process occurs only by the mechanism of shear localisation [32, 33].

The specimens M(T)-3.0-10.0, M(T)-1.0-10.0, MR(T)-1.0-1.0, and MR(T)-0.1-1.0 shown in Fig. (**5**) and Table **1** are considered to be more constrained than the others. The low-constrained specimens include the MM(T)-1.0-2.0 specimens tested along (LT direction) and across (TL direction) the rolling direction. Several MR(T)-1.0-1.0 specimens were also tested along and across the rolling direction.

MATERIAL AND TESTING

The test material is aluminium alloy D16AT in as-received condition, having the form of 1.4-1.5mm thick sheets. Its chemical composition and mechanical properties are close to those of AL 2024-T3. In particular, the properties of AL-alloy D16AT under ambient conditions were determined in tensile tests using the standard plate-type specimens are as follows: the elastic modulus E = 67.7 GPa, Poisson's ratio ν = 0.32, the 0.2% offset yield strength σ_Y = 338MPa, and the ultimate tensile strength σ_{UTS} = 465MPa. Three identical specimens were fabricated and tested in accordance with the ASTM Standard Method for Tension Testing of Metallic Materials (E8M-85). These specimens were subjected to displacement-controlled loading (with the rate 0.017 mm/s) in direction parallel to the rolling direction of the sheets.

In collecting test data, a purely mechanistic approach based on the minimum of assumptions was adopted. Uniaxial and biaxial tests were conducted in accordance with the main requirements of the ASTM Standard Practice for R-Curve Determination (E561-92a). All specimens (see Table **1**), excluding those of the MR(T) type, were tested with guide plates lightly clamped against the out-of-plane displacement. Buckling of thin plates is a competitive failure mechanism resulting from the elastic compressive stress acting parallel to the crack growth line. We deem that the various guide plate systems used in our tests do allow decoupling the fracture process from the buckling. However, the stiffness of these plates was different and unknown. It must be noted here that in wide panel tests conducted by Dawicke *et al.* [46] the load versus crack extension diagram strongly depends on the stiffness of the guide plate system. Our measurements of the out-of-plane displacements in tests of the MR(T)-1.0-1.0 specimens demonstrate that the buckling is negligibly small when the condition $c \leq 0.4W_0$ is fulfilled.

During displacement controlled tests, the MM(T) and MM(T-TC) specimens of the first set were loaded incrementally, allowing some time between steps for the crack to stabilise before measuring the load, crack length, and crack profile. The MR(T) specimens were tested under monotonically increasing displacement v(M) (with the rate 0.001mm/s, without stopping and unloading). Displacements as a function of the proportionally applied loads P and Q were measured concurrently at the extreme points on the inner and outer PD boundaries that are shown in (Fig. **5**). To develop R-curves with confidence, we usually assigned more than ten steps (data points) for each test condition. Once the crack stabilised within seconds after the loading was stopped, a close-up photograph of the crack-tip profile was taken. In most cases, four diagrams were recorded simultaneously, namely, P *vs*. $2v$ (m), P *vs*. transverse displacement $2v$(M), P *vs*. load point displacement $2v$(P), and P *vs*. displacement $2u$(N).

All the measurements mentioned above were repeated for the rest of these specimens containing an arrested tear crack after they were completely unloaded. The specimens were strained very slowly to approximate the quasi-fixed grip conditions. Thus, the fracture process could be readily stopped by the termination of loading with or without subsequent unloading. The above measurements were repeated once again at the instant t when the loading was stopped and then after the complete unloading at the instant u. Typical diagrams are shown in Figs. (**6**-**8**). In processing test data, the state t is treated as the state d on the damaging curve (i-d-f) shown in Fig. (**2**).

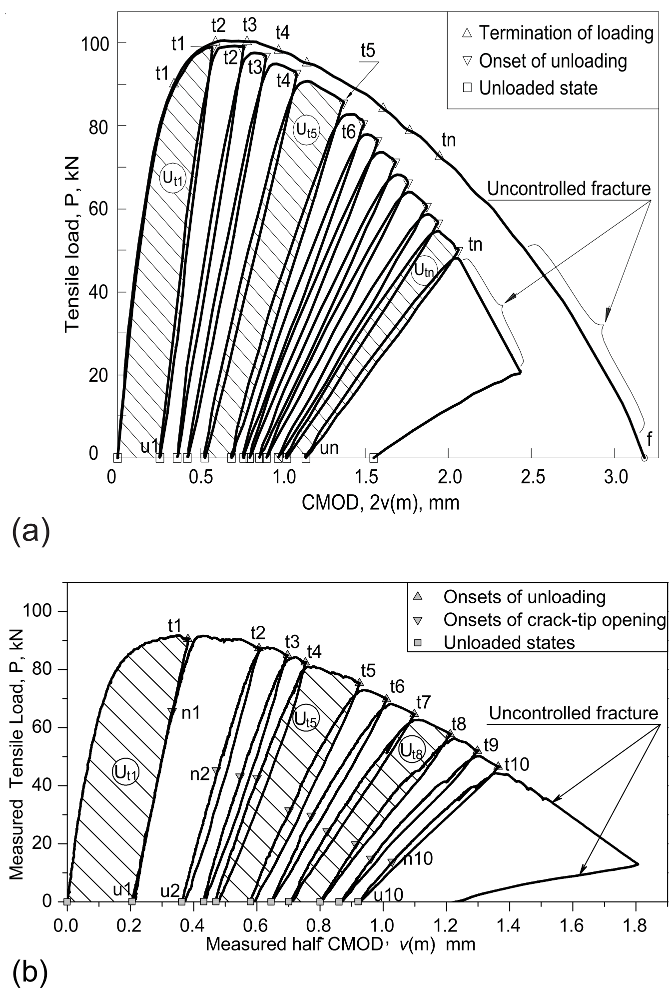

Fig. (6). $P - 2v$(m) test records for two MM(T-TC)-1.0-2.0 specimens (**a**) and an MM(T)-1.0-2.0 specimen (**b**), all tested in the LT direction. The cruciform specimens were tested in proportional biaxial tension at a constant value of load biaxiality ratio k = 0.8.

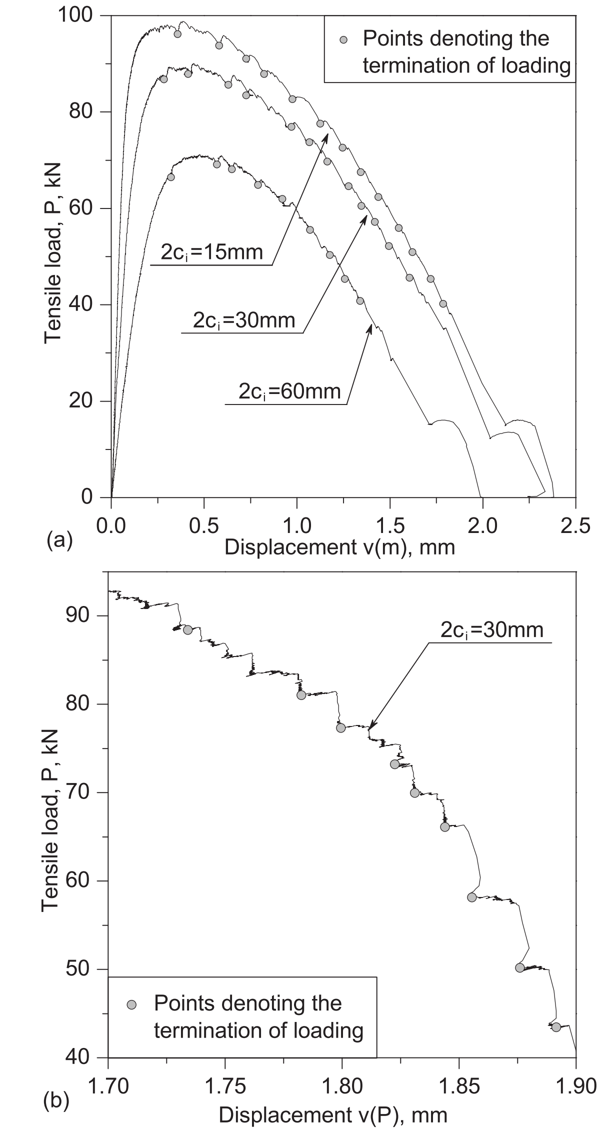

Fig. (7). Test records of tensile load *vs.* displacements v(m) measured near the points m for MM(T)-1.0-2.0 (TL direction) specimens (**a**) and displacements v(P) measured near the points P of load application for MM(T-TC)-1.0-2.0 (LT direction) specimens (**b**).

EXPERIMENTAL RESULTS

First, we consider a set of data obtained from direct measurements of the crack profiles in PDs of different shapes, sizes, and loading scheme (Figs. **9**-**17**). Taken together, they firmly support the UM approach to characterizing the tear crack profile in the BSE. One can see that the crack-mouth compliances calculated from the Eftis-Liebowitz equation [47] are lower than the measured values (Figs. **9** and **10**). This equation was included in the ASTM standard (E561-92a) in spite of the fact that in the literature, empirically determined crack-mouth compliances are always higher than those from the above equation. Schijve points out in [48] that the discrepancies vary from a few percent to 11 percent. They should not be due to the approximate character of the equation, as exemplified by the finite element analysis presented in [49]. The situation is so much unsatisfactory because the above discrepancies could not be explained by the experimental inaccuracies of measurements either. But much more important is the fact that the equation in question has no relevance to the tear crack profiles in loaded specimens (states t in Figs. **10** and **12**).

The above results are helpful for understanding the UM procedure for displacement-based assessment of plane stress tearing resistance. Initially, one has to determine a relationship between the tear crack length $2c$ and the tensile load P (Fig, **18**). In processing, test data are averaged and then approximated by cubic polynomials. Next step consists in polynomial fitting of the test data on the specimen compliance (Fig. **19**). Two relationships in question allow correlating the crack length $2c$ with the CMOD-$2v(\mathrm{m})_{\mathrm{du}}$. Thus, one can determine the values $2v(\mathrm{m})_{\mathrm{du}}$ for any crack length within the range $c_i \le c < W_f$, as it is shown in Fig. (**20**). And finally, these through-life fracture curves are used together with equations (3), (4), and (5) in accordance with the aforementioned explanations. The effect of load biaxiality on the geometric parameters characterising the near crack-tip profile is displayed in Figs. (**21**), (**22**), and (**23**).

To support the UM presentation of the through-life fracture behaviour (Fig. **2**), we consider test records obtained on specimens of the MM(T) and MM(T-TC) types (Figs. **6**, **7**, and **8**). Tear cracks were growing under well-developed or general yielding in all specimens (see as an example Fig. **24**), excluding those of the width $2W_0 = 1200$mm. The tear crack

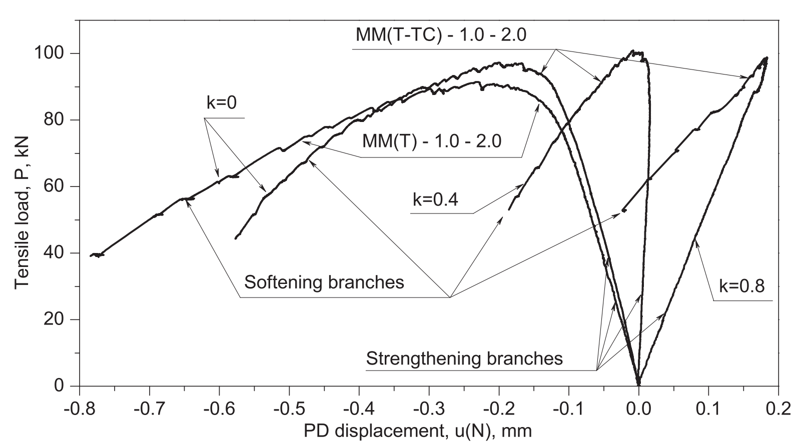

Fig. (8). P-u(N) test records for MM(T) – 1.0 – 2.0 and MM(T-TC) – 1.0 – 2.0 specimens (LT direction) containing an identical stress raiser of length $2c_{\mathrm{fi}} = 30$ mm and radius of its tips $r_{\mathrm{fi}} \approx 0.06$ mm. The specimens were loaded in uniaxial and proportional biaxial tension at different k ratios using the antibuckling guide plates.

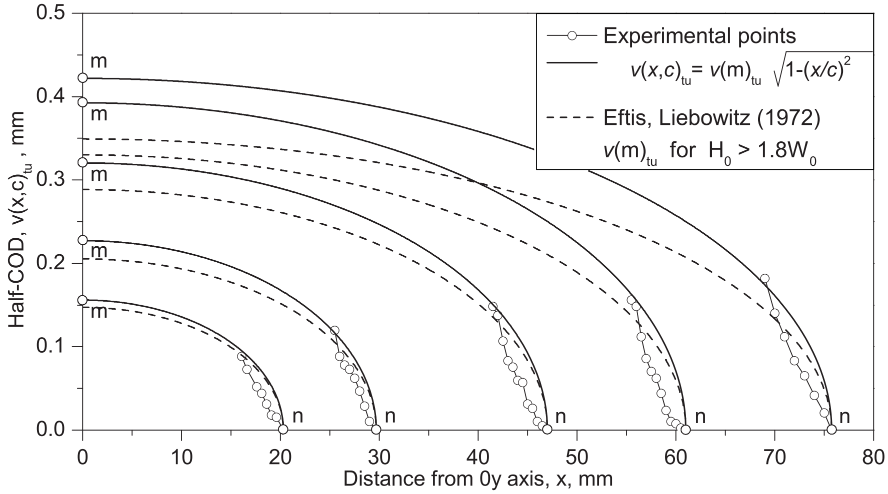

Fig. (9). Comparison of the elliptic crack profiles expressed in terms of the opening displacements, which are constructed using the directly measured (solid lines) and calculated (dashed lines) values of $v(m)_{tu}$ for an MM(T)-1.0-2.0 specimen (LT direction). The global profiles (solid lines) are matched with the corresponding displacements measured near the crack tip.

extension occurs by an intermittent attainment of the local instabilities displayed graphically in Figs. (**7**) and (**8**). These observations are in accord with the arguments of Turner and Kolednik [50], who believe that the crack growth at both micro- and macro-levels may be seen as a two-stage process of damage accumulation in a process zone followed by the actual separation being a micro-

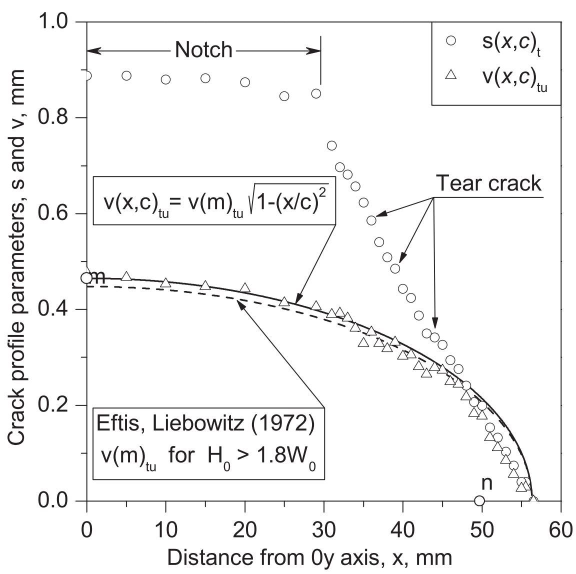

Fig. (10). Experimental data on the opening spacing $s(x,c)_t$ for a stress raiser in a large-scale M(T)-3.0-10.0 specimen of width $2W_0$=1200 mm at the termination of loading (state t) and an elliptic curve (solid line) approximating the distribution of the in-plane displacements $v(x,c)_{tu} = s(x,c)_t - s(x,c)_u$, where $s(x,c)_u$ is the opening spacing after the complete unloading. The elliptic crack profile (dashed line) was calculated assuming the linear elastic behaviour of the actual crack modelled by a mathematical cut of the length $2a = 2c$.

instability at the crack tip. It is pertinent to cite here the following conclusion of Ming Li and Richmond [51]: "In the hardening regime, plastic or inelastic deformation at modest strain is intrinsically unstable and nonuniform and develops in small temporally confined discontinuous jumps." Therefore, the SST is treated in the UM as a step-wise enlargement of the crack cavity bounded by *i-s-f* and *i-d-f* curves shown in Fig. (**2**).

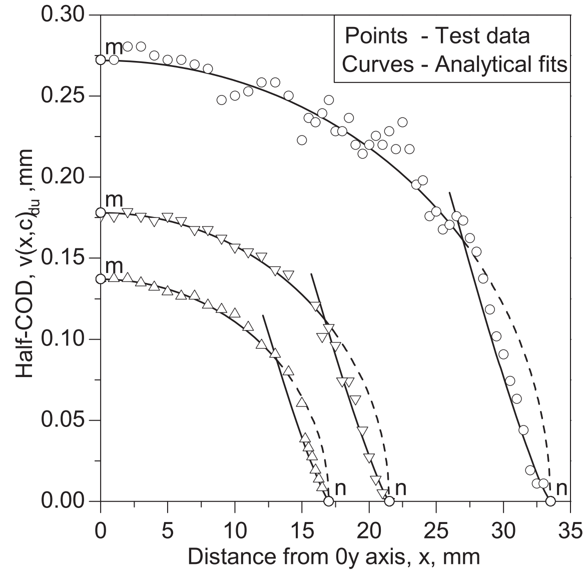

Fig. (11). Experimental data on the opening displacement $v(x,c)_{du}$ for one-quarter profile of the same tear crack in an MM(T-TC)-1.0-2.0 (LT direction) specimen after three cycles of unloading-reloading at k = 0.4.

DISCUSSION

The need to include the crack-tip length scales in the fracture mechanics analyses has long been felt and has been increasingly urgent. In studies of plane stress tearing, the commonly-used length scale is presented by the radius r_0 of a zone with a highly deformed or damaged material defined by the simplifying relationship

$$r_0 = \frac{1}{\pi} \cdot \left(K_c / \sigma_0 \right)^2 \quad \dots (7)$$

where K_c is the fracture toughness of the material and σ_0 is its characteristic strength under uniform tensile loading. The value r_0 is considered to be the intrinsic characteristic of a material because both quantities K_c and σ_0 are usually taken as physical constants, i.e., material properties. In fact, these assumptions have no definite physical meaning and reflect widespread oversimplifications often used to perform engineering calculations.

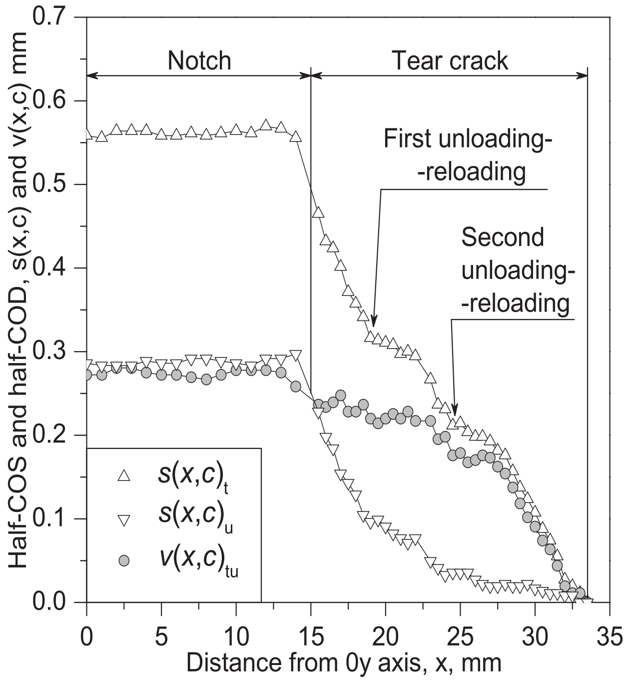

Fig. (12). Experimental data on the opening spacing $s(x,c)$ for one-quarter of the original stress raiser in an MM(T-TC)-1.0-2.0 (LT direction) specimen at the termination of loading (state t) and full unloading (state u) and the opening displacement $v(x,c)_{tu}$ defined as the difference $s(x,c)_t - s(x,c)_u$. The stress raiser comprises a centre notch and two tear cracks grown-up at $k = 0.4$ with three cycles of unloading-reloading.

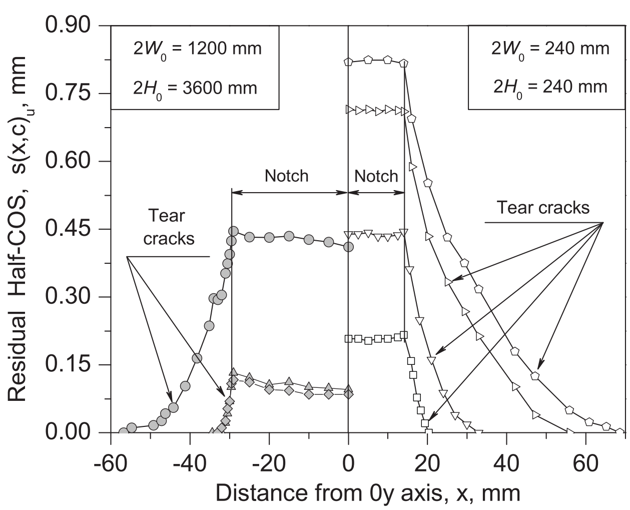

Fig. (13). Comparison of one-quarters of stress raisers in fully unloaded M(T)-3.0-10.0 (left side) and MM(T)-1.0-2.0 (right side) specimens showing very different values of irreversible displacements for raisers of the same length in low-constraint PDs with widely different sizes.

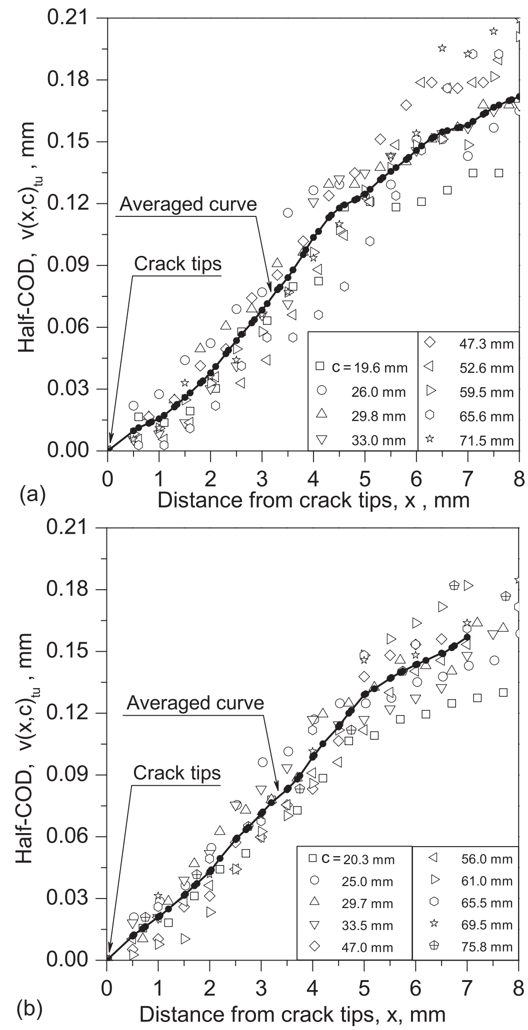

Fig. (14). Crack opening displacements measured near the tips of tear cracks of different lengths in two identical MM(T)-1.0-2.0 (LT direction) specimens during their unloading from the instant t designating the termination of loading to the instant u designating the state of complete unloading.

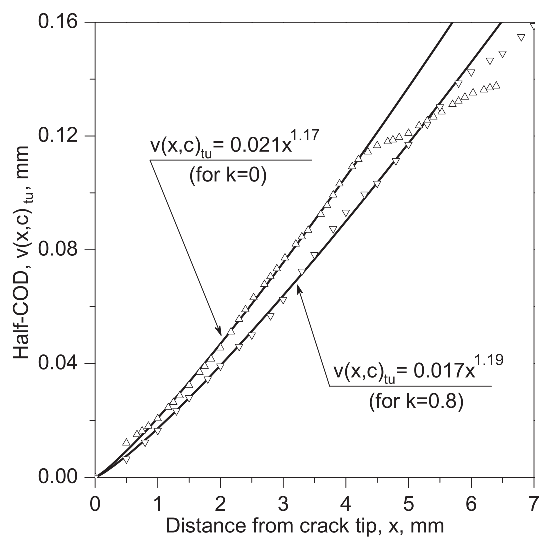

Fig. (15). Comparison of crack-tip dominated regions of the tear crack profiles in uniaxially-loaded MM(T)-1.0-2.0 and biaxially-loaded MM(T-TC)-1.0-2.0 specimens (both tested along the LT direction) used to calculate the local parameters of the crack profile.

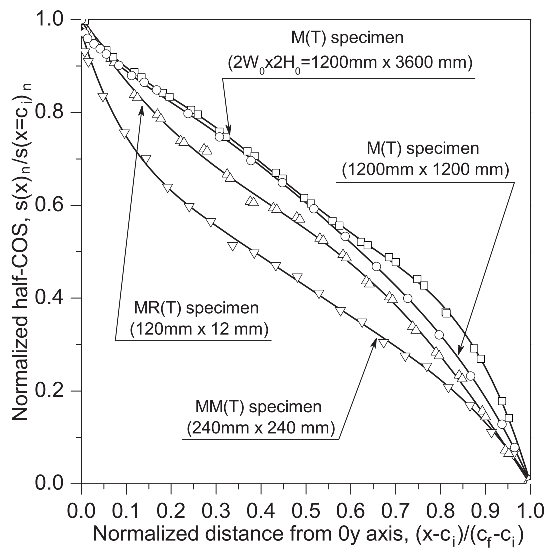

Fig. (16). Normalised presentation of one-quarter crack profiles obtained for fully-fractured specimens of different geometries and sizes that were tested under uniaxial tension in the LT direction.

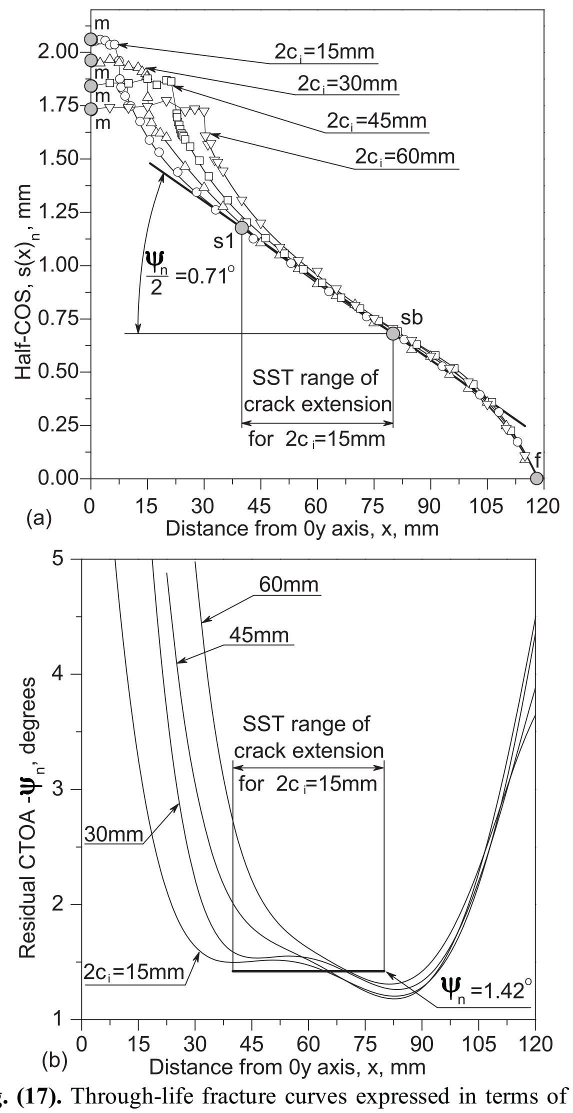

Fig. (17). Through-life fracture curves expressed in terms of the residual COS (**a**) and residual CTOA (**b**) for MM(T)-1.0-2.0 (TL orientation) specimens containing initial notches of different lengths $2c_i$.

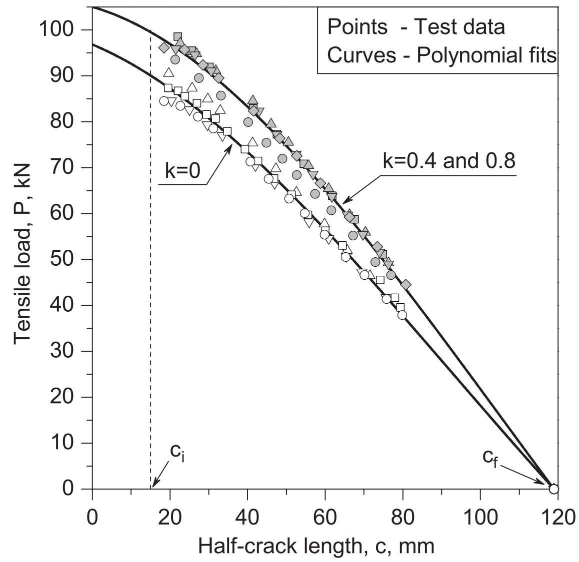

Fig. (18). Experimental diagrams for MM(T)-1.0-2.0 (LT direction) specimens tested in uniaxial tension and MM(T-TC)-1.0-2.0 (LT direction) specimens tested in biaxial tension.

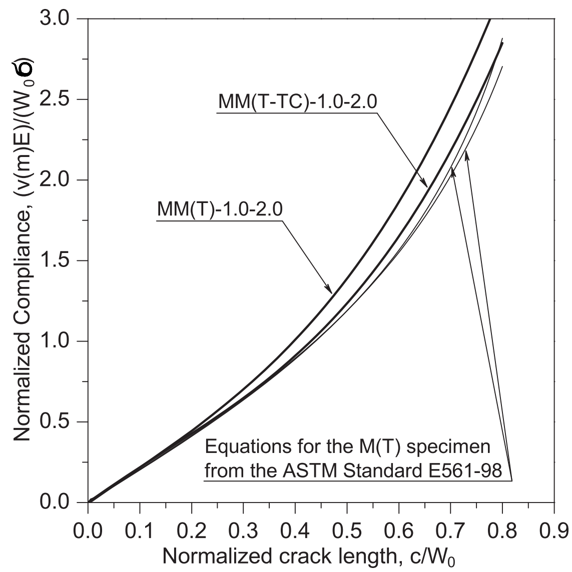

Fig. (19). Comparison of experimentally determined and calculated compliance curves for cracks in two identical MM(T)-1.0-2.0 specimens (LT direction). These curves were established on the assumption that during unloading-reloading cycles the test record can be represented by a straight line passing through the characteristic points *t* and *u* (see Fig. **6**). It means that the hysteresis behaviour observed was completely neglected. They are shown together with the averaged compliance curves for the MM(T-TC)-1.0-2.0 (LT direction) specimens tested at $k = 0.4$ and 0.8.

It should be emphasised that the current FFS procedures typically employ the following presumption: the yield strength σ_Y and the ultimate tensile strength σ_{UTS}, being the averaged net-section stresses, can be directly related to the critical parameters of local (near crack-tip) stress fields like K_c or J_c. As to the conceptual inconsistency of this statement, it is sufficient to say that the often used characteristics of tensile strength and fracture resistance all are size- and constraint-dependent quantities. Therefore, the length scale presented by equation (7) cannot be coupled in a simple and unified manner

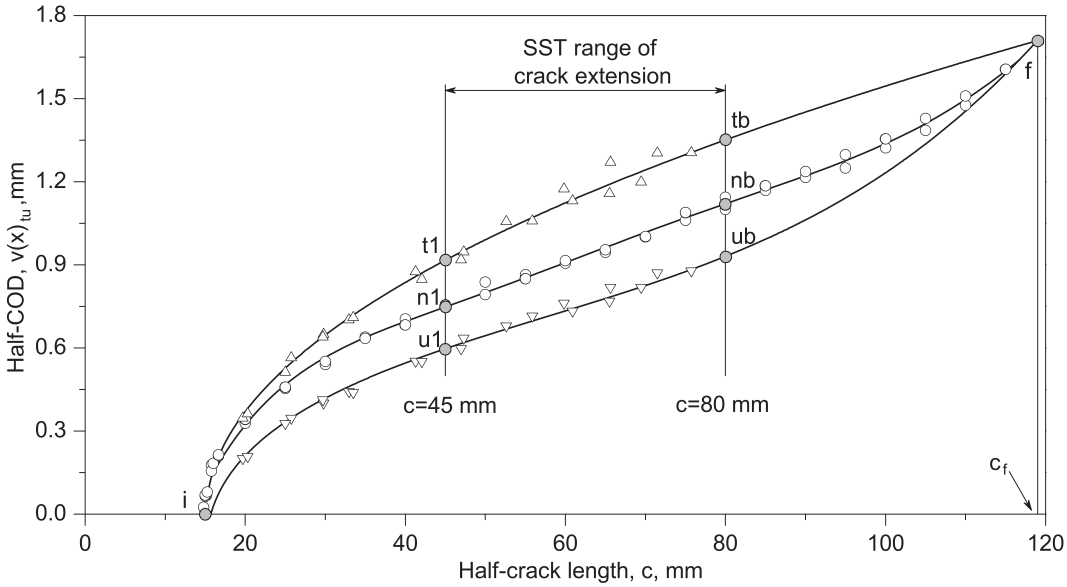

Fig. (20). Through-life fracture curves for two MM(T)-1.0-2.0 (LT direction) specimens with an identical original notch of length $2c_i$=30 mm. Both specimens were tested with the unloading-reloading cycles.

with the parameters characterising the global fracture behaviour of stationary and extending tear cracks. In other words, the characteristics like K_c, σ_0, and r_0 cannot be used in a consistent FFS procedure as interrelated physical properties of a substance.

Our experimental results call into question the very meaning of the current approach to the characterisation of ductile tearing resistance in terms of the CTOA-ψ_c parameter. It is seen from the data presented in Figs. (**25b**), (**26**), and (**27b**) that the angle ψ, as defined in standard test methods [21, 22], usually does not reach a distinct constant level ψ_c. This is also the case with the fracture resistance characterization using both procedures based on equations (1) and (2). The δ-R curves in Fig. (**27a**) can be treated as close prototypes of R curves expressed in terms of the CTOA-δ_5 values.

It is supposed that the valid criterion of SST crack growth should be reasonably independent of, at least, the PD geometry and size, as well as the geometry and size of the initial imperfection. The criterion values ψ_c, ψ_n, and ψ_{du} all depend on these geometric variables and also on the boundary restraints [53]. Besides, they are influenced by changes in the preloading history (Fig. **25a**), by load biaxiality (Fig. **23a**), and only slightly by plastic anisotropy (Table **2**). In comparison with the angle ψ_c, the novel characteristics ψ_n, and ψ_{du} are more consistent and reproducible quantities. Obviously, the large scatter in CTOA-ψ_c (Fig. **25b**) does not allow us to distinguish the small differences in the tearing resistance due

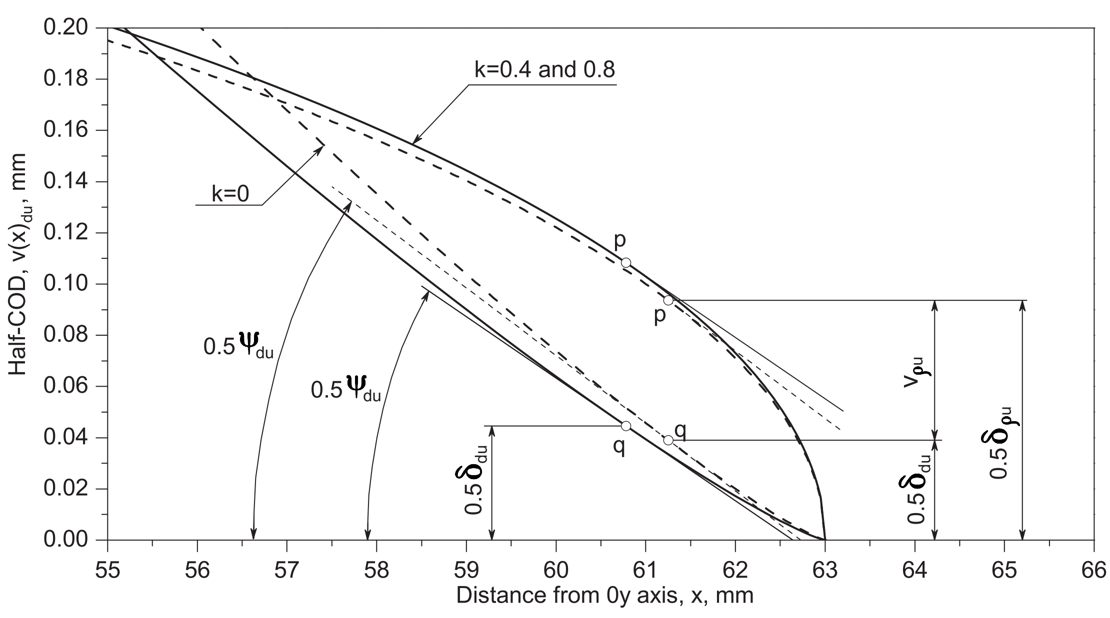

Fig. (21). Comparison of near crack-tip dominated regions for MM(T)-1.0-2.0 and MM(T-TC)-1.0-2.0 specimens (both tested along the LT direction), when the length of tear cracks at the onset of unloading was equal.

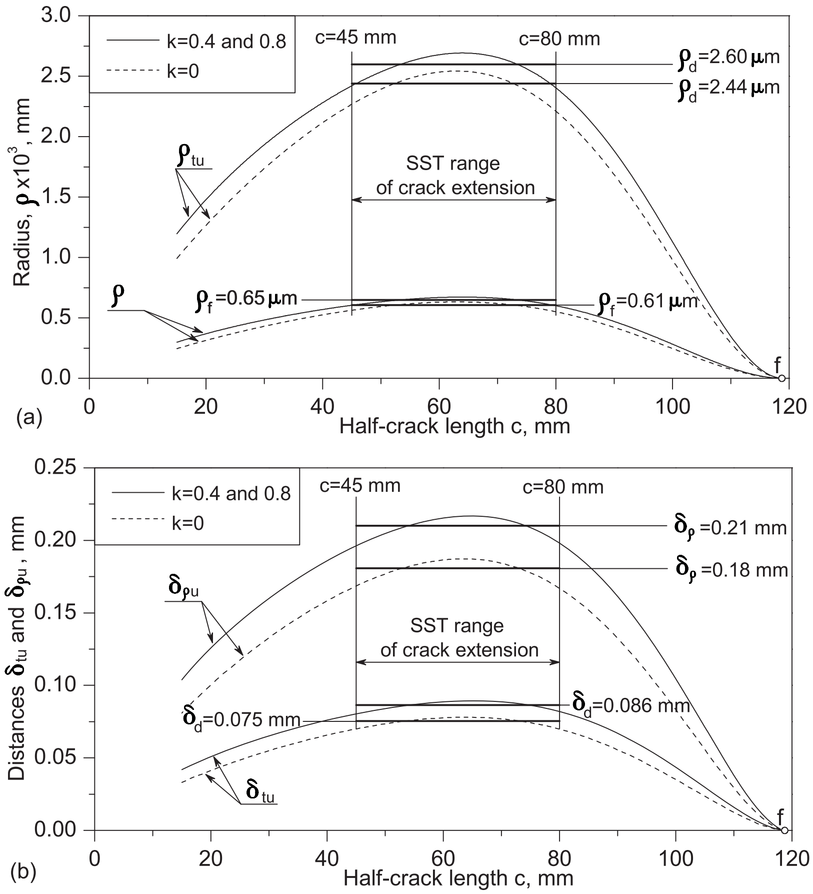

Fig. (22). Variations in the crack-tip radii ρ and ρ_{tu} in MM(T)-1.0-2.0 and MM(T-TC)-1.0-2.0 specimens (both tested along the LT direction) (**a**) and the related variations in the characteristic distances between the imaginary crack tips (**b**).

to relatively weak effects of plastic anisotropy, loading history, and load biaxiality.

It seems likely that the CTOD-δ_5 and CTOA-ψ_c concepts need to be modified or replaced by a necessarily more pragmatic approach to assessing the ductile tearing resistance. From this standpoint their combined use with displacement-based characterisations of tearing developed in the framework of the UM is very promising. Being directly connected with parameters of the global fracture behaviour, the angles ψ_n and ψ_{du} in comparison with the CTOA-ψ_c are easy to obtain in an unadulterated form. This advantage comes into a particular prominence in tests of brittle materials, when the ψ_c angles are comparatively small (fractions of a degree). Clearly, a sufficiently general engineering procedure must allow quantification of the fracture toughness for brittle and ductile materials in a simple and unified manner. The special convenience of the UM concept is that the angles ψ_n and ψ_{du} can be easily incorporated into the energy-based analysis of SST using the test records with loading-unloading cycles shown in Fig. (**6**).

GENERAL REMARKS

Though the study is still in progress, the experimental results seems to be more valuable to make the following conclusions. The constraint-dependent formulation and extension of an NFC is followed by the some set of linear and angular geometric variables.

This irreversible process occurs in an systematic arrangement and not permanently discontinuous manner. The UM relation between length scales and specific angles of SST crack growth can be readily introduced in an procedure for assessing the normal stress tearing resistance. This line of research tells us to establish a simple TL i.e., interrelation between local parameters of a travelling crack tip in laboratory sized specimen.

The overall results of our work suggest that there are a number of basic distinctions of the UM from the currently used concept of plane stress tearing. The most important among them are as follows:

1. A through crack is presented in fracture analysis by simple model equations describing the difference in distances between the crack borders in a loaded and completely unloaded specimen. It means that the deformed configuration of a tear crack profile serves as the reference state.
2. The tear crack growth is treated in fracture analysis as a step-wise extension of a two-tier model of the crack border along the mutually perpendicular directions.
3. The novel criterion of ductile tearing instability states that the transition from stable to unstable cracking occurs at the instant where the system *material-specimen-loading device* attains its minimum capacity

to absorb permanent strains and structural damage (measured by the ψ_n angle) simultaneously with the attainment of the maximum crack-driving force (measured by the ψ_{du} angle).

4. The description of the cracking initiated from a small geometric imperfection is in harmony with the description of the crack growth starting from the tips of an elongated stress raiser.

5. The displacement-based characteristics of the crack-tip and crack-mouth dominated regions on a centre crack border are related to each other in a clear-cut manner and all of them can be extracted directly from the macroscopic measurements.

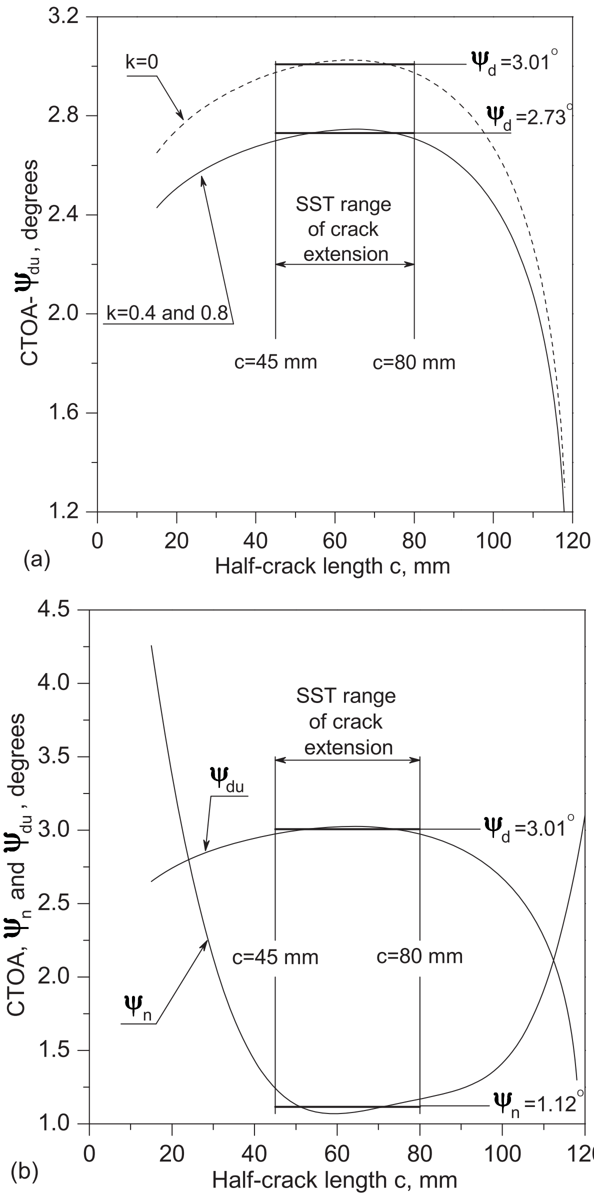

Fig. (23). Variations in the active components of resistance to plane stress tearing under uniaxial and biaxial tension in the MM(T)-1.0-2.0 and MM(T-C)-1.0-2.0 specimens with an original crack of length $2c_i$ = 30mm (LT direction) both tested with unloading-reloading cycles (**a**) and a comparison of the active and residual components of the angle ψ for the given MM(T)-1.0-2.0 specimen (**b**).

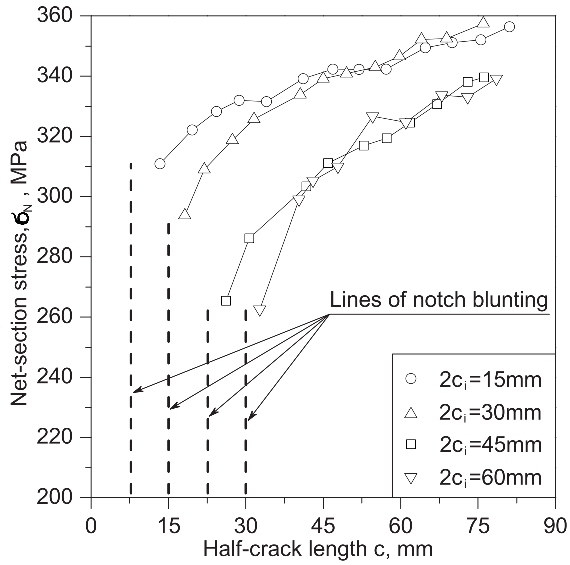

Fig. (24). A set of experimental diagrams for MM(T)-1.0-2.0 (TL direction) specimens with original notches of different lengths $2c_i$. The specimens were tested with the termination of loading (without performing the cycles of unloading-reloading).

6. The length scales reflecting variations in the geometry of the crack-tip dominated region are introduced in fracture analysis without an a priori assumption of the existence of material constants like K_c, J_c, and σ_0. That is why they fit naturally into the stress- and energy-based descriptions of the SST crack growth.

7. Attention is redirected from analysing stress-strain fields in the vicinity of an ideal crack tip to describing the behaviour of the entire crack border where the effects of buckling, plasticity, structural damage, and interaction between the inner and outer boundaries all are readily accounted for from test records. As a result, our semi-analytic approach allows prediction of fracture instability events without numerical simulations of the near crack-tip stress and strain fields.

8. The stable crack growth in thin sheets of brittle and ductile materials can be studied using fracture toughness characteristics with the same physical meaning;

9. The displacement-based characteristics of SST resistance can be easily separated into constituents suitable for predicting the mechanical behaviour of large-scale components from data collected on simple specimens of relatively small size.

These distinctive features make it reasonable to assume that the UM can provide a sound framework for the future development of a general procedure for a unified assessment of stable crack growth in damage-tolerant structural elements made from thin sheets of brittle and ductile materials subjected to tensile and/or compressive loading. However, due to a developing nature of the UM, there are several uncertainties over the end result of our explorations.

The main ones are the small number of tests on large-scale specimens and the lack of complete understanding how the SST characteristics can be correlated with the

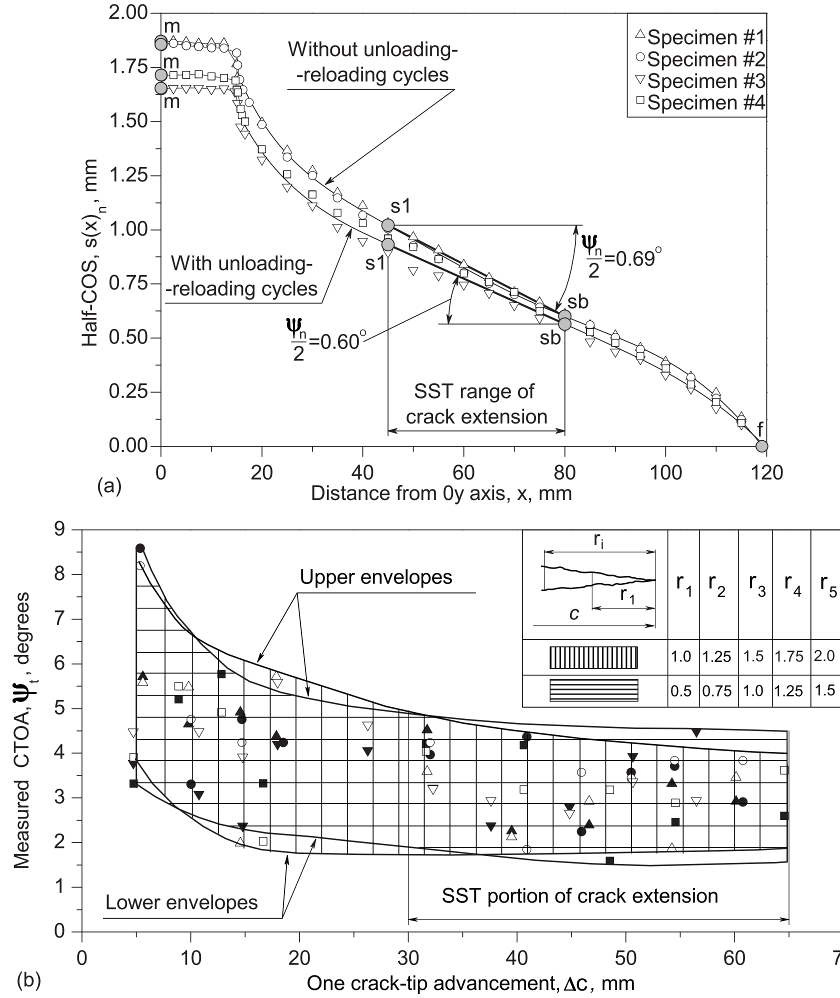

Fig. (25). Effects of introducing the unloading-reloading cycles on the COS-$s(x)_n$ in four MM(T)-1.0-2.0 (LT direction) specimens with an identical stress raiser of length $2c_i$=30 mm (**a**) and the CTOA-ψ_t (**b**) determined for these specimens using two versions of the data processing procedure developed in [52].

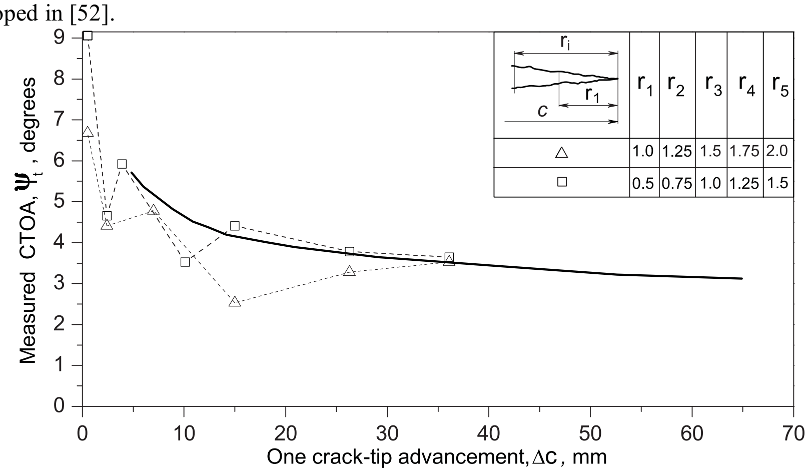

Fig. (26). Comparison of CTOA-ψ angles (points) determined for the large-scale specimen M(T) – 1.0 – 10.0 using two versions of the data processing procedure developed in [52] and the mean curve obtained by averaging the data in Fig. (**25b**).

micromechanical parameters of the moving tips of a slant crack. The limited amount of experimental data generated by this investigation for large-size specimens (Table **2**) cannot offer a sufficient basis for an extensive discussion of the size-scale effects. In addition, we deal only with a purely mechanistic approach, not taking into account the microstructural and physical aspects of the fracture process. It is clear that the results obtained in the framework of such an approach cannot be applied blindly in unexplored areas, i.e., for predicting fracture behaviour of other geometries and materials.

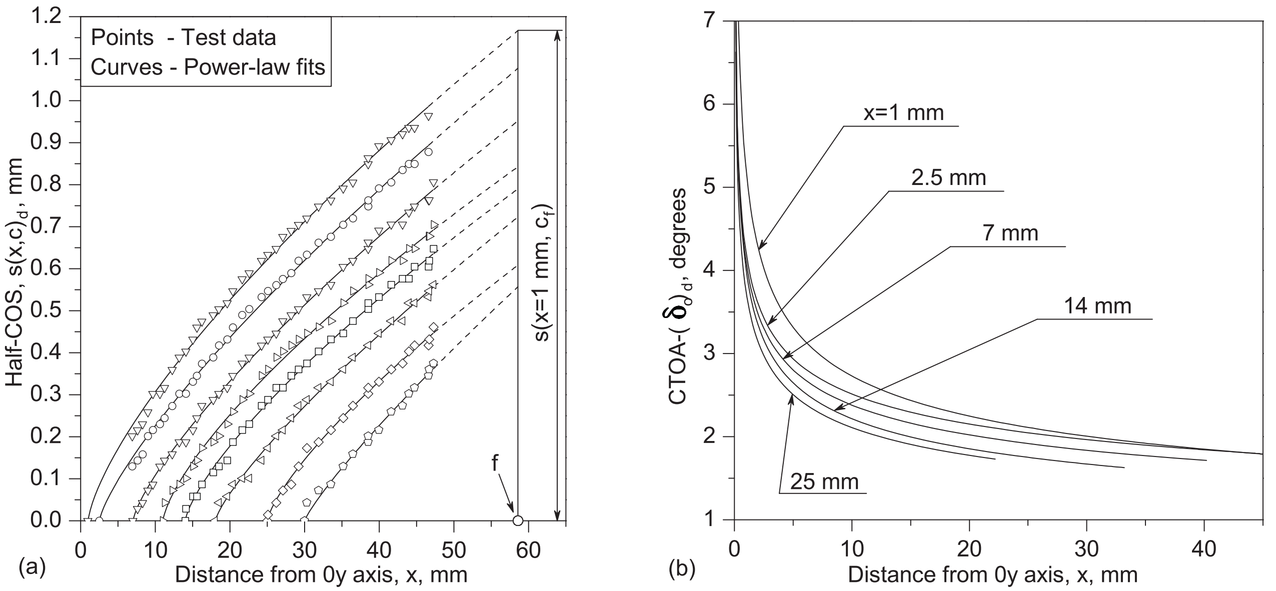

Fig. (27). Variation in the spacing between fixed points on the profile of a continuously moving crack in an MR(T)-1.0-1.0 specimen (**a**) and the related CTOA-(δ_0)$_d$ curves (**b**) determined from equation (2) on a reasonable assumption that $\delta_0 = 2s(x, c) \approx \delta_5$. The difference between the δ_0 and δ_5 values tends to become negligible as the crack elongates under continuous tearing.

At present, the UM may be thought of mainly as a complementary approach to the commonly used fracture criteria and test methods. Our experimental findings and some theoretical novelties derived from them can already be used for further refining of the engineering concept discussed in [20-22]. At the same time, the UM has a distinct potential to be treated as an alternative semi-analytic concept of ductile tearing. This assertion emerges from the aforementioned distinctions between the UM and the conventional methodology of fracture investigation. The experimental results of this study demonstrate that a universal law governing the SST crack growth has not been found yet. However, there are good reasons to believe that in the long run it will be possible to adequately cover at least the main experimental facts using the UM analysis.

ABBREVIATIONS

CTOA	=	Crack Tip Opening Angle
CTOA-ψ_c	=	Critical value of the CTOA
CTOA-ψ_n	=	Residual component of the CTOA
CTOA-ψ_{du}	=	Active component of the CTOA
CTOD	=	Crack Tip Opening Displacement
CTOD-δ_5	=	CTOD defined for a gauge length of 5 mm

Table 2. Characteristics of SST Crack Growth in Thin-Sheet Aluminium Alloy D16AT

Specimen code and *k* ratio	ψ_n (°)	ψ_d (°)	ψ_c (°)	ρ_f (μm)	ρ_d (μm)	δ_d (mm)	δ_ρ (mm)
MM(T-TC)-1.0-2.0 (LT direction)							
k=0	–	3.01	–	0.61	2.44	0.075	0.18
k=0.4 and 0.8	–	2.73	–	0.65	2.6	0.086	0.21
MM(T)-1.0-2.0							
(LT direction)	1.38	3.01	3.0±0.86	0.61	2.44	0.075	0.18
(TL direction)	1.41±0.02	–	–				
M(T)-3.0-10.0 (LT direction)	1.27	–	3.5	–	–	–	–
M(T)-1.0-10.0 (LT direction)	1.56	–	–	–	–	–	–
MR(T)-1.0-1.0 (LT direction)	1.10±0.15	–	–	–	–	–	–
MR(T)-0.1-1.0 (LT direction)	1.00	–	–	–	–	–	–

CTOD-δ_d	=	CTOD defined for the crack–tip dominated region
CTOD-δ_p	=	CTOD defined for an ideal crack represented by an open elliptic hole
COD	=	Crack Opening Displacement
COD-v_{du}	=	COD defined as the difference between values of the COS for loaded and fully unloaded specimen
CTOS-δ	=	Crack Tip Opening Spacing
CMOS-2s(m)	=	Crack Mouth Opening Spacing
COS-2s	=	Crack Opening Spacing
BSE	=	Basic Structural Element
PD	=	Problem Domain
M(T)	=	Middle-cracked Tension specimen
MM(T)	=	Modified M(T) specimen
MM(T-TC)	=	Modified Middle-cracked cruciform specimen
MR(T)	=	M(T) specimen with an open circular hole of the centre location
SST	=	Steady State Tearing
TET	=	Tail End Tearing
NFC	=	Naturally Forming Crack
ADZ	=	Active Damage Zone
TL	=	Transferring Law

REFERENCES

[1] G. S. Pisarenko and V. P. Naumenko, "Experimental Methods of the Materials Fracture Mechanics", *Soviet Material Science*, vol. 18, No. 2, pp. 110-120, 1982.

[2] G. S. Pisarenko, V. P. Naumenko and E. E. Onishchenko, "Elasto-Plastic Mode I Fracture of Thin-Sheet Steel under Biaxial Loading" [in Russian], Preprint of the Institute for Problems of Strength of the Ac. Sci. of Ukr. SSR, Kiev, 64 pp., 1983.

[3] G. S. Pisarenko, V. P. Naumenko, O. V. Mitchenko and G. S. Volkov, "Experimental determination of the value of K_I in compression of a plate along the crack line", *Strength of Materials*, vol. 16, No. 11, pp. 1497-1505, 1984.

[4] G. S. Pisarenko, V. P. Naumenko and V. M. Stepkov, "Method and results for experimental investigation into fracture kinetics and resistance to crack growth in brittle materials", *Strength of Materials*, vol. 16, No. 12, pp. 1694-1702, 1984.

[5] V. P. Naumenko and O. V. Mitchenko, "Brittle fracture of a plate with a hole in compression", *Strength of Materials*, vol. 17, No. 7, pp. 890-900, 1985.

[6] G. S. Pisarenko, V. P. Naumenko and N. I. Nedelchev, "Brittle material crack resistance characteristic: what is it", *Strength of Materials*, vol. 17, No. 11, pp. 1497-1507, 1985.

[7] G. S. Pisarenko, V. P. Naumenko and V. M. Stepkov, "Brittle fracture in uniaxial and biaxial loading" [in Russian], *Strength of Materials and Structural Components under a Complex Stress State*, Kiev, Naukova Dumka, pp. 196-201, 1986.

[8] V. P. Naumenko, "Brittle Fracture and Strength of Materials under Compression and Tension" [in Russian], Preprint, the Institute for Problems of Strength of the Ac. Sci. of Ukr. SSR, Kiev, 1987, 38p.

[9] V. P. Naumenko, "Nucleation and growth of a macrocrack in tension and compression", *Soviet Material Science*, vol. 27, No. 5, pp. 484-488, 1991.

[10] V. P. Naumenko and O. V. Mitchenko, "Deformation parameters of Mode I fracture in tension and compression", *Strength of Materials*, vol. 24, No. 8, pp. 1072-1080, 1991.

[11] V. P. Naumenko, "Modeling of brittle fracture in tension and compression," in RILEM/ESIS Conference on Fracture Processes in Concrete, Rock and Ceramics, J. G. M. van Mier, J. G. Rots and A. Bakker, Eds. London: E & F.N. Spon, pp. 183-192, 1991.

[12] V. P. Naumenko and S. I. Sopenko, "The test method for crack growth resistance and elasticity characteristics evaluation for brittle nonmetallic materials," in RILEM/ESIS Conference on Fracture Processes in Concrete, Rock and Ceramics, J. G. M. van Mier, J. G. Rots and A. Bakker, Eds. London: E & F.N. Spon, pp. 183-192, 1991.

[13] V. P. Naumenko and V. A. Rakovsky, "Crack growth onset in biaxially loded elasto-plastic plates," in ESIS/EGF9 Conference on Defect Assessment in Components-Fundamentals and Application, Berlin, pp. 363-377, 1991.

[14] V. P. Naumenko, "Griffith problem and Mode I fracture in tension and compression", *Material Science*, vol. 29, No. 4, pp. 396-405, 1993.

[15] V. P. Naumenko and O. Kolednik, "Load biaxiality effect on the fracture resistance of thin steel sheets," in 10th European Conference on Fracture (ECF 10) *Structural Integrity: Experiments, Models and Application*, Berlin, vol. 2, pp. 911-921, 1994.

[16] V. P. Naumenko and G. S. Volkov, "Assessment of plane stress tearing in terms of various crack-driving parameters", *Fatigue and Fracture Mechanics*, ASTM STP1461, S. R. Daniewicz, J. C. Newman, Jr., and K.-H. Schwalbe, Eds. West Conshohocken, PA: ASTM International, vol. 34, 20 pages, 2003.

[17] V. P. Naumenko, Yu. D. Skrypnyk and N. I. Nedelchev "Constraint-dependent fracture toughness of glass and PMMA," in 11th International Conference on Fracture, Turin, 6 pages, 2005.

[18] J. Eftis, D. L. Jones, and H. Liebowitz, "Load biaxility and fracture: synthesis and summary", *Engineering Fracture Mechanics*, vol. 36, No. 4, 537-574, 1990.

[19] FITNET, European Fitness-For-Service Network, Final report for Work Package 2 "*State-of-the-Art and Strategy*", October 2003.

[20] The Special Issue on Fundamentals and Applications of the Crack Tip Opening Angle (CTOA), *Engineering Fracture Mechanics*, vol. 70, No. 3-4, 371-577, 2003.

[21] Working document ISO/TC 164/SC 4 N413.3, Metallic Materials — Method of Test for the Determination of Resistance to Stable Crack Extension Using Specimens of Low Constraint, 2004.

[22] ASTM Standard. Test Method for Determination of Resistance to Stable Crack Extension under Low-Constraint Conditions (E2472-06).

[23] Y. J. Chao, "On a single parameter controlled fracture of solids under plane stress conditions", *International Journal of Fracture*, vol. 58, pp. 104-110, 1991.

[24] SINTAP. Structural integrity assessment procedure. EU-Project BE 95-1462:-Final Report.- Brite Euram Programme, Brussels, 1999.

[25] M. Schödel and U. Zebst, "Application of the European flaw assessment procedure SINTAP to thin wall structures", *Engineering Fracture Mechanics*, vol. 71, pp. 1035-1058, 2004.

[26] L. Xia, C. F. Shih and J. W. Hutchinson, "A computational approach to ductile crack growth under large scale yielding conditions", *Journal of Mechanics and Physics of Solids*, vol. 43, No. 3, pp. 389, 1995.

[27] V. P. Naumenko, O. Kolednik, N. P. O'Dowd, G. S. Volkov and A. I. Semenets, "Transferability of plane-stress R-curves: Effect of specimen size and crack length" in ECF 12 *Fracture from Defects*, M. W. Brown, E. R. de los Rois, and K J. Miller, Eds., vol. 2, pp. 631-636, 1998.

[28] V. P. Naumenko, O. Kolednik, N. P. O'Dowd and G. S. Volkov, "Effect of constraint on resistance to stable crack growth in thin aluminium plates", in Intern. Conference "Life Assessment and Management for Structural Components", Kiev, Ukraine, vol. I, pp. 299-304, 2000.

[29] V. P. Naumenko, G. S. Volkov and A. G. Atkins, "Comparison studies of R-curves for fatigue and tear cracks in a thin aluminum plate", in ECF 13 *Fracture Mechanics: Applications and Challenges*, San Sebastian, Spain, 2000, Online, reference No. 1A.34, 8 pages.

[30] J. C. Newman, Jr., D. S. Dawicke and C. A. Bigelow, "Finite-element analysis and measurement of CTOA during stable tearing in a thin-sheet aluminum alloy", in International Workshop on Structural Integrity of Aging Airplanes, Atlanta, pp. 167-186, 1992.

[31] V. P. Naumenko, G. S. Volkov, and A. G. Atkins, "Initiation and propagation of ductile tearing: A search for biaxial fracture criterion", in the Sixth International Conference on Biaxial/Multiaxial Fatigue and Fracture, M. M. de Freitas, Ed. Lisboa, pp. 975-982, 2001.

[32] V. P. Naumenko and Yu. D. Skrypnyk, "Sensitivity of crack nucleation parameters to the geometric imperfection", in the ECF16 *Fracture of Nano and Engineering Materials and Structures*, E. E. Gdoutos, Ed. Alexandropoulos, Greece, 2006.

[33] V. P. Naumenko, S. V. Lenzion and Yu. D. Skrypnyk, "Ductile tearing in narrow and wide strips of thin-sheet aluminium alloy", in the ESIA8 *Throughlife Management of Structures and Components,* Manchester, UK, 10 pages, 2006.

[34] W. R. Lloyd, "Microtopography for ductile fracture process characterization. Part 1: Theory and methodology", *Engineering Fracture Mechanics*, vol. 70, No. 3-4, 387-401, 2003.

[35] J. C. Newman, Jr. "An elastic-plastic finite element analysis of crack initiation, stable crack growth, and instability", *in Fracture Mechanics*, Philadelphia: ASTM STP 833, pp. 93-117, 1984.

[36] D. S. Dawicke, M. A. Sutton, J. C. Newman, Jr. and C. A. Bigelow, "*Measurement and analysis of critical CTOA for thi-sheet aluminium alloy materials*", in 25th National Symposium on Fracture Mechanics, Bethlehem, PA, 1993.

[37] J. B. Bakuskas and J. C. Newman, Jr., "Prediction of stable tearing of 2024-t3 aluminium alloy using the crack-tip opening angle approach", *in NASA Technical Memorandum 109023*, NASA Langley Research Center, 1993.

[38] K-H. Schwalbe, "Introduction δ_5 as an operational definition of the CTOD and its practical use", *in Fracture Mechanics*, ASTM STP 1256, vol. 26, pp. 763-778, 1995.

[39] G. S. Pisarenko, V. P. Naumenko, and E. E. Onishchenko, "A method for investigating the fracture of sheet materials in biaxial loading", *Strength of Materials*, vol. 14, No. 3, pp. 275-282, 1982.

[40] A. Hannon and P.Tiernan, "A review of planar biaxial tensile test systems for sheet metals", *Journal of Materials Processing Technology,* vol. 198, issues 1-3, 3, pp. 1-13, 2008.

[41] J. J. Kibler and R. Roberts, "The effect of biaxial stresses on fatigue and fracture", *Transactions of ASME*, *Journal of Engineering and Industry*, vol. 92, pp. 727-734, 1970.

[42] S. Abou-Sayed, D. Broek, T. P. Forte and R. B. Stonesifer, "Plane stress fracture under biaxial loading", in ICF5 *Advances in Fracture Research*, D. Francois, Ed. Pergamon Press, vol. 4, pp. 1707-1713, 1981.

[43] S. I. Garwood, T. G. Davey and S. I. Cresswell, "Behavior of A533B under biaxial loading at +70°C", *International Journal of Pressure Vessels and Piping,* vol. 36, pp. 199-224, 1989.

[44] C. Dalle Done and H. Döker, "Biaxial load effects on plane stress J-Δa and δ_5-Δa-curves", in ECF 10 *Structural Integrity: Experiments, Models and Applications*, Berlin, pp. 891-900, 1994.

[45] V. Boiko, L. N. Karpenko, A. A. Lebedev, N. R. Muzika and O. V. Zagornyak, "Calculation-experimental method for determining crack resistance of material under biaxial loading", *Engineering Fracture Mechanics*, vol. 64, pp. 203-215, 1999.

[46] D. S. Dawicke, A. S. Gullerud, R. H. Dodds, Jr. and R. W. Hampton, "Residual strength predictions with crack buckling", in The Second Joint NASA/FAA/DoD Conference on Aging Aircraft, C. E. Harris, Ed. NASA CP-208982, pp. 565-574, 1999.

[47] J. Eftis and H. Liebowitz, "On the modified Westergaard equations for certain plane crack problems", *International Journal of Fracture Mechanics*, vol. 8, No. 4, pp. 383-392, 1972.

[48] J. Schijve, "Some considerations on the Eftis-Liebowitz equation for the COD compliance of a center cracked sheet specimen", *Engineering Fracture Mechanics*, vol. 55, No. 3, pp. 341-346, 1996.

[49] Y. Lei and B. K. Neale, "The fracture behavior of a center cracked tensile specimen", *Fatigue and Fracture of Engineering Materials and Structures*, vol. 20, No. 2, pp. 201-216, 1997.

[50] C. E. Turner and O. Kolednik, "A micro and macro approach to the energy dissipation rate model of stable ductile crack growth", *Fatigue and Fracture of Engineering Materials and Structures*, vol. 17, pp. 1089-1107, 1994.

[51] Li Ming and O. Richmond, "Intrinsic instability and nonuniformity of plastic deformation", *International Journal of Plasticity*, vol. 13, No.s 8-9, pp. 765-784, 1997.

[52] J. Heerens and M. Schodel, *Engineering Fracture Mechanics,* vol. 70, pp. 417-426, 2003.

[53] V. P. Naumenko, S. V. Lenzion and A. G. Atkins, "Global *vs*. local characterization of crack growth in biaxially stretched plates", in the ESIA9 *Engineering Structural Integrity – Research, Development and Application,* Beijing, China, 4 pages, 2007.

Influence of Stress on Bi-Material Interface of Crack tip

Tapan Kumar Mohanty, *Department of Mechanical Engineering, Aryan Institute of Engineering & Technology, Bhubaneswar, tapankmohanty789@yahoo.co.in*
Rajaram Sahu, *Department of Mechanical Engineering, Raajdhani Engineering College, Bhubaneswar, rajaramsahu65@gmail.com*
Bipash Mohanty, *Department of Civil Engineering, Capital Engineering College, Bhubaneswar, bipashmohanty784@gmail.com*

Abstract: The optical methods of Caustics, Photoelasticity and Isopachics for the evaluation of the stress intensity factors and the distribution of the principal stresses at a bi-material interface crack-tip, were proposed. The caustics, isochromatic and isopachic fringes are developed from the stress field which results from a stress function X(r,θ). When the crack-tip, which is perpendicular to interface, is at the interface of the bi-material, the caustics, isochromatic and isopachic fringes depend on the properties of the two materials. So, the caustic, isochromatic and isopachic fringes are divided into two branches, which present a jump of values at the interface. The shape and size of the two branches of caustics, isochromatic and isopachic fringes depend mainly on the elastic modulus and Poisson's ratio of the two materials. From the caustics the stress intensity factor K_I can be calculated, while from the combination of the isochromatic and the isopachic fringes, the principal stresses σ_1, σ_2 can be theoretically and experimentally calculated. The optical evaluation of the stress intensity factors and the distribution of the principal stresses from isochromatic and isopachic fringes is presented. The stress intensity factors and the principal stresses at the bi-material interface crack-tip, were experimentally determined using the caustics and the combination photoelastic and isopachic measurements. The size and shape of the crack-tip caustics, isochromatic and isopachic fringes, at a bi-material interface under static load, were theoretically and experimentally studied.

INTRODUCTION

The experimental method of transmitted caustics was first developed by Manogg [1] while, the experimental method of reflected caustics was developed by Theocaris [2]. The experimental method of caustics, which is based on the laws of geometrical optics, transforms the stress singularity into an optical singularity. This optical singularity gives much information for the evaluation of the stress field. According to the method of caustics, a coherent light beam from a laser impinges normally on the specimen in the vicinity of the crack tip, and the reflected rays are received on a reference screen at some distance from the specimen. When a certain load is applied to the specimen, the reflected light rays in the vicinity of the crack tip, where there is an abrupt thickness variation due to the existence of a singularity, are scattered and when projected on a reference screen placed at some distance from the specimen are concentrated along a curve, the so-called caustic [3]. The optical method of reflected caustics, as it has been developed during the last thirty five years, was extensively applied to various elastic problems containing singularities and especially to the problems with cracked plates, which were made of isotropic or birefringent materials [4].

The study of the behavior of a transverse crack, propagating through the mesophase of composites, has become a subject of great interest. The problem of crack propagation in a duplex plate was studied by Williams *et al.* [5-9] and later was approached by Dally and Kobayashi [10], by means of dynamic photoelasticity. Theocaris *et al.* [11-13], have studied the influence of both the mesophase and the material characteristics of either phase, in biphase plates consisting of different materials, on the stress distribution around the crack tip. They have extended their study to the magnitude and the variation of the crack propagation velocities during fracture in duplex plates under dynamic loading [14]. Also, Theocaris *et al.* [15,16], have studied the influence of the hard or soft fiber and the mesophase layers in a soft-hard-soft or hard-soft-hard combination of biphase plate subjected to a dynamic tensile load, on the fracture mode and bifurcation process in both phases. Also, theoretical studies on this subject were carried out by Gdoutos *et al.* [17-19], Theotokoglou *et al.* [20-22]. The study of size and shape of the crack-tip caustics at a bi-material interface, was carried out by Papadopoulos *et al.* [22,23].

This work is an attempt to study the size and shape of crack-tip caustics, isochromatic and isopachic fringes, and the estimation of the principal stresses and its contour from the combination of the isochromatic and the isopachic fringes, at a bi-material interface under static load.

Stress-Field Around The Crack-Tip

Two plates of moduli E_1 and E_2 and Poisson's ratios ν_1 and ν_2, are perfectly bonded along their common interface (see Fig. (**1**)). In plate (1), there is a crack perpendicular to the interface. The crack-tip is placed exactly at the interface of the two plates. To study this problem the Airy stress function X(r,θ) used by Zak and Williams [5], is taken into account. This stress function is of form:

$$X(r,\theta) = r^{\lambda+1} F(\theta) \tag{1}$$

with:

$$F(\theta) = \alpha\sin(\lambda+1)\theta + b\cos(\lambda+1)\theta + c\sin(\lambda-1)\theta + d\cos(\lambda-1)\theta \quad (2)$$

where α,b,c,d are constants and λ takes values between 0 and 1, which depends on the ratio $E_{12}=E_1/E_2$ of the two plates moduli [22,23].

From the stress function (1) the polar stresses at the crack-tip are taken:

$$\sigma_r = -\lambda r^{\lambda-1}\begin{bmatrix} \alpha(\lambda+1)\left|\sin(\lambda+1)\theta\right| + \\ b(\lambda+1)\left|\cos(\lambda+1)\theta\right| \\ +c(\lambda-3)\left|\sin(\lambda-1)\theta\right| + \\ d(\lambda-3)\left|\cos(\lambda-1)\theta\right| \end{bmatrix} \quad (3)$$

$$\sigma_\theta = \lambda(\lambda+1)r^{\lambda-1}\begin{bmatrix} \alpha\left|\sin(\lambda+1)\theta\right| + \\ b\left|\cos(\lambda+1)\theta\right| \\ +c\left|\sin(\lambda-1)\theta\right| + \\ d\left|\cos(\lambda-1)\theta\right| \end{bmatrix} \quad (4)$$

$$\tau_{r\theta} = -\lambda r^{\lambda-1}\begin{bmatrix} \alpha(\lambda+1)\left|\cos(\lambda+1)\theta\right| - \\ b(\lambda+1)\left|\sin(\lambda+1)\theta\right| \\ +c(\lambda-1)\left|\cos(\lambda-1)\theta\right| - \\ d(\lambda-1)\left|\sin(\lambda-1)\theta\right| \end{bmatrix} \quad (5)$$

The boundary conditions of the problem are written as:

$$\tau_{r\theta_1} = 0 \quad and \quad \sigma_{\theta_1} = 0 \quad for \quad \theta_1 = \frac{\pi}{2}$$

$$\tau_{r\theta_2} = 0 \quad and \quad \upsilon_2 = 0 \quad for \quad \theta_2 = \frac{\pi}{2} \quad (6)$$

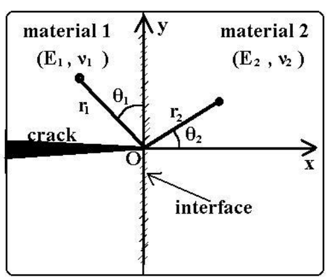

Fig. (1). Geometry of bi-material plate.

$$\sigma_{\theta_1} = \sigma_{\theta_2}, \quad \tau_{r\theta_1} = \tau_{r\theta_2}, \quad u_1 = u_2,$$

$$\upsilon_1 = \upsilon_2 \quad for \quad \theta_1 = 0 \quad and \quad \theta_2 = \frac{\pi}{2}$$

where $u_{1,2}$, $\upsilon_{1,2}$ are the displacement components.

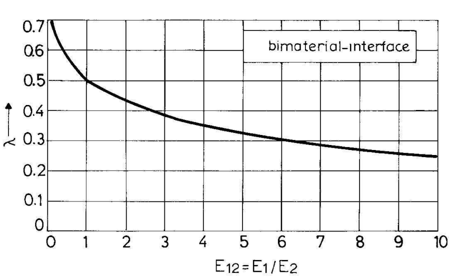

Fig. (2). Variation of λ versus ratio $E_{12}=E_1/E_2$ for Poisson's ratios $\nu_1=\nu_2=0.30$.

From the boundary conditions (6) the values of the λ can be determined. Fig. (**2**) presents the variation of λ versus the ratio E_{12} of the moduli of the plates. Various values of λ according to ratio E_{12} and Poisson's ratios ν_1, ν_2 are given in Table **1**.

Table 1. Values of λ for Various Values of E_{12} and ν_1, ν_2

E_{12}	ν_1	ν_2	λ
1.2142	0.34	0.36	0.48
0.82353	0.36	0.34	0.5192
0.10	0.30	0.30	0.6966
0.1428	0.30	0.30	0.6764
0.2016	0.30	0.30	0.6525
0.336	0.36	0.34	0.603
1.00	0.30	0.30	0.50
2.97	0.34	0.36	0.3803
4.96	0.30	0.30	0.323
7.03	0.30	0.30	0.2852
9.985	0.30	0.30	0.249

Theory of Caustics

The deflection of light, either reflected from, or passing through a generic point P of the plate in the vicinity of the crack-tip, is given by the deviation vector **W**, which, for an optically isotropic material, is expressed by [1-3]:

$$\mathbf{W}_{r,t,f} = X_{r,t,f}\mathbf{i} + Y_{r,t,f}\mathbf{j} = \mathbf{r} + \mathbf{w}_{r,t,f} \quad (7)$$

with:

$$\mathbf{w}_{r,t,f} = -\varepsilon z_0 t c_{r,t,f}\, grad_{x,y}(\sigma_r + \sigma_\theta), \qquad \mathbf{r} = r\cos\theta\,\mathbf{i} + r\sin\theta\,\mathbf{j} \quad (8)$$

where ε is a multiplying factor, which is equal to unity, for reflected from the front (f) face or transmitted (t) light rays and equal to 2 for light rays reflected from the rear (r) face of the plate, $c_{r,t,f}$ are the stress-optical constants for the material, t is the thickness of the plate and z_0 is the distance between the plate and the reference screen. The stress-optical constant $c_f = \nu_{1,2}/E_{1,2}$ for the materials 1 and 2, respectively.

The sum of the stresses σ_r and σ_θ (Eqs (3) and (4)) is:

$$\sigma_r + \sigma_\theta = r^{\lambda-1}\left[(\lambda+1)^2 F(\theta) + F''(\theta) \right] \quad (9)$$

The grad of the sum of the stresses is:

$$grad_{x,y}(\sigma_r + \sigma_\theta) = (\lambda-1)r^{\lambda-2}\left[(\lambda+1)^2 F(\theta) + F''(\theta)\right](\cos\theta\,\mathbf{i} + \sin\theta\,\mathbf{j}) + r^{\lambda-2}\left[(\lambda+1)^2 F'(\theta) + F''(\theta)\right](-\sin\theta\,\mathbf{i} + \cos\theta\,\mathbf{j}) \quad (10)$$

and from the relations (7) and (8) the parametric equations of the caustics (r) and (t) ((r) is the caustic which is formed by the reflected light rays from the rear face of the plate and (t) is the caustic which is formed by the transmitted light rays through the plate) are obtained as [22]:

$$X_{r,t} = \lambda_m r_{01,2} \left\{ \begin{matrix} \cos\theta_{1,2} - \dfrac{1}{(\lambda-2)\sqrt{c_2^2+d_2^2}} \\ \begin{bmatrix} c_2 \sin(\lambda-2)\theta_{1,2} + \\ d_2 \cos(\lambda-2)\theta_{1,2} \end{bmatrix} \end{matrix} \right\} \tag{11}$$

$$Y_{r,t} = \lambda_m r_{01,2} \left\{ \begin{matrix} \sin\theta_{1,2} - \dfrac{1}{(\lambda-2)\sqrt{c_2^2+d_2^2}} \\ \begin{bmatrix} c_2 \cos(\lambda-2)\theta_{1,2} - \\ d_2 \sin(\lambda-2)\theta_{1,2} \end{bmatrix} \end{matrix} \right\} \tag{12}$$

where λ_m is the magnification factor of the optical set-up, which is given by:

$$\lambda_m = \frac{z_0 \pm z_i}{z_i} \tag{13}$$

where z_i is the distance between plate and focus of the light beam, (+) for the reflected and (-) for the transmitted, through the plate rays.

The parametric equations of the caustic (f) ((f) is the caustic which is formed by the reflected light rays from the front face of the plate) are:

$$X_f = \lambda_m r_{01,2} \left\{ \begin{matrix} \cos\theta_{1,2} + \dfrac{1}{(\lambda-2)\sqrt{c_2^2+d_2^2}} \\ \begin{bmatrix} c_2 \sin(\lambda-2)\theta_{1,2} + \\ d_2 \cos(\lambda-2)\theta_{1,2} \end{bmatrix} \end{matrix} \right\} \tag{14}$$

$$Y_f = \lambda_m r_{01,2} \left\{ \begin{matrix} \sin\theta_{1,2} + \dfrac{1}{(\lambda-2)\sqrt{c_2^2+d_2^2}} \\ \begin{bmatrix} c_2 \cos(\lambda-2)\theta_{1,2} - \\ d_2 \sin(\lambda-2)\theta_{1,2} \end{bmatrix} \end{matrix} \right\} \tag{15}$$

The radius of the initial curve of the caustics is:

$$r_{01,2} = \left[\frac{4\lambda(\lambda-1)(\lambda-2)C_{r,t,f}}{\sqrt{c_{1,2}^2 + d_{1,2}^2}} \right]^{1/(3-\lambda)} \tag{16}$$

with:

$$C_{r,t,f} = -\frac{\varepsilon z_0 t c_{r,t,f}}{\lambda_m} \tag{17}$$

where the indices 1,2 are the materials 1 and 2 of the bi-material plate are represented. The polar coordinate $\theta_1$takes values in the region [π/2, π]U[-π, -π/2] (material 1) and θ_2 takes values in the region [-π/2, +π/2] (material 2).

The constants $\alpha_{1,2}$, $b_{1,2}$, $c_{1,2}$, $d_{1,2}$, which are calculated by the boundary conditions (6), are given by the relations:

$$\alpha_2 = c_2 = 0, \quad d_2 = arbitrary\ cons\tan t \tag{18}$$

$$\begin{aligned} &\alpha_1 = \{E_{12}(\lambda-1)[b_2(\nu_2+1)(\lambda+1) - d_2(\lambda(\nu_2 \\ &+1) + 3 - \nu_2)] - [b_2(\lambda+1) + d_2(1-\lambda)][\nu_1(\lambda-1) \\ &+\lambda+3]\}\cos(\lambda\pi/2)/4(\lambda+1) \end{aligned} \tag{19}$$

$$\begin{aligned} &b_1 = -\{E_{12}[b_2(\lambda(\nu_2+1) + \nu_2 + 1) - d_2(\lambda(\nu_2 \\ &+1) + \nu_2 - 3)] - \nu_1(\lambda+1)(b_2 - d_2) + b_2(\lambda-3) \\ &+d_2(3-\lambda)\}0.25\sin(\lambda\pi/2) \end{aligned} \tag{20}$$

$$\begin{aligned} &c_1 = -\{E_{12}[b_2(\nu_2+1)(\lambda+1) - d_2(\lambda(\nu_2+1) \\ &+3-\nu_2)] - [b_2(\lambda+1) + d_2(1-\lambda)](\nu_1 \\ &+1)\}0.25\cos(\lambda\pi/2) \end{aligned} \tag{21}$$

$$\begin{aligned} &d_1 = \{E_{12}[b_2(\nu_2+1)(\lambda+1) - d_2(\lambda(\nu_2+1) + \nu_2 \\ &-3)] - (\lambda+1)(b_2 - d_2)(\nu_1+1)\}0.25\sin(\lambda\pi/2) \end{aligned} \tag{22}$$

$$\begin{aligned} &b_2 = \{d_2[[E_{12}[\lambda(3\nu_2 - 5) + \nu_2 - 3] - [\nu_1(3\lambda \\ &+1) + 1 - \lambda]]\cos(\lambda\pi) + [\nu_1(2\lambda^2 + \lambda + 1) \\ &+(\lambda-1)(2\lambda+3)] - E_{12}[2\lambda^2(\nu_2+1) + \lambda(\nu_2+1) \\ &+\nu_2 - 3]]\}/\{[[E_{12}(\nu_2+1) \\ &+3-\nu_1]\cos(\lambda\pi) - (2\lambda+1)[E_{12}(\nu_2+1) \\ &-(\nu_1+1)]](\lambda+1)\} \end{aligned} \tag{23}$$

The variables E_{12}, ν_1, ν_2 are dependent on the materials while, the variable d_2 depends on the conditions of the experiment and mainly on the stress of loading.

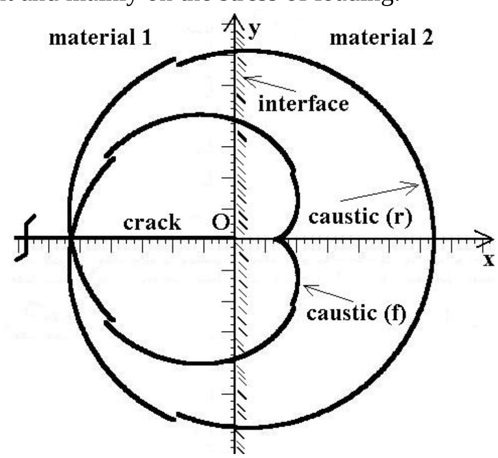

Fig. (3). Theoretical caustics for E_{12}=1.2142, ν_1=0.34, ν_2=0.36 and λ=0.48 (Plexiglas 1-Lexan 2).

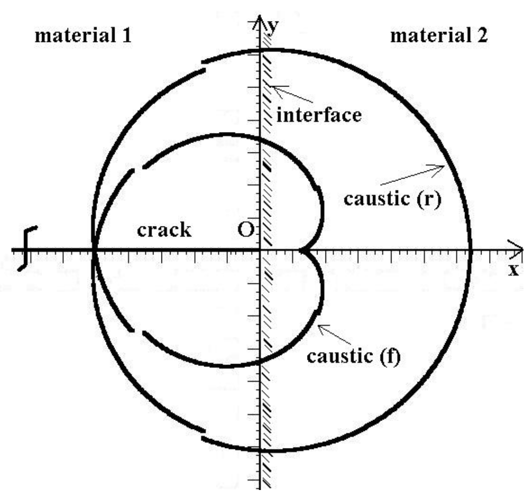

Fig. (4). Theoretical caustics for E_{12}=0.82353, ν_1=0.36, ν_2=0.34 and λ=0.5192 (Lexan 1-Plexiglas 2).

For Plexiglas (PMMA), with E_1=3.4 GPa and ν_1 =0.34, as material 1, and Lexan (PCBA), with E_2=3.8 GPa and ν_2 =0.36, as material 2 (Fig. (**1**)), the theoretical caustics at the crack-tip, at the bi-material interface were plotted according to equations (11)-(23). Fig. (**3**) presents the plotted caustics, caustic (r) and caustic (f), for Plexiglas 1 - Lexan 2 bi-material plate with E_{12}=1.2142, ν_1=0.34, ν_2=0.36, λ=0.48, b_2=0.353d_2, c_1=0.826d_2, d_1=0.78d_2, c_2=0 and d_2=1. The size of the caustic (r) depends on the initial curve radius, which further depends on the stress optical constants $c_{r,t,f}$. The jump of the values at the interface depends on the polar coordinate θ of the initial curve. This jump, which is corresponded to $\theta = \pm\pi/2$ of the initial curve, is not placed at the interface because the values of the caustic are deviated (relation (8)).

Fig. (**4**) presents the plotted caustics, caustic (r) and caustic (f), for Lexan 1 - Plexiglas 2 bi-material plate with E_{12}=0.82353, ν_1=0.36, ν_2=0.34, λ=0.5192, b_2=0.316d_2, c_1=0.607d_2, d_1=0.648d_2, c_2=0 and d_2=1.

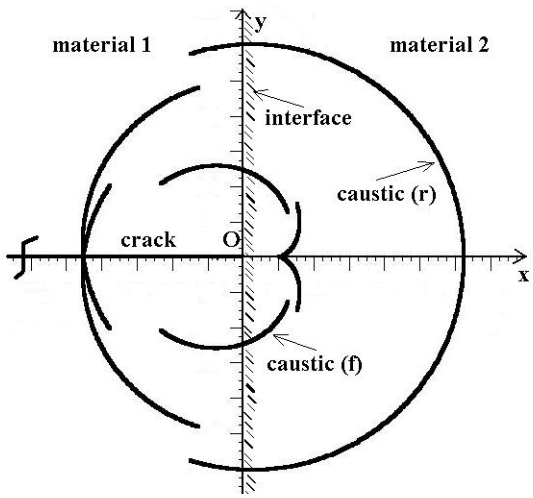

Fig. (5). Theoretical caustics for E_{12}=0.336, ν_1=0.36, ν_2=0.34 and λ=0.6003 (ductile 1-brittle 2).

Fig. (**5**) presents the plotted caustics, caustic (r) and caustic (f), for ductile material 1 - brittle material 2 bi-material plate with E_{12}=0.336, ν_1=0.36, ν_2=0.34, λ=0.603, b_2=0.275d_2, c_1=0.307d_2, d_1=0.487d_2, c_2=0 and d_2=1.

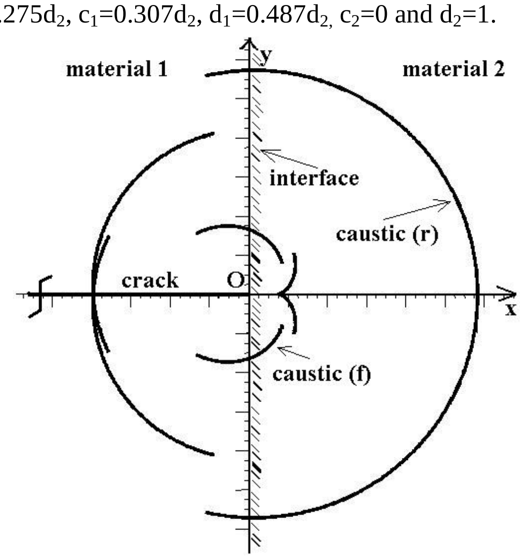

Fig. (6). Theoretical caustics for E_{12}=0.10, ν_1=ν_2=0.30 and λ=0.6966 (ductile 1-brittle 2).

Fig. (**6**) presents the plotted caustics, caustic (r) and caustic (f), for ductile material 1 - brittle material 2 bi-material plate with E_{12}=0.10, ν_1=ν_2=0.30, λ=0.6966, b_2=0.2816d_2, c_1=0.151d_2, d_1=0.406d_2, c_2=0 and d_2=1.

The relative size of the caustics (r) and (f) depends on the stress-optical constants c_r and c_f of the two materials of the bi-material plate.

The stress intensity factor K_I can be experimentally calculated from the maximum, D_{max}, so diameter of the caustic according to the relation (Papadopoulos 1993) [3]:

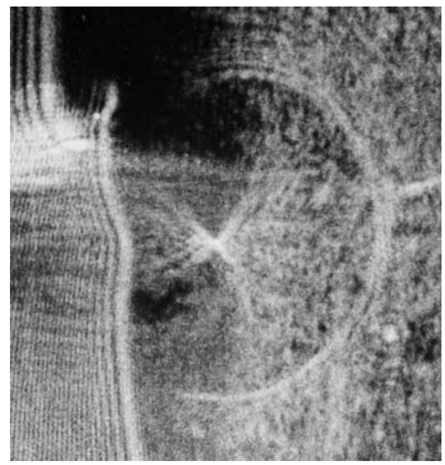

Fig. (7). Experimental caustic (r) at crack-tip of Plexiglas 1 – Lexan 2 bi-material plate.

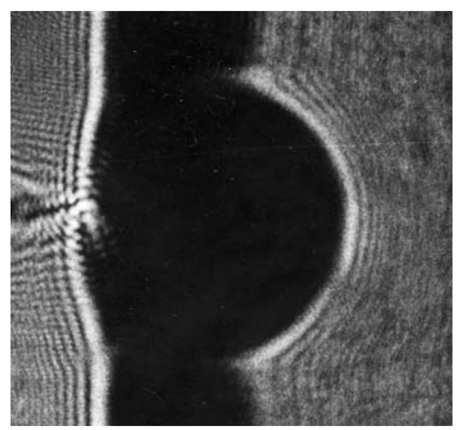

$$K_I = \frac{0.04668}{z_0 t \lambda_m^{3/2} c_{r,t}} D_{\max}^{5/2} \tag{24}$$

Fig. (8). Experimental caustic (t) at crack-tip of Plexiglas 1 – Lexan 2 bi-material plate.

Fig. (**7**) presents the experimental reflected caustic (caustic (r)) at the crack-tip of bi-material plate with material 1 (Plexiglas) – material 2 (Lexan). Fig. (**8**) presents the experimental transmitted caustic (caustic (t)) at the crack-tip for the same bi-material plate of Fig. (**7**).

Theory of Photoelasticity

Isochromatic fringes are loci of points with the same value for the difference of the principal stresses or the maximum shear stress. According to the stress optical law, the difference in the principal stresses is given by [24]:

$$\sigma_1 - \sigma_2 = 2\tau^{\max} = \frac{N_c f_c}{t} \quad (25)$$

where N_C is the isochromatic fringe order, t is the thickness of the specimens and f_c is the material fringe value or stress-optical constant, which is given by the relation:

$$f_c = \frac{E\lambda_\ell}{2\nu} \quad (26)$$

where E is the elastic modulus, λ_l is the wave length of the used monochromatic light and ν is the Poisson's ratio of the plate material.

From equations (3)-(5) and (25) is obtained:

$$r = \left\{ \frac{\dfrac{1}{\left[\begin{array}{l}[(1-\lambda^2)F(\theta)+F''(\theta)]^2 + \\ 4\lambda^2(F'(\theta))^2\end{array}\right]^{1/2}}}{\dfrac{N_c (f_c)_{1,2}}{t}} \right\}^{\frac{1}{\lambda-1}} \quad (27)$$

with:

$$\begin{aligned} F(\theta) &= \alpha_2 \sin(\lambda+1)\theta + b_2 \cos(\lambda+1)\theta + \\ & c_2 \sin(\lambda-1)\theta + d_2 \cos(\lambda-1)\theta \end{aligned} \quad (28)$$

The relation between the stress-optical constants of the materials 1 and 2 is:

$$(f_c)_2 = \frac{1}{E_{12}} \frac{\nu_1}{\nu_2} (f_c)_1 \quad (29)$$

where $E_{12}=E_1/E_2$ is the ratio of the elastic modulus of the two materials, ν_1 and ν_2 are the Poisson' s ratios of the two materials.

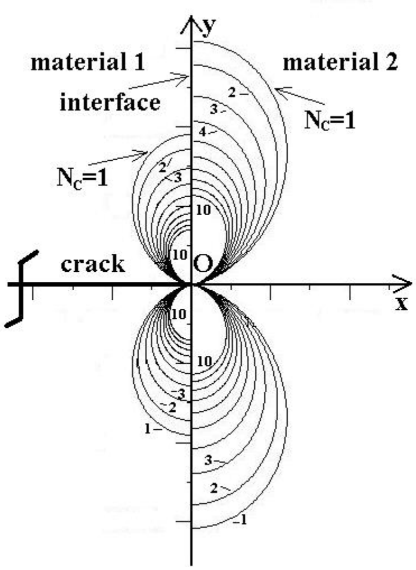

Fig. (9). Isochromatic fringes of order N_C=1 ÷ 10 for E_{12} = 1.2142, ν_1= 0.34, ν_2= 0.36 and λ=0.48 (Plexiglas 1- Lexan 2).

The isochromatic fringes are plotted around the crack-tip by the equation (27) for $(f_c)_1$=1, t=0.003m, d_2=1. Fig. (**9**) presents the plotted isochromatic fringes of order N_C=1 ÷ 10, for Plexiglas 1 - Lexan 2 bi-material plate, with E_{12} = 1.2142, ν_1= 0.34, ν_2= 0.36 and λ=0.48. It is observed that the branches of the isochromatic fringes, which correspond to the ductile material (material 2), are bigger than the branches corresponding to the brittle material (material 1). This means that the maximum shear stress at the crack-tip is considerable in brittle material (material 1). The jump of the values is exactly placed at the interface.

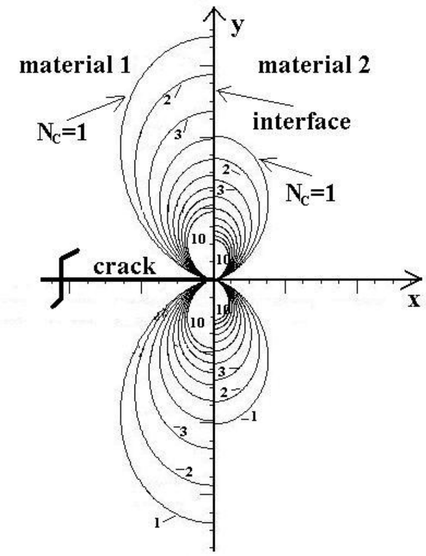

Fig. (10). Isochromatic fringes of order N_C=1 ÷ 10 for E_{12} = 0.82353, ν_1= 0.36, ν_2= 0.34 and λ=0.5192 (Lexan 1- Plexiglas 2).

Fig. (**10**) presents the plotted isochromatic fringes of order N_C=1 ÷ 10, for Lexan 1- Plexiglas 2 bi-material plate, with E_{12} = 0.82353, ν_1= 0.36, ν_2= 0.34 and λ=0.5192.

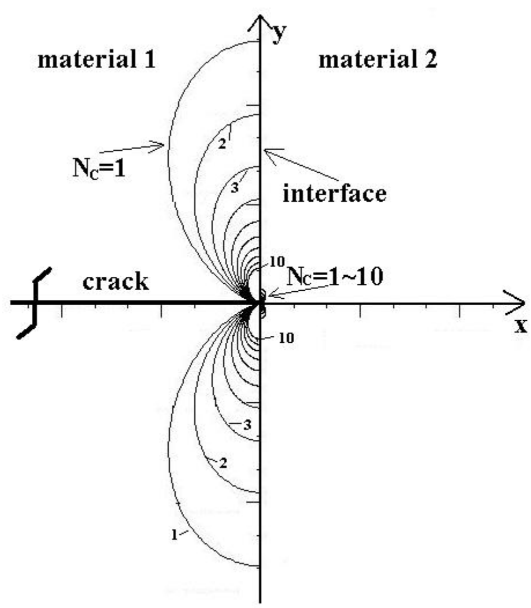

Fig. (11). Isochromatic fringes of order N_C=1 ÷ 10 for E_{12} = 0.336, ν_1= 0.36, ν_2= 0.34 and λ=0.603 (ductile 1- brittle 2).

Fig. (**11**) presents the plotted isochromatic fringes of order N_C=1 ÷ 10, for ductile material 1- brittle material 2 bi-material plate, with E_{12} = 0.336, ν_1= 0.36, ν_2= 0.34 and λ=0.603.

Fig. (**12**) presents the plotted isochromatic fringes of order N_C=1 ÷ 10, for ductile material 1- brittle material 2 bi-material plate, with E_{12} = 0.10, ν_1= ν_2= 0.30 and λ=0.6966.

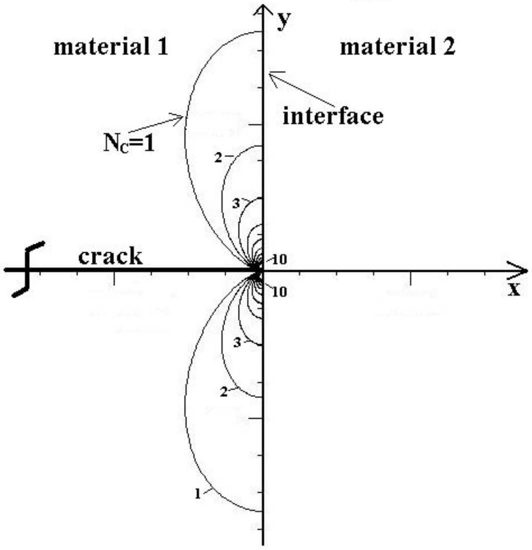

Fig. (12). Isochromatic fringes of order N_C=1 ÷ 10 for E_{12} = 0.10, ν_1= ν_2= 0.30 and λ=0.6966 (ductile 1- brittle 2).

Theory of Isopachic Fringes

Isopachics fringes are loci of points with the same value for the sum of the principal stresses. The fringe orders N_p of isopachic are related to the sum of the principal stresses by [25]:

$$\sigma_1 + \sigma_2 = \sigma_r + \sigma_\theta = \frac{N_p f_p}{t} \tag{30}$$

where N_p is the order of isopachics, t is the thickness of the plate and f_p is the isopachic fringe constant, which is given by the relation:

$$f_p = \frac{E\lambda_\ell}{2\nu} \tag{31}$$

where E is the elastic modulus, λ_l is the wave length of the used monochromatic light and ν is the Poisson's ratio of the plate material.

The sum of the stresses (from equations (3) and (4)) are:

$$\sigma_1 + \sigma_2 = \sigma_r + \sigma_\theta = r^{\lambda-1}\left[\ (\lambda+1)^2 F(\theta) + F''(\theta)\ \right] \tag{32}$$

with:

$$F(\theta) = \alpha_2 \left|\sin(\lambda+1)\theta\right| + b_2 \left|\cos(\lambda+1)\theta\right| + c_2 \left|\sin(\lambda-1)\theta\right| + d_2 \left|\cos(\lambda-1)\theta\right| \tag{33}$$

$$F''(\theta) = -\alpha_2 (\lambda+1)^2 \left|\sin(\lambda+1)\theta\right| - b_2(\lambda+1)^2 \left|\cos(\lambda+1)\theta\right| - c_2(\lambda-1)^2 \left|\sin(\lambda-1)\theta\right| - d_2(\lambda-1)^2 \left|\cos(\lambda-1)\theta\right| \tag{34}$$

By substituting the equations (32)-(34) into equation (30) is obtained:

$$r = \left\{ \frac{1}{(\lambda+1)^2 F(\theta) + F''(\theta)} \frac{N_p (f_p)_{1,2}}{t} \right\}^{\frac{1}{\lambda-1}} \tag{35}$$

with:

$$(f_p)_2 = \frac{1}{E_{12}} \frac{\nu_1}{\nu_2} (f_p)_1 \tag{36}$$

where $(f_p)_{1,2}$ are the isopachic fringe constants of the materials 1 and 2 of the bi-material plate, respectively.

The isopachic fringes are plotted around the crack-tip by the equation (34) for $(f_p)1=1$, t=0.003m, d_2=1. Fig. (**13**) presents the plotted isopachic fringes of order N_p=1 ÷ 10, for Plexiglas 1 - Lexan 2 bi-material plate, with E_{12} = 1.2142, ν_1= 0.34, ν_2= 0.36 and λ=0.48.

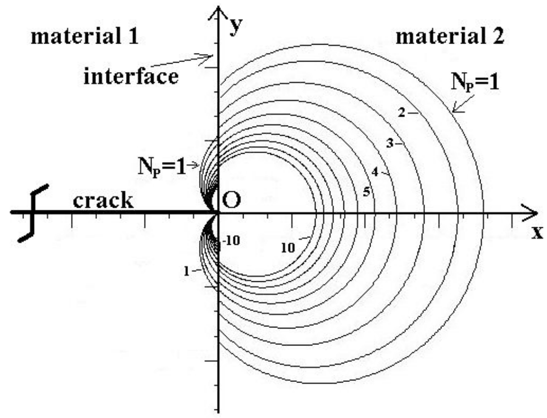

Fig. (13). Isopachic fringes of order N_p=1 ÷ 10 for E_{12} = 1.2142, ν_1= 0.34, ν_2= 0.36 and λ=0.48 (Plexiglas 1- Lexan 2).

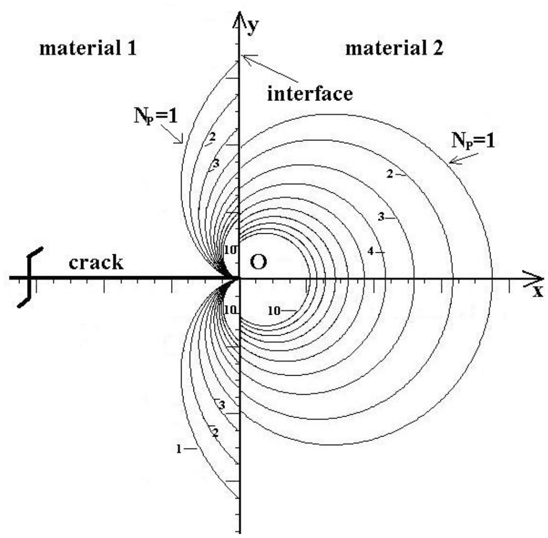

Fig. (14). Isopachic fringes of order N_p=1 ÷ 10 for E_{12} = 0.82353, ν_1= 0.36, ν_2= 0.34 and λ=0.5192 (Lexan 1- Plexiglas 2).

Fig. (**14**) presents the plotted isopachic fringes of order N_p=1 ÷ 10, for Lexan 1- Plexiglas 2 bi-material plate, with E_{12} = 0.82353, ν_1= 0.36, ν_2= 0.34 and λ=0.5192.

Fig. (**15**) presents the plotted isopachic fringes of order N_p=1 ÷ 10, for ductile material 1- brittle material 2 bi-material plate, with E_{12} = 0.336, ν_1= 0.36, ν_2= 0.34 and λ=0.603.

Fig. (**16**) presents the plotted isopachic fringes of order N_p=1 ÷ 10, for ductile material 1- brittle material 2 bi-material plate, with E_{12} = 0.10, ν_1= ν_2= 0.30 and λ=0.6966.

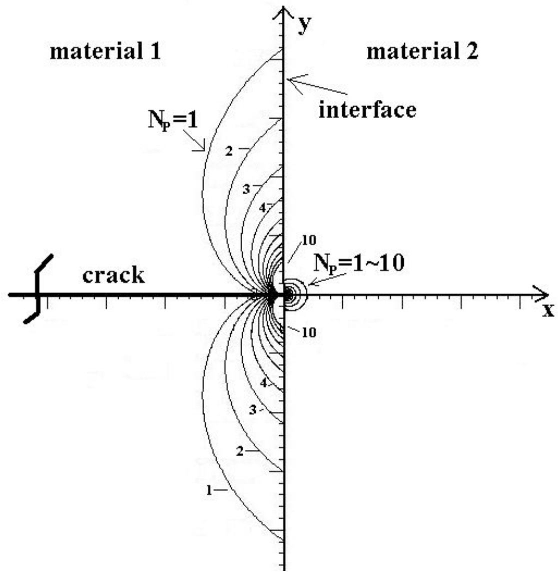

Fig. (15). Isopachic fringes of order N_p=1 ÷ 10 for E_{12} = 0.336, ν_1= 0.36, ν_2= 0.34 and λ=0.603 (ductile 1- brittle 2).

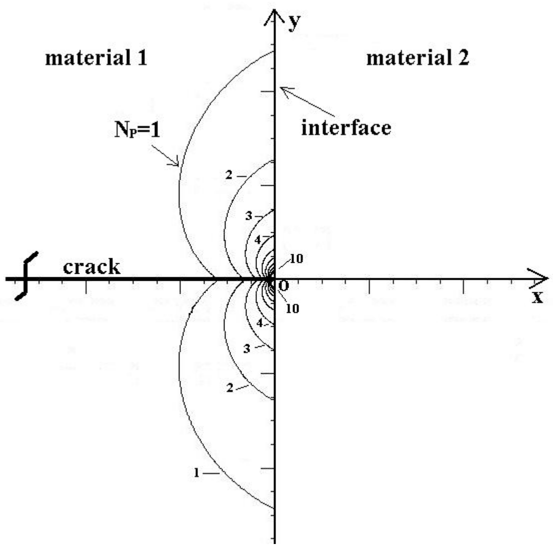

Fig. (16). Isopachic fringes of order N_p=1 ÷ 10 for E_{12} = 0.10, ν_1 = ν_2= 0.30 and λ=0.6966 (ductile 1- brittle 2).

Principal Stresses Estimation from the Isochromatic and Isopachic Fringes

The principal stresses can be estimated from the system of isochromatic and isopachic fringes (Eqs. (25), (30)). The solution of the system is valid at the cross points of the isochromatic and isopachic fringes (Fig. (**17**)). Fig. (**17**) presents the overlapping of isochromatic and isopachic fringes by Eqs. (27) and (35), for Lexan 1-Plexiglas 2 bi-material plate with E_{12}=0.82353, ν_1=0.36, ν_2=0.34, λ=0.5192, t = 0.003 and d_2 = 1 (d_2 is an arbitrary constant which represents the tensile load of the plate). Fig. (**18**) presents experimentally the overlapping of isochromatic and isopachic fringes for E_{12} = 1 (one material, Lexan). At the cross points of the fringes, the principal stresses can be calculated by the Eqs. (25) and (30). Also, at the crack tip, the caustics (r) and (f) were taken from which the stress intensity factor K_I can be calculated.

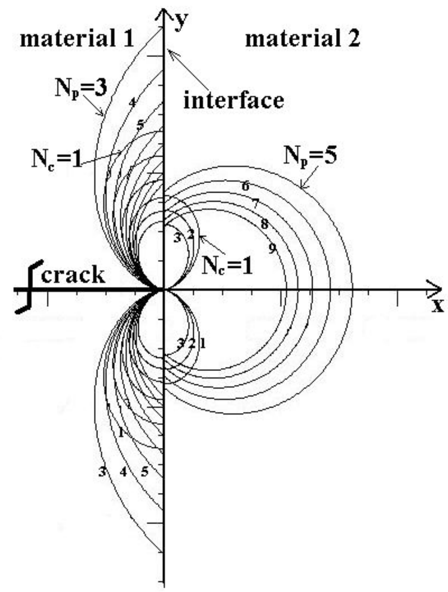

Fig. (17). Overlapping of Isochromatic (N_c) and Isopachic (N_p) fringes.

From the solution of the equations (25) and (30) system, the principal stresses are obtained:

$$\sigma_1 = \frac{\sigma_r + \sigma_\theta}{2} + \frac{1}{2}\sqrt{(\sigma_r - \sigma_\theta)^2 + 4\tau_{r\theta}^2} = \frac{N_p (f_p)_{1,2} + N_c (f_c)_{1,2}}{2t} \tag{37}$$

$$\sigma_2 = \frac{\sigma_r + \sigma_\theta}{2} - \frac{1}{2}\sqrt{(\sigma_r - \sigma_\theta)^2 + 4\tau_{r\theta}^2} = \frac{N_p (f_p)_{1,2} - N_c (f_c)_{1,2}}{2t} \tag{38}$$

By substituting the stresses from the Eqs. (3)-(5) into Eqs. (37), (38) the contour curves of the principal stresses, around the crack-tip, are obtained:

$$r_{\sigma_1} = \left\{ \frac{2\sigma_1}{\begin{bmatrix} (1+\lambda)^2 F(\theta) \\ +F''(\theta) \end{bmatrix} + \begin{bmatrix} [(1-\lambda^2)F(\theta) \\ +F''(\theta)]^2 + \\ 4\lambda^2 (F'(\theta))^2 \end{bmatrix}^{1/2}} \right\}^{\frac{1}{\lambda-1}} \tag{39}$$

$$r_{\sigma_2} = \left\{ \frac{2\sigma_2}{\begin{bmatrix} (1+\lambda)^2 F(\theta) \\ +F''(\theta) \end{bmatrix} - \begin{bmatrix} [(1-\lambda^2)F(\theta) \\ +F''(\theta)]^2 + \\ 4\lambda^2 (F'(\theta))^2 \end{bmatrix}^{1/2}} \right\}^{\frac{1}{\lambda-1}} \tag{40}$$

or:

$$r_{\sigma_1} = \left\{ \frac{\dfrac{N_p (f_p)_{1,2} + N_c (f_c)_{1,2}}{t}}{\begin{bmatrix}(1+\lambda)^2 F(\theta)\\ +F''(\theta)\end{bmatrix} + \begin{bmatrix}[(1-\lambda^2)F(\theta)\\ +F''(\theta)]^2+\\ 4\lambda^2(F'(\theta))^2\end{bmatrix}^{1/2}} \right\}^{\frac{1}{\lambda-1}} \tag{41}$$

$$r_{\sigma_2} = \left\{ \frac{\dfrac{N_p (f_p)_{1,2} - N_c (f_c)_{1,2}}{t}}{\begin{bmatrix}(1+\lambda)^2 F(\theta)\\ +F''(\theta)\end{bmatrix} - \begin{bmatrix}[(1-\lambda^2)F(\theta)\\ +F''(\theta)]^2+\\ 4\lambda^2(F'(\theta))^2\end{bmatrix}^{1/2}} \right\}^{\frac{1}{\lambda-1}} \tag{42}$$

with:

$$\begin{aligned}F(\theta) = {} & \alpha_2 \left|\sin(\lambda+1)\theta\right| + b_2 \left|\cos(\lambda+1)\theta\right| + \\ & c_2 \left|\sin(\lambda-1)\theta\right| + d_2 \left|\cos(\lambda-1)\theta\right|\end{aligned} \tag{43}$$

$$\begin{aligned}F'(\theta) = {} & \alpha_2(\lambda+1)\left|\cos(\lambda+1)\theta\right| - \\ & b_2(\lambda+1)\left|\sin(\lambda+1)\theta\right| + c_2(\lambda-1)\left|\cos(\lambda-1)\theta\right| - \\ & d_2(\lambda-1)\left|\sin(\lambda-1)\theta\right|\end{aligned} \tag{44}$$

$$\begin{aligned}F''(\theta) = {} & -\alpha_2(\lambda+1)^2 \left|\sin(\lambda+1)\theta\right| - \\ & b_2(\lambda+1)^2 \left|\cos(\lambda+1)\theta\right| - c_2(\lambda-1)^2 \left|\sin(\lambda-1)\theta\right| \\ & -d_2(\lambda-1)^2 \left|\cos(\lambda-1)\theta\right|\end{aligned} \tag{45}$$

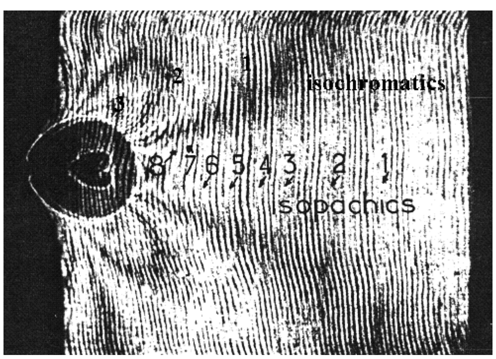

Fig. (18). Experimentally overlapping of Isochromatic and Isopachic fringes and caustics at the crack tip in one material (Lexan) plate.

Fig. (**19**) presents the contour curves of the principal stresses σ_1 and σ_2 around the crack-tip for Lexan 1-Plexiglas 2 bi-material plate with E_{12}=0.82353, ν_1=0.36, ν_2=0.34, λ=0.5192, d_2=1 and t=0.003 for isopachic fringe order $N_{p=}1$ and isochromatic fringe orders N_c=3,4. Fig. (**20**) presents the contour curves of the principal stresses σ_1 and σ_2 around the crack-tip for the same bi-material with $N_{p=}2$ and N_c=3,4 and Fig. (**21**) presents the contour curves of the principal stresses σ_1 and σ_2 around the crack-tip for the same bi-material with $N_{p=}5$ and N_c=3,4. A jump of values of principal stresses are appeared at the bi-material interface.

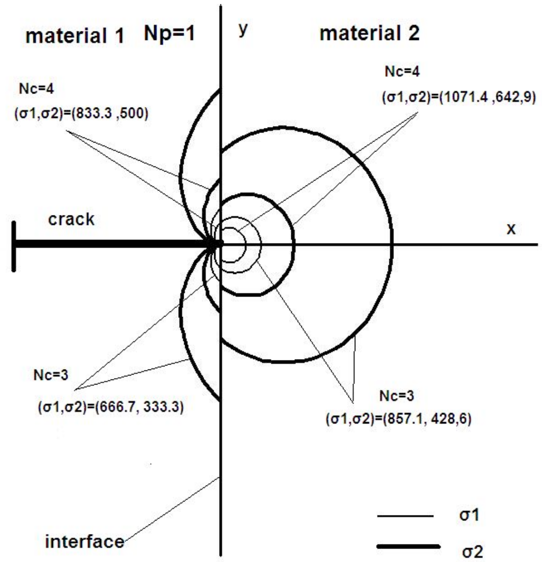

Fig. (19). Contour curves of principal stresses around the crack-tip for N_p = 1 and N_C = 3,4.

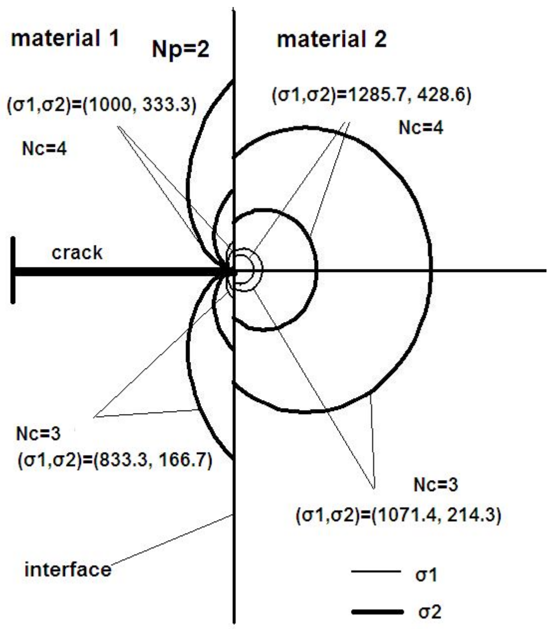

Fig. (20). Contour curves of principal stresses around the crack-tip for N_p = 2 and N_C = 3,4.

CONCLUSIONS

According to the above study it is concluded that the stress state at the crack-tip can be considered by the method of caustics, while the stress state far from the crack-tip can be considered by the methods of photoelasticity and isopachics. The stress intensity factor K_I can be calculated from the diameters of the crack-tip caustics. The contour curves of principal stresses can be plotted around the crack-tip at the interface of the bi-material from the overlapping of the isochromatic and isopachic fringes. Also, the distribution of the principal stresses close and far from the crack-tip can be experimentally considered by the methods of photoelasticity and isopachics.

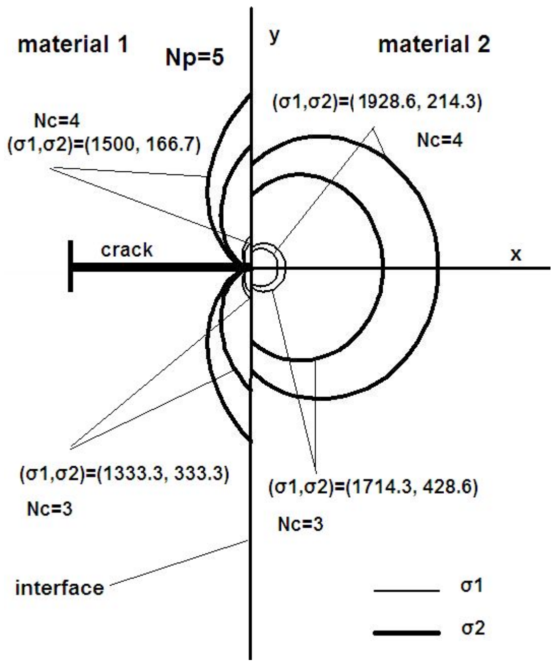

Fig. (21). Contour curves of principal stresses around the crack-tip for $N_p = 5$ and $N_C = 3,4$.

The caustics theory and the isochromatic and isopachic fringes at a bi-material interface crack-tip was developed in Refs [22,23]. In this work the evaluation of principal stresses and its contour at a bi-material interface crack-tip were developed by the combination of isochromatic and isopachic fringes. The principal stresses were calculated at cross points of the isochromatic and isopachic fringes. So, the principal stresses can experimentally be calculated from the photograph of Fig. (**18**).

Fig. (**18**) illustrates experimentally superposition of isochromatic and isopachic fringes and the caustic at the crack-tip. The stress intensity factor at crack-tip and far from crack-tip and the principal stresses can calculated experimentally. The picture of Fig. (**18**) was generated by the overlapping of three photographs. The first photograph was taken from the unloading specimen. The second photograph was taken from the loading specimen in that caustic was formed at the crack-tip. The third photograph was taken from the loading specimen in which isochromatic fringes were formed around the crack-tip. By the superposition of these three photographs, the photograph of Fig. (**18**) was formed. The isopachic fringes are the moiré which is formed by the interference fringes of the first and second photographs which are dependent on the variation of the specimen thickness [25].

REFERENCES

[1] P. Manogg, "*Anwendung der Schattenoptik zur Untersuchung des Zerreissvorgangs von Platten*". Dissertation 4/64, Universitaet Freiburg, 1964.

[2] P.S. Theocaris, "Local yielding around a crack-tip in Plexiglas",. *Journal of Applied Mechanics*, vol.37, pp. 409-415,1970.

[3] G.A. Papadopoulos, FRACTURE MECHANICS, The Experimental Method of Caustics and the Det.-Criterion of Fracture (G.A. Papadopoulos Ed.), Springer-Verlag, London, 1993.

[4] P.S. Theocaris and G.A. Papadopoulos, "Stress intensity factor from reflected caustics in birefringent plates with crack", *J. Strain Analysis*, vol.16, pp.29-36, 1981.

[5] A.R. Zak and M.L. Williams, "Crack point stress singularities at a bimaterial interface", *Journal of Applied Mechanics*, vol. 30, pp.142-143, 1963.

[6] M.L. Williams, "Surface stress singularities resulting from various boundary conditions in angular corners of plates under bending", Proceedings, First U.S.National Congress of Applied Mechanics, ASME, 1952; pp.325-329.

[7] M.L. Williams, "Stress singularities resulting from various boundary conditions in angular corners of plates in extension", *Journal of Applied Mechanics 19, Trans. ASME*, vol. 74, pp.526-528, 1952.

[8] M.L. Williams, "On the stress at the base of a stationary crack", *Journal of Applied Mechanics 24, Trans. ASME*, vol. 79, pp.109-114, 1957

[9] M.L.Williams, "The stresses around a fault or crack in dissimilar media", *Bulletin of the Seismological Society of America*, vol. 49, pp.199-204, 1959

[10] J.W. Dally and T. Kobayashi, "Crack arrest in duplex specimens", *Int. J. Solids and Structures*, vol.14, pp.121-126, 1978.

[11] P.S. Theocaris, "The Mesophase Concept in Composites", (P.S. Theocaris Ed.), Springer-Verlag, Berlin Heidelberg, 1987.

[12] P.S. Theocaris and J. Milios, "Dynamic crack propagation in composites", *Int. J. Fracture*, vol.16, pp.31-51, 1980.

[13] P.S. Theocaris and J. Milios, "Crack propagation velocities in bi-phase plates under static and dynamic loading", *Engineering Fracture Mechanics*, vol.13, pp.559-569, 1979.

[14] P.S. Theocaris and J. Milios, "Crack arrest at a bimaterial interface", *Int. J. Solids Structures* , vol. 17, pp.217-230, 1981.

[15] P.S. Theocaris, M. Siarova and G.A. Papadopoulos, "Crack propagtion and bifurcation in fiber-composite models: I Soft-hard-soft sequence of phases", *J. Reinforced Plastics and Composites*, vol. 5, pp.23-50, 1986.

[16] P.S. Theocaris and G.A. Papadopoulos, "Crack propagation and bifurcation in fiber-composite models II: Hard-soft-hard sequence of phases", *Journal of Reinforced Plastics and Composites*, vol. 5, pp.120-140, 1986.

[17] E.E. Gdoutos, "Failure of a bimaterial plate with a crack at an arbitrary angle to the interface", *Fiber Science and Technology* , vol.15, pp.27-40, 1981.

[18] E.E. Gdoutos and A. Giannakopoulou, "Stress and failure analysis of brittle matrix composites. Part I: Stress analysis", *International Journal of Fracture*, vol. 98, pp.263-277, 1999.

[19] E.E. Gdoutos, A. Giannakopoulou and D.A. Zacharopoulos, "Stress and failure analysis of brittle matrix composites. Part II: failure analysis", *International Journal of Fracture*,vol. 98, pp.279-291, 1999.

[20] E.N.Theotokoglou, G.J. Tsamasphyros and C.P. Spyropoulos, "Photoelastic study of a crack approaching the bonded half-plates interface", *Engineering Fracture Mechanics*, vol. 34, pp.31-42, 1989.

[21] C.P. Spyropoulos, E.N. Theotokoglou and G.J. Tsamasphyros, "Evaluation of the stress intensity factors for a crack approaching the bonded half-plates interface from isopachics", *Acta Mechanica*, vol.81, pp.75-89, 1990.

[22] G.A. Papadopoulos, "Crack-tip caustics at a bi-material interface", *International journal of Fracture*, vol. 98, pp.329-342, 1999.

[23] G.A. Papadopoulos and N. Moscos,Crack-tip isochromatic and isopachic fringes at a bi-material interface", *International journal of Fracture*, vol.141, pp.327-332, 2006.

[24] M.M. Frocht, Photoelasticity. John Willey, New York,1948.

[25] A.J. Durelli and W.F. Riley, Introduction to Photomechanics. Prentice-Hall Inc./Englewood Cliffs NI, USA, 1965.

Vortex Breakdown Inside a Closed Container: Simulation Analysis, PIV and Measurements of LDV

Jitendra Narayan Biswal, *Department of Mechanical Engineering, Aryan Institute of Engineering & Technology, Bhubaneswar, jnarayan679@gmail.com*
Shakyasingha Sahoo, *Department of Mechanical Engineering, NM Institute of Engineering & Technology, Bhubaneswar, shakyasinghasahoo@gmail.com*
Mdaras Aras Ansari, *Department of Civil Engineering, Raajdhani Engineering College, Bhubaneswar, mdarasansari2578@gmail.com*

Abstract: Numerical simulations and measurements using PIV and LDV have been carried out for steady vortex breakdown inside a closed container. The numerical solution has been employed as a benchmark to assess the capabilities and limitations of the experimental techniques in a difficult flow case involving a double breakdown in the limit of the steady regime.

INTRODUCTION

The swirling flow inside a closed container with a rotating end-wall has attracted significant interest from researchers since more than three decades. The simplicity of the geometry, the well-controlled flow conditions, the highly rich physics of the associated phenomena and, especially, the importance of related applications certainly explain the attention given. Initial studies on this matter were attributed to Vogel [1] but the experiments of Escudier [2], published sixteen years later, were the first reporting a systematic investigation on the occurrence of vortex breakdown in this flow geometry.

Since then, aiming to improve our knowledge about this problem, many experiments and numerical simulations have been carried out for a wide range of flow conditions. Recently, the majority of these studies have employed numerical simulations to describe the onset of unsteady, asymmetric behaviour of vortex breakdown structures [3-8]. On the other hand, and with a few exceptions only [9-12], the experimental investigations on this subject available in the literature are essentially based on the results of flow visualization techniques. In addition, it would be expected that before embarking on detailed analyses of a more complicated behaviour, such as that associated to unsteadiness and symmetry-breaking, a thorough assessment of the performance of quantitative experimental techniques should be made in the context of steady, symmetric breakdown.

In the present study, the variant proposed by Pereira and Sousa [10] to drive the swirling flow using a rotating cone instead of a flat lid has been considered with the purpose of accomplishing the foregoing task. This also differs from the numerical investigations by Yu *et al.* [13], who used stationary (concave and convex) conical lids. The velocity field in a meridional plane of the closed container has been measured by the use of both Particle Image Velocimetry (PIV) and Laser-Doppler Velocimetry (LDV), for a particular flow condition displaying steady, double breakdown of the columnar vortex at the axis. Numerical simulations have also been carried out to serve as a benchmark with the aim of assessing the capabilities and limitations of the aforementioned experimental techniques.

MATERIALS AND METHODOLOGY

The swirling flow inside the closed container was generated by the rotation of a conical end-wall at a constant value of the angular speed Ω, as shown in Fig. (**1**). The main idea behind the use of a conical driver instead of the classical flat rotor is that, from a topological point of view, the apex of a cone provides a well-defined nodal point for the central streamline impinging upon the rotor wall. The container was a cylinder with radius R and height $H = 3R$, which was kept unchanged in this study.

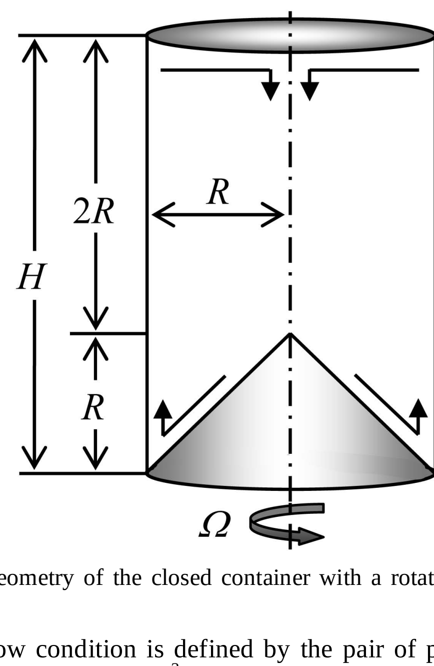

Fig. (1). Geometry of the closed container with a rotating conical end-wall.

The flow condition is defined by the pair of parameters (Re, H/R), where $Re = \Omega R^2/\nu = 2570$ is the Reynolds number and ν is the kinematic viscosity of the fluid. The stability diagram in Fig. (**2**) indicates whether single, double or no vortex breakdown occurs as well as if the flow regime is steady or time-dependent [10]. In this case, a steady, double breakdown structure is expected to be observed.

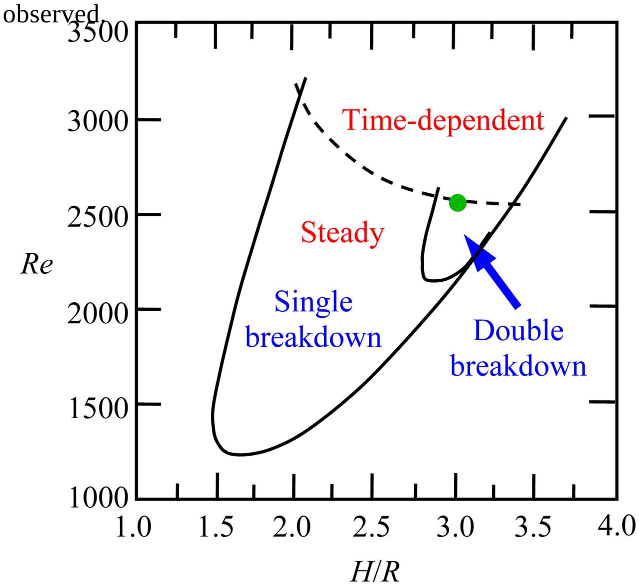

Fig. (2). Stability diagram [10] (the green spot marks the investigated flow condition).

Numerical simulations and measurements employing both PIV and LDV have been carried out for the aforementioned flow condition. A synthetic oil (ν = 31.2 x 10^{-6} m^2s^{-1} @ 21ºC) was used as working fluid in the experiments in order to allow refractive index matching between the container walls and the fluid, as depicted in Fig. (**3**). For this purpose, the oil temperature was controlled with an accuracy of ±0.1 ºC, which further allowed to minimize the uncertainty in *Re*. Additional details concerning the experimental setup were given in [10].

NUMERICAL SIMULATIONS

The mass and momentum conservation equations for the unsteady, three-dimensional flow of an incompressible fluid have been solved using the finite-volume methodology. These were discretized on a structured, non-orthogonal, fine mesh comprising 122 x 82 x 82 nodes, and integrated in space over each control volume as well as in time over a small time interval Δt. The Crank-Nicholson time-stepping method was used to advance diffusion terms in time, whereas the second-order accurate Adams-Bashforth method was applied to convection terms. The time increment was determined by stability requirements, namely max $(CFL) \leq 0.4$, where *CFL* stands for the Courant-Friedrichs-Lewy number. On the other hand, the spatial discretization of convection and diffusion terms was carried out employing second-order accurate central differences. Finally, the pressure field was obtained by an iterative procedure from the solution of a Poisson equation resulting from the combination of continuity and momentum equations. Additional details about the numerical methodology were given in [10].

A very long simulation time was required to obtain a virtually steady solution for the present values of *Re* and *H*/*R*, namely $\Omega t > 2000$. This is due to the fact that this pair of parameters is deliberately located on the boundary separating steady and unsteady regimes in the stability diagram shown in Fig. (**2**). Such flow condition was selected with the aim of emphasizing the occurrence of vortex breakdown as well as maximizing the associated field gradients.

PIV MEASUREMENTS

The digital implementation of PIV proposed in [14] was employed to collect a total of 300 flow images, which were used in the computation of ensemble-averaged velocity vectors. The associated statistical error in mean values is smaller than 2% for a 95% confidence level [15]. Following the conclusions of a previous study [16], the images have been processed in interrogation windows of 32 x 32 pixels with a 75% overlap.

In general, the dominant velocity component in swirling flows confined to closed containers is the azimuthal component. Thus, the main obstacle to an efficient application of PIV to these flows lies in its strong three-dimensionality. Such large amount of motion normal to the light sheet leads to a very significant out-of-plane loss of particle pairs, which ultimately originates an important decrease in correlation peak detectability. There is no panacea for this problem, but at least three methods have been suggested for the minimization of the foregoing effects [17]. The present work combined both the reduction of the laser pulse delay (3 ms) and the thickening of the light sheet (2.5 mm). A circular offset of the light sheet could also have been implemented at the expense of the system's simplicity. However, the efficacy of the latter procedure is rather questionable in this case due to large variations in the magnitude of the out-of-plane flow component. It must be mentioned that the laser pulse delay was further limited by exigent requirements in dynamic range, as a result of the broad range of velocities encountered in the presence of vortex breakdown. Additionally, the thickness of the light sheet had to be optimised taking into account that a reduction in illumination intensity also produces a decrease in signal-to-noise ratio.

Wide variations in the velocity field translate into a large variability in particle image shift. Thus, higher velocities occurring around the vortex breakdown structures and near the container walls are particularly vulnerable to random and bias errors due to in-plane loss of particle pairs, mainly resulting in increased noise and underestimation of displacement values by the PIV system, respectively. In order to minimise the consequences of these effects, a discrete offset of the interrogation windows coupled with a multi-grid/pass procedure was applied as well [17]. This also allowed to further increase the dynamic range in the current arrangement. It will be shown later that this issue is particularly critical when whole-field measurements of the flow inside the closed container are performed using PIV.

LDV MEASUREMENTS

A two-component LDV system from TSI Inc. was also used in the experimental characterisation of the flow structures, although only measurements of the axial velocity component are presented here. The velocimeter was based on fiberoptics and operated in backward-scatter mode. Signal

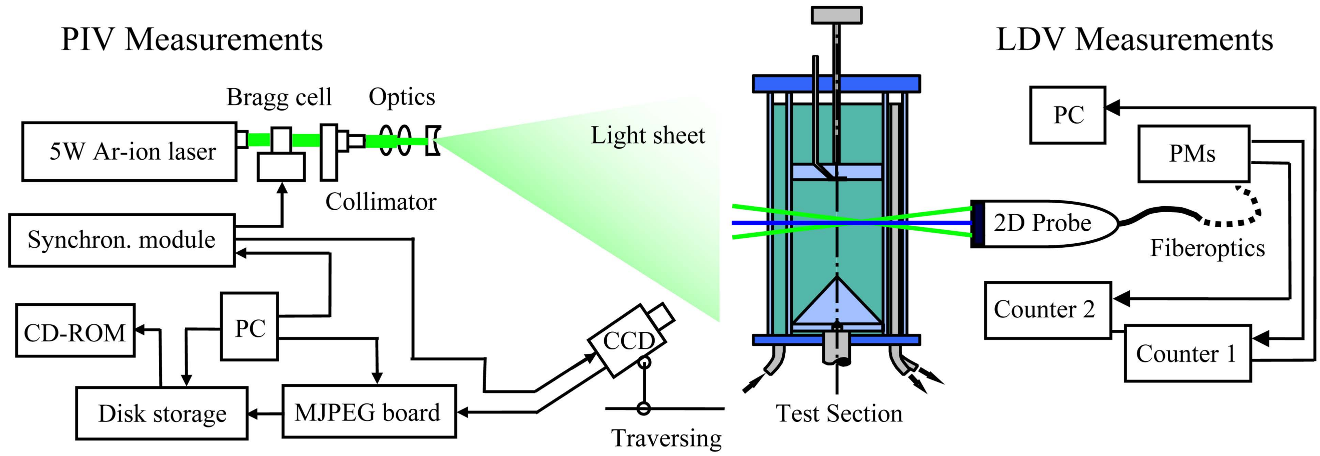

Fig. (3). Schematics of the experimental apparatus for PIV and LDV measurements.

processing was carried out using frequency counters. Velocity values were evaluated by ensemble-averaging, calculated from 5000 samples. The associated statistical error in mean values is smaller than 1% for a 95% confidence level [15]. Additional details regarding the system and the measuring effort can be found in [10].

The aforementioned refractive index matching procedure allowed to minimise the problem of distortion of the optical paths through the curved surfaces in the liquid flow [18], so that reliable measurements close to the container walls could be performed. Other systematic errors such as non-turbulent Doppler broadening due to gradients of mean velocity across the measuring volume and sampling bias are, in general, the prevalent sources of uncertainty in LDV measurements. However, the latter was lessened by the use of high seeding rates compared to the fundamental velocity fluctuation rates, and the former affects essentially the variances and other higher-order statistics of the velocity time series [15].

RESULTS AND DISCUSSION

The results obtained from PIV and LDV measurements are compared here with those produced by numerical simulation, which is used as a benchmark. This will allow a discussion on the limitations of each of these experimental techniques for a detailed characterisation of vortex breakdown and the remainder of the swirling flow inside the closed container. Taking into account that, for the investigated condition, the flow is steady and axisymmetric, only results in a meridional plane are presented. It must be emphasized that the measurement of the radial and, especially, the axial velocity components is more demanding than that of the azimuthal velocity field. Hence, the discussion is focused on the former only.

Fig. (**4**) shows the velocity field measured in a meridional plane of the closed container using PIV. The depicted flow topology strongly resembles that obtained by

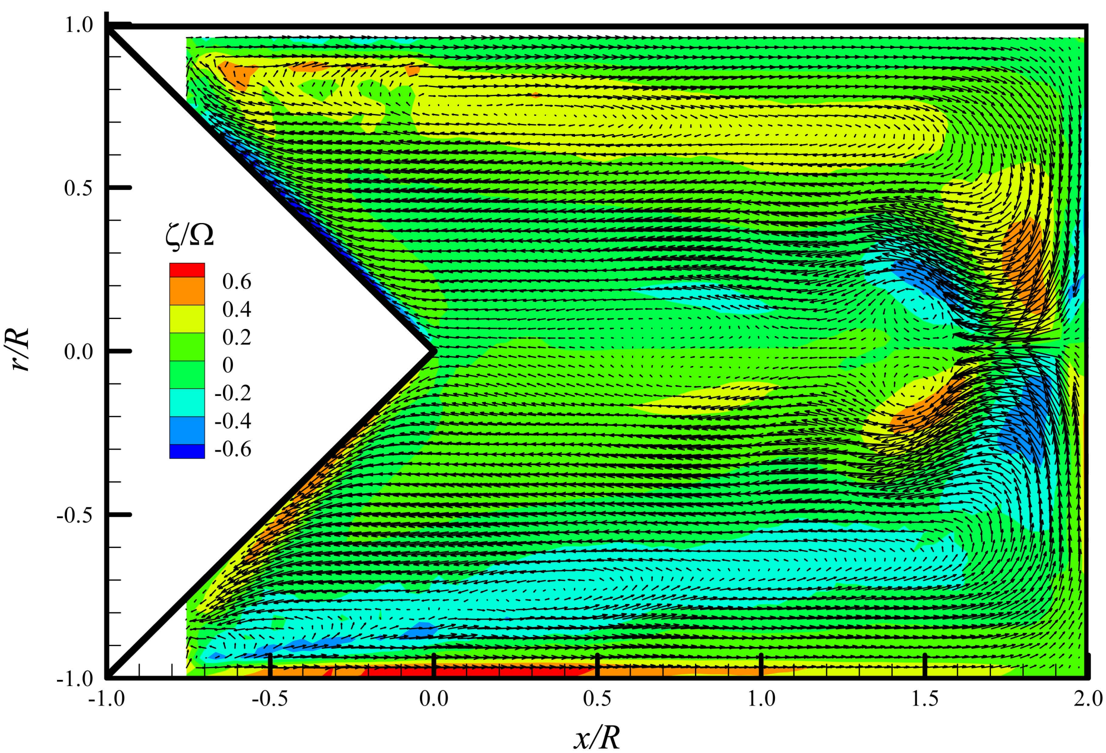

Fig. (4). Velocity vectors and vorticity contours in a meridional plane obtained by PIV measurements.

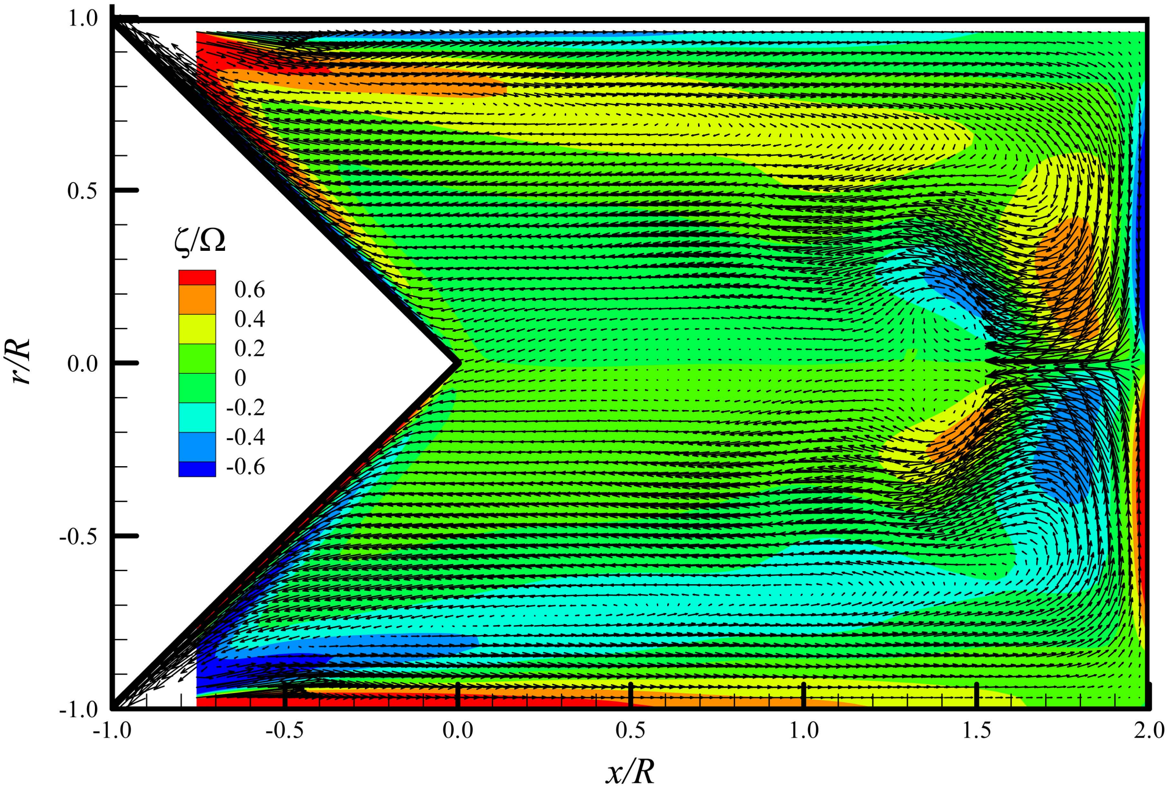

Fig. (5). Velocity vectors and vorticity contours in a meridional plane obtained by numerical simulation (as interpolated to the uniform mesh of the PIV measurements).

others for a rotating flat lid. However, as the space available at the central axis is smaller in the present case, the strength of the breakdown is also reduced for the same values of the governing parameters. This is in agreement with the findings of Yu *et al*. [13], who used a conical stationary lid to inhibit the occurrence of vortex breakdown. Altogether, this fundamentally leads to a shift of the main curve (single breakdown) in the stability diagram to larger values of H/R and Re, as already shown in Fig. (**2**).

Although whole-field quantification has been carried out with the PIV system, the double breakdown has still been captured with detail. The remaining flow features, namely the global recirculation pattern and the boundary layer over the rotating cone are evidenced as well. Vorticity contours normalized by Ω are also shown in the figure, as this quantity is of primary interest in a vortical flow. Following the conclusions of a previous study [16], the vorticity field $\zeta(r,x)$ has been directly computed from the PIV measurements using centred differences. Apart from those naturally occurring on the container walls, two main regions of concentrated vorticity are observed on top of the primary breakdown bubble. The vorticity maxima in these areas will be later used in a quantitative comparison with the numerical data.

In order to facilitate this task, the velocity field obtained by numerical simulation in a non-uniform mesh has been interpolated (Krigging method) to the same (uniform) mesh used in the PIV measurements.

Again, both velocity vectors and vorticity contours computed by centred differences are presented in Fig. (**5**) for a meridional plane. The results evidence the difficulties of PIV to cope with large velocity gradients, especially those occurring in the vicinity of solid boundaries. Wall boundary layers could not be accurately captured using the foregoing experimental technique in whole-field measurements. However, apart from these regions and the strongly decelerated flow on top of the primary breakdown bubble, a remarkably good agreement between experiments and simulations was obtained, even in the more stringent case of the vorticity field. This observation may be confirmed quantitatively as well in Table **1**, which provides a comparison between the values of local maxima of vorticity obtained with each technique.

A detailed comparison is also made for axial velocity profiles taken at several locations, as shown in Fig. (**6**). The shortcomings of PIV near the side walls (all profiles) and close to the tip of the rotating cone (x/R = 0.0) can again be seen in this figure. As mentioned before, the region on top of the primary breakdown bubble (x/R = 1.8) is also affected by the limited spatial resolution of PIV, exhibiting a clear underprediction of the axial velocity in the jet-like profile occurring at this location. Furthermore, the size of the secondary breakdown bubble seems to be slightly smaller than in the numerical predictions, whereas the size of the primary one looks slightly larger.

A similar comparison is made in Fig. (**7**) between LDV measurements and, again, numerical simulations. The consequences of the better spatial accuracy displayed by this experimental technique is evidenced in the aforementioned jet-like profile and in the vicinity of side walls and cone. However, unexpected difficulties were sometimes encountered in the measurement of the peak velocities in the side wall boundary layers. A slight asymmetry is also seen in the experiments (both PIV and LDV), which reveals the sensitivity of the flow structures to a possibly imperfect alignment of the top wall (x/R = 2.0).

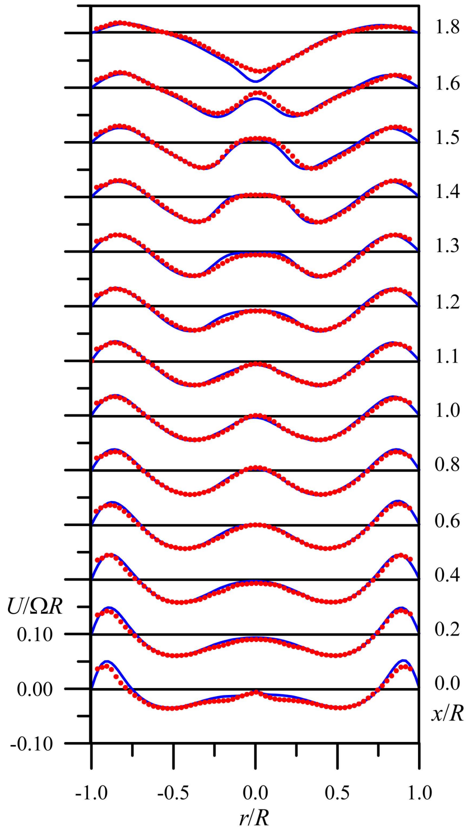

Fig. (6). Profiles of the axial velocity component: comparison between numerical simulations (blue lines) and PIV measurements (red symbols).

Table 1. Local Maxima of Vorticity at Reference Locations from Numerical Simulations and PIV

x/R	*r/R*	Numerical (no interp.)	Numerical (interpol.)	PIV
1.5	0.21	-0.52	-0.51	-0.51
1.8	0.23	-0.50	-0.50	-0.46

CONCLUSIONS

Numerical simulations of swirling flow inside a closed container have been carried out in the presence of steady vortex breakdown. These data have been used as a reference to assess the capabilities of PIV and LDV techniques for the characterisation of the associated flow topology. Flow maps embracing both axial/radial velocities and corresponding vorticity at a meridional plane have been compared in the case of numerical simulations and PIV. Several axial velocity profiles have also allowed a detailed comparison between experiments and simulations.

The results have evidenced that accurate measurements can be obtained with both PIV and LDV for a difficult flow condition, involving a double breakdown in the limit of the steady regime. The limitations of the PIV technique with respect to spatial resolution have also been noted when a whole-field characterisation is performed. This mainly affects the description of wall boundary layers and the jet-like velocity region on top of the primary breakdown bubble. Better spatial resolution is naturally obtained with LDV at the expense of a much longer measurement time. However, a few inaccuracies have also been found with this technique in the quantification of the axial velocity maxima in the side wall boundary layers.

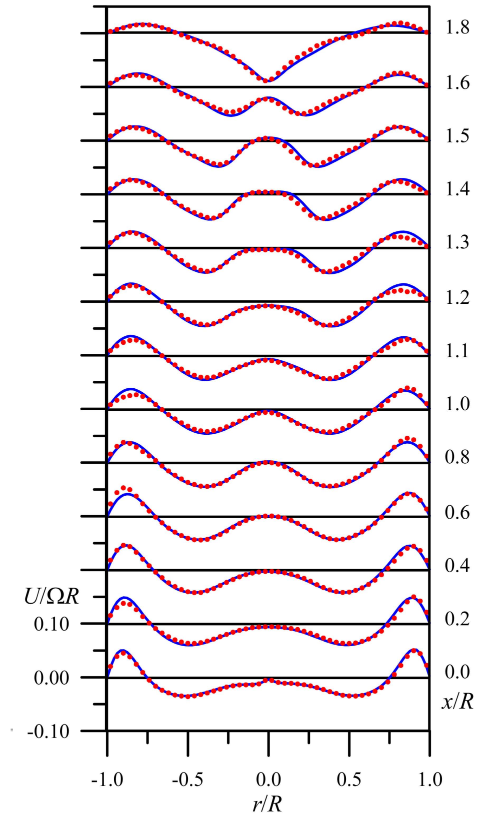

Fig. (7). Profiles of the axial velocity component: comparison between numerical simulations (blue lines) and LDV measurements (red symbols).

REFERENCES

[1] H. U. Vogel, "Experimentelle Ergebnisse über die Laminare Strömung in einem zylindrischen Gehäuse mit darin Rotierender Scheibe", Bericht 6, Max-Planck-Institut für Strömungsforschung, Göttingen, 1968.

[2] M. P. Escudier, "Observations of the flow produced in a cylindrical container by a rotating endwall", *Exps. Fluids*, vol. 2, pp. 189-196, December 1984.

[3] H. M. Blackburn and J. M. Lopez, "Symmetry breaking of the flow in a cylinder by a rotating endwall", *Phys. Fluids*, vol. 12, pp. 2698-2701, November 2000.

[4] F. Sotiropoulos and Y. Ventikos, "The three-dimensional structure of confined swirling flows with vortex breakdown", *J. Fluid Mech.*, vol. 426, pp. 155-175, January 2001.

[5] A. Y. Gelfgat, P. Z. Bar-Yoseph, and A. Solan, "Three-dimensional instability of axisymmetric flow in rotating lid-cylinder enclosure", *J. Fluid Mech.*, vol. 438, pp. 363-377, July 2001.

[6] F. Marques and J. M. Lopez, "Precessing vortex breakdown mode in an enclosed cylinder flow", *Phys. Fluids*, vol. 13, pp. 1679-1682, June 2001.

[7] E. Serre and P. Bontoux, "Vortex breakdown in a three-dimensional swirling flow", *J. Fluid Mech.*, vol. 459, pp. 347-370, May 2002.

[8] J. M. Lopez, "Rotating and modulated rotating waves in transitions of an enclosed swirling flow", *J. Fluid Mech.*, vol. 553, pp. 323-346, April 2006.

[9] C. H. Westergaard, P. Buchhave and J. N. Sørensen, "PIV measurements of turbulent and chaotic structures in a rotating flow using an optical correlator", *in Laser Techniques and Applications in Fluid Mechanics*, R. J. Adrian, D. F. G. Durão, F. Durst, T. Asanuma and J. H. Whitelaw, Eds. Berlin Heidelberg New York: Springer-Verlag, 1993, pp. 243-256.

[10] J. C. F. Pereira and J. M. M. Sousa, "Confined vortex breakdown generated by a rotating cone", *J. Fluid Mech.*, vol. 385, pp. 287-323, April 1999.

[11] I. V. Naumov, V. L. Okulov, K. E. Meyer, J. N. Sørensen and W. Z. Shen, "The LDA – PIV diagnostics and 3D simulation of oscillating swirl flow in a closed cylindrical container", *Thermoph. Aeromech.*, vol. 10, pp. 143-148, May 2003.

[12] J. N. Sørensen, I. Naumov and R. Mikkelsen, "Experimental investigation of three-dimensional flow instabilities in a rotating lid-driven cavity", *Exps. Fluids*, vol. 41, pp. 425-440, September 2006.

[13] P. Yu, T. S. Lee, Y. Zeng and H. T. Low, "Effects of conical lids on vortex breakdown in an enclosed cylindrical chamber", *Phys. Fluids*, vol. 41, pp. 117101–1-9, November 2006.

[14] C. Freek, J. M. M. Sousa, W. Wentschel, and W. Merzkirch, "On the accuracy of an MJPEG-based digital image com-pression PIV-system", *Exps. Fluids*, vol. 27, pp. 310-320, September 1999.

[15] H.-E. Albrecht, M. Borys, N. Damaschke, and C. Tropea, *Laser Doppler and phase Doppler measurement techniques*. Berlin Heidelberg New York: Springer-Verlag, 2002.

[16] J. M. M. Sousa and C. Freek, "On the advantages and pitfalls of statistical PIV analysis in the measurement of confined vortex breakdown", in Ninth International Symposium on Application of Laser Techniques to Fluid Mechanics, 1998, pp. 4.4.1-4.4.8.

[17] M. Raffel, C. Willert, and J. Kompenhans, *Particle image velocimetry*. Berlin Heidelberg New York: Springer-Verlag, 1998.

[18] J. C. F. Pereira, "Refractive index matching for LDV measure-ments near walls and in complex geometries", *in Instrumentation for Combustion and Flow in Engines*, D. F. G. Durão, J. H. Whitelaw, and P. O. Witze, Eds. Dordrecht: Kluwer Academic, 1988, pp. 267-284.

Study of Centrifugal Pump Impeller by Changing Outlet Blade Angle

Manohar Kumar Singh, *Department of Mechanical Engineering, Aryan Institute of Engineering & Technology, Bhubaneswar, manoharsingh751@gmail.com*
Abinash Sahoo, *Department of Mechanical Engineering, Capital Engineering College, Bhubaneswar, abinashsahoo719@yahoo.co.in*
Bijayalaxmi Behera, *Department of Civil Engineering, Capital Engineering College, Bhubaneswar, bijayalaxmi759@gmail.com*
Saleema Panda, *Department of Civil Engineering, NM Institute of Engineering & Technology, Bhubaneswar, saleemapanda25@gmail.com*
Hemant Ku Nayak, *Department of Mechanical Engineering, NM Institute of Engineering & Technology, Bhubaneswar, hemantnayak236@gmail.com*

Abstract: The pump design is facilitated by the development of computational fluid dynamics and the complex internal flows in water pump impellers can be well predicted. Various parameters affect the pump performance and energy consumption. The impeller outlet diameter, the blade angle and the blade number are the most critical. The present paper describes the simulation of the flow into the impeller of a laboratory pump in a parametric manner. In this study, the performance of impellers with the same outlet diameter having different outlet blade angles is thoroughly evaluated. The one-dimensional approach along with empirical equations is adopted for the design of each impeller. The predicted performance curves result through the calculation of the internal flow field and a successful correlation of local and global parameters. The numerical solution of the discretized three-dimensional, incompressible Navier-Stokes equations over an unstructured grid is accomplished with a commercial CFD finite-volume code. For each impeller, the flow pattern and the pressure distribution in the blade passages are calculated and finally the head-capacity curves are compared and discussed.

Keywords: Centrifugal pump, Impeller, CFD, Numerical study.

INTRODUCTION

The complexity of the flow in a turbomachine is primarily due to the three dimensional developed structures involving turbulence, secondary flows, unsteadiness etc. Initially, the design of a centrifugal pump was based mainly on empirical correlation, combination of model testing and engineering experience. Nowadays, the design demands a detailed understanding of the internal flow during design and off-design operating conditions. Computational fluid dynamics (CFD) have successfully contributed to the prediction of the flow through pumps and the enhancement of their design.

The complex internal flow at the outlet of the impeller appears a circumferential distortion due to the asymmetric shape of the spiral volute and tongue, especially at off design operating points. Moreover the rotor-volute interaction causes the appearance of dynamic effects which influence the overall pump performance. The non-uniform flow conditions and particularly the pressure field lead to the development of unbalanced radial forces. All these characteristics are crucial for the pump design. The predictions of the performance in combination with the investigation of the complex internal flow through the impeller have developed to fields of intense research.

Various researchers have considerably contributed to revealing the flow mechanisms inside centrifugal impellers with spiral volute or vaned diffuser volute aiming to the design of high performance centrifugal turbomachines. The reported works by Eckardt [1], Johnson *et al.* [2], Kjork *et al.* [3], Denton [4], Dawes [5], Casey *et al.* [6], Bansod *et al.* [7], Krain *et al.* [8], Farge *et al.* [9] and Zhang *et al.* [10] are an indicative collection of research efforts on the computation and the experimental verification of the flowfields within centrifugal impellers.

The last decade research becomes more sophisticated, specifically recently, Hillewaert *et al.* [11], Gonzalez *et al.* [12-14], Byskov *et al.* [15], Meakhail *et al.* [16], Majidi [17] and Feng *et al.* [18] extended the prediction of the performance at various operating conditions, different from the normal one, taking into account the dynamic effects of the flow.

Several algorithms have been proposed and developed, targeting to the numerical simulation of the flowfield of a centrifugal impeller. These algorithms apply either pressure based or density based methods for the solution of Navier-Stokes equations. Lakshminarayana [19], Rodi *et al.* [20] and Thakur *et al.* [21], provide a review of the techniques that are useful as an assessment of the state of the art.

It is evident that there is a lot of research work at the numerical and experimental evaluation of the pump flow field, however the study of important manufacturing parameters that influence the performance of a pump is infrequently available in the open literature. Kergourlay *et al.* [22] studied the influence of adding splitter blades in a hydraulic centrifugal pump impeller. A comparison between impellers with and without splitters and the predicted characteristic curves were presented. Gonzalez *et al.* [13] tested two centrifugal pump impellers with different outlet diameters for the same volute. A detailed description of the influence of the radial gap between impeller exit and tongue was presented. Anagnostopoulos [23] developed a numerical model for the simulation of the 3D turbulent flow and investigated different impeller configurations by varying crucial design parameters.

The present ongoing research is concerned with the influence of the outlet blade angle in the performance of a laboratory centrifugal pump. The design and off-design performance characteristic curves, the local and global variables of the flow field and the resulted non-uniform circumferential pressure field are numerically predicted for three shrouded radial impellers with different outlet blade angle. The computational fluid dynamics analysis is carried out with the commercial software package Fluent® [24], which has been widely used in the field of turbomachinery and the simulation results, have been proven by Sun *et al.* [25] and Gonzalez *et al.* [12] to be reliable.

THE PUMP STUDIED

The systematic research on the influence of the various design aspects of a centrifugal pump in its performance in the whole range of the flow rates requires numerical predictions and experiment. Recently, in the Fluid Mechanics Laboratory of the University of Patras, a pump test rig designed and already is in operation. The test rig is presently equipped with an industrial centrifugal pump that it will be soon replaced by a laboratory pump with the completion of its manufacture. The laboratory pump volute has been especially designed in a way that it can easily suit radial impellers of the same outlet diameter but differ in various main design parameters such as the number of blades, the mean line geometry of the blade, the inlet and outlet blade angles.

The volute of the laboratory centrifugal pump is of rectangular section with rounded corners and its diffuser extends in the radial direction. Three shrouded impellers of constant width (b=20mm) with six untwisted blades backward facing have been designed according to Pfleiderer method [26]. The blade length in the three impellers is almost equal. All impellers have the same diameters in suction and pressure side as well as the same blade's leading edge angle (β_1=14 deg) and they vary in the blade's trailing edge angle which is β_2=20, 30 and 50 deg, respectively. The diameters of the impellers at the suction and pressure side are D_1=150mm and D_2=280mm, respectively.

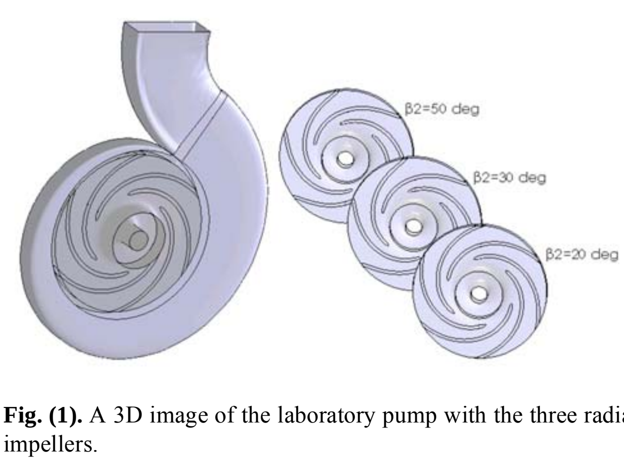

Fig. (1). A 3D image of the laboratory pump with the three radial impellers.

The CAD model of the designed laboratory pump with the three impellers and the absence of their front shroud for blade profile viewing purposes are shown in Fig. (**1**). In the rotational speed (n) of 925rpm, the normal operation of the three impellers is 0,0125m^3/sec flow rate (Q) and according to one dimensional theory the estimated pump's total head (H) is 10m that results in the value 18,4 for the specific speed ($n_q = n \cdot Q^{1/2}/H^{3/4}$). At the normal operating point, the hydraulic efficiency (η_H) of the pump reaches its maximum value 0,83.

GOVERNING EQUATIONS

The incompressible flow through the rotating impeller is solved in a moving frame of reference with constant rotational speed equal the rotational speed of the impeller. The flow through the stationary parts of the pump is solved in an inertial reference frame. The governing equations for the impeller are formulated below

$$\nabla \rho \mathbf{u}_r = 0 \ldots \tag{1}$$

$$\nabla \rho \mathbf{u}_r + 2\rho \mathbf{\Omega} \times \mathbf{u}_r + \rho \mathbf{\Omega} \times \mathbf{\Omega} \times \mathbf{r} = -\nabla p + \mu_{eff} \nabla^2 \mathbf{u}_r \ldots \tag{2}$$

where ρ is the density of the fluid, p is the static pressure, $\mathbf{u}_r$ is the vector fluid velocity in the rotating system, $\mathbf{\Omega}$ is the rotational speed and μ_{eff} is the dynamic effective viscosity which is a linear combination of laminar and turbulent viscosity derived from k-ε model of turbulence. The last two terms in the left hand side of equation (2) are the effects of the Coriolis and centrifugal forces due to the rotating frame of reference.

For the stationary parts of the centrifugal pump, the governing equations are formulated in the stationary reference frame. The continuity equation remains the same, but the momentum equation reduces to

$$\nabla \rho \mathbf{u} = -\nabla p + \mu_{eff} \nabla^2 \mathbf{u} \ldots \tag{3}$$

where **u** is the vector fluid velocity in the stationary frame of reference.

The turbulence of the flow is modelled with standard k-ε model that is rated as the most used model that combines simplicity, robustness and reasonable accuracy. Moreover, it has been tested in a wide range of industrial flows showing satisfactory results. The differential transport equations for the turbulence kinetic energy and turbulence dissipation rate are:

$$\nabla \rho \mathbf{u} k = \nabla \left(\left(\mu + \frac{\mu_t}{\sigma_k} \right) \nabla k \right) + G_k - \rho \varepsilon \ldots \tag{4}$$

$$\nabla \rho \mathbf{u} \varepsilon = \nabla \left(\left(\mu + \frac{\mu_t}{\sigma_\varepsilon} \right) \nabla \varepsilon \right) + C_{1\varepsilon} \frac{\varepsilon}{k} G_k - C_{2\varepsilon} \rho \frac{\varepsilon^2}{k} \ldots \tag{5}$$

$$\mu_t = \rho C_m \frac{k^2}{\varepsilon} \ldots \tag{6}$$

where **u** is the local velocity vector, k is the turbulent kinetic energy, ε is the dissipation rate, μ is the laminar viscosity, μ_t is the turbulent viscosity, G_k represents the generation of turbulent kinetic energy due to the mean velocity gradients, σ_κ

and σ_ε are the turbulent Prandtl numbers and $C_{1\varepsilon}$=1,44, $C_{2\varepsilon}$=1,92 and C_m=0,09 are the constants of the model.

COMPUTATIONAL ISSUES

Geometry and Grid

The numerical treatment of the radial pump implies the spatial discretization of the flow domain. All gaps between the impeller shroud and the pump casing are neglected in the present numerical simulation. The whole domain consists of three sub-domains or zones. The first and third zones are stationary while the second zone that incorporates the blade is moving with the applied rotational speed of n=925 rpm.

The first zone represents the suction or inlet pipe that is 100 mm in diameter and the third zone is the discharge or outlet portion where the flow is fully developed with a less possible reacting outlet boundary condition. The intermediate zone consists of the eye and the impeller of the pump. The three sub-domains were separated further by additional inner faces forming different blocks. In this way, the density and the quality of the cells in local flow field regions can be suitably controlled and handled depending on pressure gradients and velocities.

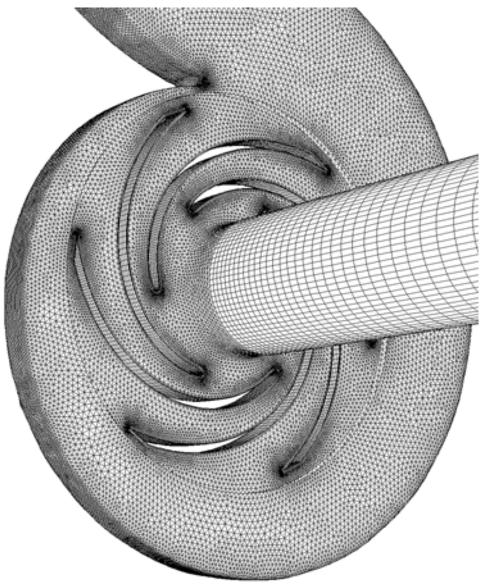

Fig. (2). Sketch of the unstructured mesh of the pump.

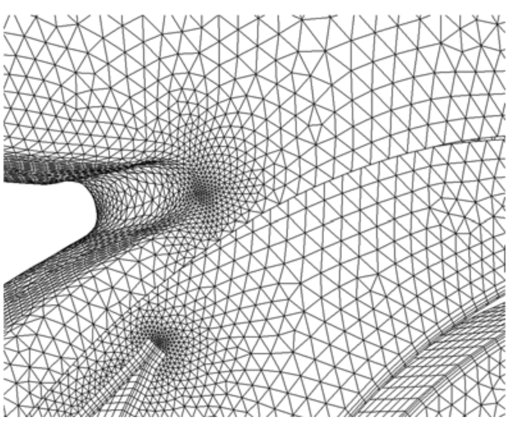

Fig. (3). Details of the unstructured mesh in the region of the tongue.

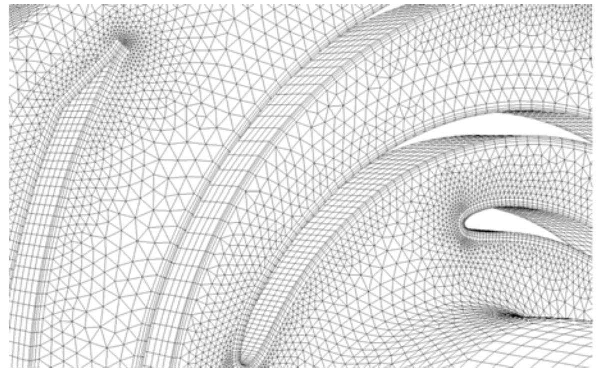

Fig. (4). The structured hexahedral cells around the blades combined with the unstructured mesh in the blade passage.

The geometry and the mesh of the computational pump domain were generated with Fluent's pre-processor, Gambit® [27]. Unstructured wedges are generated to define the inlet and outlet zones. An unstructured mesh with tetrahedral cells is also used for the zones of impeller and volute as shown in Fig. (**2**). The mesh is refined in the near tongue region of the volute (see Fig. (**3**)), as well as in the regions close to the leading and trailing edge of the blades. Around the blades, structured hexahedral cells are generated, as shown in Fig. (**4**). Though the size of the cells in the wall regions is not adequate to resolve the viscosity-affected region inside the boundary layer, the appropriate number of cells exists inside the boundary layer for the approach of standard wall functions. The latter provides correct values for the pump performance and allows a detailed analysis of the main phenomena involved.

Remarks on the Numerical Simulation

All the calculations have been performed with Fluent® CFD software package [24] that utilizes the finite volume method for the solution of the steady 3D incompressible Navier-Stokes equations, including the centrifugal force source in the impeller. Turbulence is modelled with the selection of the standard k-ε model. The involved parameters regarding the turbulence intensity and the hydraulic diameter, in the lack of realistic turbulent inflow conditions in industrial applications, are estimated with values of 5% and D/2, respectively. The pressure-velocity coupling is performed through the SIMPLE algorithm. Second order, upwind discretization is used for convections terms and central difference schemes for diffusion terms.

The applied boundary conditions involve the extension of the computational domain by adding a reasonable length at the inlet and outlet pipes of the centrifugal pump in order to better simulate the pumping circuit influence. At the inlet zone, the axial velocity is a constant based on the through flow for the pump. The absolute tangential velocity at the inlet is zero, which implies, in the rotating frame, that the relative velocity is $-r\mathbf{\Omega}$ and the radial velocity is zero. At the exit of the discharge pipe, assuming a fully developed turbulent flow, a practically zero velocity gradient is set. The walls of the model are stationary with respect to their respective frame of reference, and the no slip condition is applied.

Although grid size is not adequate to investigate local boundary layer variables, global ones are well captured. For such calculations wall functions, based on the logarithmic law, have been used.

Since the problem involves both stationary and moving zones, the multiple reference frame model has been selected. It is a quasi-steady state approximation in which individual cell zones move at different rotational speeds. As the rotation of the reference frame and the rotation defined *via* boundary conditions can lead to large complex forces in the flow, calculations may be less stable as the speed of rotation and hence the magnitude of these forces increases. To control this undesirable effect, each run starts with a low rotational speed and then the rotation is slowly increased up to the desired level.

The simulations were executed in a 3GHz Pentium IV PC. The number of iterations adjusted to reduce the scaled residual below the value of 10^{-5}, which is the criterion of convergence. For each run, the observation of the integrated quantities of total pressure, at suction as well as at discharge surface was appointed for the convergence of the solution. In many cases this drives the residuals in lower values than the initially set value. Depending on the case, the convergence was achieved at different iterations, as the result at a specific mass-flow was used to initialize the computations at another mass-flow. Aiming to smooth convergence, various runs were attempted by varying the under-relaxations factors. In that way a direct control regarding the update of computed variables through iterations, was achieved. Initializing with low values for the first iterations steps and observing the progress of the residuals, their values were modified for accelerating the convergence.

NUMERICAL RESULTS

The outlet angle of three different impellers is correlated with the slope of the H-Q performance curve of each impeller. Increasing the outlet blade angle, the shape of the curve becomes smoother and flatter. This fact is expected and is consistent with theory, i.e.

$$H = \mu\eta_H \frac{u_2^2}{g}\left(1 - \frac{c_{m3}}{u_2}\cot\beta_2\right) \ldots \tag{7}$$

where μ is the slip factor [28], η_H is the hydraulic efficiency, u_2 is the peripheral velocity at the outlet section of the impeller, c_{m3} is the meridian velocity at the exit of impeller passage and β_2 is the outlet blade angle.

Equation (7) enables the ascertainment of the effect of the two design parameters c_{m3}/u_2 and β_2 on the total head. If c_{m3}/u_2 is reduced, then the total head is increased. Certainly, the effect of the vane discharge angle is not so straightforward. If the β_2 angle increases, then the total head increases, too. However, the effect of increase the angle β_2 is partly cancelled since the slip factor formulas indicate that larger angle β_2 results to the decrease of the slip factor value. The variation of the slip factor affects the shape of the H-Q curve and it is noticeable for blade angles grater than 25 deg.

The later is in agreement with the results of the numerical prediction of the H-Q curves for the examined impellers, which are shown in Fig. (**5a**). The ordinate is the non-dimensional total head of the pump while the abscissa is the non-dimensional flow rate. The Q_N=58,5 m^3/h and H_N=8,93 m are the CFD predicted nominal volume rate and the nominal total head for the β_2=20 deg impeller, respectively.

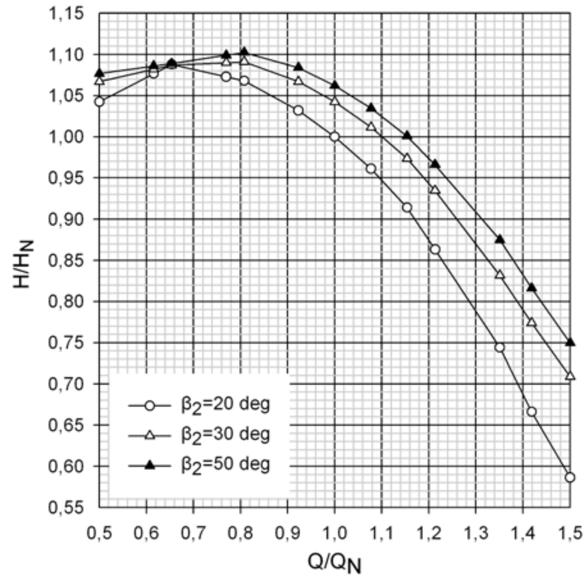

Fig. (5a). Predicted head curves for the examined pump impellers.

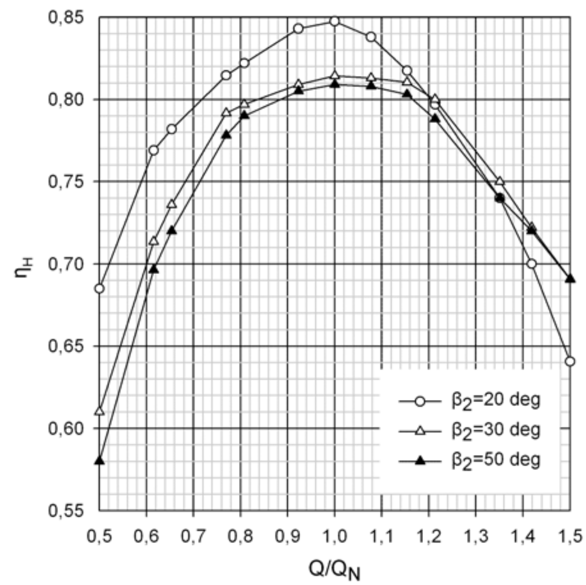

Fig. (5b). Predicted hydraulic efficiency curves for the examined pump impellers.

The nominal flow rate is defined by the point in which the hydraulic efficiency of the pump reaches its maximum value. The variation of the hydraulic efficiency against the non dimensional flow rate for the numerically studied impellers, are shown in Fig. (**5b**). At the nominal flow rate the value of the hydraulic efficiency is ranged between 0,81 and 0,845 for the three impellers which is in reasonable accuracy with the predicted value according to the applied design method. A 50% reduction of the volume rate from its nominal value results to 20%, 25% and 28% drop of the η_H relative to their nominal value for the impellers with β_2=20, 30 and 50deg respectively. A 50% increase of the volume rate from the nominal point leads to 25%, 15% and 15% drop of the η_H relative to the nominal one for the three impellers respectively.

The curve of the hydraulic efficiency for $Q<Q_N$ decreases more rapidly for the impellers with β_2=30 deg and 50 deg than for β_2=20deg. The opposite happens for $Q>Q_N$ where the η_H curve of the β_2=20 deg impeller is steeper. The comparison of the hydraulic efficiency of the three impellers at $Q=Q_N$ shows that the increase of the outlet angle more than 10 deg till to 30 deg reduce it almost 3%.

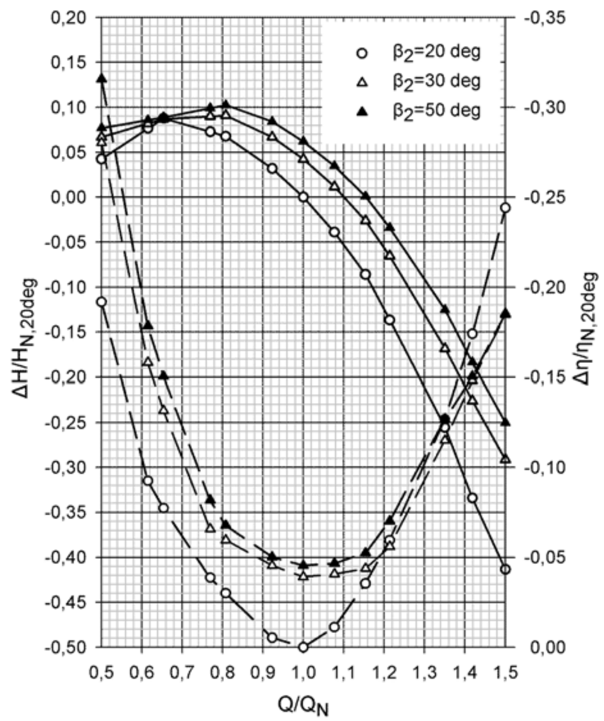

Fig. (6). Percentage variation of the head (solid lines) and hydraulic efficiency (dash lines) curves with outlet blade angle for the examined impellers.

The shift of the performance curves due to the variation of the outlet blade angle may be expressed in terms of percentage variation with reference of the corresponding values H/H_N and η_H at nominal capacity for the β_2=20 deg impeller, as shown in Fig. (**6**). Thus, at nominal capacity, a 10 deg increase of the β_2 angle causes a 4,2% increase of the head and a 3,9% decrease of the hydraulic efficiency. If the β_2 increases 30deg, i.e. from 20 deg to 50 deg, then the head increases 6,2% and the hydraulic efficiency decreases 4,5%.

Besides the predicted performance curves of the studied impellers, the assessment of the local characteristics of the internal flow field is accomplished. The static pressure fields for the plane near the back shroud for the two of the studied impellers are shown in Fig. (**7**). At constant radial position, it is confirmed that the static pressure drops from the pressure side to the suction side of the impeller blade and this pressure drop reduces at the exit of the blade passage. Moreover, the static pressure patterns are not the same in the planes between the hub and the shroud. The variation is noticed in the pressure contour field of the lateral surfaces of the blades. The observed pressure variation does not entail any additional losses in the pump and simply implies that each blade can only transmit a fixed amount of energy and certainly it is lower than the value prescribed by Euler's equation. Qualitatively, the patterns are similar for the three examined impellers. As it is expected, the variations are focused on the static pressure values that become larger with the increase of the outlet blade angle.

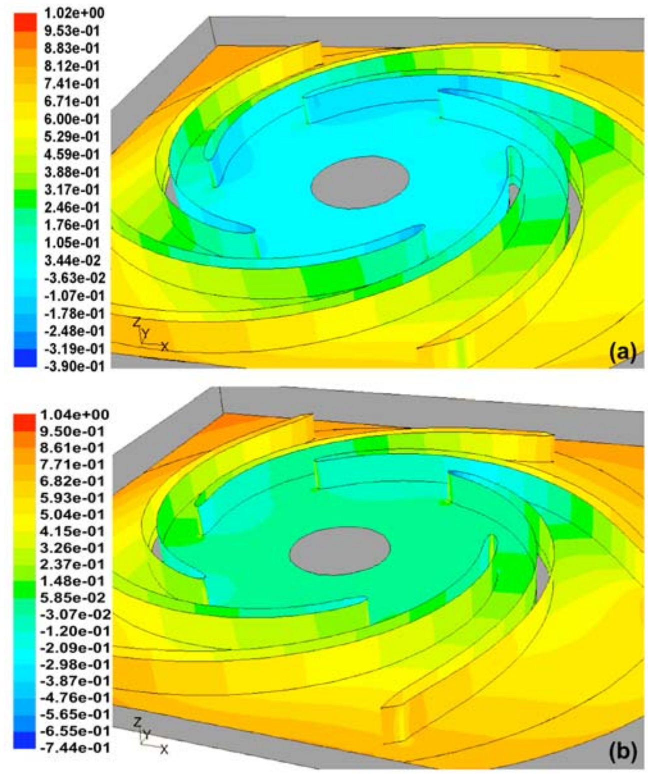

Fig. (7). Relative static pressure contours (atm) at Q_N for the β_2=20 deg (a) and β_2=50 deg (b) impellers.

The minimum value of the static pressure inside the impeller is located at the leading edge of the blades at the suction side except for the blade with trailing edge, which end up at the region of the tongue. For that blade, the minimum pressure is located at the leading edge of the blade at the pressure side primarily due to the blade - tongue interaction. Another reason for the appearance of low local pressures at the pressure side of the blade is related with the geometry and the design method of the blade, which permits the development of such pressure contours. Hence, the minimum pressure is observed at these regions. The same situation stands for flow rates greater or lower than the nominal one, as well as for different outlet angles.

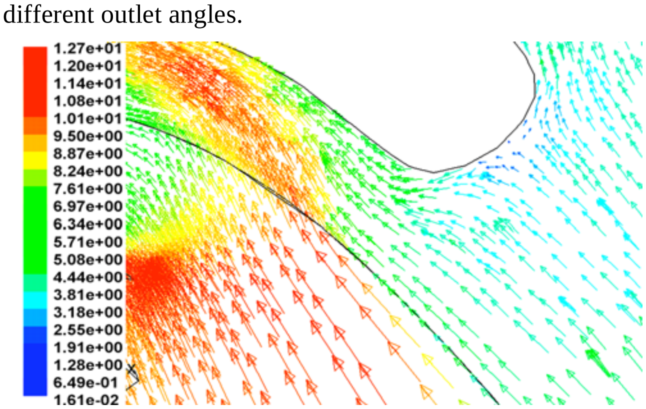

Fig. (8). The absolute velocities (m/s) in the region of the tongue for the β_2=20 deg impeller.

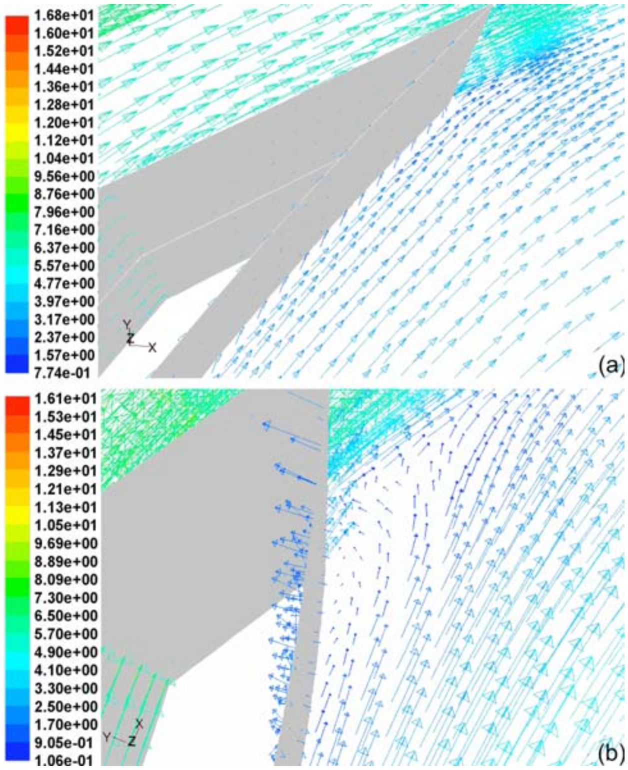

Fig. (9). The relative velocities (m/s) at the trailing edge of the blade with β_2=20 deg (a) and β_2=50 deg (b).

The flow close to the tongue and at the design operation is shown in Fig. (**8**). The pattern verifies that the position of the stagnation point is placed in the middle of the tongue edge and it is in agreement with published data [13]. Furthermore, the outlet blade angle affects and changes the relative velocity patterns. As the β_2 increases, a recirculation zone establishes at the trailing edge of the blade as Fig. (**9**) shows.

Significant variations in the absolute velocity field in the blade passage are displayed when the impeller operates off-design. Fig. (**10**) shows the absolute velocity vectors in the leading edge of one blade for the three studied impellers with each one operating in nominal capacity or at the edges of the examined capacity range. When the volume flow rate is nominal or more than nominal, the fluid flows smoothly through the impeller passage, except for the flow passage which ends up at the region of tongue. The flow direction in combination with the blade curvature exhibits a weak vortex at the pressure side of the blade just downstream the leading edge giving reasons to the appearance of low pressure in this region. Reversely, when the impeller operates in volume flow rates less than nominal, a recirculation zone is established in the leading edge of each blade.

The absolute velocity patterns which are shown in Fig. (**10**) do not suggest that the velocity distribution is uniform in the blade passage across the impeller width. Non uniformities are mainly present in the region of the leading edge and these are minimized in the outlet of the impeller. The unevenness velocity distribution in the entrance of the blade passage is due to the different wall shape of the hub and shroud as well as to inability of the fluid to adjust its path in the imposed entrance geometry. The fluid elements in the inside of the turn have

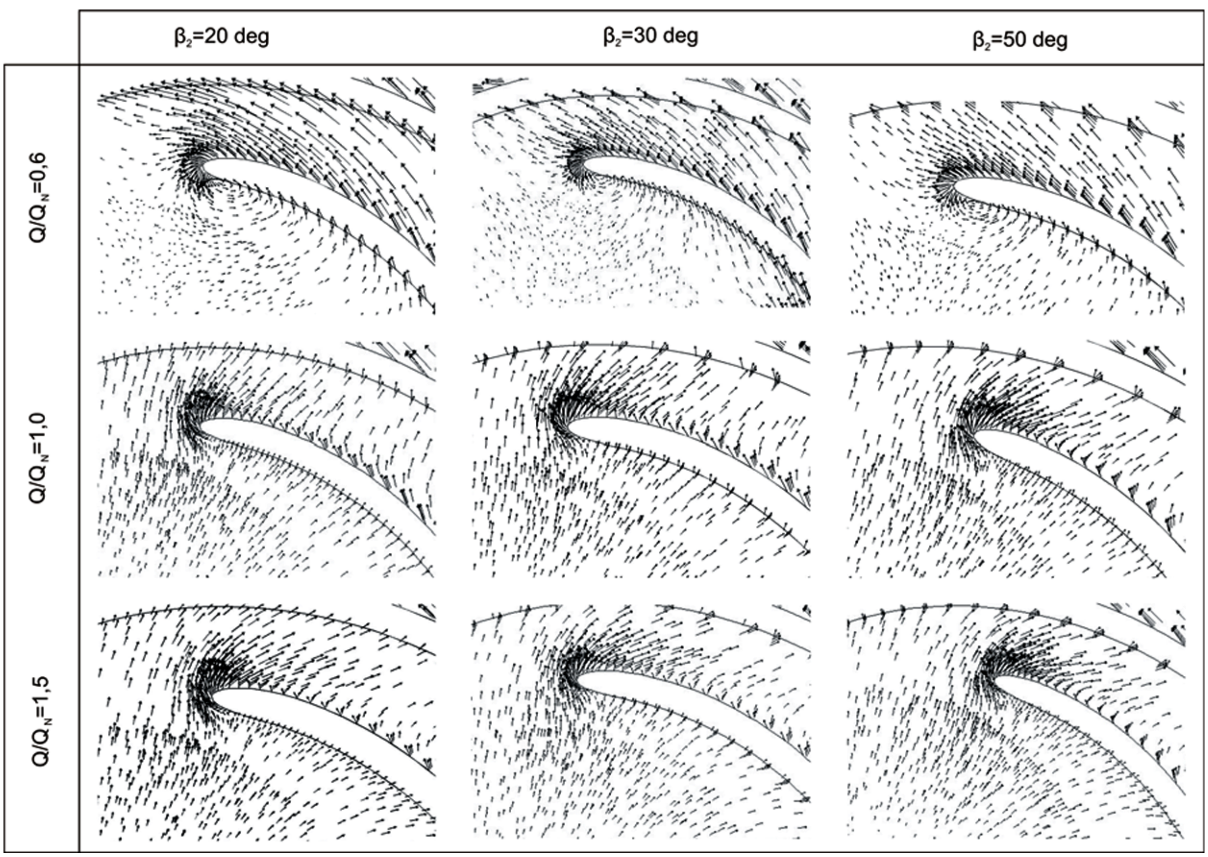

Fig. (10). Captures of the absolute velocity patterns in the region of leading edge at the middle span plane for the three studied impellers in design and off-design operation.

smaller velocities than those in the outside of curvature. These non uniformities in the velocity distribution are amplified when the pump operates off-design and especially when Q is less than Q_N where moreover the aforementioned inlet recirculation establishes.

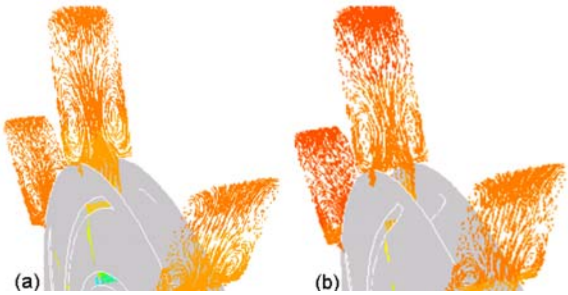

Fig. (11). Secondary flow patterns at nominal flow in three planes along the volute that suits the β_2=20 deg (a) and β_2=50 deg (b) impellers.

Published research work [14] supports the presence of secondary flow along the duct of the volute, which detected for all impellers and all volume flow rates. Fig. (**11**) shows a capture of the flow in the volute of the pump that operates in nominal flow rate and equipped with two of the studied impellers. As the fluid approaches the discharge, eddies are maintained with small changes of their size and core position.

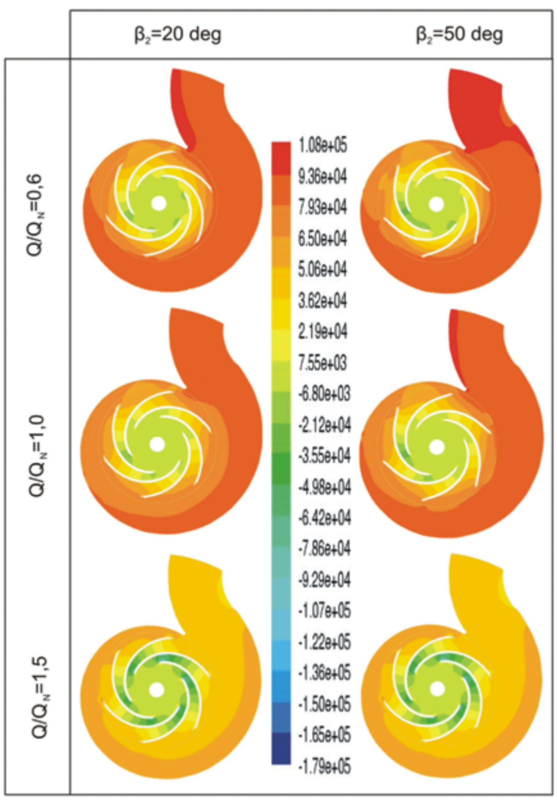

Fig. (12). The relative static pressure (atm) contours inside the laboratory pump.

The static pressure variation within the pump, for three flow rates and for two different outlet blade angles, is shown in Fig. (**12**). The pressure forces seem to be the main driven mechanism to establish the flow features both in the impeller and spiral volute. Fig. (**13**) shows the computed pressure distributions around the impeller periphery for the three examined impellers in four volume flow rates. Both figures confirm the non uniform pressure contours at the outlet of the impellers which are consistent with the global characteristics of the impellers and their performance.

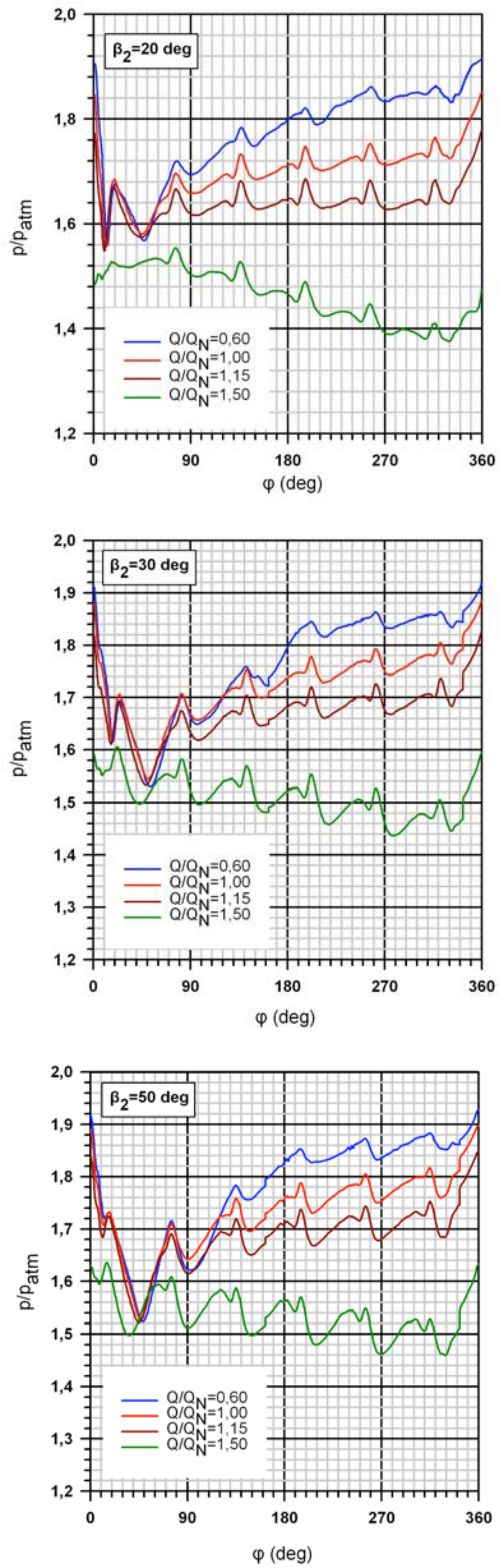

Fig. (13). Pressure distributions at the periphery of the studied impellers in four different flow rates.

For flow rates lower than nominal, the pressure reaches its lowest value directly in front of the tongue and starts to increase around the periphery of the impeller, taking its maximum value just behind the tongue. When the flow rate approaches the nominal, the pressure distribution is smoothed achieving the most uniform contour in nominal volume flow rate. At higher flow rates, the pressure decreases gradually from its maximum value in front of the tongue to a minimum value just behind the tongue. The aforementioned verify remarkable influence of the tongue in the pressure field inside the pump.

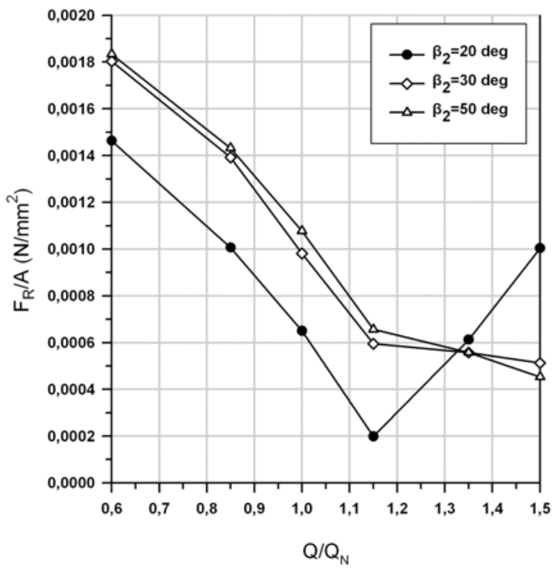

Fig. (14). Computed radial forces in the examined impellers in design and off-design operation.

The non uniform static pressure field around the impeller results in a radial force which is calculated by the integration of the pressure force distribution. For the studied impellers operating in nominal volume flow rate and away from it, the computed radial forces (F_R) divided by the impeller shroud area (A) are shown in Fig. (**14**).

For the β_2=20deg impeller with its standard volute casing, a “V” shape diagram of the radial force is obtained. For volume flow rates close to the nominal, a more uniform pressure distribution exists which implies less radial forces. On the other hand, far from the design operation the non uniformity is quite profound which results in larger forces. The minimum radial forces for that case were calculated near the best efficiency point as expected. The same trend is observed for the other two impellers with outlet blade angle β_2=30 and 50 deg. It is remarkable the shift of the minimum radial force to higher flow rates. The shift from the nominal point has been reported by researchers in literature and it has been confirmed with experiments [13]. It is explained by the fact that the pressure distribution Fig. (**13**) becomes more uniform as the exit angle of the blade increases in high flow rates. However, the simplifications of the computational pump geometry in comparison with the real one (no sided rooms for leakage flow) and the steady state approach should be taken into consideration because they affect the position of the minimum force. When $Q \approx 1{,}5\ Q_N$ the pressures around the β_2=30 and 50 deg impellers are varied almost around a mean value, which is not observed for β_2=20 deg impeller. For blade angles above 30 deg and flow rates higher than 1,5 the radial force increases, displaying the characteristic “V” shape.

CONCLUDING REMARKS

A laboratory pump that can suit radial impellers with the same diameter has been designed. Initially, three shrouded impellers with outlet blade angle 20 deg, 30 deg and 50 deg respectively were designed and with the aid of computational flow dynamics, the flow patterns through the pump as well as its performance for flow rates in design and off-design operation are predicted. On the assumption of the one dimensional flow theory, the pump was designed to operate at nominal characteristics Q=45 m^3/h and H=10 m, when the rotational speed is 925 rpm.

The CFD predicted value of the head at the nominal flow rate is approximately H=9 m. There is a shift of the numerical nominal flow rate towards greater values and a discrepancy of 10% between the theoretical head and the predicted numerical head. One reason for this shift is due to the fact that Pfleiderer design method does not take care of the complicated three dimensional flow structures and empirical formulas are applied for the account of hydraulic losses. Consequently, the increase of the nominal flow rate causes a reduction in the total head of the pump. So the discrepancy between theoretical and numerical values can be explained.

The numerical simulations seem to predict reasonably the total performance and the global characteristics of the laboratory pump. The influence of the outlet blade angle on the performance is verified with the CFD simulation. As the outlet blade angle increases the performance curve becomes smoother and flatter for the whole range of the flow rates. When pump operates at nominal capacity, the gain in the head is more than 6% when the outlet blade angle increases from 20 deg to 50 deg. However, the above increment of the head is recompensed with 4,5% decrease of the hydraulic efficiency. When the pump operates off-design, the percentage raise of the head curve, due to the increment of the outlet blade angle, is larger for high flow rates and becomes smaller for flow rates $Q/Q_N<0{,}65$. Moreover, at high flow rates, the increase of the outlet blade angle causes a significant improvement of the hydraulic efficiency.

Further research work is planned to complete this study through the validation of the CFD predictions with experimental data and simultaneously to investigate other crucial design parameters for the laboratory pump performance.

REFERENCES

[1] D. Eckardt, “Detailed flow investigations within a high-speed centrifugal compressor impeller”, *ASME Journal of Fluids Engineering*, vol. 98, pp. 390-402, 1976.

[2] M. W Johnson, and J. Moore, “The development of wake flow in a centrifugal impeller”, *ASME Journal of Engineering for Power*, vol. 102, pp. 382-390, 1980.

[3] A. Kjork, and L. Lofdahl, “Hot-wire measurement inside a centrifugal impeller”, *ASME Journal of Fluids Engineering*, vol. 111, pp. 363-368, 1989.

[4] J.D. Denton, “The calculation of three-dimensional viscous flow through multistage turbomachinery”, *ASME Journal of Turbomachinery*, vol. 114, pp. 18-26, 1992.

[5] M.W. Dawes, “Toward improved through flow capability: the use of three-dimensional viscous flow solvers in a multistage environment”, *ASME Journal of Turbomachinery* 114, pp. 8-17, 1992.

[6] M.V. Casey, P. Dalbert, and P. Roth, “The use of 3D viscous flow calculations in the design and analysis of centrifugal compressors”, *ASME Journal of Turbomachinery*, vol. 114, pp. 27-37, 1992.

[7] P. Bansod, and C.M. Rhie, “Computation of flow through a centrifugal impeller with tip leakage”, *AIAA Paper* No 90-2021, 1990.

[8] H. Krain, and W. Hoffman, “Verification of an impeller by laser measurement and 3D viscous flow calculations”, *ASME Paper* 89-GT-150, 1989.

[9] T.Z. Farge, and M.W. Johnson, “The effect of backswept blading on the flow in a centrifugal compressor impeller”, *ASME Paper* 90-GT-231, 1990.

[10] M.J. Zhang, C.G. Gu, and Y.M. Miao, “Numerical study of the internal flow field of a centrifugal impeller”, *ASME Paper* 94-GT-357, 1994.

[11] K. Hillewaert and R.A. Van den Braembussche, “Numerical simulation of impeller-volute interaction in centrifugal compressors”, *ASME Journal of Turbomachinery*, vol. 121, pp. 603-609, 1999.

[12] J. Gonzalez, J. Fernandez, E. Blanco, and C. Santolaria, “Numerical simulation of the dynamic effects due to impeller-volute interaction in a centrifugal pump”, *ASME Journal of Fluids Engineering*, vol. 124, pp. 348-355, 2002.

[13] J. Gonzalez, J. Parrondo, C. Santolaria, and E. Blanco, “Steady and unsteady forces for a centrifugal pump with impeller to tongue pump variation”, *ASME Journal of Fluids Engineering*, vol. 128, pp. 454-462, 2006.

[14] J. Gonzalez, and C. Santolaria, “Unsteady flow structure and global variables in a centrifugal pump”, *ASME Journal of Fluids Engineering*, vol. 128, pp. 937-946, 2006.

[15] R. K. Byskov, C. B. Jacobsen, and N. Pedersen, “Flow in a centrifugal pump impeller at design and off-design conditions-Part II: Large Eddy Simulations”, *ASME Journal of Fluids Engineering*, vol. 125, pp. 73-83, 2003.

[16] T. Meakhail and S.O. Park, “A study of impeller-diffuser-volute interaction in a centrifugal fan”, *ASME Journal of Turbomachinery*, vol. 127, pp. 84-90, 2005.

[17] K. Majidi, “Numerical study of unsteady flow in a centrifugal pump”, *ASME Journal of Turbomachinery*, vol. 127, pp. 363-371, 2005.

[18] J. Feng, F.K. Benra and H.J. Dohmen, “Numerical investigation on pressure fluctuations for different configurations of vaned diffuser pumps”, *International Journal of Rotating Machinery*, vol. 2007, 2007.

[19] B. Lakshminarayana, “An assessment of computational fluid dynamic techniques in the analysis and design of turbomachinery”, *ASME Journal of Fluids Engineering*, vol. 113, pp. 315-352, 1991.

[20] W. Rodi, S. Majumdar, and B. Schonung, “Finite volume methods for two-dimensional incompressible flows with complex boundaries”, *Computer Methods in Applied Mechanics and Engineering*, vol. 75, pp. 369-392, 1989.

[21] S. Thakur, J. Wright, W. Shyy, J. Liu, H. Ouyang, and T. Vu, “Development of pressure-based composite multigrid methods for complex fluid flows”, *Program in Aerospace Science*, vol. 32, pp. 313-375, 1996.

[22] G. Kergourlay, M. Younsi, F. Bakir and R. Rey, “Influence of splitter blades on the flow field of a centrifugal pump: Test-analysis comparison”, *International Journal of Rotating Machinery*, vol. 2007, 2007.

[23] J. Anagnostopoulos, “CFD Analysis and design effects in a radial pump impeller”, *WSEAS Transactions on Fluid Mechanics*, vol. 1 (7), pp. 763-770, 2006.

[24] Fluent Inc., http://www.fluent.com/.

[25] J. Sun, and H. Tsukamoto, “Off-design performance prediction for diffuser pumps”, *Journal of Power and Energy, Proceedings of I. Mech. E.*, Part A, vol. 215, pp. 191–201, 2001.

[26] C. Pfleiderer, *Die Kreiselpumpen für Flüssigkeiten und Gase*. Springer-Verlag, Berlin, 1961.

[27] Gambit: Computational Fluid Dynamics (CFD) Preprocessor, http://www.fluent.com/software/gambit

[28] D. Japikse, W.D. Marscher and R.B. Furst, *Centrifugal Pump Design and Performance*. Concepts ETI, Inc., Vermont, USA, 1997.

Study on Automatic Spray of Distribution Boom System of Truck-Mounted Concrete Pump

Tapas Kumar Panda, *Department of Mechanical Engineering, Aryan Institute of Engineering & Technology, Bhubaneswar, tapaspanda123@gmail.com*

Binoda Bihari Sahoo, *Department of Civil Engineering, NM Institute of Engineering & Technology, Bhubaneswar, bionod_bihari231@yahoo.co.in*

Niranjan Behera, *Department of Mechanical Engineering, Raajdhani Engineering College, Bhubaneswar, niranjanbehera2514@gmail.com*

Abstract: Truck-mounted concrete pumps have been adopted in many construction projects. However, the investigations about the automatization or robotization of distribution boom system of the truck-mounted concrete pump are very scattered. In this study, a scheme of automatic concrete spray of the distribution boom system of the truck-mounted concrete pump has been presented and discussed. The concrete spray process and the kinematics of the boom sections were analyzed including its inverse kinematics problem. Transient dynamic analysis was performed to validate the effect of the new control system on the boom system base on the flexible body co-simulation among ANSYS software, ADAMS software and Matlab/Simulink software. A three-dimensional simulation was programmed to imitate the process of automatic spray and verify the control algorithm. The simulation result shows that the system can pour concrete on a long narrow area automatically thereby satisfying, and the trajectory movement of boom mechanism.

Keywords: Concrete pump, boom system, automatic spray, co-simulation.

INTRODUCTION

The pumping of concrete is universally accepted as one of the main methods of concrete distribution and placement in the field of construction. As a favorable placing option, it provides advantages over other methods such as crane and skip, hoists and conveyors for building constructions. Therefore, the use of concrete pumps is increasing throughout the world, along with the pumping technologies, that are also becoming more reliable. In order to improve working efficiency of concrete pumping, much attention has been given to the automatization or robotization of the distribution boom system of Truck-mounted concrete pumps [1-7].

In many cases, pumping concrete automatically instead of manual operation will lessen the operator's labor intensity and dramatically increase the productivity (Fig. **1**). However, for a satisfactory implementation of automatic concrete distribution there are many problems needed to be solved. For example, although a robotization to the distribution boom system of concrete pump is not difficult in principle, it is not easy to eliminate the vibration problem during automatic concrete distribution in practice [8, 9]. To solve this problem, it needs to systemically consider the trajectory planning of prescribed assignments, multi-body dynamics,

Fig. (1). Pumping concrete for residential projects.

vibration of the boom system, dynamic control of kinematics and kinetics, etc. during the process of automatic concrete distribution.

Therefore, in this study, an automatic spray system of pumping concrete was schemed. We used finite element method, dynamics method, control method as well as their co-simulations by ANSYS software, ADAMS software and Matlab software to validate the effect of the whole system on the automatic spraying of the distribution boom pump. The results might provide useful references for design and development of the distribution boom system of Truck-mounted Concrete Pump.

ANALYSES ON THE AUTOMATIC SPRAY SYSTEM

Normally, the pump operator controls the entire machine *via* a radio remote control unit. This includes not only the movements of all sections (boom arms) of the multi-section boom, but also to the volume of concrete to be poured. Moreover, the control of operation sequence is submitted to guarantee that the movement of every section of boom and the location of distributed concrete are as smooth as possible [7].

Traditionally, the boom control is accomplished by using a single joystick. In this case, a pump operator controls each individual boom hydraulic cylinder and the slewing gear, preferably directly proportional, in order to secure a precise positioning of the end hose, on the construction site [7]. This means the operator has to shift at least five joysticks in turn.

However, to control the boom-end hose move along a long narrow field under the operator manipulation is not an easy task. It is almost impossible for an operator to control accurately and smoothly the hose end through a long linear narrow field. Therefore, a strong man is needed to arrange and regulate the end hose position, since the end hose is made of synthetic rubber that can be bent.

The automatic spray system was developed to simplify the spray operation in this study. The spray operation process is that in which the operator moves the end hose from one end of a wall (a prescribed trajectory) to another end, i.e. from Point 1 to Point 2 (shown in Fig. (**2**)), and lets the control system record the boom sections' postures (relative rotational angles of every boom section). Based on the two ends of the wall, the control systems draw out a straight-line equation, i.e. the trajectory of the end hose. Then the straight-line is divided into a number of sections and correspondingly, the posture of the boom is solved using Jacobian pseudoinverse algorithm. Finally, the boom mechanism, driven by a hydraulic system, can pour the wall automatically according to the solved postures one by one from the 2nd point to the 1st point. During spraying operation of the concrete, the operator has to adjust the boom movement step and concrete flow velocity if necessary.

About redundant robotic manipulators, different techniques and criteria have been used to resolve the redundancy, while optimizing certain objectives. Methods used to resolve the redundancy of the manipulators include Jacobian pseudoinverse algorithm [10, 11], singular value decomposition [12, 13], damped least-squares method [14, 15], joint torque optimization [16], minimal base reaction [17], neural network [18, 19], and genetic algorithm [20], *et al*. The singular value decomposition has played an important part in solving inverse kinematic problem of redundant robot manipulators [12, 13]. The damped least-squares method, which is based on the singular value decomposition, is an efficient method for eliminating numerical problems at the singularities [14, 15]. In this paper, we assume that the motion posture planning of the boom mechanism during concrete pouring process is defined within singularity avoidance, therefore, the conventional method, Jacobian pseudoinverse algorithm, is used to resolve the redundancy of the boom mechanism, since it is simple and effective.

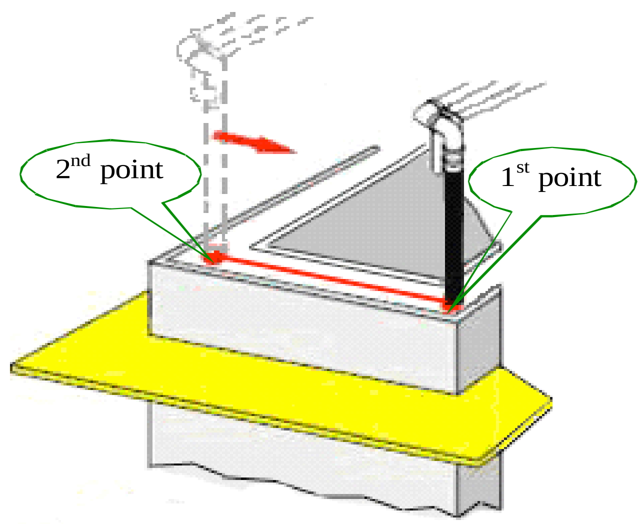

Fig. (2). Route of the end hose.

KINEMATIC RESOLUTION OF THE REDUN-DANT BOOM SYSTEM

A manipulator is said to be redundant when the dimension of the task space *m* is less than the dimension of the joint space *n*. In case of a redundant manipulator, $r = n\text{-}m$ ($r \geq 1$) is the degree of redundancy [9, 10].

The concrete boom system can be considered as a redundant manipulator, as shown in Fig. (**3**). It includes four sections, four hydraulic cylinders and one turntable. All the sections are considered as rigid bodies. In practice, there are small flexural displacements in all the sections, during spraying process of concrete. These displacements can be compensated by the control system.

For the multiple-arm boom system of a truck-mounted concrete pump, the end hose position is a function of joint variables of boom sections. The kinematic function is defined as:

$$X = f(\theta) \tag{1}$$

where X is the $m \times 1 (m = 3)$ position vector of the end hose, and θ is the $n \times 1 (n = 5)$ joint angle vector. $n > m$, in the case of redundant manipulator.

The differential kinematic function is given by

$$\dot{X} = J\dot{\theta} \tag{2}$$

where $\dot{X}$ is the 3×1 velocity vector of the end hose, $\dot{\theta}$ is the 5×1 joint velocity vector, and J is the 5×3 Jacobian matrix.

Now, the desired trajectory in workspace is given as $X(t)$ and we need to find the joint angle trajectory $\theta(t)$, corresponding to $X(t)$. We can obtain $\theta(t)$ by solving the following inverse kinematics equation:

$$\dot{\theta} = J^{+}\dot{X} + (I - J^{+}J)\phi \quad (3)$$

where J^{+} is a pseudoinverse matrix, and ϕ is a vector of arbitrary joint velocities projected in the null space of J. We can resolve the redundancy by specifying ϕ, so as to satisfy an additional constraint.

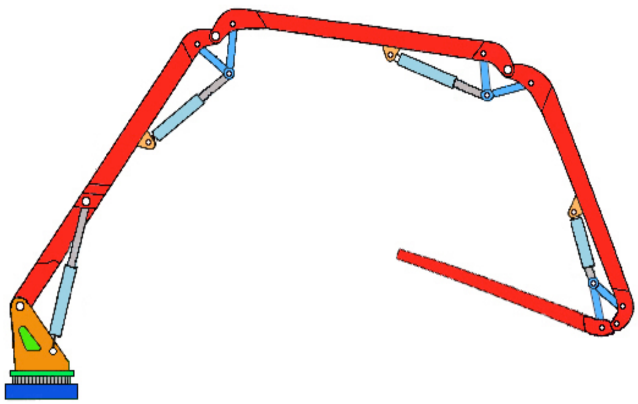

Fig. (3). A four-section boom system.

For a line trajectory to be poured, the end hose positions are definite beforehand. That is to say, a series of trajectory coordinate X is known, the trajectory coordinate X been corresponding to the joint angle θ, and the joint angle θ can be solved by Equation (3). We utilize MATLAB software to calculate the joint angle θ and the boom trajectory, is shown in Fig. (**4**). In this study, the motion posture planning of the boom mechanism during concrete pouring process is defined, within singularity avoidance.

We saved five joint angles (θ) with respect to every step (X) a data file, which will be used in the next phase. In ADAMS, these joint angles are imported and create five Splines (The Spline is a command of ADAMS and a two-order Spline is used in this study). These Splines are applied to five revolution MOTIONs to control the boom movement. As shown in Fig. (**5**), the end hose can move along the desired line.

We also produced five Splines by using Measure function on the joints (one rotational joint on the turn-table and four translational joints on the hydraulic cylinders). These Splines were exported into two columns data files and will be imported into Matlab for co-simulation.

DYNAMIC ANALYSIS USING ADAMS

In order to verify the influence of new automatic spray system on the boom, we performed a dynamic analysis using ADAMS and Simulink.

The co-simulation method used here is implemented by using ADAMS/Controls software for simulation of the mechanical system and MATLAB/Simulink for simulation of the hydraulics system. Generally, MATLAB/Simulink is also used to model the control concepts, which can drive the dynamic characteristics of a system based on sensor feedback, while ADAMS is used to model mechanical parts of the system, that are influenced by their geometric structure as well as external loads and forces imposed on them.

The mechanical parts of concrete boom system are shown in Fig. (**5**) and the hydraulic control system is shown in Fig. (**6**) [21-24].

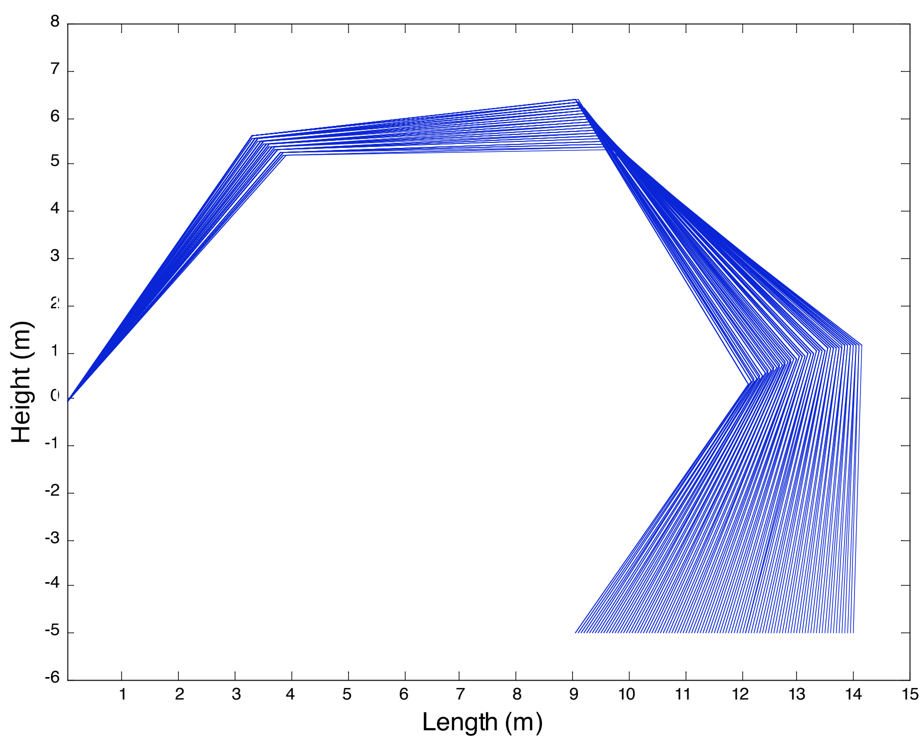

Fig. (4). The movement postures of the boom system for a straight-line trajectory.

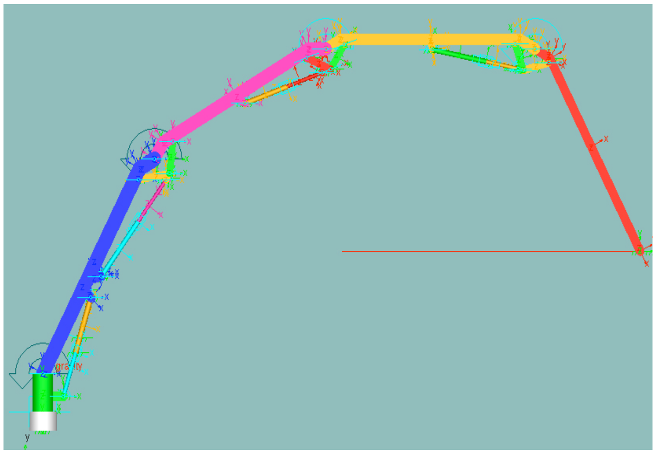

Fig. (5). Kinematics simulation in ADAMS.

In Fig. (**6**) there are four PistonRods and one Rotor. They were controlled by the five Spline data files.

One drawback of the ADAMS program is that all components are assumed to be rigid. In the ADAMS program, tools to model component flexibility, exist only for geometrically simple structures. To account for the flexibility of a geometrically complex component, ADAMS relies on the data transferred from finite-element programs such as ANSYS. The ANSYS-ADAMS Interface is a tool provided by ANSYS by which the data can be transferred from the ANSYS program to the ADAMS program [25-29].

To analyze the boom strength, we need to build flexible arms of the boom mechanism in ADAMS. Obviously, the boom arms do not belong to geometrically simple structures in a sense. It will produce wrong results if we use a box part to take the place of the boom arm. So, we have to create a flexible boom arm using ANSYS.

In ADAMS, flexible bodies are defined by importing the modal data, calculated by an external finite elements program. A special data file (MNF file) is used to transfer frequency and amplitude data for a selected number of vibration modes, from a finite element code to ADAMS program. Craig Bampton modes, which are required for defining constraint connections to flexible bodies, are transferred from the finite element code by defining master nodes. For each master node, constraint mode information is stored in the MNF file.

CREATING FLEXIBLE BODY

Since the first arm of the boom system is subjected to the biggest load, we created a flexible arm in ANSYS to substitute the first rigid arm for co-simulation in ADMAS. Because a flexible body analysis requires a high performance on the PC, we only used one flexible arm, the first arm, i.e. in this study.

Element Type

The element type will affect on the computation time and result accuracy. For the boom system, the structure is not very complicated so, we select two solid types, SOLID45 and SOLID92 in ANSYS program, for different regions of the first arm of the boom system.

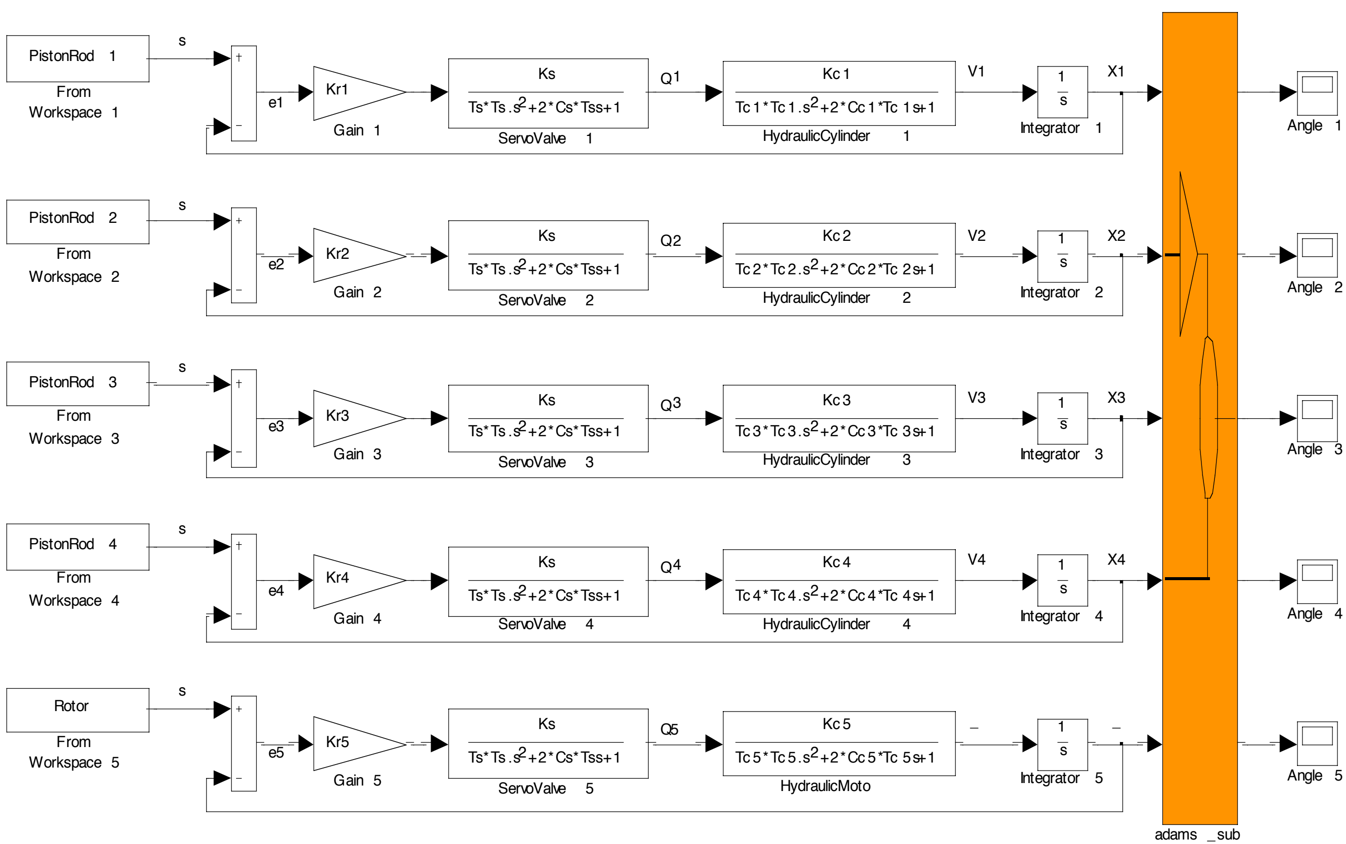

Fig. (6). The control scheme of Co-simulations in ADAMS and Matlab/Simulink.

Material Property

The boom of truck-mounted concrete pump is made of fine grained structural steel, which is a kind of high strength steel. Its material property is as follows, elastic modulus 2.1×10^{11}Pa, Poisson ratio 0.3, density 7.8×10^{3}kg/m^{3} and tensile strength 800MPa.

Master Node

The master node is the joint between the boom and other parts, such as hydraulic cylinders and the turntable. According to the constraints, loads and driving forces on the first arm, five master nodes are defined. These master nodes use MASS21 element with a tiny real constant and a huge elastic modulus.

Meshing

The first arm is divided into nine parts with workplane. The regular parts are meshed with SOLID45 element, while the others are meshed with SOLID92 element. This method reduces element number dramatically and certainly saves computation time. The meshed model of the first arm is shown in Fig. (**7**). The five pink areas are rigid coupled areas.

Finally, using ANSYS interface for ADAMS program, the first arm model is exported into a MNF file.

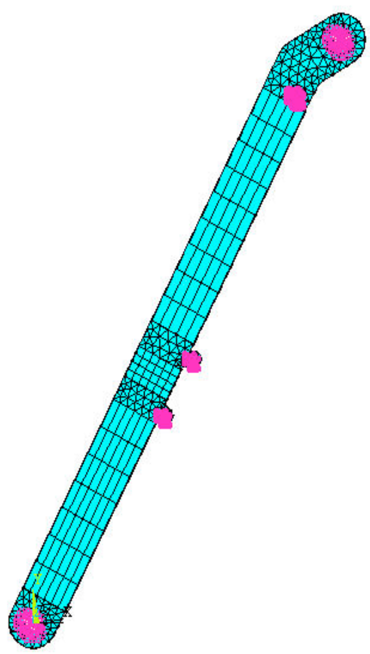

Fig. (7). Finite element model of the first arm of the boom system.

FLEXIBLE BODY SIMULATION

The flexible arm is created in ADAMS by the neutral file imported from ANSYS, to replace the first rigid arm. The boom movement is simulated again under the previous control SPLINE on the revolution MOTION, shown in Fig. (**8**). There is a slight fluctuation on the end hose trajectory since the first arm is replaced with a flexible body and it has an inevitable vibration.

In order to analyze accurately stress and strain on the first arm during automatically spraying concrete, a load step file (including the load applied on five master nodes in every time step) is exported from ADAMS. Then the data file will be imported into ANSYS, to perform a transient dynamic analysis to check the stress and strain on the first arm and will afford information to modify or optimize the structure of the boom arm.

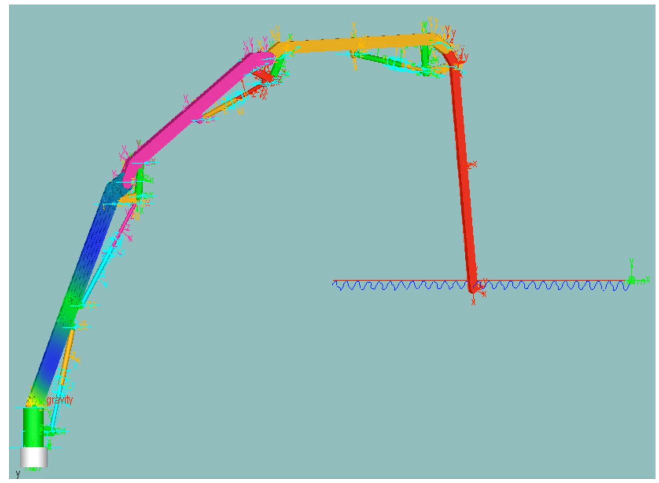

Fig. (8). Kinematics simulation of the boom system with the flexible arm (the first arm) in ADAMS.

TRANSIENT DYNAMIC ANALYSIS IN ANSYS

There are two methods to use the load file in ANSYS. One is to select the load on the arm in the most dangerous situation and then to perform a static analysis and obtain the stress and strain. Another is to carry on a transient dynamic analysis with the load changed in steps, and then to predict the time history of stress and strain. The former method is impractical because in a sense it is difficult to select the most dangerous situation. So in this paper, the latter method is applied to process the load step. In order to reduce the calculation, only the first fifty load steps are imported into ANSYS and the loads on five master nodes are applied to five rotational joints, respectively. After the transient dynamic analysis, we can view the results in ANSYS postprocessor. The relationship between stress and time-history is shown in Fig. (**9**) and equivalent stress on the second load step is shown in Fig. (**10**).

In the postprocessor of ANSYS, we find that the stress in the joint area is higher than that of other regions with respect to every load step. We select a node in the high stress area and track the stress time-history. The result is shown in Fig. (**9**). It shows that in the beginning, the stress increases rapidly and reaches the maximum at the second step, about 640MPa, and then gradually falls down and at the twentieth step the stress tends to be steady, about 350MPa. The first-order vibration frequency of the arm is 4.9Hz. The previous experiment studies [8, 30] reported that the vibration frequency is 4.69Hz.

According to the stress time-history, we load the equivalent stress on the first arm at the second step, one of the most dangerous situations, as shown in Fig. (**10**). From Fig. (**10**) we can find that the stress in most areas varies from 200MPa to 250MPa, except the joint area. The reference [30] also reported the similar stress value by experimental measurement. Considering that the arm model has no fillet,

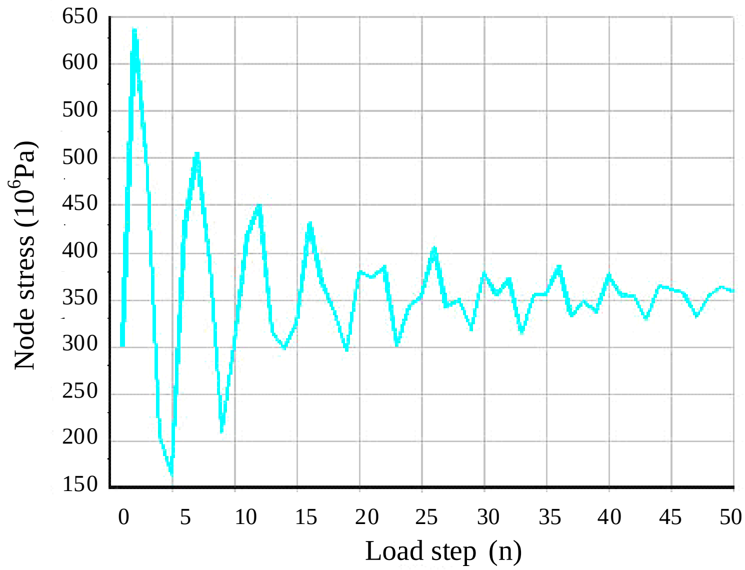

Fig. (9). The time-history curve of stress for a node on the flexible arm.

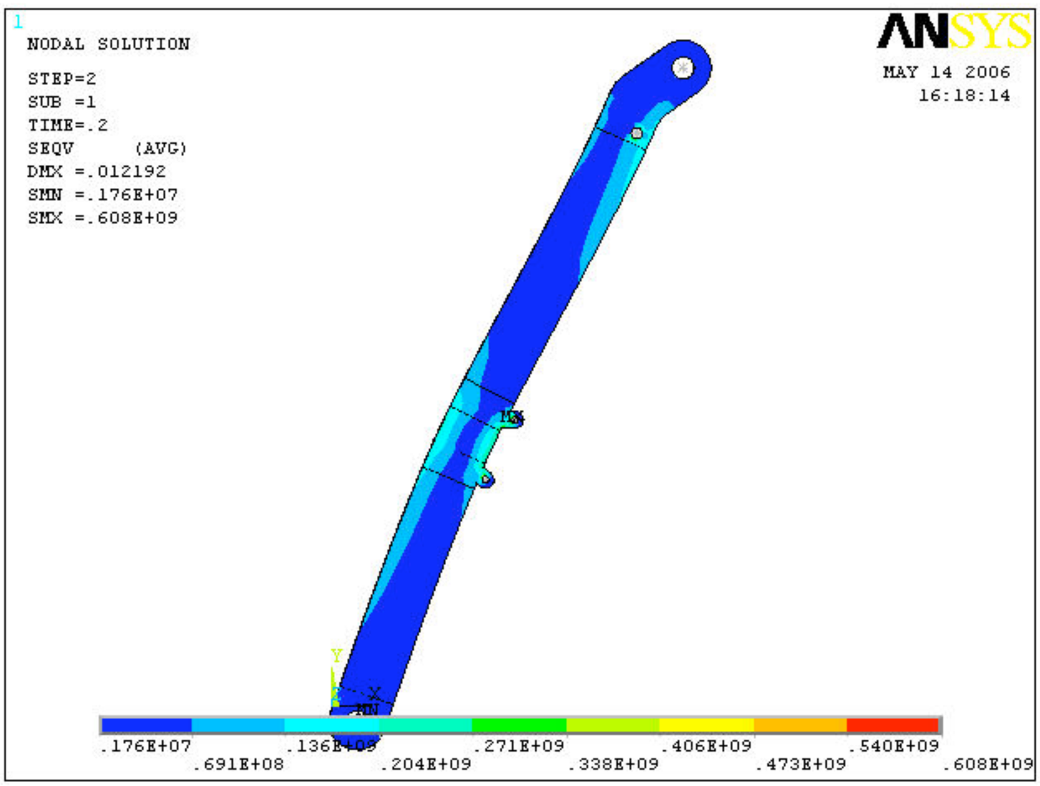

Fig. (10). The equivalent stress distribution of the first arm in ANSYS.

the number of simulation steps is less and in the beginning of loading, the arm motion acceleration is also high, so, the maximum stress at the joint region should be lower in the real arm. Therefore, the strength of the first boom arm is within a permissible range.

AUTOMATIC SPRAY SIMULATION

Virtual reality is a technology, which allows a user to interact with a model in a computer-simulated environment [31-36]. It is the result of the combination of human imagination and electronic technologies. It provides people a useful tool to study and examine a model or system before it is actually manufactured [37-39]. In order to verify the automatic spray system, we utilized virtual reality technology to simulate it in a three-dimensional environment. The simulation program was developed with Visual C++ and OpenGL. The model of a truck-mounted concrete pump and its distribution boom system was designed in 3DSMAX, and then was imported into the program [40-42]. The final model of the truck-mounted concrete pump and its boom system are shown in Fig. (**11**).

The object of this simulation is to imitate the work process of the concrete boom system. The default setting of this system is a linear spray. In the first step, we can move the end hose to a specified position through five scroll bars in the left control panel in Fig. (**12**) and press down the 'Record' button. Secondly, we can move the end hose to another end of the wall and record it. Now the control module has recorded two key points of the trajectory line. After we pressed the 'Pour' button, the whole system begins to pour concrete automatically along the trajectory line.

In Fig. (**12**), the red thin line is the predefined trajectory and the blue thick line is the actual trajectory. This

Fig. (11). Truck-mounted concrete pump and its boom system in virtual reality environment.

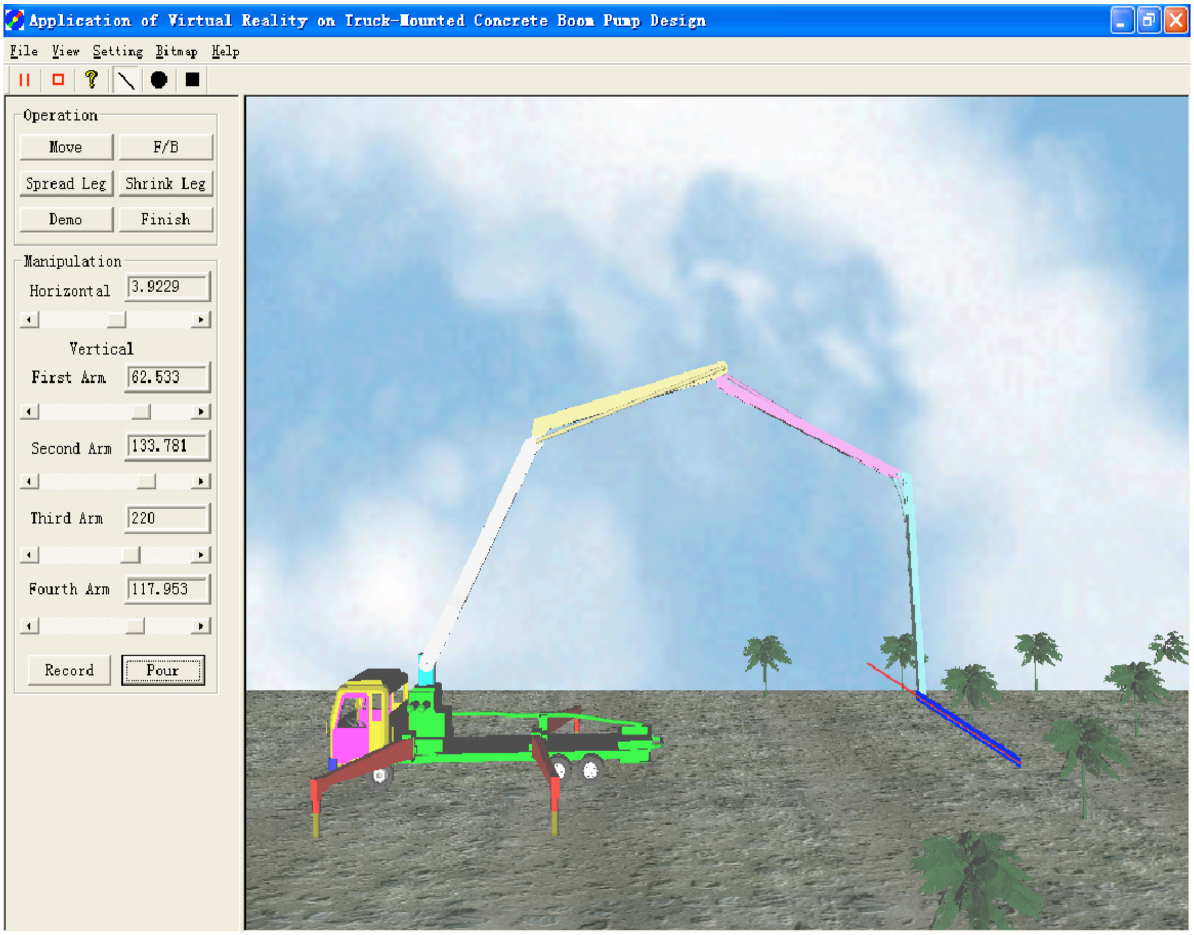

Fig. (12). Automatic spray system simulation in virtual reality environment.

simulation system can verify whether any interference occurs between boom sections and whether the boom movement is smooth. The simulation result shows that the system can pour concrete on a long narrow field automatically, and the boom movement is smooth.

CONCLUSIONS

The automatic spray system of the distribution boom system of the truck-mounted concrete pump has been studied and the kinematic redundancy is solved. A co-simulation method was used to check the dynamic response of concrete pouring process of the automatic spray system. Virtual reality technology was used to simulate the automatic spray process. Based on the dynamic loads obtained from above-mentioned analyses, the finite element method was used to analyze the structural strength of the boom system. These systemic numerical simulation methods will provide a strong assistance for the development of new concrete boom systems.

ACKNOWLEDGEMENTS

Thanks for the research grants from the Natural Science Foundation of Liaoning Province of China (20062027), the National High-Tech Research Program (2007AA04Z442), the National Basic Research Program (2007CB210305) and the Scientific Research Foundation of China Postdoctor (20070420203).

REFERENCES

[1] T.H. Cooke, *Concrete pumping and spraying: A Practical Guide.* Thomas Telford, 1990.

[2] S.W. Zhou, G.Z. Zhang and S.Q. Zhang, "Application of virtual reality on concrete pump car design", *Journal of Northeastern University (Natural Science)*, Vol. 24, pp. 464-466, Oct 2003.

[3] M. Skibniewski, P. Derrington and C. Hendrickson, "Design Impact of Robotic Construction Finishing Work", *CAD and Robotics in Architectural and Construction*, pp. 23-26, 1986.

[4] L.X. Guo, G.Z. Zhang and J.K. Li, "Approach to robotization of concrete boom truck for construction", *Machine Design and Manufacturing Engineering*, Vol. 29, pp.6-8, Mar 2000.

[5] L.X. Guo, M.Y. Zhao, G.Z. Zhang and Y. Huang, "Automtic pouring and simulation of boom system of concrete pump car", *Journal of Northeastern University Natural Science*, Vol. 21, pp. 617-619, Dec 2000.

[6] L.X. Guo and M.Y. Zhao, "A Parallel Search Genetic Algorithm Based on Multi-Peak Values and Multi-Rules", *Journal of Materials Processing Technology*, Vol. 129, pp. 539-544, July 2002.

[7] H.Benckert, "Mechydronic for boom control on truck mounted concrete pumps", *In Technical Symposium Construction Equipment Technology*, 2003, pp.1-12.

[8] L.X. Guo, G.H. Zhang and B.F. Wang, "Dynamic Analysis on Placing Boom System of Truck Concrete Pump", Proceeding of International Conference on Vibration Engineering, 1998, pp. 148-152.

[9] L.X. Guo, M.Y. Zhao, S.H. Chen, H.G. Wang, L.J. Fang and Z.G. Xu, "Automatic planning to trajectory of operating area of redundant robot", *Mechanical Science and Technology*, Vol. 21, pp. 182-184, Mar 2002.

[10] R.V. Patel and F. Shadpey, *Control of redundant robot manipulators*: *Theory and Experiments.* Springer, 2005.

[11] L. Sciavicco and B. Siciliano, *Modeling and control of robot manipulators.* McGraw-Hill, 1996.

[12] A.A. Maciejewski and C.A. Klein, "Singular value decomposition: Computation and applications to robotics", *International Journal of Robotics Research*, Vol. 8, pp. 63-79, Dec 1989.

[13] C. Stefano, "Singularity-robust task-priority redundancy resolution for real-time kinematic control of robot manipulators", *IEEE Transactions on Robotics and Automation*, Vol. 13, pp. 398-410, Jun 1997.

[14] Y. Nakamura and H. Hanafusa, "Inverse kinematic solutions with singularity robustness for robot manipulator control", *ASME Journal of Dynamic Systems, Measurement, and Control*, Vol. 108, pp. 163-171, Sep 1986.

[15] A.A. Maciejewski and C.A. Klein, "Numerical filtering for the operation of robotic manipulators through kinematically singular configurations", *Journal of Robotic Systems*, Vol. 5, pp. 527-552, 1988.

[16] J.M. Hollerbach, "Redundancy resolution of manipulators through torque optimization", *IEEE Journal of Robotics and Automation*, Vol. 3, pp. 308-316, 1987.

[17] H.P. Lee, "Motions with minimal base reactions for redundant manipulators", *Computers & Structures*, Vol. 61, pp. 651-656, Nov 1996.

[18] Y.M. Li and S.H. Leong, "Kinematics control of redundant manipulators using CMAC neural network", in The 5th World Multiconference on Systemics, Cybernetics and Informatics, pp. 274-279, 2001.

[19] S. Lee and R.M. Kil, "Redundant arm kinematic control with recurrent loop", *in Proceeding Neural Networks*, pp. 643-655, 1994.

[20] C. Nearchou, "Solving the inverse kinematics problem of redundant robots operating in complex environments *via* a modified genetic algorithm", *Mechanism and Machine Theory*, Vol. 33, pp. 273-292, 1998.

[21] MDI. *Basic ADAMS Full Simulation Training Guide*. Mechanical Dynamics Incorporated, 2002.

[22] MDI. *Basic ADAMS/Solver Training Guide*. Mechanical Dynamics Incorporated, 2002.

[23] MDI. *ADAMS/Controls Training*. Mechanical Dynamics Incorporated, 2002.

[24] M. Jelali and A. Kroll, *Hydraulic Servo-Systems*: *Modelling, Identification and Control*. Springer, 2003.

[25] ANSYS, Inc. Rigid Body Dynamics and the ANSYS-ADAMS Interface. ANSYS Advanced Analysis Techniques Guide ANSYS Release 10.0, 2005.

[26] U. Kiencke, R. Majiad and S. Kramer, "Modeling and performance analysis of a hybrid driver model", *Control Engineering Practice*, Vol. 7, pp. 985-991, Aug 1999.

[27] X.M. Zhang, C.J. Shao and A.G. Erdman, "Active vibration controller design and comparison study of flexible linkage mechanism systems", *Mechanism and Machine Theory*, Vol. 37, pp. 985-997, Sep 2002.

[28] S.Q. Yuan, Q.Y. Xu and L. Zhang, "Experiments on active vibration control of a flexible four-bar linkage mechanism", *ASME Journal of Vibration and Acoustics*, Vol. 122, pp. 82-85, Jan 2000.

[29] X.Y. Wang and K.M. James, "A FEM model for active vibration control of flexible linkages", In Proceedings of the 2004 IEEE International Conference on Robotics & Automation, 2004, pp. 4318-4323.

[30] L.X. Guo, "Studies on robotization of concrete pump car", PhD dissertation, Northeastern University, China, 1999.

[31] H.Z. Liu, *Virtual design*. Mechanical Industry Press, 1999, pp. 25-26.

[32] W. Ribarsky, J. Bolter, A. Op den Bosch and R. van Teylingen, "Visualization and analysis using virtual reality", *IEEE Computer Graphics and Applications*, Vol. 14, pp. 10-12, Jan 1994.

[33] S. Brown, "Real art and virtual reality", *Computer Graphics*, Vol. 31, pp. 36-39, Nov 1997.

[34] M. Dolinsky, "Creating art through virtual environments", *Computer Graphics*, Vol. 31, pp. 34-35, Nov 1997.

[35] S. Jayaram, H.I. Connacher and K.W. Lyons, "Virtual assembly using virtual reality techniques", *Computer-Aided Design*, Vol. 29, pp. 575-584, Aug 1997.

[36] J. Cook, R. Hubbold and M. Keates, "Virtual reality for large-scale industrial applications", *Future Generation Computer Systems*, Vol. 14, pp. 157-166, Aug 1998.

[37] J. Nomura and K. Sawada, "Virtual reality technology and its industrial applications", *Annual Reviews in Control*, Vol. 25, pp. 99-109, Oct 2001.

[38] S.A. Gomes and G. Zachmann, "Virtual reality as a tool for verification of assembly and maintenance processes", *Computers and Graphics*, Vol. 23, pp. 389-403, June 1999.

[39] A. Van Dam, D.H. Laidlaw and R.M. Simpson, "Experiments in Immersive Virtual Reality for Scientific Visualization", *Computers and Graphics*, Vol. 26, pp. 535-555, Aug 2002.

[40] B. Korves and M. Loftus, "Designing an immersive virtual reality interface for layout planning", *Journal of Materials Processing Technology*, Vol. 107, pp. 425-430, Nov 2000.

A Fast and Economical Method for Producing Self wipe Twin screw Extruder

Pradipta Kumar Das, *Department of Mechanical Engineering, Aryan Institute of Engineering & Technology, Bhubaneswar, pkdas751@gmail.com*
Hemant Ku Nayak, *Department of Mechanical Engineering, NM Institute of Engineering & Technology, Bhubaneswar, hemantnayak236@gmail.com*
Satyaprakash Mishra, *Department of Civil Engineering, Capital Engineering College, Bhubaneswar, satyaprakash_m25@gmail.com*

Abstract: After the extrusion process the remaining of polymers in the extruders cause some problems like degradation and impurity in process, therefore after each batch the extruder should be cleaned. Using self-wipe twin-screw extruder is a method, to solve this problem. Production of self-wipe screw modules is very difficult, time consuming and is not economical. In this research, we have presented a novel, quick and economical method for producing self-wipe modules with desirable profiles.

Keywords: Twin-screw extruder, self-wipe, intermeshing co-rotating screws.

INTRODUCTION

Twin-screw extrusion is extensively used for mixing, compounding, or reacting polymeric materials. Recently many researchers are trying to do some modification in polymers for specific purpose [1-3]. Reactive extrusion, reactive blending and polymer reinforcement are some of the new topics in research that are more dependent on twin-screw extruder type and configuration. The flexibility of twin-screw extrusion equipment allows this operation to be designed specifically for the formulation being processed. For a specific reaction, the residence time distribution in twin-screw extruder is less than the batch systems. Therefore, this accounts for a decrease of polymer degradation, giving better product than the batch systems. Good residence time distribution, good mixing and high capability of heat and mass transfer in twin-screw extruders led us to use this apparatus [3-6].

In twin-screw extruder, the screws may be co-rotating or counter-rotating, intermeshing or non-intermeshing, conjugated or non-conjugated. In addition, the configurations of the screws themselves may be varied by using forward conveying elements, reverse conveying elements, kneading blocks or other designs in order to achieve particular mixing characteristics [4, 7-9]. Construction features of the twin-screw extruders are shown in the Table **1**.

Screw geometry

The fundamental difference between single and twin-screw is the type of their flow pattern. The velocity profile in the twin-screw extruders is more complex than single screw extruders, thus the theoretical relations of these extruders are not improved like as single screw extruders. Fig. (**1**) shows the path of the particle in the single screw extruder, non-intermeshing counter-rotating twin-screw extruder and inter-meshing co-rotating twin-screw extruder [9-12].

(**a**) Particle path in the single screw extruder.

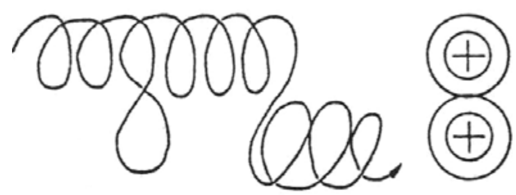

(b) Particle path in the non-intermeshing twin-screw extruder.

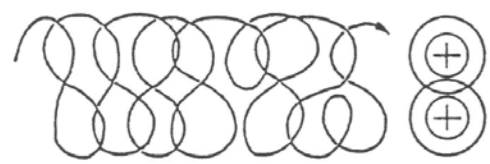

(**c**) Particle path in the intermeshing twin-screw extruder.

Fig. (1). Comparison of the Particle path between (**a**) single screw extruder, (**b**) non intermeshing counter-rotating twin-screw extruder and (**c**) inter-meshing co-rotating twin-screw extruder.

The screw geometry defined by its application of twin-screw extruders was designed in modular section form. Usually, the screws and the barrels have modular form, thus changing the arrangement of the screw modules on the main shaft make prove easy. Modular design of the screw facilitates the change in the screw configuration for proper application. Also fabricating the screws in modular form may save the time and expense [7, 12, 13].

In co-rotating twin-screw extruders, self wiping action is achieved by this procedure: one crest edge of the screw wipes the flanks of the other screw with a tangentially oriented, constant relative velocity. There is a higher relative velocity in this arrangement, and hence there is a sufficiently high shear velocity available to wipe the boundary layers, thus a more efficient and uniform self-cleaning action is achieved [11, 13-16]. Wiping action of twin-screw extruders is shown in Fig.

Table 1. Construction Features of Twin-screw Extruders

Screw intermeshing		System	Counterrotating	Corotating
Intermesh	Fully Intermesh	Length and crosswise closed		Impossible
		Lengthwise open, crosswise closed	Impossible	Screw 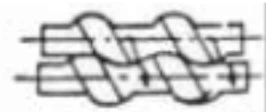
		Length and crosswise open	Impossible but useless	Disks 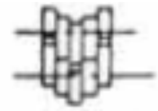
	Partially Intermesh	Lengthwise open, crosswise closed	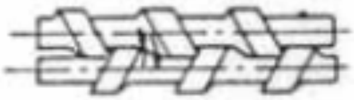	Impossible
		Length and crosswise open		
				
Non Intermesh		Length and crosswise open	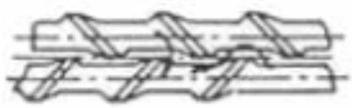	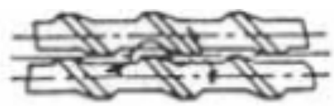

(**2**). Fabrication of counter rotating self-wipe screw is not feasible.

EXPERIMENTAL

Fabrications of Self-Wipe Screws

Some of the screws pattern quite similar to the self-wipe pattern can be prepared with special screw production machines. The type and size of these screws is limited by the producing machine because the pattern of the self-wipe screw is a unique pattern and these machines can produce only some screws with pitches that are not self-wipe [8, 11]. We have prepared some of these screws with the mentioned machine (Fig. **3**). These screws are fully intermesh but not self-wipe.

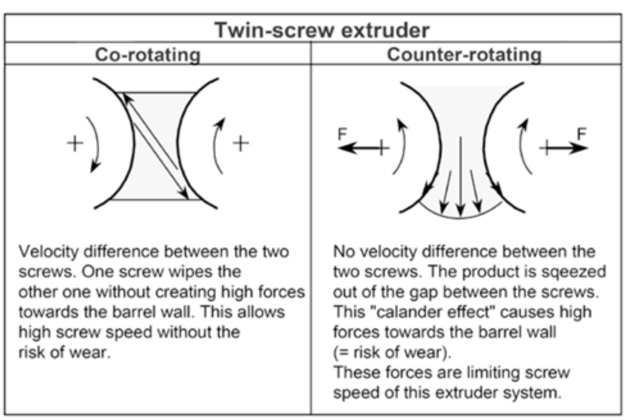

Fig. (2). Wiping action in twin-screw extruders [11].

Creating a special profile on the flank of screws that when they arranged in twin form will be fully intermesh and one crest edge of the screw wipes the flanks of the other screw and vice versa, is the most important point that should be considered in the fabrication of the self-wipe screws [12, 15]. It can be done only by creating a sinusoidal profile on the flank of the screws as shown in Fig. (**4**), [14].

Fig. (3). The sample of screws was prepared with special screw production machine.

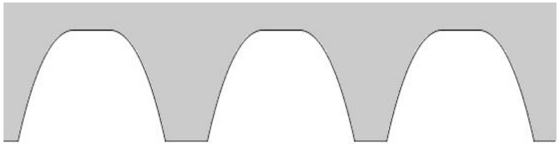

Fig. (4). Sinusoidal profile on the flank of the screw for fabrication of self-wipe screws (screw pitch 20 mm).

The main problem in the fabrication of these screws is that the creating of this profile on the flank of the screw by manual lathe machines or CNC lathe machines is not possible. The lathe machines can create sectors with certain R on the flank of the screws [13, 16]. Typical twin screws produced by lathe machine are shown in Fig. (**5**). The flank of these screws is formed of several R.

Fig. (5). Screws prepared by lathe machine by using of mould.

For flank profile modification, at first we prepared an iron mould with sinusoidal profile by CNC wire cut machine. The prepared mould is shown in Fig. (**6**). Then by using this mould, we controlled the screw flank profile during the lathing action. By successive controls and doing some modification in the screw at the end, we prepared a screw with a profile close to the self-wipe profile. This screw is not self-wipe but very similar to the self-wipe screw.

Fig. (6). The prepared mould by CNC wire cut machine for controlling of the screw flank profile.

Above methods are very difficult, expensive and time consuming. We have presented a novel, quick and Economical method for producing self-wipe modules with desirable profiles. In this method, we prepare the self-wipe screws by using of a common lathe machine with aid of a special cutting tool. At first we prepared a cutting tool from HSS (Fig. **7a**), and then created the sinusoidal profile as Fig. (**4**) by CNC wire cut machine on HSS cutting tool (Fig. **7b**). For preventing of body cutting tool interlock with shaft during the lathing, the lateral section of the cutting tool head was removed (Fig. **7c**). As regards the

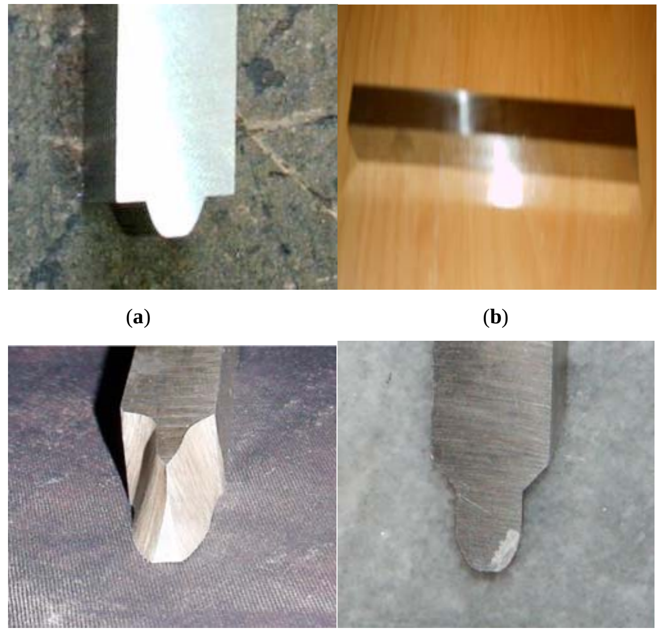

(**a**) (**b**)

(**c**) (**d**)

Fig. (7). (**a**) HSS Cutting tool lathe for creating the sinusoidal profile of screw. (**b**) The sinusoidal profile created on the cutting tool lathe by CNC wire cut machine. (**c**) The Cutting tool lathe shaped when lateral section of it is removed. (**d**) The back view of the cutting tool lathe when its additional part is removed.

head of this cutting tool lathe, for preparation of a screw, the head of the cutting tool should pass in a helical way on shaft. When the cutting tool is passed on this path, the back of cutting tool head interlocks with the flank of the screw. This problem should be solved with respect to the angle and direction of shaft torsion. In this research, the angle is 17.5° and screw is right handed. For solving this problem, we removed the left side section of the head of cutting tool lathe, that interlocked with the flank of the screw, by 17.5° angle with respect to the head section (Fig. **7d**). The prepared screws with this method are fully intermeshed and self-wipe. One sample of these screws is shown in Fig. (**8**). The needed time for preparing of one meter of these modules are about five hours. The modules arranged and fixed on the main shaft to make the screw shaft.

RESULT AND DISCUSSION

Fabrication of self-wipe modules by using of common and CNC lathe machine is not possible [8, 11]. The prepared screw by these machines may be improved with burnishing to make them similar to the self-wipe profile, but they can not act as self-wipe modules. This work is very time consuming and expensive with low accuracy. By preparing of cutting tool lathe with the mentioned method in this paper, fabricating of self-wipe screw modules with high accuracy and very low expense is facilitated. Also by applying of this method, fabricating of suitable self-wipe modules by using of a common lathe machine is feasible. The most important advantages of this method is high accuracy, low expense, simplicity and rapidity of the method. The maximum wiping efficiency of the modules prepared with conventional method is about 70% of prepared self-wipe modules with this new method. The time is

Fig. (8). The final modules of the self-wipe screw prepared with Lathe machine by using special cutting tool shape.

needed for preparing of self-wipe modules with this new method is about 10% of the conventional method.

REFERENCES

[1] J.A. Colbert, *The Extrusion, Measurement and Control of Medical Tubing*, Davis Standard Ltd, Luton, UK, March 1996.

[2] R.J. Castillo, How Do You Extrude 10 Layer Film Sheeting on a 5 Layer Die, Polymers, Laminations & Coatings Conference, San Diego, CA, 2001, pp. 115.

[3] J. Dooley, Viscoelastic Flow Effects in Multilayer Polymer Coextrusion, Ph.D. Thesis, Eindhoven University of technology, Eindhoven, ON, Netherlands, 2002.

[4] D.G. Baird, D.I. Collias, *Polymer processing principles and design*, Butterworth-Heinemann Press, USA, 1995.

[5] S.C. Garge, M.D. Wetzel and B.A. Ogunnaike, "Quantification of the melting process in a co-rotating twin-screw extruder: A hybrid modeling approach", *Polymer Engineering & Science*, Vol. 47(7), pp. 1040-1051, May 2007.

[6] Y. Wang, "Compounding in Co-rotating Twin-screw Extruders", Rapra Review Report, Vol. 10, No. 8, Report 116, 2000.

[7] J.L. White, *Twin-screw Extrusion*, Hanser/Gurdner Publications, New York, 1991.

[8] W. Szydlowski, K. Min, M.H. Kim and J.L. White, "Technology and Analysis of Flow", *Advances in Polymer Technology*, Vol. 7, pp. 177, 1987.

[9] Y. Wang and J.L. White, "Non-Newtonian Flow Modelling in the Screw Regions of an Intermeshing Corotating Twin-screw Extruder", *Journal of Non-Newtonian Fluid Mechanics*, Vol. 32, pp. 19, 1989.

[10] A. Kiani, J.E. Curry and P.G. Anderson, "Flow analysis of twin-screw extruders pressure and drag capability of various twin-screw elements", *SPE ANTEC Technical Papers*, Vol. 44, pp. 48-54, April 1998.

[11] Y. Xie, D. Bigio, P. Andersen and J. Cheng, *Imaging and Image Analysis Applications For Plastics, Behnam Pourdeyhimi*, Society of Plastics Engineers press, Chap 5, 1999.

[12] A. Rom-Rogineski and C.J.B. Dobbin, "A comparative study of the use of high intensity dispersive mixers and co-rotating twin-screw extruders in the manufacture of high quality color concentrates", *SPE ANTEC Technical Papers*, Vol. 44, pp. 189-198, April 1998.

[13] T. Ishikawa, S. Kihara and K. Funatsu, "3-D non-isothermal flow field analysis and mixing performance evaluation of kneading blocks in a co-rotating twin-screw extruder", *Polymer Engineering Science*, Vol. 41, pp. 189-849, 2001.

[14] V.L. Bravo, A.N. Hrymak and J.D Wright, "Numerical simulation of pressure and velocity profiles in mixing elements of a co-rotating twin-screw extruder", *Polymer Engineering Science*, Vol. 40, pp. 525-541, 2000.

[15] A. Lawal, S. Railkar and D. Kalyon, "3-D analysis of fully flighted screws of co-rotating twin-screw extruders", *SPE ANTEC Technical Papers*, Vol. 45, pp. 317-322, 1999.

[16] F.R. Burbank and S.M. Jackson, "New Twin-screw Element Design for Elastomer Compounding", *SPE ANTEC Technical Papers*, Vol. 57, pp. 225-230, 1999.

Interfacial Debonding in Fiber-Reinforced Polymers and its Effect on Microstructure

Ajaya Kumar Beura, *Department of Mechanical Engineering, Aryan Institute of Engineering & Technology, Bhubaneswar, akbeura25@gmail.com*

Priyabrata Jena, *Department of Mechanical Engineering, Capital Engineering College, Bhubaneswar, priyabratajena456@yahoo.co.in*

Anand Mandal, *Department of Civil Engineering, Raajdhani Engineering College, Bhubaneswar,anandmandal1@gmail.com*

Deepika Priyadarshini Palai, *Department of Civil Engineering, NM Institute of Engineering & Technology, Bhubaneswar, deepikadalai2561@gmail.com*

Abstract: This study focuses on the optimizing the microstructure to improve the efficiency for healing interfacial debonding in fiber-reinforced polymers (FRPs). Healing is accomplished by incorporating a microcapsulated healing agent and catalytic chemical trigger within a coating layer on the surface of the fiber strands. Self-healing is demonstrated on flat tensile specimens of unidirectional FRPs. The effects of microcapsule diameter and concentration, and number of filaments in the fiber strand on tensile strength of virgin and healed specimens are discussed. Microstructure of the fracture surfaces of specimens was also examined by a scanning electron microscope. Additionally, finite element analyses were performed to predict the microcapsule-matrix debonding process during uniaxial tensile loading.

INTRODUCTION

The interface between matrix and fiber has a major influence on the mechanical properties of fiber-reinforced polymers (FRPs). Damage at the interface such as fiber-matrix debonding can cause a reduction in the undamaged structural strength and stiffness of FRPs. As a result, the structural capability of the FRP is reduced, and premature failure can result if the damage is not detected and repaired. However, microscopic damage such as interfacial debonding is extremely difficult to detect and repair by conventional methods. The current research suggests that repair of microscopic damage can be accomplished by incorporating repair components into the FRP. This novel concept is that of self-healing.

The idea of a self-healing material has led to significant interest in the current literature. Many techniques have focused on the ability to heal internal damage in FRPs. Hayes *et al.* [1] reported on the optimization of a solid-state self-healing resin system and its subsequent use as a matrix for polymer composites. Trask *et al.* [2] investigated self-healing using hollow fibers embedded within both glass/epoxy and carbon/epoxy laminates. Similar approaches were adopted by Dry *et al.* [3], Motuku *et al.* [4], Bleay *et al.* [5] and Pang *et al.* [6]. White *et al.* [7] developed a self-healing polymer with a micro-encapsulated healing agent. The healing agent was dicyclopentadiene (DCPD) monomer. Kessler and colleagues [8] reported on initial studies using the self-healing polymer as the matrix material of woven glass/epoxy laminates and discussed the self-healing of interlaminar fracture (delamination). Yin *et al.* [9] studied self-healing woven glass/epoxy laminates with epoxy-filled microcapsules. Recently, Sanada *et al.* [10] proposed a methodology for self-healing of interfacial debonding in unidirectional carbon/epoxy composites by using fiber strands coated with the self-healing polymer developed by White *et al.*

The scope of this work is to optimize numerically and experimentally the microstructure to improve the performance of this self-healing system as shown in Fig. (**1**). Transverse tensile tests were carried out with flat tensile specimens of unidirectional FRPs. The influences of microcapsule diameter and concentration, and number of filaments in the fiber strand on the tensile strength of virgin and healed specimens are examined. Post-fracture specimens were also examined by a scanning electron microscope (SEM) to study the microstructure. In addition to conducting experiments, finite element analyses were employed to study the microcapsule-matrix debonding process during uniaxial tensile loading.

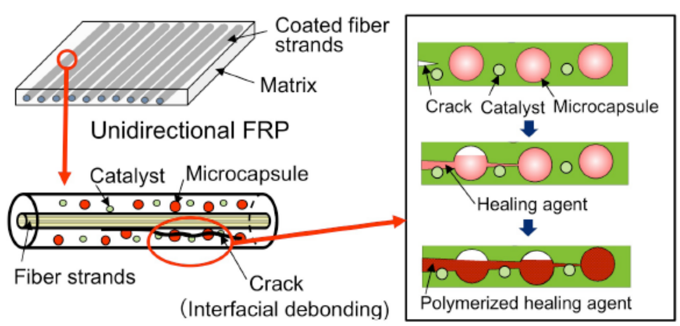

Fig. (1). Self-healing system of interfacial debonding.

EXPERIMENTAL PROCEDURES

Materials and Specimen Fabrication

Self-healing FRP plates made of unidirectional carbon fiber-reinforced polymers were prepared. Torayca T300B (Toray Industries, Inc.) carbon fiber strands were coated by manually dipping them into the Epikote 828 (Japan Epoxy

Resins Co. Ltd) /Ancamine K54 (Air Products and chemicals, Inc.) epoxy mixture containing DCPD-filled microcapsules and 2.5wt% Grubbs catalyst (Sigma-Aldrich Co.). DCPD was encapsulated in a urea-formaldehyde polymer shell via our previously reported method [10]. The number of filaments N in the fiber strand was 3000, 6000 and 12000. The mean diameters d of the microcapsules were around 50, 100, 200, 300 and 400μm and the microcapsule concentration W_f was varied from 10 to 40wt%. After coating, the fiber strands were held straight and cured for 24h at room temperature in order to obtain proper hardness.

The semi-cured fiber strands were placed in mold and impregnated with the Epikote 828 (Japan Epoxy Resins Co. Ltd)/diethylenetriamine (DETA) epoxy resin. The coated fiber strands were aligned perpendicular (90° direction) to the long direction of the plate and the fiber volume fraction was set to be about 3vol%. The mold was then closed and the samples were molded into the plate for 24h at room temperature, followed by 24h at 40 °C. Once the plates were cured, they were machined using a water cooled diamond saw and a milling machine to produce flat tensile specimens as shown in Fig. (**2**). Specimens had a nominal thickness of 3mm and a gauge length of 25mm.

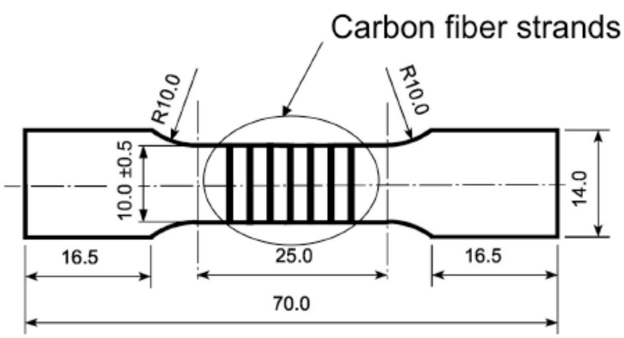

Fig. (2). Specimen geometry (dimensions in mm).

Test Methods

The specimens were tested using a tensile test machine in the displacement control at rate of 0.5mm/min. Six specimens were tested for each data point. Scatter of the data is indicated by error bars in the figures. The test procedure was as follows. First, virgin specimens were loaded to failure. After failure, the specimens were unloaded, clamped closed, and allowed to heal for 10 days at 30 °C. After healing, the specimens were reloaded to failure again.

Healing efficiency η is defined as the ability of a healed specimen to recover transverse tensile strength

$$\eta = \frac{\sigma_c^{\text{healed}}}{\sigma_c^{\text{virgin}}} \tag{1}$$

where σ_c^{virgin} is the tensile strength of the virgin specimen and σ_c^{healed} is the tensile strength of the healed specimen.

SEM observations were performed to investigate the fracture surfaces of the healed specimens. Fracture surfaces were prepared for analysis by sputter coating with gold-palladium.

FINITE ELEMENT ANALYSIS

In previous work on this self-healing system [10], an investigation of the healed fracture planes revealed that many microcapsules fractured with protruding shell materials representative of debonding. As the microcapsule-matrix debonding occurs, the release of healing agent from the microcapsules is believed to be incomplete. This leads to incomplete coverage of the healing agent on the fracture plane and a lowering of the healing efficiency. Thus, we investigated the effect of microstructure on the microcapsule-matrix debonding behavior in order to achieve high healing efficiency.

The 3D unit cell model is shown in Fig. (**3**). The form of this unit cell model is based on the assumption of a uniform and periodic distribution of microcapsules. The origin of the coordinates coincides with the center of the unit cell. Due to the symmetry of periodic packing, it is sufficient to analyze one-eighth of the cubic matrix. The diameter of the spherical microcapsule is taken as 2R, while the size of the cubic matrix is denoted as 2L. The thickness of the microcapsule membrane is t. A spherical membrane is filled with an incompressible fluid (healing agent) and is inflated by internal pressure p. The microcapsule volume fraction V_f is given by

$$V_f = \frac{\pi}{6}\left(\frac{R^3}{L^3}\right) \tag{2}$$

Symmetry conditions are applied to the boundary surfaces x_1=0, x_2=0 and x_3=0. The boundary conditions applied to surface $x_1=L$ and $x_2=L$ should enforce periodicity along the x_1 and x_2 directions. The top surface $x_3=L$ is subject to a uniform displacement u^* in the x_3 direction.

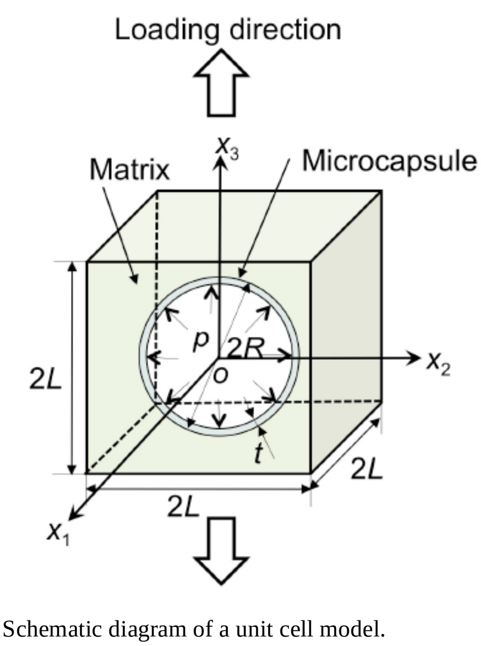

Fig. (3). Schematic diagram of a unit cell model.

The individual phase materials are modeled as linear elastic and isotropic solids. For the microcapsule membrane, the Young's modulus and the Poisson's ratio are assumed to be 1GPa and 0.3, respectively. The Young's modulus and the Poisson's ratio of the epoxy matrix are taken to be 3GPa and 0.35 [11], respectively.

In this analysis, it is assumed that mode I debonding occurs at interface between matrix and microcapsule. A bilinear cohesive zone model [12] is adopted to model the debonding behavior of the interface. As shown in Fig. (**4**), this model is governed by the maximum normal traction σ_{max} that corresponds to the interfacial strength, and δ_{cn}, which denotes the critical value of the normal displacement jump, characterizing the complete failure of material. Therefore, the critical fracture energy G_{cn} is determined by:

$$G_{cn} = \frac{1}{2}\delta_{cn}\sigma_{max} \tag{3}$$

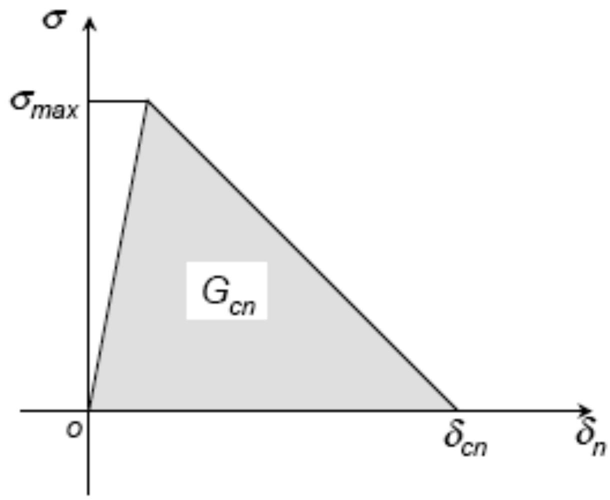

Fig. (4). Cohesive law for mode I fracture.

RESULTS AND DISCUSSIONS

Transverse Tensile Test

The virgin and healed tensile strengths (σ_c), and healing efficiency (η) of self-healing FRP specimens with W_f=30wt% and N = 6000 are presented in Fig. (**5**) as a function of d. As shown in Fig. (**5**), there is a significant amount of scatter in the data between specimens. The scatter may be attributed to the microstructural inhomogeneity of this material and the difficulty of specimen preparation. However, such behavior is characteristic of mechanical testing of FRPs in general. In this study, the test results for each group of specimens are averaged to see a trend. The d affected the average virgin tensile strength and the average virgin tensile strength of the specimens with d =400 μ m was higher as compared to other results. The average healed tensile strength and the average healing efficiency were essentially independent of d.

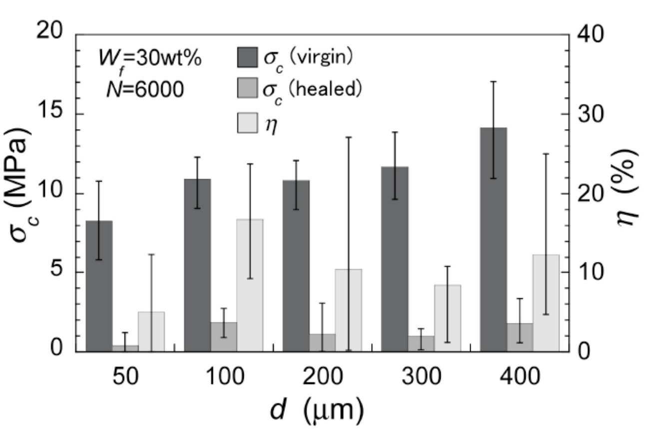

Fig. (5). Virgin and healed tensile strengths, and healing efficiency *vs*. microcapsule mean diameter.

The virgin and healed tensile strengths, and healing efficiency of self-healing FRP specimens with d =300 μ m and N = 6000 are plotted in Fig. (**6**) as a function of W_f. For the specimen with W_f =10 wt%, no healing was observed. The virgin and healed tensile strengths were insensitive to W_f as the W_f increased from 15 to 40wt%. Moreover, scatter in the virgin tensile strength is dramatically increased at higher concentrations. Large scatter was observed in the data as a result of problems with mixing of the microcapsules and the Grubbs catalyst. The W_f slightly affected the average healed tensile strength and the average healing efficiency.

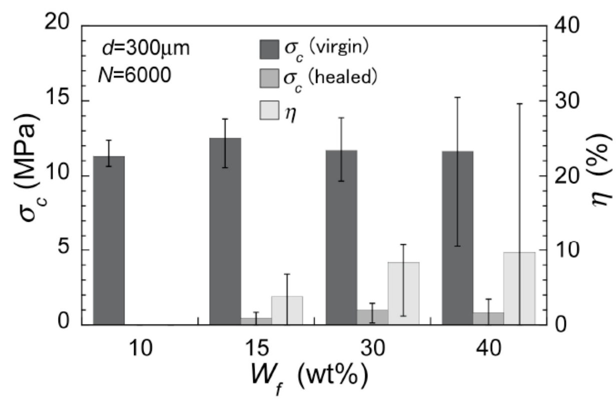

Fig. (6). Virgin and healed tensile strengths, and healing efficiency *vs*. microcapsule concentration.

Fig. (**7**) shows the virgin and healed tensile strengths, and healing efficiency of self-healing FRP specimens with W_f =30wt% and d =300μm as a function of N. The specimens with N=6000 exhibited a high average virgin tensile strength when compared to the specimens with N=3000 and 12000. In contrast, the N did not have a significant effect on the average healed tensile strength. Though the scatter in the data is appreciable, a high average healing efficiency was present at N=12000.

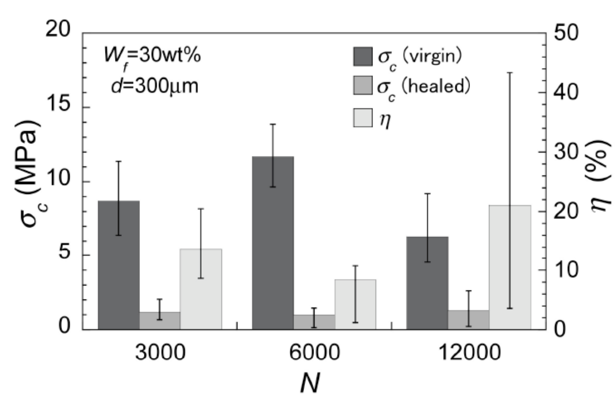

Fig. (7). Virgin and healed tensile strengths, and healing efficiency *vs*. number of filaments in reinforcements.

SEM images of the fracture surface of the healed specimens with d=50 and 100μm are shown in Fig. (**8**).

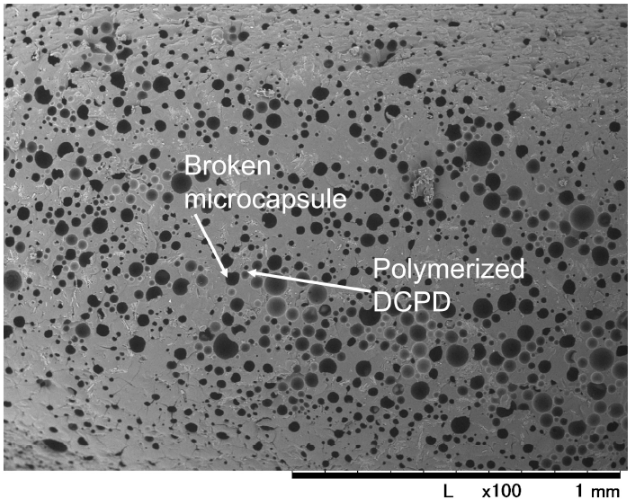

(**a**)

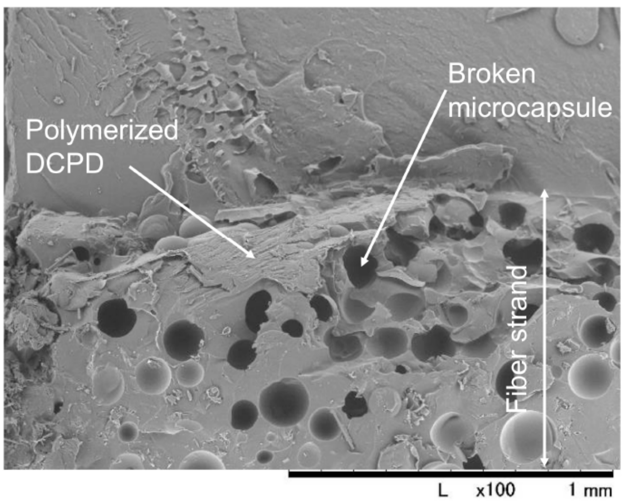

(**b**)

Fig. (8). SEM micrographs of fracture surface of healed specimens; (**a**) d=50μm, (**b**) d =100 μm.

For the specimen with d=50μm (Fig. **8a**), there are few observable polymerized healing agents. For the specimen with d =100μm (Fig. **8b**), polymerized healing agent was present in the vicinity of fractured microcapsules.

Fig. (**9**) presents SEM images of the fracture surfaces of the healed specimens with W_f =10 and 40wt%. For the specimen with W_f =10wt% (Fig. **9a**), broken fiber strands are evident on the fracture plane. For the specimen with W_f =40wt% (Fig. **9b**), it is clear from the image that crack propagation occurred through the coating layer of the fiber strand surface. The morphology of the healed fracture surface is quite distinct from the specimen with W_f =10wt% and many broken microcapsules are evident on the fracture plane.

Fig. (**10**) shows SEM images of the fracture surface of the healed specimens with N=3000, 6000 and 12000. In all images (Fig. **10a, b** and **c**), many fractured microcapsules release the encapsulated healing agent. However, there was no detectable correlation between fracture plane morphology and N.

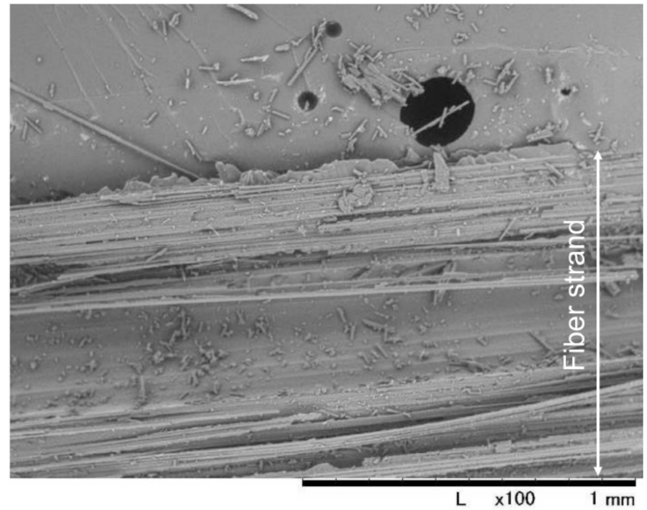

(**a**)

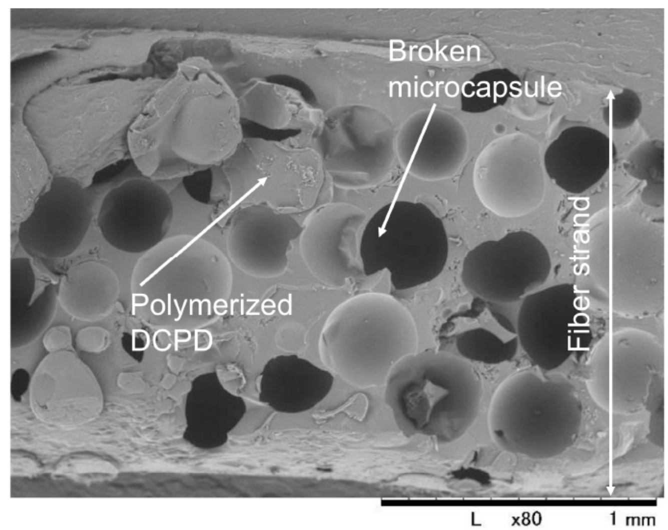

(**b**)

Fig. (9). SEM micrographs of fracture surface of healed specimens; (**a**) W_f =10wt%, (**b**) W_f =40wt%.

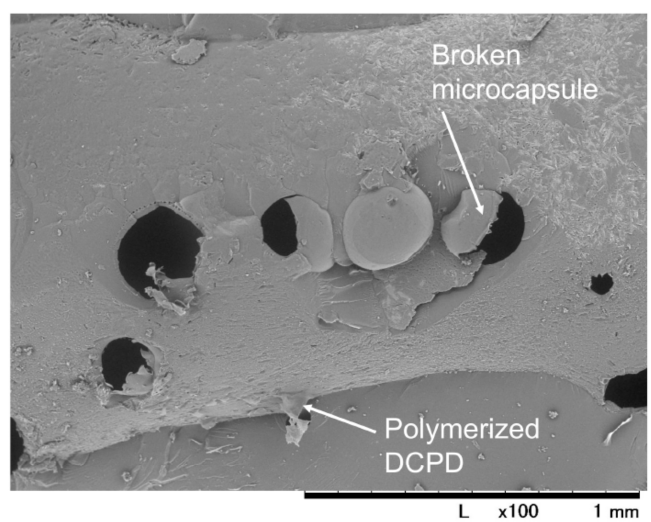

(**a**)

(Fig. 10). contd…..

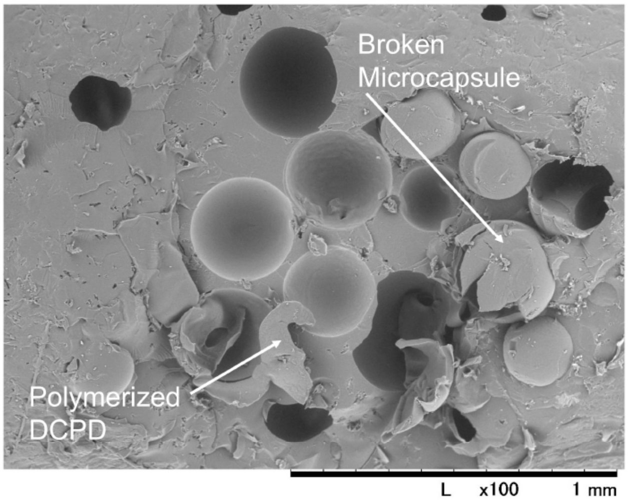

(**b**)

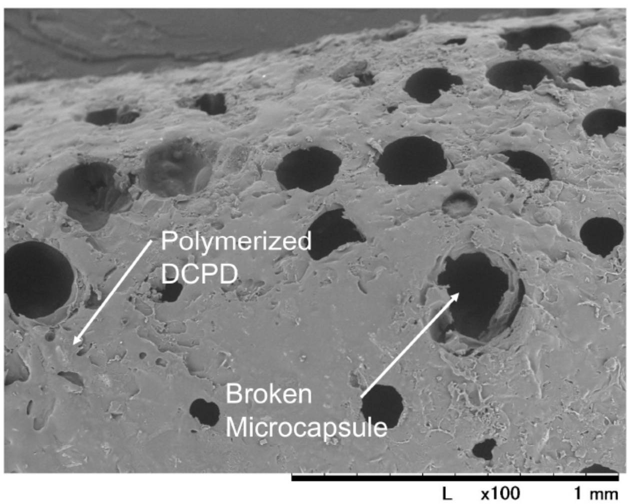

(**c**)

Fig. (10). SEM micrographs of fracture surface of healed specimens; (**a**) N=3000, (**b**) N =6000, (**c**) N=12000.

Matrix-Microcapsule Debonding Analysis

Fig. (**11**) shows the bonding area normalized by surface area of microcapsule, A/A_0, versus the nondimensional displacement, u^*/L. Calculation were carried out assuming V_f=0.1, σ_{max} = 0.1MPa, δ_{cn} = 0.1μm, p= 10kPa, 2R= 100μm and t= 0.24μm. The debonding between microcapsule and matrix initiates when the u^*/L reaches about 0.013. The debonding damage propagates rapidly as the u^*/L increases approximately from 0.013 to 0.02. As the u^*/L increases further, the damage growth rate is reduced.

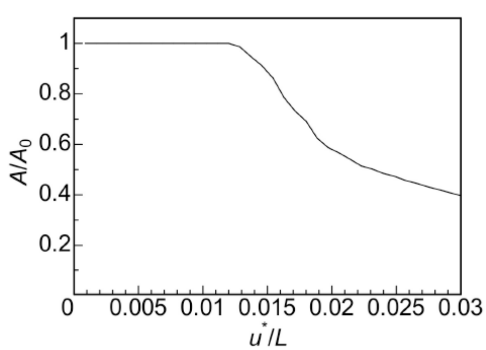

Fig. (11). Typical bonding area *vs*. displacement curve.

Fig. (**12**) shows the predicted debonding damage progression in the unit cell model viewed from surface x_2=0. It can be observed from Fig. (**12a**) that debonding initiates at the equator. As the u^*/L increases further, debonding damage propagates from the equator to the pole Figs. (**12b** and **c**).

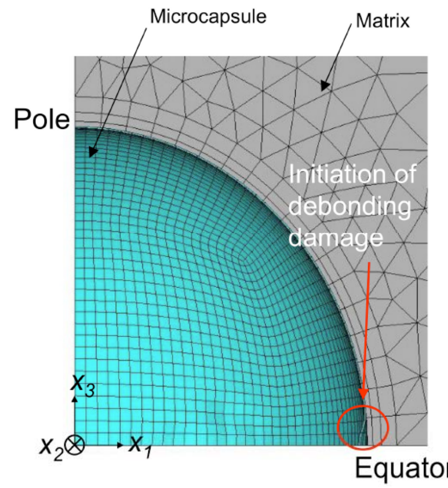

(**a**)

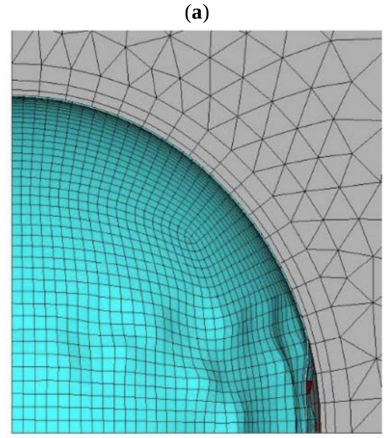

(**b**)

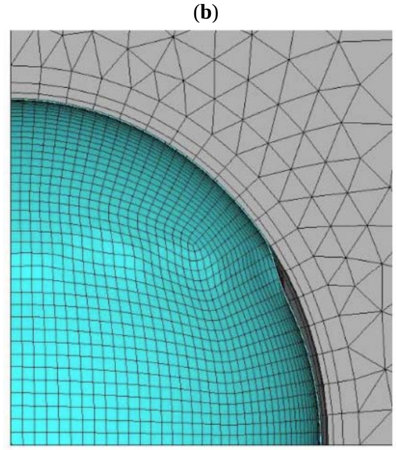

(**c**)

Fig. (12). Illustration of the predicted debonding damage growth pattern in the unit cell model viewed from surface x_2=0 as a function of the applied displacement; (**a**) u^*/L =0.013, (**b**) u^*/L =0.018, (**c**) u^*/L =0.027.

The corresponding results for the unit cell model viewed from surface x_3=0 are shown in Fig. (**13**). At u^*/L=0.013 (Fig. **13a**), the debonding damage initiates at surfaces x_1=0 and x_2=0. As the u^*/L increases further (Fig. **13b** and **c**), the debonding damage becomes larger.

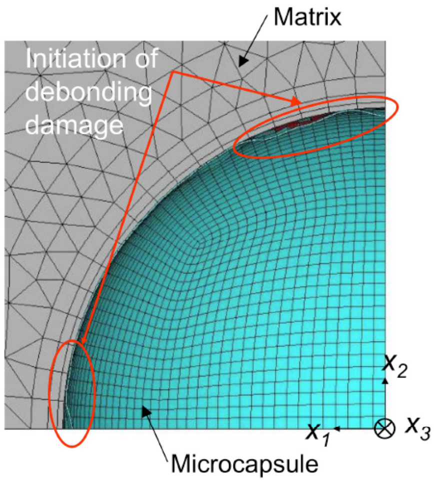

(**a**)

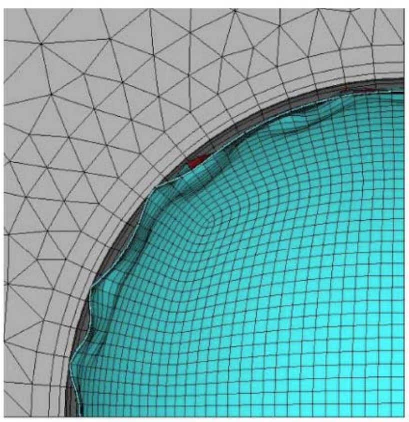

(**b**)

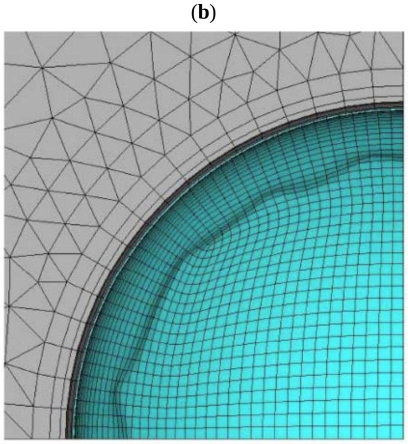

(**c**)

Fig. (13). Illustration of the predicted debonding damage growth pattern in the unit cell model viewed from surface x_3=0 as a function of the applied displacement; (**a**) u^*/L =0.013, (**b**) u^*/L =0.018, (**c**) u^*/L =0.027.

Fig. (**14**) shows the influence of σ_{max} on debonding damage behavior. As the σ_{max} decreases, the debonding damage occurs at lower displacement. Fig. (**15**) provides similar plots for various δ_{cn}. As the δ_{cn} increases from 0.01

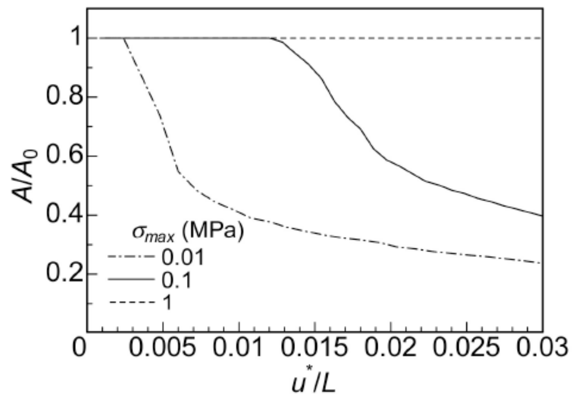

Fig. (14). Effect of interfacial strength on debonding behavior.

to 1μm, the debonding damage growth rate decreases. The debonding damage behavior changes from brittle to ductile with increasing δ_{cn}. Fig. (**16**) exhibits the effect of 2R on the debonding damage behavior. The debonding damage initiates at lower displacement as the 2R decreases. This is similar to the results for the σ_{max}. If the debonding damage occurs, the release of healing agent in the microcapsule is believed to be incomplete. The microcapsule diameter is a critical parameter to obtain higher healed strength. The corresponding results for various V_f are shown in Fig. (**17**). The debonding damage behavior is insensitive to V_f ranging from 0.01 to 0.2. The experimental results showed that the average virgin tensile strength decreased with decreasing microcapsule mean diameter. This may be attributed to the microcapsule-matrix debonding damage that occurs during the virgin test. Therefore, the numerical results are useful to interpret the experimental behavior.

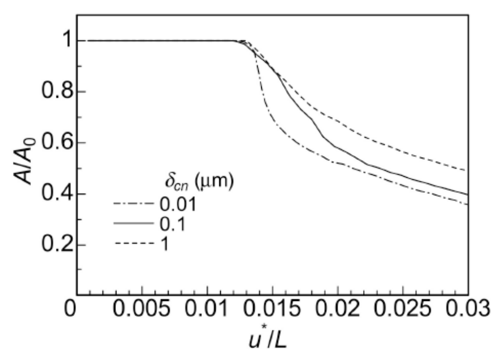

Fig. (15). Effect of critical opening displacement on debonding behavior.

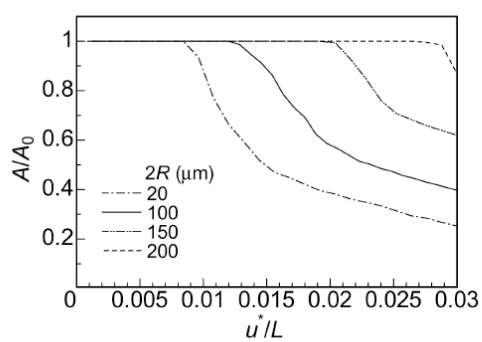

Fig. (16). Effect of microcapsule diameter on debonding behavior.

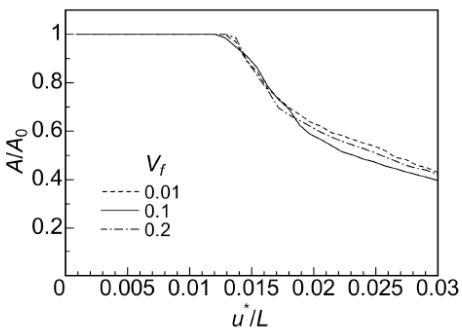

Fig. (17). Effect of microcapsule volume fraction on debonding behavior.

CONCLUSIONS

The self-healing of interfacial debonding in FRPs and the effect of microstructure on strength recovery were investigated. Transverse tensile tests were conducted using unidirectional FRP. The effects of microcapsule mean diameter and concentration, and number of filaments in the fiber strand on tensile strength of virgin and healed specimens were evaluated. Finite element analyses were also carried out to interpret the debonding behavior of the interface between the microcapsule and the matrix. Based on the study, the following conclusions can be made:

1. The N and d were shown to have an impact on the virgin tensile strength of self-healing FRP. The improvement in the average virgin tensile strength was obtained with d = 400μm and N = 6000. However, the W_f had a negligible effect on the average virgin tensile strength.
2. The effects of N and d on the healed tensile strength and the healing efficiency of self-healing FRP were weak. However, the W_f appeared to have little effect on the average healed tensile strength and the average healing efficiency.
3. The debonding damage between the microcapsule and matrix occurred at lower displacement as the microcapsule diameter decreased. This result indicates that higher healing efficiency is obtained for larger microcapsule diameter. Moreover, there is no effect of microcapsule volume fraction ranging from 0.01 to 0.2 on the debonding behavior. Because the reduction in the virgin tensile strength may be attributed to the microcapsule-matrix debonding damage, the proposed model predicted the experimental behavior well.

ACKNOWLEDGEMENTS

This work was supported by the Ministry of Education, Culture, Sports, Science and Technology of Japan under the Grant-in-Aid for Young Scientists (B), 16760572. The authors gratefully acknowledge the technical advice and guidance of Professor Makoto Kawagoe.

REFERENCES

[1] S.A. Hayes, W. Zhang, M. Branthwaite, and F.R. Jones, "Self-healing of damage in fibre-reinforced polymer-matrix composites", *J. R. Soc. Interface*, vol. 4, pp. 381-387, 2007.

[2] R.S. Trask, G.J. Williams, and I.P. Bond, "Bioinspired self-healing of advanced composite structures using hollow glass fibers", *J. R. Soc. Interface*, vol. 4, pp. 363-371, 2007.

[3] C. Dry, "Procedures developed for self-repair of polymer matrix composite materials", *Compos. Struct.*, vol. 35, pp. 263-269, 1996.

[4] M. Motuku, U.K. Vaidya, and G.M. Janowski, "Parametric studies on self-repairing approaches for resin infused composites subjected to low velocity impact", *Smart Mater. Struct.*, vol. 8, pp. 623-638, 1999.

[5] S.M. Bleay, C.B. Loader, V.J. Hawyes, L. Humberstone, and P.T. Curtis, "A smart repair system for polymer matrix composites", *Composites Part A*, vol. 32, pp. 1767-1776, 2001.

[6] J.W.C. Pang, and I.P. Bond, "Bleeding composites - damage detection and self-repair using a biomimetic approach", *Composites Part A*, vol. 36, pp. 183-188, 2005.

[7] S.R. White, N.R. Sottos, P.H. Geubelle, J.S. Moore, M.R. Kessler, S.R. Sriram, E.N. Brown, and S. Viswanathan, "Autonomic healing of polymer composites", *Nature*, vol. 409, pp. 794-797, 2001.

[8] M.R. Kessler, and S.R. White, "Self-activated healing of delamination damage in woven composites", *Composites Part A*, vol. 32, pp. 683-699, 2001.

[9] T. Yin, L. Zhou, M.Z. Rong, and M.Q. Zhang, "Self-healing woven glass fabric/epoxy composites with the healant consisting of micro-encapsulated epoxy and latent curing agent", *Smart Mater. Struct.*, vol. 17, pp. 8, 2008.

[10] K. Sanada, I. Yasuda, and Y. Shindo, "Transverse tensile strength of unidirectional fiber-reinforced polymers and self-healing of inter-facial debonding", *Plast. Rubber Compos.*, vol. 35, pp. 67-72, 2006.

[11] F.J. Guild, and A.J. Kinloch, "Predictive modeling of the mechanical properties of rubber-toughened epoxy", *J. Mater. Sci. Lett.*, vol. 13, pp. 629-632, 1994.

[12] G. Alfano, and A. Crisfield, "Finite element interface models for the delamination analysis of laminated composites: Mechanical and computational issues", *Int. J. Numer. Methods Eng.*, vol. 50, pp. 1701-1736, 2001.

Boiling Heat Transfer: Mechanisms, Models, and Correlations

Sanjeet Raj, Department of Mechanical Engineering, Aryan Institute of Engineering & Technology, Bhubaneswar, sanjeetraj4@gmail.com
Kalpana Mallick, Department of Mechanical Engineering, Raajdhani Engineering College, Bhubaneswar, kalpanamallick9@gmail.com
Alivasakhi Mishra, Department of Civil Engineering, Capital Engineering College, Bhubaneswar, alivasakhimishra258@gmail.com

Abstract: A review discusses current status of boiling heat transfer research. Basic experimental facts, physical models and correlations of experimental data on heat transfer coefficient (HTC) are reconsidered. Principal restrictions of traditional model of "the theatre of actors" (MTA) are demonstrated. Basic role of control of HTC by thermodynamic conditions on nucleation sites is demonstrated and consequent model of "the theatre of director" (MTD) is discussed. Universal MTD-based correlation of boiling HTC of all types of liquids is presented. Unified consistent research framework for developed boiling heat transfer and diverse specific boiling heat transfer regimes is outlined through supplementing MTD by so-called multifactoring concept (MFC). MFC links transition from developed boiling mode to diverse boiling curves to a phenomenon of multiplication of factors influencing HTC. Multifactoring phenomenon equally can cover any boiling process including boiling in minichannels and microchannels. Possible types of multifactoring are considered. Finally, the ways of further research of the boiling problem are discussed.

Keywords: Boiling, nucleation, heat transfer, heat transfer coefficient, heat transfer crisis.

INTRODUCTION

Complexity of boiling phenomenon is connected with combination of phase conversion and turbulence in an area with irregular internal structure. Importance of boiling heat transfer research is determined by wide sphere of application covering thermal and nuclear power engineering, space, aviation, cryogenic, refrigeration, chemical, food and other technologies.

A history of boiling heat transfer research represents an impressive example how unwillingness to deconstruct internal contradictions of applicable approaches leads to theoretical deadlock.

The first internal contradiction of traditional approach manifests itself between linking of HTC to intensity of concrete cooling mechanisms (a model of "the theatre of actors" (MTA) and real independence of heating surface superheat on changes of intensities of the same concrete cooling mechanisms.

Drastic changes in inter-phase hydrodynamics occurring with a change in the intensity of body force by several orders of magnitude, with forced convection or subcooling, with change of sizes and thermal parameters of heating surface, all of these changes have virtually no influence on heating surface superheat in the mode of developed boiling.

The main outcome of such a situation is widely known by way of numerous unsuccessful attempts of MTA-based correlation of experimental data on HTC during boiling of different groups of liquids.

The second widely used misassumption attributes universally leading role in boiling heat transfer to microlayer evaporation mechanism based only on synchronism of heating wall temperature drop with the onset of a bubble growth (against numerous experiments reflecting major role of liquid phase convection in the majority of boiling processes).

Simultaneously, the same history of boiling heat transfer research represents no less impressive example how resolution of existing contradictions opens up the ways to breakthrough in the theory.

For instance, resolution of aforementioned first contradiction leads to a model of "the theatre of director" (MTD) and universal correlation of experimental data on boiling HTC of all types of liquids opening a new avenue of attack on the problem.

In the same way, resolution of aforementioned second contradiction reveals existence of the pumping effect of growing bubble (PEGB) playing crucial role in boiling heat transfer and hydrodynamics.

Unfortunately, aforementioned misleading common background proves to be so strong that MTD and PEGB still have unnoticeable influence on the main lines of boiling heat transfer research.

Simultaneously abovementioned situation exerts certain impact on modern reviews of the problem [1-3]. It becomes topical to reanalyze modern state of boiling research [4]. An attempt to bridge this gap is made below.

Basic features of boiling phenomenon, experimental facts and physical models are reconsidered. Alternative approaches to boiling heat transfer problem (MTA and MTD) and following from them correlations are examined. Unified consistent research framework for developed boiling heat transfer and diverse specific boiling heat transfer regimes is outlined by way of supplementing of MTD by so-called multifactoring concept (MFC). In the framework of MFC potential role of PEGB is considered in generation of strong reverse vapor follows, related cyclical oscillations and flow instabilities observed in minichannels and microchannels. The ways of further research of the boiling problem are discussed.

BASIC FEATURES AND EXPERIMENTAL FACTS

The basic part of boiling heat transfer curve corresponds to so-called developed boiling mode. By common agreement developed boiling means a process with decisive contribution of cooling mechanisms unique to boiling itself. Such a boiling mode is observed in rather wide range of heat fluxes between the zones with tangible effect of natural or forced convection and boiling crisis. This is why developed boiling mode may cover different ranges of heat fluxes at constant pressure depending on geometry of boiling surface, intensity of gravity field, subcooling or liquid flow.

However, developed boiling heat transfer law (for instance, dependence between heat flux and heating surface superheat) remains uniform.

Characteristic for boiling another feature is diversity of cooling mechanisms contributing in heat transfer.

In boiling of saturated single-component liquid one can distinguish three basic cooling mechanisms associated with boiling itself. Among them only one (microlayer evaporation [5]) is linked to immediate evaporation on boiling surface (Fig. **1a**). Other two mechanisms (bubbling [6, 7] (Fig. **1b**) and jet-like [8] (Fig. **1c**) are linked to liquid phase convection.

Cooling mechanisms operating through pushing the liquid by growing bubble, through displacement of overheated liquid layer (transient conduction dominated model) or through drift liquid current subsequent to detached bubble (sometimes thought to be separate mechanisms) can presumably be regarded as being separate stages of action of bubbling mechanism.

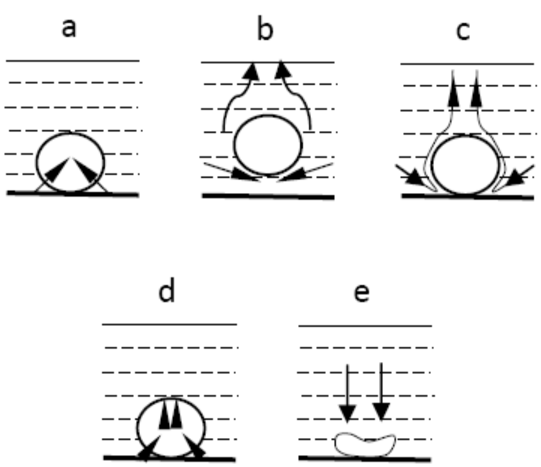

Fig. (1). Schemes of different cooling mechanisms.

Subcooling of liquid phase puts in operation two additional cooling mechanisms: evaporation-condensation [9] (Fig. **1d**), being an extra version of the microlayer evaporation mechanism, and quasi-cavitations [10] (Fig. **1e**) associated with the collapse of a bubble on the surface under the influence of subcooled liquid. It also belongs to a number of convection mechanisms micro-membrane pumping effect [11] (this poorly known dynamical effect of nongravity nature is discussed below).

Microlayer Evaporation

Discovery of heating surface temperature pulsation synchronous with a bubble formation and departure cycle [5] has led to qualitative deepening of understanding of boiling phenomenon.

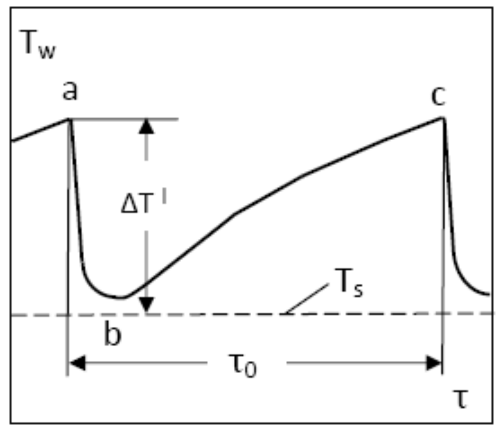

Fig. (2). Typical cycle of local temperature pulsation on heating surface [5].

Fundamental outcome of this and further studies of local temperature pulsations is establishment of coincidence of main cooling effect with onset of bubble growth (Fig. (**2**), points **a** and **c**). It also is important establishment of short-run character of intensive cooling effect (duration of intensive cooling is far less than duration of the cycle).

At the same time, in the same and in a number of further studies, exclusive role is attributed to microlayer evaporation in fixed cooling effect based only on the synchronism of temperature drop and the onset of a bubble growth. Besides, no evaluations are made of the capability of microlayer evaporation to absorb heat released by heating surface during temperature drop.

In contrast to it, questionably leading role of microlayer evaporation even in cooling of underlying local zone of heating surface is shown in an analysis [8]. Significant excess of heat removed from the boiling surface over the quantity that might be absorbed by the bubble of departure size also is revealed in experiments [12-14].

According these results fundamental evidences of dominant role of liquid phase convection in boiling heat transfer [6, 15-17] remain in force regarding to local temperature pulsations as well.

Contradiction between arising of main cooling effect at the onset of bubble growth and deficient capacity of microlayer to absorb released heat was resolved through prediction of existence of so-called pumping effect of growing bubble (PEGB) [8]. This mechanism will be discussed in detail below.

It also is noteworthy that high intensity of heat transfer in the zone of evaporating microlayer may not explain high intensity of boiling heat transfer as a whole: the share of heating surface simultaneously covered by the microlayers is quite small. It also is of essential interest peculiarities of heat transfer to evaporating liquid microlayers with low share of heating surface with intensive cooling.

The subject of the analysis [18] is evaporation of a liquid wetting the system of open triangular capillary grooves. The process really represents the case of heat transfer with prevailing role of continuous evaporation of liquid microlayers in the zones of the edges of liquid menisci.

The model of the process is presented in Fig. (**3**). The problem relates to the sphere of conjugate heat transfer. Taking in account crucial role of concentration of heat flux in the zones of the edges of liquid menisci, the cross section along bottom points of the capillary grooves is accepted as a basic isothermal surface for determination of HTC through analysis and through experiments as well [19].

Corresponding analysis of steady-state heat conduction through combined metal-liquid layer leads to following equation for average HTC during evaporation from triangular capillary grooves:

$$h = \frac{1}{\varepsilon}\sqrt{\frac{k_w k}{\sin \vartheta tg(\varphi / 2)}} \quad (1)$$

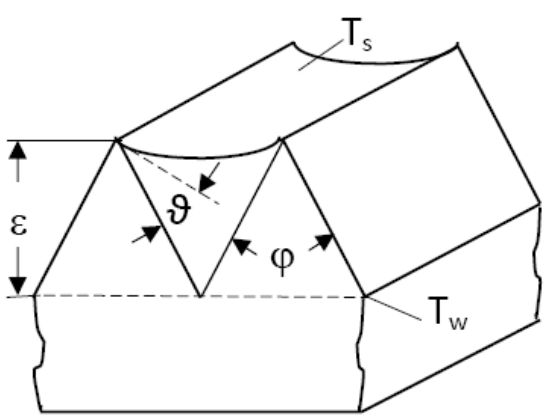

Fig. (3). Model of evaporation on triangular grooves.

Comparison of equation (1) with the experimental data [19] on distilled water evaporation and steam condensation is presented in Fig. (**4**) (concurrent arrangement of the data on evaporation and condensation reflects the range of heat fluxes with evaporation without nucleation inside grooves).

As it follows from comparison, capability of heating surface to redistribute and concentrate heat flux in the zones of liquid microlayers, in full accordance with equation (1), strongly influences average HTC (with a factor around 5 between stainless steel and copper). Besides, here is presented only the part of wide experimental data [19] confirming equation (1).

In such a manner, HTC strongly depends on thermal parameters and thickness of heating surface in any heat transfer process with prevailing role of evaporation of liquid microlayers covering only small areas distributed on all heating surface.

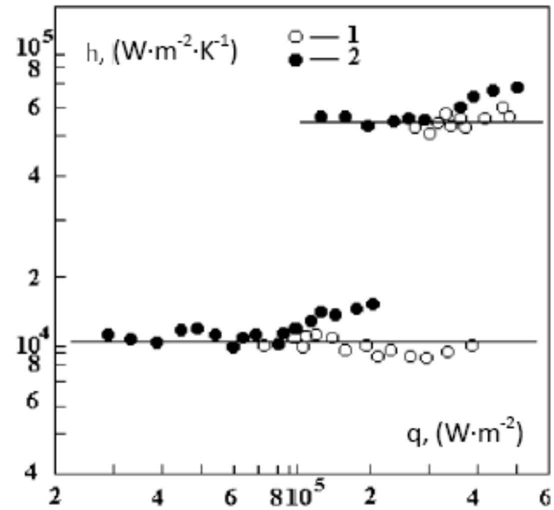

Fig. (4). Comparison of equation (1) (horizontal lines) with experimental data [19] on steam condensation and distilled water evaporation on the surfaces with triangular grooves (ε = 0.5 mm) made of stainless steel (lower data) and copper (upper data): 1 – condensation; 2 – evaporation.

Correspondingly, the fact, that such an influence of heating surface is not observed in the majority of experiments on developed boiling heat transfer, should be considered as evidence of insignificant role of microlayer evaporation mechanism in average heat transfer. Below this important issue is discussed in more detail.

At the same time aforementioned circumstances do not prohibit microlayer evaporation from the role of tangible cooling mechanism. Its contribution is higher at greater shares of contact area of bubbles with heating surface and at comparatively low superheats. In this context, microlayer evaporation may play significant and even leading role in boiling heat transfer at microgravity, at high saturation pressures, on heating surfaces with high-sized nucleation sites and, especially, at transition to prolonged action of the mechanism, for instance, in the microsystems.

Bubbling Mechanism

Bubbling mechanism is associated with exchange and displacement of liquid and vapor volumes during growth, departure and elevation of vapor bubbles. Bubbling generates complex flow including the stages of pushing the liquid by growing bubble, replacement of detaching bubbles by a liquid, displacement of overheated liquid boundary layer by detached bubble, drift liquid current subsequent to detached bubble (Fig. **5**). By tradition this mechanism claims to be the major among boiling heat transfer mechanisms.

At the same time presented in Fig. (**2**) typical cycle of local temperature variation unambiguously shows that only launched by bubble growth mechanism can play leading role in boiling heat transfer. Assuming that main cooling effect of bubbling takes place consequent to a bubble departure, a conclusion is made about major role of PEGB and second-rate intensity of the bubbling mechanism [8, 20].

In [21] the mechanism is studied through bubbling of saturated by hexane inert air through liquid hexane with simultaneous registration of local heat transfer during the cycle of air bubble growth, detachment and elevation. The most important outcome is establishment of maximum intensity of heat transfer consequent to detachment of the bubble. The bubble growth and elevation are characterized by low intensity of heat transfer.

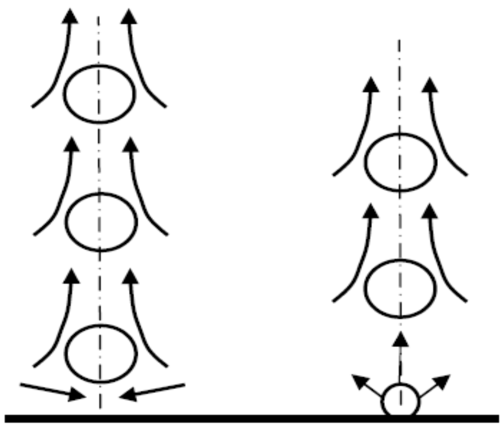

Fig. (5). A scheme of bubbling mechanism.

Insignificancy of the role of bubbling during boiling also is established in experimental study of heat transfer during bubbling of humid nitrogen into water through perforated heating surface [22].

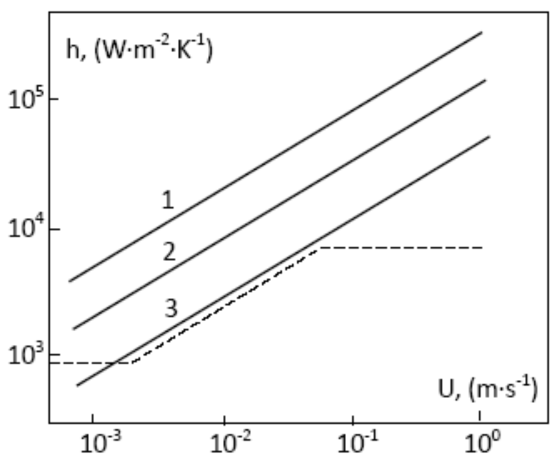

Fig. (6). Comparison of experimental data on HTC during boiling of water and during bubbling of humid nitrogen into water through perforated heating surface [22]: 1 - $h = 3.14{\cdot}q^{0.7}$, q_r/q=0.05; 2 $h = 3.14{\cdot}q^{0.7}$, q_r/q =0.2; 3 - $h = 3.14{\cdot}q^{0.7}$, q_r/q=1; dotted curve – smoothed experimental curve of heat transfer during bubbling.

In Fig. (**6**) typical dependence of HTC on heat flux during boiling of water at atmospheric pressure ($h = 3.14{\cdot}q^{0.7}$, here h is in $W{\cdot}m^{-2}{\cdot}K^{-1}$; q is in $W{\cdot}m^{-2}$) is transformed into dependence of HTC from vapor generation velocity averaged for the surface at three different values of q_r/q. The dependence also is presented of HTC during bubbling of humid nitrogen from average normal velocity of nitrogen [22] (humidity of nitrogen is sufficient for practically full prevention of water evaporation from a bubble surface).

As during boiling of water at atmospheric pressure typical values of q_r/q are much less 0.2 [6, 15-17], boiling HTC turns out to be 4-5 times higher than the same parameter in corresponding bubbling regime.

Such a result unambiguously shows secondary importance of bubbling mechanism.

It is evident also that made in [22] opposing conclusion about major role of bubbling mechanism in boiling heat transfer suffers from internal inconsistency.

This conclusion is based on experimental data accepted at very high bubbling velocities corresponding to condition of heat removal only through immediate evaporation q_r/q =1 (to say, to condition of a priori negligible role of bubbling mechanism in boiling heat transfer). Further, the results accepted through such an intensive bubbling are used as an evidence of prevailing role of bubbling mechanism in boiling process with weak vapor flow immediately generated on heating surface.

Aforementioned experiments are valuable also in terms of revelation of insignificant role of thermocapillary Marangoni convection in boiling heat transfer. This aspect of the problem is touched below.

Pumping Effect of Growing Bubble

PEGB (Fig. **7**) [8, 23] is caused by sharp variability, along bubble surface, of transverse momentum transport by evaporation, to say, by sharp variability of a reactive force applied to an interface.

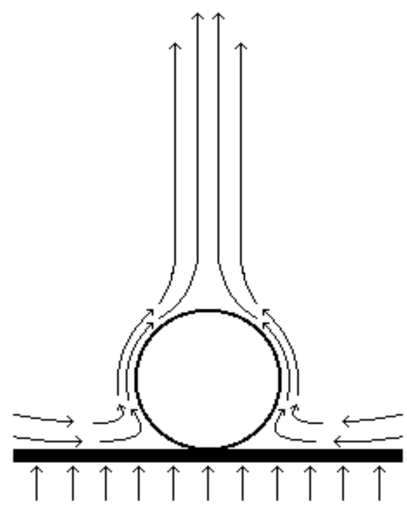

Fig. (7). A model of pumping effect of growing bubble (PEGB).

Generated in such a way superficial pressure gradient covers all thickness of liquid boundary layer (as a volume force) [24] and speeds-up liquid flow along the interface. According [11, 25] corresponding acceleration may be at two orders of magnitude above of normal gravity acceleration.

Intensity of PEGB strongly depends on initial superheat of boiling surface. Therefore PEGB is much more intensive at relatively low pressures, small-sized nucleation sites and high surface tension (e.g. in liquid metals). “Switched on” simultaneously with the onset of bubble growth, liquid flow quickly reduces initial gradient of temperature due to that it arises and “cuts off” itself even if a bubble still remains on the wall.

In such a way PEGB reconciles character of local temperature pulsation with prevailing role of liquid phase convection in the majority of boiling processes.

Decisive role could have been played by thorough interpretation of the results of the experiments [13, 26, 27] in establishment of basic role of PEGB in boiling heat transfer.

Discovery of the phenomenon of bubble departure against the gravity force (Fig. **8**) [26] unambiguously evidences high intensity of PEGB.

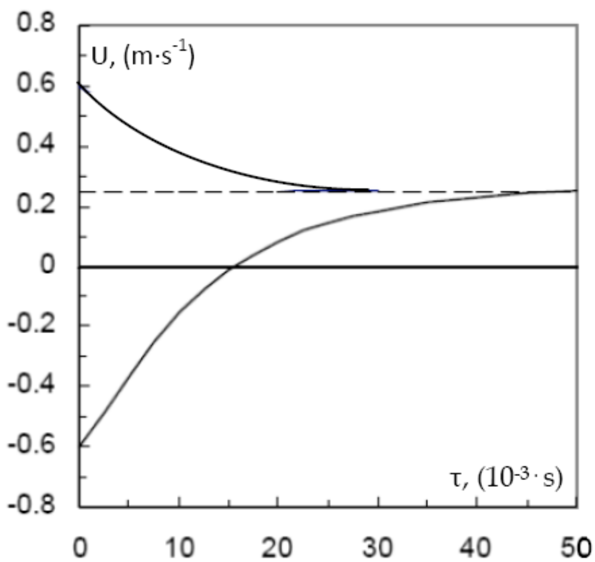

Fig. (8). Vertical velocity of vapor bubble subsequent to departure from thin wire [26]: upper curve - upward departure; bottom curve - downward departure; dotted line - equilibrium elevation velocity; point 0 - departure instant.

Roughly constant velocity of bubble departure is registered during boiling of water on thin horizontal wire (Ø 0.2 mm) under atmospheric pressure no matter the departure is oriented. Besides, departure velocity (~0.6 m/s) is more than twice higher of a bubble equilibrium elevation velocity.

As it is noted in [28-30], low heat capacity of thin wire and its rather low hydraulic resistance to transverse flow result fast transition of the bubble from the role of the accelerator of the liquid jet to the role of the object to be swept out by the same jet continuing by inertia.

As it follows from Fig. (**9**), growing bubble speeds-up jet flow directed transversely to thin wire at the stage a. In connection with low heat capacity of thin wire speeded-up liquid flow rapidly eliminates superheat serving as energy source for PEGB. Accordingly, the bubble stops pumping liquid when it still has very small diameter. Further liquid flow continues by inertia and sweeps the bubble from the wire (the stage b).

Significant role is played here by very small value of the gravity force applied to the bubble. As this force is proportional to third order of bubble diameter, small departure size of the bubble makes the gravity force extremely weak. Therefore, dynamical force wins this concrete opposition.

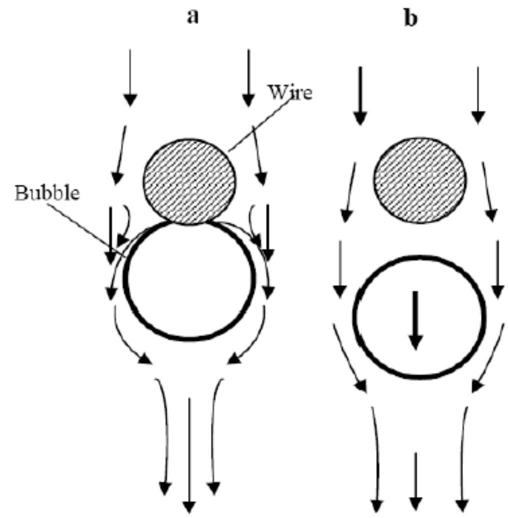

Fig. (9). A scheme of bubble departure from thin wire against the gravity force.

At the same time, as liquid flow velocity markedly reduces to the stage b, bubble departure against gravity force with velocity 0.6 m/s evidences speeding-up of much more strong flow at the stage a.

Unfortunately, in [26], observed phenomenon is not identified as a manifestation of PEGB (as an evidence of speed-up of strong liquid jet flow at initial stage of bubble growth). In unison, the authors have not fixed foregoing bubble departure liquid jet flows later clearly observed in just the same conditions [31].

In fact high intensity of PEGB directly is fixed in experiments [27] on boiling of water at atmospheric pressure. At that liquid removal velocity from the top of growing bubble is higher than 2 m/s (Fig. **10**).

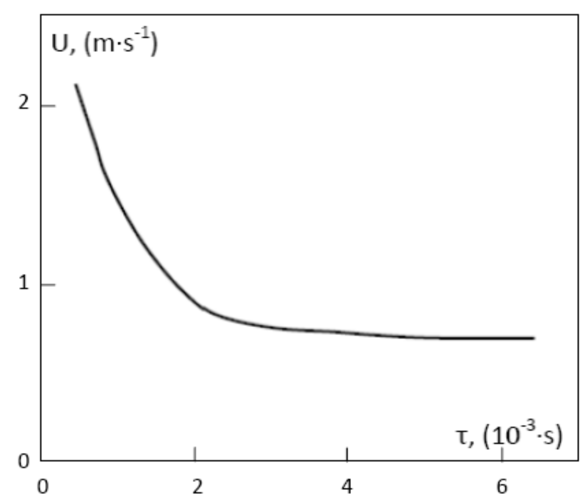

Fig. (10). Vertical velocity of superheated liquid from the top of growing bubble [27].

Unfortunately, most likely in connection with accidental arithmetic errors, these important data are interpreted as temperature wave propagation through stationary fluid by thermal conductivity (registered velocities are at two-three orders of magnitude higher than possible velocities of such a propagation).

Impressive evidences of insignificancy of the role of microlayer evaporation in local temperature pulsations and extremely high intensity of PEGB are presented in [13].

As it follows from this experiment [13], temperature pulsations of massive (Ø 60 mm) copper substrate penetrate to a depth more than 30 mm. In addition, liquid jets, speeded-up by growing bubbles up to velocity 5 m/s, are picked up on the film (Fig. **11**).

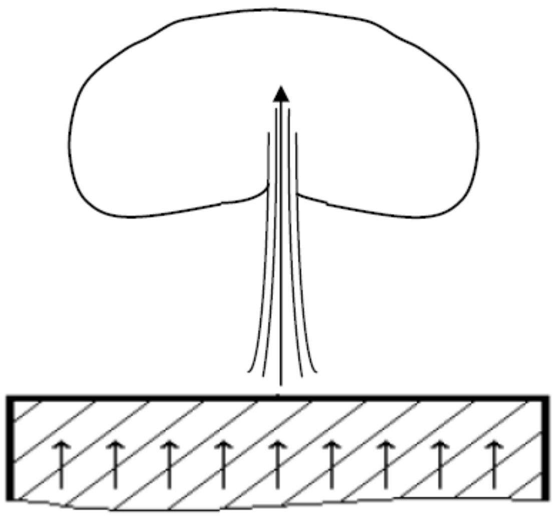

Fig. (11). Speeded-up liquid jet flow (5 m/s) penetrating through full-grown large preceding vapor bubble [13].

According simple calculations, the heat released from the substrate turned out to be at around two orders of magnitude above that expended for forming a bubble of departure size. Unfortunately, the authors lose an opportunity to demonstrate insignificancy of the role of microlayer evaporation in such a simple way. The authors also desist from any comments regarding strong manifestation of PEGB in the form of extremely strong jet flows. Leaving aside similar strong factual evidences of dominant role of PEGB, they attempt to link received experimental data to leading role of microlayer evaporation.

Effect of ejection of liquid metal with velocity 100-150 m/s is discovered during laser drilling of nickel and copper [32]. Although the effect is linked to PEGB (to vapor bubble nucleation), this specific phenomenon requires further investigation.

Real steps toward deep and systematic study of PEGB during boiling on thin wires firstly are made in works [31, 33-34].

Various rather powerful manifestations of PEGB are observed and recorded, including phenomenon of vapor bubble departure against gravity field. Experimental investigations are performed of diverse dynamical effects including bubble specific motion on microwires. Nongravity character of the observed phenomena is confirmed. Numerical model of bubble motion and adjacent jet flows through subcooled boiling on microwires is developed.

It presents particular interest discovery of so-called multi-jet flow (in addition to single jet-flow) that calls for undertaking of certain refinement of the previous scheme of PEGB (Fig. **7**).

As it follows from additional analysis, together with the previous basic case, another limiting case of realization of PEGB should be considered.

Initial bubble growth takes place within high initial temperature gradient in liquid boundary layer. In this connection driving pressure gradient is effective on all surface of the bubble. In addition, an angle between heating wall and bubble surface still remains sufficiently large for development of two-dimensional liquid flow. These circumstances result speeding-up of individual jet flow from the top of the bubble, in full accordance to the previous scheme (Fig. **7**).

Further liquid flow evolves to another limiting case when abovementioned angle becomes too small for preservation of two-dimensional flow. Concurrently, driving gradient turns out to be concentrated only on the bottom part of the bubble surface (on interface gap between the bubble and heating wall). Liquid flow in the gap becomes three-dimensional (with alternation of the zones of liquid suction and rejection) and PEGB evolves into multi-jet flow.

It can be also assumed that certain intermediate schemes of liquid flow can be realized between the limiting cases mentioned.

The phenomenon of multi-jet flow also presents interest in the context of possible contribution of Marangoni flow in observed phenomena [35].

As distinct to PEGB, Marangoni flow is driven by surface force generated by gradient of surface tension on interface with variable temperature. However, in the case of single jet flow in symmetric bubble-surface system, both of flow schemes are roughly similar.

During boiling of saturated water directly measured and indirectly evaluated jet flow velocities vary in the range 1-5 m/s [13, 27, 31]. According review of experimental data [36] maximum velocities of steady-state (needing minimum driving force) Marangoni flow are at around 2 orders of magnitude less of aforementioned values.

Taking in account that temperature gradients are near to zero on bubble surface during saturated boiling, the conclusion should be made that observed jet flows turn out to be extremely strong to be explained by Marangoni effect. The same conclusion follows from analysis [11-25] showing much greater role of the pressure gradient caused by momentum transport by evaporation in comparison with thermocapillarity.

During boiling of subcooled liquid jet flows are much weaker (characteristic velocities 15-150 mm/s) [33]. Velocities of bubble slippage are in the range 15-40 mm/s.

Contribution of Marangoni effect evidently may be tangible at such a low velocities. Nevertheless, interpretation of dynamical effects [33, 34] by the steady-state thermo-capillary Marangoni flow model [37] should be subjected to careful approach [38].

There are two potential sources of overestimation of Marangoni flow velocities: using of very small value of accommodation coefficient (0.03) and consideration of steady-state flow. According [39] accommodation coefficient is near to unity on liquid-vapor interface. However, phase conversion may be affected by presence of non-condensable air [37].

Nevertheless, absence of concrete substantiation of accepted value makes its accuracy questionable. The more so as no consideration is made of the concentration of non-condensable air on the condensation side of the bubble interface (this circumstance evidently results overestimation of intensity of Marangoni flow along evaporation zone).

The last conclusion especially concerns multi-jet flow (so-called butterfly-like structure) [34] that just is developed along the zone of evaporation (Fig. **12**).

During boiling the zone of maximum surface tension clearly is linked to the top of a bubble.

Besides, Marangoni flow-out always is directed transversely from the zone of maximum surface tension. These circumstances call into principal question possibility of speeding-up by Marangoni effect of multi-jet flow at a tangent to bottom zone of a bubble. In this connection, one may realistically assume that launching of multi-jet flow from bottom zone of a bubble evidences prevailing role of PEGB.

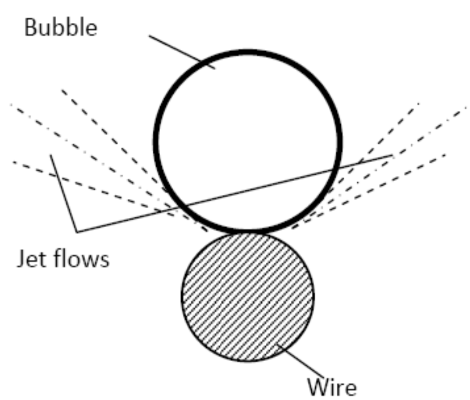

Fig. (12). Multi-jet flow during boiling of subcooled liquid on microwire [34].

Concerning the role of Marangoni flow important conclusions could have been done based at aforementioned experiments on bubbling [21, 22]. As bubbling of humid air proceeds without tangible evaporation, temperature drop on bubble surface before departure practically is equal to temperature drop between heating surface and bulk liquid.

In contrast to it, during boiling, temperature at bubble surface practically is equal to saturation temperature corresponding to the pressure in bubble itself. Only some superheat of bubble surface takes place in the zone of microlayer adjacent to heating surface. Corresponding variation of temperature along the surface of vapor bubble is small and may achieve maximum several percent of temperature drop between boiling surface and saturated bulk water.

In this connection, if variation of bubble surface temperature may be of order 10 K during bubbling, such a variation may achieve only 0.1 - 0.2 K at the same heat flux during boiling.

In such a manner, thermocapillary driving force is at around two orders of magnitude stronger during bubbling in comparison with comparable boiling process. In this connection fixed low intensity of heat transfer during air bubble growth [21] and low average HTCs during bubbling through perforated surface [22] demonstrate insignificancy of Marangoni convection in boiling heat transfer.

It also presents significant interest the role of PEGB in forced convection boiling in the microsystems. This aspect of the problem is discussed below.

Finalizing the subchapter let us discuss potential influence of PEGB on critical heat flux (CHF).

As it is known, CHF depends on intensity of mechanisms responsible for vapor phase removal from heating surface. Hydrodynamic theory of boiling crisis [40], assuming basic role of the gravity field in vapor phase removal, quite adequately describes experimental data on CHF during pool boiling of ordinary liquids.

At the same time, there is some part of pool boiling processes characterized by significantly higher values of CHF in comparison with predicted by the hydrodynamic theory.

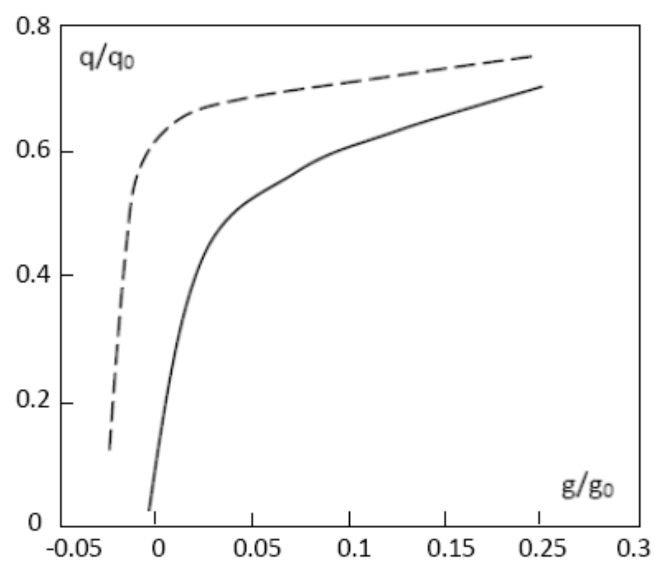

Fig. (13). Smoothed experimental curve on CHF during pool boiling of water, nitrogen and hydrogen under reduced gravity acceleration – dashed line [41]; Solid curve – according hydrodynamic theory of crisis [40].

In particular, such a lead is established during boiling of water, nitrogen, hydrogen [41] (Fig. **13**), *n*-pentane, CFC and other liquids [42, 43] in microgravity, during pool boiling of liquid metals [44] (Fig. **14**), during pool boiling of organic liquids and water under vacuum [45] (Fig. **15**).

In such a manner experimental CHFs precede theoretical ones at 300-500%. Similar result can be considered as an evidence of existence of certain rather strong nongravity mechanism of vapour phase removal from heating surface. As microgravity and low saturation pressure just are favourable for PEGB, it is supposed that just PEGB is responsible for high values of CHF [28, 29]. However, this aspect of boiling problem needs further detailed investigation.

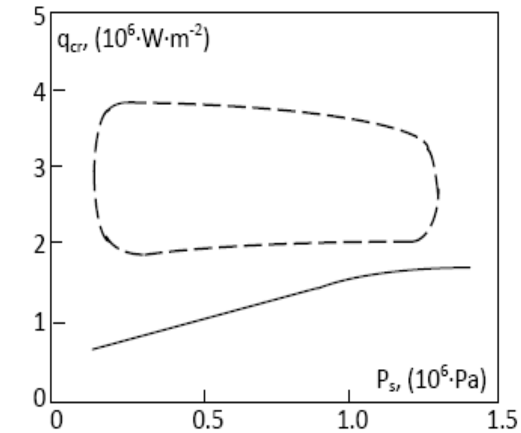

Fig. (14). Experimental data [44] on CHF during pool boiling of sodium (dotted loop); bottom curve - according hydrodynamic theory of crisis [40].

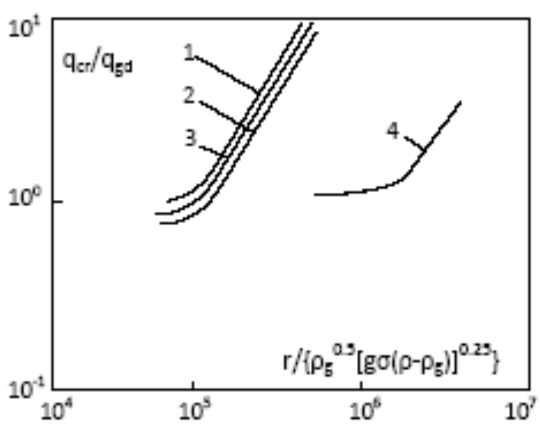

Fig. (15). Smoothed experimental curves [45] on CHF during pool boiling of dautherm-A (1), chlorbenzene (2), toluene (3), and water (4) at reduced saturation pressures; q/q_{gd} = 10^0 – according hydrodynamic theory of crisis [40].

Micro-membrane Pumping Effect

It also presents certain interest specific convective cooling mechanism linked to permanent vibration of nuclei in all potential sites, synchronously with local pulsation of heating surface temperature [11]. Such a cooling mechanism may be named as micro-membrane pumping effect (MMP).

While local temperature increases, nucleus surface (a micro-membrane) expands to critical profile, stops expansion when the nearest nuclei starts growth into the bubble with PEGB and returns to previous position when local temperature drops. Besides, in connection with quick drop of local temperature, contraction of the micro-membrane is much quicker than its expansion. Correspondingly, downward motion of the micro-membrane is much faster. The last circumstance, together with almost ideal distribution of such downward flows on heating surface, on huge number of potential sites (up to 10^3 cm^{-2}), presents important feature of MMP.

In such a manner, MMP also presents dynamical effect of nongravity nature main cooling action of which also is triggered by onset of bubble growth.

Velocity of downward motion of the micro-membrane depends on effective radius of nucleation site and on the time of local temperature drop. According preliminary evaluations, in characteristic regimes of boiling heat transfer, such a velocity may vary in rather wide range from 0.5 mm·s^{-1} to 20 mm·s^{-1}. In contrast to PEGB, cooling effect of MMP may not claim to be dominant. However, the effect deserves to be studied analytically and experimentally.

A Slope of Boiling Heat Transfer Curve

A slope of boiling heat transfer curve in coordinates $q \sim h$ or $\Delta T \sim q$ (determined by an exponent in equations of the type $h{\sim}q^n$ or $q{\sim}\Delta T_s^m$) varies in rather wide range (*n=0.5-0.9*). In the case of commercial heating surfaces this range is narrower (*n=0.65-0.75)*.

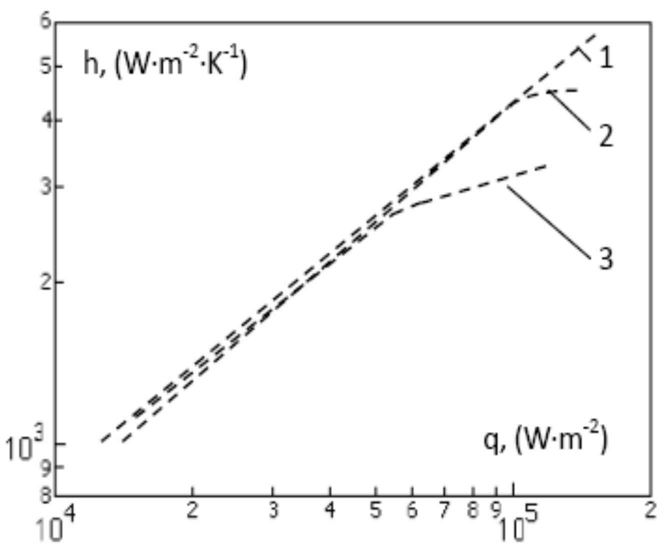

Fig. (16). Smoothed experimental curves on HTC during developed boiling of benzene at atmospheric pressure on heating surfaces with different densities of uniform big nucleation sites [46]: 1 – N/A =4·10^6m^{-2}; 2 – N/A=1·10^6m^{-2}; 3 – N/A=0.25·10^6m^{-2}.

The problem of the slope of boiling curve in certain degree is clarified in experiments [46] on boiling on heating surfaces with deferent densities of artificially created big uniform nucleation sites (Fig. **16**).

As it follows from the experimental data, at sufficient density of nucleation sites, all boiling curve equally corresponds to developed boiling with typical slope $h \sim q^{0.7}$ covered in full range by the surface with N/A=4·10^6 m^{-2} (case 1). In this case increase of heat flux evidently leads only to "switching on" of additional artificial sites with the same effective radius.

At the same time, if all artificial sites already are "switched on", further increase of heat flux may put in operation only natural sites of the basic surface. On the other hand, as activation of natural sites requires significantly higher superheat, increase of heat flux should be accompanied by tangible deviation of boiling heat transfer curve from the previous slope.

Presented data unambiguously reflect dependence of the slope of boiling curve on density and sizes of nucleation sites. Typical for majority of experiments slope turns out to be linked to heating surface with great number of nucleation sites with roughly uniform effective radius*.

Presented conclusions are supported by important experimental data [47] on sizes and distribution of operating natural nucleation sites studied through immediate optical observation of boiling process on heating surfaces with different finish classes (with standard roughness parameter R_p from 0.1 to 0.4 μm).

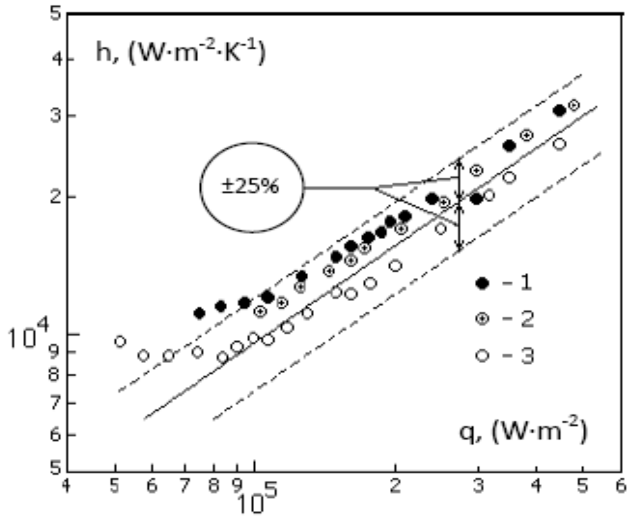

Fig. (17). Heat transfer during developed boiling of water at atmospheric pressure on heating surfaces with different finish classes [47] (1 – R_p=0.4 μm; 2 - R_p=0.125 μm; 3 - R_p=0.1 μm).

According Fig. (**17**), despite fourfold variation of the standard roughness parameter, the experimental data correspond to known empirical equation for boiling heat transfer of water on commercial surfaces at atmospheric pressure *($h = 3{,}14 \cdot q^{0.7}$)* within usual accuracy of measurement of boiling HTC.

Distribution of effective sizes of operating nucleation sites also shows insignificant stratification with surface finish classes. Besides, nucleation sites are almost at two orders of magnitude bigger than the standard roughness parameter (Fig. **18**).

Observed radii of nucleation sites vary within rather narrow limits from 3 to 10 μm (with comparatively great share of small sites) revealing absence of immediate linkage to standard roughness parameter. In certain approximation the value 5 μm can be accepted as average radius of nucleation sites. It also should stressed that practical independence of HTC on the standard roughness parameter during its fourfold variation demonstrates principal problems with using of similar parameter for evaluation of the role of heating surface in boiling heat transfer.

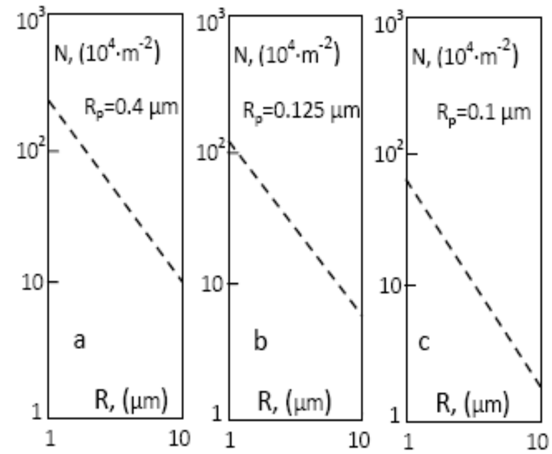

Fig. (18). Smoothed experimental distributions of radii of nucleation sites at different heat fluxes on surfaces with different finish classes [47]: **a:** q =1.67·10^5 Wm^{-2}; q =1.2·10^5 Wm^{-2}; q =0.89·10^5 Wm^{-2}; **b:** q =1.2·10^5 Wm^{-2}; q =1.13·10^5 Wm^{-2}; q =0.93·10^5 Wm^{-2}; **c:** q =1.31·10^5 Wm^{-2}; q =1.14·10^5 Wm^{-2}; q =0.92·10^5 Wm^{-2}.

In this context these results fully confirm the model [20] linking HTC to average effective radius of nucleation sites. This aspect of the problem is discussed below. At the same time coincidence of experimental data on HTC with known data on developed boiling of water on commercial surfaces supports the previous assumption [20] about rough equality of average effective radius of nucleation sites of commercial surfaces to 5 μm.

Two Basic Features of Developed Boiling Heat Transfer

According our analysis the most important features of developed boiling heat transfer are the following:

- Independence of superheat of heating surface on intensities of separate cooling mechanisms;
- Simultaneous triggering by the onset of a vapor bubble growth of the main cooling mechanisms (by liquid phase convection and microlayer evaporation).

Experimental fundamentals of such a conclusion are discussed below.

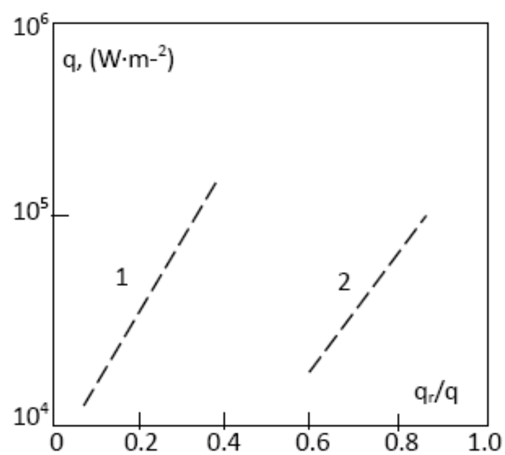

Fig. (19). Contribution of immediate evaporation and liquid phase convection mechanisms with variation of acceleration of a body force according smoothed experimental curves [48]: 1 - g/g_0 = 1; 2 - g/g_0= 0.03-0.04.

*As it was established later, the procedure of determination of effective radius of conical artificial site [46] has led to roughly fourfold overestimation of this parameter. However, this disadvantage had no influence on uniformity of artificial sites.

Presented in Fig. (**19**) experimental data [48] reflect qualitative redistribution of the shares of immediate evaporation and liquid phase convection cooling mechanisms with variation of intensity of a body force. In particular, evaporation mechanism, playing secondary role at normal gravity, gains leading role with reduction of g around 20 times.

In contrast to it, presented in Fig. (**20**) experimental data [49]) reflect independence of HTC from variation of intensity of body force at around four orders of magnitude. Similar results are received also in [50-52] carried out in the range of variation of mass acceleration from $10^{-6}g_0$ to $5{\cdot}10^3 g_0$ (almost 10 orders of magnitude).

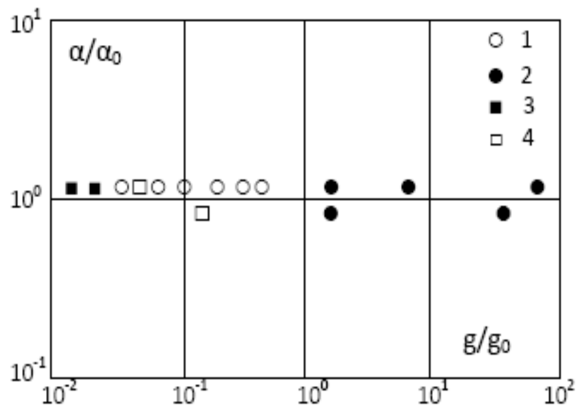

Fig. (20). Boiling HTC under different intensities of a gravity force normalized to normal gravity condition [49]: 1 – oxygen; 2 – water; 3 – ethanol; 4 – ethyl ether.

Presented in Fig. (**21**) scattering range of experimental data [52] reflects independence of HTC during boiling of CF-72 on small heaters on variation of acceleration of body force in the range $0.02g_0$ – $1.8g_0$ and on variation of subcooling of a liquid in the range 7K - 34 K.

Presented in Fig. (**22**) heat transfer curves reflect regularities of forced convection boiling on horizontal tube in the conditions of crossflow of slightly subcooled R113 [53].

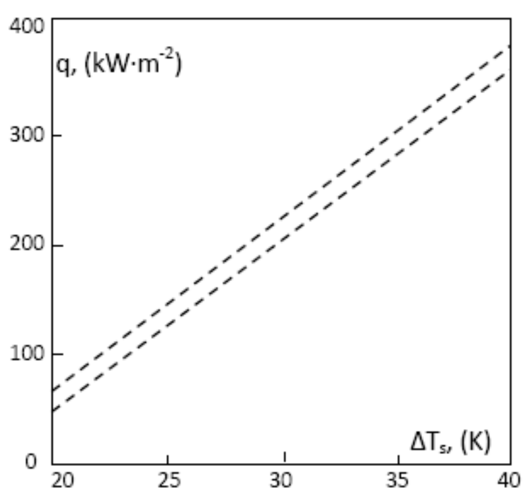

Fig. (21). Scattering range of HTC during pool boiling of CF-72 on small heaters under subcooling (in the range 7-34 K) and different gravity accelerations (in the range $0.02{\cdot}g_0 – 1.8{\cdot}g_0$) [52].

Forced convection heat transfer curve always comes together with developed pool boiling curve with the climb of heat flux. At that crossflow velocity (0.03 – 0.235 m/s) and the degree of subcooling (6 K) influence only parameters of merger of the forced convection boiling curve with the developed boiling curve. The same conclusion is made in generalized description of forced convection boiling in [54].

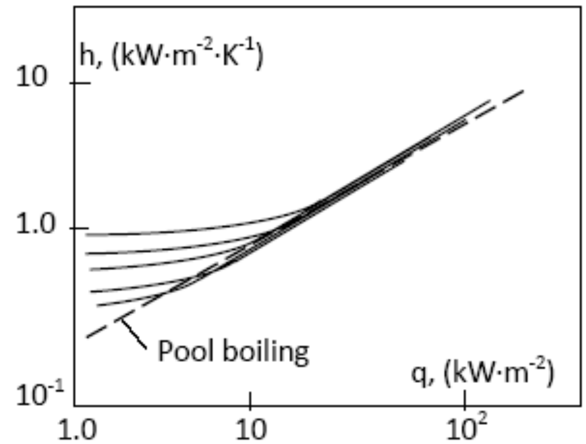

Fig. (22). Smoothed experimental curves on forced crossflow boiling on horizontal tube of slightly subcooled R113 [53]: upper curves correspond to higher crossflow velocities.

Experimental data on influence of orientation of heating surface in the gravity field on boiling heat transfer of water [55] are presented in Fig. (**23**).

As it follows from presented data developed boiling mode is conservative regarding to this type of influence as well. Similar results are received also in detailed study [56] (in this work, corresponding figures are plotted using HTC determined through ΔT).

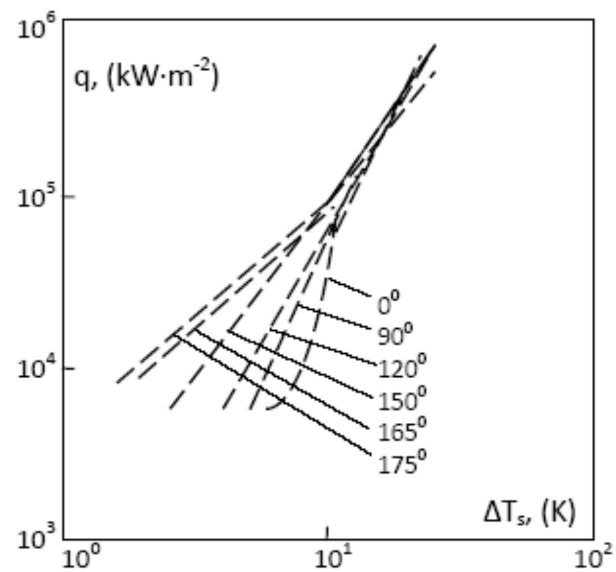

Fig. (23). Influence of inclination of heating surface on boiling heat transfer of water at atmospheric pressure. (smoothed experimental curves) [55].

The same conservatism of developed boiling heat transfer law manifests itself in the part of experiments on flow boiling in minichannels and microchannels. However, the results of some similar experiments show qualitatively differing trends. In this context it also presents significant interest coincidence of experimental curves on boiling of water on massive copper surface [47] and on thin platinum wire with diameter 0.3 mm [57] at atmospheric pressure.

Discussed above peculiarities of boiling on thin wires allow to conclude that these two processes are characterized by qualitatively differing inter-phase hydrodynamics. If in the case of massive horizontal copper surface gravity force is main driver of two-phase flow, in the case of thin wire leading role in vapor removal from heating surface is gained by nongravity dynamical effects. Despite such a drastic dissimilarity of these boiling regimes, unified developed boiling heat transfer law equally remains in force in the both cases.

In such a manner, changes in the pattern of mutual motion of the phases, in the numbers of operating sites and in the bubble departure diameters and frequencies, occurring with a change in the intensity of body force by several orders of magnitude, with change of orientation of heating surface in the gravity field, with forced convection and subcooling of bulk liquid, with drastic change of heating surface sizes, all of these conditions have virtually no influence on heating surface superheat in the mode of developed boiling.

According to our analysis this fundamental fact may be interpreted only assuming existence of certain physical mechanism that controls developed boiling heat transfer through multiple triggering of short-run actions of different heat removal mechanisms and holds certain integral cooling effect irrespective to the rates of these mechanisms.

The next in importance basic feature of developed boiling heat transfer is simultaneous triggering of the both liquid phase convection (PEGB) and microlayer evaporation mechanisms by the onset of vapor bubble growth. Although the same onset also triggers another cooling mechanism (MMP), in connection with a lack of detailed information, we shell keep it in store for the time being.

The onset of bubble growth itself is triggered by overcoming by average temperature of the meniscus of critical-size nucleus the level corresponding to thermodynamic equilibrium in the system: nucleus-liquid-site. Consequently, the process of establishment of corresponding superheat of heating surface just presents the mechanism that controls intensity of developed boiling heat transfer.

MTA AND MTD

Beginning from Jakob [6], Kruzhilin [58] and Rohsenow [59] and further [60-73] main line of development of boiling heat transfer theory is based at approaches connecting HTC to intensity of certain cooling mechanism (an actor) or certain combination of different cooling mechanisms (actors). In this connection these approaches are subsumed under the category dubbed as a model of “the theatre of actors" (MTA). Besides, approaches based at qualitative and dimensional analysis linked to concrete mechanisms also are prescribed to this category.

Principal Restrictions of MTA

MTA presents efficient universally adopted way of analysis in convection heat transfer theory. However, developed boiling heat transfer manifests exceptionally specific sequence of causes and effects.

In the framework of MTA heating surface superheat is determined by intensity of cooling mechanisms. Really maximum local superheat is found to be determined by thermodynamic conditions at transition of a nucleus through critical size at the onset of bubble growth.

In the framework of MTA so-called internal characteristics of boiling (densities of operating sites and bubble departure diameters and frequencies) naturally become main instrument for determining of temperature regime. In real situation combination of these parameters also turns out to be controlled by thermodynamic conditions at nucleation sites in correspondence with temperature regime to be hold.

Evident contradiction of MTA with the aforementioned basic feature of developed boiling heat transfer calls into principal question efficiency of MTA in terms of establishment of boiling heat transfer law.

According [1-2], among numerous MTA-based correlations, two correlations can be regarded as more accurate. Besides, these correlations fit to boiling HTC data (except liquid metals and cryogenic liquids) using different constants and powers for different surface-liquid combinations. The review [3] regards as the most comprehensive a correlation [67] dividing liquids into four groups (liquid metals once again remain outside of correlation).

At the same time reviews [1-3] fail to discuss a correlation [20, 28-29, 74-76] describing wide experimental data on developed boiling of all groups of liquids, including liquid metals, without dividing of liquids into groups and without matching different constants and powers to different surface-liquid combinations.

Given in reviews [1-3] evaluations of advances of MTA quite clearly demonstrate existence of theoretical deadlock. However, in this context, it presents certain interest discussion of some concrete disadvantages of MTA.

As bubbling and microlayer evaporation directly are linked to buoyancy driven convection in two-phase area, it is hardly achievable in the framework of MTA to get free in correct way from influence of body force on HTC. This conclusion especially concerns the models introducing vertically driven two-phase structures as the basis for analysis of boiling heat transfer [59, 63-65, 67, 70-72].

If HTC is determined by interactions on boundaries and inside such a structures, it is hardly explicable why heating surface superheat during developed boiling remains unchangeable through essential transformation or even with full disappearance of these structures (for instance, through change of gravity acceleration at several orders of magnitude or under deep subcooling).

The problem of adequate reflection of the role of gravity field also remains pressing in the case of qualitative dimensional considerations.

For instance, aforementioned correlations for four groups of liquids [67] are developed through regression analysis applied to numerous data points on HTC. The analysis starts from more than 10 dimensionless numbers obtained in the framework of MTA. Finally the following dependences of HTC on gravity acceleration are obtained for separate groups of liquids:

$h \approx g^{0.483}$ (for water)

$h \approx g^{-0.085}$ (for hydrocarbons)

$h \approx g^{-0.515}$ (for cryogens)

$h \approx g^{0.033}$ (for refrigerants)

Similar qualitatively differing dependences hardly allow to considering abovementioned approach as linked to physics of studied phenomenon.

Principal disadvantage of microlayer evaporation version of MTA is connected with contradiction between independence of HTC on thermal parameters of heating surface during developed boiling and aforementioned conclusion about significant influence of thermal conductivity of heating surface on average HTC during microlayer evaporation (by the way, this conclusion is supported by numerical MTA-based models of boiling heat transfer [70, 73]) developed based at assumption on leading role of micro and macrolayer evaporation mechanisms.

In general, comprehensive approach to boiling heat transfer problem should allow to interpreting independence of HTC on thermal parameters of heating surface during developed boiling and reality of influence of the same parameters in some other regimes. The same conclusion concerns the phenomenon of boiling heat transfer hysteresis that also is observed only in the part of experiments. No MTA-based approach meets these challenges.

Another disadvantage of MTA is connected with principal difficulties with incorporation of characteristic linear size of nucleation sites. In this connection MTA turns to be incapable to make use of wide investigations in the physics of nucleation.

As average effective size of nucleation sites strongly influences HTC (within an order of magnitude, all other things remain the same), failure to take account of such a crucial factor excludes possibility of adequate description of the process in principle. It also should be stressed that establishment of adequate set of dimensionless numbers without incorporation of the same characteristic size also is impossible in principle.

MTD and MTD-Based Analysis

Aforementioned main features of developed boiling actually predetermine alternative approach to the problem through assuming existence of certain mechanism controlling developed boiling heat transfer. This mechanism holds given average HTC by multiple triggering of short-run actions of different cooling mechanisms irrespective to variations of the rates of these mechanisms.

At that bubble growth onset is a trigger of main cooling mechanisms. The onset itself is triggered by overcoming by average temperature at the meniscus of critical size the temperature of thermodynamic equilibrium in the nucleus-liquid-site system.

Corresponding model of "the theatre of director" (MTD) [8, 20, 28-29, 74-76] incorporates one-parameter model of boiling surface with unlimited number of identical stable nucleation sites. Besides, these sites are characterized by unchangeable level of superheat triggering growth of the first and following bubbles.

The role of such a site may be played by conical recess satisfying the condition:

$$\frac{1}{2}\beta < \theta < 90^0 \qquad (2)$$

In the similar site minimum curvature radius of the nucleus (effective radius of a site ρ_0) is equal to the radius of the mouth of the recess [77] (Fig. **24**). Besides, cylindrical recess or the recess with narrowed mouth corresponds to this requirement even at zero contact angle.

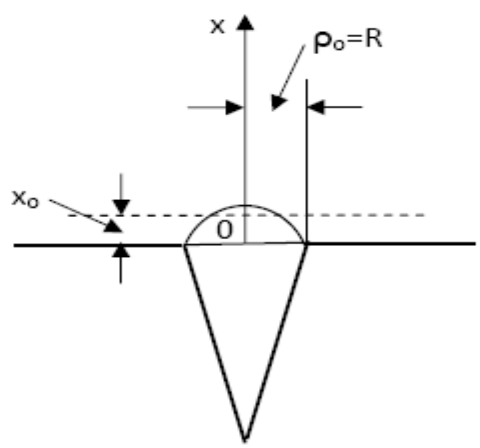

Fig. (24). A scheme of the zone of nucleation site.

To the first approximation, local temperature variation can be approximated by the curve presupposing instantaneous drop in the wall temperature down to the saturation temperature at the onset of bubble growth (instantaneous start-up and shut-down of very intensive heat removal mechanism) and further warming-up of the wall through heat conduction up to the moment of onset of the next bubble growth (Fig. **25**).

The superheat ΔT_{eq} necessary for bubble growth onset should be achieved at the meniscus of the nucleus in average. As critical nucleus is in the zone of temperature gradient concomitant heating surface superheat $\Delta T^!$ is much above ΔT_{eq}. Corresponding unsteady-state process is considered as warming-up of initially isothermal liquid semi-infinite region (with initial temperature equal to T_s) through transient heat conduction at suddenly posed boundary condition q = Const

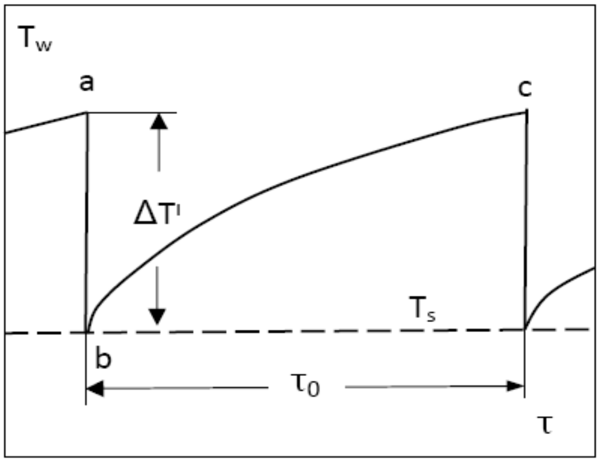

Fig. (25). The first approximation.

(nucleus growth in superheated layer is studied also in [78]). The superheat ΔT_{eq} is determined by the relationship [77]:

$$\Delta T_{eq} = \frac{2\sigma T_s}{r\rho_0\rho_g} \tag{3}$$

General solution of the problem [79] leads to the following equation:

$$T(x,\tau) - T_s = \frac{2q}{\lambda}\sqrt{\alpha\tau ierfc\frac{x}{2\sqrt{\alpha\tau}}} \tag{4}$$

The mean superheat of heating surface accordingly is equal:

$$\Delta T = \frac{1}{\tau_0}\int_0^{\tau^*}\left[T(0,\tau) - T_s\right]d\tau = \frac{2}{3\sqrt{\pi}}\frac{q}{k}\sqrt{\alpha\tau^*} \tag{5}$$

Written out in non-dimensional form this equation is:

$$Nu = \frac{3\sqrt{\pi}}{2}\frac{\rho_0}{2\sqrt{\alpha\tau^*}}, \tag{6}$$

where:

$$Nu = \frac{h\rho_0}{k} \tag{7}$$

The time of climb of heating surface temperature τ_0 is the same as the time of attainment by certain section x_0 of the meniscus of nuclei of superheat equal to ΔT_{eq}. Taking in account $x_0 \sim \rho_0$, the following relationship is acquired:

$$\frac{\rho_0}{2\sqrt{at}}\frac{1}{ierfc\frac{\rho_0}{2\sqrt{at}}} = \frac{K}{2}, \tag{8}$$

where:

$$K = \frac{q\rho_0^2 r\rho_g}{\sigma k T_s} \tag{9}$$

The results predicted by equations (6) and (8) are shown in Fig. (**26**) in the coordinates $Nu = f(K)$. Experimental data on HTC during developed boiling of water [80], nitrogen [81] and sodium [82] on commercial surfaces at atmospheric pressure also are plotted (assuming uniform value $\rho_0 \approx 5$ μm).

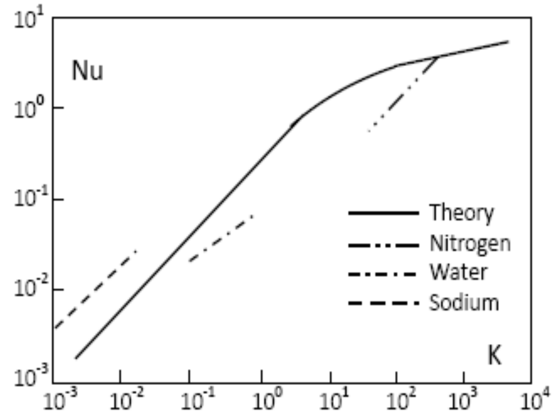

Fig. (26). Comparison of equations (6) and (8) with smoothed experimental curves on boiling at atmospheric pressure: nitrogen [81], water [80] and sodium [82].

Analytical prediction of the order of HTC for greatly differing liquids may be considered as certain support of validity of qualitative basics of MTD. Important outcome of the solution is uncovering of the role of effective radius as characteristic linear size of developed boiling heat transfer. It is important also outlining of the role of the number K. Uncovering of the role of ρ_0 stresses incompleteness of overwhelming majority of experimental studies of boiling heat transfer. Only exclusive studies have been accompanied by investigation of characteristics of nucleation sites.

Further the theory is refined making emphasis on peculiarities of heat transfer on periphery of action zone of operating nucleation site.

Superheat at the periphery of the action zone makes major contribution to average superheat of the whole zone and to average superheat of heating surface, as a whole. In the framework of MTD and one-parameter model of heating surface the action zone is determined by capability of firstly activated nucleation site to prevent by own cooling effect activation of adjacent potential sites. If the zone of influence of operating site reduces, additional site or sites with the same ρ_0 turn on operation on the periphery (and vice versa).

In such a manner the "director" holds unchangeable level of superheat just at the periphery of action zone. At that the number of operating sites automatically varies meeting this basic condition. The range of variation of the number may be quite wide, for instance, during significant change of mass acceleration.

Self-control of the number of operating sites depending on cooling effect of separate sites presents a basis for applying to boiling of a theory of self-organized structures [83]. Thereby experimental "discovery of self-organized and cooperative or competitive phenomena among sites or bubbles in boiling systems" [84] presents direct support of MTD. Besides, boiling HTC enhancement through creation of great number of large-sized nucleation sites, regarded as the main pragmatic finding

[83-84], directly was predicted by equations (6) and (8) and by the correlation (16).

Another important peculiarity is decisive role, at the periphery of action zone, of liquid convection always possessing some inertia. Correspondingly, cooling effect may not be shutdown instantly.

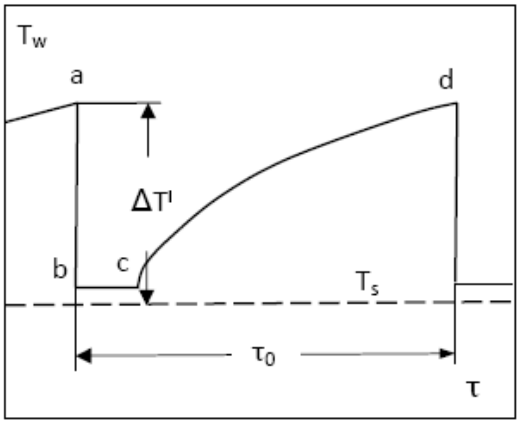

Fig. (27). Approximated temperature behaviour in peripheral zone.

Behavior of heating surface temperature on the periphery can be approximated by the curve presented in Fig. (**27**). The action of cooling mechanisms is represented by broken curve abc the equivalence of which to the real process can be ensured by suitably selected value of τ_1. Surface superheat in this period is considered to be small and its role in the time-average superheating is neglected.

Segment cd characterizes the same warming-up of initially isothermal liquid semi-infinite region. In this case the maximum superheat remains insignificantly less than $\Delta T^!$ and can be equated to it. Accordingly, functional relationship for Nusselt number can be widened through introduction of the ratio τ_1/τ_0:

$$Nu = f(K, \tau_1 / \tau_0) \tag{10}$$

The ratio τ_1/τ_0 is determined by viscous dissipation of kinetic energy of liquid motion continuing by inertia. It is, therefore, the function of appropriately specified Reynolds number. Accordingly, equation (10) will acquire the form:

$$Nu = f(K, \mathrm{Re}) \tag{11}$$

Certain assumptions also are made on characteristic liquid velocity and characteristic dynamical linear size. Considering a work of expansion as a driver of all dynamical effects, characteristic velocity is evaluated as proportional to square root from the specific work of expansion:

$$U \sim C_1\sqrt{P(v_g - v)}\,, \tag{12}$$

where C_1 is much below of unity.

Characteristic for two-phase hydrodynamics linear size is evaluated for the end of the first stage of bubble growth (to say, to the end of the period of maximum dynamical influence of growing bubble).

As a result following evaluation is derived with the kernel firstly obtained in [58]:

$$l \sim \frac{\sigma T_s \rho C_p}{\left(\rho_g r\right)^2} f_1(K) \tag{13}$$

Accordingly, Reynolds number is equal:

$$\mathrm{Re} = \frac{\sqrt{P(v_g - v)}C_p\sigma\rho T_s}{(r\rho_g)^2 \nu} f_1(K) = \mathrm{Re}_* \, f_1(K), \tag{14}$$

where modified Reynolds number comprises only physical parameters of boiling area:

$$\mathrm{Re}_* = \frac{\sqrt{P(v_g - v)}C_p\rho T_s}{(r\rho_g)^2 \nu} \tag{15}$$

Finally, through comparison with experimental data, relationship (11) acquires following form [20]:

$$Nu = 1.22 \cdot 10^{-2} K^{0.7}\, \mathrm{Re}_*^{\,0.25} \tag{16}$$

It also should be mentioned that equation (15) for modified Reynolds number could be presented in more simple form, taking in account that specific work of expansion roughly always is equal to one tenth of specific heat of evaporation. In such a case simplified Reynolds number may be written in following form:

$$\mathrm{Re}_{*,s} = \frac{C_p\sigma\rho T_s}{r^{3/2}\rho_g^2 \nu} \tag{17}$$

Accordingly, equation (16) can be transformed to the following form:

$$Nu = 0.88 \cdot 10^{-2} K^{0.7}\, \mathrm{Re}_{*,s}^{\,0.25} \tag{18}$$

In contrast to equation (16), no dependence of HTC on saturation pressure remains in actually the same equation (16). Thereby the fact is reflected that, in equation (18), specific work of expansion in reality represents specific heat of evaporation. Besides, as according (18) $Nu \sim [P(v_g-v)]^{1/8}$, calculation error connected with approximation $P(v_g-v) \approx 0.1r$ is quite insignificant. By the way, in [20] just the form (18) of the correlation is presented.

CORRELATION OF EXPERIMENTAL DATA

Longstanding disregard of the role of effective radii of nucleation sites has led to essential incompleteness of experimental studies mainly performed without investigation of nucleation sites. In addition, absence of direct dependence of effective radius on standard roughness parameters makes unfeasible attempts to using these parameters for characterization of influence of boiling surface on HTC.

Only very small part of numerous experimental works includes data on sizes and geometry of nucleation sites. It may be assessed as fortunate exclusion the work [47] including measurement of sizes and distribution of operating sites.

At the same time, in certain degree, the situation is mitigated by using in many experiments on boiling heat transfer of commercial heating surfaces (mainly rolled tubes) roughly corresponding to one-parameter model of boiling surface.

Correlation of Experimental Data on HTC on Heating Surfaces with Known ρ_0

Fortunately, a small number of comprehensive experiments including the values of effective radii covers greatly differing boiling areas and materials of heating surfaces [47, 85-86].

Boiling of water [47] is carried out on copper surfaces with average effective radius of operating nucleation sites roughly equal to 5 μm. Boiling of sodium [85] is studied on stainless steel surface with uniform, rather big (ρ_0=50μm) stable artificial sites. Boiling of refrigerants [86] is studied on steel surface with big uniform artificial nucleation sites with effective radius equal to 86μm.

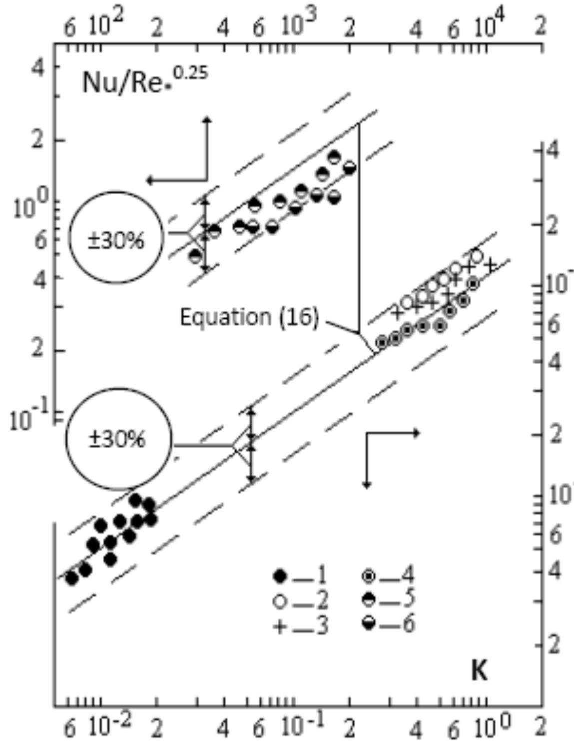

Fig. (28). Comparison of equation.(16) with experimental data on developed boiling on the surfaces with the known values of ρ_0: 1 – sodium [85], ρ_0 = 50 μm; 2-4 – water [47], ρ_0 = 5 μm; 5 – R 12 [86], ρ_0 = 86 μm; 6 - R 22 [86], ρ_0 = 86 μm.

Correlation of experimental data is presented in Fig. (**28**). The correlation reflects support of MTD by the most comprehensive experimental data. Below we should return to (Fig. **28**) in regard to the problem of enhancement of boiling heat transfer.

Correlation of Experimental Data on Developed Boiling on Commercial Surfaces

Based at some indirect evidences, commercial heating surfaces have been characterized by the average effective radius of nucleation sites equal to 5 μm [20]. This assumption is confirmed by experimental data on characteristics of operating nucleation sites [47].

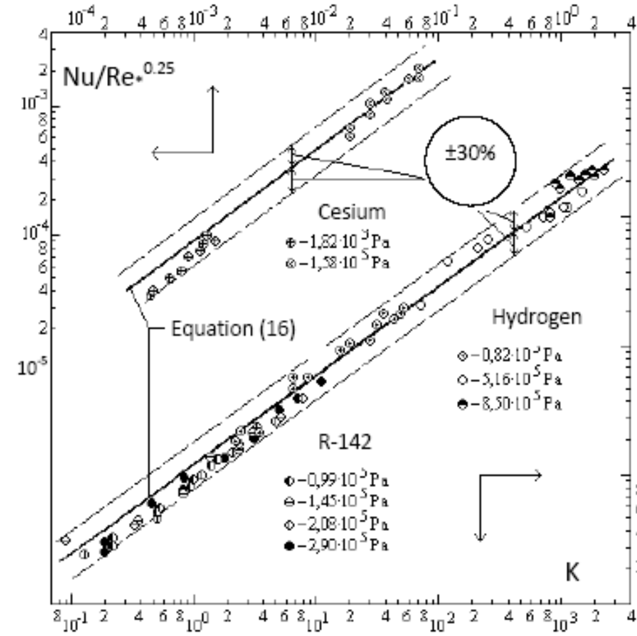

Fig. (29). Correlation of experimental data on developed boiling of cesium [87], R 142 [88] and hydrogen [89] on commercial surfaces (ρ_0= 5 μm).

In Fig. (**29**), as an example, correlation of experimental data on boiling on commercial surfaces of the most "inconvenient" liquids (liquid metals, refrigerants and cryogens) is presented.

Correlation of the data on HTC during boiling of ammonia and five refrigerants on the same heating surface (platinum wire with diameter 0.3 mm) under different saturation pressures [57, 90] is presented in the Fig. (**30**). The wire is considered as commercial surface.

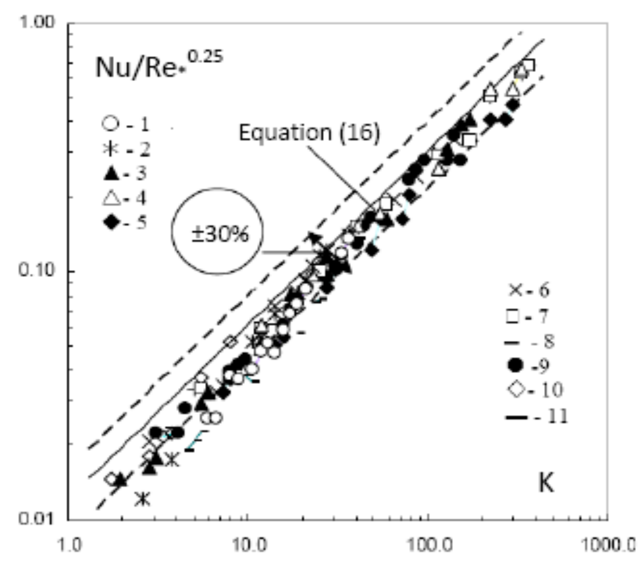

Fig. (30). Correlation of experimental data on developed boiling of 6 different liquids on thin platinum wire: [57]: Ammonia: 1 - 4-10^5 Pa; 2 - 7-10^5 Pa; [90]: R11: 3 - 4-10^5 Pa; 4 - 7-10^5 Pa; R12: 5 - 4-10^5 Pa; R22: 6 - 4-10^5 Pa; 7 - 7-10^5 Pa; R113: 8 – 2.5-10^5 Pa; 9 - 4-10^5 Pa; R134a: 10 – 2,5-10^5 Pa; 11 - 4-10^5 Pa.

Important outcome of the correlation is arrangement of all experimental data along the same unified heat transfer curve. The experimental data (related to the mode of developed boiling) corresponds to equation (16) with accuracy ± 30%.

It also should be noted that accepted value of ρ_0 is only rather well-taken rough approximation. Really this parameter may vary in certain limits even on commercial surfaces causing additional undefined error. For instance, accuracy of the correlation presented in Fig. (**30**) can be improved up to ± 15% using another value of effective radius ($\rho_0 \approx 3$ μm).

Equation (16) evidently has certain reserve of improvement of accuracy calling for detailed knowledge of nucleation sites. Heretofore we have to limit ourselves by rough evaluation of all commercial surfaces by uniform value of effective radius ($\rho_0 = 5$ μm). Thereby we avoid using of the existing uncertainty for fitting of experimental data to the recommended relationship.

Equation (16) correlates wide experimental data on developed boiling heat transfer of all groups of liquids including liquid metals and cryogenic liquids without matching different constants and powers to different surface-liquid combinations.

In particular, the correlation involves experimental data on boiling HTC of water [80], R 12 [88], R 22 [88], R 142 [88], ethyl alcohol [91], benzene [92], biphenyl [92], sodium [93], cesium [87], potassium [82], mercury [94], CO [95], NO [95], BF_3 [95], ethane [96], ethylene [96], nitrogen [81, 95], neon [89], hydrogen [89] and others. The results of correlations, as a whole, should be considered as a demonstration of fundamental character of MTD.

At the same time, unfortunately, MTD and universal MTD-based correlation more than four decades remain suppressed. Following from these works potential research lines also are left aside consideration. In contrast to it numerous correlations are developed for separate groups of liquids.

Enhancement of Boiling Heat Transfer

The line of development of high-efficient boiling surfaces presents a fortunate exception in the context of realization of MTD.

The one-parameter model and correlation (16) determine the basic principle of boiling heat transfer enhancement through creation of numerous high-sized stable artificial nucleation sites with minimum worsening of thermal conductance of boiling surface.

The correlation (16) firstly establishes boiling heat transfer enhancement law ($h \sim \rho_0^{0.4}$) quantitatively predicting achievable results.

During last decades enhanced boiling surfaces have been designed in one-to-one correspondence with this principle. In this context it is reasonable to return to discussion of correlation of experimental data presented in Fig. (**28**).

Main part of these experiments just is targeted at heat transfer enhancement. Simultaneously they quantitatively verify predicted by equation (16) heat transfer enhancement law. Real enhancement factors, as compared with commercial surfaces, in these experiments achieve around 3 in the case of refrigerants and 2.5 in the case of sodium, in full accordance with equation (16).

At the same time sensible worsening of thermal conductance of boiling surface not always may be avoided. For instance, creation of porous layers always is connected with increase of thermal resistance of heating surface. Besides, negative role of additional thermal resistance becomes more tangible with increase of heat flux. This is why in experiments on enhanced boiling surfaces (for instance, [97, 98]) heat transfer enhancement factor reduces at high fluxes.

In this context the principle of minimum worsening of thermal conductance of heating surface through creation of artificial sites still remains topical through development of enhanced boiling surfaces.

MTD AND MFC

As it follows from above correlations, developed boiling represents the most conservative basic regime of boiling heat transfer characterized by dependence of HTC on restricted number of influencing factors. Besides, even inter-phase hydrodynamics and geometry (except of the micro-level) have no influence on HTC.

According equation (18), together with physical parameters of boiling area, developed boiling HTC depends only on two "external" factors - heat flux and average effective radius.

As it follows from corresponding analysis, such a conservatism of developed boiling heat transfer can be linked to following three conditions:

- Existence of great (practically unlimited) number of stable nucleation sites with roughly uniform effective radii irrespective are they operating or potential;
- Short duration of each action of any cooling mechanism;
- Prevailing contribution of heat removal by liquid phase convection.

In the context of presented conditions more concrete and narrower definition of the term “developed boiling” can be offered, just restricted by boiling processes corresponding to these conditions.

According to multifactoring concept (MFC) [76] any failure to meet these conditions results essential transformation of heat transfer regularities up to drastic increase of the number of influencing HTC factors.

For instance, depending on concrete conditions, the circle of influencing HTC factors may be widened by parameters of inter-phase hydrodynamics, intensity of body force, contact angle, subcooling, sizes, form, orientation and thermal characteristics of heating surface, micro-geometry and distribution of nucleation sites, and prehistory of the process. Besides, multifactoring may be accompanied by "passing on the baton" from MTD to MTA.

Multifactoring, in such a manner, exhibits some characteristics of critical transition from developed boiling to qualitatively differing boiling regimes. As it follows from qualitative consideration, there can be distinguished two main types of multifactoring:

- The first – connected with onset of dependence of effective radius on a degree of penetration of liquid into nucleation site (wetting-dependent multifactoring),
- The second – connected with transition to prolonged duration or uninterrupted regime of action of any intensive cooling mechanism (duration-dependent multifactoring).

Wetting-Dependent Multifactoring

Wetting-dependent multifactoring occurs in the case $\beta/2 > \vartheta$ when effective radius of nucleation site stops to be a constant equal to the radius of the mouth of the recess.

Immediate transition from developed boiling to this type of multifactoring may be observed only in boiling system with reducing in time contact angle. In the majority of cases developed boiling and wetting-dependent multifactorous boiling of the same liquid may be observed only in separate systems. Dependence of effective radius on a degree of wetting of nucleation site by liquid phase in the case mentioned is presented in Fig. (**31**).

As it can be shown through simple analysis, in this case effective radius of the site may be determined by following relationship:

$$\rho_0 = \frac{R}{\cos(\beta/2-\theta)}(1-l/L) \tag{19}$$

As it follows from equation (19), effective radius undergoes wide-ranging variation with penetration of liquid into site. Besides, ρ_0 may be not only much less of R but even greater than R (in the case $l<<L$).

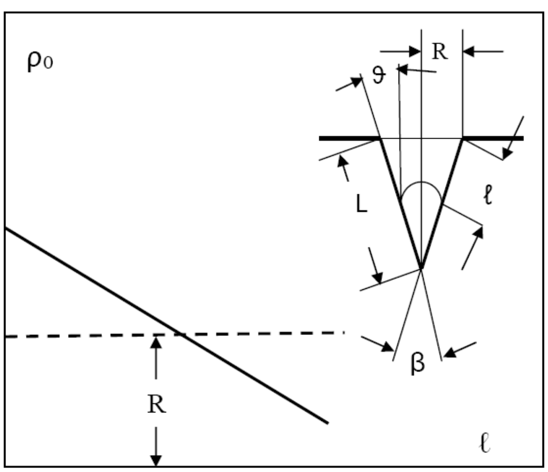

Fig. (31). Dependence of effective radius on a degree of wetting of nucleation site by liquid phase in the case $\beta/2 > \theta$.

As it is shown in [99], conditions of bubble growth onset in operating sites qualitatively differ from potential sites. As transverse size is much smaller far down from the mouth, the first onset of bubble growth in a potential site requires much higher superheat than onset of any subsequent bubble growth. In such a situation the transition of potential site to active condition and vice versa can occur only at markedly different superheats, which in fact is the basis of the hysteresis phenomenon.

Wetting of the site, in general, represents dynamical process depending on velocity and duration of wetting. These parameters, for its part, may be influenced by contact angle, heat flux, prehistory of the process, capability of heating surface to concentrate heat in the zone of wetting meniscus. If wetting length l is small, two highly differing levels of the parameter ρ_0 take place, the one of order of the radius of the mouth in operating sites and the other, very low one, in potential sites.

Corresponding so-called two-parameter model of boiling surface [74, 99] turns to be fruitful through interpreting specific families of heat transfer curves obtained in experiments on boiling of helium [100] (Fig. **32**).

Vertical line 1 corresponds to simultaneous initiation of potential nucleation sites with very small nuclei deepened in the surface (ρ_0=ρ_{min}) (in this case temperature gradient is negligible in nucleus zone).

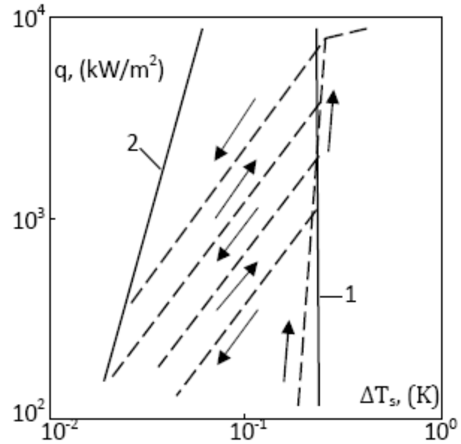

Fig. (32). Smoothed experimental boiling heat transfer curves for helium [100]: 1 - according equation (2), ρ_0=ρ_{min}=0.01 μm; 2 – according equation (16), ρ_0=ρ_{max} =20 μm.

Inclined line 2 corresponds to developed boiling according to the equation (16) for $\rho_0 = \rho_{max}$. Development of the process of boiling in the region of the line 1 is accompanied by steep increase in the number of active nucleation sites. Besides, in the context of aforementioned conclusion, decrease of heat flux at any point of line 1 cannot lead to reduction of the number of operating nucleation sites in the rather wide range of variation of superheat.

In view of this, for any change in heat flux, the process should follow along the lines between the boundaries 1 and 2 without variation in the number of operating sites. By this means a prehistory of the process (degree of climb along line 1) predetermines the boiling curve that may be realized between boundaries 1 and 2.

It also should be noted that the last comparison has qualitative character, since the actual values of ρ_{max} and ρ_{min} are unknown and have been selected on the condition of the best fit to experimental results (ρ_{min}=0.01μm; ρ_{max}=20μm).

Differing situation is to be observed on the heating surface providing stable and uniform effective radii of operating and potential sites even in the case $\theta = 0$. According MTD-MFC such a heating surface should not exhibit boiling heat transfer hysteresis.

This conclusion can be illustrated by experimental data [89] on boiling heat transfer hysteresis manifesting itself vastly on rough surfaces and virtually absent on polished ones.

As it follows from experimental data [47], effective radii of recesses survived through polishing of cooper surface are almost at two orders of magnitude larger than standard roughness parameter of the same surface. Consequently, during the polishing process only the mouths of the recesses are polished and contracted that provides stable equality of effective radii to the radius of the mouth irrespective is the site operating or potential (to say, provides fulfillment of the condition (1) even in the case $\theta = 0$). According MTD-MFC the last circumstance excludes onset of heat transfer hysteresis.

In the framework of MTD-MFC it also presents significant interest discussion of influence of thermal parameters of heating surface on HTC.

As it was mentioned above, thermal parameters of heating surface have no influence on HTC during developed boiling. In the context of wetting-dependent multifactoring, if process of wetting of a recess is accompanied by reduction of effective radius, deceleration of wetting evidently can result elevation of HTC. High thermal conductivity of heating surface, promoting concentration of heat flow in the zone of wetting meniscus (in the extent additionally dependent on the thickness of the surface), just presents such a decelerating factor.

Therefore, thermal parameters of heating surface, when its recesses correspond to condition (19), should essentially influence HTC. And vice versa, similar influence should not be exhibited by heating surfaces corresponding to condition (2) (to say, during developed boiling).

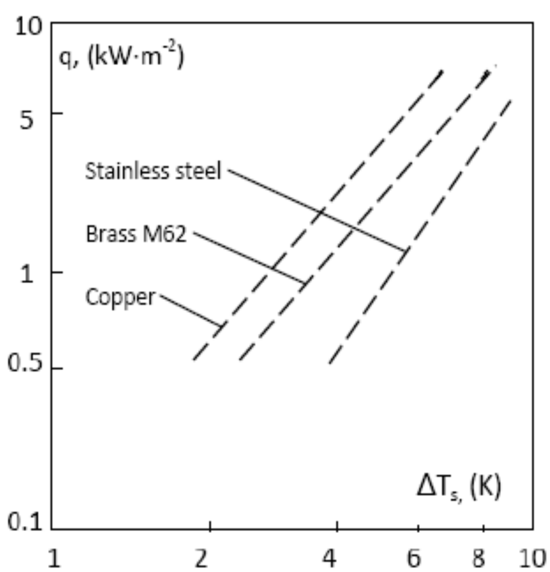

Fig. (33). Smoothed experimental boiling heat transfer curves of nitrogen on rough heating surfaces made from copper, brass and stainless steel [101].

Smoothed experimental curves [101] on boiling of nitrogen on comparatively rough heating surfaces (with the arithmetical mean roughness around 5 μm) made from copper, brass and stainless steel are presented in Fig. (**33**). According to these data HTC essentially depends on thermal properties of heating surface that can be linked to dependence of effective radius of nucleation site on degree of wetting.

Smoothed experimental curves [102] on boiling of nitrogen on polished surfaces (smooth depth 0.2 μm) made from copper, German Silver and aluminum are presented in Fig. (**34**).

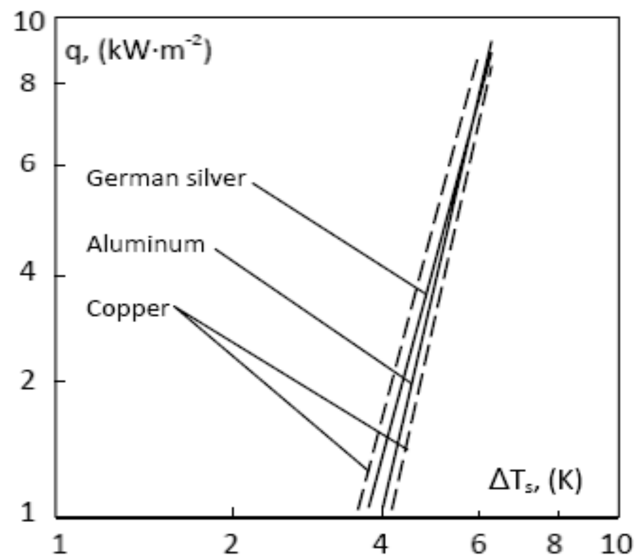

Fig. (34). Smoothed experimental boiling heat transfer curves of nitrogen on polished heating surfaces made from copper, German silver and aluminum [102].

According presented data HTC during boiling on aluminum and German silver surfaces falls within scattering range of the data for copper surface. Besides, thermal conductivity of copper is around 20 times higher than the same parameter of German silver. Practically full absence of influence of thermal properties of heating surface on HTC on polished surfaces, similar to the hysteresis phenomenon, can be interpreted by existence of great number of stable nucleation sites satisfying condition (2).

In such a manner, unified framework MTD-MFC leads to qualitative interpretation of diverse and even seemingly contradictory experimental facts connected with heat transfer hysteresis and influence of thermal parameters of heating surface.

The same framework clearly outlines boundary between developed boiling and wetting-dependent multifactorous boiling.

Despite significant increase of the number of influencing factors, bubble growth onset preserves the role of regulator of average HTC. At the same time, in contrast to developed boiling, heat transfer gains significant new peculiarities quantitative description of which requires modification of MTD, in particular, taking in account dependence of effective radius on several influencing factors.

Duration-Dependent Multifactoring and Boiling in Microsystems

Duration-dependent multifactoring quite often may origin consequent to developed boiling, for instance, through transition to prolonged or even uninterrupted action of PEGB or microlayer evaporation with structural transformation of two-phase flow.

Similar transition also may take place with change of intensity of body force or with variation of inclination angle of heating surface in the gravity field.

In contrast to wetting-dependent multifactoring, establishment of conditions of transition to duration-dependent multifactoring is much more complex problem. Clarification of quantitative regularities of transition to prolonged action of cooling mechanisms requires consideration of structural development of corresponding two-phase flows that represents independent multifaceted problem.

At the same time, duration-dependent multifactoring results transition to MTA. Thereby, in connection with diversity of cooling mechanisms, the problem of theoretical assessment of HTC becomes extremely complex. It requires comprehensive multifactorous numerical modeling of all details and stages of operation of different cooling mechanisms (similar to attempt made in [103] for the case of subcooled flow boiling).

In the context of duration-dependent multifactoring it presents significant interest boiling in microsystems.

Unfortunately, research of this important problem is affected by delay with development of adequate physical models. That is why attempts to establish efficient framework for correlation of existing data on HTC and CHF still turn out to be unsuccessful [104, 105].

There also are problems with correct choice of strategies of experimental research caused by the same absence of adequate physical models. For instance, it still insufficiently is taken in account essential role of thermal parameters of heating surface in the processes with prevailing role of microlayer evaporation.

Similar to heat transfer hysteresis and influence of thermal parameters, there also exist contradictory experimental data on boiling in the microsystems.

A part of the data shows accordance of heat transfer process to developed boiling and another part demonstrates qualitatively differing trends [104-108].

As it follows from qualitative analysis, seeming chaos in the experimental data, similar to cases considered above, can be resolved in the framework of MTD-MFC.

In general, geometry and transverse sizes of small-diameter channels support formation and longstanding preservation of vapor plugs shifting through a channel. As it is shown below, shifting vapor plug of very small diameter favors longstanding action of PEGB and microlayer evaporation mechanism. In this connection just transition to prolonged or even uninterrupted action of PEGB and microlayer evaporation claims to be main factors of multifactoring of boiling heat transfer in minichannels and microchannels.

Investigation of boiling multifactoring in small channels evidently presents complex problem covering the stage of multifactoring itself and further stage of multifactorous heat transfer. Besides, in contrast to the steady-state process studied in [18-19], areas with intensive heat transfer are distributed irregularly in space and in time in this case.

In the context of duration-dependent multifactoring it presents significant interest clarification of the role of PEGB in operation of pulsating heat pipe having quite specific peculiarities connected with self-start-up and keeping of pulsating two-phase flow [109-110].

As it follows from preliminary analysis, at very small diameter, very low thickness and possible partial drying of liquid layer between heating surface and the part of vapor plug create quite favorable conditions for strong manifestation of both related phenomena - microlayer evaporation and PEGB.

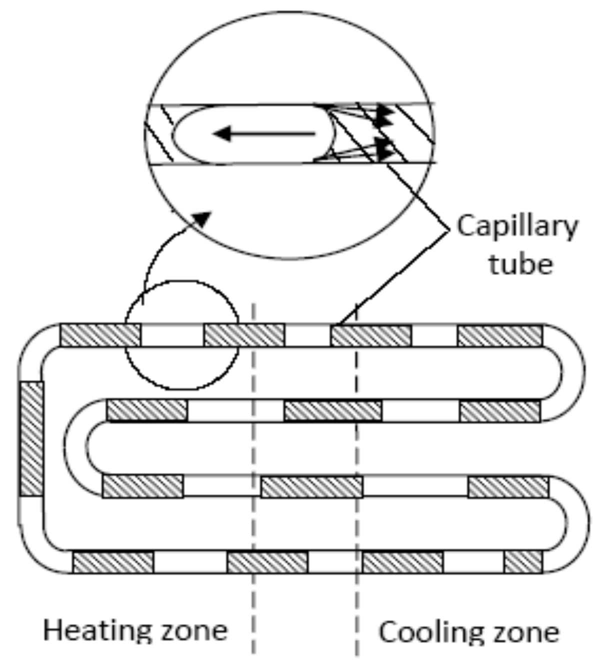

Fig. (35). Pulsating heat pipe.

In contrast to pool boiling, intensive action of the both mechanisms may turn out to be continuous in microchannel (for instance, through shifting of evaporating meniscus along superheated wall). In this context following working hypothesis can be offered regarding operation features of pulsating heat pipe [109-110] (Fig. **35**).

During heating in static conditions dynamical effects of jet flows on both sides of vapor plug mainly balance each other and dynamical influence on the system remains insignificant. However, this balance may be lost at any initial displacement of the plug (caused, for instance, by some instant pressure imbalance among different turns of pulsating heat pipe or by occurrence of temperature gradient).

The effect becomes stronger at backside of the plug (where the liquid layer becomes thinner). The plug turns into certain type of jet engine continuing shifting through the channel with self-acceleration. Further this single plug displaces other plugs with the same dynamical effect and several plugs together speed-up circulation of heat carrier in the loop.

Start-up and acceleration of circulation rather quickly returns the most cooled part of heat carrier from cooling zone. Condensation replaces evaporation on inlet plugs with change of the sign of pumping effect. In addition, evaporation weakens on other plugs.

Arising of opposite pumping effect, together with elimination of initial traction, quickly decelerates the circulation with consequent rise in temperature of heat carrier in heating zone. As a result, initial pumping effect and heat carrier circulation is reversed. Further this sequence repeats periodically.

Offered working hypothesis, with the exception of negative loop feedback aspects, is quite topical also in regard boiling in the microsystems, as a whole. In particular, prolonged duration of intensive action of PEGB and microlayer evaporation may create basis not only for boiling heat transfer multifactoring but for some specific dynamical effects as well.

For instance, it may be discussed the role of PEGB in generation of strong reverse vapor follows, related cyclical oscillations and flow instabilities observed in minichannels and microchannels [105, 111]. It may be shown also that pumping effect of a vapor slug undergoes sharp intensification near to critical regime of channel flow (in connection with partial drying of liquid layer). Generated in such a way strong liquid jet flow may push off the next slug causing reverse of its own pumping effect. As a result, just similar slug may be responsible for aforementioned reverse flows.

THE WAYS OF FURTHER RESEARCH

Following from MTD fundamental boiling heat transfer problem (establishment of interrelations between diversity of boiling heat transfer curves and sizes, geometrics and distribution of nucleation sites) still remains to be studied systematically. Only very small part of numerous experiments includes investigation of nucleation sites. Still are underway unworkable attempts to substitute standard roughness parameters for the effective radii of nucleation sites.

Despite impressive experimental evidences of crucial role of PEGB in boiling heat transfer and hydrodynamics, the effect still remains outside of scope of interests of overwhelming majority of researchers.

Wide theoretical and experimental investigations of PEGB are necessary by the goal of clarification of all spectra of important features of the effect beginning from generation of jet flow and ending by its dynamical and thermal consequences. Investigations should cover nongravity mechanism of vapor phase removal most likely playing leading role through boiling crisis at low saturation pressures and in microgravity, during forced convection boiling in minichannels and microchannels. At the same time it deserves certain interest investigation of micro-membrane pumping effect as additional convection cooling mechanism.

It still remains as the central problem physical modeling of developed boiling on one-parameter heating surfaces and on surfaces with more complex distribution of characteristic sizes and densities of nucleation sites in wide range of variation of effective radius and saturation pressure.

Two possible lines of such a modeling deserve attention: artificial creation of boiling surfaces with designed parameters of nucleation sites and improvement of methods of investigation of natural nucleation sites of heating surfaces.

Full-scale investigation of these processes in the framework MTD-MFC may create basis for analysis of wide spectra of boiling heat transfer problems including quite interesting problem of the slope of developed boiling heat transfer curve.

It is important and capacious problem theoretical and experimental investigation of the phenomenon of boiling heat transfer multifactoring. Investigation of wetting-dependent and duration-dependent multifactoring should cover such an important aspects of boiling phenomenon as heat transfer hysteresis, heat transfer at variable average effective radii of nucleation sites, heat transfer processes with prolonged action of PEGB and microlayer evaporation including boiling in minichannels and microchannels, some specific regimes of boiling in subcooled liquids, in microgravity, on down facing boiling surfaces and others. Besides, investigation of transient behavior in the framework MTD-MFC makes new potential for thorough insight into boiling phenomenon.

Unified framework MTD-MFC opens the way to comprehensive research of important problem of boiling in the microsystems. It is necessary to upgrade existing approaches and physical models taking in account dynamical and thermal consequences of prolongation of intensive action of PEGB and transition to almost uninterrupted action of microlayer evaporation mechanism.

Determined by correlation (16) basic principle of intensification of boiling heat transfer (creation of numerous high-sized stable nucleation sites with minimum worsening of thermal conductance of boiling surface) still remains as the most efficient line of development of enhanced boiling surfaces. Correspondingly, improvement of technologies of manufacturing of boiling surfaces also should be targeted at full realization of this principle.

NOMENCLATURE

A	$[m^2]$	Heating surface area
C_p	$[J \cdot kg^{-1} \cdot K^{-1}]$	Heat capacity
L	[m]	length of conical site side
N	$[m^{-2}]$	Density of operating sites
P	[Pa]	Pressure

R	[μm]	Radius of nucleation site
R_p	[μm]	Standard roughness parameter
T	[K]	Temperature
U	$[m \cdot s^{-1}]$	Velocity
ΔT	[K]	Temperature difference
ΔT_s	[K]	Temperature difference between heating surface and saturation temperature
$\Delta T^!$	[K]	Wall maximum local superheat
β	[radian]	Cone angle
g	$[m \cdot s^{-2}]$	Acceleration of a body force
h	$[W \cdot m^{-2} \cdot K^{-1}]$	Heat transfer coefficient
k	$[W \cdot m^{-1} \cdot K^{-1})]$	Thermal conductivity
l	[m]	Length of wetting of nucleation site
n		Exponent
q	$[W \cdot m^{-2}]$	Heat flux
q_r	$[W \cdot m^{-2}]$	Evaporative component of heat flux
r	$[kJ \cdot kg^{-1}]$	Heat of evaporation
v	$[m^3 \cdot kg^{-1}]$	Specific volume
x	[m]	Coordinate
x_0	[m]	Depth of liquid superheating
α	$[m^2 \cdot s^{-1}]$	Thermal diffusivity
ϑ	[radian]	Contact angle
ε	[m]	Depth of capillary groove
ρ	$kg \cdot m^{-3}$	Density
ρ_0	[m]	Effective radius of nucleation site
τ	[s]	Time
τ_0	[s]	Duration of surface temperature pulsation cycle
τ_1	[s]	Duration of intensive cooling effect
σ	$[N \cdot m^{-1}]$	Surface tension
φ	[radian]	Capillary groove angle
ν	$[m^2 \cdot s^{-1}]$	Cinematic viscosity

SUBSCRIPTS

cr	Critical value
g	Refers to vapor (fluid – without subscript)
gd	According hydrodynamic theory of crisis
eq	Refers to equilibrium condition
0	Under normal gravity
s	At saturation condition
w	On the wall

REFERENCES

[1] I.L. Pioro, W.M. Rohsenow, and S.S. Doerffer, “Nucleate pool-boiling heat transfer, 1: review of parametric effects of boiling surface”, *Int. J. Heat Mass Transf.*, vol. 47, pp. 5033-5044, December 2004.

[2] I.L. Pioro, W.M. Rohsenow, and S.S. Doerffer, “Nucleate pool-boiling heat transfer, 2: assessment of prediction methods”, *Int. J. Heat Mass Transf.*, vol. 47, pp. 5045-5057, December 2004.

[3] K.V. Dhir, “Mechanistic prediction of nucleate boiling heat transfer - achievable or hopeless task?” *J. Heat Transf.*, vol. 128, pp. 1-12, January 2006.

[4] I.G. Shekriladze, and J.G. Rusishvili, “Comments on papers L. Pioro, W. Rosenow, and S.S. Doerfer, "Nucleate pool-boiling heat transfer, 1: review of parametric effects of boiling surface; 2: assessment of prediction methods", *Int. J. Heat Mass Transf.*, vol. 49, pp. 1205-1207, March 2006.

[5] F.D. Moore and R.B. Mesler, “The measurement of rapid surface temperature fluctuations during nucleate boiling of water”, *AICHE J*., vol. 7, pp. 620-624, April 1961.

[6] M. Jacob, *Heat Transf.*. Vol. l, NY: John Wiley, 1949.

[7] H.K. Forster and R. Greif, “Heat transfer in boiling liquid, mechanism and correlations”, *Tr. ASME, J. Heat Transf.,* vol. 81, pp. 43-53, January 1959.

[8] I.G. Shekriladze, “On the mechanism of nucleate boiling”, *Bull. Acad. Sci. Georg. SSR,* vol. 41, pp. 392-396, February 1966 (English version: I.G. Shekriladze, “Mechanism of Steam bubble formation”, *NASA TM X - 59 398*, January 1967. [Online] Available: http://ntrs.nasa.gov/search.jsp?N=0&Ntk=AuthorList&Ntx=mode%20matchall&Ntt=shekriladze. [Accessed Nov 11, 2006]).

[9] T.T. Robin and N.W. Snyder, “Bubble dynamics in subcooled nucleate boiling based on the mass transfer mechanism”, *Int. J. Heat Mass Transf.*, vol. 13, pp. 305-318, February 1970.

[10] Ye.I. Nesis and I.S. Sologub, “Temperature fluctuations in subcooled boiling at a single site”, *in: Kipenie i kondensatsia*, I. Smirnov, Ed. Riga: RPI Press, 1984, pp. 5-13.

[11] I.G. Shekriladze, “Heat transfer in two-phase areas with intensive evaporation and condensation”, Dr. Tech. Sc. dissertation, Moscow Bauman Higher Technical School, Moscow, USSR, 1982.

[12] V.I. Tolubinski, A.A. Kriveshko, and Yu. N. Ostrovski, “About temperature fluctuations of heating surface under active nucleation site”, *Teplofizika i teplotekhnika,* Issue 19, V. Tolubinski, Ed. Kiev, Naukova Dumka Press, 1971, pp. 22-26.

[13] S.J. Van Stralen, W. Zijl, and D.A. De Vries, “The behavior of vapor bubbles during growth at subatmospheric pressures”, *Chem. Eng. Sci.*, vol. 32, pp. 1189-1196, October 1977.

[14] I.G. Shekriladze, Sh.A. Mestvirishvili, J.G. Rusishvili, G.I. Zhoszholiani, and V.G. Ratiani, “Study of heating surface temperature fluctuations in the process of liquid boiling“, *Bull. Acad. Sci. Georg. SSR*, vol. 89, pp. 69-72, January 1978.

[15] R.L. Judd and K.S. Hwang, “A comprehensive model for nucleate pool boiling heat transfer including microlayer evaporation”, *J. Heat Transf.,* vol. 98, pp. 623-629, May 1976.

[16] J.R. Thome, “Latent and sensible heat-transfer rates in the boiling of binary mixtures”, *J. Heat Transf.,* vol. 104, pp. 474-478, April 1982.

[17] M.V.H. Del Valle and D.B.R. Kenning, “Subcooled flow boiling at high heat flux”, *Int. J. Heat Mass Transf.,* vol. 28, pp. 1907-1920, October 1983.

[18] G.V. Ratiani, Sh. A. Mestvirishvili, and I.G. Shekriladze, “Analysis of two cases of evaporation from thin laminar films”, *Bull. Acad. Sci. Georg. SSR*, vol. 55, pp. 325-328, March 1969.

[19] I.G. Shekriladze and J.G. Rusishvili, “Evaporation and condensation on grooved capillary surfaces”, Proceedings of 6th International Heat Pipe Conference, 1987, pp. 234-239.

[20] I.G. Shekriladze and G.V. Ratiani, “On the basic regularities of developed nucleate boiling heat transfer", *Bull. Acad. Sci. Georg. SSR,* vol. 42, pp. 145-150, January 1966.

[21] L. Bard and E.F. Leonard, “Heat transfer in simulated boiling”, *Int. J. Heat Mass Transf.*, vol. 10, pp. 1727-1734, December 1967.

[22] S.S. Kutateladze and I.G. Malenkov, “The hydrogasodynamic aspects of liquid boiling heat transfer”, *Teplofizika Visokikh Temp.* vol. 14, pp. 793-803, July 1976.

[23] I.G. Shekriladze, “On the role of the “pumping effect” of a vapour bubble growing at the wall during nucleate boiling”, *in Problems of Convection Heat Transf. and Steam Purity,* V.I. Gomelauri, Ed. Tbilisi, Metsniereba Press, 1970, pp. 90-97.

[24] H. Schlichting, *Boundary-Layer Theory*. NY: McGraw-Hill, 1979.

[25] I.G. Shekriladze, Sh. A. Mestvirishvili, J.G. Rusishvili, G.I. Zhoszholiani, and V.G. Ratiani, “Studies in the mechanism of boiling and enhancement of evaporative cooling coefficients”, *Heat Transf.-Soviet Res.*, vol. 12. pp. 91-95, February 1980.

[26] V.I. Subbotin, S.P. Kaznovski, and S.K. Korotaev, “Investigation of the dynamics of vapour bubbles in boiling of water on thin wires under natural convection”, *Atomnaia Energia*, vol. 28, pp. 9-13, January 1970.

[27] O.N. Afgan, *Boiling Liquids Superheat*. Oxford: Pergamon Press, 1976.

[28] I.G. Shekriladze, “Mechanisms of heat removal in the process of developed boiling”, *Heat Transf.-Soviet Res.*, vol. 22, pp. 445-463, April 1990.

[29] I.G. Shekriladze, “Frozen pathways to breakthrough in boiling heat transfer theory”, Proceedings of. 11th International Heat Transfer Conerence, Vol. 2, 1998, pp. 474-478.

[30] I.G. Shekriladze, Comments on the paper, “Jet flow phenomena during nucleate boiling”, *Int. J. Heat Mass Transf.*, vol. 46, pp. 2711-2712, July 2003.

[31] H. Wang, X.F. Peng, B.X. Wang and D.J. Lee, “Jet flow phenomena during nucleate boiling”, *Int. J. Heat Mass Transf.,* vol. 45, pp. 1359-1363, March 2002.

[32] B.S. Yilbas and M. Sami, “Liquid ejection and possible nucleate boiling mechanisms in relation to laser drilling process”, *J. Phys. D. Appl. Phys.*, vol. 30, pp. 1996-2005, November 1997.

[33] H. Wang, X. Peng, D.M. Christopher, W.K. Lin and C. Pan, “Investigation of bubble-jet flow during subcooled boiling on wires”, *Int. J. Heat Fluid Flow*, vol. 26, pp. 485-494, March 2005.

[34] H. Wang, X. Peng, D.M, Christopher and S.V. Garimella, “Jet flows around microbubbles in subcooled boiling”, *J. Heat Transf.*, vol. 127, pp. 802, August 2005.

[35] J.L. McGraw, F.L. Bamford and T.R. Rehm, “Marangoni flow: additional mechanism in boiling heat transfer”, *Science*, vol. 153, pp. 1106-1107, 2 September 1966.

[36] J. Betz and J. Straub, “Numerical and experimental study of the heat transfer and fluid flow by thermocapillary convection around gas bubble”, *Heat Mass Transf.*, vol. 37, pp. 215-227, February 2001.

[37] D.M. Christopher, H. Wang and X. Peng, “Dynamics of bubble motion and bubble top jet flows from moving vapor bubbles on microwires”, *J. Heat Transf.*, vol. 127, pp. 1260-1268, November 2005.

[38] I.G. Shekriladze, Discussion: “Dynamics of bubble motion and bubble top jet flows from moving vapour bubbles on microwires”, *J. Heat Transf.*, vol. 127, pp. 1260-1261, December 2006.

[39] J.W. Rose, “Interphase matter transfer, the condensation coefficient and dropwise condensation”, Proceedings of 11th International Heat Transfer Conerence, Vol. 1, 1998, pp. 89-94.

[40] S.S. Kutateladze, *Heat Transf. in Condensation and Boiling*. Moscow: Mashgiz Press, 1952.

[41] D.A. Clark, “Cryogenic heat transfer”, *in Uspekhi Teploperedachi*, W.M. Rohsenow and J.P. Hartnet, Eds. Moscow: Mir Press, 1971, pp. 361-367.

[42] J. Straub, M. Zeil and B. Vogel, “Pool boiling in a reduced gravity field”, Proceedings of 9th International Heat Transfer Conerence, Vol. 1, 1990, pp. 91-112.

[43] T. Oka, Y. Abe, Y.H. Mori and A. Nagashima, “Pool boiling of n-pemtane, CFC, and water under reduced gravity: parabolic flight experiments with a transparent heater”, *J. Heat Transf.*, vol. 117, pp. 408-417, February 1995.

[44] V.I. Subbotin, D.N. Sorokin, D.M. Ovechkin, and A.P. Kudriavtsev, “*Heat Transf. during Pool Boiling of Metals*”. Moscow: Nauka Press, 1969.

[45] I.G. Shekriladze, Yu. Sh. Verulava, L. Ye. Vasadze, and M.S. Paniashvili, “An experimental investigation of heat transfer and critical heat fluxes during Boiling of organic working bodies and water under reduced pressures”, *J. Eng. Phys.,* vol. 40, pp. 689-693, June 1981.

[46] G.V. Ratiani and I.G. Shekriladze, “Study of the process of fully developed boiling of liquids”, *Heat Transf.-Soviet Res.*, vol. 4, pp. 126-141, January 1972.

[47] M. Shoukri and R.L. Judd, “Nucleation site activation in saturated boiling”, *J. Heat Transf.*, vol. 97, pp. 96-102, January 1975.

[48] R. Ziegel, *Heat Transf. Under Reduced Gravitation.* Moscow: Mir Press, 1970.

[49] A.A. Voloshko, “Effects of microgravity and dynamic acceleration on physical characteristics and heat transfer intensity under liquid boiling”, presented at International Symposium Physics and Heat Transfer Boiling Condensation, Moscow, Russia, 1996.

[50] A.I. Butuzov, S.N. Faisilberg, M.K. Bezrodny, N.I. Stogny, P.P. Kudelia, and V.I. Usenko, “Experimental data on pool Boiling of refrigerant-12 and water under inertial reloading”, *Teplofizika visokikh Temp.*, vol. 7, pp. 490-494, March 1969.

[51] J. Kim and J.F. Benton, "Highly subcooled pool boiling heat transfer at various gravity levels", *Int. J. Heat Fluid Flow*, vol. 23, pp. 497-508, February 2002.

[52] J. Kim and J.F. Benton, "Pool boiling heat transfer on small heaters: effect of gravity and subcooling", *Int. J. Heat Mass Transf.*, vol. 45, pp. 3919-3932, October 2002.

[53] L.T. Hwang, W.F. Lu, and J.C. Mollendorf, "Forced convective boiling in horizontal tube bundles", *Int. J. Heat Mass Transf.*, vol. 29, pp. 785-795, May 1986.

[54] Yu. A. Zaigarnik, "Forced convection boiling", *in International Encyclopedia of Heat and Mass Transfer*, Boca Raton: CRC Press, 2000, pp. 464-467.

[55] K. Nishikava, Y. Fujita, S. Uchida, and H. Ohta, "Effect of surface configuration on nucleate boiling heat transfer", *Int. J. Heat Mass Transf.*, vol. 27, pp. 1559-1571, September 1984.

[56] J.L. Parker, and M.S. El-Genk, "Effect of surface orientation on nucleate boiling of FC-72 on porous graphite", *J. Heat Transf.*, vol. 128, pp. 1159-1175, November 2006.

[57] T. Inoue, M. Monde, and Y. Teruya, "Pool boiling heat transfer in binary mixtures of ammonia/water", *Int. J. Heat Mass Transf.,* vol. 45, pp. 4409-4415, November 2002.

[58] G.N. Kruzhilin, "Heat transfer from heating surface to boiling single-component liquid in conditions of natural convection", *Izvestia AN SSSR, OTN*, vol. 7, pp. 967-980, July 1948.

[59] W.M. Rohsenow, "A Method of correlating heat transfer data for surface boiling of liquids", *Trans. ASME*, vol. 74, pp. 969-976, August 1952.

[60] V.I. Tolubinski, "The problem of boiling heat transfer theory", *Izvestia VUZ, Energetika*, vol. 1, pp. 15-22, January 1959.

[61] H.M. Kurihara, and J.E, Meyers, "The effects of superheat and surface roughness on boiling coefficients", *AICHE J.*, vol. 6, pp. 83-91, January 1960.

[62] J.H. Lienhard, "A Semi-rational nucleate boiling heat flux correlation", *Int. J. Heat Mass Transf.*, vol. 6, pp. 215-219, March 1963.

[63] N. Zuber, "Nucleate boiling: region of isolated bubbles and the similarity with natural convection", *Int. J. Heat Mass Transf.*, vol. 6, pp. 53-58, January 1963.

[64] S.S. Kutateladze, A.I. Leontiev, and A.G. Kirdiashkin, "Nucleate boiling heat transfer theory", *Ingenerno-Physichesi J.* vol. 8, pp. 7-12, August 1965.

[65] B.B. Micic, and W.M. Rohsenow, "A New correlation of pool-boiling data including the effect of heating surface characteristics", *J. Heat Transf.*, vol. 91, pp. 245-250, February1969.

[66] S.A. Labuntsov, "Problem of heat transfer during nucleate boiling of liquids", *Teploenegretika*, vol. 9, September 1972.

[67] K. Stephan, and M. Abdelsalam, "Heat transfer correlations for natural convection boiling", *Int. J. Heat Mass Transf.*, vol. 23, pp. 73-77, January 1980.

[68] S.A. Kandlikar, "General correlation for saturated two-phase flow boiling heat transfer inside horizontal and vertical tubes", *J. Heat Transf.*, vol. 112, pp. 219-228, January 1990.

[69] K.O. Pasamehmetoglu, P.R. Chappidi, C. Unal, and R.A. Nelson, "Saturated pool nucleate boiling mechanisms at high heat fluxes", *Int. J. Heat Mass Transf.*, vol. 36, pp. 3859-3868, August 1993.

[70] S.I. Haider and R.L. Webb, "A transient micro-convection model of nucleate pool boiling", *Int. J. Heat Mass Transf.*, vol. 40, pp. 3675-3688, August 1997.

[71] V.K. Dhir, "Numerical simulation of pool-boiling heat transfer", *AICHE J.*, vol. 47, pp. 813-834, April 2001.

[72] Y. He, M. Shoji and Sh. Maruyama, "Numerical study of high heat flux pool boiling heat transfer", *Int. J. Heat Mass Transf.*, vol. 44, pp. 2357-2373, June 2001.

[73] T. Fuchs, J. Kern, and P. Stephan, "A transient nucleate boiling model including microscale effects and wall heat transfer", *J. Heat Transf.*, vol. 128, pp. 1257-1265, December 2006.

[74] I.G. Shekriladze, "Developed boiling heat transfer", *Int. J. Heat Mass Transf.,* vol. 24, pp. 795-01, May 1981.

[75] I.G. Shekriladze, "Developed boiling heat transfer of cryogenic liquids and refrigerants", *in Heat and Mass Transf. in Refrigeration and Cryogenics*, N. Afgan, Ed. Washington: Hemisphere, 1987, pp. 580-591.

[76] I.G. Shekriladze, "Developed boiling heat transfer – forty years of the model of "the theatre of director", presented at 13th International Heat Transfer Conference, Sydney, Australia, 2006.

[77] P. Griffith and S.D. Wallis, "The role of surface conditions in nucleate boiling", *Chem. Eng. Prog. (symp. ser.)*,vol. 56 (30), pp. 49-60, December 1960.

[78] M. Madejski, "Activation of nucleation cavities on a heating surface with temperature gradient in a superheated liquid", *Int. J. Heat Mass Transf.*, vol. 9, pp. 295-300, April 1966.

[79] A.V. Luikov, *Heat Conduction Theory*. Moscow: Visshaia Shkola Press, 1967.

[80] V.M. Borishanski, A.P. Kozirev, and A.S. Svetlova, "Investigation of heat transfer during nucleate boiling of liquids", *in Convection Heat Transf. and Hydrodynamics in Two-Phase and Single-Phase Flows*, V.M. Borishanski, Ed. Moscow: Gosenergoizdat Press, 1964, pp. 71-104.

[81] A.C. Dudkevich, F.D. Akhmedov, "Experimental study of influence of thermophysical properties of heating surface on boiling of nitrogen at elevated pressures", *Trudi, MEI*; Issue 198, pp. 41-47, September 1974.

[82] V.M. Borishanski, S.S. Kutateladze, and I.I. Novikov, *Liquid Metal Heat Carriers.* Moscow: Atomizdat Press, 1967.

[83] L.H. Chai and M. Shoji, "Self-organization and self-similarity in boiling systems", *J. Heat Transf.*, vol. 124, pp. 507-515, March 2002.

[84] L.H. Chai and M. Shoji, "Closure to discussion "Self-organization and self-similarity in boiling systems", *J. Heat Transf.*, vol. 126, pp. 663-664, April 2004.

[85] P.L. Marto and W.M. Rohsenow, "Effects of surface conditions on nucleate pool boiling of sodium", *J. Heat Transf.*, vol. 88, pp. 149-157, February 1966.

[86] L.V. Chumak, L.V. Malaia, and I.V. Vinichenko, "Enhancement of heat transfer of cryogens on the pipe surface", *Kholodilnaia Tekhnika*, vol. 2, pp. 31-34, Februay 1979.

[87] V.I. Subbotin, D.M. Ovechkin, and D.N. Sorokin, "Heat transfer during pool boiling of cesium", *Teploenergetika*, vol. 6, pp. 63-66, June 1968.

[88] G.N. Danilova, "Influence of saturation pressure and temperature on heat transfer during boiling of refrigerants", *Trudi CKTI*, vol. 57, pp. 69-80, January 1965.

[89] V.A. Grigoriev, Yu. M. Pavlov, and E.V. Ametistov, *Boiling of Cryogenic Liquids*. Moscow: Energia Press, 1973.

[90] T, Inoue, N. Kawae and M. Monde, "Characteristics of heat transfer coefficient during nucleate pool boiling of binary mixtures", *Heat Mass Transf.*, vol. 33, pp. 337-344, April 1998.

[91] V.M. Borishanski, G.I. Bobrovich, and F.P. Minchenko, "Heat transfer during boiling of water and ethyl alcohol at external surface of tubes", *in Problems of Heat Transf. and Hydrodynamics in Two-Phase Area,* V. M. Borishanski, Ed. Moscow: Gosenergoizdat Press, 1961, pp. 75-93.

[92] Hene and Guber, "Boiling of benzene, biphenyl and benzene-biphenyl mixtures", *J.Heat Transf.*, vol. 85, pp. 31-38, March 1963 (Russian Translated Edition).

[93] B.S. Petukhov, S.A. Kovalev, and V.M. Zhukov, "Study of sodium boiling heat transfer", Proceedings of 3rd International Heat Transfer Conerence, Vol. 5, 1966, pp. 80-91.

[94] A.I. Pridantsev, L.S. Kokorev, V.I. Deev, and V.I. Petrovichev, "Experimental study of regimes and heat transfer during boiling of mercury under subatmospheric pressures", *in Problems of Thermophysics of Nuclear Reactors,* Issue 3, V.I. Subbotin, Ed. Moscow: Atomizdat Press, 1971, pp. 3-12.

[95] I.G. Shekriladze and J.G. Rusishvili, "Experimental study of heat transfer during boiling and condensation of cryogens", *Ingenerno-Physicheski J.*, vol. 33, pp. 486-490, March 1977.

[96] V.A. Kravchenko and L.F. Tolubinskaia, "Heat transfer during boiling of ethan and ethylene", *Teplophizika i Teplotekhnika*, V. Tolubinski, Ed. Issue 31, pp. 61-64, January 1976.

[97] Y. Xiulin, X. Hongji, Z. Yuweng, and Q. Hongzhang, "Pool boiling heat transfer to liquid nitrogen from porous metallic coatings of tube bundles and experimental research of hysteresis phenomenon", *Cryogenics*, vol. 29, pp. 460-462, April 1989.

[98] R.L Webb and Ch. Pais, "Nucleate pool boiling data for five refrigerants on plain, integral-fin and enhanced tube geometries", *Int. J. Heat Mass Transf.*, vol. 35, pp. 1893-1904, February 1992.

[99] I.G. Shekriladze, "On the mechanism of heat transfer hysteresis in the process of boiling", *Bull. Acad. Sci. Georg. SSR*, vol. 101, pp. 325-328, February 1981.

[100] V.K. Andreyev, V.I. Deyev, V.I. Petrovichev, and G.S. Shelukhina, "Heat transfer regimes in bubble pool boiling of helium", *Teplofizika visokikh Temp.*, vol. 16, pp. 882-884, April 1978.

[101] V.A. Grigoriev, Yu. M. Pavlov, E.V. Ametistov, A.V. Klimenko, and V.V. Klimenko, "Concerning the influence of thermal properties of heating surfaccce material on heat transfer intensity of nucleate pool boiling of liquids including cryogenic ones", *Cryogenics*, vol. 17, pp. 94-96, February 1977.

[102] H. Ackerman, B. Bewilogua, and H. Vinzelberg, "Bubble boiling from heated surface of different material in liquid nitrogen", *Cryogenics*, vol. 15, pp. 877-878, November 1975.

[103] N. Basu, G.R. Warrier and V.K. Dhir, "Wall heat flux partioning during subcooled flow boiling", *J. Heat Transf.*, vol. 127, pp. 131-140, January 2005.

[104] S. Kandlikar, Heat Transfer and Fluid Flow in Minichannels and Microchannels, London: Elsveier, 2006.

[105] J.R. Thome, "Fundamentals of boiling and two-phase flow in microchannels", presented at 13th International Heat Transfer Conference, Sydney, Australia, 2006.

[106] S.S. Mehendale, and A.M. Jacobi, "Evaporative heat transfer in mesoscale heat exchangers", *ASHRAE Trans.*, vol. 106, pp. 446-452, February 2000.

[107] A.E. Bergles, V.J.H. Leinhard, G.E. Kendall, and P. Griffith, "Boiling and evaporation in small diameter channels", *Heat Transf. Eng.*, vol. 24, pp. 18-40, January 2003.

[108] J.R. Thome, M. Groll, and R. Mertz, "Microscale Heat transfer: boiling and evaporation", *in Heat Exchanger Design Update*, G. Hewitt, Ed. NY: Begell House, 2003, pp. 1-27.

[109] H. Yang, S. Khandekar, and M. Groll, "Operational limit of closed loop pulsating heat pipes", *App. Ther. Eng.*, vol. 28, pp. 49-59, January 2008.

[110] W. Qu and H.B. Ma, "Theoretical analysis of start-up of pulsating heat pipe", *Int. J. Heat Mass Transf.*, vol. 50, pp. 2309-2316, June 2007.

[111] P. Cheng, H.-Y. Wu, and F.-J. Hong, "Phase-change heat transfer in Microsystems", *J. Heat Transf.*, vol. 129, pp. 101-108, January 2007.

Influence of Relative Humidity and Roughness on the Friction Coefficient

Shaik Mozammil, *Department of Mechanical Engineering, Aryan Institute of Engineering & Technology, Bhubaneswar, smozammil157@gmail.com*

Deepikarani Swain, *Department of Mechanical Engineering, NM Institute of Engineering & Technology, Bhubaneswar, depika_r19@yahoo.co.in*

Kalpana Mallick, *Department of Mechanical Engineering, Raajdhani Engineering College, Bhubaneswar, kalpanam11@outlook.com*

Biswa Ranjan Pradhan, *Department of Civil Engineering, Capital Engineering College, Bhubaneswar, biswaranjanpradhan78@gmail.com*

Saleema Panda, *Department of Civil Engineering, NM Institute of Engineering & Technology, Bhubaneswar, saleemapanda25@gmail.com*

Abstract: The present paper investigates experimentally the effect of relative humidity and roughness on friction property of mild steel under horizontal vibration. To do so, a pin-on-disc apparatus having facility of vibrating the test samples at different direction is designed and fabricated. The direction of vibration is horizontal. Horizontal vibration is created along (longitudinal direction) and perpendicular (transverse direction) to the sliding direction. The experimental setup has the facility to vary the amplitudes and frequencies of vibration while velocity of vibration is kept constant. During the experiment, relative humidity, roughness, frequency, amplitude and direction of vibration are varied. The observed ranges of relative humidity and surface roughness were 40%-80% and 0.125-2.5μm (RMS) respectively. Results show that friction co-efficient decreases with the increase of relative humidity for horizontal vibration. Friction coefficient is very high at very low roughness and it tends to be high at very high roughness for horizontal direction. It is also observed that the variation of friction co-efficient has a particular relationship with the relative humidity and roughness under horizontal vibration.

Keywords: Friction coefficient, horizontal vibration, relative humidity, roughness.

1. INTRODUCTION

Study of mechanics of friction and the relationship between friction and wear dates back to the sixteenth century, almost immediately after the invention of Newton's law of motion. The basic laws of friction are generally obeyed with a little variation which is within a few percent in many cases. It should be emphasized that coefficient of friction (μ) is strictly constant only for a given pair of sliding materials under a given set of operating conditions (temperature, humidity, normal pressure and sliding velocity). Several authors [1-4] observed that the variation of friction force depends on roughness of the rubbing surfaces, relative motion, type of material, temperature, normal force, stick slip, relative humidity, lubrication and vibration. Due to this frictional variation, they observed that no clear correlation has yet, been established. They also found that there are various hypothesis but these differ considerably. Therefore, they suggested that more research is needed for the implication of past and future results to be clearly understood.

Researchers [5-16] have concluded that mean friction force increases as well as decreases depending on the vibration parameters. The measurements of static and dynamic frictional forces by the researchers under the influence of external vibrations indicate three different or opposite trends and these trends are:

1) The frictional force is increased by vibrational assistance.
2) The frictional force is not changed or slightly changed by vibrational assistance.
3) The frictional force is reduced by vibrational assistance.

These trends were observed when the parameters involved in the process i.e. normal force, amplitude, frequency, material and surface were changed. Thus the frictional force can be increased or decreased as a result of an adequate choice of parameters. The investigation by different authors showed that either an increase or a decrease in the frictional forces can be obtained when one of the parameters like, surface pressure, frequency or amplitude is changed. The above results indicate the domain of specific behaviors i.e. certain mechanisms cause a friction to increase while others to decrease. In some cases, the mechanisms are balanced and will not affect the friction. The frictional force can be weakened mainly through a separation of the surfaces or strengthened by welding phenomena in the contact surfaces.

A decrease in frictional force can be obtained through (a) resonance between the natural frequency of the contacting asperities and that of the external vibration, (b) reversal of the friction vector, (c) superposition between static and dynamic load, which means that a lower tangential force is needed to initiate the sliding of materials in the friction surface or (d) local transformation of vibration energy into heat energy in the friction surface, so that the yield point of the material is lowered. An increase in the frictional force can be obtained through (a) viscous damping of the friction surface, (b) increased adhesion or microwelding (pick-ups) between the materials or (c) deformation and material hardening of the material (the microhardness has been affected during the investigation).

The complexity of friction makes it difficult to identify the basic mechanisms responsible for these results.

Chowdhury and Helali found that friction coefficient is a function of amplitude and roughness under vertical vibration [17]. They observed the effect of frequency and amplitude of vertical vibration on friction coefficient at a particular roughness and relative humidity [18]. They also showed that increase or decrease of friction coefficient depends on direction of vibration [19]. On the other hand friction co-efficient increases with the decrease of relative humidity [20-22]. Experiments were conducted by Chowdhury and Helali [23-24] to determine the simultaneous effect of frequency of vertical vibration and humidity on friction and wear and found that the friction coefficient and wear rate decreases with the increase of frequency of vertical vibration and relative humidity. They also found percentage reduction of friction coefficient is almost constant for a particular frequency of vertical vibration for different relative humidity. That is, the previous investigations have been carried out for mild steel to observe the effect of roughness on friction coefficient for different amplitudes, frequencies and relative humidity under vertical vibration. However, the effects humidity and roughness on friction coefficient in conjunction with frequencies and amplitudes of horizontal vibration are yet to be investigated. Therefore, in this study an attempt is made to investigate the effect of humidity and roughness on friction coefficient under horizontal vibration for mild steel. In this study vibration is generated artificially in such a way that direction, amplitude and frequency of vibration can be controlled. Within this research it is sought to better understand the relation between friction and relative humidity and roughness for horizontal vibration and to explore the possibility of adding controlled relative humidity and roughness with horizontal vibration to a mechanical process as a means to improve performance and quality. It is expected that the applications of these results will contribute to the improvement of different concerned mechanical systems.

2. EXPERIMENTAL SETUP

Fig. (**1**) shows a pin-on-disc machine which contains a pin that can slide on a rotating horizontal surface (disc). In this set-up a circular mild steel (carbon 0.19-0.2%) test sample (disc) is to be fixed on a rotating plate (table) having a long vertical shaft clamped with a screw from the bottom surface of the rotating plate. The shaft passes through two close-fit bush-bearings which are rigidly fixed with two-square plates such that the shaft can move only axially and any radial movement of the rotating shaft is restrained by the bush. All these two supporting square plates along with a base plate are rigidly fixed with four vertical square bars to provide the rigidity to the main structure of this set-up. The base plate was fixed with rubber block impagnated with steel plate. A compound V-pulley above the top supporting square

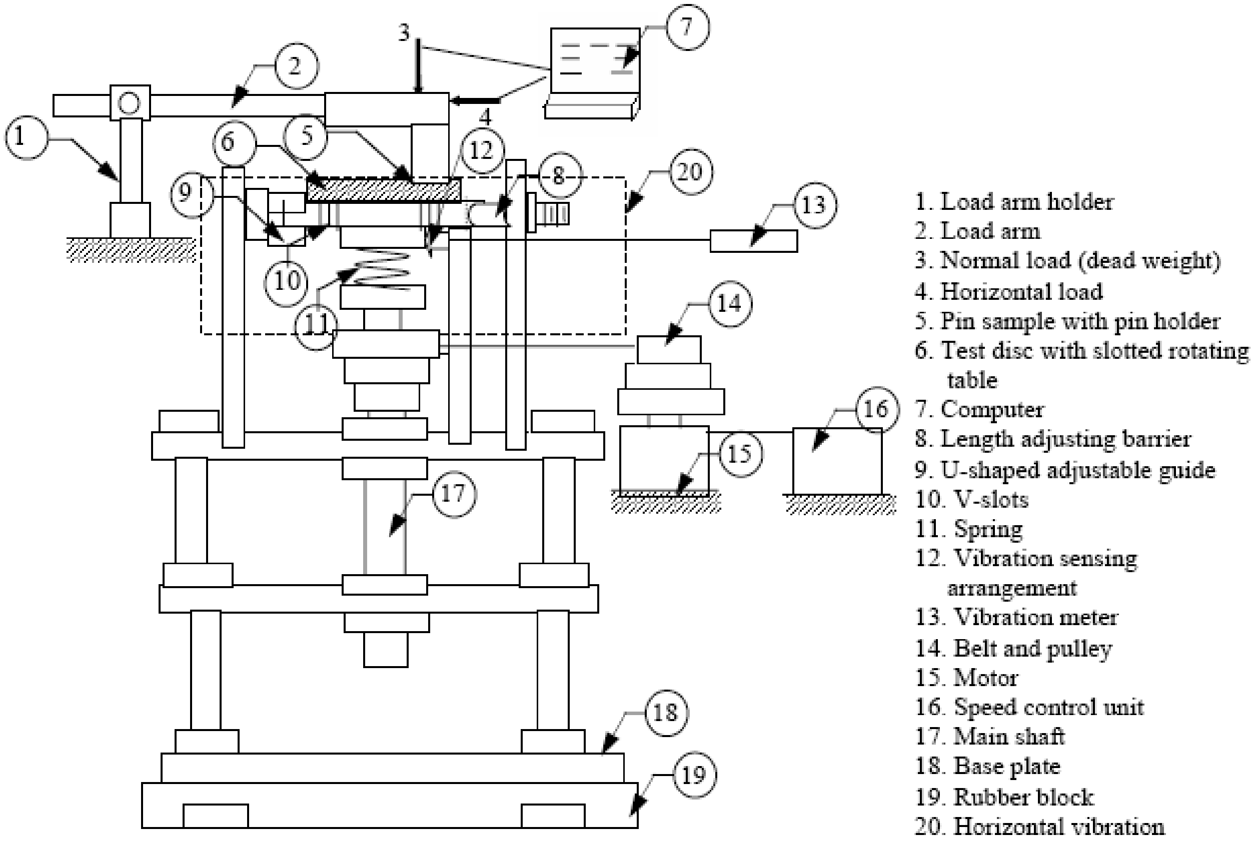

Fig. (1). Block diagram of the experimental set-up (Horizontal Vibration).

plate was fixed with the shaft to transmit rotation to the shaft from a motor. For generating horizontal vibration, one end of a coil spring is fixed with the rotating shaft and other end of the spring is fixed with the rotating table, holding the test plate. Around the circumference of the rotating table, there are a number of V-slots. An adjusting rigid barrier with spherical tip is fixed (as shown in Fig. **1**) with the basic structure of the setup. This tip may penetrate into the V-slots of the rotating table. The depth of this penetration is adjustable. Therefore when the shaft along with the spring and table rotates, the tip of the rigid barrier creates obstruction to the rotation of the slotted table. Due to spring action and rotation, the table will vibrate horizontally. To ensure the horizontality of vibration three U-shaped adjustable guides are placed at 120^0 apart. These rigid guides are fixed with the basic structure of the setup. The displacement velocity and acceleration diagrams for horizontal vibration are shown in Fig. (**2**). The direction of vibration can be either longitudinal or transverse depending on the position of sliding pin on the rotating vibrating table. By varying rotation of the shaft and the number of slots of the rotating table, the frequency of vibration can be varied. By adjusting the depth of penetration of the adjustable barrier, the amplitude of the vibration can be varied. With all these supports some vertical vibration may also arise which will be measured and presented along with the results. As the plate is vibrating and rotating, it was not possible to fix directly the vibration sensing pickup of the vibration meter for measuring vibration. So measure the vibration of the table, a spring loaded pin is kept in contact with the lower

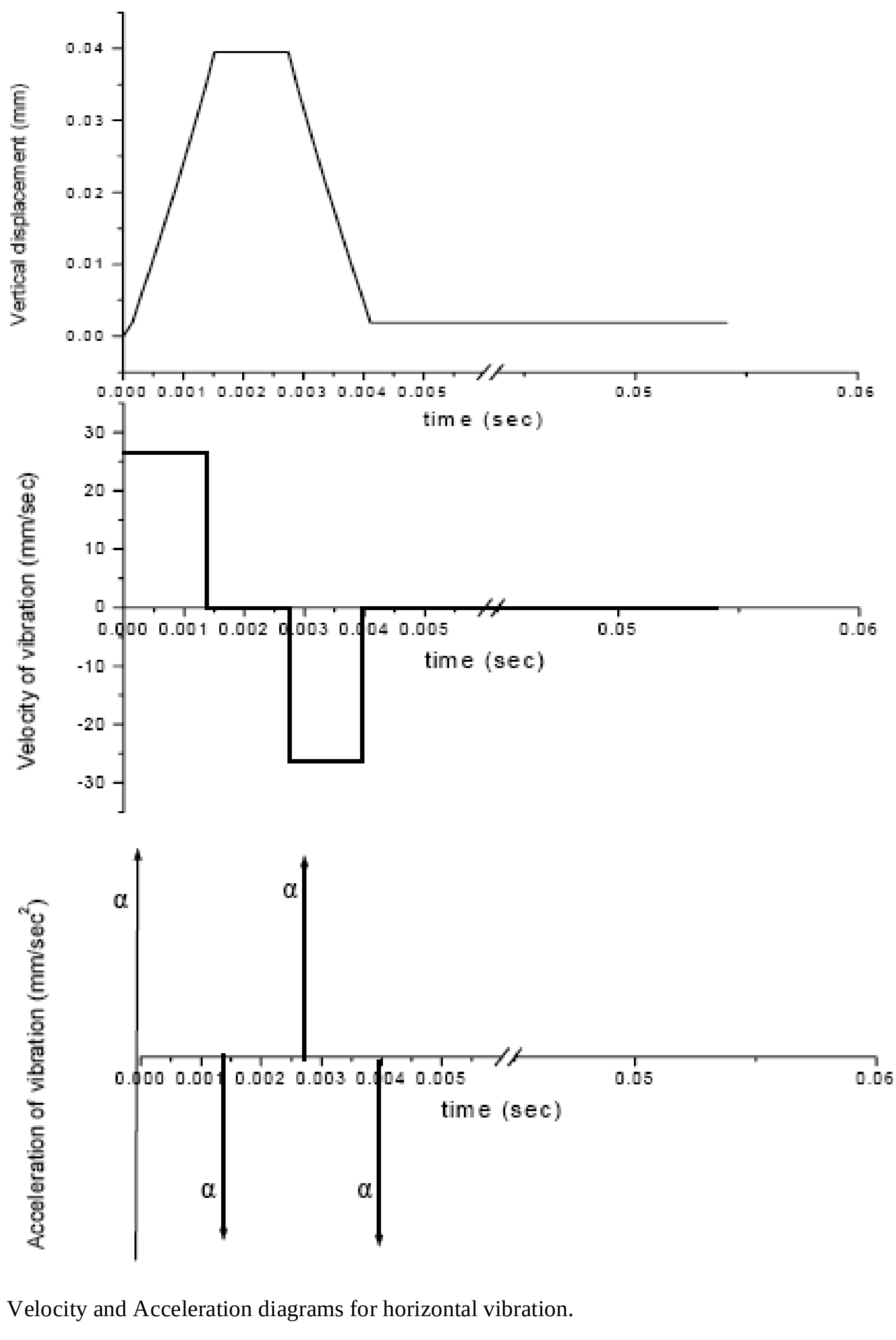

Fig. (2). Displacement, Velocity and Acceleration diagrams for horizontal vibration.

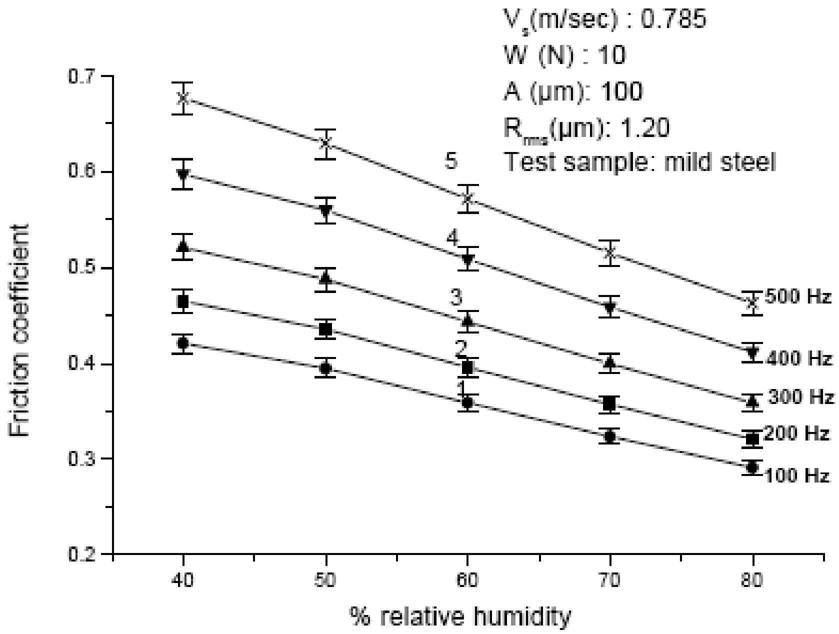

Fig. (3). Friction coefficient *vs*. relative humidity at different frequency of longitudinal horizontal vibration.

extended portion of the rotating table which will transmit vibration of the plate to the vibration sensing pickup. Sliding velocity can be varied by two ways (i) by changing the rotation of the shaft when frequency also changes and (ii) by changing the radius of the point of contact of the sliding pin when frequency does not change. But change of curvature may affect resisting force measurement. By adjusting the height of this slotted plate the amplitude of the vibration can be varied.

The pin with the holder has rocking mode of vibration due to the cantilever action of the holding arm. Considering the small area of contact of the pin and diameter of the rotating disc the sliding velocity can be taken as linear though the sliding surface is rotating.

To rotate the shaft with the table a one-horsepower motor is mounted vertically on a separate base having rubber damper. This separate base was arranged to reduce the affect of vibration of the motor, which may transmit to the main structure. An electronic speed control unit is used to vary the speed of the motor as required.

A 6mm diameter cylindrical pin whose contacting foot is flat made of mild steel, fitted on a holder is subsequently fitted with an arm. The arm is pivoted with a separate base in such a way that the arm with the pin holder can rotate vertically and horizontally about the pivot point with very low friction. This pin can be put to slide at any point of the test sample (disc). Pin holder is designed with the facility of putting dead weight on it so that required normal force will

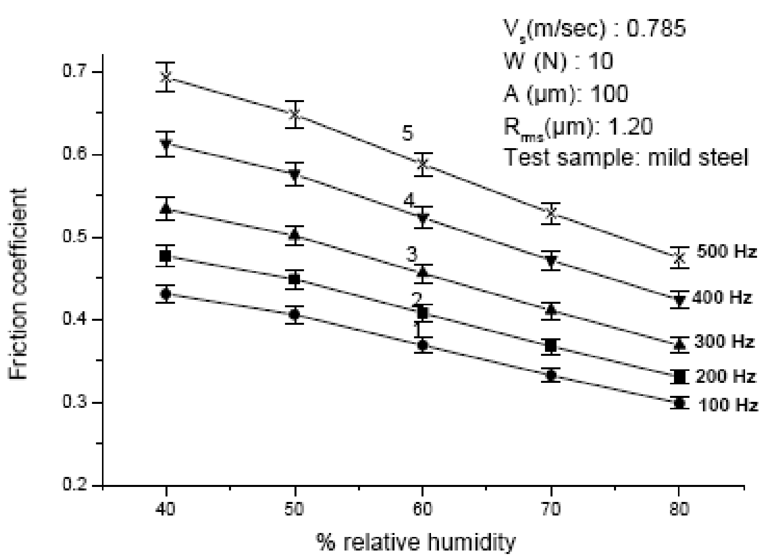

Fig. (4). Friction coefficient *vs*. relative humidity at different frequency of transverse horizontal vibration.

act on the test sample through the pin. The shapes of the pin were maintained cylindrical so that due to loss of surface material of the pin the contacting surface will remain almost constant. To measure the frictional force acting on the pin during sliding on the rotating plate, a load cell (TML, Tokyo Sokki Kenkyujo Co. Ltd, CLS-100NA, Serial no. MR2947) is fitted with a side support such that the load cell prevents the movement of the pin holder. During the rotation of the test sample, pin holder creates pressure on the load cell which gives the measure of the frictional force acting on the pin. Another load cell of the same kind was also used to measure the vertical force acting on the pin. The coefficient of friction is measured as the ratio between horizontal and vertical forces. A data acquisition system was used to measure the force continuously when the system is on and these data are sent directly to the computer. Vibration was measured by using a digital vibration meter (METRIX Instrument Co., Miniature Vibration Meter, Model no. 5500B). A load cell along with its digital indicator (TML, Tokyo Sokki Kenkyujo Co. Ltd, Model no. TD-93A) which was calibrated against a standard proving ring was used for measuring loads. Loss of frictional force at pivot point of the pin holding arm was determined and incorporated in the results. The total set-up was placed inside a chamber whose relative humidity can be adjusted by supplying requisite amount of moisture and dehumidifier. A hygrometer (Wet and Dry Bulb Hygrometer, ZEAL, England) was used to measure the relative humidity of the chamber. A tachometer was used to measure the rpm of the rotating shaft. The surface roughnesses of the test sample were also measured by surface roughness tester (Taylor Hobson Precision Roughness Checker). The first natural frequency of the test setup was found to be 820 Hz. During tests each experiment was repeated several times with fresh sample of pin and disc. In the experimental results as shown in Figs. (**3-4**) and 6-9, ±2.5% error bar has been included.

3. RESULTS AND DISCUSSIONS

In this section the results of variation of friction coefficient with the variation of relative humidity and roughness under horizontal vibration has been discussed.

Figs. (**3-4**) show the variation of friction co-efficient with relative humidity and frequency of vibration. Curves are drawn for different relative humidity with frequency of vibration 100, 200, 300, 400 and 500 Hz.

Curve 1 of Figs. (**3**) and (**4**) shows the variation of friction coefficient with the change of relative humidity from 40% to 80% for frequency of vibration 100 Hz. The values of friction coefficient of this frequency vary from 0.42 to 0.29 and 0.43 to 0.30 for longitudinal and transverse horizontal vibration respectively. Similar trends of reductions are found for 200-500 Hz frequencies i.e. the values of friction coefficient decreases almost linearly with the increase of relative humidity for horizontal vibration. The decrease of friction coefficient with the increase of relative humidity may be due to the moistening affect of the test disc surface that may have some lubricating effect reducing its value. Therefore, it may be concluded that friction coefficient decreases with the increase of relative humidity. These findings are in agreement with the findings of Yasuo Imada [22] without vibration condition and Chowdhury and Helali [23-24] under vertical vibration for mild steel. The materials Sn [20] and Ceramic [21], also show similar behavior i.e, friction co-efficient decreases with the increase of relative humidity. It is found from the experimental results that there is no effect of frequency of vibration on the percentage reduction of friction coefficient at a particular relative humidity and these percentage reductions of friction coefficient increase with the increase of relative humidity. These results are shown in Fig. (**5**) for longitudinal horizontal vibration. Similar trends are observed for transverse horizontal vibration. Note that all these

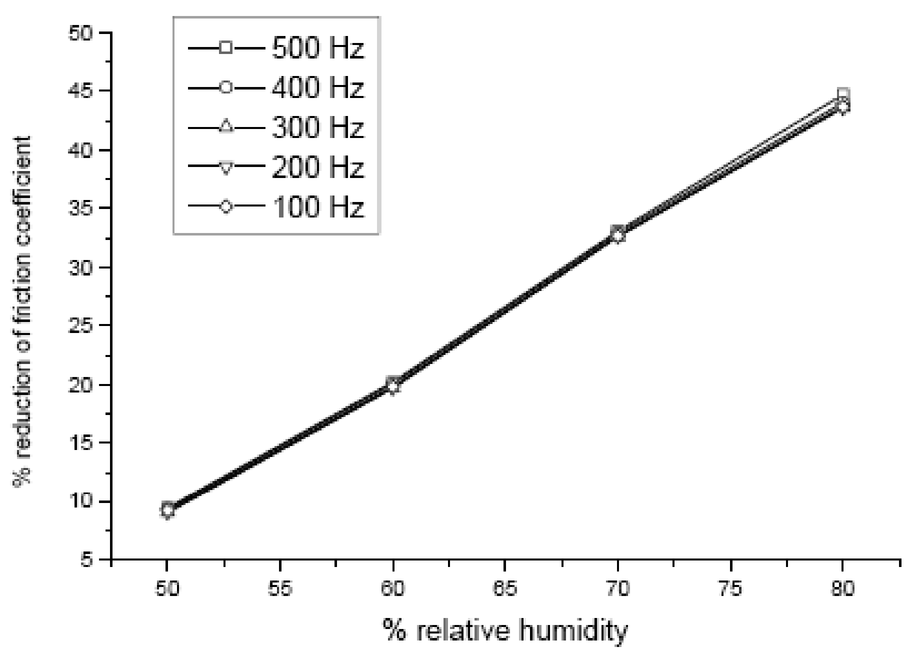

Fig. (5). Percentage reduction of friction coefficient as a function of relative humidity and frequency of longitudinal vibration.

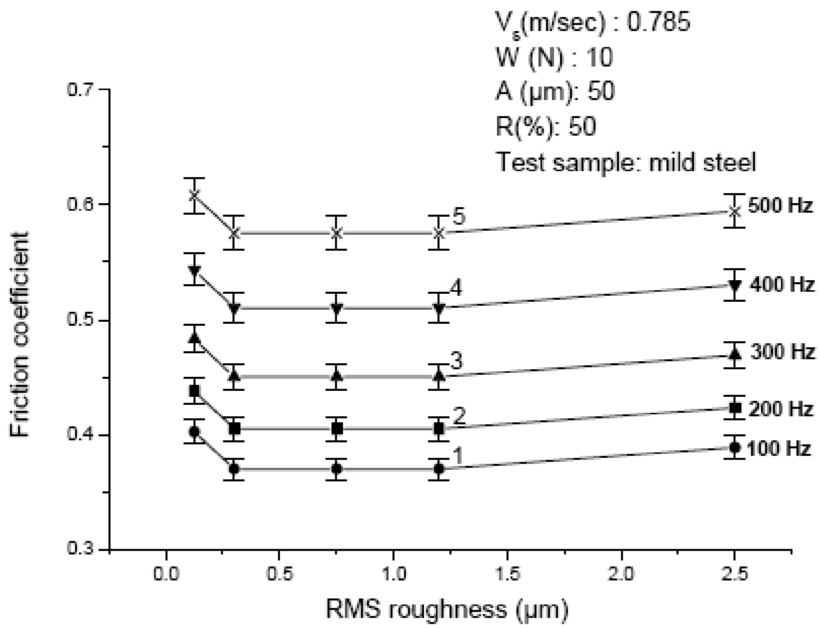

Fig. (6). Friction coefficient *vs*. RMS roughness at different frequency of longitudinal horizontal vibration.

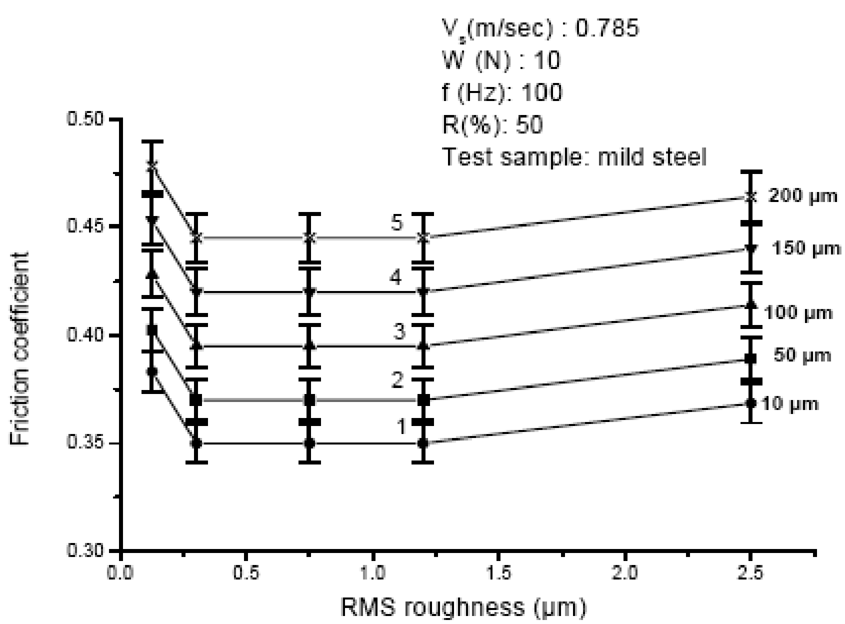

Fig. (7). Friction coefficient *vs*. RMS roughness at different amplitude of longitudinal horizontal vibration.

percentage of variations of friction coefficient are calculated with reference to the values of friction coefficient under 40% relative humidity.

Figs. (**6-9**) shows the effect of surface roughness on friction coefficient for mild steel under amplitude of vibration 10 to 200 μm and frequency of vibration 100 to 500 Hz for longitudinal and transverse vibrations. Curves 1 of Figs. (**6-8**) are drawn for frequency of vibration 100 Hz. It is shown that friction coefficient at very low roughnesses between the ranges of 0.125 to 0.30 μm varies from 0.40 to 0.37 and 0.41 to 0.38 for longitudinal and transverse vibrations respectively. For moderate range of roughnesses between 0.30 to 1.20 μm, the values of friction coefficient are almost constant. The values of friction coefficient are 0.37 for longitudinal vibration and 0.38 for transverse vibration within this range. But roughness in between 1.20 to 2.50 μm, friction coefficient varies from 0.37 to 0.39 and 0.38 to 0.4 for longitudinal and transverse vibration respectively. Curves 2 to 5 of these figures show the variation of friction coefficient at 200, 300, 400 and 500 Hz frequency of vibration, respectively. These curves show similar trend as that of curve 1. All other parameters such as sliding velocity, normal load, amplitude of vibration and relative humidity were almost identical for these five curves. Similar trends are observed for different amplitude of vibration and these results are presented in Figs. (**7**) and (**9**). Friction coefficient is very high at very low roughness because of the growth of real area of contact; it tends to be

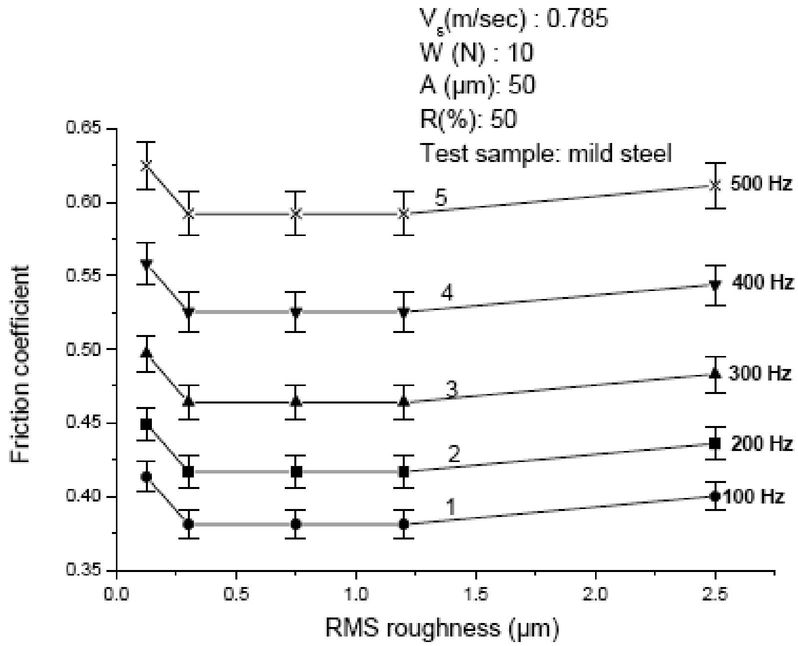

Fig. (8). Friction coefficient *vs*. RMS roughness at different frequency of transverse horizontal vibration.

high at very high roughness because of mechanical interlocking. Similar tests were done for different frequency of vibration and similar trends of results are observed. It is found from the experimental results that there is no effect of roughness on the percentage reduction of friction coefficient at a particular amplitude and frequency of vibration and these percentage reductions of friction coefficient increase with the increase of frequency and amplitude of vibration for horizontal vibrations. These findings are in agreement the findings of Chowdhury for vertical direction of vibration under different amplitudes [17]. These results are also similar to the results of Bhushan [25] and Rabinowicz [26] for no vibration condition. From the experimental results it can also be concluded that friction coefficient increases with the increase of frequency and amplitude of vibration. The increase of friction coefficient with the increase of amplitude and frequency of vibration for horizontal direction of vibration might be due to the fact that the greater the amplitude of vibration, the higher the distance travel along the sliding direction at which the slider slides. Therefore, the increase of friction coefficient for the increase of amplitude might be due to the increase of length of rubbing with the increase of amplitude of vibration. Addition to these, the increase of friction coefficient might be due to (i) fluctuation of inertia force along the direction of friction force (positive and negative), (ii) more sliding causes more abrasion

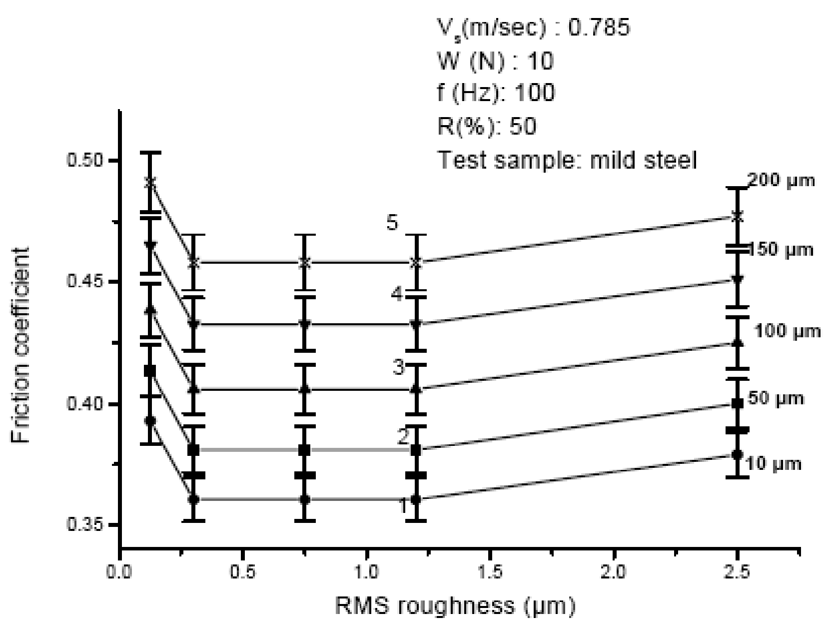

Fig. (9). Friction coefficient *vs*. RMS roughness at different amplitude of transverse horizontal vibration.

resistance. Higher abrasion results more shearing due to penetration and ploughing of the asperities between contacting surfaces that might have some effect on the increment of friction force, (iii) micro-welding, reversal of friction vector and mechanical interlocking, (iv) formation and enhance an electrically charge layer at the interface, (v) increase of solubility due to high temperature [4, 16].

4. CONCLUSIONS

The presence of relative humidity and surface roughness for horizontal direction of vibration indeed affects the friction force considerably. The coefficient of friction is function of relative humidity and frequency of vibration. The values of friction co-efficient decrease with the increase of relative humidity ranging from 40% to 80% for frequency of 100 to 500 Hz of horizontal vibration. There is no effect of frequency of vibration on the percentage reduction of friction coefficient at a particular relative humidity and these percentage reductions of friction coefficient increase with the increase of relative humidity. There is a particular relationship between friction coefficient and surface roughness under transverse and longitudinal horizontal vibration. The variation of friction coefficient with the variation of roughness shows almost similar trends both for different amplitudes and frequencies. The coefficient of friction is high at low roughness, remains constant at moderate range and also high at high roughness under horizontal vibration. Roughness has no effect on the percentage reduction of friction coefficient at a particular amplitude and frequency of horizontal vibration and these percentage reductions of friction coefficient increase with the increase of frequency and amplitude for horizontal vibrations. Results show that coefficient of friction increases with the increase of frequency and amplitude of horizontal vibration for different humidities and roughnesses. As the friction co-efficient decreases with increasing relative humidity and the friction coefficient shows different approaches with low, moderate and high ranges of surface roughness so by maintaining an appropriate level of humidity and roughness for horizontal vibrations friction may be kept to some lower optimum value.

REFERENCES

[1] J.F. Archard, "Wear Theory and Mechanisms," Wear Control Handbook, M.B. Peterson and W.O. Winer, Eds., *ASME*, New York, NY, 1980, pp. 35-80.

[2] D. Tabor, "Friction and Wear – Developments Over the Last 50 Years," Keynote Address, Proc. International Conf. Tribology – Friction, Lubrication and Wear, 50 Years On, London, *Inst. Mech. Eng*., 1987, pp. 157-172.

[3] E.J. Berger, C.M. Krousgrill and F. Sadeghi, "Stability of Sliding in a System Excited by a Rough Moving Surface," *ASME*, vol. 119, pp. 672-680, October 1997.

[4] B. Bhushan, "Principle and Applications of Tribology," John Wiley & Sons, Inc., New York, 1999, pp. 344-430.

[5] D. Godfrey, "Vibration reduces metal to metal contact and causes an apparent reduction in friction," *ASME Trans.*, vol. 10, pp. 183-192, 1967.

[6] T. Skare, and J. Stahl, "Static and dynamic friction processes under the influence of external vibrations," *Wear*, vol. 154, pp. 177-192, 1992.

[7] A. Lehtovaara, " Influence of vibration on the kinetic friction between plastics and ice," *Wear*, vol. 115, pp. 131-138, 1987.

[8] D.M. Tolstoi, G.A. Borisova, and S.R. Grigorova, "Friction reduction by perpendicular oscillations," *Sov. Phys. Dokl*., vol. 17, pp. 907-909, 1973.

[9] O. Wertheim, and I. Bucher, "On the influence of controlled vibration on friction," Research Supported by the ISARELI Academy for Science (Grant. No. 030072), 2000.

[10] W. Lenkiewicz, "The sliding process – effect of external vibrations," *Wear*, vol. 13, pp. 99-108, 1969.

[11] V. Aronov, A.F. D'souza, S. Kalpakjian, and I. Shareef, "Interactions among friction, wear, and system stiffness-part 1: effect of normal load and system stiffness," *ASME J. Tribol*., vol. 106, pp. 54-58, 1984.

[12] V. Aronov, A.F. D'souza, S. Kalpakjian, and I. Shareef, "Interactions among friction, wear, and system stiffness-Part 2: vibrations induced by dry friction," *ASME J. Tribol*., vol. 106, pp. 59-64, 1984.

[13] V. Aronov, A.F. D'souza, S. Kalpakjian, and I. Shareef, "Interactions among friction, wear, and system stiffness-part 3: wear model," *ASME J. Tribol*., vol. 106, pp. 65-69, 1984.

[14] D.H. Hess, and A. Soom, "Normal vibrations and friction under harmonic loads: part i -hertzian contacts," *J. Tribol*, vol. 113, pp. 80-86, 1991.

[15] M.D. Bryant, and J.W. LIN, "Photoelastic visualization of contact phenomena between real tribological surfaces, with and without sliding," *J. Wear*, vol. 170, pp. 267-279, 1993.

[16] T. Skare, and J. Stahl, "Static and dynamic friction processes under the influence of external vibrations," *Wear*, vol. 154, pp. 177-192, 1992.

[17] M.A. Chowdhury, and M.M. Helali, "The effect of amplitude of vibration on the coefficient of friction", *Tribol. Int.*, vol. 41, pp. 307-314, April 2008.

[18] M.A. Chowdhury, and M.M. Helali, "The frictional behavior of materials under vertical vibration", Industrial Lubrication and Tribology, Issue 3 (to be published), 2009.

[19] M.A. Chowdhury, and M.M. Helali, "The effect of direction of vibration on the coefficient of friction", *Indian J. Tribol.*, Issue 1 (to be published), 2009.

[20] Y. Imada, and K. Nakajima, "Effect of humidity on the friction and wear properties of Sn," *J. Tribol.*, vol.117, pp. 737-744, October 1995.

[21] K. Komvopoulos, and H. Li, "The effect of tribofilm formation and humidity on the friction and wear properties of ceramic materials," *J. Tribol.*, vol. 114, pp. 131-140, 1992.

[22] Y. Imada, "Effect of humidity and oxide products on the friction and wear properties of mild steel," *J. Jpn. Soc. Tribol.*, vol. 114, pp. 131-140, 1996.

[23] M. A. Chowdhury, and M. M. Helali, "The effect of frequency of vibration and humidity on the wear rate", *Wear*, vol. 262, pp. 198-203, January 2007.

[24] M.A. Chowdhury, and M.M. Helali, "The effect of frequency of vibration and humidity on the coefficient of friction", *Tribol. Int.*, vol. 39, pp. 958-962, September 2006.

[25] B. Bhushan, *Tribology and Mechanics of Magnetic Storage Devices*, 2nd ed., Springer-Verleg, New York, 1996.

[26] E. Rabinowicz, *Friction Wear Mater*, 2nd Ed., Wiley, New York, 1995.

Compression of Air Discharging from a Blowing Unit

P K Swain, *Department of Mechanical Engineering, Aryan Institute of Engineering & Technology, Bhubaneswar, pkswain25@gmail.com*
Debi Prasad Singh, *Department of Mechanical Engineering, Raajdhani Engineering College, Bhubaneswar, deboprasad_1159@gmail.com*
Ranjan Kumar, *Department of Mechanical Engineering, NM Institute of Engineering & Technology, Bhubaneswar, kumarranjan75@gmail.com*
Barsa Priyadarshini Sahoo, *Department of Civil Engineering, Raajdhani Engineering College, Bhubaneswar, barsap_sahoo@gmail.com*

Abstract: This paper aims at investigating, both through a theoretical and an experimental analysis, the discharging phase of a blowing unit of compressed air, used for the industrial production of plastic made bottles. The proposed mathematical model leads to a system of differential equations describing the flow through an open system. The solution was found by numerical simulations using the software Matlab, determining the gas density, pressure, temperature and mass flow rate, as functions of time. The pressure loss across the down flow has been tackled with a theoretical investigation, determining the mechanical loss coefficient β and evaluating the effect of these losses on the emptying time of the blowing unit. The numerical results agree with the real discharging times obtained by experimental tests, and the proposed improvements allow to reduce loss of pressure and the emptying time of 35% and 20% respectively.

INTRODUCTION

The excellent level, in terms of quality and productivity, reached by industrial bottling lines, in particular the PET bottles lines, proves that the interest in bottling industries, in the last years, is increasing.

The blowing machine here examined is based on an optimised frame, including both the oven for pre-shaped bottles heating and the stretch-blowing units. These ones are mounted on a rotating platform on which the pre-shaped bottles are conveyed, after the heating phase, and the formed bottles evacuation accomplished.

In this paper we deal with one of the main problems of the compressed air discharging phase, that is the reduction of the required time. Even if it doesn't influence the quality of the shaped bottles, it can affect the machine efficiency. With this purpose in mind, problems related to turbulent flux of a gas in not stationary conditions are considered from a theoretical point of view, with particular attention to the quantification of pressure losses and to their influence on the discharging time. On this regard, it is possible to notice a lack of reference in literature; there are no published papers concerning similar or related work by other authors. Finally, we aim at optimizing the discharging phase by acting on the more significant discharge channel obstructions.

The goals of this paper are:

- the analysis of the gas discharging path with a particular attention to geometry and obstructions;
- the proposal of mathematical model able to simulate the discharging phase;
- the evaluation of the loss of pressure coefficient β (taking account of both concentrated and distributed losses);
- the improvement of the channel geometry aimed at reducing the discharge phase time.

ANALYSIS OF THE GAS OUTFLOW

During the platform rotation, on the blowing units the stretch-blowing and air exhaust processes occur (Fig. **1**). The discharging phase of the compressed air from the blowing unit occurs after the stretch-blowing phase, when the bottle has been already shaped.

A solenoid valve controls the compressed air inlet into the blowing unit for the bottle filling. Once the valve is closed, an air volume (including the bottle, the blowing nozzle, a double effect cylinder in which is located the stem for the bottle stretching, a flexible duct and a valve control unit) is isolated. After the stretch-blowing phase, the compressed air reaches a thermodynamic equilibrium with a temperature of 10 °C and a pressure of 37 bar (the blow moulding process takes place at a temperature around 3 °C). These conditions have been measured by means of thermocouples and manometers [1]. The discharging phase starts at the opening of the solenoid valve. The compressed air flows through a second flexible duct which connects the valve control unit with a muffler, which reduces the acoustic noise caused by the gas ejection. A cooling unit is installed, aimed at reducing the air temperature and its aptitude to keep humidity, so that the risk of condensation is decreased.

The mathematical model considers a thermodynamic system constituted by a gas in a tank. At first the discharge valve is closed and the tank contains a gas whose absolute pressure is higher than the atmospheric pressure. Once the discharge valve is opened, the discharging of the gas into the atmospheric environment is studied, being well-known the volume of the tank, the exit gas cross-section, the initial and boundary thermodynamic conditions and the nature of the gas.

The following hypotheses are assumed:

- the gas is compressible with uniform physical properties;
- the process is adiabatic;
- the pressure head is described by introducing the mechanical loss coefficient β [2,3], defined as:

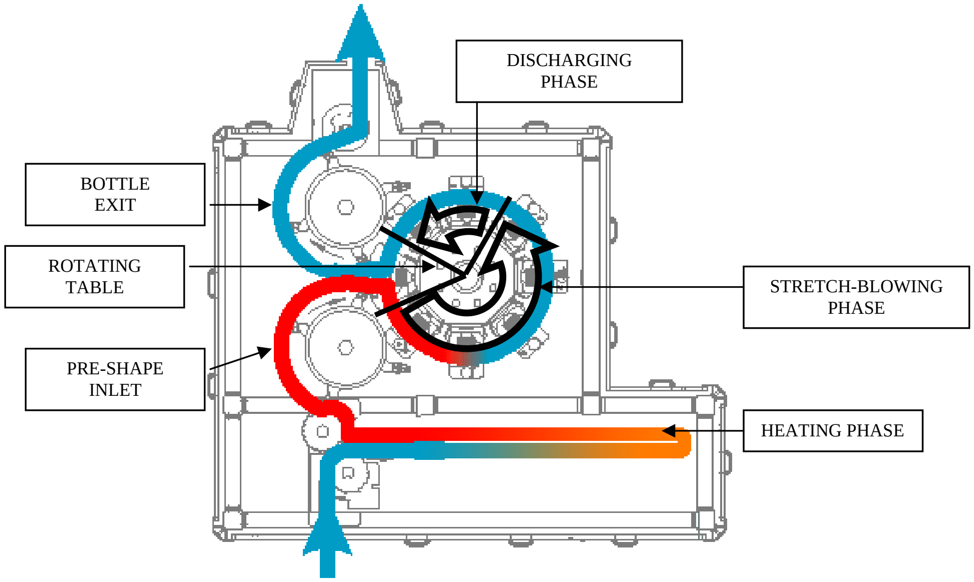

Fig. (1). Main phases of the process.

$$\frac{p-p_o}{\rho}=\beta\frac{W^2}{2} \tag{1}$$

In this model the mechanical losses, both concentrated and distributed, are located exactly in the exhaust section, which acts, in this way, as the only obstruction to the down flow. The mechanical loss coefficient β, defined in Eq. (1), connects gas pressure and density just upstream the exhaust section with gas pressure downstream and average velocity on the exhaust section. The discharging phase is extremely fast, hence the transformation can be considered adiabatic.

The parameters used in simulating the discharging process from the blowing machine, are [4] γ= 1.4, R = 287.041 J/kgK, c_v= 716.4 J/kgK, V = 1.768x10^{-3} m^3, S = 1.767x10^{-4} m^2, p_{in}= 37 bar, p_0= 1.01325 bar, T_{in}= 10 °C. For the ideal gas, the initial density would be ρ_{in}= 45.52 kg/m^3.

IDEAL GAS MODEL

In transient conditions, the energy balance equation for the ideal gas is:

$$m\left[\frac{W^2}{2}+c_v\left(T-T_R\right)+RT\right]= \\ =-\frac{\partial M}{\partial \tau}c_v\left(T-T_R\right)-M\,c_v\frac{\partial T}{\partial \tau} \tag{2}$$

The mass balance equation reads as:

$$M(\tau)=\rho(\tau)V \text{ and } -\frac{\partial M}{\partial \tau}=m \tag{3}$$

The mean velocity is linked to the mass flow rate:

$$W=\frac{m}{\rho S}=-\frac{V}{S}\frac{1}{\rho}\frac{\partial \rho}{\partial \tau} \tag{4}$$

As a consequence, the gas pressure is linked to the density, from Eq. (1), as follows:

$$\frac{W^2}{2}=\frac{p-p_o}{\rho\beta}=\frac{V^2}{2S^2}\frac{1}{\rho^2}\left(\frac{\partial\rho}{\partial\tau}\right)^2 \tag{5}$$

The pressure and its derivative are then:

$$p=\frac{\beta V^2}{2S^2}\frac{1}{\rho}\left(\frac{\partial\rho}{\partial\tau}\right)^2+p_o \\ \frac{\partial p}{\partial\tau}=\frac{\beta V^2}{2\rho S^2}\frac{\partial\rho}{\partial\tau}\left[2\frac{\partial^2\rho}{\partial\tau^2}-\frac{1}{\rho}\left(\frac{\partial\rho}{\partial\tau}\right)^2\right] \tag{6}$$

The time derivative of temperature, for the ideal gas, is:

$$\frac{\partial T}{\partial\tau}=\left(\frac{1}{\rho}\frac{\partial p}{\partial\tau}-\frac{p}{\rho^2}\frac{\partial\rho}{\partial\tau}\right)\frac{1}{R} \tag{7}$$

Hence the Eq. (2) reads as:

$$\frac{\partial\rho}{\partial\tau}\left[\frac{\partial^2\rho}{\partial\tau^2}-\frac{1}{2\rho}\left(\frac{\partial\rho}{\partial\tau}\right)^2\frac{\gamma\left(1+\beta\right)+\beta-1}{\beta}-\frac{\gamma S^2}{\beta V^2}p_0\right]=0 \tag{8}$$

valid if $\rho \neq 0$. This is a second order differential equation, not linear and written in a not normal form (that means not singleness of the Cauchy's problem).

Nevertheless, the solution investigated is not easy to obtain.

The gas density decrease is expected at the initial moment, in which the tank is opened, hence $\partial\rho/\partial\tau \neq 0$.

By defining the new function:

$$u(\rho)=\frac{\partial\rho}{\partial\tau} \tag{9}$$

the Eq. (8) can be written as:

$$u\frac{\partial u}{\partial\rho}-\frac{C_1}{2\rho}u^2=C_2 \tag{10}$$

where the known constants C_1 and C_2 are:

$$C_1 = \gamma + 1 + \frac{\gamma - 1}{\beta} \qquad C_2 = \frac{\gamma S^2}{\beta V^2} p_o \tag{11}$$

The first order differential Eq. (10) requires, to be solved, a further definition:

$$z(\tilde{n}) = u^2 \tag{12}$$

Hence the first order linear differential equation is obtained

$$\frac{\partial z}{\partial \rho} - \frac{C_1}{\rho} z = 2 C_2 \tag{13}$$

whose solution has the following form:

$$z(\rho) = \rho^{C_1} \left(\frac{2 C_2}{1 - C_1} \rho^{1 - C_1} + K \right) \tag{14}$$

with K constant of integration calculated by means of the initial condition.

Using the Eqs. (10) and (12), the solution (14) can be written as:

$$\frac{\partial \rho}{\partial \tau} = \pm \left(\frac{2 C_2}{1 - C_1} \rho + K \rho^{C_1} \right)^{\frac{1}{2}} \tag{15}$$

The only solution with physical meaning is the negative one, because, when the tank is opened, the density of the gas is expected to drop.

The existence domain for the solution to the Eq. (15) is:

$$\rho \geq \left(- \frac{2 C_2}{(1 - C_1) K} \right)^{\frac{1}{C_1 - 1}} \tag{16}$$

The steady state is represented by $\partial\rho/\partial\tau = 0$, which implies:

$$\rho^* = \left(- \frac{2 C_2}{(1 - C_1) K} \right)^{\frac{1}{C_1 - 1}} \tag{17}$$

The density function ρ is monotonically decreasing; it reaches its steady state at the time τ^*, so that the solution to the problem is the solution to the Eq. (15) for $\tau \leq \tau^*$, the Eq. (17) for $\tau \geq \tau^*$.

Even any small oscillation of ρ, due to pressure waves spreading along the exhaust duct, can be ruled out by a qualitative analysis [5] of the differential equation. The phenomenon concerning the emptying of the tank ends after a τ^* time, just when the first derivative of ρ is zero.

Coming back to the Eq. (15) and integrating it, starting from the initial state $\tau = 0$, we get:

$$\int_0^\tau d\tau' = - \int_{\rho_{in}}^{\rho} \left(\frac{2 C_2}{1 - C_1} \rho' + K \rho'^{C_1} \right)^{-\frac{1}{2}} d\rho' \tag{18}$$

Unfortunately there is not an analytical solution to the Eq. (18). So, after having reduced the beginning linear differential equation in order to obtain a qualitative analysis of the solution, it is suitable resorting to a numerical analysis.

The solution to Eq. (8) has been numerically investigated using a dedicated software: Matlab. Matlab collects additional software modules, called "toolboxes", which perform specific tasks. Many of these toolboxes can be used to solve differential equations with constant coefficients. In particular, the Runge-Kutta method of second and third class [6], has been chosen to solve this model. The respective solver function of Matlab is "ode23"; it is a one step solver which solves initial value, moderately stiff problems.

REAL GAS MODEL

Looking at the intensive properties (pressure and temperature), for both initial state and critical point of air, the reduced coordinates have been computed and, resorting to the Nelson-Obert diagram [2], the compressibility factor has been calculated. It allows quantifying the real gas deviation from the ideal gas behaviour. Fearing the ideal gas hypothesis not reliable, a second model of calculation has been accomplished: the real gas model, according to Van der Waals equation:

$$\left(p + \frac{a}{v^2} \right) (v - b) = R T \tag{19}$$

Following the same procedure as for the ideal gas model, the energy balance equation reads as:

$$\begin{aligned} \frac{\partial \rho}{\partial \tau} \Big\{ (1 - b\rho) \frac{\partial^2 \rho}{\partial \tau^2} - \frac{1}{2\rho} \left(\frac{\partial \rho}{\partial \tau} \right)^2 \Big[\frac{R}{c_v} \frac{\beta + 1}{\beta} + \\ + 2 - b\rho \Big] - \left(\frac{R}{c_v} + 2 b \rho - 1 \right) \frac{a S^2}{\beta V^2} \rho^2 + \\ - \left(\frac{R}{c_v} + 1 \right) \frac{S^2}{\beta V^2} p_o \Big\} = 0 \end{aligned} \tag{20}$$

valid if $\rho \neq 0$.

It can be observed that, if a and b were supposed negligible, the energy balance Eq. (20) would coincide with the differential Eq. (8) of the ideal gas model.

Solving this second order not linear differential equation, the behaviour the tank discharge can be described. Even in this case, the computation of the equation has been carried out numerically using Matlab, in particular the function solver "ode23".

Some more parameters of the air must be introduced, exactly: $a = 161.9\ (m^3/kg)^2$ Pa, $b = 1.26 \times 10^{-3}\ m^3/kg$ [2].

The density value at the initial state has been computed, being known pressure and temperature values, applying the Van der Waals equation. It is equal to ρ_{in}=46.98 kg/m^3, slightly different from the value for the ideal gas model (45.52 kg/m^3).

THE LOSS COEFFICIENT β

The coefficient β, defined by the Eq. (1), represents all the coefficients of mechanical losses (both concentrated and distributed) related to the flow in the control volume:

$$\beta = \sum_{1}^{n} \beta_i \tag{21}$$

with $\beta_i = \beta_{ci} + \beta_{di}$.

The computation of the coefficient β has been carried out by means of a dedicated literature [7], presenting a huge collection of tables and charts for every kind of pressure loss encountered by a fluid stream.

By the results obtained [7], it comes up that the distributed losses just represent 5% of the total losses. This gives reason to the initial hypothesis: the coefficient of mechanical losses β is particularly affected by the concentrated mechanical losses, i.e. by the duct geometry. For the particular geometry here considered, the loss coefficient is β = 39.93 [7].

RESULTS

This section shows the perfect gas model results. These results have been obtained introducing into the model, not only the known parameters related to gas properties, system

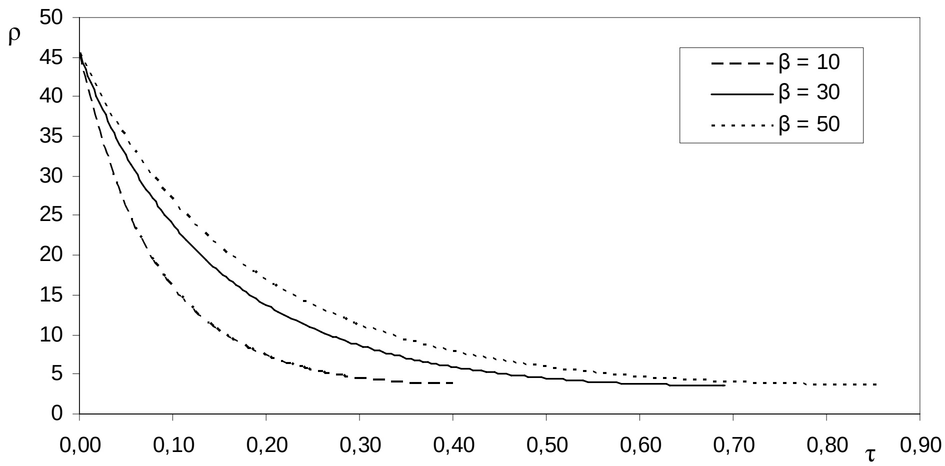

Fig. (2). Transient air density within the open thermodynamic system.

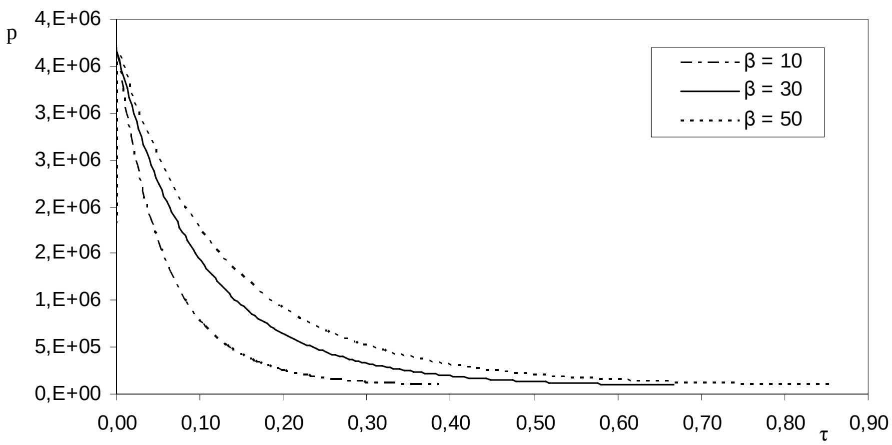

Fig. (3). Absolute air pressure within the open thermodynamic system.

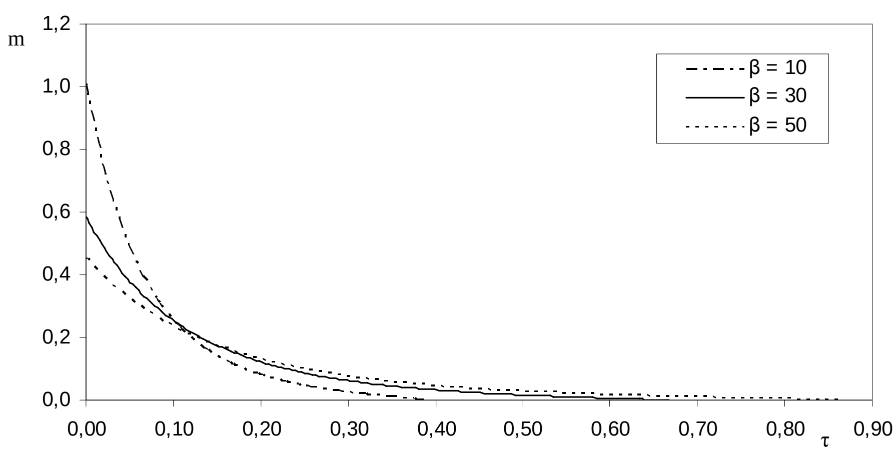

Fig. (4). Airflow rate from the open thermodynamic system.

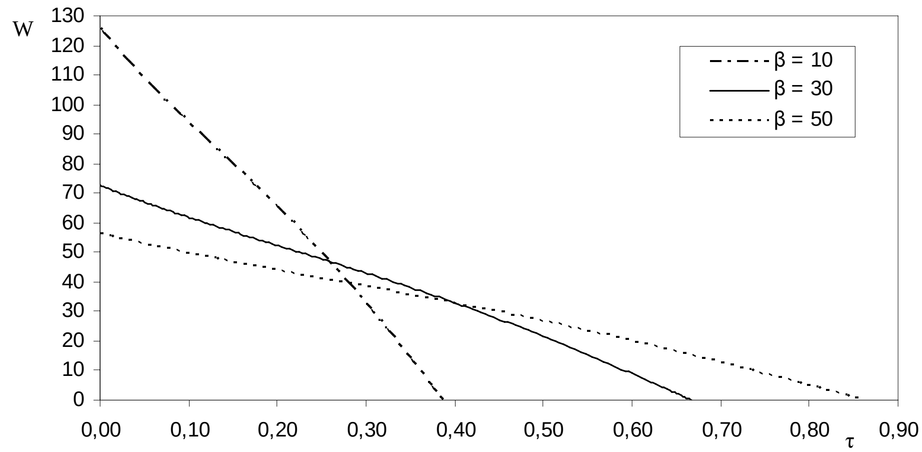

Fig. (5). Air velocity in the outflow section during the transient.

geometry, and boundary and initial thermodynamic conditions, but also the coefficient of mechanical losses β.

Figs. (**2-5**) represent a comparison between the time evolution of density, pressure, flow rate and gas velocity according to ideal gas model for three different values of the coefficient β.

Introducing into the ideal and real gas models, the value of β computed for the blowing machine, and looking at the moment in which the gas density derivative becomes zero, that is the same in which the air pressure reaches the atmospheric value, we are able to know the time needed to complete the exhaust phase:

$$\begin{cases} \tau = 0.7695\,\text{s} & \text{Perfect gas model} \\ \tau = 0.7705\,\text{s} & \text{Real gas model} \end{cases} \tag{22}$$

As the mechanical losses appeared to be mostly concentrated into the double effect cylinder, a test was carried out on the cylinder, using two digital manometers (to measure pressure upstream and downstream), a Pitot tube (to measure average velocity) and a thermocouple. Following

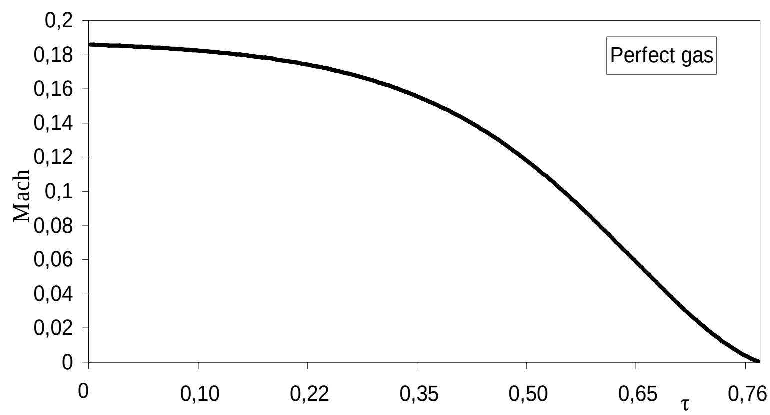

Fig. (6). Mach number during the discharge transient.

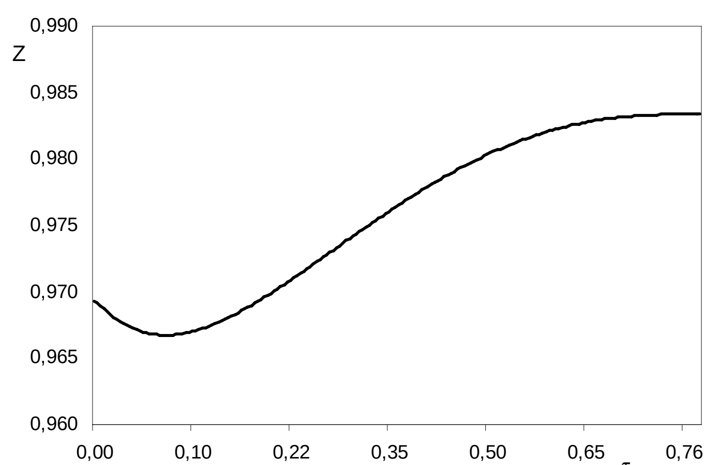

Fig. (7). Compressibility factor evolution during the discharge transient.

the results of the experimental tests [1], the time required by the blowing machine, to discharge the quantity of air needed to shape a plastic bottle (1.5 dm^3) is about 0.7÷0.8 s.

In Fig. (**6**) the Mach number is reported in the exit section, during the discharge transient. It is always less than unit. This result let us say the air discharge from a blowing station happens with a subsonic motion.

The comparisons concerning results obtained with ideal gas and real gas models, show a considerable similarity. This consideration is analytically proven; in fact Fig. (**7**) shows that the compressibility factor, calculated with the equation:

$$Z = \frac{p}{R\,\rho\,T} \tag{23}$$

is about a unitary value during the entire transient.

With the purpose of reducing the time required to carry out the complete outflow of the gas (that means to increase the machine performance) the possibility to decrease the coefficient of mechanical losses β has been investigated. Paying attention to the geometric components, in particular the two bushings of the stem set into the double effect cylinder, which appeared to be the major obstacles to the air flow, and modifying properly their geometry, the coefficient β has been reduced from 39.93 to 25.95.

Introducing the new value of β into the ideal and real gas models, it has been found a reduced time for the discharging phase:

$$\begin{cases} \tau = 0.6207\,\text{s} & \text{Perfect gas model} \\ \tau = 0.6287\,\text{s} & \text{Real gas model} \end{cases} \tag{24}$$

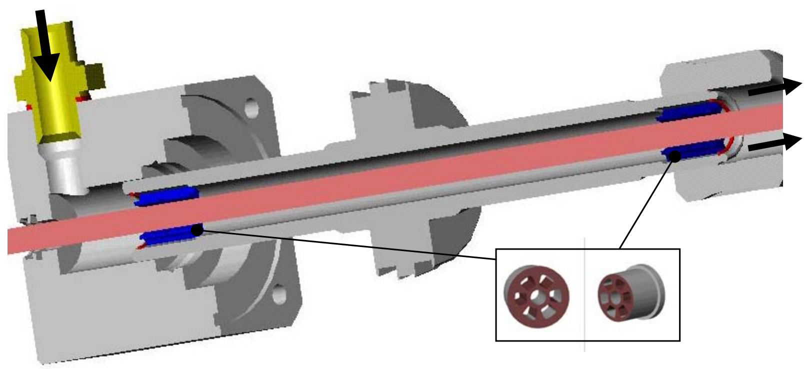

Fig. (8). Section view of the air discharging flow into the stretch-blowing unit, with a zoom view of the stem bushings.

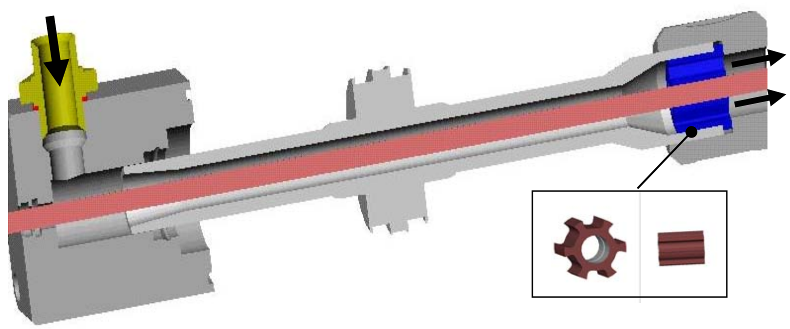

Fig. (9). Section view of the air discharging flow into the stretch-blowing unit, with a zoom view of the stem bushings, after the optimisation

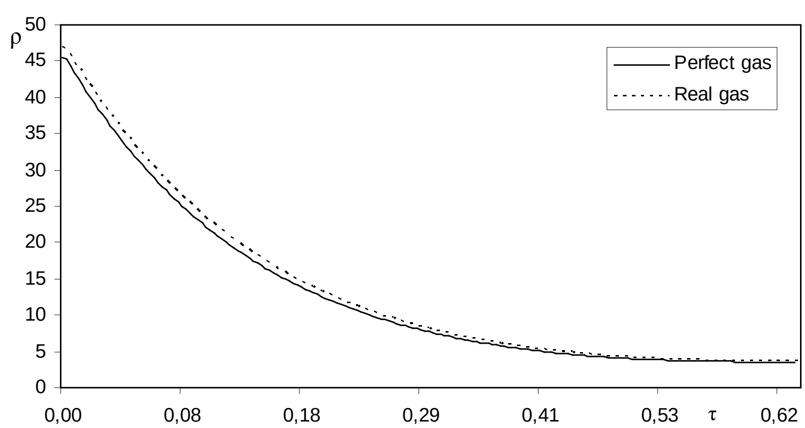

Fig. (10). Air density evolution during discharging phase, after the optimisation of the duct geometry.

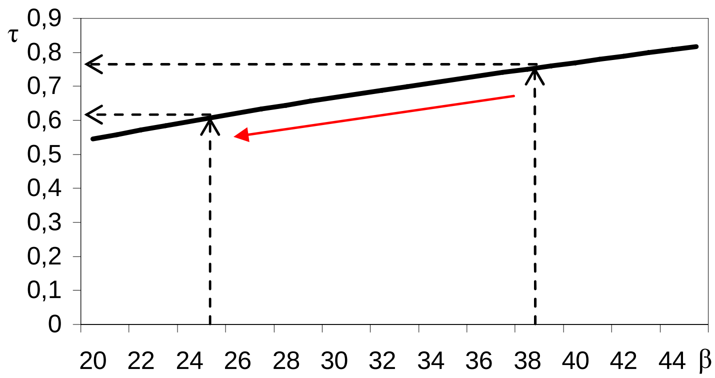

Fig. (11). Time of the discharging phase as a function of the coefficient of mechanical losses.

The stretch-blowing unit is shown in Figs. (**8-9**), focusing the stem bushings before and after the optimization, respectively.

Fig. (**10**) shows the air density evolution during the transient.

Fig. (**11**) shows the required time for the discharging phase, as a function of the coefficient of mechanical losses.

CONCLUSIONS

In this study, a numerical model has been carried out in order to analyze the discharging phase of air from a blowing machine. The model of simulation is based on the laws of thermodynamic governing the outflow of a compressible gas from an open system.

The mechanical losses, due to each geometrical singularity of the ducts crossed by the air, have been estimated. The discharging path has been modified in order to reduce their relevance. An investigation how the exhaust phase length is affected by the total coefficient of mechanical losses was carried out.

The geometry optimisation of the discharging path showed a reduction of the coefficient β of 35% and a discharging time reduction of 20% that means to increase the blowing machine efficiency.

Another parameter affecting the time reduction is the air temperature at the beginning of the discharging phase into the blowing unit.

The real gas model and the ideal gas model give very similar results, being the compressibility factor Z very close to unity. Future work will be focussed on the 3-D gas velocity and temperature, obtained through numerical analysis, slightly simplified by the ideal gas model.

GLOSSARY

a = Van der Waals coefficient in Eq. (19); $(m^3/kg)^2$ Pa

b = real gas covolume; m^3/kg

C_1 = dimensionless coefficient

C_2 = constant; $kg/m^3\ s^2$

c_p = specific heat at constant pressure; J/kg K

c_v = specific heat at constant volume; J/kg K

K = constant of integration for the Eq. (14)

m = gas mass flow rate; kg/s

M = air mass into the tank; kg

Ma = Mach number W/W_s

n = number of singularities along the discharging path

p = pressure; Pa

p_0 = atmospheric gas pressure; Pa

R = ideal gas specific constant; J/kg K

S = gas outlet section surface; m^2

T = gas temperature; K

T_R = conventional temperature corresponding to zero value of the gas internal energy; K

v = specific gas volume; m^3/kg

V = tank volume; m^3

W = average gas velocity; m/s

W_s = sound velocity in the gas; m/s

Z = compressibility factor

GREEK SYMBOLS

β = mechanical loss coefficient

γ = c_p/c_v ratio

ρ = gas density; kg/m^3

ρ* = steady state density defined in Eq. (17); kg/m^3

τ = time; s

τ* = instant time corresponding to $\rho(\tau)=\rho^*$

SUBSCRIPTS

c = concentrated mechanical losses

d = distributed mechanical losses

i = singularity along discharging path

in = initial time, $\tau = 0$

ACKNOWLEDGEMENTS

The contribution of SIG Simonazzi SpA Noceto (Parma, Italy) is gratefully acknowledged.

REFERENCES

[1] SIG Simonazzi, Noceto, Parma, Italy, personal communication. 2004.
[2] K. K. Jr Wark, *Thermodynamics.* McGraw-Hill, 5^{th} ed., New York, 1988.
[3] E. M. Greitzer, C. S. Tan and M. B. Graf, *Internal Flow*, Cambridge University Press, 2004.
[4] K. Raznjevic, *Handbook of Thermodynamic Tables*, Begell House Inc., New York, 1995.
[5] M. Abramowitz and I. A. Stegun, *Handbook of Mathematical Functions*, Dover Publications Inc., New York, 1972.
[6] T. L. Barman, J. Dabney and N. Richert, *Advanced Engineering Mathematics with Matlab*, Brooks/Cole, Pacific Grove, 2000.
[7] I. E. Idel'cik, *Mémento des pertes de charge*, Editions Eyrolles, Paris, 1986.

Computational Aerodynamics Simulation of NREL Phase Rotor

Babita Meher, *Department of Mechanical Engineering, Aryan Institute of Engineering & Technology, Bhubaneswar, baitamh784@gmail.com*

Bipash Mohanty, *Department of Civil Engineering, Capital Engineering College, Bhubaneswar, bipashmohanty784@gmail.com*

S. C. Mishra, *Department of Civil Engineering, NM Institute of Engineering & Technology, Bhubaneswar, scmishra11@yahoo.co.in*

Chinmay Swain, *Department of Mechanical Engineering, Raajdhani Engineering College, Bhubaneswar, chinmayswain1972@gmail.com*

Sidharth Pradhan, *Department of Mechanical Engineering, Capital Engineering College, Bhubaneswar, sidharthpradhan265@gmail.com*

Abstract: The work presented in this article aims to the calculation of the aerodynamic characteristics of the NREL phase II rotor that is a horizontal axis downwind wind turbine rotor and which is assumed to stand isolated in the space. The Reynolds averaged Navier-Stokes equations combined with the Spalart-Allmaras turbulence model that describes the three dimensional steady state flow about the wind turbine rotor are solved with the aid of a commercial CFD code. A structured grid of approximately 3.3 million cells formulates the computational domain. The numerical results for the considered wind turbine rotor are benchmarked against wind tunnel measurements obtained at free stream velocity of 7.2m/s in the framework of VISCEL project. The comparisons show that the used CFD code can accurately predict the span-wise loading of the wind turbine rotor.

Keywords: Wind turbine, NREL phase II rotor, VISCEL project, CFD.

INTRODUCTION

With the experience of “oil shock” in the early 1970s and the environmental impact of burning fuels, energy policy has confirmed the improvement of the environmental sustainability of energy as a primary objective and the use of renewable sources [1]. Wind power generation is an environmental friendly method of generating electric energy through the operation of a generator attached to the axis of a rotor blade that turns due to the rotational action of the resultant aerodynamic force generated by the change of wind momentum. Since wind energy is a low-density source of power, it is important to maximize the efficiency of wind machines. The prediction of the aerodynamic properties of wind turbines is more challenging in many ways than that of already complicated problems such us helicopter rotors and propellers.

The design of a wind turbine rotor requires accurate, reliable and robust numerical predictions. The literature reports various methods that compare numerical predictions to experiments. The methods vary from blade element momentum (BEM) theory [2], vortex lattice [3], coupled viscous/potential panel [4] to variants of Reynolds averaged Navier-Stokes (N-S) [5, 6]. The computer related requirements which set in full N-S simulations [7-9] are overcome with hybrid N-S solver/free wake method. In this method, the computational domain is divided in N-S regions near the rotor blade and potential flow regions on outer field where free vortex methods are used to model the vortical flowfield [10-12].

BEM methods although based on a “two-dimensional” theory provide acceptable approximations to the axisymmetric distribution of inflow and loads found under conditions where the wind is normal to the plane of the rotor (i.e., the turbine is in zero yaw angle with respect to the oncoming wind), and there are no dynamic stall effects [13]. This explains their use in the preliminary studies concerning the performance of horizontal axis wind turbine (HAWT) rotors. A full aerodynamic analysis however should take into account important operational parameters like wind turbulence and shear. This can be accomplished with the full Navier-Stokes solvers. This class of methods has the potential to provide a consistent and physically realistic simulation of the turbine flow field. The field of CFD applied to rotating-blade problems is reviewed by McCroskey [14], Landgrebe [15], Hansen *et al.* [16] and Hu *et al.* [17].

The aim of the present work is to perform a 3-D flow analysis of a three-bladed small-sized rotor from the Viscous and Aeroelastic Effects on Wind Turbine Blades - Phase II (VISCEL-II) project [18] with the aid of a commercially available CFD package. Several 2-D and 3-D simulations were carried out to yield information on different aspects involved, ranging from aerodynamic calculations to wake development. The calculations are compared with experimental data for validation purposes.

TURBINE GEOMETRY

The National Renewable Energy Laboratory (NREL) phase-II rotor mounted on a downwind machine is a small three bladed HAWT rotor with 5.029m radius [19], as shown in Fig. (**1**). The blades of the phase-II rotor are non-twisted and non-tapered with a constant cord of 0.4572m. The NREL S809 airfoil series is used, except for the root. At 14.4% span the airfoil thickness is t/c=43% and decreases linearly to t/c=20.95% at 30% span, while outboard of 30%, thickness is constant at that value. The nominal rotation speed is 71.68 rpm and the pitch is 12 deg. This HAWT rotor was chosen to use data from the NREL phase-II experiment as reported in ‘IEA Annex XIV:Field Rotor Aerodynamics’ [18] where also the geometry of the rotor is thoroughly described.

Fig. (1). Different views of the NREL Phase II Rotor.

DESCRIPTION OF THE N-S SOLVER

The physico-mathematical modeling of the complicated HAWT rotor flow is provided by the steady, incompressible, isothermal Reynolds Averaged Navier-Stokes (RANS) equations [20, 21], i.e.

$$\nabla(u_i) = 0 \qquad (1)$$

$$\rho\frac{\partial}{\partial x_j}(\bar{u}_i\bar{u}_j) = -\frac{\partial\bar{p}}{\partial xi} + \frac{\partial}{\partial x_j}(\bar{\tau}_{ij} - \overline{\rho u_i u_j}) \qquad (2)$$

combined with one of the existing options for turbulence modeling. The one-equation Spalart-Allmaras model [22, 23] with standard wall functions ($y^+ \geq 30$) is proposed due to its efficiency in combining accuracy with low computing cost.

$$\frac{\partial}{\partial t}(\rho\bar{v}) + \frac{\partial}{\partial x_i}(\rho\bar{v}u_i) =$$

$$G_v + \frac{1}{\sigma_{\bar{v}}}\left\{\frac{\partial}{\partial x_j}\left[(\mu+\rho\bar{v})\frac{\partial\bar{v}}{\partial x_j}\right] + C_{b2}\rho\left(\frac{\partial\bar{v}}{\partial x_j}\right)^2\right\} - Y_v + S_{\bar{v}} \qquad (3)$$

where G_v is the production of turbulent viscosity, Y_v is the destruction of turbulent viscosity that occurs in the near-wall region due to wall blocking and viscous damping, ν is the molecular kinematic viscosity, $\tilde{\nu}$ is identical to the turbulent kinematic viscosity except in the near-wall region, $\sigma_{\tilde{\nu}}$ and C_{b2} are constants and $S_{\tilde{\nu}}$ is a user defined source term.

The transport variable $\tilde{\nu}$ is related to the turbulent viscosity as follows

$$\mu_t = \rho\tilde{\nu}f_u \qquad (4)$$

The viscous damping function f_u is given by

$$f_u = \frac{\chi^3}{\chi^3 + C_u^3} \qquad (5)$$

where χ relates the molecular velocity and the transport variable and is defined by the following equation

$$\chi \equiv \frac{\tilde{\nu}}{\nu} \qquad (6)$$

The equations are solved by the commercial code Fluent [21] using the single reference frame (SRF) technique attached to the blades of the rotor. The non-linear system of equations implies the segregated solver, thus is solved sequentially. PRESTO and QUICK discretization schemes are used for the continuity and the momentum equations respectively. The PRESTO scheme [24] uses the discrete continuity balance for a "staggered" control volume about the face to compute the "staggered" pressure. QUICK-type schemes [25] are based on a weighted average of second-order-upwind and central interpolations of the variable. As the code solves the incompressible flow equations, no equation of state exist for the pressure, and the SIMPLE algorithm is used to enforce pressure-velocity coupling.

COMPUTATIONAL DOMAIN AND GRID

In the current research work, the wind turbine tower and the ground are neglected, which is a fair approximation for HAWT rotor simulation. The computational domain is enclosed between a small inner cylinder and an outer cylinder with diameter equal to 6 times the rotor diameter, both axial centered. Thus, the region, which includes the hub of the rotor, is completely removed from the domain. The field is extended to 8 rotor diameters downwind of the turbine and 2 diameters upwind. Exploiting the 120 degrees periodicity of the three-bladed rotor, only one of the blades is explicitly modeled using the SRF technique as shown in Fig. (**2**).

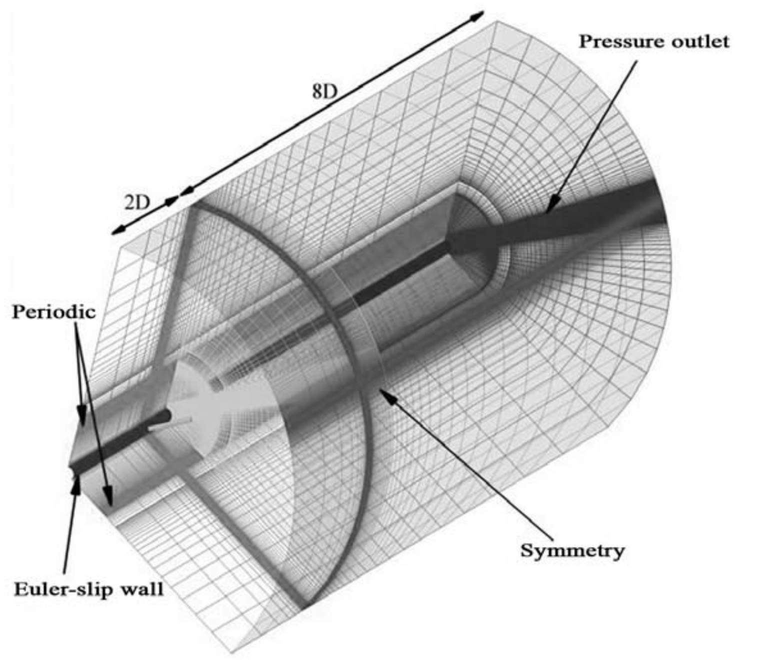

Fig. (2). The control volume meshing in 120 degrees section and definition of the boundary conditions.

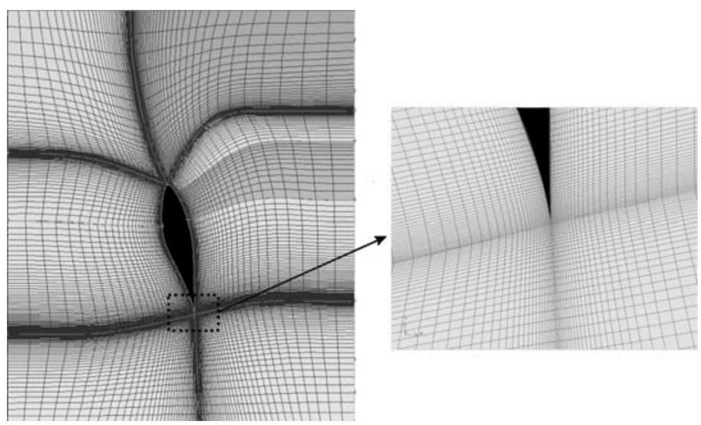

Fig. (3). Mesh construction around the blade of the rotor. Left picture shows the mesh around the blade and the right picture shows detail of the mesh near the trailing edge of the blade.

The Fluent's pre-processor Gambit is used to create the volume mesh. It is a hexahedral mesh of approximately 3.3 million cells (145x135x167 cells in x, r and ϑ directions respectively). As shown in Fig. (**3**), the grid around the blade is H-type which is optimized to resolve the boundary layer for standard wall functions ($y^{+}\geq 30$). All the calculations were carried out in an Intel Core 2 quad Extreme QX6800 with 8Gb Ram. The number of iterations adjusted to reduce the scaled residual below the value of 10^{-5} which is the criterion of convergence. For each run, the observation of the static pressure, at a specific point in the free-stream behind the rotor and the value of the rotor power were appointed for the convergence of the solution. Aiming to smooth convergence, various runs were attempted by varying under-relaxations factors. In that way, a direct control regarding the update of computed variables through iterations, was achieved. Initializing with low values for the first iterations steps and observing the progress of the residuals, their values were modified for accelerating the convergence. For a typical run of a case the cpu time was approximately 20 days and the construction time of the domain grid was about a month. This is a factor that does not permit a grid independence task procedure.

The working fluid for this analysis is the air with density equal to the reference value in the experimental data which is $0.997 kg/m^3$ [18]. A uniform wind speed profile of 7.2m/s is assumed at the entrance of the domain as boundary condition with fixed turbulence intensity and turbulence viscosity ratio. The nominal rotation speed is 71.68 rpm. The boundary condition for the inner cylinder is Euler-slip and for the outer one is symmetry, as shown in Fig. (**2**). The no-slip wall condition is assigned to the rotor blade surface and the pressure outlet condition to the downwind extreme of the field.

RESULTS

The commercial CFD code Fluent [21] is used for all the calculations presented. In order to validate the numerical results, experimental data are used from the 'IEA Annex

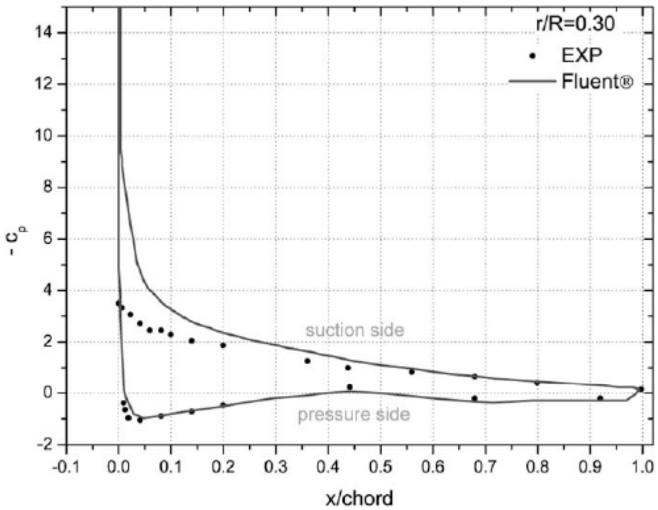

Fig. (4a). Computed and experimental "EXP" [19] chord-wise pressure distributions at r/R=0.30 span-wise location.

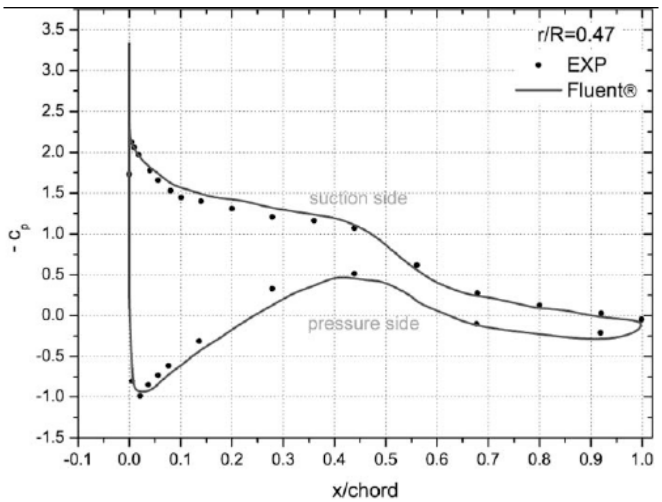

Fig. (4b). Computed and experimental "EXP" [19] chord-wise pressure distributions at r/R=0.47 span-wise location.

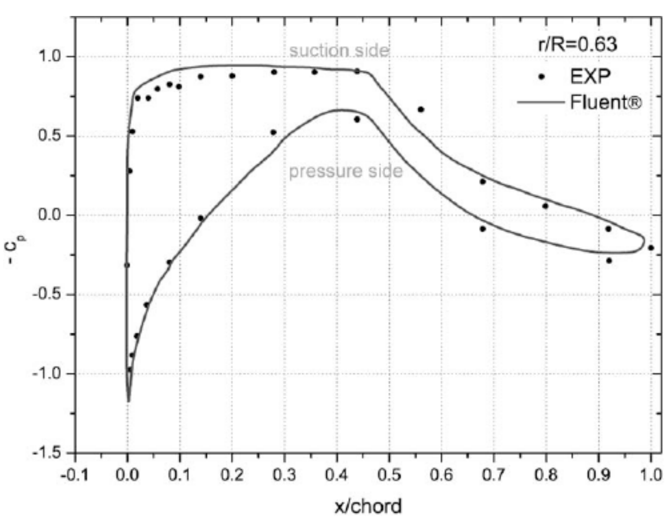

Fig. (4c). Computed and experimental "EXP" [19] chord-wise pressure distributions at r/R=0.63 span-wise location.

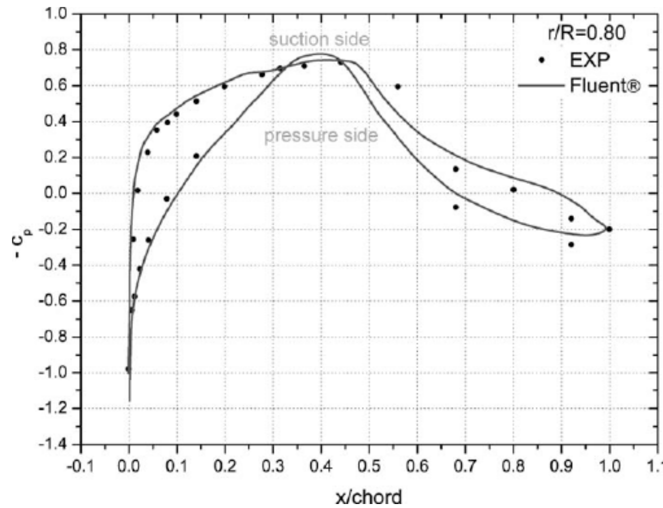

Fig. (4d). Computed and experimental "EXP" [19] chord-wise pressure distributions at r/R=0.80 span-wise location.

XIV: Field Rotor Aerodynamics' report [19]. In Figs. (**4a**, **4b**, **4c** and **4d**), the numerical pressure coefficient distribution is presented and compared with experimental results for 30, 47, 63 and 80% spanwise locations, respectively. The calculated pressure coefficient follows the definition applied in experimental data for reasons of direct comparison. Therefore, the pressure coefficient is:

$$c_p = \frac{\left(p - p_{hub}\right) + p_{cent}}{q_{ref}^2} \quad (7)$$

where p is the local pressure on the blade surface, p_{hub} is the reference pressure on the hub of the rotor, $p_{cent} = 0.5\rho(\Omega r)^2$ is the static pressure that accounts the centrifugal action of the flow and q_{ref} is the reference dynamic pressure in a distance of about half chord upstream of the blade in the corresponding radial position.

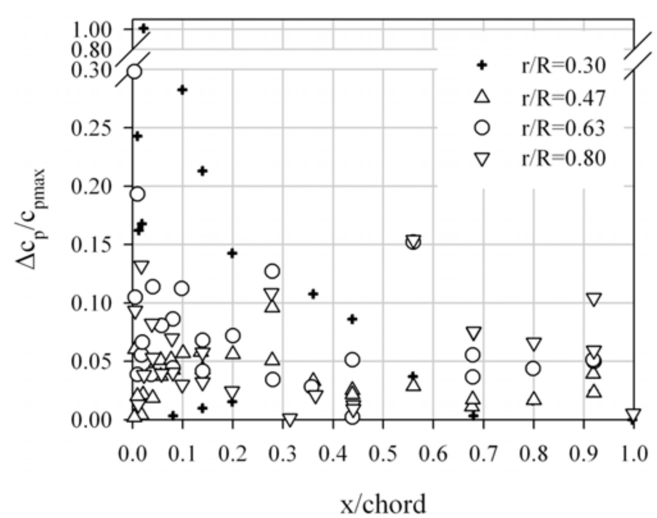

Fig. (5). Deviation of the computed pressure coefficients from the corresponding experimental in the four sections examined alongside blade.

To minimize the influence of the tower on the experimental results instantaneous data at an azimuthal blade positions of 90 deg are used, i.e. when the blade is horizontal

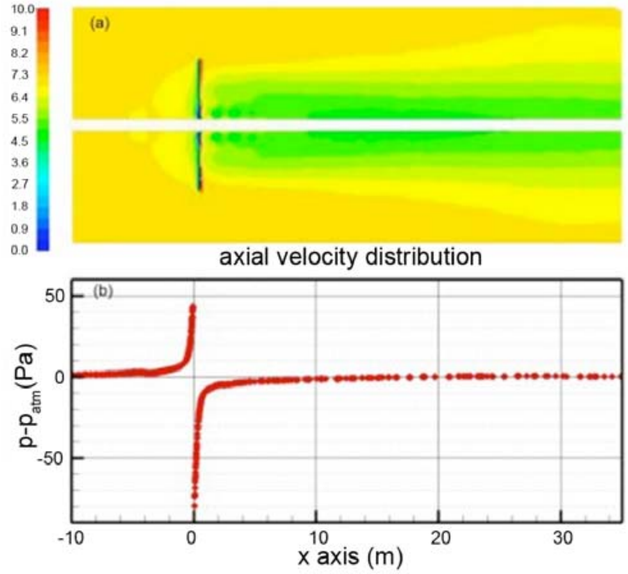

Fig. (6). Near wake axial velocity distributions (a) and pressure distribution (b) along longitudinal axis of the NREL Phase II rotor at hub height.

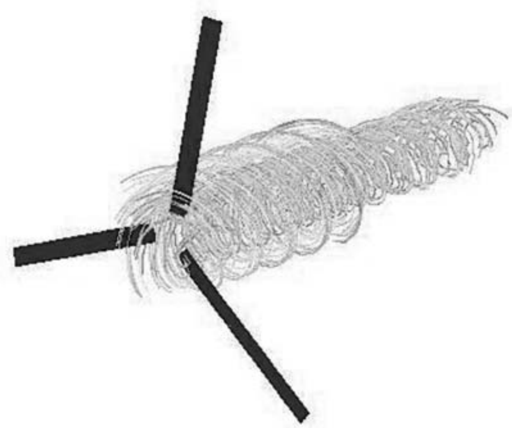

Fig. (7). Pathlines at blade root.

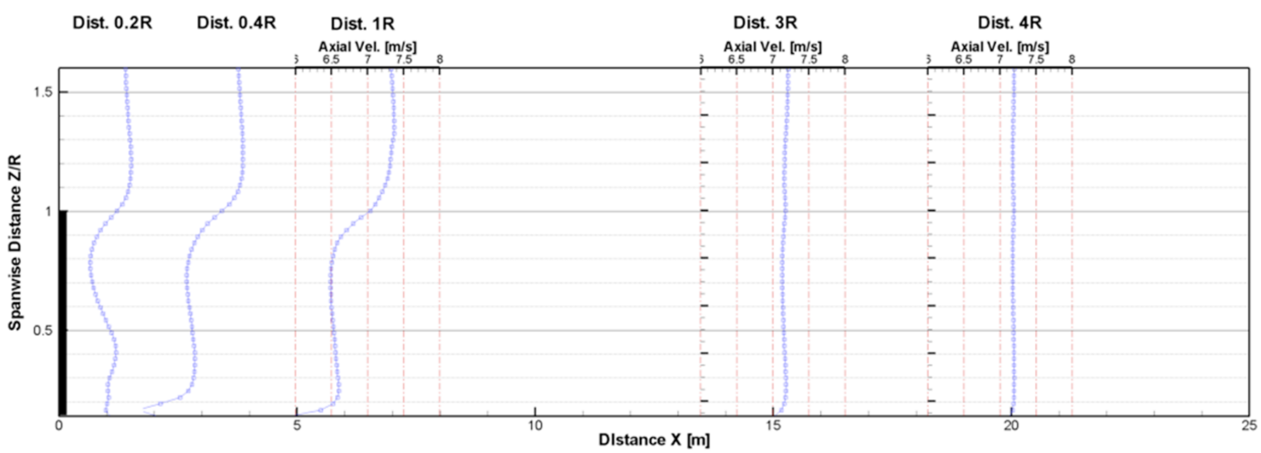

Fig. (8). Axial velocity distribution at various stations alongside free stream.

and moving down towards the tower. The comparison between the calculated pressure distribution and the experimental data is in satisfactory agreement. Some inaccuracies occur on the leading edge of the blade section and seem to increase at span-wise positions closer to the rotor hub.

The accuracy of the computed pressure coefficients against the corresponding experimental values are verified in terms of their percentage deviation at the four spanwise examined stations, as shown in Fig. (**5**). The majority of the deviations are less than 6%. However, some important discrepancies are observed in the r/R=0.30 station near the blade root. The above observed discrepancies are probably due to the highly separated flow region which is not properly resolved with the RANS approximation.

The evolution of the produced wake from the rotor blade is depicted in the axial velocity contour plot which is shown in Fig. (**6a**). As expected, the cone shape of the wake evolution downward the rotor is clearly shown. Strong tip vortices are not clearly visible in this plot. However, in Fig. (**6b**), the relative to atmospheric static pressure variation along the longitudinal dimension of the field, it can be observed. The pressure increases gradually, approaching the rotor blade where a deep drop occurs, as expected, and after 1.5 rotor diameters downwind the pressure gradients diminish. The pressure rises before the rotor is in agreement with the theory, while the sudden pressure drop gradient is associated with the power extraction of the wind.

Theoretically, behind a HAWT rotor the generated wake central vortices developed near the blade root. This is represented in the latter contour plot and at the pathlines of Fig. (**7**), where the relative flowfield is shown near the blade root with strong three dimensional effects.

The development of the limiting streamlines (i.e. the curves whose directions coincide with that of the vanishing fluid velocity or the shear stress, at the surface) for both blade sides is shown in Fig. (**9**). It is clear that near the root, strong 3D effects occur and the flow separates. The effect of rotation, which becomes more pronounced at inboard locations of the blade, is to suppress vortex shedding and the development of separation bubbles. When the flow separates, the Coriolis force acts as a favorable pressure gradient, causing the reattachment of the flow, and the reduction in the separation bubble volume. The reduction of

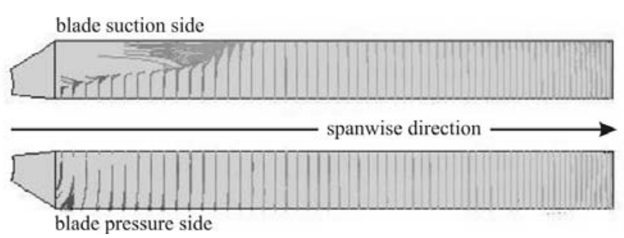

Fig. (9). Development of the limiting streamlines for the NREL Viscel II rotor blade.

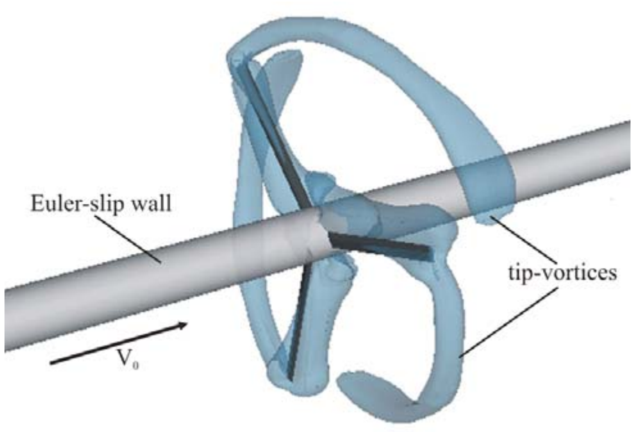

Fig. (10). Vorticity iso-surface (U_0=7.2m/s).

the bubble volume produces a pressure drop along the suction side of the airfoils increasing, thus, the blade loading.

The axial velocity distributions in the wake are observed in the axial velocity contour plots of the Figs. (**11**) and (**8**). It can be noticed that outside the wake shape downwind of the rotor, the axial velocity attains the free stream value. The deviation of the axial velocities from the free stream values is noticeable, rotor is further amplified after the upwind. Vortices are shed from the trailing edges of the blades which are diffusing in the far wake. These contours are used to identify the transition from the near to the far wake. In the near wake the shed vortices appear as distinct vortex spiral tubes as shown in Fig. (**10**). The involved vorticity strength decays in the downstream direction following the theoretical signature for such vorticity field structure.

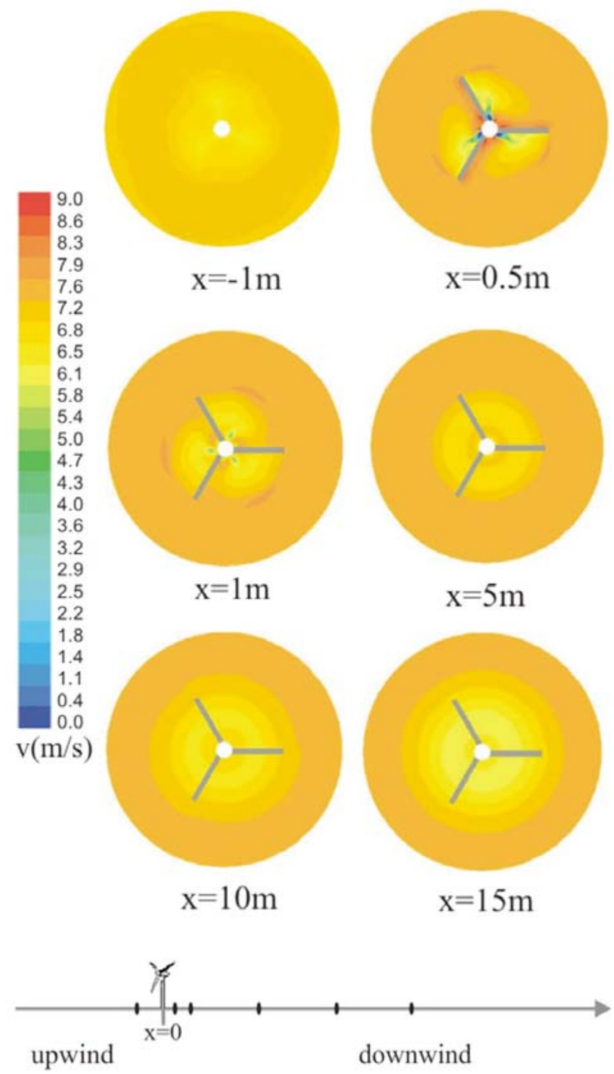

Fig. (11). Calculation of the axial velocity contours at different positions upwind and downwind of the NREL Phase II rotor.

CONCLUSIONS

The aerodynamic characteristics of a model HAWT are predicted by means of the commercial CFD code Fluent. Despite the evident simplicity of the wind turbine flowfield, there are three-dimensional effects, separated flows, wakes interactions and vortices which transform it to a complicated one.

The purpose of the current work is the numerical study on aerodynamic behavior of HAWT rotor and the validation of the simulation with available experimental data. The numerical simulations also allow the prediction of the basic features of the wake development downwind the rotor. Different aspects of HAWT flowfield are resolved with good accuracy, despite the different relevant scales involved. The simulations were validated and assessed against detailed wind turbine aerodynamic data. Nevertheless, the code and turbulence models failed to predict experimental power curves and further research is needed in that direction.

The study confirms that RANS simulations are capable to solve with a fair accuracy the different aspects involved in HAWT flowfield, thus this confirms that nowadays CFD simulations can be the most important tool for analysis and design of wind turbine rotors.

Finally, one of the future research directions will be the CFD simulation of the wind turbine flowfield with the detached-eddy simulation (DES) approach in order to better understand and fully simulate the complicated 3-d phenomena produced.

NOMENCLATURE

c_p = Pressure coefficient [dimensionless]

G_ν = Production of turbulent viscosity

p = Pressure [Pa]

p_{atm} = Atmospheric pressure [Pa]

R = Radius of the wind turbine rotor [m]

SRF = Single Reference Frame technique

t = Time [s]

u_i = Overall velocity component [m/s]

U_0 = Free-stream velocity [m/s]

y^+ = Dimensionless wall distance

Y_ν = Destruction of turbulent viscosity

GREEK LETTERS

μ_t = Turbulent viscosity [m^2/s]

ν = Molecular kinematic viscosity [m^2/s]

$\tilde{\nu}$ = Turbulent kinematic viscosity [m^2/s]

ρ = Density [kg/m^3]

REFERENCES

[1] Executive Committee for International Energy Agency, *Wind Energy*, IEA Annual Report 2004, 2005.

[2] R.E. Wilson and P.B.S. Lissaman, “Applied aerodynamics of wind power machines”, NTIS PB 2385594, Oregon State University, 1974.

[3] F.J. Simoes and J.M.R. Graham, “A free vortex model of the wake of a horizontal axis wind turbine”, 12th British Wind Energy Association Conference, 1990, pp. 161-165.

[4] N.S. Tachos, A.P. Fragias, E.G. Fenekos, D.P. Margaris and D.G. Papanikas, “Aerodynamic noise prediction of a horizontal axis wind turbine rotor”, Special Topic Conference, The Science of making Torque from Wind, EWEA, 2004, pp. 273-281.

[5] N.N. Sørensen and M.O.L. Hansen, “Rotor performance predictions using a Navier-Stokes method. In: ASME Wind Energy Symposium, 36th AIAA Aerospace Sciences Meeting and Exhibit, AIAA-98-0025, Reno, NV, 1998.

[6] G. Xu and L.N. Sankar, “Computational study of horizontal axis wind turbines”, ASME Wind Energy Symposium, 37th AIAA Aerospace Sciences Meeting and Exhibit, AIAA-99-0042, Reno, NV, 1999.

[7] J.N. Sørensen and W.Z. Shen, “Numerical modelling of wind turbine wakes”, *J. Fluids Eng.*, vol. 124, pp. 393-399, 2002.

[8] N.N. Sørensen, “3-D background aerodynamics using CFD”, Risø-R-1376, Risø National Laboratory, Denmark, 2002.

[9] N.N. Sørensen, J. Johansen and S. Conway, “CFD computations of wind turbines blade loads during standstill operation”, Know-Blade Task-3.1 Report, Risø-R-1465(EN), Risø National Laboratory, Denmark, 2004.

[10] G. Xu and L.N. Sankar, “Effects of transition, turbulence and yaw on the performance of HAWT”, 38th AIAA Aerospace Sciences Meeting and Exhibit, January 10-13, Paper 2000-0048, Collection of Technical Papers (A00-16885 03-44), Reno, NV, 2000.

[11] S. Benjanirat, L.N. Sankar and G. Xu, “Evaluation of turbulence models for the prediction of wind turbine aerodynamics”, *Wind Energy Symp.*, AIAA Paper 2003-0517, Reno, NV, 2003.

[12] G. Xu and L.N. Sankar, “Application of a viscous flow methodology to the NREL phase VI rotor”, Proceedings of the 21st ASME Wind Energy Conference and the 40th AIAA Aerospace Sciences Meeting, Paper 2002-0030, Reno, NV, Jan. 14-17, 2002, pp. 83-93.

[13] J.L. Tangler, “The nebulous art of using wind tunnel airfoil data and blade-element momentum theory for predicting rotor performance”, 21st ASME Wind Energy Symposium and the 40th AIAA Aerospace Sciences Meeting, Paper 2002-0040, Reno, NV, Jan. 14-17, 2002.

[14] W.J. McCroskey, “Vortex wakes of rotorcraft”, 33rd AIAA Aerospace Sciences Meeting and Exhibit, Paper 95-0530, Reno, NV, Jan. 9-12, 1995.

[15] A.J. Landgrebe, “New directions in rotorcraft computational aerodynamics research in the U.S.”, In: AGARD, Aerodynamics and Aeroacoustics of Rotorcraft, AGARD CP-552, Berlin, 1994.

[16] M.O.L. Hansen, J.N. Sørensen, S. Voutsinas, N. Sørensen and H.A. Madsen, “State of the art in wind turbine aerodynamics and aeroelasticity”, Progress in Aerospace Sciences, 42, pp. 285-330, 2006.

[17] D. Hu, O. Hua and Z. Du, “A study on stall-delay for horizontal axis wind turbine”, *Renewable Energy*, 31, pp. 821-836, 2006.

[18] J.G. Schepers, A.J. Brand, A. Bruining, J.M.R. Graham, M.M. Hand, D.G. Infield, H.A. Madsen, R.J.H. Paynter and D.A. Simms, “Final report of IEA Annex XIV: field rotor aerodynamics”, ECN-C-97-027, Energy Research Center of the Netherlands, 1997.

[19] D. Simms, S. Schreck, M. Hand and L. Fingersh, “NREL Unsteady Aerodynamics Experiment in the NASA-Ames Wind Tunnel: A Comparison of Predictions to Measurements”, National Renewable Energy Laboratory, NREL/TP-500-29494, 2001.

[20] J.C. Tannehill, D.A. Anderson and RH. Pletcher, “Computational Mechanics and Heat Transfer”. Taylor & Francis Inc., NY, 2nd ed., 1997.

[21] Fluent Inc., Fluent 6.2 Documentation-User’s Guide, 2004.

[22] P.R. Spalart and S.R. Allmaras, “A one-equation turbulence model for aerodynamic flows”, Technical Report AIAA-92-0439, American Institute of Aeronautics and Astronautics, 1992.

[23] D.C Wilcox, “Turbulence modelling for CFD”. DCW Industries Inc., 2nd ed., 1998.

Cost-Cotrol Skyhook for Vehicle Suspension System

Alok Sunder Mohanty, *Department of Mechanical Engineering, Aryan Institute of Engineering & Technology, Bhubaneswar, aloksundar75@gmail.com*
Subhasis Sarkar, *Department of Mechanical Engineering, NM Institute of Engineering & Technology, Bhubaneswar, subhasissarkar14@yahoo.co.in*
Sidharth Pradhan, *Department of Mechanical Engineering, Capital Engineering College, Bhubaneswar, sidharthpradhan265@gmail.com*
Jagruti Swain, *Department of Civil Engineering, Capital Engineering College, Bhubaneswar, jagrutiswain26@yahoo.co.in*

Abstract: Skyhook control, which is now widely applied to vehicle suspension control, requires two sensors to measure sprung mass acceleration and relative displacement, respectively. In the practical implementation, these two measurement signals are converted into corresponding velocities; then per the skyhook control policy the velocities are employed to decide the desired damping level; finally the damping control signal will be sent to a controllable damper to reduce vibration. For automotive application, the cost as well as reliability is always one of the primary concerns. In this paper, a new scheme is proposed to simplify skyhook control implementation by eliminating one sensor instead of traditionally using two. This design can reduce cost and improve system reliability by reducing the semiactive system complexity. According to a quarter car model, the idea is expatiated on through analysis of the phase relationship between the two velocities that are essential for skyhook control. Then the estimation of the relative velocity from the sprung mass acceleration is formulated. A cost effective skyhook control is derived from using only one accelerometer, and the effectiveness of this new skyhook control approach is demonstrated with ride control through a simulation study of a full car suspension system with application of magneto-rheological (MR) dampers.

INTRODUCTION

The skyhook control was developed in the early 1970s [1] using controllable semiactive dampers. The characteristic of such dampers can be illustrated with Fig. (**1**). The tunable damping ranges between hard and soft envelopes. With respect to compression and extension, they offer symmetric damping forces. As such, this kind of semiactive damper is referred to as a HH/SS damper. The HH/SS damper can be realized by using a hydraulic, magneto-rheological (MR), or electro-rheological (ER) fluid. High-end automotive markets have seen the rise of applications of semiactive suspensions for better ride and handling performance. Some successful examples are high-performance cars from BMW, Mercedes-Benz and Toyota, to name a few, which use hydraulic HH/SS dampers. Another semiactive suspension in the current market is MagneRide® with application of MR dampers, which is developed by Delphi and Lord Corp. These semiactive suspensions utilize the skyhook controls to achieve the desired vehicle driving performance.

With application of HH/SS dampers, a semiactive quarter-car suspension in Fig. (**2**) lends itself to interpretation of the skyhook control. It requires two measurement signals of the sprung mass acceleration $\ddot{y}_1$ and suspension relative displacement y_{12}. These two signals need to be converted into the sprung mass velocity $\dot{y}_1$ and the relative velocity $\dot{y}_{12}$ by using properly designed filters, respectively. Then the two-sensor based skyhook control can be expressed to produce the damping control signal $C_{skyhook}$ as the following formula

$$C_{skyhook} = \begin{cases} G\dot{y}_1 & \dot{y}_1\dot{y}_{12} \geq 0 \\ 0 & \text{otherwise} \end{cases} \quad (1)$$

where G is the skyhook control gain.

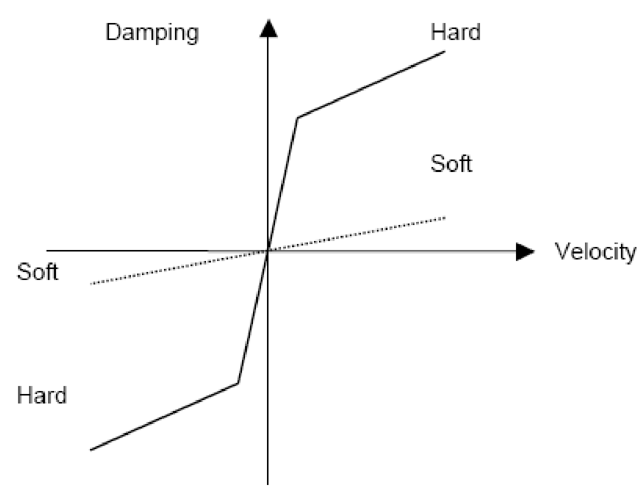

Fig. (1). Damping characteristics of HH/SS Semiactive dampers.

Since the advent of this two-sensor based skyhook control, a significant number of studies have discussed how to improve and effectively implement this damping control [2-9]. However, there has not been much study about the implementation cost, which actually is sensitive and essential for market success in the competitive automotive industry. This report develops a new and easily implemented approach to estimate the relative velocity around the primary resonant frequency region by using the sprung mass acceleration instead of the relative displacement. Thus the proposed

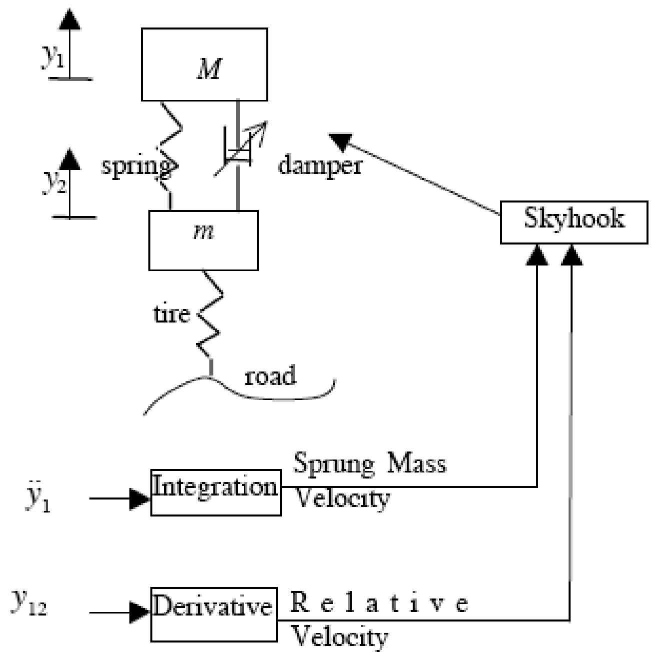

Fig. (2). Two-sensor based Skyhook control.

skyhook control policy can reduce the number of sensors by half and can improve system reliability.

The following sections will elaborate on the development of acceleration sensor based skyhook control. First the phase relationship between velocities will be analyzed. This analysis leads to a new estimation method to obtain the relative velocity from the sprung mass acceleration. Then laid out is a full car model setup with application of MR dampers for simulation study. Next the formulation of skyhook controls for a full car suspension system is elucidated. Finally simulation results are used to demonstrate the effectiveness of this new cost-effective skyhook control.

PHASE RELATIONSHIP BETWEEN VELOCITIES

The skyhook control in Eq. (1) says that the damping level needs to be changed immediately as soon as the two velocities have different signs. When both velocities have the same sign, the damping required is proportional to the sprung mass velocity. As described above, an accelerometer can be used to derive this velocity. Therefore, one question that can be asked is whether this acceleration signal can be used to estimate the relative velocity. The enlightenment is that skyhook control can create a damping command if the suspension relative velocity direction is known regardless of its magnitude. This inspires the pursuit of the accelerometer based skyhook control instead of using two sensors described in Eq. (1). In this section, the phase relationship between these two velocities is analyzed. Then in the following section a new estimation of relative velocity will be provided to develop a new skyhook control.

According to Fig. (**2**), the equation of motion for the sprung mass M can be derived as

$$M\ddot{y}_1 + C(\dot{y}_1 - \dot{y}_2) + K(y_1 - y_2) = 0 \tag{2}$$

$$M\ddot{y}_1 + (Cs + K)y_{12} = 0 \tag{3}$$

where K is the spring stiffness and C represents the damping coefficient of the damper. A proper manipulation of the above two equations leads to the following displacement transmissibility function

$$\frac{y_{12}}{y_1} = \frac{M}{Cs + K}(-s^2) \tag{4}$$

Then the velocity relationship can be expressed as

$$\frac{\dot{y}_{12}}{\dot{y}_1} = \frac{M}{Cs + K}(-s^2) \tag{5}$$

The above equation is used to declare the following phase relationship between these two velocities.

$$\angle\dot{y}_{12} - \angle\dot{y}_1 = \angle\frac{M}{Cs + K} \tag{6}$$

Eq. (6) clearly shows that the relative velocity lags behind the sprung mass velocity up to 90 degrees. For a semiactive suspension system with unchanged M and K, the phase delay depends solely on the damping coefficient C. If C is zero, then two velocities are in phase. In general the higher the damping level C the larger the phase-delay. Since C is varying during vibration controls, a feasible solution is to derive an approximate phase relationship between these two velocities. That will be further explained in the following section.

ONE-SENSOR BASED SKYHOOK CONTROL POLICY

As discussed above, the traditional skyhook control needs two sensors with application of HH/SS dampers. Now one-senor approach will be developed here. If the sprung mass acceleration is measured, then integration of this acceleration can deliver the sprung mass velocity (i.e., the absolute velocity) as following:

$$\dot{y} = \frac{1}{s}\ddot{y}_1 \tag{7}$$

However, for practical implementation, it is strongly recommended to include a washout filter to remove accelerometer DC component to improve accuracy. Eq. (6) states that the relative velocity lags behind the sprung mass velocity between 0 and 90 degrees. Therefore, the formulation of a first order filter as Eq. (8) is proposed to estimate the relative velocity $\dot{x}$ around the primary resonant frequency

$$\dot{x} = \frac{\beta}{s+\alpha}\left(\frac{1}{s}\ddot{y}_1\right) \tag{8}$$

where α and β are pre-determined constant values.

As such, this approach requires firstly specifying the range of the sprung mass M, minimum mass m_{min} and maximum one m_{max}. Usually we know the suspension stiffness K. Furthermore we need to know a priori damper characteristics such as minimum and maximum damping coefficients, C_{min} and C_{max}. Then α and β are recommended to be decided as follows:

$$\begin{aligned} \alpha &= K / C_{mean} \\ \beta &= (m_{\min} + m_{\max}) / C_{mean} \\ C_{mean} &= (C_{\min} + C_{\max}) / 2 \end{aligned} \tag{9}$$

Based on the estimated velocity signals from Eqs. (7) and (8), the one-sensor based skyhook control policy can be expressed (similar to no-jerk skyhook [5]) as:

$$C_{skyhook} = G\dot{x}\dot{y}(\dot{x}\dot{y} >= 0) \tag{10}$$

where $(\dot{x}\dot{y} >= 0)$ is a binary logic function, either one or zero, and G is the skyhook control gain.

One advantage of Eq. (8) is that in the estimate of the relative velocity the high frequency components are significantly reduced because of dropping out s^2 in comparison to Eq. (5). This reduction implicitly means to automatically attenuate the high frequency components in the skyhook damping control signal. This kind of high frequency attenuation in the control signal is truly desirable for suspension control, because the vehicle suspension needs to have low transmissibility for high frequency vibrations.

SIMULATION MODEL SETUP

In order to show its effectiveness, a full-car suspension system with application of MR dampers will be set up for this study. In this section, the models of MR damper and the vehicle suspension system are briefly introduced.

MR Damper Model

The MR damper configuration is shown in Fig. (**3**). Magneto-rheological fluids exhibit rheological properties that are controllable by a tunable magnetic field around coils. This property is used in MR dampers to provide different damping forces dependent on the strength of the magnetic field that is created within the damper. The magnetic field is controlled by the electrical current supplied to the coils of the MR valve, which is commonly used to restrict the fluid flow as the damper piston moves relative to the damper body. MR damper force is continuously tunable between maximum HH and minimum SS damping level. The higher the current to the MR damper the larger the damping force as illustrated in Fig. (**4**).

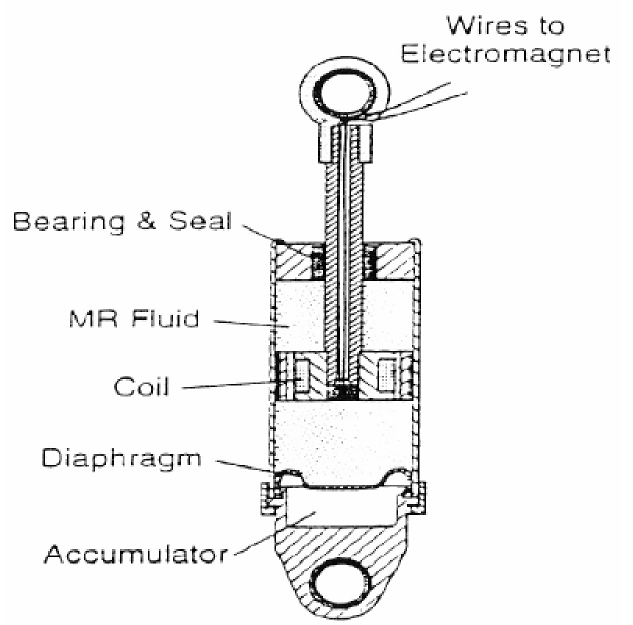

Fig. (3). Magneto-Rheological (MR) damper (In courtesy of Lord corporation).

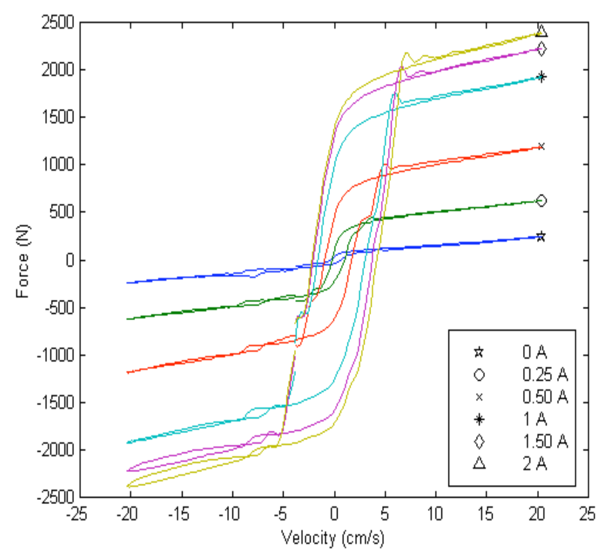

Fig. (4). MR Damper experimental data.

There are several ways to model the MR dampers [10-12], for example, the Bouc-Wen and Preisach hysteresis model. For this study the nonparametric modeling approach is adopted [10]. This MR damper model is composed of the following three functions:

1) An amplitude function

$$A_{mr}(I) = \sum_{i=0}^{n} a_i I^i \tag{11}$$

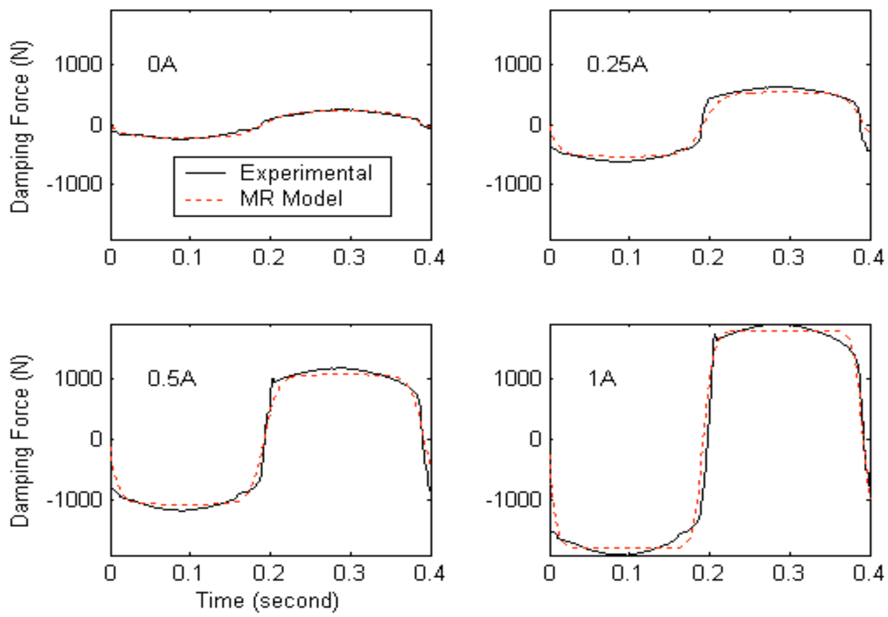

(a) Time Domain

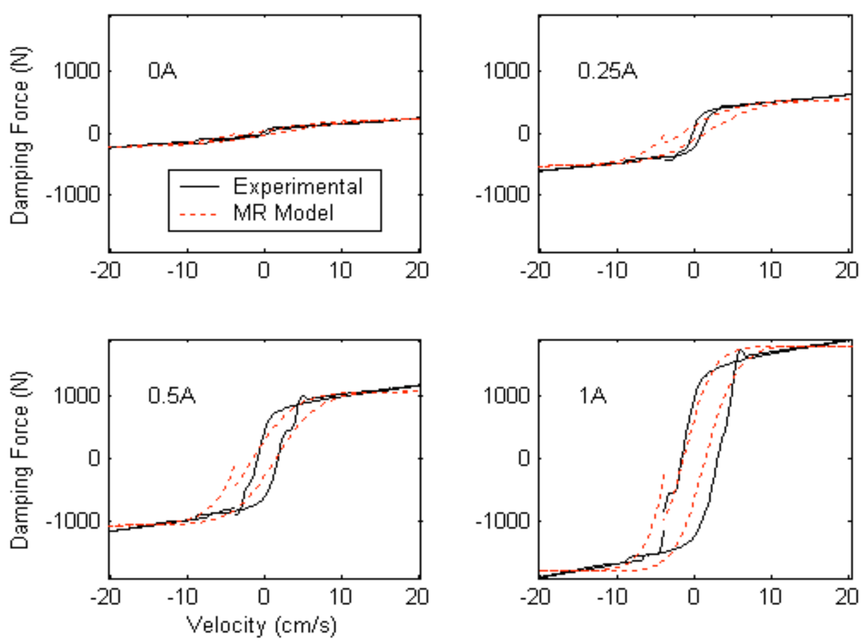

(b) Force *vs*. Velocity

Fig. (5). MR Damper model validation: (**a**) Time domain; (**b**) Force *vs.* Velocity.

2) A backbone-shape function

$$S_b(I,V) = \tanh[(b_1 I + b_2)V] \quad (12a)$$

$$F_s = A_{mr}(I)S_b(I,V) \quad (12b)$$

3) A delay function (used to create the hysteresis)

$$\begin{cases} \dot{x} = -Ax + BF_s \\ F_h = Ax + CF_s \end{cases} \quad (13)$$

Fig. (**5**) shows that the composition of these three equations can well represent this MR damper. In the model, *A*= 186.5, *B*=1, *C*=0, and the other parameters are shown in Fig. (**6**). Furthermore, it is worth noting that Eq. (13) is an expanded first-order filter that is used to mimic the hysteresis loops of the damper, while Eq. (12) captures the bilinear behavior of the MR damper.

Full Car Model Setup

Skyhook control has been studied to improve vehicle ride comfort in the automotive industry for decades. For this

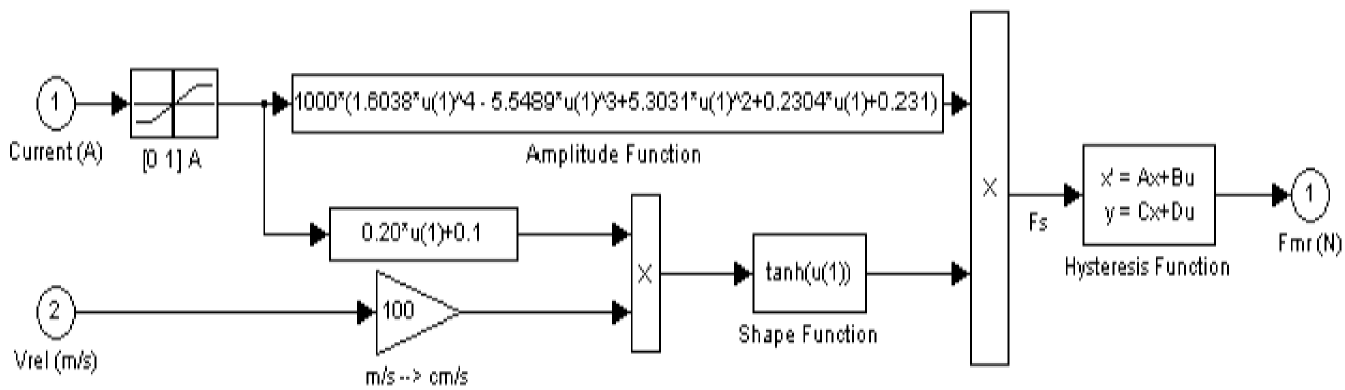

Fig. (6). Non-parametric MR damper model in Simulink.

study, a full car model in Fig. (**7**) is built to test the effectiveness of the skyhook controls. It has 7 degrees-of-freedom (DOFs): four relative motions in correspondence to four suspension corners, and three vehicle body DOFs of bounce, pitch and roll. The four independent suspensions consist of springs and MR dampers. Bounce, pitch and roll accelerations are used to evaluate the vehicle ride control and comfort.

The suspension-related parameters are presented in Table **1**, which specifies the rocker arm ratio, spring rate, unsprung mass, and tire stiffness and damping for each corner, respectively. The inertia parameters for this simulated vehicle are:

Vehicle Sprung Mass = 1720 Kg

Inertia at Longitudinal Axis = 475 Kg-m^2

Inertia at Lateral Axis = 2730 Kg-m^2

Table 1. Suspension Related Vehicle Parameters

	Front Left	Front Right	Rear Right	Rear Left
Rocker Arm Ratio	0.75	0.75	0.75	0.75
Spring Rate (KN/m)	33.8	33.0	34.0	34.7
Unsprung Mass (Kg)	45	45	40	40
Tire Stiffness (KN/m)	300	300	300	300
Tire Damping (N/(m/s))	50	50	50	50

According to the above vehicle setup, the natural frequencies can be approximately estimated by linearizing

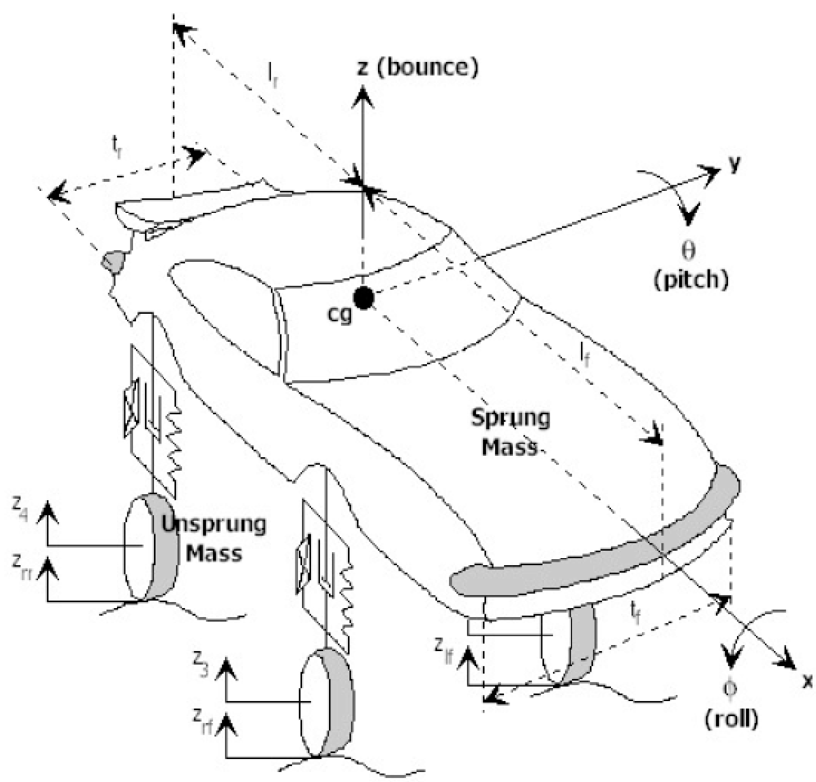

Fig. (7). Full car model with respect to inertial coordinate.

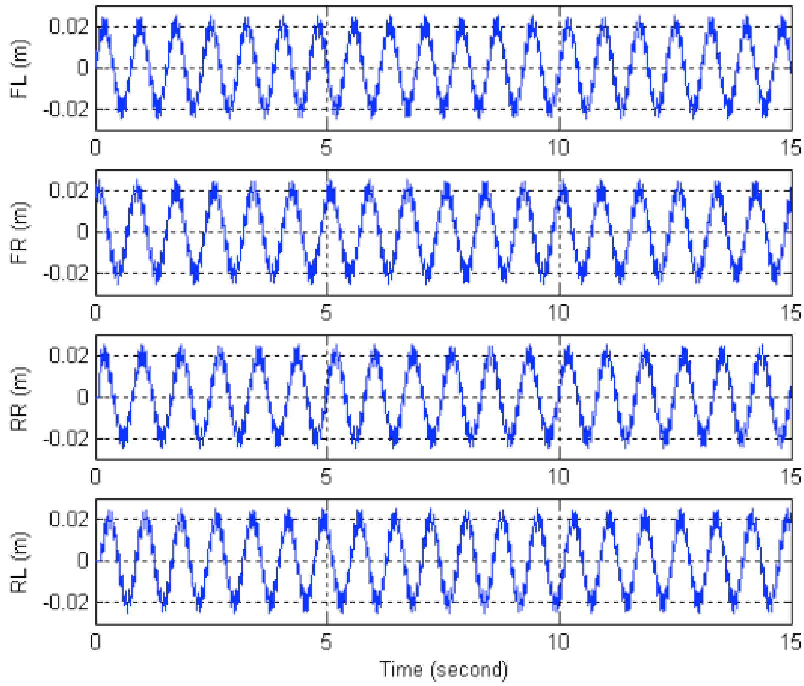

Fig. (8). Excitations on four wheels for simulation study.

the full car model. The suspension system has two bounce modes of 1.26 and 13.30 Hz, two pitch modes of 1.45 and 14.10 Hz, and two roll natural frequencies of 2.10 and 13.30 Hz. So in order to test the effectiveness of studied skyhook controls, the road excitation is designed to have a mixture of 1.30 and 13.50Hz, as shown in Fig. (**8**). As such, each suspension corner can be exposed to an appropriate vibration excitation for this simulation study.

SKYHOOK CONTROL SETUP

Compared to a semiactive quarter car in Fig. (**2**), application of skyhooks to a full car suspension system is more complicated. The vehicle rigid body (i.e., the sprung mass) has three DOFs of bounce, pitch and roll, which are abbreviated as BPR in the rest of the paper. As shown in Fig. (**7**), the bounce acceleration along the vertical direction has units of m/s^2, while both roll and pitch accelerations are rotational signals in rad/s^2. Four suspension corners are labeled as LF (left front), RF (right front), LR (left rear), and RR (right rear), respectively. The following section goes into implementation details.

Two-Sensor Based Skyhook

The traditional skyhook control for a full car suspension system can be realized by using three BPR velocities together with four suspension relative velocities, as shown in Fig. (**9**). That means the suspension control system needs to use seven sensors. Similar to the quarter-car system, three BPR accelerations can be measured and then used to obtain the BPR velocities $\dot{y}_1^i$ $(i = B, P, R)$ of the vehicle body per Eq. (7). The relative velocities at each suspension corner

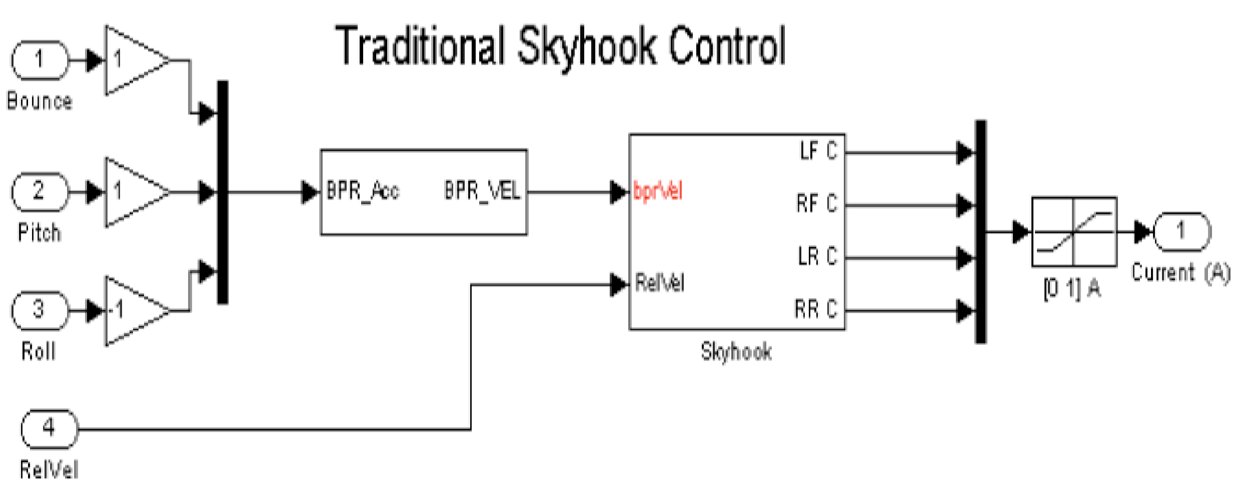

Fig. (9). Traditional two-sensor based skyhook control application in Simulink.

$\dot{y}_{12}^{j}$ $(j = LF, RF, LR, RR)$ are derived from the measured relative suspension displacements. Each of the BPR velocities creates a damping command for each damper with the corresponding relative velocity, as further explained in Eq. (14a).

$$C_j^i = \begin{cases} G_j^i \dot{y}_1^i & \dot{y}_1^i \dot{y}_{12}^j \geq 0 \\ 0 & \text{otherwise} \end{cases} \tag{14a}$$

where $i = B$, P, and R, and $j = LF$, RF, LR, and RR.

Then the dampers can have the following damping control commands

$$\begin{aligned} C_{LF} &= C_{LF}^B + C_{LF}^P + C_{LF}^R \\ C_{RF} &= C_{RF}^B + C_{RF}^P - C_{RF}^R \\ C_{LR} &= C_{LR}^B - C_{LR}^P + C_{LR}^R \\ C_{RR} &= C_{RR}^B - C_{RR}^P - C_{RR}^R \end{aligned} \tag{14b}$$

One-Sensor Based Skyhook

This section will explain the application of the newly proposed skyhook control of Eqs. (7-10) to the full car suspension control system. Like the two-sensor based skyhook, three inertia sensors at the gravity center of the vehicle body are used to measure BPR accelerations, respectively. Similarly, the accelerations are used to calculate the BPR velocities of the vehicle body, $\dot{y}^i$ $(i = B, P, R)$. But for this one-sensor based control, these three accelerations are also used to estimate three relative velocities $\dot{x}^i$ $(i = B, P, R)$. The two parameters of α and β of Eq. (8) for BPR relative velocities are defined in Table **2** for this simulation study. Then these velocity signals are used to produce the BPR damping commands as:

$$C^i = G^i \dot{x}^i \dot{y}^i (\dot{x}^i \dot{y}^i >= 0) \tag{15a}$$

where $i = B$, P, and R. Next C^i is properly split to each damper empirically as well as per vehicle chassis design. Finally, the damper commands can be formulated as following:

$$\begin{aligned} C_{LF} &= \mu^B C^B + \mu^P C^P + \mu^R C^R \\ C_{RF} &= \mu^B C^B + \mu^P C_{RF}^P - (1-\mu^R) C_{RF}^R \\ C_{LR} &= (1-\mu^B) C_{LR}^B - (1-\mu^P) C_{LR}^P + \mu^R C_{LR}^R \\ C_{RR} &= (1-\mu^B) C_{RR}^B - (1-\mu^P) C_{RR}^P - (1-\mu^R) C_{RR}^R \end{aligned} \tag{15b}$$

Table 2. Relative Velocity Filter Setup for One-Sensor Based Skyhook Control

	Bounce Estimator	Pitch Estimator	Roll Estimator
α	4	5	6
β	3.8	4.8	5.8

Fig. (**10**) shows the cost-effective implementation diagram in Simulink using the one-sensor based skyhook control strategy. This suspension control system requires only three inertia sensors.

SIMULATION RESULTS

The simulation focuses on vehicle ride comfort, representative of the vehicle body accelerations. For comparison purpose, a passive suspension is also simulated with application of 0.5A to the two front MR dampers and 0.35A for rear dampers, respectively. The passive suspension is treated as a baseline for skyhook controls.

The BPR accelerations from all three simulation cases are presented from Figs. (**11-13**) in the frequency domain. The legend 'Skyhook' represents the two-sensor based strategy, while 'Cost Effective Skyhook' stands for the one-sensor based strategy.

From Fig. (**11**), it can be observed that the bounce vibration around both primary and secondary suspension frequencies is significantly reduced with both skyhook strategies in comparison to the passive suspension. Figs. (**12** and **13**) show the pitch and roll accelerations, respectively. Both controls can lower the peaks at the secondary suspension frequency. One subtle observation is that the one-sensor based control provides better control of the primary pitch peak. That may be induced by smaller relative velocity estimation in the high frequency range from Eq. (8). Overall, the cost effective skyhook control provides competitive

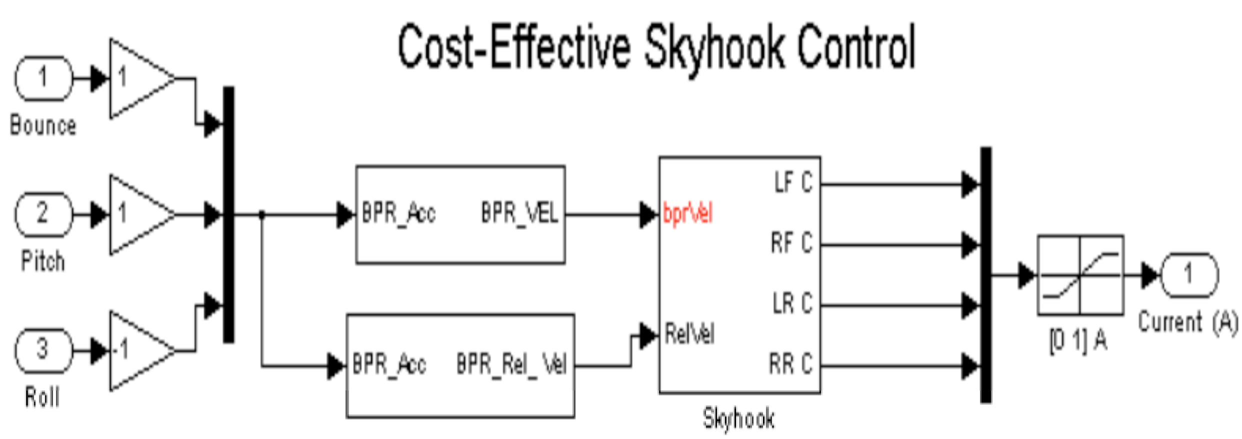

Fig. (10). Cost-effective implementation of one-sensor based skyhook control in Simulink.

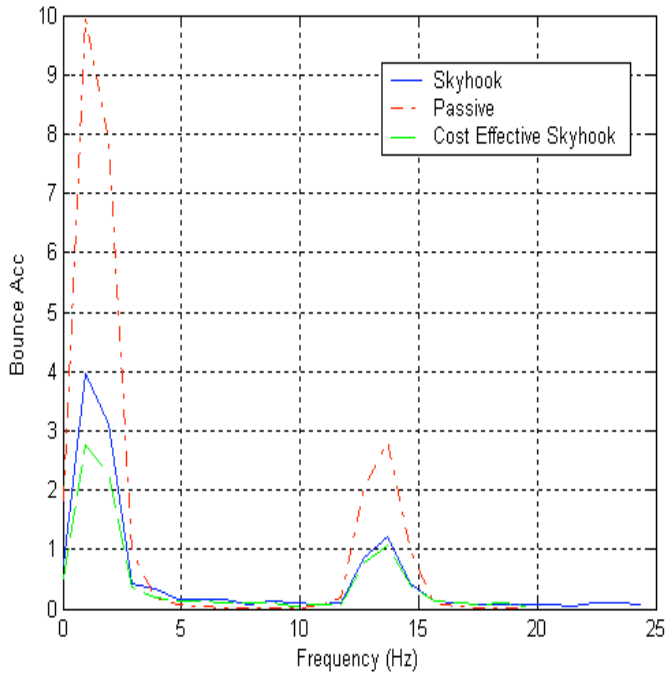

Fig. (11). Comparisons of Bounce acceleration.

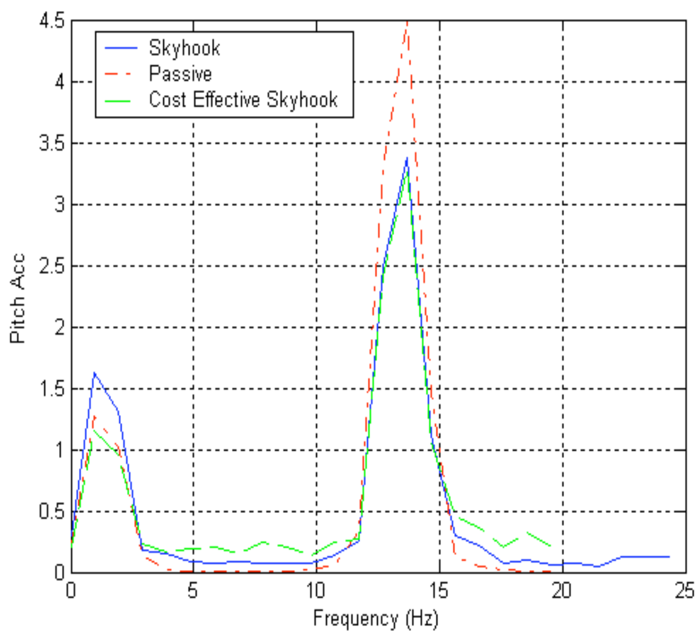

Fig. (12). Comparisons of Pitch acceleration.

performance against the traditional skyhook control. Thus, the one-sensor based skyhook control provides another new avenue to simplify semiactive vehicle suspension implementation.

CONCLUSIONS

The traditional two-sensor based skyhook control is briefed first. Then using a quarter-car suspension configuration the phase relationship between sprung mass and relative velocity is analyzed. From this phase analysis, a new one-sensor based skyhook control strategy is developed for this study.

A full car suspension system model is then used to demonstrate the effectiveness of the one-sensor based skyhook control compared to the traditional skyhook control as well as the passive suspension. The simulation results show that the proposed skyhook with three sensors can achieve competitive ride comfort performance in comparison

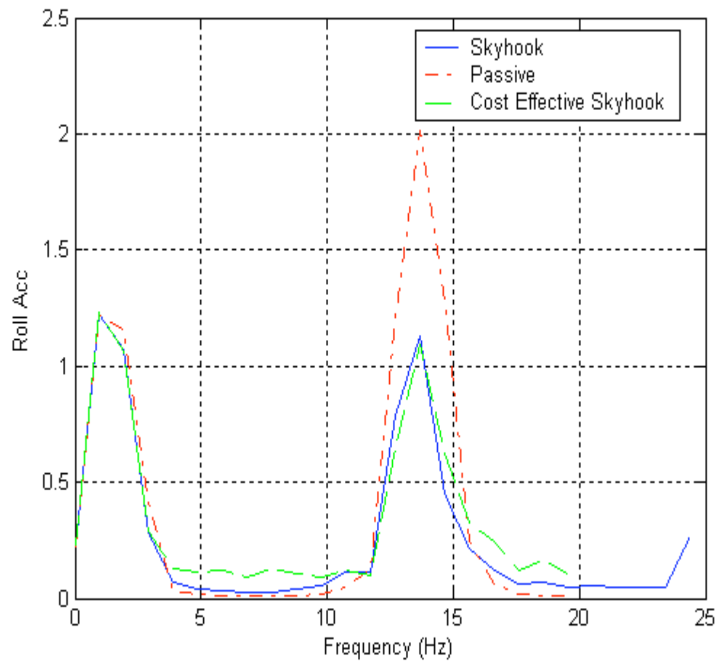

Fig. (13). Comparisons of Roll acceleration.

to the seven-sensor based traditional skyhook. However, more studies need to be done to further investigate the application of this simplified one-sensor based skyhook control with other suspension-related vehicle performances.

For the automobile industry, both cost and reliability are always a big concern. This will also challenge the control engineers to develop more cost-effective control algorithms for reducing system complexity and cost but maintain a high-quality bar for productions. This study highlights one example of such engineering efforts that can lead to that goal.

ACKNOWLEDGEMENT

The author uses the MR damper data from Lord Corporation. His working experience at Visteon Corp motivates him to continue to explore the vehicle semiactive suspension development, even though he is now working at Eaton Corp and focusing on powertrain controls for commercial vehicles.

REFERENCES

[1] D.C. Karnopp, and M.J. Crospy, “System for Controlling the Transmission of Energy between Spaced Members”, U.S. Patent 3,807,678, April 1974.

[2] D. E. Ivers and L. R. Miller, “Semiactive suspension technology: an evolutionary view”, *ASME Advanced Automotive Technologies*, DE-40, Book No. H00719-1991, pp. 327-346, 1991.

[3] X. Song, “Design of adaptive vibration control systems with application to magneto-rheological dampers”, Doctor of Philosophy Dissertation, Virginia Polytechnic Institute and State University, Blacksburg, Virginia, 1999.

[4] M. Bieber, S. M. Mackool, and D. S. Rhode, “Vehicle Suspension Control Systems”, Patent No. 5,864,768, Jan. 26, 1999.

[5] M. Ahmadian, X. Song, and S.C. Southward, “No-jerk skyhook control methods for semiactive suspensions”, *ASME Journal of Vibration and Acoustics*, Vol. 126, No. 4, pp. 580-584, October 2004.

[6] S. B. Choi, J. H. Choi, Y. S. Lee, and M. S. Han, “Vibration control of an ER seat suspension for a commercial vehicle”, *Journal of Dynamic Systems, Measurement, and Control, ASME*, Vol. 125, pp. 60-68, March 2003.

[7] Y. T. Choi, and N. M. Wereley, “Biodynamic response mitigation to shock loads using magnetorheological helicopter crew seat suspension”, *Journal of Aircraft*, Vol. 42, No. 5, pp. 1288-1295, September-October 2005.

[8] Y. Liu, T. P. Waters and M. J. Brennan, “A comparison of semi-active damping control strategies for vibration isolation of harmonic disturbances”, *Journal of Sound and Vibrations*, Vol. 280, pp. 21-39.

[9] K. S. Hong, H. C. Sohn and J. K. Hedrick, “Modified skyhook control of semi-active suspensions: a new model, gain scheduling, and hardware-in-the-loop tuning,” *Journal of Dynamic Systems, Measurement and Control*, ASME, Vol. 124, pp. 158-167, March 2002.

[10] M. Ahmadian, and X. Song, “Non-parametric model of magneto-rheological dampers”, Proceedings of 17th Biennial Conference on Mechanical Vibration and Noise, ASME DETC, September 12-14, Las Vegas, NV, 1999.

[11] B. F. Spencer, S. J.Dyke, M. K. Sain, and J. D. Carlson, “Phenomenological model of a magnetorheological damper,” *ASCE Journal of Engineering Mechanics*, 1996.

[12] R. B. Gobert, K. A. Morris and D. W. L. Wang, “Passivity-based stability and control of hysteresis in smart actuators,” IEEE *Transactions on Control Systems Technology*, Vol. 9, No. 1, pp. 5-16, January 2001.

Novel Model for Two-Cup Horizontal Wind-Turbine Analysis

Sarat Kumar Mishra, *Department of Mechanical Engineering, Aryan Institute of Engineering & Technology, Bhubaneswar, skmishra784@gmail.com*

Jyotikusum Acharya, *Department of Civil Engineering, NM Institute of Engineering & Technology, Bhubaneswar, jyotikusumacharya@yahoo.co.in*

Abinash Sahoo, *Department of Mechanical Engineering, Capital Engineering College, Bhubaneswar, abinashsahoo719@yahoo.co.in*

Sikendar Sharma, *Department of Civil Engineering, Raajdhani Engineering College, Bhubaneswar, sikendarsharma92@gmail.com*

Abstract: Typical wind turbine systems are sufficiently large so as to require extensive physical space for their installa-tion and operation. These requirements preclude the use of turbines in crowded, urban environments. On the other hand, smaller turbine systems may find practical application as rooftop units, installed atop tall buildings. Such rooftop units must be much smaller than their ground-based counter parts. In this paper, a new, vertical-axis wind turbine has been ana-lyzed by using a two-step numerical procedure. The design consists of two turbine cups that are positioned with 180^o separation. In the first step of the analysis, a complete numerical simulation of the wind-flow patterns across the cup with wind impacting angles spanning 360^o was completed. From these calculations, it was possible to determine the functional relationship between rotational forces, relative wind speed, and the relative angle of wind approach. The second stage of numerical procedure was a time-wise integration of the instantaneous angular velocity of the wind turbine. These calcula-tions were carried out until the turbine had achieved quasi-steady motion. The corresponding cycle-averaged angular ve-locity (*terminal angular velocity*) was then determined. This second stage was completed for a wide range of wind speeds so that a functional dependence of the turbine rotational velocity on the wind speed could be found. This functional rela-tionship enables a user to predict the operational response of the wind turbine based on a known and steady wind velocity.

INTRODUCTION

Wind-based electrical generation is a fast-growing source of clean power production [1]. Typically, wind-based elec-tricity is produced in large, relatively remote wind-farms which are constituted by turbine populations that vary from tens to hundreds of units. Electricity is then transferred to residential and commercial centers through extensive power grids.

Another future mode of wind-energy generation is through on-sight production and utilization. In this mode, wind-based electricity is generated at a residential or com-mercial location for immediate use. Such local wind turbines are much smaller than their wind-farm counterparts that typically reach heights of hundreds of feet above ground. Effective local power production requires small wind tur-bines that are readily adapted to a variety of geometric con-straints.

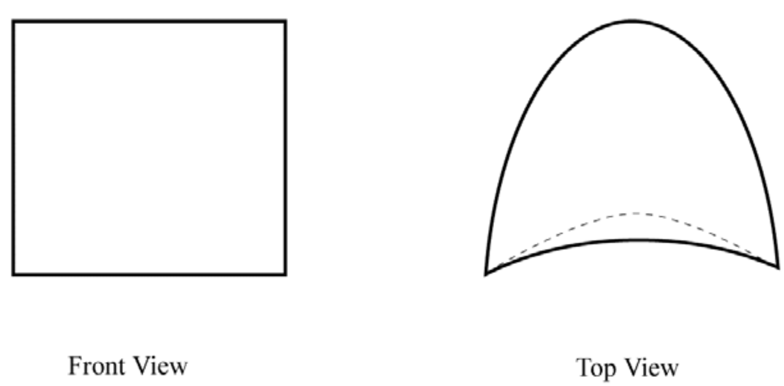

Fig. (1). Front and side view of cup design.

For grid-size wind turbines, larger and taller turbines generally perform better than smaller counterparts due to the physics of wind-power extraction and wind speeds that in-crease with elevation [2]. The rotational rate of grid-size wind turbines is also restricted for environmental and safety concerns. In rooftop applications, there are fewer restrictions on rotation rate and furthermore, some of the designs are even screened for safety reasons. As a consequence, the de-

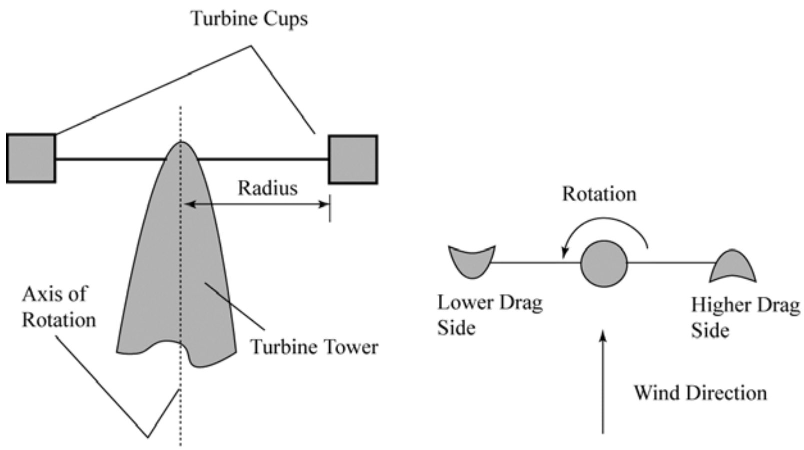

Fig. (2). Schematic diagram of the turbine system with front and side views shown.

sign space for rooftop wind turbines is quite different from their grid-sized cousins. The relatively smaller size of rooftop units also limits the power generation to a few kilowatts. Hence, for simplicity and cost reasons the associated electrical generators are typically permanent magnet machines with very efficient conversion and grid-synchronization power electronics.

In this research effort, a novel turbine system has been designed with a number of features that facilitates its use in urban or constrained environments. The major innovations are related to the use of a rectangular profiled cup design and a vertical axis of rotation. A detailed investigation of the first of these features is facilitated by reference to Fig. (**1**). The figure shows two views of the turbine cup. In the left view, the square profile of the front surface is shown. On the right, a top view of the cup is displayed which clearly exhibits the streamlined nature of the back surface of the cup.

When positioned in an airflow, the front and back surfaces of the cup generate differing drag forces due to their blunt and streamlined shapes. As a consequence, the turbine will rotate as shown in the rightmost portion of Fig. (**2**). The left half of the figure shows the turbine cups attached to a schematic tower with the vertical axis of rotation clearly indicated.

The design that is analyzed in this paper consists of two cups, located at 180 degree increments about the axis of rotation. The analysis will include a detailed numerical study of the flow of air across the cups at all circumferential locations. The outcome of the numerical study will be used in a dynamic analysis of the rotational motion. The results of the two-part study will enable a determination of the resulting rotational velocity of the new turbine design. While the analysis completed here will be specific to a specific cup design, the method is universal and would allow calculations for design variations. The profiles of the concave and convex surfaces of the blade structure are, at this point, proprietary so only the general shape of a cup will be disclosed.

NUMERICAL MODEL

Fluid Flow Modeling

The fluid modeling was completed using a finite volume computational scheme. The calculations were completed for all combinations of incoming wind speeds and directions. The complexity of the numerical simulations was great due to the rotational motion of the turbine cup which causes a continuously changing relative wind velocity and direction, even though the wind itself was assumed to be steady with regard to speed and direction. Discussion of these issues is aided by reference to Fig. (**3**) which shows the wind impacting at angle θ on the concave surface of the cup. As the cup completes a cycle about the axis of rotation, the angle θ varies continuously over a 360 degree range. In addition, the rotational velocity dramatically affects the incoming wind velocity relative to the cup. When the cup moves in the same direction as the wind, the relative wind velocity is decreased. On the other hand, when the motion of the cup is into the wind, the relative velocity increases.

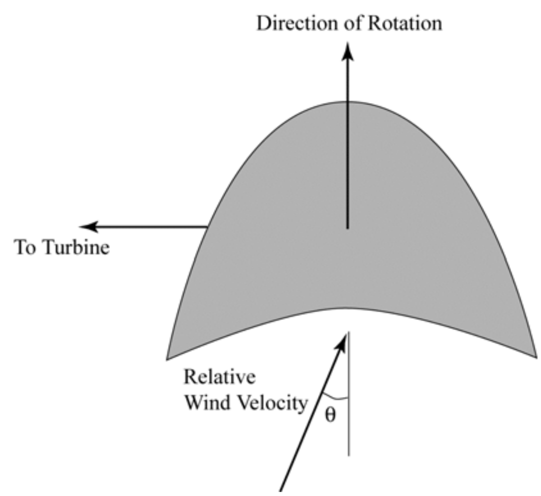

Fig. (3). Diagram showing cup and incoming wind orientation. The angle θ varies continuously over a 360 degree range.

All calculations were completed by solving equations which balance mass and momentum flowrates over all finite-volume cells which constitute the fluid region. Those equations, hereby referred to as continuity and momentum conservation, are shown in Equations (1) and (2) in tensor form [3].

$$\frac{\partial u_i}{\partial x_i} = 0 \tag{1}$$

$$\rho\left(u_i \frac{\partial u_j}{\partial x_i}\right) = -\frac{\partial p}{\partial x_i} + \frac{\partial}{\partial x_i}\left((\mu+\mu_t)\frac{\partial u_j}{\partial x_i}\right) \quad j = 1,2,3 \qquad (2)$$

All air properties are evaluated at atmospheric pressure and a temperature of 20°C. The high velocities and the inevitable recirculation patterns guarantee that turbulence will exist within the domain. The present calculations have accommodated turbulence by means of the eddy viscosity, μ_t, which is displayed on the right-hand side of Equation (2). The shear stress transport model (SST) of Mentor [4] has been used. That model combines the κ–ε model of Jones and Launder [5] with the κ–ω approach set forth by Wilcox [6, 7]. The combination of these approaches is performed in such a manner that the k-ω equations dominate in the near-wall region while k-ε holds away from the wall. In this way, the advantage of the near-wall calculations of k-ω are realized yet its sensitivity to free-stream values of the turbulent frequency is mitigated [8]. It has been shown that the SST approach provides superior results for near-wall and separated flow calculations [9-15].

The expression of the SST is provided in two extra transport equations for the turbulence kinetic energy, k and the specific rate of turbulence dissipation, ω. The new transport equations, are provided in Equations (3) and (4).

$$\frac{\partial(\rho u_i k)}{\partial x_i} = P_k - \beta_1\rho k\omega + \frac{\partial}{\partial x_i}\left[\left(\mu + \frac{\mu_t}{\sigma_k}\right)\frac{\partial k}{\partial x_i}\right] \qquad (3)$$

and

$$\frac{\partial(\rho u_i \omega)}{\partial x_i} = A\rho S^2 - \beta_2\rho\omega^2 + \frac{\partial}{\partial x_i}\left[\left(\mu + \frac{\mu_t}{\sigma_\omega}\right)\frac{\partial \omega}{\partial x_i}\right] + 2\left(1-F_1^{'}\right)\rho\frac{1}{\sigma_{\omega 2}\omega}\frac{\partial k}{\partial x_i}\frac{\partial \omega}{\partial x_i} \qquad (4)$$

The solution of Equations (3) and (4) yields the turbulent viscosity, μ_t, in terms of k and ω. It is,

$$\mu_t = \frac{a\rho k}{\max\left(a\omega, SF_2^{'}\right)} \qquad (5)$$

where $F_2^{'}$ is a blending function that limits the eddy viscosity within the boundary layer.

In these equations, P_k is the rate of production of the turbulent kinetic energy and the σ terms are the Prandtl numbers for transport of turbulent kinetic energy and specific rates of turbulence destruction (ω and $\omega 2$). $F_1^{'}$ is a blending function that facilitates the combination of the standard κ–ε model and the κ–ω model. The term S is the absolute value of the shear strain rate, and the β terms are model constants.

At all solid-fluid interfaces, the no-slip condition was employed so that the fluid velocity was zero. The turbulent kinetic energy is also zero at these surfaces. A portion of the computational domain nearest the cup is shown in Fig. (**4**). That figure is a two-dimensional top view of the three dimensional extent of the volume under consideration. The figure, which is not drawn to scale, shows that the fluid region completely encloses the cup. Airflow is applied at two orthogonal surfaces of the fluid region. The modeled inlet condition was steady so that the direction and magnitude of the wind did not change in time (no gusts). Also, it was assumed that the wind passed parallel to the base of the wind turbine and did not spatially vary at the blade surface. The calculations were carried out for values of θ which spanned the entire 360° range. They also covered the expected range of relative wind velocities.

Opening conditions are used to complete the enclosure which allows air to flow either into or out of the domain. The use of an opening condition is required by the potential for the formation of eddies downstream of the cup. A detailed

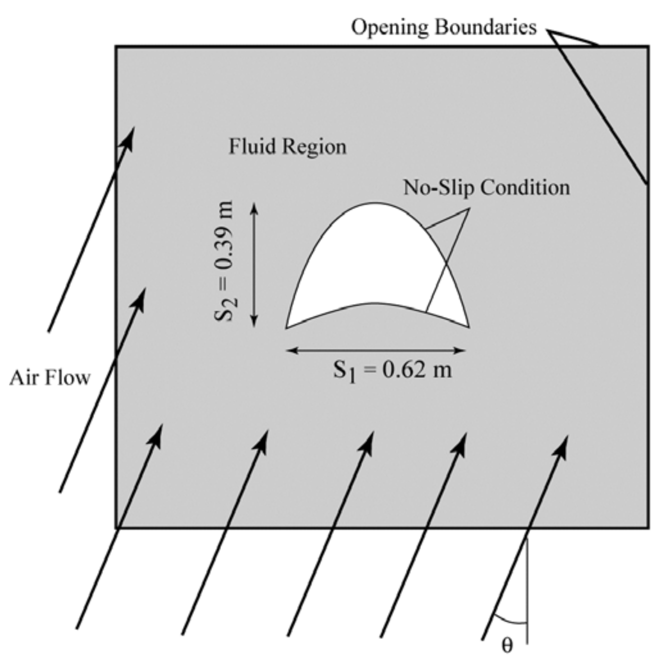

Fig (4). Boundary conditions used in the fluid simulation.

study was made on the required extent of the solution domain so that the positioning of all boundaries were sufficiently far from the cup so as to not affect the calculations.

The fluid region was subdivided into 2,000,000 elements which were preferentially deployed in regions of high gradients, such as at all fluid-solid interfaces. To accomplish this deployment, thin prismatic elements were placed along all boundaries. A view of the element deployment is shown in Fig. (**5**), which is a projection of the control volumes taken from a horizontal slice through the three-dimensional region. The CFX 11.0 solver was used to complete the calculations.

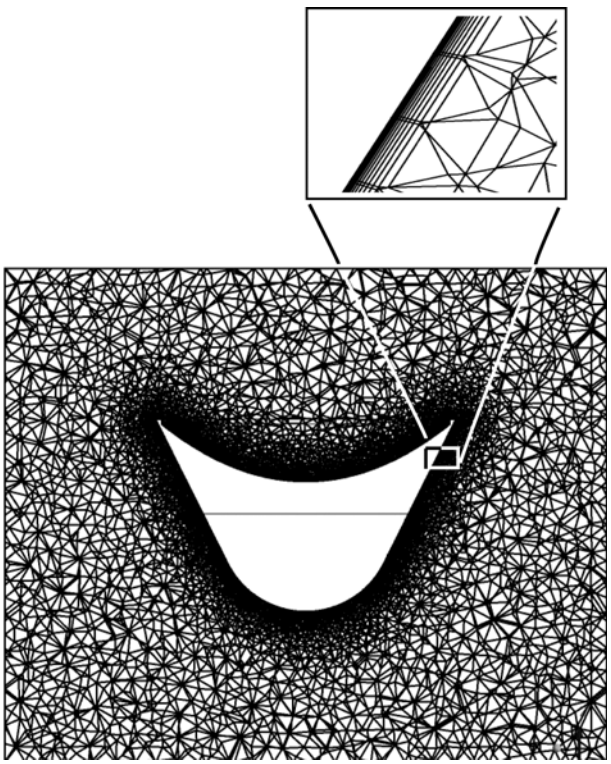

Fig. (5). Depiction of the mesh near the surfaces of the cup.

Coupling of the velocity-pressure equations was achieved on a non-staggered, collocated grid using the techniques developed in [16] and [17]. The inclusion of pressure-smoothing terms in the mass conservation equation suppresses oscillations which can occur when both the velocity and pressure are evaluated at coincident locations.

The advection terms in the momentum equations were evaluated by using the upwind values of the momentum flux, supplemented with an advection-correction term. The correction term reduces the occurrence of numerical diffusion and is of second-order accuracy. Further details of the advection treatment can be found in [18].

The calculations were performed using a false-transient algorithm. Mesh and time-step values were sufficiently small to ensure a solution that was independent of their values. The selected values resulted from an independence study during which both the element sizes and time steps were reduced and results were compared. When the sequential reductions failed to yield noticeable changes in the results, it was determined that the settings were sufficiently refined.

Model of Rotational Motion

The calculations of the proceeding section were completed for multiple angles θ and for a number of relative wind velocities. For each calculation, the circumferential force was determined by integrating pressure and shear forces over all surfaces of the cup. The resulting circumferential force, which at all instances is tangent to the direction of motion, provides the torque about the axis of rotation. A diagram of the circumferential forces on the two cups is shown in Fig. (**6**). It is worthy of note that in most positions, the two forces provide opposing moments, with one force acting to continue rotation and the other acting to slow the rotational velocity.

With the two forces now determined, it is possible to construct an equation which describes the rotational motion of the two-cup system. That equation, shown below contains

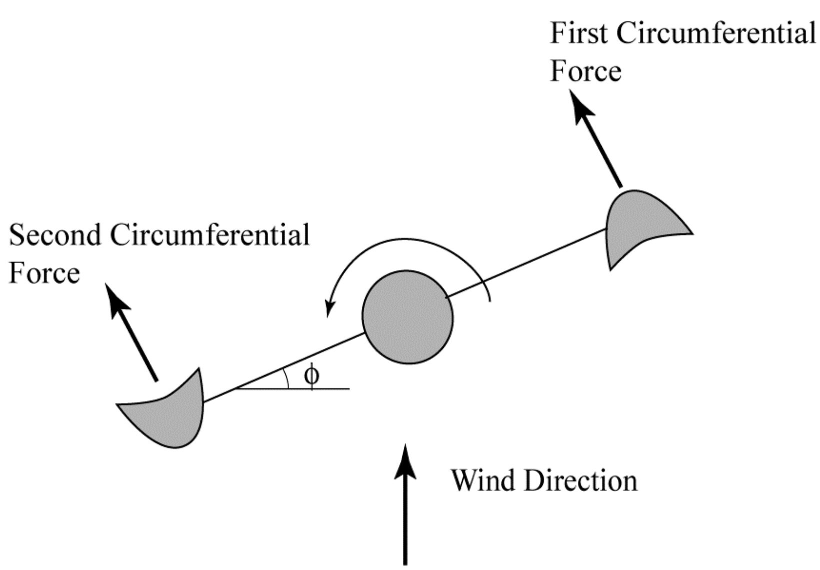

Fig. (6). Schematic showing circumferential forces acting on turbine cups the moment of inertia of the system, $I=2.9\ kg\ m^2$, and the instantaneous angular acceleration, α.

$$I\alpha = M_1 - M_2 = \left(F_1 - F_2\right)\cdot Radius \tag{6}$$

The model, as presented in Equation 6 ignores frictional losses due to rotation, and drag forces in the thin beams which connect the cups to the turbine.

In Equation (6), F_1 and F_2 are, respectively, the forces promoting and opposing rotation. As evident from the description of the fluid flow calculations, the two forces F_1 and F_2 are continuous functions of both the relative wind speed and of the angle of incidence of the wind. The functional dependence of the circumferential forces can be represented as,

$$F = f\left(\theta,\left|V_{rel}\right|\right) \tag{7}$$

When this expression is inserted into Equation (6), the motion equation becomes,

$$I\frac{d\omega'}{dt} = \left(f\left(\theta_1,\left|V_{rel}\right|_1\right) - f\left(\theta_2,\left|V_{rel}\right|_2\right)\right)\cdot Radius \tag{8}$$

In Equation (8), ω' is the instantaneous angular velocity and is equal to,

$$\frac{d\varphi}{dt} = \omega' \tag{9}$$

where angle ϕ is the angle of inclination of the turbine system with respect to the wind, as shown in Fig. (**6**).

Equations (8) and (9) completely determine the progression of motion. The non-linearity of the system requires that the solution of these coupled equations be obtained numerically using a time-stepping solution procedure. The algorithm provides the progression of the angular position and velocity of the turbine based on initial conditions for both ϕ and ω'.

Using the symbol n to reference the current time step, Equation (8) is evaluated based at the current time-step as shown in Equation (10).

$$I\frac{d\left(\omega'\right)^n}{dt} = \left(f\left(\theta_1,\left|V_{rel}\right|_1\right)^n - f\left(\theta_2,\left|V_{rel}\right|_2\right)^n\right)\cdot Radius \tag{10}$$

Then, with $(\omega')^n$ determined, the incremental change in the angular position and velocity of the turbine is calculated from a forward-stepping integration, as shown in the following:

$$\varphi^{n+1} = \left(\omega'\right)^n \cdot \Delta t + \varphi^n \tag{11}$$

and

$$\left(\omega'\right)^{n+1} = \left(\alpha\right)^n \cdot \Delta t + \left(\omega'\right)^n \tag{12}$$

where α is the angular acceleration. In all calculations, the time step was selected to ensure both numerical stability and accuracy. Accuracy was ensured by successively reducing the numerical integration time steps until no difference in outcome was observed.

The new information is used to update the wind speed and angle of incidence which then allow a determination of newly updated forces F_1 and F_2, and a continuation of the calculation procedure.

The time-stepping calculations of Equations (11) and (12) were carried out until the wind turbine reached a quasi-steady motion. The motion of the turbine accelerated during part of its rotation and decelerated during other portions. Quasi-steady motion is achieved when the time integrated acceleration equaled the same integration of deceleration throughout one complete cycle. For quasi-steady motion, the instantaneous angular velocities evaluated at one cycle are identical to those evaluated at a subsequent cycle.

RESULTS AND DISCUSSION

Fluid Flow Results

Results from the fluid analysis are best illustrated by visualization of the flow field. To facilitate the following

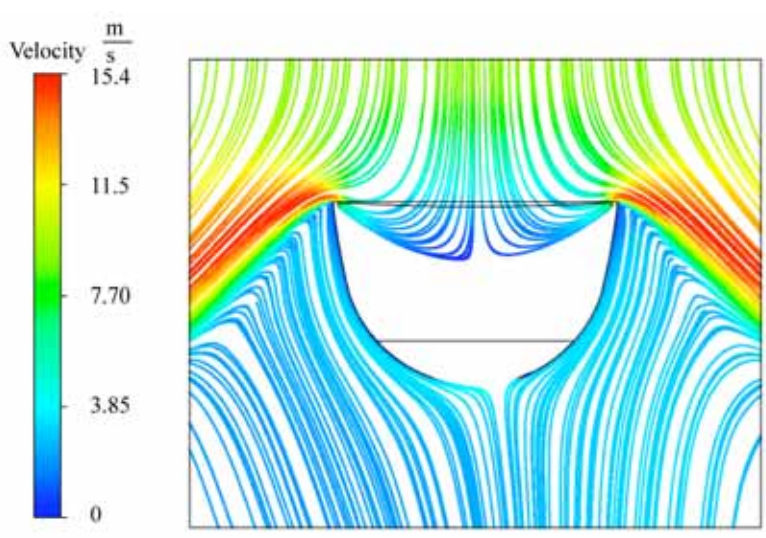

Fig. (7). Streamline pattern for flow with an incident angle of 0 degrees, color-coded by velocity magnitude corresponding to a relative wind speed of 20 miles/hour (9 m/s).

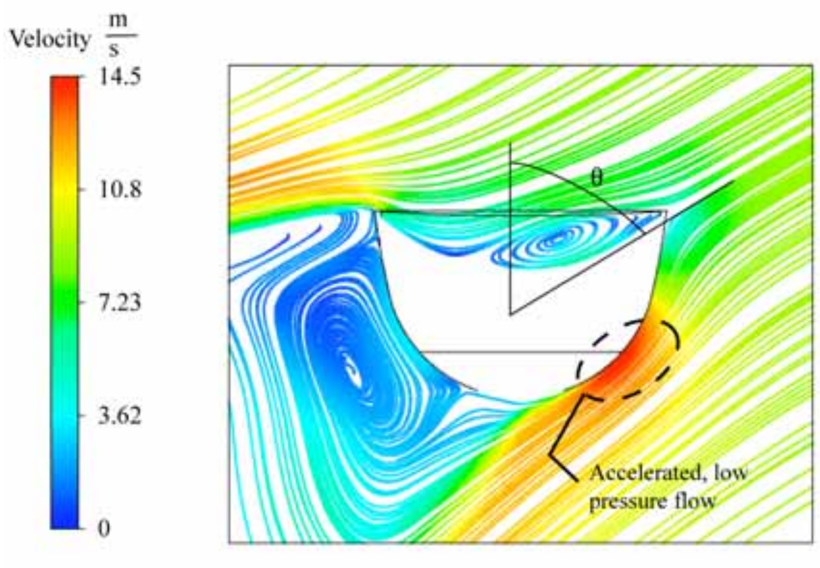

Fig. (8). Streamline pattern for flow with an incident angle of 60 degrees, color-coded by velocity magnitude corresponding to a relative wind speed of 20 miles/hour (9 m/s).

discussion, representative results corresponding to airflow angles-of-incidence of 0, 60 and 120 degrees are shown. The first set of results is displayed in Fig. (**7**), which shows streamlines of the flow passing normal to the concave surface of the cup. The streamlines, which are color-coded by the velocity scale on the left side of the figure, have been obtained on a two-dimensional cross-sectional cut through the cup and fluid region. It should be noted that the solution was, in fact, fully three dimensional. The results of Fig. (**7**) are for an incident velocity of 20 miles per hour (9 m/s). The deflection of streamlines on the front face of the cup is evident, as is the separation of flow on the downstream surfaces. In the figure, the airflow passes downwards, over the front surface of the cup.

The aforementioned deflection of flow at the front surface of the cup causes a rise in local air pressure as the kinetic energy of the air is converted to pressure. The pressure and shear stress distributions across the entire surface of the cup were integrated to provide the overall net circumferential force which results in rotation of the turbine blade.

A corollary set of figures for the cases of incident angles of 60 and 120 degrees are presented in Figs. (**8**) and (**9**), respectively. The figures show the streamline pattern including separation and the pressure distribution on the front face of the cup. Of note is a region of high velocity flow which, with its corresponding low pressure, creates a component of tangential force (cup lift) which aides in rotating the turbine blade.

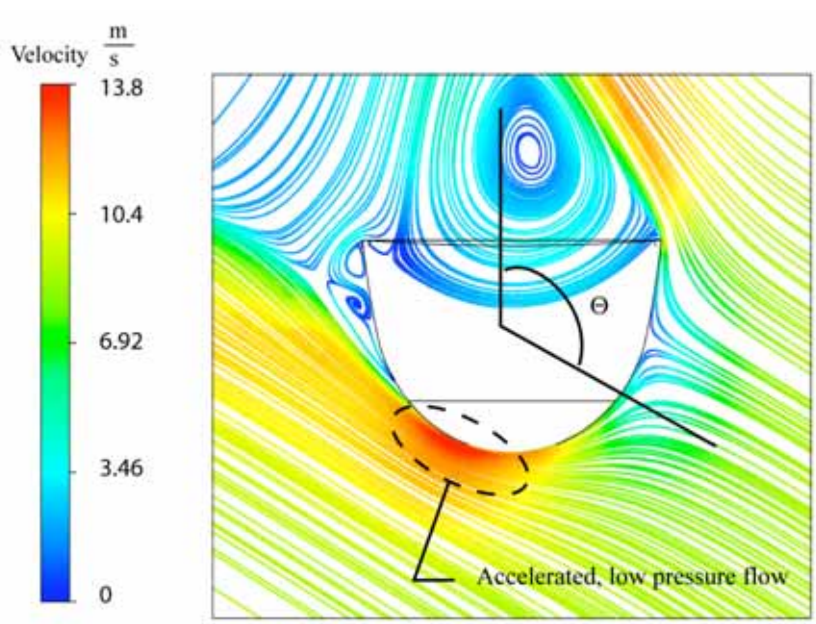

Fig. (9). Streamline pattern for flow with an incident angle of 120 degrees, color-coded by velocity magnitude corresponding to a relative wind speed of 20 miles/hour (9 m/s).

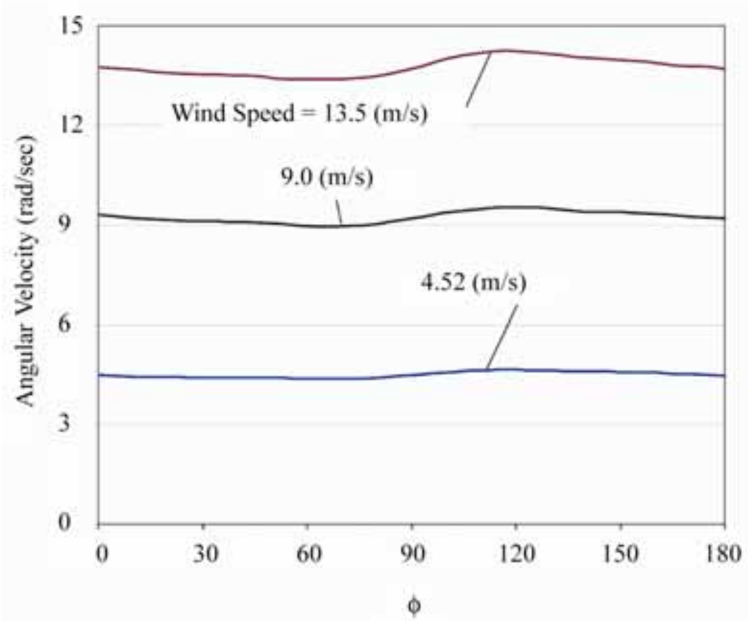

Fig. (10). Values of the angular velocity for wind speeds of 4.52, 9.0, and 13.5 (m/s) which correspond, respectively, to 10, 20, and 30 miles/hour.

The flow depictions set forth in Figs. (**7-9**) are illustrative and serve to demonstrate the complicated flow patterns which exist in the region near the turbine cup. Similar results have been obtained for multiple angles θ and relative wind velocities but are not shown here for brevity.

Rotational Motion Results

With the flow field calculations completed and tangential forces available at multiple relative wind velocities and angles, the numerical integration shown in Equations (11) and (12) can be completed. The calculations utilized a time-step increment, Δt, of 0.01 seconds. The calculations were continued from an imposed initial value of both ω' and ϕ until a quasi-steady state was reached. The achievement of quasi-steady motion was determined when the cycle-to-cycle variation of the angular velocity ω' was less than 1%.

The cycle-average angular velocity which corresponds to the quasi-steady state, hereafter called the *terminal angular velocity*, was obtained for multiple wind velocities so that the turbine response can be determined for any wind speed. A depiction of sample results is shown in Fig. (**10**) where the angular velocity is shown for an entire cycle and for three wind velocities, 4.52, 9.0, and 13.5 m/sec, which are equivalent to, respectively 10, 20, and 30 miles per hour. The figure shows results for a 180^o variation of the angle ϕ. The two cup system experiences periodic motion so that the pattern of angular velocity is repeated for every 180^o of motion.

For all cases presented in Fig. (**10**), it is seen that the angular velocity of the turbine varies slightly throughout the cycle. The terminal angular velocity for a given case is calculated by integrating the instantaneous angular velocity over the entire period of motion. When the terminal velocity

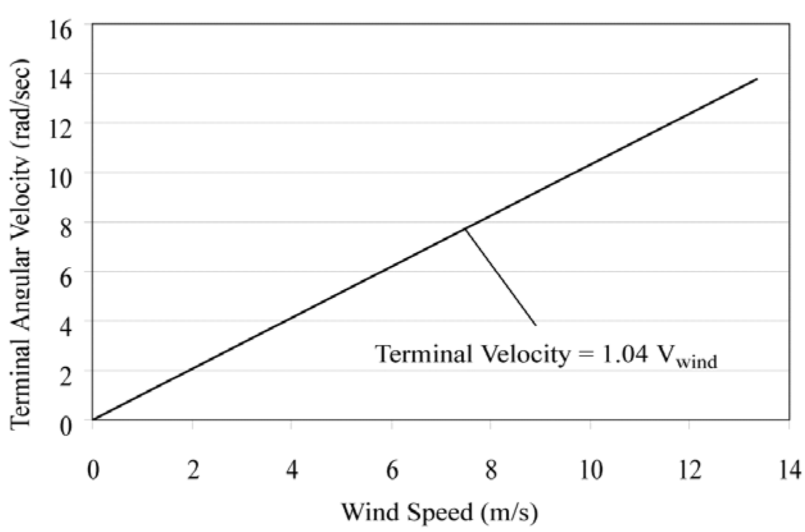

Fig. (11). Variation of terminal velocity with wind speed.

is obtained for a sequence of wind velocities, it is possible to develop a functional relationship between the two variables. Such a functional relationship is shown graphically in Fig. (**11**).

The results of Fig. (**11**) show that the terminal velocity depends linearly on the magnitude of the wind speed. This linear dependence is somewhat unexpected because in general, the circumferential force exerted on the cup varies as V_{wind}^2. On the other hand, it must be recognized that for most of the rotational period, the two cups experience two, counteracting forces. This fact tends to diminish the sensitivity of the angular velocity on the wind speed. The data illustrated in Fig. (**11**) has great utility in that it can be used to predict the final rotational velocity of the wind turbine for any incoming, steady wind speed and ultimately, the power generated by the wind turbine.

Of critical importance is the expected power generation which results from the rotating turbine. Based on the rotational results obtained with this candidate two-cup turbine design, the electrical output will be 12, 100, and 325 watts, respectively for wind speeds of 4.5, 9, and 13.5 meters per second.

CONCLUDING REMARKS

A two-step numerical simulation has been used to evaluate the efficacy of a new, vertical axis, small-scale wind turbine. The turbine possesses cups with a square front face and a smoothly contoured rear body which results in a net positive moment when the turbine is positioned in blowing air. Other features of the turbine include its very small profile which facilities its use in crowded, urban rooftop applications.

The numerical analysis consisted of a detailed simulation of the airflow patterns which exist across the cup surfaces. Calculations were made for a wide range of approach velocities and angles. These results enabled the continuous calculations of circumferential forces to be made on a two-cup system. Based on the circumferential forces, it was possible to determine the quasi-steady rotational motion of the turbine for a collection of steady wind velocities. The calculations ignored frictional losses within the turbine housing. Calculations of the rotary motion were completed using a forward-stepping numerical integration in time. Convergence was determined when the cycle-to-cycle variation in the angular velocity was less than 1%.

The results presented here are summarized in a function which relates the terminal angular velocity to the wind speed. That functional relationship enables a user to predict angular velocity of the turbine system.

ACKNOWLEDGEMENTS

The authors would like to acknowledge Horizontal Winds for the grant to the University of St. Thomas' School of Engineering. This grant enabled the directed student research that was instrumental to the success of the project.

NOMENCLATURE

a	Turbulent model constant
A	Turbulent model constant
F_1 and F_2	Circumferential forces [N]
F_1' and F_2'	Turbulent model blending functions
i,j	Tensor indices
I	Moment of inertia [kg m^2]
k	Turbulent kinetic energy
M_1 and M_2	Moments
p	Pressure [Pa]
P_k	Turbulence model production term
S	Shear strain rate
t	Time [s]
u_i	Local velocity [m/s]
V_{rel}	Relative wind velocity [m/s]
x	Coordinate direction [m]

Greek

α	Angular acceleration of turbine [rad/s^2]
β_1 and β_2	Turbulent model constants
θ	Incident angle of wind
ϕ	Angular position of turbine
ω	Specific rate of turbulence dissipation
ω'	Angular velocity [rad/s]
ρ	Air density [kg/m^3]
μ	Molecular viscosity [N s/m^2]
μ_t	Turbulent viscosity [N s/m^2]
σ	Prandtl number

REFERENCES

[1] "Annual report on U.S. wind power installation, cost, and performance trends: 2007", U.S. Department of Energy, May 2008.
[2] T. Ackermann, Ed., *Wind Power in Power Systems*. New York: John Wiley and Sons, 2005.
[3] W. Kays, M. Crawford, and W. Bernhard, *Convective Heat and Mass Transfer*, 4th ed. London: McGraw-Hill, 2004.
[4] F. Menter, "Two-equation eddy-viscosity turbulence models for engineering applications", *AIAA J.*, vol. 32, pp.1598-1605, 1994.
[5] B. Launder and D. Spalding, "Numerical computation of turbulent flows", *Comput. Meth. Appl. Mech. Eng.*, vol. 3, pp. 269-289, 1974.

[6] D. Wilcox, "Re-assessment of the scale-determining equation for advanced turbulence models", *AIAA J.*, vol. 26, pp. 1299-1310, 1988.

[7] D. Wilcox, "Comparison of two-equation turbulence models for boundary layers with pressure gradient", *AIAA J.*, vol. 32, pp. 1414-1421, 1993.

[8] F. Menter, "Influence of freestream values on k-omega turbulence model predictions", *AIAA J.*, vol. 30, pp. 1657-1659, 1992.

[9] M. Malone, "Turbulence model evaluation for free shear dominated flows", *AIAA paper 1996-2038*, New Orleans, LA, 1996.

[10] J. Ladd and T. Korakianitis, "On the assessment of one- and two-equation turbulence models for the computation of impinging jet flowfields", *AIAA paper 1996-2545*, 1996.

[11] R. Bush, "A two-equation large eddy stress model for high sub-grid shear", *AIAA Paper 2001-2561*, 2001.

[12] C. Rumsey, T. Gatski, and J. Morrison, "Turbulence model predictions of strongly curved flow in a U-duct", *AIAA J.*, vol. 38, pp. 1394-1402, 2000.

[13] J. Ekaterinas, "Computation of oscillating airfoil flows with one- and two-equation turbulence models", *AIAA J.*, vol. 32, pp. 2359-2365, 1994.

[14] F. Menter, M. Kuntz, and R. Langtry, "Ten years of industrial experience with the SST turbulence model", in International Symposium on Turbulence Heat and Mass Transfer 4, Antalya, Turkey, October 12-17, 2003.

[15] J. Abraham and A. Thomas, "Induced co-flow and laminar-to-turbulent transition with synthetic jets", *Comput. Fluids*, (in press).

[16] C. Rhie and W. Chow, "A numerical study of the turbulent flow past an isolated airfoil with trailing edge separation", *AIAA paper 82-0998*, 1982.

[17] S. Majumdar, "Role of underrelaxation in momentum interpolation for calculation of flow with nonstaggered grids", *Num. Heat Transfer*, vol. 13, pp. 125-132, 1998.

[18] T. Barth and D. Jesperson, "The design and applications of upwind schemes on unstructured meshes", *AIAA paper 89-0366*, 1989.

Corelation of S-N and da/dN- K Curves for any Particular Materials

Suraj Kumar Patel, *Department of Mechanical Engineering, Aryan Institute of Engineering & Technology, Bhubaneswar, surajpatel26@gmail.com*

Priyabrata Jena, *Department of Mechanical Engineering, Capital Engineering College, Bhubaneswar, priyabratajena456@yahoo.co.in*

Bijayalaxmi Behera, *Department of Civil Engineering, Capital Engineering College, Bhubaneswar, bijayalaxmi759@gmail.com*

Saruk Mallick, *Department of Civil Engineering, Raajdhani Engineering College, Bhubaneswar, sarukmallik57@yahoo.co.in*

Abstract: The *S-N*, *ε-N* and d*a*/d*N*-Δ*K* curves are the basic data of fatigue property for materials, and they are used in the stress-life method, the local strain method and the LEFM (Linear elastic fracture mechanics) crack propagation method to predict fatigue life of structures, respectively. In the present paper, the relations between these fatigue curves and their probability of predicting each other were discussed through several fatigue-life models. The discussed subjects include (1) predicting the *S-N* curves from the d*a*/d*N*-Δ*K* curves of materials, (2) predicting the *S-N* curves from the *ε-N* curves, and (3) predicting the d*a*/d*N*-Δ*K* curves from the *ε-N* curves. It is shown that there are certain relations between the *S-N*, *ε-N* and d*a*/d*N*-Δ*K* curves of materials and it is predictable from one curve to another.

Keywords: d*a*/d*N*-Δ*K* curve, *ε-N* curve, *S-N* curve, relation.

1. INTRODUCTION

Since the concept of fatigue *S-N* curve, i.e. the stress-life curve, was put forward by Wöhler in the 1860s, various methods of fatigue-life predictions have been developed. Among the methods the stress-life method, the local strain method and the LEFM (Linear elastic fracture mechanics) crack propagation method have become the most classical ones. For the three methods, the *S-N*, *ε-N* (strain-life) and d*a*/d*N*-Δ*K* (crack propagation rate *vs*. stress intensity factor range) curves are their bases to predict fatigue-life, respectively. In order to obtain the *S-N*, *ε-N* and d*a*/d*N*-Δ*K* data for one material, three sets of tests, i.e. the *S-N*, *ε-N* and d*a*/d*N*-Δ*K* tests of standard specimens under constant amplitude loading, must be performed, respectively, which always needs much money, time and manpower.

In fact, the *S-N*, *ε-N* and d*a*/d*N*-Δ*K* curves are only the characterization of fatigue property for materials under different cases. Now let's suppose that there are certain relations between the three curves of materials and one curve can be predicted from another through the relations, then, the existing fatigue curve will educe two others, its value will double, and a great amount of experimental expense will be saved.

In the present paper, through several fatigue-life models we will discuss the relations between the *S-N*, *ε-N* and d*a*/d*N*-Δ*K* curves of materials, as well as their probability of predicting each other.

2. PREDICTING THE *S-N* CURVES FROM THE d*a*/d*N*-Δ*K* CURVES

From the viewpoint of fracture mechanics, fatigue crack emanates from the surface or near-surface defects of structure, and then evolves into 3D (three-dimensional) crack until the structure fails. In Reference [1] a 2D (two-dimensional) fracture mechanics based full-life model was put forward. In the model, one standard d*a*/d*N*-Δ*K* curve, i.e. the Pairs curve of material, is extrapolated toward small crack to obtain "the equivalent initial crack length a_0" (also called as "the equivalent initial defect a_0") of the material; further the a_0 is regarded as the inherent parameter of this material and is considered to be applicable to any other structure of same material and same environment; at last, with the a_0 as initial crack length, the total fatigue-life of other structures of same material and same environment can be predicted through the routine LEFM method. In Reference [1], with one experimental data-point as subject, the 2D fracture mechanics method, with the linearly extrapolated Pairs curve in logarithm coordinate, is used to calculate the fatigue life for crack propagating from a_0 to a_L, and the trial-and-error method is applied to determine the a_0 of material, i.e., a series of a_0 are tried one by one until the calculated life is equal with the experimental result. The idea of Reference [1] is inspirational, but the 2D fracture mechanics based model has vital defects. Firstly, the a_0 through the extrapolated Pairs curve is very difficult to be equivalent with the 3D initial defects of the actual 3D structures; secondly, the geometrical size effect [2] during 3D crack growth is ignored. In Reference [3, 4] we put forward a 3D fracture mechanics method to predict the *S-N* curves of material through the d*a*/d*N*-Δ*K* data. In the 3D fracture mechanics method the effective SIF (stress intensity factor) ΔK_{eff} for the crack closure model, i.e., d*a*/d*N*=$C(\Delta K_{eff})$, takes the Newman's expression [5]. In the Newman's expression, the 3D constraint factor a_g is given by Reference [2].

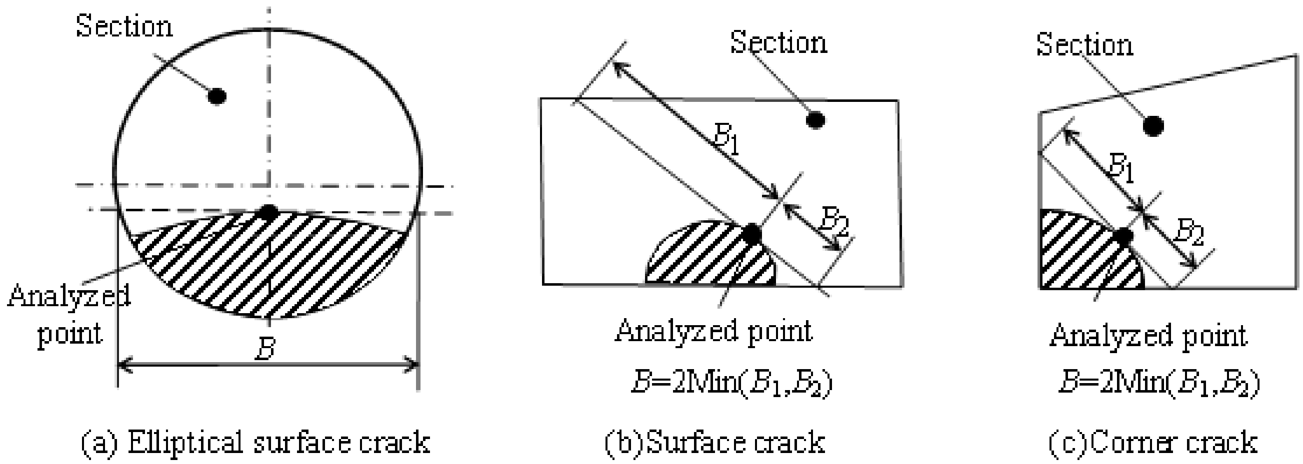

Fig. (1). Fatigue crack and the definition of equivalent thickness *B*.

$$a_g = \frac{1 + a_1 f(r_{po}/B)}{1 - 2\nu + b_1 f(r_{po}/B)} \tag{1}$$

where $f(x) = x^{0.5} + 2x^2$; $r_{po} = \frac{\pi}{8}\left[\frac{K}{\sigma_{flow}}\right]^{1/2}$; K is the SIF of the investigated point of crack border; r_{po} is the plastic zone size; ν is the Poisson's ratio; σ_{flow} is the flow stress of material, namely, the average value of the yielding stress σ_s and the fracture stress σ_b; a_1=0.6378; b_1=0.5402; B is the equivalent thickness of specimen. For through-thickness cracked bodies, the B is the thickness of the specimen; for 3D cracked bodies, the B is defined as B=2min(B_1+B_2), where B_1 and B_2 are the distances from the analyzed point P on the crack border to the boundary of the cracked bodies along the tangential line of the crack front-line at P, as shown in Fig. (**1**). For elliptical surface crack in a round bar, the equivalent thickness B of the deepest point P is defined in Fig. (**1a**).

Apparently the constraint factor a_g of Eq. (1) is a function of the analyzed points on the 3D crack border, and the present crack closure model considers the effects of the specimen size and stress status.

By using the above closure model as well as one standard da/dN-ΔK curve of material, the da/dN-ΔK_{eff} curve can be obtained with the stress ratio, the specimen size and the stress status considered. According to the obtained da/dN-ΔK_{eff} curve of material, the "cycle-by-cycle" method, the SIFs of 3D cracks published in the SIF handbooks [6] (or calculated by the finite element method [7]), and the crack shape evolvement given according to the theoretical method of Reference [8] or the analogous experiments [9], as well as the above 3D fracture mechanics method, we can predict the full-life of 3D structure, i.e. the fatigue life of crack propagating from the initial defect a_0 to the critical crack lengthen a_L in one direction of crack propagation, such as the propagation direction of the deepest point of 3D crack. Here the initial defect a_0 of material is given according to the following principles:

(1) Supposing that the initial defect of material is small semi-circular surface crack or fan-shaped corner crack. The radius of the cracks is a_0.

(2) With one experimental data-point as subject, the above 3D fracture mechanics method is used to calculate its fatigue life for crack propagating from a_0 to a_L. During the calculation, a series of a_0 are tried one by one until the calculated life is equal with the experimental result.

Apparently the a_0 is relative with environment and material. Once the a_0 is obtained, it can be repeatedly used to predict the total fatigue life of other 3D structures for same environment, same material and same quality of material by the above 3D fracture mechanics method. In other words, we can predict the *S-N* curves through the da/dN-ΔK curves of material.

By the above method and the da/dN-ΔK curves of 30CrMnSiA steel and LC9Cgs aluminum [10], the *S-N* curves of the rotating-bending round-bars of the two metals are predicted respectively. The 30CrMnSiA and LC9Cgs bars have the diameters of 7.5mm and 20mm respectively, and both their stress ratio r = -1. The predicted *S-N* curves as well as the experimental results [11] are shown in Fig. (**2**). In Fig. (**2**) the experimental data points marked by the "↑" are used to determine the a_0 of two materials through the trial-and-error method. Here the obtained a_0 of 30CrMnSiA steel and LC9Cgs aluminum is 0.015mm and 0.03mm respectively. From Fig. (**2**), it is shown that the predicted *S-N* curves are close to the experimental results [11].

3. PREDICTING THE *S-N* CURVES FROM THE *ε-N* CURVES

Considering that the classical local strain method is only valid to low cycle fatigue, in References [12] a modified local strain method was put forward by us for the life calculation of high cycle fatigue. In fact, the modified method has the same processes as the classical one. Their only difference lies in that the *ε-N* curve used in the modified

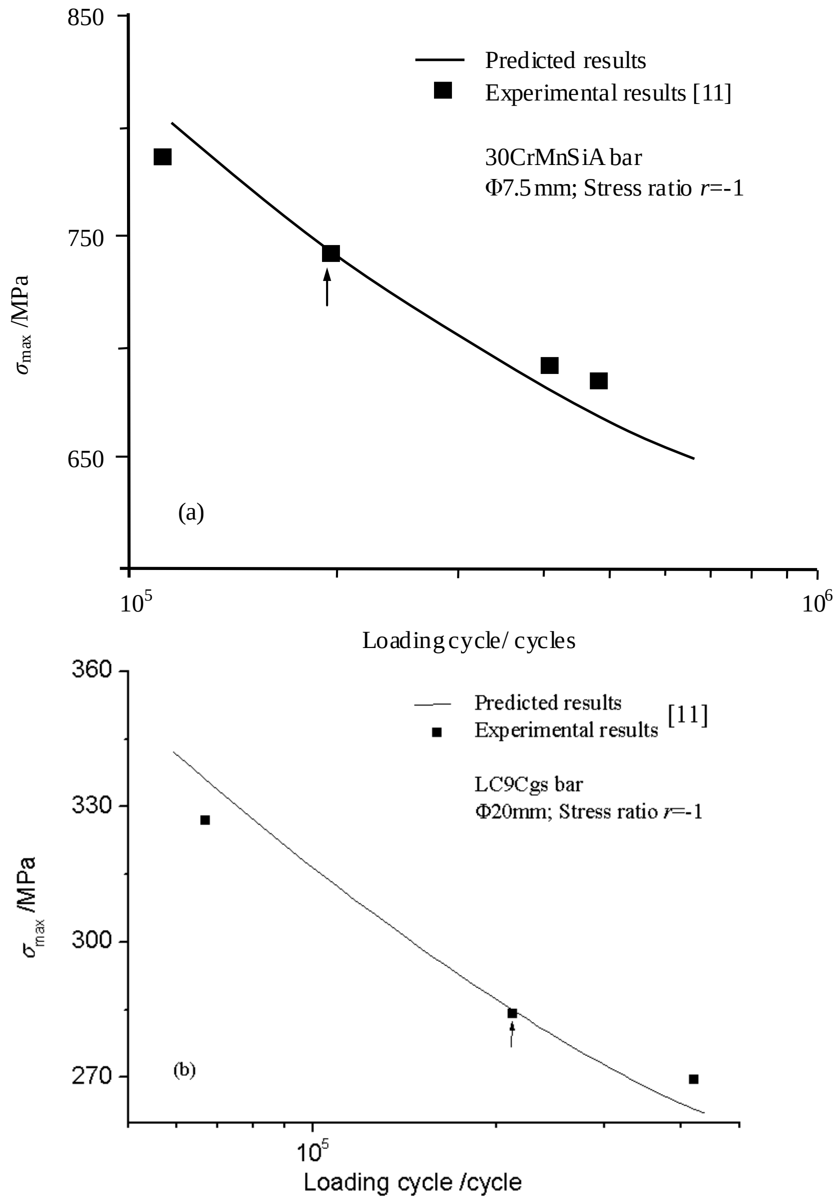

Fig.(2). The *S-N* curves of the rotating-bending round-bars.

method must have its elastic component modified according to the specimen size and surface quality. The followings are the modification procedures of the *ε-N* curve used in the modified local strain method.

In Fig. (**3**) Line1, i.e.; the AB line, is the elastic component of the *ε-N* curve for the classical local strain method. For high cycle fatigue, when the specimen size and surface quality are considered the fatigue-limit falls to the C point from the B point. Log(2*N*)=0 corresponds to the monotone load, and the specimen size and surface quality have no effect on the monotone load, so the A point has no change in position. Line2, i.e. the AC line, is the modified elastic component of the *ε-N* curve with the specimen size and surface quality considered. Considering that the specimen size and surface quality have only little effect on low cycles fatigue, the plastic component of the *ε-N* curve, i.e. Line 3, needs no modification. After the elastic component is modified, the *ε-N* curve changes into Line 5 from Line 4. The modified elastic component, i.e. Line 2, has the slope of

$$b' = \frac{\log(\sigma_{-1}\gamma_c\varepsilon_d\beta) - \log(\sigma'_f\gamma'_c)}{\log(2N_0)} \tag{2}$$

where σ'_f is the fatigue strength coefficient; γ'_c is the crystallite size coefficient for fracture strength; $\sigma_{-1}$is the fatigue-limit corresponding to the stress ratio r = -1; γ_c is the crystallite size coefficient for fatigue-limit; log(2N_0)≈7; ε_d and β are the specimen size coefficient and the surface quality coefficient respectively, and the ε_d and β for some typical metal specimens are given in Reference [13, 14].

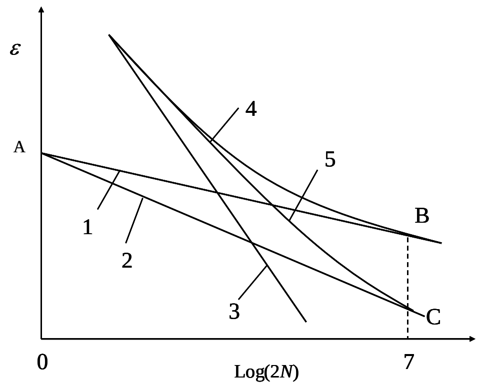

Fig.(3). The ε -N curves of materials.

The unmodified elastic component, i.e. Line 1, has the slope of,

$$b = \frac{\log(\sigma_{-1}\gamma_c) - \log(\sigma'_f\gamma'_c)}{\log(2N_0)} \tag{3}$$

Combining Eq. (2) and Eq. (3), the slope of Line 2

$$b' = b\frac{\log(\sigma_{-1}\gamma_c\varepsilon_d\beta) - \log(\sigma'_f\gamma'_c)}{\log(\sigma_{-1}\gamma_c) - \log(\sigma'_f\gamma'_c)} \tag{4}$$

After the modification, the Morrow equation for ε-N curves changes into,

$$\frac{\Delta\varepsilon}{2} = \frac{\sigma'_f\gamma'_c - \sigma_m}{E}\left(2N\right)^{b'} + \varepsilon'\left(2N\right)^{c} \tag{5}$$

where E is the elastic module; ε' is the fatigue ductility coefficient; c is the fatigue ductility exponent; b is the fatigue strength exponent; b' is the modified fatigue strength exponent; σ_m is the average stress.

By using the modified method with the same steps as the classical local strain method [15], in addition to the standard ε-N curve of material, the specimen size coefficient ε_d and the surface quality coefficient β, the S-N curves for standard specimens of the material can be predicted.

Fig. (**4**) presents the experimental fatigue-life results for 3Cr13 and 2Cr11NiMolV stainless-steel plates (steam-

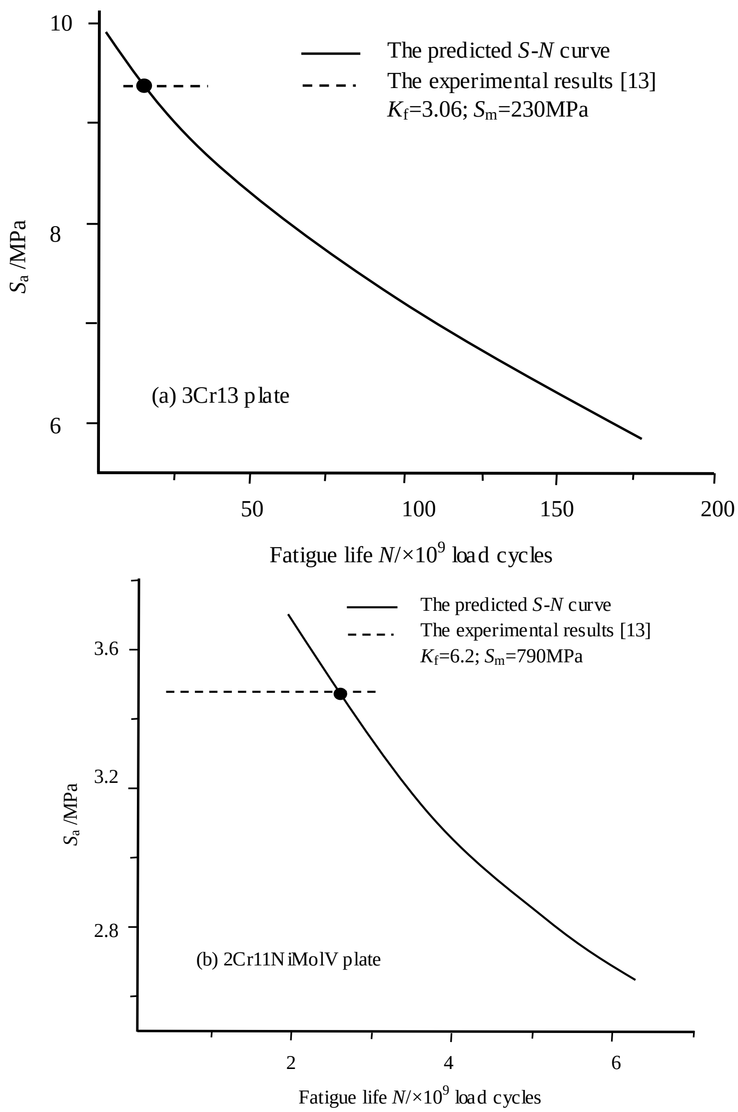

Fig. (4). The S-N curves for 3Cr13 and 2Cr11NiMolV plates.

turbine blades) under constant amplitude fatigue loading [13]. The 3Cr13 plate has the fatigue notch coefficient K_f = 3.06, the average nominal-stress S_m=230Mpa, and the nominal-stress amplitude S_a=9.73MPa; the 2Cr11NiMolV plate has K_f = 6.2, S_m=790Mpa, and S_a=3.47MPa. The experimental fatigue-life for the 3Cr13 plates distributes in the range from 8.8×10^9 to 35.3×10^9 load cycles, and that for 2Cr11NiMolV plate in the range from 0.32×10^9 to 3.2×10^9 load cycles. Their strain-fatigue parameters are as followings: $E=210Gpa$, ε' =0.381, c =-0.5791, σ_{-1} =301MPa, σ'_f =930MPa, b = -0.0743, cyclic strength coefficient K'=1325MPa, cyclic strain hardening exponent n'=0.099, and γ_c =1 for 3Cr13 steel; $E=210Gpa$, ε'=0.5561, c=-0.664, σ_{-1}=461MPa, σ'_f = 1249MPa, b=-0.0656, K'=1056MPa, n'=0.124, and γ_c = 1 for 2Cr11NiMolV steel. All the parameters come from Reference [16].

By using the present modified local-strain-method with ε_d = γ'_c =1 and β=0.5 [11], Fig. (**4**) gives the predicted *S-N* curves for the two stainless-steel plates. From Fig. (**4**), it is found that the corresponding life-results, marked by solid circles in the predicted *S-N* curves, are close to the experimental ones [13].

4. PREDICTING THE D*a*/d*N*-Δ*K* CURVES FROM THE *ε-N* CURVES

From the view of low cycle fatigue, the fatigue crack propagation can be considered to be the process of the material at crack-tip continually fracturing under high-strain fatigue loading. In Reference [17] the strain-fatigue damage was introduced into crack-tip, and basing the idea the fatigue crack propagation was described. However, the model includes too many experimental parameters and is very inconvenient to analyze crack propagation. In Reference [18-20], we put forward a fatigue crack propagation model basing the concept of "crack-tip damage zone". In the model, it is assumed that:

(1) Within the plastic zone ω of crack-tip there is one small zone x^*, called as "crack-tip damage zone". In the damage zone, stress and strain have little gradient, see Fig. (**5**).

(2) The material in the zone x^* undergoes cyclic strain; when the life reaches N cycles, the material of the zone x^* cracks and the crack grows x^*.

(3) Outside the damage zone x^*, the stress and strain have very large gradient and attenuate very quickly, so the damage is relatively small and can be ignored.

(4) The stress and strain of the damage zone x^* can be respectively characterized with those at the midpoint of the zone, i.e. the position of 0.5 x^*.

Reference [18] gave the expressions of the stress σ and ε strain of the damage zone, i.e. the stress and strain at the position of $0.5x^*$, for power hardening material.

$$\sigma(0.5x^*) = \sigma_s\left(\frac{K^2}{0.5\pi(1+n)\sigma_s^2 x^*}\right)^{\frac{n}{1+n}}$$
$$\varepsilon(0.5x^*) = \varepsilon_s\left(\frac{K^2}{0.5\pi(1+n)\sigma_s^2 x^*}\right)^{\frac{1}{1+n}} \qquad (6)$$

where σ_s is the yielding stress; ε_s (=σ_s/E) is the yielding strain; K is the SIF of the crack; n is the hardening exponential. Under cyclic loading, according to Eq. (6) the maximum stress σ_{max} and strain ε_{max} of the damage zone have the following relation:

$$\sigma_{max}\varepsilon_{max} = \frac{K_{max}^2}{0.5\pi E(1+n)x^*} \qquad (7)$$

where K_{max} is the SIF corresponding to the maximal loading.

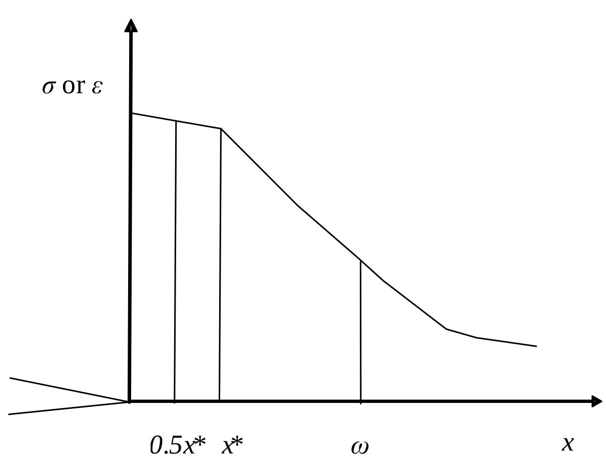

Fig.(5). The stress and strain distribution of crack-tip.

Supposing that material complies with the Ramberge-Osgood relationship, then

$$\varepsilon_{\max} = \frac{\sigma_{\max}}{E} + \left(\frac{\sigma_{\max}}{K'}\right)^{1/n} \quad (8)$$

For the center cracked plate, when the crack propagates x^* the released energy $U = \frac{K_{\max}^2}{E} x^*$ and the stress work of the damage zone $\bar{U} = \int \frac{1}{2}\sigma 2v(x)\,dx$. The U and $\bar{U}$ are equal in value, i.e.,

$$\frac{K_{\max}^2}{E} x^* = \int \frac{1}{2}\sigma 2v(x)\,dx \quad (9)$$

where $v(x)$ is the displacement vertical to the crack surface, and

$$v(x) = 4K_{\max} / E\sqrt{\frac{x^*-x}{2\pi}} \quad [21]$$

According to Eq. (7-9), the size x^*, the maximum stress $\sigma_{\max}$ and strain $\varepsilon_{\max}$ of the damage zone under $K_{\max}$ can be worked out.

Under constant amplitude fatigue loading, according to Eq. (7, 8), the stress amplitude $\Delta\sigma$ and the strain amplitude $\Delta\varepsilon$ have the following relations:

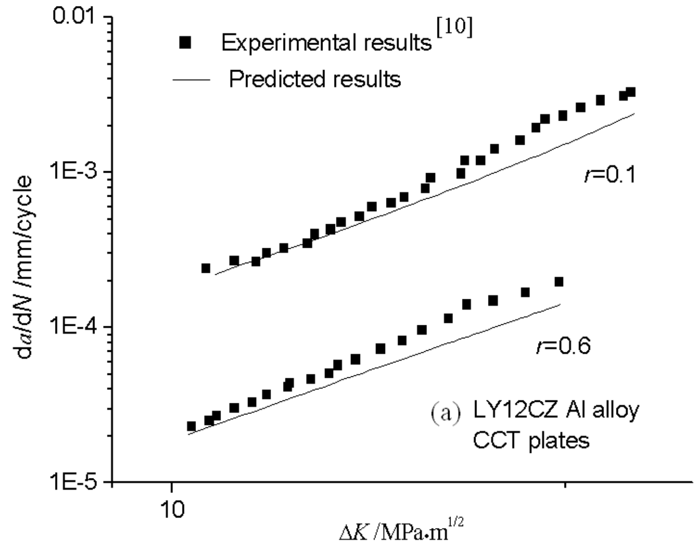

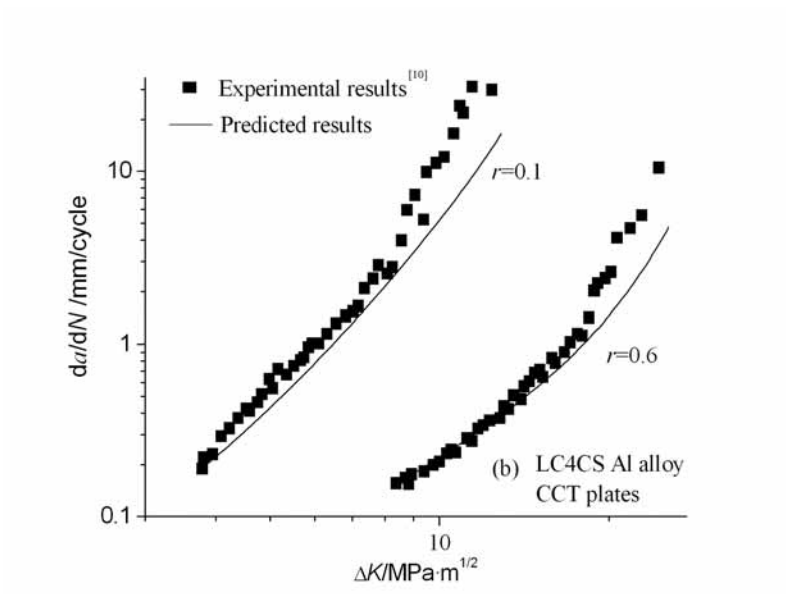

Fig. (6). The da/dN-ΔK curves of LY12CZ and LC4CS aluminum plates.

$$\Delta\sigma\Delta\varepsilon = \frac{K_{eff}^2}{0.5\pi E(1+n')x^*} \tag{10}$$

$$\Delta\varepsilon = \frac{\Delta\sigma}{E} + \left(\frac{\Delta\sigma}{K''}\right)^{1/n'} \tag{11}$$

where n' is the cyclic hardening exponential; K'' is the cyclic hardening coefficient; the effective SIF range $\Delta K_{eff} = U'\Delta K$, and the closure factor $U' = (0.55+0.35r+0.1r^2)$ [22].

According to the Manson-Coffin equation for the ε-N curves,

$$\frac{\Delta\varepsilon}{2} = \frac{\sigma_f' - \sigma_m}{E}(2N)^b + \varepsilon'(2N)^c \tag{12}$$

The load-cyclic number N at the time of the damage zone x^* cracking, as well as the crack propagation ratio $da/dN = x^*/N$ under the present ΔK, can be obtained.

Repeatedly using Eq. (7)-Eq. (12), we will obtain the d*a*/d*N* corresponding to different ΔK, *i.e.* the d*a*/d*N*-ΔK curves of the material. Fig. (**6**) shows the experimental d*a*/d*N*-ΔK data [10] for LY12CZ and LC4CS aluminum plates under constant amplitude fatigue loading. All the aluminum plates are the standard CCT specimens, and the stress ratio r takes 0.1 and 0.6. The ε-N data (namely the parameters of Eq. (12)) of LY12CZ and LC4CS aluminum come from Reference [11].

According to Eq. (7)-Eq. (12), we predict the d*a*/d*N*-ΔK curves of the above LY12CZ and LC4CS aluminum plates. The predicted results are shown in Fig. (**6**). From Fig. (**6**), it is found that the predicted d*a*/d*N*-ΔK curves from the ε-N curves [11] are close to the experimental results [10].

Note: Here the plane stress assumption is taken, so the method is only suitable to the sheet materials.

5. CONCLUSIONS

Through several fatigue-life models the relations between the *S*-*N*, ε-N and d*a*/d*N*-ΔK curves of materials, as well as their probability of predicting each other, are discussed. It is found that it is possible to predict the *S*-*N* curves from the d*a*/d*N*-ΔK curves of material, to predict the *S*-*N* curves from the ε-N curves, and to predict the d*a*/d*N*-ΔK curves from the ε-N curves. The work in the present paper is very valuable for extending the available fatigue properties database and significant for unitizing the fatigue theory and the fracture theory.

NOMENCLATURE

a	=	Crack length
a_0	=	Initial crack length
a_L	=	Critical crack length
a_g	=	3D constraint factor
b	=	Fatigue strength exponent
b'	=	Modified fatigue strength exponent
B	=	Specimen equivalent thickness
β	=	Surface quality coefficient
c	=	Fatigue ductility exponent
ε	=	Strain
$\Delta\varepsilon$	=	Strain amplitude
ε_d	=	Specimen size coefficient
E	=	Elastic module
ε'	=	Fatigue ductility coefficient
ε_{max}	=	Maximum strain
ε_s	=	Yielding strain
K	=	Stress intensity factor (SIF)
K_f	=	Fatigue notch coefficient
K_{max}	=	Maximal SIF
K'	=	Cyclic strength coefficient
K''	=	Cyclic hardening coefficient
ΔK	=	SIF amplitude
ΔK_{eff}	=	Effective SIF amplitude
n	=	Hardening exponential
N	=	Fatigue life (loading cycle)
n'	=	Cyclic strain hardening exponent
r_{po}	=	Is the plastic zone size
S,σ	=	Stress
r	=	Stress ratio
γ_c	=	Crystallite size coefficient
γ_c'	=	Crystallite size coefficient
S_m	=	Average nominal-stress
S_a	=	Nominal-stress amplitude
U	=	Released energy
$\bar{U}$	=	Stress work
U	=	Closure factor
v	=	Displacement vertical to the crack surface
ν	=	Poisson's ratio
ω	=	Plastic zone
x^*	=	Crack-tip damage zone
σ_{flow}	=	Flow stress of material
σ_s	=	Yielding stress
σ_b	=	Fracture stress
σ'_f	=	Fatigue strength coefficient
σ_{-1}	=	Fatigue-limit
σ_m	=	Average stress

σ_{max} = Maximum stress

$\Delta\sigma$ = Stress amplitude

REFERENCES

[1] X.J. Fu and Y.Q. Zhou, "The full-life model of the fatigue crack propagation", In Proceeding of the 8th National Fracture Academic Conference, 1996, pp. 252-255.

[2] W.L. Guo and F. Rose, "Three-dimensional strip-yielding modeling for constraint factors". In Proceeding of the 7th International Fatigue Congress, 1999, pp. 685-690.

[3] H.J. Shen and W.L. Guo, "Three dimensional fracture method for prediction of fatigue *S-N* curves". *Trans. Nanjing Univ. Aeronaut. Astronaut.*, vol. 34, pp. 216-220, Jun 2002.

[4] H.J. Shen and W.L. Guo, "3D constraint effect on 3D fatigue crack propagation", *Int. J. Fatigue*, vol. 27, pp.617-623, May 2005.

[5] J.C. Jr. Newnan, *Effects of Constraint on Crack Growth under Aircraft Spectrum Loading*. Delft University Press, 1992.

[6] Z.T. Gao, Stress intensity factors. Beijing: Scientific Press, 1993.

[7] H.J. Shen and W.L. Guo, "3D FE analyses of corner-crack near dimple holes", *Acta Aeronaut. Astronaut. Sin.*, vol. 23, pp. 106-110, Feb 2002.

[8] X.B. Lin and A. Smith. Roderick, "Fatigue life prediction for irregular racks", *China Mech. Eng.*, vol. 11, pp. 43-45, Nov 1998.

[9] H.J. Shen and W.L. Guo, "Modified James-Anderson method for stress intensity factors of three-dimensional cracked bodies", *Int. J. Fatigue*, vol. 27, pp. 624-628, May 2005.

[10] M.M. Yan, *Handbook of the Velocity of Fatigue Crack Propagation of Aviation Metal Materials*. Beijing: Beijing Institute of Aviation Materials, 1984.

[11] Z.T. Gao, *Handbook of Fatigue Performance of Aviation Metal Materials*. Beijing: Beijing Institute of Aviation Materials,1981.

[12] B.T. Zhu, "Modified local stress-strain method for the life calculation of stream turbine lamina under low cycles and high cycles fatigue (I)", *Therm. Power Generation*, vol. 12, pp. 9-14, May 1997.

[13] B.T. Zhu, "Modified local stress-strain method for the life calculation of stream turbine lamina under low cycles and high cycles fatigue (II)", *Therm. Power Generation*, vol. 12, pp. 4-8, Jun 1997.

[14] J. Wan, *Handbook of Electromechanical Engineering Materials.* Shanhai: Science and Technology Press, 1990.

[15] W.X. Yao. *Fatigue Life Prediction of Structures.* Beijing: Press of National-defence Industry, 2003.

[16] C. Boller and T. Seeger, *Material Data for Cyclic Loading*. Amsterdam: Elservier Science Publishers. B. V., 1987.

[17] G. Glinka, "A cumulative model of fatigue crack growth", *Int. J. Fatigue*, vol. 4, pp. 337-347, April l982.

[18] H.J. Shen, Corrosion fatigue mechanism of high strength aluminum alloy and full-life model for corrosion fatigue, PhD dissertation, Northeastern Poly-technology University, China, 2000.

[19] J.F. Ma, "A fatigue crack propagation model basing on crack-tip damage zone", *Mech. Sci. Technol.*, vol. 18, pp. 701-703, May 1999.

[20] J.F. Ma, "An analytical model for determining ΔK_{eff}", *Mech. Sci. Tech.*, vol. 18, pp. 384-385, Apr 1999.

[21] W.Y. Huang, *Engineering Fracture*, Beijing: Aviation Industry Press, 1991.

[22] J. Schijve, " Some formulas for the crack opening stress level", *Engng. Fracture Mech.*, vol. 14, pp. 461-465, Nov 1981.

Fluid Friction Factor Abandoned, and the Transformed Moody Chart

Bidyuta Ranjan Rout, *Department of Mechanical Engineering, Aryan Institute of Engineering & Technology, Bhubaneswar, bidyutaranjan1@gmail.com*

Sidharth Pradhan, *Department of Mechanical Engineering, Capital Engineering College, Bhubaneswar, sidharthpradhan265@gmail.com*

Rajaram Sahu, *Department of Mechanical Engineering, Raajdhani Engineering College, Bhubaneswar, rajaramsahu65@gmail.com*

Abstract: The "fluid friction factor" (f) should be abandoned because it is a mathematically undesirable parameter that complicates the solution of fluid flow problems. f is the dimensionless group $\pi^2 g\rho\Delta PD^5/8LW^2$. This group is mathematically undesirable because it includes ΔP, W, and D. Therefore if f is used in the solution of a problem, the problem must be solved with ΔP, W, and D in the same term, even though fluid flow problems are generally much easier to solve if ΔP, W, and D are in separate terms. (Just as it is generally much easier to solve equations if x and y are in separate terms). The mathematical complication introduced by f is illustrated by the Moody chart (Fig. **1**). Because the chart is based on f, it must be read iteratively (or by trial-and-error) to determine W or D. But if the Moody chart is transformed in order to eliminate f, the transformed chart (Fig. **2**) is read directly to determine ΔP, W, or D. The fluid flow methodology described herein altogether abandons f, and allows fluid flow problems to be solved in the simplest possible manner.

INTRODUCTION

In the modern view, fluid flow behavior is described by the "Darcy equation" (also known as the "Darcy-Weisbach equation"), Expression (1). In the laminar regime, f is described by Eq. (2). In the turbulent regime, f is described by Expression (3). The function in Expression (3) is described by the Moody [1] chart, Fig. (**1**).

$\Delta P = fL\rho V^2/2gD$ . . . (1)

$f_{laminar} = 64/Re$ . . . (2)

$f_{turbulent}$ = function of Re and ε/D . . . (3)

Oftentimes, the "Darcy equation", f, and the Moody chart are not used, and fluid flow behavior is approximated by empirical, analytical correlations in the literature, such as,

$\Delta P_{turbulent} = aL\rho V^n/2gD$ . . . (4)

HISTORICAL BACKGROUND FROM BROWN [2]

In 1845, the fluid friction factor was presented by Weisbach [3] in the "Darcy equation", Expression (1).

In Weisbach's view, this expression was a general description of the behavior of fluids flowing in pipes. It was not accepted for some time because Weisbach "did not provide adequate data for the variation in f with velocity. Thus, his equation performed poorly compared to the empirical Prony equation in wide use at the time;

$\Delta P = \rho L/D(aV + bV^2)$ . . . (5)

in which a and b are empirical friction factors for the velocity and velocity squared."

Darcy [4] was the first to recognize that ΔP depends on wall roughness. Fanning [5] was the first to reduce fluid flow data to friction factor values that quantified the effect of both V and wall roughness.

(This article is an extension of the friction factor view presented in Adiutori [6].)

THE "DARCY EQUATION" IS NOT AN EQUATION

The "Darcy equation" is not an equation, even though it is written in the form of an equation. Equations describe the relationship between the parameters on the left side of the equation and those on the right side. The "Darcy equation" does not do this, and therefore it is not an equation.

For example, the "Darcy equation" does not describe the relationship between ΔP and V, even though it appears to state that ΔP is proportional to V^2.

The "Darcy equation" would be an equation if f were a constant coefficient, in which case the equation would in fact state that ΔP is proportional to V^2.

f IS NOT A CONSTANT COEFFICIENT

The f in the "Darcy equation" is not a constant coefficient, even though the symbolism in the "Darcy equation" indicates that f is a constant coefficient. f is a variable that depends on Re and ε/D, and it should be written in the form f{Re, ε/D}.

Rouse and Ince [7] state that Weisbach "found the coefficient f to vary not only with the velocity . . . but also with the diameter and wall material". Since Weisbach viewed the fluid friction factor as a variable that depends on V, D, and wall material, it is surprising that he presented it in

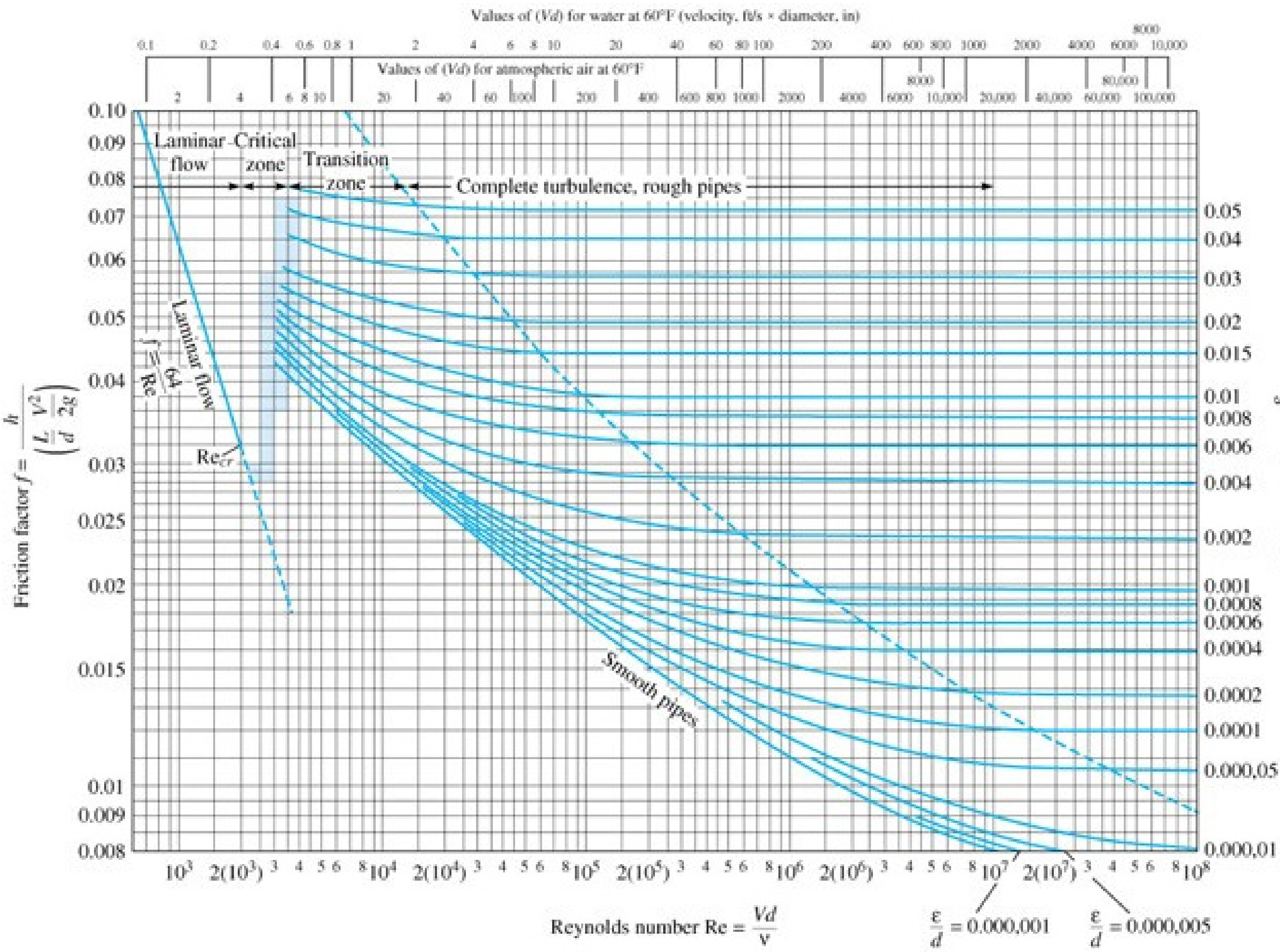

Fig. (1). The Moody [1] chart.

the form "f" rather than the correct form "f{V, D, wall material}".

THE "DARCY EQUATION" IS A DEFINITION

The "Darcy equation" is a definition. It defines f to be $2\Delta PgD/L\rho V^2$, and should be written in the form of a definition, as in Definition (6).

$$f \equiv 2\Delta PgD/L\rho V^2 \ldots \quad (6)$$

f IS A DIMENSIONLESS GROUP

f is a dimensionless group defined by the "Darcy equation", just as Re is a dimensionless group defined by Definition (7).

$$Re \equiv 4W/\pi\mu D \ldots \quad (7)$$

Dimensionless groups are best defined by independent parameters in order to readily reveal the true nature of the group. For example, Definition (6) seems to state that the f group includes D, when in fact it states that the f group includes D^5. This seeming contradiction results because V is not an independent parameter in Definition (6).

Combining Definition (6) and Eq. (8) eliminates V, and results in Definition (9).

$$V = 4W/\pi\rho D^2 \ldots \quad (8)$$

$$f \equiv \pi^2 g\rho\Delta PD^5/8LW^2 \ldots \quad (9)$$

Definition (9) is the most desirable form of the "Darcy equation" because it reveals that the "Darcy equation" is not an equation, and because it defines f in the clearest possible way.

THE MODERN VIEW OF FLUID FLOW BEHAVIOR IN TERMS OF PHYSICAL PARAMETERS

Equation (2) and Expression (3) describe the modern view of fluid flow behavior in terms of the dimensionless groups f and Re. Substituting $\pi^2 g\rho\Delta PD^5/8LW^2$ for f and $4W/\pi\mu D$ for Re in Eq. (2) and Expression (3) results in Eq. (10) and Expression (11), the modern view of fluid flow behavior expressed in terms of physical parameters:

$$(\pi^2 g\rho\Delta PD^5/8LW^2)_{laminar} = 16\pi\mu D/W \ldots \quad (10)$$

$$(\pi^2 g\rho\Delta PD^5/8LW^2)_{turbulent} = \text{function of } 4W/\pi\mu D \text{ and } \varepsilon/D \quad (11)$$

The function in Expression (11) is described by the Moody chart.

THE MOODY [1] CHART, (FIG. 1)

The Moody chart appears in most texts and handbooks on fluid flow engineering. Moody prepared the chart by plotting widely used correlations that were applied over narrow ranges of Reynolds numbers, then fairing curves between the different ranges.

In terms of dimensionless groups, the Moody chart is in the form of Eq. (2) and Expression (3). In terms of physical parameters, the Moody chart is in the form of Eq. (10) and Expression (11).

Moody explained why the coordinates in the Moody chart are f and Re, since other coordinates were also used to describe fluid flow behavior in 1944:

> *R. J. S. Pigott [8] published a chart for the (Darcy friction factor), using the same coordinates (used in the Moody chart). His chart has proved to be most useful and practical and has been reproduced in a number of texts.*

THE "DARCY EQUATION", f, AND THE MOODY CHART ARE SUPERFLUOUS IN THE LAMINAR REGIME

The "Darcy equation", f, and the Moody chart are superfluous in the laminar regime because fluid flow behavior is described by Eq. (12), obtained by rearranging Eq. (10).

$$\Delta P_{laminar} = 128\mu WL/\pi g D^4\rho \ldots \quad (12)$$

Note that the "Darcy equation" appears to indicate that ΔP is generally proportional to V^2, even though ΔP is proportional to V in the laminar regime. The seeming contradiction results because f in the "Darcy equation" is written as though it were a constant coefficient, when in fact f is a variable that depends on Re and ε/D, and should be written in the form f{Re, ε/D}.

In summary, the "Darcy equation", f, and the Moody chart serve no useful purpose when dealing with laminar flow.

WHY f IS MATHEMATICALLY UNDESIRABLE

f is the group $\pi^2 g\rho\Delta PD^5/8LW^2$. The f group is mathematically undesirable because it includes ΔP, W, and D. This makes it necessary to solve turbulent fluid flow problems with ΔP, W, and D together in f, whereas the problems would be easier to solve if ΔP, W, and D were in separate terms.

Using f methodology, turbulent fluid flow is described by Expression (11). With regard to ΔP, W, and D, Expression (11) is in the form of Expression (13), whereas the mathematically desirable form is Expression (14).

$$\Delta PD^5/W^2 = \text{function of W/D and D} \ldots \quad (13)$$

$$\Delta P = \text{function of W and D} \ldots \quad (14)$$

In summary, f is mathematically undesirable because f makes it necessary to solve turbulent fluid flow problems with the variables together as in Expression (13), even though the problems would be easier to solve if the variables were separated as in Expression (14). (Just as it is generally much easier to solve equations if x and y are separated).

Using the Moody chart (Fig. **1**) to solve practical problems illustrates why f is mathematically undesirable—i.e. why $\pi^2 g\rho\Delta PD^5/8LW^2$ is mathematically undesirable.

THE MOODY CHART MUST BE READ ITERATIVELY TO DETERMINE W OR D

The Moody chart must be read iteratively (or by trial-and-error) to determine W or D because the chart is based on f, a dimensionless group that includes ΔP, W, and D.

Note that if the chart is used to determine W, the coordinates of f and Re cannot be calculated from the given information because f and Re are groups that include W. Therefore the chart must be read iteratively (or by trial-and-error).

Also note that, if the chart is used to determine D, the coordinates of f, Re, and ε/D cannot be calculated from the given information because f, Re, and ε/D are dimensionless groups that include D. Therefore the chart must be read iteratively (or by trial-and-error).

HOW THE MOODY CHART CAN BE TRANSFORMED TO A FORM THAT IS READ WITHOUT ITERATING

The Moody chart can be transformed to a form that is read without iterating to determine ΔP, W, or D. The transformation is based on noting the following:

$$f \equiv \pi^2 g\rho\Delta PD^5/8LW^2 \ldots \quad (15)$$

$$Re \equiv 4W/\pi\mu D \ldots \quad (16)$$

$$fRe^2(\varepsilon/D)^3 \equiv 2\Delta Pg\rho\varepsilon^3/L\mu^2 \ldots \quad (17)$$

$$Re(D/\varepsilon) \equiv 4W/\pi\mu\varepsilon \ldots \quad (18)$$

Identity (17) indicates that $fRe^2(\varepsilon/D)^3$ includes ΔP, but does not include W or D. Identity (18) indicates that Re(D/ε) includes W, but does not include ΔP or D.

Therefore ΔP, W, and D are in separate terms in charts based on $fRe^2(\varepsilon/D)^3$, Re(D/ε), and ε/D—ie charts based on $2\Delta Pg\rho\varepsilon^3/L\mu^2$, 4W/πμε, and ε/D. Since ΔP, W, and D are separated, the charts are in the form of Expression (14), and can be read without iterating to determine ΔP, W, or D.

THE MOODY CHART TRANSFORMED TO A FORM THAT IS READ WITHOUT ITERATING, FIG. (2)

Fig. (**2**) is the Moody chart transformed to Expression (19), a form that is read without iterating.

$$\log(W/\mu\varepsilon) = \text{function of } \log(\varepsilon/D) \text{ and } \log(\Delta Pg\rho\varepsilon^3/L\mu^2) \quad (19)$$

The transformation was accomplished in the following steps:

1. Obtain f, Re, and ε/D coordinates for eleven curves in the Moody chart by reading the chart for relative roughness from .00001 to .05 at Reynolds numbers from 10^4 to 10^8.
2. Use the f, Re, and ε/D coordinates obtained in Step 1 to calculate coordinates of $0.5fRe^2(\varepsilon/D)^3$ and (π/4)Re (D/ε).

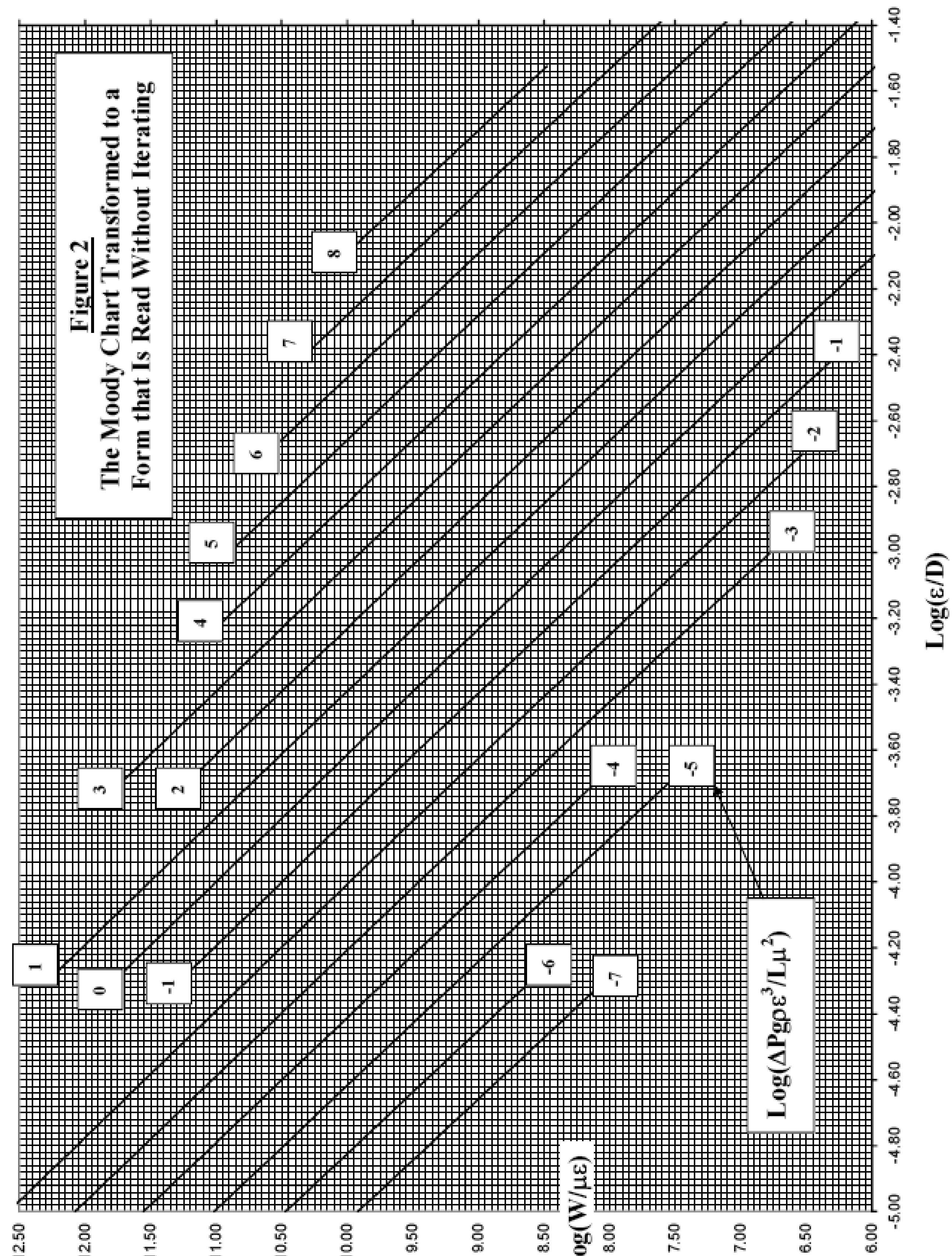

Fig. (2). The Moody Chart Transformed to a Form that Is Read Without Iterating.

3. Use the $0.5fRe^2(\varepsilon/D)^3$ and $(\pi/4)Re(D/\varepsilon)$ coordinates calculated in Step 2 to prepare Fig. (**2**), a chart of $\log((\pi/4)Re(D/\varepsilon))$ *vs.* $\log(\varepsilon/D)$, parameter $\log(0.5fRe^2(\varepsilon/D)^3)$. Note that Fig. (**2**) is presented in terms of physical parameters rather than dimensionless parameters. It is labeled $\log(W/\mu\varepsilon)$ *vs.* $\log(\varepsilon/D)$, parameter $\log(\Delta Pg\rho\varepsilon^3/L\mu^2)$.

Note the following in Fig. (**2**):

- The y coordinate is dependent on W, but is independent of ΔP and D.
- The x coordinate is dependent on D, but is independent of ΔP and W.
- The chart parameter is dependent on ΔP, but is independent of D and W.
- If W is to be determined from Fig. (**2**), the coordinates on the x axis and the chart parameter are calculated from the given information, and the chart is read without iterating.
- If D is to be determined from Fig. (**2**), the coordinates on the y axis and the chart parameter are calculated from the given information, and the chart is read without iterating.
- If ΔP is to be determined from Fig. (**2**), the coordinates on the y axis and the x axis are calculated from the given information, and the chart is read without iterating.

It is important to note that, over the range of Re and relative roughness common to both charts, the Moody chart and Fig. (**2**) are essentially identical. They differ only in form.

THE MOODY CHART *VS*. FIG. (2)

- The Moody chart and Fig. (**2**) are essentially *identical* except for form. They provide essentially the same answers to problems.
- The Moody chart is based on groups $\pi^2 g\rho\Delta PD^5/8LW^2$, $W/\pi\mu D$, and ε/D. Fig. (**2**) is based on groups $\Delta Pg\rho\varepsilon^3/L\mu^2$, $W/\mu\varepsilon$, and ε/D.
- The Moody chart must be read iteratively (or by trial-and-error) when it is used to determine W or D in the turbulent regime. Fig. (**2**) is read without iterating when it is used to determine ΔP, W, or D.
- The Moody chart describes both the laminar and turbulent regimes. Fig. (**2**) describes only the turbulent regime because the laminar regime is described by Eq. (12).
- The imprecision in reading Fig. (**2**) is one-fourth of a division. The resulting imprecision is ±1.2% of D, ±3% of W, and ±6% of ΔP. The imprecision in reading a Moody chart of the same size is considerably smaller.

EXAMPLE PROBLEM USING THE MOODY CHART, FIG. (1)

A pipe line is to be laid to transport fluid from Plant A to Plant B. Using the given information and the Moody chart (Fig. **1**), determine the pipe diameter that will result in a flow rate of 2.50 kg/s with a pressure drop of 20000 kg/m^2.

Given

Pipe roughness ε = .000050 m

Equivalent length of pipe line = 60 m

μ = .000750 Kg/m s

ρ = 950 kg/m^3

Analysis

(The analysis is to be performed by the reader.)

Answer

A pipe diameter of **.0331 m** will result in a flow rate of 2.5 kg/s with a pressure drop of 20000 kg/m^2.

EXAMPLE PROBLEM USING FIG. (2)

Repeat the above problem using Fig. (**2**) instead of Fig. (**1**).

Analysis

Use the given information to calculate values for the y coordinate and the chart parameter in Fig. (**2**).

$\log(W/\mu\varepsilon) = \log(2.5/(.00075x.00005) = 7.82$ (20)

$\log(\Delta Pg\rho\varepsilon^3/L\mu^2) =$

$\log(20000x9.82x950x.00005^3/(60x.00075^2)) = -.16$ (21)

Use the above values and Fig. (**2**) to determine the value of the x coordinate. Then solve for the value of D.

$\log(\varepsilon/D) = -2.82$ (from Fig. (**2**)) . . . (22)

$\therefore (\varepsilon/D) = .00151$ . . . (23)

$D = \varepsilon/(\varepsilon/D) = .00005/.00151 = .0331$ m. . . . (24)

Answer

A pipe diameter of .0331 m will result in a flow rate of 2.50 kg/s with a pressure drop of 20000 kg/m^2.

(The Moody chart solution obtained by iterating is:

D = .0328 m, f = .0232, Re = $1.29x10^5$, ε/D = .00152.)

HOW FLUID FLOW BEHAVIOR IS DESCRIBED WHEN F IS ABANDONED

When f is abandoned, fluid flow behavior is described by

$\Delta P_{laminar} = 128\mu WL/\pi gD^4\rho$ . . . (12)

$$(\Delta P g \rho \varepsilon^3 / L\mu^2)_{turbulent} = \text{function of } W/\mu\varepsilon \text{ and } \varepsilon/D \qquad (25)$$

The function in Expression (25) is obtained by transforming the Moody chart in the manner described above.

Note that Eq. (12) is used currently, but is usually written in the friction factor form of Eq. (2). Also note that Expression (25) can be rearranged, as in Expression (19).

Expression (25) replaces Expression (11) used in f methodology. The particular advantage of Expression (25) is that ΔP, W, and D are in separate terms, whereas ΔP, W, and D are together in the f group in Expression (11). Separating ΔP, W, and D makes it possible to solve fluid flow problems in the simplest possible manner, as illustrated above.

CONCLUSIONS

- f is mathematically undesirable because it includes ΔP, W, and D. This makes it necessary to solve problems with ΔP, W, and D in the same term, whereas problems are easier to solve if ΔP, W, and D appear only in different terms.
- The "Darcy equation", f, and the current form of the Moody chart should be abandoned because f is superfluous in the laminar regime, and because f complicates the solution of turbulent fluid flow problems.
- In the laminar regime, fluid flow behavior should be described by Eq. (12). This equation is used currently, but is often written in the friction factor form of Eq. (2).
- In the turbulent regime, fluid flow behavior should be described by a chart based on $\Delta P g \rho \varepsilon^3/L\mu^2$, $W/\mu\varepsilon$ and ε/D, such as Fig. (**2**). The chart is obtained by transforming the Moody chart as described above.

NOMENCLATURE

a = An arbitrary constant
b = An arbitrary constant
D = Pipe diameter
f = Fluid friction factor, $\pi^2 g \rho \Delta P D^5/8LW^2$
g = Gravity constant
L = Length
n = An arbitrary constant
P = Pressure
Re = Reynolds number, $4W/\pi\mu D$
V = Velocity
W = Mass flow rate
ε = Surface roughness
μ = Viscosity
ρ = Density

REFERENCES

[1] L. F. Moody, "Friction factors for pipe flow", *Transactions of the ASME*, vol. 66, pp. 671-684, Nov 1944.
[2] G. Brown, "The history of the Darcy-Weisbach equation", 2002, Available from: http://biosystems.okstate.edu/darcy/DarcyWeisbach/Darcy-WeisbachHistory.html
[3] J. Weisbach, *Lehrbuch der Ingenieur und Maschinen-Mechanik,*, Braunschweig, Germany: Vieweg und Sohn, 1845.
[4] H. Darcy, "Experimental research relating to the movement of water in pipes", in *Recherches Experimentales Relatives au Mouvement de L'Eau deans les Tuyaux*, Paris: Mallet-Bachelier, 1857.
[5] J. T. Fanning, *A Practicle Treasite on Water Supply Engineering*, New York: Van Nostrand, 1877.
[6] E. F. Adiutori, in *The New Engineering*, USA: Ventuno Press 2002, pp. 192-194.
[7] H. Rouse and S. Ince, *History of Hydraulics*, Iowa city, IA: Iowa Institute of Hydraulic Research, 1957.
[8] R. J. S. Pigott, "The flow of fluids in closed conduits", *Mechanical Engineering*, vol. 55, pp. 497-501, 515, 1933.

Optimization Algorithm for Two-Finger Grippers Kinematic Mechanisms

Nirmal Charan Mallik, *Department of Mechanical Engineering, Aryan Institute of Engineering & Technology, Bhubaneswar, nirmal_m26@gmail.com*
Niranjan Behera, *Department of Mechanical Engineering, Raajdhani Engineering College, Bhubaneswar, niranjanbehera2514@gmail.com*
Abinash Sahoo, *Department of Mechanical Engineering, Capital Engineering College, Bhubaneswar, abinashsahoo719@yahoo.co.in*
Binoda Bihari Sahoo, *Department of Civil Engineering, NM Institute of Engineering & Technology, Bhubaneswar, bionod_bihari231@yahoo.co.in*

Abstract: In this paper, an analysis of mechanisms in two-finger grippers has been discussed to formulate an optimum design procedure. The design problem has been approached and formulated as a new optimization problem by using fundamental characteristics of grasping mechanisms. In particular, in order to optimize a mechanism for two-finger gripper, an original multi-objective optimum algorithm has been used by considering four different objective functions, such as grasping index, encumbrance of grasping mechanism, acceleration and velocity for finger gripper with respect to the imposed working area. A case study has been reported by using an 8R2P linkage for a proposed two-finger gripper mechanism. Numerical example has been computed to show the soundness of the proposed new optimum design procedure by referring to computational and practical results.

Keywords: Grippers, grasp mechanics, mechanisms, analysis, design, experimental validation.

INTRODUCTION

A gripper is an important component of industrial robots because it interacts with the environment and objects, which are grasped for manipulative tasks. Usually, a gripper of industrial robots is a specialized devise, which is used to grasp one or few objects of similar shape, size, and weight in repetitive operations [1-3].

The manipulative operations are usually performed by using two-finger grippers, which are powered and controlled for the grasping action by one actuator only, [4, 5]. In addition, two-finger grippers are used both for manipulation and assembling purposes since most of these tasks can be performed with a two-finger grasp configuration [6, 7].

Since a gripper gives a great contribution to practical success of using an automated and/or robotized solution, a proper design may be of fundamental importance. The design of a gripper must take into account several aspects of the system design together with the peculiarities of a given application or a multi-task purpose. Strong constraints for the gripping system can be considered for lightness, small dimensions, rigidity, multi-task capability, simplicity and lack of maintenance. These design characteristics can be achieved by considering specific end-effectors or grippers. In the last case a two-finger gripper corresponds to the minimum number of fingers and the minimum complexity of a hand.

An early work on gripper designs can be considered the publication by Lundstrom, [1], who described several gripper designs with rigid fingers and flexible fingers, and even vacuum grippers, and magnetic grippers.

Chen, [2], described several mechanisms for different gripper functions. He also classified mechanical grippers according to pair elements used in their construction as linkage, gear and rack, cam, screw, rope and pulley types and miscellaneous. The selection of a particular mechanism is mainly affected by type of actuators to be employed and type of grasping modalities to be used.

Chelpanov and Kolpashnikov, [8], reported a definition and formalization of the basic problems of gripper mecha-nisms. In particular, a grasping mechanism can be classified into five classes, namely clamping elements; elements for linking the clamping with the executive elements; executive elements; transmission mechanisms between the drive and executive mechanism.

Belfiore and Pennestrì, [9], presented an atlas of 64 linkage-type grippers. For each mechanism one possible functional scheme has been provided for a better unders-tanding of its kinematic properties. The proposed atlas can be useful to designers in the field of robotics.

Several procedures to design grippers have been reported in literature, as for given in refs. [3, 10-23].

In particular, refs. [3, 10] a description of several gripper mechanisms has been reported with design conside-rations.

Dwivedi, Sharma and Sharifi, [11], proposed the design of an intelligent gripper. The intelligent gripper has been composed as a combination of the general-purpose gripper mechanism and force/torque sensor mechanism. In parti-cular, a translational-type gripper mechanism has been chosen as the basis of the general purpose-gripper.

Shimoga, [12], reported algorithms to achieve dexterity primarily to solving an unconstrained linear programming problem where an objective function can be chosen to represent one or more of the currently known dexterity measures for grippers.

Salunkhe, Mao, and Tasch, [13], developed a mathematical formulation for robust and high quality grasp. In particular, the grasping quality has been obtained by minimizing the entropy of the finger normal force whereas the robustness is ensured by minimizing the perturbations in finger contact locations.

Dubey, Crowder and Chappell, [14], formulated an optimal control of fingertip force during grasping operation. In particular, a controller that is based on fuzzy logic has been considered in order of performing optimal stable grasp of objects without knowing their mass and frictional properties and with a minimum applied force.

Hester, Cetin, Kapoor and Tesar, [15], used multiple performance criteria both at the finger and hand levels to generate a preliminary grasp and then an optimum grasp.

Osyczka and Krenich, [16], described a new genetic algorithm for solving nonlinear multi-criterion optimization problem. In the proposed method the tournament selection has been considered as the core of the procedure.

Penisi, Carbone and Ceccarelli, [17], developed an optimum design procedure and validation testing for mechanisms of two-finger grippers. In particular, an optimization problem has been formulated by taking into account both the kinematics and statics of the gripper action.

Ceccarelli, Cuadrado and Dopico, [18], presented a simple and efficient procedure for optimum dimensional synthesis of grasping mechanisms. The proposed design has been based on a suitable formulation of grasping performance of grasping mechanisms by using natural coordinates.

Krenich, [19], formulated a design optimization problem of robot grippers by taking into account six objective functions and several constraints.

Ceccarelli, [20, 21], proposed an optimum design for grasping mechanism of two-finger gripper in the form of a suitable optimization problem by defining a grasping index, which takes into account some fundamental characteristics of the grasp action.

Zheng and Qian, [22], formulated an optimal grasp planning and dynamic force distribution in multi-fingered grasping.

Lanni, [23], studied the design problem for two-finger gripper by considering the numerical and experimental characterization as regarding with the impact during a grasp. In particular, in order to optimize a mechanism for two-finger gripper, a multi-objective optimum algorithm has been used by considering four different objective functions, such as grasping index, encumbrance of gripper mechanism, acceleration and velocity for finger gripper with respect to the imposed working area.

In this paper, performance criteria are investigated and a design problem has been approached and formulated as an optimization problem by using the basic characteristics of grasping mechanisms. A suitable algorithm has been developed for a general optimum design of grasping mechanisms.

A study has been reported as a numerical example in the paper to show the soundness of the proposed optimum design procedure by referring to computational and practical results.

MECHANISMS FOR GRIPPERS

Among all the problems encountered in designing robots, the most crucial one concerns with the end-effector. Basic features for a gripper depend strongly of the grasping mechanism. Thus, factors can be considered before choosing a grasping mechanism as following:

- Characteristics of the gripper, which include maximum payload, dimensions, orientations, number of the composed links;
- Characteristics of the objects, which include weight, body rigidity, nature of material, geometry, dimensions, condition, position and orientation, contact surfaces, forces acting on the object and environmental conditions;
- Gripper technology, for the construction of components (mechanism links and finger parts) with proper manufacturing and materials;
- Flexibility of the gripper, whether it allows rapid replacement, or easy adjust and external modification, or adaptation to a family of objects that are contained within a range of specifications;
- Cost for design, production and application to robot operation and maintenance.

In fact, those characteristics are fundamental from a practical viewpoint for the grasping purpose, since they may describe the range of exerting force on the object by the fingers, the size range of the objects which may be grasped and a particular manipulation type. Thus, a dimensional design of gripper mechanisms may have great influence on the maximum dimensions of the grasped object by a gripper, and on the grasping force, since the mechanism size may affect the grasp configuration and transmission characteristics. These peculiarities can be considered well known when it is taken into account the great variety of mechanisms which have been used.

The basic components of a two-finger gripper are given in ref. [21], (Fig. **1**): fingers are the elements that execute the grasp on objects; finger tips are directly in contact with a grasped object; grasping mechanism is the transmission component between the actuator and the fingers; actuator is the power source for the grasping action of a gripper.

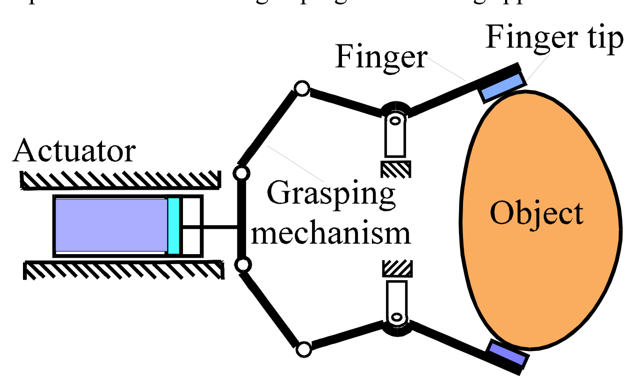

Fig. (1). A scheme for mechanical design for two-finger grippers.

In order to execute a specific grasping task a design problem consists in selecting a proper gripper mechanisms and sizing its kinematic design.

Many different types of kinematic chains can be used as for example those that are reported and shown in refs. [1-3, 9, 11]. Special attention requires the motion of the fingers. This motion can be linear, rotative or a combination of both. Needs of limited encumbrance, stiff design, light mechanical design and easy operation may limit the number of the mechanism links. In fact, most of industrial gripper mechanisms show kinematic chains that are composed by four-bar, slider-crank linkages as shown in Fig. (**2**), [2].

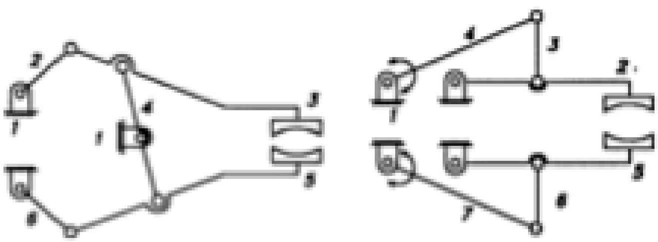

a)

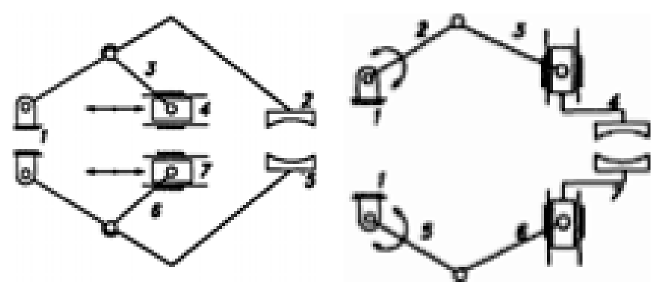

b)

Fig. (2). Examples of grasping mechanism in [2] as based on: **a**) four-bar linkage; **b**) slider-crank linkage.

In particular, Fig. (**2**) shows examples of grasping mechanism in industrial grippers, which are actuated by linear or rotative actuator using revolute and prismatic joints with one or two actuators. The fingers can move with a swinging or a parallel motion. In Fig. (**2a**) the grasping mechanisms are based on a mechanisms composed by four-bar linkages which are based on revolute joints. The two fingers move with an approximately parallel motion. In Fig. (**2b**) the grasping mechanisms are based on a mechanisms composed by slider-crank linkages which are based on prismatic and revolute joints. The two fingers move with an approximately linear motion.

Most of industrial grippers are actuated by a linear actuator. However, two actuators can be useful when the fingers can operate independently with a symmetric or unsymmetrical behaviour.

Many others types of gripper mechanisms are used in order to achieve suitable mechanical design with grasping efficiency, small size, robust design, light and low-cost devices.

There are many different types of industrial grippers composed by two-fingers that are implemented in commercial grippers, like those given in refs. [1, 24-27].

Examples of two-finger grippers that are actuated pneumatically are shown from Figs. (**3**) to (**7**). In particular, Fig. (**3a**) shows a view of a commercial industrial 2-jaws parallel-acting self-centering pneumatic gripper that is produced by Gimatic Handling [24]. Fig. (**3b**) shows the complex mechanical design, corresponding to the gripper in Fig. (**3a**), in which the identification of the kinematic chain can be very difficult if the gripper is not observed during the operation with and without an object. The mechanical design of the gripper in Fig. (**3b**) shows how to obtain a parallel motion of the fingers by the chain reported in Fig. (**3c**).

Fig. (**4a**) shows a view of commercial industrial 2-jaws self centering radial pneumatic gripper that is produced by Gimatic Handling [24]. Fig. (**4b**) shows the related mechanical design of a gripper in Fig. (**4a**). The kinematic scheme of Fig. (**4c**) emphasize the use of cam system. The cam connection can be very useful to have small-sized designs with an easy understanding of the gripper operation.

Fig. (**5a**) shows a view of a commercial industrial gripper that is produced by GMG System [25]. Fig. (**5b**) shows the related mechanical design of a gripper in Fig. (**5a**). The kinematic scheme of Fig. (**5c**) shows how is possible to obtain different combination of the motion during opening and closing phases. In fact, depending to the dimensions of the links of the fingers is possible to obtain parallel open /

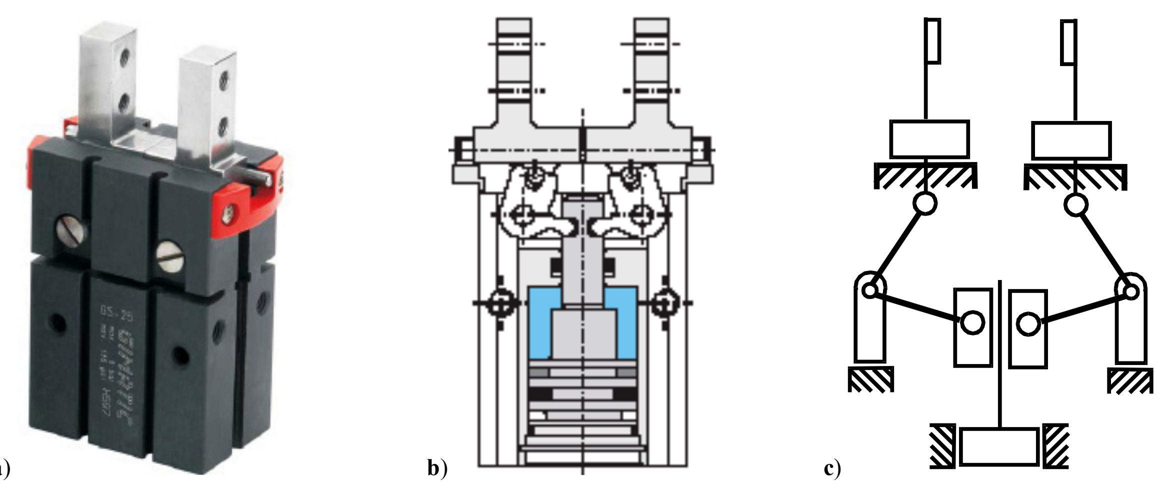

a) **b**) **c**)

Fig. (3). An industrial 2-jaws parallel-acting self centering pneumatic gripper, [24]: **a**) a view of GIMATIC GS-25 type; **b**) a mechanical design; **c**) a kinematic scheme.

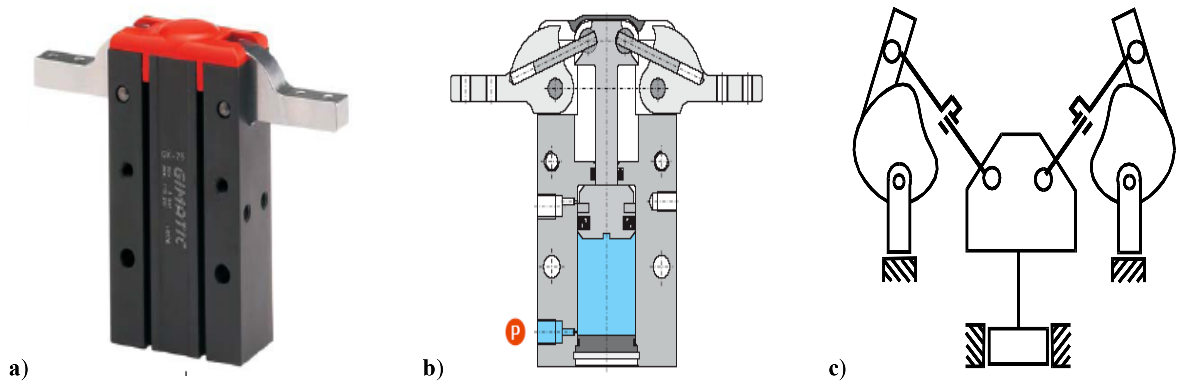

Fig. (4). Industrial 2-jaws self centering radial pneumatic gripper [24]: **a**) a view of GIMATIC GX-25 type; **b**) a mechanical design; **c**) a kinematic scheme.

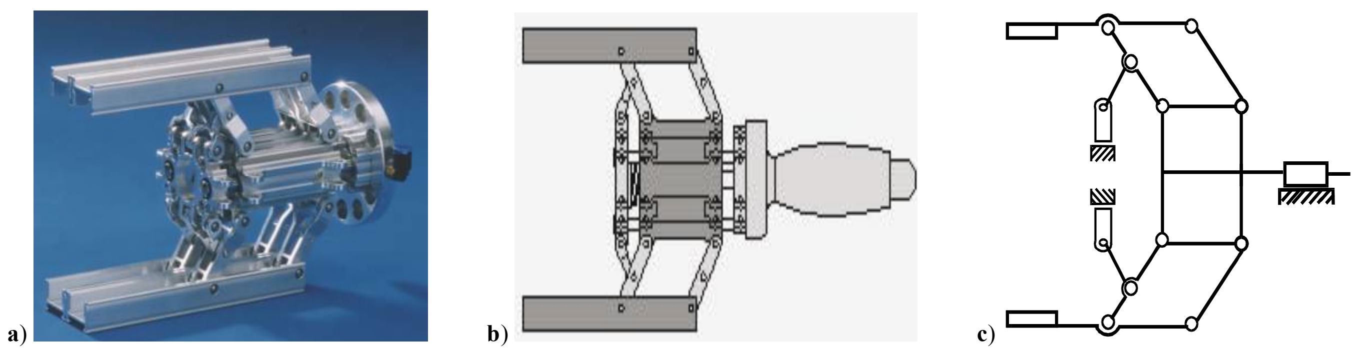

Fig. (5). An industrial gripper, [25]: **a**) a view of GMG 102 type; **b**) a mechanical design; **c**) a kinematic scheme.

parallel close, parallel open/swivelling close, and swivelling open/swivelling close action.

Fig. (**6a**) shows a view of an industrial toggle gripper that is produced by AGI Components [26]. Fig. (**6b**) shows the related mechanical design of a gripper in Fig. (**6a**). The kinematic scheme of Fig. (**6c**) shows how is possible to obtain the synchronized parallel motion of the fingers as generated by a pinion mechanism that is powered by a double-acting piston. The jaws are supported by a T-SLOT way.

Fig. (**7a**) shows a view of a commercial industrial toggle gripper that is produced by SMC Components [27]. Fig, (**7b**) shows the related mechanical design of a gripper in Fig. (**7a**). The kinematic scheme of Fig. (**7c**) shows that the moving prismatic joints and rolling contact ensure an approximately circle trajectory for each finger.

DESIGN PROBLEMS

A fundamental problem both for designing and operating a gripper mechanism can be recognized in the modeling of

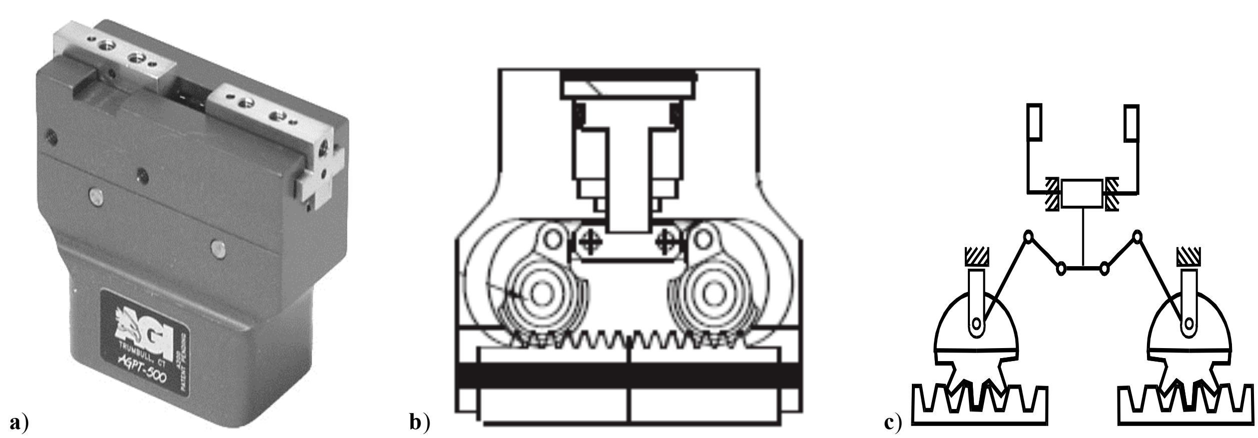

Fig. (6). An industrial toggle gripper, [26]: **a**) a view of AGI PT500 type; **b**) a mechanical design; **c**) a kinematic scheme.

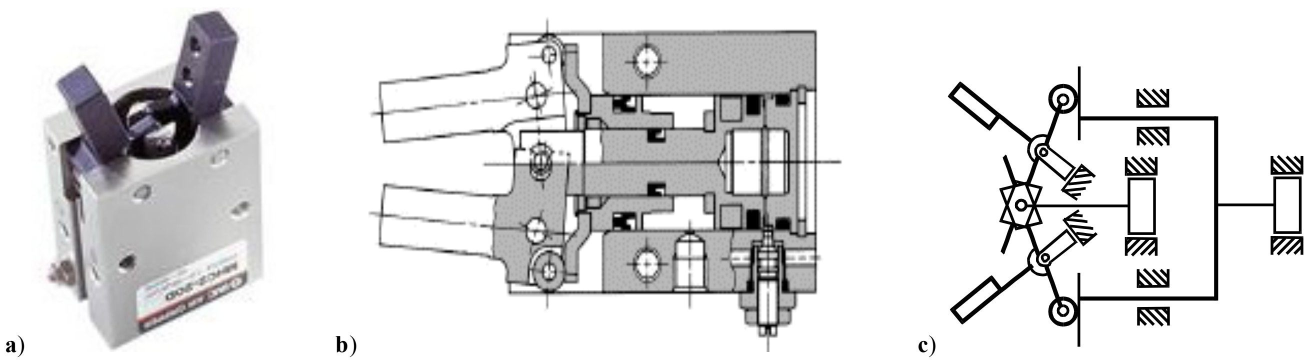

Fig. (7). An industrial toggle gripper, [27]: **a**) a view of SMC MHC2 type; **b**) a mechanical design; **c**) a kinematic scheme.

the basic characteristics of a gripper in order to identify the mechanism chain and its kinematic characteristics but by considering yet the integration with the other components in a Mechatronics design.

The design problem for grippers consists of sizing all the components of a gripper in order to ensure suitable grasping performances for a proper grasping manipulation.

A design procedure can be proposed in the following steps:

1. To determine the basic characteristics of the grasped object, in terms of dimensions, weight, shape, material, density, delicateness;
2. To individuate the environments in which the object should be grasped;
3. To evaluate the required grasping force as a function of maximum dimension of the grasped object;
4. To design finger tips and their sensors;
5. To design a control system;
6. To choose a chain type and to size the gripper mechanism and its operation;
7. To size the actuator by considering the efficiency of the grasping mechanism;
8. To design all the components that are needed to control the gripper operation.

In particular, it is to note that for step 3, the model and formulation for the equilibrium of the grasp can be elaborated in order to evaluate the maximum grasping force. An in-depth analysis can be focused on the interactions among object and fingers. The static equilibrium of a grasped object between the fingers can be expressed by considering all the forces that can be determined along the directions of the contact, squeezing and slipping lines [21].

At step 5, a control system can be designed as depending of the level of grasping force regulation, which is required for the grasping task.

At step 6, a specific kinematic chain can be chosen by a designer by considering atlas, books, catalogs of existing industrial grippers, expert systems for searching, and even designers expertise. The dimensional design of gripper mechanisms can be approached by using traditional techniques for dimensional synthesis of mechanisms. Alternatively, an optimum design of a gripper mechanism can be formulated. In this case, by using commercial computational tools a suitable design procedure can give optimum characteristics for an optimum use of a grasping mechanism as a function of specific grasping purposes.

At step 8, all the components of the control system can be designed for the given gripper tasks. The power circuit and actuator can be pneumatic, hydraulic and electric. Thus, the components of the control system can be sized as function of actuator performances, gripper mechanism and control grasping force.

In general, a design of two-finger grippers can be expressed explicitly through suitable formulations to give an analytical system of design equations which express the relations between all the components.

The design parameters can be summarized as, (Fig. **8**):

- Link sizes l_i, i=1, 2, …, N in which N indicates the number links;
- Configuration angles α_J, J=1, 2, …, N_g in which N_g is the number of joint of gripper mechanism;
- Actuation force Q;
- Characteristics of the control systems in term of K_P, K_D, K_I, proportional, derivative and integrative gains, respectively.

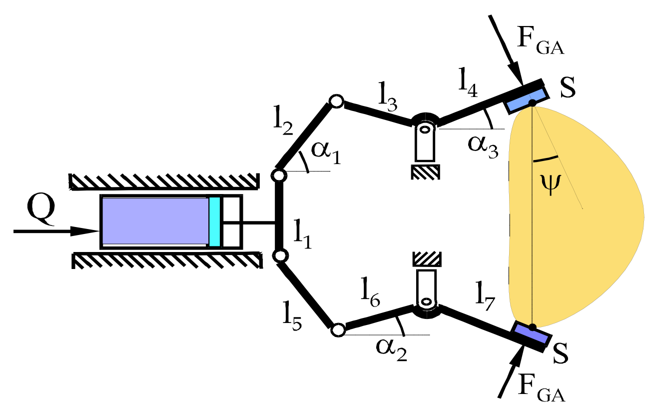

Fig. (8). Design parameters for a two-finger gripper.

A FORMULATION FOR OPTIMUM DESIGN

The problem of optimum design of mechanisms has quite a long history. In fact, most of these problems have been modelled as non-linear programming problems [28].

Similarly, the design problem of grippers can be formulated as a multi-criteria optimization problem in which several criteria can be considered.

An optimum design formulation for gripper mechanisms consists of minimizing an objective function F that is subject to satisfy constraints, material properties, object characteristics, and peculiarities of the grasping task.

A critical point of such a design formulation is to choose a suitable objective function F, which must include peculiarity aspects of the gripper mechanism and its design parameters in order to obtain solutions with proper optimal performance characteristics.

A design formulation can be expressed in the form of optimization problem in the form of:

$$\min \mathbf{F}(\mathbf{x}) \tag{1}$$

subject to,

$$\mathbf{G}_i\,(\mathbf{x}) < \mathbf{0} \quad i = 1, \ldots, k \tag{2}$$

$$\mathbf{H}_i\,(\mathbf{x}) = \mathbf{0} \quad i = 1, \ldots, m \tag{3}$$

where $\mathbf{x} = [x_1, x_2, \ldots, x_n]$ is the vector of the n design variables; $\mathbf{F}(\mathbf{x})$ is the vector of objective functions f_i ($i = 1,\ldots, N$) that express the optimality criteria, $\mathbf{G_i}$ ($\mathbf{x}$) is the vector of k inequality constraint functions that describes limiting conditions, and $\mathbf{H_i}$ ($\mathbf{x}$) is the vector of m equality constraint functions that describes the design prescriptions.

The multi-objective function **F** can be formulated with computer-oriented algorithms when its components f_i are computed numerically through suitable analysis procedures.

Similarly, the constraint functions **G** and **H** can be formulated by using suitable evaluation of design and operation constraints as well as those additional constraints that are needed for computational issues. Thus, the problem for achieving optimal results from the formulated multi-objective optimization problem consists mainly in two aspects, namely to choose a proper numerical solving technique and formulate the optimality criteria with computational efficiency.

The constraints can be expressed for so many and different characteristics but they should be analytically formulated by considering geometrical characteristics of the grasping mechanisms, forces acting on the joints, maximum and minimum dimensions of the grasped object, minimum and maximum grasping force acting for a specific grasped object, minimum dimensions of the gripper [19].

Indeed, the solving technique can be selected among the many available ones, even in commercial software packages, by looking at a proper fit and/or possible adjustments to the formulated problem in terms of number of unknowns, non-linearity type, and involved computations for the optimality criteria and constraints. On the other hand, the formulation and computations for the optimality criteria and design constraints can be conceived and performed by looking also at the peculiarity of the numerical solving technique.

Those two aspects can be very helpful in achieving an optimal design procedure that can give solutions with no great computational efforts and with possibility of engineering interpretation and guide. Since the formulated design problem is intrinsically high no-linear, the solution will be obtained when the numerical evolution of the tentative solutions due to the iterative process converges to a solution that can be considered optimal within the explored range. Therefore a solution can be considered an optimal design but as a local optimum in general terms. This last remark makes clear once more the influence of suitable formulation with computational efficiency for the involved criteria and constraints in order to have a design procedure, which is significant from engineering viewpoint and numerically efficient.

OPTIMALITY CRITERIA

In general, an optimum design procedure can be considered by means the following steps:

1) Identification of design constraints and performance characteristics for a given application;
2) Formulation of basic performances;
3) Analysis of optimality criteria through numerical algorithms;
4) Formulation of a single and/or multi-objective optimization problem for design purposes;
5) Numerical solution of the multi-objective optimization and interpretation of results;
6) Determination of a design solution through a suitable model;
7) Mechanical design of all the components and details.

In this paper, we have addressed attention mainly to the design step 3 that are related with optimality criteria and an optimum design procedure has been proposed using a multi-objective optimization problem in terms of grasping index PI, encumbrance of grasping mechanism, acceleration and velocity of the gripper mechanism.

An optimum synthesis is useful to find the mechanism that has the better efficiency which is variable with the configuration adopted by the mechanism. Thus, the optimum solution should have a small variation of the efficiency in the whole range of objects that can be grasped. In order to satisfy the proposed requirements and to consider an expression for the mechanical efficiency, the grasping index PI can be defined as proposed in [21].

$$\mathrm{PI} = \frac{F_{GA} \cos \psi}{Q} \tag{4}$$

where Q indicates the actuating force, F_{GA} is the grasping force applied to the contact point S and ψ is the angle grasp configuration, Fig. (**8**). The grasping index PI can be evaluated for several gripper mechanisms by using a principle of virtual work. Thus, in order to optimize a gripper mechanism, one can define the following optimality criterion f_1, [23].

$$f_1 = \mathrm{PI} \tag{5}$$

The number of the links affects the dimension and weight of the device. Minimizing the dimension of the gripper can be useful to reduce its weight and costs and to provide better

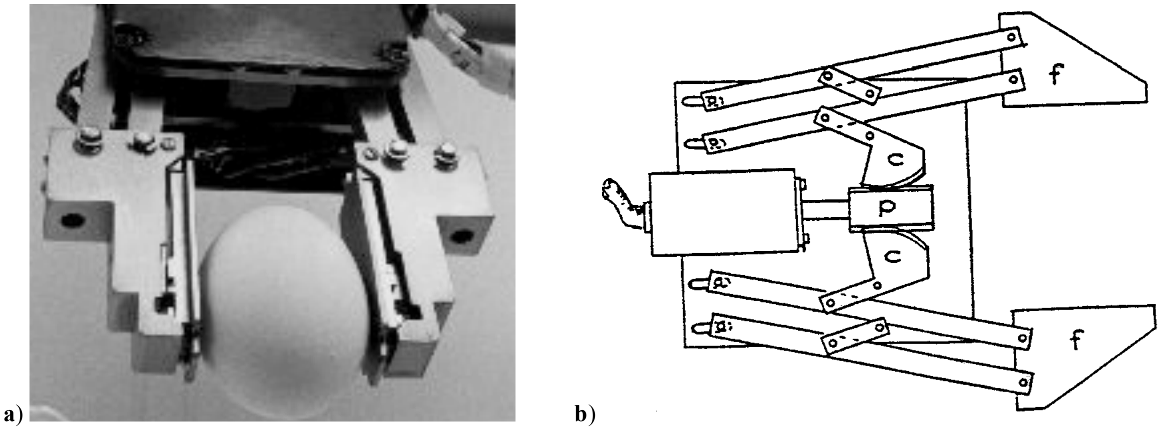

Fig. (9). A commercial industrial gripper, [30]: **a**) a view of IBM-7565 type; **b**) a mechanical design [31].

clearances in a specific workstation, [29]. Thus, in order to optimize the gripper mechanism, one can define the following optimality criterion f_2, [23]

$$f_2 = \sqrt{\sum_{i=1}^{N} l_i^2} \tag{6}$$

The acceleration of the gripper should not be too large because it causes inertia phenomenon which may increase the disturbance acting on the grasped object during a grasp. Thus, in order to optimize the gripper mechanism, one can define the following optimality criterion f_3, [23]

$$f_3 = \frac{acc_{max} - acc_{min}}{acc_{med}} \tag{7}$$

where acc_{max}, acc_{min} and acc_{med} indicate the maximum, minimum and average acceleration during the grasping action, respectively.

The velocity of the gripper should be constant in order to avoid sudden variation of vibrations and external disturbances during the grasped object. Thus, in order to optimize the gripper mechanism, one can define the following optimality criterion f_4, [23].

$$f_4 = \frac{vel_{max} - vel_{min}}{vel_{med}} \tag{8}$$

where vel_{max}, vel_{min} e vel_{med} indicate the maximum, minimum and average velocity during the grasping action, respectively.

The purpose of the above proposed formulation is to simplify the required computations and reduce the overall computational cost for gripper optimization by giving also the possibility to a designer to understand and guide the computational evolution in a numerical technique for optimization problem solution.

A NUMERICAL EXAMPLE

The example refers to an IBM gripper, in Fig. (**9**), whose gripper mechanism can be modelled as a 8R2P linkage in Fig. (**10**). A parallel motion of a finger f is obtained by actuating the 8R2P linkage through a double acting pneumatic piston that is connected to the crank c by a rack-pinion gear sector. In particular, in Fig. (**10**) a link is added to l_0 to model the rack-pinion gear sector from which the piston actuates the crank l_0.

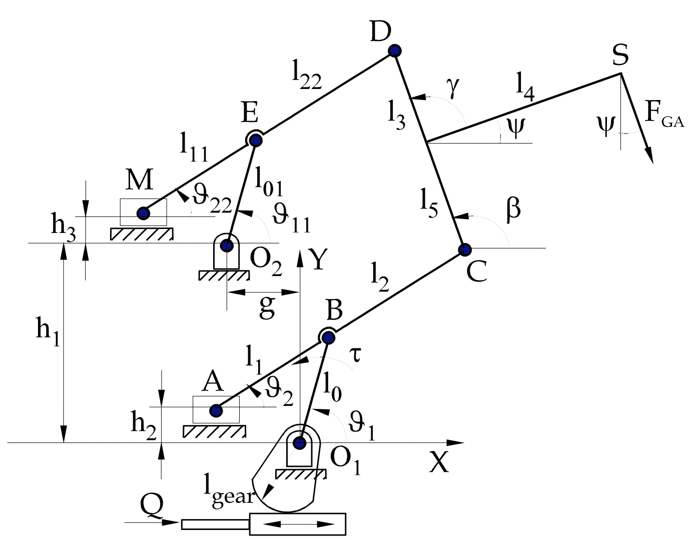

Fig. (10). A kinematic scheme of two-finger gripper mechanism in Fig. (**9**).

The analysis of kinematic characteristics of the gripper mechanism can be obtained as referring to a frame O_1XY in Fig. (**10**), where l_0, l_1, l_{01}, l_{11}, l_2, l_{22}, l_3 and l_5 are the lengths of the links; l_4 is the finger link length; ϑ_1 is the input angle of the crank l_0; ϑ_2 is the angle of the crank l_1; h_1 is the vertical offset between revolute joints; h_2 and h_3 are the slider joint offsets; g is the horizontal offset between the frame revolute joints; γ is the finger angle between l_4 and l_3; β is the orientation angle between l_2 and l_5; l_{gear} is the radius of rack-pinion gear sector.

The position, velocity, and acceleration of point S can be computed by considering the closure equations for 8R2P linkage as follows. The position of point S can be evaluated through the expressions

$$x_S = x_C + l_4\cos(\psi) + l_5\cos(\beta)$$

$$y_S = y_C + l_4\sin(\psi) + l_5\sin(\beta) \tag{9}$$

The orientation angles β and ψ can be computed by

$$\beta = \tan^{-1}\left(\frac{y_D - y_c}{x_D - x_c}\right)$$

$$\psi = \begin{cases} pi - \beta - \gamma & \text{if} \quad x_C > x_D \quad \text{and} \quad y_D > y_C \\ \beta - \gamma & \text{if} \quad x_D \geq x_C \quad \text{and} \quad y_D > y_C \end{cases} \tag{10}$$

where

$$x_C = l_0\cos(\vartheta_1) + l_2\cos(\vartheta_2)$$

$$y_C = l_0\sin(\vartheta_1) + l_2\sin(\vartheta_2) \tag{11}$$

$$x_D = l_{01}\cos(\vartheta_{11}) + l_{22}\cos(\vartheta_{22}) + g$$

$$y_D = l_{01}\sin(\vartheta_{11}) + l_{22}\sin(\vartheta_{22}) + h_1 \tag{12}$$

The velocity of point S can be computed through the derivative expressions of Eq. (9) by using Eqs. (10)-(12) in the form,

$$\dot{x}_S = \dot{x}_C - l_4\dot{\psi}\sin(\psi) - l_5\dot{\beta}\cos(\beta)$$

$$\dot{y}_S = \dot{y}_C + l_4\dot{\psi}\cos(\psi) + l_5\dot{\beta}\cos(\beta) \tag{13}$$

whose terms are computed by expressions that are given in Appendix **1**.

The acceleration of point S can be computed through the derivative expressions of Eq. (13) to obtain,

$$\ddot{x}_S = \ddot{x}_C - l_4\ddot{\psi}\sin\psi - l_4\dot{\psi}^2\cos\psi - l_5\ddot{\beta}\sin\beta - l_5\dot{\beta}^2\cos\beta \tag{14}$$

$$\ddot{y}_S = \ddot{y}_C + l_4\ddot{\psi}\cos\psi - l_4\dot{\psi}^2\sin\psi + l_5\ddot{\beta}\cos\beta - l_5\dot{\beta}^2\sin\beta,$$

in which the involved derivatives can be expressed as the derivatives of the expressions in Appendix **1**.

The above-mentioned analysis is also useful to compute the values of the objective functions f_i during the optimization process.

By applying the principle of virtual power one can obtain, (Fig. **10**),

$$\tau\dot{\vartheta}_1 = F_{GA}v_S \tag{15}$$

in which τ indicates the actuation torque applied on the input link l_0, and v_s is the velocity of contact point S.

Finally, the Eq. (4) can be written as,

$$IP = \frac{l_{gear}\cos(\psi)\dot{\vartheta}_1}{\dot{y}_s\cos(\psi) + \dot{x}_s\sin(\psi)} \tag{16}$$

where $\dot{x}_s$ and $\dot{y}_s$ are the components of the velocity v_s in Eqs. (13). Thus Eq. (16) has been deduced from Eq. (4) by considering that $\tau = Ql_{gear}$ as a torque on an input link that is given by an actuating force Q acting on it at a distance l_{gear}, (Fig. **10**).

The size L of a gripper mechanism can be given as fuction of the design parameters in the form,

$$L = \sqrt{l_0^2 + l_1^2 + l_2^2 + l_3^2 + l_4^2} \tag{17}$$

Results of these computations are illustrated in Figs. (**11**) and (**12**). In particular, in Fig. (**11**) the coupler path of point S has been reported together with the gripper mechanism for two-finger gripper.

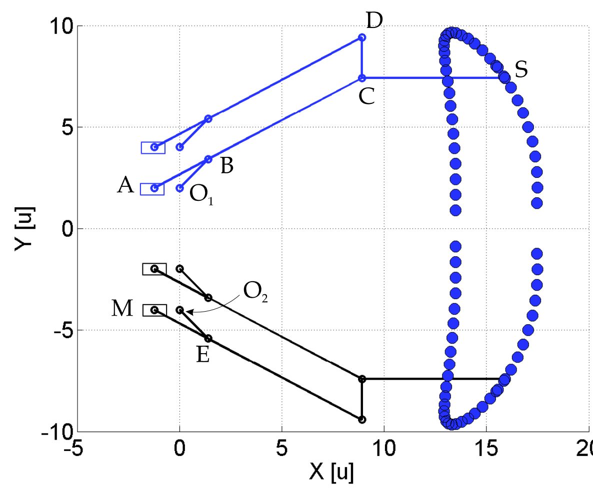

Fig. (11). A kinematic scheme of 8P2R mechanism with path, as described by point S.

Fig. (**12**) shows kinematic characteristics of 8R2P mechanism. In particular, Fig. (**12a**) show the trajectory described by contact point S during the grasping action; Fig. (**12b**) shows the trajectory described by contact point S with respect the input angle ϑ_1; Fig. (**12c**) shows the velocity of point S during the grasping action; Fig. (**12d**) shows the acceleration of point S; Fig. (**12e**) shows the variation of IP with respect the input angle ϑ_1, [23].

The displacement curves in Figs. (**12b**) and (**12e**) have been plotted with the aim to show the continuous character of the motion that starts from ϑ_1 = -10deg. up to ϑ_1 = 190deg., according to the scheme in Fig. (**10**).

The above-mentioned considerations can be used in a design formulation in the form of an optimization problem.

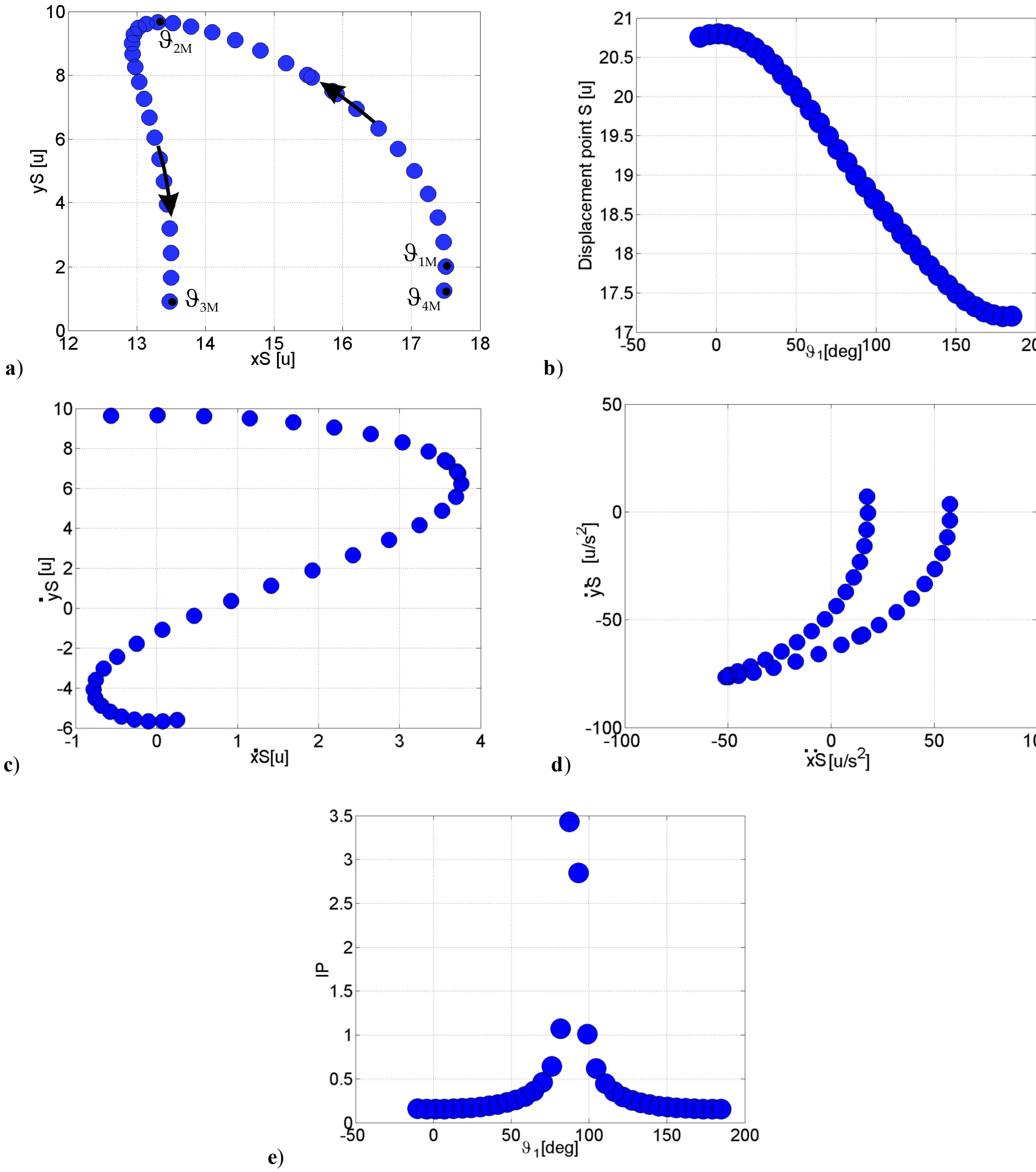

Fig. (12). Kinematic characteristics of 8R2P mechanism in Fig. (**10**): **a**) path described by point S; **b**) displacement point S; **c**) velocity of point S; **d**) acceleration of point S; **e**) IP versus ϑ_1.

Referring to the scheme in Fig. (**10**), the design parameters can be chosen as,

$$x_k = [l_0 = l_{01}, l_1 = l_{11}, l_2 = l_{22}, l_3, l_4, h_1, h_2 = h_3 = g = 0,$$
$$\gamma = \pi/2, l_5 = 0.1, l_{gear} = 1.4] \quad (18)$$

In order to consider the above-mentioned requirements and constrains and find an optimum solution in the whole range of objects that can be grasped, the optimisation design problem can be defined as,

$$\min \quad \mathbf{F}(\mathbf{x}) \quad (19)$$

subject to,

$$g_1 = \text{Min } X_S - \min X_{S0} \geq 0 \quad (20)$$

$$g_2 = \text{Min } Y_S - \min Y_{S0} \geq 0 \quad (21)$$

$$g_3 = \text{Max } X_S - \max X_{S0} \leq 0 \quad (22)$$

$$g_4 = \text{Max } Y_S - \max Y_{S0} \leq 0 \quad (23)$$

where $F_i = f_i$ is the i-th component of the vector **F** as a function of the design variables in vector **x**.

The objective functions f_i (i = 1, 2, 3, 4) have been expressed as a synthetic criterion of the grasping requirements for a grasping mechanism. IP can be computed for each possible configuration of grasping mechanism. The design constraints defined in Eqs. (20)-(23) are expressed in term of the area that can be reached by the contact point S. If the mechanism is symmetric only one finger mechanism can be analysed, and this area can be defined by the given co-ordinates $\min X_{S0}$, $\min Y_{S0}$, $\max X_{S0}$ and $\max Y_{S0}$ of the generic contact point S in a fixed frame as shown in Fig. (**13**).

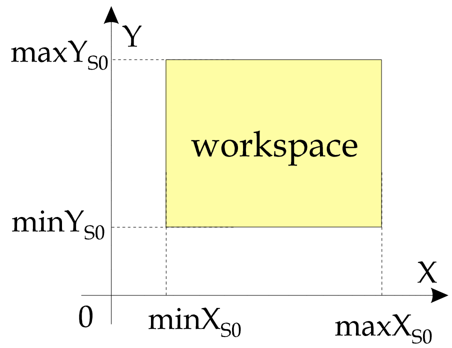

Fig. (13). Workspace area for a contact point S.

The numerical procedure, which has been adopted in this work, is summarized in the flowchart in Fig. (**14**) where the utilization of the proposed formulation has been emphasized as well as a Sequential Quadratic Programming procedure for the non linear design problem. Indeed, the Optimization Toolbox of Matlab [32] has been used to perform the numerical solution with a Sequential Quadratic Programming procedure. This numerical procedure works in such a way that at each step k a solution is found along a search direction δ_k with a variable update ψ_k. The iteration continues until the objective vectors converge.

The procedure has been developed so that the formulation has been easily included within the solving procedure for the optimization problem by using the facilities of the Optimization Toolbox of Matlab, [32], which permits an easy arrangement for an optimum design with analytical expressions.

Once the numerical computations are convergent to a feasible solution, the velocity and the accuracy of the solution can be enhanced by the designer by updating the convergence parameters ε_f and ε_g, which refer to the multi-objective functions f_i (i = 1, 2, 3, 4) in Eq. (19) and the constraints functions g_i (i = 1, 2, 3, 4) in Eqs. (20)-(23), respectively.

Eqs. (9) to (17) have been used in order to optimize the design procedure developed by using the routine "minimax" of Matlab Optimization Toolbox, [32], by considering the objective functions expressed by Eq. (19) and constraints expressed by Eqs. (20) to (23), [23].

The design parameters have chosen as $l_0 = l_{01}$= 1. 8 u, l_1 = l_{11}= 3. 0 u, $l_2 = l_{22}$ = 12. 0 u, l_3 = 1. 4 u, l_4 = 7. 0 u, l_5 = 0. 1 u,

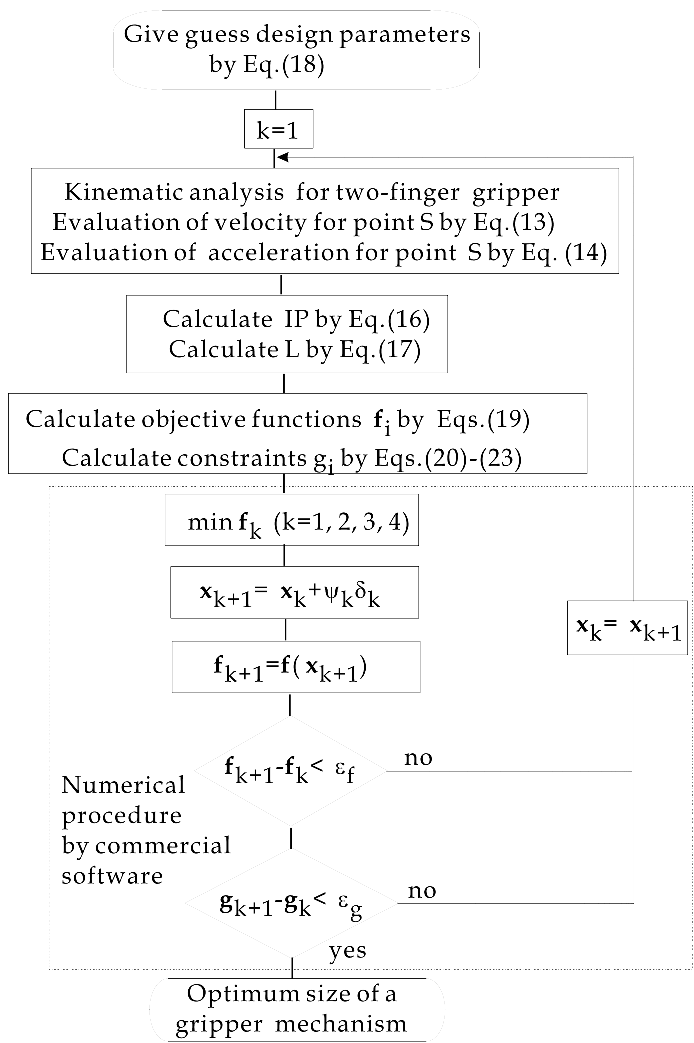

Fig. (14). Flowchart of a numerical procedure for optimum design of two-finger gripper mechanism.

h_1 = 1.4 u, $h_2 = h_3 = g$ = 0 u, $\gamma = \pi/2$ deg., l_{gear} = 1.4 u (Lengths are expressed in u unit and angles in degrees).

Referring to Fig. (**15**), the inequality constraints have been chosen, referring to Eqs. (20)-(23) as $minX_{S0}$ = 18 u, $minY_{S0}$ = -4.5 u, $maxX_{S0}$ = 20.5 u e $maxY_{S0}$ = 8 u, respectively. The prescribed workspace has been chosen with an asymmetric area with the aim to stress how the algorithm can give optimal solution with suitable symmetrical workspace even when the starting guess could be not suitably assigned.

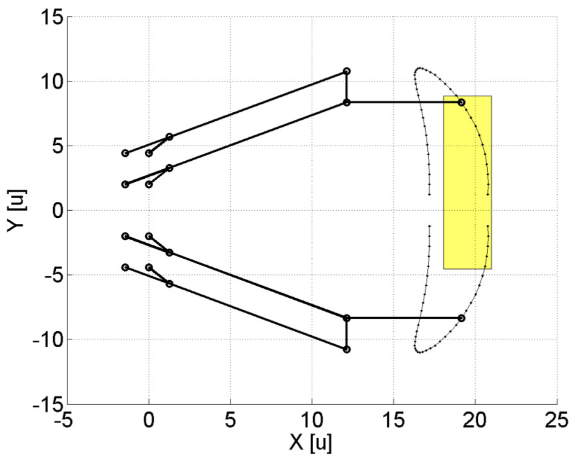

Fig. (15). A prescribed working area.

The results of the proposed case of study are shown in the plots of Figs. (**16**) to (**19**).

In particular, Fig. (**16**) show the evolution of the multi-objective functions versus the number of iteration. It is worth noting that the optimization algorithm has converged very rapidly to an optimum solution in 76 iterations as reported in Table **1**.

Table 1. Optimal Values of Objective Functions

Solution	f_1	f_2	f_3	f_4	nr. iteration
Guess	0.117	14.40	2.00	0.99	-
Optimal	0.101	14.13	1.93	0.86	76

Fig. (**17**) shows the evolution of the design parameters versus the number of iteration, whereas Table **2** shows the numerical results.

Table 2. Optimal Values of Design Parameters

Solution	$l_0 = l_{01}$ [u]	$l_1 = l_{11}$ [u]	$l_2 = l_{22}$ [u]	l_3 [u]	l_4 [u]	h_1 [u]
Guess	1.80	3.00	12.00	1.40	7.00	1.40
Optimal	1.23	3.23	9.71	1.59	9.52	1.28

In particular, Fig. (**17a**) shows the evolution of the design parameters l_0, l_1 and l_2, whereas Fig. (**17b**) shows the evolution of the design parameters of l_3, l_4 and h_1.

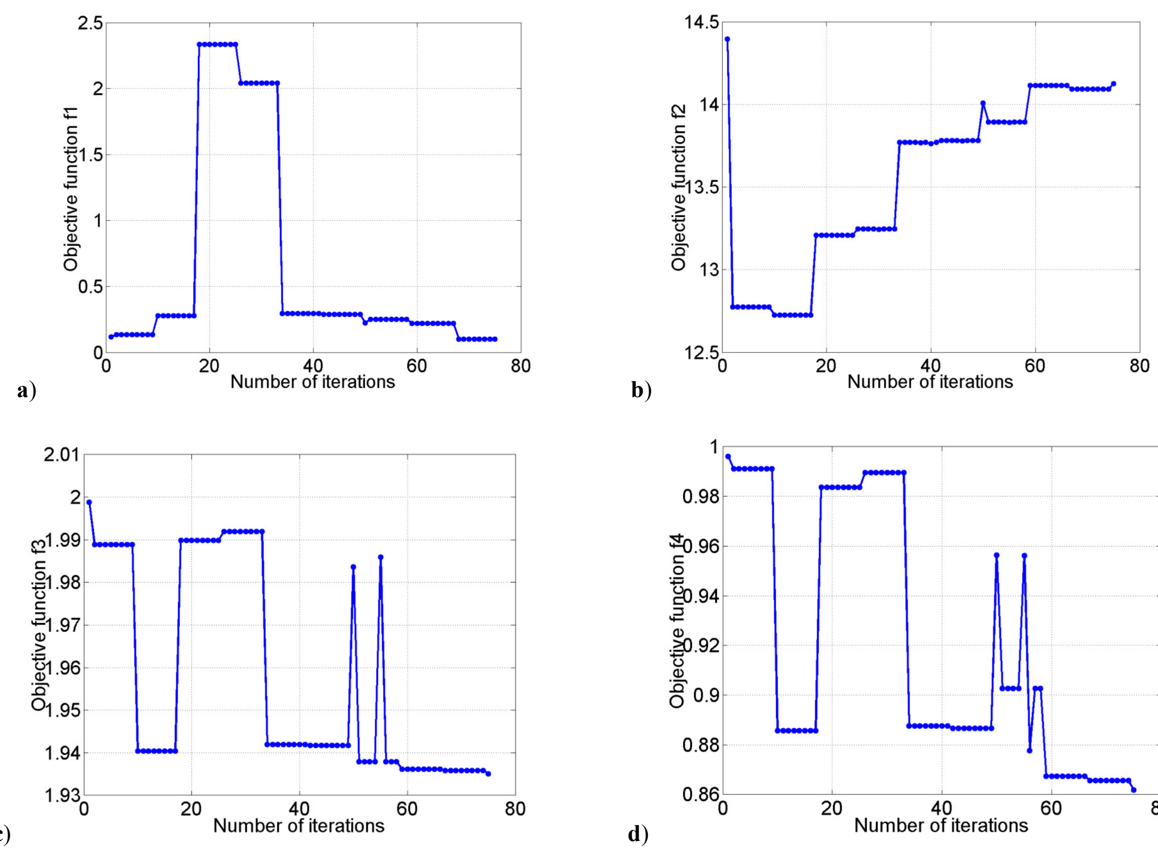

Fig. (16). Evolution of the objective functions versus number of iterations for the case of study in Table **1**: **a)** f_1; **b)** f_2; **c)** f_3; **d)** f_4.

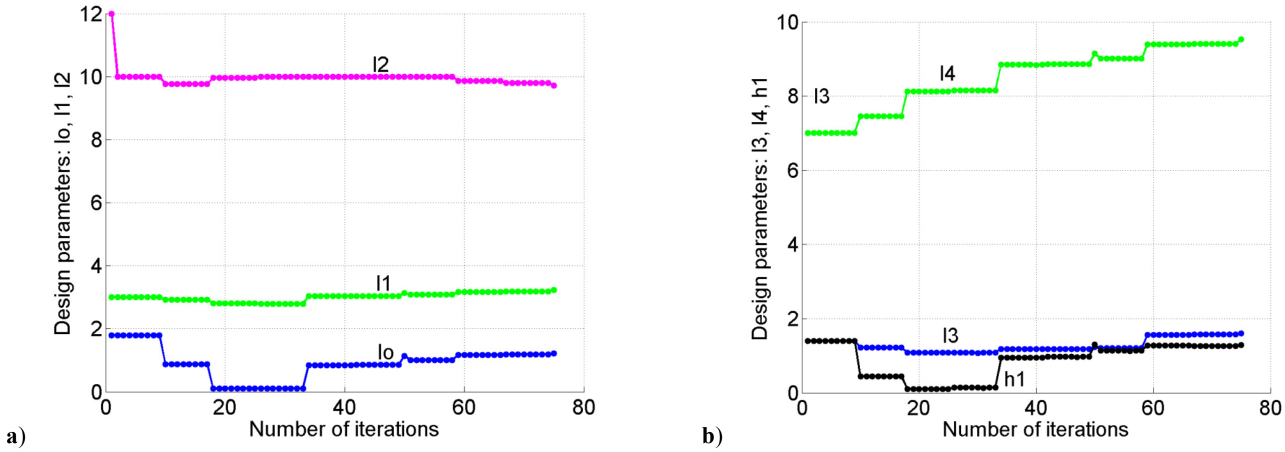

Fig. (17). Evolution of design parameters versus number of iterations: **a)** l_0, l_1 and l_2; **b)** l_3, l_4 and h_1.

Fig. (**18**) shows the evolution of the constraints versus the number of iteration, whereas Table **3** shows the numerical results. In particular, Fig. (**18a**) shows the evolution of significant constraints g_1, g_2, whereas Fig. (**18b**) shows the evolution of significant constraints g_3 and g_4.

Table 3. Optimal Values Constraints

Constraints	g_1 [u]	g_2 [u]	g_3 [u]	g_4 [u]
Initial	2.15	1.90	0.30	2.57
Optimal	0	0	-0.04	-2.71

In particular, Fig. (**18a**) shows the evolution of two significant constraints g_1 and g_2 during the optimization process to illustrate how fast and accurately the constraints have been satisfied. Similarly, Fig. (**18b**) shows the evolution of two significant constraints g_3 and g_4 during the optimization process. In particular, it has been shown how fast and accurately constraint g_3 has been satisfied.

Fig. (**19**) shows the optimum kinematic chain obtained by considering the optimum design parameters listed in Table **1**.

In particular, Fig. (**19a**) shows the path described by contact point S. Fig. (**19b**) shows the related obtained working area with respect the imposed constraints sketched by a rectangle, which shows how accurately constraints have been satisfied.

The optimal grasping mechanism satisfies requirements and constraints and the given working area.

CONCLUSIONS

In this paper, a review of existing industrial two-finger grippers has been used to formulate an optimum design procedure for two-finger gripper mechanisms as based on main characteristics of gripper operation.

An original multi-objective optimum algorithm has been used by considering four different objective functions, namely grasping index, encumbrance of mechanism, acceleration and velocity for fingers with respect to a prescribed working area.

This new formulation will achieve a kinematic design of gripper mechanism with optimal characteristics even as improvement of existing solutions.

A case of study has been presented for designing a gripper mechanism with an 8R2P linkage. The newly design

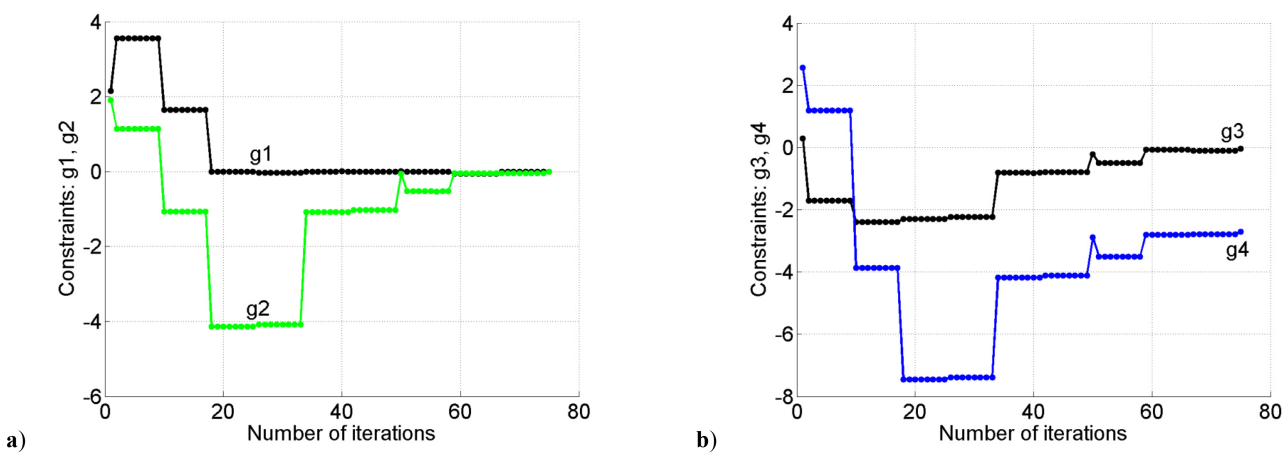

Fig. (18). Evolution of constraints versus number of iterations: **a)** g_1 and g_2; **b)** g_3 and g_4.

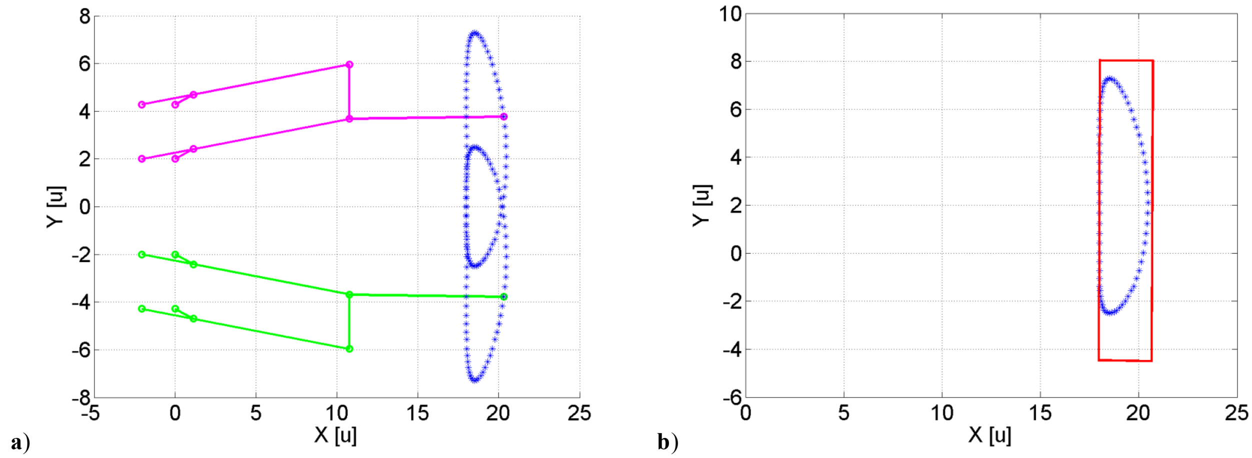

Fig. (19). Optimum results for the 8R2P mechanism: **a**) chain; **b**) working area with respect the prescribed one.

mechanism show more compact structure and optimal operation features as compared with the guess industrial example.

Numerical results have been reported to show the soundness of the proposed new optimum design procedure by referring to computational and practical results.

APPENDIX 1

$$\dot{x}_C = -l_0\dot{\vartheta}_1 \sin(\vartheta_1) - l_2\dot{\vartheta}_2 \sin(\vartheta_2)$$

$$\dot{y}_C = l_0\dot{\vartheta}_1 \cos(\vartheta_1) + l_2\dot{\vartheta}_2 \cos(\vartheta_2)$$

$$\dot{\vartheta}_2 = \frac{l_0\dot{\vartheta}_1 \cos(\vartheta_1)}{l_1 \cos(\vartheta_2)}, \qquad \dot{\beta} = C_1\dot{\vartheta}_1 + C_2\dot{\vartheta}_{11}$$

$$\dot{\vartheta}_{11} = \left(\frac{A - C_1 l_3 \sin(\beta)}{A_1 + C_2 l_3 \sin(\beta)}\right)\dot{\vartheta}_1$$

$$\dot{\psi} = \begin{cases} -\dot{\beta} & \text{if} \quad x_C > x_D \quad \text{and} \quad y_D > y_C \\ \dot{\beta} & \text{if} \quad x_D \geq x_C \quad \text{and} \quad y_D > y_C \end{cases}$$

$$C_1 = \frac{-B(x_D - x_C) + (y_D - y_C)A}{(x_D - x_C)^2 + (y_D - y_C)^2}$$

$$C_2 = \frac{B_1(x_D - x_C) - (y_D - y_C)A_1}{(x_D - x_C)^2 + (y_D - y_C)^2}$$

$$A = \left\{-l_0 \sin(\vartheta_1) - \frac{l_0 l_2 \cos(\vartheta_1)\sin(\vartheta_2)}{l_1 \cos(\vartheta_2)}\right\}$$

$$B = \left\{\frac{l_0 l_2 \cos(\vartheta_1)}{l_1} + l_0 \cos(\vartheta_1)\right\}$$

$$A_1 = \left\{-l_{01} \sin(\vartheta_{11}) - \frac{l_{01} l_{22} \cos(\vartheta_{11})\sin(\vartheta_{22})}{l_{11} \cos(\vartheta_{22})}\right\}$$

$$B_1 = \left\{\frac{l_{01} l_{22} \cos(\vartheta_{11})}{l_{11}} + l_{01} \cos(\vartheta_{11})\right\}$$

$$\ddot{x}_C = -l_0\ddot{\vartheta}_1 \sin\vartheta_1 - l_0\dot{\vartheta}_1^2 \cos\vartheta_1 - l_2\ddot{\vartheta}_2 \sin\vartheta_2 - l_2\dot{\vartheta}_2^2 \cos\vartheta_2$$

$$\ddot{y}_C = l_0\ddot{\vartheta}_1 \cos\vartheta_1 - l_0\dot{\vartheta}_1^2 \sin\vartheta_1 + l_2\ddot{\vartheta}_2 \cos\vartheta_2 - l_2\dot{\vartheta}_2^2 \sin\vartheta_2$$

$$\ddot{x}_D = -l_{01}\ddot{\vartheta}_{11} \sin\vartheta_{11} - l_{01}\dot{\vartheta}_{11}^2 \cos\vartheta_{11} - l_{22}\ddot{\vartheta}_{22} \sin\vartheta_{22} + \\ - l_{22}\dot{\vartheta}_{22}^2 \cos\vartheta_{22}$$

$$\ddot{y}_D = l_{01}\ddot{\vartheta}_{11} \cos\vartheta_{11} - l_{01}\dot{\vartheta}_{11}^2 \sin\vartheta_{11} + l_{22}\ddot{\vartheta}_{22} \cos\vartheta_{22} + \\ - l_{22}\dot{\vartheta}_{22}^2 \sin\vartheta_{22}$$

$$\ddot{\vartheta}_2 = \frac{l_0\ddot{\vartheta}_1 \cos\vartheta_1 - l_0\dot{\vartheta}_1^2 \sin\vartheta_1 + l_1\dot{\vartheta}_2^2 \sin\vartheta_2}{l_1 \cos\vartheta_2}$$

$$\ddot{\vartheta}_{22} = \frac{l_{01}\ddot{\vartheta}_{11} \cos\vartheta_{11} - l_{01}\dot{\vartheta}_{11}^2 \sin\vartheta_{11} + l_{11}\dot{\vartheta}_{22}^2 \sin\vartheta_{22}}{l_{11} \cos\vartheta_{22}}$$

$$\ddot{\beta} = \frac{-l_3\dot{\beta}^2 \cos\beta - \ddot{x}_D + \ddot{x}_C}{l_3 \cos\beta}$$

$$\ddot{\vartheta}_{11} = \frac{l_{22}}{l_0}\ddot{\vartheta}_{22} \cos(\vartheta_{11} + \vartheta_{22}) - \frac{l_{22}}{l_0}\ddot{\vartheta}_{11} \sin(\vartheta_{22} - \vartheta_{11})$$

$$\ddot{\psi} = \begin{cases} -\ddot{\beta} & \text{if} \quad x_C > x_D \quad \text{and} \quad y_D > y_C \\ +\ddot{\beta} & \text{if} \quad x_D \geq x_C \quad \text{and} \quad y_D > y_C \end{cases}$$

REFERENCES

[1] G. Lundstrom, “Industrial robot grippers”, *The Industrial Robot,* Vol. 1, pp. 72-82, 1973.

[2] F. Y. Chen, “Gripping mechanisms for industrial robots”, *Mechanism Machine Theory,* Vol. 17, pp. 299-311, 1982.

[3] S. Y. Nof, *Handbook of industrial robotics:* New York: Editorial Wiley, 1985.

[4] G. Belforte, "Industrial robot gripper", *Notiziario Tecnico AMMA*, Torino, 128-136, 1985.

[5] D. T. Pham, and W. B. Heginbotham, *Robot grippers*, Bedford: IFS Publications Limited, 1986.

[6] R. D. Potter, "End-of-arm tooling", in *Handbook of Industrial Robotics*, S. Y. Nof, Ed, New York: Wiley, 1985, pp. 775-787.

[7] M. Ceccarelli, "Design problems for industrial robot two-finger grippers", in *Proceedings of the 4th International Workshop on Robotics in Alpe-Adria Region*, Bled, 1994, pp. 568-571.

[8] I. B. Chelpanov, and S. N. Kolpashnikov, "Problems with the mechanics of industrial robot grippers", *Mechanism and Machine Theory*, pp. 295-299, 1983.

[9] N. P. Belfiore, and E. Pennestrì, "An atlas of linkage-type robotic grippers", *Mechanism and Machine Theory*, Vol. 32, (n. 7), pp. 811-833, 1997.

[10] F. Lhote, J. M. Kauffmann, P. Andrè, and J. P. Taillard, in *Robot Technology: Robot Components and Systems*, Vol. 4, Chapter 8: End Effectors, Kogan Page, London, 1987, pp. 297-312.

[11] S. N. Dwivedi, S. C. Sharma, and M. Sharifi, "Design of an intelligent gripper for space application" in *The 8th World Congress on the Theory of Machines and Mechanisms*, Prague, 1991, pp. 453-456.

[12] K. B. Shimoga, "Robot grasp synthesis algorithms: a survey", *International Journal of Robotics Research*, Vol. 4, (n. 4), pp. 3-17, 1986.

[13] B. Salunkhe, W. X. Mao, and U. Tasch, "Optimal grasping formulations that result in high quality and robust configurations", *Journal of Robotic Systems*, Vol. 15, (n. 12), pp. 713-729, 1998.

[14] V. N. Dubey, R. M. Crowder, and P. H. Chappell, "Optimal object grasp using tactile sensors and fuzzy logic", *Robotica*, Vol. 17, (n. 6), pp. 685-693, 1999.

[15] R. D. Hester, M. Cetin, C. Kapoor, and D. Tesar, "A criteria-based approach to grasp synthesis", in *Proceedings of the 1999 IEEE International Conference on Robotics & Automation, Detroit*, 1999, pp. 1255-1260.

[16] A. Osyczka and S. Krenich, "A new constraint tournament selection method for multicriteria optimization using genetic algorithm", in *Proceedings of the Congress of Evolutionary Computing*, San Diego, 2000, pp. 501-509.

[17] O. H. Penisi, G. Carbone, and M. Ceccarelli, "Optimum design and testing of mechanisms for two-finger gripper", in *Proceedings of MUSME2002, The International Symposium on Multibody Systems and Mechatronics*, Mexico City, 2002, Paper n. M03.

[18] M. Ceccarelli, J. Cuadrado, and D. Dopico, "An optimum synthesis for gripping mechanisms by using natural coordinates", *Journal of mechanical Engineering Science*, *IMechE 2002*, Vol. 216, Part C, pp. 643-653, 2002.

[19] S. Krenich, "Multicriteria design optimization of robot gripper mechanisms", in *IUTAM Symposium on Evolutionary Methods in Mechanics, Proceedings of the IUTAM Symposium*, 2002, Vol. 117, pp. 207-218.

[20] M. Ceccarelli, "An optimum design for a gripping mechanism", in *Proceedings of the International Symposium Machines and Mechanisms ISMM'97*, Beograd, 1997, pp. 23-26.

[21] M. Ceccarelli, Ed., in *Fundamentals of mechanics of robotic manipulation*, Dordrecht: Kluwer Academic Publisher, 2004.

[22] Y. Zheng, and W. H. Qian, "Limiting and minimizing the contact forces in multifingered grasping", *Mechanism and Machine Theory*, Vol. 41, pp. 1247-1257, 2006.

[23] C. Lanni, "A characterization of impact grasping and optimum design of gripper mechanisms", PhD thesis, LARM, University of Cassino, Cassino, Italy, 2008.

[24] Gimatic Handling, 2008. Available from: www.gimatic.com

[25] GMG System, 2008. Available from: http://www.gmg-system.com/en/fr_home. html

[26] AGI Components, 2008. Available from: www.agi-automation.com/index.html

[27] SMC Components, 2008. Available from: www.smcworld.com/ 2002 / e / webcatalog / docs / actuator / gripper / gripper. html

[28] S. S. Rao, "Multicriteria optimization in mechanisms", *Transaction of ASME, Journal of Mechanical Design*, Vol. 101, pp. 398-406, 1985.

[29] K. Tanie, "Design of robot hands" in *Handbook of Industrial Robotics*, S. Y. Nof, Ed, New York: Wiley, 1985, pp. 112-137.

[30] IBM 7565, *IBM 7565 manufacturing system*, IBM Hardware Library, 1985.

[31] M. Ceccarelli, and J. Nieto, "Kinematic evaluation of a robotic gripper", *Anales de Ingenieria Mecanica, Año 6*, Vol. 1, pp. 159-164, 1988.

[32] A. Grace, *Optimization Toolbox for use with matlab*, Natick: The Math Works Inc., 1992.

In a microreactor, non-catalytic and glycerol-free biodiesel generation

Priyabrata Jena, *Department of Mechanical Engineering, Capital Engineering College, Bhubaneswar, priyabratajena456@yahoo.co.in*

Suraj Kumar Patel, *Department of Mechanical Engineering, Aryan Institute of Engineering & Technology, Bhubaneswar, surajpatel26@gmail.com*

Hemant Ku Nayak, *Department of Mechanical Engineering, NM Institute of Engineering & Technology, Bhubaneswar, hemantnayak236@gmail.com*

Shradha Jena, Department of Civil Engineering, Capital Engineering College, Bhubaneswar, shradhajena98@gmail.com

A R T I C L E I N F O

Keywords:
Biodiesel
Microreactor
Rice bran oil fatty acid distillate
Supercritical process
Dimethyl carbonate

A B S T R A C T

Rice bran oil fatty acid distillate (RBOFAD) is a low-value, non-edible, and undesirable by-product of the rice bran oil refining process that can be used as a promising alternative raw material for biodiesel manufacturing. However, due to the high quantity of free fatty acids, the traditional biodiesel process cannot handle this material (FFA). This paper proposes a novel supercritical biodiesel synthesis process in a microreactor employing dimethyl carbonate (DMC) as an acyl acceptor for high FFA input materials. Our technique produced high-quality biodiesel and a value--added by-product (glyoxal). The biodiesel content of RBOFAD as feedstock was attained at 80.9 percent in this method, compared to just 43.6 percent for refined rice bran oil as feedstock. Response surface approach was used to study and optimise the impact of operating variables on biodiesel and glyoxal content, including reaction temperature, residence time, and DMC-to-RBOFAD molar ratio. At the ideal conditions (reaction temperature of 360°C, residence duration of 35 minutes, and RBOFAD-to-oil molar ratio of 11:1), a biodiesel content of 97.1 -◦percent was reached. In comparison to prior procedures, the necessary pressure and amount of DMC were greatly lowered. Most of the biodiesel properties met the international standards except for some impurities (mono- and diglycerides). These results provided the new insight for the development of biodiesel production from low-grade feedstocks.

Introduction

Although biodiesel has been reported as an effective substitute for diesel fuel, there are certain issues to further improve the production especially for the economic aspect. The raw material cost is one of the significant barriers contributing to the overall cost of biodiesel. Conceivably, the worldwide use of biodiesel would be greatly increased if the low-cost feedstock can be used. Another challenge is the low biodiesel yield associated with the production limitation due to low-grade materials. Hence, advanced production techniques such as the two-step process and supercritical process may be required. However, such techniques are still being intensified to improve the process efficiency and cost-effectiveness in a practical way.

In our previous works [1], the supercritical conditions were applied with microreactor technology to enhance the biodiesel production in terms of process efficiency and cost reduction. The requirements of extreme operating conditions, such as reaction pressure, residence time, and alcohol usage, to provide the high yield were significantly reduced, i.e., the molar ratio of alcohol-to-oil ratio of 25:1, residence time of 4.7 min and reaction pressure of 8 MPa achieving 97% of biodiesel yield was successfully demonstrated. Similar successes were also confirmed in the literature [2,3]. Therefore, the integration of supercritical process with microreactor technology is one of the promising methods to be implemented for an efficient and economical solution for biodiesel production.

Rice bran oil fatty acid distillate (RBOFAD) is a low-price and unwanted by-product obtained from rice bran oil production. RBOFAD is a non-edible fat that comprised of mostly free fatty acid (FFA) compounds, presenting a great potential to be used as an abundant source for biodiesel production. While various results on crude/refined rice bran oil-based biodiesel research have been extensively studied [4,5], research is rarely reported on the biodiesel production using RBOFAD as a low-quality feedstock [6]. Thus, it would be worth investigating this RBOFAD as a novel feedstock for biodiesel production.

Another factor affecting the biodiesel price is a by-product (glycerol) obtained from biodiesel production. The biodiesel price cannot be compensated due to the low value of glycerol, caused by the surplus of glycerol in the world market. Therefore, a new biodiesel production route to obtain a value-added by-product (instead of glycerol) is an advantage to promote biodiesel as a strong competitor to diesel. Recently, an interesting route emerged as the biodiesel production from refined vegetable oil and dimethyl carbonate (DMC) [7,8,9]. In this route, the high-value glycerol carbonate (GC), highly demanded in various industries such as coating and painting, pharmaceutical, and cosmetics [10], is produced (see Equation (1)). Apparently, this route offers an excellent potential for improving the economic competitiveness of biodiesel production. For example, Rathore et al. [11] reported that 96.8% of ester content was obtained from the alkaline (KOH) transesterification of jatropha oil and DMC using DMC-to-oil molar ratio of 10:1, reaction temperature of 80 °C, and reaction time of 8 h. Another successful demonstration was reported by Jung et al. [12]. The avocado oil and DMC were used to produce biodiesel with the yield of 92.6% at 380 °C. The high yield and strong thermal cracking resistance of biodiesel were offered when DMC was used as an acyl acceptor instead of methanol. Although the influence of operating conditions on the yield of biodiesel via this production route was investigated, the influence of operating conditions on the yield of by-product (GC) has rarely been observed [8]. Moreover, using low-grade materials (high FFA) as a feedstock for DMC biodiesel production has rarely been investigated, indicating another knowledge gap of this production route.

The free fatty acids can also be used as a feedstock for DMC biodiesel production via esterification reaction route to obtain the high-value by-product, named as glyoxal (see Eq. (2)). Glyoxal, commercially produced from the oxidation reaction of ethylene glycol or acetaldehyde [13], is a useful substrate for wood-processing, petrochemical, and pharmaceutical applications [14]. Due to the issue of catalyst performance, these processes provided low productivity of glyoxal [15]. Hence, a by-product obtained from biodiesel production might be a potential supply of glyoxal.

$$\text{Triglyceride} + \text{DMC} \leftrightarrow \text{Biodiesel} + \text{GC} \quad (1)$$

$$\text{FFA} + \text{DMC} \leftrightarrow \text{FAME} + \text{Glyoxal} + H_2O \quad (2)$$

One of the experimental design techniques for analyzing and optimizing the production process is the response surface methodology (RSM), which has extensively contributed to developing the process of biodiesel production [16,17]. Both mathematical and statistical techniques can be applied for interpreting the relation of output variable (response) and input variables. The basic concept of this method for biodiesel application can be found elsewhere [18]. This method provides a reliable and accurate model for predicting the desired output response. For example, in the work of Chamola et al. [19] who applied RSM for optimizing biodiesel production from algae, the regression model as a function of process parameters was obtained with the low relative error of 3.9%. Hence, the correlation between process variables (such as reaction temperature, residence time, and molar ratio of oil and alcohol) and response (biodiesel content) of our novel DMC-supercritical biodiesel process can be analyzed via this method.

In this work, the DMC biodiesel production from low-value feedstock in a microreactor was proposed to fulfill the knowledge gaps in the field of biodiesel development. The RBOFAD was used as a low-value feedstock for synthesizing with DMC to produce biodiesel and high-value by-product (glyoxal). The influence of major factors affecting the biodiesel purity (%FAME) and by-product content was explored including reaction temperature, residence time, and molar ratio of DMC to RBOFAD. The optimization based on %FAME was determined via response surface methodology. The production performance in our work was compared with the other processes reported in the literature. Our biodiesel properties were compared with the biodiesel from literature and international standards. The prototype of our novel production of biodiesel from low-grade raw material (high content of free fatty acid) without catalyst can be used as a foundation to further enhance the production performance.

Materials and methods

Materials

Refined RBO and RBOFAD were obtained from Surin Bran Oil company. Both types of oil were used without further purification. DMC (AR grade, 99%) was purchased from Sigma-Aldrich. HPLC grade of acetonitrile (99.9%) and acetone (99.8%) were supplied by RCI Labscan Limited. Analytical standards were purchased from Sigma-Aldrich including glyoxal, and FAME (AOCS No. 6).

Biodiesel synthesis

In this work, biodiesel synthesis was carried out in a microreactor under supercritical DMC condition. First, the RBOFAD (or refined RBO) was premixed with DMC at the desired proportion (molar ratios of DMC-to-oil ratio between 1.8:1 and 25.7:1) in a beaker to obtain the homogeneous substrate solution. The stream of RBOFAD (or refined RBO) and DMC was then introduced into a microreactor via HPLC pump (LKB Bromma 2150) at the desired residence time (8 to 67 min). The microreactor, where transesterification/esterification reactions took place, was placed inside a convection oven (adapted from a gas chromatography oven; Varian 3600) to control the reaction temperature (275 to 375 °C). The reactor outlet was connected to a back-pressure regulator for controlling the pressure at 8 MPa. After exiting the reactor, the outlet stream was rapidly cooled down to stop the reactions. The product was collected for product analysis. The purity of biodiesel (%FAME) and glyoxal content were used to evaluate the reaction performance. The experimental setup is shown in Fig. 1.

To determine the %FAME, the product was purified via the washing process. The product was washed with a mixture of DI water and methanol (1:1 (v/v)) to remove the impurity. The upper and lower phases were separated using a centrifugal separator. The upper phase (biodiesel) was then rewashed twice and dried at 105 °C for 2 h to remove the remaining solvents. After that, the biodiesel sample was analyzed using HPLC technique. For glyoxal analysis, the glyoxal content was also evaluated with HPLC method without further purification.

Raw material and product analysis

The composition of biodiesel product (biodiesel, triglycerides, and glyoxal) was analyzed using HPLC equipped with a refractive index detector (RI; model YL9170, YL Instrument). The analysis was performed on the ACE Excel 5 Super C_{18} column (4.6 mm × 250 mm, 5 μm particle size) at the temperature of 40 °C. The 70:30 (v/v) of acetone and

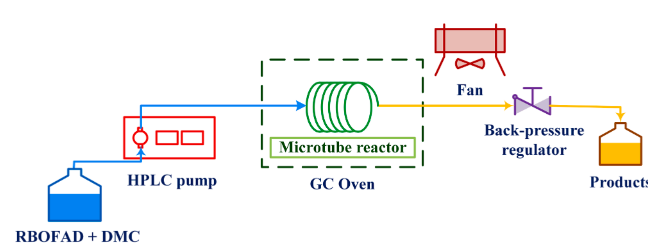

Fig. 1. Schematic diagram of an experimental setup for biodiesel process.

acetonitrile was used as a mobile phase at a flow rate of 0.7 mL/min. The peak identification was analyzed by comparing the retention time between the sample and the standard compounds.

Response surface methodology

In this work, the regression analysis was performed to obtain the correlation between process variables and %FAME via response surface methodology (RSM) based on the Box-Behnken design (BBD). The polynomial regression equation as shown in Eq. (3) can be used to describe this relationship, which will be used for the optimization of % FAME (Section 3.4).

$$Y = \beta_0 + \sum_{i=1}^{3} \beta_i X_i + \sum_{i=1}^{3} \beta_{ii} X_i^2 + \sum_{i=1}^{2} \sum_{j=i+1}^{3} \beta_{ij} X_i X_j \tag{3}$$

where Y is the biodiesel content (%), X_i and X_j are the process variables and β_0, β_i, β_j, and β_{ij} are polynomial regression coefficients.

Results and discussion

Raw material analysis

The properties and composition of RBOFAD and refined RBO are summarized in Table 1. The main difference between the RBOFAD and refined RBO for biodiesel production was the quality of the feedstock. The high amount of FFAs was found in RBOFAD (61.5 wt%), whereas the refined RBO contained mostly triglyceride compounds (92.5 wt%). This was also in line with the acid value results. Using RBOFAD (high FFA content) as raw material for the conventional alkaline-based biodiesel process using DMC generally requires the additional purification steps or the advanced production techniques [20,21]. In this work, the supercritical method was applied in combination with microreactor technology for highly efficient biodiesel production. The chromatogram of RBOFAD and refined RBO are shown in Fig. 2.

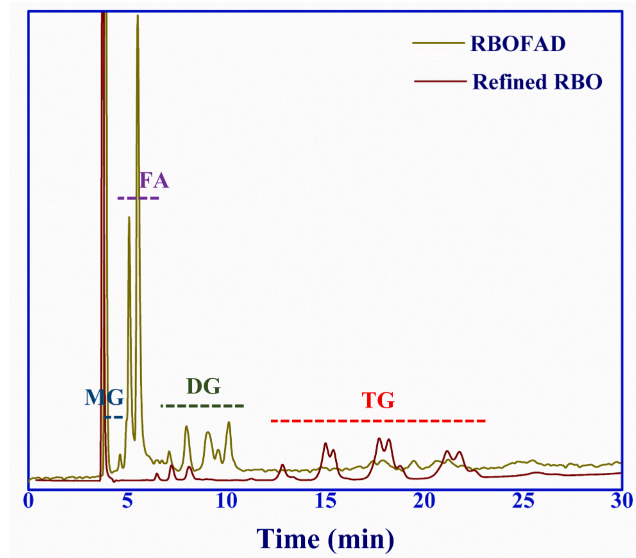

Fig. 2. Chromatograms of RBOFAD and refined RBO; MG: monoglycerides, FA: free faty acids, DG: diglycerides, TG: triglycerides.

Biodiesel production from RBOFAD and refined RBO

The first experiment of biodiesel production using RBOFAD as feedstock via glycerol-free under supercritical conditions in a microreactor was investigated at the temperature of 325 °C, residence time of 20 min, and DMC-to-RBOFAD molar ratio of 3.7:1 (1:1 (v/v)). The chromatogram of sample is shown in Fig. 3 and the biodiesel content of 80.9% was achieved. The esterification reaction was the main pathway responsible for this result (see Eq. (2)) due to the large amount of free fatty acid in the raw material. The biodiesel content could be increased by converting the remaining di- and triglycerides to biodiesel through the transesterification reaction (see Eq. (1)), which could be promoted by modifying the operating conditions.

The transesterification reaction of triglycerides and DMC was further studied by using refined RBO as raw material to better understand the behavior of DMC transesterification reaction. The experiments were performed at temperatures in the range of 275 to 325 °C and residence times of 8 to 67 min, while the DMC-to-refined RBO volumetric ratio of 1:1 was held constant. As shown in Fig. 4, results suggested that the

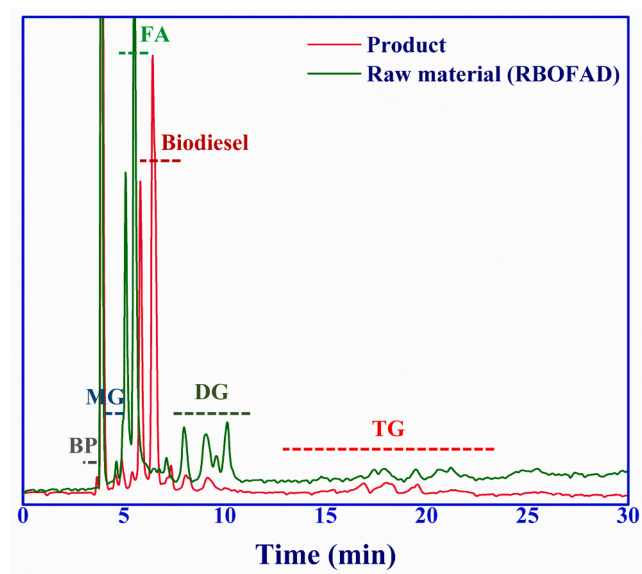

Fig. 3. Comparison of chromatograms between raw material (RBOFAD) and biodiesel obtained from RBOFAD synthesized under the temperature of 325 °C, residence time of 20 min, and DMC-to-RBOFAD molar ratio of 3.7:1; BP: by-product, MG: monoglycerides FA: free faty acids, DG: diglycerides, TG: triglycerides.

transesterification rate of triglyceride and DMC was relatively slower when compared to that of the esterification reaction of RBOFAD and DMC. For example, at the temperature of 325 °C and residence time of 20 min, 3.5% of %FAME was obtained from the case of RBO, whereas 80.9% of %FAME was achieved for the esterification reaction. Increasing of the reaction temperature (up to 375 °C) and residence time (up to 67 min) could not enhance the %FAME as expected, i.e., the % FAME of 43.6% was obtained at the temperature of 375 °C and residence time of 20 min (see Fig. 4(a)) or the %FAME of 35.6% was obtained at the temperature of 325 °C and residence time of 67 min as shown in Fig. 4(b).

In contrast, as reported in our previous works (see Table 2), relatively fast reaction rate was observed for supercritical alcohol transesterification/esterification reactions using refined raw material

Table 1
Physico-chemical properties of RBOFAD and refined RBO.

Properties	RBOFAD	Refined RBO
Density (kg/m3)	930	900
Viscosity (cSt)	27.53	39.8
Acid value (mg_{KOH}/g)	140 ± 3.5	0.1 ± 0.05
Free fatty acids (wt%)	61.5 ± 1.4	NA
Monoacylglycerides (wt%)	1.0 ± 0.2	NA
Diacylglycerides (wt%)	27.8 ± 1.0	7.5 ± 1.3
Triacylglycerides (wt%)	9.7 ± 2.6	92.5 ± 1.3

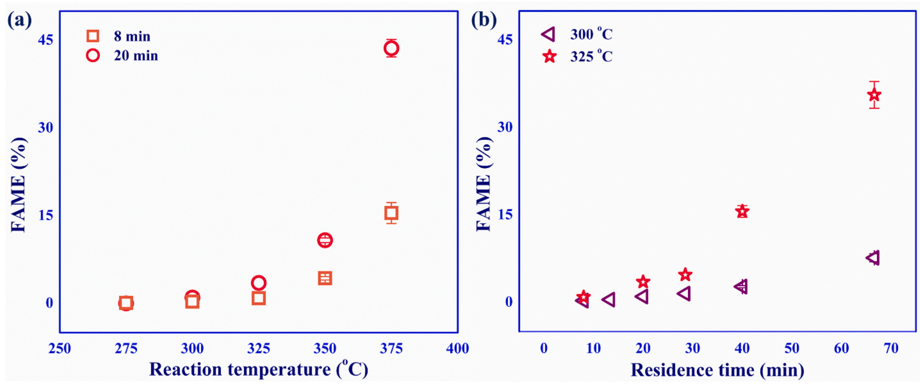

Fig. 4. Effect of operating conditions on the %FAME (a) effect of residence time (b) effect of reaction temperature.

Table 2
Supercritical biodiesel production from various substrates.

Raw material	Temperature (°C)	Pressure (MPa)	Residence time (min)	Solvent-to-oil molar ratio	Biodiesel content (%)	Reference
Refined palm oil + Ethanol	350	8	3.5	11:1	60.1[a]	[22]
RBOFAD + Ethanol	300	8.5	24	5:1	75[a]	[6]
Refined RBO + DMC	375	8	20	11:1	43.6[a]	In this work
RBOFAD + DMC	325	8	20	3.7:1	80.9	In this work

[a] The optimal conditions for obtaining the highest biodiesel content

compared to that of the aforementioned reaction between DMC and RBOFAD in this work. A similar observation was also reported in the work of Kwon et al. [23]. Conversely, when the low-grade oil was applied as a feedstock (instead of refined oil), the DMC supercritical process provided better performance than that of alcohol supercritical process. These results suggested that the low-grade raw material was highly eligible for the DMC esterification reaction, as the high rate of transesterification reaction comparable to the case of refined raw material was also provided. The preliminary results as discussed previously confirmed these findings. Hence, this evidence suggested a great potential of using this material for improving the economic aspect of the production of biodiesel via simultaneous DMC esterification and transesterification reactions.

Effect of operating conditions on biodiesel and glyoxal contents

In this work, the effect of operating conditions including reaction temperature, residence time, and DMC-to-oil molar ratio was investigated under supercritical conditions. The first operating variable studied was the reaction temperature since the reaction temperature was considered as the most significant effect on the biodiesel content [24]. The reaction temperature in the range of 275 to 375 °C was investigated to cover the recommended range for biodiesel production [25,26,27]. Note that, the thermal decomposition of biodiesel would be detected when operating at temperatures above 375 °C. The experiments were carried out with different residence times between 8 and 60 min while the DMC-to-oil molar ratio was kept constant at 3.7:1. The results as shown in Fig. 5(a) indicated that, at 8 min, only 5.6% of biodiesel content was obtained at 275 °C. The %FAME increased with increasing the reaction temperature, achieving 91.0% at 375 °C. Similar trends were observed when different residence times were applied (up to 60 min). It can be observed that the effect of reaction temperature on the % FAME was mitigated when the residence time was increased. The addition of catalyst can also be used to lower the reaction temperature required [28]. The maximum biodiesel content of about 93.4% was achieved when the reaction temperature and residence time were adjusted accordingly.

The effect of residence time on the %FAME was also observed in Fig. 5(a). To obtain the high %FAME, the short residence time could be used for the reaction at high temperature, and vice versa. For example, %FAME of 91.0% was obtained at the reaction temperature of 375 °C and residence time of 8 min, while the residence time of 40 min was required for the operation at 325 °C to achieve the similar %FAME (93%). Although the high %FAME was obtained, the triglyceride trace still appeared in biodiesel as shown in Fig. 6. The triglyceride compounds were still detected even when the residence time was further

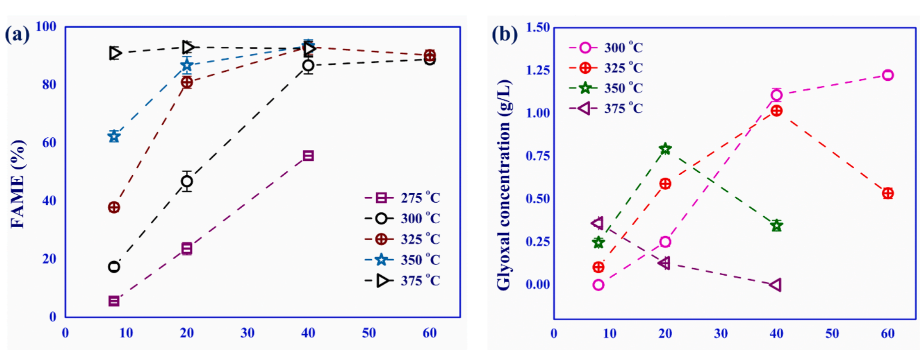

Fig. 5. Effect of reaction temperature on the %FAME and glyoxal content under various residence times.

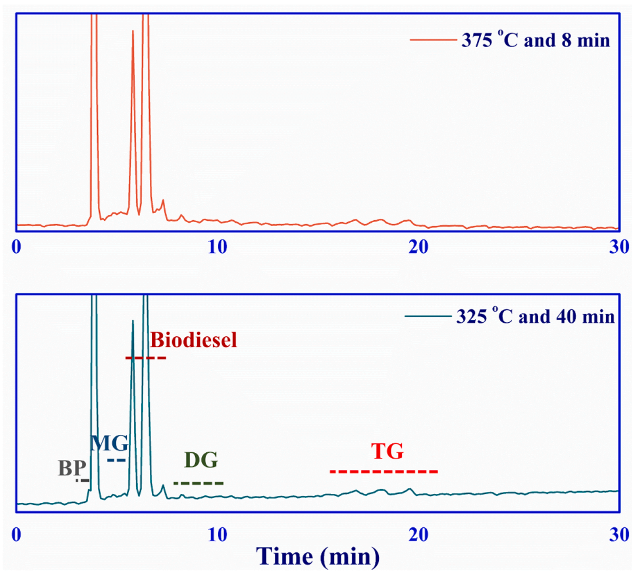

Fig. 6. Chromatograms of biodiesel product with high %FAME.

increased to 60 min (constant temperature at 325 °C). This was due to the difficulty of converting triglycerides to biodiesel, which requires both high reaction temperature (>325 °C) and long residence time (>8min). These results were in line with those observed from the cases of refined RBO (see Section 3.2).

The effects of reaction temperature and residence time on the glyoxal content were considered in the range of 275–375 °C and 8–60 min, respectively. Fig. 5(a) shows that the %FAME increased with increasing residence time, followed by a plateau for the residence time exceeding 40 min except for the cases of the reaction temperature of 275 °C. This indicated that the appropriate residence time allowed the system to reach the equilibrium. For the concentration of glyoxal, as shown see Fig. 5(b), it was found that the concentration of glyoxal increased with increasing reaction temperature from 300 to 350 °C when the residence time was shorter than 20 min. Conversely, for cases with residence time exceeding 20 min, the glyoxal content decreased upon increasing the reaction temperature from 300 to 375 °C. This might be due to the thermal instability of glyoxal under the prolonged exposure [29]. Note that the operating condition at the reaction temperature of 300 °C and the residence time of 60 min was suitable for obtaining the maximum glyoxal content; however, the unsatisfied %FAME was provided (88%). Apparently, when the %FAME and glyoxal content were both considered, there was a trade-off between the %FAME and glyoxal content, i.e., reduced concentration of glyoxal was obtained in order to achieve high %FAME.

The effect of DMC-to-RBOFAD molar ratio on the %FAME was investigated in the range of 1.8:1 to 25.7:1. The investigation was carried out at various reaction temperatures (300 to 375 °C) with the constant residence time of 20 min. As shown in Fig. 7(a), the high sensitivity of DMC-to-RBOFAD molar ratio on the %FAME was observed at the low reaction temperatures (300 and 325 °C). The increase in molar ratio negatively affected the %FAME, i.e., at 325 °C, %FAME of 82.1% dropped to 50.4% when the molar ratio was increased from 0.5:1 to 7:1. This was due to the dilution effect of the reactant. The effect of DMC-to-RBOFAD molar ratio on the %FAME was switched to the positive side by operating at elevated temperatures (350 to 375 °C). Further increasing the molar ratio beyond 11:1 could not significantly promote the %FAME due to the difficult conversion of triglyceride compounds into biodiesel. Therefore, the DMC supercritical process should not be performed with the DMC-to-RBOFAD molar ratio exceeding 11:1. In addition, the molar ratio required for the supercritical DMC reaction was smaller when compared to that of the supercritical alcohol process [6]. Similar results were reported in the work of Ilham and Saka [30].

The effect of DMC-to-RBOFAD molar ratio on the glyoxal content is shown in Fig. 7(b). Increasing the molar ratio significantly decreased the glyoxal content. This was due to the slow rate of esterification as the low %FAME was obtained. Another possible reason was the side reactions of glyoxal to the other products at high temperatures (>350 °C) and high DMC amounts. Methanol, one of the decomposition products of DMC [31], would react with glyoxal to other products [32]. Hence, the molar ratio of 1.8:1 was required to achieve the high glyoxal content. On contrary, the biodiesel production was not effective at this condition (high DMC content was required to achieve the high %FAME).

Apparently, the trade-off between %FAME and glyoxal content was the constraint of this process. Therefore, in this work, our process was developed based on the maximum %FAME. The appropriate operating conditions for optimization experiments were the reaction temperatures of 325 to 375 °C, DMC-to-RBOFAD molar ratios of 3 to 11, and residence times of 10 to 60 min as reported in Table 3. These conditions were used to determine the optimal operating conditions as discussed in the next section.

Table 3
Variables, levels of variable and constrains used for optimization.

Variables	Symbol	Levels			Constrains
		−1	0	1	
Independent variables					
Reaction temperature (°C)	X_1	325	350	375	In the range
DMC-to-RBOFAD molar ratio (mol/mol)	X_2	3	7	11	In the range
Residence time (min)	X_3	10	35	60	In the range
Dependent variable					
%FAME (%)	Y				Optimize

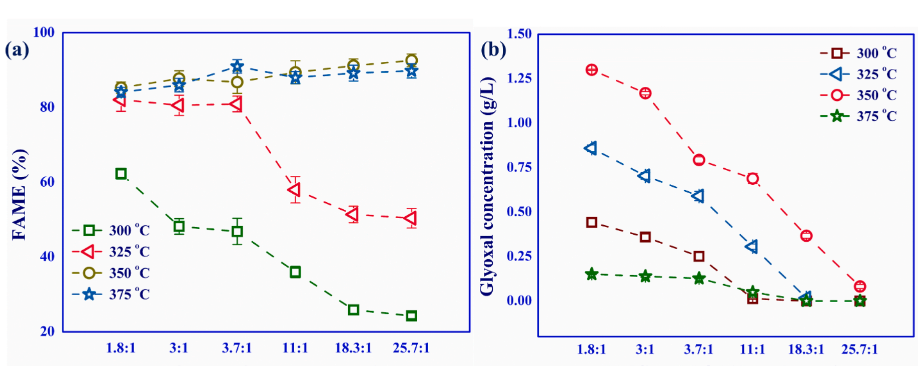

Fig. 7. Effect of DMC-to-RBOFAD molar ratio on the %FAME and glyoxal content under various reaction temperatures.

Correlation and optimization

The relationship between operating conditions (reaction temperature, DMC-to-RBOFAD molar ratio, and residence time) and %FAME was used for optimization via the response surface methodology. The experiments were performed, and results were analyzed based on the Box-Behnken design (BBD). The response surface plots of process variables on the %FAME are shown in Fig. 8. These results provided the relationship between process variables and responses. The relationship between the operating conditions and %FAME is described by Equation (4).

$$Y = -1150 + 6.09X_1 - 3.95X_2 + 8.79X_3 - 0.01X_1^2 + 0.3X_2^2 - 0.02X_3^2 - 0.02X_1X_3 \quad (4)$$

where, Y is the biodiesel content (%FAME, %), X_1 is the reaction temperature (°C), X_2 is the DMC-to-RBOFAD molar ratio, and X_3 is the residence time (min).

The accuracy of the model was verified by measuring the coefficient of determination (R^2). The R^2 of 98% (see Fig. 9) indicated that the prediction results were satisfactory. According to the optimization analysis, the reaction temperature of 360 °C, DMC-to-RBOFAD molar ratio of 11:1, and residence time of 35 min were the optimal operating conditions to achieve the maximum %FAME of 97.8%. Another experiment was carried out at the optimal conditions to validate the model prediction. The %FAME of 97.1% was obtained with the relative error of 0.7%. The glyoxal content of 0.23 g/L was also obtained as by-product.

Biodiesel quality

The properties of biodiesel synthesized at the optimal conditions were analyzed and compared with the literature and the international standards as reported in Table 4. The main composition of product was fatty acid methyl ester (biodiesel), followed by the small amount of mono- and diglyceride compounds. The content of mono- and diglyceride compounds in our fuel did not meet the specification of the European standard EN14214. It may involve the formation of precipitates in the engine system [33,34]. Hence, using our synthesized biodiesel at low temperatures should be avoided. Alternatively, the fuel can be transesterified with alcohol to eliminate these compounds (our future work). Note that, there is no requirement regarding these compounds in the ASTM standard. Other fuel properties including ester content, density, acid value, and viscosity were within the range of the international standards (EN14214 and ASTM D6751). When compared to the biodiesel fuel obtained from various sources of rice bran oil (different FFA content), as reported in Table 4, our fuel properties were comparable to that of other fuels (except the content of mono- and diglyceride compounds). Results indicated that our process was capable of handling the raw material with high FFA content, highlighting one of the promising alternative methods for low-quality (cost) vegetable oil.

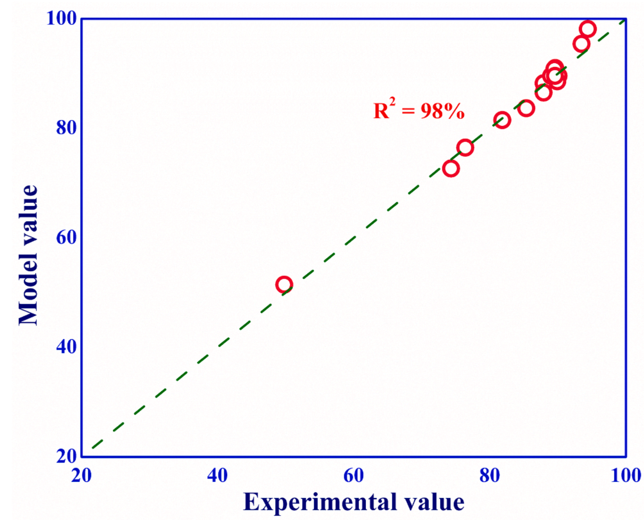

Fig. 9. Parity plot of %FAME obtained from experimental results and model prediction.

Performance comparison

The comparison of reaction performance between our proposed method for biodiesel production and other processes from the literature was evaluated as reported in Table 5. To achieve the high yield of biodiesel (>90%) for the transesterification of refined oil and DMC, large amount of DMC was required (DMC-to-oil molar ratio of around 40:1) as well as high reaction pressure of 15 to 20 MPa. Besides, different processes using high FFA as feedstock were also reported. The multi-processing steps such as the two-step batch process were required to obtain the high yield of biodiesel. High production performance of our method was clearly observed when compared to that of the two-step process. In addition, our work was the first to investigate the continuous DMC biodiesel process for such high FFA feedstock. High yield of biodiesel produced from our process was achieved with the relatively lower requirements of DMC amount and reaction pressure. However, a slightly higher reaction temperature was the downside of this method when compared to those of refined oil-based biodiesel processes. Our method might be improved to lower the reaction temperature by adding alcohol (such as methanol) in the system as a co-reactant. Presumably, the alcohol can react with triglyceride compounds more easily than with DMC. The improvement of our method to meet the international fuel standards as well as to reduce the reaction temperature and residence time will be further investigated in our future work.

Conclusion

High performance of DMC supercritical biodiesel production in a microreactor was proposed in this work as the glycerol-free and non-catalytic biodiesel process. Our proposed process was effective for the

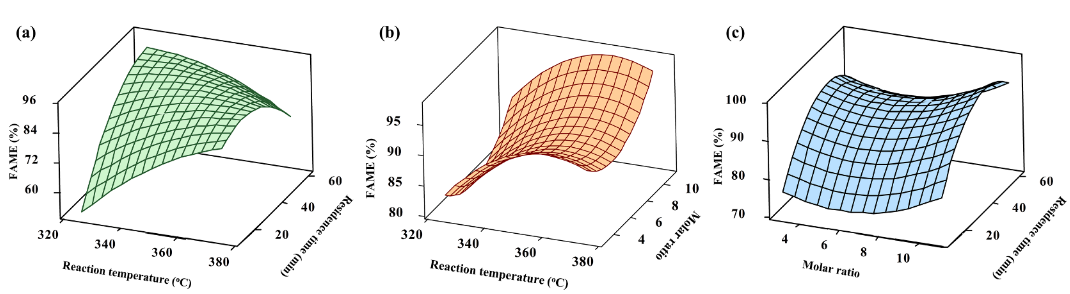

Fig. 8. Surface plots of process variable pairs and %FAME.

Table 4
Properties of biodiesel obtained in our work in comparison with the literature and the international standards.

Properties	RBOFAD biodiesel[a]	CRBO biodiesel[c]	RRBO biodiesel[d]	RRBO BIodiesel[e]	EN 14,214	ASTM D6751
Density (kg/m^3)	890 ± 5	884	877	NA	860 to 900	–
Kinematic viscosity (mm^2/s)	3.8 ± 0.2	4.12	5.29	4.3	3.5 to 5	1.9 to 6.0
Acid value (mg_{KOH}/g)	0.2 ± 0.05	0.45	NA	0.14	0.5 max	0.5 max
Ester content (wt%)	97.1 ± 0.08	98.3	NA	97.4	96.5 min	–
Free fatty acids (wt%)	ND[b]	NA	NA	NA	–	–
Monoacylglycerides (wt%)	1.4 ± 0.04	0.06	NA	0.1	0.80 max	–
Diacylglycerides (wt%)	1.4 ± 0.08	0.04	NA	0.06	0.20 max	–
Triacylglycerides (wt%)	ND	0.04	NA	ND	0.20 max	–

[a] Biodiesle from rice bran oil fatty acid distillate (RBOFAD; 61.5% FFA) produced at the optimal condition (this work).
[b] Not detectable.
[c] Biodiesle from crude rice bran oil (CRBO; 20% FFA) produced with subcritical two-step process (esterification and transesterification) [35].
[d] Biodiesle from refined rice bran oil (RRBO; 2.8% FFA) produced with conventiona alkaline process [36].
[e] Biodiesle from refined rice bran oil (RRBO; <1% FFA) produced with supercritical DMC process [27].

Table 5
Performance assessment of supercritical DMC biodiesel production.

Process type	Raw material	Optimal process conditions[a]				Biodiesel yield (%)	Reference
		T (°C)	P (MPa)	Ratio[a] (mol/mol)	Time (min)		
Batch	Schizochitrium Limacinum microalgae	370	20	10:1	30	50	[37]
Batch	Refined jatropha oil	325	15	40:1	45	99	[38]
Batch	Refined palm oil	380	15	39:1	30	91	[39]
Continuous	Refined rapeseed oil	300	20	42:1	30	97	[27]
Two-step batch	Jatropha curcas oil (FFA:13.6 wt%)	270[b]/300[c]	27[b]/9[c]	217:1[b]/NA[c]	25[b]/15[c]	97	[30]
Continuous	RBOFAD (FFA: 61.5 wt%)	360	8	11:1	35	97.1[d], 94[e]	This work

[a] T: Reaction temperature, P: Pressure, Ratio: DMC-to-oil molar ratio, Time: reaction time
[b] Subcritical water process
[c] DMC supercritical process
[d] Biodiesel content (%FAME)
[e] Biodiesel yield ($kg_{biodiesel}/kg_{RBOFAD}$) × 100

low quality of raw material as demonstrated by using the RBOFAD as feedstock. High quality of biodiesel and high-value glyoxal (by-product) were simultaneously obtained. In addition, the reaction temperature, RBOFAD-to-oil molar ratio, and residence time were the significant operating variables to control the product yield. The trade-off between %FAME and glyoxal content was found in this process. As predicted by the model based on the maximum %FAME, the reaction temperature of 360 °C, residence time of 35 min, and RBOFAD-to-oil molar ratio of 11:1 were the optimal conditions achieving the %FAME of 97.1%. Lower requirements of reaction pressure and DMC amount were the benefits of this process when compared to the transesterification of DMC and refined oil. Based on our fuel quality, most of our biodiesel properties met the requirements of the international standards except for the mono- and diglyceride contents, limiting our biodiesel for cold temperature applications. The areas for improvement of our process would be further investigated to mitigate the requirements on the high reaction temperature and long residence time. The quality of fuel should be improved by reducing the content of impurities, which will be studied in our future works.

CRediT authorship contribution statement

Nattee Akkarawatkhoosith: Conceptualization, Methodology, Investigation, Formal analysis, Validation, Funding acquisition, Writing - original draft. **Tiprawee Tongtummachat:** Investigation, Methodology, Resources, Formal analysis, Writing - original draft. **Amaraporn Kaewchada:** Conceptualization, Project administration, Writing - review & editing. **Attasak Jaree:** Resources, Supervision, Writing - review & editing.

Declaration of Competing Interest

The authors declare that they have no known competing financial interests or personal relationships that could have appeared to influence the work reported in this paper.

References

[1] N. Akkarawatkhoosith, A. Kaewchada, A. Jaree, Simultaneous development of biodiesel synthesis and fuel quality via continuous supercritical process with reactive co-solvent Fuel, 237 (2019), pp. 117-125, DOI:10.1016/j.fuel.2018.09.077.
[2] Silva CD, Castilhos FD, Oliveira JV, Filho LC. **Continuous production of soybean biodiesel with compressed ethanol in a microtube reactor**. Fuel Process Technol 2010;91:1274–81. https://doi.org/10.1016/j.fuproc.2010.04.009.
[3] Trentin CM, Lima AP, Alkimim IP, Silva CD, Castilhos FD, Mazutti MA, et al. Continuous production of soybean biodiesel with compressed ethanol in a microtube reactor using carbon dioxide as co-solvent. Fuel Process Technol 2011; 92:952–8. https://doi.org/10.1016/j.fuproc.2010.12.016.
[4] Gunawan S, Maulana S, Anwar K, Widjaja T. **Rice bran, a potential source of biodiesel production in Indonesia**. Ind Crop Prod 2011;33:624–8. https://doi.org/10.1016/j.indcrop.2010.12.027.
[5] Choi N, Kim H, Kim BH, Kwak J, Lee JS, Kim IH. In situ lipase-catalyzed transesterification in rice bran for synthesis of fatty acid methyl ester. Ind Crop Prod 2018;120:140–6. https://doi.org/10.1016/j.indcrop.2018.04.049.
[6] Akkarawatkhoosith N, Kaewchada A, Jaree A. Continuous catalyst-free biodiesel synthesis from rice bran oil fatty acid distillate in a microreactor. Energy Rep 2020; 6:545–9. https://doi.org/10.1016/j.egyr.2019.11.117.
[7] Lee Y, Lee JH, Yang HJ, Jang M, Kim JR, Byun EH, et al. Efficient simultaneous production of biodiesel and glycerol carbonate via statistical optimization. J Ind Eng Chem 2017;51:49–53. https://doi.org/10.1016/j.jiec.2017.03.010.
[8] Lee Y, Kim SB, Lee T, Jang M, Shin A, Park SJ, et al. Efficient and simultaneous cleaner production of biodiesel and glycerol carbonate in solvent-free system via statistical optimization. J Clean Prod 2019;218:985–92. https://doi.org/10.1016/j.jclepro.2019.01.331.
[9] Ilham Z, Saka S. Dimethyl carbonate as potential reactant in non-catalytic biodiesel production by supercritical method. Bioresour Technol 2019;100:1793–6. https://doi.org/10.1016/j.biortech.2008.09.050.

[10] Wang X, Zhang P, Cui P, Cheng W, Zhang S. Glycerol carbonate synthesis from glycerol and dimethyl carbonate using guanidine ionic liquids. Chin J Chem Eng 2017;25:1182–6. https://doi.org/10.1016/j.cjche.2017.06.025.

[11] Rathore V, Tyagi S, Newalkar B, Badoni RP. Jatropha and Karanja oil derived DMC-biodiesel synthesis: A kinetics. Fuel 2015;140:597–608. https://doi.org/10.1016/j.fuel.2014.10.003.

[12] Jung JM, Oh JI, Kwon D, Park YK, Zhang M, Lee J, Kwon EE Synthesis of fatty acid methyl esters via non-catalytic transesterification of avocado oil with dimethyl carbonate Energy Convers Manage, 195 (2019), pp. 1-6, DOI:10.1016/j.enconman.2019.04.095.

[13] Vodyankina OV, Koscheev SV, Yakushko VT, Salanov AN, Boronin AI, Kurina LN. Physicochemical investigation of the copper and silver catalysts of the ethylene glycol oxidation. J Mol Catal A Chem 2008;158:381–7. https://doi.org/10.1016/S1381-1169(00)00109-6.

[14] Zhu Y, Yao X, Chen S, Cui Q, Wang H. HPLC determination of glyoxal in aldehyde solution with 3-methyl-2-benzothiazolinone hydrazine. Front Chem Sci Eng 2011; 5:117–21. https://doi.org/10.1007/s11705-010-0535-4.

[15] Chumbhale VR, Awasarkar PA. Oxidative dehydrogenation of ethylene glycol into glyoxal over phosphorus-doped ferric molybdate catalyst Appl Catal A-Gen, 205 (2001), pp. 109-115, DOI:10.1016/S0926-860X(00)00580-9.

[16] Foroutan R, Mohammadi R, Ramavandi B. Waste glass catalyst for biodiesel production from waste chicken fat: Optimization by RSM and ANNs and toxicity assessment Fuel, 291 (2021), Article 120151, DOI:10.1016/j.fuel.2021.120151.

[17] Rahimi T, Kahrizi D, Feyzi M, Ahmadvandi HR, Mostafaei M. Catalytic performance of MgO /Fe_2O_3-SiO_2 core-shell magnetic nanocatalyst for biodiesel production of Camelina sativa seed oil: Optimization by RSM-CCD method. Ind Crops Prod 2021;113065:159. https://doi.org/10.1016/j.indcrop.2020.113065.

[18] Mumtaz MW, Adnan A, Mukhtar H, Rashid U, Danish M. Chapter fifteen - biodiesel production through chemical and biochemical transesterification: trends technicalities, and future perspectives. Clean Energy Sustain Dev Comparisons Contrasts New Approaches 2017:465–85. https://doi.org/10.1016/B978-0-12-805423-9.00015-6.

[19] Chamola R, Khan MF, Raj A, Verma M, Jain S. Response surface methodology based optimization of in situ transesterification of dry algae with methanol, H2SO4 and NaOH Fuel, 239 (2019), pp. 511-520, DOI:10.1016/j.fuel.2018.11.038.

[20] Farobie O, Matsumura Y. State of the art of biodiesel production under supercritical conditions. Prog Energy Combust Sci 2017;63:173–203. https://doi.org/10.1016/j.pecs.2017.08.001.

[21] Esan AO, Adeyemi AD, Ganesan S. A review on the recent application of dimethyl carbonate in sustainable biodiesel production J Clean Prod, 257 (2020), Article 120561, DOI:10.1016/j.jclepro.2020.120561.

[22] Akkarawatkhoosith N, Kaewchada A, Jaree A. Enhancement of continuous supercritical biodiesel production process: influence of co-solvent types Energy Procedia, 156 (2019), pp. 48-52, DOI:10.1016/j.egypro.2018.11.085.

[23] Kwon EE, Yi H, Jeon YJ. Boosting the value of biodiesel byproduct by the non-catalytic transesterification of dimethyl carbonate via a continuous flow system under ambient pressure Chemosphere, 113 (2014), pp. 87-92, DOI:10.1016/j.chemosphere.2014.04.055.

[24] Andreo-Martínez P, Martínez VMO, Martínez NG, Ríos APDL, Fernández FJH, Medina JQ. Production of biodiesel under supercritical conditions: State of the art and bibliometric analysis Appl Energy, 264 (2020), Article 114753, DOI:10.1016/j.apenergy.2020.114753.

[25] Marulanda VF, Anitescu G, Tavlarides LL. Investigations on supercritical transesterification of chicken fat for biodiesel production from low-cost lipid feedstocks. J Supercrit Fluid 2010;54:53–60. https://doi.org/10.1016/j.supflu.2010.04.001.

[26] Quesada-Medina J, Carrillo PO. Evidence of thermal decomposition of fatty acid methyl esters during the synthesis of biodiesel with supercritical methanol. J Supercrit Fluid 2011;56:56–63. https://doi.org/10.1016/j.supflu.2010.11.016.

[27] Ilham Z, Saka S. Optimization of supercritical dimethyl carbonate method for biodiesel production. Fuel 2012;97:670–7. https://doi.org/10.1016/j.fuel.2012.02.066.

[28] Dawodu FA, Ayodele OO, Xin J, Zhang S. Dimethyl carbonate mediated production of biodiesel at different reaction temperatures. Renew Energy 2014;68:581–7. https://doi.org/10.1016/j.renene.2014.02.036.

[29] Friedrichs G, Colberg M, Dammeier J, Bentz T, Olzmann M. HCO formation in the thermal unimolecular decomposition of glyoxal: rotational and weak collision effects. Phys Chem Chem Phys 2008;10:6520–33. https://doi.org/10.1039/b809992h.

[30] Ilham Z, Saka S. Two-step supercritical dimethyl carbonate method for biodiesel production from Jatropha curcas oil Bioresour Technol, 101 (2010), pp. 2735-2740, DOI:10.1016/j.biortech.2009.10.053.

[31] Stehmann F, Wiegmann E, Scholl S. Decomposition of dimethyl carbonate caused by adsorption onto activated carbon. Adsorption 2017;23:341–8. https://doi.org/10.1007/s10450-016-9858-x.

[32] Mielke Z, Mucha M, Bil A, Golec B, Coussan S, Roubin P. Photo-induced hydrogen exchange reaction between methanol and glyoxal: formation of hydroxyketene. Chem Phys Chem 2008;9:1774–80. https://doi.org/10.1002/cphc.200800249.

[33] Tang H, Salley SO, Simon Ng KY. Fuel properties and precipitate formation at low temperature in soy-, cottonseed-, and poultry fat-based biodiesel blends. Fuel 2008; 87:3006–17. https://doi.org/10.1016/j.fuel.2008.04.030.

[34] Paryanto I, Prakoso T, Suyono EA, Gozan M. Determination of the upper limit of monoglyceride content in biodiesel for B30 implementation based on the measurement of the precipitate in a Biodiesel-Petrodiesel fuel blend (BXX) Fuel, 258 (2019), Ariticle 116104, DOI:10.1016/j.fuel.2019.116104.

[35] Lin L, Ying D, Chaitep S, Vittayapadung S. Biodiesel production from crude rice bran oil and properties as fuel. Appl Energy 2009;86:681–8. https://doi.org/10.1016/j.apenergy.2008.06.002.

[36] Sinha S, Agarwal AK, Garg S. Biodiesel development from rice bran oil: Transesterification process optimization and fuel characterization. Energy Convers Manag 2008;49:1248–57. https://doi.org/10.1016/j.enconman.2007.08.010.

[37] Rathnam VM, Madras G. Conversion of Shizochitrium limacinum microalgae to biodiesel by non-catalytic transesterification using various supercritical fluids Bioresour Technol, 288 (2019), Article 121538, DOI:10.1016/j.biortech.2019.121538.

[38] Rathore V, Tyagi S, Newalkar B, Badoni RP. Glycerin-free synthesis of jatropha and pongamia biodiesel in supercritical dimethyl and diethyl carbonate. Ind Eng Chem Res 2014;53:10525–33. https://doi.org/10.1021/ie5011614.

[39] Tan KT, Lee KT, Mohamed AR. Optimization of supercritical dimethyl carbonate (SCDMC) technology for the production of biodiesel and value-added glycerol carbonate. Fuel 2010;89:3833–9. https://doi.org/10.1016/j.fuel.2010.07.010.

Hybrid Electrical Air-Cushion Tracked Vehicle for Swamp Peat

Deepikarani Swain, *Department of Mechanical Engineering, NM Institute of Engineering & Technology, Bhubaneswar, depika_r19@yahoo.co.in*

Debi Prasad Singh, *Department of Mechanical Engineering, Raajdhani Engineering College, Bhubaneswar, deboprasad_1159@gmail.com*

Bhagyashree Panda, *Department of Mechanical Engineering, Aryan Institute of Engineering & Technology, Bhubaneswar, bhagyashree2561@gmail.com*

Biswa Ranjan Pradhan, *Department of Civil Engineering, Capital Engineering College, Bhubaneswar, biswaranjanpradhan78@gmail.com*

Abstract: The aim of this paper is to present a hybrid electrical air-cushion tracked vehicle (HETAV) for the operation on swamp peat. Mathematical models are incorporated with accounting kinematics and dynamics behaviors of the vehicle. Sinkage of the HETAV is sensed by an ultrasonic displacement (UD) sensor, in order to operate the air-cushion system. The air-cushion of HETAV is protected with a novel-design auto-adjusting supporting (AAS) system. A propeller is equipped with the vehicle to develop additional thrust for overcoming the dragging motion resistance of the air-cushion system . The performance of the HETAV is defined by traction and motion resistance. The mean value of traction for the swamp terrain with propeller over without propeller increases 10.21% and 6.47% for the vehicle weight of 1.02 kN and 2.04 kN, respectively. Similarly, it was found that the mean values of vehicle's motion resistance decrease 12.63% and 25.81% for the vehicle weight of 2.45 kN and 3.43 kN, respectively.

Keywords: Hybrid vehicle, air-cushion, auto-adjusting-supporting system, UD sensor, propeller.

1. INTRODUCTION

The transportation operation of palm oil fresh fruit bunches (FFB) over the swamp peat terrain is considered as the biggest issue of Malaysia. Different types of University's research institute, government organization, and private companies were introduced different types of vehicles for solving the transportation problems on moderate peat terrain Ref. [1-4]. But still no one offered any vehicle on low bearing capacity swamp peat terrain. *The bearing capacity in this study is defined as maximum load that a material (soil) can support before failing; and swamp is defined as a tract of wet or water-covered ground overgrown with trees and shrubs.*

The main objective of the study is to design and develop the vehicle for justifying the concept to introduce a full-scale vehicle for the transportation operation of agricultural and industrial goods on the low bearing capacity swamp peat terrain in Malaysia. The propulsion system of the vehicle is comprised of track and air-cushion system. The track mechanism is used as the driving system to overcome the rolling motion resistance and the air cushion system is used to increase the floatation capacity of the vehicle. The driving force is provided to each of the track by an individual DC motor. The air-cushion system of this vehicle was designed in such a way that it would not slid on the terrain all the while with the vehicle movement. It only touches the ground and supports the partial load of the vehicle once the vehicle sinkage was closed to 50 mm or more. As the air is compressible fluid, so during the vehicle testing it was found that by increasing the vehicle sinkage the air-cushion supporting system was not sink. But, it slides over the ground once it touches the ground and supports the vehicle. The additional thrust (or tractive effort) is provided to the vehicle by using two propellers for overcoming the drag resistance of the air-cushion system. As the terrain is unprepared and different types of decomposed materials are on the terrain, the air-cushion was protected by a novel design protecting system. It can adjust on the terrain automatically when the vehicle traverse over the root and any other obstacles by absorbing its longitudinal displacement with two horizontally attached shock absorbers and vertical displacement with four vertically attached springs. The air-cushion system makes the vehicle ground contact pressure 5 kN/m^2. The power transmission system of the vehicle is shown in Fig. (**1**). The magnetic pick-up sensor is used in this study to measure the vehicle theoretical speed.

2. MATHEMATICAL MODEL

Mathematical model is formulated with understanding the terrain nature and analyzing the mechanics of track-terrain interaction and the interaction of air-cushion supporting system-terrain. The vehicle is designed mainly for the operation on the swamp peat bearing capacity of 5 kN/m^2. So, the vehicle has chanced to sink even though its operating load is estimated, based on the bearing capacity of the terrain. The tractive effort and motion resistance of the vehicle are formulated in this study, based on two sinkage conditions: (i) sinkage, $0 \le z \le 5cm$ when the vehicle is considered to operate on the moderate peat terrain, and (ii) sinkage, $z \ge 5cm$ when the vehicle is considered to operate

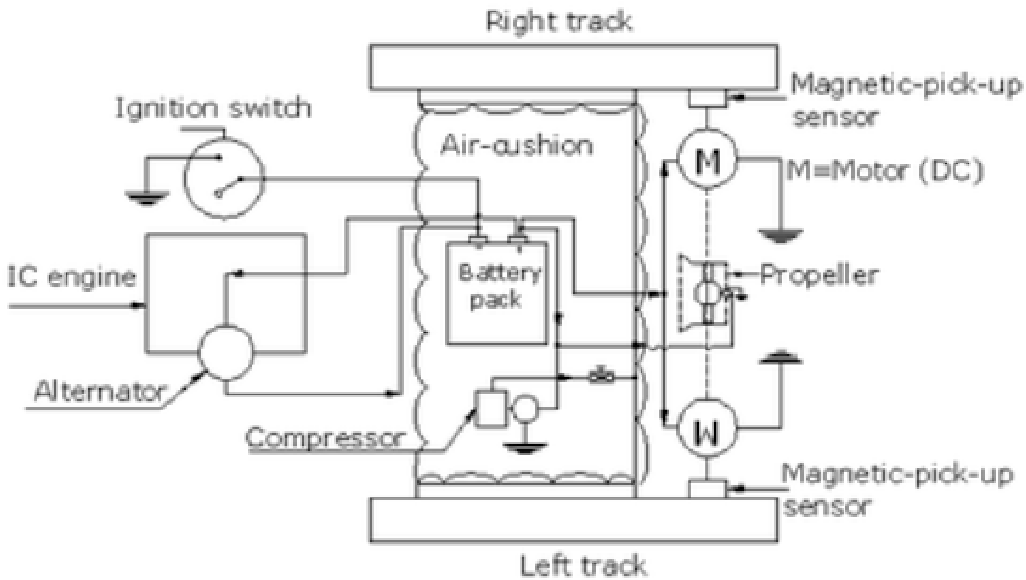

Fig. (1). Vehicle power transmission system.

on swamp peat. Assumptions are made in order to establish the mathematical models: (i) the pressure distribution in the track-terrain interface is assumed to be uniform by locating the vehicle C.G at the mid point of the track system, and (ii) critical sinkage of the vehicle is considered to be 120 mm based on the study of author ref. [5].

Consider a segmented rubber track vehicle of total weight W, track size including track ground contact length L, width B, pitch T_p, and grouser height H, radius of the rear sprocket R_{rs}, and radius of the road-wheels R_r, that is traversing under traction on a swamp peat terrain at a constant speed of v_t as soon as applying the driving torque Q at the rear sprocket. The pressure distribution in the track-terrain interface is assumed to be uniform by locating the vehicle C.G at the mid point of the track system. The pressure at main straight part P, and rear sprocket P_{rs}, and the sinkage of the vehicle z_{rw} and the sinkage of the rear sprocket z_{rs} are revealed same as C.G of the vehicle is located at the middle of the track system, shown in Fig. (**2**).

Traction

The traction equations of the vehicle are developed, mainly based on the vehicle tracked-terrain and tracked-

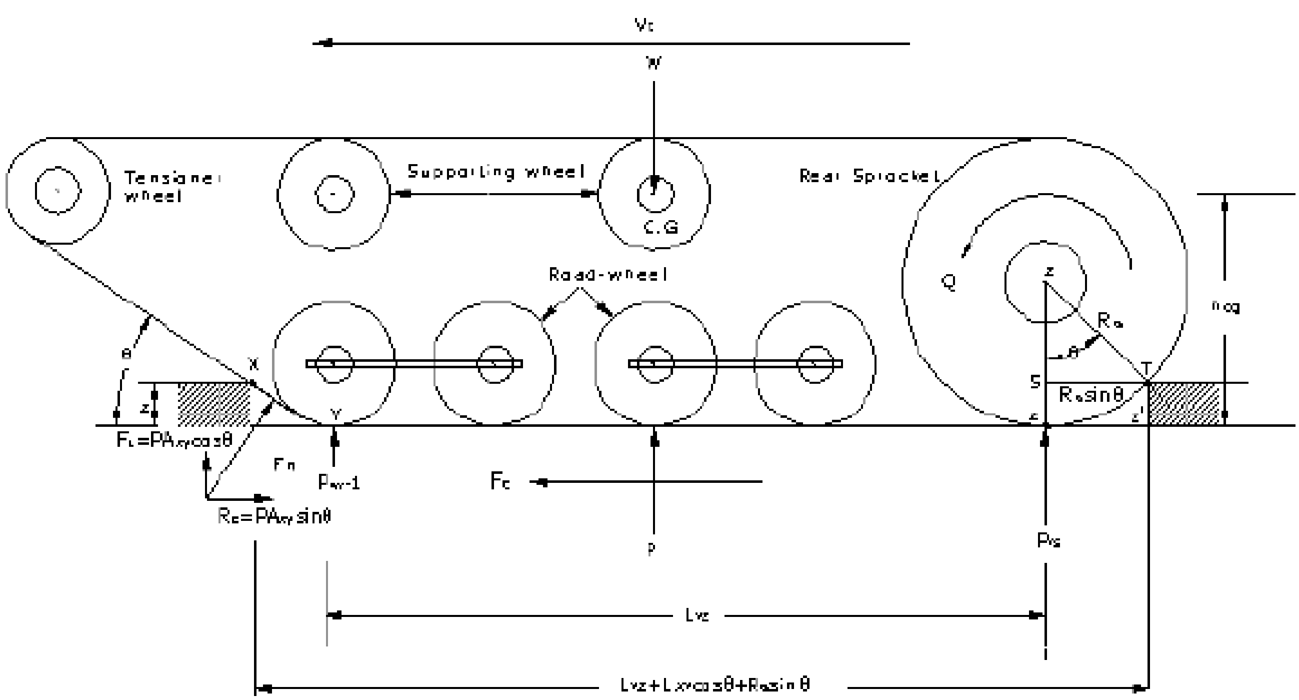

Fig. (2). Force acting on track system.

cushion-terrain interaction mechanism. However, only the traction equation of the vehicle for the moderated terrain is computed based on the track-terrain interaction mechanism by using the recommended equation of ref. [6]:

For sinkage, $0 \le z < 50\ mm$

$$F_b = \left(A_t c + (W_t)\tan\varphi\right)\left[\frac{K_w}{iL}e^1 - \left(1+\frac{K_w}{iL}\right)exp\left(1-\frac{iL}{K_w}\right)\right] \quad (1)$$

where, $A_t = 2(L_{YZ})(B)$ and $L = L_{YZ}$

In Equation (1), F_b is the traction that develops at the bottom part of the track in kN, L is the ground contact part of the track in m, A_t is the area of the track ground contact length in m^2, W_t is the vehicle load supported by the track system in kN, c is the cohesiveness in kN/m^2, φ is the terrain internal friction angle in degree, K_w is the shear deformation modulus of the terrain in m, i is the slippage of the vehicle in percentage, and B is the width of the track in m.

For sinkage, $z \ge 50\,mm$

The vehicle will start to sink severely when the vehicle is assumed to operate on the swamp peat. In this case, the vehicle load will be partially supported by the air-cushion system. It is assumed that the air-cushion system of the vehicle will be in contact with the terrain when the vehicle sinkage is more than 50mm (i.e, $z \ge 50\,mm$). The drag motion resistance develops due to the dragging of the air-cushion support system with the terrain, which will significantly affect on the vehicle mobility. Therefore, the additional thrust of the vehicle will be needed to develop, in order to overcome the dragging motion resistance of the vehicle. The traction of the vehicle F_t is calculated by using the recommended equation of ref. [7]:

$$F_t = \left(A_t c + W_t \tan\varphi\right)\left[\begin{matrix}\frac{K_w}{iL}e^1 - \\ \left(1+\frac{K_w}{iL}\right)exp\left(1-\frac{iL}{K_w}\right)\end{matrix}\right] + F_{tac(add)} \quad (2)$$

where, $A_t = \left(L_{XY}\cos\theta + L_{YZ} + R_{rs}\sin\theta\right)\left(2B\right)$,

$$L = \left(L_{XY}\cos\theta + L_{YZ} + R_{rs}\sin\theta\right) \text{ and } L_{XY} = \frac{z}{\sin\theta}$$

In Equation (2), $F_{tac(add)}$ is the additional tractive effort developed by the propeller in kN, and θ is the angle between the track of 1st road-wheel to tensioned wheel and the ground in degree.

Fig. (**3**) shows the mechanics of the automated adjusted - air-cushion protecting system. It is made in such a way that its weight does not affect on the vehicle's ground contact pressure and its vertical and longitudinal displacements don't affect the air-cushion inflation pressure as well. The basic objective of this system is to protect the air-cushion system from the external threat on the ground by adjusting its vertical and longitudinal displacements automatically.

The air-cushion system is attached with the HETAV, only for stopping the vehicle sinkage and increasing the vehicle floatation capacity. It would be incurred for the vehicle, once the vehicle transfers its load to the air-cushion system. Load transferring of the vehicle to the air-cushion system starts when the vehicle gets its sinkage 50 mm or more. The load transfer of the vehicle to the air-cushion system could be formulated as follows:

$$W_{v(ac)} = \left(P' - P\right)\left(A_{BC}\right) = \left(P_0'\right)\left(A_{BC}\right) \quad (3)$$

For sinkage, $z_{acs} = 0.0\,mm$

$$W_{v(ac)} = \left[P' - \left(k_p z_{acs} + \frac{4}{D_{hac}} m_m {z_{acs}}^2\right)\right]\left(A_{BC}\right) \quad (4)$$

where, $$z_{acs} = \frac{-\left(\frac{k_p D_{acs}}{4m_m}\right) \pm \sqrt{\left[\left(\frac{k_p D_{acs}}{4m_m}\right)^2 + \frac{D_{acs}}{m_m}P_0'\right]}}{2}$$ and

$$D_{acs} = \frac{4\left(B_{acs}\right)\left(L_{BC}\right)}{2\left(L_{BC} + B_{acs}\right)}$$

For sinkage, $z > 50\,mm$

$$W_{v(ac)} = \left[P' - \left(k_p z_{acs} + \frac{4}{D_{hac}} m_m {z_{acs}}^2\right)\right]\left(A_{BC} + 2A_{BC'}\right) \quad (5)$$

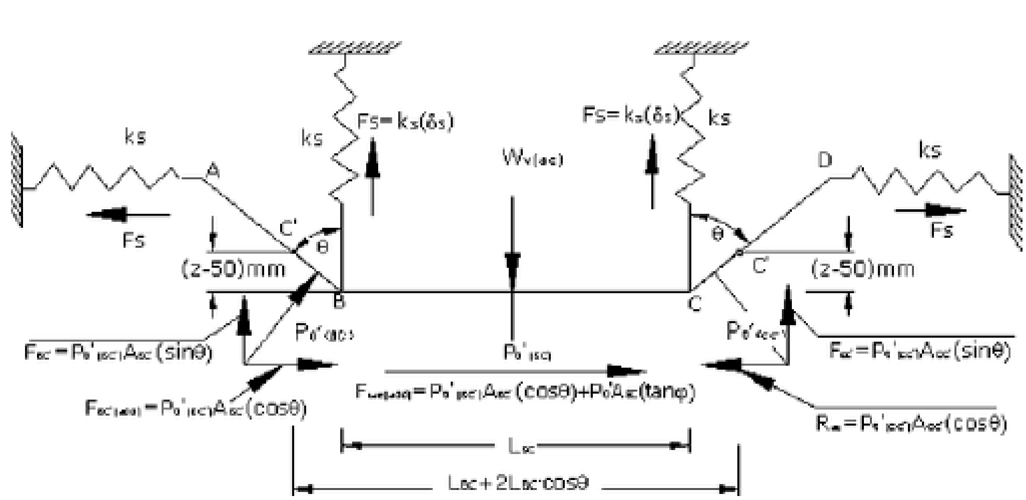

Fig. (3). Air-cushion support system.

where, $z_{acs} = \dfrac{-\left(\dfrac{k_p D_{acs}}{4m_m}\right) \pm \sqrt{\left[\left(\dfrac{k_p D_{acs}}{4m_m}\right)^2 + \dfrac{D_{acs}}{m_m} P_0'\right]}}{2}$ and

$D_{acs} = \dfrac{4(B_{acs})(L_{BC} + 2L_{BC}\cos\theta)}{(L_{BC} + 2L_{BC}\cos\theta + B_{acs})}$

In Equation (3), P_0' is the ground nominal pressure which could exist due to the transfer load of the vehicle to the air-cushion system in kN/m^2, P' is the vehicle ground contact pressure in kN/m^2, and A_{BC} is the contact area of the air-cushion support system as shown in Fig. (**3**). It is noted that the vehicle sinkage will be zero or less than 50 mm (i.e, $0.0\, mm \le z < 50\, mm$ or $P_0' = 0$), which indicates that the air-cushion will not be in contact with the terrain. In swamp peat terrain, it is absolutely not possible to make the sinkage zero (i.e.,z = 0) for any vehicle. While in some instant it could be less than 50mm. The sinkage of this vehicle will be more than 50 mm, if the vehicle is not equipped with air-cushion. Therefore, the vehicle sinkage will be limited to 50 mm by using an air-cushion system. The air-cushion system supports the vehicle's partial load and makes the vehicle ground contact pressure less than the ground (terrain) nominal pressure.

In Equations (4) and (5), z_{acs} is the sinkage of the air-cushion-support system in m, and D_{acs} is the hydraulic diameter with respect to the air-cushion-support system in m.

The additional thrust that was developed by the vehicle at the air-cushion system could be calculated as follows:

For sinkage, $z < 50\, mm$ when the vehicle load is considered 2.45 kN.

$$F_{tac(add)} = P_0' A_{BC}(\tan\varphi) \tag{6}$$

For vehicle sinkage, $z > 50\, mm$ when the vehicle load is considered 3.43 kN.

$$F_{tac(add)} = P_0' A_{AB}(\cos\theta) + P_0' A_{BC}(\tan\varphi) \tag{7}$$

Motion Resistance

The motion resistance is due to the rolling resistance of the track system, which is mainly due to the terrain compaction. Furthermore, the external motion resistance of the vehicle will also be incurred due to the dragging of the air-cushion, when the vehicle will sink 50 mm or more. The motion resistance of the vehicle due to the train compaction:

For sinkage, $z = 0.0\, mm$

$$R_c = 2(P)(B)(L_{YZ})(\tan\varphi) \tag{8}$$

where, $P = \left(k_p z + \dfrac{4}{D_{ht}} m_m z^{\ 2}\right)$,

$z = \dfrac{-\left(\dfrac{k_p D_{ht}}{4m_m}\right) \pm \sqrt{\left[\left(\dfrac{k_p D_{ht}}{4m_m}\right)^2 + \dfrac{D_{ht}}{m_m} p'\right]}}{2}$,

$D_{ht} = \dfrac{4BL_{YZ}}{2(L_{YZ} + B)}$ and $P' = \dfrac{W}{(L_{YZ})(2B)}$

For sinkage, $z = 50\, mm$

$$R_c = (2)(B)(L_{YZ} + L_{XY}\cos\theta + R_{rs}\sin\theta)(P) + P_0' A_{BC}(\tan\varphi) \tag{9}$$

where, $P = P_0'$, P is the nominal ground pressure that is considered for tracked system, while P_0' is for cushion support system. The pressure P could be computed by using the following equation of ref. [8]:

where, $P = \left(k_p z + \dfrac{4}{D_{ht}} m_m z^{\ 2}\right)$,

$D_{ht} = \dfrac{(4)(B)(L_{YZ} + L_{XY}\cos\theta + R_{rs}\sin\theta)}{2(L_{YZ} + L_{XY}\cos\theta + R_{rs}\sin\theta + B)}$ and

$P = \dfrac{W}{(L_{YZ} + L_{XY}\cos\theta + R_{rs}\sin\theta)(2B)}$

For vehicle sinkage, $z > 50\, mm$

$$R_c = (2)(B)(L_{YZ} + L_{XY}\cos\theta + R_{rs}\sin\varphi)(P) + P_0' A_{CD}(\cos\theta) + P_0' A_{BC}(\tan\varphi) \tag{10}$$

For the sinkage, $z > 50\, mm$, the hydraulic diameter D_h of the vehicle for the track system will follow the same equation as stated in Equation (18). Only the L_{XY} will change due to the change in the position of X on the track, as shown in Fig. (**2**).

3. SIMULATION

Fig. (**4**) shows the swamp peat terrain in Malaysia. The bearing capacity of swamp peat in Malaysia is considered 5kN/m² based on the study of ref. [9] and surface mat thickness 50 mm have been considered in this study. Authors ref. [8] reported that the surface mat of the peat or muskeg terrain is the traficability of the terrain to allow the vehicle to travel rather than to sink. The swamp peat terrain parameters include: ω is the moisture content in percentage, c is the cohesiveness in kN/m^2, φ is the internal frictional angle in degree, K_w is the shear deformation modulus in m, m_m is the surface mat stiffness in kN/m^3, and k_p is the underlying peat

Fig. (4). Photo of swamp peat in Malaysia.

Table 1. Terrain Parameters

Parameters	Un-drained	
	Sepang	Sarwak
	Mean Value	Mean Value
ω, (%)	90.51	98
γ, (g/cm^3)	0.082	0.045
c, (kN/m^2)	0.78	0.38
φ, degree)	12.64	20
K_w, (cm)	0.635	1.24
M_m, (kN/m^3)	14.42	7.42
K_p, (kN/m^3)	119.65	59.65

Source: Ataur *et al.* (2004).

stiffness in kN/m^3, as shown in Table **1**. As the mechanical properties of the swamp peat terrain is very difficult to measure and is not available, in this study the swamp peat terrain is considered 50% worst than the peat terrain parameters of Sepang based on the study of ref. [10]. The vehicle loading conditions of 2.45 kN and 3.43 kN and the traveling speed of 12 km/h are considered for the study of vehicle design parameters. The simulation on the vehicle design parameters and performance are conducted by using the MATLAB.

Fig. (**5**) shows the relationship between the vehicle tractive effort and motion resistance. Result shows that the vehicle is able to traverse on the terrain, if the vehicle terrain compaction motion resistance remains within the shaded area. In this study, the vehicle with total contact area 1.052 m^2 including 0.544 m^2 of air-cushion area was optimized based on the bearing capacity of the terrain. Therefore, the track system will only be able to develop 0.75 kN, while the additional 0.15 kN tractive effort has needed to develop by the propeller, in order to traverse the vehicle on the peat terrain with overcoming the motion resistance.

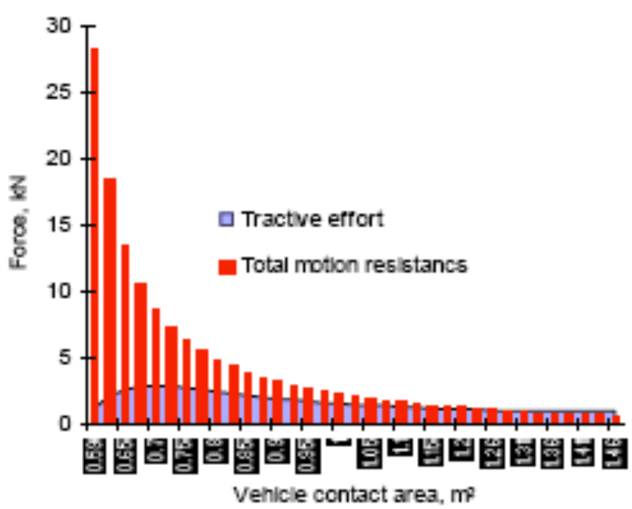

Fig. (5). Relationship between the force and the motion resistance for the vehicle weight =3.43 kN.

Fig. (**6**) shows the load distribution (defined as the load transferred from the traveling system to air-cushion system in order to limit the vehicle sinkage and to maintain the vehicle ground contact pressure). The load distribution to the air-cushion system is decreased linearly by increasing the track ground contact area. The vehicle with ground contact area of 1.052 m^2 has distributed load of 0.45 kN and power consumption by the propeller of 1.02 kW.

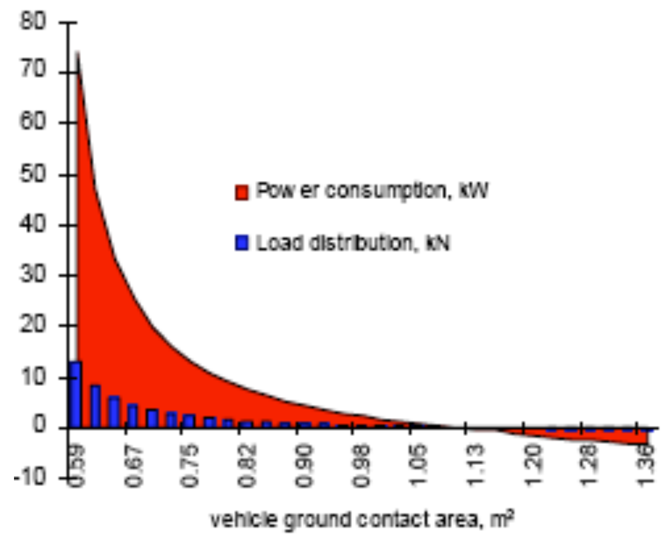

Fig. (6). Relationship of the power consumption and load distribution for the vehicle weight = 3.43 kN.

The vehicle optimum ground contact area of 1.052 m^2 which included track ground contact area of (2 x 1.0 m x 0.254 m) or 0.508 m^2 and air-cushion area of 0.544 m^2, the vehicle traveling length of 200 m over the swamp peat terrain and the vehicle loading conditions of 2.45 kN and 3.43 kN are considered for the simulation of vehicle ground contact pressure, traction, and load distribution. Fig. (**7**) shows the difference of vehicle ground contact pressure over the ground nominal pressure (GNP). *Ground nominal pressure is defined as the pressure that exists from the ground with respect to the static or dynamic vehicle on that ground. While the vehicle ground contact pressure is defined as the pressure that distributes to the ground with the ground contact area of the vehicle.* Result showed that the VGP-without air-cushion is always higher than the ground nominal pressure. It is noted earlier in this study that the

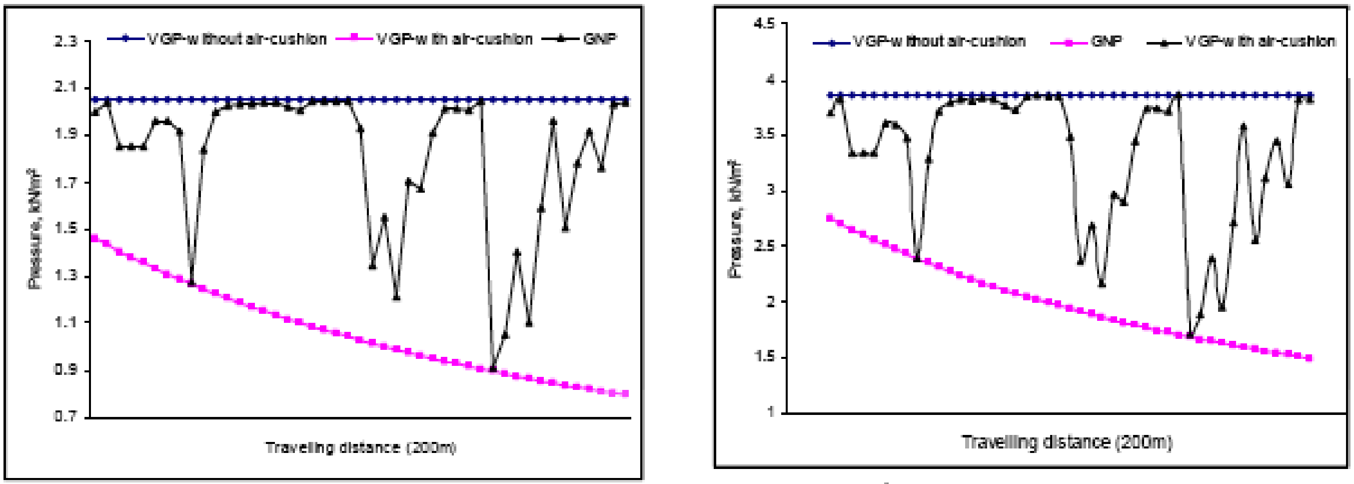

(a) Vehicle weight = 2.45 kN (b) Vehicle weight = 3.43 kN

Fig. (7). Variation of the vehicle ground contact pressure (VGP) and ground nominal pressure (GNP).

vehicle will sink, if $P > P_0'$ and it is also supported by ref. [11]. Therefore, air-cushion system is attached with the vehicle in order to maintain the vehicle sinkage and ground contact pressure. By using the air-cushion system, the VGP is always lower than the GNP. So, the vehicle would be able to travel on the terrain without any risk.

The vehicle was designed in such a way that it would travel on the moderate type of peat terrain with the help of tracked system by overcoming the motion resistance as the tracked total ground contact area was optimized based on the minimum motion resistance exist on the tracked system, bearing capacity of the moderate terrain of 12 kN/m^2, and maximum traction developed by the tracked system both in straight and turning motion. In this study, the simulation on the motion resistance and traction was conducted for the vehicle on 200 m traveling distance swamp peat terrain. Fig. (**8**) shows that the vehicle would stuck on the terrain if $(VT - without\ air - cushion) < VRT$. *VT is defined as the vehicle traction (tractive effort) and VRT is defined as the vehicle total motion resistance.* But, it would traverse on the terrain if $(VT - with\ air - cushion) > VRT$. Therefore, it would be concluded that the air-cushion system is a crucial part for the vehicle, which reduce the vehicle motion resistance with reducing the vehicle sinkage. Furthermore, the traction of this vehicle would need to increase in order to overcome the vehicle total motion resistance. So, emphasis has been given to equip a propeller with the vehicle to develop additional thrust.

Fig. (**9**) shows that the load transfer to the air-cushion system increases with increasing the vehicle loading conditions which significantly affect the power consumption by the vehicle for overcoming the motion resistance. This conclusion is also supported by ref. [12]. Therefore, the loading condition for this vehicle is limited to 3.43 kN, as the power of the vehicle battery pack is 3.5 kW.

4. VEHICLE DEVELOPMENT

Fig. (**10**) shows the designed and developed HETAV. Steering of this vehicle was achieved by means of an individual switch of the DC motor with a power of 0.500kW@2.94 Nm. The dry weight of the vehicle equals to 1.02 kN. The vehicle is designed mainly for operating maximum load of 3.43 kN, including 1.02 kN payload over

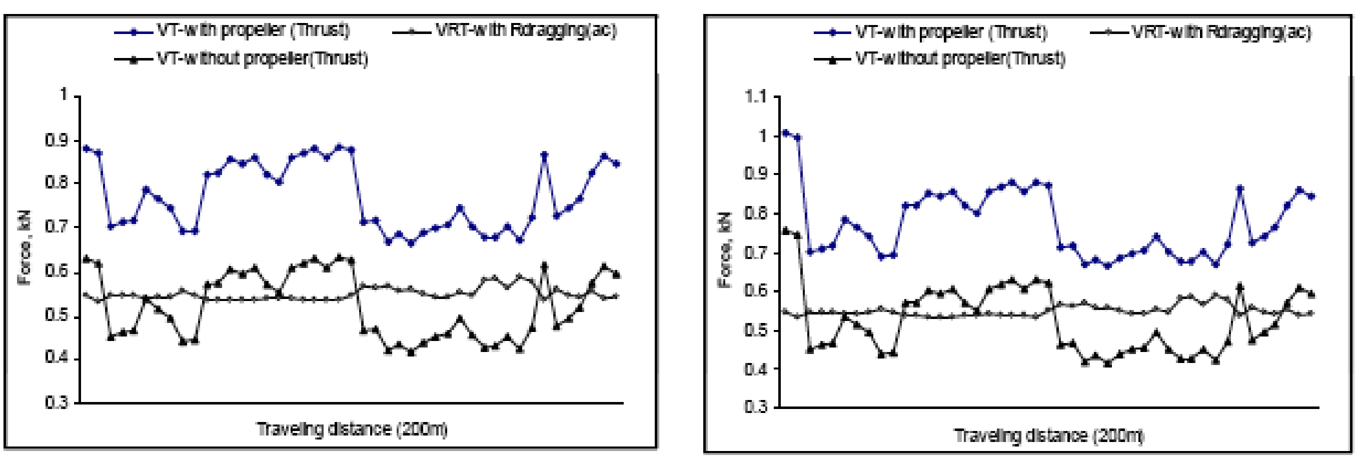

(a) Vehicle weight = 2.45 kN (b) Vehicle weight = 3.43 kN

Fig. (8). Variation of the vehicle traction (VT) and vehicle motion resistance (VRT).

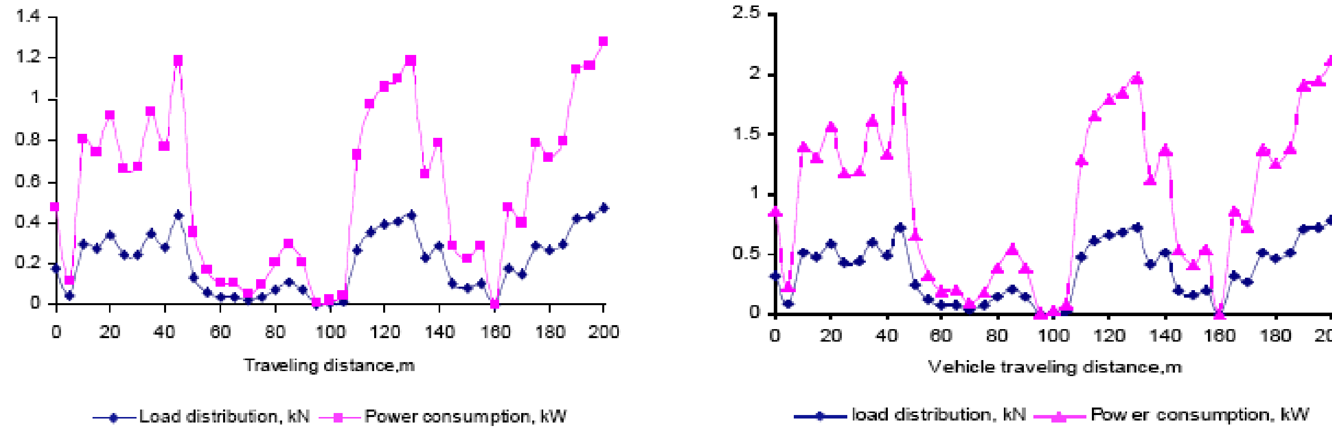

(a) Vehicle weight = 2.45 kN

Vehicle weight = 3.45 kN

Fig. (9). Affect of load distribution of air-cushion on the vehicle power consumption.

the swamp peat terrain. The total ground contact area of the vehicle is 1.052 m^2, which sum-up the track ground contact area of (2x1 m x 0.254 m) or 0.508 m^2 and the air-cushion contact area of 0.544 m^2. The vehicle is powered by a battery pack comprising of four batteries (4 x 3 kg) of 12 volts, connected in parallel. The vehicle can travel 15km by using the power from the single charged battery pack. A small IC Engine power of 2.5 kW@4000 rpm is installed on the vehicle to recharge the battery pack with the help of an alternator. The vehicle is controlled by a remote control system from the road side in order to avoid the risk, if there is any.

Fig. (10). Photo of the vehicle.

5. FIELD (LABORATORY) EXPERIMENT

Vehicle was tested on the swamp peat terrain at a traveling speed of 10 km/h and 15 km/h with the loading conditions of 2.45 kN and 3.43 kN including the dry weight of .02 kN. The vehicle traveling distance during testing was considered 50 m. During testing it was found that to travel over the swamp peat without payload is not a problem for vehicle, but the vehicle starts to sink when its load increased to 2.45 kN and 3.43 kN. Furthermore, the vehicle was tested on the swamp terrain by using the air-cushion system with two conditions: (i) without operating the propeller, and (ii) with operating the propeller. The output torque of the DC motor was measured and was converted into tractive effort. The motion resistance test was performed by pulling the vehicle with an auxiliary vehicle. It was noted that a loaded cell was placed in between the tested and auxiliary vehicle. Data were recorded from the loaded cell in every 5 seconds. Figs. (**11-13**) show the typical variations of tractive effort and motion resistance of the HETAV. The mean values of vehicle tractive effort and motion resistance are shown in Table **2**.

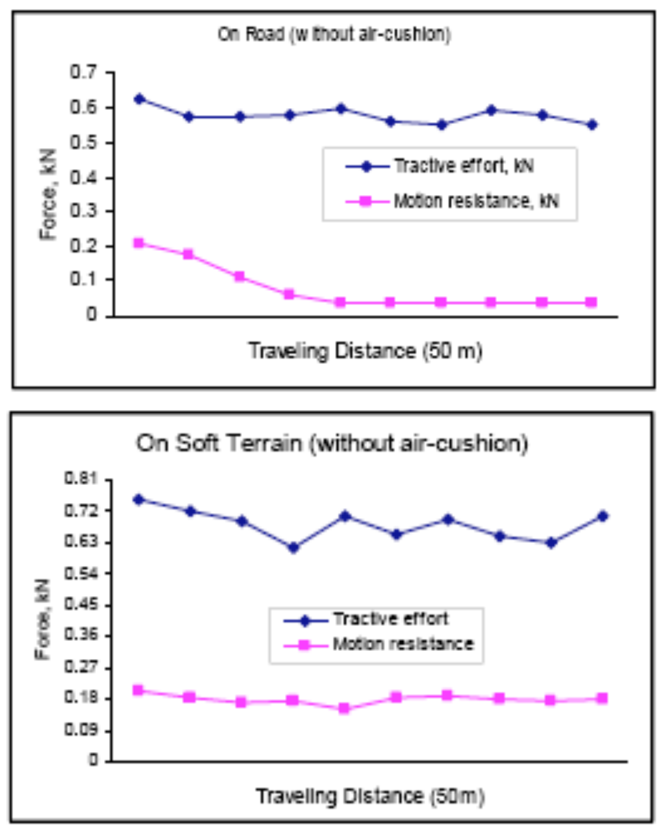

Fig. (11). Variation of tractive effort and motion resistance for the vehicle weight=2.45 kN.

The results show that the mean value of traction for the swamp terrain with the propeller over without propeller increases 10.21% and 6.47% for the vehicle weight of 2.45

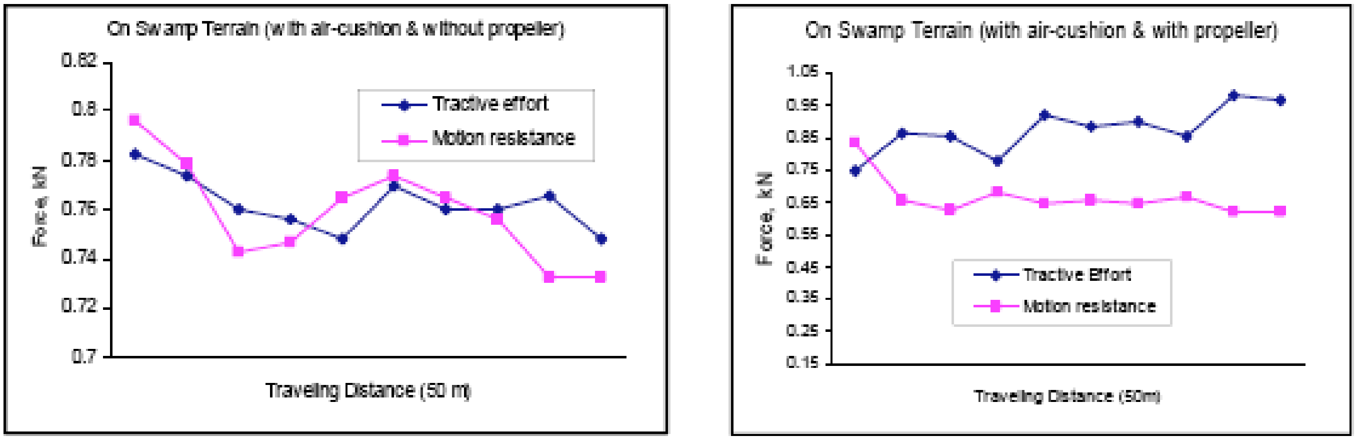

Fig. (12). Variation of tractive effort and motion resistance for the vehicle weight=2.45 kN.

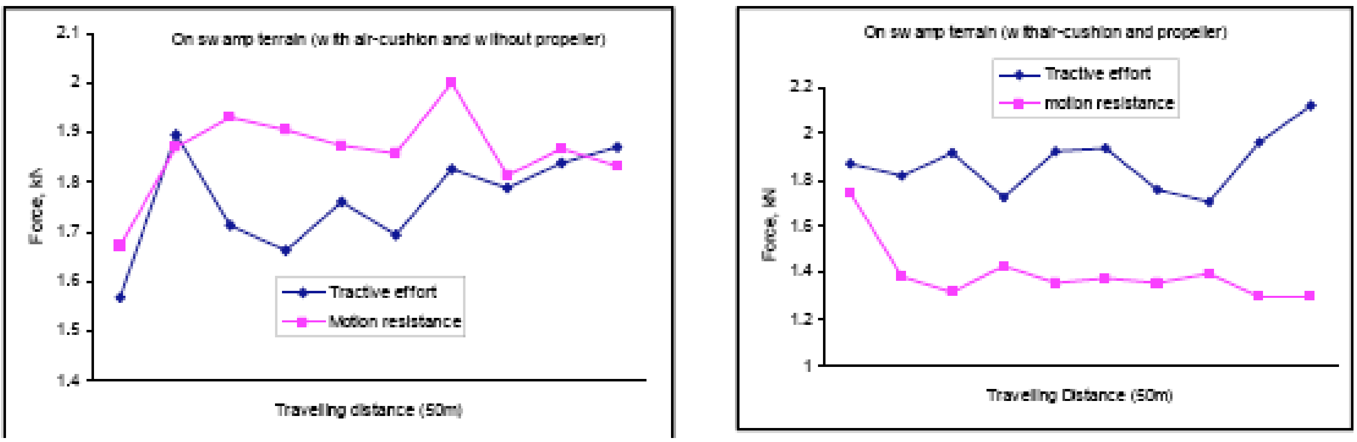

Fig. (13). Variation of tractive effort and motion resistance for the vehicle weight =3.43 kN.

kN and 3.43 kN, respectively. Similarly, it was found that the motion resistance decreases 12.63% and 24.81% for the vehicle weight of 2.45 kN and 3.43 kN, respectively. It is concluded that the increment and decrement of the tractive effort and motion resistance are due to the additional tractive effort developed by the propeller. Furthermore, the mean value of tractive effort increases swamp terrain mainly due to the increment of loading conditions of the vehicle as the cohesiveness of the field is approximately constant for all the traveling length. The conclusion is also supported by the conclusion remarks of ref. [8], ref. [10], and ref. [11].

6. CONCLUSIONS

The conclusions that are made based on the discussion of this study are as follows:

1. The air cushion was activated as soon as the vehicle sinkage was closed to 0.05 m.

2. Based on the simulation result, the following conclusions could be made:

(i) The vehicle load distribution to the air-cushion system would not be too much, since the power consumption by the air-cushion drag motion resistance is too high

Table 2. Mean Values of Tractive Effort and Motion Resistance

Tractive Effort (kN)				Motion Resistance (kN)			
Vehicle Weight = 1.02 kN							
Road	Soft-terrain	Swamp-terrain (equipped with air-cushion)		Road	Soft-terrain	Swamp-terrain (equipped with air-cushion)	
		Without Propeller	Without Propeller			Without Propeller	Without Propeller
0.579	0.682	0.793	0.874	0.077	0.1796	0.76	0.664
Vehicle Weight = 2.04 kN							
0.976	1.86	1.76	1.874	0.201	0.3625	1.862	1.4

which is also supported by the author ref. [3]. Other than that, the power of the battery pack is too limited.

(ii) The vehicle must have needed to develop an additional thrust of at least 0.2 kN, as the vehicle track ground contact area is optimized by 0.505 m^2.

(iii) Air-cushion system of the vehicle makes the vehicle ground contact pressure less than 5 kN/m^2, with partially supporting the vehicle load.

(iv) The propellers must have to manage an additional thrust of 0.20 kN, while the track system developed only 0.665 kN and 1.674 kN.

3. The battery pack provided the power to the DC motor only for a 15 km traveling distance, which was found based on the depth-of-discharge of the battery.

4. Based on the laboratory experimental results, the following conclusion could be made:

(i) According to the mean values of vehicle tractive performance in terms of tractive effort and motion resistance, the vehicle would not be able to traverse on the swamp terrain with air-cushion and the additional thrust of the propeller.

(ii) The mean value of the tractive effort of the vehicle increases by increasing the vehicle loading conditions and it could be due to the changing of the track ground contact area. Since the track width is constant and the track ground contact length increases with increasing the sinkage. So that the track ground area is the function of the track ground contact length i.e $A = \oint(L, W)$

where, $L = L_{YZ} \; or \; L_{YZ}(1+\cos\theta) + R_{RS}\sin\theta$ and vehicle load as well.

(iii) Traction coefficient of the vehicle in the range of 77-85% make the vehicle highly potential to operate on the swamp peat terrain.

(iv) The vehicle sinkage is not possible to limit at 50 mm, if the vehicle is not equipped with air-cushion system. Furthermore, the vehicle will stuck on the swamp terrain, if the vehicle is equipped with air-cushion and the dragging motion resistance of the air-cushion system is considerably high. Therefore, the vehicle must have to equip with air-cushion system and propeller in order to operate on the swamp terrain without any difficulties.

(v) The novel-design-air-cushion supporting system will make the vehicle more vulnerable to operate on the real swamp peat, as it allows the vehicle to traverse on any unprepared terrain with adjusting the air-cushion automatically by absorbing the longitudinal and vertical displacement.

5. Based on the operating performance of this small-scale vehicle, it could be justified that by introducing the same concept, a full-scale vehicle could be introduced in the swamp peat terrain which would be highly potential for the transportation operation of agricultural goods and others industrial products.

REFERENCE

[1] H. S. Ooi, "Theoretical investigation on the tractive performance of MALTRAK on soft padi soil," MARDI, Report no.116, 1993.

[2] H. S. Ooi, "Design and development of peat prototype track type tractor", MARDI, Report no. 184, 1996.

[3] A. Shuib, and A. Hitam, "Wakfoot the FFB evacuation vehicle. PORIM Information Series. Palm Oil Research Institute of Malaysia," PORIM TT No. 20, Pamphlet, 1998.

[4] A. Yahya, M. S. Jaafar, and K. Aribi, "Mechanical infield collection of oil palm fresh fruit bunches," Fruit, Nut, and vegetable production engineering, Vol. 1, pp. 317-326, 1997.

[5] R. Ataur, Y. Azmi, M. Zohadie, D. Ahmad, and W. Ishak, "Design and development of a segmented rubber tracked vehicle for Sepang peat terrain in Malaysia," International Journal of Heavy Vehicle Systems, Inderscience. Vol. 12, No. 3, pp. 239-267, 2005.

[6] R. Ataur, Y. Azmi, and A. K. M. Mohiuddin, "Mobility investigation of a designed and developed segmented rubber track vehicle for sepang peat terrain in Malaysia," Journal of Automobile Engineering, Proceedings of the IMech E Part D, Vol. 221 (D7), pp. 789-800.

[7] Z. Luo, F. Yu, and B.C. Chen, "Design of a novel semi-tracked air-cushion vehicle for soft terrain", International Journal of Vehicle Design, Vol. 31, No. 1, pp. 112-123, 2003.

[8] J. Y. J. Wong, R. Radforth, and J. Preston-Thomas, "Some further studies on the mechanical properties of muskeg in relation to vehicle mobility," Journal of Terramechanics, Vol. 19, No. 2, pp. 107-127, 1982.

[9] B. J. Jamaluddin, 2002, "Sarawak peat agricultural uses," [online]. Available: http://www.Alterra.dlo.nl/ [Accessed Feb 2005].

[10] R. Ataur, Y. Azmi, B. Zohaide, D. Ahmad, and I. Wan, "Mechanical properties in relation to mobility of Sepang peat terrain in Malaysia," Journal of Terramechanics, Vol .41, No. 1, pp. 25-40, 2004.

[11] A. Bodin, "Development of a tracked vehicle to study the influence of vehicle parameters on tractive performance in soft terrain," Journal of Terramechanics, Vol. 36, pp.167-181, 1999.

[12] I. C. MacFarlane, Muskeg Engineering Handbook, Toronto, University of Toronto Press, 1969.

POSTER PRESENTATION

Suspension System Based on Genetic Algorithm and Neural Network Control

Shakyasingha Sahoo, *Department of Mechanical Engineering, NM Institute of Engineering & Technology, Bhubaneswar, shakyasinghasahoo@gmail.com*

Alok Sunder Mohanty, *Department of Mechanical Engineering, Aryan Institute of Engineering & Technology, Bhubaneswar, aloksundar75@gmail.com*

Satyaprakash Mishra, *Department of Civil Engineering, Capital Engineering College, Bhubaneswar, satyaprakash_m25@gmail.com*

Abstract: In this paper, a five degree of freedom half body vehicle suspension system is developed and the road roughness intensity is modeled as a filtered white noise stochastic process. Genetic algorithm and neural network control are used to control the suspension system. The desired objective is proposed as the minimization of a multi-objective function formed by the combination of not only sprung mass acceleration, pitching acceleration, suspension travel and dynamic load, but also the passenger acceleration. With the aid of software Matlab/Simulink, the simulation model is achieved. Simulation results demonstrate that the proposed active suspension system proves to be effective in the ride comfort and drive stability enhancement of the suspension system. A mechanical dynamic model of the five degree of freedom half body of vehicle suspension system is also simulated and analyzed by using software Adams.

INTRODUCTION

Suspension is the term given to the system of springs, shock absorbers and linkages that connects a vehicle to its wheels. Suspension systems can not only contribute to the car's handling and braking for good active safety and driving pleasure, but also keep vehicle occupants comfortable and reasonably well isolated from road noise, bumps, and vibrations. The suspension also protects the vehicle itself and any cargo or luggage from damage and wear. The ride quality of a vehicle is significantly influenced by its suspension system, the road surface roughness, and the speed of vehicle. A vehicle designer can do little to improve road surface roughness, so designing a good suspension system with good vibration performance under different road conditions become s a prevailing philosophy in the automobile industry. Passive suspension systems use conventional dampers to absorb vibration energy, the dampers and stiffness coefficients are constant. The active suspension system use extra power to provide a response-dependent damper, which is capable of producing an improved ride comfort. Over the years, both passive and active suspension systems have been proposed to optimize a vehicle's ride quality. O. GD used genetic algorithm to obtain the optimal set and suspension design (O. GD. IJIE 2007) [1], Sun L, Cai XM, Yang J. got the minimum dynamic pavement load through the genetic algorithm (Sun L, Cai XM, Yang J. JSV 2007) [2]. A simplified algorithm for the evaluation of a small car suspension model can be found in the papers of T.G. Chondros (T.G. Chondros, S. Michalitsis, S. Panteliou and A.D. Dimarogonas 1994) [3] and (T.G. Chondros, P.A. Belokas, K. Vamvakeros and A.D. Dimarogonas 1997) [4], Furthermore, a more detailed model for heavy vehicles suspension systems are given in the paper (Chondros T. G., Michalos G, Michaelides P, Fainekos E 2007) [5]. The state-of-the-art review on neural networks in automotive applications can be found in the papers (J.T. Papadimitropoulos, T.G. Chondros, S.D. Panteliou, B. Carlsson, S. Kalogirou and A.D. Dimarogonas 1999) [6] and (S. Kalogirou, T.G. Chondros, A.D. Dimarogonas 2000) [7].

A variety of research projects and publications deal with different types of active suspension systems have been discussed (Yeh, E.C. and Tsao, Y.J. 1994) [8]. Different vehicle dynamic models have been adopted according to different study purposes during research. A two degree-of - freedom quarter body of vehicle suspension system model had been widely applied in vehicle suspension control research, it can indicate the vehicle body vertical movement, but not include the pitching movement of the vehicle body. Although a seven degree-of -freedom whole-body of vehicle suspension system model can describe not only the vertical movement of the four wheels and the body center of gravity, but also the pitching and lateral movement, the model is too complicated to be widely applied. In our research, a five-degree-of -freedom half body of vehicle suspension system model is established, which can describe both the vertical movement and the pitching movement of the body, what's more, it can demonstrate the effect of the passenger, which makes it to be a relatively ideal model for suspension dynamic description.

From the flow chart before using ADAMS, we can see that the mechanical engineer and the control engineer use different software, build repeated model for one concept design, moreover, different design validation and tests are made. Once there is something wrong, no matter what kind of fault appears, both the mechanical system and the control system will have to be designed again. Fig. (**1**) shows the flow chart before using ADAMS, and Fig. (**2**) shows the flow chart after using ADAMS.

From Fig. (**2**), the flow chart after using ADAMS, we can see that the mechanical engineer and the control engineer share the same virtual model, thus the mechanical design can

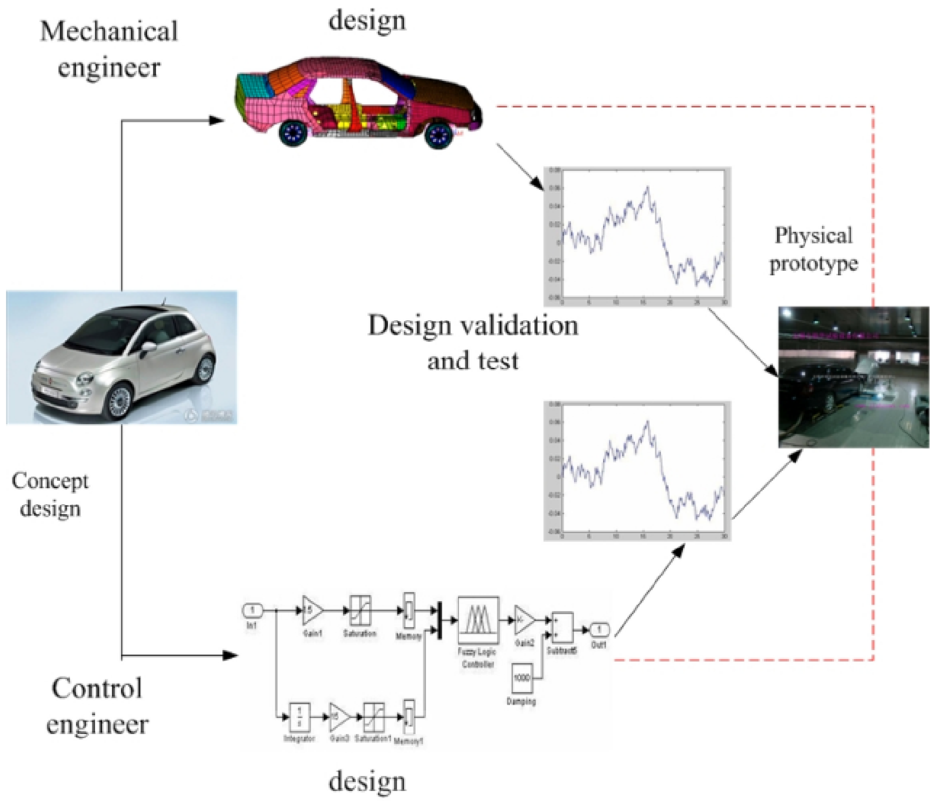

Fig. (1). The flow chart before using ADAMS.

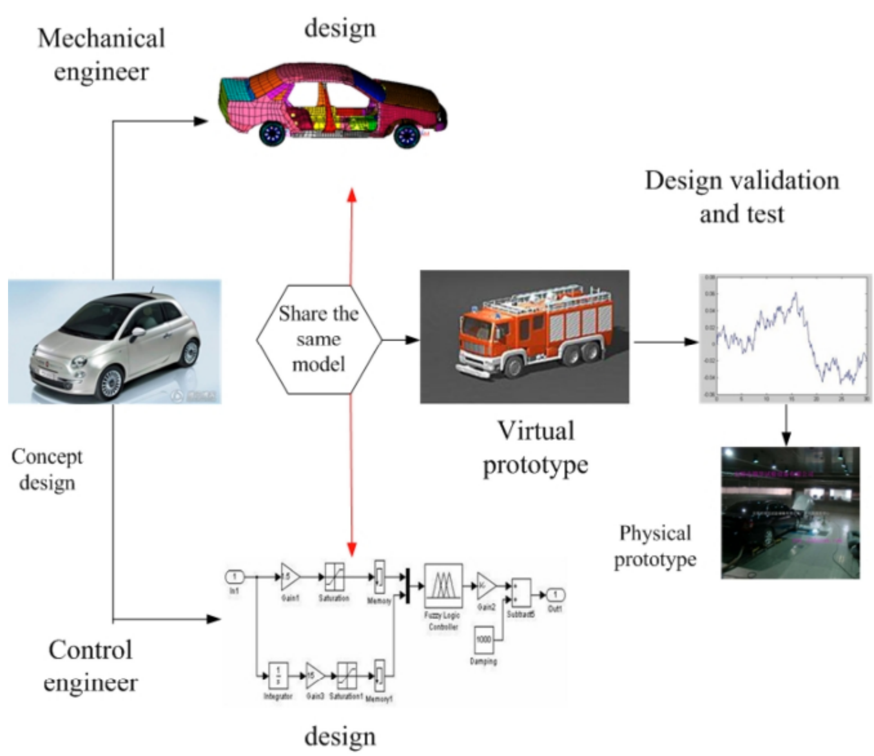

Fig. (2). The flow chart after using ADAMS.

correspond with the control design. Furthermore, more complex model, such as the nonlinear model can be obtained, and design time is decreased and the design reliability is improved.

The paper proposes an active suspension system for vehicles, using the genetic and neural network algorithm to control the system, which integrates the merits of two algorithms. A mechanical dynamic model of the five degrees

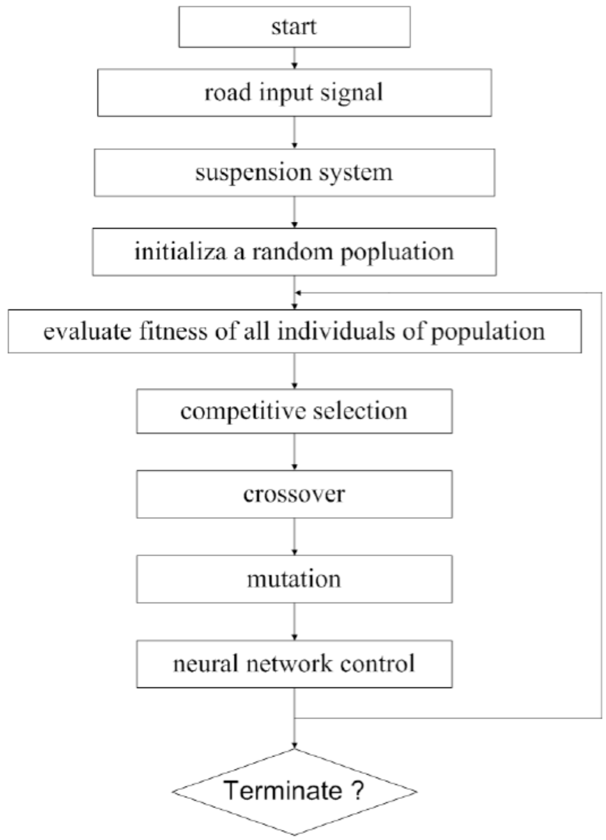

Fig. (3). Model of five degrees of freedom of suspension system.

of freedom half body of vehicle suspension system is also simulated and analyzed by using software Adams. Computer simulations demonstrate the effectiveness of the proposed system.

VEHICLE MODEL

A schematic diagram of active suspension control system is shown in Fig. (**3**). The half-body suspension system is represented as a five degrees of freedom system.

The assumptions during the process of modeling are considered as following: (1) the irregular road excitation of the left tire and right tire is same, the vehicle is symmetrical to the longitudinal line, thus the roll and yaw movement is omitted; (2) the vehicle body, including the engine part is considered as a rigid body, which means the effect of engine is neglected. The vehicle consists of a single sprung mass connected to two unsprung masses and the passenger mass; (3) the axle and the tires connected are regarded as the unsprung mass, the contact manner of the center tire line and the road is point to point method; (4) the tires are modeled as simple linear springs without damping. For simplicity, all pitch angles are assumed to be small (Yu. ZS. 2002) [9].

The essence of the control of the semi-active suspension is the regulation of the adjustable shock absorber, thus the nonlinearity of the adjustable shock absorber is the main characteristics of nonlinear suspension model. For simplicity, tires are still assumed as the linear elements. The shock absorber indicate strong nonlinearity during certain region. The shock absorber is partitioned as the fundamental damping and the controller damping, and the controller damping can be separated as the control force, thus only the fundamental damping of the adjustable shock absorber is considered during modeling. The adjustable throttle orifice hydraulic shock absorber can obtain the regulation of the damping through the control of angles of the stepping motor.

According to the different peculiarity of extend and compress stroke, the relationship of damping force and the velocity of the shock absorber is considered as followings (Zhou LK. 2005) [10]:

$$F = CV \tag{1}$$

If $V < 0$ then $C = 1034 Ns/m$;

If $V < 0$ then $C = 2502 Ns/m$

Where F is the damping force, V is the velocity of the shock absorber, C is the fundamental damping.

The relationship between the is adopted, which is expressed as following:

$$\begin{aligned}\theta &= 1000 \times (-0.5012c^4 + 2.9153c^3 \\ &+ - 6.2572c^2 + 5.8246c - 1.9370)\end{aligned} \tag{2}$$

Where θ is the angle of the stepping motor; c is the average damping of adjustable shock absorber. With the aid of matlab file M, the nonlinear differential equation can be obtained by programming.

After applying a force- balance analysis to the model in Fig. (**1**) the dynamics equation is governed by,

$$m_s \ddot{Z}_1 + f_{ks} + f_{cs} = 0 \tag{3}$$

$$m \ddot{Z}_2 + f_{kf} + f_{kr} + f_{cf} + f_{cr} - f_{ks} - f_{cs} = 0 \tag{4}$$

$$J\ddot{\theta} + b(f_{kr} + f_{cr}) + e(f_{ks} + f_{cs}) - a(f_{kf} + f_{cf}) = 0 \tag{5}$$

$$m_f \ddot{Z}_4 + f_{ktf} - f_{kf} - f_{cf} = 0 \tag{6}$$

$$m_r \ddot{Z}_6 + f_{ktr} - f_{kr} - f_{cr} = 0 \tag{7}$$

The system states are expressed as follows:

$f_{ks} = K_s[Z_1 - Z_3 - (a-e)(Z_5 - Z_3)/L]$; $f_{cs} = C_s[\dot{Z}_1 - \dot{Z}_3 - (a-e)(\dot{Z}_5 - \dot{Z}_3)/L]$, are the seat spring force and seat damping force, respectively; $f_{kf} = K_f(Z_3 - Z_4)$ and $f_{kr} = K_r(Z_5 - Z_6)$ are the front suspension spring force and rear suspension spring force, , respectively; $f_{cf} = C_f(\dot{Z}_3 - \dot{Z}_4)$ and $f_{cr} = C_r(\dot{Z}_5 - \dot{Z}_6)$ are the front suspension damping force and rear suspension damping force, respectively; where the coefficients C_f and C_r come from Equation (1). $f_{ktf} = K_{tf}(Z_4 - Z_{01})$ and $f_{ktr} = K_{tr}(Z_6 - Z_{02})$ are front tire spring and force rear tire spring force.

This results in the system state equations below:

$X = [\ X_1\ X_2\ X_3\ X_4\ X_5\ X_6\ X_7\ X_8\ X_9\ X_{10}\ X_{11}\ X_{12}\ X_{13}\ X_{14}\ ]^T$

$= [\ \dot{Z}_1\ \dot{Z}_2\ \dot{Z}_3\ \dot{Z}_4\ \dot{Z}_5\ \dot{Z}_6\ Z_1\ Z_2\ Z_3\ Z_4\ Z_5\ Z_6\ Z_{01}\ Z_{02}\ ]^T$ The state space equations in matrix are given by $\dot{X}(t) = AX(t) + BW(t)$, with the disturbance input defined as $W = \begin{bmatrix} w_1 & w_2 \end{bmatrix}^T$.

GENETIC ALGORITHM AND NEURAL NETWORK CONTROL

Genetic algorithm is a stochastic global search method which is based on the metaphors of natural biological evolution, according to Darwin (1809-1882) evolution theory. Genetic algorithm has abilities that differ substantially from more traditional search and optimization methods. Neural network provides a fast method for autonomously learning to produce a set of output states, given a set of input states. The emergence of neural networks as effective learning systems for a wide variety of applications has resulted in the use of these networks as learning models for dynamical systems (Wang YJ 2007) [11]. One of the important advantages of using neural networks for control applications is that the dynamics of the controlled system need not be completely known as a prior condition for controller design. This is a very desirable feature in the design of the controller, because of the nonlinearities arising from rigid-body coupling. The ability of networks and adaptation and their highly parallel nature of computation make approach suitable for real time and simulations applications.

The combination of neural network and genetic algorithm is one methods of the scientific optimization arithmetic. The proportion of the index, the spring mass and the suspension stiffness have important influence on the stability of the system.

There are three characteristics commonly used to access the performance of vehicle suspension system. (1) ride comfort, which improves as the magnitude of the seat acceleration is reduced; (2) system stability, which is acceptable for restricted or low tire road contact forces and is quantified by tire deflection; (3) the suspension travel, which must be restricted.

To consider the ride comfort and drive stability synthetically, the spring mass acceleration, tire dynamic load and suspension deflection are selected as the significant indexes for the evaluation of active suspension control effect, and the weighted objective function is generally defined by the following equation:

$$J = \rho_1 \ddot{z}_2^{\,2} + \rho_2 \ddot{\theta}^{\,2} + \rho_3 \ddot{z}_1^{\,2} + \rho_4 \frac{y_f^2 + y_r^2}{2} + \rho_5 \frac{(z_{1f} - z_{0f})^2 + (z_{1r} - z_{0r})^2}{2} \tag{8}$$

And $y_f = z_3 - a\theta - z_4$ $y_r = z_2 + bq - z_6$; z_1 is the passenger displacement; z_2 is the vehicle body vertically displacement θ is the pitching angle.

The fitness function *f* is given by $f = \frac{1}{J}$.

Ride quality as the suspension system design criterion mainly stems from taking a human ride comfort perspective. P. E. Uys investigates the spring and damper settings that will ensure optimal ride comfort of an off-road vehicle on different road profiles and at different speeds (P. E. Uys. JF. 2007) [12].

On the other hand, from a cost-effectiveness of vehicle infrastructure system perspective, another performance measure is also of significant importance, that is, the dynamic tire load applied on the road. Thus, the objective function includes not only the sprung mass acceleration, the sprung pitching acceleration, but also the suspension deflection and the dynamic tire load. And ρ_1, ρ_2, ρ_3, ρ_4, ρ_5 are the weighted coefficients of the sprung mass acceleration the sprung pitching acceleration the passenger acceleration the suspension deflection and the dynamic tire load, respectively.

The general steps of genetic algorithm and neural network are shown by a chart in Fig. (**4**).

To take advantage of genetic algorithms as well as neural network, we implement the combination of genetic algorithm and neural network in this paper to solve the vehicle suspension problem.

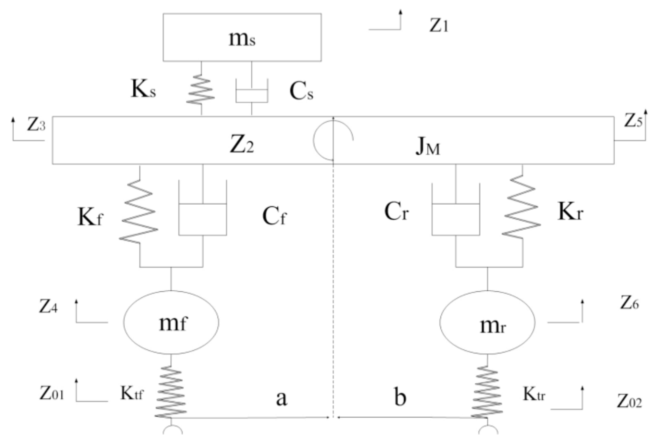

Fig. (4). Schematic diagram of the system.

Crossover

This is the exchange of chromosomes characteristics among randomly selected pairs from the parent root. The crossover rate has proper value, the excessive large value will damage the excellent mode, and the excessive small value will decrease the velocity of new chromosome. In the present work, 0.5 is the considered probability rate of the crossover.

Mutation

This operator executes by switching zero with one, at a binary bit. Mutation is randomly applied with low probability, typically in the range of 0.01-0.1. Here, a value of 0.01 is the considered for mutation probability.

The NN of this active control system has two hidden layers, the input, hidden and output neurons are 1, 10, 3 and 1, respectively. The advanced back propagation is adopted and we added momentum in the back propagation to prevent the network from getting stuck in a shallow local minimum point. An adaptive learning rate was applied to decrease the training by keeping the learning reasonably high while insuring stable learning. We pick random values as initial weights and biases.

(1) The input of NN is the time response of the acceleration of sprung mass, the objective output is the optimized suspension control force. The transfer function is nonlinear function.

$$y = \frac{2}{1+e^{-x}} - 1 . \qquad (9)$$

(2) The objective function E_p is determined as:

$$E_p(t) = \frac{1}{2}\sum_k \left[d_{kp} - y_{kp}(t)\right]^2 \qquad (10)$$

Where $y_{kp}(t)$ is the network output after t times weighting factors adjusting, with the p th sample applied to the network. And k is the kth neuron of the output layer.

The mathematical expression of back propagation wit momentum can be written as:

$$w_{ij}(t+1) = w_{ij}(t) - \eta(t)\sum_p \frac{\partial E_p(t)}{\partial w_{ij}(t)} + \alpha \Delta w_{ij}(t) \qquad (11)$$

To get variable η from function,

$$Fd = \begin{cases} \min \ f\left(w(t+1) - f(w(t))\right) \\ s.t.\ \eta \ge 0 \end{cases} \qquad (12)$$

Where $\delta_{m_1 p}$ is sensitivity degree value of the m_1 th neuron's state $x_{m_1 p}$ with E_p m_1 is the m_1 th neuron of next layer of neuron i ; η is the learning coefficients and α is the coefficient of momentum.

SIMULATION RESULTS

To verify the validity of the method, the paper includes a great deal of calculating process based on the simulation software "Matlab/Simulink". The performance of the active control scheme is illustrated through a series of simulations.

Denoting the irregular road excitation as band limited white noise, which is determined by different road surface condition and velocity, the equations (ISO 2631-1:1997 (E)) [13] of font and rear road are expressed as following:

$$\dot{z}_{01}(t) = -2\pi f_0 z_{01}(t) + 2\pi\sqrt{G_q V_0}\,\omega_1(t);$$

$$\dot{z}_{02}(t) = -2\pi f_0 z_{02}(t) + 2\pi\sqrt{G_q V_0}\,\omega_2(t)$$

Where f_0 is the lowest frequency irregular road coefficients $G_q(n_0) = 256\times10^{-6}\ m^2/m^{-1}$ and velocity is $20m/s$.

The NN controller with optimal acceleration parameters computed by GA-based optimization is designed as follows: The NN uniformed the input data and objective matrix, and revert the output result to the actual range. If the fitting tolerance of testing samples are within the desired, the NN perform normally, and save the weighting factors, otherwise, print" the network is over-fitting and can not work properly". In the NN simulations system, a momentum value of 0.9, error ratio value of 1.04, and an adaptive learning rate value of 0.01 with an increase multiplier of 1.05 and a decrease multiplier of 0.6 were applied to speed up the training time. The initial population size is 45; the end number is 100; set the probability of crossover to be 0.5, and the mutation probability to be 0.01.

Fig. (**5**) indicates the controlled system and the passive system sprung mass vertical acceleration response. For compare, they are shown in one figure. The dash line represents the system before control, and the solid line indicates the system after control. Fig. (**6**) shows the controlled pitching angular acceleration response and the passive system pitching angular acceleration response. And Fig. (**7**) shows the controlled acceleration response and the passive system acceleration response of passenger. Then Fig. (**8**) demonstrates the front suspension travel response. Figs. (**9** and **10**) presents the dynamic front and rear tire load response, respectively. From these figures, we can see that the vertical control of the sprung mass and passenger accele-ration is decreased by the controlled systems, which indi-cates that the GA&NN control system is effective in impro-ving the system ride comfort. The response of suspension travels and the dynamic tire deflections emphasizes the fact that the controlled system can improve the system stability.

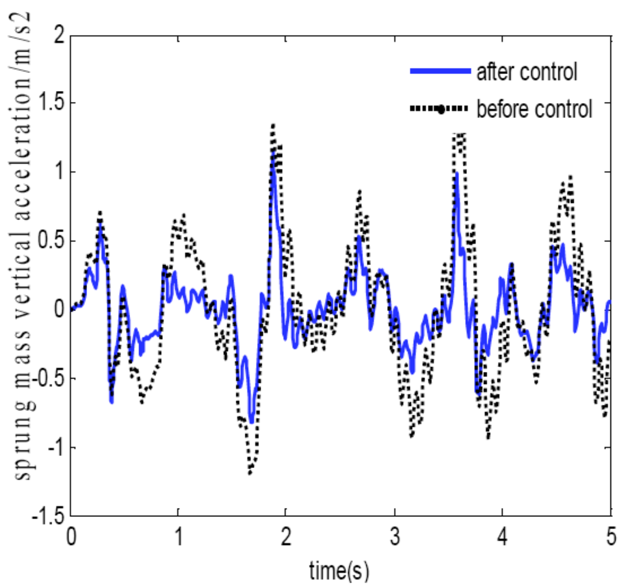

Fig. (5). Sprung mass vertical acceleration response.

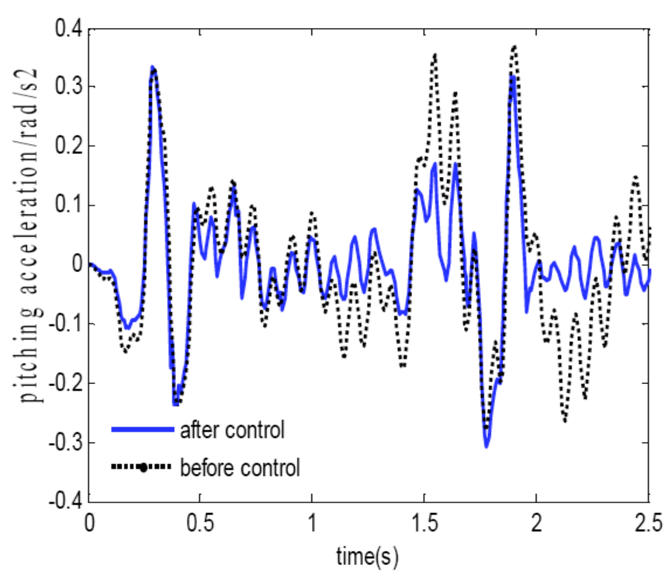

Fig. (6). Pitching angular acceleration response.

Table **1** includes the performance analysis of the system. The body acceleration and pitching angular acceleration is greatly decreased, and the passenger acceleration is reduced dramatically, which indicates that the genetic algorithm and neural network controller is effective in improving the sys-tem riding comfortability. The tire dynamic load is reduced, which indicates that the system stability is meliorated.

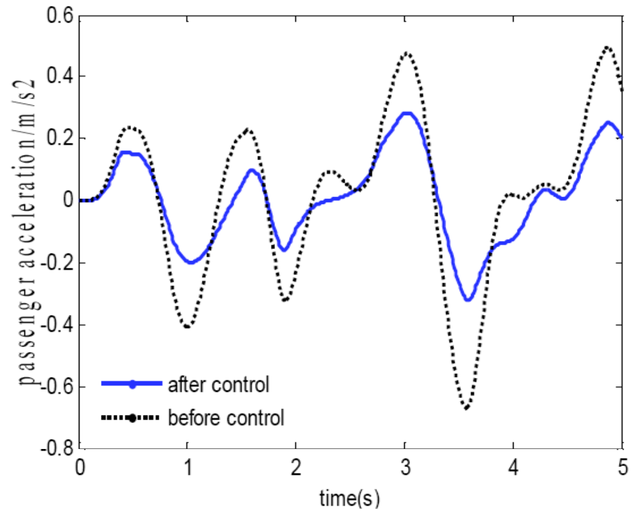

Fig. (7). Passenger vertical acceleration response.

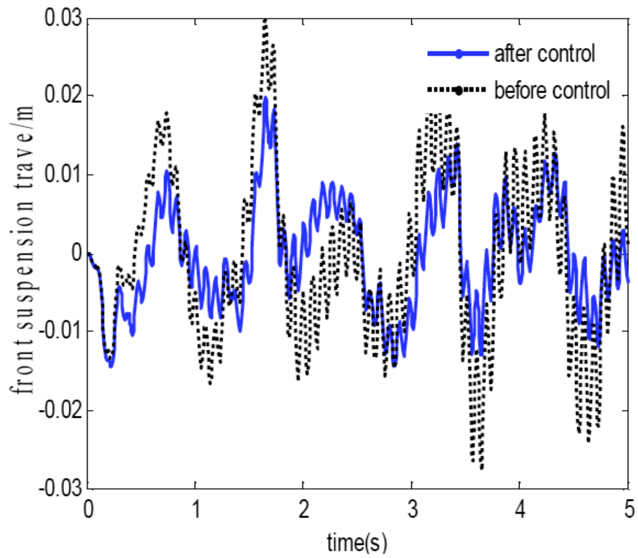

Fig. (8). Front suspension travel response.

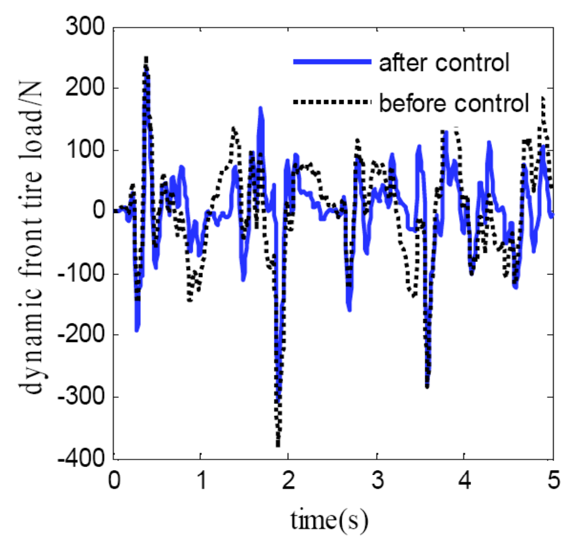

Fig. (9). Dynamic front tire load response.

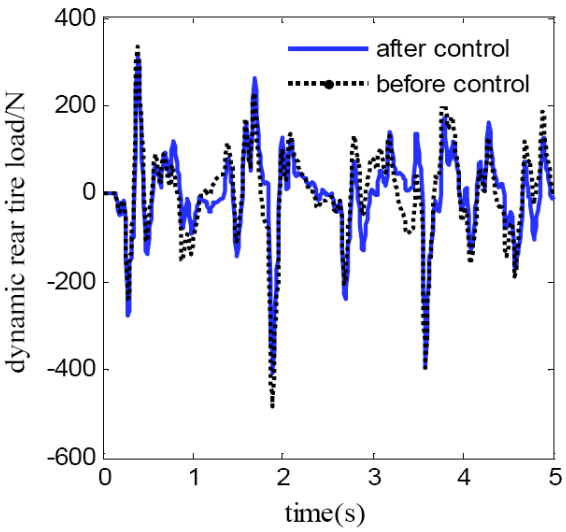

Fig. (10). Dynamic rear tire load response.

Table 1. Performance Analysis

	Body Acceleration (m/ s2)	**Pitching Angular Acceleration (rad/s2)**
Before control	0. 4620	0.1745
After control	0. 2524	0.1226
Performance melioration	45. 4%	29. 7%
	Passenger Acceleration (m/ s2)	Front suspension travel (m)
Before control	0. 2109	0.0089
After control	0.1150	0.0058
Performance melioration	45. 5%	34. 8%
Before control	Front tire dynamic load (N)	Rear tire dynamic load (N)
After control	82. 8	102. 5
Performance melioration	61. 4	89. 9
Before control	25. 8%	12. 3%

ASSOCIATED SIMULATION

First, using the software ADAMS, the mechanical model of five DOF suspension system is established (Chen Y 2007) [14], as shown in Fig. (**11**). The ADAMS model is imported into the Matlab/Simulink model, to accomplish the associated simulation with Matlab/Simulink (Chen LP 2007) [15]. Figs. (**12** and **13**) indicate the vertical acceleration and pitching angular acceleration response of the sprung mass of the constituted mechanical model. The solid line is the curve of matlab simulation, the dash line is the curve of combination of matlab and Adams. From the results, we can see that although the variation trend of the vertical response and the pitching acceleration response of the established mathematical model and the mechanical are in consistence, there is difference between the solid line and the dash line. The method of modeling of matlab and Adams differs from each other. Through matlab/simulink we constitute the suspension model; for Adams, the virtual mechanical model is constituted by plentiful accessory storeroom of Adams, such as the vehicle body, the wheel and the spring part, then we have to inflict the restriction between the components, the restriction between the components constitutes the difference between the matlab response and the Adams response.

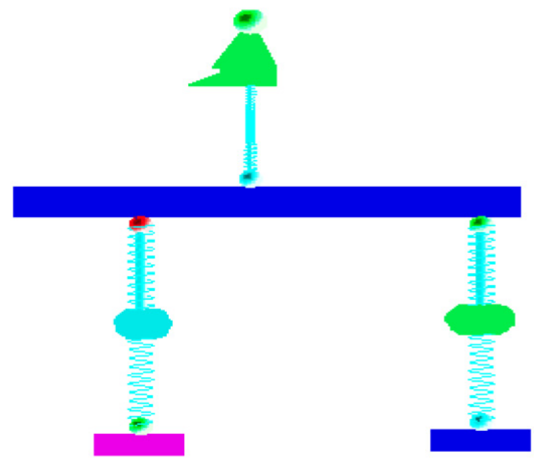

Fig. (11). Mechanical dynamic model.

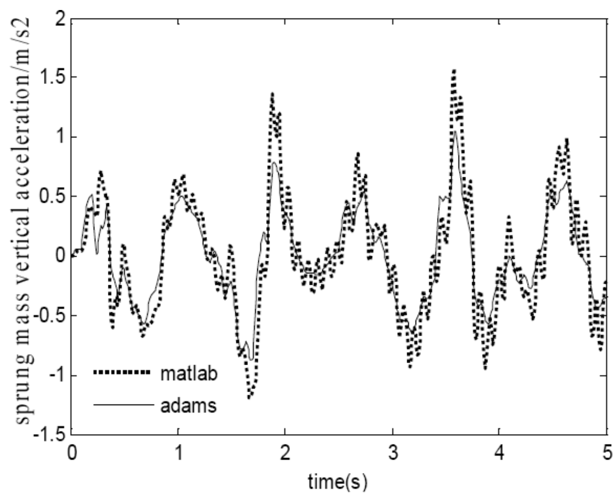

Fig. (12). Sprung mass vertical acceleration response.

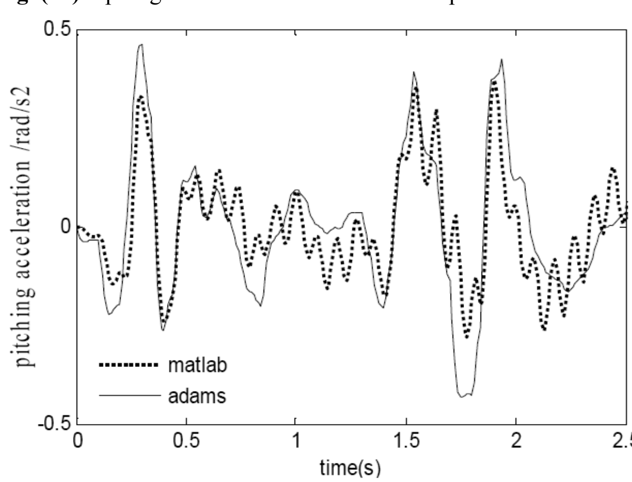

Fig. (13). Pitching angular acceleration response.

CONCLUSIONS

In this work, the specified half body vehicle model with passenger involving five degree of freedom is presented to achieve the excellent ride comfort and drive stability of the system. The model is assumed to have five masses attached with linear springs and nonlinear dampers. It is also assumed that the system does not vibrate in lateral direction, only oscillates in vertical and longitudinal directions. Furthermore, the tires are assumed not losing the contact with the road surface. Approaches are presented for suspension design which uses genetic algorithm and neural network control algorithm. It is obvious from the response plots that vehicle body vertical acceleration, passenger response and pitching angular response decreased compared with the passive suspension system, which naturally brings ride comfort. And the suspension travel and dynamic load reduced compared with the passive suspension system, which indicates that the proposed controller proves to be effective in the stability improvement of the suspension system.

REFERENCES

[1] O. GD, "Optimal seat and suspension design for a quarter car with driver model using genetic algorithms", *International Journal of Industrial Ergonomics*, vol. 37, pp. 327-332, 2007.

[2] L. Sun, X. M. Cai, and J. Yang, "Genetic algorithm-based optimum vehicle suspension design using minimum dynamic pavement load as a design criterion", *Journal of Sound and Vibration*, vol. 301, pp.18-27, 2007.

[3] T. G. Chondros, S. Michalitsis, S. Panteliou, and A. D. Dimarogonas, "Chassis design for a small electric city car", *Society of Automotive Engineers Special Publication*, vol.1023, pp. 5-12, 1994.

[4] T. G. Chondros, P. A. Belokas, K. Vamvakeros, and A. D. Dimarogonas, "Vehicle dynamics simulation and suspension system design", *SAE Steering and Suspensions Technology*, vol.1223, pp.169-180, 1997.

[5] T. G. Chondros, G. Michalos, P. Michaelides, and E. Fainekos, "An approximate method for road tankers roll stiffness evaluation", *Proceedings of the Institution of Mechanical Engineers*, Part D, *Journal of Automobile Engineering*, vol. 221, pp.1499-1512, 2007.

[6] J. T. Papadimitropoulos, T. G. Chondros, S. D. Panteliou, B. Carlsson, S. Kalogirou, and A. D. Dimarogonas, "Advances in electric vehicle technology", Expert system for energy management of electric cars, *SAE Technical Paper Series*, SP-1417, 01-1154, 1999.

[7] S. Kalogirou, T. G. Chondros, and A. D. Dimarogonas, "Development of an artificial neural network based fault diagnostic system of an electric car", 01-1154. Reprinted from Design and Technologies for Automotive Safety – Critical Systems *2000 SAE Technical Paper Series* SP-1507, 1999.

[8] E. C. Yeh, and Y. J. Tsao, " A fuzzy preview control scheme of active suspension for rough road", *International. Journal of Vehicle Design*, vol.15, pp.166-180, 1994.

[9] Z. S. Yu, *Automobile Theory*, Beijing: China Machine Press, 2002, pp. 170-182.

[10] L. K. Zhou, *Study on Fuzzy Dynamic System Design and Test of Semi-Active Suspension*, Jiangshu: Jiangshu University, 2005.

[11] Y. J. Wang, *Analysis of Vehicle Suspension Control Using Neural Networks*, Shenyang: Northeastern University, 2007.

[12] P. E. Uys, P. S. Els, and M. Thoresson, "Suspension settings for optimal ride comfort of off-road vehicles travelling on roads with different roughness and speeds", *Journal of Terramechanics*, vol. 44, pp.163-175, 2007.

[13] Mechanical vibration and shock-Evaluation of human exposure to whole-body vibration-Part 1: General requirements, ISO 2631-1: 1997 (E).

[14] Y. Chen, "*Active Suspension System of Automobile Based on Fuzzy Control*", Shenyang: Northeastern University, 2007.

[15] L. P. Chen, *Mechanical System Dynamic Analysis and ADAMS Application Tutorial*, Beijing: Tsinghua University Press, 2005, pp. 80-120.

Numerical Simulation Analysis of Circular Synthetic Jets with Asymmetric Forcing

Kalpana Mallick, *Department of Mechanical Engineering, Raajdhani Engineering College, Bhubaneswar, kalpanam11@outlook.com*

Nirmal Charan Mallik, *Department of Mechanical Engineering, Aryan Institute of Engineering & Technology, Bhubaneswar, nirmal_m26@gmail.com*

Binapani Mohapatra, *Department of Civil Engineering, Raajdhani Engineering College, Bhubaneswar, binapanimohapatra@yahoo.co.in*

Abstract: This paper presents a detailed numerical simulation of the fluid flow characteristics of a synthetic jet. The fluid motion is caused by an oscillating piston within a circular channel which is connected to a larger cavity. The oscillating piston utilized a sawtooth forcing profile, and the solution encompassed the channel geometry, the cavity, and the fluid domain external to the cavity. Momentum fluxes through the orifice and over the exterior of the cavity are calculated. The contribution of the external flow to the induced momentum, by means of the co-flow, is investigated numerically. These findings support previous experimental and computational investigations of the existence of co-flow and its overall contribution to mass and momentum flowrates. The effects of the asymmetric forcing profile on the net and instantaneous momentum fluxes, as well as the co-flow mass flux, are presented. Of particular note, it was found that the shape of the sawtooth profile has a significant impact on direction of momentum transferred to the fluid, however, the absolute magnitudes of this momentum flowrate were found to be negligible compared to the momentum flowing through the orifice.

Keywords: Induced co-flow, synthetic jet, momentum flux, propulsion, sawtooth forcing.

INTRODUCTION

Recently, the viability of synthetic jets as propulsors for underwater vehicles has been demonstrated [1-5]. Inspiration for their use in this application is taken from living creatures that successfully use pulsed jets for their locomotion [6-8]. In a typical synthetic jet, an orifice plate is situated on one wall of a cavity through which fluid is exhausted during a compression stroke. On an expansion stroke, fluid is drawn into the cavity so that throughout an entire cycle, there is no net mass efflux from the cavity. Despite this, synthetic jets are capable of imparting a net momentum to the fluid surrounding the cavity and are also able to promote mixing. In this paper the impact of asymmetric actuation profiles on momentum flux is investigated.

Past investigations demonstrate an evolving understanding of the phenomena which characterize synthetic jet development and the propulsion developed thereby. Experimental work has allowed the clear visualization of jets produced by vibrating motion, acoustic excitation, and other means [9,10]. Smith and Glezer performed Schlieren and smoke imaging to identify vortex rings which are ejected from a cavity orifice [11]. Average velocities along the central axis showed the cyclical ingestion and ejection of fluid. In work by Mallinson [12], complementary experimental and numerical studies were performed and comparisons were made. That numerical simulation included both laminar and turbulent models, although the simulations did not extend into the cavity proper. Rather, the presence of a cavity was simulated by an imposed velocity profile at the orifice. Calculations have been performed, by Lee and Goldstein on the effect of cavity size and shape on the synthetic jet [13]. In that work, the interaction between a synthetic pulsating jet and a crossflow was investigated. The geometry was planar and the orifice plate was infinite in its extent. More recently, numerical simulations have been conducted looking at the flow induced by synthetic jets on the fluid outside of the jet chamber, upstream of the orifice [14]. That study, inspired by the experimental results of [2] discussed the implications of this induced coflow on the thrust produced by a synthetic jet.

The computations performed in this paper relate to the physical geometry shown in Fig. (**1**), which is based on information from [2] in which a piston-created flow, in connection with a cylindrical cavity, was used to create synthetic jets and co-flow around the perimeter of the cavity. The piston, modeled here as a moving plate, reciprocates vertically, pulling fluid into the cavity on the upstroke and expelling fluid from the cavity on the downstroke. In addition, fluid surrounds the entire chamber which was submerged within a large volume of water.

One significant difference between the majority of the synthetic jets in the literature and the one presented here is the use of an asymmetrical forcing profile for the piston. Many researchers [15-18] used piezoelectric actuation which allowed for inflow and outflow membrane velocity profiles that were mirror images of one another. Krieg [3] and Mohseni [1], used a plunger with an oscillating velocity profile which was also symmetric with respect to time. Experimental results have been published for a voice-coil actuated synthetic jet with a sawtooth forcing profile [4, 5] but to the best of the authors' knowledge, no numerical studies have been done on asymmetricly forced synthetic jets.

The present calculations will simulate a moving piston, rather than an imposed time-varying velocity profile within the channel which has been more typical of past research. This modification was made to more accurately model the physical situation presented in [2]. The results are focused on the flow patterns at the orifice, within the cavity space, and in the fluid region surrounding the device. Momentum calculations are made to assess the various contributions to the overall momentum transfer to the fluid.

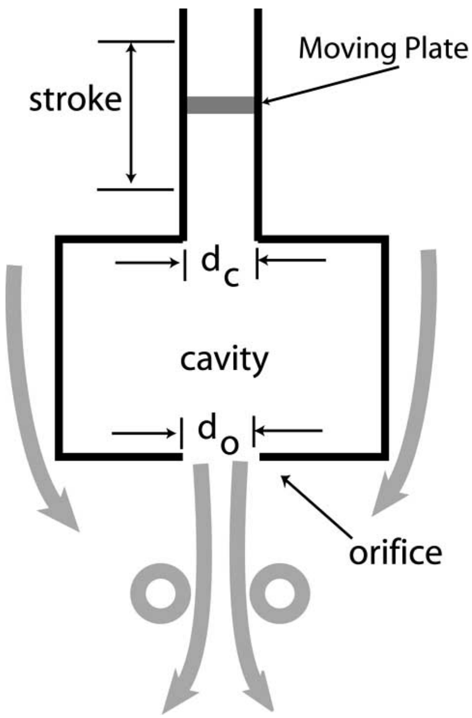

Fig. (1). Schematic diagram of the synthetic jet device.

NUMERICAL MODEL

Solution Domain

The physical domain used in the calculations includes the fluid within the channel and cavity and extends both upstream and downstream of the orifice. Both the cavity and channel are circular in shape and the channel is centrally located at the top surface of the cavity. At the top edge of the channel there is a moving plate which reciprocates vertically. The fluid region encompassing the channel-cavity extends laterally and downwards. The size of the solution domain was selected so that the boundary conditions imposed there did not influence the computational results near the investigated cavity.

Arrows in Fig. (**1**) show the general direction of fluid motion during the outstroke. This motion includes co-flow around the cavity proper, a fluid jet emerging from the orifice, and the vortex rings which are shed from the orifice. The investigations performed in [2, 14, 19] and the simulations presented here used values of physical parameters shown in Table **1**. For the present study, the “co-flow” region refers to the fluid domain outside the cavity, emanating horizontally from the bottom surface of the cavity proper.

Table 1. Synthetic Jet Geometry Used in this Paper

Parameter	Symbol	Value (cm)
Cavity Width	w_c	7.0
Cavity Height	h_c	9.9
Channel Width	d_c	2.5
Orifice Width	d_o	1.9

Forcing Profile

As described above, the plate at the top of the chamber is given a velocity profile defined by a sawtooth. Three different sawteeth profiles, as shown in Fig. (**2**), were used:

- *25/75 Profile*: in which the plate is being raised (bringing fluid into the chamber) for 25% of the period, and being lowered (ejecting fluid from the orifice) for 75 % of the period.
- *50/50 Profile*: in which the plate is raised and lowered for equal durations of time.
- *75/25 Profile*: in which the plate is being raised (bringing fluid into the chamber) for 75% of the period, and being lowered (ejecting fluid from the orifice) for 25 % of the period.

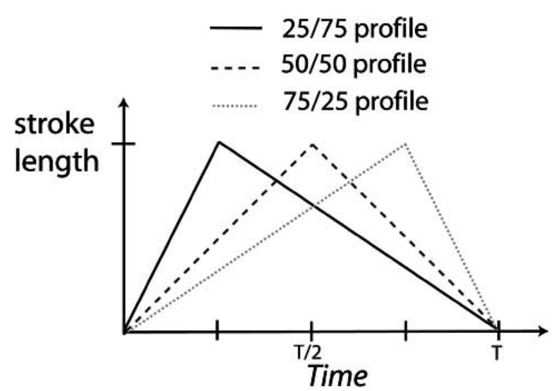

Fig. (2). Sawtooth forcing profiles.

A base case was tested in which the period (T) was one second, and the total stroke of the moving plate was 5 *cm*. Once this initial case was tested for the three forcing profiles, additional cases were tested with strokes of 2.5, 5.0, and 10 cm each with periods of 0.5, 1, and 2 seconds in order to assess the impact of stroke length and period on the results.

The Governing Equations

The flow was modeled as unsteady and incompressible with a timewise deforming mesh that enabled the moving piston. The Navier-Stokes equations for unsteady flow are found in standard fluid flow texts [20, 21]. For some of the cases represented by the parameters in Table **1** and the forcing profiles in Fig. (**2**), the flow is turbulent in the channel and at the orifice whereas it is laminar within the cavity itself. In [14], it was shown that the results relevant to this study were independent of whether the turbulence was accounted for. Therefore, only results extracted from the laminar solver will be presented here.

The unsteady mass and momentum conservation equations for an incompressible Newtonian fluid are shown in two-dimensional tensor form as

$$\frac{\partial u_i}{\partial x_i} = 0 \tag{1}$$

$$\rho\left(u_i \frac{\partial u_j}{\partial x_i}\right) = -\frac{\partial p}{\partial x_i} + \mu \frac{\partial^2 u_j}{\partial x_i^2} \quad j = 1,2,3 \tag{2}$$

where μ is the dynamic viscosity and ρ is the fluid density.

Initial and Boundary Conditions

A requirement for the completion of the calculations is that conditions be provided on all boundaries of the fluid domain. At the upper edge of the outer fluid domain, a condition was prescribed which enabled fluid to enter or leave the fluid region (zero gradient was applied to all transport variables). At the rightmost and leftmost boundaries, a wall was employed so that fluid here would be motionless. These boundaries were sufficiently far from the cavity (more than seven times the orifice diameter) so that their impact on the flow was negligible.

At the lower boundary, an exit condition was given with weak closure conditions enforced on the second derivative in the flow direction. This condition allows for flow to exit the domain with minimal impact on the flow near the cavity. Furthermore, the outlet was placed far from the cavity so that its presence did not impact the cavity flow. The location of the outlet, as measured from the bottom of the cavity was 20 times the diameter of the orifice.

The interfaces of solid walls with the fluid were all prescribed as no slip because physically, fluid in contact with a solid wall has no motion.

Initially, at t = 0, the entire fluid region was at rest. The simulation spanned ten full reciprocating cycles of the piston to ensure that timewise periodic flow was achieved.

The Numerical Method

The circular geometry of the cavity, channel, and the surrounding fluid body facilitated an axisymmetric simulation. The computations were completed using the CFX-11.0 software. In total, more than 80,000 elements were used to resolve the spatial domain. These elements were preferentially deployed in regions were large variations in the transported variables were expected. In addition, thin prismatic elements were deployed along interfaces between the fluid and solid surfaces to ensure proper resolution of the boundary layers. Fig. (**3**) has been prepared which shows the computational mesh used in the simulation. The figure clearly shows a highly refined region extending throughout the domain and an expanded view showing the wall-adjacent mesh. The utilization of this mesh was based on a rigorous mesh-refinement study so that the solution was independent of element size and deployment. Further details of the mesh refinement are provided in a prior work which utilized the same geometry [14, 19].

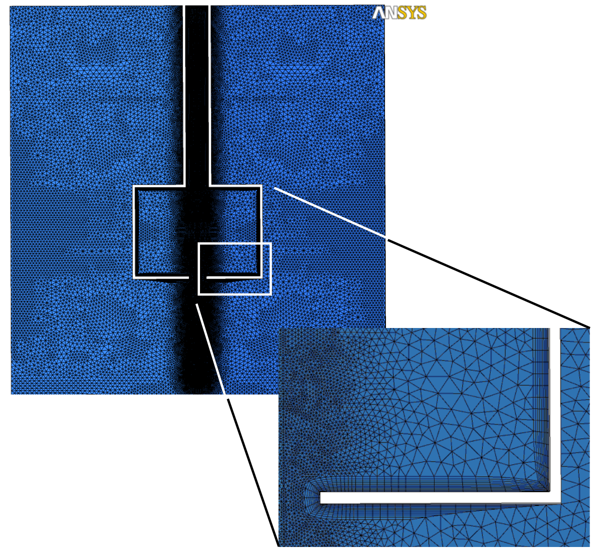

Fig. (3). Computational mesh used in the numerical solution.

The unsteady computations were performed with 100 timesteps for each reciprocating cycle. All timesteps contained 10 internal iterations, each of which was performed using a two-step multi-grid computational algorithm. The time stepping was carried out using a second-order Euler backward scheme. To each time step, a convergence criterion was applied on the root-mean-square value of the residuals of each dependent variable. The convergence criterion that was employed was 0.0001 for all variables. The selection of 100 calculations per period with 10 internal iterations was based on a previous time-step convergence study. During that study, the integration time step and the number of iterations per time step were sequentially reduced until the results were independent of both settings. Independence was based on comparisons of the instantaneous velocity field and on the integrated mass and momentum flowrates through the orifice and co-flow region. Results from the time-step study led to timewise integration steps that were sufficient for all the operating conditions of this study.

Coupling of the velocity-pressure equations was achieved on a non-staggered, collocated grid using the techniques developed by [22] and [23]. The inclusion of pressure-smoothing terms in the mass conservation equation suppresses oscillations which can occur when both the velocity and pressure are evaluated at coincident locations.

The advection term in the momentum equations was evaluated by using the upwind values of the momentum flux, supplemented with an advection-correction term. The correction term reduces the occurrence of numerical diffusion and is of second-order accuracy.

RESULTS AND DISCUSSIONS

For a finite-sized cavity, momentum is imparted to the fluid in two distinct spatial regions: at the orifice and in the co-flow zone. The results below will be focused on the momentum and mass fluxes in these regions. As synthetic jets have been proposed as a method for mixing fluids, particular interest will be paid to mass flowrates throughout the region. The total mass flow through the orifice plane consists of both the flow through the orifice and the flow through the co-flow region. The total mass which passes through the orifice was calculated by numerical integration across the orifice opening at a sequence of times. The actual integration is performed numerically in both space and time and it was found that, as expected, there was no net mass flow through the orifice region so that globally, conservation of mass was achieved.

$$m_{orifice} = \int_0^T \left(\int_{Orifice\ Area} \rho\upsilon\, dA \right) dt = \sum_{t=0}^{t=T} \left[\sum_{Orifice\ Area} \rho\upsilon_i\, \Delta A_i \right] \Delta t = 0kg \quad (3)$$

The term υ signifies the axial component of the fluid velocity. The inner integration (summation) evaluates the instantaneous flow rate through the orifice. The outer integration (summation) calculates the total flow throughout a cycle period. For Eq. (3), the values of the velocity at each elemental area i is orthogonal to both the orifice and the element surface area. Eq. (4) calculates the mass flow through the co-flow region.

$$m_{co-flow} = \int_0^T \left(\int_{Co-flow} \rho\upsilon dA \right) dt = \sum_{t=0}^{t=T} \left[\sum_{Co-flow} \rho\upsilon_i\, \Delta A_i \right] \Delta t \quad (4)$$

Fig. (**4**) and Table **2** show the total mass which passes through the co-flow region during a single cycle. Fifteen cases were tested, spanning all combinations of the five period/stroke configurations and three sawtooth profiles. As would be expected by conservation of mass and previous work [14, 19], the greatest mass flow is present in the case where the stroke is doubled. However, by using the 75/25 profile, the net mass flow is doubled compared to the 50/50 case and tripled compared to the 25/75 case. It can also be seen that for the double period and double stroke cases, there is a greater sensitivity of co-flow to the time-period split.

Table 2. Net Mass Flow through the co-Flow Region during a Single Up/Down Cycle of the Plate

	25/75	50/50	75/25
Base Case	1.29 x 10^{-3} *kg*	2.07 x 10^{-3} *kg*	4.46 x 10^{-3} *kg*
Double Period	6.07 x 10^{-4} *kg*	1.08 x 10^{-3} *kg*	6.63 x 10^{-3} *kg*
Half Period	2.71 x 10^{-3} *kg*	4.23 x 10^{-3} *kg*	9.00 x 10^{-3} *kg*
Double Stroke	7.34 x 10^{-3} *kg*	1.03 x 10^{-2} *kg*	2.18 x 10^{-2} *kg*
Half Stroke	5.40 x 10^{-4} *kg*	1.08 x 10^{-3} *kg*	2.78 x 10^{-3} *kg*

A critical measure of the propulsive capability of synthetic jets is the momentum imparted by the jet to the fluid. For the finite-sized cavity investigated here, momentum was found to be imparted to the fluid in two distinct spatial regions, at the orifice and in the co-flow zone. The momentum flow through the orifice exists even in the absence of a net mass flow. The timewise variation of the orifice momentum flow was determined by spatial integration of the momentum flux at the orifice at a number of successive times, which in turn, were integrated in time. The momentum which has passed through the co-flow region was calculated in a similar fashion. The respective orifice and co-flow momentum flow rates are calculated in Eqs (5) and (6) respectively.

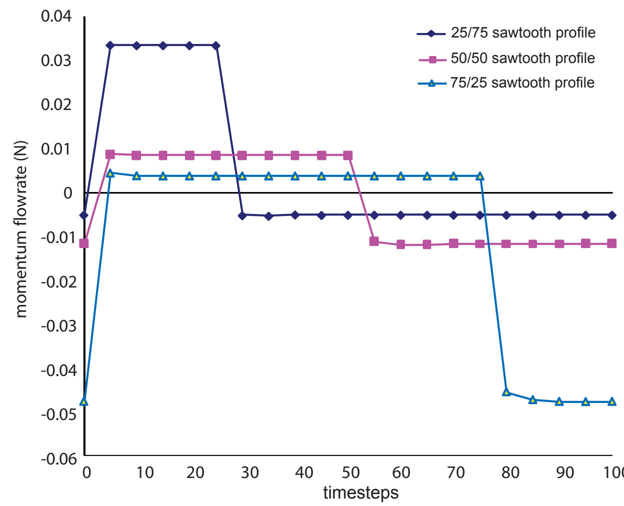

Fig. (4). Single cycle, mass through the co-flow region.

$$M_{orifice} = \int_0^T \left(\int_{Orifice\ Area} \rho\upsilon^2\, dA \right) dt = \sum_{t=0}^{t=T} \left[\sum_{Orifice\ Area} \rho\upsilon_i^2 \Delta A_i \right] \Delta t \quad (5)$$

$$M_{co-flow} = \int_0^T \left(\int_{Co-flow\ Area} \rho\upsilon^2\, dA \right) dt = \sum_{t=0}^{t=T} \left[\sum_{Co\text{-}flow\ Area} \rho\upsilon_i^2 \Delta A_i \right] \Delta t \quad (6)$$

As would be expected from observing synthetic jets in nature, changing the piston's velocity profile changes the momentum flowrate as a function of time, as well as the overall momentum flowrate per cycle. Table **3** shows the time-integration of momentum of fluid passing through the orifice, the co-flow region, and their sum for the base case. Similar results are available for the other reciprocation parameters but are not shown here for sake of brevity. Of particular note are the signs of the flowrates. Note that by changing the profile, the direction of the net momentum transfer can be changed. It can be seen that a 50/50 or 75/25 profile results in a downward thrust (negative) through the orifice, while the 25/75 profile would result in an upward thrust (positive). On the other hand, in every case, it can be seen that the net momentum of the fluid flowing in the co-flow region has a negative momentum (directed downwards). Also, a comparison of the orifice momentum flow to that in the co-flow region reveals that in all cases, the momentum flow through the orifice dominates that in the co-flow region.

Table 3. Singlecycle Timewise Integrated Momentum Flow-rates (kg m/s) for the Base Case

	25/75	50/50	75/25
Net momentum transfer (orifice)	0.0896	-0.0335	-0.179
Net momentum transfer (co-flow region)	-3.06 x 10^{-4}	-2.64 x 10^{-4}	-3.08 x 10^{-4}
Total	0.0892	-0.0338	-0.180

Figs. (**5**) and (**6**) have been prepared to show the time variation of the momentum flowrates through the orifice and co-flow region respectively throughout one complete cycle (100 time steps).

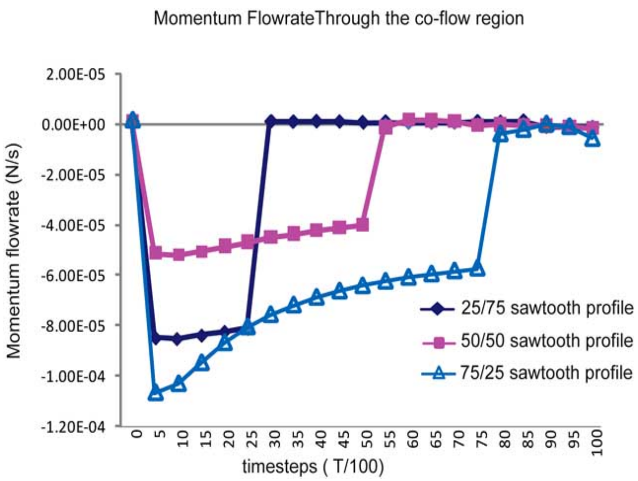

Fig. (5). Momentum flowrate through the orifice with three different forcing profiles for the base case throughout one complete cycle (100 time steps).

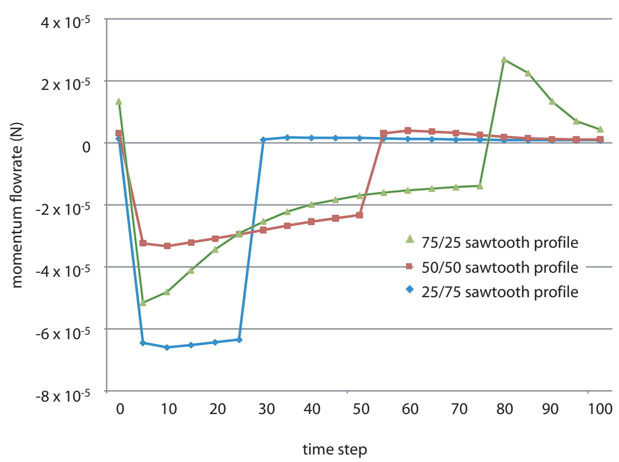

Fig. (6). Momentum flowrate through the co-flow region with three different forcing profiles for the base case.

Finally, Table **4** gives the total net momentum transfer to the fluid considering both the orifice and the co-flow region for the fifteen cases investigated in this study.

An overview of the results of Table **4** show that the momentum transferred to the fluid varies nearly as

$$\dot{M}_{orifice} \sim \frac{stroke\ length^2}{Period^2} \tag{7}$$

Thus, doubling the period results in approximately the same change to momentum as halving the stroke length. As seen in Table **3**, $\dot{M}_{orifice} >> \dot{M}_{co-flow}$, and thus Eq. (7) can be rewritten as

$$\dot{M}_{total} \sim \frac{stroke\ length^2}{Period^2} \tag{8}$$

Table 4. Total Net Momentum Transferred to the Fluid during a Single Up/Down Cycle of the Plate (Units are kg m/sec)

	25/75	50/50	75/25
Base Case	0.0892	-0.0338	-0.180
Double Period	0.00292	-0.00788	-0.0444
Half Period	0.352	-0.141	-0.726
Double Stroke	0.351	-0.149	-0.751
Half Stroke	0.00227	-0.00735	-0.0422

This is consistent with the results in a prior investigation which only considered sinusoidal forcing functions [14, 19] and to experimental work carried out previously [2]. This finding is remarkable in that it holds universally for a multitude of forcing functions.

To provide further perspective, Fig. (**7**) has been prepared. As shown there, the result of changing the period can greatly affect the net momentum transfer to the fluid. Consistent with Eqs. (7) and (8), the difference in single cycle momentum flowrates between the half period and double period cases is nearly a factor of 16.

As expected, the asymmetric profile significantly impacts the momentum transfer to the fluid. Most dramatic for the half period and double stroke cases, the 75/25 profile results in the doubling of the net momentum transfer compared to the base case. More importantly, however, is the change in direction of the momentum flow. This shows that the same synthetic jet thruster can be used in both “forward” and “reverse” modes as a propellor. A symmetrically forced synthetic jet has only a “forward” mode, significantly constricting the maneuverability of a vehicle using these thrusters.

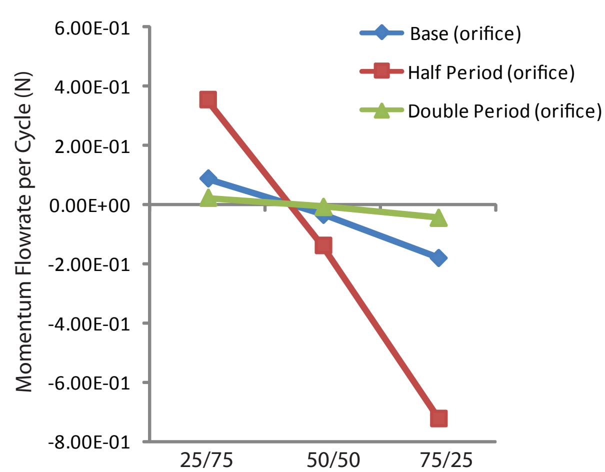

Fig. (7). Single cycle momentum flowrate through the orifice with three different forcing profiles and three different periods.

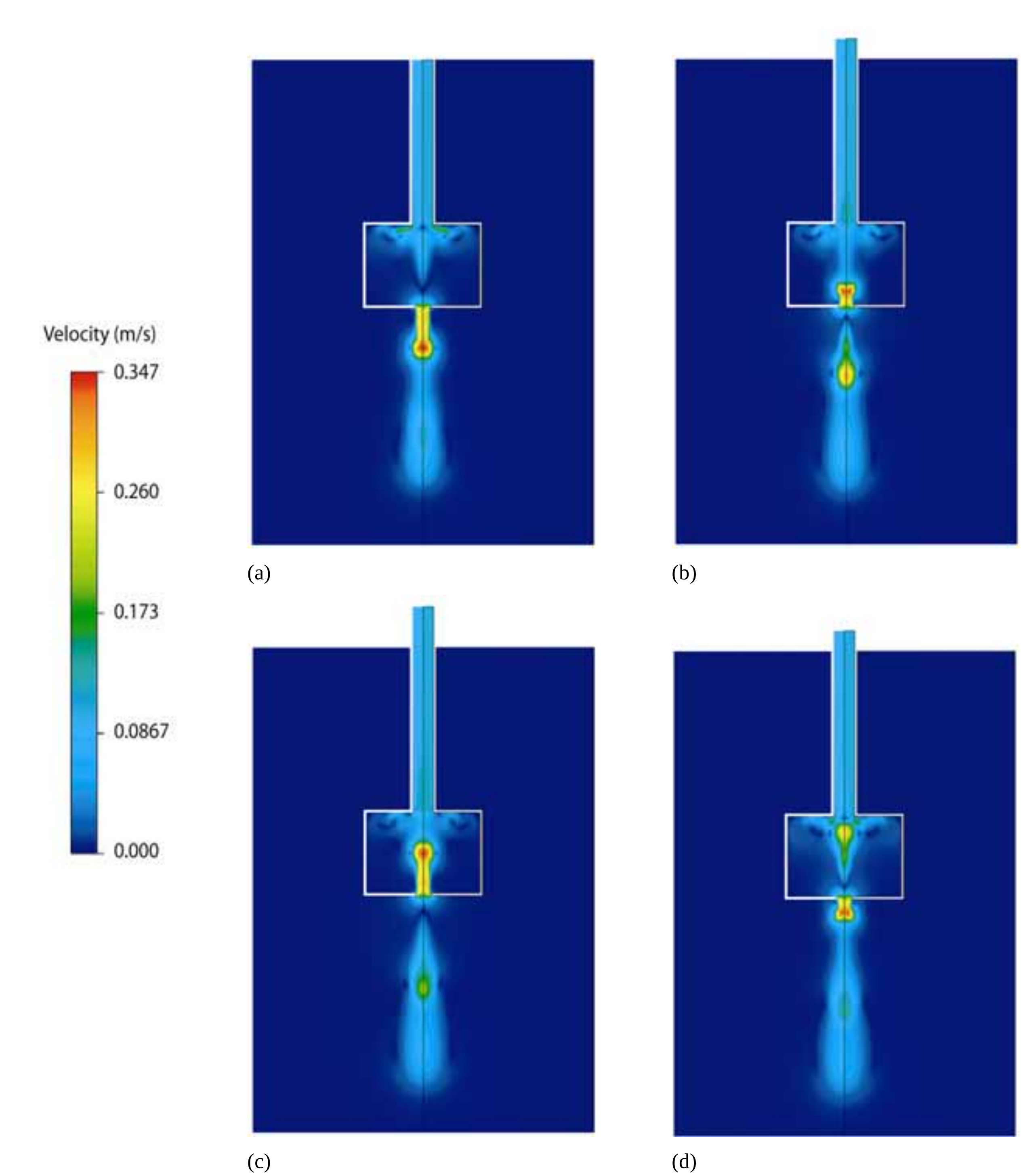

Fig. (8). Contour plots showing velocity field for the 50/50 base case at *t*/*T* values of (**a**) 0, (**b**) 25, (**c**) 50, and (**d**) 75. Velocities are keyed to the color contour legend on the left-hand side.

Flow Patterns

The last presentation of results will display the flow patterns which occur throughout a single period of cyclic motion. The results are extracted from the base case and for a 50/50 sawtooth profile. To facilitate the discussion, Figs. (**8a**) through (**8d**) have been prepared which show velocity contours at *t*/*T* values of 0, 0.25, 0.50, and 0.75, respectively.

The sequence of figures shows the development of a jet-like slug of fast moving fluid which is being expelled in the (**a**) part of the figure. The clearly defined slug of fluid is sent into the larger surrounding fluid region. It follows a remnant slug of fluid which was generated during the previous cycle. In (**b**), the piston is retracting and drawing fluid into the cavity. The slug generated in (**a**) continues to move away from the orifice and its maximum velocity is decreasing, as evidenced by the yellow color of that fluid. In (**c**), the ingested jet is shown extending deeply into the cavity and the piston is at its uppermost position. Finally, in (**d**), the fluid is again being ejected from the cavity as the piston is in a downward trajectory. During the motion, complex recirculation patterns and evident which are similar to those previously identified in [14, 19].

CONCLUDING REMARKS

Numerical simulation of the fluid motion induced by an asymmetrically forced, reciprocating piston within a circular channel has been carried out. The focus of the simulations was on the flow patterns near the orifice plate which comprises one wall of the cavity and in the region surrounding the cavity. Results were provided for the mass and momentum flows through the orifice and in the region of fluid surrounding the cavity. It was found that both the direction and magnitude of a synthetic jet's momentum flow can be altered by using an asymmetric forcing profile. As synthetic jets are increasingly being discussed as a means of underwater vehicle propulsion, the ability to produce a wider range of thrust magnitudes and direction from a single jet expands the range of applications for which these jets might be used.

NOMENCLATURE

A = area [m^2]

d_c = channel width [cm]

d_o = orifice width [cm]

h_c = cavity height [cm]

i,j = tensor indices

m = mass [kg]

M = momentum [kg m/s]

p = pressure [Pa]

t = time [s]

T = period [s]

u_i = local velocity [m/s]

x = coordinate direction [m]

w_c = cavity width [cm]

Greek

ρ = density [kg/m^3]

μ = molecular viscosity [N s/m^2]

υ = axial component of velocity [m/s]

REFERENCES

[1] K. Mohseni, "Pulsatile vortex generators for low-speed maneuvering of small underwater vehicles", *Ocean Eng.*, vol. 33, pp. 2209-2223, 2006.

[2] A. Thomas, "*Exploration into the Feasibility of Underwater Synthetic Jet Propulsion*" Ph.D. Thesis, California Institute of Technology, Pasadena, CA, 2006.

[3] M. Krieg, and K. Mohseni, "Thrust characterization of a bio-inspired vortex ring generator for locomotion of underwater robots", *J. Oceanic Eng*, vol. 33, pp. 123-132, 2008.

[4] A. Thomas-Polsenberg, M. Milano, M. Grazier G'Sell, K. Fischer, and J. Burdick, "Synthetic jet propulsion for small underwater vehicles", *IEEE Int. Conf Robotics Automation*, Barcelona, Spain, 2005.

[5] A. Polsenberg-Thomas, J. Burdick, and K. Mohseni, "An experimental study of voice-coil driven synthetic jet propulsion for underwater vehicles", *MTS/IEEE OCEANS Conf.*, Washington, DC, Sept.19–23, 2005, pp. 923-927.

[6] J. Seikmann, "On a puslating jet from the end of a tube, with applications to the propulsion of certain aquatic animals", *J. Fluid Mech.*, vol. 15, pp. 399-418, 1963.

[7] D. Weihs, "Periodic jet propulsion of aquatic creatures", *Fortsch. Der. Zool.*, vol. 24, pp. 171-175, 1977.

[8] J. Dabiri, S. Colin, J. Costello, and M. Gharib, "Flow patterns generated by oblate medusan jellyfish", *J. Exp. Biol.*, vol. 208, pp. 1257-1265, 2005.

[9] E. Davidson, and N. Riley, "Jets induced by oscillatory motion", *J. Fluid Mech.*, vol.53, pp. 287-303, 1972.

[10] R. Jacobs, J. Jacobs, and A. Glezer, "A round turbulent jet produced by an oscillating diaphragm", *Phys. Fluids*, vol. 8, pp. 2484-2495, 1996.

[11] B. Smith, and A. Glezer, "The formation and evolution of synthetic jets", *Phys. Fluids*, vol. 10, pp. 2281-2297, 1998.

[12] S. Mallinson, J. Reizes, and G. Hong, "An experimental and numerical study of synthetic jet flow", *Aeronaut. J.*, vol. 105, pp. 41-49, 2001.

[13] C. Lee, and D. Goldstein, "Two-dimensional synthetic jet simulation", *AIAA J.*, vol. 40, no. 3, pp. 510-516, 2002.

[14] J. Abraham, and A. Thomas, "Induced co-flow and laminar-to-turbulent transition with synthetic jets", *Comput. Fluids*, vol. 38, pp. 1011-1017, 2009.

[15] A. Crook, A.M. Sadiri, and N.J. Wood, "The development and implementation of synthetic jets for the control of separated flow", *30th Appl Aerodyn Conf*, Norfolk, VA, 1999.

[16] S. Mallinson, G. Hong, and J. Reizes, "Some Characteristics of Synthetic Jets", *30th AIAA Fluid Dyn Conf*, Norfolk, VA, 1999.

[17] F.-J. Chen, C. Yao, G.B. Beeler, R.G Bryant, and R.L. Fox, "Development of synthetic jet actuators for active flow control at NASA Langley", *AIAA Paper* 2000-2405, 2000.

[18] B. Smith and A. Glezer, "Vectoring and small-scale motions effected in free shear flows using synthetic jet actuators", *AIAA Paper* 97-0213, 1997.

[19] Abraham, and A. Thomas, "Numerical simulation of induced coflow and laminar-to-turbulent transition associated with syntheticjets", *Proc Flucome 2007*, Tallahassee, FL, Sept. 16-19, 2007.

[20] H. Schlichting, and K. Gersten, *Boundary Layer Theory*, 8th ed., Berlin: Springer Verlag, 2000.

[21] F. White, *Viscous Fluid Flow*, 3rd ed., New York: McGraw Hill, 2005.

[22] C. Rhie, and W. Chow, "A numerical study of the turbulent flow past an isolated airfoil with trailing edge separation", *AIAA J.*, vol. 21, 1982, pp. 170-183.

[23] S. Majumdar. "Role of underrelaxation in momentum interpolation for calculation of flow with nonstaggered grids", *Numer. Heat Transf.*, vol. 13, pp. 125-132, 1998.

Sensitivity Analysis on the Stress Levels in a Human Mandible

Debi Prasad Singh, *Department of Mechanical Engineering, Raajdhani Engineering College, Bhubaneswar, deboprasad_1159@gmail.com*

Bidyuta Ranjan Rout, *Department of Mechanical Engineering, Aryan Institute of Engineering & Technology, Bhubaneswar, bidyutaranjan1@gmail.com*

S. C. Mishra, *Department of Civil Engineering, NM Institute of Engineering & Technology, Bhubaneswar, scmishra11@yahoo.co.in*

Alivasakhi Mishra, *Department of Civil Engineering, Capital Engineering College, Bhubaneswar, alivasakhimishra258@gmail.com*

Abstract: In this work the structural behaviour of a mandible considering a unilateral occlusion is numerically analysed by means of the Finite Element Method (FEM). The mandible, considered as completely edentolous, is modelled together with its articular disks, whose material behaviour is assumed as elastic or hyper-elastic. The mandible model is obtained by computer tomography scans. The anisotropic and non homogeneous bone material behaviour is considered and the loads applied to the mandible are those related to the active muscle groups during unilateral occlusion. The results of FEM analysis are presented mainly in terms of stress distribution on the mandible. Because of uncertainty on the determination of the adopted parameters, a sensitivity analysis is provided, showing the way in which the variation of articular disc stiffness and temporomandibular joint friction coefficient has an impact on the mandible stress peak and occlusal force.

Keywords: Mandible, finite element method, articular disc, sensitivity analysis.

INTRODUCTION

The mathematical modelling of the whole mandible, with the addition of the articular joint, certainly represents a powerful tool for the determination of the stress-strain distribution related to the human masticatory system.

Many studies have strongly simplified the geometry of the joint surfaces, restricting it to a two-dimensional analysis in the sagittal plane [1,2], or neglecting the presence of anatomical components between the surfaces of the joint [3]. Other authors, even if analysing the temporomandibular joint in its three-dimensional configuration, limited their analysis only to a part of the whole mandible [4,5], or considered the whole mandible without explicitly modelling the disks [6], or considered only elastic material behaviour [7,8], whereas the high level of disk compliances requires a consideration of a hyper-elastic material type [9]. Some of the previously mentioned limitations have been overcome by recent works that accurately analyses the articular disc stresses, considering its viscolelastic [10] or poroelastic behaviour [11,12].

In this paper, in continuation of a consolidated research activity by the authors [6-9, 13], the structural behaviour of a mandible which included temporomandibular joint, considering the occlusal phase of a unilateral mastication, has been analysed by the finite element method (FEM). The accuracy of the FEM adopted approach can be based also on the comparison between FEM and BEM (Boundary Element Method) results [6-9]. The mandible, considered completely edentulous, is modelled together with the articular disks whose behaviour is modelled alternatively as elastic or hyper-elastic. The objective is to provide a sensitivity analysis for the stresses in the mandible as influenced by the values of some parameters related to the temporomandibular joint (TMJ), for which there is uncertainty in assessing the precise values. This objective prevents from adopting a more complicate TMJ modelling as done in [10,11], that would ask for a huge computational effort.

Such sensitivity analyses are useful to the dentists in order to assess the importance of retrieving accurate and patient specific values for the parameters under analysis.

The mandible model has been obtained by the reconstruction of an image obtained by a computerised tomography (C.T.) scan.

CAD MODEL

In this work the file DICOM (Digital Imaging and Communications in Medicines) has been translated by using the MIMICS software, produced by MATERIALISE. The automatic upload of the DICOM images in a CAD environment offered satisfactory results, allowing to visualise the mandible projected on three planes: the sagittal plane, the horizontal plane and the frontal plane (Fig. **1**).

Subsequently the images have been modified and refined in order to clear them from the supports on which the patient has been positioned during the C.T. scan and the metal parts, related to fillings with bio-compatible material. Then, the image segmentation phase (*regiongrowing*) was realised, by a previous calibration of the optimal contrast value (*threshold*). Once the complete mandible anatomy is defined, it is possible to realise a 3D reconstruction. This operation is strongly linked to the correct choice of a threshold value that is peculiar of each patient, because the bone density differs for each patient.

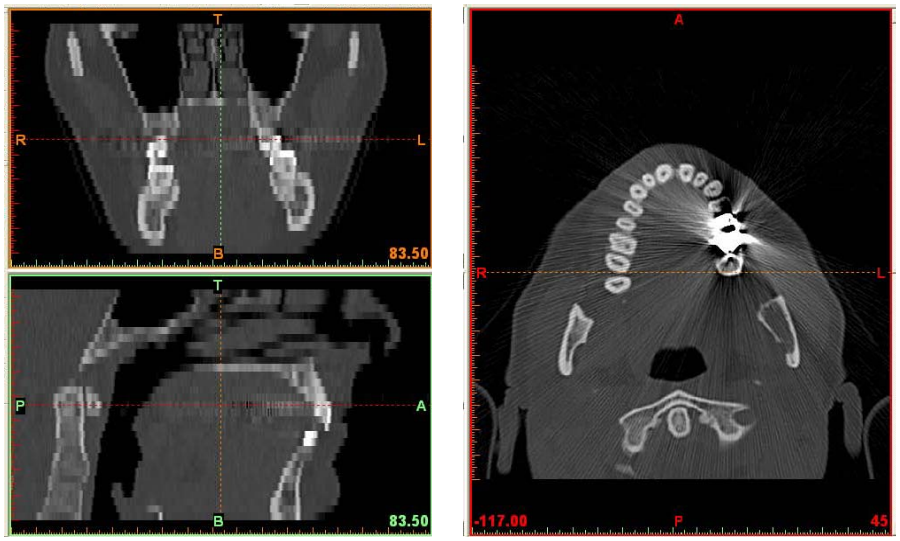

Fig. (1). Projection on sagittal, frontal and horizontal planes of human mandible imported by MIMICS software.

At this point the visualised image is a simple standard triangulation language (STL) representation of the vertex positions and not a mathematical representation of surfaces and volumes. The mathematical reconstruction of the surfaces was then realised by using the MEDCAD module of MIMICS. In this phase it was particularly important to correctly distinguish the parts of cancellous bone from those of cortical bone, because of the nature of the C.T., which does not allow a clear assessment of the layer separating the two materials. Therefore, the contours (polylines) of the objects contained inside the selected mask were generated in an automatic way (Fig. **2**) in order to subsequently interpolate them and generate the related surfaces.

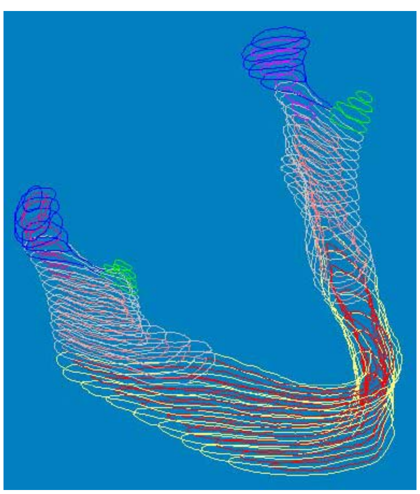

Fig. (2). Twelve sets of polylines (twelve colours) used for generation of mandible geometry.

For the generation of the whole mandible it was necessary to select twelve sets of polylines, seven of which were for the cortical bone parts and five for the cancellous bone parts.

Starting from each of these sets, the corresponding fitting surfaces were automatically produced; in this way twelve surfaces were created, one for each set of polylines (Figs. **3a** and **3b**).

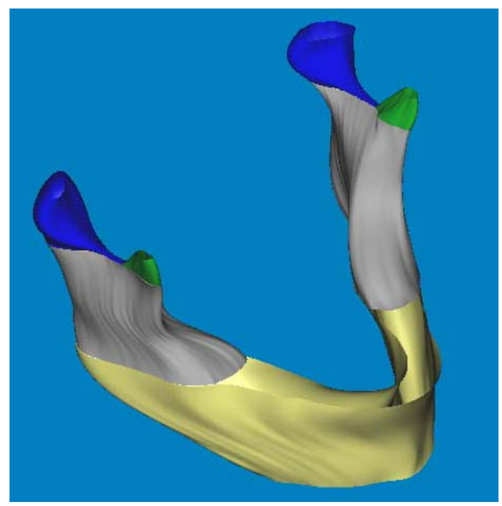

Fig. (3a). Reconstruction of the 7 surfaces related to cortical bone zone.

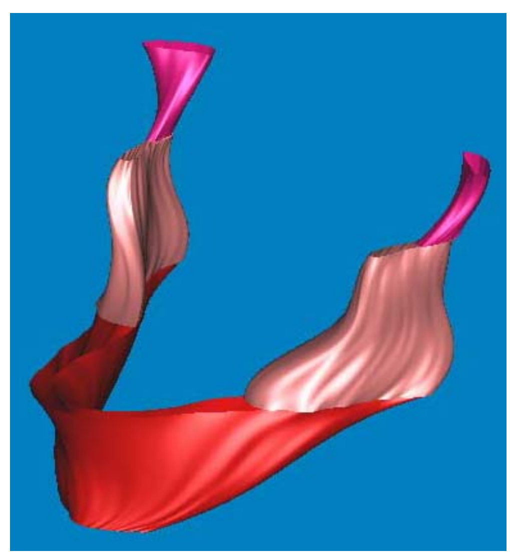

Fig. (3b). Reconstruction of the 5 surfaces related to cancellous bone zone.

The created geometry was finally exported in an IGES format (Initial Graphics Exchange Specification), that assures the maximum compatibility and the lowest loss of information in the export phase.

The articular disks allow the relative movements within the TMJ, reducing the stress level on the mandible during the masticatory phase. The disks are primarily constituted by cartilage and they are kept in their position by means of the retrodiscal tissue and the constraints imposed by the condyles and the glenoid fossa. The disk geometric reconstruction from C.T. scan was not feasible so it was made from reference to literature data [2, 4], but, in order to improve the accuracy of results that are specific to the single patient, it would be better to reconstruct the numerical model of the articular disk by using a Magnetic Resonance and to adapt the estimation of masticatory forces for patient-specific analysis [14].

Considering that the articular disk is positioned between the condyle and the infratemporal cavity and is completely overlapped with the former, it was possible to start their reconstruction from the condyles CAD model.

Once the disk surface was created in contact with the infratemporal cavity (the disk is nearly completely in contact with both the infratemporal cavity and the anterior and superior parts of the condyle), the other four side surfaces embedding the volume of the joint disk and not in contact with other parts of the TMJ were modelled as planar for simplicity (Fig. **4**). Actually there is not a fully unloaded state of the disk and this determines a limitation of the modelling approach.

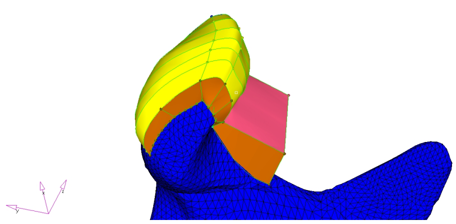

Fig. (4). Disk geometry.

FEM MODEL

The commercial software used is Ansys. The mandible and related disks were modelled by both tetrahedral 4-noded elements (first model) and hexahedral 8-noded elements (second model). The first model is preferred when there is a need for an automatic pre-processing phase; the second one requires a user intervention but allows a faster solution.

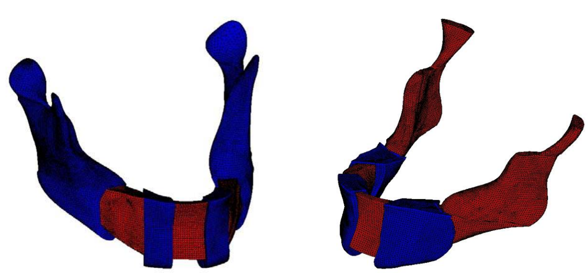

Fig. (5). Tetrahedral FE mesh of mandible (blue colour for cortical zone, red colour for cancellous zone).

Fig. (**5**) shows the first FE model of the mandible with tetrahedral elements, whereas Fig. (**6**) shows the second model with hexahedral elements. Figs. (**7**) and (**8**) show the FE disk models.

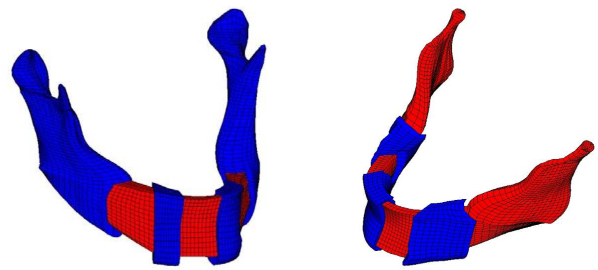

Fig. (6). Hexahedral FE mesh of mandible (blue colour for cortical zone, red colour for cancellous zone).

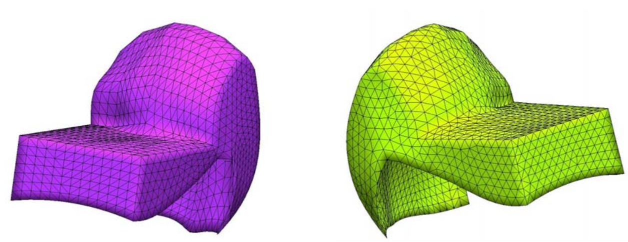

Fig. (7). Tetrahedral FE mesh of ipsilateral (left) and controlateral (right) articular disks.

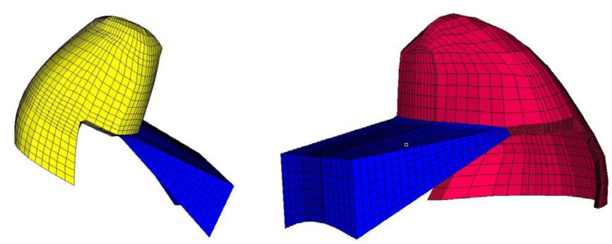

Fig. (8). Hexahedral FE mesh of ipsilateral (left) and controlateral (right) articular disks.

The interaction between the condyles and the joint disks has been modelled by contact elements (contact 173 and target 170 elements from Ansys library). The whole tetrahedral model of the TMJ is characterised by 73,210 nodes and 361,024 elements, 330,596 of which model the mandible and 20,760 the joint disk; 9,668 elements are contact elements interposed between disks and condyle and between disks and infratemporal cavities (Fig. **9a**). The hexahedral

Fig. (9a). Tetrahedral FE mesh of whole temporomandibular joints.

model is constituted of 16,534 nodes and 18,133 elements (Fig. **9b**). The mesh density is in both cases the result of a convergence analysis.

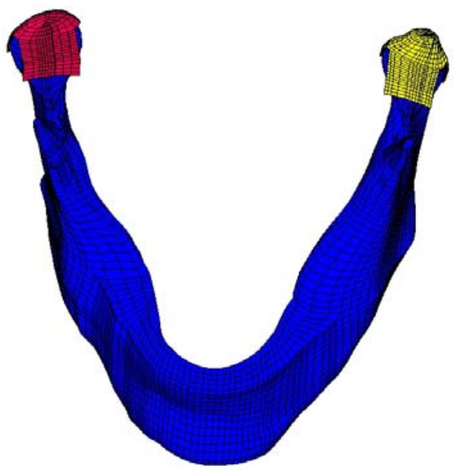

Fig. (9b). Hexahedral FE mesh of whole temporomandibular joints.

The models take into account the non homogeneity and the anisotropy of the bone mandible properties [15-21]. The mandible is divided into an internal zone, where the stiffness is that of the bone cancellous part (Fig. **10a**) and an external zone with the material properties of the cortical bone (Fig. **10b**). The mandible is further divided in fourteen sectors, characterised by varying stiffness properties (the stiffness increases from the posterior part to the anterior part of the mandible). In each of the considered zones the material has been modelled as transversally isotropic, with specified material directions and elastic compliances (Table **1**). With reference to Figs. (**10a,b**), the global reference system is indicated as xyz, whereas the local material reference system in indicated x'y'z' (z' ≡ z).

The disk material is considered as linear elastic or hyper elastic (large deformations). In the latter case the well known formulation of Mooney-Rivlin for the equation of the deformation energy has been considered:

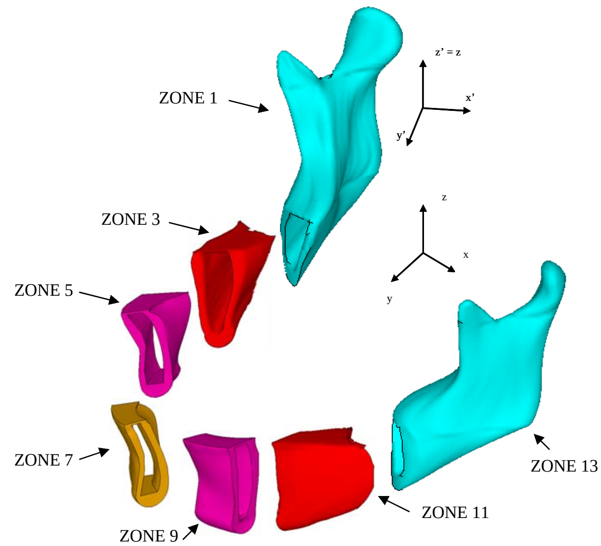

Fig. (10a). Mandible scheme of cortical bone to highlight the different zones considered.

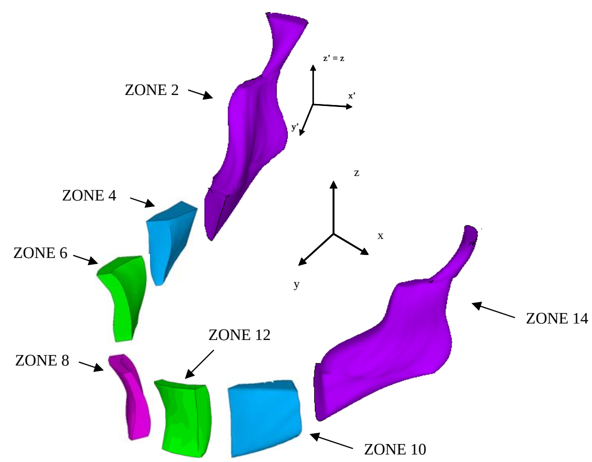

Fig. (10b). Mandible scheme of cancellous bone to highlight the different zones considered.

Table 1. Material Properties and Material Axis Orientations of the Mandible (Zones from 9 to 14 are Symmetric with Respect to Zones from 1 to 6)

ZONE	1	2	3	4	5	6	7	8
$\theta_{xx'}$ [degrees]	-28	-28	-28	-28	-59	-59	0	0
$E_{x'}$ [MPa]	1.00E+04	2.42E+02	1.22E+04	2.78E+02	1.36E+04	3.46E+02	1.35E+04	2.94E+02
$E_{y'}$ [MPa]	1.00E+04	2.42E+02	1.93E+04	8.35E+02	2.40E+04	1.04E+03	2.04E+04	8.83E+02
$E_{z'}$ [MPa]	1.68E+04	7.27E+02	1.22E+04	2.78E+02	1.36E+04	3.46E+02	1.35E+04	2.94E+02
$G_{x'y'}$ [MPa]	3.72E+03	1.61E+02	4.37E+03	1.89E+02	4.80E+03	2.08E+02	4.60E+03	1.99E+02
$G_{x'z'}$ [MPa]	4.09E+03	5.37E+01	4.54E+03	1.04E+02	5.06E+03	1.29E+02	5.02E+03	1.09E+02
$G_{y'z'}$ [MPa]	4.09E+03	5.37E+01	4.37E+03	1.89E+02	4.80E+03	2.08E+02	4.60E+03	1.99E+02
$\nu_{x'y'}$	3.45E-01	3.45E-01	2.36E-01	2.36E-01	2.36E-01	2.36E-01	2.36E-01	2.36E-01
$\nu_{x'z'}$	2.36E-01	2.36E-01	3.45E-01	3.45E-01	3.45E-01	3.45E-01	3.45E-01	3.45E-01
$\nu_{y'z'}$	2.36E-01	2.36E-01	2.36E-01	2.36E-01	2.36E-01	2.36E-01	2.36E-01	2.36E-01

$$W = \sum_{i+j=1}^{N} c_{ij}(I_1 - 3)^i (I_2 - 3)^j + \sum_{k=1}^{N} \frac{1}{d_k}(J-1)^{2k} \qquad (1)$$

where W is the strain energy potential, I_1 and I_2 are the first and the second deviatoric strain invariant, J is the determinant of the elastic deformation gradient, c_{ij} are material constants characterising the deviatoric deformation of the material and d_k are material constants characterising the hydrostatics part of the deformation. For relatively small nominal deformations, less than 6%, as it is hypothesised in the case of the disk, N can be set equal to 1, for which, in the hypothesis of hyper-elastic incompressible material, eq. (1) becomes:

$$W = c_{10} (I_1 - 3) + c_{01} (I_2 - 3). \qquad (2)$$

In this work, according to [2], it has been assumed that c_{10} = 27.91 MPa and c_{01} = -20.81 MPa. The six main muscle groups, activated in the masticatory phase by the occlusal loads are: deep and superficial masseter (DM and SM), medial and lateral pterygoid (MP and LP), and the temporalis muscle, divided into anterior and posterior portions (AT and PT).

The intensity and the direction of the resultant load of every muscle are obtained by experimental measurements, in particular by means of electromyography combined with measurement of the section of the muscular bundles [22]; these results are reported in Table **2**. The muscular loads have been modelled as forces applied on the nodes belonging to the surfaces on which the muscular bundles are attached (Figs. **11A** and **11B**); their values have been obtained by

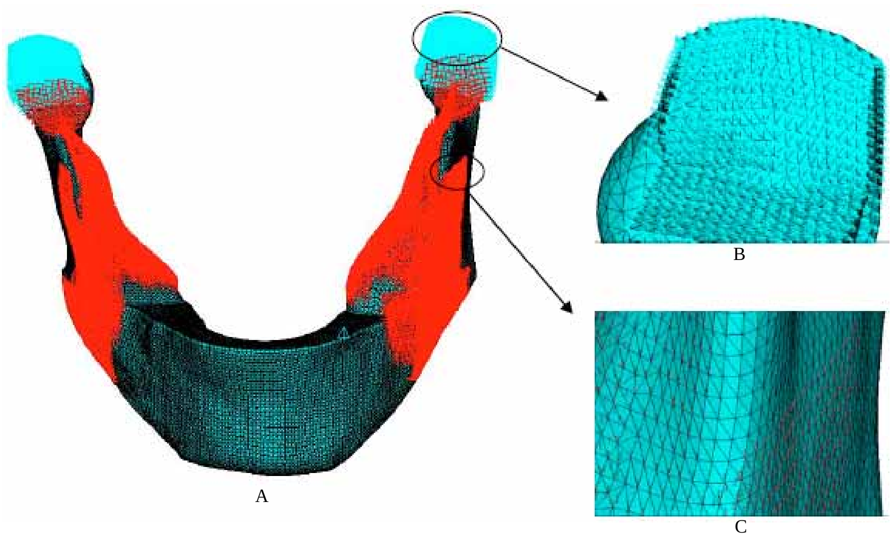

Fig. (11). A) Muscular loads (red) and boundary conditions on disk and occlusal point (blue). **B**) Close-up of boundary conditions modelling on disk. **C**) Close-up of muscle loads modelling.

Table 2. Magnitude and Direction of the Mandible Muscle Forces on the left (L _ _) and Right (R _ _) Side. (PT = Posterior Temporalis; AT = Anterior Temporalis; DM = Deep Masseter; SM = Superficial Masseter; MP = Medial Pterygoid; LP = Lateral Pterygoid)

Muscle	Components of the Unit Force Vector (See Figure 10)			Muscle Force Magnitude [N]	Muscle Insertion Area [mm^2]
	x	y	z		
LPT	0.10	0.76	0.64	11.0	363
LAT	0.07	-0.34	0.94	27.9	363
LDM	-0.27	0.18	0.94	27.3	470
LSM	-0.27	-0.15	0.95	20.2	1098
LMP	-0.32	-0.03	0.94	17.1	1199
LLP	0.25	0.94	-0.25	7.4	123
RPT	-0.10	0.76	0.64	20.2	363
RAT	-0.07	0.34	0.94	21.9	363
RDM	0.27	0.18	0.94	13.5	470
RSM	0.27	-0.15	0.95	9.8	1098
RMP	0.32	-0.03	0.94	16.1	1199
RLP	-0.25	0.94	-0.25	7.4	123

dividing the components of the resultant of each muscular load by the number of the involved nodes. Intensity and direction of the muscular actions have been considered as constant during the occlusion. The bite force location, in correspondence of the first molar, has been modelled by imposing a constraint on the mandible in the normal direction to the occlusal plane in correspondence of the considered occlusal point.

The disk is able to slide among the joint surfaces of the condyle and of the infratemporal cavity, being kept in its position by contact forces (the contribution of the retrodiscal tissue attached to the articular disk is neglected because it is very soft). The infratemporal cavity is supposed infinitely rigid and completely constrained (Figs. **11A** and **11C**).

RESULTS

The numerical simulations have been primarily oriented to a sensitivity analysis, useful to assess the impact on the mandible stress state of the friction values related to the slippage between disk and condyles and between disk and infratemporal cavity [23]. Moreover the influence of the disk stiffness has been taken into account, by considering hyper elastic material and linear elastic material with different values of Young modulus [24].

All the performed simulations, including those under the hypothesis of linear elastic material for the joint disk and absence of friction, become non linear due to the presence of the contact elements.

Figs. (**12,13**) show the FEM contour plots of von Mises equivalent stress for respectively tetrahedral and hexahedral mandible models (with included TMJ) when considering hyper-elastic disk material properties and TMJ friction coefficient equal to 0.3.

The results based on tetrahedral and hexahedral models show a level of discrepancy that is not such to affect the main conclusions of the work; so, in the following, only the tetrahedral models are used for sensitivity analyses.

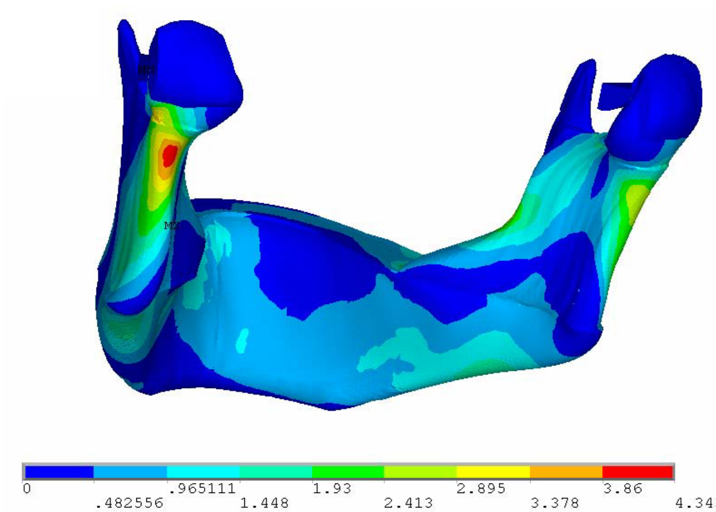

Fig. (12). von Mises equivalent stresses [MPa] on the mandible and TMJ - tetrahedral model.

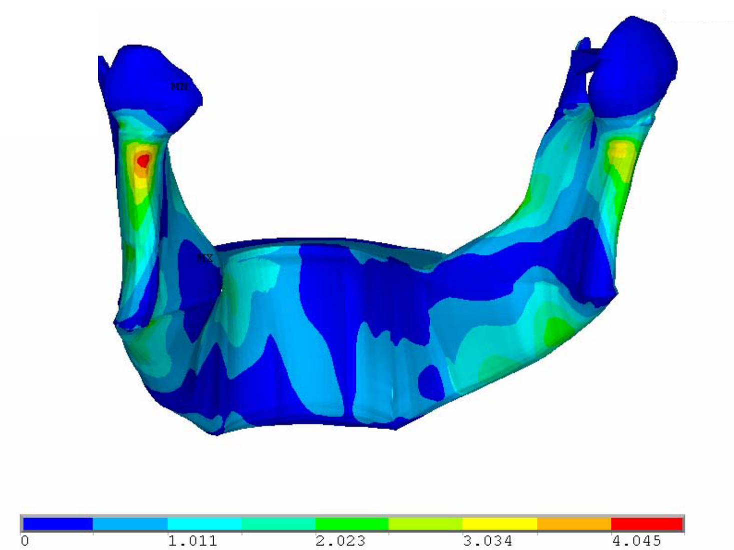

Fig. (13). von Mises equivalent stresses [MPa] on the mandible and TMJ - hexahedral model.

Fig. (**14**) shows the sensitivity analyses for the reaction force on the occlusion point against varying values of TMJ friction coefficients and disk material properties (hyper elastic and elastic with different values of the Young modulus). The adopted TMJ friction coefficients reach very high values, typical of a pathologic condition characterised by the absence or reduced effectiveness of synovial liquid. Such reaction force on the occlusal point (bite force) is not strongly influenced by increasing values of friction coefficient or disk stiffness.

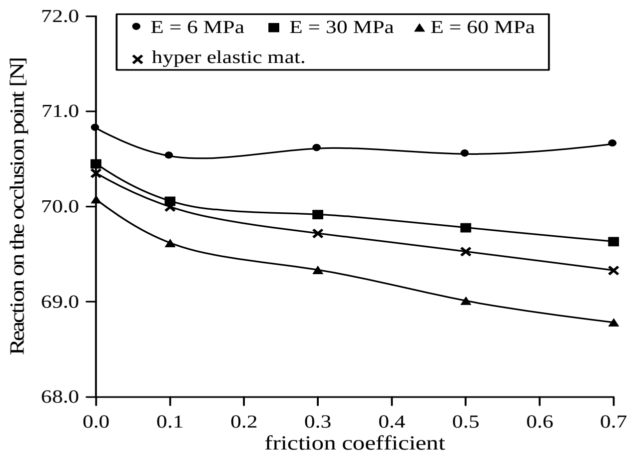

Fig. (14). Reaction on the occlusion point [N].

On the contrary, the maximum stress (von Mises) in the mandible, which is always located in the area below the ipsilateral condyle (Fig. **15**), is affected in non negligible manner by the values chosen for the friction coefficient. Once the loss of lubrication occurs on the joint surface, the mandible appears less stressed.

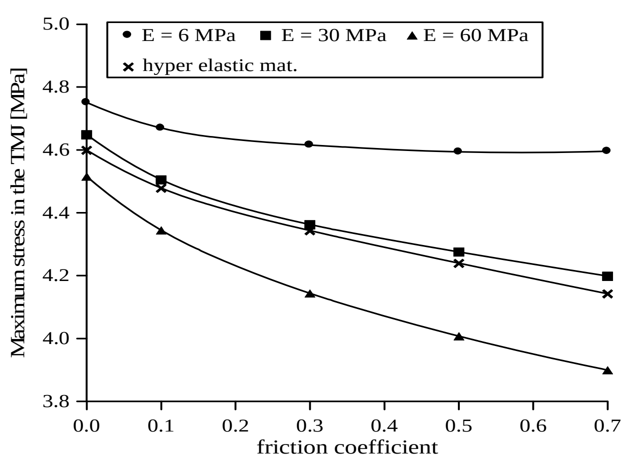

Fig. (15). Maximum stress (von Mises) in the mandible (cortical part) [MPa].

Within the range of the investigated loads, associated to low deformations values for the disks, it turns out that, considering the mandible bone behaviour and for the chosen hyperelastic parameters, there is a good approximation in modelling the disk material as elastic, with Young modulus equal to 30 MPa, instead of a more realistic, but more demanding from a computational point of view, choice of hyper-elastic material properties.

CONCLUSIONS

Stresses in a mandible undergoing mechanical loading play an important role in different clinical situations (fracture healing, callus stabilisation or transplant healing): their knowledge allow the assessment of the bone regenerative capacity.

Concerning the biomechanics of bones, stress evaluation in different anatomical locations can be used to investigate potential fracture sites under artificial or traumatic loading (e.g. forensic evaluation).

The critical point in these numerical analyses resides in the correct boundary condition evaluation and consequently in the availability of realistic anatomic data like bone density (that is proportional to the stiffness) and muscle forces.

But anyway, based on the obtained results, the following conclusions can be drawn.

Within the range of the muscle forces considered, a more complex modelling of the articular disc material does not considerably affect the reaction force on the occlusal point, whereas the peaks of the mandible stresses are influenced in a non negligible manner by both friction coefficient and disk stiffness values at least considering a non pathological range of TMJ friction coefficient values (less than 0.2).

REFERENCES

[1] J. Chen, L. Xu, "A finite element analysis of the human temporomandibular joint", *Journal of Biomechanics Engineering*, vol. 116, pp. 401-407, 1994.

[2] J. Chen, U. Akyuz, L. Xu, R. M. V. Pidaparti, "Stress analysis of the human temporomandibular joint", *Medical Engineering and Physics*, vol. 20, pp. 565-572, 1998.

[3] N. Paydar, H. U. Akay, C. L. Poyraz, W. E. Roberts, "Finite element model of a human mandible for investigating joint reactions and bone stresses during mastication", *Advances in Bioengineering*, ASME, vol. 20, pp. 163-166, 1991.

[4] M. Beek, J. H. Koolstra, L. J. van Ruijven, T. M. G. J. van Eijden, "Three-dimensional finite element analysis of the human temporomandibular joint disc", *Journal of Biomechanics Engineering*, vol. 33, pp. 307-316, 2000.

[5] R. del Pozo, E. Tanaka, M. Tanaka, M. Kato, T. Iwabe, M. Hirose, K. Tanne, "Influence of friction at articular surfaces of the temporomandibular joint on stresses in the articular disk: a theoretical approach with the finite element method", *Angle Orthodontist*, vol. 73, no. 3, pp.319-327, 2003.

[6] E. Armentani, C. Calì, F. Caputo, R. Citarella, M. Infante, G. Lavorgna, "Modello agli elementi di contorno per l'analisi tensionale dell'articolazione temporo-mandibolare", in *XXXI Convegno Nazionale AIAS Conference Proceedings*, Parma, Italy, 2002.

[7] E. Armentani, F. Caputo, R. Citarella, M. Infante, G. Lavorgna, A. Naddeo, "Analisi FEM di una mandibola umana con relativa articolazione temporo-mandibolare", in *XXXI Convegno Nazionale AIAS Conference Proceedings*, Parma, Italy, 2002.

[8] E. Armentani, C. Calì, F. Caputo, R. Citarella, G. Lavorgna, "Analisi non lineare FEM e BEM di una mandibola umana in presenza del disco articolare", in *XXXII Congresso Nazionale AIAS Conference Proceedings*, Salemo, Italy, 2003.

[9] E. Armentani, F. Caputo, R. Citarella, G. Lavorgna, "Analisi FEM di una mandibola in presenza di disco articolare a comportamento iperelastico", in *Convegno Nazionale XIV ADM - XXXIII AIAS Conference Proceedingas*, Bari, Italy, 2004.

[10] M. Hirose, E. Tanaka, M. Tanaka, R. Fujita, Y. Kuroda, E. Yamano, T. M. G. J. van Eijden, K. Tanne, "Three-dimensional finite-element model of the human temporomandibular joint disc during prolonged clenching", *European Journal of Oral Sciences*, vol. 114, pp. 441-448, 2006.

[11] A. Pérez Del Palomar, M. Doblaré, "Anterior displacement of the TMJ disk: Repositioning of the disk using a mitek system. A 3D finite element study", *Journal of Biomechanical Engineering*, vol. 128, no. 5, pp. 663-673, 2006.

[12] A. Pérez del Palomar, M. Doblare, "Finite element analysis of the temporomandibular joint during lateral excursions of the mandible", *Journal of Biomechanics*, vol. 39, pp. 2153-2163, 2006.

[13] G. Sammartino, G. Marenzi, R. Citarella, R. Ciccarelli, H. L. Wang, "Analysis of the occlusal stress transmitted to the inferior alveolar nerve by an osseointegrated threaded fixture", *Journal of periodontology*, vol. 79, no. 9, pp. 1735-44, 2008.

[14] M. Koseki, N. Inou, K. Maki, "Estimation of masticatory forces for patient-specific stress analysis of the human mandible", *Modelling in Medicine and Biology*, vol. 6, pp. 491-500, 2005.

[15] R. S. Hobson, "A pilot study of mineralization distribution in the cortical bone of the human mandible", *Archives of Oral Biology*, vol. 43, pp. 633-639, 1998.

[16] J. Y. Rho, L. Kuhn-Spearing, P. Zioupos, "Mechanical properties and the hierarchical structure of bone", *Medical Engineering & Physics*, vol. 20, pp. 92-102, 1998.

[17] P. Homolkaa, A. Beer, W. Birkfellner, A. Gahleitner, R. Nowotny, H. Bergmann, "Local calibrated bone mineral density in the mandible presented using a color coding scheme", *Medical Engineering and Physics*, vol. 23, no. 9, pp. 673-677, 2001.

[18] M. Soncini, R. Rodiguez, R. Pietrabissa, V. Quaglini, S. Rizzo, D. Zaffe, "Experimental procedure for the evaluation of the mechanical properties of the bone surrounding dental implants", *Biomaterials*, vol. 23, pp. 9-17, 2002.

[19] K. Maki, A.J. Miller, T. Okano, Y. Shibasaki, "A three-dimensional quantitative computed tomographic study of changes in distribution of bone mineralization in the developing human mandible", *Archives of Oral Biology*, vol. 46, pp. 667-678, 2001.

[20] C. Verna, B. Melsen, F. Melsen, "Differences in static cortical bone remodeling parameters in human mandible and iliac crest", *Bone*, vol. 25, no. 5, pp. 577-583, 1999.

[21] R. T. Hart, N. Thongpreda, "A finite element based study of the biomechanics of the mandible", in *IEEE Engineering in Medicine and Biology Society 10th Annual International Conference*, 1988.

[22] M. G. Faulkner, D. C. Hatcher, A. Hay, "A three-dimensional investigation of temporomandibular joint loading", *Journal of Biomechanics Engineering*, vol. 20, pp. 997-1002, 1987.

[23] E. Tanaka, M. S. Detamore, K. Tanimoto, N. Kawai, "Lubrication of the temporomandibular joint", *Annals of Biomedical Engineering*, vol. 36, no. 1, pp. 14-29, 2008.

[24] J. W. deVocht, V. K. Goel, D. L. Zeitler, D. L. Lew, "A study of the control of disc movement within the temporomandibular joint using the finite element technique", *Journal of Oral and Maxillofacial Surgeons*, vol. 54, pp. 1431-1437, 1996.

A Performance Evaluation of Four Bar Mechanism

Sarat Kumar Mishra, *Department of Mechanical Engineering, Aryan Institute of Engineering & Technology, Bhubaneswar, skmishra784@gmail.com*
Abinash Sahoo, *Department of Mechanical Engineering, Capital Engineering College, Bhubaneswar, abinashsahoo719@yahoo.co.in*
Suryaleen Rout, *Department of Civil Engineering, NM Institute of Engineering & Technology, Bhubaneswar, suryaleenrout@yahoo.co.in*
Sidhanta Behera, *Department of Civil Engineering, Raajdhani Engineering College, Bhubaneswar, sidhantabehera89@gmail.com*

Abstract: This paper deals with the study of joint clearance on kinematics of mechanism and bearing stiffness along with links flexibility on modal analysis at higher frequency. Literature survey reveals that the studies were carried out for high-speed mechanism considering linkage flexibility without considering bearing stiffness.

The method of calculating clearance at joints, checking for orientation of linkages and estimation of exact mechanical error using sensitivity analysis is discussed. An attempt is also made to analyze the actual dynamic performance of mechanism by determining natural frequencies of flexible mechanism at high speed considering the effect of bearing stiffness. Bearing stiffness depends upon speed, bearing load and also on wear, out of run, play etc during operation. It is observed that as the stiffness of joint increases natural frequency also increases and converges when stiffness reaches a value close to $1.6x10^9$N/m.

Keywords: Clearance link, bearing stiffness, flexible linkages.

1. INTRODUCTION

A mechanical system is made-up of several components, which can be divided into two major groups namely links and joints. The functionality of a joint relies upon the relative motion allowed between the connected components. This implies the existence of a clearance between the mating parts. The joint clearance has motivated a number of investigations on the subject [1-3]. Gilardi G. [1] presented a literature review concerned with contact dynamics taking into account the effects of friction and lubrication. P. Flores *et al.* [2] have focused on dynamics of joint of slider-crank system with joint clearance. Schwab [3] modeled analytically joint clearances in mechanical systems considering both the dry contact and the lubrication effects.

In the past few years the number of publications, which deal with elastic behavior of mechanisms, has increased considerably. Dwivedy [4] conducted survey of the literature related to dynamic analyses of flexible robotic manipulators for both link and joint flexibility. An effort has been made to critically examine the methods used in these analyses. Turcic [5, 6] presented dynamic analysis of elastic mechanism system with experimental validation of analytical methods. S.D Yu and F. Xi [7] presented a methodology for free vibration analysis of flexible mechanisms by modeling a beam with higher–order elements. Yu and Cleghorn [8] dealt with procedure for determining values of critical running speeds that cause a high speed flexible mechanism to become dynamically unstable due to parametric resonance.

Various methods including finite element method, lump-mass method, substructure method and continuum mechanics method have been discussed by various researchers. Among other methods, the finite element models have been employed in more general to flexible mechanisms. Flexible links in a mechanism are commonly modeled as elastic beams with and without consideration of the effects of large deformations, shear deformations, rotary inertia and axial deformations. Once modeling of an unconstrained link is completed, the Lagrange multiplier method or the augmented Lagrange equations may be used to formulate the equations of motion for the entire mechanism by enforcing continuity conditions across the interfaces. These differential equations governing the kineto-elastodynamic behaviors of a mechanism are solved directly using numerical or analytical methods to study modal analysis, deflections and stresses in a planar mechanism using a cubic polynomial mode shape.

In the present work, a simple method is presented to estimate the error in the output angle and path generation due to clearance between crank-coupler-follower. Estimation of clearance link, its orientation and bearing stiffness is explained in section 2. Section 3 deals with modal analysis of flexible linkages considering stiffness of joint. Results obtained were compared with results of earlier researchers in Section 4. Conclusions are presented in Section 5.

2. ESTIMATION OF CLEARANCE LINK

Linkages in mechanism are connected with bearing as shown in Fig. (**1**). A bearing comprised of an inner rotating cylinder (JOURNAL) and outer cylinder (BEARING). The two cylinders are closely spaced and angular gap between two cylinders is known as clearance, which is very small as compared to link lengths as shown in Fig. (**2**). The angle δ is an angle of clearance link with reference to crank orientation. The clearance in joints does not constrain any degree of freedom in the system; it imposes some kinematics restrictions limiting the journal to move within the bearing.

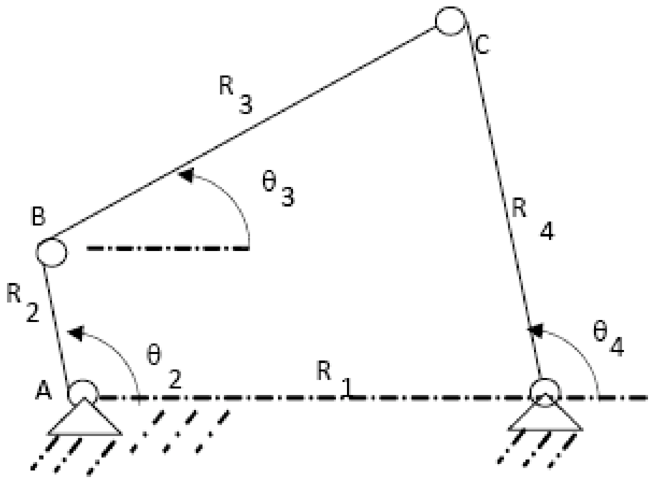

Fig. (1). Four bar linkage without clearance.

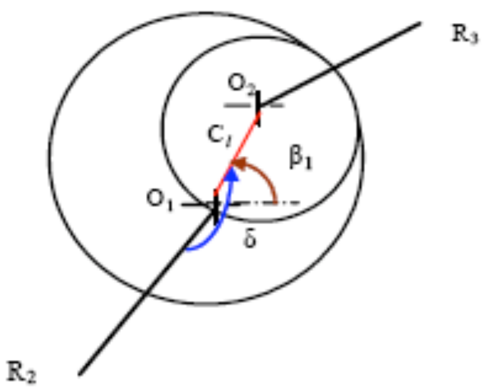

Fig. (2). Clearance link.

The clearance can be allocated from functional point of view or estimated for acceptable deviation in output angle. In this research paper clearance estimated for acceptable deviation in output angle is discussed.

The displacement equation for mechanism can be written using Frudenstein's equation

$$\theta_4 = f(\theta_2, R_i) \quad \text{(i= 1.......4)} \tag{1}$$

The deviation in the output angle due to small deviation in the link parameters follows a statistical pattern which can be expressed probabilistically as

$$\delta\theta_4 = \{\sum_{i=1}^{4}[(\partial\theta_4 / \partial R_i)\delta R_i]^2\}^{1/2} \tag{2}$$

Where allowable deviations in link parameter and specified output deviation is represented by δR_i and $\delta\theta_4$.

Assuming that all tolerance and clearance have the same effect upon output deviation, Eq. 2 will result into

$$(\partial\theta_4 / \partial R_1)\delta R_1 = (\partial\theta_4 / \partial R_2)\delta R_2 = (\partial\theta_4 / \partial R_3)\delta R_3 = (\partial\theta_4 / \partial R_4)\delta R_4 \tag{3}$$

On simplifying

$$\delta R_i = \frac{\ddot{a}\grave{e}_4}{\sqrt{4}\left(\frac{\partial \grave{e}_4}{\partial R_i}\right)} \tag{4}$$

The effective distance between the joints of the links is given by

$$R_{li} = R_i + \ddot{a}R_i \tag{5}$$

R_i is the nominal length of link i as shown Fig. (**3**).

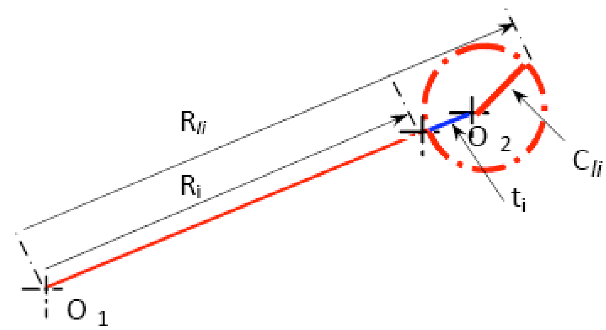

Fig. (3). Details of link.

Total deviation in the link depends upon tolerance in the link (t_i) and clearance at the joint (C_{li}). Assuming ratio of clearance to tolerance equal to unity.

$$C_{li} = t_i \tag{6}$$

The magnitude of $\delta R_i = \sqrt{t_i^2 + C_{li}^2}$ (7)

$$\Rightarrow t_i = C_{li} = \frac{\delta R_i}{\sqrt{2}} \tag{8}$$

Eqs. 1-8 can be used to get required tolerances and clearance on link lengths for specified error in output angle.

2.1. Effect of Joint Clearance on the Orientation of Linkages

It has been observed that, in single loop linkage, joint clearances with same value contribute equally to deviation of the link from its ideal position [9]. It is possible to asses the output position or direction variation, due to clearances allocated at the joints, by using geometrical model.

Let each joint clearance represented by a clearance link C_l, an N-bar linkage is equivalent to a (2N)-bar linkage and the number of Degree of freedom (DOF) is increased from (N -3) to (2N - 3). Because the sum of all clearance link lengths is much smaller than any nominal link length, adding clearance links does not change the classification of the resulting chain, the linkage becomes one with an eight-bar chain including four clearance links as shown in Fig. (**4**). It may be noted that the expression $R_4+R_1<R_2+R_3$ for ideal

mechanism is equivalent to $R_4+(R_1+4C_l)<(R_2+R_3)$ for mechanism considering clearance linkages.

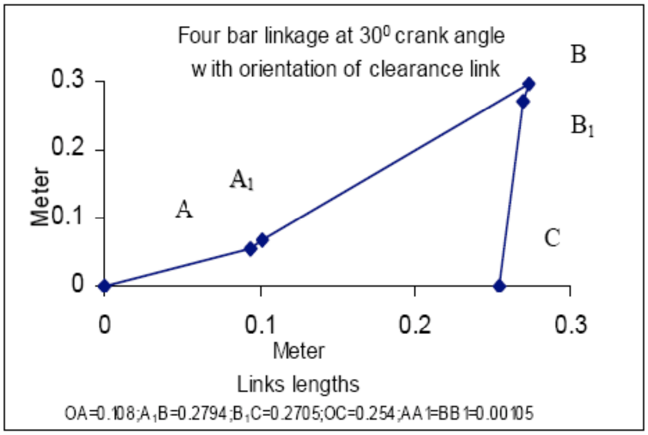

Fig. (4). Linkages with clearance at both end of coupler.

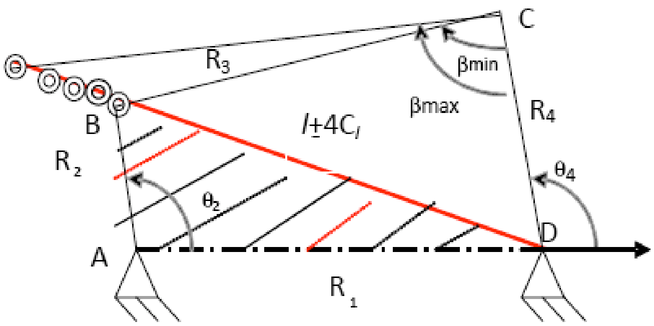

Fig. (5). The limiting value of β.

As shown in Fig. (**5**), sum of all clearance links to diagonal line BD gives two angles between coupler and follower. The length of diagonal (l) is given by cosine formula as

$$l = \sqrt{R_1^2 + R_2^2 - 2R_1R_2Cos\theta_2} \tag{9}$$

The possible range of angle β can be found between β_{min} and β_{max} as

$$\beta_{\min,\max} = \cos^{1} 22\{[R_4^2 + R_3^2 - (l \pm 4C_l)^2]/(2R_4R_3)\} \tag{10}$$

The proposed method makes it possible for designers to predict and set the limits of the uncertain range within the desired safety range by estimating the clearance value.

2.2. Orientation of the Clearance Link (β_1)

Once the clearance has been estimated for the joints of four bar mechanism, its orientation can be obtained from joint forces between the links of mechanism. The joint forces are obtained from the kinematics and dynamics analysis of four bar mechanism with the assumption of rigid–body motion of all linkages and zero clearance in all joints.

$$\beta_1=\tan^{-1}(F_y/F_x) \tag{11}$$

2.3. Sensitivity Co-efficient and Mechanical Error

Clearance links affect kinematics performance of linkages. Jae Kun Shin and Jin Han Jun [10] presented a general method of finding mechanical error using sensitivity coefficients for one revolution of clearance link at fixed crank angle. The method transforms the problem of calculating sensitivity coefficients into one of the velocity analysis. The pattern of the error is elliptical for one cycle of clearance link. In the present work however the exact orientation of clearance link is determined for a given crank angle as explained in Sec.2.2. Using this clearance link and its orientation, exact error has been calculated [11]. Mechanical error of the path point P resulting from a clearance at the pin joint B (Fig. **6**) is defined as:

$$E_p(r,\delta) = R_p(r,\delta) - R_p(0,\delta) \tag{12}$$

r and δ represents the relative position of the pin within clearance circle (Fig. **2**). As the magnitude of the clearance remains small compared to the lengths of links. $R_p(r,\delta)$ can be approximated by Taylor's series

$$R_p(r,\delta) = R_p(0,\delta) + \left.\frac{\partial R_p}{\partial r}\right|_{(0,\delta)} r \tag{13}$$

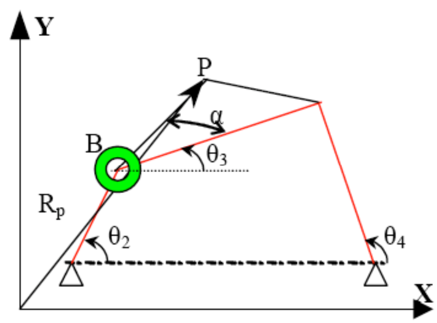

Fig. (6). Four bar mechanism with clearance at B-joint.

Eqs. 12 and 13 give

$$E_p(r,\delta) = \left.\frac{\partial R_p}{\partial r}\right|_{(0,\delta)} r \tag{14}$$

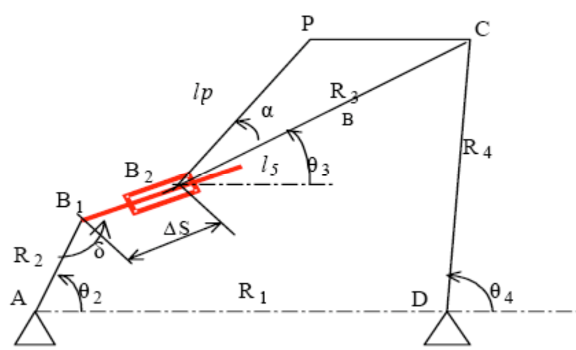

Fig. (7). Sensitivity linkage for the clearance.

The term $\partial R_p/\partial r$ is known as sensitivity co-efficient. Sensitivity linkage is formed by adding, two more links to the original four bar mechanism (Fig. **7**). A slider 'S' is pinned at B_2 and a link 'l_5' through the slider is pinned at B_1

to get a new linkage of 3-DOF. Let 'l_5' be fixed relative to the input link by an angle δ. Then sensitivity coefficients is given by input velocity.

$$\left.\frac{\partial R_p}{\partial r}\right|_{(0,\delta)} = \lim_{\Delta s \to 0}\left(\frac{\Delta R_p}{\Delta S}\right)$$

$$= \lim_{\Delta s \to 0}\left(\frac{\Delta R_p / \Delta t}{\Delta S / \Delta t}\right) = V_p / S^1 \tag{15}$$

Required velocity ratio can be obtained by setting slider input velocity equal to one and Eq.15 will be

$$\left.\frac{\partial R_p}{\partial r}\right|_{(0,\delta)} = V_p\Big|_{\theta_2=\theta_2;\delta=\delta;S^1=S^1} \tag{16}$$

X-Y component of mechanical error $E_{px} = V_{px} C_l$; $E_{py} = V_{py} C_l$ (17)

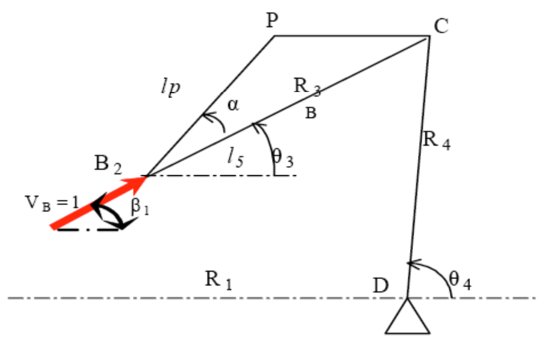

Fig. (8). Open kinematics chain.

Resultant of E_{px} and E_{py} and its orientation (θ_{Ep}) will be

$$TE_p = \sqrt{E_{px}^2 + E_{py}^2} \ ; \ \theta_{Ep} = \tan^{-1}(E_{py} / E_{px}) \tag{18}$$

As shown in Fig. (**8**), the magnitude of R_p (position vector for point P) without clearance $R_{p(Cl,0)}$ is obtained as

$$Rp = \sqrt{R_{px}^2 + R_{py}^2} \tag{19}$$

Position of coupler point P_1, refer Figs. (**8 and 9**), from origin because of clearance between crank and coupler $R_{p(Cl,\,\beta)}$ will be

$$R_{p(cl,\beta)} = \sqrt{R_{p(Cl,0)}^2 + TE_p^2 - R_{p(Cl,0)} TE_p Cos(\Omega)} \tag{20}$$

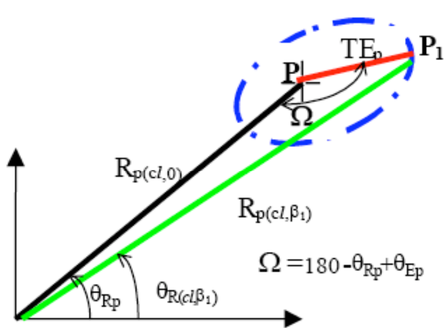

Fig. (9). Magnitude of coupler point with mechanical error.

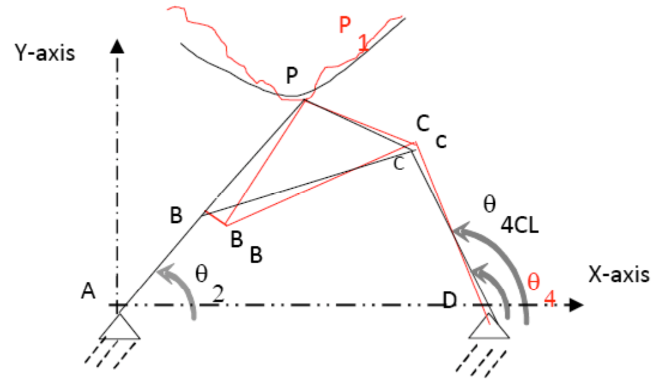

Fig. (10). Four bar linkage with and without clearance.

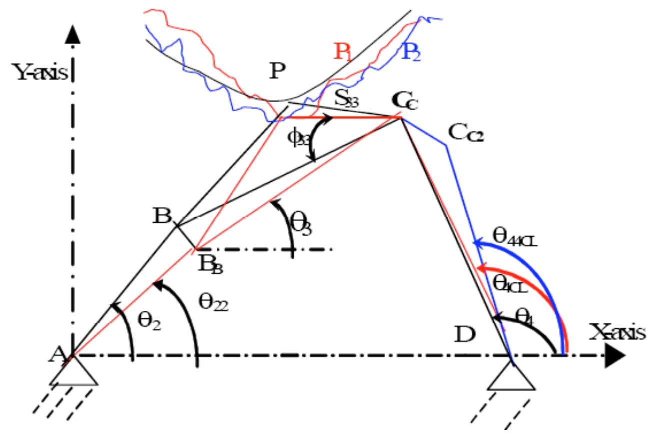

Fig. (11). Four bar linkage with clearance at joints at joint crank and coupler (Joint-1) Crank–Coupler-Follower (Joint-1and Joint-2).

The orientated clearance link (δ) at crank-coupler B-B_B (Fig. **10**) causes the journal center between coupler and follower to shift from C to C_c which causes the error in output angle from θ_4 to θ_{4cl} and coupler point shift from P to P_1. Similarly clearance link at coupler-follower C_c-C_{c2} (Fig. **11**) causes further error in output angle θ_{4cl} to θ_{44cl} and coupler point curve shift from $P_1$to P_2. To obtain the said parameters computer code has been developed. It is observed that obtained error was minimum for optimum transmission angle which is ranging from 60^o-288^o crank angle. Also, clearance links at both end of coupler are used to find total error in the path and function generation.

Clearances in the bearing not only affect kinematics performance but also modal performance of linkages. By knowing the fluctuation of forces at bearing, bearing stiffness can be model as a linear spring using clearance link as discussed in following section.

2.4. Bearing Stiffness

The literature survey indicates that during analysis of elastic linkages bearings have been considered as ideal i.e. without any clearance and elasticity. However, clearance in bearing induces error both in path generation, function generation and also affect the stiffness property of bearing.

Bearings are subjected to horizontal and vertical vibrations due to the joint and unbalance forces. The shaft or journal center always moves about an equilibrium position described by eccentricity (e) and eccentricity angle (φ) as shown in Fig. (**12**). However, the orbit of the shaft motion is small compared to the bearing clearance. Three different types of motion between the journal and bearing can be observed during the dynamics of the revolute joint namely, (i) permanent contact, in which contact is always maintained although the relative penetration depth between the bearing and journal varies along the circumference of the journal; (ii) impact mode, which occurs at the termination of the free flight mode, being impact forces applied to and removed from the system; (iii) free flight mode, in which the journal moves freely within the bearing's boundaries, that is, the journal and the bearing are not in contact. Bearing can be dynamically represented as spring in liberalized model to represent the stiffness. Stiffness coefficient depends on journal speed, load and have significant implication during operation.

For free flight mode, the positive spring constant or stiffness as shown in Fig. (**13**), is defined as the amount of force that is required to obtain a unit displacement in a particular direction. The fluid film forces are functions of journal center displacements and velocities. It is assumed that the journal is subjected to small displacements, which are less than the bearing clearance. The bearing forces can be expressed by Taylor series expansion around the journal.

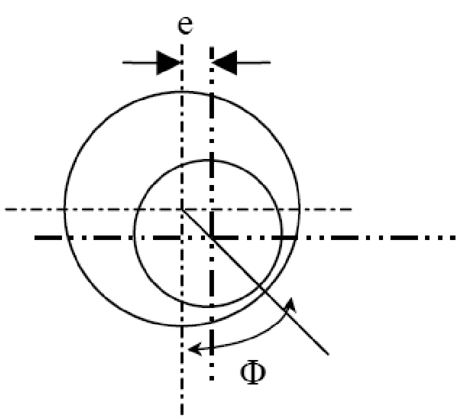

Fig. (12). Equilibrium position.

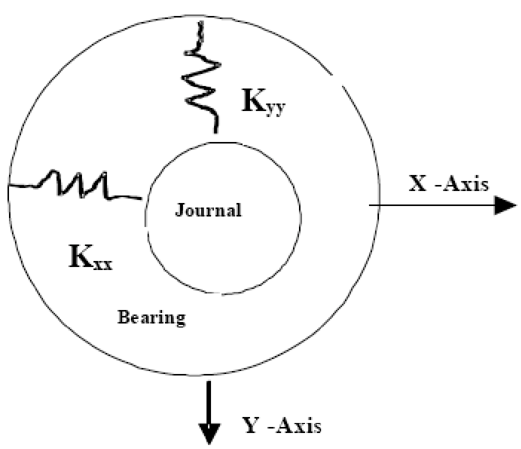

Fig. (13). Dynamic properties of bearing.

$$F_x = F_{x0} + (\delta F_x / \delta X)\Delta X + (\delta F_x / \delta Y)\Delta Y + (\delta F_x / \delta \dot{X})\Delta \dot{X} + (\delta F_x / \delta \dot{Y})\Delta \dot{Y}$$

$$F_y = F_{y0} + (\delta Fy / \delta X)\Delta X + (\delta F_y / \delta Y)\Delta Y + (\delta F_y / \delta \dot{X})\Delta \dot{X} + (\delta F_y / \delta \dot{Y})\Delta \dot{Y} \quad (21)$$

When the journal is subjected to a small displacement in either the ΔX or ΔY direction, a corresponding change in force occurs in both ΔF_x and ΔF_y directions. Thus, stiffness can be defined as in Eqs. 22 and 23.

$$K_{ij} = \Delta F / (.05 * C_l)\ ;\ \text{ij=x, y} \quad (22)$$

$$K_{xx} = \Delta F_x / \Delta x\, ; K_{yy} = \Delta F_y / \Delta y \quad (23)$$

The perturbation constants selected are the fractional amounts of journal displacement from the equilibrium point used in calculating the stiffness coefficients. Over the small changes on the journal position or motion, the dynamic coefficients will be approximately constant and given by .05C_l [12]. Thus perturbation constant defined as

$$\Delta X = \Delta Y = 0.05\ C_l \quad (24)$$

C_l is clearance.

Eqs. 22-24 indicate that bearing stiffness depend upon change in force and clearance value. For free flight mode, bearing stiffness values varying from $2.5\text{x}10^4$N/m to $1.56\text{x}10^9$N/m.

During permanent contact or impact mode, the generalized stiffness parameter K depends on the geometry and physical properties of the contacting surfaces. For two spherical contacting bodies with radii R_i and R_j, the stiffness parameter is expressed by

$$K = \frac{4}{3\pi(\sigma_i + \sigma_j)}\left[\frac{R_i R_j}{R_i - R_j}\right]^{1/2} \quad (25)$$

in which the material parameters σ_i and σ_j are given by

$$\sigma_z = \frac{1-\nu_z^2}{E_z}\ ;\ (z = i, j)$$

Variables υ_z and E_z are the Poisson's coefficient and the Young's modulus associated with each body, respectively. The radius of curvature is taken as positive for convex surfaces and negative for concave surfaces [13]. In Eq. 25, the value (R_i-R_j) represent clearance value. The sphere with radius R_i=8.95mm, R_j=-10mm, E=$2.06\text{x}10^{11}$N/m^2 and Poisson's coefficient ν=0.3 value of stiffness $1.5\text{x}10^{11}$N/m.

The bearing has to overcome torsional stiffness of the link attached. The compliance for torsional stiffness of link attached is represented by a torsional spring. The torsional spring constant K_t for a cantilever beam with a force at the free end is given by [14].

$$K_t = \gamma\, K\varphi\, EI/l \quad (26)$$

Where E is the Young's Modulus, I is the area moment of inertia, l is the beam length and K_Φ is the pseudo-rigid-body model stiffness coefficient, which has the value of K_t =2.65 and γ = 0.85.

Using above expressions, values of linear and torsional stiffness are calculated. Linear spring stiffness values are chosen from 4.5 x10^5N/m to 1.6x10^9N/m depending upon different types of motion. These values are cross checked with the values given in the literature and available software for numerical values for rotor dynamic coefficients for constant speed and load.

3. FINITE ELEMENT MODELING OF FOUR BAR MECHANISM

The mathematical model of four bar flexible linkages must generally capture the mass and stiffness charactertics of links using Lagrang's equation and theory from structural mechanics. Generally 2D-Euler's beam element is selected for system-oriented element matrices. Research dealing with dynamic behavior of four bar crank–rocker mechanism containing elastic effects has been carried out since long. Researchers treated elastic links as continuous system or as discrete system. The finite element theory of structural analysis or lumped parameter approach has been applied for modeling an elastic linkage using force method or the displacement method. Using various analysis methods, researchers have verified their respective techniques by conducting experimental investigations. The main assumption made in the analysis are (i) frictionless bearing representing free-free motion between journal and bearing (ii) no play in the bearings (iii) small elastic deformation from rigid-body equilibrium position (iv) constant crank speed.

However, in reality motion between bearing and journal is governed by dynamics of bearing due to joint forces, hydrodynamic forces etc. Hence in present work, bearing is represented by linear and torsional spring constant as discussed in section 2.4. The effects of these stiffnesses on modal analysis are studied and results are compared with analytical method available for dynamic response of elastic mechanisms presented by D.A Trucic [5, 6].

Eq. 27 shows the motion of the elastic beam element described by Lagrange's Equation,

$$\frac{d}{dt}\left(\frac{\partial KE_i}{\partial\{\dot{U}\}_i}\right)-\frac{\partial KE_i}{\partial\{U\}_i}+\frac{\partial P_i}{\partial\{U\}_i}=\{Q\}_i+\{F\}_i \qquad (27)$$

$\{U\}_i$ represents the generalized nodal DOF, KE_i is kinetic energy of the element, P_i is potential energy, $\{Q\}_i$ the generalized forces acting on the element, $\{F\}_i$ applied external forces.

Eq. 27 is used to develop the element mass and stiffness matrix as given in Eq. 28.

$$[M_e]=\begin{bmatrix} 2a & 0 & 0 & a & 0 & 0 \\ & 156b & 22l_e b & 0 & 54b & -13l_e b \\ & & 4l_e^2 b & 0 & -13l_e b & -3l_e^2 b \\ & & & 2a & 0 & 0 \\ & \text{Symmetric} & & & 156b & -22l_e b \\ & & & & & 4l_e^2 b \end{bmatrix}$$

$$[K_e]=\begin{bmatrix} EA/l_e & 0 & 0 & -EA/l_e & 0 & 0 \\ & 12EI_e/l_e^3 & 6EI_e/l_e^3 & 0 & 12EI_e/l_e^3 & 6EI_e/l_e^2 \\ & & 4EI_e/l_e & 0 & -6EI_e/l_e^3 & 2EI_e/l_e^2 \\ & & & EA_e/l_e & 0 & 0 \\ & \text{Symmetric} & & & 12EI_e/l_e^3 & -6EI_e/l_e^2 \\ & & & & & 4EI_e/l_e \end{bmatrix} \qquad (28)$$

where $a=\dfrac{\rho A_e l_e}{6}, b=\dfrac{\rho A_e l_e}{420}$

The above mass and stiffness matrices are for individual elements in their local coordinates. These elements matrices in the global coordinate system can be defined using transformation matrix [R].

$$[R]=\begin{bmatrix} \lambda & \mu & 0 & 0 & 0 & 0 \\ -\mu & \lambda & 0 & 0 & 0 & 0 \\ 0 & 0 & 1 & 0 & 0 & 0 \\ 0 & 0 & 0 & \lambda & \mu & 0 \\ 0 & 0 & 0 & -\mu & \lambda & 0 \\ 0 & 0 & 0 & 0 & 0 & 1 \end{bmatrix}$$

as $[m] = [R]^T[m_e][R]$; $[k]= [R]^T[k_e][R]$ (29)

where λ= Cos θ : μ= Sinθ and θ is the orientation of element with reference to global co-ordinate system.

To simplify the computational, assumptions made are:

Each link is modeled by one finite-beam element.

The input shaft is assumed to be connected to a flywheel with high inertia, ensuring that no undue fluctuations occur in the input angular velocity.

The input crank is treated as "instantaneous structure" in each position of the moving mechanism for one cycle.

In earlier work to simulate a pin joint between adjacent links two independent rotational deformation in each of the two elements were chosen. These two independent deformations represent free-free motion between adjacent links (bearing and journal). However, here joints are modeled by assigning suitable linear and torsional stiffness. A total system oriented global stiffness matrix of linkage is suitably modified by adding these stiffnesses at appropriate positions.

As shown in Fig. (**14**), system-oriented generalized displacements are labeled to describe the structural deformations of the linkage as well as to maintain compatibility between the elements at the node (bearing joint). For example, at node B, U_4 and U_5 are required to describe the nodal translations from the rigid-body position of linkage, two more independent displacements, U_6 and U_7, are necessary at node B to describe the rotational deformations in each of the two elements, 1 and 2 with respect to their respective rigid-body orientations. In earlier papers movement between journal and bearing was considered as free-free. Actually, the movement is controlled by forces and clearance link of bearing, which can be represented by spring stiffness. The joint characteristic is represented by stiffness values of joint and adding to respective generalized displacements (U_4, U_5 and U6) as shown in Fig. (**15**).

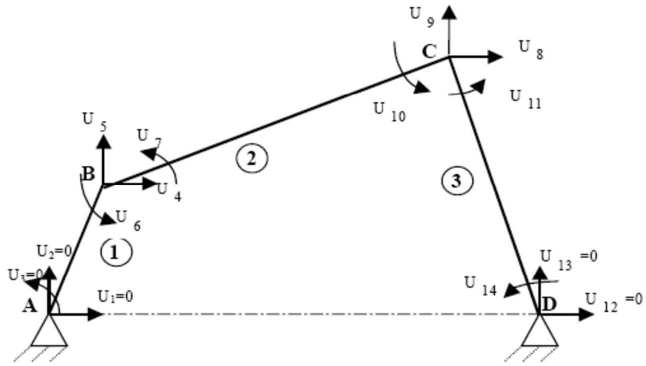

Fig. (14). Elastic mechanism with 3-Elements and 9-DOF.

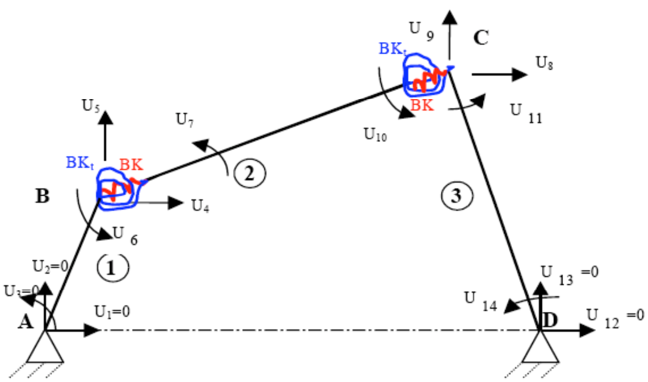

Fig. (15). Elastic mechanism 3-Elements and 9-DOF with flexible Bearing (BK & BK_t).

The total system stiffness matrix [K] is derived as shown in Eq. 30 by superpositioning and considering the required displacements with bearing stiffness at appropriate locations.

[K]=

$$\begin{bmatrix} S^1_{44}+S^2_{44}+BK_{1x} & S^1_{45}+S^2_{45} & S^1_{46} & S^1_{47} & S^1_{48} & S^1_{49} & S^1_{410} & 0 & 0 \\ & S^1_{55}+S^2_{55}+BK_{1y} & S^1_{56} & S^1_{57} & S^1_{58} & S^1_{59} & S^1_{510} & 0 & 0 \\ & & S^1_{66}+BK_{1t} & 0 & 0 & 0 & 0 & 0 & 0 \\ & & & S^2_{77} & S^2_{78} & S^2_{79} & S^2_{710} & 0 & 0 \\ & & & & S^2_{88}+S^3_{88}+BK_{2x} & S^2_{89}+S^3_{89} & S^2_{810} & S^2_{811} & S^2_{814} \\ & & & & & S^2_{99}+S^3_{99}+BK_{2y} & S^2_{910} & S^2_{911} & S^2_{914} \\ & Symetrical & & & & & S^2_{1010}+BK_{2t} & 0 & 0 \\ & & & & & & & S^3_{1111} & S^3_{1114} \\ & & & & & & & & S^2_{1414} \end{bmatrix} \tag{30}$$

In above equation only non-zero generalized coordinates have been labeled. The first element of above stiffness matrix ($S^1_{44}+S^2_{44}+BK_x$) corresponds to the stiffness for displacement vector U_4 of element 1(S^1_{44}), U_4 of element 2 (S^2_{44}) and BK_{1x} stiffness of bearing in X-direction. The superscripts 1 are added to represent stiffness matrix elements of the element numbered 1.

After idealization of linkage structure and system–orientated element mass and stiffness matrices; the next step is to obtain the natural frequencies and natural modes of a system, undamped free vibration equation is used because the damping has very little influence on the natural frequencies of a system. From the free vibration of the system the following modal equation is solved.

$$[M]\{\ddot{U}\}+[K]\{U\}=0 \tag{31}$$

For the free vibration of the system, modal Eq. 31 will be,

$$([K]-\lambda_i[M])\{X_i\}=\{0\} \quad (i=1,2,3\ldots\ldots,n) \tag{32}$$

The condition of Non-zero solution of Eq. 32 is,

$$\left|\,\left|[K]-\lambda_i[M]\right|\right|=\{0\} \quad (i=1,2,3\ldots\ldots,n) \tag{33}$$

From Eq. 32 we can obtain the eigenvalues λ_i (i=1, 2,…, n) of the system and $\lambda_i = \omega_i^2$. The cyclic frequency $f_1=\omega/2\pi$ Hertz. By substituting each eigenvalue λi into Eq.33, the eigenvector $\{X_i\}$or the i^{th} natural mode of the system can be determined. The modal matrix is defined as,

$$[\phi]= [\{X_1\},\{X_2\},\{X_3\}\text{------}\{X_n\}] \tag{34}$$

Natural frequencies (First to Fifth) for mechanism are obtained by solving stiffness and mass matrix using Jacobi Program by accommodating the stiffness of joint. The stiffness of joints is incorporated by changing the stiffness values of joints for axial and transverse directions also the stiffness of pseudo coupler link is added to represent the torsional stiffness as given by Eq. 26.

A complete Computer code FLBMA (FLEXIBLE LINKAGE-BEARING MODAL ANALYSIS) is developed as per the flowchart shown in Fig. (**16**) to find mechanical error due to clearance in joints and to carry modal analysis of linkages considering bearing stiffness for one end and both ends of coupler. The programme is developed using Fortran-77 for kinematic and dynamic analysis while for modal analysis Turbo-C compiler is used. A total 36305 statements are executed by FORTRAN program with time of execution 0.06S.

4. NUMERICAL RESULTS

In this section, for above listed procedure, numerical simulations are performed for a mechanism selected on a case study. Obtained results are compared for flexible mechanism. The geometrical and material properties for a mechanism are presented in Table **1**.

Table 1. Details of Four Bar Mechanism

	Crank	Coupler	Follower
Length (R_i); cm	10.80	27.94	27.05
Area (A_i); cm^2	1.077	0.406	0.406
Area Movement of inertia; cm^4	$1.616*10^{-2}$	$8.674*10^{-4}$	$8.674*10^{-4}$
Fixed pivots; cm	25.4		
Modulus of Elasticity; kPa	$7.10*10^{7}$		
Clearance; cm	0.105		

Position of coupler Point(P) $\alpha=38^o$ w.r.t. coupler link and lp=5.0cm. Weight density of links $2.66*10^{-2}N/cm^3$. Weight of bearing 0.42N. RPM of crank is 340.

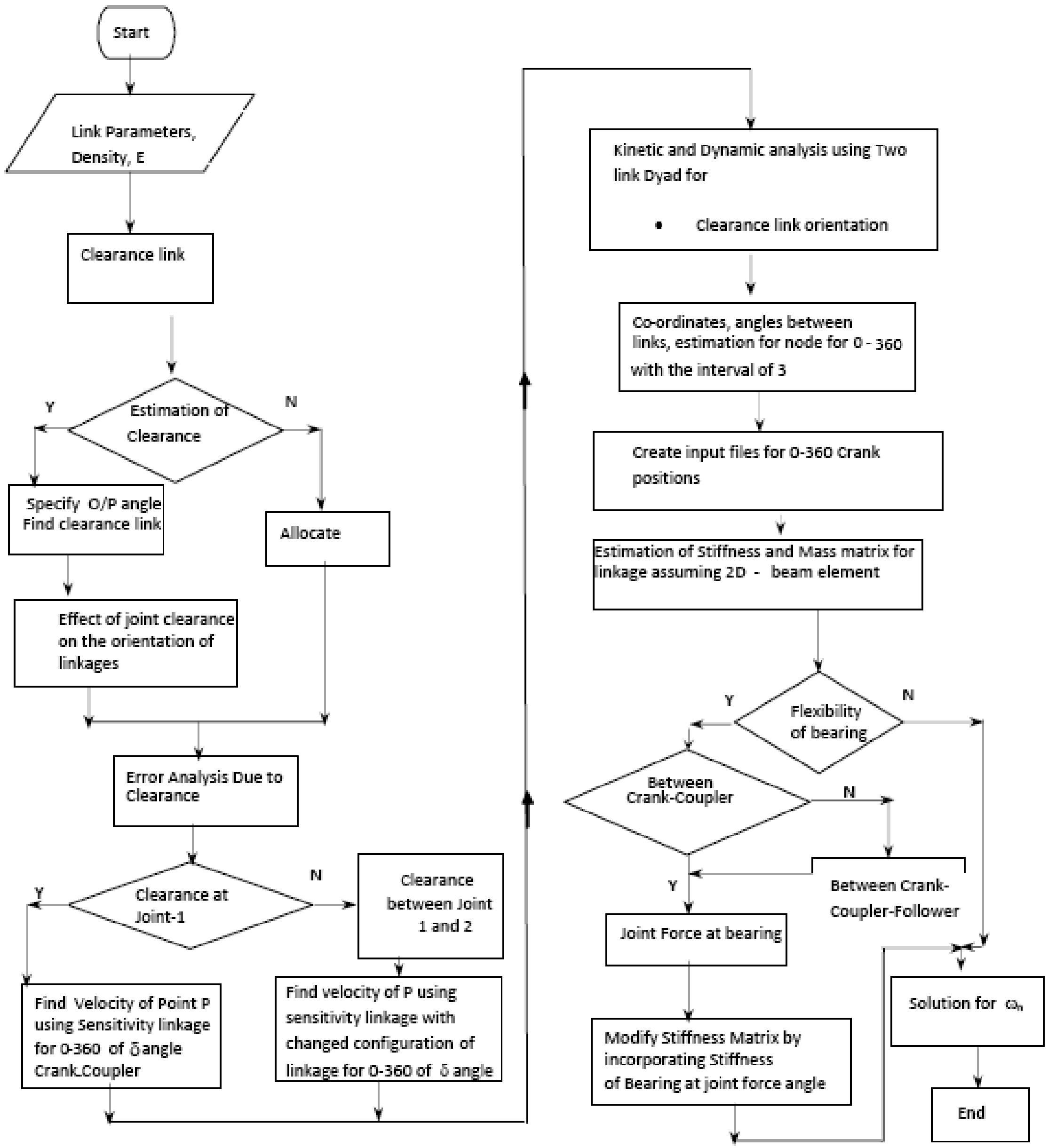

Fig. (16). Flow chart for procedure used in development of computer code.

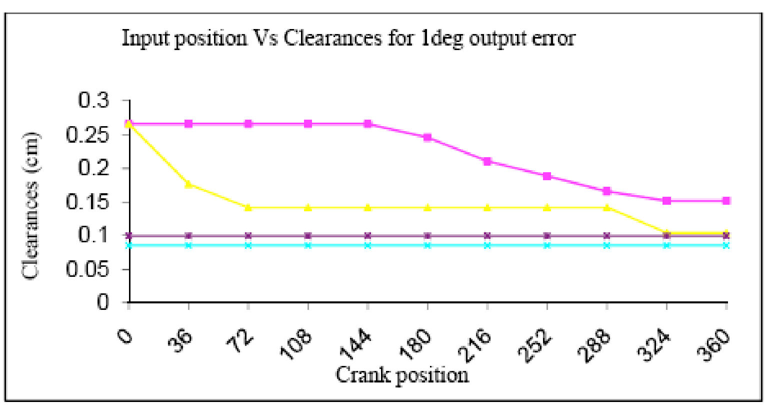

Fig. (17). Crank Angle *vs*. magnitude of clearance.

The magnitude of clearances on each joint of mechanism for 1^o error in output angle is obtained using procedure of section 2 and depicted (Fig. **17**). Clearance link between joint R_1-R_2 is ranging from 0.266 to 0.125cm, between joint R_2-R_3 is ranging 0.266 to 0.105 cm and between joint R_3-R_4 and R_4-R_1 is constant.

As joint clearance affect configuration of linkages from its ideal positions, obtained clearances are checked as per section 2.2 for ensuring the mobility and characteristics of mechanism. Results are given in Fig. (**18**) for coupler angle θ_3 and clearance link of magnitude 0.105cm. It shows that due to addition of clearance links at point B as shown in Fig. (**5**), coupler angle θ_3 deviate by 1.8^o in the present case.

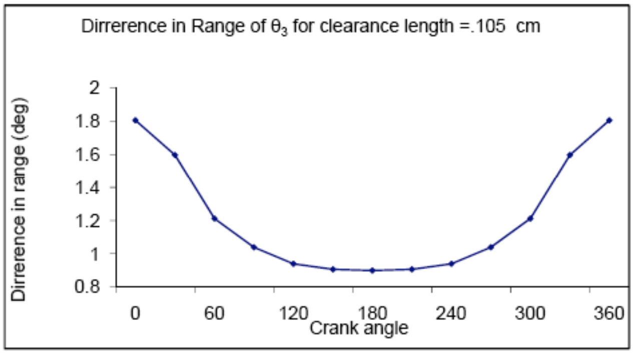

Fig. (18). Difference in Range of θ_3.

The mechanical error, for constant crank angle of 150^o and one complete revolution of clearance link is elliptical in nature as shown in Fig. (**19**).

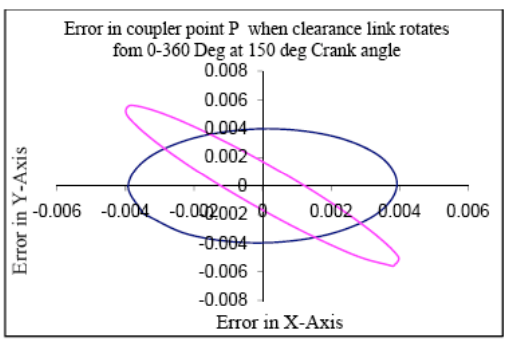

Fig. (19). Distribution of Error at $\Theta_2 = 150^o$ and δ varies 0-360^o for coupler point.

For exact estimation of mechanical error, the angle δ is obtained through kinematics and dynamic of given mechanism [11]. The results are obtained for rigid body angular velocity and acceleration of coupler and follower for constant anticlockwise crank angular velocity of 340rpm (35.6rad/s). The joint forces are obtained with assumption of zero clearance in all joints. Detail results for velocity, acceleration of coupler and follower, components of joint forces at crank-coupler (Joint-1) are presented in Fig. (**20a-c**).

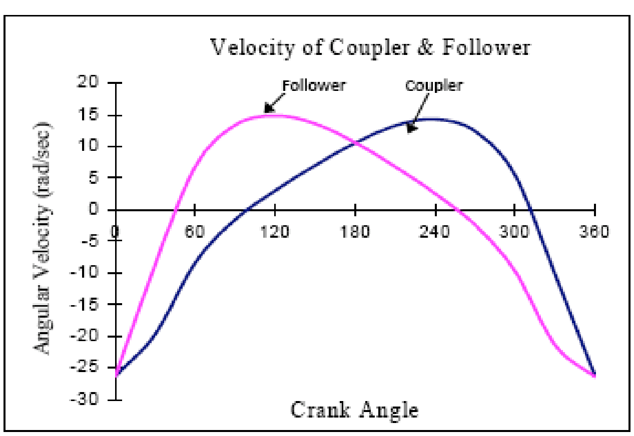

Fig. (20a). Velocity analysis.

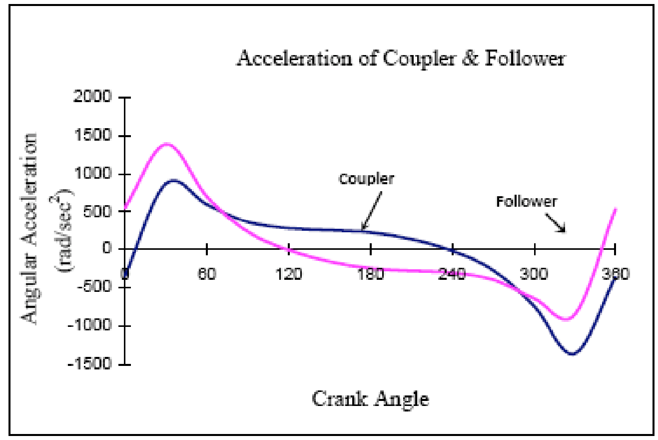

Fig. (20b). Acceleration analysis.

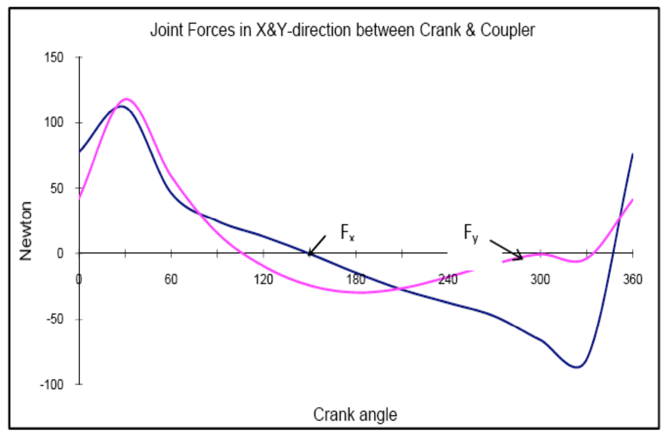

Fig. (20c). Joint forces between Crank and Coupler.

Fig. (20a-c). Graphical representation of Kinematics and Dynamic Analysis.

The significant part of current results, which distinguishes from earlier results, is that in present work exact estimation of mechanical error in coupler point curve is carried out considering clearance link orientations at one and both ends of the coupler. Results of which are shown in Fig. (**21**).

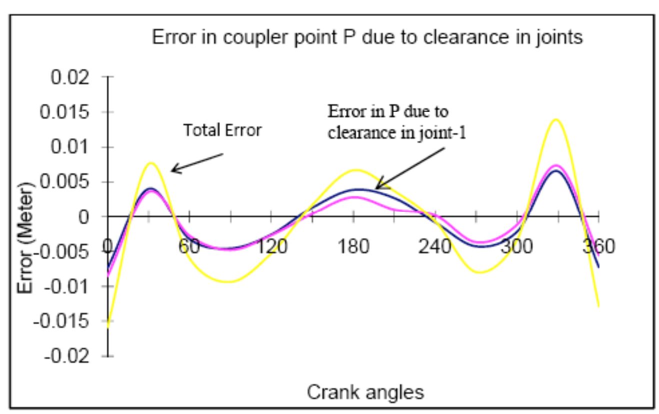

Fig. (21). Error in Coupler point P due to clearances at both ends of coupler.

Clearance links which are established for 1^o permissible errors in the output angle are used to find out actual error in the output angle considering joint first at only one end and than at both the ends of the coupler. The variation of error is given in Fig. (**22a-b**). The results show that error is within limit except at few points (close to 0^o crank position), hence the method proposed for finding clearance in joint within permissible error limit in output angle has been validated.

After finding the clearance link, its orientation, error in function and path generation, modal analysis is carried out considering ideal joint i.e. free-free movement and joint with clearance having stiffnesses. The stiffnesses of joint calculated as per the Eqs. 22-25 are transformed in X-Y component using resultant joint force angle and incorporated in the stiffness matrix in U_4 and U_5 displacement direction as shown in Fig. (**15**). For torsonal stiffness Eq. 26 is used. Modal analysis is carried out and results are presented in Table **2(a-c)** along with Fig. (**23a-e**). The natural frequencies of the mechanism considering ideal joint are exactly matching with earlier established results for the same mechanism by the ref. [5].

For exact modal analysis of flexible mechanism, joints are added with appropriate linear and torsional stiffness. Finite element approach is used for modal analysis and it is

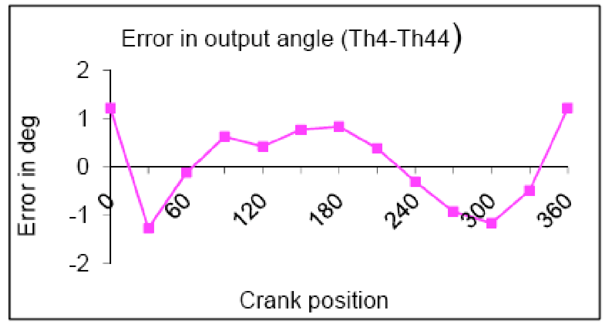

Fig. (22a). Crank Angle *vs*. Clearance for 1deg Error in.

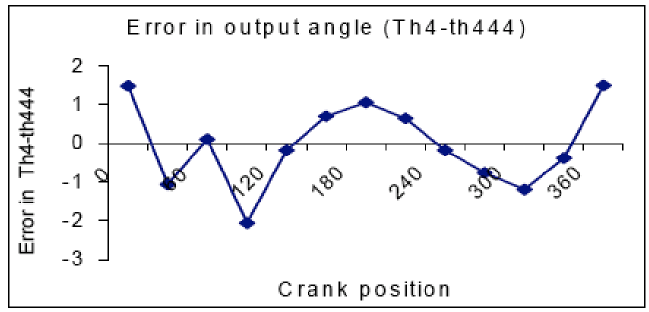

Fig. (22b). Crank Angle *vs*. Clearance for Output angle 1deg Error in Output angle.

Table 2a. Third Natural Frequencies (Rad/s) Bearing at Joint-1

Crank Angle (degree)		0	30	60	90	120	150	180	210	240	270	300	330	360
Sr.No	**Stiffness (N/m)**													
1	0	716	1120	1300	945	834	924	985	1060	1290	1320	1230	811	705
2	4.48E+05	715	1460	1510	1520	1520	1490	984	1490	1510	1520	1520	1440	705
3	9.17E+05	716	1490	1520	1520	1520	1510	985	1510	1510	1520	1520	1500	706
4	1.23E+07	716	1510	1520	1520	1520	1520	986	1520	1520	1520	1520	1520	710
5	8.00E+07	715	1520	1520	1520	1520	1520	992	1520	1520	1520	1520	1520	721
6	1.06E+08	716	1520	1520	1520	1520	1520	992	1520	1520	1520	1520	1520	723
7	6.00E+08	715	1520	1520	1520	1520	1520	995	1520	1520	1520	1520	1520	732
8	1.56E+09	716	1520	1520	1520	1520	1520	997	1520	1520	1520	1520	1520	733

Table 2b. Fourth Natural Frequencies (Rad/s) Bearing at Joint-1 and 2

Crank Angle (degree)		0	30	60	90	120	150	180	210	240	270	300	330	360
S. No.	**Stiffness (N/m)**													
1	0	1560	1600	1570	1530	1520	1530	1550	1590	1620	1620	1530	1530	1570
2	4.48E+05	1560	1600	1570	1530	1520	1530	1550	1590	1620	1620	1550	1530	1570
3	9.17E+05	1560	1600	1580	1530	1520	1530	1550	1600	1620	1620	1580	1530	1570
4	1.23E+07	1560	1610	1610	1610	1610	1600	1550	1620	1620	1620	1620	1580	1570
5	8.00E+07	1560	1620	1620	1620	1620	1620	1550	1620	1620	1620	1620	1620	1570
6	1.06E+08	1560	1620	1620	1620	1620	1620	1550	1620	1620	1620	1620	1620	1570
7	6.00E+08	1560	1620	1620	1630	1620	1620	1550	1620	1620	1620	1620	1620	1570
8	1.56E+09	1560	1620	1620	1630	1620	1620	1550	1620	1620	1620	1620	1620	1570

Table 2c. Fifth Natural Frequencies (Rad/s) Bearing at Joint-1

Crank Angle (degree)		0	30	60	90	120	150	180	210	240	270	300	330	360
S. No.	Stiffness (N/m)													
1	0	1820	1980	1750	1690	1670	1680	1690	1730	1970	1910	1720	1740	1830
2	4.48E+05	1820	3290	4890	3880	3030	2080	1690	2890	5540	6190	4290	2080	1830
3	9.17E+05	1820	4230	6520	5340	4180	2710	1690	3840	7160	7860	5820	2620	1830
4	1.23E+07	1820	9480	10600	10700	10400	8050	1690	9320	10600	10800	10600	7490	1830
5	8.00E+07	1820	10700	11000	11000	10900	10600	1690	10600	10900	11000	10900	10400	1830
6	1.06E+08	1820	10700	11000	11000	11000	10700	1690	10700	11000	11000	10900	10500	1830
7	6.00E+08	1820	10800	11000	11000	11000	10800	1690	10800	11000	11000	11000	10800	1830
8	1.56E+09	1820	10800	11000	11000	11000	10800	1690	10800	11000	11000	11000	10800	1830

observed that for first and second natural frequency, the difference in the magnitude of frequencies with ideal joint and joint with stiffness 1.56E9N/m is minimal and can be neglected. However, third natural frequency for ideal joint is varying from 716rad/s to 1320 rad/s and for joint with equivalent stiffness of 1.56E9N/m is varying from 760 rad/s to 1520 rad/s. There is maximum difference of approximately 760 rad/s. As regards to the fifth natural frequency for ideal joint, is varying from 1670rad/s to 1980 rad/s. and for joint with equivalent stiffness of 1.56E9N/m is varying from 1690 rad/s to 11000rad/s. There is a maximum difference of approximately 9300rad/s Table **2(a-c)** and Fig. (**23a-e**).

In the Table, natural frequencies are given for different values of stiffness assigned to the clearances, varying from 4.48E5 to 1.56E9N/m.

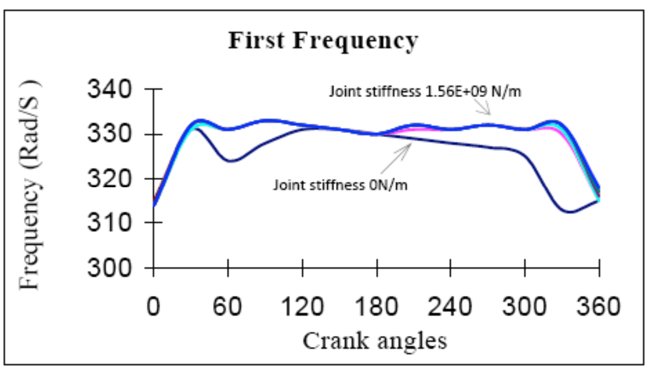

Fig. (23a).

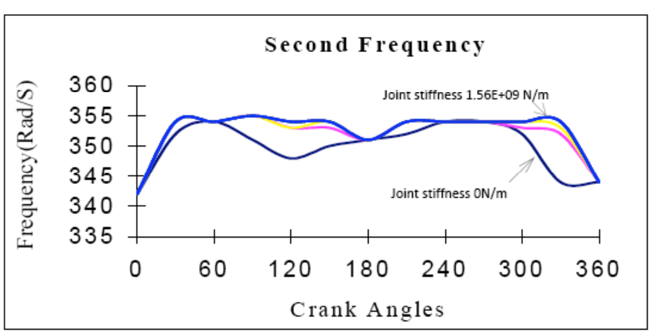

Fig. (23b).

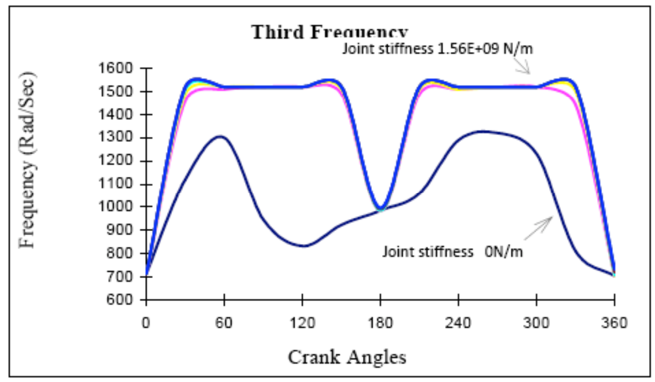

Fig. (23c).

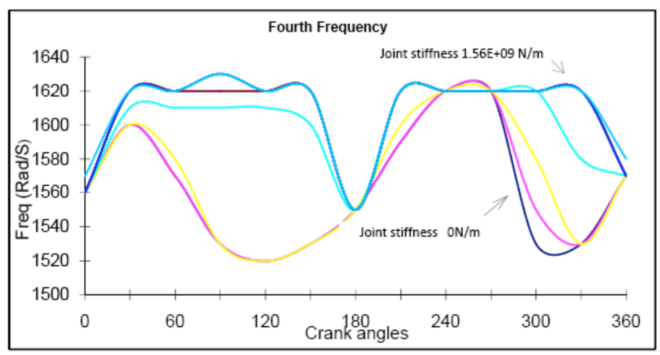

Fig. (23d).

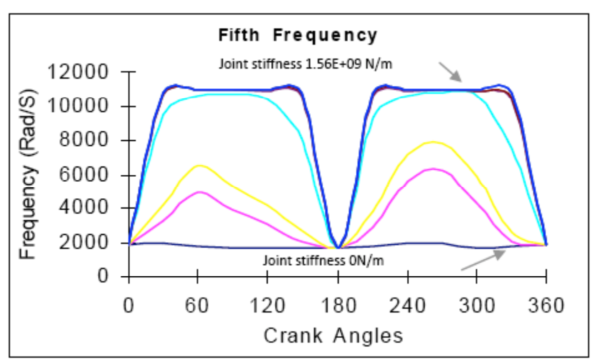

Fig. (23e). Fifth Natural frequency.

Fig. (23a-e). Frequencies considering Bearing Stuffiness between Crank –Coupler.

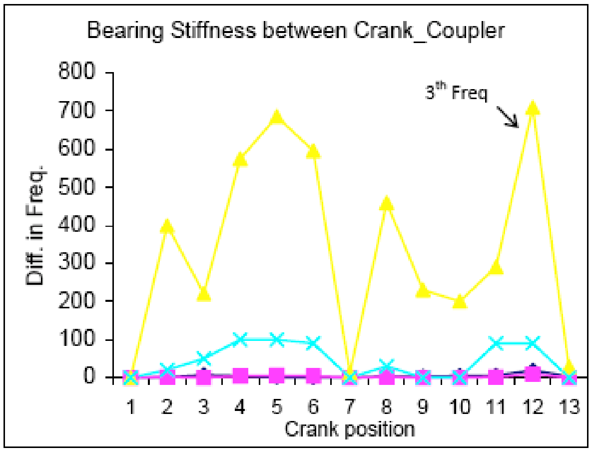

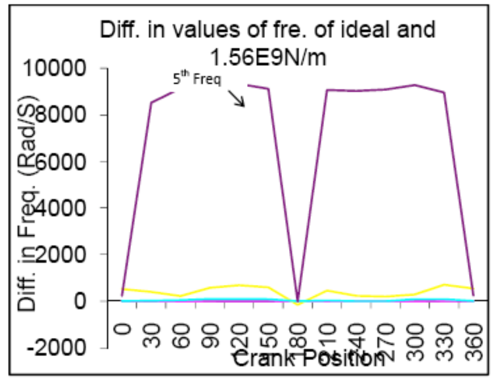

Fig. (24a-b). Difference in Ideal Joint and Joint with Stiffness.

It is observed that as the stiffness of joint is increased from 4.5 x10^5N/m to 1.6x10^9N/m, natural frequency also increases and converges when stiffness reaches approximately to 1.56E9N/m. This is expected and also justified by the earlier work [5, 6]. Fig. (**24a-b**) also indicate that for higher frequencies the difference increases drastically for Third and Fifth frequency. This fact indicates that the effect of bearing stiffness be incorporated in the analysis of flexible linkages operating at higher frequencies to get the actual performance and to study the natural frequencies due to change in stiffness of bearing due to wear, out of run, play etc during operation.

The mid point coupler bending strain are obtained for ninety equal crank angle positions shown in Fig. (**25**). Bending strain and elemental joint forces are minimum from 60^o to 288^o crank angle where the transmission angle is within recommended range ($90^o \pm 40^o$) as shown in Fig. (**26**).

Figs. (**25** and **26**) show coupler mid point bending strain at 340rpm varying from -9.38x10^{-4} to 8.31x10^{-4} *Meter/Meter*. The magnitude of bending strain and therefore stress is minimum for optimum transmission angles and matches with [15]. Optimum transmission variation in the strain with crank angle is also crossed checked with the earlier researcher.

CONCLUSION

In this paper, error in coupler point location and output angle of a four bar mechanism due to clearance link orientation at one end and both ends of coupler is examined. Finite element approach is carried out for modal analysis for linkage and joint flexibility. The study reveals following conclusions:

- For four bar mechanism the coupler point location and output angle is greatly affected by joint clearances and flexibility in linkages.
- The error in the output angle and coupler position is minimum for optimal transmission angles.
- In four bar mechanism joints can be exactly modeled with the help of clearance link assigned with proper

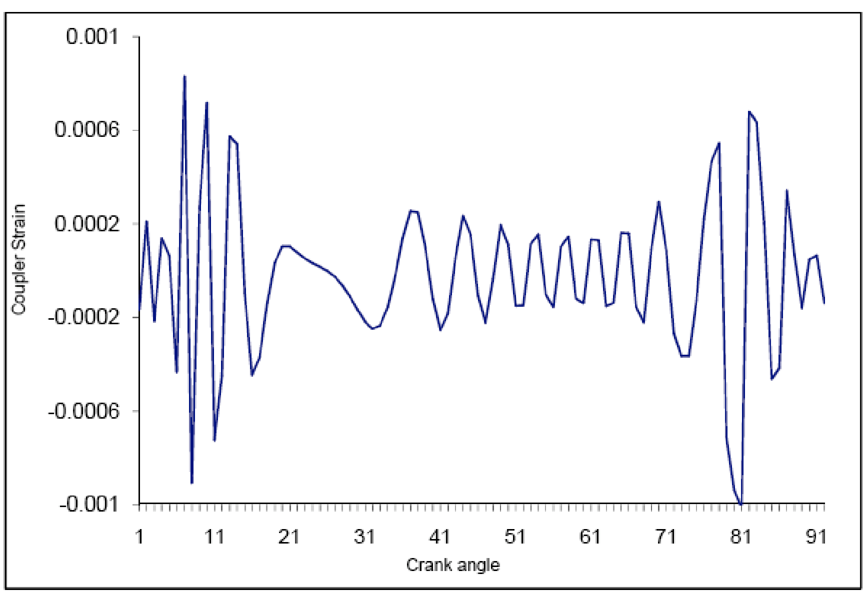

Fig. (25). Coupler mid point bending strain.

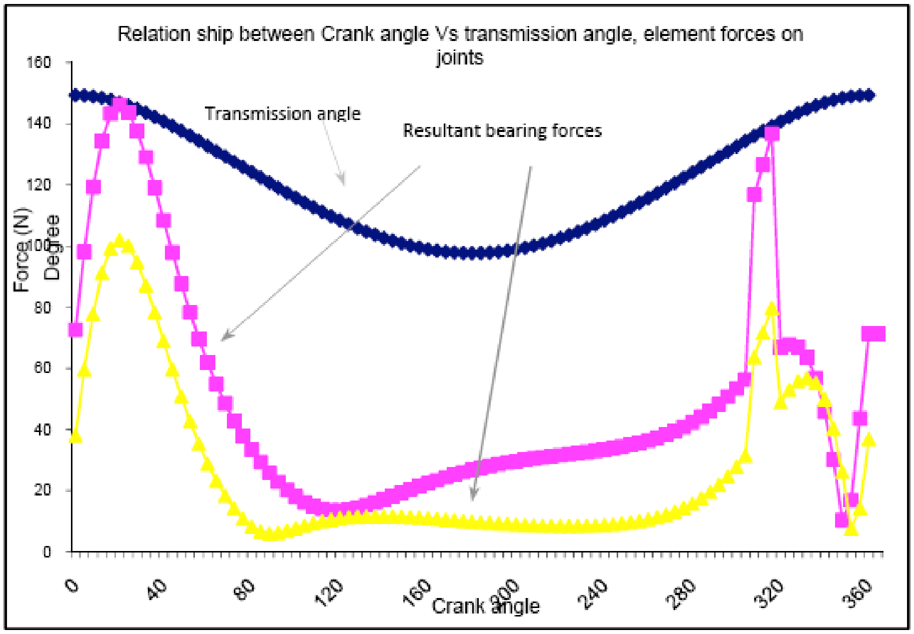

Fig. (26). Transmission angle and elemental joint forces.

axial, longitudinal and torsional stiffness.

- Joint stiffness does affects the model analysis of the four bar mechanism especially at higher order frequencies.

REFERENCES

[1] G. Gilardi, and I. Sharf, "Literature survey of contact dynamics mode-ling," *Mechanism and Machine Theory*, vol. 37, no. 10, pp. 1213-1239, 2002.

[2] P. Flores, J. Ambro´sio, J.C.P. Claro, H.M. Lankarani, and C.S. Koshy, "A study on dynamics of mechanical systems including joints with clearance and lubrication," *Mechanism and Machine Theory*, vol. 41, pp. 247-261, 2006.

[3] A.L. Schwab, J.P. Meijaard, and P. Meijers, "A comparison of revolute joint clearance model in the dynamic analysis of rigid and elastic mechanical systems," *Mechanism and Machine Theory*, vol. 37, no. 9, pp. 895-913, 2002.

[4] S.K. Dwivedy, and P. Eberhard, "Review dynamic analysis of flexible manipulators, a literature review," *Mechanism and Machine Theory*, vol. 41, pp. 749-777, 2006.

[5] D.A. Turcic, and A. Midha, "Dynamic analysis of elastic mechanism systems. Part I: Applications, measurement and control," *Journal of Dynamic Systems*, vol. 106, pp. 249-254, 1984.

[6] D.A. Turcic, A. Midha, and J.R. Bosnik, "Dynamic analysis of elastic mechanism systems. Part II: Experimental Results measurement and control," *Journal of Dynamic Systems*, vol. 106, pp. 255-260, 1984.

[7] S.D. Yu, and F. Xi, "Free Vibration analysis of planar flexible mechanisms," *Journal of Mechanical Design,* vol. 125, 764-772, 2003.

[8] S.D. Yu, and W.L. Cleghorn, "Dynamic instability analysis of high-speed flexible four-bar mechanisms," *Mechanism and Machine Theory*, vol. 37, pp. 1261-1285, 2002.

[9] K.-L. Ting, J. Zhu, and D. Watkins, "The effect of joint clearance on the position and orientation deviation of linkages and manipulators," *Mechanism and Machine Theory*, vol. 35, pp. 391-401, 2000.

[10] J.K. Shin, and J.H. Jung, "On the mechanical errors in planar linkages," *Mechanism and Machine Theory*, vol. 97, pp. 378-382, 1997.

[11] A.M. Vaidya, and P.M. Padole, "Error analysis of four bar planar mechanism considering clearance between crank & coupler," In: *13th National Conference on Mechanisms and Machines (NaCoMM07), IISc*, Bangalore: India, December 2007, pp. 12-13.

[12] R.S. Balupari, "*Validation of finite element program for journal bearing- static and dynamic properties*," MS thesis, College of engineering, University of Kentucky, Lexington, UK 2004.

[13] J. Rhee, and A. Akay, "Dynamic response of a revolute joint with clearance", *Mechanism and Machine Theory,* vol. 31, pp. 121-134, 1996.

[14] L.L. Howell, and A. Midha, "Parametric deflection approximation for end-loaded, large-deflection beams in compliant mechanisms," *Journal of Mechanical Design, Transaction, ASME*, vol. 11 no. 1, pp. 156-165, 1995.

[15] Z. Yang, and J.P. Sadler, "Large-displacement finite element analysis of flexible linkages," *Journal of Mechanical Design*, vol. 112, pp. 175-182, 1990.

Investigation on Cervical Spine Injuries in Vehicle Side Impact

P. Paulpandian, *Department of Mechanical Engineering, Aryan Institute of Engineering & Technology, Bhubaneswar, p_pandian@gmail.com*

Chinmay Swain, *Department of Mechanical Engineering, Raajdhani Engineering College, Bhubaneswar, chinmayswain1972@gmail.com*

Sudeepta Kishor Dash, *Department of Civil Engineering, NM Institute of Engineering & Technology, Bhubaneswar, sudeeptakishordash1@gmail.com*

Raushan Gupta, *Department of Civil Engineering, Capital Engineering College, Bhubaneswar, raushangupta26@yahoo.co.in*

Abstract: This paper presents the development and study of a three-dimensional multi-body model of the 50th percentile male human and discretized neck for the study of cervical spine injuries in vehicle side impact. The neck is composed of cervical spine vertebrae, intervertebral discs, ligaments, and muscles. Following motor crash evaluations, an impactor with a deformable front end representing the front of a car was propelled straight ahead into the sides of the vehicles being assessed. A EuroSID-2 adult male dummy was seated on a sled, restrained using safety belt, and lateral velocity measured from side impact was applied to simulate cervical spine injuries. The results show that the methods used in this paper have the potential to provide a costeffective and versatile platform to examine local loadings on the cervical spine and soft tissues, including the kinetics and the kinematics of the cervical spine and its components, as well as the mechanical response of the intervertebral discs under other complex dynamic loading environment.

Keywords: Cervical spine, multibody model, side impact, biomechanics, soft tissues.

INTRODUCTION

Side impact, commonly known as T-bone collisions, is where the side of one vehicle is hit by the front or rear of another vehicle or a fixed object. An occupant on the struck side of a vehicle may sustain far more severe injuries than an otherwise similar front or rear collision crash. Serious cervical spine injury will result in a huge economic burden of medical and insurance costs and loss of work force. If misdiagnosed or untreated, soft tissue injuries in cervical spine may lead to clinical instability and chronic pain.

Neck sprains and strains are the most frequently reported injuries in US insurance claims. In 2007, an estimated 66 percent of all insurance claimants under bodily injury liability coverage and 57 percent under personal injury protection coverage — two important insurance injury coverages — reported minor neck injuries. For 43 and 34 percent of bodily injury liability and personal injury protection claimants, respectively, neck sprains or strains were the most serious injuries reported. The cost of the claims in which neck pain was the most serious injury was about $8.8 billion, representing approximately 25 percent of the total dollars paid for all crash injuries combined.

What happens to the soft tissue in an accident? The answer to that is even in a slow speed collision, the forces applied to bones, muscles, and joints of the body are clearly capable of inflicting significant injury. Almost all joints are pulled and twisted. Why? Because the body of the occupant is first accelerated in his seat due to the side impact, the head remains static. This inflicts tremendous force on the neck. Then, just as the neck is stretched to (or even beyond) its normal limits, the head starts its lateral motion, the neck snaps back. When this takes place the head has accelerated up to five times the G-force of the impact — and then back. Muscles and ligaments can be stretched beyond their breaking strength. Discs can be damaged. Nerve roots or the spinal cord can be injured permanently [1].

Therefore, the cervical spine receives utmost attention in bioengineering discipline, not only to investigate the head-and-neck to determine the biomechanical limits of its components for a better evaluation of the injury risk, but also to have an insight for the common injuries it is subjected to [2-7].

Injury mechanisms of the cervical spine soft tissues during motor vehicle collisions remain elusive [3-5]. There are few biomechanical studies documenting injuries to the cervical spine ligaments due to flexion-type loading, the most likely injury mechanism during frontal impact [4]. Typically two methods, Multibody Dynamics (MBD) [6-13] and Finite Element Methods (FEM) [14-22] are being using widely to study human spine and soft tissues mechanisms in order to have a better understanding of its kinetics, kinematics, and clinical aspects.

Some literatures investigated chest, pelvis and neck injuries, mechanisms, tolerances, and comparison with impact dummies using postmortem human subjects (PMHS) [23-26]. Some literatures studied cervical spine injuries based on different anthropometric measurements on human volunteer test series [27, 28]. As is well known, it is impossible to carry out experiments on living volunteers to such a degree that injuries are produced. Therefore there has been great emphasis on computational simulation [29-39]. FE models need a great deal of computational power, but can provide detailed information about tissue deformations and injury prediction. Multi-body models can also include many anatomical details while being computationally efficient. This makes them suitable for parameter variation and optimization analyses [3-7].

Therefore, in this study we performed simulation to cervical spine injuries in motor vehicle collisions, with risk analysis when they are involved in side impact collisions. The side impact test is carried out by firing a deformable cart at 53km/h into the driver's side of a stationary car as shown in Fig. (**1**). Under these circumstances, the most frequently seriously injured part of the body is the driver's head, which can obtain substantial safety from the introduction of side impact airbags. So in this paper, the cervical spine injuries are our main concern. The impact problem of adult male dummy in driver seat was analyzed.

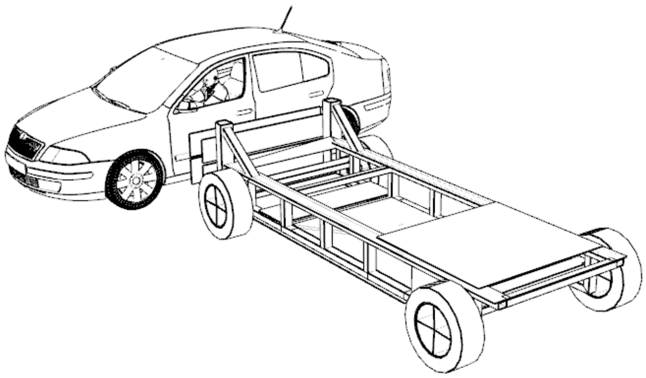

Fig. (1). Motor vehicle side crash sketch.

CERVICAL SPINE ANATOMY

The cervical spine consists of the first seven vertebrae running from the base of the skull to the chest. Sandwiched in between each of these vertebrae is a disc that is made of a gel-like material (the nucleus pulposus) enclosed within a more rigid covering, the annulus fibrosis. These discs act to cushion the vertebrae and absorb shock. The cervical spine anatomy is shown in Fig. (**2**).

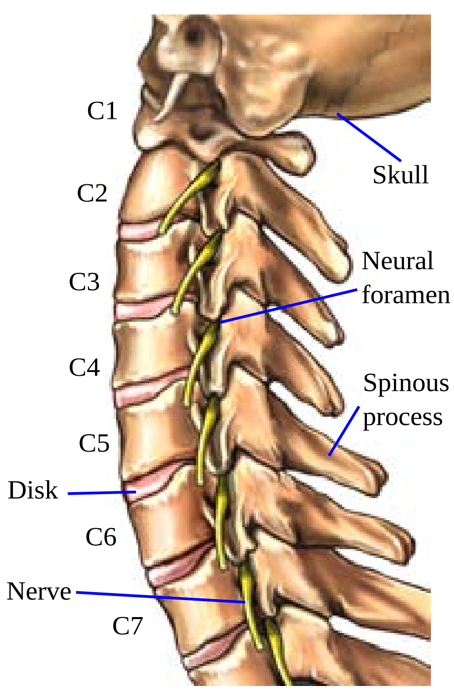

Fig. (2). Cervical spine anatomy.

The cervical spine has a backward "C" shape (lordotic curve) and is much more mobile than either of the thoracic or lumbar regions of the spine. Unlike the other regions of the spine, the cervical spine has special openings in each vertebrae for the arteries that carry blood to the brain.

C1-C7 (Cervical Vertebrae)

C1 through C7 are the symbols for the cervical (neck) vertebrae, the upper 7 vertebrae in the spinal column (the vertebral column). C1 is called the atlas. It supports the head and is named for the Greek god Atlas who was condemned to support the earth and its heavens on his shoulders. (Because the god Atlas often adorned maps, a compilation of maps came to be known as an atlas). C2 is called the axis because the atlas rotates about the odontoid process of C2. The joint between the atlas and axis is a pivot that allows the head to turn. C1 and C2 have special bony structures for supporting the movement of the skull.

Cervical vertebrae 3-7 are more typical. Although the general structures of the cervical spine are similar to the bony structures of the lower spine, there are key differences. The typical cervical vertebrae (C3-C7) are smaller than the vertebrae in the thoracic or lumbar areas. The disc material between the bones is about half as thick. Also, the cervical vertebrae have more of a rectangular shape in the body of the bone. There are two lips on the superior surface of the body of the cervical vertebrae. These lips interlock with the vertebrae above it. The cervical vertebrae are designed to allow more range of motion than the thoracic or lumbar areas, but also provide good stability in the neck region. The spinous processes project posteriorly, the longest of which is C7. C7 is sometimes called the prominent vertebra because of the length of its spinous process (the projection off the back of the vertebral body). Side collision survivors who experience chronic pain often sustain injuries that are undetectable radiographically.

A strain refers to an injury to a muscle, occurring when a muscle-tendon unit is stretched or overloaded. Cervical muscles that are commonly strained include the sternocleidomastoid (SCM), the trapezius, the rhomboids, the erector spinae, the scalenes, and the levator scapulae.

A sprain refers to a ligamentous injury, and the diagnosis of cervical sprain implies that the ligamentous and capsular structures connecting the cervical facet joints and vertebrae have been damaged. Practically, a cervical sprain may be difficult to differentiate from a strain, and the two injuries often occur simultaneously. Pain referred to the muscle can arise from any source that is modulated by the dorsal rami.

The cervical spine or the neck is usually subjected to several forms of injuries that are not seen in the thoracolumbar spine. Injuries to the upper cervical spine, particularly at the atlanto-occipital joint, are considered to be more serious and life-threatening than those at the lower level. The atlanto-occipital joint can be dislocated either by an axial torsional load or a shear force applied in the anteroposterior direction, or vice versa. A large compression force can cause the arches of C1 to fracture, breaking it up into two or four sections. The odontoid process of C2 is also a vulnerable area. Extreme flexion of the neck is a common cause of odontoid fractures, and a large percentage of these injuries are related to motor vehicle collisions. Some survivors will suffer acute strains and sprains of the musculature of the neck, as well as soft-tissue contusions.

SIDE IMPACT SIMULATION

Since 1997 the federal New Car Assessment Program, which compares crashworthiness among new passenger vehicles, has included side impacts. In these tests, an impactor with a deformable front end representing the front of a car is used to strike the sides of the vehicles being assessed. This moving deformable barrier was developed in the early 1980s, when cars represented most of the vehicles on the road. The height of the barrier's front end is below the heads of the dummies that measure injury risks in the side-struck vehicles. Injuries commonly associated with this type of impact include head trauma, maxillofacial injury, spine fracture, thoracic injury, aortic transection, solid organ injury, hollow viscus perforation, and fractures of the femur, knee, and acetabulum.

When a passenger car is hit on the side by another vehicle, the crumple zones of the striking vehicle (the simulation reproduces the situation with a deformable cart attached of aluminum honey comb, the impact absorption material, to all impact areas) will absorb some of the kinetic energy of the collision. The passenger compartment which is inherently rigid and resistant to large deformation is designed to protect the occupants. The car begins accelerating as soon as the crumple zone of the striking vehicle starts crumpling, extending the acceleration over a few extra tenths of a second.

In this paper, a side impact model was built with Finite Element Methods, i.e. explicit, 3-D, dynamic FE computer codes were used to simulate side impact. The lateral velocity of the vehicle side panel can be measured through the side impact simulation and will be used as the initial condition of the analysis on the cervical spine injuries. Fig. (**3**) is the 90-degree side impact test simulation under FMVSS 214 requirements. The vehicle was hit by an impactor with a deformable front end representing the front of a car propelled

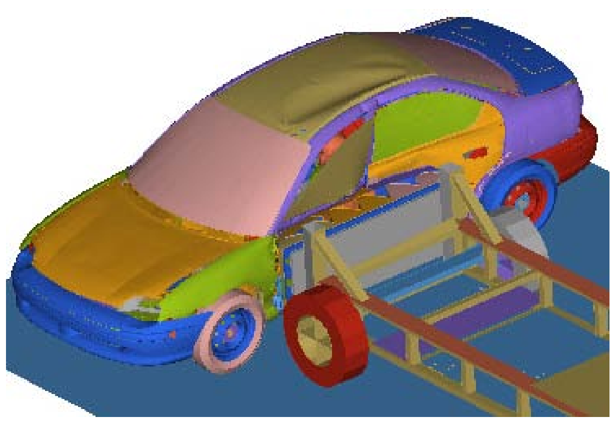

Fig. (3). Side impact simulation.

at a speed of 53 kilometers per hour (km/h). From the figure, less deformation can be seen on the motor side panel because of the inherently rigid passenger compartment comparing to the deformation of the impactor. Because of the buffer function of the aluminum honey comb of the moving deformable barrier, the impact on the test vehicle was decreased. Fig. (**4**) is the lateral velocity of left door measured in the side impact simulation, and will be used in the neck injuries simulation.

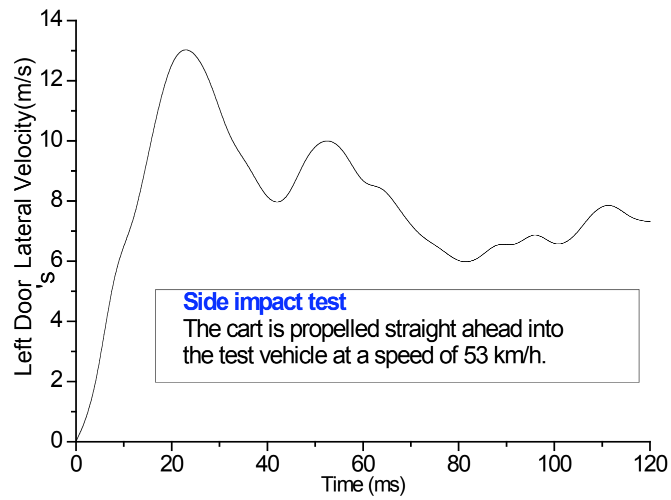

Fig. (4). Left door's lateral velocity.

In this paper, the body of the occupant is first accelerated in his seat due to the side impact, the head remains static. This inflicts tremendous force on the neck. Then, just as the neck is stretched to (or even beyond) its normal limits, the head starts its lateral motion, the neck snaps back.

DRIVER MODEL CONSTRUCTION

The aim of our study was to evaluate the muscle cervical spine load of human in motor vehicle collisions, for this purpose, A EuroSID-2 adult male dummy seated on a sled, restrained using safety belt, was built for a vehicle collision simulation.

The LifeMOD™ Biomechanics Modeler, from Biomechanics Research Group, Inc. is a plug-in module to the ADAMS physics engine. It allows for full functionality of ADAMS/View during the creation of human models. Since human models are built entirely within ADAMS/View, the human models may be combined with any type of physical environment or system for full dynamic interaction. The dummy of EuroSID-2 in this paper was designed based on biomechanics modeler commercially software.

The simulation dummy allows designers and engineers to test and evaluate product performance and characteristics while interacting with the validated 'virtual' model of a human body. Thousands of design iterations can be assessed for user comfort, safety, and fatigue - without expensive physical prototypes or crash-test dummies.

An anthropometric database is used to build the model body segments configurations; this database will relate the data of age, height, weight and sex (user defined) with the size of the several ellipsoids that bring together model parts. The values of joints stiffness and damping of the simulation dummy were set according to the parameters of EuroSID-2 dummy developed in Europe. The driver model was built with the following main parameters.

• Age- 288 months

• Sex-Male

• Height- 178 cm

• Weight- 72 kg

All joints (Scapular, Shoulder, Elbow and Wrist) are passive joints with nominal stiffness. Fig. (**5**) is the driver model built with EuroSID-2 dummy parameters, seated on a sled and restrained using safety belt.

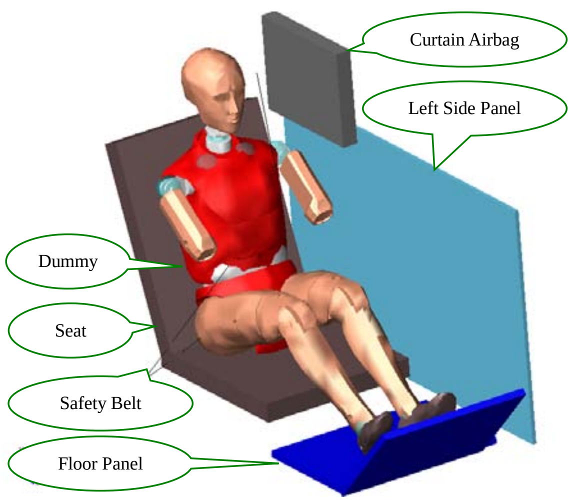

Fig. (5). Driver model construction.

In this paper, the single base segment of the neck is discretized into C1-C7 vertebrae elements. In addition to the individual parts, bushing forces representing disk compression and shear forces are automatically generated between the segments. Fig. (**6**) is the discretized neck. The model is stabilized with a set of ligament forces for the interspinous, flaval, anterior longitudinal and capsule, as shown in Fig. (**6**).

Muscle force sets representing the trapezius, semispinalis capitis, semispinalis cervicis, longus colli and the sternocleidomastoid are created on the model. The Hill-Formulation muscle model is used to model the muscle dynamics. Tissue sliding elements are created for each muscle to permit the interaction between the tissue and bone.

The Hill muscle formulas combine the A(t) curve and the physiological characteristics of the Hill-based muscles, which operate on the traditional combination of active contractile elements (CE) and parallel passive elements (PE) with force-length and force-velocity contraints.

$$F = (F_{\mathrm{CE}} + F_{\mathrm{PE}}) \cdot T \qquad (1)$$

Equation 1 shows the formula used to place the strength-conditioning limits on Hill muscles where FCE can be found using the formula shown in Equation 2.

$$F_{\mathrm{CE}} = \mathrm{A}(t) \cdot F_{\max} \cdot \mathrm{F_H}(V_{\mathrm{r}}) \cdot \mathrm{F_L}(L_{\mathrm{r}}) \qquad (2)$$

Where:

A(t) = activation state (normalized between 0 and 1)

Fmax = product of the physiological cross sectional area and maximum isometric muscle stress (σmax)

FH = the normalized active force-velocity relation (Hill-curve)

FL = the normalized active force-length relation

Vr = dimensionless lengthening velocity

Lr = dimensionless muscle length

T = muscle force output filter value between 0 and 2

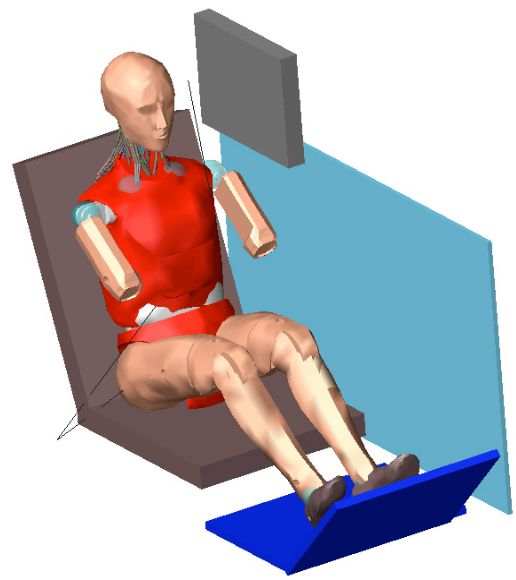

Fig. (6). Discretized neck.

A translational joint is used between the side panel and ground to provide a translational acceleration profile to the model representing a side impact. And the translational joint is driven with a translational joint motion using a velocity spline created from two dimensions velocity data according to Fig. (**4**). So the side panel can move as being hit by the moving deformable barrier.

NECK INJURES SIMULATION

Following motor crash evaluations, a EuroSID-2 adult male dummy were seated on a sled, restrained using belts, and lateral velocity was applied.

The cervical spine muscle force provided postural stability to maintain the neutral posture and passive resistance to intervertebral motion following the side impact, thus approximating the response of an unwarned occupant. Although a driver may be able to foresee the side impact, he may not respond quickly enough to develop sufficient neck muscle force in time to alter the intervertebral kinematics during the impact [4]. Therefore, there was no active force to exert on the joints of C1-C7 vertebrae elements.

Fig. (**7**) is the dummy body movement after side impact. As we can see from the figures, due to the huge impact energy, the neck sprains and strains are inevitable.

RESULTS ANALYSIS

The human cervical spinal column is a three dimensional structure, and the ligaments responsible for maintaining functional interrelationships among the various spinal compo-

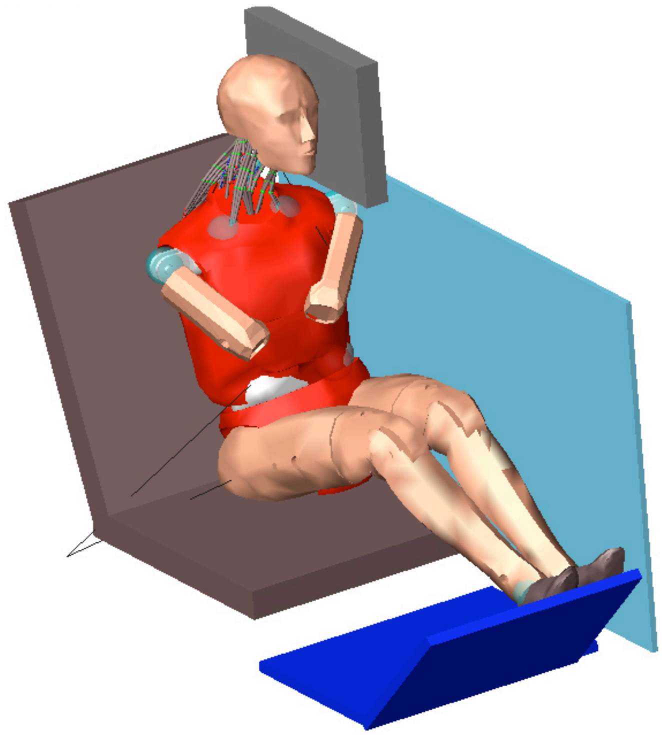

Fig. (7). Dummy body movement after side impact.

nents are complex in geometry and material property. Fig. (**8**) to Fig. (**11**) provide an overview of disk bending loads, extension muscle loads, interspinous ligament loads disk shear strain at head-c1, c1-c2, c2-c3, c3-c4, c4-c5, c5-c5, c6-c7 and c7-t1.

Compressive forces are transferred through the intervertebral disc, the vertebral body, and the facet joints. The intervertebral disc is a viscoelastic material and its mechanical properties are dependent on the rate of loading. At low load rates the disc deforms and is more flexible, but at higher rates the disk becomes stiff [40].

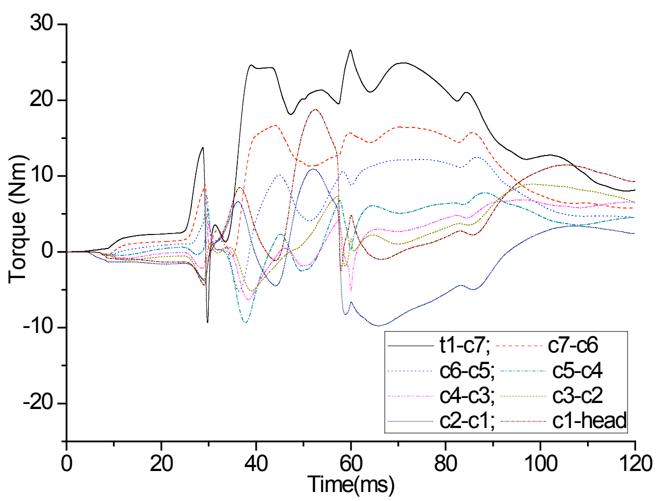

Fig. (8). Disk bending loads.

The results show that bending torque in the discs increases with flexion of the vertebrae and reaches a maximum at all levels at around 48 ms in conjunction with maximum neck rotation. A peak in anterior shear of the discs at all levels can be seen at around 30 ms. During the whole side impact, the load of the t1-c7 interspinous ligament is predominant, as well as the shear strain force of the t1-c7 disc. Therefore, for a neck injured patient, the t1-c7 of the cervical spine is the important inspection area because it is the most likely to be sprained and strained.

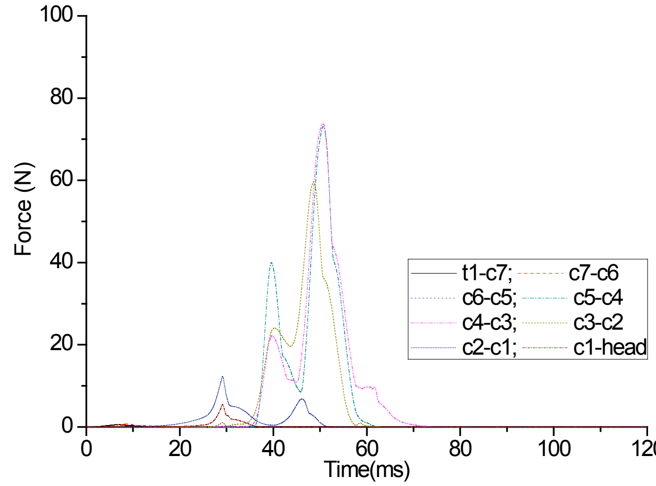

Fig. (9). Interspinous ligament loads.

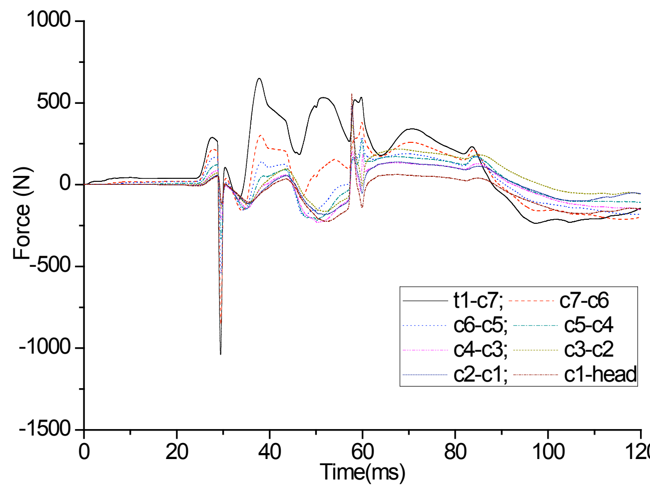

Fig. (10). Disk shear strain for the lateral impact.

c7 and t1 injuries can be classified as either complete or incomplete injuries. Complete injuries result in the total loss of movement and sensation below the point of injury, while incomplete injuries indicate that some function below the level of injury is retained.

Forces and moments causing disc injury increase progressively down the vertebral column. Hiroshi Yamada, Anthony Sances Jr. et al and Bradford Burton et al (and others) found that cervical discs fail at mean loads and moments about 1/5 to 1/3 of lumbar disc values [41]. Since injury thresholds are reduced by up to 1/3 for degenerated discs, the values the 1/5 proportion most likely reflects some degree of disc degeneration.

At more a severe load rate found in higher velocity collisions (44 J of energy) disc failure occurred at a mean bending moment of 185 Nm, and min of 149 Nm.

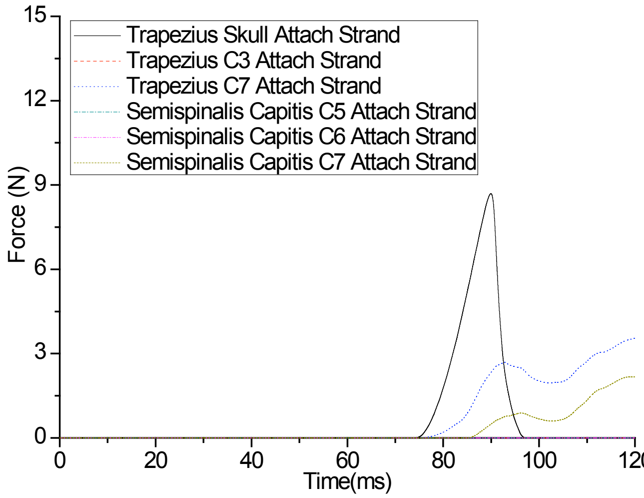

Fig. (11). Extension muscle loads for the lateral impact.

Using the higher 1/3 proportional value, the mean bending moment injury threshold for the cervical region for a somewhat higher speed collision is about 61 Nm, and the corresponding minimal threshold value is about 50 Nm. (Mean and min at 1/5 proportion is 37 Nm and 30 Nm).

The disk bending loads maximum at head-c1 and c2-c3 are about 27 Nm and 28 Nm respectively, which are close to the minimal injury threshold value, which means this driver's cervical spine was injured to a certain extent.

The greatest interspinous ligament load tended to occur at 53 ms, with the largest interspinous ligament load observed at c3-c4. Excessive interspinous ligament load may lead to neck sprains and strains.

CONCLUSIONS

The purpose of this study was to preliminarily evaluate the utility of the multibody approach in cervical spine injuries analysis.

Numerous epidemiologic studies have been completed in the hopes of identifying the cervical spine injury risk patterns that are associated with motor vehicle collisions. Some cervical spine injury may result in a huge economic burden of medical and insurance costs and loss of work force. The mainstay of prevention and treatment of cervical spine injuries is to diagnose exactly in time and maintain good strength and flexibility through conditioning.

This study shows that the methods used in this paper have the potential to provide a costeffective and versatile platform to examine local loadings on the cervical spine and soft tissues, including the kinetics and the kinematics of the cervical spine and its components and the mechanical response of the intervertebral discs under complex dynamic loading environment.

REFERENCES

[1] Insurance Research Council, *Auto Injury Insurance Claims: Countrywide Patterns in Treatment, Cost, and Compensation*, 2008 Edition, Insurance Research Council, Malvern, PA, 2008.

[2] M. J. Van Der Horst, *Human Head Neck Response in Frontal, Lateral and Rear End Impact Loading Modelling and Validation*, Ph.D. dissertation, Tech. Univ. of Eindhoven, Eindhoven, North Brabant, 2002.

[3] A. M. Pearson, M. M. Panjabi, P. C. Ivancic, S. Ito, B. W. Cunningham, W. Rubin, and S. E. Gimenez, "Frontal impact causes ligamentous cervical spine injury," *Spine*, vol. 30, no. 16, pp. 1852-1858, 2005.

[4] M. M. Panjabi, A. M. Pearson, S. Ito, P. C. Ivancic, S. E. Gimenez, and Y. Tominaga, "Cervical spine ligament injury during simulated frontal impact", *Spine*, vol. 29, no. 21, pp. 2395-2403, 2004.

[5] P. C. Ivancic, A. M. Pearson, Y. Tominaga, A. K. Simpson, J. J. Yue, and M. M. Panjabi, "Mechanism of cervical spinal cord injury during bilateral facet dislocation," *Spine*, vol. 32, no. 22, pp. 2467-2473, 2007.

[6] V. Esat, D. W. Van Lopik, and M. Acar, "Combined multi-body dynamic and FE models of human head and neck," in *Proc. of IUTAM Symp. on Impact Biomechanics*, Dublin, 2005, pp. 91-100.

[7] S. Himmetoglu, M. Acar, A. J. Taylor, and K. Bouazza-Marouf, "A multi-body head-and-neck model for simulation of rear impact in cars," *Proc. IMechE, Part D: J. Automobile Eng.*, vol. 221, no. 5, pp. 527-541, 2007.

[8] D. W. Van Lopik, and M. Acar, "A computational model of the human head and neck system for the analysis of whiplash motion," *Int. J. Crashworthiness*, vol. 9, no. 5, pp. 465-473, 2004.

[9] D. W. Van Lopik and M. Acar, "Development of a multi-body computational model of human head and neck," *Proc. IMechE, Part K: J. Multi-body Dyn*, vol. 221, no. 2, pp. 175-197, 2007.

[10] D. W. Van Lopik, and M. Acar, "Dynamic verification of a multi-body computational model of human head and neck for frontal, lateral, and rear impacts," *Proc. IMechE, Part K: J. Multi-body Dyn.*, vol. 221, no. 2, pp. 199-217, 2007.

[11] A. Veloso, G. Esteves, S. Silva, C. Ferreira, and F. Brandao, "Biomechanics modeling of human musculoskeletal system using Adams multibody dynamics package," in *Proc. of the 24th IASTED Int. Conf. on Biomedical Engineering*, Innsbruck, 2006, pp. 401-407.

[12] S. M. Kim, I. C. Yang, and M. P. Lee, "Cervical spine injury analysis regarding frontal and side impacts of wheelchair occupant in vehicle by LifeMOD," in *IFMBE Proc.*, 2007, vol. 14, no. 4, pp. 2521-2524.

[13] L. X. Guo, M. Zhang, Z. W. Wang, Y. M. Zhang, B. C. Wen, and J. L. Li, "Influence of anteroposterior shifting of trunk mass centroid on vibrational configuration of human spine," *Comput. Biol. Med.*, vol. 38, no. 1, pp. 146-151, 2008.

[14] Z. P. Li, J. E. Alonso, J. E. Kim, J. S. Davidson, B. S. Etheridge, and A. W. Eberhardt, "Three-dimensional finite element models of the human pubic symphysis with viscohyperelastic soft tissues," *Ann. Biomed. Eng.*, vol. 34, no. 9, pp. 1452-1462, 2006.

[15] H. Yu, M. B. Medri, Q. Zhou, F. P. DiMasi, and F. A. Bandak, "Head-neck finite element model of the crash test dummy THOR," *Int. J. Crashworthiness*, vol. 9, no. 2, pp. 175-186, 2004.

[16] P. Tropiano, L. Thollon, P. J. Arnoux, R. C. Huang, K. Kayvantash, D. G. Poitout, and C. Brunet, "Using a finite element model to evaluate human injuries application to the HUMOS model in whiplash situation," *Spine*, vol. 29, no. 16, pp. 1709-1716, 2004.

[17] E. C. Teo, Q. H. Zhang, and T. X. Qiu, "Finite element analysis of head-neck kinematics under rear-end impact conditions," in *Int. Conf. on Biomedical and Pharmaceutical Engineering*, Singapore, 2006, pp. 206-209.

[18] E. C. Teo, and H. W. Ng, "First cervical vertebra (atlas) fracture mechanism studies using finite element method," *J. Biomech.*, vol. 34, no. 1, pp. 13-21, 2001.

[19] H. W. Ng, E. C. Teo, and Q. H. Zhang, "Prediction of inter-segment stability and osteophyte formation on the multi-segment C2–C7 after unilateral and bilateral facetectomy," *Proc. IMechE, Part H: J. Eng. Med.*, vol. 218, no. 3, pp. 183-191, 2004.

[20] Q. H. Zhang, S. H. Tan, and E. C. Teo, "Finite element analysis of head–neck kinematics under simulated rear impact at different accelerations," *Proc. IMechE, Part H: J. Eng. Med*, vol. 222, no. 5, pp. 781-790, 2008.

[21] M. J. Fagan, S. Julian, and A. M. Mohsen, "Finite element analysis in spine research," *Proc. IMechE, Part H: J. Eng. Med.*, vol. 216, no. 5, pp. 281-298, 2002.

[22] W. Z. Golinski, and R. Gentle, "The influence of seat back rake on ligament loadings in rear-end impact," *Proc. IMechE, Part D: J. Automobile Eng.*, vol. 219, no. 2, pp. 197-205, 2005.

[23] N. Yoganandan, S. Kumaresan, and F. A. Pintar, "Geometric and mechanical properties of human cervical spine ligaments," *J Biomech. Eng.*, vol. 122, no. 6, pp. 623-629, 2000.

[24] N. Yoganandan, F. A. Pintar, J. Zhang, B. D. Stemper, and M. Philippens, "Upper neck forces and moments and cranial angular accelerations in lateral impact," *Ann. Biomed. Eng.*, vol. 36, no. 3, pp. 406-414, 2008.

[25] N. Yoganandan, F. A. Pintar, D. J. Maiman, M. Philippens, and J. Wismans, "Neck forces and moments and head accelerations in side impact," *Traffic Inj. Prev.*, vol. 10, no. 1, pp. 51-57, 2009.

[26] B. D. Stemper, N. Yoganandan, and F. A. Pintar, "Validation of a head-neck computer model for whiplash simulation," *Med. Biol. Eng. Comput.*, vol. 42, no. 3, pp. 333-338, 2004.

[27] W. Hell, S. Schick, K. Langwieder, and H. Zellmer, "Biomechanics of cervical spine injuries in rear end car impacts: influence of car seats and possible evaluation criteria," *Traffic Inj. Prev.,* vol. 3, no. 2, pp. 127-140, 2002.

[28] J. Latchford, E. C. Chirwa, T. Chen, and M. Mao, "The relationship of seat backrest angle and neck injury in low-velocity rear impacts," *Proc. IMechE, Part D: J. Automobile Eng.*, vol. 219, no. 11, pp. 1293-1302, 2005.

[29] M. M. Panjabi, P. C. Ivancic, Y. Tominaga, and J. L. Wang, "Intervertebral neck injury criterion for prediction of multiplanar cervical spine injury due to side impacts," *Traffic Inj. Prev.*, vol. 6, no. 4, pp. 387-397, 2005.

[30] P. C. Ivancic, S. Ito, M. M. Panjabi, A. M. Pearson, Y. Tominaga, J. L. Wang, and S. E. Gimenez, "Intervertebral neck injury criterion for simulated frontal impacts," *Traffic Inj. Prev.*, vol. 6, no. 2, pp. 175-184, 2005.

[31] M. M. Panjabi, P. C. Ivancic, T. G. Maak, Y. Tominaga, and W. Rubin, "Multiplanar cervical spine injury due to head-turned rear impact," *Spine*, vol. 31, no. 4, pp. 420-429, 2006.

[32] M. Fukushima, K. Kaneoka, K. Ono, M. Sakane, S. Ujihashi, and N. Ochiai, "Neck injury mechanisms during direct face impact," *Spine*, vol. 31, no. 8, pp. 903-908, 2006.

[33] J. W. Lee, K. H. Yoon, and G. J. Park, "A study on occupant neck injury in rear end collisions," *Proc. IMechE, Part D: J. Automobile Eng.*, vol. 217, no. 1, pp. 23-29, 2002.

[34] C. R. Gentle, W. Z. Golinski, and F. Heitplatz, "Computational studies of 'whiplash' injuries," *Proc. IMechE, Part H: J. Eng. Med.*, vol. 215, no. 2, pp. 181-189, 2001.

[35] B. S. Zuckerbraun, K. Morrison, B. Gaines, H. R. Ford, and D. J. Hackam, "Effect of age on cervical spine injuries in children after motor vehicle collisions: effectiveness of restraint devices," *J. Pediatr. Surg.*, vol. 39, no. 3, pp. 483-486, 2004.

[36] R. K. Wilcox, "The biomechanical effect of vertebroplasty on the adjacent vertebral body: a finite element study," *Proc. IMechE, Part H: J. Eng. Med.*, vol. 220, no. 4, pp. 565-572, 2006.

[37] R. J. Oakland, R. M. Hall, R. K. Wilcox, and D. C. Barton, "The biomechanical response of spinal cord tissue to uniaxial loading," *Proc. IMechE, Part H: J. Eng. Med.*, vol. 220, no. 4, pp. 489-492, 2006.

[38] E. M. K. P. Barros, C. J. Rodrigues, N. R. Rodrigues, R. P. Oliveira, T. E. Barros, and A. J. Rodrigues, "Aging of the elastic and collagen fibers in the human cervical interspinous ligaments," *Spine J.*, vol. 2, no. 1, pp. 57-62, 2002.

[39] P. C. Ivancic, M. P. Coe, A. B. Ndu, Y. Tominaga, E. J. Carlson, W. Rubin, F. H. Dipl-Ing, and M. M. Panjabi, "Dynamic mechanical properties of intact human cervical spine ligaments," *Spine J.*, vol. 7, no. 6, pp. 659-665, 2007.

[40] A. A. White, R. M. Johnson, M. M. Panjabi, and W. O. Southwick, "Biomechanical analysis of clinical stability in the cervical spine," *Clin. Orthop. Relat. Res.*, vol. 109, pp. 85-96, 1975.

[41] H. Yamada, *Strength of Biological Materials*. Baltimore, MD: Williams and Wilkins, 1970.

FEM Analysis of High-Speed Motorized Spindle

Sanjeet Raj, *Department of Mechanical Engineering, Aryan Institute of Engineering & Technology, Bhubaneswar, sanjeetraj4@gmail.com com*

Niranjan Behera, *Department of Mechanical Engineering, Raajdhani Engineering College, Bhubaneswar, niranjanbehera2514@gmail.com*

Anjan Kumar M. U., *Department of Civil Engineering, NM Institute of Engineering & Technology, Bhubaneswar, anjankumar28@yahoo.co.in*

Kankan Mandal, *Department of Civil Engineering, Capital Engineering College, Bhubaneswar, kankanmandal26@gmail.com*

Abstract: This paper presents a method to investigate the characteristics of a high-speed motorized spindle system. The geometric quality of high-precision parts is highly dependent on the dynamic performance of the entire machining system, which is determined by the interrelated dynamics of machine tool mechanical structure and cutting process. This performance is of great importance in advanced, high-precision manufacturing processes. The state-of-the-art in machine tool main spindle units is focus on motorized spindle units for high-speed and high performance cutting. This paper taking the high-speed milling motorized spindle of CX8075 produced by Anyang Xinsheng Machine Tool Co. Ltd. as an example, a finite element model of the high-speed motorized spindle is derived and presented. The model takes into account bearing support contact interface, which is established by spring-damper element COMBIN 14. Furthermore, the static analysis, modal analysis, harmonic response analysis and thermal analysis were done by means of ANSYS commercial software. The results show that the maximum rotating speed of the motorized spindle is far smaller than the natural resonance region speed, and the static stiffness of the spindle can meet the requirements of design. The static and dynamic characteristics of the motorized spindle accord with the requirements of high-speed machining. The thermal deformation of spindle is 6.56μm, it is too small to affect the precision of the spindle. The results illustrate the rationality of the spindle structural design.

Keywords: Motorized spindle, finite element analysis, ANSYS.

1. INTRODUCTION

In today's prosperous industrial development, with the multifarious design of products and reduction of production cycle, high speed machining technology has been widely adopted by manufacturers [1]. With the development of the science and technology, the high frequency spindles has been taken place of the normal mechanical spindles more and more, and also be used of the numerical control machine with great effects.

Classically, main spindles were driven by belts or gears and the rotational speeds could only be varied by changing either the transmission ratio or the number of driven poles by electrical switches. Later simple electrical or hydraulic controllers were developed and the rotational speed of the spindle could be changed by means of infinitely adjustable rotating transformers.

The need for increased productivity led to higher speed machining requirements which led to the development of new bearings, power electronics and inverter systems. The progress in the field of the power electronics led to the development of compact drives with low-cost maintenance using high frequency three-phase asynchronous motors. Through the early 1980's high spindle speeds were achievable only by using active magnetic bearings. Continuous developments in bearings, lubrication, the rolling element materials and drive systems have allowed the construction of direct drive motor spindles which currently fulfill a wide range of requirements.

Today, the overwhelming majority of machine tools are equipped with motorized spindles. Unlike externally driven spindles, the motorized spindles do not require mechanical transmission elements like gears and couplings [2].

High-speed motorized spindle is an important component of the high-speed machine tools its performance decides the level of the whole machine tools development to some extent. So high-speed machine tools have strict requirements for technical indexes of the motorized spindle, which is different from traditional spindle system. The safety and reliability due to imperfect dynamic performance have become the primary problem of structural design and machine operation. Therefore, the dynamic performance research of the high-speed motorized spindle has an important theoretical and practical significance [3]. As the FEM (finite element method) has become an essential solution technique in many areas of engineering concerned static and dynamic process, the FEM is utilized in the design of motorized spindle bearing system [4]. The static and dynamic characteristics, the thermal characteristics, and the centrifugal-force induced characteristic variations of motorized spindle bearing system were analyzed by using FEM [5-7].

CX series vertical milling compound machining center is one of the national major technology subjects of "High-grade NC machine tools and basic manufacturing equipment". It is one of the national key research projects of China. Motorized spindle is used in CX8075 series vertical milling compound machining center. The maximum rotating speed of the motorized spindle is greater than or equal to 12,000rpm. Motorized spindle is one of the key parts of CX8075.

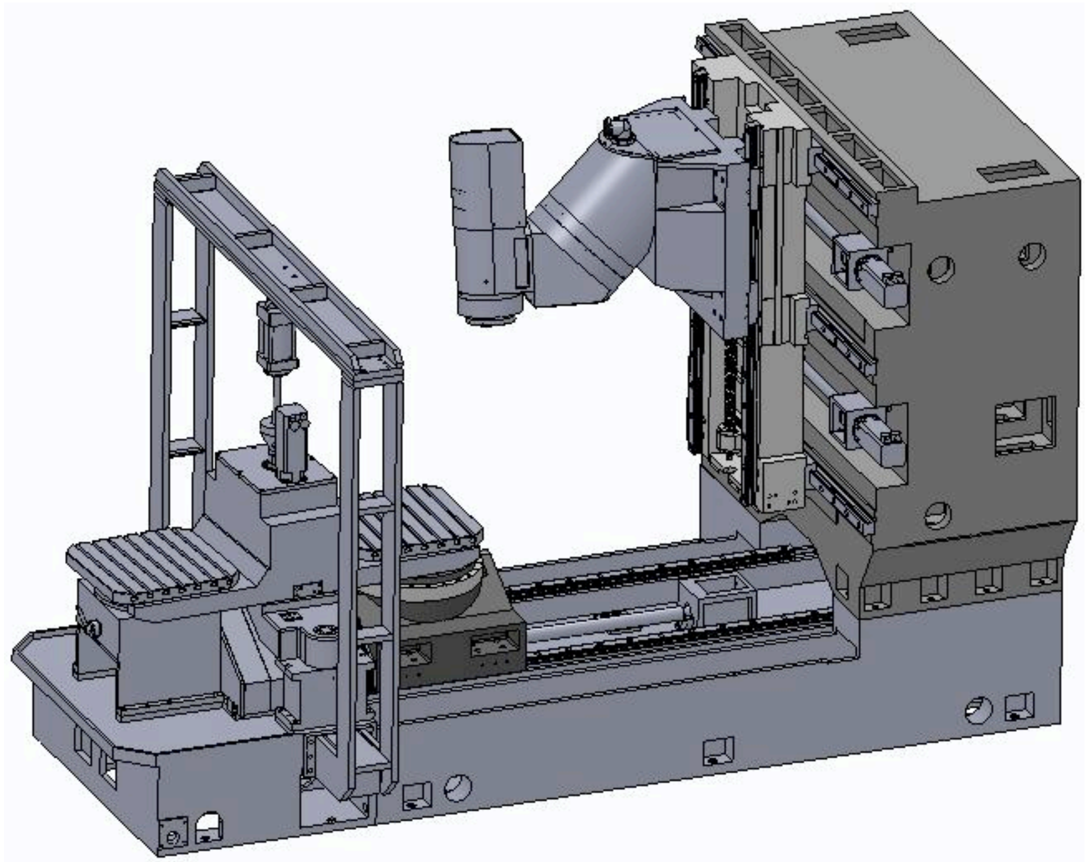

Fig. (1). Assembly drawing of CX8075.

The aim of this paper is to develop a finite element model of the high-speed motorized spindle. The model takes into account bearing support contact interface. The simulations of static, modal, harmonic response and thermal deformation are conducted by using ANSYS commercial software. The static, dynamic and thermal characteristics of the motorized spindle are analyzed and verified by the result of simulation.

2. CX8075 AND MOTORIZED SPINDLE STRUCTURE

Taking the swing milling head of the CX8075 vertical milling compound machining center produced by Anyang Xinsheng Machine Tool Co. Ltd. as an example, the maximum rotating speed of the motorized spindle is greater than or equal to 12,000rpm, and the fast moving speed of feeding system (X/Y/Z axis) is greater than or equal to 60m/min. The virtual assembly result of CX8075 is shown in Fig. (**1**).

The structure of the spindle is shown in Fig. (**2**). In order to meet the requirements of high-speed processing, the standardized tool interface HSK(Hohlschaftkegel) is placed at the spindles front end. The spindle is supported by two sets of angular contact ball bearings which are XCB series super precision spindle bearings produced by the FAG in Germany. For the sake of reducing the axial runout of the spindle and improving the axial stiffness of the spindle, the two sets of angular contact ball bearings are installed in the back to back.

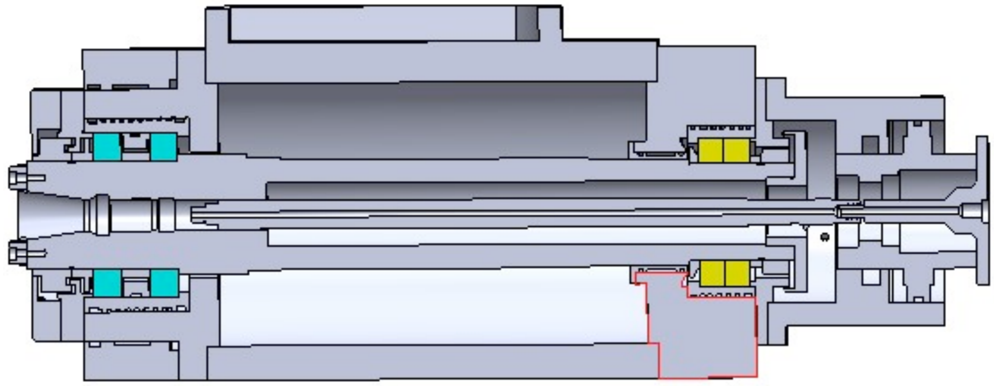

Fig. (2). Mechanical structure of a spindle.

3. FOUNDATION OF THE FINITE ELEMENT MODEL

A motorized spindle assembly is composed of a large number of different parts and subassemblies, many of which are complex. However, research has shown that a model of a motorized spindle may be obtained experimentally [8]. In fact, the spindle can be modeled as a shaft, supported at each end by a set of bearings. This representation has been used in [9, 10]. Fig. (**3**) shows a diagram of the simplified representation of the spindle system considered herein [11]. The model of the high-speed milling motorized spindle is established by ANSYS commercial software. Spring-damper element is applied to simulate the elastic support of the two sets of bearings. Four spring damper units uniformed along the circumferential direction of the spindle, which is shown in Fig. (**4**).

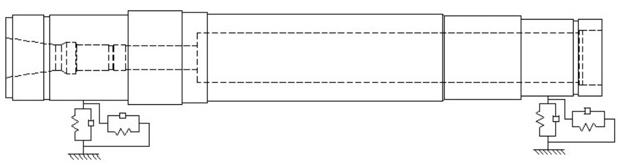

Fig. (3). Equivalent dynamic model of a spindle.

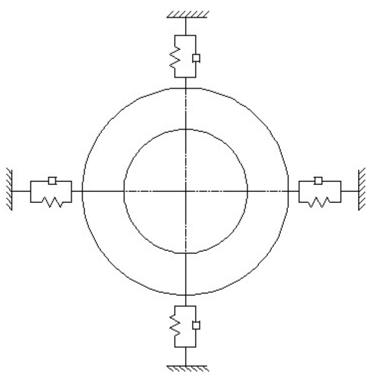

Fig. (4). Layout of spring damper unit.

COMBIN14 element which can be applied to simulate springs and dampers is provided in ANSYS commercial software. The Solid 92 element which is a tetrahedral element with ten nodes is used to simulate spindle part. The finite element model is shown in Fig. (**5**). The total numbers of nodes and elements are 55,689 and 35,231, respectively. The material of the spindle is 40Cr. When assigned material number to the model in ANSYS, the quality of the spindle is 27.6263 kg. The required mass of the spindle is 27.5kg. For the necessary simplification in the process of model establishment, the model of the spindle is reasonable.

The spring stiffness and damper parameter of the spring-damper element COMBIN 14 are necessary for finite element analysis. In the condition of having known the axial preloading Fa_0, the radial stiffness of the angular contact ball bearings can be calculated as follows [12]:

$$K_r = 1.77236 \times 10^7 \times k_m \left(z^2 \cdot D_w\right)^{1/3} \frac{\cos^2 \alpha}{\sin^{1/3} \alpha} \left(F_{a0}\right)^{1/3} \left(N/m\right) \tag{1}$$

The bearing types are XCB7017C.T.P4S and XCB7018C.T.P4S [13]. The spring stiffness of each set of bearings is 310.3N/μm and 274.3N/μm according to Eq. 1. Because the damper has little influence on the natural frequency of the transversal vibration, the damper element can be ignored.

4. STATIC ANALYSIS OF THE SPINDLE

In the engineering, there are few cases of machine failure owing to the fatigue fracture of the spindle, but there are many cases of machine failure as a result of spindle's large deformation self-excited vibration under the action of the cutting force. Therefore, the static design of the milling spindle unit is mainly related with the static stiffness of the spindle which is referred to spindle stiffness. The spindle stiffness is closely related with the load capacity and vibration resistance, which is an important performance index of the motorized spindle.

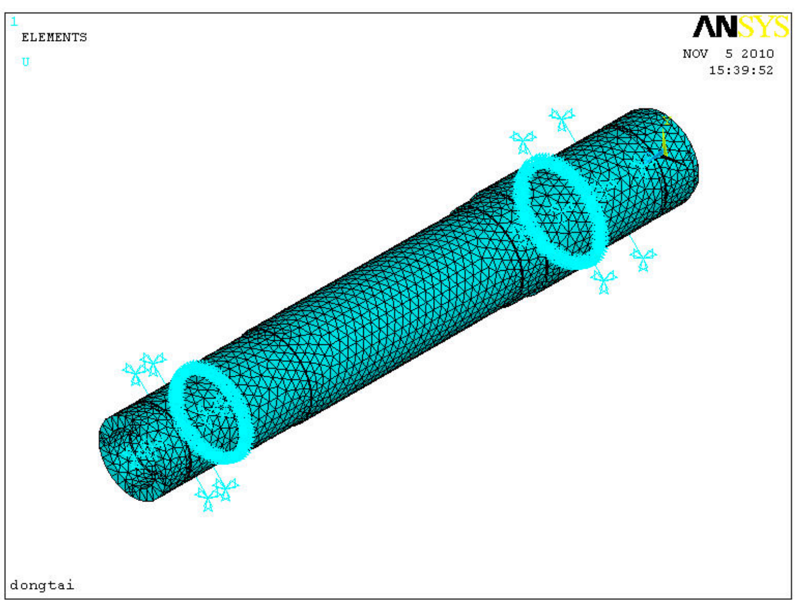

Fig. (5). Model of FEM mesh.

The spindle stiffness includes the axial and bending stiffness. In normal operating condition, the bending stiffness is more important than axial stiffness. The bending stiffness (K) of the spindle unit is defined as follows: if the front part of the spindle generates unit radial displacement δ, the force required to be imposed on the direction of the displacement is Fr [12]:

$$K = Fr/\delta \text{ (N/}\mu\text{m)} \quad (2)$$

In the study of the static load analysis of spindle, the rotating speed loading analysis is done at first, and the maximum rotating speed of the motorized spindle is greater than or equal to 12000rpm. The analysis result of rotating speed loaded is shown in Fig. (**6**). The maximum deformation is only 3.67 micron, which basically does not affect the precision of the spindle.

Then the loading cutting force analysis is done. The PIPE16 element is applied to simplify the spindle, and COMBIN14 element to simplify spindle bearing support. The result is shown in Fig. (**7**). The maximum deformation is 11.1 micron when loading the main cutting force 2305N. Thus, the static stiffness of spindle can be calculated, whose result is 207.66N/μm according to Eq. 2.

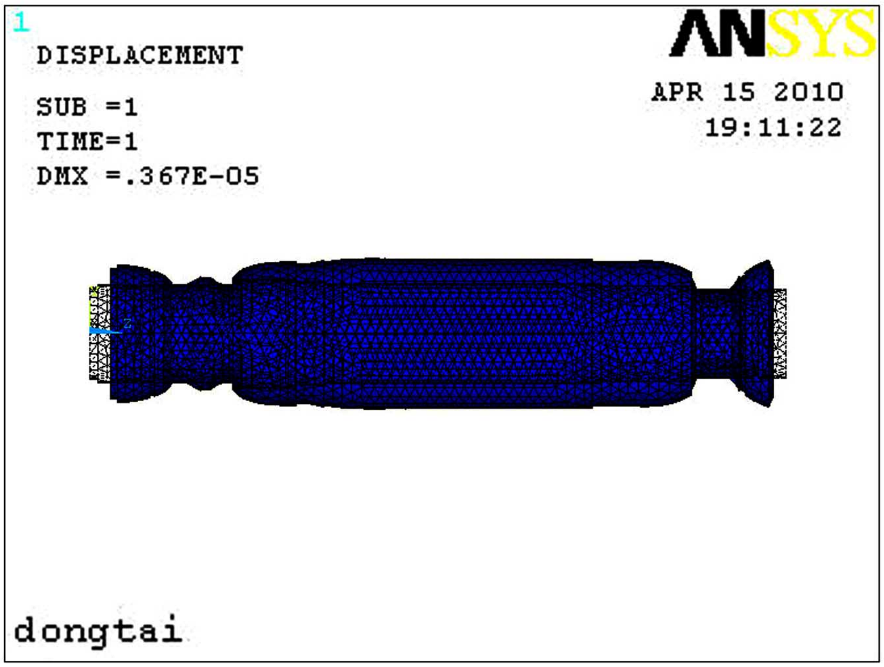

Fig. (6). Deformation of rotating speed loading.

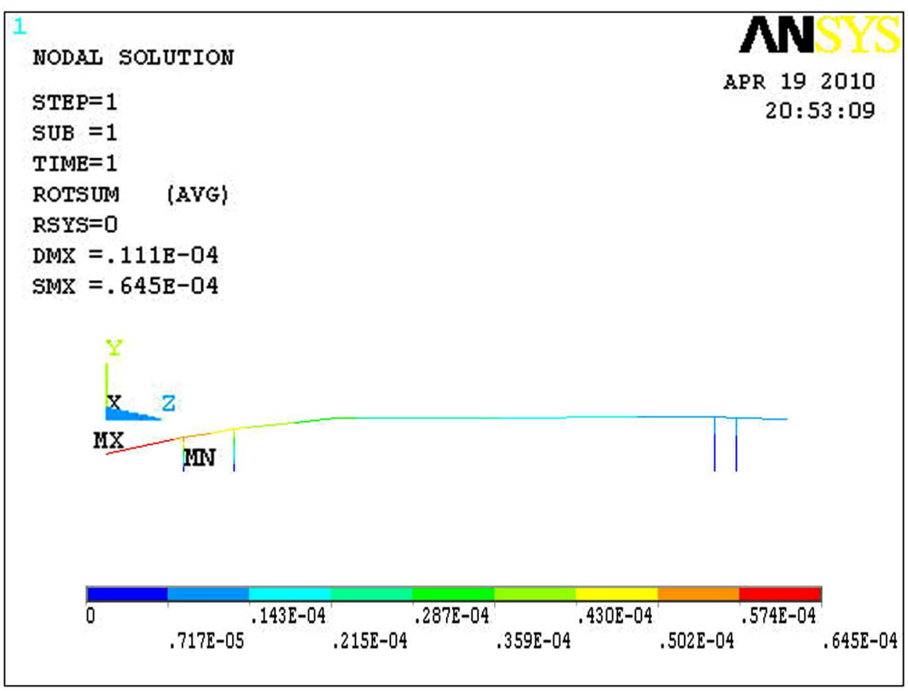

Fig. (7). Deformation of cutting force loading.

5. MODAL ANALYSIS OF THE SPINDLE

Milling motorized spindle vibration is inevitable during milling, which not only changes the relative position of work pieces and milling cutters to influence the machining accuracy, but also accelerates the wears of milling cutter, further influencing the machining accuracy. Research shows that the processing quality largely depends on the vibration produced by machine. Especially for high speed machine tools with high accuracy, the influence of vibration is even more serious. Therefore, the modal of spindle is the primary problem of dynamic characteristics analysis.

5.1. The Spindle Modal without Bearing Support

The spindle each order natural frequencies and corresponding rotating speed are shown in Table **1**. Because all freedoms of the spindle are not restricted actually, the former 6 order natural frequencies of the spindle are zero.

Table 1. Frequency and Rotating Speed in each Order without Bearing Support

Order	6	7	8	9	10
Freq(HZ)	0	1091.3	1091.3	2518.9	2579.8
Rev(r/min)	0	65478	65478	151134	154788

The natural frequency of the 7th and the 8th of the spindle are equal, the vibration model is shown in Fig. (**8**) and Fig. (**9**). They are mutually orthogonal, as first-order bending vibration. The corresponding rotating speed is 65,478rpm,

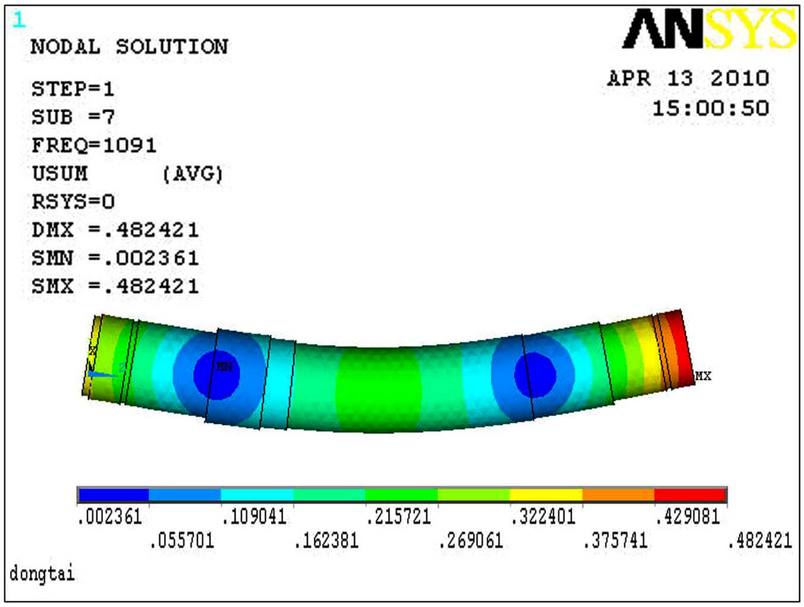

Fig. (8). The 7th vibration mode of a spindle without bearing support.

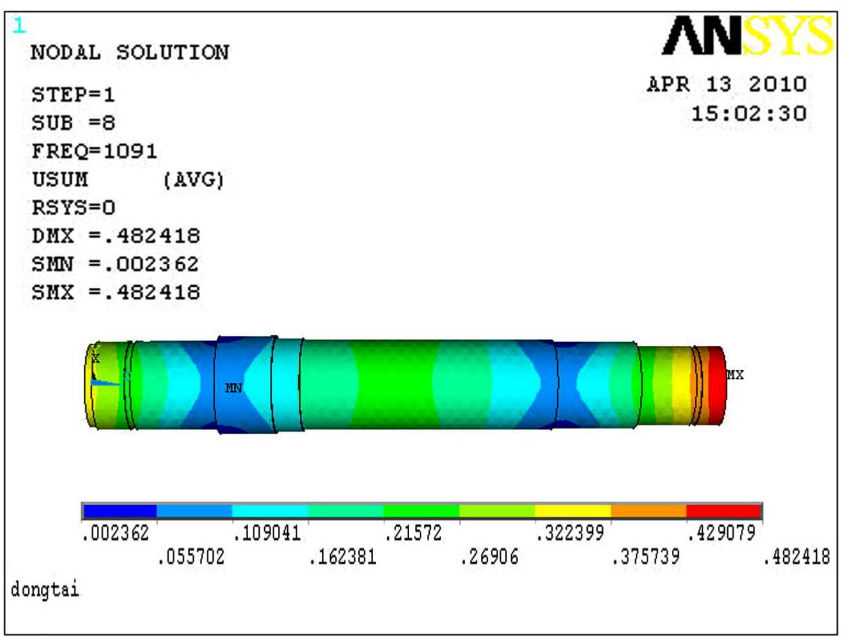

Fig. (9). The 8th vibration mode of a spindle without bearing support.

which is much greater than the working rotating speed 12,000rpm.

5.2. The Spindle Modal with Bearing Support

With the bearing bounded state, the spindle former 5 natural frequencies and corresponding rotating speed are shown in Table **2**. The first-order frequency is zero which is the result of the axial rotating freedom of the spindle is not restricted actually.

Table 2. Frequency and Rotating Speed in each Order with Bearing Support

Order	1	2	3	4	5
Freq(HZ)	0	1054.6	1056.0	1602.3	1602.6
Rev(r/min)	0	63276	63360	96138	96156

As the spindle is restricted by the spring-damper element, the 2nd and the 3rd natural frequency of the spindle is similar, the vibration mode is shown in Fig. (**10**) and Fig. (**11**). They are mutually orthogonal too. The corresponding rotating speed is 63,276rpm, which is far away from the working rotating speed 12,000rpm. Through the above analysis, it is very obvious that the design of the spindle avoids the resonance region effectively, and the design of the milling motorized spindle is reasonable.

6. HARMONIC RESPONSE ANALYSIS OF THE SPINDLE

Harmonic response analysis is done on the basis of the modal analysis of the spindle in the way of the modal superposition. The computing time is effectively reduced on the basis of the completed modal analysis. For harmonic response, 100N force is applied on the end of the spindle

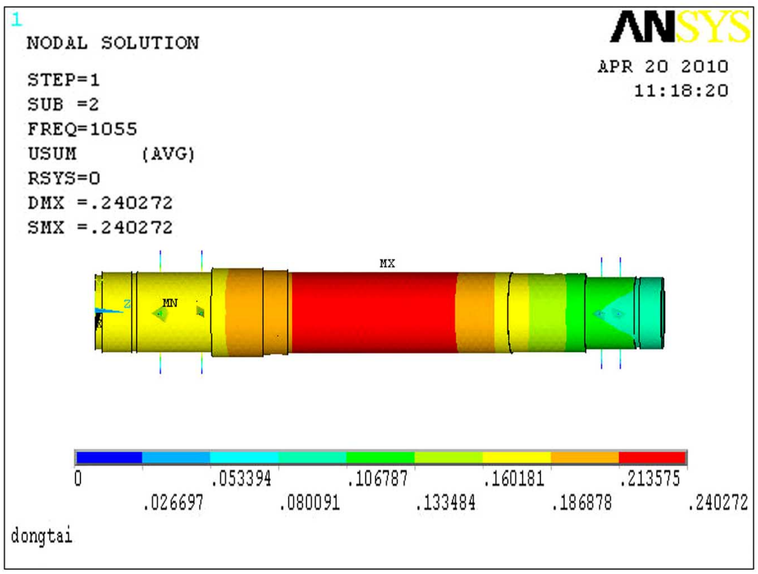

Fig. (10). The 2nd vibration mode of a spindle with bearing support.

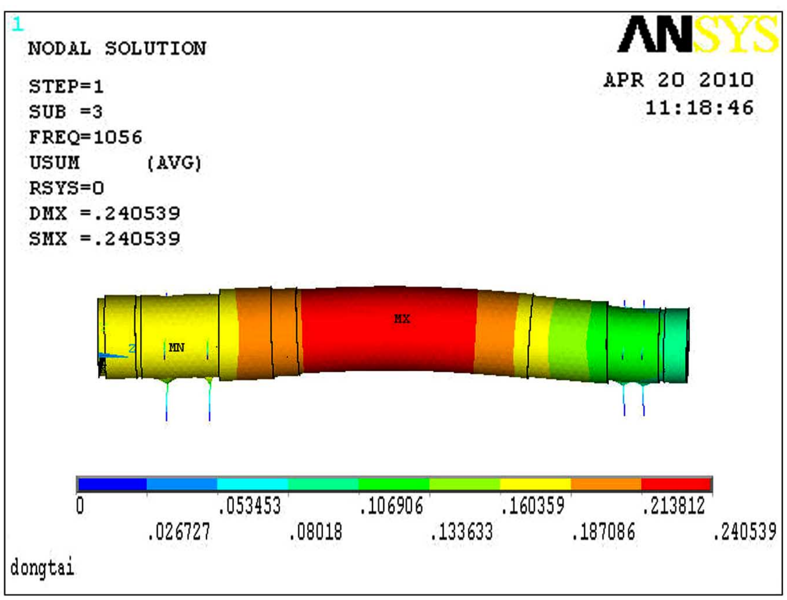

Fig. (11). The 3rd vibration mode of a spindle with bearing support.

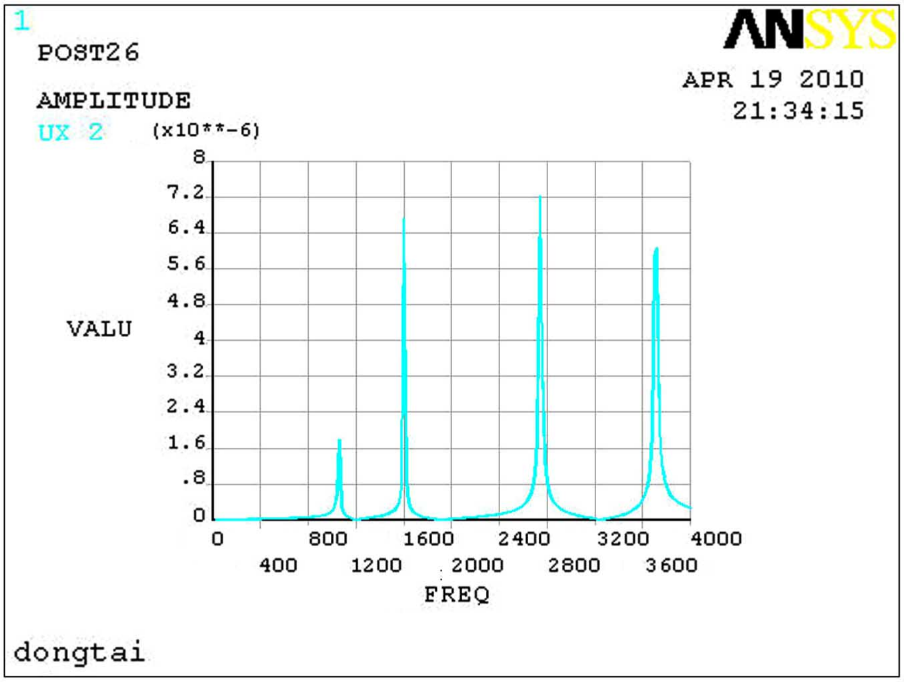

Fig. (12). Node harmonic response curve.

taper to analyze the 10 order frequency, whose range is from 0Hz to 4,000Hz with step 400Hz. Selecting a node from the cone part of spindle to analyze, the analysis result is shown in Fig. (**12**). From the graph, it can be seen that the node has vibration peak at 1,056Hz, 1,602Hz, 2,746Hz and 3,710Hz. The maximum vibration peak appears at 2,746Hz which is 7.22µm. The vibration is only 0.009,93µm at the working frequency of 200Hz, which has virtually no influence on spindle.

7. THERMAL ANALYSIS OF THE SPINDLE

Limits of a spindle's speed, reliability and performance are usually constrained by properties of its bearings, which are affected by the uneven thermal expansion of spindle parts and degraded condition of lubricants due to high temperature. The most significant parameter affecting the spindle thermal displacement is the friction heat in the front and back bearings of the spindle. When the spindle rotates, heat occurs at the front and back bearings because of friction, and the heat is then transmitted to the spindle head and tool header etc. Thermal displacement consequently occurred at the spindle because of temperature increase.

7.1. The Finite Element Model of Thermal Analysis

In order to analysis the thermal deformation of motorized spindle, the analysis of thermal-structural coupled field is

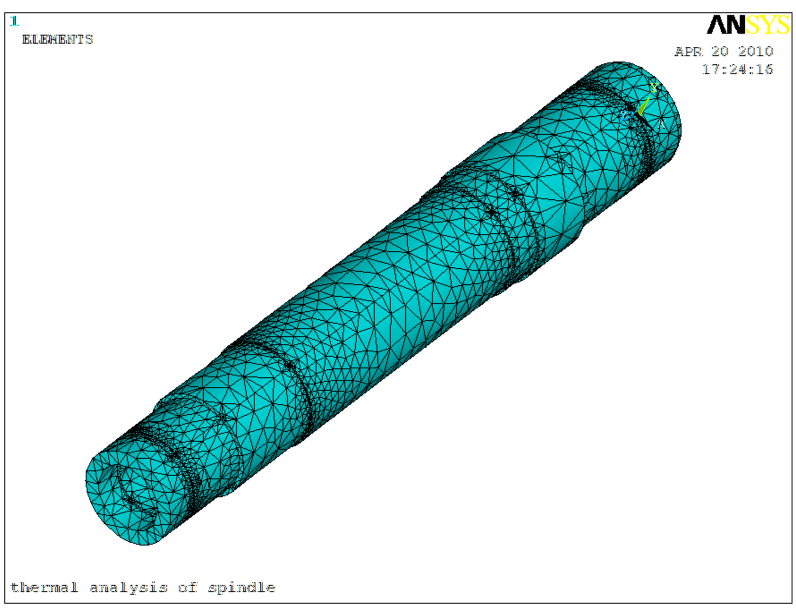

Fig. (13). The thermal deformation model of spindle.

needed. Analysis of thermal-structural coupled field can be carried out by direct coupling method and indirect coupling method. The element of direct coupling method requires thermal and structure of degrees of freedom, direct coupling method can draw coupling field analysis results only through one solution, such as temperature distribution and structure deformation. Indirect coupling method takes the results of the first analysis as the load of the second analysis to realize two field coupling. Direct coupling method is used to analyze the motorized spindle in this paper. The Solid 227 element which is a thermal-structural coupled element, is used to mesh the spindle part. In order to be used in direct thermal-structural coupling analysis, the freedom of Ux, Uy, Uz and Temp need to be selected when definition the attributes of solid 227 element. The bearings on both ends of spindle need to be simplified in the finite element model, structure freedom and the thermal load are set at bearing installation site. The finite element model of spindle thermal deformation is showed in Fig. (**13**).

7.2. The Boundary Conditions of Thermal Deformation

Considering the high-speed axial load factor, and the spindle bearing pressure angle for 15°, the thermal value of bearing is according to Eq. 3.

$$Q = 1.047\times10^{-4} nM \tag{3}$$

In Eq. 3, n is the rotating speed of bearing, M is the friction torque of bearing. The friction torque $M=M_0+M_1$, and M_0 is relevant with the rotating speed of bearing. When bearing in low speed and heavy load conditions, M_1 is occupied the main part of M, when bearing in high-speed and light load conditions, M_0 is occupied the main part of M.

In the motorized spindle thermal analysis, the thermal value of bearing load applied to bearing installation position. The thermal production rate of bearing is 6×10^6W/m^3 according to calculation.

Convection, conduction and radiation are three kinds of method of heat transmittance. Because the temperature rise of machining center spindle system is smaller than the other method, the lost thermal of radiation is rarely. Therefore the former two kinds of methods are considered into this analysis.

The working environment temperature of motorized spindle is set to 25°, the rotating speed is 12000rpm, the convection heat transfer coefficient between spindle and ambient air is 250~260W/(m$^2\cdot$°C). The material of the spindle is 40Cr, its thermal conductivity is 91.3 W/(m·K).

Considering the support type of spindle bearing, the freedom of Ux, Uy and Uz at one bearing are fixed, and the freedom of Ux and Uy at another bearing are fixed. The boundary conditions of thermal deformation loading are shown in Fig. (**14**).

7.3. The Thermal Deformation of Motorized Spindle

The thermal steady-state analysis is done by means of ANSYS, the temperature distribution of motorized spindle is shown in Fig. (**15**). Because calorific value of bearing is larger than other place, the bearing in front and back of motorized spindle is in high temperature. The highest temperature occurs in the inner ring of the former bearing. Research shows that thermal deformation is the main factors which causing deformation of the spindle.

After spindle reached thermal equilibrium, the thermal deformation analysis of spindle is done according to the results of temperature distribution. The thermal deformation of spindle is shown in Fig. (**16**). The largest thermal deformation of spindle is 6.56μm, appears in the front-end of the spindle. It basically does not affect the precision of the spindle.

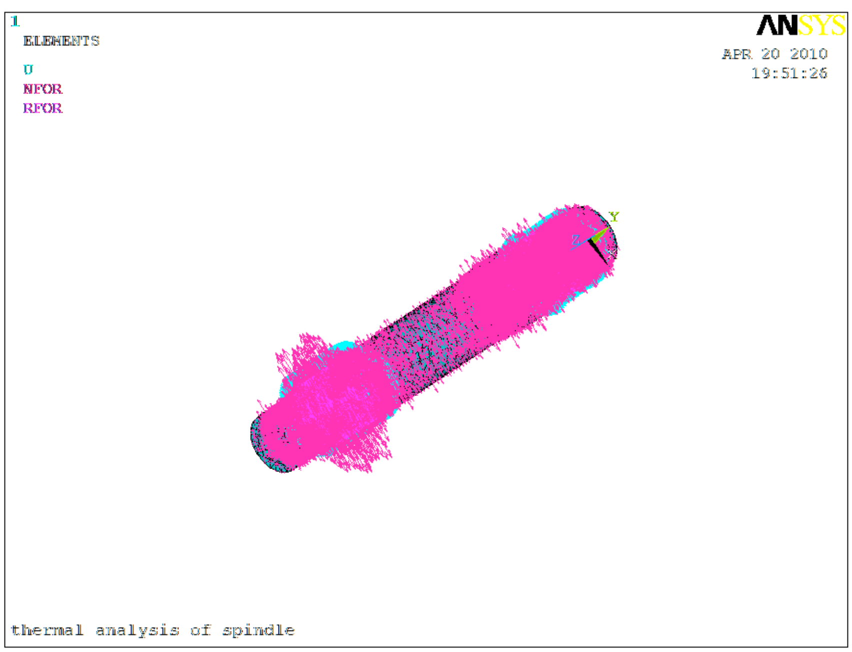

Fig. (14). The boundary conditions loading.

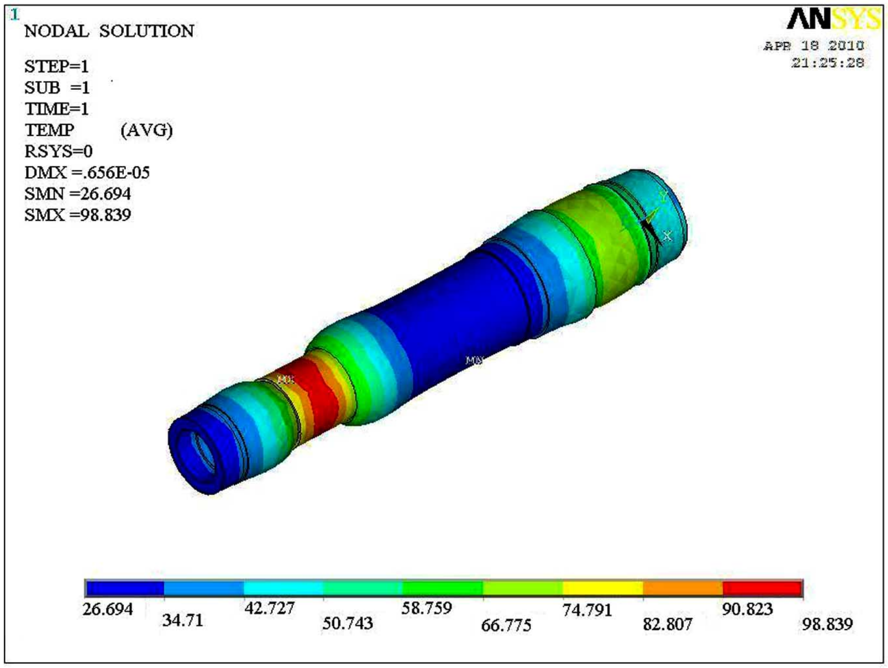

Fig. (15). The temperature distribution of spindle.

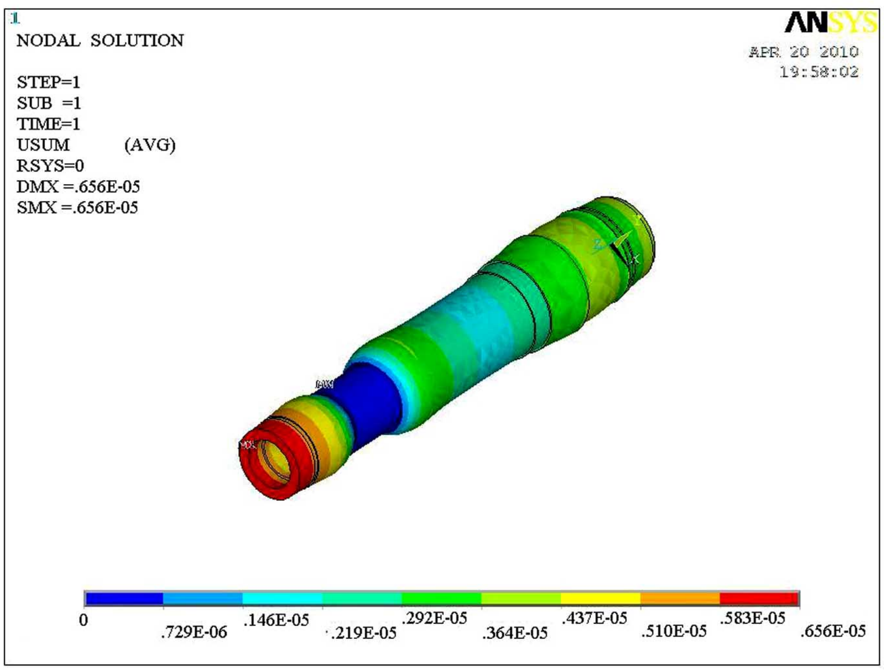

Fig. (16). The thermal deformation of spindle.

8. CONCLUSIONS

(1) The method of finite element modeling about milling motorized spindle of CX8075 vertical milling compound machining center was studied. A finite element model of the high-speed motorized spindle is derived and presented. The model takes into account bearing support contact interface, which is established by spring-damper element COMBIN 14.

(2) The static analysis, the model analysis harmonic response and thermal analysis were done by means of ANSYS. The method to establish the finite element model of the bearing support by spring-damper element COMBIN 14 was investigated and tested.

(3) The results of static analysis show that the stiffness of spindle is 207.66N/µm, which is strong for a motorized spindle. The results of modal analysis show that the first-order natural frequency of the spindle is 1054.6Hz, the first-order critical rotating speed is 63,276rpm which is away from the maximum rotating speed of the motorized spindle, 12,000rpm. The results of thermal analysis show that the thermal deformation of spindle is 6.56µm, which is too small to affect the precision of the spindle.

(4) The requirements of high-speed processing are meet by analyzing static and dynamic characteristics of the motorized spindle. The rationality of the spindle structural design is verified by FEM analysis. The result shows that the method to establish the finite element model of the bearing support by spring-damper element can be applied to the spindle component analysis and optimization.

REFERENCES

[1] Z.-C. Lin, and J.-S. Chang, "The building of spindle thermal displacement model of high speed machine center", *Int. J. Adv. Manuf. Technol.*, vol. 34, pp. 556-566, Sept. 2007.

[2] E. Abele, Y. Altintas, and C. Brecher, "Machine tool spindle units", *CIRP Annals – Manuf. Technol.*, vol. 59, pp. 781-802, 2010.

[3] C. Li, Y. Ding, and B. Lu, "Development and Key Technology in High Speed Cutting", *J. Qingdao Technol. Univ.*, vol. 30, pp. 7-16, Feb. 2009.

[4] W. Li, H. Pu, Q. Liu, G. Chen, and S. Zhang, "ANSYS-Based dynamic analysis of high-speed motorized spindle", *Int. Conf. Comput. Eng. Technol.*, 2009, pp. 336-340.

[5] J. K. Choi, and D. G. Lee, "Characteristics of a spindle bearing system with a gear located on the bearing span". *Int. J. Mech. Tool. Manuf. Pergamon*, vol. 37, pp. 171-173, Aug. 1997.

[6] J. K. Choi, and D. G. Lee, "Thermal characteristics of the spindle bearing system with a gear located on the bearing span", *Int. J. Mech. Tool. Manufact. Pergamon*, vol. 38, pp. 1017-1030, Sept. 1998.

[7] J.-S. Chen, and Y.-W. Hwang, "Centrifugal force induced dynamics of a motorized high-speed spindle", *Int. J. Adv. Manuf. Technol.*, vol. 30, pp. 10-19, Aug. 2006.

[8] A. G. Rehorn, "*Spindle Dynamics: Identification, Modeling and Effects*", M. S. thesis, University of Western Ontario, Ontario, Canada, 2001.

[9] E. V. Bordatchev, and R. Henriksen, "State space modeling of machine tool spindle units using subspace identification", *Proceedings of the 2nd IASTED International Conference on Control and Application*, 1999, pp. 120-123.

[10] E. V. Bordatchev, "Modeling and parameter identification of the impulse response matrix of mechanical systems", *Proceedings of SPIE - The International Society for Optical Engineering*, 1998, pp. 106-117.

[11] A. G. Rehorn, J. Jiang, P. E. Orban, and E. Bordatchev, "Modelling and experimental investigation of spindle and cutter dynamics for a high-precision machining center", *Int. J. Adv. Manuf. Technol*., vol. 24, pp. 806-815, Dec. 2004.

[12] W. Xie, "*The FEM Analysis of Dynamic and Static Characteristic of High Speed Motorized Spindle*", M. S. thesis, Harbin Institute of Technology, Harbin, PRC, 2001.

[13] R. A. Burton, and H. E. Staph, "Thermally Activated Seizure of Angular Contact Bearings". *A.S.L.E. – Transactions*, vol. 10, pp. 408-417, Oct. 1967.

Numerical Analysis for Composite Wing Structure Design

Rajaram Sahu, *Department of Mechanical Engineering, Raajdhani Engineering College, Bhubaneswar, rajaramsahu65@gmail.com*

Ajaya Kumar Beura, *Department of Mechanical Engineering, Aryan Institute of Engineering & Technology, Bhubaneswar, akbeura25@gmail.com*

Suchampa Bagchi, *Department of Civil Engineering, NM Institute of Engineering & Technology, Bhubaneswar, suchampabagchi@yahoo.co.in*

Abstract: To improve the structure performances of minitype unmanned aerial vehicle (UAV) wing, numerical simulation and optimization design principle was carried out for designing the best composites wing structure. Thus tradeoff can be obtained between the general performance and the weight of the wing. Advanced composite material has its own outstanding features, such as high specific strength, high specific modulus, designable performance and integral forming easily. The application of advanced composite material on the aerocraft structure can significantly reduce the weight, and improve the aerodynamic and flight performances. In this paper, the parametric finite element model is established using parametric modeling technique for stress and stain analysis. Given any set of geometric parameters, the geometric modeling, meshing, strain and stress analysis can be automatically carried out in sequence. The global optimal solution is guaranteed by the proposed two-step optimization search strategy combing genetic algorithm (GA) and sequential quadratic programming (SQP). Comparative studies show that the optimization efficiency can be greatly improved with the two-step optimization search strategy.

Keywords: Advanced composite material, structure design, parametric finite element modeling, optimization design.

1. INTRODUCTION

As a kind of new material, the advanced composite material brings about great revolution to the aerocraft industry since it was introduced in the 1960s. With its wide application in aerospace structure, the advanced composite material is named as “the four main materials of aerospace structure” along with aluminum alloy, titanium alloy, and alloy steel. The advanced composite material has its own prominent features, such as high specific strength, high specific modulus, designable performance and integral forming easily, etc. With the application of the advanced composites, the weight of the aerocraft structure can be reduced by about 25% ~ 30% compared to the conventional metal structures. Moreover, the aerodynamic and flight performances can be improved to the levels that the conventional materials can hardly achieve. The extensive application of advanced composites is also able to promote some further technology development of structure stealth and intelligent structure design. The aerocraft structure performance is significantly dependent on the part and quality of the advanced composites used in aerocraft. However, it is difficult to achieve good designs of the composites in aerocraft structure to guarantee requirements for different missions. Therefore, to fully explore the directional properties of composites, the designable ability of structure performance and the excellent manufacturability of large component integral forming, it is necessary to introduce the principle of optimization to the composite structure design [1-6].

In this paper, the optimization design and numerical simulation for composite structure of wing on a UAV is implemented. By using parametric modeling technique, the parametric finite element model is established to conduct stress and strain analysis of the wing. Given any set of geometric parameters, the geometric modeling, meshing, strain and stress analysis can be automatically carried out in sequence. To ensure the optimal solution can be obtained, a two-step optimization search strategy which combines genetic algorithm (GA) and sequential quadratic programming (SQP) is proposed during optimization. It is concluded that this two-step optimization search strategy can greatly enhance the efficiency of finding the true optimal solution through comparing this method with GA.

2. THE PARAMETRIC FINITE ELEMENT MODELING OF UAV

2.1. Geometric Modeling and Meshing

Wing box is the main load bearing structure of airfoil surface, including skin panels, beams and core sandwich panel, etc. Aerofoil B-8306-b 5 depicted in Fig. (**1**) is considered in this work [7]. Fig. (**2**) displays the geometric model with mesh of the minitype UAV wing. The parameters involved in the geometric modeling process are: the quality of UAV W=5kg, reference area of wing s=0.16 m2, taper ratio λ=0.8, aspect ration A=8, wing span b, length of root chord c_{r}, length of tip chord c_{t}, sweepback angle (leading edge sweepback angle L_{LE}, a quarter chord sweepback angle $L_{\mathrm{c/4}} = 10^{\circ}$) and b, c_{t}, L_{LE} ($A = \frac{b^2}{s}$, $c_{\mathrm{t}} = \frac{2s}{b(1+l)}$, $\tan L_{\mathrm{LE}} = \tan L_{\mathrm{c/4}} + \frac{1-l}{A(1+l)}$).

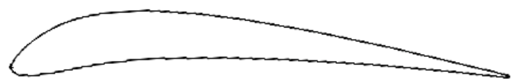

Fig. (1). Aerofoil B-8306-b.

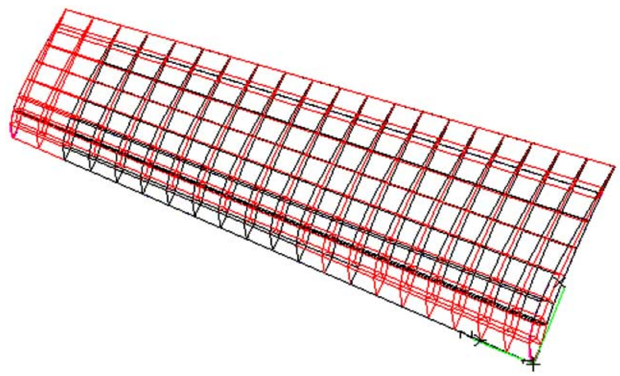

Fig. (2). Geometric model of UAV wing.

2.2. Finite Element Analytical (FEA) Modeling

The true pressure distribution of the upper and lower surfaces of the UAV wing is illustrated in Fig. (**3**) [8]. It is very difficult to exert such load on the FEA model for practical applications. Therefore, the true load curves in Fig. (**3**) are simplified within the precision requirement, and the load adopted in this work is shown in Fig. (**4**). In these Figures, the solid line represents the wing geometry shape, the dash dot line represents the pressure distribution of upper surface of the wing, and the dotted line represents the pressure distribution of lower surface of the wing.

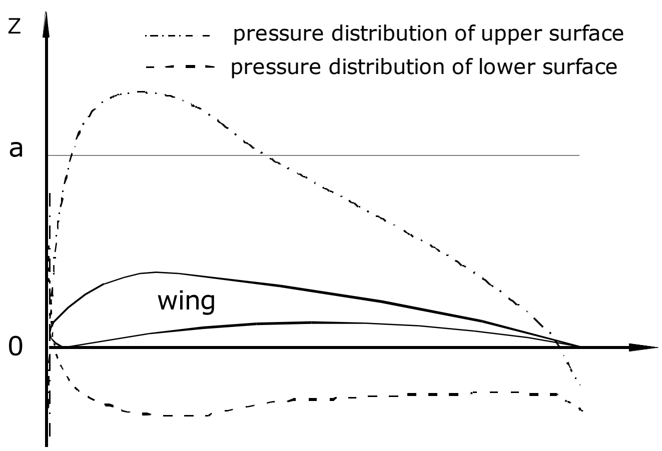

Fig. (3). True load curve.

In Figs. (**3** and **4**), *a* is a constant coefficient (a = 2.64×10^{-4}), which can be calculated according to the equilibrium condition of forces between the load suffered by the wing and the weight of UAV. According to the geometric relationship, the chord length of any section can be expressed as $c = c_b - \frac{c_b - c_t}{b/2} y$. Then the values determining the pressure distribution of upper and lower surfaces of the wing (z_1, z_3, z_2, z_4) can be calculated. Because the wing is fixed on the aircraft body, both the displacement and rotation angle at the root chord are considered as zero.

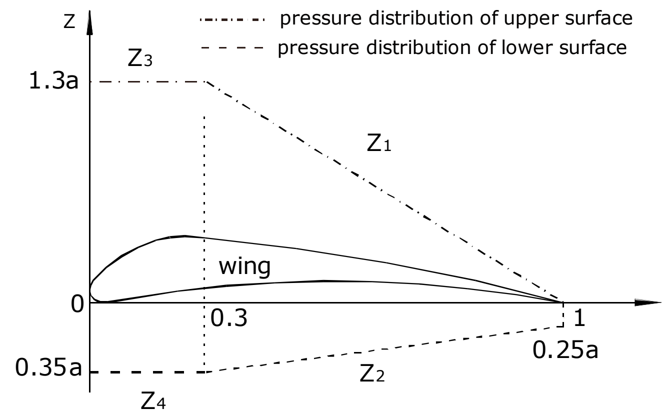

Fig. (4). Approximate load curve.

The material used in the core sandwich panels is foam adhesive, of which the elastic modulus is E=5.7MPa, the shear modulus is G=3MPa and the density is $0.04 g/cm^3$. The material used for beams is Korean pine, of which the elastic modulus is E=10400MPa and the density is $0.5 g/cm^3$. The material used for skin panels is carbon fiber/epoxy resin, of which the single layer sickness is 0.28mm and the density is $1.4\ g/cm^3$. The mechanical properties of unidirectional laminates can be found in Reference [1]. The upper surface of the skin suffers pressure, while the lower surface suffers tension. Meanwhile, carbon fiber is two-dimensional anisotropic, which means that it has different capability to resist tensile and compressive strength. Therefore, in order to achieve the optimal overall performance of the wing, different materials are respectively used in the skin panels in the upper and lower surface. The number of composites layer is considered as the variable *N*, and laying angle equals to $\frac{180^{\circ}}{N}$.

2.3. Model Parameterization

To facilitate the design optimization, the parametric model with the geometric parameters as control parameters of the minitype UAV wing is established using the parametric modeling technique in the MSC. Patran software [9]. The automatic process of FEA modeling is called model parameterization. The detailed description of this process is: 1) the design parameters are given by the designers; 2) geometric model are updated according to the current design parameters; 3) the FEA model based on the updated geometric model is automatically rebuilt by the parametric finite element modeling program. Thus the designers can be freed from tedious work full of details design, and concentrate on the control feature of design object without

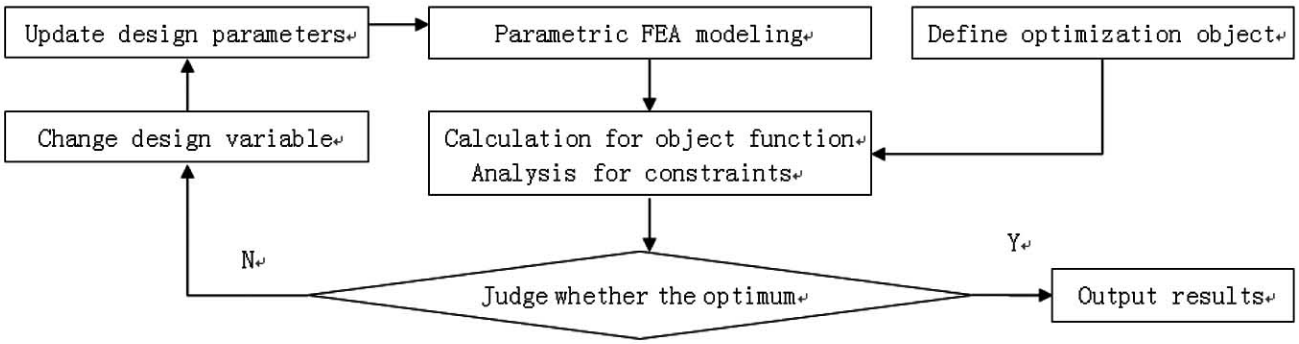

Fig. (5). The process of design optimization.

having to start with the geometric details. Furthermore, design parameters can be changed in the following design process and then design object will be automatically updated. Given any set of geometric parameters, the geometric modeling, meshing, strain and stress analysis can be automatically carried out in sequence.

3. OPTIMIZATION DESIGN FOR COMPOSITE WING STRUCTURE OF MINITYPE UAV

3.1. Description of the Wing Structure Optimization

In order to reduce the mass of wing, the optimization design principle is employed to choose the best composites wing structure of minitype UAV in this paper. The process of design optimization is shown in Fig. (**5**). Optimization object is defined after parametric FEA modeling, and then the calculation for object function is conducted. Meanwhile, the analysis for constraints is conducted. After the results come out, the first thing is to judge whether they are the optimal results; if they are the optimal results, they will be exported; otherwise, the input values of design variables should be changed, in order to automatically update the design parameters according to their corresponding relationship, and then rebuild the geometric model. Thereby, the corresponding FEA model can be reestablished for renewed analysis computation. This cycle continues until the optimal results are available.

The optimization design problem of the minitype UAV composite wing structure is formulated as equation (1).

$$\begin{aligned}
&\min \quad W(X)=\sum \rho_j * V_j(X) \\
&s.t. \quad |\sigma_1| \le X', \qquad |\sigma_2| \le Y', \qquad |\tau_{12}| \le S \\
&\quad d_{\max} \le 10\text{mm}, \qquad R_{\max} \le 1^\circ \\
&\quad 0.5 \le x_1 \le 0.99, 8 \le x_2 \le 15, 0 \le x_5 \le 90, 0.01 \le x_6 \le 0.9 \\
&\quad 0.01 \le x_7 \le 0.95, \quad 0.1 \le x_8 \le 30, \quad 0.1 \le x_9 \le 30 \\
&\quad x_3 = 1,2,3,4,5,6, \quad x_4 = 1,2,3,4,5
\end{aligned} \tag{1}$$

where $W(X)$ is the weight function of the wing; ρ_j is the density of component j; $V_j(X)$ is the volume of component j; σ_1, σ_2 is the largest positive axis stress occurring in each layer of the wing, τ_{12} is the largest shear stress of the wing, and X', Y', S are the allowable strength of materials respectively corresponding to σ_1, σ_2 and τ_{12}; $d_{\max}$ and $R_{\max}$ are the maximum deformation and largest torsion angle of the wing, respectively. The design variables $X=\{x_1,x_2,x_3,x_4,x_5,x_6,x_7,x_8,x_9\}$ are the structure and geometry parameters of the wing. Table **1** lists the design variables and their range. The design objective is to minimize the mass of the wing. The constraints are imposed

Table 1. Descriptions of the Design Variables

Design vars.	Optimization variables	Variable type	LB	UB
x_1	Taper ratio	Continuous Real	0.5	0.99
x_2	Aspect ratio	Continuous Real	8.0	15
x_3	Layer number of carbon fibers	Discrete Integer	[1,2,3,4,5,6]	
x_4	Materials of skin panels	Discrete Integer	[1,2,3,4,5]	
x_5/(°)	Laying angle of materials	Continuous Real	0.0	90
x_6	Position of front beam	Continuous Real	0.01	0.9
x_7	Position of back beam	Continuous Real	0.01	0.95
x_8/mm	Thickness of front beam	Continuous Real	0.1	30
x_9/mm	Thickness of back beam	Continuous Real	0.1	30

on the stiffness and strength of the wing structure, the maximum deformation and the largest torsion angle of the wing. Generally, to trade off between minimizing the structure weight and optimizing the structure performance, the number of layers of carbon fibers is considered to be smaller than 7 in the literature. So x_3 can vary among the six integral (1 to 6). $x_4 \in [1\text{-}5]$ represents the materials of the five most common carbon fiber/epoxy resins (G814NT/3234, G803/5224, G827/55, G803/QY891, G827/QY891) used in this work correspondingly [10].

3.2. Realization of Optimization

iSIGHT is a software which can carry out system integration, design optimization and automation processing. Through a graphical interface, this software is able to integrate simulation code and provide intelligent support. The product design period can be significantly reduced; meanwhile, the product quality and reliability can be improved. Therefore, iSIGHT is applied to realize design integration and optimization in our work. The optimization is accomplished in the iSIGHT software.

Genetic algorithm (GA) is applicable to optimization problems with both continuous and discrete design variables. The global optimal solution can be achieved with high possibility. However, it may converge to the vicinity of the optimal point causing inaccurate solution [11-14]. What's more, it suffers heavy calculation burden and slow convergence rate because of too many searching times. Sequential quadratic programming (SQP) is only applied to continuous problems. With fewer reanalysis, it converges quickly, and the accurate optimal solution can be achieved in high efficiency [15].

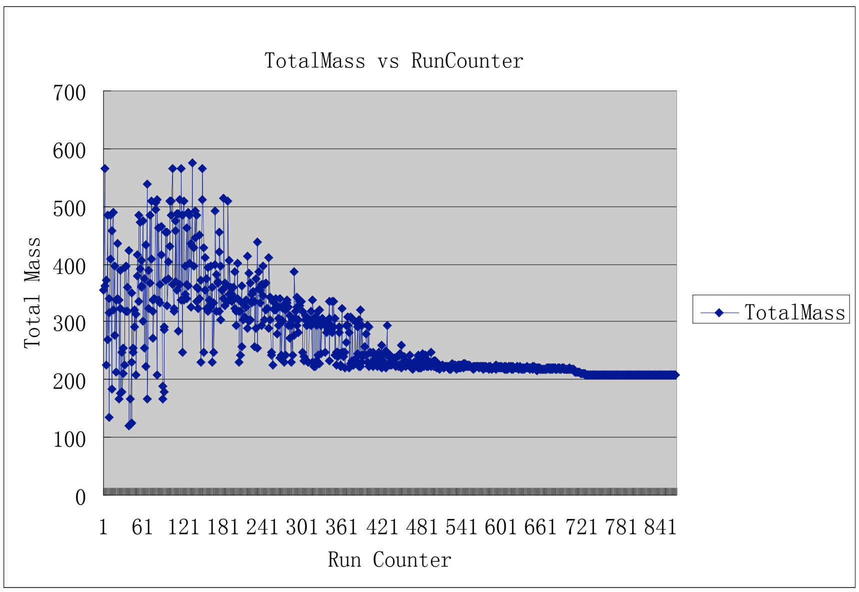

a. Convergence plot of optimization parameter Total Mass.

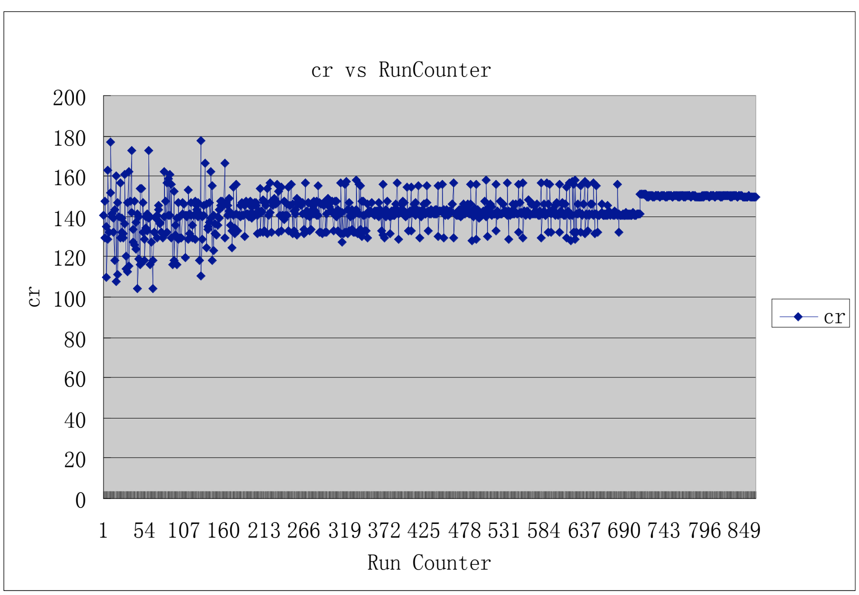

b. Convergence plot of optimization parameter c_r.

(Fig. 6) Contd…..

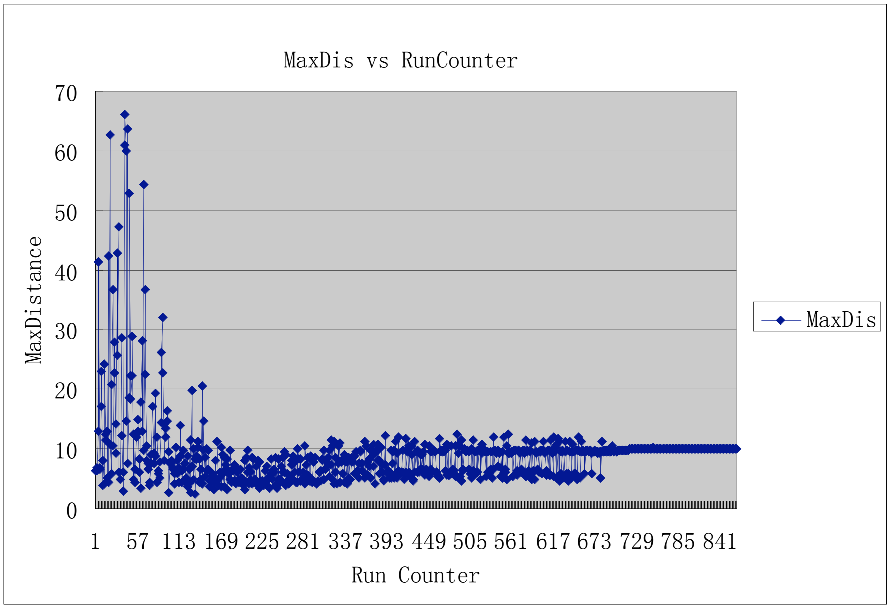

c. Convergence plot of optimization parameter d_{max}.

Fig. (6). Convergence plots of optimization parameters (Total Mass, c_r, d_{max}).

Table 2. Design Variables and System Performances

	Design vars. $X \begin{cases} x_1, x_2, x_3, x_4, x_5, \\ x_6, x_7, x_8, x_9 \end{cases}$	Total Mass	c_r	c_t	d_{max}	σ_1	τ_1	R_{max}
Init.	0.8,10,5,4,45, 0.15,0.8,5,5	355.243	140.5457	112.44	6.3302	0.0072	0.0041	-0.1036
GA	0.78,9.92,3,3,2.596, 0.01,0.95,0.101,0.1	208.979	143.0193	110.93	9.9922	0.0319	0.0184	-0.2892
GA+ SQP	0.64,10.59,3,3,45, 0.017,0.95,0.1,0.14	208.582	149.9999	95.858	9.9999	0.0225	0.013	-0.2404

Since both continuous and discrete design variables are involved in this optimization problem, GA is applied. Considering the slow convergence rate and stochastic properties of GA, SQP is used to conduct further optimization search to guarantee the true global optimal solution and improve the convergence rate. GA is first applied to obtain a sub-optimal design point, and then SQP is used to conduct the second round of optimization search with the sub-optimal design point from GA as the initial start point. During this second round, the discrete variables x_3 and x_4 are fixed at the values of the sub-optimal design point. In order to investigate the efficiency of our numerical simulation model, another method is carried out for a detailed comparison, in which GA is alone applied to obtain the optimal design point.

3.3. Optimization Results Analysis

In order to verify the effectiveness of our approach, the wing structure performances at the initial start point are also calculated for comparison. Both the initial design variables and optimal ones of these two methods are plugged input into the FEA model to estimate the structure performances. The convergence plots for optimization parameters (Total Mass, c_r, and d_{max}) are depicted in Fig. (**6**). The design variables and the system performances generated by our approach and those at the initial points are shown in Table **2**. To more clearly show the improvement of the optimal design solutions, the stress and displacement distribution at initial point (P0), the optimal point of GA (P1), and the final optimal point of GA+SQP (P2), are also illustrated in Figs. (**7**, **8** and **9**), respectively.

From Table **2** and Figs. (**7**, **8** and **9**) three noteworthy results are drawn below:

(1) The mass of wing is greatly reduced at the optimal design. The Total Mass at the final optimal design point P2 is 208.582g, which is reduced by 41.3% compared to that at the initial design point P0 (355.243g).

(2) The material can be fully utilized with optimal design. Although, the constraints at both the initial design point P0 and the final optimal design point P2

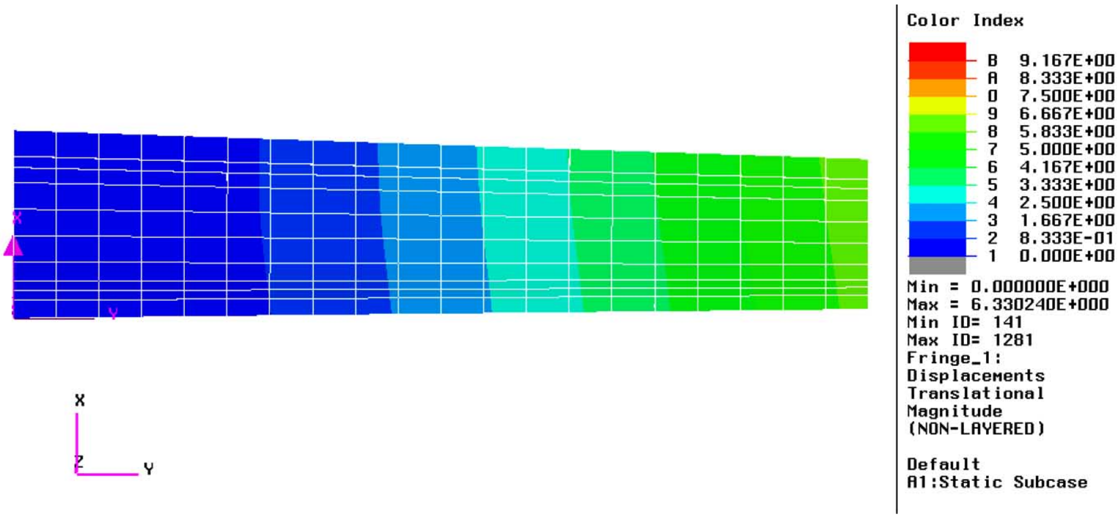

a. Displacement distribution at P0.

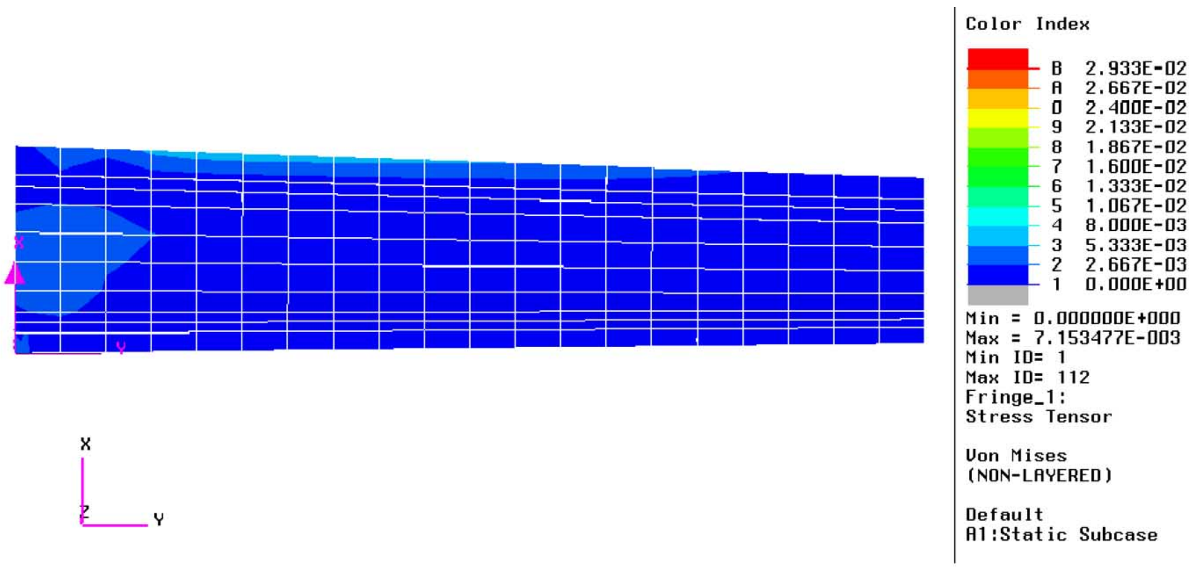

b. Stress tensor distribution at P0.

Fig. (7). Stress and displacement distribution at the initial point (P0).

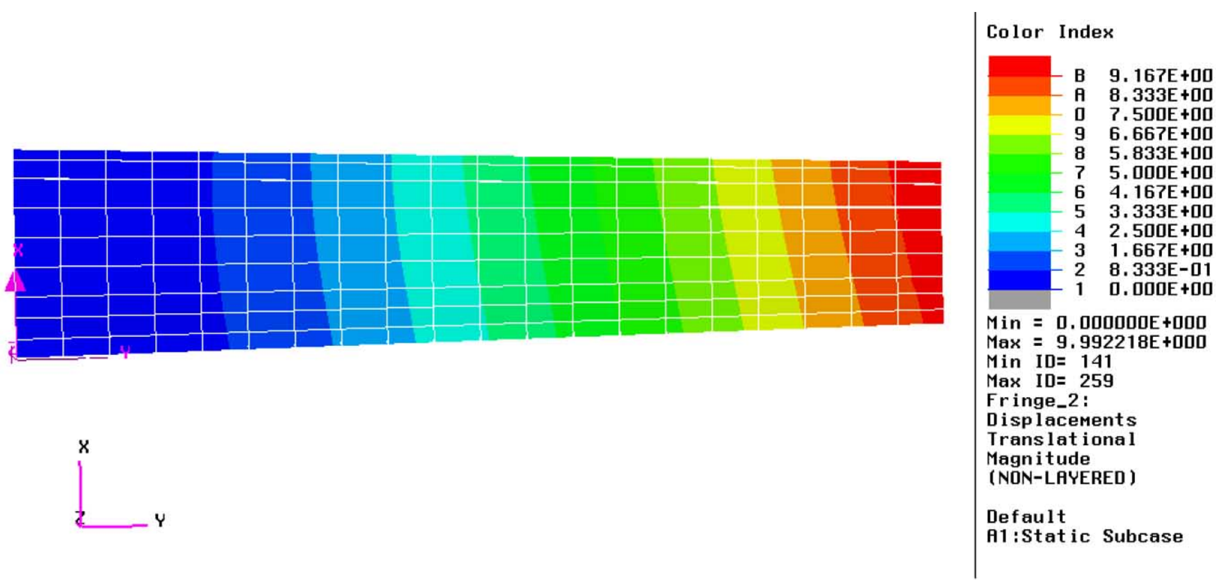

a. Displacement distribution at P1.

(Fig. 8) Contd…..

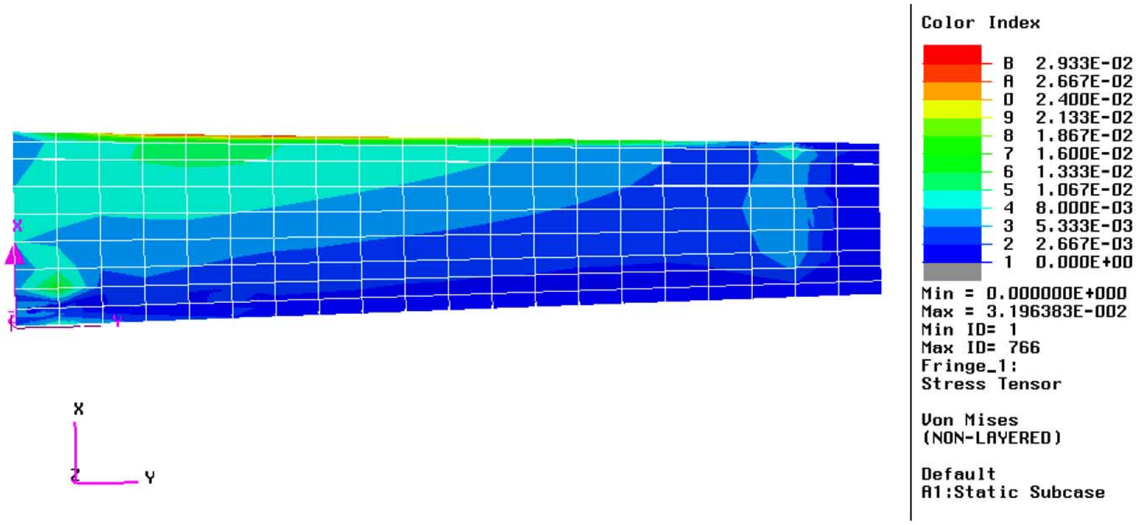

b. Stress tensor distribution at P1.

Fig. (8). Stress and displacement distribution at the GA optimal point (P1).

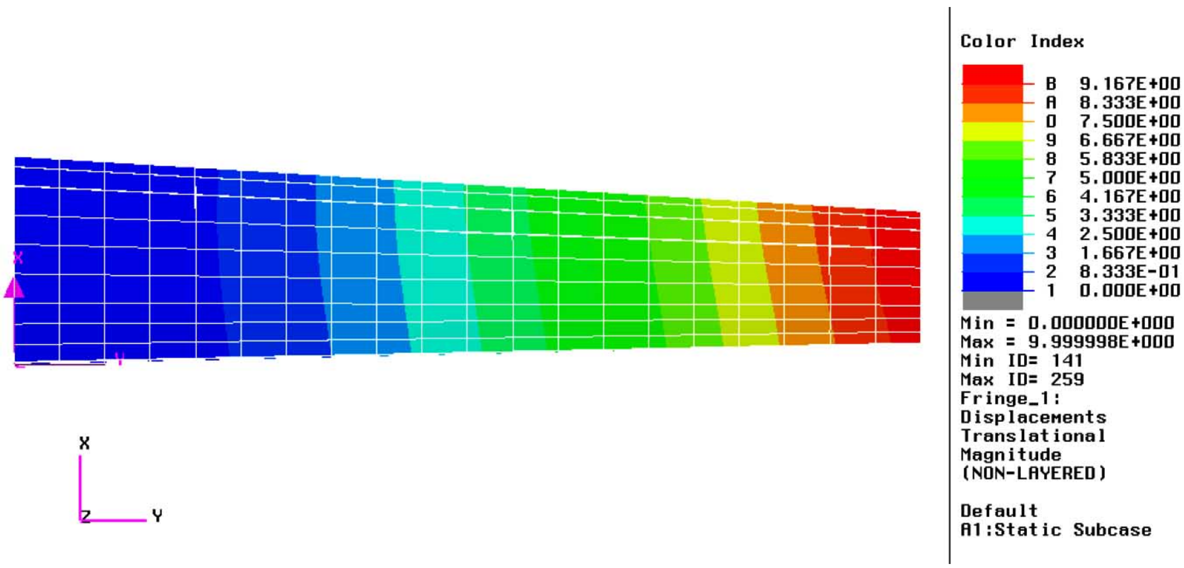

a. Displacement distribution at P2.

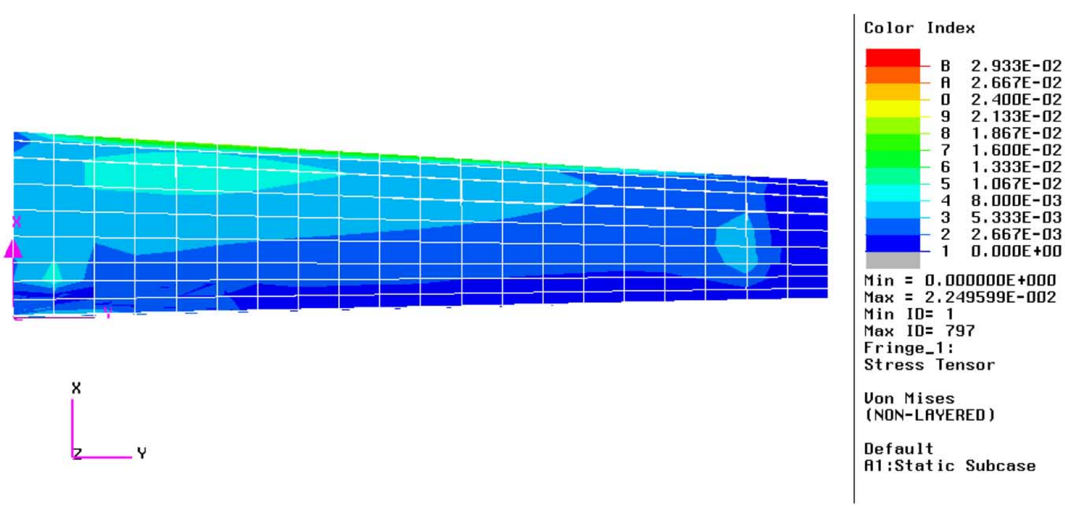

b. Stress tensor distribution at P2.

Fig. (9). Stress and displacement distribution at the GA+SQP optimal point (P2).

are satisfied, the latter show smaller gap to the constraints upper bound. Just take the maximum deformation as an example, the initial design and the optimal design respectively produce values of 6.3302mm and 9.9999mm (see in columns 6 in Table **2**). It is clear that the optimal design is much closer to the constraint upper bound (10mm), which indicates that the material utilization ratio is greatly increased through composites optimization design by our approach. The maximum deformations in Figs. (**7a**) and (**8a**) show the same trend.

(3) The Total Mass at the final optimal design point P2 is 208.582g compared to that at the point P1(208.979g). The run time for the GA simulation method was around 12 CPU hours on a Pentium IV 3.0G machine as the data of the optimal point was achieved, and that for our two-step simulation method was only 2.5 CPU hours on the same machine. Moreover, take the length of root chord as an example, the values at P1 and the final optimal design point P2 are respectively 143.0193mm and 149.99mm (see in columns 4 in Table **2**). It is clear that the final optimal design is much closer to the constraint upper bound (150mm). The final optimal results are significantly improved compared to that of GA, which indicates the effect-iveness of our two-step optimization search.

4. CONCLUSIONS

The application of the advanced composites plays an important role in improving the aerocraft structure perfor-mances. In this work, the parametric finite element model is established to accomplish the stress and strain analysis for UAV composite wings. In the process of optimization, the combination of GA and SQP algorithms ensure that the global optimal solution can be obtained. The optimization results show that the mass of the wing is greatly reduced using our proposed approach, and the utilization rate of material is evidently increased compared to that of the initial design. Meanwhile, the optimization efficiency can be greatly improved with the two-step optimization search strategy.

REFERENCES

[1] Chinese Institute of Aviation, Composites design manual. Beijing, Aviation Industry Press, 2001.

[2] D. Liu, and V. V. Toropov, "Optimization of blended composite wing panels using smeared stiffness technique and lamination parameters", In: *51st AIAA/ASME/ASCE/ AHS/ASC Structures, Structural Dynamics, and Materials Conference*, Orlando: Florida, 2010.

[3] N. Chang, W. Yang, J. Wang, and W. Wang, "Design optimization of composite wing box for flutter and stiffness", In: *48th AIAA Aerospace Sciences Meeting Including the New Horizons Forum and Aerospace Exposition*, Orlando: Florida, 2010.

[4] O. Seresta, M. M. Abdalla, and Z. Gurdal, "Minimum weight design of composite structures with local postbuckling and blending constraints", In: *47th AIAA/ASME/ ASCE/AHS/ASC Structures, Structural Dynamics, and Materials Conerence*, Newport: Rhode Island, 2006.

[5] V. V. Volovoi, S. Yoon, C. Y. Lee, and D.H. Hodges, "Structural optimization of composite rotor blades", In: *45th AIAA/ASME/ ASCE/AHS/ASC Structures, Structural Dynamics & Materials Conf*erence, Palm Springs: California, 2004.

[6] J.P.T.J. Berends, M.J.L. van Tooren, and D.N.V. Belo, "A distributed multi-disciplinary optimization of a blended wing body UAV using a multi-agent task environment", In: *47th AIAA/ASME/ASCE/AHS/ ASC Structures, Structural Dynamics and Materials Conference*, Newport: Rhode Island, 2006.

[7] Aero Model Research Department of Chinese Aviation Club, Model Aircraft Aerofoil Collection. Beijing, People's Sports Press, 1956.

[8] X. N. Mei, *"Research of The Multidisciplinary Design Optimization Method for Rocket-Borne UAV"*, PhD thesis, Beijing Institute of Technology, Beijing, China, 2010.

[9] S. H. Zhang, X. M. Yu, and E. Johnson, "A practical global optimization procedure", In: *44th AIAA/ASME/ASCE/AHS Structures, Structural Dynamics, and Materials Conference*, Norfolk: Virginia, 2003.

[10] S. R. Swanson, "Strength design criteria for carbon/epoxy pressure vessels", *J. Spacecr. Rockets*, Vol.27, no.5, pp. 522-526, 1990.

[11] T. D. Robinson, K. E. Wollcox, M. S. Eldred, and R. Haimes, "Multifidelity optimization for variable-complexity design". In: *11th AIAA/ISSMO Multidisciplinary Analysis and Optimization Conference*, Portsmouth: Virginia, 2006.

[12] J. L. Liu, "Intelligent genetic algorithm and its application to aerodynamic optimizaion of airplanes", *AIAA J.*, Vol. 43, no.3, pp. 530-538, 2005.

[13] O. Seresta, M. M. Abdalla, and Z. Gurdal, " A genetic algorithm based blending scheme for design of multiple composite laminates", In: *50th AIAA/ASME/ASCE/AHS/ASC Structures, Structural Dynamics, and Materials Conference*, Palm Springs: California, 2009.

[14] N. Rastogi, D. K. Ghosh, and G.Vanderplaats, "Discrete optimization capabilities in genesis structural analysis and optimization software", In: *9th AIAA/ISSMO Symposium on Multidisciplinary Analysis and Optimization*, Atlanta: Georgia, 2002.

[15] L. Pan, and H. J. Du. "Structure topology optimization for dynamics performance using SQP method", In: *8th AIAA/USAF/ NASA/ISSMO, Symposium on Multidisciplnary Analysis and Optimization*, Long Beach: CA, 2000.

Cutting Geometry and Base-Cone Parameters of Manufacturing

Pradipta Kumar Das, *Department of Mechanical Engineering, Aryan Institute of Engineering & Technology, Bhubaneswar, pkdas751@gmail.com*

Nalinikanta Swain, *Department of Mechanical Engineering, Capital Engineering College, Bhubaneswar, nalini_526@yahoo.co.in*

Shradhanjali Moharana, *Department of Civil Engineering, Raajdhani Engineering College, Bhubaneswar, shradhanjalimoharana1@gmail.com*

Deepika Priyadarshini Palai, *Department of Civil Engineering, NM Institute of Engineering & Technology, Bhubaneswar, deepikadalai2561@gmail.com*

Abstract: Generating-line method, which is based on the generating process of spherical involute curve, is a new processing theory of cutting ideal spherical involute gears. Based on the principle of the new method, this paper expands the traditional geometrical relationship into the cutting geometry of generating-line method, and proposes the base-cone parameters with their formulas to provide necessary parameters for further study. The application examples, such as establishing the coordinate systems and the equation of gear generating line, show the importance of these researches, and the example of calculating geometric parameters illustrate the way to adjust the base-cone parameters. It can be seen from the researches, the cutting geometry contains the tangent relationships between two base cones and a base plane respectively, and the planar conjugated relationship between two generating lines of pinion and gear. The base-cone parameters determine the relationships among base cones, base plane and generating lines. If some of the base-cone parameters need to be adjusted, it can be realized by modify the value of the parameter r_2, ε or Z_0.

Keywords: Hypoid gear, generating-line method, cutting geometry, base-cone parameters.

1. INTRODUCTION

Hypoid gears are widely used to transmit crossed-axis power and motion in vehicles, ships and aircrafts, and could offer higher load capability and axis position flexibility than spiral bevel gears. The basic geometry of hypoid gears were established by Wildhaber [1] and Baxter [2], after decades of development, there are two major processes called face milling and face hobbing for cutting hypoid and spiral bevel gears in the current gear manufacturing industry [3].

In recent years, a large number of developments in the field of manufacturing spiral bevel and hypoid gears have been obtained. Qi Fan developed mathematical models of hypoid gear drives processed by face milling and face hobbing, and researched the tooth contact analysis and the tooth surface error correction [4-6]; in order to improve the load distribution and reduce the transmission error, Vilmos Simon proposed the optimal machine tool setting and tooth modifications of spiral bevel and hypoid gears [7-9]. All of these developments above were built on the traditional methods of face milling and face hobbing. As a result of applying engineering approximation, the tooth profile curves cut by these methods are not ideal spherical involutes, therefore the advantages of using spherical involute profiles, such as transmission ratio constancy and angular displacement insensitivity, are partly lost. Also the calculation and adjustment of machine tool settings are complex, and the interchangeability of the gears cut by these traditional methods is relatively poor [10]. Y.C. Tsai *et al.* [11] and M.J. Al-Daccak *et al.* [12] respectively proposed the modeling of bevel gears by using exact spherical involute profiles, but they did not discuss the feasibility of cutting ideal spherical involute gears.

Based on the generating principle of spherical involute and the theory of conjugated tooth surfaces, we have proposed *the generating-line method of cutting spherical involute gears* [13, 14]. This new theory can be used to process ideal spherical involute bevel gears; however the principle of cutting hypoid gears by this method still needs to be researched systematically. Therefore, in order to facilitate the further studies of the shape of generating lines and the cutting motion parameters, this paper develops the cutting geometry and base-cone parameters of manufacturing hypoid gears by this new method, and indicates the important effects of the researches through the application examples.

2. BASIC GEOMETRY

The axodes of hypoid gears are two tangent revolving hyperboloids. In order to simplify the designing and manufacturing, axodes are usually replaced by a pair of pitch cones [15]. As shown in Fig. (**1a**), the angle between pinion axis X_1 and gear axis X_2 is shaft angle Σ, and the length of common perpendicular O_1O_2 is the pinion offset E; two pitch cones are in tangency at point M which is usually the center point of the tooth surfaces, and the common tangent plane, which is also called pitch plane, is T; at point M, pitch cone distances of pinion and gear are A_1 and A_2, and pitch radius are r_1 and r_2; pitch angles are δ_1 and δ_2, and the distance from point O_2 to the center of gear pitch circle is Z_0; the pitch cone vertexes of pinion and gear are H_1 and H_2, and the angle between H_1M and H_2M is ε'; the line K_1K_2, which crosses the point M and is vertical to the T plane, intersects X_1 and X_2 at points K_1 and K_2; in the vertical plane of axis X_1, the angle between projections of X_2 and K_1K_2 is η; in the vertical plane of axis X_2, the angle between projections of X_1 and K_1K_2 is ε. As shown in Fig. (**1b**), in the pitch plane T, the helix angles at the point M of pinion and gear are β_1 and β_2, and this paper calls β_1 and β_2 pitch helix angles. In addition, the number of teeth of pinion and gear are N_1 and N_2.

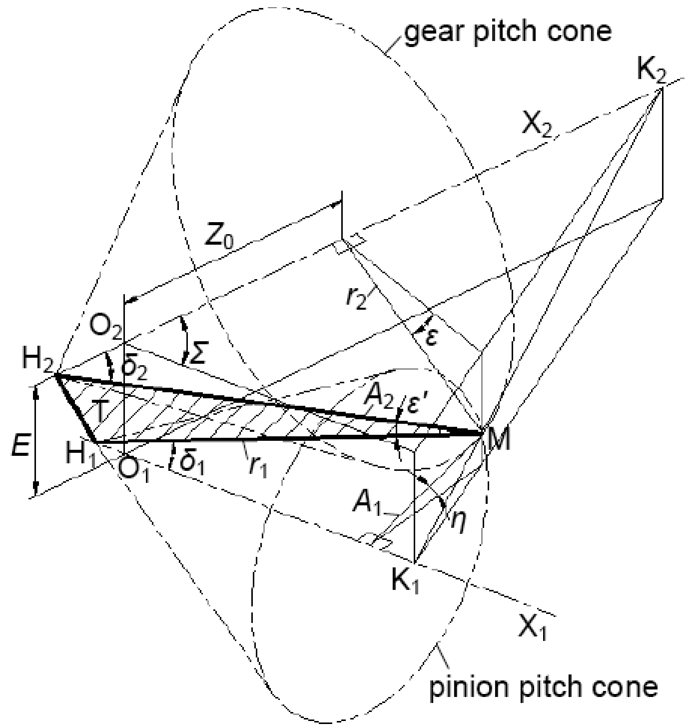

a

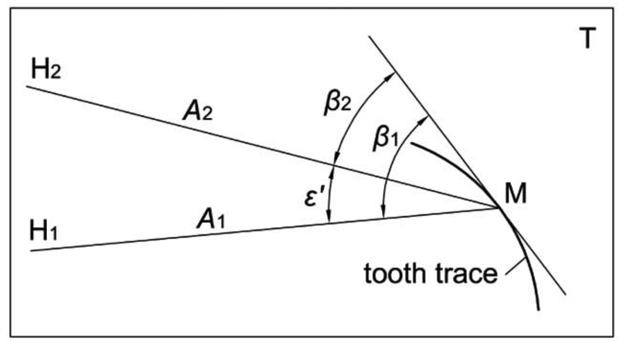

b

Fig. (1). Basic geometry of hypoid gears.

The position of point M can be determined by given the parameters r_2, ε and Z_0, if we know the parameters N_1, N_2, Σ, E and the position of point M, all of other parameters mentioned above can also be determined uniquely [2]. Hypoid gears can be designed and manufactured by traditional methods according to this basic geometry. But for the new generating-line method in this paper, this geometry needs to be expanded according to the new cutting principle.

3. CUTTING GEOMETRY OF GENERATING-LINE METHOD

For a bevel gear drive, as shown in Fig. (**2**), pitch plane T and two pitch cones are in tangency alone line OM, while base plane Q and two base cones are in tangency alone line OU_1 and OU_2, and the angle α between plane T and plane Q is the pressure angle on the back cone. When the motion of

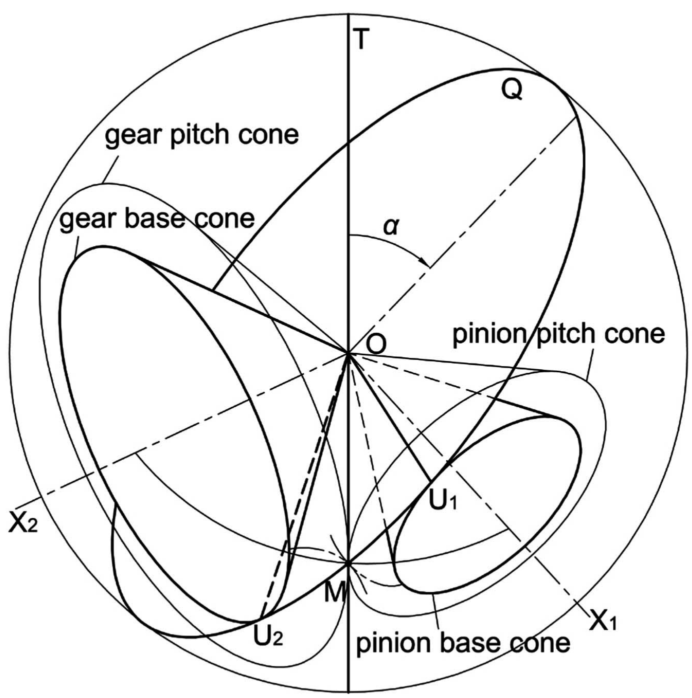

Fig. (2). Schematic of a bevel gear drive.

this pair of pitch cones is pure-rolling in tangency with the pitch plane T, the motions of two base cones are also pure-rolling in tangency with the base plane Q along their own tangent lines respectively, and a pair of ideal spherical involutes with respect to the base cones could be formed by the traces of point M which is fixed on and rolling with the plane Q.

As shown in Fig. (**3**), M′C′ and M″C″ are two spherical involutes on the toe and on the heel of gear respectively; if there is a curve between M′ and M″ in plane Q, a spherical involute profile tooth surface will be formed between toe and heel of the gear. According to this theory, generating-line method takes *generating line* M′M″ as the cutting edge, which removes excess material with the appropriate relative motion between tool and gear blanks. In theory, using the same generating line as the cutting edge could process a pair of bevel gears which are conjugated in line contact.

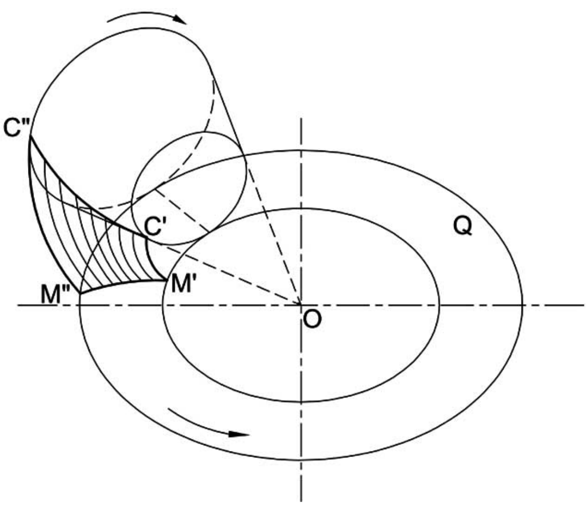

Fig. (3). Principle of generating-line method.

As can be seen from the description above, determining the position of base plane Q and the equation of generating line is the key point of the generating-line method. Therefore, this new method could also be used to cut hypoid gears if these two elements can be determined properly. However, traditional methods of designing and manufacturing hypoid gears do not have the concepts of base cone and base plane, so this paper proposes the following method to establish the base cones and base plane of hypoid gears.

As shown in Fig. (**4**), the final position of rotating pitch plane T about H_2M at an angle α could be defined as plane Q which is the base plane of a hypoid gear drive; the axis X_1 and plane Q intersect at point V, and the tangent relationship between plane Q and two base cones can be used to determine base cones of the pinion and the gear; the tangent lines are VU_1 and H_2U_2, and the base angles of pinion and gear are δ_{b1} and δ_{b2}.

As the base cone vertexes of pinion and gear are not coincident, the generating lines of pinion and gear can not be the same one. Therefore as shown in Fig. (**5**), the generating planes Q_1 and Q_2 are set up in the base plane Q. When the gears are being processed or driving, the motion of pinion base cone and the generating plane Q_1 are pure-rolling in tangency along VU_1, while the motion of gear base cone and the generating plane Q_2 are pure-rolling in tangency along H_2U_2. Based on the principles of gear connection, it can be proved that if the following two conditions are met, a pair of hypoid gears cut by generating-line method will be conjugated in point contact.

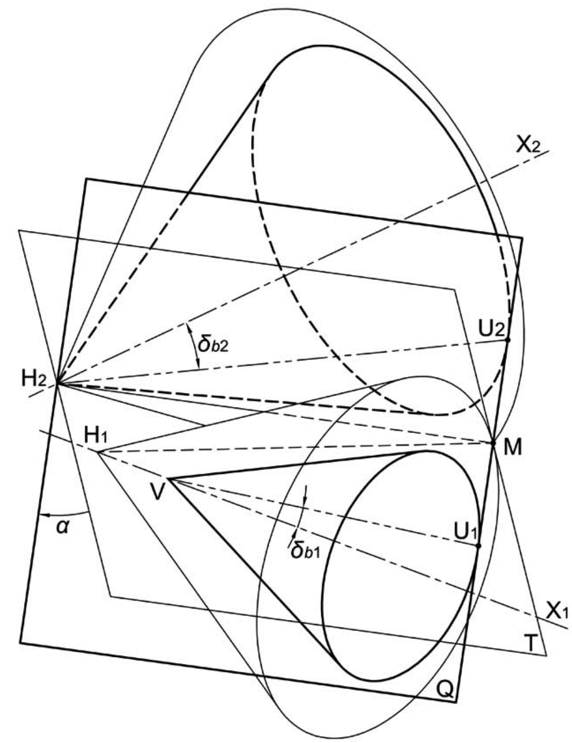

Fig. (4). Geometry of cutting hypoid gears.

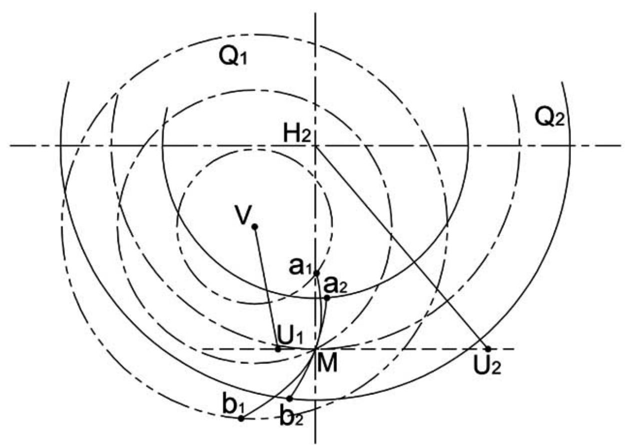

Fig. (5). Relationship of generating lines.

Condition 1: The rotation speeds of generating plane Q_1 and Q_2 meet the transmission ratio of the gears.

Condition 2: As the pinion generating line a_1b_1 rotates with Q_1 and the gear generating line a_2b_2 rotates with Q_2, a_1b_1 and a_2b_2 is a pair of planar conjugated curves, while point M was one of their contact points, and there is no curvature interference between the two generating lines.

Because the shape of generating lines have not been determined, similar to the concepts of the convex and concave of spiral bevel gears, this paper defines the left and

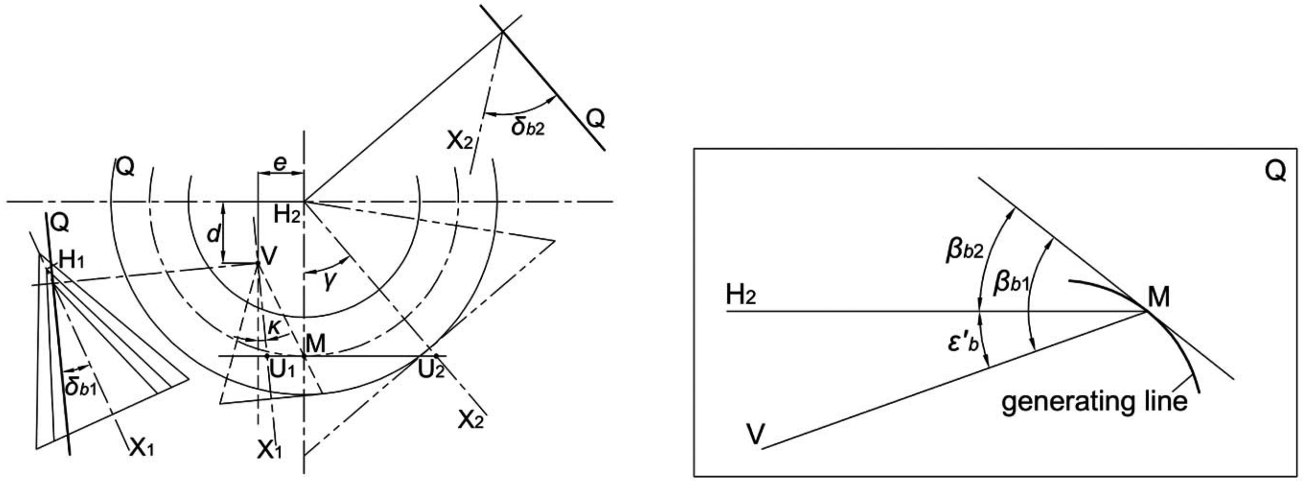

a

b

Fig. (6). Schematic of base-cone parameters.

right sides of tooth surfaces of hypoid gears as follows: observing a gear tooth alone the tooth trace from the heel to the toe, putting the topland above and the root below, and then two sides of the tooth in sight are called the left side and right side respectively. Therefore, the situation shown in Fig. (**4**) is the geometry of cutting left sides of tooth surfaces of hypoid gears which the pinion is offset below from the center of the gear, and this paper mainly researches the situation of cutting left sides of tooth surfaces, if the angle α is rotating to the opposite direction, the cutting geometry of right sides of tooth surfaces can be easily obtained.

4. BASE-CONE PARAMETERS

In order to facilitate the further studies of the parameters of the machine tool and the blade, it is necessary to determine the geometrical relationships among base cones, base plane and generating lines. On base of the cutting geometry as shown in Fig. (**6**), this paper defines *the base-cone parameters* as below to determine those geometrical relationships.

On the basis of designing, assume the pitch-cone pressure angle α_n, which indicates the angle between normal direction of the tooth surface and the pitch plane T at point M, is known. Then the angle α between pitch plane T and base plan Q can be determined by

$$\alpha = \sin^{-1}\frac{\sin\alpha_n}{\sqrt{1-\cos^2\alpha_n\sin^2\beta_2}} \tag{1}$$

The base cone angles of pinion and gear are determined, respectively, by

$$\delta_{b1} = \sin^{-1}\left(\cos\alpha\sin\delta_1 + \sin\alpha\cos\delta_1\sin\varepsilon'\right) \tag{2}$$

$$\delta_{b2} = \tan^{-1}\sqrt{\frac{\sin^2\delta_2}{\tan^2\alpha+\cos^2\delta_2}} \tag{3}$$

As shown in Fig. (**6a**), in the base plane Q, d denotes the distance from the projection of point V on the line H_2M to point H_2, provided d is positive if the projective point lies between M and H_2; otherwise, d is negative. Furthermore, e denotes the distance from point V to line H_2M; κ denotes the angle between VU_1 and H_2M; and γ denotes the angle between H_2U_2 and H_2M. These parameters are determined, respectively, by

$$d = A_2 - \frac{A_1\tan\delta_1\cos\varepsilon'}{\tan\alpha\sin\varepsilon' + \tan\delta_1} \tag{4}$$

$$e = \frac{A_1\sin\delta_1\sin\varepsilon'}{\cos\alpha\sin\delta_1 + \sin\alpha\cos\delta_1\sin\varepsilon'} \tag{5}$$

$$\kappa = \tan^{-1}\left(\frac{\sin\varepsilon'\cos\alpha - \sin\alpha\tan\delta_1}{\cos\varepsilon'}\right) \tag{6}$$

$$\gamma = \cos^{-1}\frac{\cos\delta_2}{\cos\delta_{b2}} \tag{7}$$

As shown in Fig. (**6b**), in the base plane Q, ε'_b denotes the angle between VM and H_2M; β_{b1} denotes the angle between the tangential direction of generating lines at point M and VM, and β_{b2} denotes the angle between the tangential direction of generating lines at point M and H_2M, so this paper calls β_{b1} and β_{b2} base helix angles. These parameters are determined, respectively, by

$$\varepsilon'_b = \tan^{-1}\frac{e}{A_2 - d} \tag{8}$$

$$\beta_{b2} = \tan^{-1}\left(\cos\alpha\tan\beta_2\right) \tag{9}$$

$$\beta_{b1} = \beta_{b2} + \varepsilon_b \tag{10}$$

5. APPLICATION EXAMPLES

Based on the researches of the cutting geometry and the base-cone parameters, many further researches can be done, such as establishing the coordinate systems to build the tooth

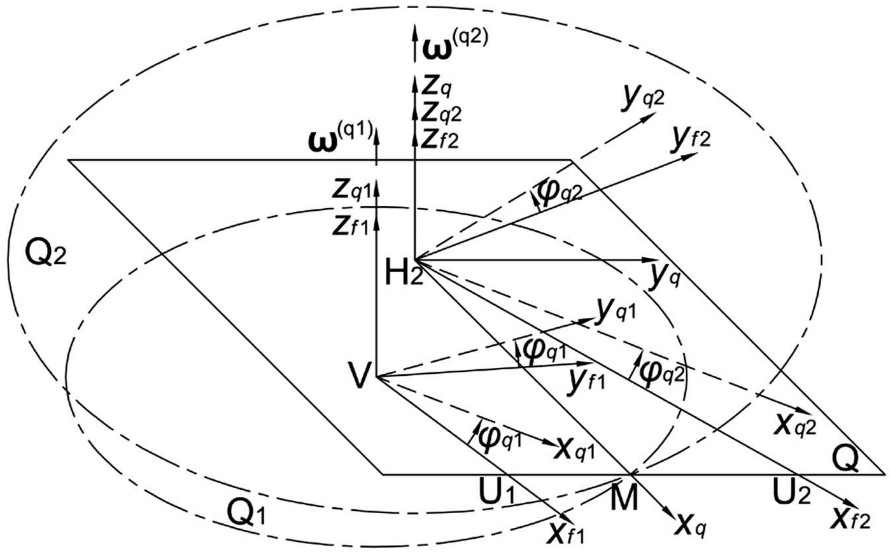

Fig. (7). Coordinate systems S_q, S_{f1}, S_{f2}, S_{q1}, S_{q2}.

surfaces model and analyze the situation of meshing, establishing the equation of gear generating line to study the shape of generating lines and the influence of shape errors, and so on.

5.1. Coordinate Systems

As shown in Fig. (**7**) and Fig. (**8**), the coordinate systems S_q, S_{f1}, S_{f2}, S_{q1}, S_{q2}, S_1 and S_2 are established as given below.

Fixed system $S_q(x_q, y_q, z_q)$ is fixed with the initial position of plane Q and attached to the machine house.

Auxiliary fixed systems $S_{f1}(x_{f1}, y_{f1}, z_{f1})$ and $S_{f2}(x_{f2}, y_{f2}, z_{f2})$ are fixed with the initial positions of generating planes Q_1 and Q_2 respectively.

Moving systems $S_{q1}(x_{q1}, y_{q1}, z_{q1})$ and $S_{q2}(x_{q2}, y_{q2}, z_{q2})$ are fixed with generating planes Q_1 and Q_2 respectively, and simulated motions of cutting edges. S_{q1} and S_{q2} are supposed to rotate about z_{q1} and z_{q2} respectively with the angular velocity $\boldsymbol{\omega}^{(q1)}$ and $\boldsymbol{\omega}^{(q2)}$, and the rotation angles starting from the initial positions are φ_{q1} and φ_{q2}.

Moving systems $S_1(x_1, y_1, z_1)$ and $S_2(x_2, y_2, z_2)$ are fixed with base cones and simulated motions of gear blanks. The initial position of S_1 is the position of rotating S_{f1} about y_{f1} at an angle δ_{b1}, and the initial position of S_2 is the position of rotating S_{f2} about y_{f2} at an angle δ_{b2}. S_1 and S_2 are supposed to rotate about x_1 and x_2 respectively with the angular velocity $\boldsymbol{\omega}^{(1)}$ and $\boldsymbol{\omega}^{(2)}$, and the rotation angles starting from the initial positions are φ_1 and φ_2.

Then, on the basis of the cutting geometry and base-cone parameters proposed above, the transformation matrixes can be determined as below.

$$\mathbf{M}_{q\_f1} = \begin{bmatrix} \cos\kappa & -\sin\kappa & 0 & d \\ \sin\kappa & \cos\kappa & 0 & -e \\ 0 & 0 & 1 & 0 \\ 0 & 0 & 0 & 1 \end{bmatrix} \tag{11}$$

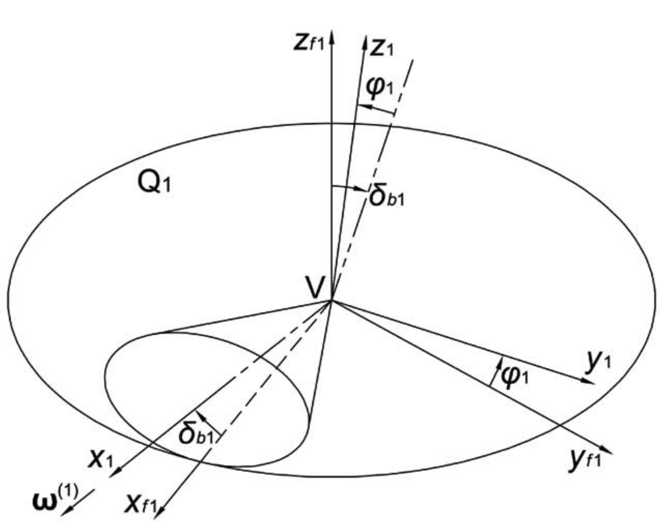

a

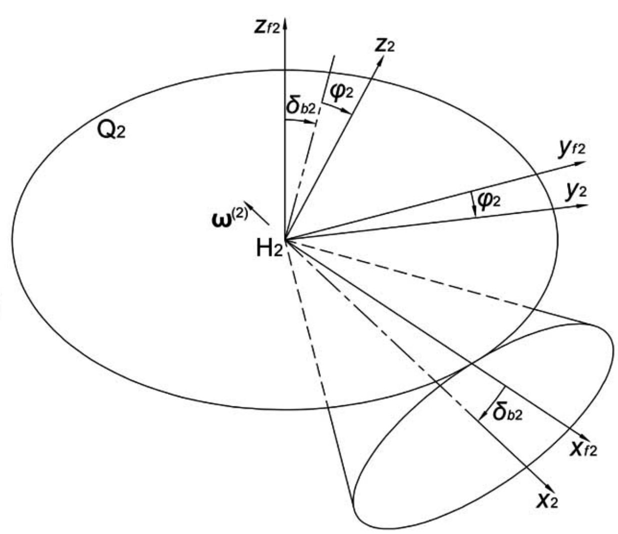

b

Fig. (8). Coordinate systems S_1, S_2.

$$\mathbf{M}_{q\_f2} = \begin{bmatrix} \cos\gamma & -\sin\gamma & 0 & 0 \\ \sin\gamma & \cos\gamma & 0 & 0 \\ 0 & 0 & 1 & 0 \\ 0 & 0 & 0 & 1 \end{bmatrix} \tag{12}$$

$$\mathbf{M}_{f1\_q1} = \begin{bmatrix} \cos\phi_{q1} & -\sin\phi_{q1} & 0 & 0 \\ \sin\phi_{q1} & \cos\phi_{q1} & 0 & 0 \\ 0 & 0 & 1 & 0 \\ 0 & 0 & 0 & 1 \end{bmatrix} \tag{13}$$

$$\mathbf{M}_{f2\_q2} = \begin{bmatrix} \cos\phi_{q2} & -\sin\phi_{q2} & 0 & 0 \\ \sin\phi_{q2} & \cos\phi_{q2} & 0 & 0 \\ 0 & 0 & 1 & 0 \\ 0 & 0 & 0 & 1 \end{bmatrix} \tag{14}$$

$$\mathbf{M}_{f1\_1} = \begin{bmatrix} \cos\delta_{b1} & -\sin\delta_{b1}\sin\phi_1 & -\sin\delta_{b1}\cos\phi_1 & 0 \\ 0 & \cos\phi_1 & -\sin\phi_1 & 0 \\ \sin\delta_{b1} & \cos\delta_{b1}\sin\phi_1 & \cos\delta_{b1}\cos\phi_1 & 0 \\ 0 & 0 & 0 & 1 \end{bmatrix} \tag{15}$$

$$\mathbf{M}_{f2\_2} = \begin{bmatrix} \cos\delta_{b2} & -\sin\delta_{b2}\sin\phi_2 & \sin\delta_{b2}\cos\phi_2 & 0 \\ 0 & \cos\phi_2 & \sin\phi_2 & 0 \\ -\sin\delta_{b2} & -\cos\delta_{b2}\sin\phi_2 & \cos\delta_{b2}\cos\phi_2 & 0 \\ 0 & 0 & 0 & 1 \end{bmatrix} \tag{16}$$

where matrix $\mathbf{M}_{q\_f1}$ denotes the coordinate transformation from system S_{f1} to S_q, and other matrix have the same subscript meaning.

5.2. Equation of Gear Generating-Line

To make the structure and movement of machine tool simple, the shape of generating lines should be simple and easy to form a continuous movement. Therefore the most appropriate shapes are straight line and circular arc. In order to improve processing efficiency, the shape of the gear generating line should be determined preferentially.

If the gear generating line a_2b_2 is a straight line, then its equation in coordinate system S_{q2} should be represented as,

$$\begin{cases} x_{q2c}(u) = x_1 + u\cos\theta \\ y_{q2c}(u) = y_1 + u\sin\theta \\ z_{q2c}(u) = 0 \end{cases} \tag{17}$$

where u is a parameter, x_1, y_1 and θ can be determined by the cutting geometry and the base-cone parameters, namely,

$$\begin{cases} x_1 = A_2\cos\gamma \\ y_1 = -A_2\sin\gamma \end{cases} \tag{18}$$

$$\theta = -\beta_{b2} - \gamma \tag{19}$$

If the gear generating line a_2b_2 is a circular arc, then its equation in coordinate system S_{q2} should be represented as

$$\begin{cases} x_{q2c}(\theta) = x_0 + r\cos(\theta + \mu) \\ y_{q2c}(\theta) = y_0 + r\sin(\theta + \mu) \\ z_{q2c}(\theta) = 0 \end{cases} \tag{20}$$

where θ is a parameter, r is the arc radius of gear generating line, x_0, y_0 and μ can be determined by the cutting geometry and the base-cone parameters, namely

$$\begin{cases} x_0 = A_2\cos\gamma - r\sin(\beta_{b2} + \gamma) \\ y_0 = -A_2\sin\gamma - r\cos(\beta_{b2} + \gamma) \end{cases} \tag{21}$$

$$\mu = 90° - \beta_{b2} - \gamma \tag{22}$$

5.3. Example of Calculating Geometric Parameters

Consulting the data of designing a pair of Gleason hypoid gears, mainly geometrical parameters of cutting hypoid gears by generating-line method can be calculated as follows.

The basic parameters are shown in Table **1**, and these parameters are given by the basic conditions of designing. As shown in Table **2**, the key geometrical parameters r_2, ε and Z_0, which determining the position of point M, are assumed known based on the data of Gleason gears, and so is the average pressure angle α^*. Then, on the basis of traditional formulas, the basic geometrical parameters can be calculated easily, the results are shown in Table **3**. Finally, based on the equations (1) to (10), the results of the base-cone parameters are calculated and shown in Table **4**.

Table 1. The Basic Parameters of Designing

Symbols	Data	Symbols	Data
N_1	11	Σ (deg)	90
N_2	43	E (mm)	34

Table 2. The Key Geometrical Parameters Assumed in Advance

Symbols	Data	Symbols	Data
r_2 (mm)	88.16	Z_0 (mm)	30.56
ε (deg)	20.3	α^* (deg)	19

Table 3. The Results of the Basic Geometrical Parameters

Symbols	Data	Symbols	Data
r_1 (mm)	30.688	A_2 (mm)	92.618
η (deg)	6.375	ε' (deg)	21.237
δ_1 (deg)	16.707	β_1 (deg)	49.981
δ_2 (deg)	72.151	β_2 (deg)	28.744
A_1 (mm)	106.964	α_n (deg)	25.668

Table 4. The Results of the Base-Cone Parameters

Symbols	Data	Symbols	Data
α (deg)	28.728	κ (deg)	10.537
δ_{b1} (deg)	24.762	γ(deg)	56.180
δ_{b2} (deg)	56.585	ε'_b (deg)	23.901
d (mm)	32.611	β_{b1} (deg)	49.588
e (mm)	26.593	β_{b2} (deg)	25.686

During the process of researching the shape of generating lines, the parameters of the gear generating line could influence the shape of the pinion generating line, and we can see from the conditions above, the parameters of the gear generating line are determined by the base-cone parameters. Therefore, when some of the base-cone parameters need to be adjusted to optimize the shape of the pinion generating line, it can be realized by modify the value of the parameter r_2, ε or Z_0. For example, if the value of Z_0 is changed from 30.56 to 30.00, the other parameters should be changed as shown in Table **5**.

Table 5. The Results of Changing the Value of Z_0

Symbols	Data	Symbols	Data
r_1 (mm)	30.194	α (deg)	27.997
η (deg)	6.493	δ_{b1} (deg)	24.896
δ_1 (deg)	16.997	δ_{b2} (deg)	57.033
δ_2 (deg)	71.839	d (mm)	33.767
A_1 (mm)	103.287	e (mm)	26.020
A_2 (mm)	92.782	κ (deg)	10.745
ε' (deg)	21.271	γ(deg)	55.054
β_1 (deg)	48.283	ε'_b (deg)	23.793
β_2 (deg)	27.012	β_{b1} (deg)	48.027
α_n (deg)	25.344	β_{b2} (deg)	24.234

6. CONCLUSIONS

On the basis of the theory of generating-line method, this paper established the cutting geometry and base-cone parameters, and these researches made the new method suitable to manufacture hypoid gears. The cutting geometry contains the tangent relationships between pinion base cone and base plane, and between gear base cone and base plane, respectively, and also contains the planar conjugated relationship between two generating lines of pinion and gear. The base-cone parameters determine the relationships among base cones, base plane and generating lines, and they are necessary to be used to establish the coordinate systems and the equations of generating lines. It can be seen from the example, if some of the base-cone parameters need to be adjusted, it can be realized by modify the value of the parameter r_2, ε or Z_0.

REFERENCES

[1] E. Wildhaber, "Basic Relationship of Hypoid Gears I-VII", *American Machinist*, vol. 90, pp. 108-111, pp. 131-134, February 1946; vol. 90, pp. 132-135, March 1946; vol. 90, pp. 110-114, pp. 150-152, June 1946; vol. 90, pp. 106-110, July 1946; vol. 90, pp. 104-106, pp. 122-128, August 1946.

[2] M. L. Baxter, "Basic geometry and tooth contact of hypoid gears", *Ind. Math.*, vol. 11, pp. 19-42, 1961.

[3] Y. P. Shih, Z. H. Fong, and Grandle C. Y. Lin, "Mathematical model for a universal face hobbing hypoid gear generator", *J. Mech. Des.*, vol. 129, pp. 38-47, January 2007.

[4] Q. Fan, "Computerized modeling and simulation of spiral bevel and hypoid gears manufactured by gleason face hobbing process", *J. Mech. Des.*, vol. 128, pp. 1315-1327, November 2006.

[5] Q. Fan, "Enhanced algorithms of contact simulation for hypoid gear drives produced by face-milling and face-hobbing processes", *J. Mech. Des.*, vol. 129, pp. 31-37, January 2007.

[6] Q. Fan, "Tooth surface error correction for face-hobbed hypoid gears", *J. Mech. Des.*, vol. 132, pp. 011004–1-8, January 2010.

[7] V. Simon, "Optimal machine tool setting for hypoid gears improving load distribution", *J. Mech. Des.*, vol. 123, pp. 577-582, December 2001.

[8] V. Simon, "Optimal tooth modifications in hypoid gears", *J. Mech. Des.*, vol. 127, pp. 646-655, July 2005.

[9] V. Simon, "Design and manufacture of spiral bevel gears with reduced transmission errors", *J. Mech. Des.*, vol. 131, pp. 041007–1-11, April 2009.

[10] J. L. Wu, C. C. Liu, C. B. Tsay, and S. Nagata, "Mathematical model and surface deviation of helipoid gears cut by shaper cutters", *J. Mech. Des.*, vol. 125, pp. 351-355, June 2003.

[11] Y. C. Tsai, and P. C. Chin, "Surface geometry of straight and spiral bevel gears", *J. Mech. Trans. Autom. Des.*, vol. 109, pp. 443-449, December 1987.

[12] M. J. Al-Daccak, J. Angeles, and M. A. González-Palacios, "The modeling of bevel gears using the exact spherical involute", *J. Mech. Des.*, vol. 116, pp. 364-368, June 1994.

[13] Z. J. Yang, F. H. Peng, and X. C. Zhang, "*Cutting method and machine tool of spherical involute tooth profile spiral bevel gear*," China Patent 200810051354.3, March 25, 2009.

[14] F. H. Peng, *Involute Gear Cutting on the Tracing Line*, China: Jilin Science and Technology Press, 2008.

[15] F. L. Litvin, *Gear Geometry and Applied Theory*, USA: Cambridge University Press, 2004.

Intelligent Prediction of Process Parameters for Bending Forming

Saswati Nayak, *Department of Mechanical Engineering, Capital Engineering College, Bhubaneswar, saswatinayak2574@gmail.com*

Chinmay Swain, *Department of Mechanical Engineering, Raajdhani Engineering College, Bhubaneswar, chinmayswain1972@gmail.com*

Tapas Kumar Panda, *Department of Mechanical Engineering, Aryan Institute of Engineering & Technology, Bhubaneswar, tapaspanda123@gmail.com*

Abstract: The choice of the process parameters in the conventional tube bending forming is often based on experience and adjusted by repeated bending tests. The method of constantly testing to adjust has seriously affected the production efficiency and increased production costs. In this paper, neural network is used to establish the intelligent prediction model of the pipe forming process parameters. The obtained datum from analytical calculations, numerical simulations and experiments then serve as the training samples and test samples of neural network training. By the trained neural network, the intelligent prediction for the main process parameters including the bending moment and the boost power can be executed. The test results show that the average relative error between the simulation output and target output of bending moment and boost power is less than 2%, and the predicted process parameters, i.e. bending moment and boost power, can be directly used for actual production.

Keywords: Neural network, intelligent prediction, process parameters, bending forming.

1. INTRODUCTION

The technology of tube bending is widely used in many fields, such as modern automobile, aerospace industry and shipbuilding, so it plays an important role in society. The shaping quality of bending tube mainly includes ellipticity, exine thinness rate and inner wall thickness rate, and there are many factors that could influence the shaping quality, such as pipe size, material, the rotating velocity of pipe die, the technological parameters in bending process, and so on. These factors have an inter-coupling relationship, so they have a non-liner and complicated influence on shaping quality of bending tube. The manipulator, lack of theoretic calculation and convenient method, always adjust and confirm technological parameters by experience and experiments when they machine different batches and type pipes with the traditional tube bender using cold bending, so the precision of shape can't be achieved by single bending forming. These results in long period, high cost, low efficiency and can't satisfy the need of rapid manufacture.

There are many researches in this field in some domestic and foreign universities. Yongjun Wang from Northwestern Polytechnical University has made an in-depth study on the intelligent control of sheet metal bending forming, established its intelligent control model by using the artificial neural network, and the technology of online prediction controlling in stretch bending process is realized [1]. His work provides a valuable reference for the intelligence of sheet metal forming. By using finite element method, Yongle Kou has investigated the influence of the pushing equipment on the wall thickness thinning and cross section ovalisation [2]. The achievements of his study lay foundations for the establishing of an accurate finite element model and the analyzing of the forming mechanism and quality in Aluminum alloy thin-walled tube NC bending with small bending radius; it also provides some bases for the selection of reasonable process parameters and the control of wall thickness thinning and cross section ovalisation in Aluminum alloy thin-walled tube NC bending process. Guangxiang Wang studied the influence of processing parameters on wrinkling cracking spring-back and deformation of thin-walled NC bending tube by experimentation [3]. The major reason for the extension length of mandrel influencing wrinkle and crack of tube is deeply analyzed, and the calculation formula of the most reasonable extension length of mandrel is deduced and proved. At the same time, the effects of angularity on spring-back angle and deformation of cross-section are researched, and the conclusion of the linear relationship between angularity and spring-back angle is obtained. Changping Pan from Jilin University analyzed the bending mechanism of thin-walled tube, and focused on the bending spring-back control of thin-walled tube, and analyzed and elaborated the working principle of the self-developed CNC tube bender [4]. Through the method of numerical simulation, the finite element analysis and experiment of bending process parameters on curvature stretch bending of rectangular aluminum have been achieved by Arild H. Clausen and Odd. S. Hopperstad, *et al.* [5]. The researchers found that the work piece spring-back is controlled by the pretension and the strain hardening index.

Lingyi Sun researched the key technologies of neural network bending spring-back prediction [6]. He effectively solved the nonlinear mapping problem between the tension control parameters and resilience amount by establishing a kind of artificial neural network model which has been achieved by using Matlab neural network toolbox, achieved a good prediction accuracy, and verified the validity of the prediction model. A numerical wrinkling prediction system is developed for NC thin-walled bending process by Yang He [7]. The analysis of the bending process of aluminum and stainless tube has been carried out by the system. The system can be used to both predict the wrinkling phenomena and

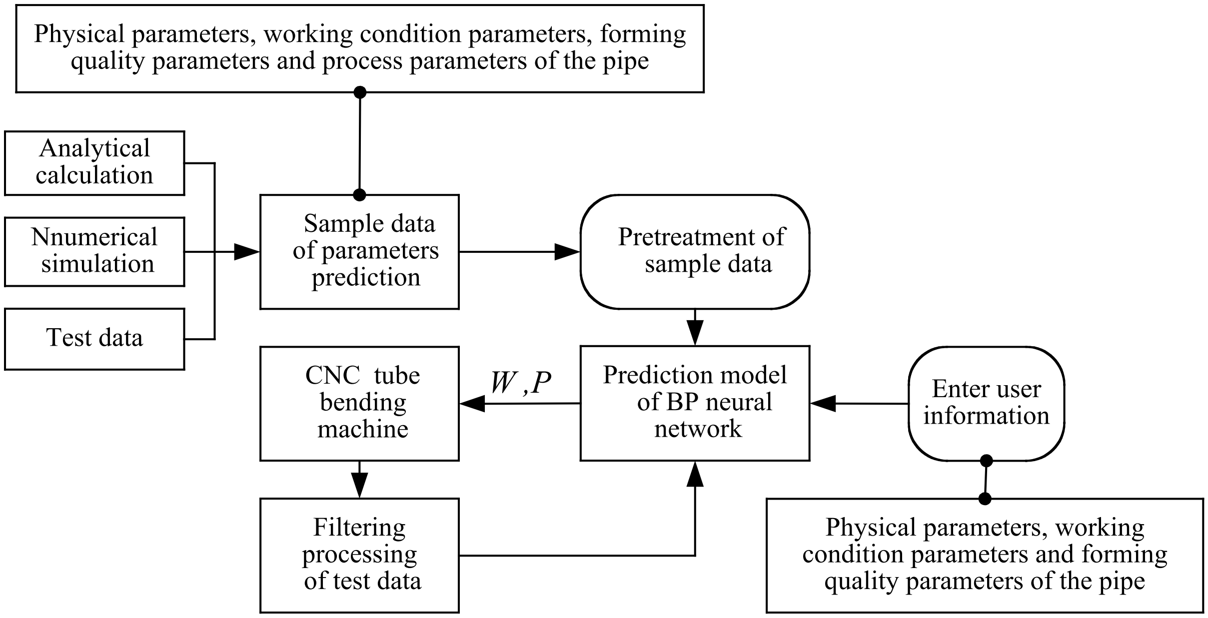

Fig. (1). Schematic drawing of prediction scheme of the tube bending forming process parameters.

analyze the bending process. Lehua Qi and Junjie Hou, who used artificial neural network method, applied 81 sets of experimental data to the neural network modeling and testing, and then established a parameters knowledge base of liquid extrusion tube and bar, which can more accurately predict the key process parameters [8]. In this paper, BP neural network has been used to predict the process parameters of tube bending, which makes the tube bending process realize intelligentization and automation, and enhance the productivity and reduce the production costs.

2. PREDICTION OF TUBE BENDING FORMING PROCESS PARAMETERS BASED ON BP NEURAL NETWORK

The neural network is used as the prediction model, and the obtained datum from analytical calculations, numerical simulations and experiments serve as the training samples. The process parameters database is established by the analytical calculations of the bend forming, finite element simulations and experiments. The retrieved processing parameters serve as the initial value of the predictive control. According to the different material parameters, process parameters can be dynamically adjusted by the model predictive control model so as to achieve the predictive control of the bend forming quality.

The prediction scheme of the tube bending forming process parameters for utility boiler based on BP neural network is shown in Fig. (**1**).

The original samples of the prediction model of process parameters are obtained by methods of analytical calculations, numerical simulations and experimental data. There are fourteen parameters in the samples, two of which, i.e. bending moment and boost power, are chosen as the goal of the network prediction. The original samples for the neural network must be pretreatment before applied to neural network. Trained neural network prediction model can be directly used in production. Users would obtain the process parameters W and P by inputting the pipe physical parameters, working parameters and objectives forming quality parameters. Then the predictive values will be sent to the tube bending machine for real-time control. The data obtained from operation by users are eventually returned as the new sample data of the neural network prediction model.

3. ESTABLISHMENT OF THE PREDICTION MODEL OF TUBE BENDING FORMING PROCESS PARAMETERS

BP neural network algorithm can approximate nonlinear functions with arbitrary precision, it is widely used to solve the industrial process control problem of the nonlinear characteristics and the unknown structure, and it is also suitable for building the model of multivariable nonlinear and uncertain time-varying complex system. The establishment of BP neural network model can be divided into three parts: the sample data acquisition and processing; determination of the network structure; neural network training and testing [9].

3.1. Sample Data Acquisition and Processing

The sample data acquisition and processing including sources of initial data samples, determination of input and output, design of the total sample network and pretreatment of input and output data.

3.1.1. Sources of Initial Data Samples

In the process of tube bending forming of utility boiler, the sample data of network training and testing mainly come from three ways: One is the experience data accumulated by the bending machine operators. This part of the data can also be obtained by the repeated bending test. Second one is the simulation of tube bending forming process by using the FEA software. The conditions of tube bending forming are added and changed in order to make the end results tend to the ideal of the best value. Third one is the establishment of bending mechanical analysis model for analytical calculation.

3.1.2. Determination of Input and Output

In the bending process, the processing parameters are affected by the pipe size parameters, physical parameters and the quality parameters. Hence, in the original sample the original sample, pipe outer diameter, the 12 variables of wall thickness, yield strength, elastic modulus, strength coefficient, stiffness index, bending radius, bending speed, bending angle, exine thinness rate, inner wall thickening and ellipticity are designed as network input variables, bending moment and boost power as the network output variable.

3.1.3. Design of the Total Sample Network

The design of the total sample determines the advantages and disadvantages of network training results. According the rule of thumb, the sample size required for the network training needs to account for 5 to 10 times of the total number of the connection weights. 320 sets of data selected from the original sample are regarded as the total sample data set of BP neural network. In the process of selecting the total sample, the balance principle of sample type has been fully considered during the sample selection. Finally, 224 sets of data were selected as the training sample set, 96 sets of data as the test sample set.

3.1.4. Pretreatment of Input and Output Data

The total samples must be pretreated in network training, namely the uniform normalized. Through the transform processing network's input and output data will be limited in the [-1,1] or [0,1] interval. BP neural network can use the Matlab toolbox built-in data to convert functions. Training samples and test samples can be normalized uniformly by using prestd function, while the input data during prediction by using trastd function, and the poststd function must be used for the reduction treatment of final predictive Output.

3.1.5. Design of the Process Parameters Database

The process parameters database is established by the analytical calculations of the bend forming, finite element simulations and experiments. The retrieved processing parameters serve as the initial value of the predictive control. According to the different material parameters, process parameters can be dynamically adjusted by the model predictive control model so as to achieve the predictive control of the bend forming quality, and improve the bending quality.

3.2. Determination of the Network Structure

In this paper, predictive control model was established by BP neural network with three hidden layers, the predictive model is shown in Fig. (**2**).

Input Layer: pipe outer diameter α, wall thickness t, yield strength σ, elastic modulus E, strength coefficient n, stiffness index K, bending radius R, bending speed v, bending angle θ, outer wall thinning rate β, inner wall thickening χ and ellipticity α, a total of 12 input nodes. Output layer: moment and boost power, a total of 2 output nodes.

Hidden Layer Nodes: The role of the hidden layer node is to extract and store the internal law of the sample. The number of hidden nodes directly affects its ability of generalizing and reflecting the sample laws. Theoretically, a three-layer BP neural network can make a full approximation arbitrarily with any complex nonlinear function. Therefore, only one hidden layer is usually enough. In this paper, the number of the input network layer and output layer nodes are 12 and 2, respectively. The results showed that using a single hidden layer neural network, the network training time is very long, it is difficult to achieve the target accuracy even though the iterative steps is more than 5000. Considering the time limits in practical application, the three-hidden layer neural network can be controlled iterations within 50 steps, which greatly improved the training efficiency.

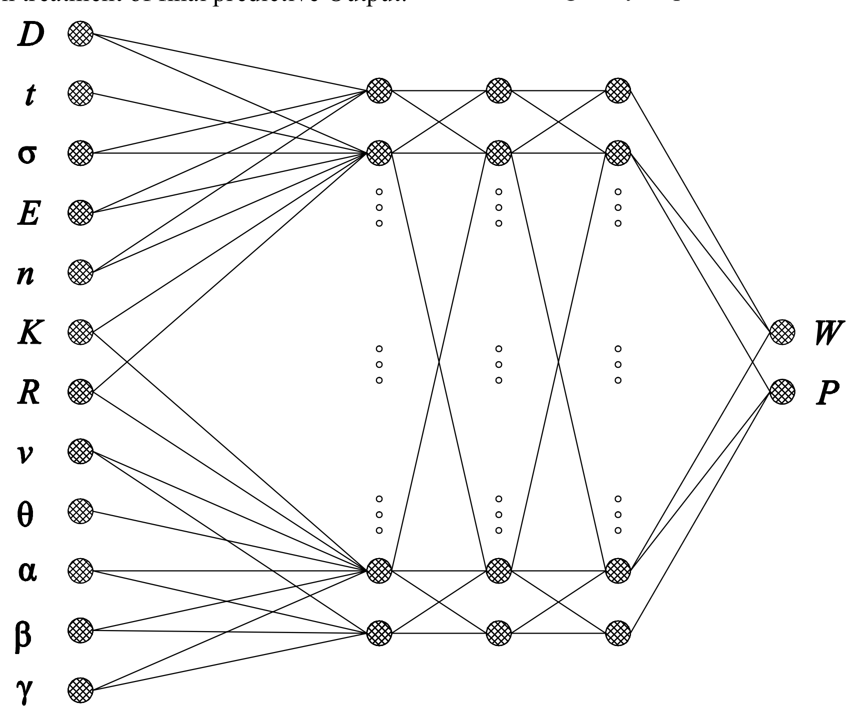

Fig. (2). Neural network prediction model of process parameters of tube bending forming.

Firstly, the number of nodes in hidden layer has been estimated by using the empirical formula. Then through commissioning tests based on the estimated value, the best group of hidden nodes has been selected. The following is a kind of empirical formula of hidden nodes:

$$m = \sqrt{n+l} + \alpha m \tag{1}$$

Where m is the number of hidden layer nodes, n is input nodes, l is output nodes; α is a constant between 1 to 10.

According to empirical formula, taking the estimated number of hidden layer nodes as 10-10-6, and gradually increasing the number of nodes for training the same sample set, then the following results was obtained by several experiments in Table **1**:

Table 1. The Results of Hidden Nodes from Several Experiments

Hidden layer nodes	Training steps	Moment fitting	Boost power fitting
10—10—6	22	0.995	0.902
12—12—8	18	0.993	0.924
16—16—8	16	0.995	0.907
16—15—12	11	0.998	0.983
18—18—15	25	0.956	0.924

The above table shows that hidden nodes is selected as 16-15-12, the network training convergence can be achieved just within 10 steps, and get the best fitting degree.

3.3. BP Network Trainning and Testing

After determining the network structure and training sample set, network training can be stated. During the training, the feedbacks of advantages and disadvantages of the network performance are used to adjust the network design. The main advantages and disadvantages of network performance are to see whether it has good generalization ability, namely the approximate capacity between the predicted results and expected results. In addition, the speed of network training for some special problems is also a basis to determine network performance. Since the input data are all more than zero, so the tansig transfer function is used in the hidden layer, the purelin transfer function is used in output layer, and trainlm function based on a LM algorithm is used in the training. The experiment results shows that target error can be achieved only within 20 iteration steps.

The partial training sample data of process parameters prediction network for utility boiler are listed in Table **2**.

Final determination of the network is to constantly adjust based on the advantages and disadvantages of the training performance, and when the test results of test samples meet the expectations, then it can be say that the form of network was finally established.

4. EXAMINATIONS AND ANALYSIS OF RESULTS

According to the process of network training above, it can be found that the network training is a kind of process in which a output result constantly feedback to adjust the network training. Then, the final qualified BP neural network must satisfy the desired effect. Otherwise, the network is still unsatisfactory and requires further improvement. The bending moment and boost power as the network output must meet the requirements of actual production, i.e. errors between predictive value and expectation value need to be controlled within 2%, that is, the relative error must be controlled below 2%. In addition, the training speed must be fast. Neural network training error gradient is shown in Fig. (**3**).

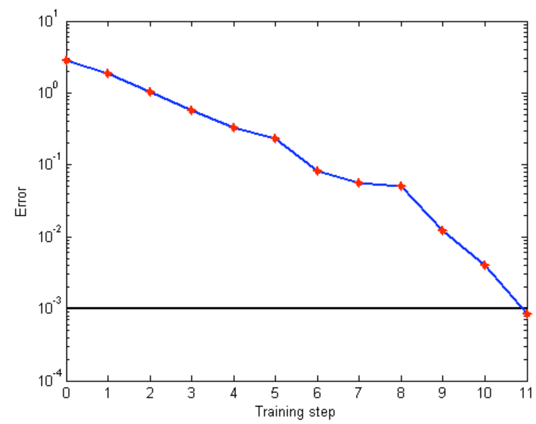

Fig. (3). Schematic drawing of neural network training error gradient.

Table 2. Partial Training Sample Data of Process Parameters Prediction Network for Utility Boiler

Network input data												Target output	
D	t	σ	E	n	K	R	v	θ	α %	β %	χ%	W	P
63	7	310	211	0.3	390	130	0.5	90	4.28	10.55	13.67	1.008	4.9
63	7	318	217	0.31	380	130	0.5	90	4.25	10.52	13.68	1.009	4.8
63	11	315	225	0.26	386	130	0.5	90	2.5	10.6	12.66	1.562	5.5
63	11	309	213	0.34	392	130	0.5	90	2.473	10.55	12.65	1.563	5.5
54	7	310	217	0.34	396	118	0.5	90	3.49	9.8	12.67	1.038	5.3
54	7	312	214	0.29	406	118	0.5	90	3.48	9.77	12.68	1.025	5.2
54	4	310	217	0.27	396	130	0.5	180	5.95	8.81	12.84	0.574	3.9
54	4	314	203	0.34	402	130	0.5	180	5.82	8.72	12.9	0.567	4.0

Table 3. Comparison of the Simulation Output and Target Output of the Bending Moment *W*

Target output *W*	Simulation output *W*				Standard deviation	Maximum relative error (%)
0.671	0.6698	0.6682	0.6672	0.6731	0.0026	-0.57
0.645	0.6442	0.6394	0.6464	0.6386	0.0038	-0.99
1.138	1.1369	1.1395	1.1391	1.1388	0.0012	0.13
1.025	1.0239	1.0261	1.0236	1.0195	0.0028	-0.53
1.681	1.6832	1.6792	1.6831	1.6792	0.0023	0.13

Table 4. Comparison of the Simulation Output and Target Output of the Boost Power *P*

Target output *P*	Simulation output *P*				Standard deviation	Maximum relative error (%)
4.6	4.6138	4.6154	4.5347	4.6491	0.0485	-1.42
4.3	4.2764	4.3156	4.4012	4.3235	0.0522	-1.24
6.7	6.6837	6.6378	6.6714	6.7154	0.0321	-0.93
5.8	5.7645	5.9010	5.8226	5.7761	0.0712	1.74
7.1	7.1843	7.0347	7.1352	7.2130	0.0783	1.59

From the Fig. (**3**), it can be seen that the accuracy of the network training has reached 0.00083405 in the 11-step, the precision of target error is 0.001, and hence both of the training speed and training accuracy achieved the intended target. Partial results of simulation output and target output of test samples for the bending moment and boost power are listed in Table **3** and Table **4**, which are selected from 4-time consecutive network prediction.

The linear fitting charts of moment linear and boost power of network input and target output of the test sample are shown in Fig. (**4**) and Fig. (**5**) respectively.

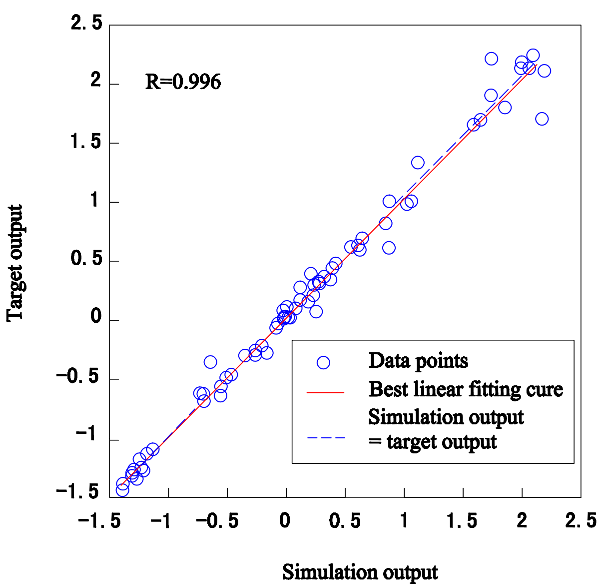

Fig. (4). Moment linear fitting chart.

According to the linear fitting charts of moment linear and boost power above, it can be seen that the correlation coefficient R reflecting the fitting degree is 0.996 and 0.983 respectively, very close to 1. The predictive value and expected value are in high fitting degree. Through the 4-time consecutive network tests, the maximum relative errors between the simulation output and the target output are all controlled within 2%, which meets the accuracy requirement of this case and confirms the reliability and validity of BP neural network technology for the tube bending process parameters prediction.

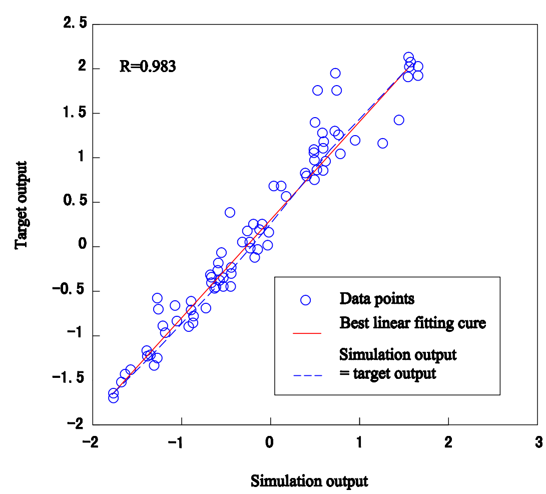

Fig. (5). Boost power linear fitting chart.

5. CONCLUSIONS

There are many factors that could influence the shaping quality, and the relationship between these factors is inter-coupling and nonlinear. Hence, the determination of process parameters by continuously adjusting the parameters often takes a lot of time and increases the production cost in the actual production of tube bending. In this paper, BP neural network is used to establish the intelligent prediction model of the pipe forming process parameters, and the main process parameters including the bending moment and the boost power were predicted. The main results are as follows:

(1) The prediction scheme of the tube bending forming process parameters for utility boiler was established based on BP neural network, the moment and boost power network serve as the prediction targets.

(2) The BP Neural network prediction model was established, and the network structure, network training and testing methods were designed.

(3) The test results show that the prediction error of the bending moment and the boost power can be maintained at below 2%, fully meet the required precision of tube bending. The trained neural network model can be directly used to guide the production practice.

REFERENCES

[1] Y. J. Wang, *Study on Intelligent Control of Precise Stretch Bending Forming*, D.S. thesis, Northwestern Polytechnical University, Xian, China, 2005.

[2] Y. L. Kou, *Experimental Research on NC Bending with Small Bending Radius of Aluminum Alloy Thin-Walled Tube*, Northwestern Polytechnical University, Xian, China, 2007.

[3] G. X. Wang, H. Yang, H. Li, M. Zhan, and R. J. Gu, *Experimental Study of the Influence of Processing Parameters on Forming Quality of Thin-Walled NC Bending Tube*, *Mech. Sci. Tech.*, vol. 24, pp. 995-998, August 2005.

[4] Ch. P. Pan, *Research on the Bending Spring-Back of Thin-Walled Tube and the Control System of Tube Bending Machine*, Jilin University, Changchun, China, 2008.

[5] A. H. Clausen, O. S. Hopperstad, and M. Langseth, "Sensitivity of model parameters in stretch bending of aluminum extrusions", *Int. J. Mech. Sci.,* vol. 43, pp. 427-453, February 2001.

[6] L. Y. Sun, Y. J. Wang, and J. B. Wang, " Springback prediction of stretch bending using artificial neural network", *Mech. Sci. Tech.,* vol. 27, pp. 65-68, January 2008.

[7] Y. He, and L. Yan, "Wrinkling analysis for forming limit of tube bending processes", *J. Mater. Process. Technol.*, vol. 152, pp. 363-369, October 2004.

[8] L. H. Qi, J. J. Hou, F. Yang, and H. J. Li, "Establishing the knowledge base of parameters for shaping tube and bar products on the neural network", *Acta Aeronautica Et Astronautica Sinica*, vol. 19, pp. 744-747, November 1998.

[9] Y. W. Li, *Research and Implement Intelligent Forecast System Based on ANN*, North China University of Technology, Beijing, China, 2006.

Thermal Process of MIG Welding of Aluminum Alloy

Manohar Kumar Singh, *Department of Mechanical Engineering, Aryan Institute of Engineering & Technology, Bhubaneswar, manoharsingh751@gmail.com*

Sidhanta Behera, *Department of Civil Engineering, Raajdhani Engineering College, Bhubaneswar, didhantabehera21@gmail.com*

Kalpana Mallick, *Department of Mechanical Engineering, Raajdhani Engineering College, Bhubaneswar, kalpanam11@outlook.com*

Abstract: In order to study MIG welding process of aluminum alloy with longitudinal magnetic field, thermal efficiency with longitudinal magnetic field was analyzed, as well as softening behavior of heat-affected zone (HAZ) and base metal were investigated. The results showed that under the action of longitudinal magnetic field, welding current decreased and resultingly total heat input reduced as the exciting current increased, meanwhile at the anode surface current density and heat flux density decrease in the arc core and rise at the edge of arc, which made arc thermal efficiency increasing and melting efficiency decreasing. As a result of action of the magnetic field, the trend of grain growth of HAZ slowed down and the influence on base metal of heat input decreased. When the exciting current was 20A, microhardness of HAZ and base metal improved evidently. However, as the exciting current continued to increase, the effect of magnetic field on softening behavior did not change significantly.

Keywords: Magnetic field, MIG welding, thermal process, softening behavior.

1. INTRODUCTION

Welding thermal process consist in the whole welding process. Welding heat input and the distribution of heat flux influence the crystal structure, residual stresses and welding distortion of the weld zone and HAZ, sequentially to determine the final weld quality [1]. Therefore, the study on the welding thermal process has always been an important research subject in welding field. A variety of welding methods and techniques has been developed to reduce the impact of heat input. The applications of electromagnetic field in welding is a new developed technology in recent years, by which the welding arc shape, melting droplet transition and crystallization process of liquid metal in the molten pool are influenced through additional magnetic field, accordingly refining weld crystal organization and improving mechanical properties [2]. Another important action of magnetic field has not been noticed widely yet, which is to change the arc shape by the magnetic field and thus to affect the heat input and heat flux distribution, thereby decreasing the influence of welding heat input on the base material, particularly to reduce the welding deformation and improve welding quality when welding the thin pieces metal. In this paper, the thermal efficiency and melting efficiency in MIG welding of aluminum alloy with longitudinal magnetic field were analyzed, as well as the influence on softening behavior was investigated.

2. EXPERIMENTAL MATERIAL AND METHODS

In the study the base metal used was 6061 aluminum alloy plate which size was 300×300×15mm and welding wire used was ER5356 which diameter was 1.2mm. The chemical compositions of the base metal and welding wire are shown in Table **1**. A TPS-4000 digital DC pulsed MIG welding source was used. Shielding gas was argon, which purity is 99.99% and the flow rate is 15L/min. Additional longitudinal magnetic field was produced via the excitation coil installed on the welding torch. The excitation coil was made of enameled wire which diameter was 2.5 mm. The turns of excitation coil was 230, and the range of magnetic flux density was 0~30mT. The direction of magnetic lines of flux paralleled the arc axis, and made a symmetrical distribution relative to arc axis. Excitation current was provided by a self-designed excitation power, which excitation current and frequency could be adjusted. Diagram of welding equipment is shown in Fig. (**1**). In the experiment beads were made by choosing different welding parameters and exciting current intensity. These parameters were shown in Table **2**. After welding, the geometry of bead was measured and microstructure of HAZ was observed. The microhardness of different zone was measured including coating, fusion line, HAZ and base metal. Hardness measurement points are shown in Fig. (**2**). Heat flux density and current density of the arc with longitudinal magnetic field were simulated by using ANSYS FEA software.

Table 1. Compositions of Base Metal and Filler Wire (wt. %)

Material	Si	Fe	Cu	Mn	Mg	Cr	Zn	Ti	Al
6061	0.4~0.8	0.7	0.15~0.4	0.15	0.8~1.2	0.04~0.35	0.25	0.15	Bal
ER5356	0.25	0.10	0.10	0.05~0.2	4.5~5.5	0.05~0.20	0.10		Bal

3. RESULTS AND ANALYSIS

3.1. Welding Thermal Process under the Action of Additional Magnetic Field

The physical model of welding heat source involves two aspects: how much heat is applied to the weldment and how

Table 2. Welding and Electromagnetic Field Parameters

Weld No.	Welding Speed [mm·s^{-1}]	Wire Feed Speed [m·min^{-1}]	Magnetic Field Frequency [Hz]	Exciting Current [A]	Welding Current [A]	Welding Voltage [V]
1	24	8	0	0	136	19
2	24	8	10	10	130	19
3	24	8	10	20	112	19
4	24	8	10	25	105	19

the heat is distributed in weldment. The majority of total energy in welding process is provided by the welding arc, while a small portion is generated by the electrode. According to the law of conservation of energy [3], the total energy balance can be expressed as:

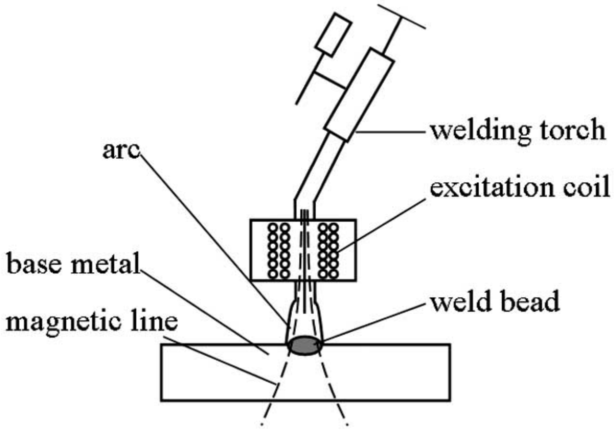

Fig. (1). Diagram of welding equipment.

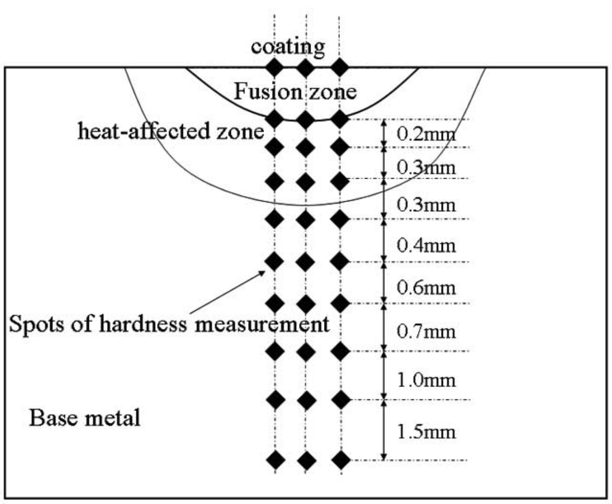

Fig. (2). Locations of measured points.

$$E_{total} = E_{losses} + E_{fz} + E_{bm} \tag{1}$$

Where E_{total} is the total energy generated by the arc and electrodes resistance, E_{losses} is the energy lost to the surrounding environment, E_{fz} is the energy used to melt the fusion zone (including the latent heat of fusion), E_{bm} is the energy passed to the base metal (used to form the HAZ and heat base metal). E_{fz}+E_{bm} is the total energy transferred to the work piece, E_{fz} is used for melting metal, called effective energy. Therefore, the arc heat efficiency η_a, and the melting efficiency η_m, can be defined as:

$$\eta_a = \frac{E_{fz} + E_{bm}}{E_{total}} \tag{2}$$

$$\eta_m = \frac{E_{fz}}{E_{fz} + E_{bm}} \tag{3}$$

During the welding process voltage remained the same and welding current decreased with the increase of exciting current, as is shown in Fig. (**3**). The reason is that charged particles circumgyrated under the action of Lorentz force and the moving path of charged particles changed from the straight line to spiral, which made total path and the distance of the conduction current increased, as well as the arc resistance increased, thus welding current reduced [4].

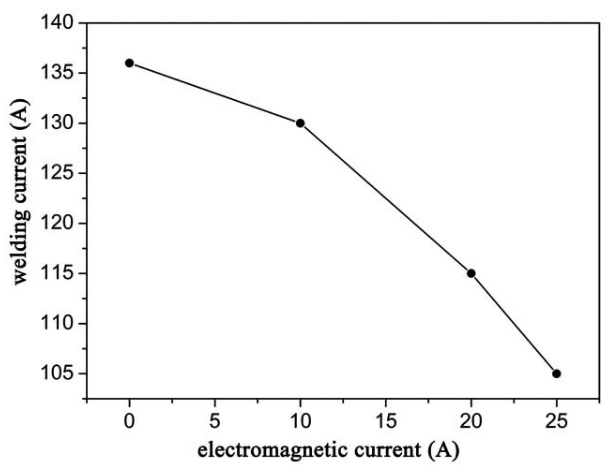

Fig. (3). Effects of electromagnetic current intensity on welding current.

As arc voltage remained the same and the welding current decreased under the action of magnetic field, the heat input E_{total} reduced. Arenas gave the approximate empirical equation of computing the arc heat efficiency by generalizing Tsai and Eagar's experimental data [5, 6]. The equation can be expressed as:

$$\eta_a = 7.48\frac{I^{0.63} R_c^2}{L^{0.8} IU} \tag{4}$$

Where, L, I, U and R_c represent length of arc, welding current, welding volt and radius of arc respectively. So under action of longitudinal magnetic field, arc expanded and radius of arc increased and welding current reduced, which made arc heat efficiency increased. But owing to the total heat input reduced, the total effective energy of arc decreased. Guan Qiao gave method of testing welding thermal efficiency and melting efficiency under different weld heat input, and the result showed that effective energy factor of thermal decreased as effective heat input of arc decreased, namely the melting efficiency η_m decreased [7]. DuPont had demonstrated that melting efficiency could be predicted from the welding parameters and material properties by the equation 5 [8].

$$\eta_m = 0.5\exp\left(\frac{-175}{\eta_a UI\mathrm{v}/E\alpha v}\right) \tag{5}$$

In the equation 5, $\eta_a UI$ is effective energy of arc, v is welding speed, E is the total enthalpy change due to melting, α is the thermal diffusivity at 300K, v is kinematic viscosity at the melting point. DuPont's research showed that melting efficiency decreased as total energy decreased, and melting efficiency increased rapidly when welding speed increased. But when welding speed increased to some extent, melting efficiency reached a maximum.

The comparison of the effective heat input under different exciting current can be transformed into the comparison of the cross-sectional area of fusion zone by the equation (6) [9].

$$E_{fz} = F\mathrm{v}\rho\left(\int_{T_0}^{Tm} c\,dT + H\right) \tag{6}$$

Where F is the cross-sectional area of fusion zone, v is the welding speed, ρ is the density of weld material, c is heat capacity, H is the latent heat of fusion, T_0 is the environment temperature, T_m is the melting point. As welding speed and density of weld material are constant, effective heat input ratio δ under different exciting current can be expressed as,

$$\delta = \frac{E_{fz1}}{E_{fz2}} = \frac{F_1}{F_2} \tag{7}$$

Where E_{fz1} and E_{fz2} are the effective weld heat input under different exciting current, F_1 and F_2 are the cross-sectional area of fusion zone under exciting current. As the fusion line shape can approximately be seen as parabolic shape and weld width and penetration are known, the equation of fusion line can be expressed as,

$$y = -\frac{4h}{b^2}x^2 + h \tag{8}$$

So the cross-sectional area of fusion zone can be got according to equation (9):

$$F = \int_{-\frac{b}{2}}^{\frac{b}{2}}(-\frac{4h}{b^2}x^2 + h)dx = \frac{2}{3}bh \tag{9}$$

Where b is weld width and h and is penetration. The cross-sectional area of fusion zone under the action of different exciting current is shown in Fig. (**4**), from which it is observed that the cross-sectional area of fusion zone decreased with the exciting current increasing, so the effective weld heat input E_{fz} reduced according to the equation (7).

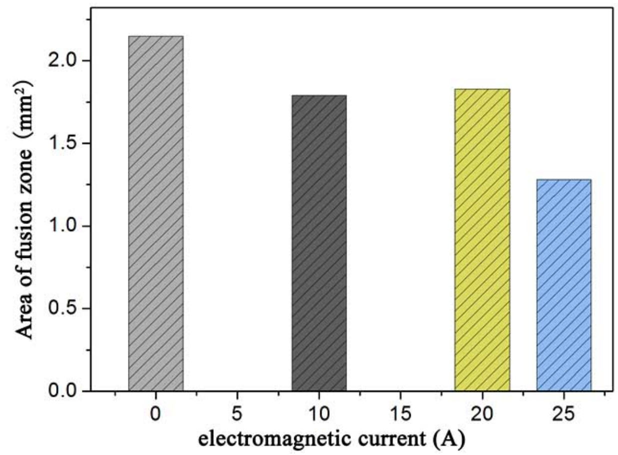

Fig. (4). Cross-sectional area of fusion zone under different exciting current intensity.

3.2. Current Density and Heat Flux Density under the Action of Additional Magnetic Field

Current density distribution of welding arc is one of the most fundamental matters. It affects the distribution of heat flux directly and decided the final welding quality. Move of charged particle is the main mode by which arc transmits heat energy to welding pool. So move of charged particle under the action of longitudinal magnetic field is analyzed.

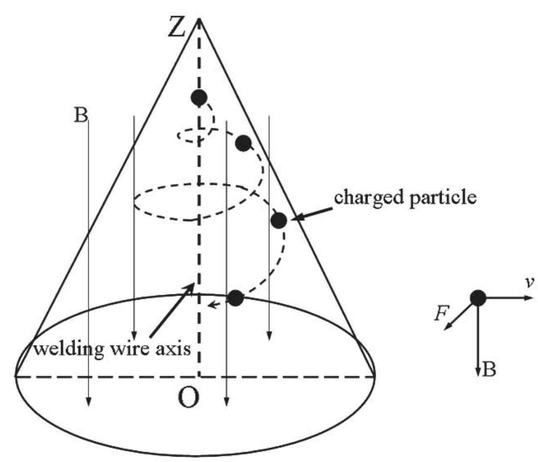

Fig. (5). Move of charged particle under the action of longitudinal magnetic field.

When longitudinal magnetic field is introduced into welding process, charged particle was act by Lorentz force as is shown Fig. (**5**). Under the action of Lorentz force F charged particle rotate around the welding wire axis and away from the welding wire axis, which made shape of arc expand and density of charged particle decrease. As density of charged particle decrease, current density decreased and heat flux decreased. Fig. (**6**) and Fig. (**7**) gave the simulated results of current density of arc under the action of different magnetic field condition, which can refer to Ref. [10]. From the simulated results it can be concluded that at the tip of welding wire current density has maximum and the max is 1.25×10^8 when the welding current is 136A. As the distance

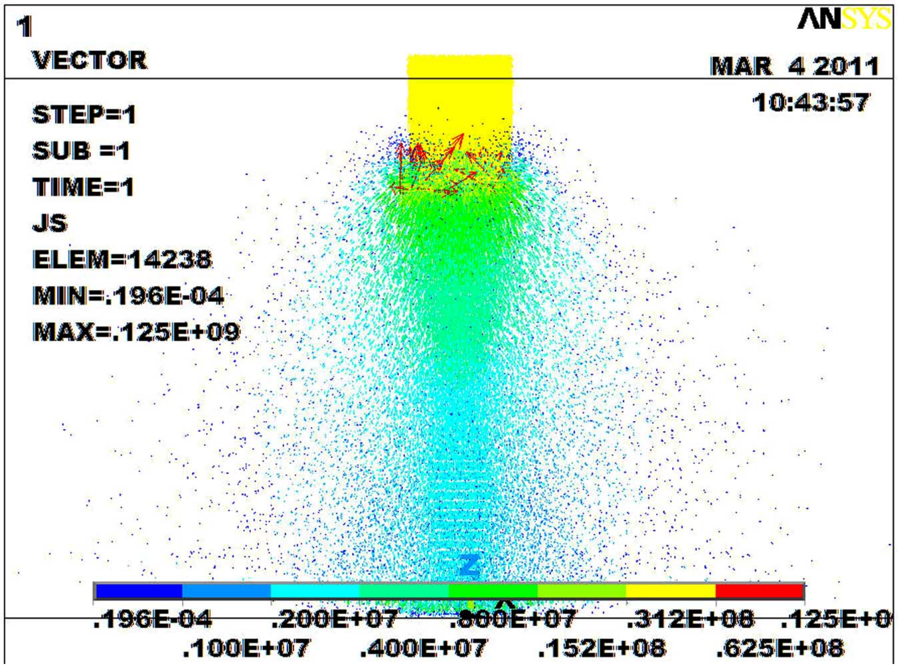

Fig. (6). Current density distribution without longitudinal magnetic field.

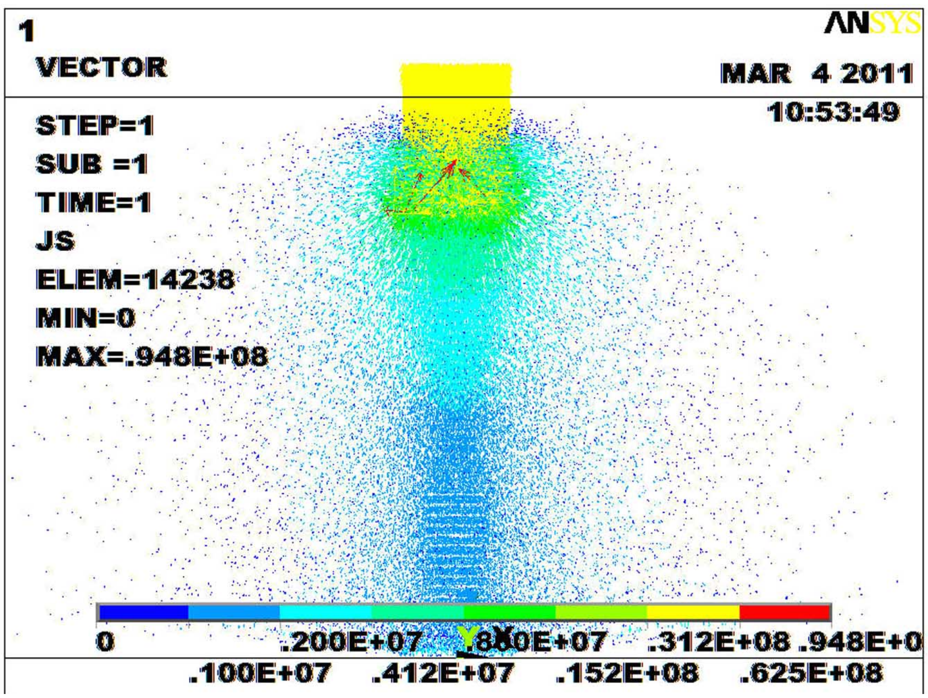

Fig. (7). Current density distribution with longitudinal magnetic field.

from cathode increased, current density decreased gradually. When longitudinal magnetic field is introduced into welding process and other process parameters are invariable, average of current density decreased and the max of current density is 0.9×10^8.

Fig. (**8**) and Fig. (**9**) show heat flux distribution and current density distribution on the anode under different magnetic field conditions. It is seen that the rule of current density distribution and heat flux are similar. Heat flux density and current density on the anode decreased in the arc core and increased at the edge of arc when longitudinal magnetic field is introduced into welding process. As radial distance to arc core increase, current density and heat flux on the anode decrease. Yet velocity of decrease is different. Current density and heat flux of arc with additional longitudinal magnetic field is slower than that having no longitudinal magnetic field. Consequently at the edge of arc current density and heat flux of arc with longitudinal magnetic field are greater than arc without longitudinal magnetic field.

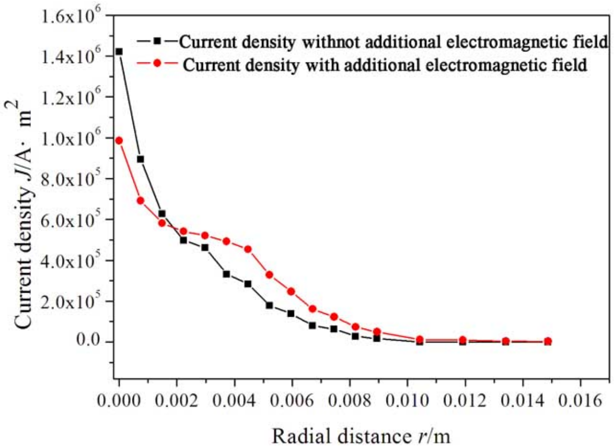

Fig. (8). Current density distribution at anode.

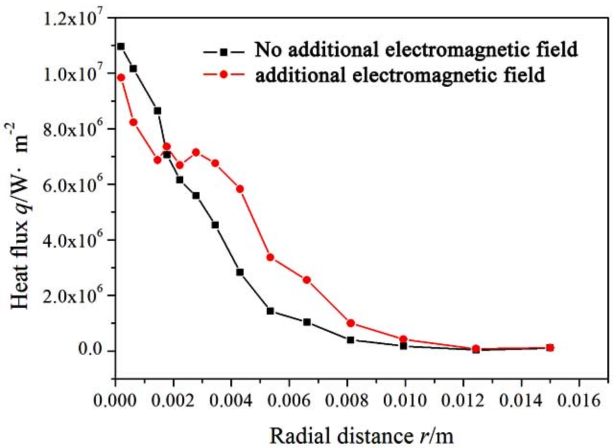

Fig. (9). Heat flux distribution at anode.

3.3. Softening Behavior of HAZ under the Action of Additional Magnetic Field

Microstructure and properties of base metal changed owing to the heat input decreasing and the redistribution of heat flux on the surface of base metal under the action of magnetic field.

Fig. (**10**) shows the microstructure of HAZ under different exciting current intensity. It can be observed when the exciting current is 0 A, the organization of HAZ became thick obviously and apparently belonged to the typical overheated organizations. As the exciting current increased, the effect of heat input on base material organizations reduced and the grain growth trend of HAZ slowed down. When the exciting current is between 10 A and 20 A, effectiveness of grain refining is the best. Therefore when the longitudinal magnetic field is suitable, it is beneficial to improve the grain organization of HAZ.

Fig. (**11**) shows trend of micro-hardness of HAZ and base metal under different exciting current intensity. It can be observed that softening behavior of HAZ due to weld heat input is obvious and magnetic field has an obvious effect to hardness of base metal. The farther the distance from the fusion line, the greater the hardness gradually became. When the exciting current intensity was 0, the base metal hardness was lower. As exciting current intensity increased, the over-all hardness of base metal increased. Base metal hardness is the greatest when exciting current intensity is 20 A. How-ever, when the exciting current intensity continued to increase, the base metal hardness did not change signifi-cantly. These results show that the impact of heat input on softening behavior of HAZ and base metal becomes weaker under the action of longitudinal magnetic field.

Fig. (**12**) shows cross section and HAZ of bead under different exciting current intensity. It is observed that shape

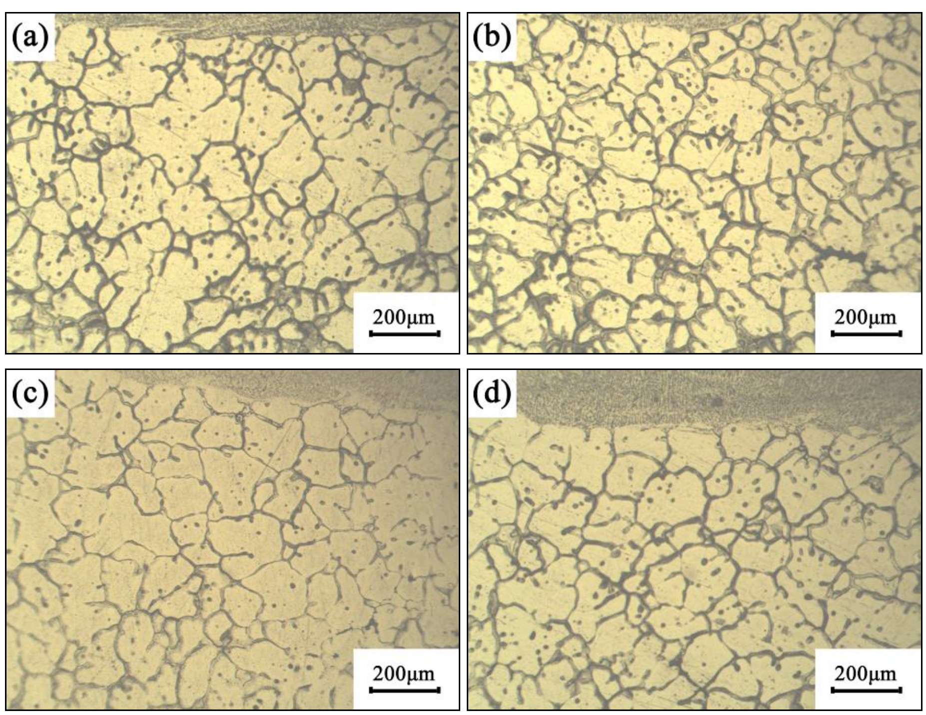

Fig. (10). Microstructure of HAZ under different exciting current intensity. (**a**) I=0A; (**b**) I=10A; (**c**) I=20A; (**d**) I=25A.

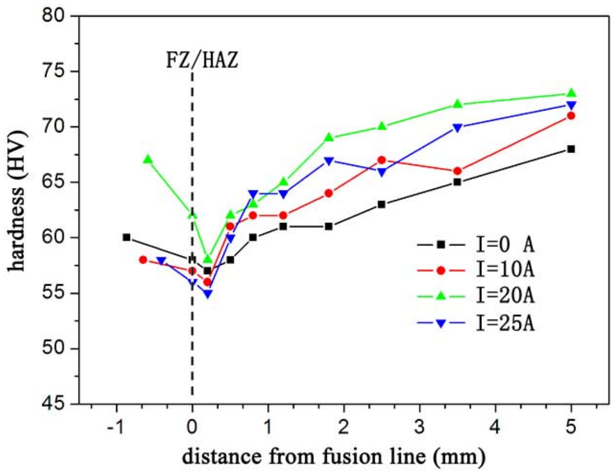

Fig. (11). Hardness distribution of HAZ and base metal under different exciting current intensity.

change with different magnetic field conditions, which are shown in Fig. (**13**). The penetration was 0.87mm when there have no additional longitudinal magnetic field. Under the action of magnetic field as exciting current intensity increased, penetration of bead reduced. While the exciting current intensity is 25A, penetration reduced to 0.41mm. As the exciting current intensity changed from 0 to 25A, the width of HAZ changed little and average width was 0.6mm. The overall impact of heat input on the base metal should be the total of penetration and width of HAZ, so the depth of influence on the base metal reduced with the exciting current intensity increasing.

4. CONCLUSIONS

During the welding process with additional longitudinal magnetic field, welding current and total heat input decreased as the exciting current increased, meanwhile arc

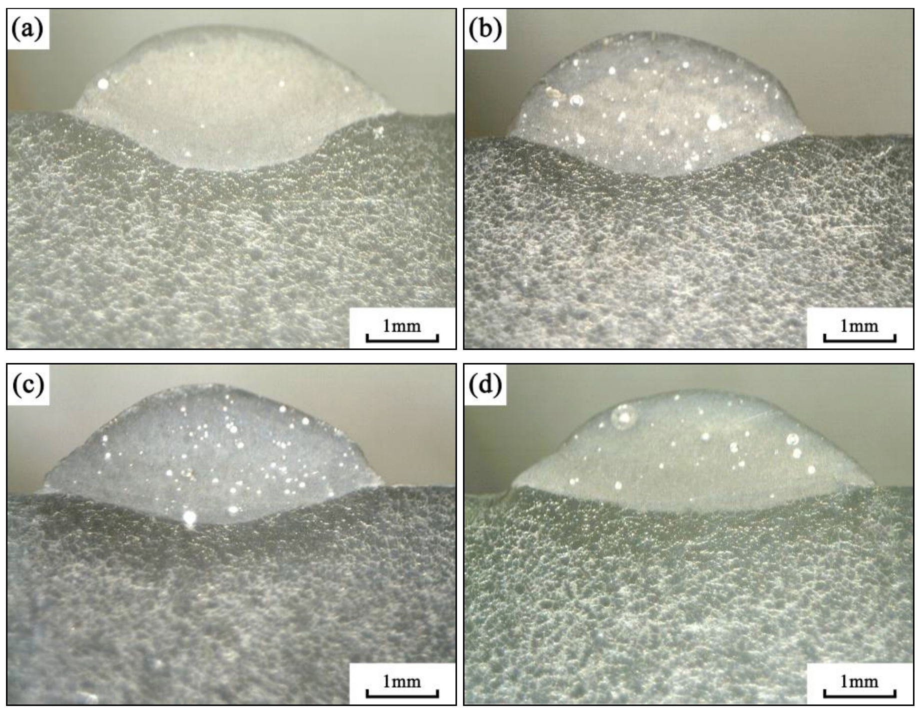

Fig. (12). Cross section and HAZ under different exciting current intensity. (**a**) *I*=0A; (**b**) *I*=10A; (**c**) *I*=20A; (**d**) *I*=25A.

of cross section changed under the action of longitudinal magnetic field. Penetration of bead and width of HAZ had a

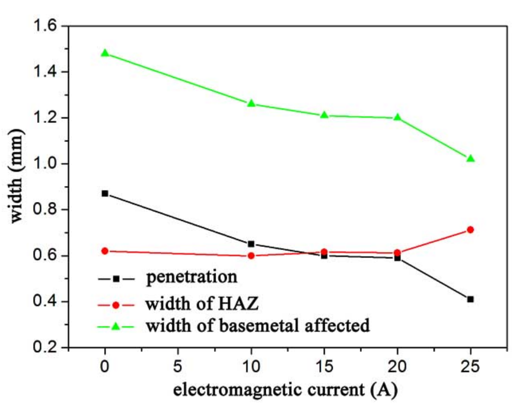

Fig. (13). Effects of magnetic condition on penetration and width of HAZ.

thermal efficiency increased and melting efficiency decreased. Thermal actions of arc weaken in long direction and cover with more area in lateral direction with exciting current intensity increasing, which made bead width increased, penetration and area of fusion zone reduced, as well as influence extent of heat input on base metal decreased. The trend of the grain growth of HAZ slows down and softening behavior lower with exciting current intensity increasing. As the exciting current intensity was 20A, the micro-hardness of HAZ and base metal improves evidently. But when exciting current intensity continued to increase, microstructure and mechanical property of HAZ did not change obviously.

REFERENCES

[1] C. S. Wu, *Numerical Analysis of Welding Thermal Process*. Harbin: Harbin Institute of Technology Press 1990.

[2] X. Q. Yin, J. Luo and H. G. Li, "Optimization of magnetic parameters for grain structure refinement of LD10CS aluminum alloy weldment", *J. Xi'an Jiao Tong University*, Vol. 33, pp. 71-74, July 1999.

[3] H. X. Wang, "Thermal efficiencies of fusion welding processes", *Welding & Joining*, pp. 15-19, October 2007.

[4] Y. L. Chang, L. G. Shao, D. Li and D. Y. Li, "Research on MIG welding arc with additional longitudinal alternating magnetic field", *Welding Technol.*, Vol. 38, pp.14-16, May 2009.

[5] N. S. Tsai and T. W. Eager, "Distribution of the heat and current fluxes in gas tungsten arcs", *Metall. Trans. B*, Vol. 16B, pp. 841-846, April 1985.

[6] M. Arenas, V. L. Acoff and N. El-Kaddah, "Effect of arc length on weld penetration in GTA welding of gamma titanium aluminide", in *Proceedings of the Conference*, 2001, pp. 142-147.

[7] Q. Guan, W. X. Peng, J. D. Liu, Y. C. Shao and W. L. He, "Test method of effective utilization rate of Welding heat source", *Transactions of the China Welding Institution*, Vol. 3, pp. 10-23, March 1982.

[8] J. N. Dupont, and A. R. Marder, "Thermal efficiency of arc welding processes", *Welding Journal*, Vol.74, pp. 406-416, December 1995.

[9] Y. F. Fan, J. H. Liu, X. N. Luo and W. F. Xu, "Study on penetration of low power laser-TIG arc hybrid welded stainless steel", *Aeronautical Manufacturing Technol.*, Vol. 22, pp. 84-87, 2008.

[10] S. Zhu, Q. W. Wang, F. L. Yin, Y. Y. Liang and X. M. Wang, "Numerical simulation of MIG welding arc with longitudinal magnetic field", in *Sixth International Conference on Physical and Numerical Simulation of Materials Processing*, 2010.

Thermal Performance of Copper Mould in Slab Continuous Casting

Jitendra Narayan Biswal, *Department of Mechanical Engineering, Aryan Institute of Engineering & Technology, Bhubaneswar, jnarayan679@gmail.com*

Kalpana Mallick, *Department of Mechanical Engineering, Raajdhani Engineering College, Bhubaneswar, kalpanam11@outlook.com*

Priyabrata Jena, *Department of Mechanical Engineering, Capital Engineering College, Bhubaneswar, priyabratajena456@yahoo.co.in*

Sikendar Sharma, *Department of Civil Engineering, Raajdhani Engineering College, Bhubaneswar, sikendarsharma92@gmail.com*

Biswa Ranjan Pradhan, *Department of Civil Engineering, Capital Engineering College, Bhubaneswar, biswaranjanpradhan78@gmail.com*

Abstract: Based on the cooling parameters of the mold copper plate for slab continuous casting in a steelmaking plant, the three-dimensional calculating model of the copper plate was established, and three-dimensional distributions of temperature, thermal stress and strain were simulated numerically by using finite element method (FEM). The maximum deformation of the mold copper plate, the highest temperature and thermal stress were obtained. This research is useful for the structure design of the mold.

Keywords: Slab continuous casting, mold copper plate, temperature, thermal stress, thermal deformation.

1. INTRODUCTION

Mold is the core part of continuous caster. Heat transfer effect of mold has a direct impact on continuous casting production process and internal quality of slab. In the cooling process, the mold not only carried out the heat transferred from liquid steel, but also supports static pressure from molten steel, and friction, etc. The mold copper plate (or called mold copper) works under an extremely poor condition which includes high temperature, friction between the slab and the mold, the mechanical and thermal stresses and the pressure of the cooling water. In order to make the mold work properly, the mold structure and the materials of the mold copper must be suitable. For example, to make the molten steel cooled efficiently, the mold copper should contact perfectly with the slab surface, and there should be no gap between them. This demands the mold should be tapered, and the taper design should take the deformation of the mold copper into account. The cooling water pressure is very high, so the thermal deformation of the mold copper should not be big enough to make the cooling water leak. The mold copper should have a better resistance to abrasion. The inner surface of the mold copper is heated by the slab, and the outside surface is cooled by the cooling water, so the temperature difference would cause the thermal stress and deformation. The deformation and thermal stress should be taken into account when the mold structure, such as the taper, seam size and the strength are designed.

Yang *et al.* had done some research works about three-dimensional heat transfer analysis on thin slab continuous casting mold copper [1]. Feng *et al.* had simulated the temperature field on the slab continuous casting mold copper with finite element method (FEM) [2]. In accordance with the result, they re-allocated the water seam. Liu and Zhu conducted the research on analysis of thermal elastoplastic behavior of continuous casting slab mold [3]. Wang *et al.* optimized the mold taper in high speed casting of steel billets [4]. Long and Peng analyzed the thermal deformation of mold copper by using FEM [5].

In this paper, based on the method of coupling the mold copper heat transfer with the stress/strain and deformation, the temperature field, stress/strain and thermal deformation of the mold copper during slab continuous casting process were successfully analyzed by using FEM.

2. CALCULATING MODEL AND PARAMETERS

2.1. Finite Element Model

Before modeling, some assumptions are made as following without causing large calculation error.

1. Ignore the impact of molten steel fluctuation on the mold copper near the meniscus.
2. Ignore the impact of mold oscillation on the mold copper.
3. Consider that the contact between the mold copper and the backplane is closely. Ignore the impact of bolts on the mold copper.
4. Consider that the mold copper is isotropic.

Because the distribution of water seam is symmetric, half of the cross-sectional area between two bolts is taken as the computational domain. The mesh used in FE simulation is shown in Fig. (**1**).

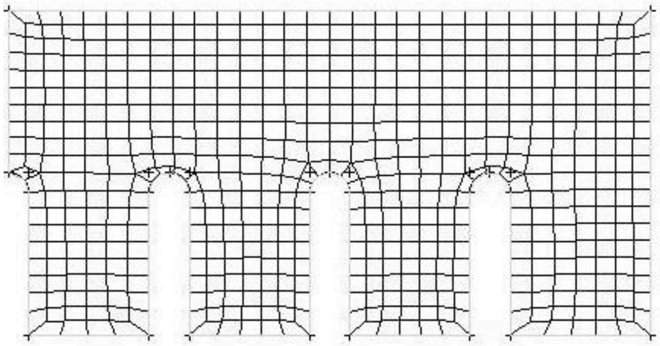

Fig. (1). Mesh of mold copper.

2.2. Parameters of the Mold Copper

The structural parameters of the mold copper are shown in Table **1**. The material of the mold copper is chromium - zirconium - copper alloy, which the mass fraction of three elements is:

Cr: 0.5-1.5%; Zr: 0.05-0.3%; Cu: 98%

Table 1. Structural Parameters of the Mold Copper

Items	Units	Values
Mold copper thickness	mm	40
Bolts spacing	mm	160
Bolt type		M30
Water seam spacing	mm	20
Width of water seam	mm	5
Depth of water seam	mm	20

The alloy not only has high hardness and strength, but also good thermal conductivity, wear and corrosion resistance. Its softening temperature is 500 degree, and the linear expansion coefficient is 1.7×10^{-5}/degree. The thermal conductivity coefficient is a function of temperature which can be described as (1).

$$k = 317.75 + 0.1224\times T - 0.0001\times T^2 \quad (1)$$

where the unit of temperature T is degree. k is the thermal conductivity coefficient, the unit is W/(m·degree). The specific heat is 384 J/(kg·degree). Young's modulus E is 115 GPa. Poisson ratio is 0.34.

3. HEAT TRANSFER AND MECHANICAL BOUNDARY CONDITIONS

To analyze the temperature, stress and deformation of the mold copper, the corresponding boundary conditions must be determined firstly.

3.1. Inner Surface of the Mold Copper

On the inner surface of the mold copper which contacts with the slab, the heat flux can be calculated using Eq. (2) [6],

$$q = 2680 - 335\sqrt{t} \quad (2)$$

where q is the heat flux, KW/m^2. t is the time that the slab stays in the mold, and its unit is second, and $t=L/v$ (where L is the distance from the calculating position to the meniscus, the unit is m. v is the casting speed, in this study, v is 0.9 m/minute).

3.2. Surface of Water Seam

On the surfaces of water seams which contact with the cooling water, the heat flux can be calculated using Eq. (3),

$$q = h(T_{copper} - T_{water}) \quad (3)$$

where q is the heat flux, W/m^2. T_{copper} is the temperature of the water seam surface which contacts with the cooling water, degree. T_{water} is the temperature of the cooling water, degree. h is the heat transfer coefficient between the mold copper and cooling water, W/(m^2·degree), and it can be calculated using Eq. (4) [7].

$$h = 0.023\cdot\left(\frac{D\cdot v\cdot\rho}{\mu}\right)^{0.8}\cdot\left(\frac{C\cdot\mu}{\lambda}\right)^{0.4}\cdot\frac{\lambda}{D} \quad (4)$$

where D is the equivalent diameter of water seam, its unit is m. v is the flow speed of cooling water, which equals 10.5 m/s. ρ is the density of cooling water, kg/m^3. μ is the viscosity of cooling water, kg/(m·s). λ is the thermal conductivity coefficient of cooling water, W/(m·degree). C is the specific heat of cooling water, J/(kg·degree).

3.3. Surface of the Mold Copper Contacting with the Backplane

On the surface of the mold copper contacting with the backplane, the heat flux can be calculated using Eq. (5).

$$q = h_a(T_{back} - T_0) \quad (5)$$

where T_{back} is the temperature of the mold copper surface which contacts with the backplane, degree. T_0 is the temperature of the backplane, degree. h_a is the heat transfer coefficient between the mold copper and the backplane, which equals 10000 W/(m^2·degree), and the initial temperature of backplane is T_0=20 degree.

3.4. Mechanical Boundary Conditions

The backplane of the mold is considered as a rigid body, and its displacements at any direction equal zero. The mold copper is considered as elastomer, and at any bolt position the displacement of the mold copper is zero.

4. ANALYSIS OF SIMULATION RESULTS

4.1. Temperature, Stress and Deformation Analysis of the Mold Copper at Meniscus

The distributions of the temperature, thermal stress and deformation of the mold copper at meniscus are shown in Figs. (**2-4**). And at the middle of mold copper, along the thickness direction the distributions of the temperature, thermal stress and deformation are shown in Fig. (**5-7**). From these figures it can be seen that:

1. The highest temperature at the inner surface of the mold copper is 218.8 degree. It is far away from the molten temperature. However, the high temperature will lower the hardness of the mold copper. So the mold copper here is easy worn down.
2. The temperature gradient near the inner surface is relatively large. Therefore, the thermal stress near the inner surface is greater than that of other parts.
3. Due to the strong cooling effect of cooling water, the rapid temperature change results in the stress concentration near the bottom of the water seam.

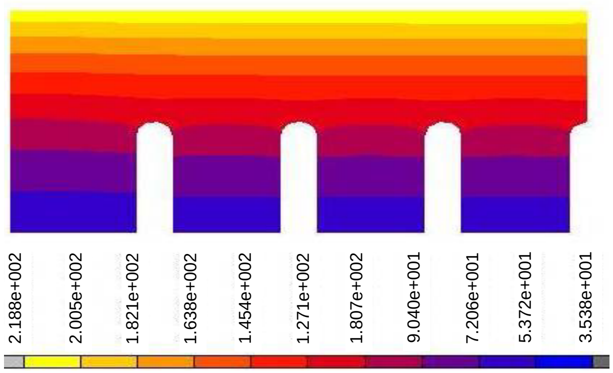

Fig. (2). Temperature distribution of the mold copper.

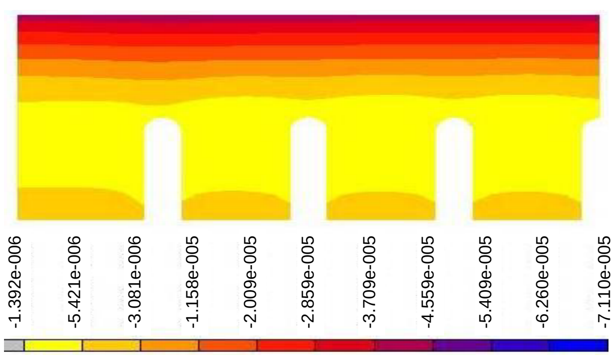

Fig. (3). Deformation distribution of the mold copper.

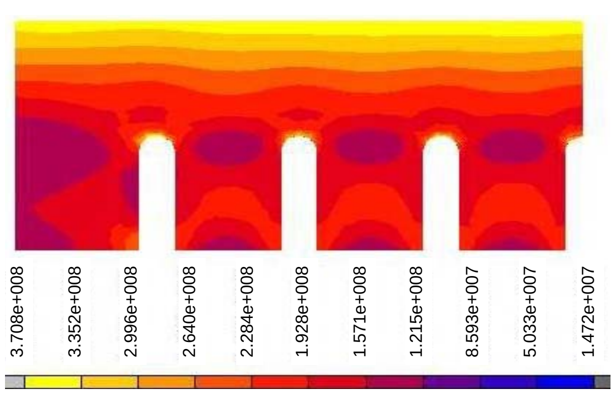

Fig. (4). Thermal stress distribution of the mold copper.

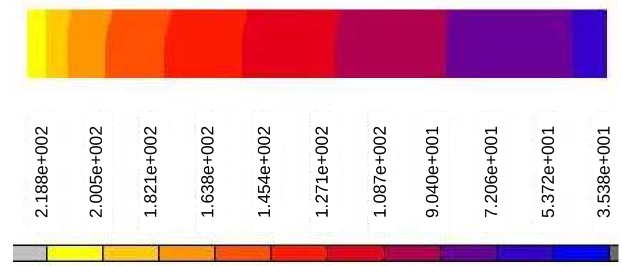

Fig. (5). Temperature distribution at the middle of mold copper.

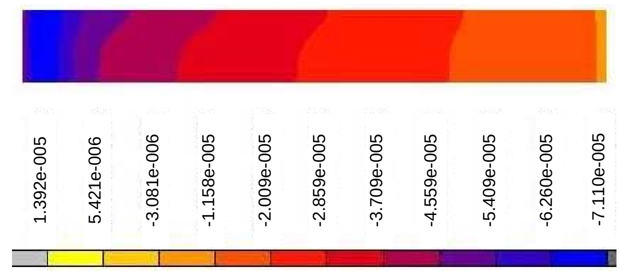

Fig. (6). Deformation distribution at the middle of mold copper.

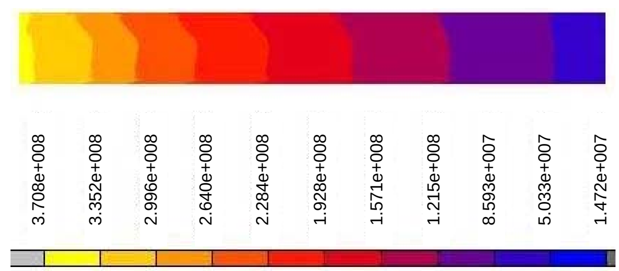

Fig. (7). Thermal stress distribution at the middle of mold copper.

4.2. Curves of Temperature, Stress and Deformation

Along the casting direction, the temperature, the thermal deformation and the thermal stress distributions at the middle position of the inner surface of the mold are shown in Fig. (**8**) to Fig. (**10**).

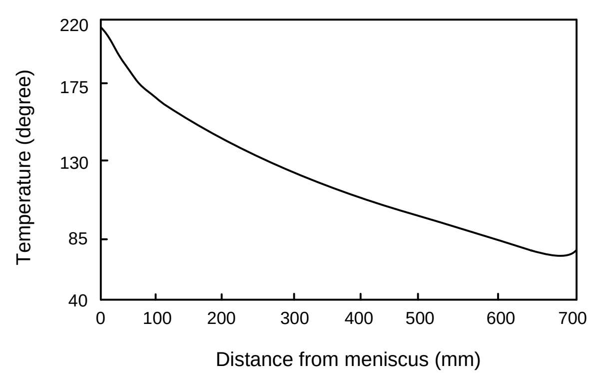

Fig. (8). The inner surface temperature distribution.

It can be seen form Fig. (**8**) that the temperature of the mold copper changes in accordance with the heat flux, which was expressed in Eq. (2). The highest temperature is at the meniscus, and along the casting direction, the inner surface temperature falls sharply. But at the position of 40 mm from mould outlet, it begins to return a little. This is due to there are no water seams near the bottom of the mold copper. The poor heat transfer results in the temperature increase.

It can be seen from Fig. (**9**) that the largest deformation is about 0.07 mm, which appears in the vicinity of meniscus. The deformation decreases rapidly with the decrease of the inner surface temperature of the mold copper.

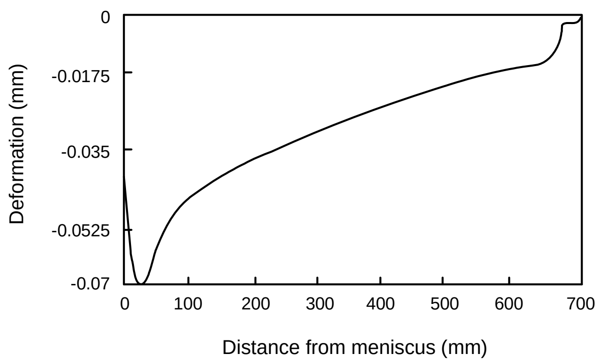

Fig. (9). The deformation distribution.

It can be seen from Fig. (**10**) that the thermal stress decreases rapidly along the casting direction. The biggest thermal stress appears at the meniscus, and its value is about 360 MPa, and at the outlet of the mold, the thermal stress is lower. Because the high temperature of the mold copper lowers its hardness near the meniscus, the bigger thermal stress, the oscillation of mold, the fluctuation of the molten steel surface together with the erosion effect of the powder would make the mold copper surface near the meniscus more erosive and abrasive.

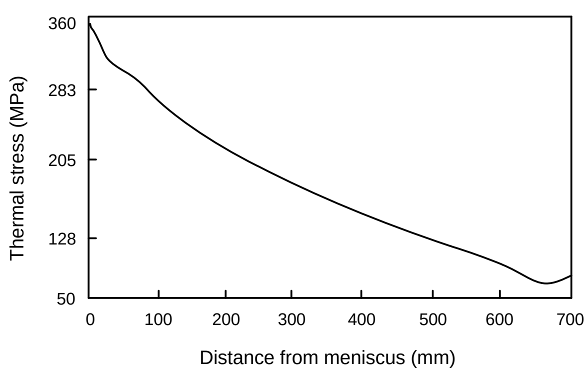

Fig. (10). The thermal stress distribution.

5. CONCLUSION

The highest temperature of the mold copper appears on the inner surface at the meniscus position. The inner surface temperature of the mold copper declines rapidly along the casting direction, and it increases a little near the outlet of the mold. The surface temperature of water seam changes little along the casting direction, and the biggest temperature difference from the top to the bottom is not bigger than 10 degree.

The maximum thermal deformation of the mold copper appears at position 30 mm downwards from the meniscus. The deformation is not big enough to cause the leaking problem of the cooling water.

The thermal stress on the inner surface of the mold copper is bigger than that of the water seam surface. There is a little stress concentration at the bottom of the water seam, but it is not severe enough to result in cracks.

REFERENCES

[1] G. Yang, B. K. Li, and Y. Yu, “There dimensional heat transfer of cooling copper plate of thin slab continuous casting mold”, *Acta Metal. Sin.*, vol. 43, pp. 332-336, March 2007.

[2] K. Feng, Z. W. Han, and J. H. Mao, “Finite element simulation of temperature field of mold copper plate for continuous casting”, *Foundry Technol.,* vol. 28, pp. 135-138, January 2007.

[3] X. D. Liu, and M. Y. Zhu, “An analysis of thermal elastoplastio behavior of continuous casting slab mold”, *Acta Metal. Sin.*, vol. 42, pp. 1137-1142, November 2006.

[4] J. G. Wang, B. F. Wang, and F. Dong, “Optimization of the mold taper in high speed casting of steel billets”, *Continuous Casting*, pp. 10-14, April 2009.

[5] X. S. Long, and X. H. Peng, “FEM analysis of thermal and deformation of mold copper”, *Iron Steel*, vol. 41, pp. 35-38, October 2006.

[6] M. Y. Liu, P. Li, and X. J. Luan, *Slab Continuous Caster*, Beijing: Mechanical Industry Press, 1990.

[7] J. Q. Sun, and Q. G. Liu, *Heat Transfer*, Harbin: Northeat Forestry Univeristy Press, 1997.

Algorithms of Graphic Element Recognition for Precise Vectorization

Tapan Kumar Mohanty, *Department of Mechanical Engineering, Aryan Institute of Engineering & Technology, Bhubaneswar, tapankmohanty789@yahoo.co.in*

Hemant Ku Nayak, *Department of Mechanical Engineering, NM Institute of Engineering & Technology, Bhubaneswar, hemantnayak236@gmail.com*

Saleema Panda, *Department of Civil Engineering, NM Institute of Engineering & Technology, Bhubaneswar, saleemapanda25@gmail.com*

Barsa Priyadarshini Sahoo, *Department of Civil Engineering, Raajdhani Engineering College, Bhubaneswar, barsap_sahoo@gmail.com*

Abstract: Circle, line and circular arc are the common basic graphic elements in industrial computed tomography (ICT) image. The algorithm of recognizing such elements is the key to industrial CT image precise vectorization. An industrial CT image vectorization system has been studied, including different recognition methods for these elements. Firstly, based on facet model, the sub-pixel edge of an industrial CT image is extracted. Then, the circles are recognized by an improved algorithm based on probability of existence map, while the lines are recognized with the set intersection algorithm of fitting a straight line, and the circular arcs are recognized by the combination of the perpendicular bisector tracing algorithm and least squares function. Finally, the graphic element parameters are measured according to recognition results, and the drawing exchange file (DXF) is produced and transmitted into the computer aided design (CAD) system to be edited and consummated. The experimental results show that these methods are capable of recognizing graphic elements in industrial CT image with an excellent accuracy, besides, the absolute errors of circles are less than 0.1 mm, and the relative errors are less than 0.5%. It can satisfy the industrial CT vectorization requirements of higher precision, rapid speed and non-contact.

Keywords: Computed tomography, facet model, edge detection, vectorization.

1. INTRODUCTION

There has been remarkable research achievement in developing and applying computerized tomography (CT) technology for medical and industrial applications, particularly in the industrial area, such as aerospace, aviation, military, machinery and automobile. Industrial CT is not only effective to detect the inner construction and flaws of an object, but also necessary to nondestructively measure the size of workpiece [1, 2]. However, the two dimensional slice images acquired by the 3rd generation ICT device can't be edited in the existing computer aided design (CAD) system. And most industrial CT images are the workpieces' dislocation images, which have many geometrical elements, such as lines, circular arcs and circles. Several conventional vectorizaion methods, applied in engineering drawings and maps, come with disadvantages, including noise sensitivity, computational complexity and low accuracy. These shortcomings make it difficult to accurately measure the size of workpieces' inner construction. In order to overcome these problems, in this paper we investigate methods of industrial CT images precise vectorization.

Since the research of image vectorization started in the early 1970s, numerous approaches have been developed [3, 4]. Broadly, these algorithms can be divided into several groups: thinning algorithm, contour tracking, Hough Transform (HT), dynamic window method and global recognition algorithm. The main advantage of thinning algorithm is that it holds a better reservation of image topology information, and its processing data points are decreased. Nevertheless, it is sensitive to noise. As a solution of this problem, the contour tracking method is provided. Its processing rate is high, and the impact of the air bubble and burr defects on the vectorization effect is reduced. However, the recognition accuracy is low since the vector image is discontinuous. In terms of accuracy and robustness, the HT and its variants have been successfully used in image vectorization. These methods are robust against outlier and occlusion, but computationally expensive. Dynamic window vectorization algorithm was proposed as a relatively novel method. A major advantage of this method presents at its high recognition accuracy to crossing point. Unfortunately, the window is changing continually, so the robustness is not enough. With the vectorization technology improving, some researchers have presented global recognition method. In process of vectorization, the line width can be obtained. Meanwhile, the corresponding tracking mode is adopted for reducing the impact of line fracture and missing data. But the accuracy of crossing point should be further improved.

In view of the disadvantages of the current image vectorization methods, the key contribution of this paper is to investigate a vectorization system for industrial CT image. In this system, the sub-pixel edge of an industrial CT image is extracted based on facet model. Its execution time is reduced significantly by removing invalid data points. Then, the circles, lines and circular arcs are recognized respectively with the corresponding recognition algorithms. These algorithms improve recognition accuracy. Also, in the process of recognition, the obtained elements parameters are dynamically saved in the corresponding linked lists. Hence, the required computation storage space is much cheaper than the previous methods.

2. SYSTEM OVERVIEW

In the process of industrial CT image vectorization, it is critical to detect edges in the image which is an important stage as the quantity and quality of edge data will affect greatly the vectorization performance of the system. The sub-pixel edge contour is extracted by the edge detection algorithm based on facet model, after the pre-processing as Gaussian filter, binarization. For this contour, the recognition algorithms of graphic elements are implemented. Firstly, determine whether the contour is a circle by calculating the center's probability. If it is a circle, the improved fast algorithm of circle detection based on probability of existence map is utilized to recognize it. The obtained circle parameters by the least squares function (LSF) are saved in the circle chained list. Reversely, if it is not a circle, the contour curve is fitted into many short line segments by adopting the improved set intersection algorithm of fitting a straight line. Then, merge the short line segments into the long line segments. Finally, the perpendicular bisector tracing algorithm is adopted to find the long line segments which can be fitted into circular arcs. And the merged circular arcs' parameters are derived from the least squares function. These parameters are saved in the circular arc linked list. Another long line segments' parameters are saved in the line linked list. After recognizing these elements, their parameters are outputted for vector graph. The system architecture is summarized in Fig. (**1**).

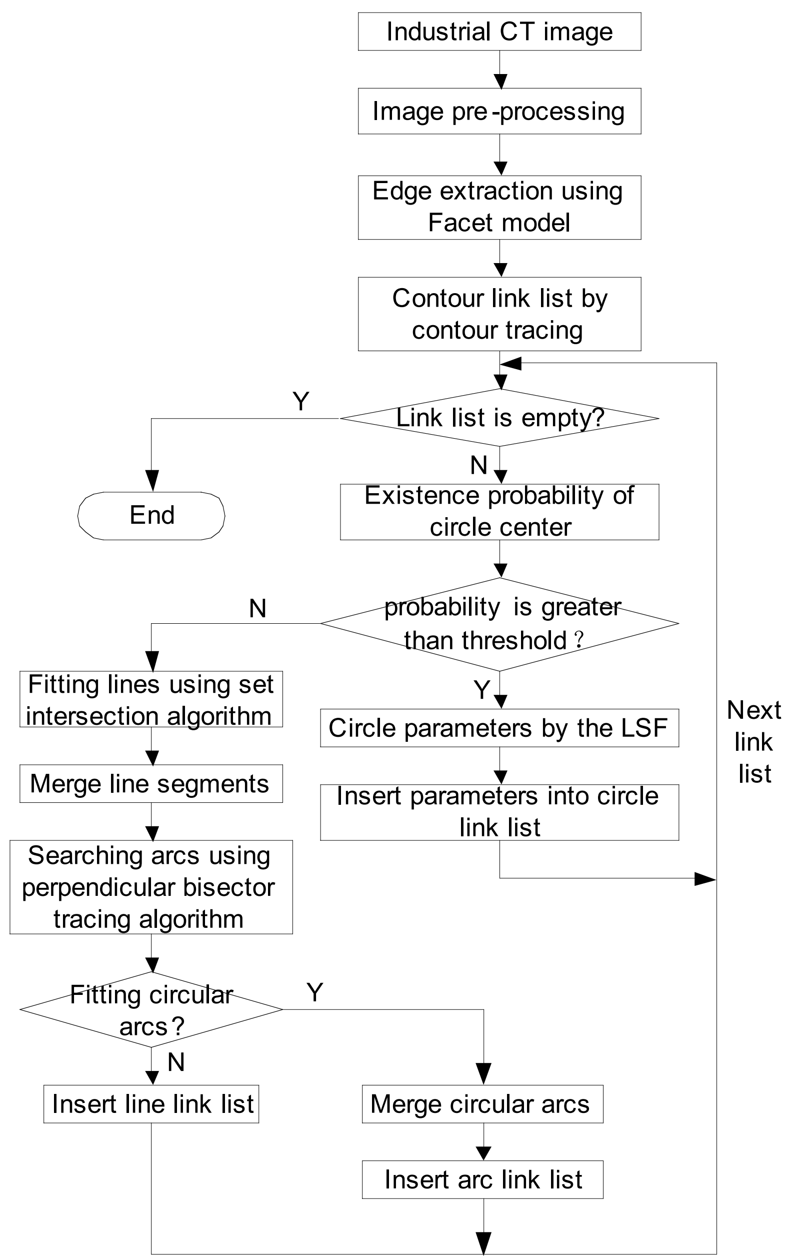

Fig. (1). Architecture of system.

3. EDGE DETECTING ALGORITHM BASED ON FACET MODEL

The exact location of edge is obtained by using the edge detection algorithm based on facet model. Through calculating the second-ordered directional derivative, edge point is defined as the zero-crossing point of facet model along the gray gradient direction [5]. Third-ordered facet model of the pixel (x, y) in 5×5 regions can be expressed as follows:

$$f(r,c) = k_1 + k_2 r + k_3 c + k_4 r^2 + k_5 rc + k_6 c^2 + k_7 r^3 + k_8 r^2 c + k_9 rc^2 + k_{10} c^3 \tag{1}$$

$$r, c \in [-2, -1, 0, 1, 2].$$

Where (r, c) is the coordinate of any point in this pixel's neighborhood; $k_1 \sim k_{10}$ are the coefficients which are obtained by the least square method [6]. So

$$\sin\alpha = k_2 \Big/ \sqrt{k_2^2 + k_3^2}, \cos\alpha = k_3 \Big/ \sqrt{k_2^2 + k_3^2} \tag{2}$$

Define $r = \rho\sin\alpha$, $c = \rho\cos\alpha$ (ρ is the distance between edge point and the center of pixel), the first-ordered, second-ordered and third-ordered partial derivatives of the model can be expressed as follows:

$$\begin{cases} f'(\rho) = m_1 + 2m_2\rho + 3m_3\rho^2 \\ f''(\rho) = 2m_2 + 6m_3\rho \\ f'''(\rho) = 6m_3 \end{cases} \tag{3}$$

The edge point is the location of local extremum of the first-ordered derivative in local fitting surface; meanwhile it is the zero-crossing point of the second-ordered derivative as well. (r, c) is the edge point, if we can obtain ρ_0 (ρ_0 is within the 5×5 sub-region whose center is (r, c)) which satisfies (4), and the third-ordered partial derivative negative, as in (5).

$$f''(\rho) = 2m_2 + 6m_3\rho = 0 \Rightarrow |m_2/3m_3| = \rho_0 \tag{4}$$

$$f'''(\rho) < 0 \Rightarrow m_3 < 0 \tag{5}$$

Adopting this algorithm, the subtle image detail is located. The edge detection accuracy is high enough, and the image noise is restrained to some extent.

4. RECOGNITIION OF GRAPHIC ELEMENTS

4.1. Recognition of Circle

4.1.1. Existence Probability of Circle

Circles in the X-Y plane can be completely represented by the following quadratic equation with three parameters (u, v, r) as other 2nd order curves can be.

$$(x-u)^2 + (y-v)^2 = r^2 \tag{6}$$

In order to obtain the size and position of circles in industrial CT image, the method based on probability of existence map is applied [7]. P_e is the existence probability of the circle whose center is (u, v) and radius is r. It is given by:

$$P_e = A(r)/2\pi r \tag{7}$$

Where $A(r)$ is the amount of edge points, whose distance from the center equals r; $2\pi r$ is the amount of discrete pixels of the circle with radius r.

Every pixel (x, y) in the image is regarded as the center, the existence probability P_e is calculated and saved in the two dimensional array $\{P(x, y)\}$. The probability of existence map is produced, and the radius r is saved in the two dimensional array $\{R(x, y)\}$. Each peak in probability of existence map represents that a circle may exist in this image, taking the peak coordinates as the center and r as the radius. P_e is the probability of such existence. Fig. (**2**) is an industrial CT image with a circle. The existence probability of the center point is calculated, and the probability map is shown in Fig. (**3**). The following information can be obtained: Center point (139, 139), r =42.4946, P_e =0.8996.

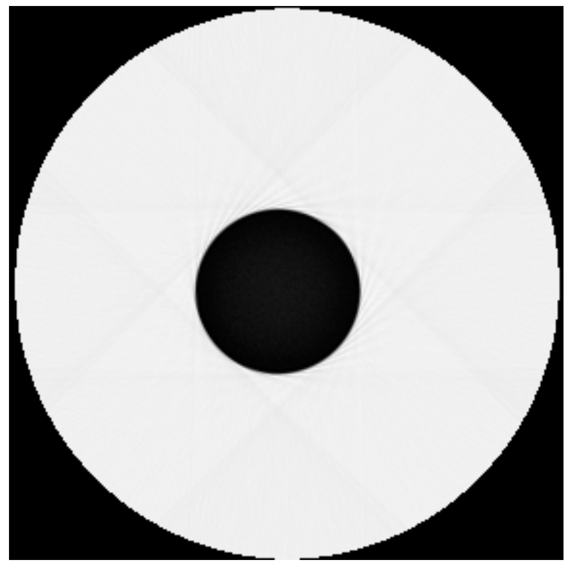

Fig. (2). Industrial CT image.

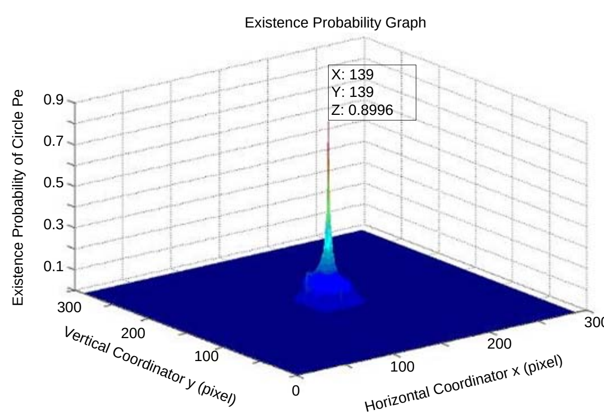

Fig. (3). Probability map of circle.

4.1.2. Improved Algorithm of Existence Probability

The above algorithm regards each pixel in the image as the center of a circle, but most pixels in the image are not the center of the circle actually. As a result, the computation is complicated and the required computational storage is expensive. The center of the circle should lie in a mini-realm in the target region, thus, we improve the above algorithm by decreasing the select range of circle center to the square *C* [8]. If a closed curve has been recognized as a circle, the maximum distance of two points on the circle is defined as diameter, and the middle point of the diameter is the circle center. As illustrated in Fig. (**4**), for every closed contour, we first have to find the nethermost point *A*, then, calculate all distances from *A* to the other points. The point *B* that has the maximum distance *D* is the endpoint of the diameter. The midpoint *O* of the diameter is approximately regarded as the centroid of the closed contour. Therefore, a square *C* is obtained, whose center and sides are the centroid *O* and $D \times w$ ($D = 100$, $w = 0.1$), respectively. The square *C* is the area within which the potential circle center will be sought. In this way, the improved method constrains the search for potential circle center only in the specified small range and thereby reduces the computational cost.

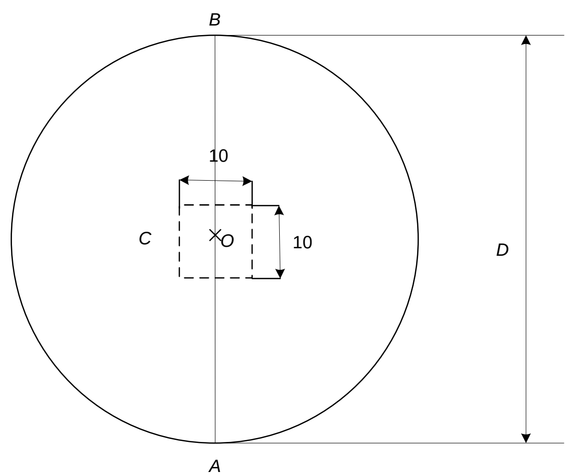

Fig. (4). Select range of circle center.

Besides, we improved the storage mode for saving memory space as well. Circle parameters, such as the coordinates of the circle center, radius and existence probability, are stored by a series of two dimensional arrays in the previous algorithm, which has to allocate memory beforehand. Thus, different types of images require different memory size. If the allocated memory is oversize, the memory space will be wasted; on the contrary, if undersized, memory space will cause data overflow. In this paper, we store the above parameters using the chained-list, referred to as the mode of allocating memory is dynamic, not beforehand. There is no need for this rule to redefine the memory size, even though the image size is different. As described in the following, the constructed list structure is effective in that it influences not only memory allocation, but also the recognition efficiency of a circle.

```
typedef struct
    {int x; // x-coordinate of circle center
    int y; // y-coordinate of circle center} Point;
struct NODE
    {Point point; // coordinates of circle center
    float r; // radius of circle
    int k; // number of edge points
    float p; // existence probability of circle
    NODE *next; // the pointer of next node};
```

4.2. Recognition of Line

After recognizing the circles in industrial CT image, the remaining contours are fitted into short line segments by an improved method of fitting a straight line. Based on the set intersection algorithm of fitting a straight line [9], the method makes use of least square technique [10] to get line segment parameters. Generally, the procedure of the method is as follows:

As shown in Fig. (**5a**). For a contour, the starting point is P_0, the current point is P_c. At the beginning of fitting, P_c=P_0. First, determine whether the next field of P_c is empty. If the next field is empty, end tracking the current line, get the line segment P_0P_c. If the next field isn't empty, judge whether the following point P_n belongs to the current line. If P_n is in the current line, then $P_n \rightarrow P_c$, and continue determining the following one. Or else, terminate tracking the current line, and get the line segment P_0P_c. Next, let P_n be the new starting point, and continue recognizing other line segments of the contour. After finishing a contour recognition, the above process is repeated for another contour of industrial CT image.

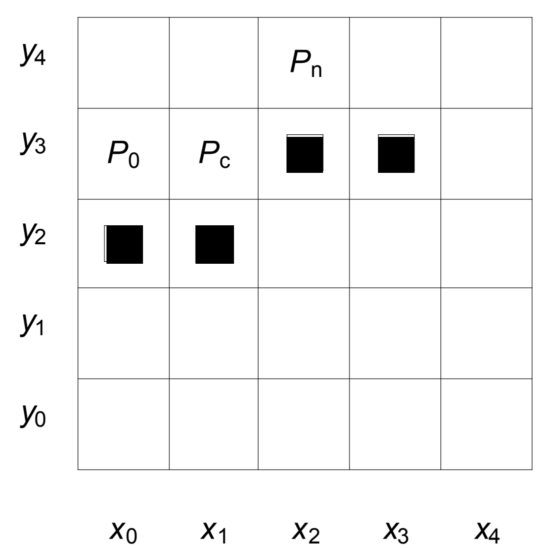

Fig. (5) (a). Sketch map of straight line fitting.

Due to low image quality and improper image preprocessing, the straight line may be mistaken as a series of short line segments, which we should merge into the long segments. The merging condition of two adjacent short line segments: the difference of slopes between two line segments must fall within the prescribed limits; and the distance between the endpoint of line segment and the merged long segment should be less than the specified value. As illustrated in Fig. (**5b**), if the angular difference between the adjacent line segments *AB* and *CD* is less than the prescribed value (using the angle value to represent the slope of line segment; here we choose 10°); and the distance from the point *B* to the line segment *AC* is less than the specified value (here 3 is appropriate), we will merge the short line segments *AB* and *BC* into the long segment *AC*. Then, determine whether the distance between the point C and the line segment AD is less than 3, and determine whether the angle difference between the line segment CD and the line segment AC is less than 10°. If the above two conditions are both met, get the long line segment AD. Or else, insert the merged line segment AC into the merged line link list, then, let CD be the new starting line segment, and continue merging the subsequent line segments.

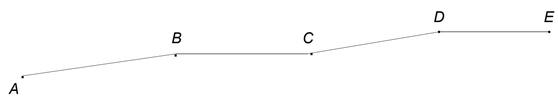

Fig. (5) (b). Sketch map of merging line segment.

4.3. Recognition of Circular Arc

The obtained short line segments by implementing the above strategy are merged into the long line segments. These long line segments are fitted into circular arcs by means of the perpendicular bisector tracing algorithm [11]. The basic idea of the algorithm is that the perpendicular bisector of any chord on a circle passes through the circle center, and every endpoint of the chord is at an equal distance from the circle center.

As illustrated in Fig. (**6a**), any obtained line segment may be an approximation of an arc. We first consider the obtained line segment L_0 as seed arc, its perpendicular bisector P_0 is constructed. For every line segments L_i (i =1, 2…N), we then construct its perpendicular bisector P_i, and calculate the intersection C_i of P_i and P_0. Due to errors, the intersection C_i is not unique. However, all C_i are located along the line P_0. We define the point C_{min} is the nearest point from L_0, and the point C_{max} is the farthest point from L_0. Therefore, a rectangle C is obtained, whose length is the distance between C_{min} and C_{max}, and whose width is equal to the length of L_0 and is bisected by P_0. The rectangle C is the area within which the potential arc center is sought.

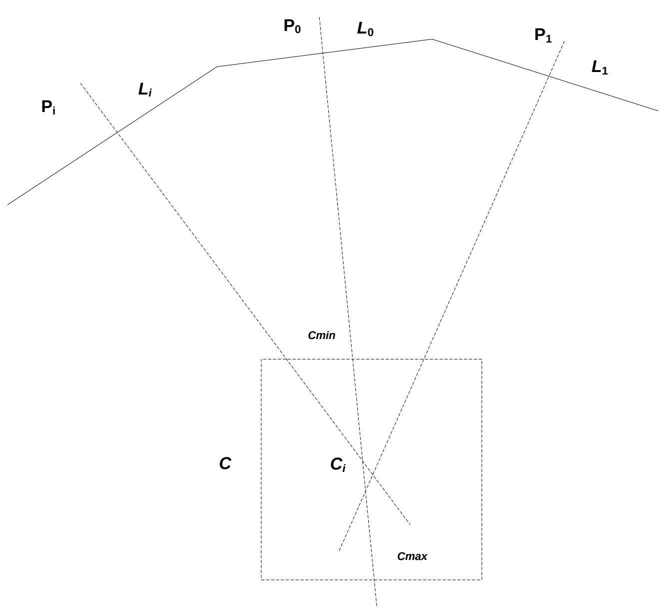

Fig. (6) (a). Sketch map of circular arc fitting.

Having determined the potential center area, we check every pixel within it as a center candidate $c(x, y)$, the distances $R_i(x, y)$ between $c(x, y)$ and endpoints of line segments are gained. Then, we calculate the average radius $R(x, y)$ and the mean square error $ASD(x, y)$, using (8) and (9), respectively.

$$R(x,y) = \frac{1}{N+1}\sum_{i=0}^{N} R_i(x,y) \tag{8}$$

$$ASD(x,y) = \frac{1}{N+1}\sum_{i=0}^{N}(R(x,y) - R_i(x,y))^2 \tag{9}$$

The point whose $ASD(x, y)$ is minimal is taken as the circle center of circular arc, and the corresponding $R(x, y)$ is the radius of circular arc.

The long circular arc may be recognized as some short circular arcs by using the perpendicular bisector tracing algorithm, so we merge these short circular arcs into the long circular arc. As shown in Fig. (**6b**), the merging condition of two adjacent short circular arcs: the coordinate difference between the circle centers O_1 and O_2 must fall within the prescribed limits (5 is fine); the radius difference between the radius R_1 and the radius R_2 should be less than the specified value (also 5 is enough); and the angular difference between the ending angleα_2 of the first circular arc and the starting angle α_3 of the second circular arc should be less than the threshold value (the threshold value is 3°). If there are two circular arcs meeting the above-mentioned three conditions, they can be merged into a new longer circular arc. The new circle center coordinates of this longer arc can be defined by the average value of the circle center coordinates of the two shorter arcs, and the radius of this new longer arc can be replaced by the average value of the radius of the two shorter ones. Also, the starting angle and ending angle of this new arc are substituted with the starting angleα_1 of the first arc and the ending angleα_4 of the second arc, respectively.

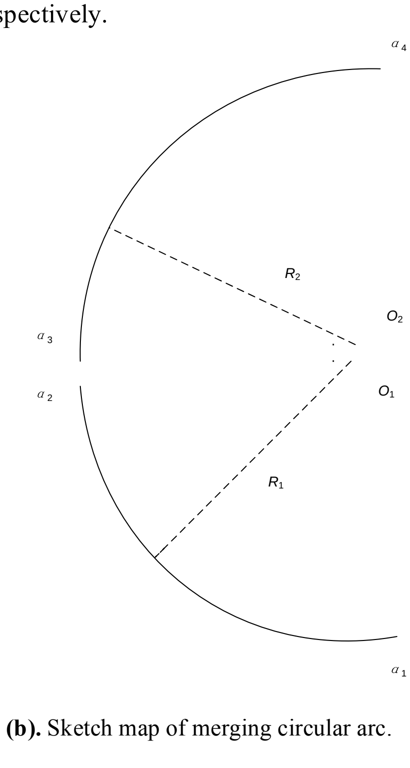

Fig. (6) (b). Sketch map of merging circular arc.

5. EXPERIMENTAL RESULTS AND EVALUATION

5.1. Recognition of Circle

In this section, the performance of the proposed algorithms has been tested with the real industrial CT images. The algorithms are implemented in C++ with MS Visual C++ 6.0 complier on a desktop PC with AMD 64 processor 1.81GHZ and 512MB RAM. The vectorization system for industrial CT image is designed, which provides the platform for our experiments. Fig. (**7a**) is an original industrial CT image of a socket set by the ICT system of CD-650BX in Chongqing University ICT Research Center. The technical indexes of the ICT system are as follows: the ray source is a 6/9MeV electron linear accelerator, the spatial resolution is 2.0lp/mm, the density resolution is better than 0.5%, the diameter of field of view is 398.872mm, the size of image is 800pixel*800pixel. Fig. (**7b**) is the sub-pixel edge image of circles in Fig. (**7a**); Fig. (**7c**) is the probability map of circles in Fig. (**7a**).

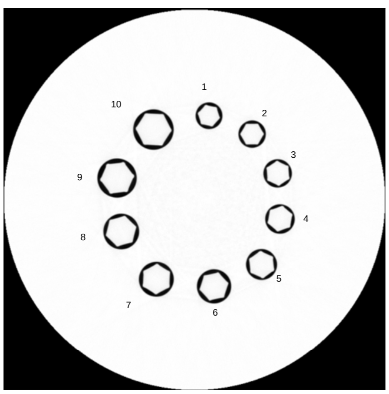

Fig. (7) (a). Industrial CT image of a socket set.

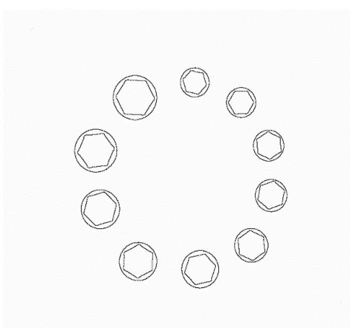

Fig. (7) (b). Sub-pixel edge image.

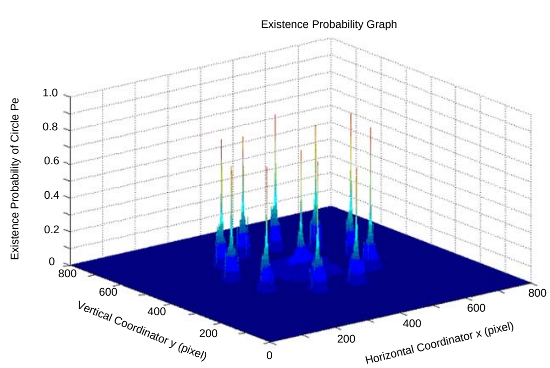

Fig. (7) (c). Probability map of circles.

5.2. Measurement of Circle Parameters

The results of our algorithms on the industrial CT image of the socket set are summarized in Table **1**. While in Table **2**, we list the absolute error *e* between the true and measured values of a parameter, and we evaluate the relative error e_r as well. As can be seen from Table **2**, our algorithms are able to achieve good accuracy. The absolute errors *e* of radius are less than 0.10mm, and the relative errors e_r are less than 0.5%.

Table 1. Measurement Results of Circles

Number	Circle Center (pixel)	Radius (pixel)	Radius (mm)	P_e
1	(430, 576)	27.798	13.860	0.867
2	(520, 538)	28.452	14.186	0.919
3	(573, 455)	29.520	14.718	0.908
4	(578, 360)	30.635	15.274	0.774
5	(540, 264)	32.172	16.040	0.870
6	(440, 219)	35.642	17.770	0.785
7	(320, 233)	36.254	18.076	0.847
8	(246, 333)	37.170	18.533	0.729
9	(237, 445)	40.871	20.378	0.841
10	(314, 547)	42.133	21.007	0.877

Table 2. Measurement Errors of Circles

Number	True Value (mm)	Measured Value (mm)	Error (mm)	Relative Error (%)
1	13.925	13.860	-0.065	0.467
2	14.240	14.186	-0.049	0.379
3	14.780	14.718	-0.062	0.419
4	15.350	15.274	-0.076	0.495
5	16.075	16.040	-0.035	0.218
6	17.810	17.770	-0.040	0.225
7	18.125	18.076	-0.049	0.270
8	18.590	18.533	-0.057	0.307
9	20.420	20.378	-0.042	0.206
10	21.230	21.007	-0.023	0.109

5.3. Vectorization Results of Whole industrial CT image

In addition, we evaluate the vectorization performance on two complicated images shown in Figs. (**8a** and **9a**). Fig. (**8a**) displays an original industrial CT image of a car engine. Based on facet model, its edge image is extracted and shown in Fig. (**8b**). As seen from the edge image, the contour is clear and intact. Also, all small contours are extracted correctly. Fig. (**8c**) is the vector graph of the car engine by our algorithms; it is edited and perfected in AutoCAD2008. In this experiment, a threshold is set for determining whether the closed graphic element is circle. As observed in Fig. (**8c**), setting the threshold is 0.7, our algorithms not only detect these four large circles correctly, but also fit them with good accuracy. The sizes of circles are marked in AutoCAD2008. Nevertheless, the small circles and slight contours can't be detected completely. If we decrease the threshold value appropriately, these small circles and slight contours will be detected. But the vectorization accuracy may be dropped.

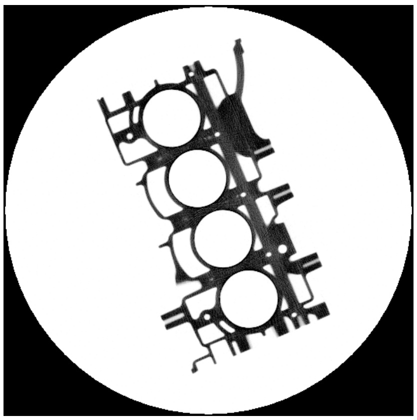

Fig. (8) (a). Industrial CT image of car engine.

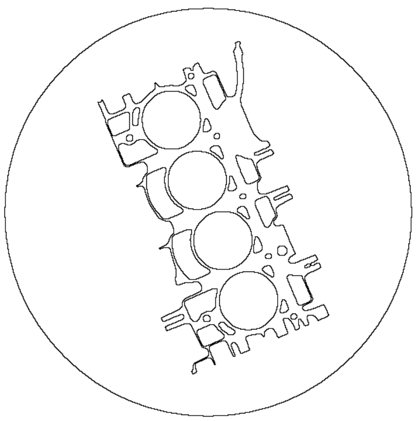

Fig. (8) (b). Sub-pixel edge image of car engine.

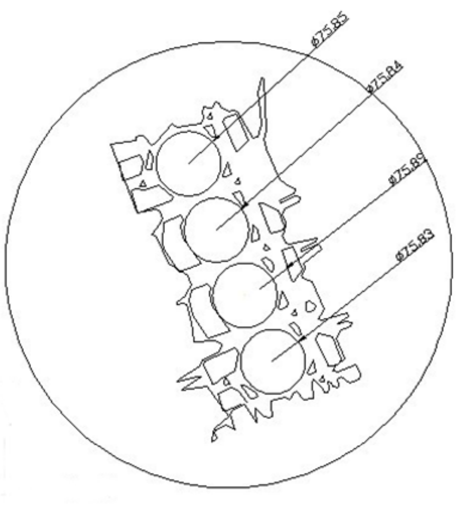

Fig. (8) (c). Vector graph of car engine.

Fig. (**9a**) shows an original industrial CT image of a gearbox cover. Unlike the previous industrial CT image of the car engine, this image has relative complex contours. In the top left corner are several small contours, which are difficult to be detected correctly. Despite this, its edge map is extracted completely and shown in Fig. (**9b**). Of particular interest is the vector graph of the gearbox cover in Fig. (**9c**) which evaluates our algorithms, and it is edited in AutoCAD2008. As shown in this picture, all circles are detected. Furthermore, several small circles are also detected and fitted correctly. Notice that the left isolated circle, which has the inner and outer concentric contours, is detected correctly. Also, the line contour can be fitted with ideal precision. However, Fig. (**9c**) also shows the limitation of our algorithms in the slight and complicated details of image. The circle with diameter of 16.55mm is nonexistent, it should not be found. And some contours are not with respect to the original contours ideally. For instance, the circular arc is represented by the irregular arc segments and curves. The following work will aim to resolve these problems.

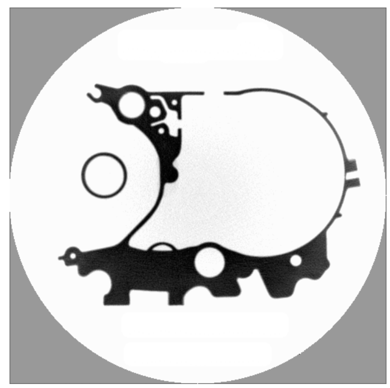

Fig. (9) (a). Industrial CT image of gear box cover.

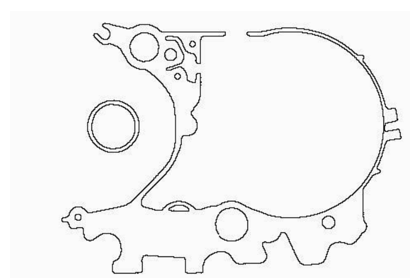

Fig. (9) (b). Industrial CT image of gear box cover.

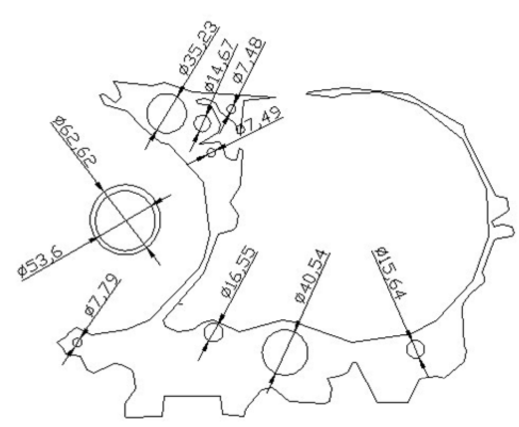

Fig. (9) (c). Industrial CT image of gear box cover.

6. CONCLUSIONS

In this paper, an algorithm for sub-pixel edge detecting based on facet model is adopted for the pre-processed industrial CT image. For the obtained contour, we can calculate the parameters of circle using the improved fast algorithm based on probability of existence map. Then, a set intersection algorithm of fitting a straight line is applied for recognizing the line. Finally, use the perpendicular bisector tracing algorithm and the least squares function to recognize circular arc. Thus, a vectorization system of industrial CT image is designed, which provides the platform for our experiments.

Experimental results show indeed that our algorithms are capable of recognizing the circle, line and circular arc with an excellent accuracy. Furthermore, the vectorization performance for the whole image is preferable. It can satisfy the industrial CT image vectorization requirements of higher precision, rapid speed and non-contact. In the future, we will focus on extending this work by recognizing the relative complex graphic elements as ellipse, regular polygon.

REFERENCES

[1] F. L. Liu, G. F. Qiao and B. Zou, "Precise measurement of circles in industrial computed tomographic images", *Optics Precision Eng.*, vol. 17, no. 11, pp. 2842-2848, 2009.

[2] N. Y. Lee, S. H. Jung and J. B. Kim, "Evaluation of the measurement geometries and data processing algorithms", *Appl. Radiat. Isot.*, vol. 67, pp. 1441-1444, 2009.

[3] B. Cheng, S. S. Zhang and Y. F. Shi, "Research on Vectorization and Recognition for Engineering Drawings: a Survey", *J. Eng. Graph.*, vol. 29, no. 6, pp. 7-12, 2008.

[4] V. Nagasamy and N. A. Langrana, "Engineering drawing Processing and vectorization system", *Comput. Vis. Graph. Image Proc.*, vol. 49, no. 3, pp. 379-397, 1990.

[5] J. W. Tian, Y. Shu, D. P. Tian and Y. X. Huang, "Image sub-pixel feature location algorithm on vision measurement system", *Chin. J. Mech. Eng.*, vol. 42, no. 11, pp. 75-80, 2006.

[6] S. Zheng, J. W. Tian and J. Liu, "Efficient facet-based edge detection approach", *Opt. Eng.*, vol. 44, no. 4, pp. 1-10, 1990.

[7] Y. C. Zhang, H. M. Wang, Z. Z. Liang, M. Tan, W. B. Ye and B. Lian, "Existence Probability Map Based Circle Detection Method", *Comput. Eng. Appl.*, no. 29, pp. 49-51, 2006.

[8] F. L. Liu and G. F. Qiao, "A Fast Algorithm of Circle Detection for Industrial CT Images Based on Probability of Existence", *China Mech. Eng.*, vol. 19, no. 19, pp. 2335-2339, 2008.

[9] Q. H. Li, D. Q. Wang and Z. Y. Chen, "Research on Image Vectorization Methods and Algorithms", *Appl. Res. Comput.*, no. 6, pp. 9-12, 1995.

[10] H. Y. Guan, J. Q. Zhang, Q. Hu and L. Zhong, "Line Extraction of industrial parts based on least square template matching," *Proc. - Int. Congr. Image and Signal Processing (CISP 08)*, IEEE Press, July 2008, pp. 696-700.

[11] D. Dori and W. Y. Liu, "Stepwise Recovery of Arc Segmentation in Complex Line Environment", *Int. J. Doc. Anal. Recog.*, vol. 1, no. 1, pp. 62-71, 1998.

Meshing of Spiral Bevel Gears Manufactured by Generating Line Method

Pili Kumari Sahoo, *Department of Mechanical Engineering, Aryan Institute of Engineering & Technology, Bhubaneswar, p.kumari4gmail.com*

Niranjan Behera, *Department of Mechanical Engineering, Raajdhani Engineering College, Bhubaneswar, niranjanbehera2514@gmail.com*

Abinash Sahoo, *Department of Mechanical Engineering, Capital Engineering College, Bhubaneswar, abinashsahoo719@yahoo.co.in*

Abstract: The theory of generating-line method has been discussed in this study. It is a new theory of manufacturing spiral bevel gears of which tooth surfaces are formed by exact spherical involutes. The tooth surface of spiral bevel gears is obtained by the pure-rolling motion between the base cone and the great circular plane of the fundamental sphere. Based on the cutting motions the equations to describe tooth surfaces have been derived by using theory of gearing, and the equation of meshing of spiral bevel gears with spherical involute tooth surface is obtained in the text. This study can provide some fundamentals for manufacturing and contact analysis of spherical involute spiral bevel gears.

Keywords: Equations of meshing, generating-line, spiral bevel gears.

1. INTRODUCTION

Spiral bevel gears are widely used for intersecting shafts, they are the most efficient means of transmitting rotations between intersecting shafts. Design and manufacturing of such gear drives has been a topic of research [1-4]. In most of the current work, the tooth profile of spiral bevel gear manufactured by exclusive machines is not a spherical involute curve, the tooth-surface geometry is analyzed by expanding on the planar involute geometry [5]. The companies like Gleason Works and Klingelnberg-Oerlikon have developed advanced technology and equipments for manufacturing the spiral bevel gears, but there are still some disadvantages: the cutting machines are expensive, the gear ratio is not constant during the tooth engagement cycle [6], in order to reduce the kinematical errors and transmission errors the complicated machine tool settings are needed [7]. Tooth Contact Analysis computer program for simulation of meshing and contact of gear drive has been used to enhance the meshing quality [8, 9].

The spiral bevel gears with spherical involutes tooth profile have many good properties such as the interchange-ability and the constant ratio of angular speed [10]. Tsai and Chin described the tooth-surface of bevel gears by a family of spherical involutes curves initiating from a radial straight line on the base cone [11]. A suitable formulation and its implementing algorithms have been proposed for involute and octoidal bevel-gear generation [12]. A solid model of straight and spiral bevel gears were obtained by using simple sweeping techniques to their tooth profiles described by the exact spherical involutes [13].

In this paper the spiral bevel gears with exact spherical involutes tooth profile can be obtained by generating-line method. The equations of tooth surfaces and the equation of meshing of spiral bevel gears with spherical involutes tooth profile are deduced based on the cutting moment and the theory of gearing. It is the foundation of design, manufacture and contact analysis of spherical involutes spiral bevel gears.

2. THE BASICS OF GENERATING-LINE METHOD

The exact spherical involutes can be obtained by the pure-rolling motion between the base cone and the great circle of the fundamental sphere. The generating process of exact spherical involutes is shown in Fig. (**1**). The arc TP is the spherical involute traced by a point P of the great circle C during the pure-rolling motion of its disk plane on the base cone. The principle of surfaces generated by generating-line method is shown in Fig. (**2**). S is an arc in the plane Q. The plane Q and the base cone in tangency along line OJ, δ_b is the base cone angle. In order to keep the pure-rolling motion between them, plane Q and the base cone rotate with their respective angular velocities ω_q and ω, the relation between ω and ω_q is described as,

$$\omega_q / \omega = \sin\delta_b \tag{1}$$

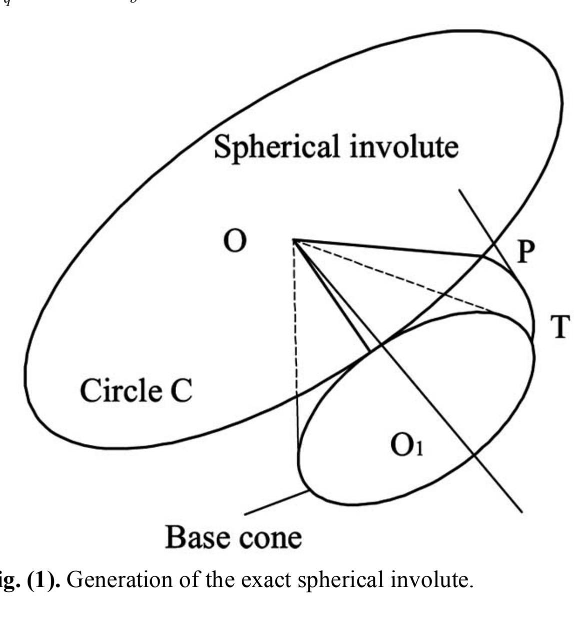

Fig. (1). Generation of the exact spherical involute.

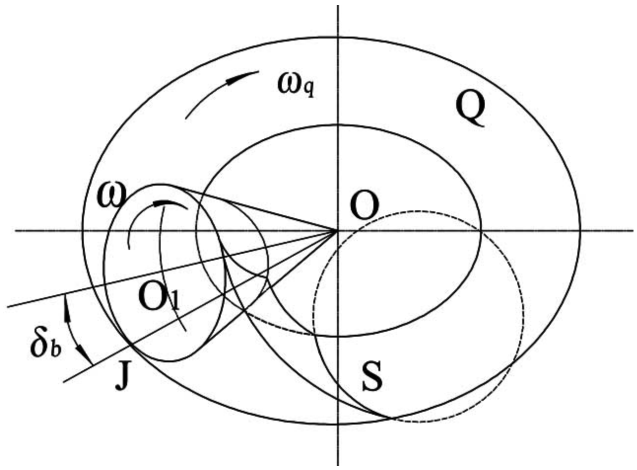

Fig. (2). Generation of the tooth surface formed by spherical involutes.

When the arc S on the plane Q rotates together with plane Q to keep pull-rolling motion with the base cone, the trace of the arc S should be a right-hand concave tooth surface formed by a family of exact spherical involutes. If the cutting edge on the plane Q shaped identical to the generating line S keeps pull-rolling with the base cone, and rotates about its geometrical center to enhance the cutting velocity simultaneity, the surface is obtained [14].

3. COORDINATE SYSTEMS AND EQUATIONS OF THE SURFACES

The equation of meshing is the fundamental starting point for developing the computerized gear design and meshing quality. In order to deriving the equation of meshing, the equation of tooth surface should be deduced. So the coordinate systems should be set up firstly.

Coordinate systems applied are shown in Fig. (**3**). Coordinate system $S=[O;X,Y,Z]$ is the fixed one which origin O coincidence with the center of Q plane, the common tangent of the plane Q and the base cone 1 is defined as axis OX, the axis OZ is perpendicular to Q plane, the axis OY in Q plane is perpendicular to OX and OZ. The coordinate system of gear 1 is set up like this: $S_1=[O\,;X_1,Y_1,Z_1]$ is connected to the base cone of gear 1, OX_1 in the coordinate plane O-XZ is designed to represent the rotary axis of base cone 1, OY_1 coincides with OY, the angle between axis OX and axis OX_1 labeled δ_{b1} is denoted as the base angle of gear 1. Coordinate system $S_f=[O\,;X_f,Y_f,Z_f]$ is an auxiliary coordinate system of which the axis OZ_f coincides with OZ, they are all perpendicular to plane O-XY, and α denoted as the angle between OX_f and OX, axis OX_f is the common tangent of Q plane and cone 2. The coordinate system $S_2=[O\,;X_2,Y_2,Z_2]$ is connected to the base cone of gear 2, OX_2 is the rotary axis of base cone 2, the angle between axis OX_2 and axis OX_f labeled δ_{b2} is denoted as the base angle of gear 2, OY_2 coincides with OY_f in Q plane. Fig. (**4**) shows the relationship between coordinate systems S_q and S_d. Coordinate system $S_q=[O\,;X_q,Y_q,Z_q]$ is a moving coordinate system, it is coincidence with the fixed coordinate system S at the beginning, then rotated about the axis OZ with the angular velocities of ω_q with plane Q, the angle ϕ between OX_q and OX is denoted by $\omega_q t$. Coordinate system $S_d=[O\,;X_d,Y_d,Z_d]$ is connected to the arc generating line, the origin O_d is the center of the arc whose position is denoted by length b and angle between OY_d and OY_q labeled β. The generating line is an arc with the radius r_d, in coordinate system S_q, the generating line can be represented by,

$$r_q=\begin{bmatrix} r_d\cos(\beta+\theta)-b\sin\beta \\ r_d\sin(\beta+\theta)+b\cos\beta \\ 0 \end{bmatrix} \tag{2}$$

Here, θ is the parameter of the generating line.

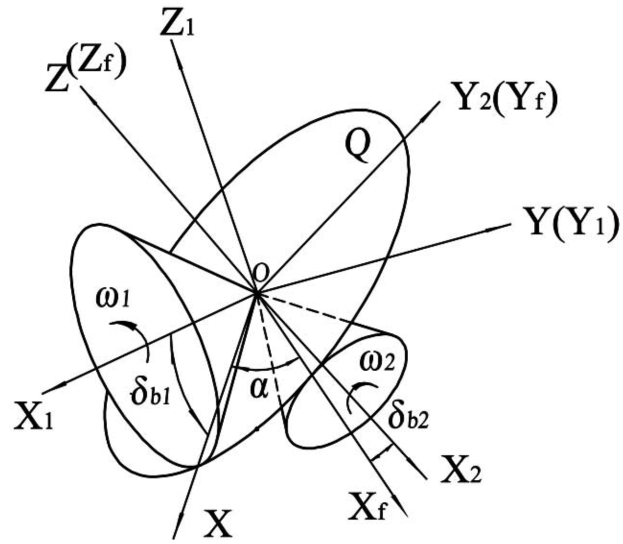

Fig. (3). Coordinate systems.

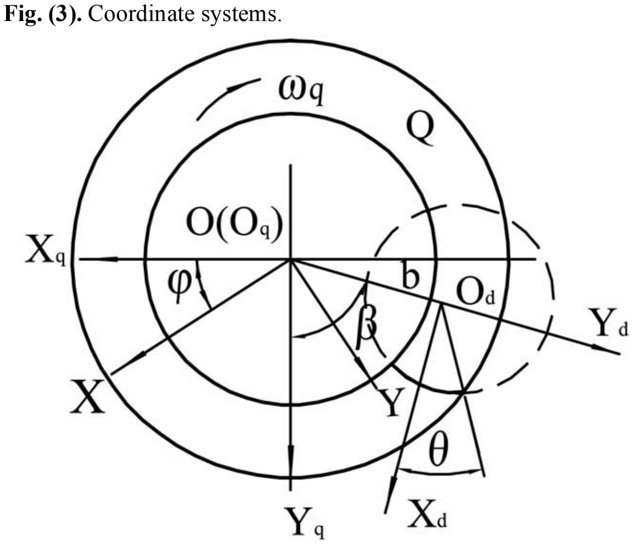

Fig. (4). Coordinate system of generating line.

In coordinate system S_1 the equation of surface r_1 is represented by,

$$r_1(\theta,\phi) = x_1 i_1 + y_1 j_1 + z_1 k_1 \tag{3}$$

Here,

$$A = \phi - \beta \tag{4}$$

$$\begin{aligned} x_1 &= \cos\delta_{b1}[r_d\cos(A-\theta)+b\sin A] \\ y_1 &= \cos\psi_1[-r_d\sin(A-\theta)+b\cos A]+\sin\psi_1\sin\delta_{b1} \\ &\quad [r_d\cos(A-\theta)+b\sin A] \\ z_1 &= \sin\psi_1[-r_d\sin(A-\theta)+b\cos A]-\cos\psi_1\sin\delta_{b1} \\ &\quad [r_d\cos(A-\theta)+b\sin A] \end{aligned} \tag{5}$$

And, $\psi_1 = \phi / \sin\delta_{b1}$.

In coordinate system S_2 the equation of surface r_2 is represented by,

$$r_2(\theta,\phi) = x_2 i_2 + y_2 j_2 + z_2 k_2 \tag{6}$$

Here,

$$B = \phi - \beta + \alpha \tag{7}$$

$$\begin{aligned} x_2 &= \cos\delta_{b2}[r_d\cos(B-\theta)+b\sin B] \\ y_2 &= \cos\psi_2[-r_d\sin(B-\theta)+b\cos B]+\sin\psi_2\sin\delta_{b2} \\ &\quad [r_d\cos(B-\theta)+b\sin B] \\ z_2 &= -\sin\psi_2[-r_d\sin(B-\theta)+b\cos B]+\cos\psi_2\sin\delta_{b2} \\ &\quad [r_d\cos(B-\theta)+b\sin B] \end{aligned} \tag{8}$$

And, $\psi_2 = \phi / \sin\delta_{b2}$.

The expression of unit normal vector of surface r_1 in coordinate system S_1 is represented by,

$$n_1 = n_x i_1 + n_y j_1 + n_z k_1 \tag{9}$$

Here,

$$\begin{aligned} n_{x1} &= \cos\delta_{b1}\cos(A-\theta) \\ n_{y1} &= -\cos\psi_1\sin(A-\theta)+\sin\delta_{b1}\sin\psi_1\cos(A-\theta) \\ n_{z1} &= -\sin\psi_1\sin(A-\theta)-\sin\delta_{b1}\cos\psi_1\cos(A-\theta) \end{aligned} \tag{10}$$

4. EQUATION OF MESHING

The concept of relative velocity is used for the derivation of the equation of meshing. According to the theory of gearing, consider the two gears are rotated about crossed axes with angular velocities ω_1 and ω_2, respectively, the conjugated points N_1 and N_2 are the points of gear tooth surfaces r_1 and r_2. When the two gears rotated, points N_1 and N_2 coincidences at point N. The relative velocity V^{12} of point N_1 of gear 1 with respect to point N_2 of gear 2 can be represented by the equation,

$$V^{12} = \omega^{12} \times r \tag{11}$$

Here r is the position vector that is drawn to contact point in the fixed coordinate system, which is described by,

$$r = xi + yj + zk \tag{12}$$

The surface equation and normal vector of r_1 are represented in coordinate system S_1, they should be determined in the fixed coordinate system S. The transformational matrix from S_1 to S is represented by,

$$M_{s1} = \begin{bmatrix} \cos\delta_{b1} & 0 & -\sin\delta_{b1} \\ 0 & 1 & 0 \\ \sin\delta_{b1} & 0 & \cos\delta_{b1} \end{bmatrix} \tag{13}$$

When gear 1 rotated with angle ϕ_1, gear 2 rotated with angle $i_{21}\phi_1$, the rotational matrix of coordinate system S_1 rotated about axis OX_1 is represented by,

$$M_{\varphi 1} = \begin{bmatrix} 1 & 0 & 0 \\ 0 & \cos\varphi_1 & -\sin\varphi_1 \\ 0 & \sin\varphi_1 & \cos\varphi_1 \end{bmatrix} \tag{14}$$

Therefore, the expression of vector of meshing point in fixed coordinate system is represented by,

$$r = M_{\varphi 1} M_{s1} r_1 = xi + yj + zk \tag{15}$$

Here,

$$\begin{aligned} x &= \cos\delta_{b1}x_1 - \sin\delta_{b1}z_1 \\ y &= \cos\phi_1 y_1 - \sin\phi_1(\sin\delta_{b1}x_1 + \cos\delta_{b1}z_1) \\ z &= \sin\phi_1 y_1 + \cos\phi_1(\sin\delta_{b1}x_1 + \cos\delta_{b1}z_1) \end{aligned} \tag{16}$$

The relative angular velocity ω^{12} should be deduced. The gear ratio i_{21} is represented by the equation,

$$i_{21} = \frac{\omega_2}{\omega_1} \tag{17}$$

The angular velocity ω_1 and ω_2 are shown in Fig. (**3**). Conveniently, consider ω_1=1, then ω_2=i_{21}. In fixed coordinate system ω_1 and ω_2 can be represented as,

$$\omega_1^S = \begin{bmatrix} \cos\delta_{b1} & 0 & \sin\delta_{b1} \end{bmatrix}^T \tag{18}$$

$$\omega_2^S = \begin{bmatrix} -i_{21}\cos\delta_{b2}\cos\alpha & i_{21}\cos\delta_{b2}\sin\alpha & i_{21}\sin\delta_{b2} \end{bmatrix}^T \tag{19}$$

Thus, the expression for ω^{12} can be represented in fixed coordinate system as,

$$\omega^{12} = \omega_1^S - \omega_2^S = \begin{bmatrix} \cos\delta_{b1} + i_{21}\cos\delta_{b2}\cos\alpha \\ -i_{21}\cos\delta_{b2}\sin\alpha \\ \sin\delta_{b1} - i_{21}\sin\delta_{b2} \end{bmatrix} \tag{20}$$

Then, subscribed (15), (20) into（11), the relative velocity V^{12} is represented in fixed coordinate system by the following expressions:

$$\begin{aligned} V_x^{12} &= -zi_{21}\cos\delta_{b2}\sin\alpha - y(\sin\delta_{b1} - i_{21}\sin\delta_{b2}) \\ V_y^{12} &= -z(\cos\delta_{b1} + i_{21}\cos\delta_{b2}\cos\alpha) + x(\sin\delta_{b1} - i_{21}\sin\delta_{b2}) \\ V_z^{12} &= y(\cos\delta_{b1} + i_{21}\cos\delta_{b2}\cos\alpha) + xi_{21}\cos\delta_{b2}\sin\alpha \end{aligned} \tag{21}$$

According to the theory of gearing, in the fixed coordinate system the equation of meshing of the surfaces is represented by equation,

$$\varphi(\theta,\phi,t) = n \cdot V^{12} = n_x V_x^{12} + n_y V_y^{12} + n_z V_z^{12} = 0 \tag{22}$$

And in fixed coordinate system, the unit normal vector of meshing point is represented by equation,

$$n = M_{\varphi 1} M_{s1} n_1 = n_x i + n_y j + n_z k \tag{23}$$

Here,

$$\begin{aligned} n_x &= \cos\delta_{b1} n_{x1} - \sin\delta_{b1} n_{z1} \\ n_y &= \cos\varphi_1 n_{y1} - \sin\varphi_1 (\sin\delta_{b1} n_{x1} + \cos\delta_{b1} n_{z1}) \\ n_z &= \sin\varphi_1 n_{y1} + \cos\varphi_1 (\sin\delta_{b1} n_{x1} + \cos\delta_{b1} n_{z1}) \end{aligned} \tag{24}$$

Subscribed (21), (24) into (22), then obtained the expression of meshing equation in fixed coordinate system as follows:

$$U\cos\phi_1 - V\sin\phi_1 = W \tag{25}$$

Here,

$$\begin{aligned} U &= [-z(\cos\delta_{b1} + i_{21}\cos\delta_{b2}\cos\alpha) + x(\sin\delta_{b1} - i_{21}\sin\delta_{b2})]n_{y1} \\ &\quad + [y(\cos\delta_{b1} + i_{21}\cos\delta_{b2}\cos\alpha) + x i_{21}\cos\delta_{b2}\sin\alpha] \\ &\quad (\sin\delta_{b1} n_{x1} + \cos\delta_{b1} n_{z1}) \\ V &= [-z(\cos\delta_{b1} + i_{21}\cos\delta_{b2}\cos\alpha) + x(\sin\delta_{b1} - i_{21}\sin\delta_{b2})] \\ &\quad (\sin\delta_{b1} n_{x1} + \cos\delta_{b1} n_{z1}) - [y(\cos\delta_{b1} + i_{21}\cos\delta_{b2}\cos\alpha) \\ &\quad + x i_{21}\cos\delta_{b2}\sin\alpha] n_{y1} \\ W &= -[-z i_{21}\cos\delta_{b2}\sin\alpha - y(\sin\delta_{b1} - i_{21}\sin\delta_{b2})] \\ &\quad (\cos\delta_{b1} n_{x1} - \sin\delta_{b1} n_{z1}) \end{aligned} \tag{26}$$

When i_{21} and δ are given, the values of U, V, W only relate to the position of meshing point (x_1, y_1, z_1), U, V, W are the function of θ and φ. Thus, when the position of meshing point is given, the rotate angle $\phi_1$which is the function of θ and φ can be calculated by equation of meshing. It is represented by equation,

$$\phi_1 = \arccos\left(\frac{W}{\sqrt{U^2 + V^2}}\right) - \arctan\left(\frac{V}{U}\right) \tag{27}$$

From the equation above, it showed that a set of values of θ and φ determined the values of ϕ_1, it means that when the gear rotated with angles ϕ_1, the correspondence of point determined by θ and φ becomes the meshing point. If the surfaces are line contact, the certain contact line exists. Generally, when considering the value of parameter t is t_0, the equation of instantaneous contact line is represented by equations,

$$\begin{cases} \phi(\theta,\varphi,t_0) = 0 \\ r_1 = r_1(\theta,\varphi) \end{cases} \tag{28}$$

5. CONCLUSIONS

Generating-line method is a new method of designing and manufacturing spiral bevel gears with spherical involute tooth profile. The spiral bevel gears manufactured by generating-line method can avoid errors caused by using the planer involute tooth profile on the back cone to replace the spherical involute tooth profile. The tooth surface formed by spherical involutes has been obtained by making the cutting edge shape be identical to the generating line which is arc or line. This kind of spiral bevel gear has many advantages, the structure of machine and the cutting motions are not so complicated.

The equations of tooth surfaces which describe the new kind of spiral bevel gears have been deduced, and the equations of meshing which provide the foundations for the design, modeling and contact analysis of this kind of spiral bevel gears are obtained.

REFERENCES

[1] F. L. Litvin, A. Fuentes, and K. Hayasaka, "Design, manufacture, stress analysis, and experimental tests of low-noise high endurance spiral bevel gears", *Mech. Mach. Theory*, vol. 41, pp. 83-118, January 2006.

[2] Y. C. Tsai, and W. Y. Hsu, "The study on the design of spiral bevel gear sets with circular-arc contact paths and tooth profiles", *Mech. Mach. Theory*, vol. 43, pp. 1158-1174, September 2008.

[3] J. Argyris, A. Fuentes, and F. L. Litvin, "Computerized integrated approach for design and stress analysis of spiral bevel gears", *Comput. Methods Appl. Mech. Eng.*, vol. 191, pp. 1057-1095, 2002.

[4] A. Fuentes, F. L. Litvin, B. R. Mullins, R. Woods, and R. F. Handschuh, "Design and stress analysis of low-noise adjusted bearing contact spiral bevel gears", *J. Mech. Des.*, vol. 124, pp. 524-532, September 2002.

[5] F. L. Huston, and J. J. Coy, "Surface geometry of circular cut spiral bevel gears", *J. Mech. Des.*, vol. 104, pp. 743-748, October 1982.

[6] F. L. Litvin, and A. Fuentes, *Gear Geometry and Applied Theory*, Cambridge University Press, USA 2004.

[7] V. V. Simon, "Design and manufacture of spiral bevel gears with reduced transmission errors", *J. Mech. Des. Trans. AsME*, Vol. 131, pp. 0410071-04100711, 2009.

[8] F. L. Litvin, A. Fuentes, Q. Fan, and R. F. Handschuh, "Computerized design, simulation of meshing, and contact and stress analysis of face-milled formate generated spiral bevel gears", *Mech. Mach. Theory*, vol. 37, pp. 441-459, May 2002.

[9] F. L. Litvin, M. De Donno, A. Peng, A. Vorontsov, and R. F. Handschuh, "Integrated computer program for simulation of meshing and contact of gear drives", *Comput. Methods in Appl. Mech. Eng.*, vol. 181, pp. 71-85, January 2002.

[10] G.. Figliolini, and J. Angeles, "Algorithms for involute and octoidal bevel-gear generation", *J. Mech. Des.*, vol. 127, pp. 664-672, July 2005.

[11] Y. C. Tsai, and P. C. Chin, "Surface geometry of straight and spiral bevel gears", *J. Mech. Transm. Autom. Des.*, vol. 109, pp. 443-449, December 1987.

[12] H. W. Lee, K. O, Lee, and D. H. Chung, "A kinematic investigation of a spherical involute bevel-geared system", Proc. IMechE Part C: *J. Mech. Eng. Sci.*, vol. 224, pp. 1335-1348, 2009.

Particle Focusing and Separation through Lab-On-Chip Device

Babita Meher, *Department of Mechanical Engineering, Aryan Institute of Engineering & Technology, Bhubaneswar, baitamh784@gmail.com*

Shakyasingha Sahoo, *Department of Mechanical Engineering, NM Institute of Engineering & Technology, Bhubaneswar, shakyasinghasahoo@gmail.com*

Rajaram Sahu, *Department of Mechanical Engineering, Raajdhani Engineering College, Bhubaneswar, rajaramsahu65@gmail.com*

Bipash Mohanty, *Department of Civil Engineering, Capital Engineering College, Bhubaneswar, bipashmohanty784@gmail.com*

Abstract: A Lab-On-Chip micro-device has been introduced for the focusing and separation of particles which exploits negative dielectrophoretic (nDEP) force. A 3D numerical computational model was presented to simulate the focusing and separation process. In particular, the model will solve for bioparticle movement and Joule heating. In the experimental study, the mixture of viable and nonviable yeast cells was used to demonstrate the focusing and separation effect of the designed microfluidic device. The fabricated chip performs a desired focusing result for the conditions with the electric fields frequency of 1MHz, the medium conductivity of 0.01S/m and the applied voltage $V = 20V_{pp}$. The mixture of viable and nonviable yeast cells were focused to the central plane of the micro-channel and then separated by non-equilibrium nDEP induced by the single part of the last pair of electrodes with conductivity $\sigma = 0.01$S/m, applied voltage $V = 20V_{pp}$ and applied electric field frequency of 5Mhz, which validities the prediction of the proposed 3D model. This Lab-On-Chip device provides a simple and effective mean of particle focusing.

Keywords: Lab-On-Chip, dielectrophoresis, particle focusing, particle separation.

1. INTRODUCTION

The recent development of bio-microfluidic devices makes it possible to perform complex functions of biological assays on a Lab-On-Chip device. Lower cost, lower volumes of sample and shorter time are considered to be the advantages of bio-microfluidic devices. For typical biomedical applications, the focusing of cells from dilute suspension or even a targeted location is desired using a bio-microfluidic device. Many focusing techniques have been developed to accomplish the focusing of targeted particles through sheath flow confine the particles within a certain volume of fluid stream. These methods are effective for focusing and later on for separation but the device are complex and require multiple inlets with precise flow rates. Due to these constraints the device is difficult to be fabricated and sometimes cannot be used commercially due to its cost effectiveness. Dielectrophoresis provides an attractive alternative to conventional separation and focusing methods because of its ability to separate bioparticles in a convenient, controllable, selective and rapid means [1, 2]. Braschler *et al.* proposed a multiple frequencies dielectrophoresis method to separate cells continuously [3]. They produced electric field gradients by a novel geometrical arrangement of lateral metal electrodes and a patterned insulator. And the performance of this device was demonstrated by separating a mixed yeast cell population into pure fractions of viable and nonviable cells. In addition, red blood cells infected with Babesia bovis were enriched by using the same device which confirms the hypothesis that infection with B. bovis causes significant changes in the dielectric response of red blood cells. The proposed geometrical arrangement of the lateral dielectrophoresis or “liquid electrodes” is characterized and optimized for shaping electric field to achieve lateral deviation of particles in liquid flow.

DEP means the creation of forces on polarizable particles and the resulting movement of them in a nonuniform electric field. The magnitude and direction of DEP forces depend on the frequency of the AC electric field, conductivity and permittivity of both particles and the medium where particles suspended, and the gradient of electric field. Confining the sample to the center of the microfluidic channel ensures that all the particles move at a constant velocity. It also eliminates signal interference from the chamber wall, as well as particle-wall interactions [4]. Chu *et al.* proposed a microfluidic device using lateral dielectrophoresis to focus and continuously separate cells [5].

In this work, a 3D computational model was presented to predict and investigate the particle behavior and the impact of Joule heating. The present microfluidic device, similar to that of Demierre *et al.*, can focus particles eliminating the use of sheath flow and pumps. Experiments were conducted to verify the proposed 3D computational model.

2. NUMERICAL MODEL AND GOVERNING EQUATIONS

Microfluidic devices often have complex electrode patterns, which require solving the full set of governing equations using numerical method. Comsol Multiphysics was used to simulate the effects of temperature distribution on AC electrothermal microflow. Three modules are used to find the electric field, temperature distribution and fluidic velocity. First, the electric field distribution in the fluidic chamber is derived. The resulting electric field distribution is

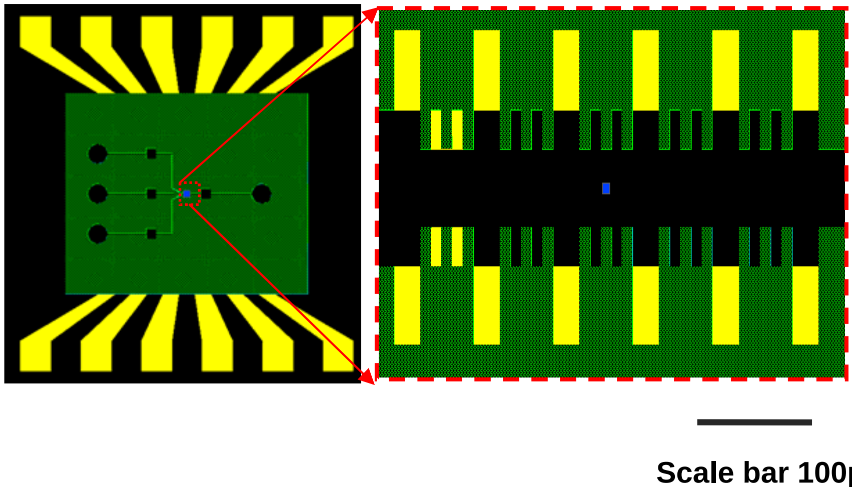

Fig. (1). The schematic of the lateral microfluidic microelectrodes structure.

used to calculate the temperature field according to the energy equation. Then the fluid volume force in the chamber is calculated using the temperature gradient and the electric field distribution from the first two steps. Lastly, the fluid flow field is obtained by Navier-Stokes equation. The problem space and boundary conditions for the electrical and thermal problem are modeled similarly to the work by Green *et al.* [6], and the lateral microfluidic microelectrodes structure is shown schematically in Fig. (**1**).

The thermal and electrical problems are decoupled since induced fluid convection does not contribute to the thermal problem. The electrical problem is bounded to within the fluid medium. The Laplace equation for a potential (ϕ) in a homogeneous medium is first solved with [6].

$$\nabla^2\phi = 0, \qquad \vec{E} = -\nabla\phi \tag{1}$$

where the boundary condition for the electrode strip V_0 refers to the root mean square (rms) value of the applied potential.

The electrical force per unit volume for an incompressible fluid can be expressed as:

$$\vec{F}_{et} = -\frac{1}{2}\left[\left(\frac{\nabla\sigma}{\sigma} - \frac{\nabla\varepsilon}{\varepsilon}\right)\vec{E}\,\frac{\varepsilon\vec{E}}{1+(\omega\tau)^2} + \frac{1}{2}\left|\vec{E}\right|^2\nabla\varepsilon\right] \tag{2}$$

The gradients in conductivity and permittivity can be replaced by corresponding gradients in temperature for aqueous buffer near room temperature

$$\frac{\nabla\sigma}{\sigma} = 0.002\nabla T; \frac{\nabla\varepsilon}{\varepsilon} = -0.004\nabla T \tag{3}$$

Then, the fluid velocity, u, is solved for using Navier-Stokes equation.

$$-\nabla p + \eta\nabla^2 u + \vec{F}_{et} = 0 \tag{4}$$

where p is pressure, η is fluid viscosity. The water properties are given as $\rho = 1{,}000 kg/m^3$ and $\eta = 0.001 pa\cdot s$ at 20^{o}C. No slip boundary condition, u = 0 is applied to all the solid boundaries.

The time averaged DEP force is given by [7]

$$\left\langle \bar{F}_{DEP}(t)\right\rangle = 2\pi\varepsilon_m r^3\,\mathrm{Re}[K(\omega)]\nabla\left|\bar{E}_{rms}\right|^2 \tag{5}$$

where ε_m is the medium permittivity, $\nabla\left|\bar{E}_{rms}\right|^2$ is the gradient of the square of rms electrical field, ω is the angular field frequency, $\mathrm{Re}[K(\omega)]$ is the real part of $K(\omega)$. $\mathrm{Re}[K(\omega)] > 0$ means that cells show pDEP response while $\mathrm{Re}[K(\omega)] < 0$ means that nDEP response.

Numerical simulations were conducted for different experimental fluid conductivities and applied voltage. Fig. (**2**) shows the FEM simulation of the particle tracing of yeast cells for a fluid sample with conductivity $\sigma = 0.01$S/m, applied voltage V = 20V_{pp}, and electric field frequency of 1MHz. From simulation results it can be seen that evenly distributed yeast cells in the inlet channel were focused to the central plane of the channel. Both viable (green lines) and nonviable yeast cells (red lines) present a similar focusing effect, and their stream lines overlapped when yeast cell pass a certain distance (here four electrodes gap). Fig. (**3**) shows FEM simulation result for the separation process of viable and nonviable yeast cells. 5MHz electric field frequency was applied at the single part of the last pair of electrodes to obtain the spatial separation of viable and nonviable yeast cells mixture with conductivity σ = 0.01S/m and applied voltage V = 20V_{pp}. Viable and nonviable yeast cells demonstrate an obviously distinctive stream line due to the different nDEP response. Strong electric field will act on the conducting fluid medium, which may result in Joule heating. This could damage temperature sensitive biological samples. It is important to monitor the temperature field in a fluid medium. Fig. (**4**) shows FEM simulation of the temperature field for a fluid sample with conductivity σ = 0.01S/m and applied voltage V = 20V_{pp}. The maximum temperature increase from numerical simulation was less than 0.5^{o}C, which is safe for the yeast cells.

3. DEVICE FABRICATION

Device fabrication involves two parts, the electrodes and the microfluidic channel. First, the electrode array with

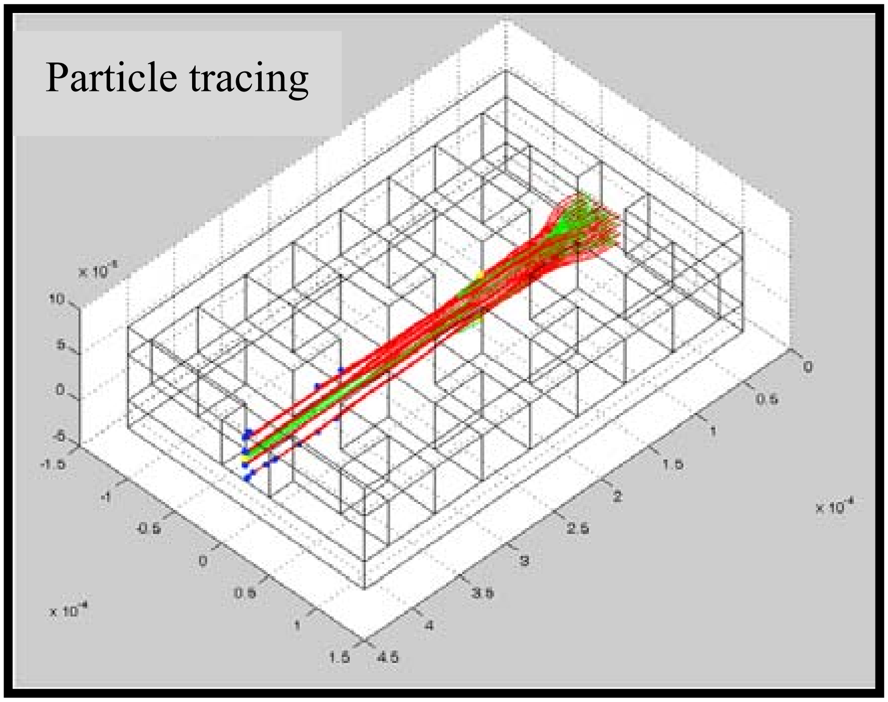

Fig. (2). FEM simulation of the particle tracing of yeast cells for a fluid sample with conductivity $\sigma = 0.01$S/m and applied voltage $V = 20V_{pp}$.

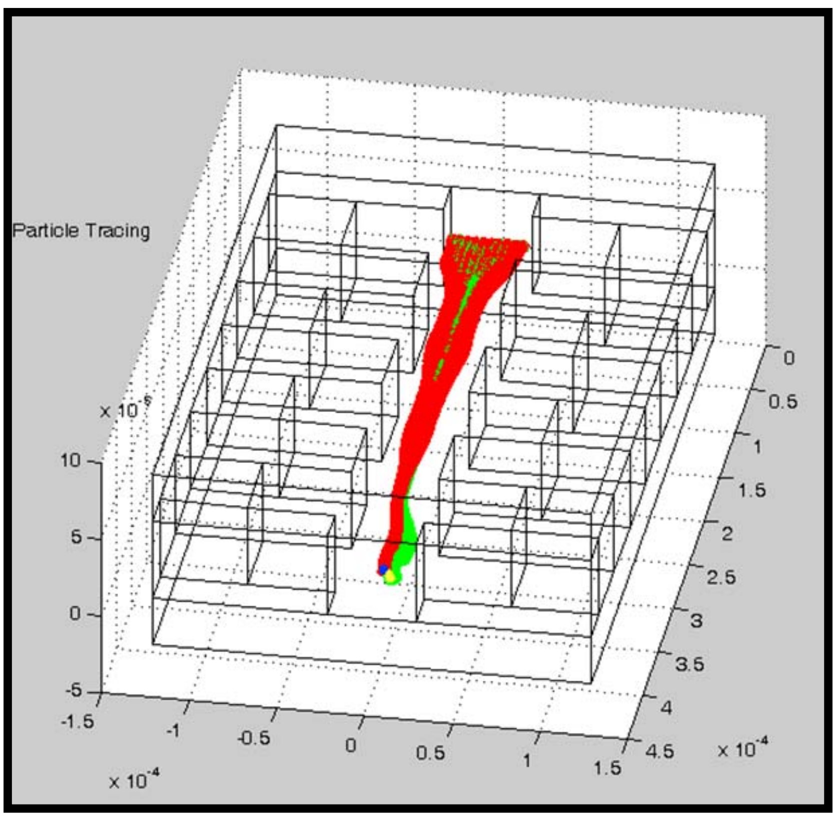

Fig. (3). FEM simulation of the separation process viable and nonviable of yeast cells for a fluid sample with conductivity $\sigma = 0.01$S/m, applied voltage $V = 20V_{pp}$ and frequency 5Mhz.

$50\mu m$ wide, $50\mu m$ spaced, were fabricated from Indium Tin Oxide (ITO) coated glass slide (SPI). These glass slides provide high transparency and good electrical conductivity, enabling visualization of the flow of particle in the micro-channel. The chambers and the channels were structured in an insulating material. The microfluidic channels were made

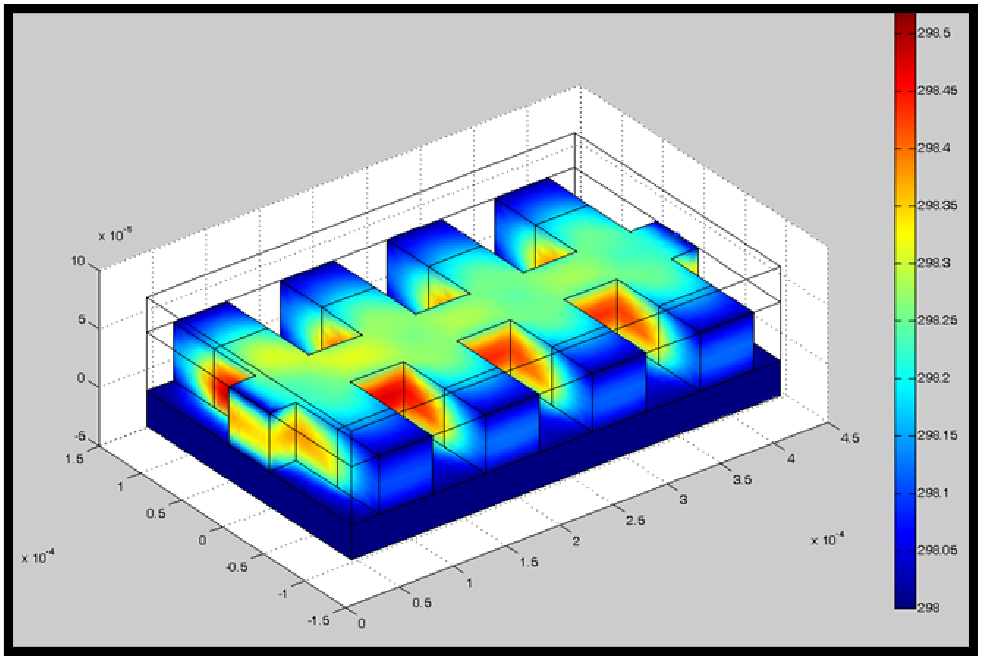

Fig. (4). FEM simulation of the temperature field for a fluid sample with conductivity σ= 0.01S/m and applied voltage $V = 20V_{pp}$.

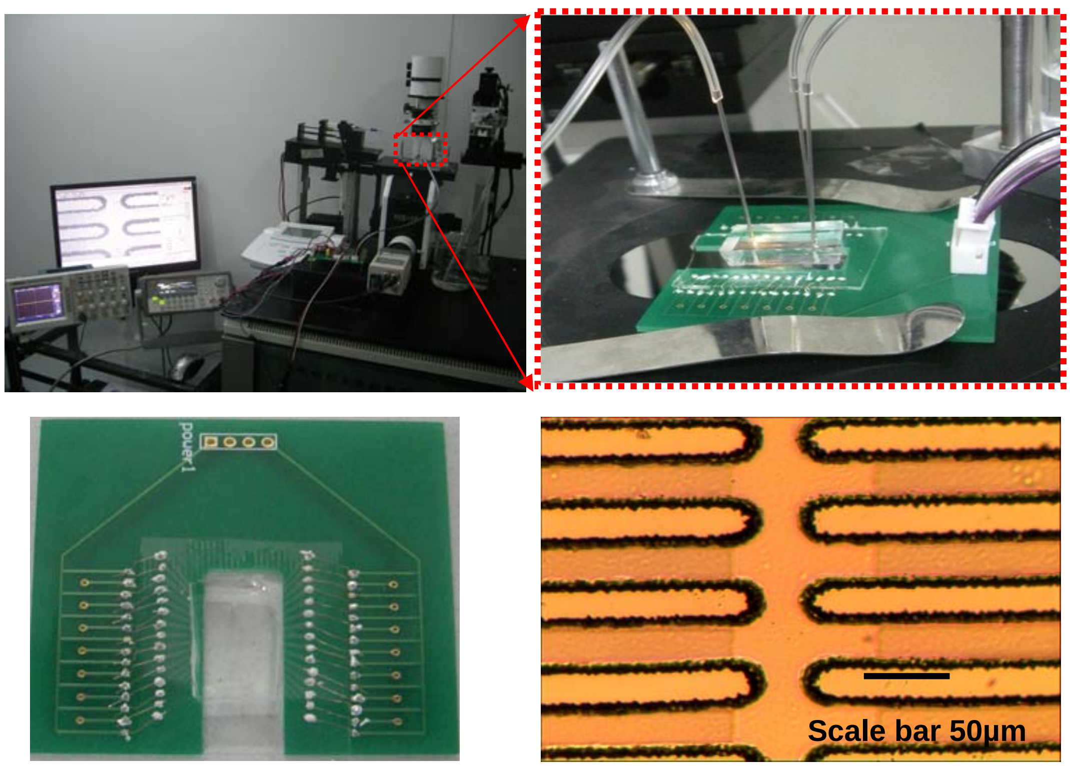

Fig. (5). The structure of the designed microfluidic chip system.

from PDMS structures that patterned on the bottom ITO glass substrate by standard photolithography process. The bottom-patterned structure was accurately positioned under a mask aligner. More details can be found in reference [7]. The structure of the designed microfluidic chip system is shown in Fig. (**5**). There are totally fifteen pairs of electrodes were fabricated on the bottom of the prototype microfluidic chip.

4. TEST METHOD AND RESULTS

The mixture of viable (live) and nonviable (dead) yeast (Sacchararomyces cerevisiae) cells was selected to serve as sample cells to be focused. Yeast cell are cultured in culture medium at 30^{o}C for 24h, washed and then resuspended four times through deionized water. Conductivity of the medium is adjusted by adding a small amount of NaCl and conduc-

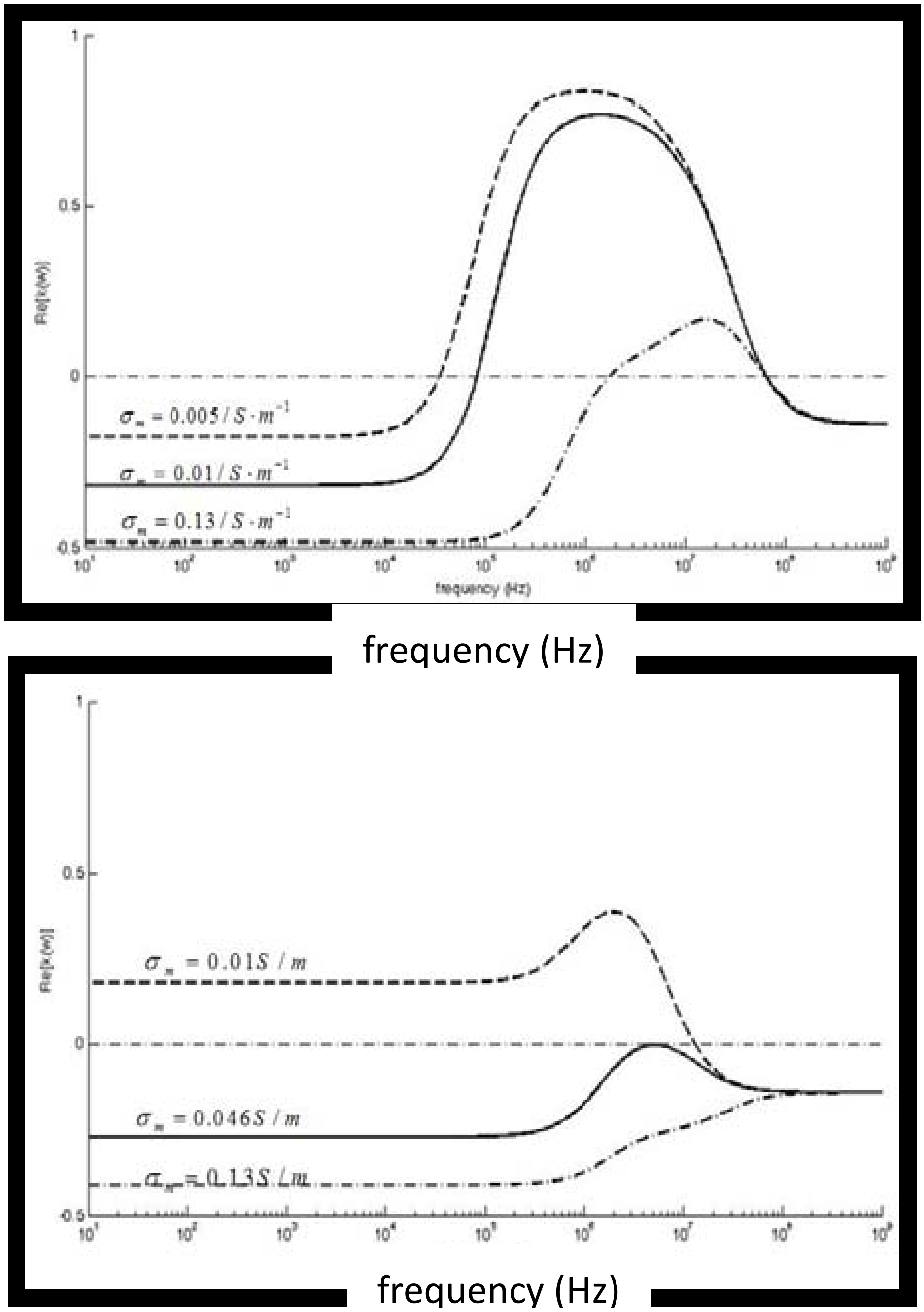

Fig. (6). The DEP frequency response at three different medium conductivities of viable (Upper) and nonviable (Lower).

tivity is measured by conductive meter TN2301. Nonviable yeast cells are prepared by heat treatment (90°C for 20 min) and viability is visualized using a methylene blue stain. In this stain, the color of those dead cells changes into blue. Such a sample preparation follows the process proposed by Doh *et al.* [8]. In order to obtain the optimal condition of separation; we measure DEP response of viable and nonviable yeast cells using test devices in terms of the medium conductivity and the electric fields frequency before the particles focusing experiment. The results of DEP frequency response at three different medium conductivities of viable and nonviable were shown in Fig. (**6**).

The measurements using the mixture of viable and nonviable yeast cells were conducted to verify their focusing effect. The medium conductivity of 0.01S/m and electric frequency of 1MHz were chosen as the focusing condition because viable and nonviable yeast cells show same nDEP response at this conditions and low medium conductivity is good to avoid heat problem which can damage cells. Under these conditions, the mixture of viable and nonviable yeast cells was focused towards the center line across the channel, as shown in Fig. (**7**). The focusing effect was obtained by generating two opposite negative DEP-forces with the same low frequency signals. In order to separate the viable and nonviable yeast cell mixture from the focused fluid medium, a 5MHz electric field frequency was applied at the single part of the last pair of electrodes to obtain the spatial separation of viable and nonviable yeast cells mixture with

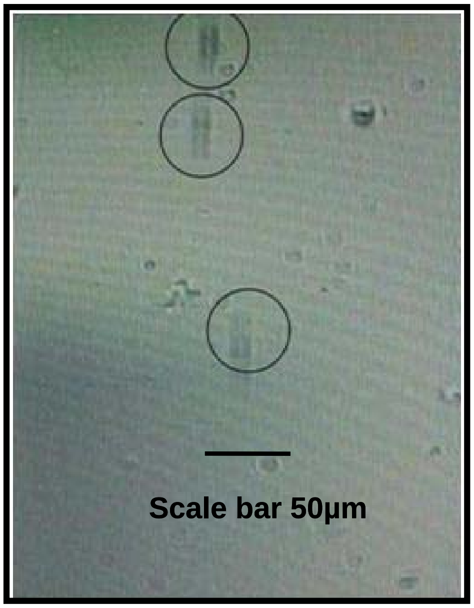

Fig. (7). The DEP focusing result of the mixture of viable and nonviable yeast cells with conductivity σ = 0.01S/m and applied voltage $V = 20V_{pp}$.

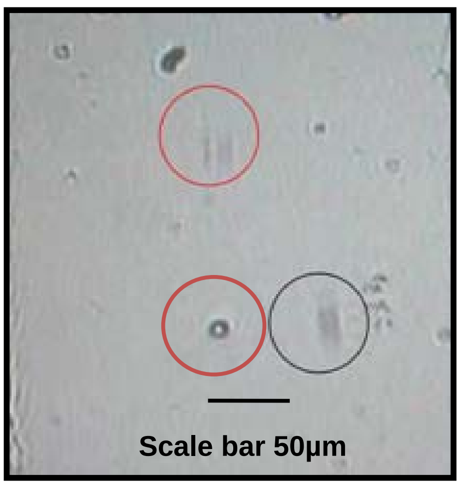

Fig. (8). The DEP separation result of the mixture of viable (indicated by the red circle) and nonviable yeast cells (indicated by the black circle) with conductivity σ = 0.01S/m and applied voltage $V = 20V_{pp}$.

conductivity σ = 0.01S/m and applied voltage $V = 20V_{pp}$. Fig. (**8**) shows the separation effect of viable (indicated by the red circle) and nonviable yeast cell (indicated by the black circle) which caused by the different nDEP response. There is a qualitatively agreement between the FEM simulation results and the experimental test results.

4. CONCLUSIONS

In this work, we present a cell focusing and separation microfluidic chip using negative dielectrophoresis. A 3D computational model was proposed to predict and investigate the behavior of particles. In the experimental study, viable and nonviable yeast cells were chosen to verify the focusing and separation effect of the proposed microfluidic chip. The mixture of viable and nonviable yeast cells were focused to the central plane of the micro-channel with conductivity σ = 0.01S/m and applied voltage $V = 20V_{pp}$, and then separated by non-equilibrium nDEP induced by the single part of the last pair of electrodes which is in accordance with the prediction of the proposed 3D model. The present chip is capable of performing the work of hydrodynamic focusing and separation, and is promising to be integrated into biological analysis system.

REFERENCES

[1] H. Pohl, "The motion and precipitation of suspensoids in divergent electric fields", *Appl. Phys. (Berl)*, vol. 22, pp. 869-871, 1951.

[2] E. Cummings, and A. Singh, "Dielectrophoresis in microchips containing arrays of insulating posts: theoretical and experimental results", *Anal. Chem.*, vol. 75, pp. 4724-4731, 2003.

[3] T. Braschler, N. Demierre, E. Nascimento, T. Silva, A. G. Oliva, and P. Renaud, "Continuous separation of cells by balanced dielectrophoretic forces at multiple frequencies", *Lab. Chip.*, vol. 8, pp. 280-286, 2008.

[4] H. Morgan, D. Holmes, and N. G. Green, "3D focusing of nanoparticles in microfluidic channels", *IEE Proc. Nanobiotechnol.*, vol. 150, pp. 76-81, 2003.

[5] N. Demierre, T. Braschler, R. Muller, and P. Renaud, "Focusing and continuous separation of cells in a microfluidic device using lateral dielectrophoresis", *Sensors Actuat.*, vol. 132, pp. 388-396, 2008.

[6] N. G. Green, A. Ramos, A. Gonazalez, A. Castellanos, and H. Morgan, "Electric field induced fluid flow on microelectrodes: The effect of illumination", *J. Phys. D: Appl. Phys*., vol. 33, pp. L13-L17, 2000.

[7] H. H. Cui, J. Voldman, X. F. He, and K. M. Lim, "Separation of particles by pulsed dielectrophoresis", *Lab. Chip*, vol. 9, pp. 2306-2312, 2009.

[8] Doh and Y. Cho, "A continuous cell separation chip using hydrodynamic dielectrophoresis (DEP) process", *Sensors Actuat. A: Phys*., vol. 121, pp. 59-65, 2005.

Transient Preheating Process of a Regenerative Oxidation Bed

Bhagyashree Panda, *Department of Mechanical Engineering, Aryan Institute of Engineering & Technology, Bhubaneswar, bhagyashree2561@gmail.com*

Sidharth Pradhan, *Department of Mechanical Engineering, Capital Engineering College, Bhubaneswar, sidharthpradhan265@gmail.com*

S. C. Mishra, *Department of Civil Engineering, NM Institute of Engineering & Technology, Bhubaneswar, scmishra11@yahoo.co.in*

Mdaras Aras Ansari, *Department of Civil Engineering, Raajdhani Engineering College, Bhubaneswar, mdarasansari2578@gmail.com*

Abstract: The transient preheating process of a regenerative oxidation bed placed in a coal mine methane thermal reverse-flow reactor is numerically investigated in this paper. The regenerative oxidation bed is heated by the burned gas which is generated from a burner and is distributed through manifolds, which is modeled in a three-dimensional, unsteady state and laminar flow system, and is assumed as a semitransparent porous media. Non-local thermal equilibrium between gas and solid is accounted for introducing separate energy equations for two phases in porous media, and the finite volume method is used to solve the radiative transfer equation of the solid phase to calculate the local radiation source term. The calculating results indicate that the regenerative oxidation bed is preheated mainly by the hot gas passing through the manifold, and increasing the inlet mass flow could shorten the time of preheating, specific heat and porosity have a great influence on the heat storage capacity of the regenerative oxidation bed, and the contribution of the solid phase radiation to heat transfer can not be ignored, the temperature is highest in the middle of the regenerative oxidation bed, and it decreases gradually along the direction of height of the regenerative oxidation bed. All these work can help to understand the transient preheating process of a regenerative oxidation bed and the heat transfer phenomena and mechanism during the process.

Keywords: Preheating, regenerative oxidation bed, heat transfer, porous media, manifold.

1. INTRODUCTION

Methane vented from coal mine exhaust shafts constitutes an unused source of energy and a potent atmospheric greenhouse gas (GHG). Technologies that can reduce ventilation air methane (VAM) emissions while harnessing methane's energy offer significant benefits to the world community. The thermal flow-reversal reactor (TFRR) and the catalytic flow-reversal reactor (CFRR) are both candidates for utilizing the low methane concentrations contained in VAM streams [1-3]. TFRR has been commercially used in Australia and China, but no reports of commercial applications of CFRR are found [4-6].

The regenerative oxidation bed, consisting of a number of honeycomb ceramic, is the site for methane oxidation in TFRR [7]. To start the operation, the middle of the regenerative oxidation bed must be preheated to the temperature required to initiate methane oxidation or hotter by the electric heating elements embedded in it or the burned gas generated from a burner placed outside. For the second case, the burned gas coming from the burner is transported to the middle of the regenerative oxidation bed, and is distributed through manifold. During the preheating process, the temperature and heat storage capacity of the regenerative oxidation bed increases gradually due to the heat transfer between the hot gas and the bed. The mechanism of the heat transfer is very complicated, including radiation, conduction and convection [8-11].

In recent years, there were numerous investigations on heat transfer in a porous media [12-14]. C. Ben Kheder, B. Cherif and M.S. Sifaoui studied numerically the transient heat transfer in semitransparent porous medium using a fully implicit time-marching algorithm to solve the nonlinear coupled energy equations for gas and porous medium, and reported that the Reynolds number, optical characteristic and conduction–radiation parameter have obvious effects on the temperatures.

The main purpose of this study is to numerically investigate the transient preheating process of the regenerative oxidation bed heated by the burned gas, and analyze the effects of some important parameters on the heat storage capacity in order to better understand the heat transfer phenomena and mechanism during the preheating process.

2. PHYSICAL MODEL

The coal mine VAM TFRR which was made and tested at Shan Dong University of Technology is used in this study, as shown in Fig. (**1**). It is a simple apparatus that consists of a regenerative oxidation bed, a heating and starting system, an upper header and a lower header, four control valves and ducts. The regenerative oxidation bed, consisting of a number of honeycomb ceramic, is the main part of the TFRR, where the methane is oxidized and the energy is stored. It is a vertical structure (2100mm × 1350mm × 2400mm), in which gas flows along the vertical direction, as shown in Fig. (**1**). In the middle of the TFRR is the hot gas distribution system of the heating and starting system, through which the hot gas is distributed and the oxidation bed is heated uniformly within the starting stage. The upper header and the lower header are used to guide the feed into the oxidation

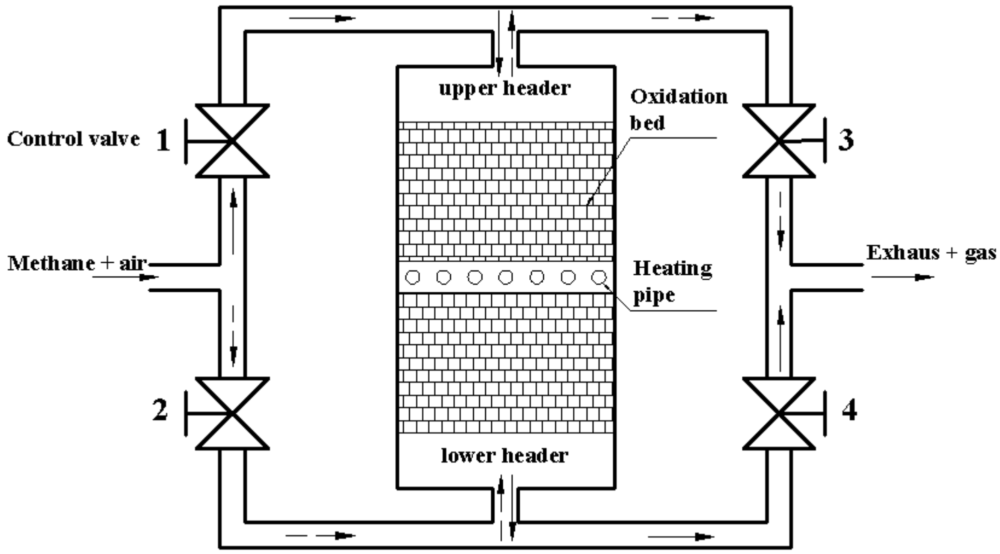

Fig. (1). The schematic of the coal mine VAM TFRR.

bed uniformly. Four control valves are used to control the direction of VAM flowing in the regenerative oxidation bed.

The operating process employs the principle of regenerative heat exchange between a gas (ventilation air) and a solid (bed of honeycomb ceramic). One cycle of the process is comprised of two flow reversals, so each flow reversal is a half-cycle. Referring to Fig. (**1**), assume that during the first half-cycle both the control valves 1 and 4 are open while the control valves 2 and 3 are closed. Thus, the flow through the reactor takes place from bottom to top. After a time interval, the reactor reverses flow direction by closing the control valves 1 and 4 and opening the control valves 2 and 3. Flow then takes place from top to bottom.

To start the operation, the burned hot gas coming from the heating and starting system preheat the middle of the regenerative oxidation bed to the temperature required to initiate methane oxidation (above 900°C) or hotter. This preheating process takes about experiences dozens of hours. After completion of the preheating process, VAM at ambient temperature enters and flows through the oxidation bed in one direction, and its temperature increases until oxidation of the methane takes place near the center of the oxidation bed. The hot oxidate continue through the oxidation bed, transferring heat to the far side of the oxidation bed. When the far side of the oxidation bed is sufficiently hot, the reactor automatically reverses the direction of VAM. The VAM now enters the far (hot) side of the oxidation bed, where it is heated gradually to auto-oxidation temperatures near the center of the oxidation bed and then oxidizes.

Fig. (**2**) shows the schematic of the heating and starting system, which consists of two parts, one is the hot gas production and adjustment system, the other is the hot gas distribution system. The burned gas coming from the burner and the air coming from the blower are mixed in hot gas mixing chamber firstly. In the hot gas mixing chamber, a thermocouple is used to measure the temperature of the mixing hot gas. And in order to get some certain temperature of the mixing hot gas, a valve is needed to control the mass flow of the air. Fig. (**3**) shows the sectional view of the middle part of the regenerative oxidation bed. The manifolds placed in the center of the oxidation bed have many holes through which the hot gas is distributed uniformly. In order to reduce workload, only one manifold is chosen to be studied in this paper, as shown in Fig. (**4**).

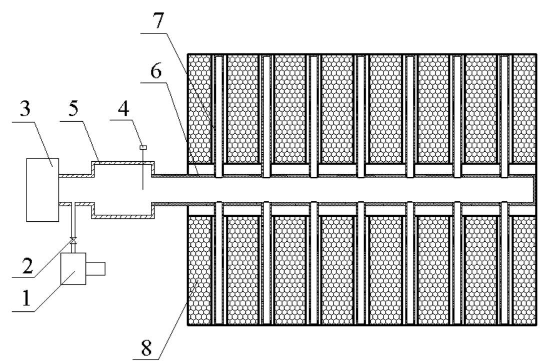

Fig. (2). The schematic diagram of the system of heating and starting (1-blower; 2-valve; 3-burner; 4-thermocouple; 5-hot gas mixing chamber; 6- main pipe; 7-manifold; 8- honeycomb ceramic).

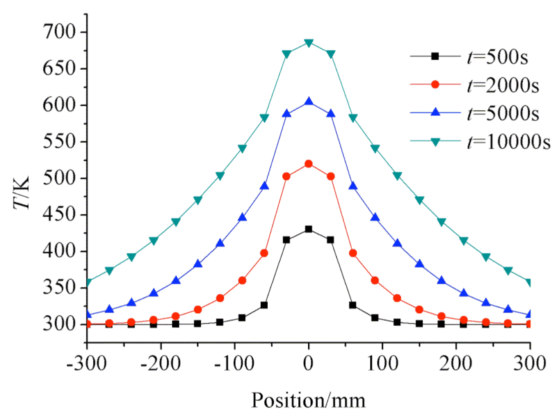

Fig. (3). The schematic diagram of the regenerative oxidation bed.

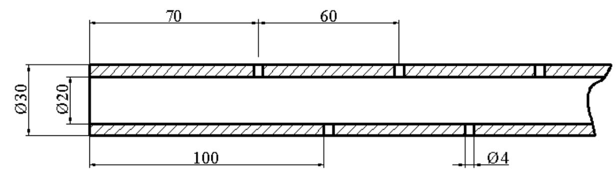

Fig. (4). The sketch of the manifold.

3. GOVERNING EQUATION

For the mathematical analysis, the following basic assumptions are made: (a) the honeycomb ceramic is assumed as porous media; (b) the mass and heat fluxes of the hot air through the holes are uniform; (c) the hot air is compressible and its thermophysical properties are designed as piecewise-linear of temperature, and is listed in Table **1**; (d) the radiation of the hot air is negligible; (e) the gas flow in porous media is assumed to be laminar; (f) the thermophysical properties of all porous media are taken to be constants.

Table 1. The Thermophysical Properties of the Hot Gas

$\frac{T}{K}$	$\frac{\rho}{kg/m^3}$	$\frac{c_p}{kJ/(kg\cdot k)}$	$\frac{\lambda\times10^2}{W/(m\cdot K)}$	$\frac{\mu\times10^6}{kg/(m\cdot s)}$
273	1.293	1.005	2.44	17.2
473	0.746	1.026	3.93	26.0
673	0.524	1.068	5.21	33.0
873	0.404	1.114	6.22	39.1
1073	0.329	1.156	7.18	44.3
1273	0.277	1.185	8.07	49.0

Based on these assumptions, the governing conservation equations used in this simulation calculation to solve the problems are given as follows.

For a three-dimensional, unsteady state and laminar flow system, the continuity equation can be written as

$$\frac{\partial \rho_g}{\partial t} + \nabla(\rho_g \vec{v}) = 0 \tag{1}$$

where ρ_g is the hot gas density, kg·m^{-3}; v is the hot gas velocity, m·s^{-1}.

The momentum conservation equation of the gas in porous media can be described by the Darcy law

$$\nabla p = -\frac{\mu}{\alpha}\vec{v} \tag{2}$$

in which, α is permeability of porous media; μ is the hot gas viscosity, pa·s.

The temperature between gas and solid is different during the preheating process, so separate energy equations for the two phases are introduced [15, 16]. Solid phase energy equation is expressed as

$$(1-\varphi)(\rho c)_s \frac{\partial T_s}{\partial t} = (1-\varphi)\nabla\cdot(\lambda_s \nabla T_s) + h(T_g - T_s) - \nabla\cdot\vec{q} \tag{3}$$

in which, T is temperature, K; c is specific heat, J·kg^{-1}·K^{-1}; h is volumetric the heat transfer coefficient, W·m^{-3}·K^{-1}; ϕ is porosity; q is radiative heat flux, W·m^{-2}; λ is thermal conductivity of the medium, W·m^{-1}·K^{-1}. The subscripts "g" and "s" stand for gas and solid phase, respectively.

Gas phase energy equation is expressed as,

$$\varphi(\rho c_p)_g \frac{\partial T_g}{\partial t} + (\rho c_p)_g V\cdot\nabla T_g = \varphi\nabla\cdot(\lambda_g \nabla T_g) + h(T_g + T_s) \tag{4}$$

The porous media in this study is considered as a gray medium. The heat source term due to radiation that appears in equation (3) is calculated by,

$$\nabla\cdot\vec{q} = \kappa\left\{4\pi I_b\left[T(\vec{r})\right] - \int I(\vec{r},\vec{s})\,d\Omega\right\} \tag{5}$$

where κ is the absorption coefficient, m^{-1}; Ω is solid angle, sr; I is radiation intensity, W·m^{-2}, calculated by

$$(\vec{s}\cdot\nabla)I(\vec{r},\vec{s}) = -\beta I(\vec{r},\vec{s}) + \kappa I_b(\vec{r}) + \frac{\sigma_s}{4\pi}\int_{4\pi} I(\vec{r},\vec{s})\phi(s' \to \vec{s})\,d\Omega \tag{6}$$

where β is the extinction coefficient, m^{-1}; σ_s is the scattering coefficient, m^{-1}.

4. NUMERICAL METHOD

The three-dimensional coupled heat transfer problem is solved using the software FLUENT6.2. Laminar flow is assumed for the gas flow in porous media and the K-ε turbulent model is used in the numerical calculations for the turbulent flow in the manifold. Pressure and velocity are coupled by the SIMPLE algorithm. The discrete ordinate method (DOM) is used to solve the radiative transfer equation [17, 18].

Because the hot air is compressible, so the mass flow boundary is used for the inlet boundary condition of the manifold.

For the hot air

$$q_0 = q_{in},\ T_0 = T_{in} \tag{7}$$

T_{in}, q_{in} are initial temperature and mass flow of the hot air. Initially, the porous media is at room temperature throughout.

At the inner wall of the manifold, coupled thermal conditions is chosen, where

$$T_g = T_w \tag{8}$$

T_g is the temperature of the hot air nearby the inner wall of the manifold, T_w is the temperature of the inner wall of the manifold.

At the regenerative oxidation bed wall, the usual no-slip and impenetrability condition is applied. These surfaces are assumed to be gray, emitting and reflecting diffusely. Therefore, the boundary intensity for outgoing direction is

$$I(\vec{r}) = \varepsilon I_b(\vec{r}) + \frac{1-\varepsilon}{\pi} \int_{\vec{s}\cdot n \le 0} I(\vec{r},\vec{s}) |\vec{s}\cdot n| \, d\Omega \quad (9)$$

where n and ε are unit vector normal to the surface and emissivity, respectively.

The top and bottom of the regenerative oxidation bed are defined as outlet, where pressure outlet boundary is introduced due to the reverse flow of the hot gas. And the radiation transfer between the porous media and environment is considered.

$$(1-\varphi)\lambda_s \frac{\partial T_s}{\partial z} = -\varepsilon\, \sigma\left(T_s^4 - T_0^4\right), \; I = \frac{\sigma T_s^4}{\pi} \quad (10)$$

5. RESUILTS AND DISCUSSION

Because the regenerative oxidation bed is structure symmetrical along the vertical direction, as shown in Fig. (**1**). And the hot gas is distributed through the hot gas distribution system located in the middle of the regenerative oxidation bed. So the top of the regenerative oxidation bed is chosen in the following analysis at the heating and starting stage. Fig. (**5**) shows the temperature difference between gas and solid phase in the regenerative oxidation bed at the conditions of T_{in}=1200K, q_{in}=0.00155kg·s^{-1}. In Fig. (**5**), the x-coordinate represents the position in the regenerative oxidation bed along the vertical direction and the middle of the regenerative oxidation bed is defined at x = 0. The y-coordinate represents the change of temperature. It can be seen that the temperature of gas is higher than the solid's. Along the vertical direction, the difference of temperature becomes smaller gradually, which means the heat transfer between the two phases is more completely.

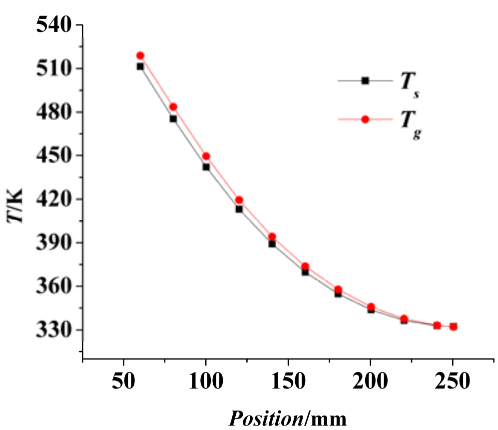

Fig. (5). The temperature of gas and solid phase.

5.1. Ways of Preheating of the Porous Media

Fig. (**6**) shows the changes of different ways of preheating during the preheating process. It can be seen that the porous media can be preheated directly by the hot gas passing through the manifold and the heat transfer between the outer wall of the manifold and the porous media. Besides, Fig. (**6**) shows that the heat mass flow passing through the manifold is less than 40% at the beginning of the preheating process, but it increases with the increase in heating time. Within the first 100s, because the temperature of the outer wall of the manifold is less than that of hot gas outside of the manifold, the heat flow between the outer wall of the manifold and the porous media keeps zero. The heat transfer between the outer wall of the manifold and the porous media reaches to the biggest value at the time of 1000s, and then it turns down and becomes smaller and smaller with the increase of the preheating time.

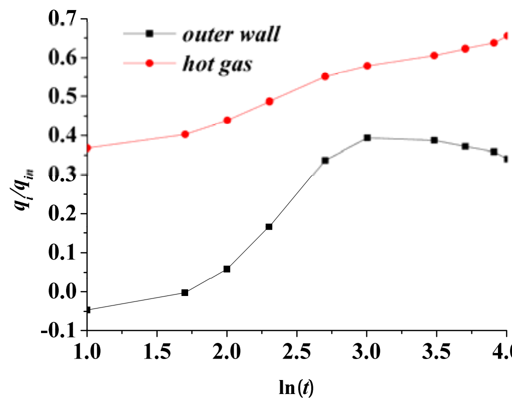

Fig. (6). The changes of different ways of preheating during the preheating process.

The transient temperature distribution of porous media for various inlet mass flows is shown in Fig. (**7**). It is seen that the temperature of the regenerative oxidation bed increases with the increase in inlet mass flow during preheating process. This phenomenon can be understood as that the greater the inlet mass flow is, the more heat energy is transported to the porous media within one unit time.

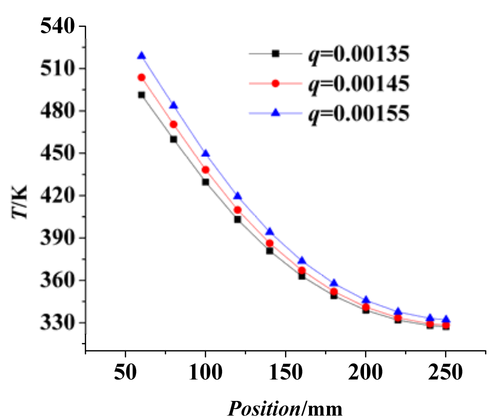

Fig. (7). The temperature distribution for different inlet mass flow.

5.2. Influence of Specific Heat of the Porous Media

Fig. (**8**) illustrates the effect of specific heat of the porous media on the temperature of the outlet at different time. The conditions are: T_{in}=1200K, q_{in}=0.00155kg·s^{-1}. From Fig. (**8**), it can be seen that the temperature of the outlet decreases significantly with the increase in the specific heat after the bed is preheated for a long time. At the time of 3000s, the temperature difference is even over 50K.

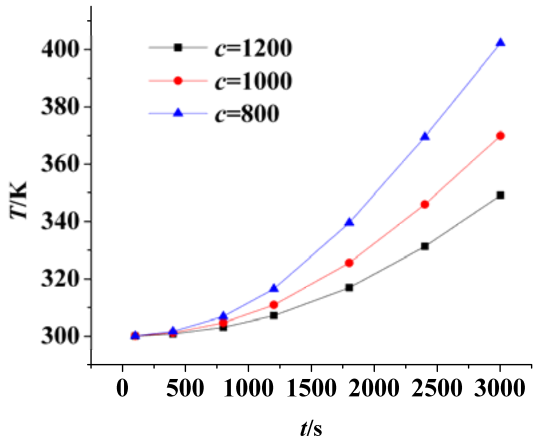

Fig. (8). The outlet temperature of porous media for different specific heat.

This fact can be explained that specific heat is an important parameter affecting the heat storage capacity of porous media. The larger the specific heat is chosen, the greater the heat storage capacity will be gained. That is to say when the inlet mass flow fixed, more heat energy would be stored by the regenerative oxidation bed with high specific heat.

5.3. Influence of Porosity

At the conditions of T_{in}=1200K, q_{in}=0.00155kg·s^{-1}, t=2000s, the effects the porosity of the porous media on the heat transfer are shown in Fig. (**9**). It can be seen that the trends of temperature distribution for different porosity along the vertical direction of the regenerative oxidation bed are similar. But the higher porosity, the higher temperature profile for the regenerative oxidation bed.

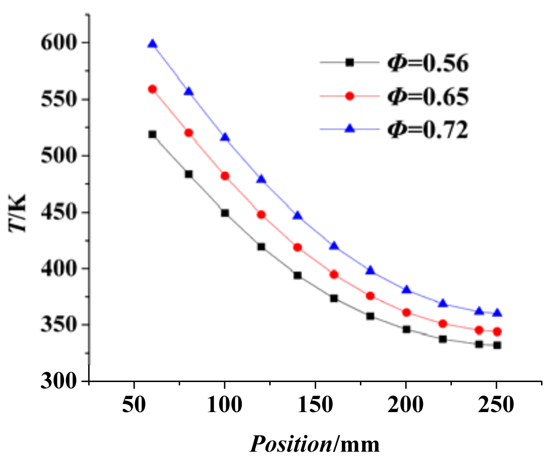

Fig. (9). The temperature distribution for different porosity.

The reasons are explained as follows. The higher porosity is, the smaller density for certain volumetric porous media is. So the heat storage capacity of porous media would decreases with the decrease in density, and the temperature will rise quickly along the vertical direction in the regenerative oxidation bed accordingly, resulting in the temperature of the outlet increase and more heat energy loss.

5.4. Influence of Radiation Heat Transfer

Fig. (**10**) shows the difference of enthalpy distribution along the vertical direction in the centerline of the regenerative oxidation bed for considering the influence of radiation or not at the conditions of T_{in}=1200K, q_{in}=0.00155kg·s^{-1}, t=1600s. The enthalpy without the radiation heat transfer initially is higher than that with the radiation heat transfer. Then the difference between them decreases gradually along the vertical direction in the centerline of the regenerative oxidation bed. After x=142mm, the enthalpy without the radiation heat transfer is smaller than that with the radiation heat transfer. This can be explained as follows. When the radiation is not care in the heating process, the heat transfer in the porous media just by conduction and convection, leading to less heat transfer along the vertical direction in the regenerative oxidation bed. So radiation takes an important role in the process of heat transfer, it is must be taken into account when the transient heat transfer in porous media is analyzed.

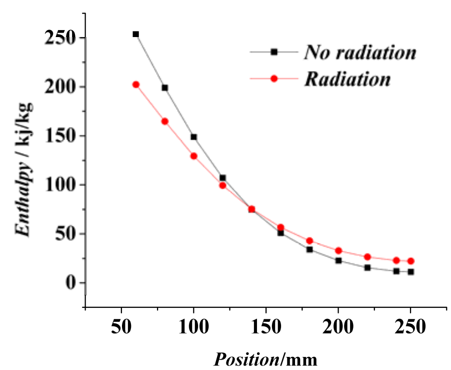

Fig. (10). The changes of enthalpy for considering the influence of radiation or not.

5.5. The Temperature Distribution of the Regenerative Oxidation Bed

Fig. (**11**) indicates the changes of temperature distribution of the regenerative oxidation bed along the direction of

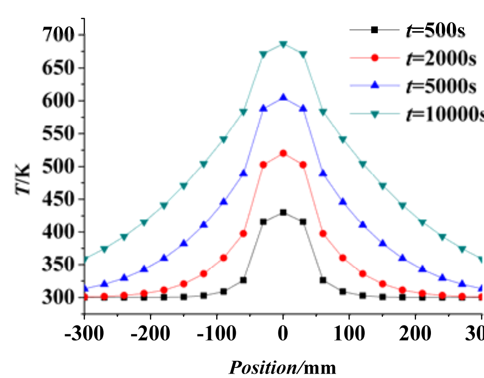

Fig. (11). The changes of temperature distribution of the regenerative oxidation bed (along the direction of height in the middle facet of it).

height in the middle facet of it during the preheating process. It can be seen that the temperature is the highest in the middle of the regenerative oxidation bed, and it decreases gradually along the direction of height. With the preheating process progresses, the outlet temperature of the regenerative oxidation bed is increasing, which leads to the loss of more energy.

6. CONCLUSIONS

A numerical study is performed to explore the transient preheating process of the regenerative oxidation bed heated by the burned gas generated from a burner placed outside. The main conclusions are summarized as follows.

When the burned gas initially flows into the regenerative oxidation bed, the temperature of the gas is higher than the solid's. The difference of temperature becomes smaller gradually with the heat transfer going on. The hot gas passing through the manifold is the main resource of the heat to preheat the regenerative oxidation bed. Increasing the inlet mass flow of the pipe could shorten the time of preheating. As the main parameters of porous media, specific heat and porosity have a great influence on the heat storage capacity of the regenerative oxidation bed. The larger the specific heat is, the greater the heat storage capacity for the regenerative oxidation bed will be. While the porosity has an opposite effect on the heat storage capacity. The importance of solid phase radiation on the temperature profiles in porous media is numerically assessed, whose contribution on heat transfer in the preheating process can not be ignored. The temperature is the highest in the middle of the regenerative oxidation bed, and it decreases gradually along the direction of height of the regenerative oxidation bed.

REFERENCES

[1] G. Q. Niu, "Prospect and utilization status of Low concentration gas in vitiated air at mine", *Ind. Safety Environ. Prot.*, vol. 28, pp. 3-5, 2002.

[2] Pablo Marin, Miguel A. G. Hevia, Salvador Ordonez and Fernando V, "Combustion of methane lean mixture reverse flow reactors: comparison between packed and structured catalyst beds", *Catalysis Today*, vol. 105, pp. 701-708, 2005.

[3] S. Su, J. Agnew, "Catalytic combustion of coal mine ventilation air methane", *Fuel,* vol. 85, pp. 1201-1210, 2006.

[4] S. Su, A. Beath, H. Guo, and Cliff Mallettet, "Characteristics of coal mine ventilation air flows", *J. Env. Manag*., vol. 86, pp. 44-62, 2008.

[5] B. ZHeng, Y. Q. Liu, "Oxidation of coal mine ventilation air methane in thermal reverse-flow reactor", *J. China Coal Soc.*, vol. 34, pp. 1475-1478, 2009.

[6] T. N. Haynes, C. Georgakis, and H. S. Caram, "The design of reverse flow reactors for catalytic combustion systems", *Chem. Eng. Sci.*, vol. 50, pp. 401-416, 1995.

[7] Y. Q. Liu, R. X. Liu, ZH. Q. Gao, "*Coal mine ventilation air methane thermal flow-reversal reactor*", CHINA. Patent ZL2,008,102,498,60.3, December 27, 2008.

[8] T. W. Tong, and S. B. Sathe, "Heat transfer characteristics of porous radiant burners", *Heat Transfer*, vol. 113, pp. 423-428, 1991.

[9] I. Malico, and J. C. F. Pereira, "Numerical study on the influence of radiative properties in porous media combustion", *J. Heat Transfer*, vol. 123, pp. 951-957, 2001.

[10] P. Talukdar, S. C. Mishra, D. Trimis, and F. Durst, "Combined radiation and convection heat transfer in a porous channel bounded by isothermal parallel plates", *Int. J. Heat Mass Transfer*, vol. 47, pp. 1001-1013, 2004.

[11] Y. T. Yang, and M. L. Hwang, "Numerical simulation of turbulent fluid flow and heat transfer characteristics in heat exchangers fitted with porous media", *Int. J. Heat Mass Transfer*, vol. 52, pp. 2956-2965, 2009.

[12] K. Ichimiya, and T. Matsuda, "Effects of a porous medium on local heat transfer and fluid flow in a forced convection field", *Heat Mass Transfer*, vol. 40, pp. 1567-1576, 1997.

[13] C. Ben Kheder, B. Cherif and M. S. Sifaoui, "Numerical study of transient heat transfer in semitransparent porous medium", *Renewable Energy*, vol. 27, pp. 543-560, 2002.

[14] P. Talukdar, S. C. Mishraa, D. Trimisb, and F. Durst, "Combined radiation and convection heat transfer in a porous channel bounded by isothermal parallel plates", *J. Quant. Spectrosc. Radiat. Transfer*, vol. 47, pp. 1001-1013, 2004.

[15] M. Farzaneh, R. Ebrahimi, M. Shams, and M. Shafiey, "Two-dimensional numerical simulation of combustion and heat transfer in porous burners", *Eng. Lett.*, vol. 15, No. 2, EL_15_2_28, 2007.

[16] H. Amiri, S. H. Mansouri, and A. Safavinejad, "Combined conductive and radiative heat transfer in an anisotropic scattering participating medium with irregular geometries", *Int. J. Therm. Sci.*, vol. 49, pp. 492-503, 2010.

[17] A. A. Mohamad, "Local analytical discrete ordinate method for the solution of the radiative transfer equation", *Int. J. Heat Mass Transfer*, vol. 39, pp. 1859-1864, 1996.

[18] P. X. Jiang, and X. C. Lu, "Numerical simulation and theoretical analysis of thermal boundary characteristics of convection heat transfer in porous media", *Int. J. Heat Fluid Flow*, vol. 28, pp. 1144-1156, 2007.

Tooth Modification of Spur Bevel Gear

Alok Sunder Mohanty, *Department of Mechanical Engineering, Aryan Institute of Engineering & Technology, Bhubaneswar, aloksundar75@gmail.com*

Subhasis Sarkar, *Department of Mechanical Engineering, NM Institute of Engineering & Technology, Bhubaneswar, subhasissarkar14@yahoo.co.in*

Jagruti Swain, *Department of Civil Engineering, Capital Engineering College, Bhubaneswar, jagrutiswain26@yahoo.co.in*

Abstract: Isometric modification is proposed as a new method of axial modification of spur bevel gear. Based on the gear geometry theory and the normal meshing motion equation of gear pairs, changes of meshing points and angles are analyzed and the effect of axial modification on meshing movement of gear pairs is discussed. After that, a method of drawing spherical involute with the aid of SolidWorks software is achieved, by which the accuracy of solid modeling of spur bevel gear is improved. After solid modeling, bevel gear analysis is carried out by ANSYS/LS-DYNA software so that the contact stress and acceleration changes of driven wheel during the meshing process which was used to guide the modification of spur bevel gear can be calculated. The simulation results show that the stress distribution of gear surface is controlled by tooth modification. The load concentration, agglutination and pitting of the gear can be avoided effectively.

Keywords: Solid modeling, tooth modification, spur bevel gear, finite element analysis (FEA).

INTRODUCTION

Spur bevel gears can be utilized to transmit rotary motions between the orthogonal intersecting axes and they are usually applied to decelerate, differential operations, etc. The special use of spur bevel gear calls for high driving accuracy and transmission stability. However, it is difficult to avoid the impact and load concentration of a pair of meshing gears due to many complex factors such as the variety range of bearing amplitudes, manufacture and installation tolerances, contact deformations, bending deflections and torsional deformations of the shaft and bearing clearances, etc. To abate these problems, one can increase the size of shaft, the hardness of bearing or support as well as restrict the width of every gear. Apart from these, another effective method of axial modification was developed recently.

Dynamic simulation analysis will be operated explicitly with the nonlinear software ANSYS/LS-DYNA in this paper. Compared with static analysis, the results of dynamic analysis will reveal much more specific meshing situation [1-4]. In spite of this, accurate solid modeling remains the basis of dynamic simulation. The spherical involute can not be obtained directly through 3D software and therefore the plane involute or the three-point arc is often used instead. In this sense, the accuracy of solid modeling can not be guaranteed. This paper will endeavor to propose a method of drawing spherical involute and to get an accurate model of spur bevel gear.

ISOMETRIC MODIFICATION OF SPUR BEVEL GEAR

Isometric modification, as the name implies, is a method of axial modification of the standard tooth with the aim to create a new surface in normal direction [5, 6]. The new surface will contact with the standard tooth instead of the original one. Therefore, the contact area of the gear can be controlled by both the position and the size of isometric modification. Fig. (**1**) is the schematic diagram of isometric modification. As is shown in Fig. (**1**), Σ is the non-modified tooth surface, Σ' is the modified tooth surface, *p* is a point in surface Σ and point *p* is in surface Σ', h stands for the size of modification, that is, the distance between P and *p*'.

The advantages of isometric modification include improving the contact area, avoiding the contact at the edge and reducing the impact caused by load change and the sensitivity of assembling error.

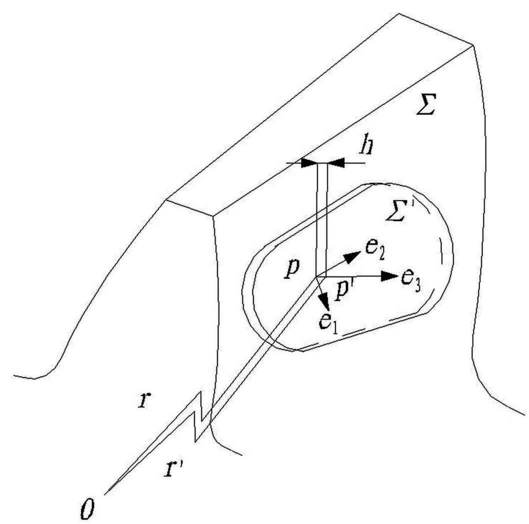

Fig. (1). Schematic diagram of isometric modification.

When a gear pair is in normal contact, the ideal contact area will take up 40-70% along the tooth height and 35-65% along the tooth length. The size and position of the contour of isometric modification can be determined on the basis of the ideal contact area. Fig. (**2**) is the schematic diagram of the contour shape and position of isometric modification.

The size of h plays a decisive role in the effect of isometric modification. If the size is too big, the contact area will decrease and the load concentration will increase, on the contrary, the target of modification can not be reached. From the above, many factors should be considered to determine the size, including manufacture and installation tolerances, contact deformations, bending and torsional deformations of the shaft, hot deformations in high-speed operation, etc. Mechanics of Materials, elastic mechanics theory and numerical method can be utilized to calculate the size but all of the three methods are very complex. H is always determined by one's experience in practical work and the recommended size is 0.03~0.05 mm or 0.004~0.005m (m is the modulus) [7].

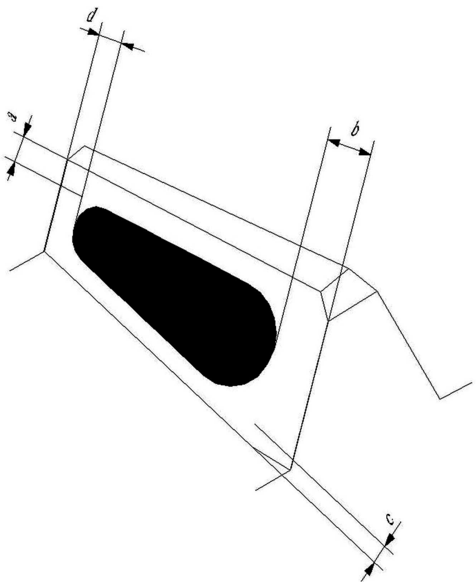

Fig. (2). Schematic diagram of the contour shape and position of isometric modification.

INVOLUTE CHARACTERISTICS OF ISOMETRIC MODIFICATION GEAR

Fig. (**3**) is the schematic diagram of the characteristics of the involute. According to the principle of involute forming, the generating line KN is the normal of the involute at the point N and the size of modification y is uniform in the normal direction. Therefore, the new profile is still an involute profile that meets the requirements of modification.

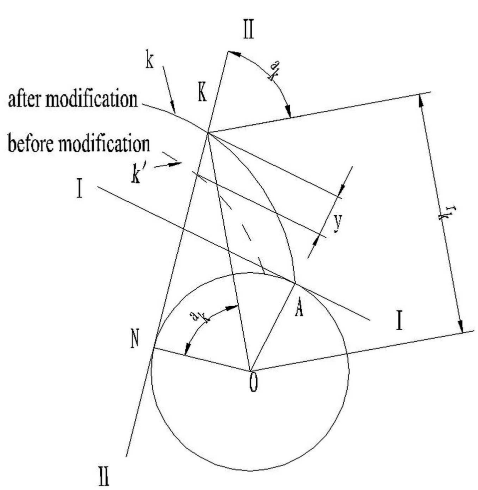

Fig. (3). Schematic diagram of involute characteristics.

MESHING OF ISOMETRIC MODIFICATION SPUR BEVEL GEAR

On the basis of the gear geometry theory and the normal meshing motion equation of gear pairs, changes of meshing points and angles can be analyzed with the help of isometric modification.

Position of Meshing Point

As is shown in Fig. (**1**), e_1, e_2 are unit vectors in tooth depth and width of point P, e_3 is surface Σ's unit vector in the normal direction, point O is in the rotation axis, r, r' are vectors of O to P and P'.

The changes of the normal direction are caused by different modification sizes h. After isometric modification, surface Σ is parallel to surface Σ' with h which is a constant magnitude, that is to say, the normal direction of the gear surface does not change.

Denote δ_1, δ_2, δ_3 as the variable quantities of the meshing point in the direction of e_1, e_2, e_3. The variable position of the meshing point caused by the change of the tooth thickness is shown as follows:

$$r' = (r + e_3 h) + \mathrm{d}r + e_3\delta_3 + e_3\mathrm{d}h \tag{1}$$

With the theory of differential geometry, calculate the second derivative of radius vector $r(u,v)$.

$$\mathrm{d}^2 r = r_{uu}\mathrm{d}u^2 + 2r_{uv}\mathrm{d}u\mathrm{d}v + r_{vv}\mathrm{d}v^2 \tag{2}$$

n is the unit normal vector. Define $\mathrm{d}^2 r \cdot n$ as the second basic form of surface [8], thus $n = r_u \times r_v \Big/ \sqrt{(r_u \times r_v)^2}$. The second form can also be expressed as follows:

$$\varphi_{II} = c_{11}\delta_1^2 + c_{12}\delta_1\delta_2 + c_{22}\delta_2^2 \tag{3}$$

In Eq. (3), c_{11}, c_{22} respectively represent the induced normal curvatures in the direction of e_1, e_2; c_{12} is the negative induction geodesic torsion in the direction of e_1.

Therefore, δ_3 can be expressed as follows:

$$\delta_3 = \frac{1}{2}\varphi_{II} = \frac{1}{2}(c_{11}\delta_1^2 + c_{12}\delta_1\delta_2 + c_{22}\delta_2^2) \tag{4}$$

Known from Eq. (4), δ_3 is the second-order small element and the changed position of the meshing point has little effect on the rotational angle of the gear pair.

Rotational Angle

The angle tolerance of a gear can be measured through a comprehensive survey instrument. Denote Φ_1 as the angle of the master gear, Φ_2 is the theoretical angle of the measured gear before modification, Φ_2' is the actual angle of the measured gear after modification, $\Delta\Phi_2$ is the angle variation caused by modification. Obviously,

$$\Phi_2' = \Phi_2 + \Delta\Phi_2 \tag{5}$$

Denote r_1', r_2' as the vectors of the master gear and the measured gear respectively. The gear pair will reach the actual meshing point P_1', P_2' when r_1', r_2' turn around the certain angle Φ_1, Φ_2. Known from Eq. (1)

$$p_1' = p_1 + e_3 h^{(1)} + \left(e_1\delta_1^{(1)} + e_2\delta_2^{(1)}\right) + e_3\delta_3^{(1)} \tag{6}$$

$$p_2' = p_2 + e_3 h^{(2)} + \left(e_1\delta_1^{(2)} + e_2\delta_2^{(2)}\right) + e_3\delta_3^{(2)} + e_3\delta_3^{(2)} + e_3 \mathrm{d}h^{(2)} + k_2 \times p_2 \Delta\Phi_2 \tag{7}$$

Where P_1, P_2 are respectively the points on the tooth surfaces of the master gear and the non-modified measured gear; k_2 is the equivalent gear's rotation vector of the measured bevel gear and it is in the same direction with e_3.

The modified gear pair should meet the requirement as follows:

$$p_1' - p_2' = p_1 - p_2 \tag{8}$$

After finishing, to

$$(k_2 \times p_2)\Delta\Phi_2 e_3 = h^{(2)} + \left(\delta_3^{(1)} - \delta_3^{(2)}\right) \tag{9}$$

Known from Eq. (4), δ_3 is a second-order small element and the term $\delta_3^{(1)} - \delta_3^{(2)}$ in Eq. (9) can be neglected. $(k_2 \times p_2)e_3$ stands for the basic circle radius and $\Delta\Phi_2$ can be expressed as follows:

$$\Delta\Phi_2 = \frac{h}{R} \tag{10}$$

The establishment of the relationship between angle change and modification size provides not only the basis for calculation and the selection of the modification size, but also reference for the detection of the modification effect in the future work.

ACCURATE SOLID MODELING OF SPUR BEVEL GEAR

The basic idea of modeling is solving spherical involute equation, generating curve in the 3D software SolidWorks, filling surface and creating tooth space entities, arraying and cutting entities combined with gear matrix [9, 10]. The modeling details of differential planetary gear will be listed in the following example.

Solution to the Involute Equation

The spherical involute equation in Cartesian coordinate system is presented as follows:

$$\begin{aligned} x &= l(\sin\varphi\sin\phi + \cos\varphi\cos\phi\cos\theta) \\ y &= l(\sin\varphi\cos\phi\sin\theta - \cos\varphi\sin\phi) \\ z &= l\cos\varphi\cos\theta \end{aligned} \tag{11}$$

Where $\sqrt{x^2+y^2+z^2} = l$; $\phi = \varphi\sin\theta$; l is the initial radius of the gear; θ is the base angle; φ is the angle between the starting line which is on the contact surface and the instantaneous rotor. When the starting point of the involute is on the base circle bevel, $\varphi = 0$.

Take a differential bevel gear for instance. Its parameters are shown in Table **1**.

Table1. Parameters of Differential Bevel Gears

Parameters	Planet Gear	Half Axle Gear
Shaft angle	90°	
Tooth number	10	15
Module	4.438	
Pressure angle	22.5	
Reference diameter	44.38	66.57
Outer cone distance	40±0.025	
Reference circle cone angle	33.69°	56.31°
Tip circle cone angle	46°	66°
Root circle cone angle	24°	44°
Addendum	4.98	3.28
Tooth depth	9.17	9.17

Solve the coordinates of x, y, z under the condition that φ is in [0, π/3] according to Eq. (11). The corresponding Matlab program is as follows:

```
clc; clear;
z1=10; % Tooth number of planetary gear
z2=15; % Tooth number of axle gear
m=4.438; % Gear module
r=m*(sqrt(z1^2+z2^2))/2; % Outer cone distance
l=r+5; % Initial radius of gear
alpha=22.5*pi/180; % Pressure angle
theta=33.69*pi/180; % Pitch angle
gamma=asin(sin(theta)*cos(alpha)); % Base angle
counter=0;
for t=0:0.01:1 % Step is 0.01
phi=t*pi/3; % Angle between the starting line which is on the contact surface and the instantaneous rotor
counter=counter+1;
x=l*cos(phi*sin(gamma))*cos(gamma)*cos(phi)+l*sin(phi*sin(gamma))*cos(phi);
y=l*cos(phi*sin(gamma))*sin(gamma)*sin(phi)-l*sin(phi*sin(gamma))*cos(phi);
z=l*cos(phi*sin(gamma))*cos(gamma);
D(counter,1)=phi;
D(counter,2:4)=[x y z];
End
```

The calculation results are shown in Fig. (**4**).

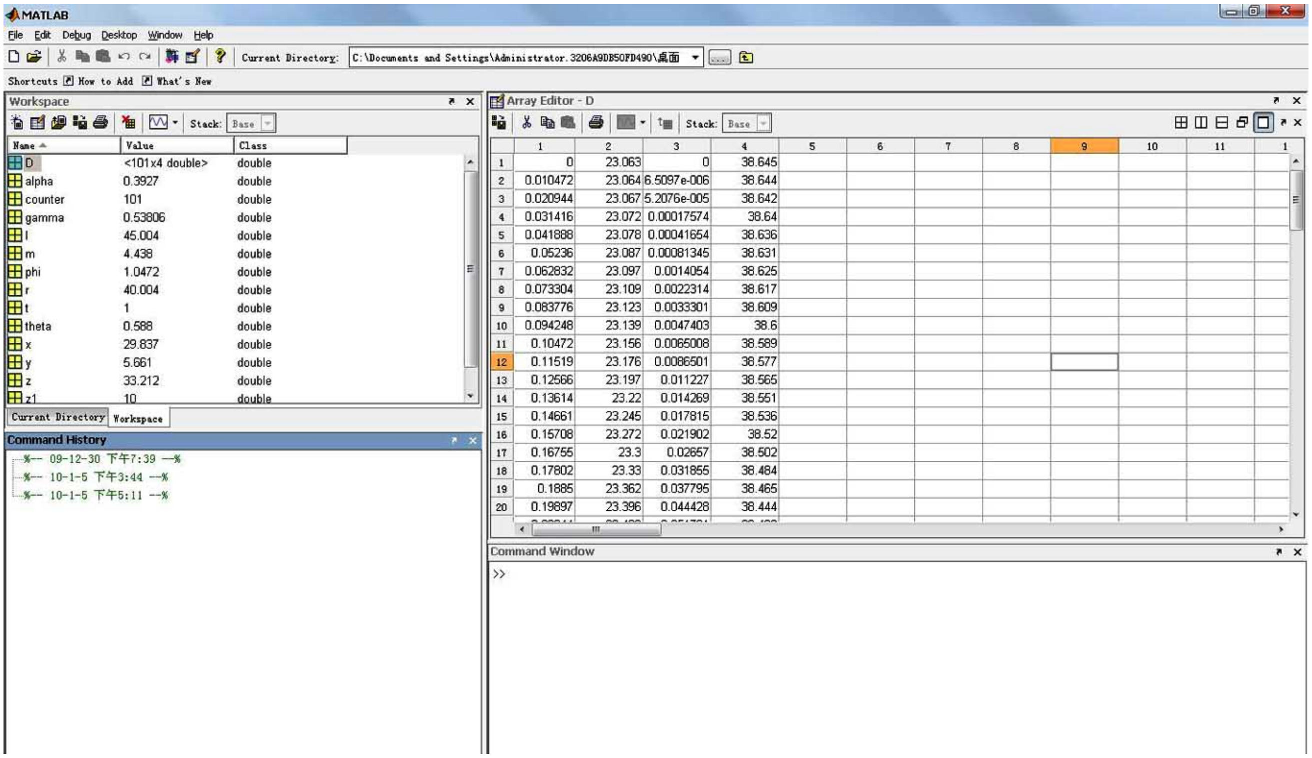

Fig. (4). Calculation results.

Create Entity of Spur Bevel Gear

First, create a new part drawn in SolidWorks, then choose "curve by xyz point" under the command of "curve" and the spherical involute will be formed by importing *x*, *y*, *z* coordinates. Next, generate a closed interval by connecting the starting and the end point of the involute, then fill the closed interval and the tooth surface will be obtained. Then, a base level should be determined according to the width of tooth space. The two-dimensional figures of the gear entity can be drawn on this base level. The base level can also be used as a symmetric plane of the tooth surface which is shown in Fig. (**5**). Fig. (**6**) is the schematic diagram of addendum and tooth root surface, which is generated by rotating the two-dimensional figure.

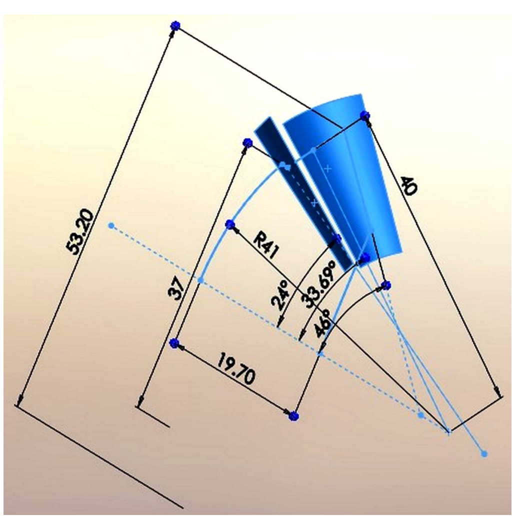

Fig. (5). Symmetric tooth surface.

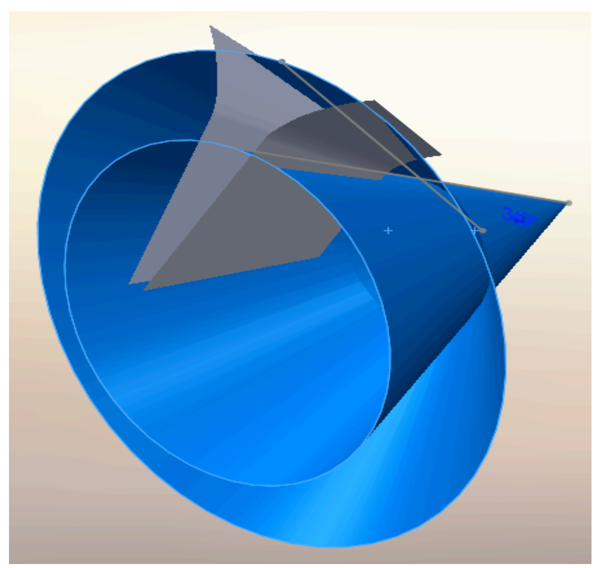

Fig. (6). Addendum and tooth root surface.

To get the entity of tooth space, the surface of addendum and tooth root should be trimmed and filled. After circularly arraying, the entity is obtained as is shown in Fig. (**7**).

Finally, the entity of spur bevel gear is obtained by cutting the combination of the gear matrix. Fig. (**8**) shows the solid model of a planetary gear.

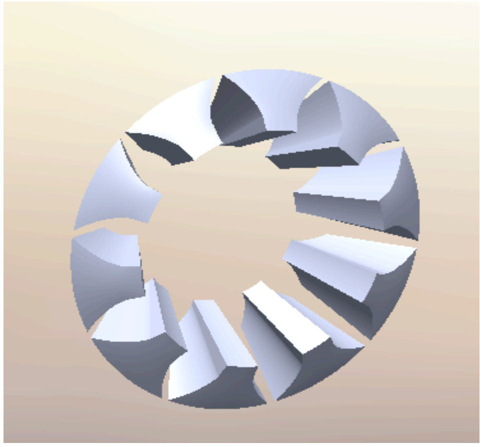

Fig. (7). Entity of tooth space.

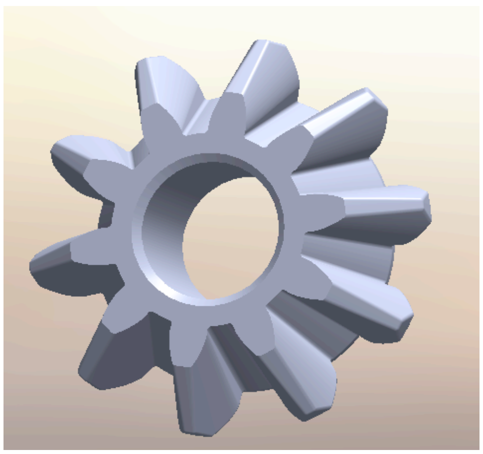

Fig. (8). Solid model of planetary gear.

Build the Model of Isometric Modification Gear

Draw a closed curve in tooth section in the interfical environment of sketch editing, and then withdraw it from the edit mode. Fig. (**9**) shows the two-dimensional schematic diagram of the closed curve.

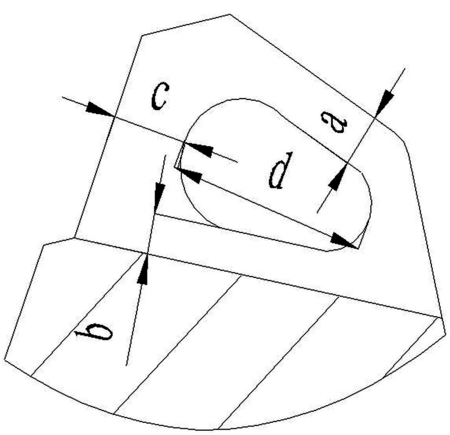

Fig. (9). Two-dimensional schematic diagram of closed curve.

Execute the order “tension-to a surface in a specified distance”. Set the distance according to the modification size *h* and the new surface is the isometric modification surface, as is shown in Fig. (**10**).

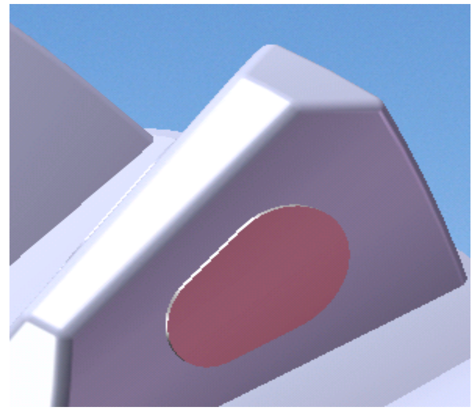

Fig. (10). Isometric modification surface.

DYNAMIC SIMULATION OF SPUR BEVEL GEAR

Basic Theory of Gear Simulation

As for the gear pair, the meshed gears will not only have to meet the elasticity equation, but also have to satisfy the displacement of embedded conditions in the normal direction of the meshing point and obey the law of coulomb in the tangent direction. According to the contact statement, the contact surfaces can be divided into three kinds of boundary conditions as long as the input torque of driving gear does not change, namely the continuous state, the sliding state and the separation state. The gear pair can be divided into the drive and the driving gear, which are two separate objects. The finite element equations of the two gears can be established in the global coordinate. The equations are as follows:

$$\begin{aligned} K_1U_1 &= P_1R_1 \\ K_2U_2 &= P_2R_2 \end{aligned} \tag{12}$$

Where K_1, K_2 are the rigidity matrixes of the drive and the driving gear, U_1, U_2 are the displacement vectors of the drive and the driving gear, P_1, P_2 are the load vectors force on the drive and the driving gear, R_1, R_2 are the contact load vectors.

In the local coordinate (x, y), we respectively apply *r* and *u* to represent the contact node and the displacement components of the meshing point *i,* which is in the direction of *j*. Therefore,

In continuous state,

$$\begin{aligned} r_{ij}^{)(2} &= -r_{ij}^{1} \\ u_{ix}^{)(2} &= u_{ix}^{1} + \delta_{ix} \quad (j = x, y) \\ u_{iy}^{)(2} &= u_{iy}^{1} + \delta_{iy} \end{aligned} \tag{13}$$

In sliding state,

$$\begin{aligned} r_{ij}^{(2)} &= -r_{ij}^{(1)} \\ u_{ix}^{(2)} &= u_{ix}^{(1)} + \delta_{ix} \quad (j = x, y) \\ R_{iy} &= \pm u \left| R_{ix} \right| \end{aligned} \tag{14}$$

In separation state,

$$r_{ij}^{(2)} = -r_{ij}^{1} = 0 \quad (j = x, y) \tag{15}$$

Where u is the friction coefficient, δ_{ix} is the initial clearance in the normal direction of the meshing point i, δ_{iy} is the initial clearance in the tangent direction of the meshing point i, R_{ix} is the contact load in the normal direction of the meshing point i, R_{iy} is the contact load in the tangent direction of the meshing point i.

Fundamental Assumptions of Gear Meshing Procession

Before simulation, a collection of fundamental assumptions, which the simulation scheme has to satisfy, should be listed:

1. The material of the gear has the characteristics of continuity, linear elasticity, uniformity and isotropy.
2. The deformation of the meshing point is along the normal direction of the tooth profile. The contact load is along the normal direction of the tooth surface. The contact interface is in a smooth and continuous fashion.
3. The gear that used in simulation is in an ideal model in which manufacture and installation tolerances are excluded. The mechanical and geometric boundary conditions of the contact interface can be denoted by node parameters.
4. Thermal deformation of the transmission system and the elastic hydrodynamic lubrication mechanism are out of consideration. Lubrication is represented by the friction coefficient and the friction coefficient should obey the law of coulomb.

Simulation Procedures

Dynamic simulation analysis of spur bevel gear is operated explicitly with the nonlinear software ANSYS/LS-DYNA [11, 12]. Fig. (**11**) is a procedure chart of the application of Solid Works- ANSYS-DYNA.

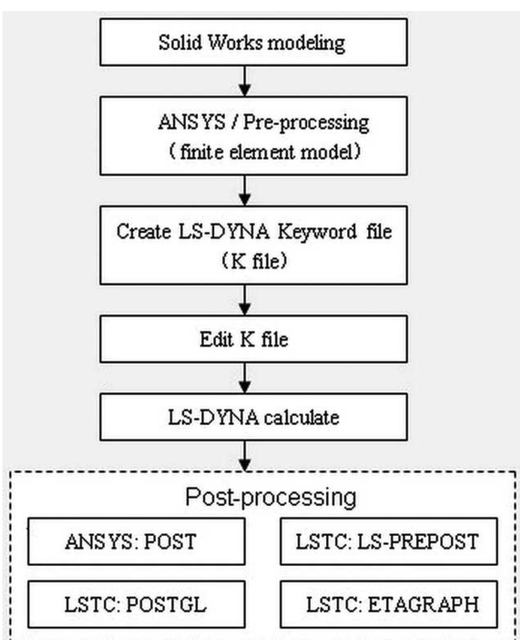

Fig. (11). Procedure chart of the application of Solid Works-ANSYS-DYNA.

The assembly model of a gear pair which is created by SolidWorks can be imported into ANSYS/LS-DYNA in the manner of "Parasolid". In ANSYS/LS-DYNA, penalty function is used to deal with contact information and its principles are as follows: Check whether the associate node penetrates the main surface. If it does, a contact force should be introduced between the associate node and the main surface. In physics, there is a normal spring between the associate node and the main surface, which is used to avoid penetrating. The size of the contact force is proportional to the penetration depth and the hardness of the main surface. The contact force is expressed by the value of the penalty function. Penalty function method has many advantages such as little hourglass effect, little numerical noise and exact algorithm conservation of momentum. Because of these factors, dynamic analysis results can clearly show the specific meshing situation.

The simulation procedures consist of three main steps: Pre-processing, Solution to dynamic analysis and Post-processing.

Pre-processing includes defining element type, setting real constants, choosing material model, meshing and defining contact, and load and constraints.

When the assembly model was introduced into ANSYS/ LS-DYNA, the properties of the material should be defined. Set the differential gear as an example. Its material is 20CrMnTiH, its elastic modulus is 207GPa, the density is $7.8 \times 10^3 kg/m^3$ and the Poisson ratio is 0.25.

Elements SOLID164 and SHELL163 are adopted in this paper. SOLID164 is used for 3D modeling of solid structures. It is defined by eight nodes which have the following degrees of freedom at each node: translations, velocities, and accelerations in the nodal x, y, and z directions. SOLID164 does not have rotational degrees of freedom, so SHELL163 is needed in order to apply angular velocity and torque to gear pair. SHELL163 is a 4-node element with both bending and membrane capabilities. It is permitted both in-plane and normal loads. The element has 12 degrees of freedom at each node. They are translations, accelerations, and velocities in the nodal x, y, and z directions and rotations about the nodal x, y, and z-axes [13].

Many factors must be taken into consideration before meshing, such as the number of grid, the meshing density, the unit order, the meshing quality, the interface and demarcation point of grid, the grid distribution and the coordination of displacement. To improve the accuracy of the simulation, the grid in both the tooth root and the mating surface should be designed more sophisticated. Fig. (**12**) is the schematic diagram of the meshed gear pair.

The torque and the speed are all parameters of time. As a result, the array of time, the torque and the speed should be defined and assigned. After that, angular velocity is applied to planetary gear and the negative torque is applied to axle gear. The axial displacement of the two gears must be restricted when a gear pair is meshing. The load command is "EDLOAD, Option, Lab, KEY, Cname, Par1, Par2, PHASE, LCID, SCALE, BTIME, DTIME".

Control parameters should be assigned before getting a solution, such as the control of the calculation time, the control of the output file and the advanced control of the solution. The termination time of calculation is set according to angular velocity of the gear (termination time is very short in the physical process, generally in milliseconds). In time-step control, the calculation time of CPU will increase if the time step is too small. Mass scaling is an effective way to control minimum time step and to cut down the calculation time of CPU. Mass scaling is only used in elements which are smaller than minimum time step, that is to say, the minimum time step should be a negative value. The types of output file are ".RST"、".HIS"、"d3plot" and "d3thdt" and they can be used in post-processor POST1, POST26 of ANSYS and LS-Prepost of LS-DYNA.

The purpose of isometric modification is to control the stress distribution and to compensate tooth deformation. The additional dynamic load is the direct result of tooth deformation, and therefore, messages of stress distribution and acceleration are needed. The special post-processor Ls-prepost can meet these requirements.

Fig. (**13**) is the dynamic stress nephogram of the meshing of a gear pair. Known from Fig. (**13**), the stress distribution is not uniform ,and the load concentration is in the big end. For these reasons, pitting, wearing and other tooth injuries will appear and the lifespan of gear will also be reduced. These aspects are usually caused by tooth deformation, which is mainly caused by the different curvature in the big end and the small end. In addition, manufacture and installation tolerances, bending and torsional deformations of the shaft, hot deformations in high-speed operation will exacerbate them. In order to improve these aspects, one can apply axial modification as a good way.

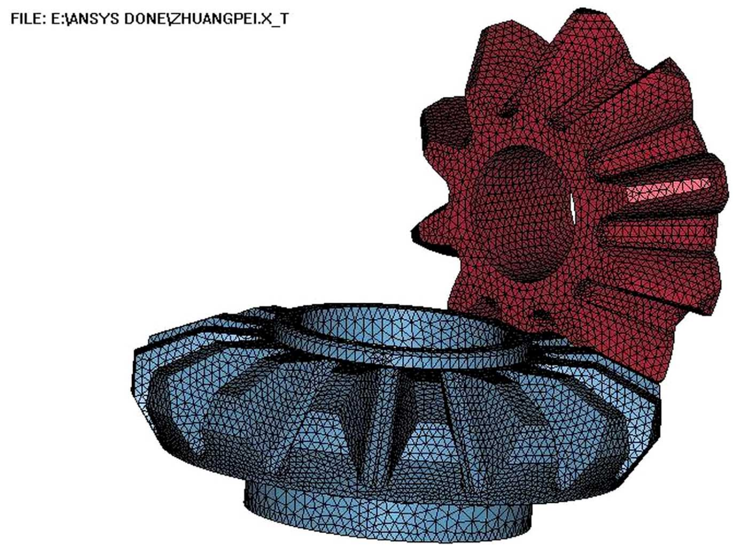

Fig. (12). Schematic diagram of meshed gear pair.

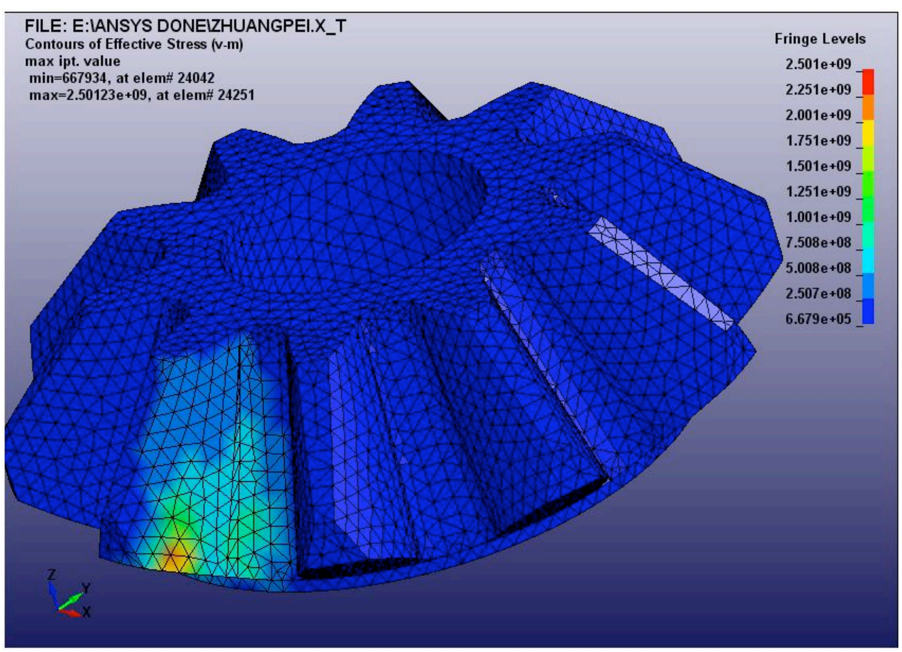

Fig. (13). Diagram of stress distribution before modification.

EFFECTS OF ISOMETRIC MODIFICATION

The characteristics of the strain and stress of planetary gear and axle shaft gear are similar. Only planetary gear's messages are listed in this paper.

Fig. (**14**) and (**15**) are the diagrams of stress distribution after isometric modification and the planetary gear's stress distribution curve in tooth width after isometric modification. Known from Fig. (**14**) and (**15**), the contact area and stress distribution are controlled effectively by axial modification in the direction of the tooth width. The maximum effective stress has a slight increase after modification while the effective stress that in the big end is reduced and the contact area is improved.

Many factors such as the manufacture and installation tolerances, contact deformations, bending and torsional deformations of the shaft, and hot deformations in high-speed operation are difficult to avoid for the reason that the base pitch is no longer equal. Transmission ratio is also changed and the additional dynamic load, vibration, noise, impact will appear [14]. Fig. (**16**) shows the angular acceleration

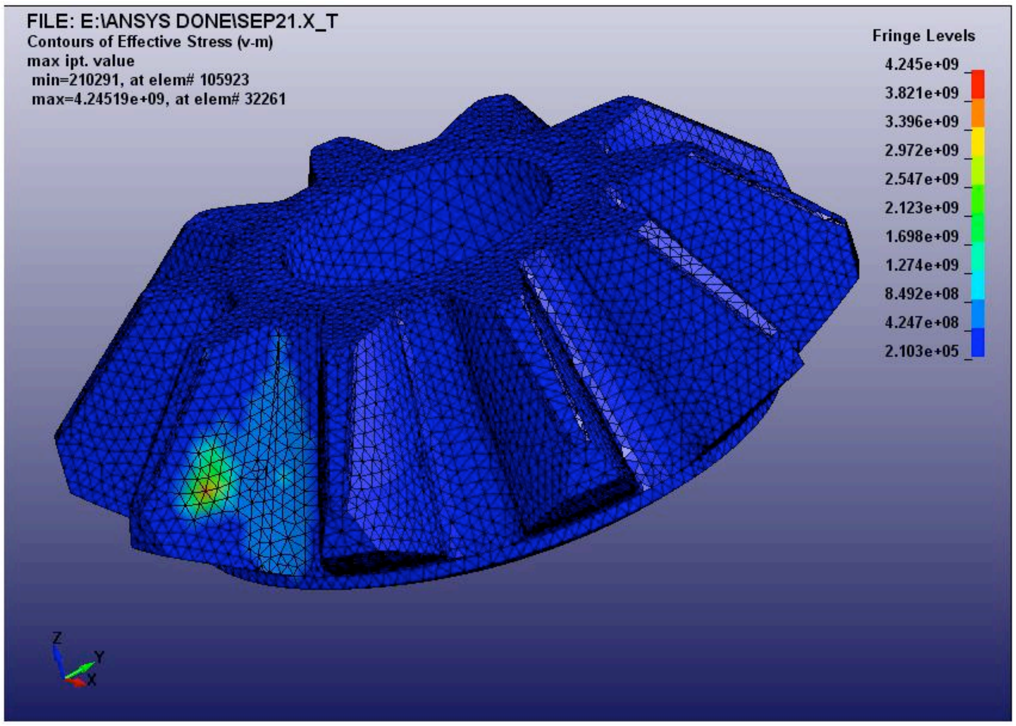

Fig. (14). Diagram of stress distribution after isometric modification.

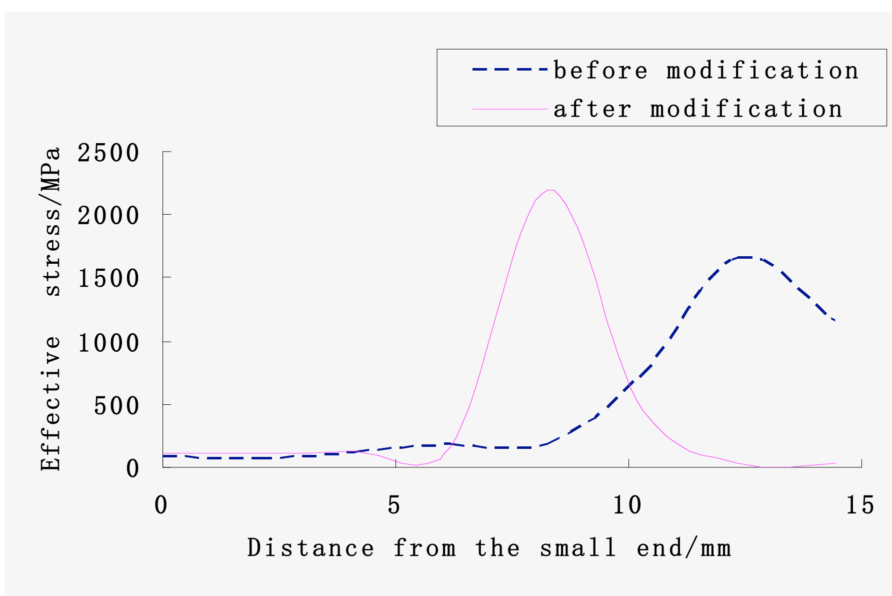

Fig. (15). Planetary gear's stress distribution curve in tooth width after isometric modification.

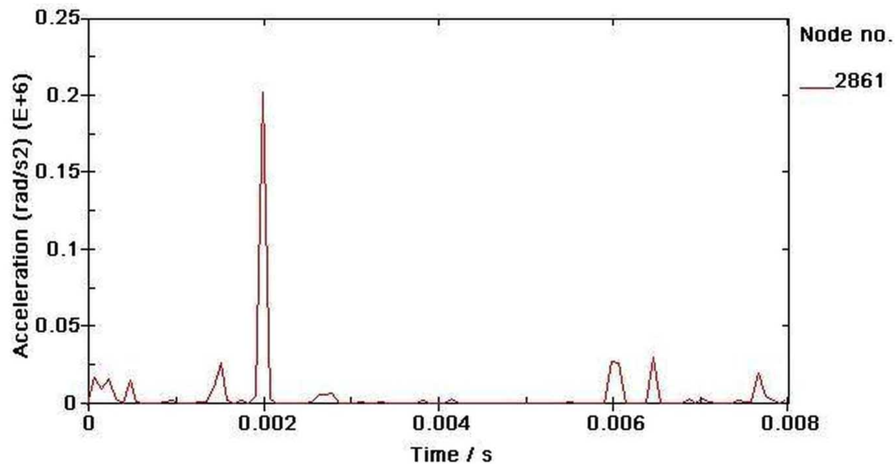

(**a**) Before modification

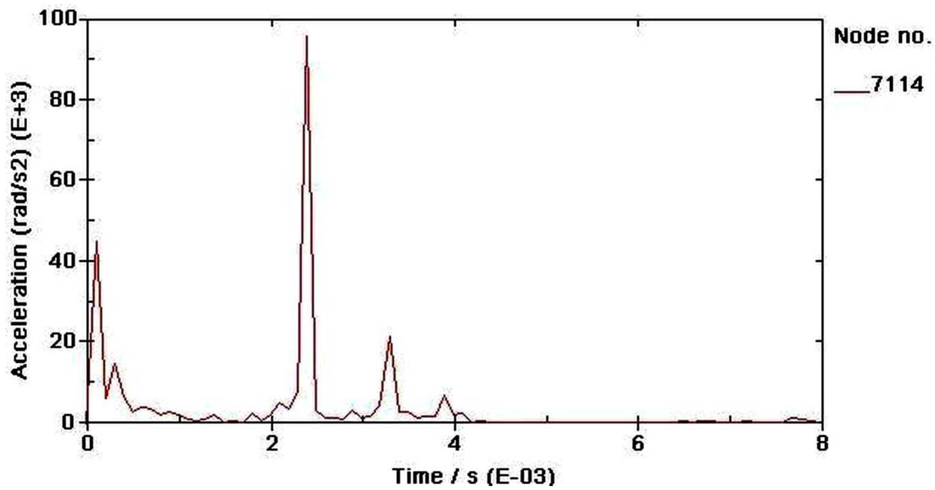

(**b**) After modification

Fig. (16). Angular acceleration curve of one point on the top land.

curve of one point on the top land before and after modification. The curve can obviously reflect the influence that the modification has generated. Known from Fig. (**16**), the additional load is reduced significantly by isometric modification and the maximum angular acceleration is changed from 0.205×10^6 rad/s^2 before modification to 0.098×10^6 rad/s^2 after modification; and the size has depreciated by 52.2%. Vibration and noise will also be reduced.

SUMMARY

Through the combination of both experience and the traditional theory of gear modification, the concept of isometric modification was proposed. By selecting the appropriate modification size and modification location, tooth deformation would be compensated and the stress distribution would be controlled in the central part of the tooth; the load concentration, agglutination, pitting of the gear could also be avoided effectively.

According to the gear geometry theory and the normal meshing motion equation of gear pairs, changes of meshing points and angles were analyzed, and then, the effect of axial modification on gear pair's meshing movement was discussed. The establishment of the relationship between angle changes and modification size provided not only the basis for calculation and the selection of the modification size, but also a reference for the detection of modification effect in the future work.

Based on the 3D software SolidWorks, a method of drawing spherical involute was achieved, and the solid modeling accuracy of spur bevel gear was improved. After solid modeling, dynamic emulation analysis was operated by FEA software. The analytical results had shown that stress distribution was controlled by isometric modification and the additional load was reduced effectively.

This technology has been applied in small batch production of automobile differential bevel gear, and the results showed that the modified gears' kinematic accuracy and motion smoothness accuracy were up to 7 degree (GB11365-89), the lifespan of gear was increased by more than 10%. The users' feedback showed that the meshing noise of gears has significantly decreased.

REFERENCES

[1] A. Kahaman, "Dynamic analysis of multi-mesh helical gear train", ASME, *Journal of Mechanical Design*, vol. 116, pp. 35-37, 1994.

[2] V. Ramamurti, Nayak H. Vijayendra, and C. Sujatha, "Static and dynamic analysis of spur and bevel gears using FEM", *Mechanism and Machine Theory*, vol. 33, pp. 1177-1193, 1998.

[3] R. F. Li, and C. Y. Yang, "Finite element simulation of the dynamical behavior of a speed-increase gearbox", *Journal of Materials Processing Technology*, vol. 150, pp. 170-174, 2004.

[4] S.-W. Zhou, L.-X. Guo, S.-Q. Zhang, and C.-Y. Tang, "Study on cervical spine injuries in vehicle side impact", *The Open Mechanical Engineering Journal*, vol. 4, pp. 29-35, 2010.

[5] N. Sigg, "Tooth profile modification of high speed duty gear", In: *Proceedings of International Conference on Gearing*, 1958, pp. 313-316.

[6] B. W. Dudlcy, *Handbook of Practical Gear Design*. New York: McGraw-Hill Co, 1984.

[7] Gear Guide Editorial, *Gear Guide*, Beijing: China Machine Press, 2000.

[8] F. L. Litvin, *Gear Geometry and Applied Theory*, New Jersey: Prentice Hall PTR, 1994.

[9] J. Wang, and I. Howard, "The torsional of involute spur gears", *Journal of Mechanical Engineering Science*, vol. 218, pp. 131-142, 2004.

[10] J. Wang, and I. Howard, "FEA of high contact ratio spur gears in mesh", *Journal of Tribology*, vol. 127, pp. 469-483, 2005.

[11] S. J. Nalluveettil, and G. Muthuveerappan, "Finite element modeling and analysis of a straight bevel gear", *Computers & Structures*, vol. 48, pp. 739-744, 1993.

[12] J. D. Andrews, "A finite element analysis of bending stresses induced in external and internal involute spur gears", *Journal of Strain in Analysis*, vol. 26, pp. 153-163, 1991.

[13] Livemore Software Technology Corporation, *LS-DYNA Keyword User's Manual*, 2001.

[14] H. N. Ozguven, and D. R. Houser, "Mathematical models used in gear dynamics", *Journal of Sound and Vibration*, vol. 121, pp. 383-411, 1988.

Analysis on Jet Characteristics of Combined Plasma Arc

Nirmal Charan Mallik, *Department of Mechanical Engineering, Aryan Institute of Engineering & Technology, Bhubaneswar, nirmal_m26@gmail.com*

Chinmay Swain, *Department of Mechanical Engineering, Raajdhani Engineering College, Bhubaneswar, chinmayswain1972@gmail.com*

Saswati Nayak, *Department of Mechanical Engineering, Capital Engineering College, Bhubaneswar, saswatinayak2574@gmail.com*

Jyotikusum Acharya, *Department of Civil Engineering, NM Institute of Engineering & Technology, Bhubaneswar, jyotikusumacharya@yahoo.co.in*

Abstract: A three-dimensional axisymmetric mathematical model, including the influence of the swirl exiting in the plasma torch, was developed to describe the heat transfer and fluid flow within a combined plasma arc. In the model, a mapping method and a meshing method of variable step-size were adopted to mesh the calculation domain and to improve the results precision. To overcome a problem from a coexistence of non-transferred arc and transfer arc and a complicated interaction between electric, magnetic, heat flow and fluid flow phenomena in the combined plasma arc, a sequential coupling method and a physical environment approach were introduced into the finite element analysis on jet characteristics of the combined plasma arc. Furthermore, the jet characteristics of combined plasma arc such as temperature, velocity, current density and electromagnetic force were studied; the effects of working current, gas flow and the distance from the nozzle outlet to the anode on the distributions of temperature, velocity and current density were also revealed. Compared with the collection and diagnosis on the combined plasma arc by CCD, the results show that the simulated value appears to be in good agreement with measured value, and the temperature of combined plasma arc is much dependent on the working current, while is less sensitive to the argon flow rate and the distance from the nozzle outlet to the workpiece anode.

Keywords: Combined plasma arc, jet characteristics, numerical simulation, plasma diagnosis.

1. INTRODUCTION

Plasma arc has generally been applied to material processing such as plasma welding, plasma cutting, plasma spraying, etc. Its jet characteristic has a crucial and direct influence on above processing quality. However, the generation of plasma arc involves complex physical phenomena, such as electromagnetic, heat flow and fluid flow, etc. Furthermore, the behavior of the coupling between these physical phenomena makes it quite difficult to grasp the distributions of temperature, velocity and current density of plasma arc with experimental methods. Aimed at above problem, numerical simulation method has been applied to plasma arc and it is proved feasible by some investigations. Westhoff and Szekely [1] made a numerical analysis of fluid, heat flow and electromagnetic phenomena in a non transferred arc plasma torch. Though provided an important finding that the electromagnetic forces may markedly modify the velocity profiles and may significantly affect the swirl of the plasma, they assumed the cathode tip as flat rather than pointed. Bauchire *et al*. [2] modeled a DC non-transferred plasma arc both in laminar and turbulent flow and found the result of the laminar flow model was more agreement with experimental measurements, while current density distribution was assumed when electromagnetic field being analyzed. Seungho Paik *et al*. [3] also made a numerical analysis of non transferred plasma arc with the Steenbeck theory, and investigated the effect of arc root position on the temperature and fluid flow of DC non-transferred plasma torch. In addition, Ushio *et al*. [4,5] made a numerical simulation on the distribution of velocity and temperature in the non-constricted transferred plasma based on continuous equation, momentum equations, energy equation and Maxwell equation. Lu *et al*. [6,7] established an integral mathematic model of fluid flow and heat transfer of GTAW transferred arc and weld pool, and analyzed the behavior of transferred arc and weld pool including arc temperature field and current density distribution with finite element method. Especially, Yin *et al*. [8] developed a two-dimensional mathematical model to research the behavior of the transferred argon plasma arc constricted by a torch. The model also took the plasma arc as laminar flow and included the torch region to consider the influence of cathode figure and the restricted role of the nozzle.

Up to now, many studies on the jet characteristics of transferred plasma arc and non-transferred plasma arc have been published, however, little attentions are given to a numerical simulation of the combined plasma arc. Furthermore, as an ideal heat source, combined plasma arc has been generally applied to precise welding and also involves complex physical phenomena. Therefore, it is necessary to make a numerical analysis on the combined plasma arc. Unfortunately, it is quite difficult to apply above methods to simulate the combined plasma arc, due to the coexistence of non-transferred arc and transfer arc and the more complicated coupling between electric, magnetic, heat flow and fluid flow phenomena in the combined plasma arc. In this paper, a three-dimensional axisymmetric mathematical model on the combined plasma arc is established according to the theories of magneto- hydrodynamics (MHD) and electromagnetics, and is solved with the finite element methods including a sequential coupling method and a physical environment approach. In this model, a conservation of azimuthal momentum is introduced to avoid the assumption of plasma flow independent of the swirl existing in combined plasma arc. A mapping method and a variable step-size meshing method are also adopted to improve the calculation precision. Moreover, the distributions of the current density, electromagnetic force, temperature and velocity of combined plasma arc are described. The influence of processing parameters, such as working current, argon flow rate and the distance from the nozzle outlet to the workpiece anode on above distributions are also investigated. As well as, the simulated results are compared with the measured values obtained from the collection and diagnosis on the combined plasma arc by CCD.

2. MODELING APPROACH

Calculation Domain

Fig. (**1**) presents a schematic sketch of a combined plasma arc. Firstly, the non-transferred arc between the tungsten cathode and the nozzle is be ignited, then the transferred arc between the tungsten cathode and anode workpiece is also ignited. Consequentially, the combined plasma arc will be generated. Being a main working arc, the transferred arc plays a key role in the combined plasma arc, and non transferred arc can remarkably improve the stability of the transferred arc. Wherefore, it can be seen that the combined plasma arc consists of a non-transferred arc and a transferred arc, and results in a complicated coupling between physical phenomena such as electricity, magnetism, heat and force, etc. In order to objectively simulate the generation of combined plasma arc as much as possible, and to ensure boundary conditions easily determined, the calculation domain of the combined plasma arc is shown in Fig. (**2**). The whole calculation domain can be divided into the domain of electromagnetic field and the domain of flow field, as well as each domain is composed of a domain of non-transferred arc and a domain of non-transferred arc. The domain of ABCDEIJKLB is used for solving the electromagnetic field in non-transferred arc, and the domain of AEFGHIJKLBCDE is used for solving the electromagnetic field in transferred arc. To avoid an assumption of the current density distribution on the cathode surface, the tungsten cathode ABCDE is included into above both calculation domains. In addition, the domain of BCDEFGHIJKLB is used for solving the fluid field in the combined plasma arc.

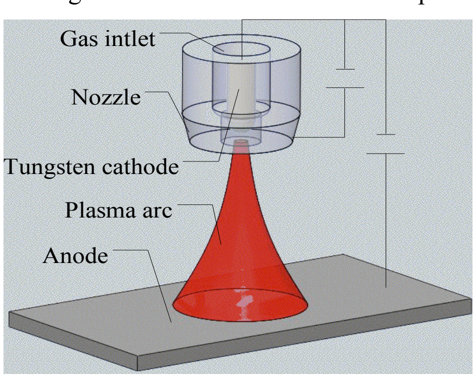

Fig. (1). Schematic of the combined plasma arc.

In order to establish a mathematical model of the combined plasma arc and to simplify its calculation, the following assumptions have to be summarized as follows:

1. The plasma arc is assumed to be pure argon in local thermodynamic equilibrium (LTE), which is taken to mean that electron and heavy particle temperature are not significantly different.
2. The plasma arc is radially axisymmetric and its flow is laminar, which is reasonable for the operating conditions considered.
3. The heating effects of viscous dissipation and compressibility effects are negligible.
4. The plasma arc is steady and optically thin to radiation, so the governing equations are not time dependent.

MHD Equations

With above-mentioned assumptions, a group of magnetohydrodynamics equations are expressed in terms of cylindrical coordinates as follows:

Equation of Mass Continuity

$$\frac{1}{r}\frac{\partial(r\rho v)}{\partial r}+\frac{\partial(\rho u)}{\partial z}=0 \tag{1}$$

where ρ is the mass density of the gas, u and v are axial and radial velocity, respectively.

Conservation of Axial Momentum

$$\frac{1}{r}\frac{\partial}{\partial r}(\rho r u v)+\frac{\partial}{\partial z}(\rho u^2)=-\frac{\partial P}{\partial z}+j_r B_\theta+\frac{\partial}{\partial z}\left(2\mu\frac{\partial u}{\partial z}\right)+\frac{1}{r}\frac{\partial}{\partial r}\left(r\mu\left(\frac{\partial v}{\partial z}+\frac{\partial u}{\partial r}\right)\right)+\rho g \tag{2}$$

where P is pressure, j_r is radial component of the current density, B_θ is self-induced magnetic field intensity, μ is the gas viscosity, g is the acceleration of gravity.

Conservation of Radial Momentum

$$\frac{1}{r}\frac{\partial}{\partial r}(r\rho v^2)+\frac{\partial}{\partial z}(\rho u v)=-\frac{\partial P}{\partial r}-j_z B_\theta+\rho\frac{w^2}{r}-2\mu\frac{v}{r^2}+\frac{\partial}{\partial r}\left(2\mu r\frac{\partial v}{\partial r}\right)+\frac{\partial}{\partial z}\left(\mu\left(\frac{\partial v}{\partial z}+\frac{\partial u}{\partial r}\right)\right) \tag{3}$$

where w is the azimuthal velocity, j_z is the axial component of the current density vector. The terms of $j_r B_\theta$ and $j_z B_\theta$ are the electromagnetic forces, where **J** is the current density vector and **B** is the magnetic flux density vector.

Conservation of Azimuthal Momentum

$$\frac{1}{r}\frac{\partial}{\partial r}(r\rho v w)+\frac{\partial}{\partial z}(\rho u v)+\rho\frac{vw}{r}=\frac{1}{r}\frac{\partial}{\partial r}\left(\mu r^2\frac{\partial}{\partial r}\left(\frac{w}{r}\right)\right)+\mu\frac{\partial}{\partial r}\left(\frac{w}{r}\right)+\frac{\partial}{\partial z}\left(\mu\frac{\partial w}{\partial z}\right) \tag{4}$$

Conservation of Energy

$$\frac{1}{r}\frac{\partial}{\partial r}(r\rho v T)+\frac{\partial}{\partial z}(\rho u T)=\frac{1}{r}\frac{\partial}{\partial r}\left(\frac{rk}{c_p}\frac{\partial T}{\partial r}\right)-S+\frac{\partial}{\partial z}\left(\frac{k}{c_p}\frac{\partial T}{\partial z}\right)+\frac{5k_b}{2e}\left(j_r\frac{\partial T}{\partial r}+j_z\frac{\partial T}{\partial z}\right)+\frac{j_r^2+j_z^2}{\sigma} \tag{5}$$

where T is temperature, c_p is specific heat, σ is electric conductivity, k is thermal conductivity, k_b is Boltzman constant, e is electronic charge, and S is the volumetric radiative loss term.

Maxwell Equations

There exit Lorentz force terms in above momentum equations. Moreover, the energy equation contains the joule heating term and an additional term which represents the transport of electron enthalpy due to the drift of electrons. Therefore, it is necessary to solve Maxwell equations for the electromagnetic field.

Current Continuity Equation

$$\frac{1}{r}\frac{\partial}{\partial r}\left(r\sigma\frac{\partial\phi}{\partial r}\right)+\frac{\partial}{\partial z}\left(\sigma\frac{\partial\phi}{\partial z}\right)=0 \tag{6}$$

where Φ is the electrical potential.

Ohm's Law

$$j_r=-\sigma\frac{\partial\phi}{\partial r}\;;\quad j_z=-\sigma\frac{\partial\phi}{\partial z} \tag{7}$$

Ampere's Law

$$\frac{1}{r}\frac{\partial}{\partial r}(rB_\theta)=\mu_0 j_z \tag{8}$$

where μ_0 is the vacuum permeability ($4\pi\times10^{-7}$H/m).

According to the characteristic of non-transferred arc coexisting with transferred arc in the combined plasma arc, it is necessary to apply a sequential coupling method. That is to say, the solving process of above MHD equations and Maxwell equations can be divided into one stage when non-transferred arc is calculated and another stage when transferred arc is solved. When the distributions of the current density, temperature and velocity in the first stage are introduced into the second stage, then iteratively calculated, the solution of above mathematical model of combined plasma arc will be convergent. Consequentially, the distributions of electromagnetic field and fluid field in the combined plasma arc will be also obtained.

3. FINITE ELEMENT ANALYSIS

Owing to the complicated interaction of electric field, magnetic field, flow field and thermal field and the coupling of physical phenomena such as electric, magnetic, heat flow and fluid flow, etc in the combined plasma arc, it is difficult to simulate the combined plasma arc with conventional methods. In this section, the physical environment approach has to be introduced into the analysis of above mathematical model of combined plasma arc. Firstly, current density distribution is obtained from the electric field, which is loaded into the magnetic field in succession. Then electromagnetic coupling computation is performed to gained Lorenz force and Joule heat, which are loaded into the flow field as its body force and volume heating subsequently. Finally, the temperature and velocity of the combined plasma arc are acquired through coupling computation of flow field and thermal field. Repeatedly, coupling computation of electric field, magnetic field, flow field and thermal field is carried out until results convergence.

Mesh Generation

The thermophysical properties of working gas must be considered before above calculation domains are meshed. In this paper, argon is taken as the working gas of combined plasma arc. However, its electric and thermodynamic properties are strongly temperature dependent, including density, constant pressure specific heat, viscosity, electrical and thermal conductivities and radiation losses. The relationship between above properties with temperature can be ascertained from the expression of Szekely [9].

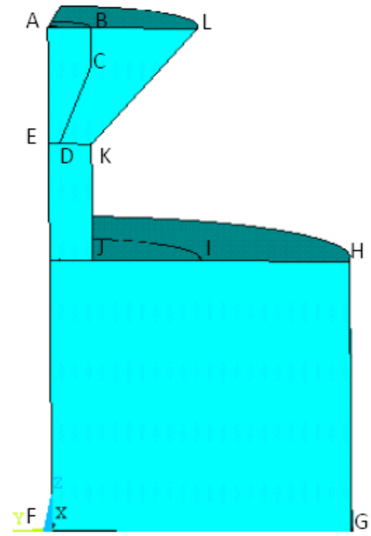

Fig. (2). Computational domain of the combined plasma arc.

In view of the influence of the cathode geometric shape and the accuracy of the finite element simulation, as shown in Fig. (**3**), a mapping method is introduced into the finite element model of combined plasma arc to obtain the finer hexahedral meshes. Because of the steep gradients between the cathode and the anodes, a variable step-size meshing method has to be also introduced into the finite element model of the combined plasma arc. Then the region near to the model center line will be hold finer meshes.

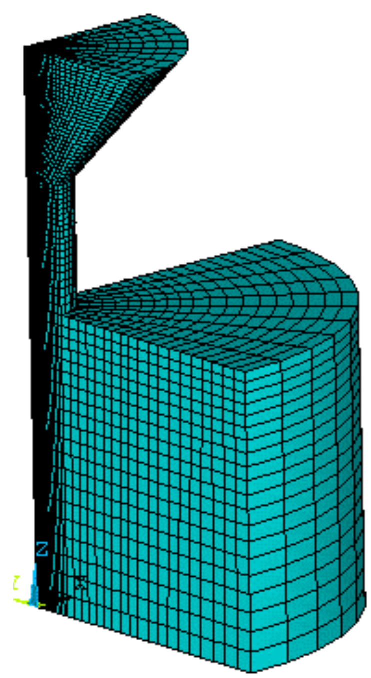

Fig. (3). Mesh generation of the finite element model of the computational domain.

Boundary Conditions

Due to the finite element model of combined plasma arc being axisymmetric, a quarter of this model is regarded as the substitution of whole calculation model to save computation time, and its boundary conditions are shown in Table **1**. For solving the potential equation, the working current passing through tungsten cathode is considered as uniform, so the current density of AB can be taken from the investigation of Lee [10]. At the anode surfaces FG and JL, the electrical potential is assumed to be zero. Meanwhile, $\partial \Phi/\partial n=0$ has been set on other places to represent the condition that no current flow crosses this boundary. For solving the momentum and energy equations, at BE and FG, a temperature of 3000K is assumed. An adiabatic condition is applied to the symmetrical surface EF. At other surfaces, the temperature is assumed to be 1000K. Furthermore, at the interior wall of the nozzle IL, wall of the cathode BE and anode surface FG, a no-slip condition is used. At the gas outlet GH, relative pressure P is assumed to *0*. $\partial u/\partial r=0$, $v=0$, $w=0$ are specified to the symmetrical surface AF and shielding gas inlet HI. Along the working gas inlet BL, the radial and azimuthal velocity components are neglected, and the axial velocity component is determined from the equation of the pipe flow [10] as follows:

$$u_0 = 2\frac{Q}{\pi\rho}\frac{\left(R_2^2 - r^2 + \left(R_2^2 - R_1^2\right)\frac{\ln\left(r/R_2\right)}{\ln\left(R_2/R_1\right)}\right)}{\left(R_2^4 - R_1^4 + \frac{\left(R_2^2 - R_1^2\right)^2}{\ln\left(R_2/R_1\right)}\right)} \tag{9}$$

where Q is argon flow rate, R_1 is the cathode radius and R_2 is the internal radius of the shielding nozzle.

Table 1. Boundary Conditions for the Solution of the Finite Element Model of the Combined Plasma arc. ("-" Substitutes Natural Boundary Conditions)

	u	*v*	*w*	*Φ*	*T*
AB	0	0	0	*I*	3000K
AE	0	0	0	-	3000K
BE	0	0	0	-	3000K
EF	0	$\partial v/\partial r = 0$	$\partial w/\partial\theta = 0$	-	-
FG	0	0	0	0	3000K
GH	-	-	-	-	1000K
HI	$\partial u/\partial z = 0$	0	0	-	1000K
IJ	0	0	0	0	1000K
JK	0	0	0	0	1000K
KL	0	0	0	0	1000K
LB	u_0	0	0	-	1000K

In addition, in the process of analysis of electro- magnetic coupling field, magnetic lines of force are assumed to perpendicularly pass the symmetry plane and the boundary condition of the magnetic vector potential being zero is imposed on other surfaces in the calculation domain of the combined plasma arc.

Technique of Solution

Owing to the physical environment approach being mostly applied into the iterative analysis on coupled phenomena, in this paper, three physical environment files are created by finite element software ANSYS, including electric field, magnetic field and flow field. In the finite element analysis process, the operation command LDREAD is introduced to help these physical environment files successively correlated, that is, the results from one file can be loaded into another file using LDREAD. To ensure above iterative analysis convergent, a minor convergence of temperature is set, which results from the normalization value of the temperature change between two adjacent iterative steps. In addition, to make argon gas fully ionize, a temperature of 100000K is imposed to the region of arc column in the initial calculation of electric field. Convergence is declared when the following condition is satisfied:

$$\frac{\sum_{i=1}^{N}\left|T_i^k - T_i^{k-1}\right|}{\sum_{i=1}^{N}\left|T_i^k\right|} \le 0.01 \tag{10}$$

where N is the total number of nodes, *Tk-1 i* and *Tk i* are the upper iterative (*k*-1) temperature and current *k* temperature, respectively.

4. CALCULATION AND DISCUSSION

The process parameters adopted in the simulation are that the diameter of tungsten cathode is 1mm, its cone angle and length in the calculation domain is 60° and 3mm respectively, the interior radius of nozzle inlet and outlet is 3.5mm, its length is 6mm, and the radius of workpiece anode is 7mm. Moreover, the working current *I* is 15A, 20A and 25A, respectively. The distance *D* from the nozzle outlet to the workpiece anode is 6mm, 7mm and 8mm, respectively. The argon gas flow rate *Q* is 4L/min, 5L/min and 6L/min, respectively.

The Distributions of Current Density and Electromagnetic Force

The calculated current density distribution is shown in Fig. (**4**). As shown, the current departs from the anode

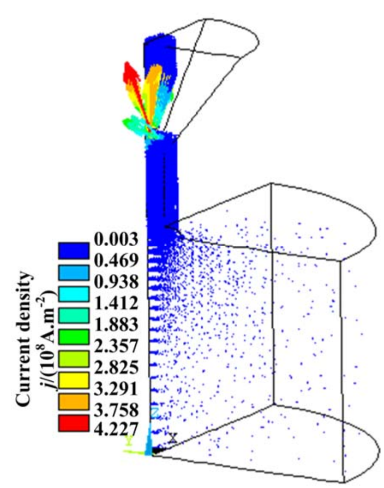

Fig. (4). Current density distribution in the combined plasma arc.

surface and enters the electrode tip through the tungsten cathode spot. The current density achieves highest value at the cathode tip for its smaller area and higher temperature. Furthermore, due to the effect of temperature distribution of combined plasma arc on argon gas electric conductivity, which affects current density distribution of combined plasma arc, the current density becomes larger with axial distance nearing to the cathode, and decreases with radial distance increasing.

Fig. (**5**) shows the calculated distribution of the electromagnetic force both in the arc column and tungsten cathode. Based on the left-hand rule, the direction of electromagnetic force can be determined with the current density and magnetic flux density. As shown, in the region of combined plasma arc column, the direction of electro-magnetic force is inward and downward, which compels the combined plasma arc to flow towards the workpiece anode and to be compressed at the same time. Furthermore, it can be seen that the electromagnetic force at the cathode tip is larger than the one at the lower portion of the arc, which also makes the combined plasma arc flow downward and inward.

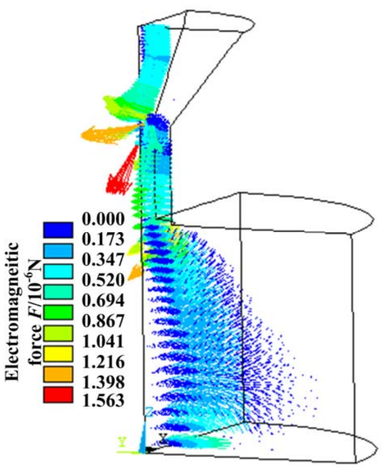

Fig. (5). Electromagnetic force distribution in the combined plasma arc.

The Distributions of Temperature and Velocity

The calculated temperature distribution of combined plasma arc is shown in Fig. (**6**). As shown, there exists a

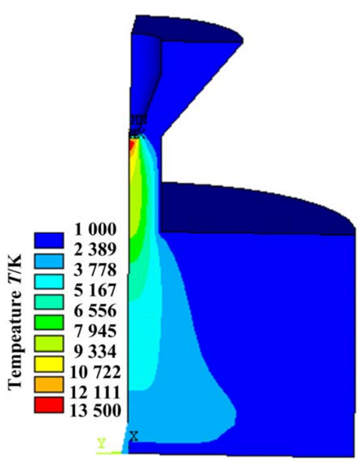

Fig. (6). Temperature distributions in the combined plasma arc.

maximum temperature in the region near to the tungsten cathode where the current density is higher, and larger temperature gradients in the cathode region and workpiece anode regions, respectively. It can be also seen that the temperature of combined plasma arc becomes smaller with axial distance away from the cathode, and increases with radial distance decreasing.

Fig. (**7**) shows the velocity distribution of the combined plasma arc. It can be seen that after passing the nozzle inlet, argon gas flows downward and inward. Once it reaches the cathode tip, the combined plasma arc will be accelerated from the cathode towards the workpiece anode, and be forced to turn around radial direction when approaching this working anode, which causes a bell shape of combined plasma arc and transforms the momentum of the high speed flow into the impact force of the combined plasma arc.

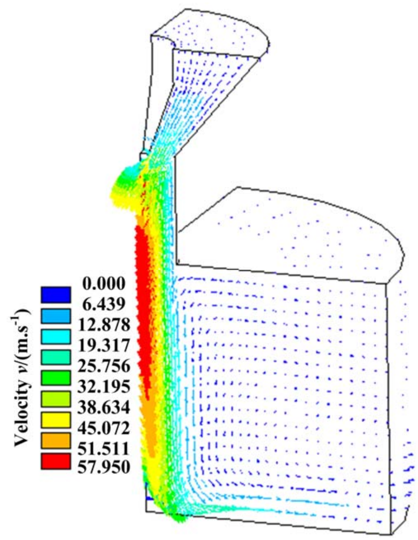

Fig. (7). Velocity distributions in the combined plasma arc.

The Effects of Process Parameters on the Jet Characteristics of Combined Plasma arc

The Working Current Effects

The temperature, velocity and current density of combined plasma arc under typical operation conditions (argon flow rate is 5L/min and the distance is 7mm) are discussed in this section by inputting three different working currents: 15, 20 and 25A.

Fig. (**8a** and **8b**) show the temperature of combined plasma arc along the axial direction and the radial direction under three different working currents, respectively. It can be seen that, the temperature field in the plasma jet greatly depends on the working current. At the same position, the higher the working current is, the higher the temperature is, because of the temperature being directly related to the input power. Since the input power is proportional to the working current, increasing it will definitely increase the input power, thus raise the temperature of the combined plasma arc. It can be also seen that with increasing the axial distance, after quickly reaching its maximum, the temperature decreases due to the current density becoming weakened. Moreover, with increasing the radial distance, the temperature also decreases due to these regions being far from the center of arc column and the influence of the turbulent boundary layers.

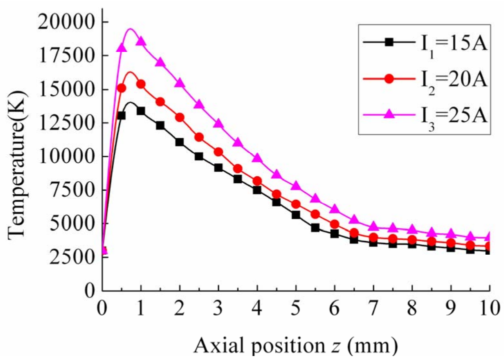

Fig. (8a). Effect of working currents on the axial temperature.

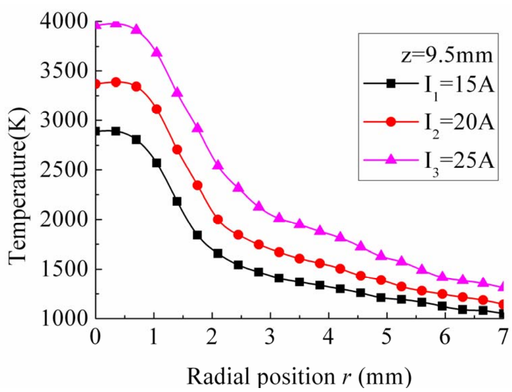

Fig. (8b). Effect of working currents on the radial temperature.

Figs. (**8c** and **9d**) show the velocity along the axial direction and current density along the radial direction on the workpiece anode, respectively. As shown, the influences of working currents on the velocity of combined plasma arc are similar to the effect on temperature, due to the electromagnetic force having a significant effect on the shape of the velocity profiles and its effect being more important with

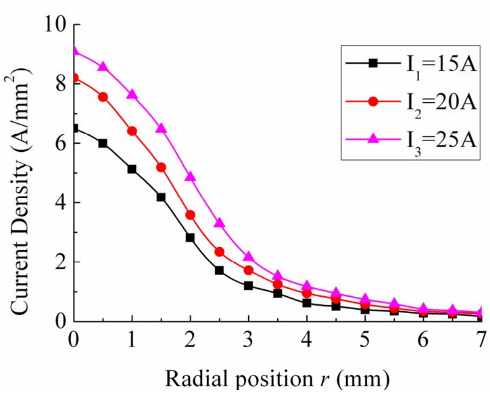

Fig. (8c). Effect of working currents on the axial velocity.

increasing current. At the same position, the relatively higher working current corresponds to relatively higher velocity and current density. With increasing the axial distance, after quickly reaching its maximum, the velocity decreases in succession. Due to the violent thermal expansion of the high temperature plasma gas, increasing the working current, argon density decreases, the degree of thermal ionization and electrical conductivity increase, which induce the peak value and radius of the current density on the workpiece anode to be increased.

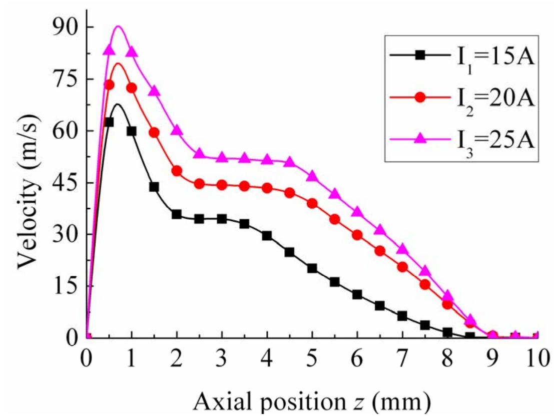

Fig. (8d). Effect of working currents on the radial current density on the anode.

The Argon Gas Flow Rate Effects

The temperature, velocity and current density of the combined plasma arc under typical operation conditions (the working current is 15A and the distance is 7mm) are discussed in this section by inputting three different argon gas flow rates: 4, 5, 6L/min.

Fig. (**9a** and **9b**) show the temperature distributions along the axial and radial direction, respectively, under different argon gas flow rates. It can be seen that the higher the flow rates of argon gas, the higher the temperature are along the axial and radial direction (r<2mm). However, the temperature slightly increases with argon gas flow rate increasing,

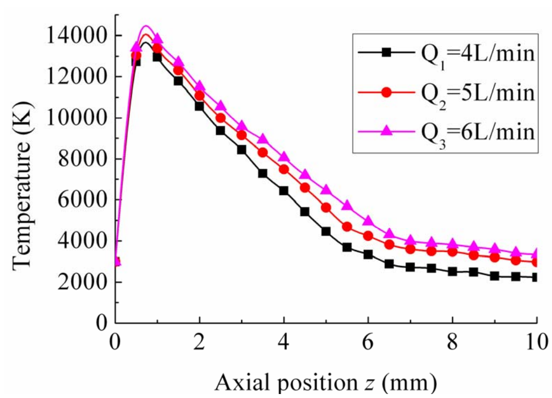

Fig. (9a). Effect of argon flow rate on the axial temperature.

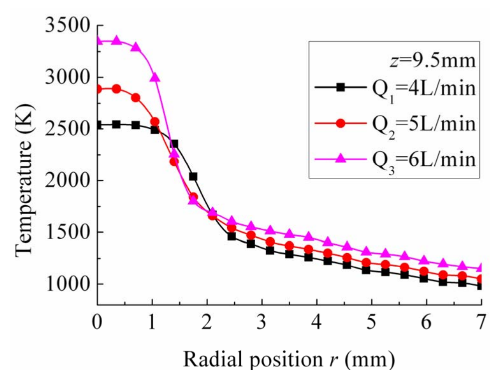

Fig. (9b). Effect of argon flow rate on the radial temperature.

even the temperature along the radial direction (r>2mm) decreases with argon flow rate increasing. The reason is that increasing argon flow rate will expand the length of plasma arc in the nozzle and induce the arc voltage and relevant input power to be increased, which results in higher temperature of combined plasma arc. On the other hand, increasing argon flow rate will force the more argon gas to be heated and ionized, which brings on the temperature descending. Completely considered above two effects of argon flow rate on the temperature, it can be concluded that the temperature is not proportional to argon flow rate. In addition, it will enhance the compression effect on combined plasma arc with the increase of argon flow rate increase, and reduce the radius of the temperature distribution along the radial direction because of its energy density distribution concentrating.

Fig. (**9c** and **9d**) present the velocity distribution along the axial direction and the current density distribution on the anode along the radial direction, respectively, under different argon flow rates. As shown, the influence of argon flow rate on the velocity is similar to its effect on the temperature of combined plasma arc. It can be also seen that the peak value of current density on the workpiece anode along its radial direction increases with the accretion of argon flow rate, however, the radius of the current density distribution reduces with increasing argon flow rate.

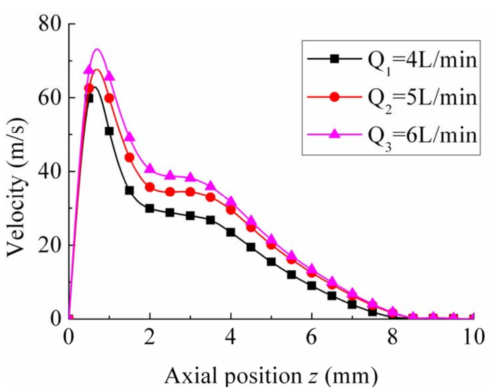

Fig. (9c). Effect of argon flow rate on the axial velocity.

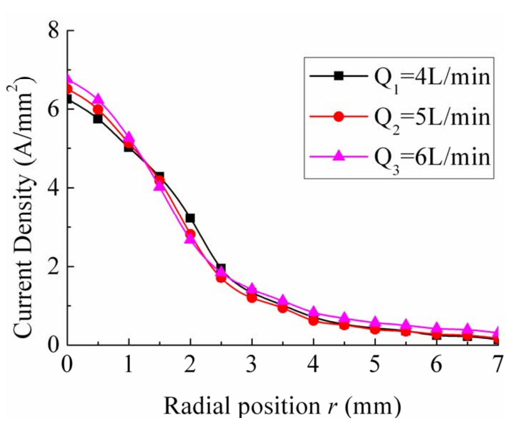

Fig. (9d). Effect of argon flow rate on the radial current density on the anode.

The Effects of the Distance from the Nozzle Outlet to the Workpiece Anode

The temperature, velocity and current density of combined plasma arc under typical operation conditions (the working current is 15A and argon flow rate is 5L/min) are discussed in this section by inputting three different distances from the nozzle outlet to the anode: 6, 7, 8mm.

Fig. (**10a** and **10b**) show the temperature distributions along the axial and radial direction, respectively, under different distances from the nozzle outlet to the workpiece anode. As shown, increasing the distance, the temperature along the axial direction slightly increases. However, along the radial direction, the temperature near to the workpiece anode decreases. The reason is that increasing the distance will lengthen the combined plasma arc and the arc voltage to be ascended, which will consequentially lead to the increase of the temperature along the axial direction. On the other hand, increasing the length of combined plasma arc will result in the extension of contact field with the ambient cool gas and the increase of the heat loss, which will consequentially bring on the decrease of the temperature near to the anode along the radial direction.

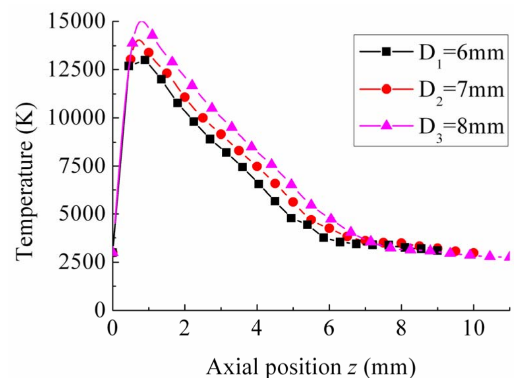

Fig. (10a). Effect of the distance on the axial temperature.

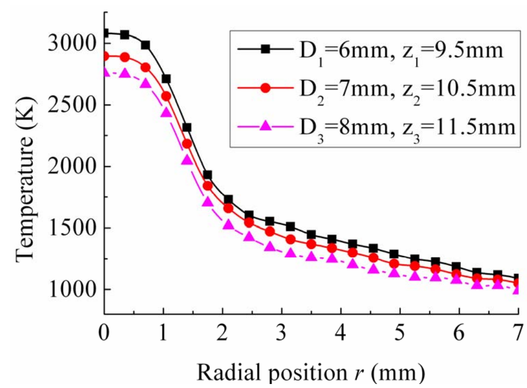

Fig. (10b). Effect of the distance on the radial temperature.

Fig. (**10c** and **10d**) present the velocity distribution along the axial direction and the current density distribution on the anode radial direction, respectively, under different argon flow rates. As shown, the influence of the distance on the velocity is similar to the effect on the temperature along axial direction. The longer the distance from the nozzle outlet to the anode, the higher the velocity is. On the contrary, the peak value of current density along the anode radial direction is reciprocal proportional to the distance. However, the longer the distance, the more the radius of current density along anode radial direction is, due to the expansion of the conduction region on the workpiece anode with the distance increasing.

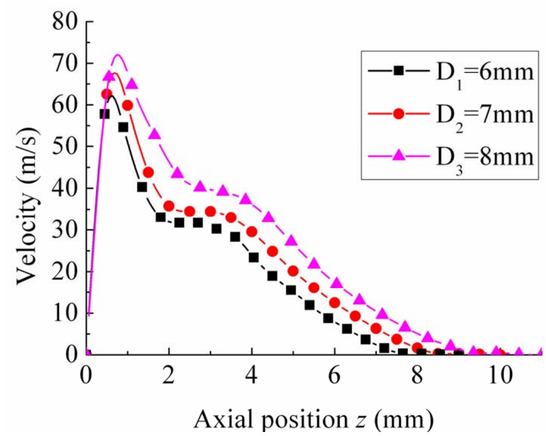

Fig. (10c). Effect of the distance on the axial velocity.

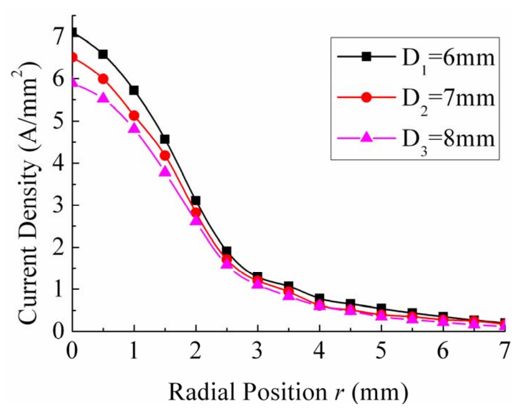

Fig. (10d). Effect of the distance on the radial current density on the anode.

Experimental Verifying

It is well known that the temperature of plasma is usually in the more than 100000K, it is too high to use the contact thermometry. So it is difficult to precisely measure the experimental temperature by only using the thermocouple probe. Fortunately, in recent years, the emergence of computer-controlled photoelectric direct-reading diagnosis device and special equipment not only improved the resolution of spectral diagnostics in time and space, but also enhanced the capabilities of data processing and the accuracy of experimental measurement. Thus it provides a favorable method for the spectrum diagnosis of plasma arc. Based on our previous investigations [11, 12] on spectral diagnosis of the plasma jet, in this paper, a result from the numerical simulation is compared with that from the collection of plasma arc image by CCD and its corresponding spectral diagnosis under the same process parameters (working current is 25A, argon gas flow rate is 5L/min and the distance from the nozzle outlet to the workpiece anode is 5mm). As shown in the Fig. (**11**), the shape of the combined plasma arc between the nozzle outlet and the workpiece anode is in good agreement with that obtained from the image collection by CCD. In addition, it can be also seen that the maximum temperature 18695K in the former is very close to the maximum temperature 19025K in the latter. As a result, it can be proved that the numerical simulation on the combined plasma arc is feasible and the results from its analysis are reliable.

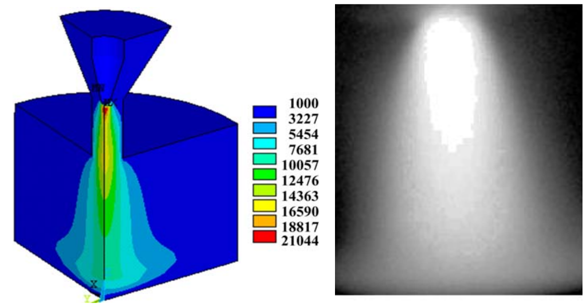

Fig. (11). Comparison of simulated results with diagnosed measured results by CCD.

5. CONCLUSIONS

It's well known that the transferred arc and non-transferred arc have poor stability when working current is less, however, as an ideal heating source for precise welding, the arc current of micro plasma is usually less than 15A and more stable due to the use of combined plasma arc. In this paper, a three-dimensional mathematical model on the combined plasma arc is established, including the influence of the swirl exiting in the plasma torch, without the assumption of plasma flow independent of the swirl existing in the combined plasma arc. Using the sequential coupling method and physical environment approach, the coexistence of non-transferred arc and transfer arc in the combined plasma arc is successively simulated. Consequentially, it proved that the non-transferred arc can provide a good conducting channel for the transferred arc in combined plasma arc and improve the stability of this transferred arc.

An important finding of this work is that the distributions of current density, electromagnetic force, temperature and velocity in the plasma arc are interesting. The peak values of the current density and electromagnetic force emerge at the cathode tip. Far from the cathode tip, the current density will descend and the electromagnetic force will be smaller. And the direction of electromagnetic force is inward and downward. Furthermore, there exists a maximum temperature in the region near to the cathode tip. Far from the cathode tip or the center line of the arc column, the temperature will become smaller. The electromagnetic force plays a very important role in determining both the distributions of the temperature and velocity. Consequently, the combined plasma arc will be accelerated from the cathode towards the workpiece anode and be forced to constrict inward

Another important finding of this work is that the effects of the process parameters on the current density, the temperature and the velocity are unique, including the working current, the argon flow rate and the distance from the nozzle outlet to the working anode. It is found that the working current is significantly influential to the temperature, velocity and current density. Increasing the current will tend to increase above all jet characteristics of the combined plasma arc, because of the current increase resulting in higher input power and higher electromagnetic force of the combined plasma arc. However, the jet characteristics is less sensitive to the argon flow rate at a constant current for two physical reasons, one being that the electromagnetic force will remain essentially constant, the other is that the thermal generation will be somewhat reduced, due to the expansion of the gas with the increase of argon flow rate. Meanwhile, the jet characteristics is less sensitive to the distance from the nozzle outlet to the anode at a constant current for two physical reasons, one being that the input power will improve with the distance increasing, the other is that the thermal loss will be increased, because of the extension of contact region with the ambient cool gas.

The shape and character of the combined plasma arc obtained from the numerical simulation are quite agreeable with the measurements of CCD collection and spectral diagnosis. The results proved that the numerical simulation and analysis on the combined plasma arc in this paper are reliable and effective.

REFERENCES

[1] R. Westhoff, and J. Szekely, "A model of fluid, heat flow and electromagnetic phenomena in a non transferred arc plasma torch", *J. Appl. Phys.*, vol. 70, pp. 3455-3466, 1991.

[2] J. M. Bauchire, J. J. Gonzalez, and A. Gleizes, "Modeling of DC plasma torch in laminar and turbulent flow", *Plasma. Chem. Plasma. Process.*, vol. 17, pp. 409-432, 1997.

[3] S. Piak, P. C. Huang, J. Heberlein, and E. Pfender, "Determination of the arc root position in a DC plasma torch", *Plasma. Chem. Plasma. Process.*, vol. 13, pp. 379-397, 1993.

[4] M. Ushio, J. Szekely, and C. W. Chang, "A mathematical modeling of flow field and heat transfer in high current arc discharge", *Ironmaking Steelmaking*, vol. 6, pp. 279-286, 1981.

[5] J. Szekely, J. Mchelliget, and M. Choudhary, "Heat transfer fluid flow and bath circulation in electric arc furnaces and DC plasma furnaces", *Ironmaking Steelmaking*, vol. 10(4), pp. 169-179, 1983.

[6] S. C. Chu, and S. S. Lian, "Numerical analysis of temperature distribution of plasma arc with molten pool in plasma arc melting", *Comput. Mater. Sci.*, vol. 30, pp. 441-447, 2004.

[7] F. G. Lu, X. H. Tang, H. L. Yu, and S. Yao, "Numerical simulation on interaction between TIG welding arc and weld pool", *Comput. Mater. Sci.*, vol. 35, pp. 458-465, 2006.

[8] F. L. Yin, S. S. Hu, C. L. Yu, and L. L, "Computational simulation for the constricted flow of argon plasma", *Comput. Mater. Sci.*, vol. 40, pp. 389-394, 2007.

[9] R. T. C. Choo, J. Szekely, and R. C. Westhoff, "On the calculation of the free surface temperature of gas-tungsten arc weld pools from first principles: Part A. Modeling the welding arc", *Metall. Trans. B*, vol. 23(B), pp. 357-369, 1992.

[10] S. Y. Lee, and J. Na, "Analysis of TIG welding arc using boundary-fitted coordinates", *Proc. Inst. Mech. Eng. Part B: J. Eng. Manu*, vol. 209B, pp. 153-164, 1995.

[11] J. P. Xu, J. C. Fang, and Z. G. Li, "Plasma jet imaging by CCD technology in rapid mold manufacturing", *J. Mater. Proc. Technol.*, vol. 129, pp. 250-254, 2002.

[12] J. C. Fang and W. J. Xu. "Plasma jet collection of temperature field image processing", *Chin. J. Mech. Eng.*, vol. 38, pp. 82-84, 2002.

Testing and Manufacturing of Advanced Composite Material

Debi Prasad Singh, *Department of Mechanical Engineering, Raajdhani Engineering College, Bhubaneswar, deboprasad_1159@gmail.com*

Suraj Kumar Patel, *Department of Mechanical Engineering, Aryan Institute of Engineering & Technology, Bhubaneswar, surajpatel26@gmail.com*

Deepika Priyadarshini Palai, *Department of Civil Engineering, NM Institute of Engineering & Technology, Bhubaneswar, deepikadalai2561@gmail.com*

Abstract: Due to the problems of potential corrosion and thermal expansion differences between traditional metal connecting pieces and carbon fiber poles, it is difficult for them to meet the operating requirements of truss structures in the environment of stratosphere. Based on the large scale composite space truss structure of stratosphere aerostats, the carbon fiber flange connection joints were studied in the present paper. Adopting the three-dimensional full five-directional braiding technology, Toray T700S – 12K carbon fiber is used as the raw material to manufacture flange joint preform, and to manufacture flange forming by RTM(resin transfer molding) process. As demonstrated by tensile and bending tests, the composite flange joints have better mechanical properties than flanges manufactured by aviation aluminum alloy, and meet requirements of stratosphere truss structure connecting pieces. In conjunction with the results of finite element analysis, mechanical properties can be further enhanced by the improvements of the braiding process, the forming process and the physical dimension.

Keywords: Advanced composite material flange, manufacture, test, finite element analysis.

1. INTRODUCTION

Three-dimensional braided composite material, a new type of composite material, is a combined product of the three-dimensional braiding technology and the advanced composite material technology. It is essentially developed and applied in high and new technology fields represented by the aerospace technology. As the fiber bundles extend along a plurality of spatial directions and cross with each other, the integrity of the composition is good and the drawbacks of low intensity and easy lamination between layers of the laminated composite material are overcame [1-6]. Meanwhile, the high specific strength, the high specific stiffness, and the very strong designability of the three-dimensional braided composite material play an essential role in the weight reducing of aerospace structures.

Aerostats have become the public research hotspot. One of the key technologies is the research of large scale truss structure which is light in weight and high in strength. The large scale truss structure in spacecraft is usually composed of carbon fiber poles and metal joints. Through the improvements of the connection between the carbon fiber poles, the weight of the truss structures is further reduced, the bearing efficiency of the structure is improved, and problems of the potential corrosion and the thermal expansion rate between the aluminum alloy and carbon fiber are solved.

In the present paper, the carbon fiber flange preform is manufactured by the four steps three-dimensional braiding technology, and the three-dimensional braided flange specimen is developed in combination with the RTM process. Also, advanced composite material flange is used to substitute the aviation aluminum alloy joint of carbon fiber truss structure. As tested by tensile and bending tests, under the condition of same quality, the tensile and bending property of the former is better than latter, so that the expected result is reached. The whole manufacturing process is divided into five steps: manufacture of three-dimensional braided preform, manufacture of the RTM process mold, injection, curing and release of the resin.

2. THE PROCESSING OF THE THREE-DIMENSIONAL BRAIDED PREFORM

One of the characteristics of three-dimensional braiding is that different shapes of heterotype whole pieces can be directly braided. As for the reasons, in one aspect, the size of the cell cube of the basic structure of three-dimensional braidings can be changed with the changes of the shape and size dimension of the preforms. In another aspect, braiding process is varied, and processing parameters can be changed to adjust the process to meet the requirements of the shape of the preforms, thereby to achieve whole braiding.

In the present paper, the four steps three-dimensional braiding process is used to manufacture the flange preform. Many structures with different cross-sectional shapes can be braided by the four steps, for example, tabular, tubular, semi-cylinder, and cylinder. The four steps braiding method is introduced as follows, taking tabular structure as example. A square machine is used to braid the tabular structure. The theory of the four steps process of the 6 lines 4 rows structure is described in Fig. (**1**). In the first step, all the bobbins in row move horizontally, in which, adjacent rows move in reverse directions, as shown by the arrows in Fig. (**1b**). In the second step, all the bobbins in column move vertically, in which, adjacent rows move in reverse directions, as shown by the arrows in Fig. (**1c**). The third step is similar with the first step, except that the rows move reversely, that is to say, all the rows return to the state of the first step (Fig. **1d**). In the fourth step, all the columns return to the state of the second step, only the position of respective bobbin is changed (Fig. **1e**). Thus, one braiding cycle is completed and the braider returns to the initial state of the circle again, only that the position of respective bobbin is changed (Fig. **1a**). These four steps are repeated afterwards, and the four steps braiding is achieved.

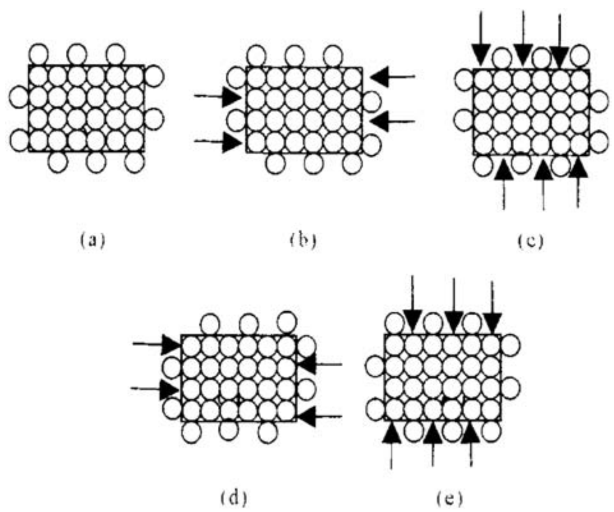

Fig. (1). The theory of four steps tabular braiding process of three-dimensional braiding.

The braider used for tubular braiding is a round machine. The round machine is actually a square machine and the rows of which are connected between the beginning and the end. The process of a four steps tubular braiding is similar to the tabular braiding, only that the horizontal movement is changed to the tangential movement and the vertical movement is changed to radial movement.

The fabric construction is divided into many types including three-dimensional four directions, three-dimensional five directions, three-dimensional full five-directions, three-dimensional six directions or even three-dimensional seven directions. In the structure of three-dimensional four directions, there is no axial direction yarn passing through the pitch of the braiding. In the structure of three-dimensional five directions, there is one axial direction yarn passing through the pitch every other pitch length. Whereas in the structure of three-dimensional full five-directions, there are axial direction yarns passing through all pitches, and the thickness of which is far larger than the structure of three-dimensional four directions or three-dimensional five directions. The present flange which has the structure of three-dimensional full five-directions [7] is shown as Fig. (**2**).

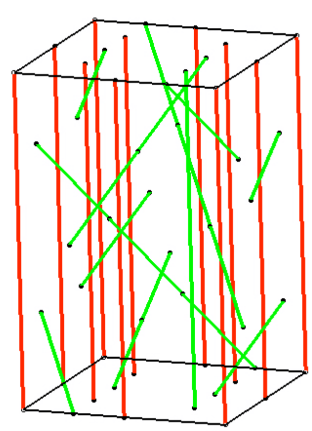

Fig. (2). Schematic illustration of the fiber structure of the three-dimensional braiding.

T700S-12K carbon fiber from Toray Co., Japan is chosen as the braiding material, its basic characteristics are listed in Table **1**.

The resin chosen is tri-functioned epoxy resin TDE - 85# from jindong chemical plant, its properties are listed in the following Table **2**.

Table 1. Basic Characteristics of T700S - 12K

Type	**T700S-12K**	**Fiber density (g/cm3)**	**1.74~1.79 g/cm3**
monofilament diameter	8μ	Elongation (%)	≥1.5
tensile strength(GPa)	4.827	Carbon content	≥95%
elastic modulus(GPa)	210		

Table 2. Performance Parameters of Epoxy Resin TDE - 85#

Properties of the curing	Impact strength Kg-cm/cm2	13.9
	Bending strength Kg/cm2	1690
	Compressing strength Kg/cm2	1636
	Brinell hardness Kg/cm2	1807
	Tensile strength Kg/cm2	638
	Elongation %	2.1
	Shear strength(RT)	142
	Sueface resistance Ω	1.7×10^14
	Volume resistanceΩcm	3.4×10^16
	Dielectric constant ζ	3.7
	Dielectric loss tg δ	2.2×10^-2
	Breakdown voltage strength KV/mm	23.3

3. PHYSICAL DIMENSION OF THE FLANGE

According to the requirements of the connection size of the truss structure, the internal diameter of the flange cylinder is 45mm, and the external diameter is 51mm; the external diameter of the flange disc is 90mm, and the thickness is 3mm. According to the requirements of bonding strength, the length of the flange cylinder is 90mm, and there is a round transition with a radius of 10mm between the flange disc and the flange cylinder, to decrease the stress concentration. The shape and size of the flange is shown in Fig. (**3**).

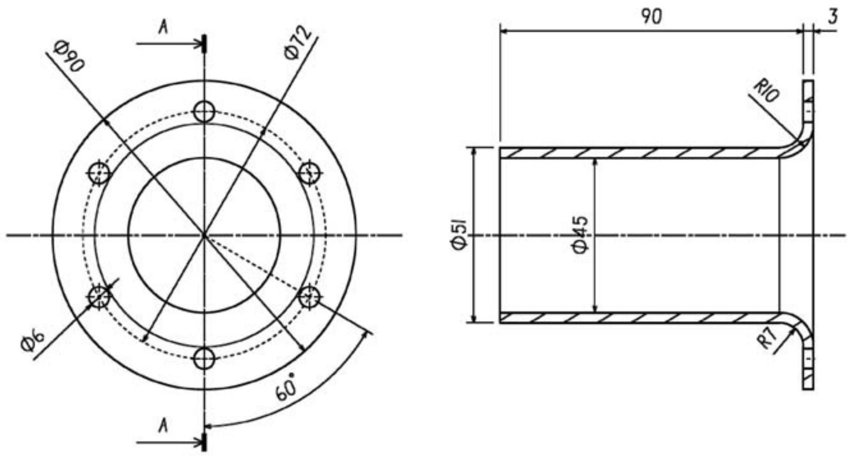

Fig. (3). Physical dimension of the flange.

Since the mechanical properties of the composite material are greatly impacted by processing parameters, and theories on design criteria of the mechanical properties of three-dimensional braiding composite material are not yet completed, the one dimension quantity method is adopted to carry out the research. The volume content of the fiber is set as 50%(±2%), the braiding angle of the flange as 20°, and the pitch length as 5mm, the braiding is completed by Beijing Boruiding Science and Technology Co. Ltd. under set-up parameters adopting three-dimensional full five-directions braiding technology. The flange preform is shown in Fig. (**4**). After braiding by the weaving technology, the preform units are cut and separated one by one. Because of the cutting, the flange neck and the edges of the flange disk are provided with burr, and the braiding parameters can not be guaranteed, such that after curing, this region can not reach the requirements of the designed properties. But in view of the process, the loosening at the edges can not be avoided. Therefore, it is only necessary to make the braiding size of the preform lager than the physical dimension of the part, and cut off the related region after curing.

Fig. (4). Manufacture of the flange preform.

4. THE FORMING PROCESS OF THE FLANGE

The RTM process is adopted to form the flange, it mainly includes steps of the manufacture of the RTM process mold, injection, curing and release of the resin.

4.1. Designing of the Mold

The designing of the mold is one of the key steps of the RTM forming process. The quality of the mold not only decides the inherent quality of the composite material, but also decides the surface grade of the composite material. As the property of the composite material is greatly impacted by the composite process, the dispersibility of the properties of the product is frequently large. Therefore, designing an appropriate mold can insure that the dispersibility of the properties of the cured composite material is relatively smaller.

The height of the projection of the male mold is slightly higher than the flange neck, and the higher part is the area for the main passage and bypass passage. The end face of the projection of the male mold is in connection with the end face of the intra-cavity of the female mold. The resin is injected from the pores at the end face and flew from the four pores at the side surface to the braiding uniformly. The design figure of the mold is shown as Fig. (**5**). The male mold and the female mold is shown as Fig. (**6**).

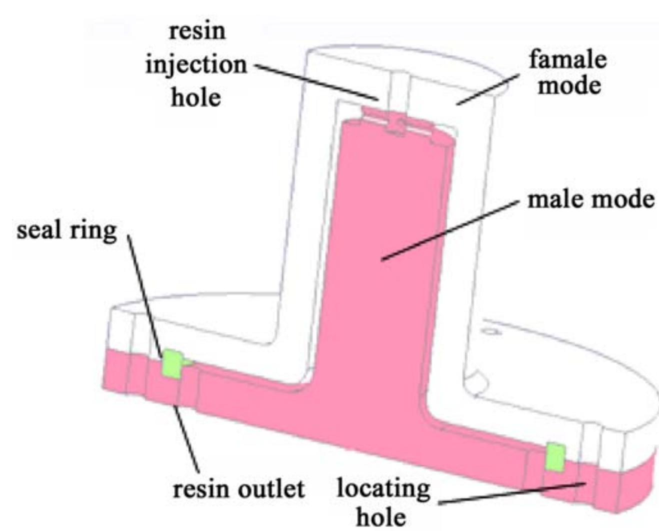

Fig. (5). Half sectional view of the mold.

Fig. (6). Photos of the male mold and the female mold.

4.2. Forming

In the three-dimensional braided carbon-fiber composite flange, the base material is TDE - 85# epoxy resin, and the reinforcement material is carbon fiber. Also, 70# anhydride is chosen as the curing agent, and aniline is chosen as the accelerant. Upon curing, the resin, curing agent and the accelerant is mixed in the ratio of 100:113.7:0.1, and the curing is carried out at an injection pressure of 0.3mpa and at 85 ^{o}C for one hour, then raised to 120 ^{o}C for another one hour, followed by natural cooling and releasing. The flange joint is shown as Fig. (**7**).

Fig. (7). Advanced composite material flange.

5. TESTS

Through the tensile and bending tests of advanced composite material flange, the mechanical properties of which is obtained, and in conjunction with the tensile and bending tests of aviation aluminum alloy flange, the mechanical properties of both are compared. In the tests, the physical dimensions and the test methods of the aviation aluminum alloy flange are in accordance with those of the advanced composite material flange.

5.1. Tensile Tests of Advanced Composite Material Flange

A tensile test is carried out to the flange joint to test its tensile property. Currently, there are no test criteria as reference on the mechanical properties of composite material flange joints. The present paper designed the above mentioned experiment according to the operating requirements of the flange. The loading rate of the testing machine is 0.5mm / min, and the loading mode for tensile test of the flange joint is shown as the Fig. (**8**).

Fig. (8). Composite material flange tensile test.

As observed by the test, when the experimental load reached 20000N, the specimen started to make a cracking sound. As the load continued, the bolt holes for connecting of the flange started to deform, after which, a crack was first seen at the round corner which connects the flange disc and the flange cylinder. At last, the whole round corner of the flange neck and the flange disc were seriously deformed, and the flange neck was completely broken. The whole destructed flange is shown as Fig. (**9**).

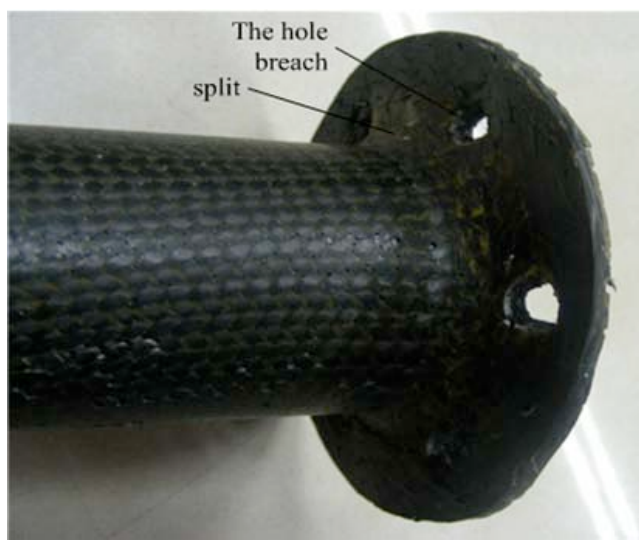

Fig. (9). Destroy of the composite material flange by the tensile test.

The load - displacement curve of the flange by the tensile test is shown as Fig. (**10**). It can be recognized in the curve that the whole test curve of the flange is changed as a line. The load is decreased rapidly after reaching a maximum of 29321N, and the test is finished after the load is decreased to 24000N, by then the flange is completely damaged.

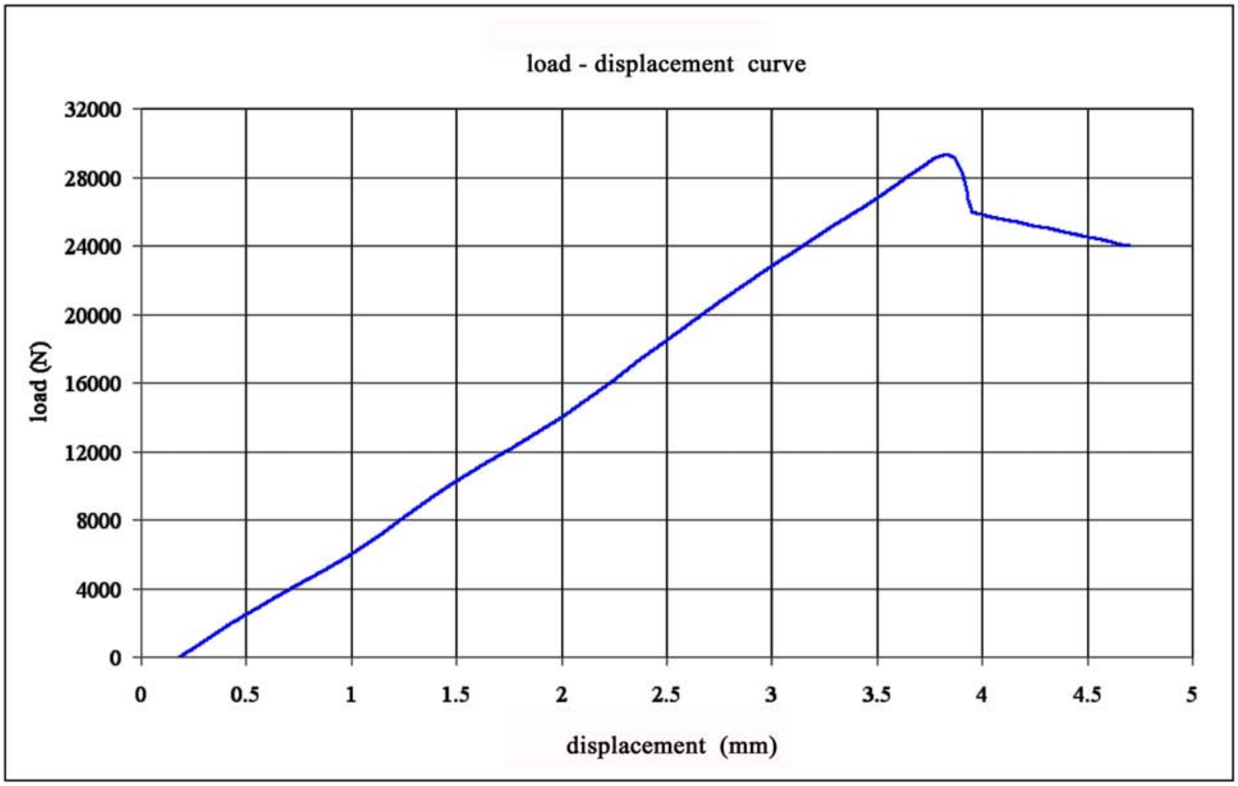

Fig. (10). Load - displacement curve of the composite material flange by the tensile test.

5.2. Bending Tests of Advanced Composite Material Flange

A bending test is carried out to an advanced composite material flange joint, to measure its bending property. Considering the use and the stress conditions of the flange joint on the aerostat truss structure, the present paper designed an experiment program: the distance between the bearings of both sides of the specimen is 520mm, the distance from the loading head to the bearing is 260mm, and the loading rate of the test machine is 0.5mm / min. The bending test of the flange joint is shown in Fig. (**11**).

Fig. (11). Composite material flange bending test.

As observed by the test, when the experimental load reached 3620N, the specimen started to make a cracking sound. As the load continued, the sound did not stop, and the connecting bolt holes at the down side of the flange started to deform, after which, a crack condition appeared at the transition round corner near the bolt holes. Along with the increasing of the load, the crack enlarged and extended along both sides. At last, the flange disc was seriously deformed. The destructed form of the whole flange by the test is shown as Fig. (**12**).

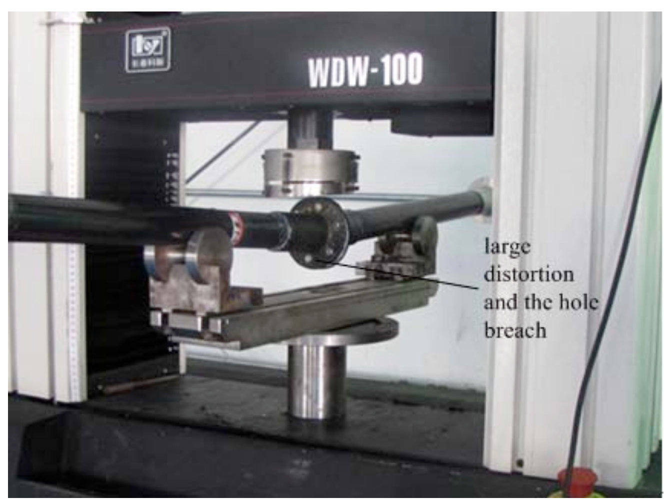

Fig. (12). Destroy of the composite material flange by the bending test.

The load - displacement curve of the flange bending test is shown as Fig. (**13**). From the load curve, it can be seen that the whole test curve of the flange is basically changed in line. The slope of the curve is slightly decreased when the load reaches 4000N. After the maximum of 5110N, the load rapidly drops, and when the load draps to 3800N, the test is stopped, by then the flange is completely damaged.

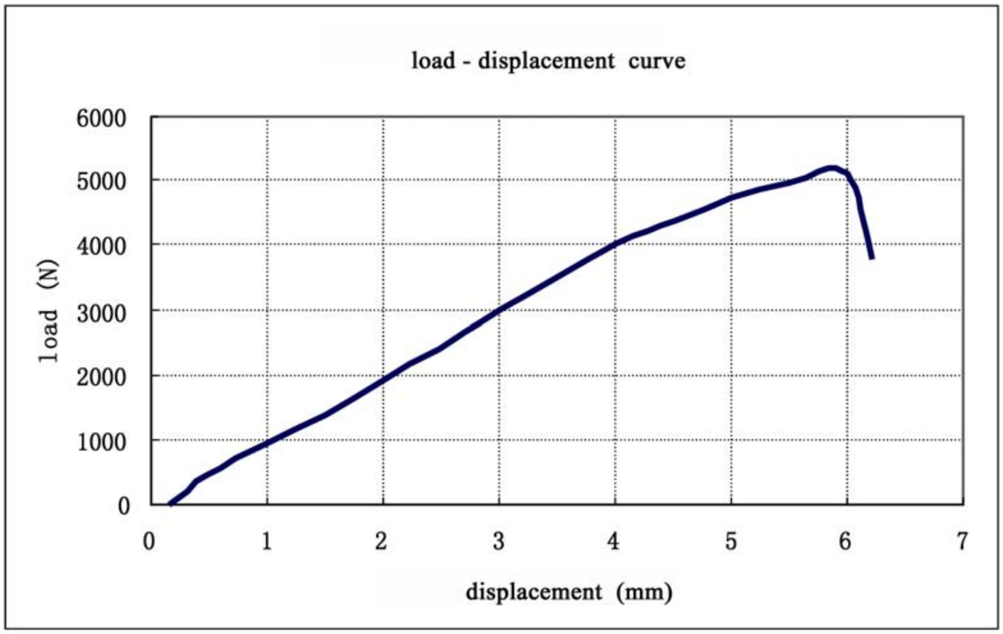

Fig. (13). Load - displacement curve of the composite material flange by the bending test.

5.3. Tensile Tests of the Aviation Aluminum Alloy Flange

Referring to the tensile test method of advanced composite material flange, the tensile test of aviation aluminum alloy flange is carried out. The flange is fixed with the test machine by adhesively bonding carbon fibre pipes. The loading rate of the test machine is 0.5mm / min. The loading test is shown as Fig. (**14**). When the load reaches 30000N, the flange begins to deform, and when reaching 40000N, the bolt holes crack and the flange is destroyed. The destroyed flange is shown as Fig. (**15**).

The load - displacement curve of the tensile test of a typical metal flange is shown as Fig. (**16**). The whole load curve is basically changed in line. The flange reaches its maximum tensile load at 40000N.

5.4. Bending Tests of the Aviation Aluminum Alloy Flange

Referring to the bending test method of advanced composite material flange, the bending test of aviation aluminum alloy flange is carried out. The flange is fixed

Fig. (14). Aviation aluminum alloy flange tensile test.

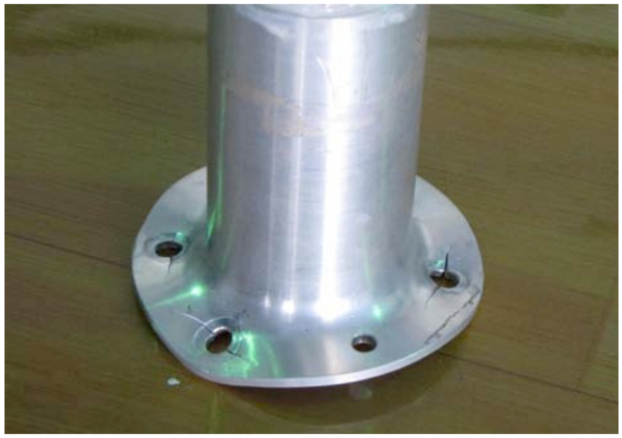

Fig. (15). Destroy of the aviation aluminum alloy flange by the tensile test.

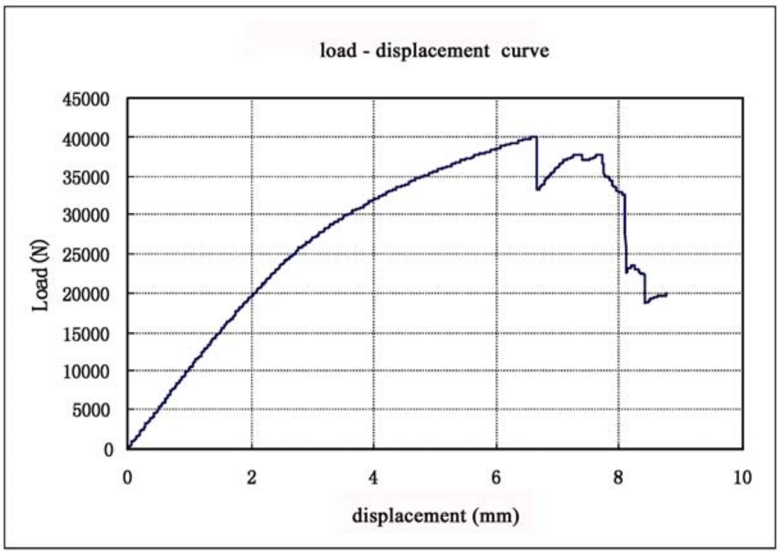

Fig. (16). Load - displacement curve of the aviation aluminum alloy flange by the tensile test.

with the bearing by adhesively bonding carbon fibre pipes. The distance between two bearings is 520mm, the distance from the bearing to the center loading point is 260mm, and the loading rate of the test machine is 0.5mm / min. The bending test is shown as Fig. (**17**). When the load reaches 4500N, the flange begins to deform, and when reaching

Fig. (17). Aviation aluminum alloy flange bending test.

Fig. (18). Deform of the aviation aluminum alloy flange by the bending test.

6150N, a bigger deform appears at the bottom of the flange, by then the test is stopped. The deform condition is shown as Fig. (**18**).

The load - displacement curve of the tensile test of a typical metal flange is shown as Fig. (**19**). The whole load curve is basically changed in line, although the load vibrates in small amplitude after 5800N. When the load reaches its maximum of 6150N, the flange is largely deformed and the test is stopped.

5.5. Summary of the Tests

As is known from the tensile and bending tests of the advanced composite material flange and the aviation aluminum alloy flange, under the condition of same physical dimension, the tensile and bending properties of the advanced composite material flange are slightly lower than those of the aviation aluminum alloy flange. However, the weight of the former is 57% of the latter, thus under the condition of same weight, the tensile property of the advanced composite material flange is 1.28 times of that of the metal flange, and the bending property 1.45 times. The equivalent mechanical properties of the former are apparently better than those of the latter.

6. FINITE ELEMENT ANALYSIS

Since the radius of the circular arc of the flange disc at the concentration of stress on the advanced composite material flange joint is relatively small, the desired distribution of strain and stress can not be directly measured. Thus, through simulations of finite element analysis, the limiting loads in the above tests are adopted to analyze the stress distribution of the whole flange, to derive the breaking strength. Since currently there are not yet calculation methods for mechanical properties of three-dimensional full five-directional

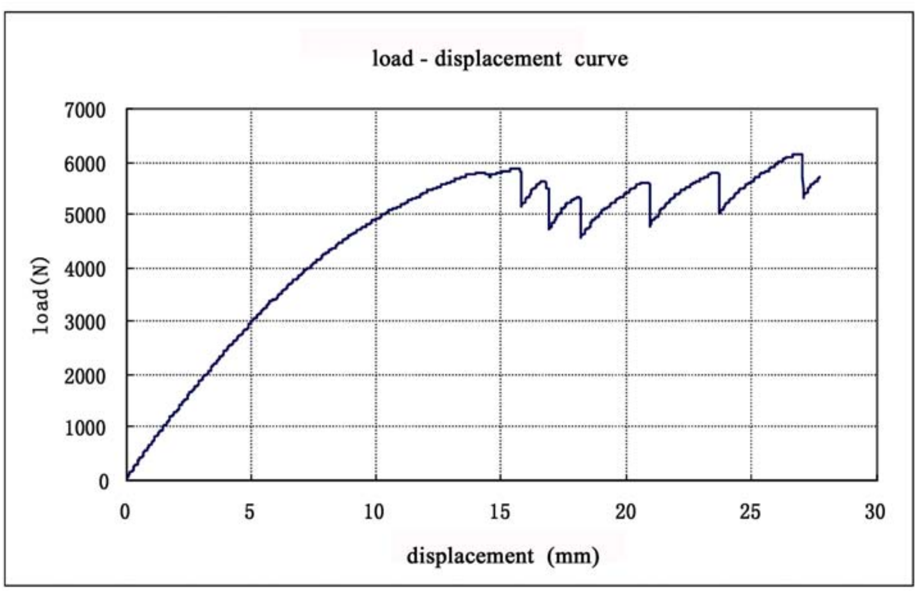

Fig. (19). Load - displacement curve of the aviation aluminum alloy flange by the bending test.

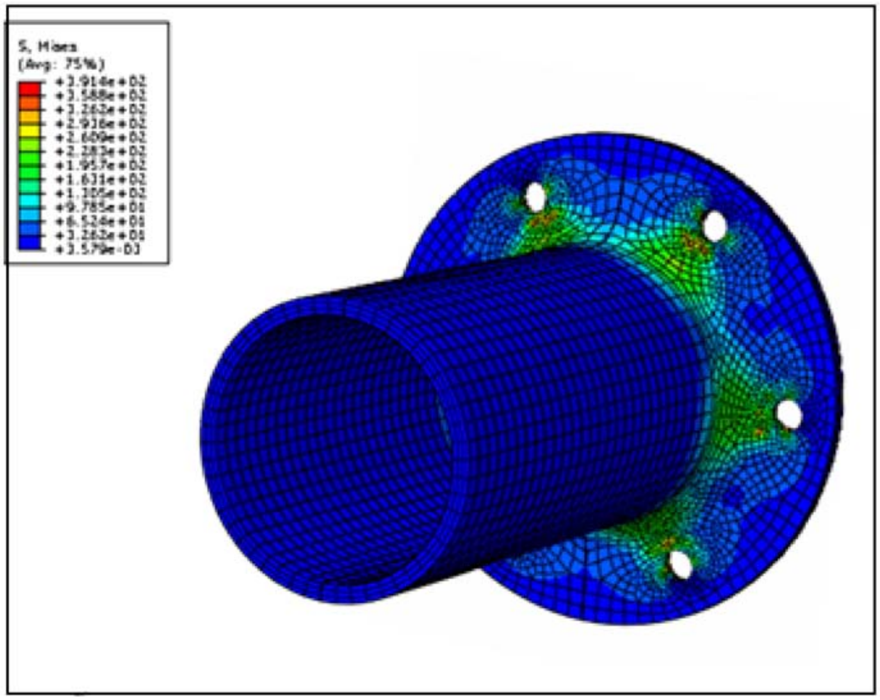

Fig. (20). Stress nephogram of flagne by the tensile test.

advanced composite material flange, the present paper adopts the calculation methods for isotropy homogeneous materials to proceed the model analysis, and carry out the demonstrations in conjuntion with the test results. The tensile modulus of the material is 106GPa, and the Poisson ratio is 0.3 [8]. The loads of the tensile and bending finite element analysis are the breaking loads in the tests. The flange model is analyzed as linear elasticity.

As is obtained from the finite element analysis, the maximum stress of the advanced composite material flange under the function of the breaking load of the tensile test is 391mpa, and locates at the flange hole and the round corner. The stress distribution of the flange under stress is shown as Fig. (**20**), which is in good agreement with the destroy condition of the tensile tests. In the finite element analysis of the bending tests, for the convenience of loading, the flange and the adhesively bonded carbon fibre pipes are considered as a whole to build the model. Since the root of the flange is the area with the biggest load, the analysis precision is not affected. The stress analysis is shown as Fig. (**21**). The maximum stress of the flange is 366mpa, and locates at the flange holes and the round corners near the flange holes, which is in good agreement with the test results.

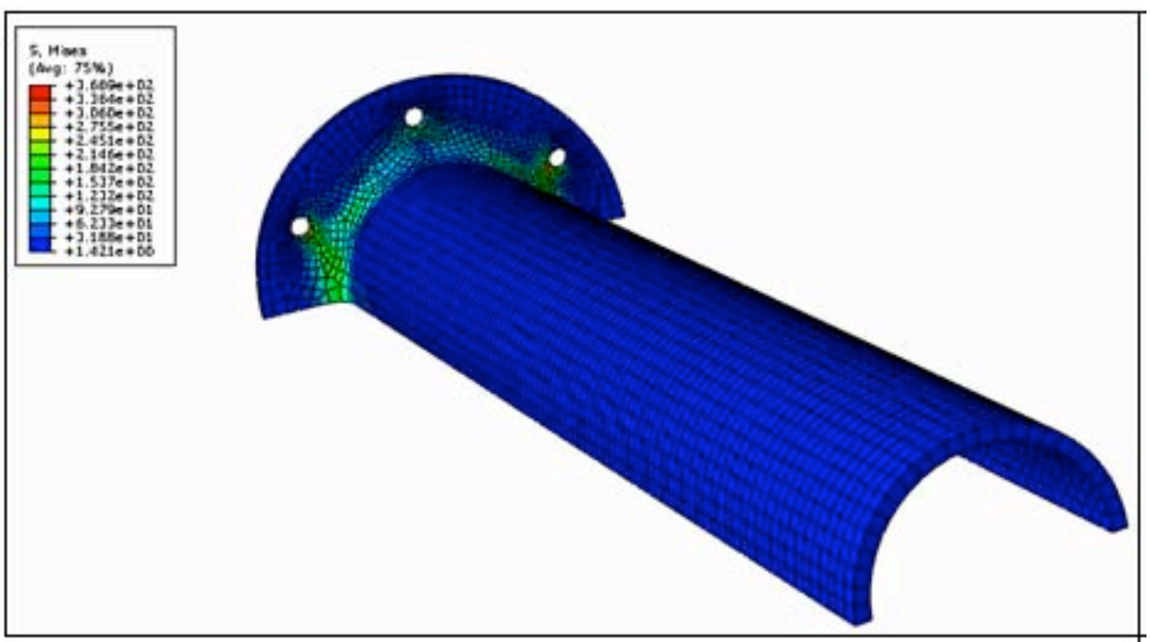

Fig. (21). Displacement nephogram of flange by the bending test.

From the stress and strain distribution resulted from the finite element analysis, it is known that the round corner joints and the flange holes of the flange are the weakness, which have to be strengthened, and the stress of the flange cylinder is relatively smaller, which can be properly weakened.

7. CONCLUSION

The present flange is manufactured by a weaving pre-form and the RTM forming process. The manufacturing process is feasible and the processing efficiency is high. By this process, three-dimensional braided composite material joint can be manufactured in mass production.

The carbon fiber braided composite material joint in concern with the present paper is better than aviation aluminum alloy joint under the condition of the same quality, which suggests that the carbon-fiber composite flange joint researched in the present paper has obvious advantages in substituting aluminum alloy joint in the manufacturing of the truss structures for stratosphere aerostats.

The use of advanced composite material flange connecting pieces has solved the problems of electrical erosion and thermal stress which existed in carbon fibre composite truss structure when using traditional metal connecting pieces.

In conjunction with the results of the finite element analysis, mechanical properties can be further enhanced by the improvements of the braiding process, the forming process and the physical dimension.

REFERENCES

[1] R. M. Crane, and A. B. Macander, “Mutidimensionally braided fiber reinforced composite material characterization”, *Naval Engineers Journal*, vol. 96, No. 6, pp. 52-560, 1984.

[2] L. Jialu, “Three dimensional braiding composites for structural components”, *Journal of Spacecraft Recovery & Remote Sensing*, vol. 28, No. 2, pp. 53-58, 2007. [in Chinese].

[3] E. D. Reese, A. P. Majidi, and R. B. Pipes, “Friction and wear behavior of fiber FP/aluminum composites”, *Journal of Reinforced Plastics and Composites*, vol. 7, No. 11, pp. 500-514, 1988.

[4] R. A. Florentine, “Characterization of 3D braided composites-status of structure-property design data for magnaweave-reinforced carbon-epoxy aircraft composites”, *SAMPE*, pp. 433-443, 1989.

[5] L. W. Gause, and J. Alper, “Structural properties of braided graphite/epoxy composites”, ASTM *Journal of Composites Technology Research*, vol. 9(4), pp. 141-150, 1987.

[6] S. Huiyu, “RTM process and mechanical properties of 3D braided composite materials”, *Journal of Materials Engineering*, vol. 5, pp. 34-40, 1998. [in Chinese].

[7] L. Zhenguo, “Concept of three-dimensional full five-direction braided preforms”, *Journal of Materials Engineering*, pp. 305-308. 2008 [in Chinese].

[8] Z. Fan, “A new scheme and micro-structural model for 3D full 5-directional braided composites”, *Chinese Journal of Aeronautics*, vol. 23, No. 1, pp. 61-67, 2010.

Traction Motor Sizing for Optimal Fuel Economy

Bidyuta Ranjan Rout, *Department of Mechanical Engineering, Aryan Institute of Engineering & Technology, Bhubaneswar, bidyutaranjan1@gmail.com*

Binapani Mohapatra, *Department of Civil Engineering, Raajdhani Engineering College, Bhubaneswar, binapanimohapatra@yahoo.co.in*

Ranjan Kumar, *Department of Mechanical Engineering, NM Institute of Engineering & Technology, Bhubaneswar, kumarranjan75@gmail.com*

Shradha Jena, *Department of Civil Engineering, Capital Engineering College, Bhubaneswar, shradhajena98@gmail.com*

Abstract: This paper presents the traction motor sizing for optimal urban fuel economy in two mild and three strong hybridization propulsion on front-wheel-drive vehicles. The traction motor sizes, by means of motor rated torque and speed, are optimized for maximum urban fuel economy. The two mild hybrids are Belt-Integrated-Starter-Generator (B-ISG) and Crankshaft-Integrated-Starter-Generator (C-ISG) systems. The three strong hybrid configurations include a strong C-ISG system where motor is placed between a starting clutch and the transmission, one-mode Electric Variable Transmission (EVT), and two-mode EVT. Using the simulated vehicle performance data as constraints and the motor rated torque and speed as the design variables, the objective function is to maximize the urban fuel economy. The purpose of this study is to provide a design guideline for hybrid propulsion configurations and component sizing of the traction motors.

Keywords: Component sizing, Electric-variable-transmission, EVT, Hybrid electric vehicle, ISG, Traction motor.

1. INTRODUCTION

Hybrid propulsion systems provide an additional control dimension, as they can control not only engine speed but also the fraction of engine power that is transferred to the driving wheels. This additional level of control enables fuel economy improvement by adding operation features not available with conventional powertrains [1-3]. The Hybrid Electric Vehicle (HEV) can be propelled via the internal combustion engine (ICE), the electric motor, or both. At low speeds when little power is needed, the vehicle moves along silently on just electric power. As the driver accelerates, more power is needed and the engine automatically starts, providing additional power. At cruising speeds, the engine runs alone, driving the electric machine and charging the batteries if needed. The electric motor engages for aggressive acceleration as needed. While braking, electricity gets generated and stored in the batteries for use with the electric motor (regenerative braking). The above features are described next.

The first operation feature enabled by hybridization is that the engine can be turned off when idling or during periods of low power output – two highly inefficient stages of typical ICE operation. This feature is used when engine load is low and operates at a highly inefficient level, such as in deceleration and vehicle launch stages. The vehicle accessories, such as power steering and air conditioning, are electrically powered to maintain the auxiliary functions during engine turn-off stage. The vehicle is propelled by the electric system in the launch stage (assuming that the battery is sufficiently charged). The second hybrid operational feature that can increase fuel economy is electric machine power assist. This assist function has two primary elements. The first element provides assist during varying power demand. This function enables a more fuel-efficient transmission calibration because the required amount of reserve engine power needed for pleasing operation is reduced. The second element of power assist is engine downsizing. During peak demand, the electric machine augments engine power thereby allowing a smaller engine to provide similar performance as a larger engine. Reducing the size of the engine improves fuel economy since the engine operates at a higher percentage of its peak capacity more of the time. Finally, hybrid systems can improve fuel economy by allowing the recuperation of vehicle kinetic energy into stored electrical energy during deceleration or braking actions. When the driver lifts a foot off the accelerator, the electric motor slows the vehicle and at the same time acts as a generator, recharging the battery pack. When the brake is applied, the electric motor actually slows the vehicle while it also charges the battery pack. As additional braking torque is needed, the traditional frictional brakes take over. This recapture energy can be used at a later time to power the auxiliaries or propel the vehicle instead of being lost to heat in the brake rotors.

A hybrid propulsion is comprised of electric motors with power electronics, energy storage devices such as batteries and ultracapacitors, and sophisticated controllers, in addition to such classical components as internal combustion engines, transmissions, clutch, drive shafts, differentials, etc. Therefore, hybrid propulsion is much more complicated than a conventional powertrain. The drivetrain configuration, energy balance optimization, and component optimal sizing have been the focus of research and development in hybrid vehicles in both academic community and industry. Sizing the traction motor is a key point in a HEV to improve fuel economy and dynamic performances [4, 5]. The process of selecting the appropriate electric propulsion systems is however difficult and should be carried out at the system level. The objective of this paper is to optimize the traction motor sizes, by means of motor rated torque and speed, such that the fuel economy of the urban driving cycle is maximized. The vehicle fuel economy and performance of two mild and three strong hybridization propulsions on front-wheel-drive vehicles are first simulated. Using the simulated vehicle performance data as constraints and the motor rated torque and speed as the design variables, the objective function is to maximize the urban fuel economy.

2. PROPULSION HYBRIDIZATION

In a typical vehicle drive train system, four primary components are engine, transmission, final drive and axle, and drive wheels. The engine's primary function is to supply power to the other components of the system. The transmission controls the speed ratio and the level of torque multiplication between the engine and the final drive. The final drive and drive axle assembly multiplies transmission output torque and transfers power to the wheel assembly. Finally the tire and wheel assembly transfers power from the axle to ground. To hybridize a vehicle propulsion system, electric machine must be connected somewhere in the power flow. Based on the ratio of electric power to total power of a vehicle, the degree of propulsion hybridization [6, 7] is typically classified into two levels: mild and strong (or full) hybrids. The front-wheel-drive vehicle in which engine drives the primary front axle is selected in this study.

2.1. Mild Hybrid

The mild hybrids provide limited functions, such as engine stop/start and regenerative braking energy capture. The “mild” means that the vehicle uses a relatively small motor for torque assist of the engine. Belt-Alternator-Starter (BAS) system [8, 9] or Belt-Integrated-Starter-Generator (B-ISG) [10] and Flywheel-Alternator-Starter (FAS) [11], Crankshaft-Integrated-Starter-Generator (C-ISG) [12], or Integrated-Motor-Assist (IMA) systems [13, 14] are currently available mild hybrid propulsions. The B-ISG system replaces the standard alternator with an electric motor/ generator that is connected to the ICE via a belt or chain. The system enables early fuel cut-off during deceleration and shut off of the engine during idle. It operates in two modes: (1) motoring – provides cranking torque to restart the engine when the brake pedal is released and to assist vehicle acceleration; (2) generating – charges the battery when the engine is running. The battery provides electric power to run vehicle accessories and passenger comfort systems while the engine is off. Regenerative braking capabilities are also included to further enhance fuel economy. The B-ISG system strikes a compromise between fuel efficiency and price. It is designed to fit in the same space as a typical engine and work with conventional transmissions to minimize integration effort and cost. Fig. (**1**) illustrates a typical B-ISG system layout.

The C-ISG system replaces the conventional starter motor and alternator with a larger (than in B-ISG) electric machine located between the engine flywheel and transmission. The C-ISG has the similar functions as the B-ISG. A C-ISG system typically utilizes conventional transmissions with significant packaging changes to accommodate

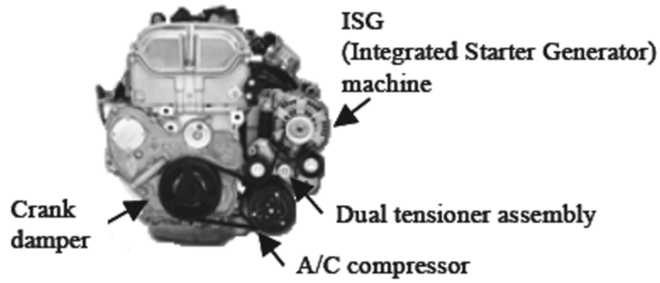

(a) Layout of front engine accessory drive

(b) Assembly of ISG and power electronics box

Fig. (1). Layout of a typical B-ISG system [9].

the increased envelope of the electric machine. The electric machine in the C-ISG system may be packaged around torque converter (using a ring type motor) such as [12], or between the engine and the transmission where the torque converter is removed, such as in Honda IMA system [13, 14]. The C-ISG systems can be changed from mild to strong hybridization by adding starter clutch and increasing the power rating of the electric machine and the corresponding battery capacity [15]. Fig. (**2a**) and (**2b**) respectively shows the mild and strong C-ISG systems.

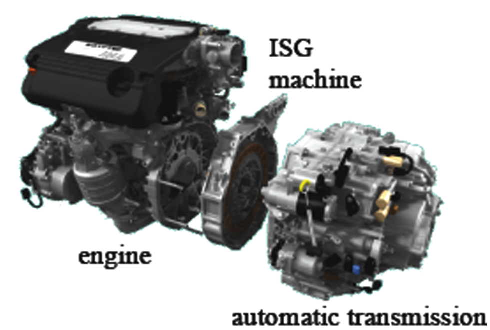

(a) Mild C-ISG

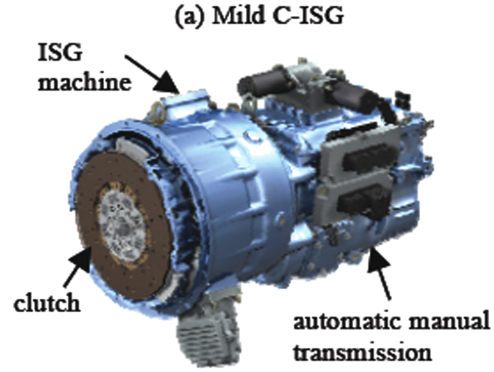

(b) Strong C-ISG

Fig. (2). Layout of a typical C-ISG system [14, 15].

2.2. Strong or Full Hybrid

In addition to enhancing the features of a mild hybrid, the electric motor used in full hybrid architectures provides a larger percentage of total power for longer durations. They also enable electric-only launch and the capability to run solely in electric mode at lower speeds (including reverse) without engaging the ICE. This enables higher levels of fuel efficiency. Three strong hybridization vehicle propulsions are presented and considered in this study. The first configuration is a strong C-ISG system, where motor is packaged between a starting clutch and the transmission. The other two configurations are one-mode Electric-Variable-Transmission (EVT) and two-mode EVT.

The strong C-ISG configuration is attractive because one electric machine can be used to start the engine, to propel the vehicle, and to be function as generator. Fig. (**3a**) illustrates that motor is connected to the transmission input shaft and takes advantage of the torque multiplication of the transmission. The engine is connected to the drive train via a starting clutch. The vehicle may be launched with the motor only where the starting clutch is disengaged and the engine may be turned off or it may be left idling. If the engine participates in the launch, the starting clutch will slip until the transmission input shaft is synchronized with the engine speed. During deceleration, the motor/generator regenerates braking energy to the battery. The engine may be disconnected from the transmission for maximum regeneration or it may be left connected for ease of control. Eaton hybrid drive unit [15] is a strong C-ISG system coupled with automated manual transmissions that have been implemented in production city buses and medium-duty trucks.

The EVT combines planetary gear sets with electric machines and clutches to eliminate the use of a conventional transmission. The one-mode EVT is the major framework of the hybrid fleet from Toyota, Ford and Nissan [16-18]. Another major EVT design on the market is the Allison Hybrid System, also known as AHSII [19]. This system as a two-mode system is applied to several mid-sized SUV's and pickup trucks [20]. A one-mode EVT, shown in Fig. (**3b**) and (**3c**) [21], is studied in this project. The mode means a range of infinitely variable gear ratios. The one-mode is an input split mode that is used for launching the vehicle from a stop or driving at low speeds [17, 22]. The input power split is a parallel hybrid which uses planetary gear set to divide the engine power into an electrical path and a mechanical path. The planetary gear set multiplies engine torque and allows the engine to operate over a continuous range of

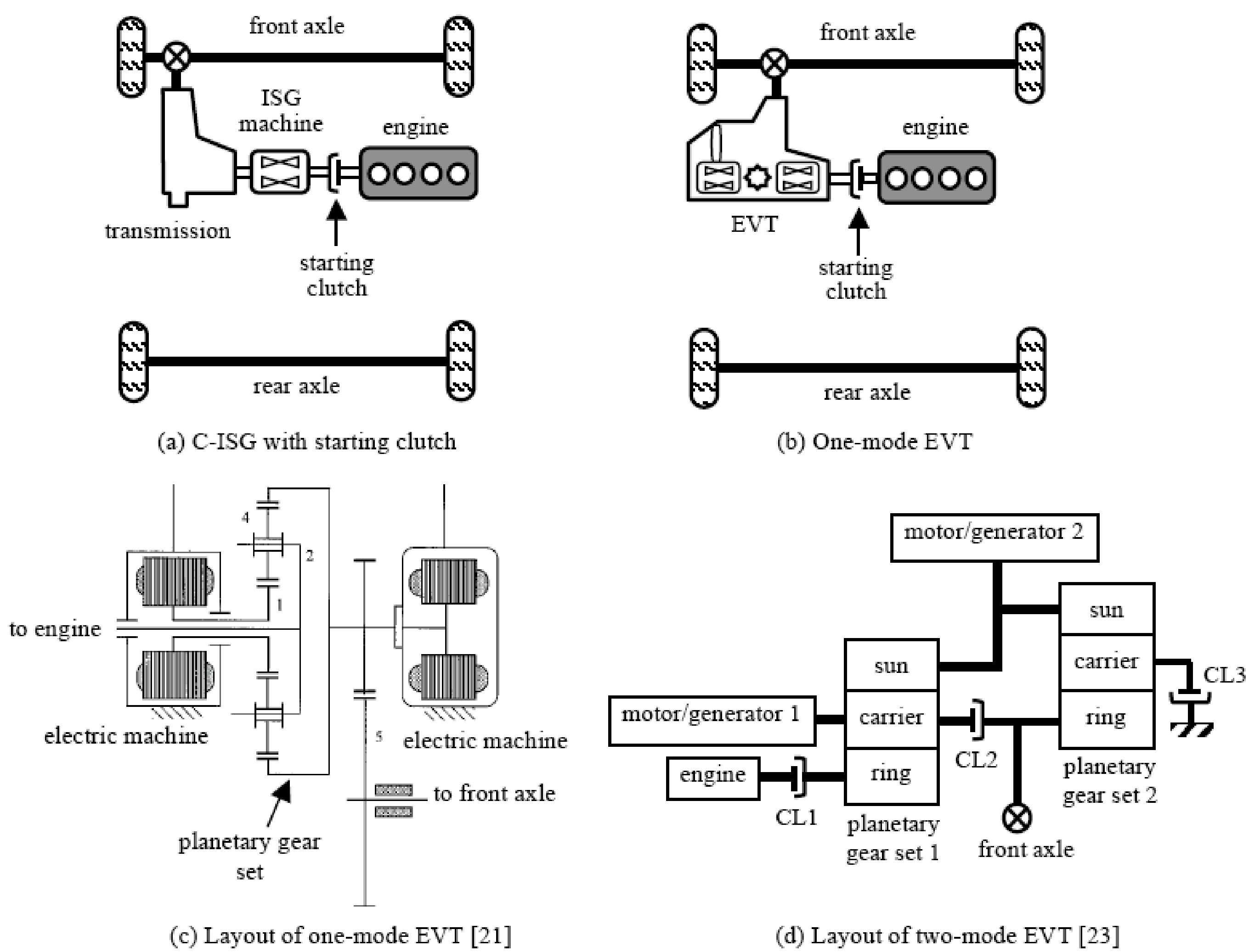

Fig. (3). Configurations of three strong HEVs.

speeds. This architecture utilizes a power-flow where the engine is connected to a planetary carrier (input 1), a generator is connected to the corresponding sun gear (input 2), and another electric motor is connected on the ring gear (transmission output). This configuration allows a great deal of engine control flexibility and also provides full hybrid functionality.

The two-mode EVT for front-wheel-drive vehicle consists of two planetary gear sets and three clutches as shown in Fig. (**3d**) [23]. By selectively engaging and disengaging of the clutches, the compound input power split EVT establishes different torque multiplication ratios between the engine, electric motors and transmission output shaft. This allows for additional flexibility and better performance with the same size electrical components. The first and second planetary gear sets split mechanical power from the input. The first mode of the power-split (Mode 1) exists when the output shaft is driven by the planetary gear set 2 where CL3 is applied, and the second mode (Mode 2) exists when the output shaft is driven by the planetary gear set 1 and CL2 is on. The electric launch of the vehicle has two regions that depend on the vehicle velocity, and the engine is always off (CL1 off). The first region is for low speeds (CL1 and CL2 are off, CL3 is on, and motor/generator 2 is on while motor/generator 1 is off), the second region (CL1 is off, CL2 and CL3 are on, and both electric machines are motoring) is for faster speeds. As significant transmission power is required: the engine is on (CL1 is on or engaged) and there is power flow from the battery pack. At low speeds, Mode 1 is selected and then Mode 2 is selected as fast speeds are attained. The continuous variable gear ratio regime has engine power and no power flow to or from the battery pack, and occurs when the vehicle road load is relatively small. When the vehicle is moving slowly in this regime, Mode 1 is chosen; when the vehicle is moving at medium or fast speeds, Mode 2 is selected.

This paper investigates the traction motor sizing for optimal urban fuel economy in two mild hybrids (B-ISG and C-ISG) and three strong hybrid configurations (strong C-ISG, one- and two-mode EVT).

3. HEV MODELING AND SIMULATION

The component sizing and system prototyping of a hybrid propulsion is difficult because of the many design options and the rapidly developing technologies in the automotive industries. Modeling and simulation is needed to analyze component sizing and quantify benefits of hybrid propulsion configurations. Vehicle simulation model can be generally classified as two types: kinematic and dynamic methods. In the kinematic method, the force required to accelerate the vehicle through the time step is calculated directly from the required speed trace. The required force is then translated into a torque that must be provided by the component directly upstream. This power/energy requirement at the wheel is passed backward through all the propulsion components to compute fuel and electricity consumption. The dynamic method is solved forward approach where the desired vehicle speed is an input to the driver/PID controller which actuates the accelerator position therefore requesting torque from the engine which in turn produces a response through the driveline. This method is more realistic in that it controls the engine similar to the way an actual driver does and does not impose or directly control the driveline components. The adjustment of the driver/PID determines how accurately the analytical vehicle follows the desired vehicle speed trace. The dynamic method was applied in this project.

The GT-Drive software [24] was used for the analytical simulation in this project. For this study, a relatively simple approach was taken that uses steady state engine performance maps to determine fuel rate for a desired engine torque at a given engine speed. It has been shown that fuel economy can be accurately predicted using simple steady state engine maps [25, 26]. For accurate simulation, the model requires considerable driveline information: clutch and torque converter performance tables; transmission with gear ratios, inertias, efficiencies and shift schedule; drive shaft and axle with inertias; final drive with gear ratio and inertias; tires with radius, rolling resistances; brake with braking torque maps; and any other data related to vehicle resistances such as aerodynamic loading. Other control algorithms were added to the model for simulating an idle speed controller and a simple fuel shutoff control during deceleration events. A GT-Drive vehicle model with one-mode EVT is presented in Fig. (**4**). Fig. (**4a** and **4b**) respectively shows the vehicle and powertrain model.

The fuel economy prediction is based on the U.S. Environmental Protection Agency (EPA) drive schedule. The EPA drive schedule is divided into two main portions: urban and highway drive cycles respectively represented by FTP-75 (Federal Test Procedure) and HWFET (Highway Fuel Economy Test) [27]. The urban cycle contains lower vehicle speeds and more stop and go (or accelerating, decelerating, and idle). Cold start fuel penalty also applies to urban cycle. The highway cycle represents freeway conditions and contains higher vehicle speeds and more steady state cruise regions. These two cycles are combined into a formula, as illustrated in Eq. (1), to obtain the composite fuel economy value. The composite fuel economy is defined as:

$$\frac{1}{\dfrac{0.55}{\text{urban fuel economy}}+\dfrac{0.45}{\text{highway fuel economy}}} \quad \ldots \quad (1)$$

The label numbers that appear on the vehicle stickers are adjusted by the EPA to represent fuel economy closer to on the road conditions.

Adjusted or label urban fuel economy = Simulated or test of urban fuel economy*0.9 … (2)

Adjusted or label highway fuel economy = Simulated or test of highway fuel economy*0.78 … (3)

In this paper, all the fuel economy data are converted to adjusted data. Additional to the fuel economy data, vehicle performance data is also important. The standard performance categories are vehicle maximum velocity and peak acceleration, time to peak acceleration, time to reach 48 kilometer per hour (kph), time to reach 96 kph, time to reach 128.7 kph from 80.5 kph, and gradeability at 88.5 kph.

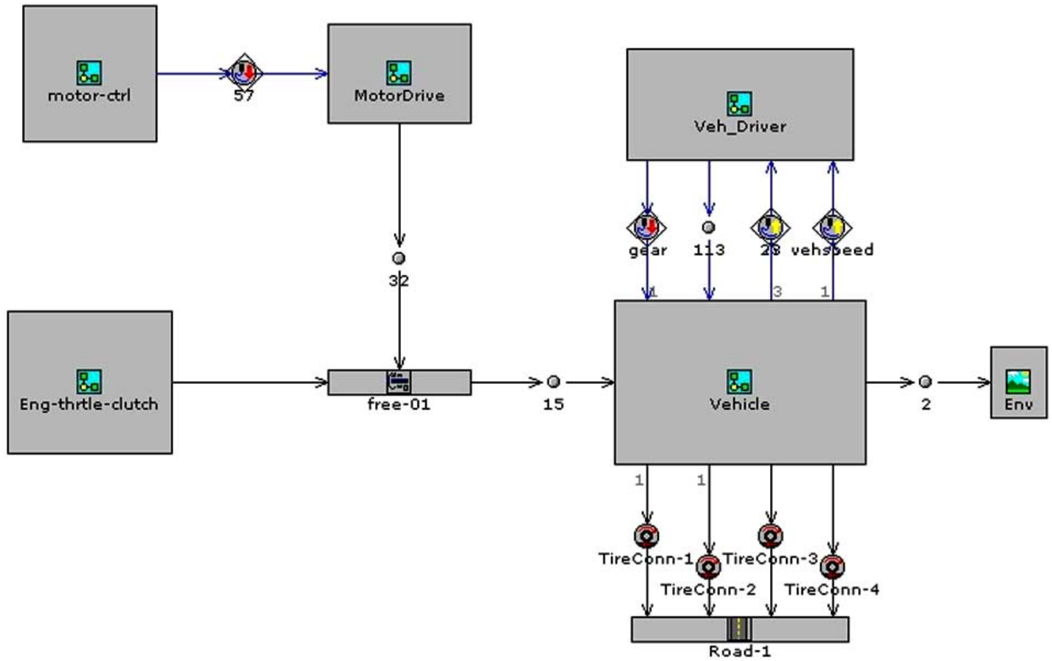

(a) Vehicle system model

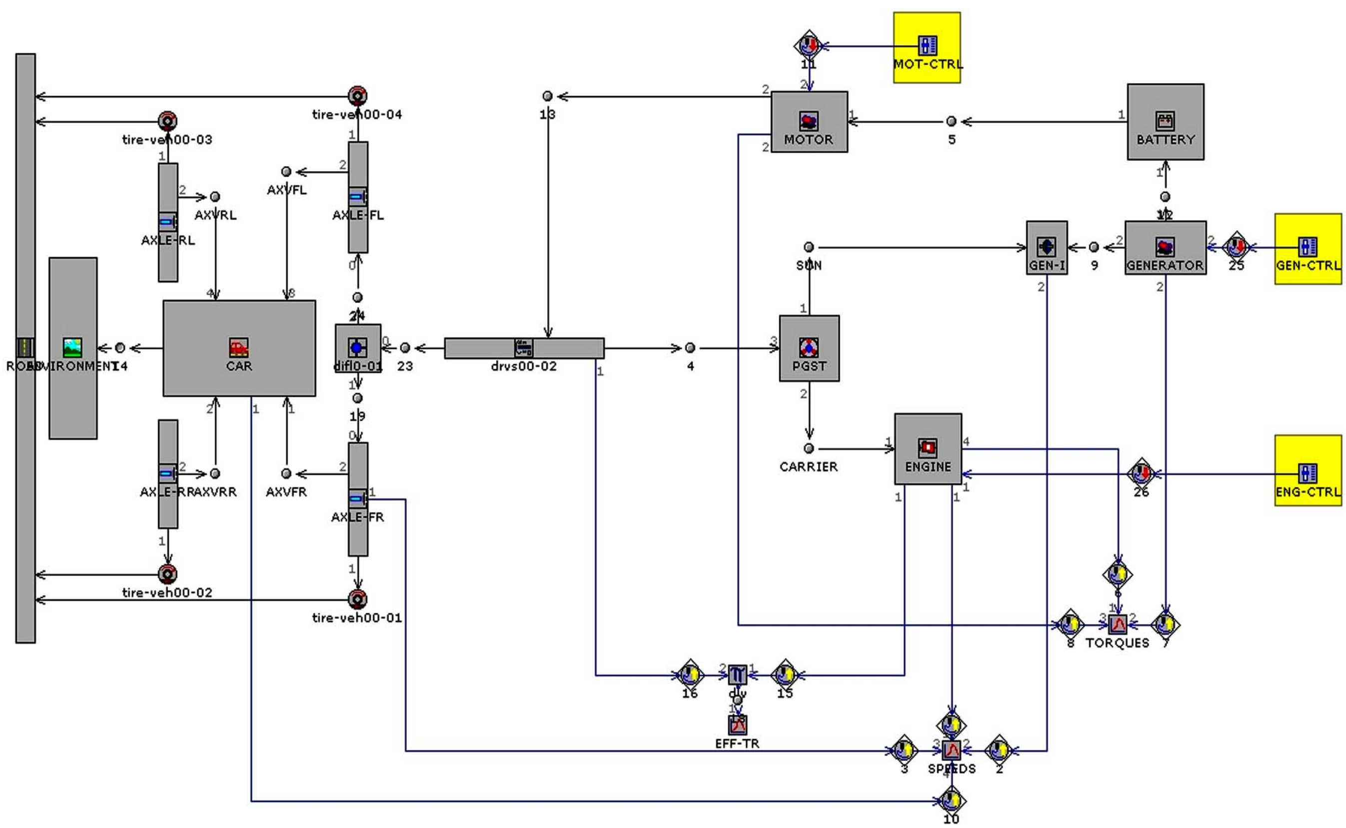

(b) One-mode EVT powertrain model

Fig. (4). Layout of a GT-Drive model.

3.1. Conventional Vehicle Analysis

The fuel economy and vehicle performance of conventional powertrain, two mild, and three strong hybrid configurations are predicted using GT-Drive software. The purpose of conventional vehicle analysis is to validate the simulation model and to use the simulated results as a baseline for gauging the vehicle fuel economy and performance of the

HEVs. The base vehicle is a front-wheel-drive compact size sport utility vehicle equipped with an inline four-cylinder 2.2-liter engine (102 kW at 5200 rpm and 198 N-m at 4400 rpm), CVT (ratio range from 2.63 to 0.47), and 4.98 final drive ratio. The vehicle mass is 1588 kg with aerodynamic characteristics as: 2.59 m^2 frontal area, 0.397 drag coefficient, and 1.2555 kg/m^3 air density. The simulated urban fuel economy is 22.2 mile per gallon (mpg) or 10.59 liter/100km, which is 5.6% higher than the test vehicle data or label data (21 mpg or 11.2 liter/100km). The simulated highway fuel economy is 28.2 mpg (8.34 liter/100km), which is 0.7% higher than the test vehicle data (28 mpg or 8.4 liter/100km). Therefore the composite fuel economy is 24.6 mpg (9.56 liter/100km) and 2.5% higher than label data (24 mpg or 9.8 liter/100km). Based on this correlation, the predicted fuel economy is acceptable. The fuel economy improvements on hybrid vehicles will use these simulation data (on conventional vehicle) as a comparison base. The predicted vehicle performance is: 184.2 kph vehicle top speed, 3.81 m/s^2 (0.39 g) peak acceleration, 1.8 sec to the peak acceleration, 4.3 sec to reach 48 kph, 9.6 sec to reach 96 kph, 9.0 sec to reach 128.7 kph from 80.5 kph, and 20.8% gradeability at 88.5 kph.

3.2. B-ISG (Mild Hybrid) Analysis

The engine, transmission, torque converter and final drive ratio are identical to conventional vehicle in the B-ISG configuration. The hybrid vehicle mass is 1688 kg which adds 100 kg for hybrid components. For comparison purpose, the aerodynamic characteristics are the same as conventional vehicle. The hybrid components include an inverter, battery (36 Volt, 20 amp-hrs, 4.7 kW max power charge and 8.4 kW max power discharge) and one electric machine (induction motor, 4.0 kW rated power, 10000 rpm rated speed, and 70 N-m rated torque). The belt ratio between motor and crankshaft is 1.60.

The simulated urban fuel economy is 24.3 mpg (9.68 liter/100km), which is 9.4% improvement over the conventional vehicle (22.2 mpg or 10.59 liter/100km). The simulated highway fuel economy is 28.4 mpg (8.28 liter/100km), which is only 0.7% improvement over the conventional vehicle (28.2 mpg or 8.34 liter/100km). Therefore the composite fuel economy is 26.0 mpg (9.05 liter/100km) and 5.7% improvement (24.6 mpg or 9.56 liter/100km). The predicted vehicle performance is: 179 kph vehicle top speed, 3.60 m/s^2 (0.37 g) peak acceleration, 2.2 sec to peak acceleration, 4.3 sec to reach 48 kph, 10.2 sec to reach 96 kph, 10.2 sec to reach 128.7 kph from 80.5 kph, and 18.4% gradeability at 88.5 kph.

3.3. C-ISG (Mild Hybrid) Analysis

The C-ISG mild hybrid vehicle mass is 1688 kg which adds 100 kg for hybrid components. For comparison purpose, the aerodynamic characteristics are the same as conventional vehicle. The hybrid components include an inverter, battery (42 Volt, 55 amp-hrs, 8 kW max power charge and 12 kW max power discharge) and one electric machine (induction motor, 7.0 kW rated power, 10000 rpm rated speed, and 123 N-m rated torque). The motor is directly mounted to the engine flywheel, therefore the ratio is 1.00.

The simulated urban fuel economy is 25.0 mpg (9.41 liter/100km), which is 12.6% improvement over the conventional vehicle. The simulated highway fuel economy is 28.7 mpg (8.19 liter/100km), which is only 1.8% improvement over the conventional vehicle. Therefore the composite fuel economy is 26.6 mpg (8.84 liter/100km) and 8.2% improvement. The predicted vehicle performance is: 179 kph vehicle top speed, 3.61 m/s^2 (0.37 g) peak acceleration, 2.7 sec to peak acceleration, 4.3 sec to reach 48 kph, 10.1 sec to reach 96 kph, 10.1 sec to reach 128.7 kph from 80.5 kph, and 18.5% gradeability at 88.5 kph.

3.4. Strong C-ISG Analysis

The engine, transmission, and final drive ratio are identical to conventional vehicle for the strong C-ISG architecture. The torque converter is replaced by a starting clutch. For comparison purpose, the aerodynamic characteristics are the same as the conventional vehicle. The hybrid vehicle mass is 1738 kg which adds 150 kg for hybrid components. The hybrid components include an inverter, battery (300 Volt, 6.5 amp-hrs, 20 kW max power charge and 28 kW max power discharge) and one electric machine (20.9 kW rated power, 14000 rpm rated speed, and 90 N-m rated torque). The energy management and control strategy are the same as [6].

The simulated fuel economy is 32.7 mpg (7.19 liter/100km) in urban (47.2% improvement) and 28.9 mpg (8.14 liter/100km) in highway (2.5% improvement), which results in 30.9 mpg (7.61 liter/100km) composite fuel economy (25.5% improvement). The predicted vehicle performance is: 178.8 kph vehicle top speed, 3.51 m/s^2 (0.36 g) peak acceleration, 2.3 sec to peak acceleration, 3.8 sec to reach 48 kph, 9.9 sec to reach 96 kph, 10.4 sec to reach 128.7 kph from 80.5 kph, and 18.0% gradeability at 88.5 kph.

3.5. One-Mode EVT Analysis

In the one-mode EVT, the engine and final drive ratio are identical to conventional vehicle. The hybrid components include two inverters, battery (300 Volt, 6.5 amp-hrs, 20 kW max power charge and 28 kW max power discharge), two electric machines (25.1 kW rated power, 14000 rpm rated speed, and 90 N-m rated torque), and one planetary gear set (2.21 ratio) with clutches. A gear ratio of 2.21 is connected to motor because motor rotates faster than planetary output shaft. The energy management and controls are similar to the previous two configurations with the following modifications:

• *Engine Control Strategy*: load following with battery assist. The engine operates at the lowest possible speed with the battery assisting if required.

• *Instantaneous Optimization Method*: lowest system loss. The valid engine speed and torque range is analyzed at each time step, and the torque combination resulting in the lowest total system loss is selected [28].

The total system loss represents the overall driving efficiency of the vehicle and is calculated as:

Total system loss = w_e * engine loss + w_m * electric machine losses + w_t * transmission loss + w_b * battery loss + (w_{c1} + w_{c2}(current SOC – final SOC)) * battery recharging loss (4) where w_e, w_m, w_t, w_b, w_{c1} and w_{c2} are weight factors defined by user. The initial values of w_e, w_m, w_t, and w_b are set to 1.0. The w_{c1} is the weight factor for battery recharging base and set to 1.70 and 1.97 respectively in the urban and highway driving cycle. The w_{c2} is the weight factor for battery recharging slope and set to –3.0. The loss of each component is defined as:

Engine loss = (fuel power in) – (engine mechanical power out) … (5)

Electric machine loss = sum of losses of all motors in the system … (6)

Transmission loss = gear mesh, spin and pumping loss of transmission … (7)

Battery loss = $I_{bat}^2 * r_{bat}$ … (8)

Battery recharging loss = $I_{bat} * V_{bat}$ … (9)

The battery recharging loss is a measure of the fuel energy required to replace energy removed from the battery. If the battery assists the engine in propelling the vehicle at a given time, engine power is reduced but this represents a debit that must be returned to the battery.

The simulated fuel economy is 35.4 mpg (6.64 liter/100km) in urban (59.7% improvement) and 29.8 mpg (7.89 liter/100km) in highway (5.8% improvement), which results in 32.7 mpg (7.19 liter/100km) composite fuel economy (32.8% improvement). The predicted vehicle performance is: 176.2 kph vehicle top speed, 5.7 m/s^2 (0.58 g) peak acceleration, 0.7 sec to peak acceleration, 4.1 sec to reach 48 kph, 12.4 sec to reach 96 kph, 14 sec to reach 128.7 kph from 80.5 kph, and 13.1% gradeability at 88.5 kph.

3.6. Two-Mode EVT Analysis

The engine and final drive ratio are identical to conventional vehicle. The hybrid components include two inverters, battery (300 Volt, 6.5 amp-hrs, 20 kW max power charge and 28 kW max power discharge), two electric machines (25.1 kW rated power, 14000 rpm rated speed, and 90 N-m rated torque), three planetary gear sets and four clutches. The planetary gear ratios (ring gear teeth number / sun gear teeth number) are selected as: planetary gears one and two is 1.9545; planetary gear three is 2.6923. The simulated fuel economy is 36.3 mpg in urban (63.5% improvement) and 29.5 mpg in highway (4.6% improvement), which results 32.9 mpg combined fuel economy (33.7% improvement). The predicted vehicle performance is: 192.7 kph vehicle top velocity, 5.03 m/s^2 (0.51 g) peak acceleration, 0.6 sec to peak acceleration, 3.2 sec to reach 48 kph, 9.4 sec to reach 96 kph, 8.2 sec to reach 128.7 kph from 80.5 kph, and 19.8% gradeability at 88.5 kph.

4. OPTIMIZATION OF ELECTRIC MACHINE SIZE

An electric machine delivers high torque at low speeds and high power at high speeds. These speed torque characteristics of the electric machine are ideally suited for traction function of the ground vehicles. The motor gives a constant torque for variable speed up to the 'base (rated) speed' of the motor; beyond the base speed, the torque of the motor decreases with increase in the speed. The main requirement that is related to the electric propulsion control is the ability to operate at constant power over a wide speed range, good overload performance, and high efficiency.

The objective of this paper is to optimize the traction motor in HEV to increase the fuel economy on an urban driving cycle. The vehicle fuel economy and performance data of two mild and three strong hybridization propulsions on front-wheel-drive vehicles are initially predicted using GT-Drive software. Using the simulated vehicle performance data (max. velocity, max. acceleration, and time to reach 96 kph vehicle speed) as constraints and the motor rated torque and speed as the design variables, the objective function is to maximize the urban fuel economy. The objective function only targets on the urban driving cycle because most of the HEVs gain the fuel economy improvement mainly from the urban or city driving cycle. The urban or city driving cycle consists of stop-start operations and lower vehicle speed using electric launch. A completed design exploration software, iSight platform optimization algorithm [29, 30], is integrated with the GT-Drive for optimization study.

The basic overview of the integration process between the two software is described as (1) GT-Drive is used to build the vehicle model, make parameters of the independent variables, and run the model; (2) iSight is used to parse the independent parameters in the GT-Drive .dat file, parse the output variables in the GT-Drive .rlt file, and set up the command line execution of the GT-Drive. After choosing a strategy in the iSight, the model is ready to be executed. The iSight reads the output variables from the .rlt file at the end of each iteration and then replaces the independent variables in the .dat file before the next iteration begins.

The optimization problem statement is to size the motor in a manner that minimizes fuel consumption while meeting performance characteristics for a given driving cycle. Using a strong C-ISG hybrid vehicle as an example, the problem statement is described below.

Maximize: FE_u, Urban fuel economy (average mile per gallon of gasoline from all initial SOC load cases)

Subject to:

$t_1 \leq 9.9$ sec (accelerate time to 96 kph from 0) … (10)

$t_2 \leq 10.4$ sec (accelerate time to 128.7 kph from 80.5 kph or quarter-mile acceleration) … (11)

$S_{top} \geq 178$ kph … (12)

$a_{max} \geq 3.5$ m/s^2 … (13)

By varying design variables:

M_t (motor rated torque)

M_s (motor rated speed)

With:

$SOC_u = 0.68$, upper SOC limit … (14)

$SOC_l = 0.52$, lower SOC limit … (15)

$SOC_b = \{0.52, 0.60, \text{and } 0.69\}$ (multiple initial SOC load cases) … (16)

Using the above simulated performance data ($S_{top} \geq 180$ kph; $a_{max} \geq 3.5$ m/s^2; $t_1 \leq 10$sec) as constraints and the motor rated torque and speed as the design variables, the objective function is to maximize the urban fuel economy. For a strong

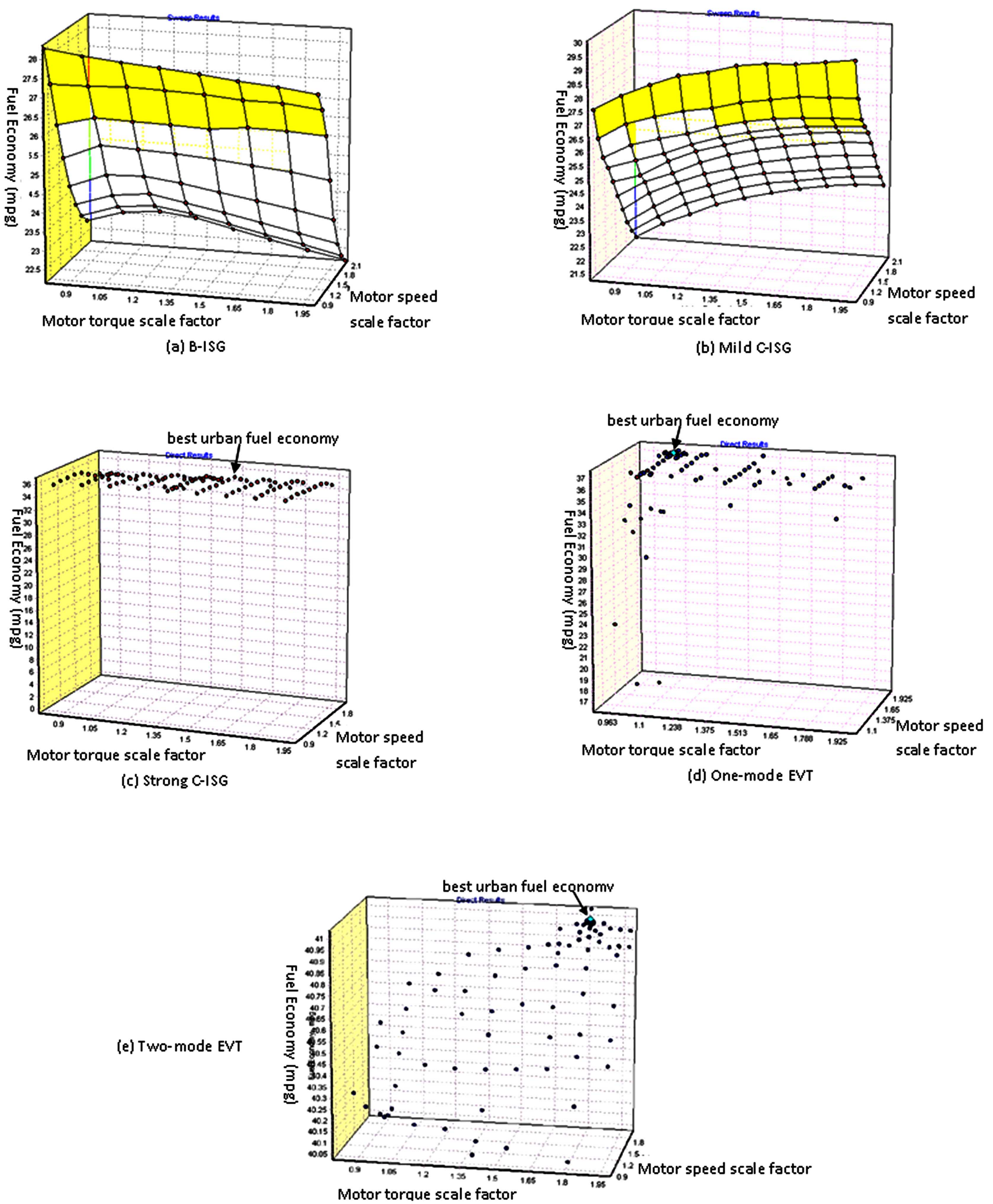

Fig. (5). Optimization results of two mild and three strong hybrid configurations.

Table 1. Summary of Simulation Results

		Fuel Economy (mpg)						Performance (sec)
		Composite	**% gain**	**Urban**	**% gain**	**Highway**	**% gain**	**0 ~ 96 kph**
Conventional		**24.6**		**22.2**		**28.2**		**9.6**
Mild HEV	B-ISG	26.0	5.7%	24.3	9.4%	28.4	0.7%	10.2
	Mild C-ISG	26.6	8.2%	25.0	12.6%	28.7	1.8%	10.1
Strong HEV	Strong C-ISG	30.9	25.5%	32.7	47.2%	28.9	2.5%	9.9
	One-mode EVT	32.7	32.8%	35.4	59.7%	29.8	5.8%	12.4
	Two-mode EVT	32.9	33.7%	36.3	63.6%	29.5	4.6%	9.4

Table 2. Summary of Simulation Results with Optimal Traction Motor Sizes

		Optimal traction motor size			Fuel economy (mpg)	
		Rated power (kW)	**Rated speed (rpm)**	**Rated torque (N-m)**	**Urban**	**% gain**
Conventional					**22.2**	
Mild HEV	B-ISG	6	13000	84	25.5	14.9%
	Mild C-ISG	10	14000	120	26.4	18.9%
Strong HEV	Strong C-ISG	26	11620	135	33.1	49.0%
	One-mode EVT	41	21238	97	36.7	65.3%
	Two-mode EVT	56	17500	162	37.2	67.6%

C-ISG configuration, the optimal motor size (26 kW rated power, 11620 rpm rated speed, and 135 N-m rated torque) results in a maximum urban fuel economy at 33.1 mpg which is 49% improvement.

The same approach is applied to the other hybrid configurations to determine the optimal electric machine size. The optimal B-ISG motor size (6.0 kW rated power, 13000 rpm rated speed, and 84 N-m rated torque) results in a maximum urban fuel economy at 25.5 mpg which is 14.9% improvement while sustaining the vehicle performance. An optimal mild C-ISG motor size (10 kW rated power, 14000 rpm rated speed, and 120 N-m rated torque) results in a maximum urban fuel economy at 26.4 mpg which is 18.9% improvement while sustaining the vehicle performance. For the strong hybrid configurations, the front axle optimal motor size (26 kW rated power, 16786 rpm rated speed, and 92 N-m rated torque) results in a maximum urban fuel economy at 33.4 mpg which is 50.5% improvement while sustaining the vehicle performance. The optimal motor size (41 kW rated power, 21238 rpm rated speed, and 97 N-m rated torque) for a one-mode EVT results in a maximum urban fuel economy at 36.7 mpg which is 65.3% improvement. In the two-mode EVT, the optimal motor size (56 kW rated power, 17500 rpm rated speed, and 162 N-m rated torque) results in a maximum urban fuel economy at 37.2 mpg which is 67.6% improvement. Figs. (**5a**) and (**5b**) respectively show the optimization results for B-ISG mild C-ISG. Figs. (**5c**) to (**5e**) show the optimization results for three strong hybrid propulsion configurations.

Simulation results are summarized in Table **1**, indicating that mild and strong hybrid configurations can result in urban fuel economy gains respectively up to 12.6% and 63.6% over conventional powertrain. Using the simulated vehicle performance data (top speed, maximum acceleration and time to reach 96 kph vehicle speed) as constraints and the motor rated torque and speed as the design variables, the objective function is to maximize the urban fuel economy. Since the main fuel economy gains is in the urban driving cycle and the electric motor plays an important role in improving urban fuel economy, the optimal motor sizes are investigated only in the urban cycle. Table **2** summarizes the optimal motor size and maximum urban fuel economy for five hybrid configurations. The purpose of this study is to provide a design guideline for hybrid propulsion configuretions and component sizing of the traction motors.

5. CONCLUSIONS

This paper presents the modeling and simulation of vehicle fuel economy and performance for two mild and three strong hybridization propulsions on front-wheel-drive vehicles. Based on the simulation results, the traction motor sizes, by means of motor rated torque and speed, are optimized for maximum urban fuel economy. The two mild hybrids are B-ISG and C-ISG systems. The three strong hybrid configurations include a strong C-ISG system where motor is placed between a starting clutch and the transmission, one-mode and two-mode EVTs. The main fuel economy improvement is in the urban driving cycle, this is due to (1) allowing the engine to shut-off under vehicle coast-down and stop conditions, and (2) launching vehicle by electric motor. In order to keep the same towing capability as conventional vehicle, engine downsizing advantage was not adopted. If a smaller engine were implemented, the fuel economy improvements would be larger.

The significant packaging change to accommodate the increased envelope of the optimal electric motor and the corresponding battery are not taken as the constraints in the optimization process. It would be difficult to pack two electric motors and planetary gear sets (an EVT system) in a small or compact front-wheel-drive vehicle. The optimal motor size might not be feasible in the actual design and manufacturing stage. This study does not investigate the driveability which could be a major issue for strong C-ISG configuration since torque converter is replaced by a starting clutch.

ABBREVIATIONS

a_{max}	=	Vehicle maximum acceleration
FE_u	=	Urban fuel economy
I_{bat}	=	Battery current
kph	=	Kilo meters per hour
kW	=	Kilo Watts
M_t	=	Motor rated torque
Ms	=	Motor rated speed
mpg	=	Miles per gallon
N-m	=	Newton-meter
rpm	=	Revolutions per minute
r_{bat}	=	Battery resistance
SOC	=	State Of Charge on battery
SOC_u	=	Upper SOC limit
SOC_l	=	Lower SOC limit
SOC_b	=	Initial SOC load cases
S_{top}	=	Vehicle top speed
t_1	=	Accelerate time to 96 kph from 0
t_2	=	Accelerate time to 128.7 kph from 80.5 kph or quarter-mile acceleration
V_{bat}	=	Battery voltage
w_b	=	Weight factor of battery loss
w_{c1}	=	First weight factor of battery charging loss
w_{c2}	=	Second weight factor of battery charging loss
w_e	=	Weight factor of engine loss
w_m	=	Weight factor of electric machine loss
w_t	=	Weight factor of transmission loss

ACKNOWLEDGEMENTS

This work was supported in part by the National Science Foundation, CCLI-Phase I: Exploratory, under grant number DUE-0941809.

CONFLICT OF INTEREST

None declared.

REFERENCES

[1] K.T. Chau, and S. Wong, "Overview of power management in hybrid electric vehicles", *Energ. Convers. Manage.*, vol. 43, pp. 1953-68, 2002.

[2] K. Oh, J. Min, D. Choi, and H. Kim, "Optimization of control strategy for a single-shaft parallel hybrid electric vehicle", *IMechE Proc. Part D: J. Automob. Eng.*, vol. 221, 2007, pp. 555-65.

[3] Y. Zhang, H. Lin, B. Zhang, and C. Mi, "Performance modeling and optimization of a novel multi-mode hybrid powertrain", *ASME Trans. J. Mech. Des.*, vol. 128, pp. 79-89, 2006.

[4] M. Zeraoulia, M. Benbouzid, and D. Diallo, "Electric motor drive selection issues for HEV proulsion systems: a comparative study", *IEEE Trans. Veh. Technol.*, vol. 55, no. 6, pp. 1756-64, 2006.

[5] M. Ehsani, Y. Gao, and S. Gay, "Characterization of electric motor drives for traction applications", *In: IEEE annual conference,* vol. 1, 2003, pp. 891-6.

[6] Y.G. Liao, T. Weber, and D. Pfaff, "Modeling and analysis of powertrain hybridization on all-wheel-drive sport utility vehicles", *IMechE Proc. Part D: J. Automob. Eng.*, vol. 218, pp. 1125-34, 2004.

[7] E. Odvarka, A. Mebarki, D. Gerada, N. Brown, and C. Ondrusek, "Electric motor-generator for a hybrid electric vehicle", *Eng. Mech.*, vol. 16, no. 2, pp. 131-39, 2009.

[8] H. Kusumi, K. Yagi, Y. Ny, S. Abo, H. Sato, S. Furuta, and M. Morikawa, "42V power control system for mild hybrid vehicle (MHV)", *SAE paper 2002-01-0519*, 2002.

[9] G. Tamai, M. Jeffers, C. Lo, C. Thurston, S. Tarnowsky, and S. Poulos, "Development of the hybrid system for the Saturn VUE hybrid", *SAE paper 2006-01-1502*, 2006.

[10] M. Canova, K. Sevel, Y. Guezennec, and S. Yukovich, "Control of the start/stop of a diesel engine in a parallel HEV with a belted starter/alternator", *SAE paper 2007-24-0076*, 2007.

[11] D. Evans, M. Polom, S. Poulos, K. VanMaanen, and T. Zarger, "Powertrain architecture and controls integration for GM's hybrid full-size pickup truck", *SAE paper 2003-01-0085*, 2003.

[12] X. Chen, and S. Shen, "Comparison of two permanent-magnet machines for a mild hybrid electric vehicle application", *SAE paper 2008-01-1552*, 2008.

[13] K. Hanada, M. Kaizuka, S. Ishikawa, T. Imai, H. Matsuoka, and H. Adachi, "Development of a hybrid system for the V6 midsize sedan", *SAE paper 2005-01-0274*, 2005.

[14] A. Kabasawa and K. Takahashi, "Development of the IMA motor for the V6 hybrid midsize sedan", *SAE paper 2005-01-0726*, 2005.

[15] C. Lin, H. Peng, J. Grizzle, J. Liu, and M. Busdiecker, "Control system development for an advanced-technology medium-duty hybrid truck", *SAE paper 2003-01-3369*, 2003.

[16] L. Tsai, G. Schultz, and N. Higuchi, "A novel parallel hybrid transmission", *ASME Trans. J. Mech. Des.*, vol. 123, pp. 161-8, 2001.

[17] K. Ahn, S. Cho, S. Cha, and J. Lee, "Engine operation for the planetary gear hybrid powertrain", *IMechE Proc. Part D: J. Automob. Eng.*, vol. 220, pp. 1727-35, 2006.

[18] S. Cho, K. Ahn, and J. Lee, "Efficiency of the planetary gear hybrid powertrain", *IMechE Proc. Part D: J. Automob. Eng.*, vol. 220, pp. 1445-54, 2006.

[19] D. Zhang, J. Chen, J. Hsieh, J. Rancourt, and M. R. Schmidt, "Dynamic modelling and simulation of two-mode electric variable transmission", *IMechE Proc. Part D: J. Automob. Eng.*, vol. 215, pp. 1217-23, 2001.

[20] G. Tamai, S. Reeves, and T. Grewe, "Truck utility and functionality in the GM 2-mode hybrid", *SAE paper 2010-01-0826*, 2010.

[21] Toyota Hybrid System THSII, Toyota Motor Corporation, Public Affairs Division, 2003. [Online] Available: http://www.evworld. com/library/ toyotahs2.pdf [Accessed May 11, 2011].

[22] J. Meisel, "An analytical foundation for the Toyota Prius THS-II powertrain with a comparison to strong parallel-electric powertrain", *SAE paper 2006-01-0666*, 2006.

[23] M.R. Schmidt, "*Two-mode, input-split, parallel, hybrid transmission*", U. S. Patent 5,558,588, September 24, 1996.

[24] GT-Drive, Gamma Technologies, Inc., Westmont, IL, USA: [Online] Available: http://www.gtisoft.com/. [Accessed May 25, 2011].

[25] S. Hausberger, and M. Rexeis, "Emission behaviour of modern heavy duty vehicles in real world driving", *Intl. J. Environ. Pollut.*, vol. 22, no. 3, pp. 275-86, 2004.

[26] M. Ward, C. Brace, T. Hale, and R. Ceen, "Investigation of sweep mapping approach on engine testbed", *SAE paper 2002-01-0615*, 2002.

[27] U.S. Environmental Protection Agency (EPA), Testing and Measuring Emissions: [Online] Available: http://www.epa.gov/ fueleconomy/420f06069. htm#background_existing. [Accessed June 6, 2011].

[28] G. Paganelli, T.M. Guerra, S. Delprat, J. Santin, M. Delhom, and E. Combes, "Simulation and assessment of power control strategies for a parallel hybrid car", *IMechE Proc. Part D: J. Automob. Eng.*, vol. 214, pp. 705-17, 2004.

[29] B. Tillock, and C. Yuan, "iSIGHT/GT-Power coupling: brake torque design exploration with constrained knock index and NOx", In: *GT-Suite Conferences*, Frankfurt: Germany, 2008.

[30] Isight, Dassault Systems Simulia Inc., Providence, RI, USA: [Online] Available: http://www.simulia.com/products/isight.html. [Accessed Apr. 5, 2011].

A Manufacturing Model for Ball-End Mill Gashing

Nalinikanta Swain, *Department of Mechanical Engineering, Capital Engineering College, Bhubaneswar, nalini_526@yahoo.co.in*

Sarat Kumar Mishra, *Department of Mechanical Engineering, Aryan Institute of Engineering & Technology, Bhubaneswar, skmishra784@gmail.com*

Saruk Mallick, *Department of Civil Engineering, Raajdhani Engineering College, Bhubaneswar, sarukmallik57@yahoo.co.in*

Satyaprakash Mishra, *Department of Civil Engineering, Capital Engineering College, Bhubaneswar, satyaprakash_m25@gmail.com*

Suryaleen Rout, *Department of Civil Engineering, NM Institute of Engineering & Technology, Bhubaneswar, suryaleenrout@yahoo.co.in*

Abstract: To facilitate the manufacturing of a ball-end mill, this paper presents an algorithm for ball-end mills gashing by using a five-axis computer numerical control (CNC) grinding machine. In this study, the normal helix models are proposed. Then, based on the cutting edge geometric model and the machining mode of the five-axis computer numerical control (CNC) grinding machine, the coordinate of the grinding point when the step of the gash out is grinded will be calculated. With the input data of ball-end mill geometry, wheels geometry, wheel setting and machine setting, the NC code for machining will be generated. Then the code will be used to simulate the ball-end mill machining in 3 Dimension. The 3D simulation system of the ball-end mill grinding is generated by VBA and AutoCAD2008. The algorithm of ball-end mill gashing can be verified by the 3D simulation system. Result shows that the algorithm presented in this paper provides a practical and efficient method for the manufacture of a ball-end mill gashing.

Keywords: CNC grinding, ball-end mill, gash out, grinding wheel.

1. INTRODUCTION

The ball-end mills used in a Computer Numerical Control (CNC) machine play a vital role in a successful High-Speed Machining (HSM) process, which directly affect the quality of a machined surface [1]. In order to save time and reduce the cost of manufacturing process, it is necessary to control the prediction of the ball-end mill geometry .In addition, there is a need to develop a cutting tool with high performance and long product life with low price. The shape of a ball-end mill contributes a lot to machining accuracy and dynamic stability, and it is defined by a few elements like relief angle, rake angle, and helix angle. The grinding of a ball-end mill with a complex geometry is related to some complicated processes in machining with a CNC grinding machine. Therefore, the research on the helical-groove grinding, the cutting tool manufacturing and the cutting edge geometric model has drawn great interest of many researchers [2, 3]. When traditional design method is used to determine the structure and the parameters of a ball-end mill, the designers need to access large amounts of data and rules. Not only the design cycle time is long, but also it is hard to control the quality of the design. To reduce the cost and save the time for designing a ball-end mill, a 3D solid model is used.

One key feature of modern CAD/CAM system is the automatic generation of NC-machining programs directly from a CAD model [4, 5]. In our CAM system, the NC code of all processes for the ball-end mill manufacturing is generated automatically in the program based on its 3D solid model. These NC code files will be loaded for machining in the CNC grinding machines. It is necessary to verify the performance of the NC code before actual manufacturing. However, traditional CAM systems cannot provide the method to realize this type of simulations and specific applications. The algorithm of producing a ball-end mill can be authenticated by the 3D simulation system. This paper presents how to calculate the grinding data of gash, and how to generate and simulate NC code for all grinding processes in 3D manner.

2. THE SETTING OF MACHINE REFERENCE FRAME AND BALL-END MILL GEOMETRY

In the study, the ball-end mill is machined on the CNC grinding machine tool, which has 5 degrees of freedom: three axes in translation (X-axis, Y-axis, and Z-axis) and two in rotation (A-axis, C-axis). The machine coordinate system is established as shown in Fig. (**1**). When the C-axis coordinate is 0, the axial direction of the end mill is in accordance with X-axis. The wheel spindle is Y-axis. The origin of coordinates is the intersections of X-axis and Y-axis. Z-axis is vertical with XY plane. The tool is fixed on the tool holder, which has three degrees of freedom; two rotation (A-axis, C-axis) and translation (X-axis). The grinding wheels are arranged at the wheel spindle, which has two degrees of freedom; translation (Y-axis) and translation (Z-axis). Fig. (**2**) shows the arrangement of the grinding wheels for the ball-end mill manufacturing. There are four major machining steps for the ball-end mill manufacture: fluting, first and second reliefs, gashing out, and tip clearance. Wheel 1 and 2 are used for the operation of the gash out and the flute. Wheel 3 is used for the first and the second relief operations. The tip clearances are performed by wheel 2.

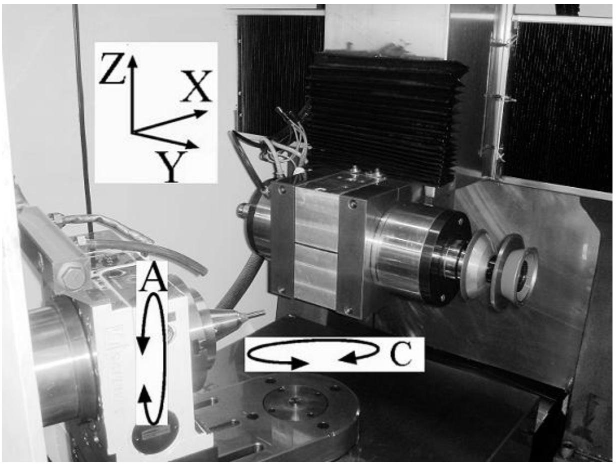

Fig. (1). The applied five-axis grinding machine.

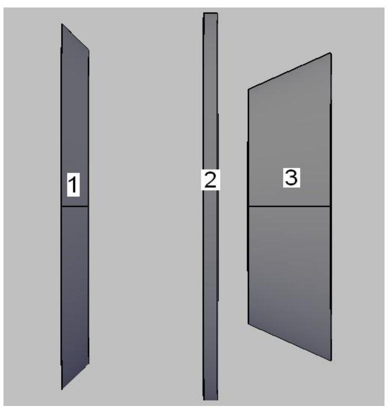

Fig. (2). Grinding wheels for ball-end millmanufacturing.

2.1. Dimensional Parameters

Fig. (**3**), Fig. (**4**) and Table **1** show the geometric dimensions that define the shape of the ball-end mills. It should be noted that the helical groove and the neck groove shape will not be determined by the design parameters but by other factors, such as the grinding wheel shape and the grinding position. In general, the geometry of a ball-end mill consists of two parts: the geometries of the flute surface and the ball-end surface.

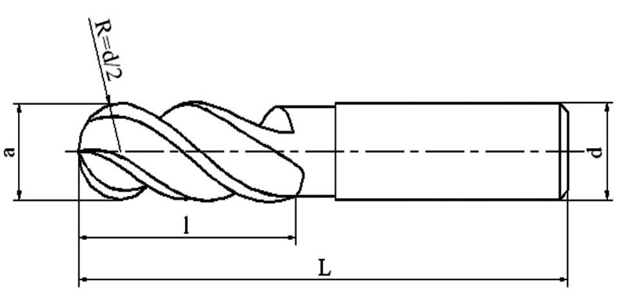

Fig. (3). External shape dimensions of ball-end mill.

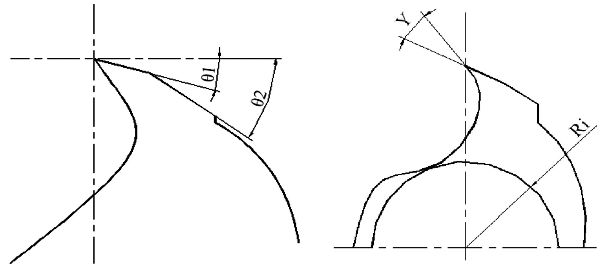

Fig. (4). Section dimensions of ball-end mill.

Table 1. Parameters to Define a Ball-End-Milling Cutter Dimensions

Φ_1	First relief angle	l	Cutter length
Φ_2	Second relief angle	β	Helix angle
Γ	Rake angle	N_f	Number of flutes
R_i	Radius of inner circle	D_1	Shank diameter
d	Cutter diameter	L_s	Shank length
L	Overall length	R	Ball end radius
θ_1	First ball-end relief angle	θ_2	Second ball-end relief angle

2.2. Basic Algorithm for a Ball-End Mill Grinding

The machining of a cutting tool is to be done with sets of operation steps, each of which has a specific name in the CNC jargon. Each operation is performed with dedicated wheel. This information is contained in the CNC file. Specifically, the main steps are (in their usual order): Helical-flute, Relief angle and Gashing. The mathematical models for the helical flute and the gash out machining are based on the enveloping theory and the fundamental analytical conditions of engagement between the wheel surface and the helical groove surface [6]. As shown in Fig. (**5**), an independent right hand Cartesian coordinate system other than the system created for the CNC machine is established. Origin O is in the ball centre of the ball-end mill, X-axis is the axial direction of the end mill, cylindrical and ball junction plane is YOZ surface, Z-axis has an intersection with the cutting edge geometric curve. The cutting edge geometric curve can be considered as the intersection between an orthogonal helical surface and a ball surface. We use $\vec{r}$ to represent the cutting edge curve on the orthogonal helical surface, which can be expressed as:

$$\vec{r} = \begin{cases} X = \dfrac{P}{2\pi}\phi \\ Y = R\cos\theta\sin\phi \\ Z = R\cos\theta\cos\phi \end{cases} \tag{1}$$

Where X, Y, Z stand for 3-dimention coordinates, β is the helix angle, R is the radius of the ball-end mill, P is the lead value, and φ is the angle between the any point on the cross section to the center and the X axis. The equation of ball can be expressed as:

$$\vec{r} = \begin{cases} X = R\sin\theta \\ Y = R\cos\theta\sin\phi \\ Z = R\cos\theta\cos\phi \end{cases} \tag{2}$$

Where R is the radius of the ball-end mill, θ and φ are parameters. From the theory of normal helix, we know that $P = 2\pi R / \tan\beta$. Combine this with the equation (1) and (2), the cutting edge geometric model of the ball-end mill can be derived, which can be expressed as:

$$\vec{r} = \begin{cases} X = Rc\phi \\ Y = R\sqrt{1-(c\phi)^2}\sin\phi \\ Z = R\sqrt{1-(c\phi)^2}\cos\phi \end{cases} \tag{3}$$

Where $c = 1/\tan\beta$, β is the helix angle, R is the radius of the ball-end mill, φ is the angle between the any point P on the cross section to the center and the X axis. $0 \le \phi \le \tan\beta$.

Per the knowledge of differential geometry, the tangent vector T of the any point P on the cutting edge can be deduced as:

$$\vec{T} = \begin{bmatrix} T_X \\ T_Y \\ T_Z \end{bmatrix} = \begin{bmatrix} \frac{dX}{d\phi} \\ \frac{dY}{d\phi} \\ \frac{dZ}{d\phi} \end{bmatrix} = \begin{bmatrix} cR \\ -\frac{R(\cos\phi.c^2.\phi^2 + \sin\phi.c^2.\phi - \cos\phi)}{\sqrt{1-(c\phi)^2}} \\ \frac{R(\sin\phi.c^2.\phi^2 + \cos\phi.c^2.\phi - \sin\phi)}{\sqrt{1-(c\phi)^2}} \end{bmatrix} \tag{4}$$

The unit tangent vector $\vec{T}_0 = \frac{\vec{T}}{|\vec{T}|}$, $|\vec{T}|$ is expressed as:

$$|\vec{T}| = \sqrt{T_X^2 + T_Y^2 + T_Z^2} = \frac{R.\sqrt{(1-c^2.\phi^2)^2 + c^2}}{\sqrt{1-(c\phi)^2}} \tag{5}$$

Substituting equation (5) into equation (4), the unit tangent vector of the any point P on the cutting edge becomes:

$$|\vec{T}_0| = \begin{bmatrix} \vec{T}_{OX} \\ \vec{T}_{OY} \\ \vec{T}_{OZ} \end{bmatrix} = \begin{bmatrix} \frac{\sqrt{1-(c\phi)^2}}{R.\sqrt{(1-c^2.\phi^2)^2 + c^2}} \\ -\frac{\cos\phi.c^2.\phi^2 + \sin\phi.c^2.\phi - \cos\phi}{R.\sqrt{(1-c^2.\phi^2)^2 + c^2}} \\ \frac{\sin\phi.c^2.\phi^2 + \cos\phi.c^2.\phi - \sin\phi}{R.\sqrt{(1-c^2.\phi^2)^2 + c^2}} \end{bmatrix} \tag{6}$$

In addition, in the direction of the ball meridian line, the vector of the any point P on the cutting edge can be expressed as:

$$\vec{r}_\theta = \frac{\partial \vec{r}}{\partial \theta} = \begin{bmatrix} R.\sqrt{1-c^2.\phi^2} \\ -R.c.\phi.\sin\phi \\ -R.c.\phi.\cos\phi \end{bmatrix} \tag{7}$$

Then, by the definition of the spiral angle in rotary surface spirals, the spiral angle β in the tip ball cutting edge can be deduced as:

$$\beta = \arccos\left(\frac{\vec{r}_\theta.\vec{T}_o}{|\vec{r}_\theta|.|\vec{T}_o|}\right) = \arccos\left(\frac{c}{\sqrt{(1-c^2.\phi^2)^2 + c^2}}\right) \tag{8}$$

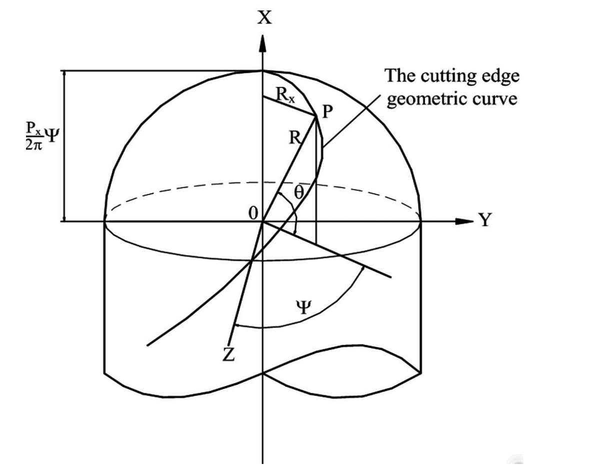

Fig. (5). The cutting edge geometric model of the ball-end mill.

2.3. The Helical-Gash Out Grinding And The Calculation Of The Grinding Data

The helical- gash out surface is generated by the combined motion of the grinding wheel 2 and the tool. The gash out surface of the end mill can be formed by the motion of the tool along the curve of the cutting edge and the motion of the grinding wheel 2 along the grinding wheel outline. The shape of the gash out is related to the grinding wheel shape. Fig. (**6**) shows the schematic illustration of the gashing operation. Differing from other steps, five axes need to move simultaneously in certain matter in this step. The coordinates of contact point between the tool and the wheel will be generated by the CAM system. If the diameter of the end mill, the diameter of the wheel and the location of the wheel is fixed, the contact point data can be calculated accordingly. Table **2** shows the parameters that are used to calculate the coordinate of the contact point.

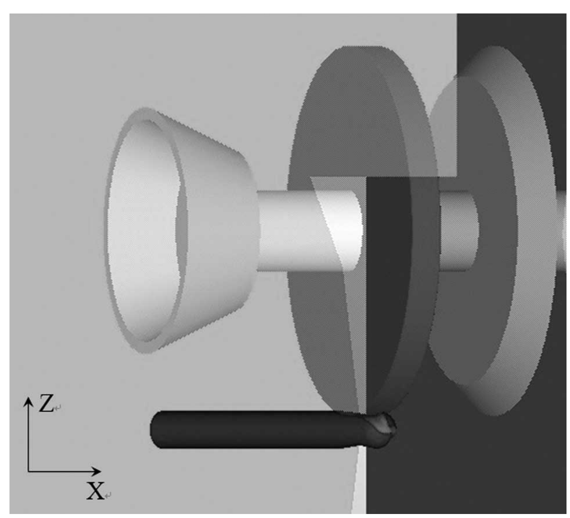

Fig. (6). Schematic illustration of the gashing operation.

Table 2. Parameters to Calculate the Coordinate of the Contact Point

R	Ball end radius	L_2	Length from X axis zero to C axis rotation center
R_1	Wheel radius	L_3	Wheel spindlel length
θ_3	Gash out angle	N_f	Number of flutes
θ_4	Gash runout angle	L_4	Grinding wheel flange length
d	Cutter diameter	β	Helix angle
L_1	Tool holder length	D_2	Core thick diameter

There are two ways of processing gash out, one is from the ball head root to the ball head end, and the other is from the ball head end to the ball head root. In this study, the first one is selected. The coordinates of starting contact point can be calculated. Table **3** shows the starting contact point coordinate between the tool and the grinding wheel. In the gash out grinding process, the tool rotates along the A-axis from its original position to 0, along the C-axis from $-\beta$ to 0 and also moves in the X directions to find the contact point of the gash out grinding process. At the same time, wheel 2 moves in the Y, Z directions to avoid the possible collision to the cutting tool.

Table 3. The Starting Contact Point Coordinate between the Tool and the Grinding Wheel

C_0	$\mathrm{acos}(c/\sqrt{(1-c^2.\phi^2)^2+c^2})$
X_0	$(-L_2+L_1-R).\cos C_0+L_2+R_1.\sin\theta_4$
Y_0	$-(-L_2+L_1-R).\sin C_0-L_4-L_3$
Z_0	$R_1.\cos\theta_4+D_2/2$
A_0	$\tan\beta$
c	$1/\tan\beta$

Table **4** shows the calculation of the grinding data for gash out grinding:

Through the above calculation, the CAM system can automatically generate NC code. Users input the parameters in the dialog box of ball-end mill grinding program, then the corresponding NC machining code can be automatically generated.

Table 4. The Calculation of the Grinding Data for Gash Out Grinding

T_1	$90^\circ-\theta_3-\theta_4$
t	Change from 0 to T_1
A_1	$t.\tan\beta/T_1$
C_1	$\mathrm{acos}(c/\sqrt{(1-c^2.A_1^2)^2+c^2})$
X_1	$R_1\sin(\theta_3+t)+R.A_1.c+(-L_2+L_1-R)\cos C_1$
Y_1	$(-L_2+L_1-R+R.A_1.c)\sin C_1$
Z_1	$R_1.\cos(\theta_3+\mathrm{t})+(R-R.A_1.c).(D_2/2)/R$
c	$1/\tan\beta$

3. DESIGN SIMULATION SYSTEM BASE ON BOOLEAN OPERATIONS

The representation of 3D CAD model forms the basic cornerstone of the computer controlled manufacturing process. We develop the simulation system on the basis of AutoCAD2008 Open API and VBA in the MS Windows environment. The main functions applied in this system include the end mill shape modeling, the prediction of wheel geometry and the tool path verification.

According to the machine mechanical structure, the CAM system generates the wheel model and the tool model. In simulation, machining can be considered as a dynamic Boolean operation of difference between the grinding wheel and the tool through NC code [7, 8]. It is dynamic because that both the tool and the wheels move along through rotations and translations. Then the major design parameters of a cutter, such as relief angle and inner radius, can be verified by interrogating the section profile of its solid model. The movements are divided into blocks; each one corresponds to a CNC operation or even to one cut within an operation. Each block is performed in sequence of the machining process which has absolute coordinate and relative coordinates.

4. GRINDING PERFORMANCE AND RESULTS

4.1. Generation of NC Codes for Ball-End Mill Machining

Using the input data for ball-end mill geometry, wheel geometry and machine configuration data, the computer program will generate the grinding points for helical-flute, relief angle and gashing. The NC codes for manufacturing in 5-axis CNC grinding machine are generated by the program and stored as txt file. Each machining process is carried out through the rotation and the translation of the axis of the wheel and the tool. The design parameters and cutting conditions of the ball-end mill as example are described in Table **5**.

Table 5. Design Parameters of the Ball-End Mill

Diameter	6mm	First relief angle	8°
Radius of inner circle	1.8mm	Second relief angle	16°
Number of teeth	2	First ball-end relief angle	12°
Helix angle	35°	Secondball-end relief angle	24°
Rake angle	10°	Overall length	30mm
Gash out angle	35°	Cutting length	10mm

4.2. Simulation Results

Simulation software works as following:

A. The creation of the scene model starts from a textual description of the wheels and the initial tool.

B. The translation of the CNC code into a linear list of movement instructions. This step consists of removing loops and alternative structures, filtering unnecessary expressions as well as evaluating variables.

C. Machining simulation on each block.

D. Measurements of the tool on 2D cross-sections.

The NC code is used to simulate all the machining processes in 3D. From Fig. (**7**) to Fig. (**12**), they show the tool-path verification procedure in which the solid models in the CAM system are constructed and simulated, and the interference detection is performed, such as the collision between machine components or axis stroke-over. Fig. (**7**) is showing how to simulate the helical-gash using wheel 2. The Fig. (**8**) shows the final gashing after grinding. Fig. (**9**) is the process of grinding the relief angle using the wheel 3. Fig. (**10**) shows the final relief surface after grinding. Fig. (**11**) is the process of grinding the Helical-gashing after grinding, relief angle and tip clearance operations. Fig. (**12**) is the final cutter after grinding.

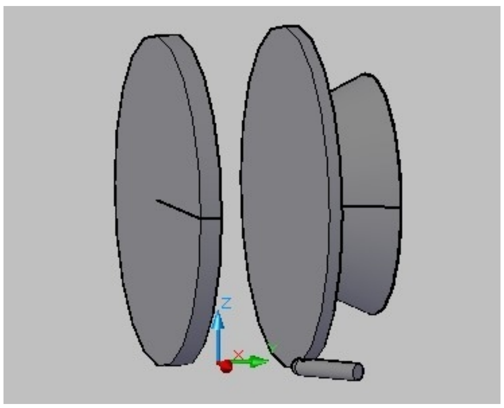

Fig. (7). The grinding of Helical-gashing.

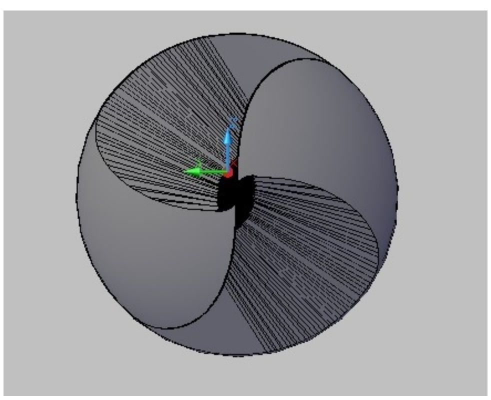

Fig. (8). The final gash after grinding.

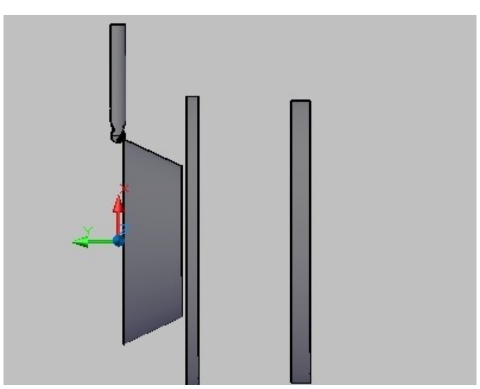

Fig. (9). The grinding of relief angle.

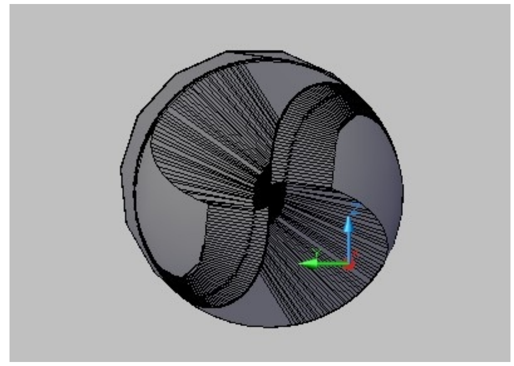

Fig. (10). The final relief after grinding.

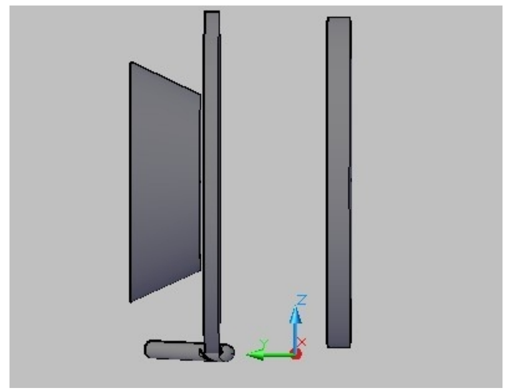

Fig. (11). The grinding of Helical-gashing.

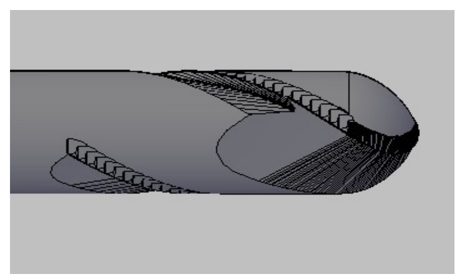

Fig. (12). A final cutter after grinding.

4.3. Experiment Results

From above example of simulation, we can see that this model can well describe a cutting tool with computer language. This allows engineers to try and study different shape and geometry of ball-end mill tool before doing any real grinding work. The cycle time and material cost of developing new ball-end mill tool is reduced dramastically.

Fig. (**13**) is the ball-end mill sample produced by a CNC machine based on the simulation result discussed in the paper. The physical tool matches the simulation result of manufacturing model very well.

Fig. (13). Sample of a ball-end mill machined by the developed software.

CONCLUSIONS

The paper presents a new method which is used to grind the gashing out of the ball-end mill. The calculation, simulation and experiment results indicate that the manufacturing model presented in this paper provides a simple and efficient method of fabricating a grinding end mill. The CAM system is developed to predict and optimize geometric ball-end mill configuration before machining. The NC codes for all steps of manufacturing in 5-axis CNC grinding machine are generated from the CAM software for the CNC machine. It is necessary to simulate ball-end mill geometry and verify the NC code before processing the real materials to save time and to reduce the manufacturing cost. The developed CAM system has been used to manufacture ball-end mills together with the developed five-axis CNC grinding machine.

CONFLICT OF INTEREST

None declared.

ACKNOWLEDGEMENT

None declared.

REFERENCES

[1] Reuteler, “Cutting tool technology in high-speed milling (HSM)”, *FRAISA SA*, 1997.

[2] W. Zhang, X. Wang, F. He, and D. Xiong, “A practical method of modelling and simulation for drill fluting”, *Int. J. Mach. Tools. Manuf.*, vol. 46, pp. 667-672, 2006.

[3] J. Hsieh, “Mathematical model and sensitivity analysis for helical groove machining”, *Int. J. Mach. Tools. Manuf.*, vol. 46, pp. 1087-1096, August 2006.

[4] Y. Lu, Y. Takeuchi, I. Takahaki, and M. Anzai, “An integrated system development for ball end mill design, creation and evaluation”, *Int. J. Adv. Manuf. Tech.*, vol. 25, pp. 628-646, 2005.

[5] S.L. Ko, T.T. Pham, and Y.H. Kim, “Visualization process for design and manufacturing of ball-end mills”, *LNAI, Springer-Verlag: Berlin Heidelberg*, vol. 3613, pp. 1133, 2008.

[6] T.T. Pham, and S.L. Ko, “A practical approach for simulation and manufacturing of a ball-end mill using a 5-axis CNC grinding machine”, *J. Mech. Sci. Technol.,* vol. 24, pp. 159-163, 2010.

[7] D. Tost, A. Puig, and L.P. Vidal, “Boolean operations for 3D simulation of CNC machining of drilling tools”, *Comput.-Aided Des.*, vol. 36, pp. 315-323, 2004.

[8] J.H. Kim, J.W. Park, and T.J. Ko, “End mill design and machining via cutting simulation”, *Comput.-Aided Des.*, vol. 40, pp. 324-333, 2008.

Simulation of Bifurcate Fracture of Linear Red Copper Penetrator

P. Paulpandian, *Department of Mechanical Engineering, Aryan Institute of Engineering & Technology, Bhubaneswar, p_pandian@gmail.com*

Deepikarani Swain, *Department of Mechanical Engineering, NM Institute of Engineering & Technology, Bhubaneswar, depika_r19@yahoo.co.in*

Debi Prasad Singh, *Department of Mechanical Engineering, Raajdhani Engineering College, Bhubaneswar, deboprasad_1159@gmail.com*

Abstract: The Red copper has been widely used in shaped charge liner because of good ductility. Red copper penetrator is a Linear Explosively Formed Penetrator (LEFP) when linear red copper shaped charge liner overturned under the effect of detonation production. Compared with ordinary jet swords, red copper penetrator has a wider range of stand-off, bigger cratering and significant aftereffect, which can meet the requirements in various environments. It was observed that bifurcate fracturing of red copper penetrator occurred in the performance testing of LEFP initiated on edge midpoint as the stand-off increased, which resulted in the separate craters on the target and the cratering effect was weakened. The Propagation of detonation wave and the interaction with red copper shaped charge liner were theoretically and experimentally studied, also numerical simulations were conducted. The results showed that velocities of charge liner elements were directly proportional to those of detonation waves, which caused different velocity directions and values of different elements, and great velocity gradient formed in the penetrator. The penetrator fractured as the elongations both on the vertical and horizontal directions were greater than the dynamic elongation of red copper. It was concluded that the main factor which resulted in the bifurcate fracture phenomenon was velocity gradient in the penetrator.

Keywords: Linear red copper penetrator, bifurcate fracture, stand-off, numerical simulation.

INTRODUCTION

A linear shaped charge (LSC) has a liner with wedge-type (or V-shaped) profile. The liner is surrounded with explosive. When explosive detonated, the liner collapsed under pressure and a plane jet sword formed. LSCs are commonly used in the cutting of rolled steel joists (RSJ) and other structural targets [1,2]. Because the performance of the linear shaped charge is determined by the jet which is restricted by the charge structure, there are serious limitations in stand-off and aftereffect for some special applications.

The linear metal charge case is overturned under the effect of detonation production after the explosive in the linear shaped charge was detonated [2], then a Linear Explosively Formed Penetrator (LEFP) is formed on the symmetrical surface of the charge with certain length along vertical direction. Compared with ordinary jet swords, LEFP has some characteristics such as a wide range of stand-off, big cratering and significant aftereffect and can meet lots of specific requirements in various environments.

The structure of LEFP charge is three-dimensional and complicated, and can be detonated in several ways such as

Fig. (1). Charge structure scheme and test setup.

point detonation at end face, or edge, etc. LEFP charge simultaneously detonated on the edge is substantially same to EFP conical charge except that projectile shapes are different. But this simultaneous detonation is difficult to implement because of its high precision requirement. The end face point initiation and edge midpoint initiation are mainly applied for linear shaped charge.

Liner is the core part of shaped charge structure [3]. Metal materials with the better ductility were often chosen to forge the projectile, preferred red copper. Yet bifurcate fracturing of red copper penetrator was observed in the performance testing of LEFP initiated on edge midpoint as the stand-off increased. It results in the separate craters on the target and the cratering effect is weakened. In this paper, the bifurcate fracture model of LEFP is numerically simulated, and is discussed based on experiments and theoretical analysis.

EXPERIMENT

The charge structure is shown in Fig. (**1**). Shells of the shaped charges are made of 45# steel (2mm thick). Explosives used are composition B and material of the liner is oxygen-free copper.

Target is made of 45# steel; booster charge is insensitive PETN. Detonator is 8# military detonator. Stand-off is controlled by U-shaped wood blocks.

Figs. (**2**, **3** and **4**) showed the experiment results when the stand-off is 5, 10 and 20 times of charge caliber respectively.

From experimental results, it can be seen that LEFP has been formed when the stand-off was 5 times of charge caliber. The separating crater phenomenon arose near detonation point when the stand-off was 10 times of charge caliber, and came to more evident when the stand-off was 20 times of charge caliber. This indicates that bifurcate fracture phenomenon occurs in the course of the LEFP movement.

NUMERICAL SIMULATION

A half model was set according to the symmetry, which represented to the left half charge from the detonation point. The model length is 100 mm from the detonation point. LS-

Fig. (2). Target result on the condition 5 times charge caliber stand-off.

Fig. (3). Target result on the condition 10 times charge caliber stand-off.

Fig. (4). Target result on the condition 20 times charge caliber stand-off.

Dyna code was employed and total computing time was set to 240μs. Fig. (**5**) showed the simulation of the penetrator shapes in time sequence.

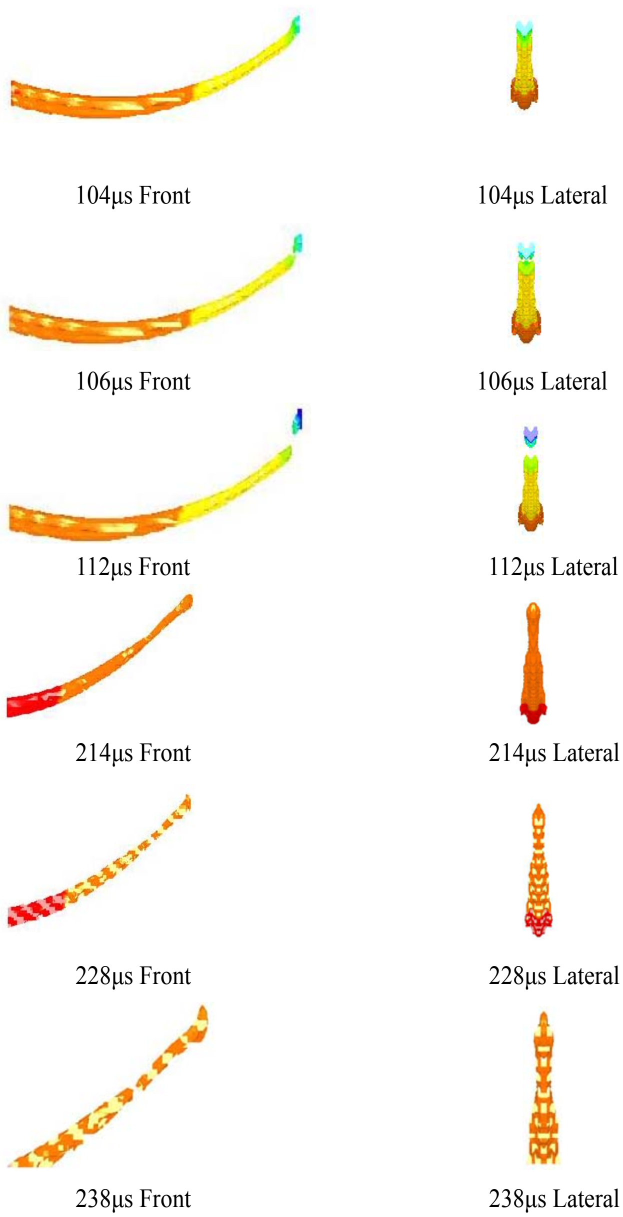

Fig. (5). The simulation of bifurcate fracturing of linear red copper penetrator.

It can be seen that in Fig. (**5**) a bifurcate fracture showed up near the detonation point at 104 μs, and completed at 112μs. More fractures showed up at 228μs, and the top one completed at 238μs. Owing to the continuous bifurcate fracturing, the penetrator broke into several parts which resulted in the separate carters on the target.

Fig. (**6**) illustrated that the variations of V_y (the vertical components of the velocity vectors of the penetrator tip) along the longitudinal direction, each curve for one moment. V_y was increasing along the charge length as the distance from the detonation point increased. The changes of V_y at different positions were different, as shown in the figure. On the part near the detonation point (between 0 ~ 22.5 mm) it increased more quickly than that on the other part. The nearer to the detonation point, the greater change of V_y was. The increase of V_y was slowed down, and almost no increase at the point of 22.5mm. It decreased cross the point of 22.5mm. The decreases of V_y at different points were similar in the range of 22.5~80mm, while the decreases changed to different at the points greater than 80mm because of the effect of rarefaction wave from the other end. Consequently, the velocity gradient in LEFP were gradually decreasing after 80 mm, as shown in the figure, the curves slowly approached to horizontal direction, and met to the same end. The reason is that as continuum medium there are mutual implications between different elements of the penetrator, which reduce the great velocity and enlarge the less one.

Fig. (**7**) illustrated that the variations of V_x (the horizontal components of the velocity vectors of the penetrator tip) along the longitudinal direction. It can be seen that V_x was also increasing along the charge length as the distance from the detonation point increased. The changes of V_x were also different at different positions. The nearer to the detonation point, the greater change of V_x was. The increase of V_x was slowed down at the far end, and almost no increase between 60 ~ 70mm. On the other hand, the nearer to the other end, the value of V_x decreased more quickly. Thus, there were significant gradients of V_x in the parts near to two ends of the penetrator model, which result in that the penetrator stretched on horizontal direction. Under the combining stretch effect both horizontal and vertical, bifurcate fracture formed in the penetrator.

RESULTS AND DISCUSSIONS

Mechanism of Bifurcate Fracture

The primary cause of the bifurcate fracture was the velocity gradient in the penetrator, which made the penetrator close to detonation point bend, and simultaneously stretched the penetrator on two directions. The velocity gradient was caused by the detonation growth in the situations of which the charge was detonated at the midpoint of the edge or the point on end face.

LEFP Bifurcate Fracture Model

The generation mechanisms of bifurcate fracture were same for both situations of the edge midpoint and end face detonating. Here the mechanism was analyzed in the latter case.

The LEFP model as shown in Fig. (**8**), R axis is along the length direction of the charge, and the bottom of the liner is set to S=0. The detonating face is set to R=0.

The change of detonation wave velocity from detonation point is expressed as:

$$\left(\frac{D}{D_s}\right)^2 = 1 + \frac{2\gamma^2 L^\alpha}{(\gamma+1)\gamma^\alpha R^\alpha}$$

The reversal velocity of the liner can be expressed as [4]:

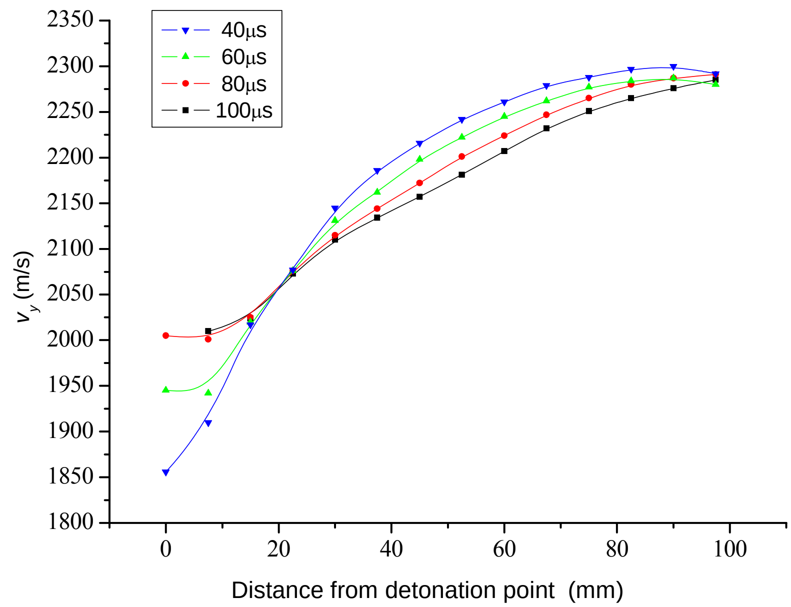

Fig. (6). Vertical velocity variation of the penetrator tip along the longitudinal direction.

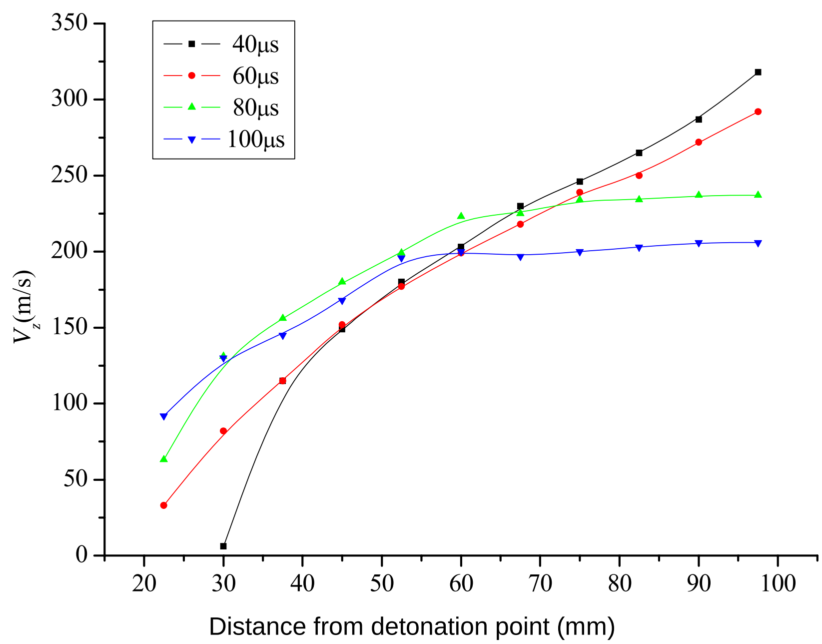

Fig. (7). Horizontal velocity variation of the penetrator tip along the longitudinal direction.

$$V_F = \sqrt{2E}\left\{\frac{1}{3}\left[\left(\frac{2M}{C}\right)^2 + \frac{5M}{C} + 1\right]\right\}^{-\frac{1}{2}}$$

Where

$\sqrt{2E}$ = Gurney constant of explosive, $\sqrt{2E} = 0.52 + 0.28D_S$;

D = ideal of detonation velocity;

M = mass of liner element;

C = explosive mass corresponding to the liner element;

r = adiabatic index of detonation products;

L = width of reaction zone;

R = propagation radius of detonation wave.

It takes time T that the detonation wave travels to the end of the charge, and the penetrator has been formed in this period. Assuming the elements reversal velocity of shaped charge liner is constant, and only considering the movements in y-direction, the distance that the liner element traveled till time T:

$$S = V_F t = V_F\left(T - t_R\right)$$

Where t_R is the time when detonation wave arrived at R position.

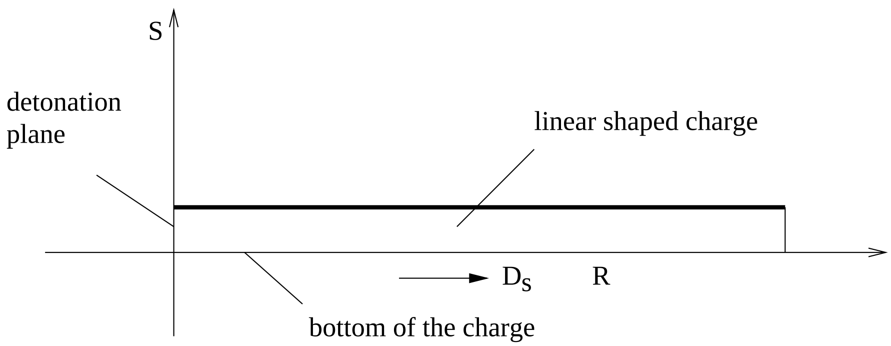

Fig. (8). The coordinate on the charge model.

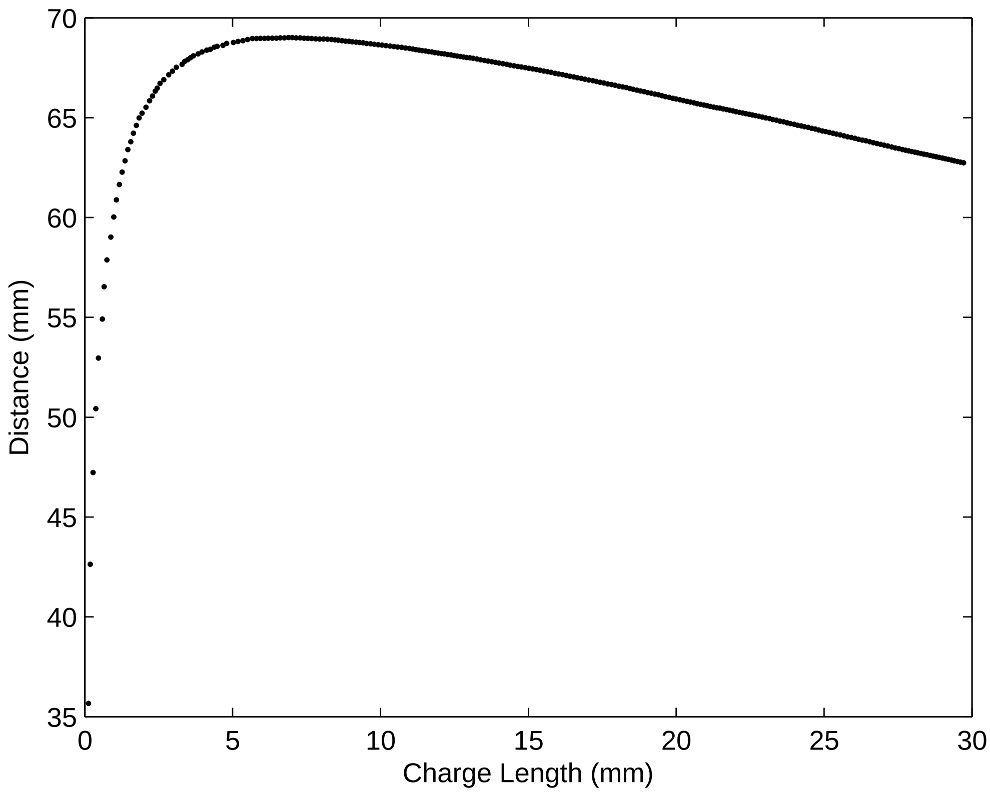

Fig. (9). The calculated shape of the penetrator tip.

$$R = \int_0^{t_R} D_S dt = D_S t_R$$

$$t_R = \frac{R}{D}\sqrt{1+\frac{2\gamma L}{(1+\gamma)R}}$$

With the parameters of real charge, the shape of LEFP tip is calculated and as shown in Fig. (**9**).

As can be seen from Fig. (**9**), the shape curve of LEFP was more bent near initiation point due to the velocity gradients. Bifurcate fracture showed up firstly in this part of LEFP as it continued to move. The shape curve of the last part was less bent.

Fig. (**10**) showed the position of the penetrator at time t_0 and t_1. The velocity of detonation end face A is V^A and it can be decomposed to V_x^A, V_y^A, V_z^A. B is the lowest point of LEFP and its velocity and corresponding velocity components are V^B, V_x^B, V_y^B, V_z^B respectively. AB is stretched out on A′B′ in LEFP movement. The main reason of the stretching is that there is velocity gradient in the direction of y and z.

$$y_{A'} = \int_0^{t_1} V_y^A(t)dt$$

$$y_{B'} = \int_0^{t_1} V_y^B(t)dt + Y_0$$

The elongation number of A′B′ in the direction of y:

$$\Delta y = y_{B'} - y_{A'} - Y_0$$

The horizontal distances from A′, B′ to o respectively are as follow:

$$z_{A'} = 0$$

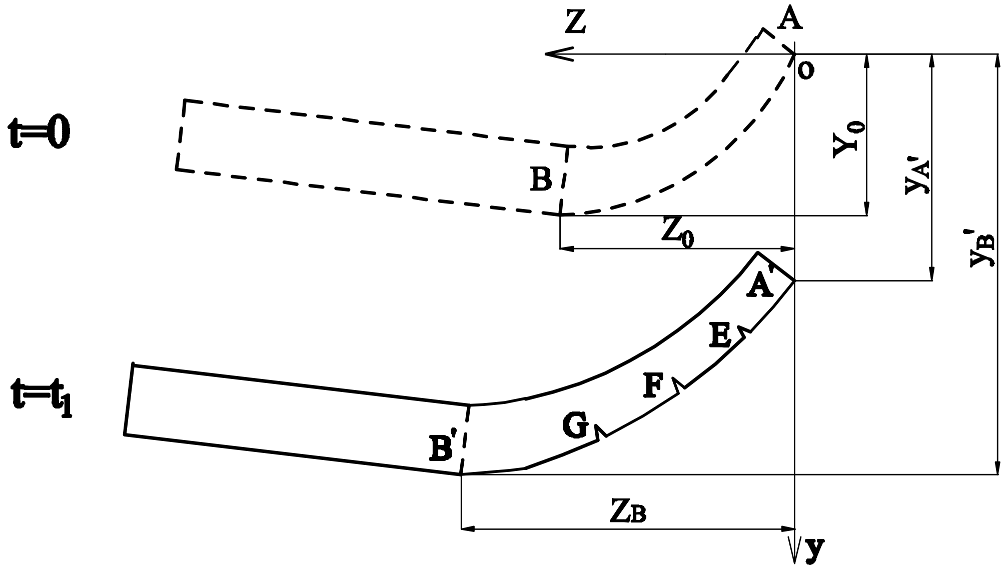

Fig. (10). The penetrator movement and extension process.

$$z_{B'} = \int_0^{t_1} V_z^B(t)dt + Z_0$$

The extension in the direction of z is:

$$\Delta z = z_B - Z_0$$

The total extension of AB is approximately

$$\Delta l = \sqrt{(\Delta y)^2 + (\Delta z)^2}$$

And the elongation of AB is:

$$\delta = \frac{\Delta l}{l_0}$$

Criterion of LEFP Bifurcate Fracture

The oxygen-free copper crystal grain size of shaped charge liner has turned refiner under explosion loading and its tensile strength and fracture elongation are increased [5]. Assuming the maximum dynamic elongation is $\delta_{\max}$, if

$$\delta \geq \delta_{\max}$$

the bifurcate fracture will arise, which leads to the separating craters on the target.

Analysis

The AB segment is curve and the elongation percentage of LEFP head is bigger than that of LEFP tail, so the bifurcate fracture point of AB segment arises on the head of LEFP firstly. With the movement of LEFP, the bifurcate fracture points go up on the corresponding plane and the bifurcate fracture breach is bigger until the two parts separate completely.

In the process of LEFP stretching, the velocity of B point decreases with the deceasing of the adjacent element velocity. There is the velocity gradient in the course of LEFP due to the effect of velocity between every breach of LEFP, The longer the distance of LEFP movement in air is, the longer the stretching of LEFP will be, which leads to bifurcate fracture. Therefore the penetrating results are obtained in LEFP upon target experiment.

CONCLUSIONS

The results of theoretical analyze and numerical simulation agreed with that of experiment. On the discussions above, the following conclusions can be drawn:

1) Element velocities of the red copper penetrator were directly proportional to those of detonation wave. Near the detonation point, they increased when detonation grew up. The penetrator was bent when it has been formed, and there were velocity difference between sections.
2) The bent part would get more stretch effect on both y and z directions, and when the combined elongation was great than the dynamic elongation of red copper, the penetrator fractured.
3) The development of bifurcate fractures related to the distance which it traveled, and the more distance the penetrator traveled, the larger bifurcate fractures obtained.
4) Thus, as the stand-off was getting large, it caused separate craters on the target; as a result the cratering effect was weakened.
5) The way to eliminate bifurcate fractures is to decrease the velocity gradient in the penetrator, which can be approached by enlarge the initializing area.

CONFLICT OF INTEREST

None declared.

ACKNOWLEDGEMENTS

None declared.

REFERENCES

[1] F. Rondot, Tracking the "Poorness" of a Linear Shaped Charge[C]. *23rd International Symposium on Ballistics Tarragona*, Spain, vol. 16-20, p. 167, 2007.

[2] Y. Luo, S. Zhao-Wu and C. Xiao-Rong, Application Study on Blasting with Linear Cumulative Cutting Charge in Rock[J]. *Chin. J. Energetic Mater.*, vol. 14, p. 236, 2006.

[3] L. Wei, F. Ning-Jun and Wang Zheng-Jie, Warhead Missile Fuze Analysis and Simulation[J]. *J. Beijing Inst. Technol.*, vol. 17, p. 290, 2008.

[4] W.P. Walters, and J.A. Zukas, *Fundamentals of Shaped Charge[M]*, John Wiley & Sons, New York, 1989.

[5] Y. Zhuoyue, L. Baocheng and Z. Jiaping, The Formation Mechanism of Ultrafine Grain in Pure Iron Under Explosive Shock Loading[J]. *Trans. Mater. Heat. Treat.*, vol. 22, p. 56, 2001.

Limit and Shakedown Analysis of Circular Tube Containing External Pit

Sanjeet Raj, *Department of Mechanical Engineering, Aryan Institute of Engineering & Technology, Bhubaneswar, sanjeetraj4@gmail.com*

Ranjan Kumar, *Department of Mechanical Engineering, NM Institute of Engineering & Technology, Bhubaneswar, kumarranjan75@gmail.com*

Sidhanta Behera, *Department of Civil Engineering, Raajdhani Engineering College, Bhubaneswar, sidhantabehera29@outlook.com*

Swarup Sahoo, *Department of Civil Engineering, Capital Engineering College, Bhubaneswar, swarupsahoo16@live.com*

Abstract: The circular tubes containing external pit defects are analyzed in a lower-bound finite element computational form based on the static shakedown theorem. The shakedown analysis has not been commonly used in the engineering due to the large amount of computations. To overcome the numerical difficulties, a temperature parameter method is used, in which a pseudo-temperature field is applied to the structure and the resulting self-equilibrium thermoelastic stress is treated as the residual stress field which is used in the analysis. The pseudo temperature is assumed as a harmonic function satisfying the uniqueness theorem, therefore the nodal temperature matrix of the whole structure can be expressed by the boundary nodal temperature matrix. The nonlinear yield condition is piece-wise linearized so that the shakedown analysis is transformed into a linear programming problem in which the strategic variable is boundary nodal temperature and objective variable is the loading multiplier. The relations of limit and shakedown pressures to geometric parameters of various defects are presented.

Keywords: Shakedown analysis, thermo elastic stress, residual stress, circular tube, mathematical programming.

INTRODUCTION

In assessing the load carrying capacity of structures, besides fracture mechanics method which is used for assessing controlling crack, limit and shakedown methods are commonly used for assessing the overall structure collapse, in which limit analysis is for monotonous load, while for the structures subjected to multiple and variable load, shakedown analysis should be required. A combination of the two assessment method by using interpolation between fracture and plastic collapse is called the two-criteria method [1]. In the early time, main concern is paid for the limit analysis using theoretical method. For circular tube with a rectangular slot part through the thickness Kitching and Zarrabi [2] presented experimental limit pressure and lower bound limit analysis [3] based on the assumption of stress resultants in thin shell. The analysis in [3] is similar to that for a circular tube with a rectangular part through slot. No account has been taken of the fact that the mid-surface of the shell in the regions of the slot is offset from the mid-surface of the surrounding thicker shell and that the stress field in the regions of slots and near the slot could not be similar to the stress in thin shell. In the review by Miller [4] a number of approximate results of limit pressure for cylindrical and spherical shells containing defects are reported. All results were based on 2-D or thin shell analysis, however the stress characteristic in a circular tube with defect is a real 3-dimensional problem.

As to plastic limit and shakedown analysis of structure, although the classical shakedown theorem founded by Melan [5] and Koiter [6] and recently developed by Konig [7] is elegant, it is computationally very difficult in applying to 3-D structures due to the large number of variables and constraints. Feng *et al.,* [8-10] investigated a global/local shakedown computational form for three-dimensional elastoplastic strain-hardening and damage structures with cracks. Liu and Cen [11,12] presented a upper bound numerical method for limit analysis of 3-D structures and investigated the upper bound limit analysis of cylindrical shells with part through slots. Later, Konig [13] discussed the exactness of the kinematical approach in the structural shakedown and limit analysis, in which appropriately defined parameters called generalized stresses and strains are used in the analysis.

Comparing with upper bound limit analysis based on displacement variables, lower one on stress has more variables and restraints so that it is computationally more difficult. Fuschi and Polizzotto [14] presented a shakedown load boundary for an elastic-perfectly plastic structure. Giambanco [15] considered the optimal shakedown design of structures discretized by elastic perfectly plastic finite elements. Four alternative methods were presented in his paper to formulate the design problem. Polizzotto [16] provided a unified approach to quasi-static shakedown problems for elastic-plastic solids with piecewise linear yield surface. A general inequality was given by using a perturbation method, from which, by simply specializing the perturbing terms, the generalized Melan theorem as well as bounds on various deformation parameters (such as displacements or plastic strain intensities) were obtained.

The lower bound shakedown analysis of axisymmetric structures is presented by the authors [17] and the limit and shakedown loading for spherical shells containing part through slots and gas holes [18] is investigated. In [17, 18] a pseudo-temperature field is put into a structure discretized by finite element method and the resulting thermo-elastic stress is considered as a self-equilibrated stress field. The yield condition is linearized piecemeal. Then the shakedown analysis is transformed into a linear programming containing unknown element temperature variables and constraints. By means of the further steps the numerical difficulties for plastic shakedown analysis of 3-D structures are overcome and the results are verified by experiments and by upper bound solution.

DERIVATION OF COMPUTATIONAL FORM

Static shakedown theorem by Melan [6] is presented as following mathematical programming form

Max: μ

s.t. $f(\mu\sigma_{ij}^{e}(x_k) + \rho_{ij}(x_k)) \leq \sigma_s \quad \forall x_k \in v$ (1a)

$\rho_{ij,j} = 0 \quad \forall x_k \in v$ (1b)

$\rho_{ij} n_j = 0 \ \forall x_k \in S_F$ (1c)

where σ_{ij}^{e} is the elastic stress field, ρ_{ij} is the self-equilibrate residual stress field, f is the yielding function and μ is the load multiplier, v and SF represent the structure body and its surface, respectively. The difficulty in lower bound shake-down analysis is to find $\rho_{ij}(x_k)$, which has six independent components at each point x_k in a 3-D structure. Since a ther-moelastic stress field automatically satisfy self-equilibrate conditions (1b) and (1c) so that a temperature (scalar) field $\theta(x_k)$, instead of the two-order stress tensor fields $\rho_{ij}(x_k)$, can be considered as the optimization variables of the program-ming problem (1). The procedure may largely simply the programming analysis.

Suppose that the structure which is discretized by finite element method, has M nodes. A pseudo node temperature matrix $\boldsymbol{\theta}$ is applied to the structure. Thus the node thermal stress matrix $\boldsymbol{\rho}$ in the structure has the linear relation with $\boldsymbol{\theta}$ as follows:

$$\boldsymbol{\rho} = \boldsymbol{W\theta} \tag{2}$$

where $\boldsymbol{W}$ is (6M×M) thermo-elastic matrix of the structure. The yielding function is simulated by an inscribed poly-hedron consisting of J planes as shown in [4,5]:

$$\boldsymbol{N}_j\boldsymbol{Q} = k_j \qquad j = 1,2 \ldots \mathrm{J} \tag{3}$$

where $\boldsymbol{N}_j$ is the normal vector to the linearized plane in the stress space and k_j is the perpendicular distance from point O to the j-th linearized plane. $\boldsymbol{Q}$ is the stress of current node, including both elastic stress, $\boldsymbol{Q}^e$ and pseudo-residual stress:

$$\boldsymbol{Q} = \mu \boldsymbol{Q}^e + \boldsymbol{W\theta} \tag{4}$$

Therefore the programming problem (1) is transformed into the following problem:

Max: μ

s.t. $\mu \boldsymbol{NQ}^e + \boldsymbol{NW\theta} \leq \boldsymbol{K}$ (5)

where N is composed of Nj, and K is a vector composed of kj of all nodes. Problem (5) contains (M+1) variables includ-ing both μ and node temperature matrix and (M×J) cons-traints, so that the scale of the linear programming usually dependent on the number of nodes of discretized structure. For a 3-D solid finite element analysis the scale of the programming is still too large.

In order to overcome the above mentioned difficulty, the equation for sustained heat conduction without a heat source in the structure is considered. Suppose that there are total M nodes in the structure in which the number of boundary nodes is B, the heat conduction equation in finite element form can be expressed as:

$$\boldsymbol{K^{\theta}\theta} = \mathbf{0} \tag{6}$$

where $\boldsymbol{K}^{\theta}$ is a (M×M) heat conduction matrix and $\boldsymbol{\theta}$, (M×1) node pseudo-temperature matrix. Suppose that the sub-matrix of the temperature at the boundary nodes, $\boldsymbol{\theta_b}$, has been known and $\boldsymbol{\theta_i}$ is the sub-matrix of temperature at the nodes inner the structure, then equation (6) is transformed into:

$$\begin{Bmatrix} \mathbf{K}_{ii}^{(\theta)} & \mathbf{K}_{ib}^{(\theta)} \\ \mathbf{K}_{bi}^{(\theta)} & \mathbf{K}_{bb}^{(\theta)} \end{Bmatrix} \begin{Bmatrix} \theta_i \\ \theta_b \end{Bmatrix} = \mathbf{0} \tag{7}$$

Therefore, we have

$$\theta_i = -\boldsymbol{K}_{ii}^{(\theta)-1} \boldsymbol{K}_{ib}^{(\theta)} \theta_b \tag{8}$$

Thus, $\boldsymbol{\theta}$, can be expressed by

$$\theta = \boldsymbol{T}\theta_b \tag{9}$$

where $\boldsymbol{T}$ is a (M×B) matrix:

$$\mathbf{T} = \begin{Bmatrix} -\mathbf{K}_{ii}^{(\theta)-1}\mathbf{K}_{ib}^{(\theta)} \\ \mathbf{I} \end{Bmatrix} \tag{10}$$

where I is the identity matrix. Substituting equation (9) into problem (5), the programming problem is transformed into:

Max: μ

s.t. $\mu \boldsymbol{NQ}^e + \boldsymbol{NWT\theta_b} \quad \leq \boldsymbol{K}$ (11)

In programming problem (11) the number of optimiza-tion variables is reduced from (M+1) to (B+1) .The dual programming of problem (11) is solved directly as follows:

Min: $\mu = \boldsymbol{K}^T\boldsymbol{Y}$

s.t. $(\boldsymbol{NQ}^e)^{\mathrm{T}}\boldsymbol{Y} = 1$

$(NWT)^{\mathrm{T}} Y = 0$

$Y \geq 0$ (12)

Problem (12) is a standard linear programming form containing (M×J) variables $\boldsymbol{Y}$ and (B+1) constraints. The problem is solved by using Fortran program coded by the authors.

THE LIMIT AND SHAKEDOWN ANALYSIS OF CIRCULAR TUBE WITH PART THROUGH PIT

The tubes containing four kinds of part-through pit, which are spherical, ellipsoidal, circular and rectangular, on the outside surface shown in Fig. (**1**) and named for types A, B, C and D, respectively, are computed by the presented approach. It is simplified by assuming the two symmetrical planes of each defect to be in the longitudinal and circum-ferential directions of the cylinder and the region of the defect to be far from the two end of the shell. Therefore, the computing model could be taken a quadrant of the cylinder shown in Fig. (**2**).

The models are discretized by 3-D 8-node Wilson incom-patible element [19] with nine additional degrees of freedom which is accurate to 20-node isoparametric element but the number of degree of freedom decreased by 3/5 (Fig. **3**).

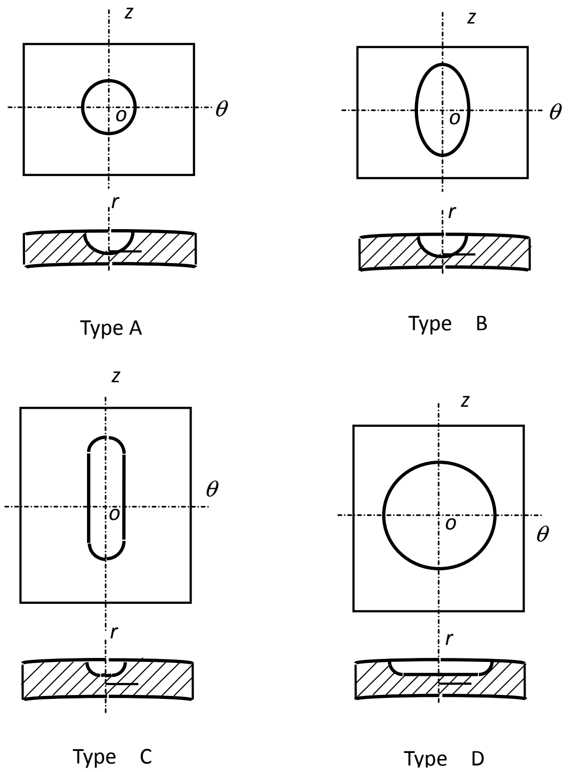

Fig. (1). Four types of defects.

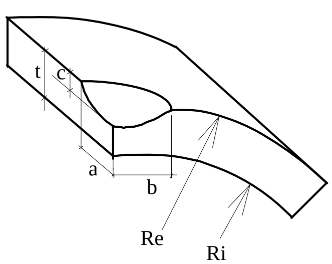

Fig. (2). Computational model.

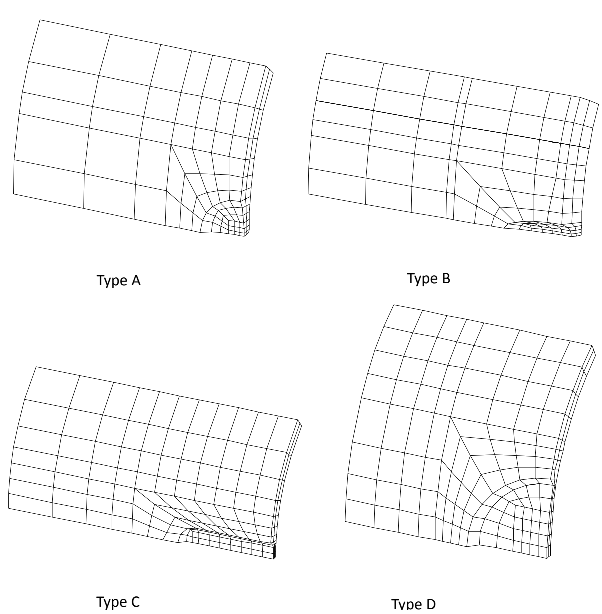

Fig. (3). Finite element meshes.

As to the linearization of the yield condition, as the difference between three principal stresses and stress components σ_θ, σ_z and σ_r is not significant, θ, z and r are assumed to be principal axis of stress and Tresca yield condition is chosen as linearized yield condition.

Six steel models are tested and calculated by the presented method. The outer diameter of the tested cylinders are 140mm and the yielding and ultimate strength of material: σ_s = 400 Mpa, σ_b = 620 Mpa. The basic parameters of six models are shown of in Table **1**, where a and b are longitudinal and circumferential dimension of slot, respectively, c, the depth of the slot and t, the thickness of cylinder. According to work criterion for choice of the deformation parameter [20] for each model the experimental limit pressure $p_l^{(ex)}$ is obtained from diagram pressure p/volume change ($\Delta v/v$) and is that for which the permanent volume change is twice the volume change at the initial departure from linearity. This definition corresponds to the definition of ASME code. However, for No1,3,6 models having large areas of defect the definition of ASME code is not appropriate because the volume change at the initial departure from linearity is too large ($\Delta v/v$ large than 1.5%) to find the limit pressure according to the definition of ASME code. Therefore for the three models the limit pressure is that giving 0.2% permanent volume change. The tested burst pressure $p_b^{(ex)}$ for the experimental models is measured too. The comparison between experimental and calculated results for the six models are given in Table **2**. Here, the limit pressure of each test model, p_o, is calculated with the thickness of each model as follow:

$$p_o = \sigma_s \ln(R_o / R_i) \tag{13}$$

Table 1. Basic Parameters of Six Tested Models

No.	Defect Type	a(mm)	b(mm)	c(mm)	t(mm)
1	C	43.2	8.2	2.8	5.1
2	B	22.2	7.4	2.9	5.4
3	D	26.5	26.5	2.9	5.3
4	A	11.6	11.6	2.9	5.8
5	B	14.9	2.6	2.5	5.1
6	C	89.0	8.4	2.7	5.4

The calculated limit and shakedown pressure, $p_l^{(lw)} / p_o$ and $p_{sd}^{(lw)} / p_o$ by the present method are given in Table **2**. The upper bound solution, $p_l^{(up)} / p_o$, for the six models is calculated by Liu with the method given in [11] and shown in Table **2** as well.

Table **2** shows that:

(1) The presented results are lower than the upper bound solution for all models but they are closed each other.

(2) The presented results are in good agreement with and lower than the experimental ones.

Table 2. The Comparison between Numerical and Experimental Results

No	Tested Results			Numerical Results		
	$p_b^{(ex)}$ **(MPa)**	$p_l^{(ex)}$ **(MPa)**	$p_l^{(ex)} / p_o$	$p_l^{(lw)} / p_o$	$p_l^{(up)} / p_o$	$p_{sd}^{(lw)} / p_o$
1	26.0	22.4	0.74	0.65	0.69	0.44
2	28.0	24.1	0.73	0.72	0.73	0.52
3	28.0	23.2	0.74	0.74	0.78	0.69
4	40.5	32.3	0.93	0.90	0.92	0.86
5	30.0	27.3	0.90	0.83	0.90	0.43
6	23.5	17.9	0.56	0.54	0.59	0.40

THE EFFECT OF PARAMETERS OF THE DEFECT ON THE CARRYING CAPACITY OF THE TUBES

The lower bound limit and shakedown pressure of cylinders with four kinds of part-though pits having different parameters are obtained by the present method and given in Figs. (**4**)~(**7**) which are for Type A, B, C and D, respectively.

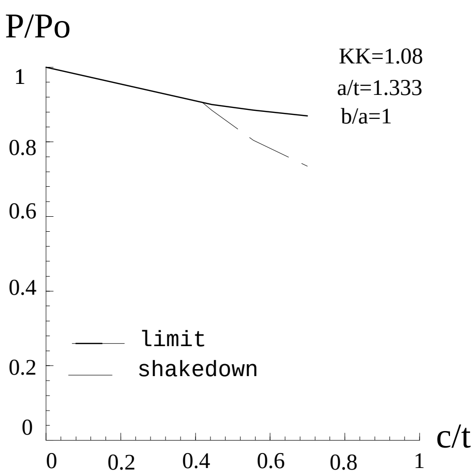

Fig. (4). Effect of depth of type A part-through pit on the carrying capacity.

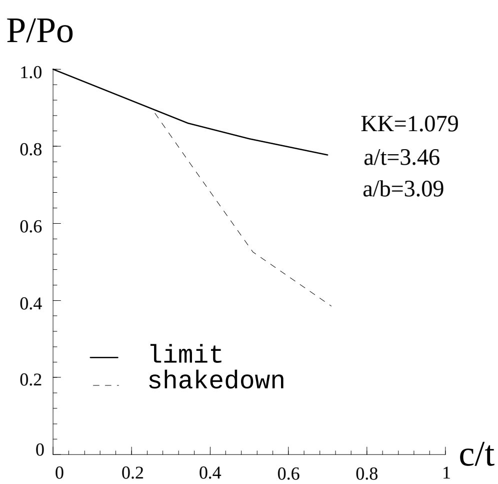

Fig. (5). Effect of depth of type B part-through pit on the carrying capacity.

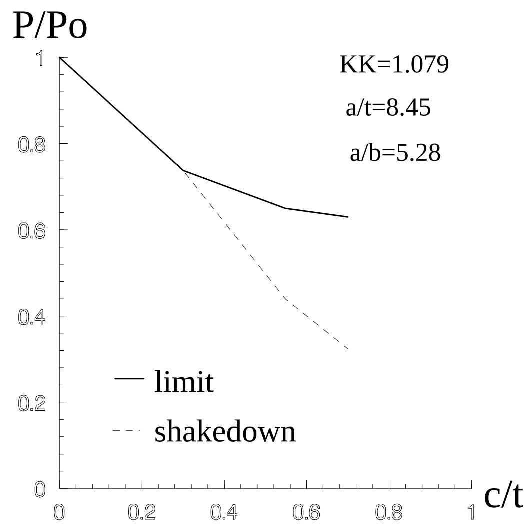

Fig. (6). Effect of depth of type C part-through pit on the carrying capacity.

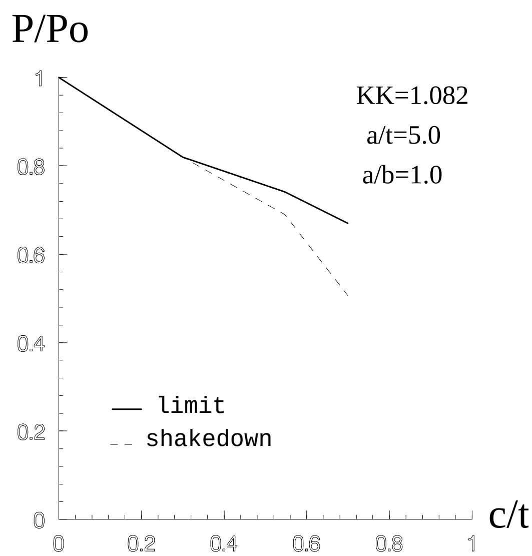

Fig. (7). Effect of depth of type D part-through pit on the carrying capacity.

The diagrams show that: (1) The carrying capacity of the tube with rectangular defect (its long axis is in the longitudinal direction of the cylinder) is the lowest and that with spherical one is the highest. (2) The carrying capacity of the tubes with rectangular or ellipsoidal defect decrease with their b/a. (3) The carrying capacity goes down with the expansion of the area of the pit, no matter what kinds of the pit is. (4) For the same model the shakedown pressure are coincident with limit one when the pit is shallow, but it descends more rapidly than limit one when the pit is deepened.

CONCLUSIONS

A FEM computational form based on the static shake-down theorem was developed in this paper. The circular tubes containing external pit defects were analyzed using Temperature Parameter Method, in which the computational quantity was largely decreased by simulating the residual stress field with a pseudo self-equilibrium thermal stress field. The approach was verified by the experimental results of six models. Due to the intrinsic characteristics of dis-placement element, the computational results should be greater than the theoretic lower-bound values, which are more closed to the real values. From the numerical results for the circular tubes with four types of part-though pits, it is found that rectangular defect is the most danger defect. The carrying capacity of the tubes decreases monotonously with the expansion of the pit. When a pit is shallow, the shake-down pressure of the tube is coincident with the limit one, however with deepening the pit, the two load carrying capa-cities becomes bifurcated, the shakedown pressure descends more rapidly than the limit one.

CONFLICT OF INTEREST

None declared.

REFERENCES

[1] I. Milne, R.A. Ainsworth, A.R. Dowling, and A.T. Stewart, *Assessment of the Integrity of Structures Containing Defects*, R/H/R6-Rev.3, CEGB Report, UK, 1986.
[2] R. Kitching, and K. Zarrabi, “Lower bound to limit pressure for cylindrical shell with part-through slot”, *Int. J. Mech. Sci.*, vol. 23, pp. 31-48, 1981.
[3] R. Kitching, and K. Zarrabi, “Limit and burst pressures for cylindrical shells with part-through slots”, *Int. J. Press. Vessels Piping*, vol. 10, pp. 235-270, 1982.
[4] A.G. Miller, “Review of limit loads of structures containing defects”, *Int. J. Press. Vessels Piping*, vol. 32, pp. 197-327, 1988.
[5] E. Melan, “Theoric statisch unbestimmter tragwerke aus ideal-plastischem baustoff”, *Sitzungsbericht der Akademie der Wissenschaften,* Abt.IIA 145, Wien, p. 195, 1938.
[6] W.T. Koiter, “General theorems for elastic-plastic solids”, In: *Progress in Solid Mechanics* I.N. Sneddon and R. Hill, Eds. Amsterdam: North-Hollad 1960, pp. 165-221.
[7] J.A. König, *Shakedown of Elastic-Plastic Structures*, *PWN*, Warsaw, Poland, 1987.
[8] X. Feng, and D. Gross, “A global/local shakedown analysis method of elastoplastic cracked structures”. *Eng. Fract. Mech*., vol. 63, pp. 179-192, 1999.
[9] X.Q. Feng, and X.S. Liu, “On shakedown of three-dimensional elastoplastic strain-hardening structures”. *Int. J. Plasticity*, vol. 12, pp. 1241-1256, 1997.
[10] X.Q. Feng, and S.W. Yu, “Damage and shakedown analysis of dtructures with strainhardening”. *Int. J. Plasticity*, vol. 11, pp. 237-249, 1995.
[11] Y.H. Liu, Z.Z. Cen, and B.Y. Xu, “A numerical method for plastic limit analysis of 3-D structures”, *Int. J. Solids Struct.*, vol. 32, pp. 1645-1658, 1995.
[12] Y.H. Liu, Z.Z. Cen, and B.Y. Xu, “Numerical limit analysis of cylindrical shells with part-through slots”, *Int. J. Press. Vessels Piping*, vol. 64, pp. 73-82, 1995.
[13] J.A. König, “On exactness of the kinematical approach in the structural shakedown and limit analysis”, *Arch. Appl. Mech*., vol. 52, Number 6, pp. 421-428, 2004.
[14] P. Fuschi, and C. Polizzotto, “The shakedown load boundary of an elastic-perfectly plastic structure”, Meccanica, vol. 30(2), pp. 155-174, 2005.
[15] F. Giambanco, L. Palizzolo, and L. Cirone, “Computational methods for optimal shakedown design of FE structures”, *Struct. Optim*., Vol. 5, Numbers 3-4, pp. 284-295, 1998.
[16] C. Polizzotto, “A unified approach to quasi-static shakedown problems for elastic-plastic solids with piecewise linear yield surface”, Meccanica, vol. 13, Number 2, pp. 109-120, 2005.
[17] M.D. Xue, X.F. Wang, F.W. Williams, and B.Y. Xu,” Lower-bound shakedown analysis of axi-symmetric structures subjected to variable mechanical and thermal loads”, *Int. J. Mech. Sci.*, vol. 39, pp. 965-976, 1997.
[18] M.D. Xue, X.F. Wang, and B.Y. Xu. “Lower-bound shakedown analysis of spherical shells containing defects”, *Int. J. Press. Vessels Piping*, vol. 68, pp. 287-292, 1996.
[19] K.J. Bathe, and E.L. Wilson, Numerical methods in finite element analysis, *Prentice-Hall, Inc:* Englewood Cliffs, New Jersey, 1976.
[20] J.C. Gerdeen, A critical evaluation of plastic behavior data and a united definition of plastic loads for pressure components, *WRC Bul.,* No. 254, 1979, pp. 1-64.

Experimental Analysis of Plastic Zone at Crack Tip

Sarat Kumar Mishra, *Department of Mechanical Engineering, Aryan Institute of Engineering & Technology, Bhubaneswar, skmishra784@gmail.com*

Saswati Nayak, *Department of Mechanical Engineering, Capital Engineering College, Bhubaneswar, saswatinayak2574@gmail.com*

Chinmay Swain, *Department of Mechanical Engineering, Raajdhani Engineering College, Bhubaneswar, chinmayswain1972@gmail.com*

Abstract: The study of this paper was to determine the plastic zone dimension at the crack tip by the experimental method of caustics. The caustics shape at the crack tip depends on plastic zone which is small for brittle materials and large for ductile ones. The plastic zone dimensions depends on the crack length, the plates thickness and the loading level. The experimental method of caustics is an excellent tool for the plasticity and stress intensity factors evaluation of loaded cracked structures.

Keywords: Cracks, caustics, stress intensity factors, plastic zone.

INTRODUCTION

The optical method of caustics is suitable for the experimental study of singularities in stress fields created either by geometric discontinuities or by loading. For many crack problems, the stress intensity factors at the crack-tip were calculated by caustics [1-3]. According to the method of caustics, the light rays impinging normally at the thin plate are partly reflected from either the front or the rear faces of the plate. The reflected rays are deviated because of the important constraint of the plate at the vicinity of the applied concentrated load and the significant variation of the refractive index there. The deviated light rays, when projected on a reference screen, are concentrated along a singular curve which is strongly illuminated and forms a caustic. It was proved that the shape and size of the caustic depend on the stress singularity at the point of application of the load. The initiation of crack propagation is essential for security problems. The study of initiation of crack propagation is presupposed the extension of the plastic zone at crack tip. Among the experimental techniques used to investigate the neighborhood of a crack tip, optical methods are widely employed, as the interferometry, photoelasticity and caustics. The method of reflected and transmitted caustics has been used to determine the static and dynamic stress intensity factors for elastic materials, Manogg [1], Theocaris [2], Papadopoulos [3], Spitas *et. al*. [4] and Badalouka *et al*. [5]. Recent work, Unger *et al.* [6] and Hedans *et al.* [7], has demonstrated that the method of caustics can be used to study the plasticity around the crack tip. The aim of this work is to study the dependence of the caustic shape on the plastic zone and to show that the optical method of caustics can be used to determine the extension of the plastic zone ahead of the crack tip.

METHOD OF REFLECTED CAUSTICS

The optical method of caustics is able to transform the stress singularity into an optical singularity, using the geometric reflection laws. For divergent light beam the reflected light rays from front (f) and rear (r) plate faces form two caustics, the caustic (f) and the caustic (r). For a cracked isotropic elastic specimen, the parametric equations of the two caustics are [3]:

$$\text{Caustic (f):}\quad \begin{aligned} X_f &= \lambda_m r_{of}(\cos\theta - \frac{2}{3}\cos\frac{3\theta}{2}) \\ Y_f &= \lambda_m r_{of}(\sin\theta - \frac{2}{3}\sin\frac{3\theta}{2}) \end{aligned} \tag{1}$$

$$\text{Caustic (r):}\quad \begin{aligned} X_r &= \lambda_m r_{or}(\cos\theta + \frac{2}{3}\cos\frac{3\theta}{2}) \\ Y_r &= \lambda_m r_{or}(\sin\theta + \frac{2}{3}\sin\frac{3\theta}{2}) \end{aligned} \tag{2}$$

where r_{of} and r_{or} are the radii of initial curves of the caustics, respectively. These radii are given by:

$$r_{of} = \left(\frac{3}{2}C_f\right)^{2/5} \quad with \quad C_f = \frac{z_o d c_f K_I}{\lambda_m \sqrt{2\pi}} \tag{3}$$

and:

$$r_{or} = \left(\frac{3}{2}C_r\right)^{2/5} \quad with \quad C_r = \frac{2 z_o d c_r K_I}{\lambda_m \sqrt{2\pi}} \tag{4}$$

and:

$$\lambda_m = \frac{z_o + z_i}{z_i} \tag{5}$$

where z_o is the distance between specimen and reference plane, d is the thickness of the specimen, λ_m is the magnification ratio of the experimental set-up, z_i is the distance between specimen and light beam focus and K_I is the stress intensity factor for the mode-I stress state. c_r and

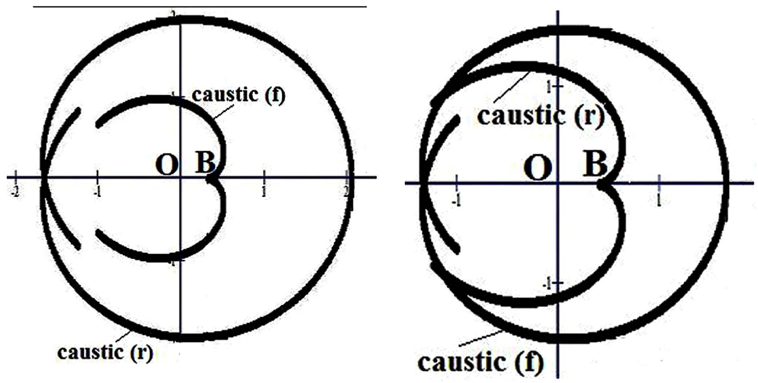

Fig. (1). Geometry of caustics (r) and (f), (**a**) for divergent light beam and (**b**) for convergent light beam.

c_f are the material stress-optical constants. The stress-optical constant c_f is given by:

$$c_f = \frac{\nu}{E} \tag{6}$$

where ν is the Poisson's ratio and E is the material modulus of elasticity.

Fig. (**1**) illustrates the plotting of the two caustics, (r) and (f), for (a) divergent light beam and (b) convergent light beam. As it is appears from Fig. (**1**) the two caustics change shape depending on light beam (divergent or convergent). For the plotting, this change is corresponding to switching the (-) with (+) in relations (1) and the (+) with (-) in relations (2).

The experimental stress intensity factor K_I is estimated by the relation [3]:

$$K_I = \frac{\sqrt{2\pi}}{3z_o d\lambda_m^{3/2} c_r}\left(\frac{D_t}{3.1702}\right)^{5/2} \tag{7}$$

where D_t is the maximum diameter of the caustic (r).

EXPERIMENTAL PROCEDURE

For the present investigation Lexan (PCBA) specimens with a length of $0.300m$, a width of $0.080m$ and a thickness of $d = 0.003m$ were used during the tensile tests. The edge crack lengths were $\alpha = 0.028m, 0.040m, 0.056m, 0.069m$. The Lexan stress optical constant was $c_r = 2.04 \times 10^{-10} m^2 / N$. For divergent light beam, the magnification ratio was $\lambda_m = 4.7179$ and the distance between specimen and reference plane was $z_0 = 1.45m$ and the distance between specimen and light beam focus was $z_i = 0.390m$.

RESULTS AND DISCUSSION

Fig. (**2**) illustrates the experimental and plotting caustics corresponding to experiments with tensile stress $\sigma = 2.37MPa$ and edge crack lengths a) $\alpha = 0.028m$, b) $\alpha = 0.040m$, c) $\alpha = 0.056m$ and d) $\alpha = 0.069m$. As it appears in photos (c) and (d), the caustics became oval. This means that in front of the crack tip a small plastic zone was appearing. In photos (a) and (b) the ratio of the diameters of the caustics (transverse D_t and longitudinal D_l) is $D_t / D_l = 1.056$ as the ratio of the plotting (theoretical) caustics. The diameters ratio of the caustics in photos (c) and (d) is $D_t / D_l < 1.056$. This means that the longitudinal diameter becomes bigger than the transverse diameter. The biggest longitudinal diameters is depended from the size of the created plastic zone in front of the crack tip.

Fig. (**3**) illustrates the experimental and plotting caustics obtained from tensile experiments for edge crack lengths $\alpha = 0.040m$ and tensile stresses a) $\sigma = 4.9MPa$, b) $\sigma = 6.13MPa$, c) $\sigma = 8.58MPa$ and d) $\sigma = 11.03MPa$.

Fig. (**4**) illustrates the variation of diameters ratio of the caustic versus the stresses for various edge crack lengths as obtained from tensile experiments. From these curves the effect of the size of plastic zone on the diameters of the caustics can be observed. The diameters ratio is rapidly decreasing (mainly for $\alpha = 0.069m$) because the longitudinal diameter of the caustic was increased by the plastic zone increased.

Fig. (**5**) illustrates the percentage variation of the caustic shape (deformation) ($D\%$) versus the stresses for various edge crack lengths as obtained from tensile experiments. The value size of the deformation D was calculated by the relation:

$$D = \frac{\left(D_t / D_l\right)_i - \left(D_t / D_l\right)_0}{\left(D_t / D_l\right)_0} \tag{8}$$

From these curves the effect of the crack length on the values of caustic shape deformation D can be observed (mainly for $\alpha = 0.069m$).

Fig. (**6**) illustrates the percentage variation of the permanent caustic shape deformation per cent ($D_{perm.}\%$) versus the crack length as obtained from tensile experiments and from caustics at the crack tip after unloading the specimens. The size of the permanent caustic shape deformation $D_{perm.}$ was calculated by relation (8). From this curve the effect of crack length on the size of permanent caustic shape deformation can be observed.

Fig. (**7**) illustrates the variation of the percentage plastic zone size ($R_{pl.zon.}\%$) in front of the crack tip versus stresses

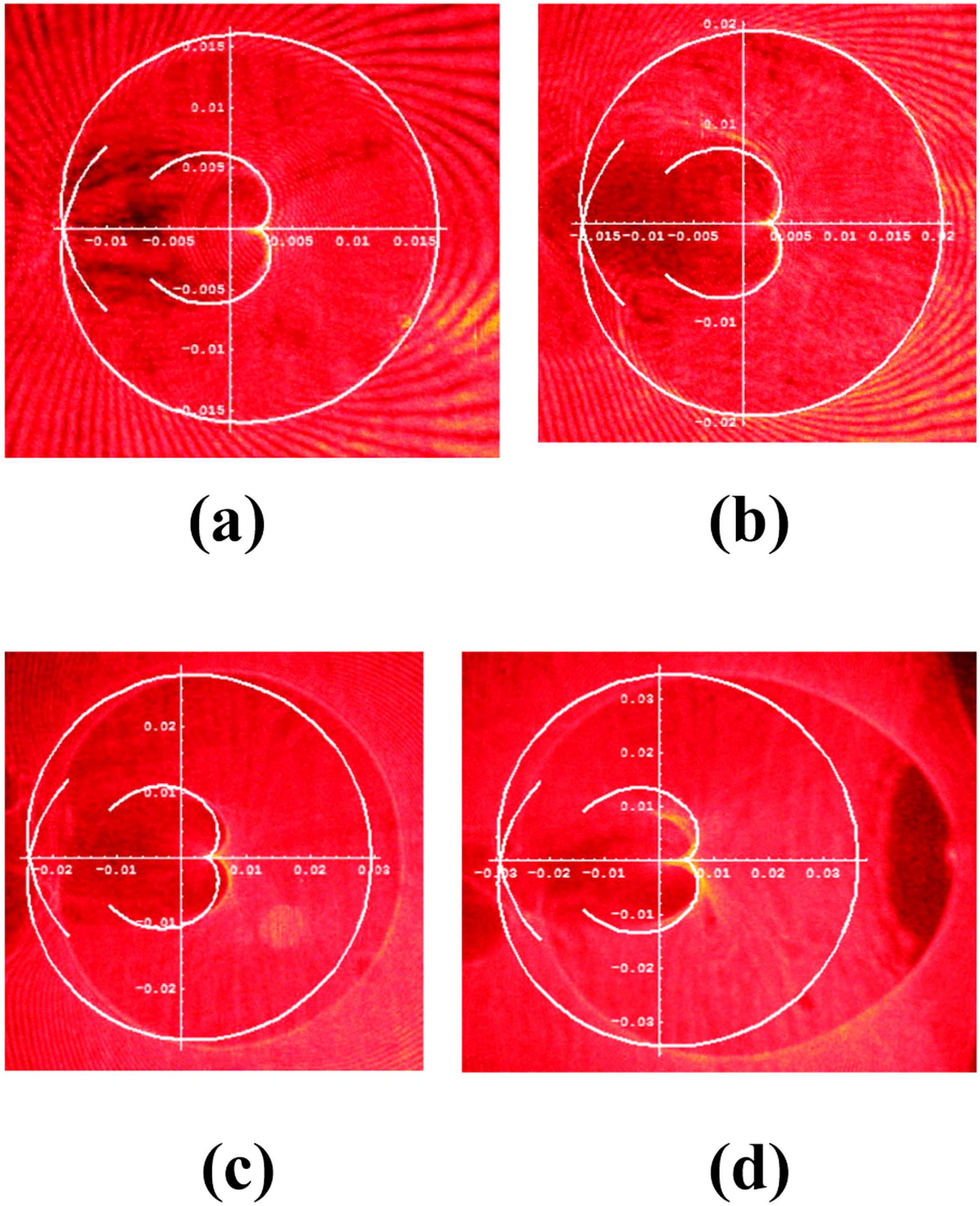

Fig. (2). Experimental and plotting caustics obtained from tensile experiments for tensile stress $\sigma = 2.37 MPa$ and edge crack lengths **a**) $\alpha = 0.028m$ **b**) $\alpha = 0.040m$ **c**) $\alpha = 0.056m$ and **d**) $\alpha = 0.069m$.

for various edge crack lengths as obtained from tensile experiments. The size of the plastic zone $R_{pl.zon.}$ was calculated by the relation:

$$R_{pl.zon.} = \frac{\Delta D_l}{D_{l0}} \% \tag{9}$$

From these curves the effect of stress on plastic zone size $R_{pl.zon.}$ can be observed.

Fig. (**8**) illustrates the variation of the experimental stress intensity factor $K_I^{exp.}$ versus the edge crack length for a stress $\sigma = 2.37 MPa$ and a specimen width $w = 0.080m$. The stress intensity factor $K_I^{exp.}$ was calculated by the relation (7) for crack length $\alpha = 0.040m$ and specimen width $w = 0.080m$. From this curve a nearly linear variation can be observed for great crack lengths. While, for small crack length a non-linear variation can be observed because a triaxiality stress state was created.

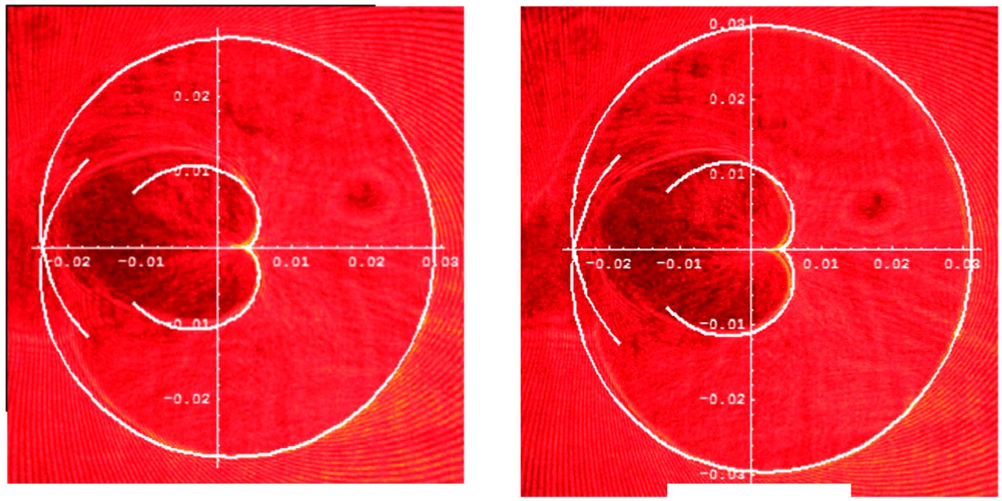

(a) **(b)**

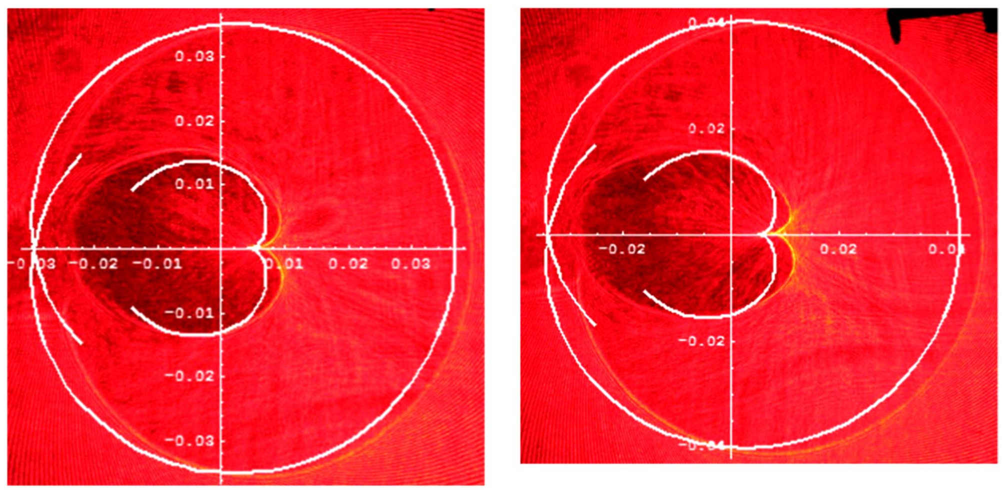

(c) **(d)**

Fig. (3). Experimental and plotting caustics obtained from tensile experiments for edge crack lengths $\alpha = 0.040m$ and tensile stresses **a**) $\sigma = 4.9MPa$ **b**) $\sigma = 6.13MPa$ **c**) $\sigma = 8.58MPa$ and **d**) $\sigma = 11.03MPa$.

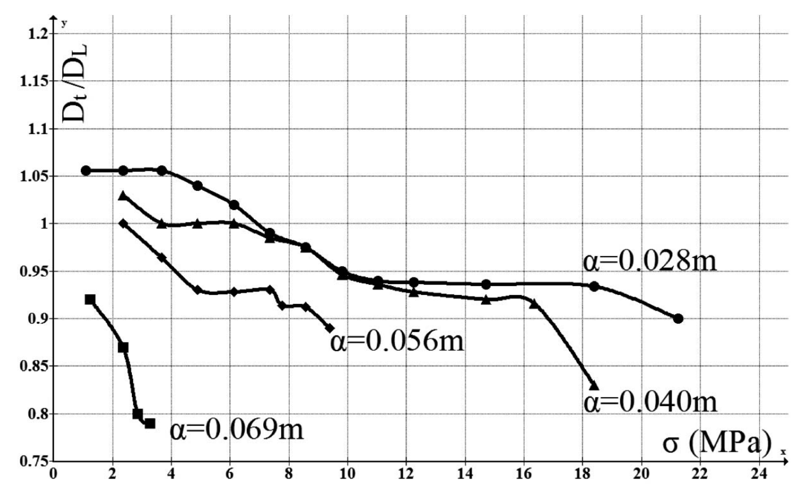

Fig. (4). Variation of the caustic diameter ratio versus stresses.

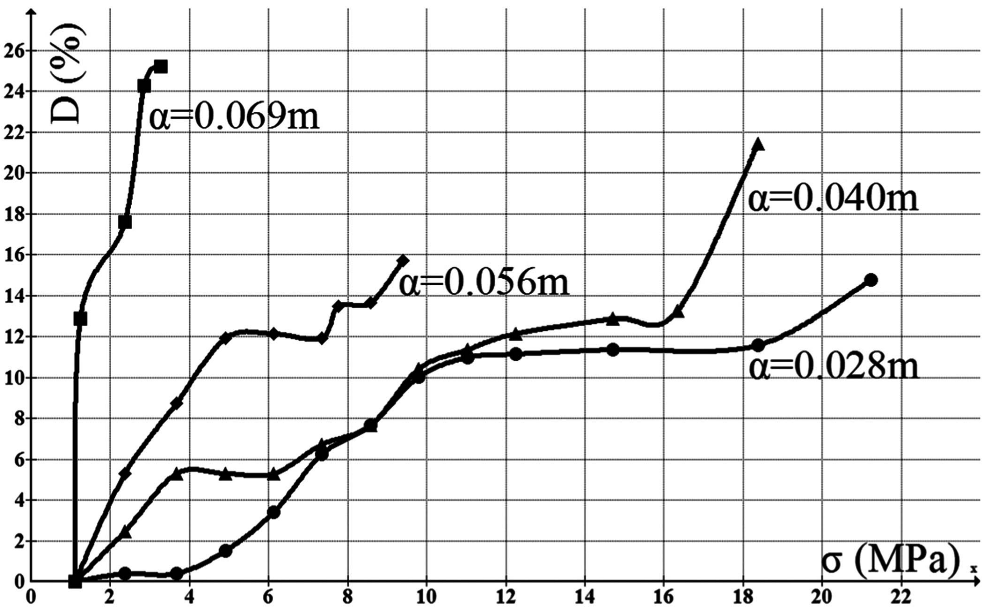

Fig. (5). Variation of the caustic shape deformation per cent (*D*%) versus stresses for various edge crack lengths.

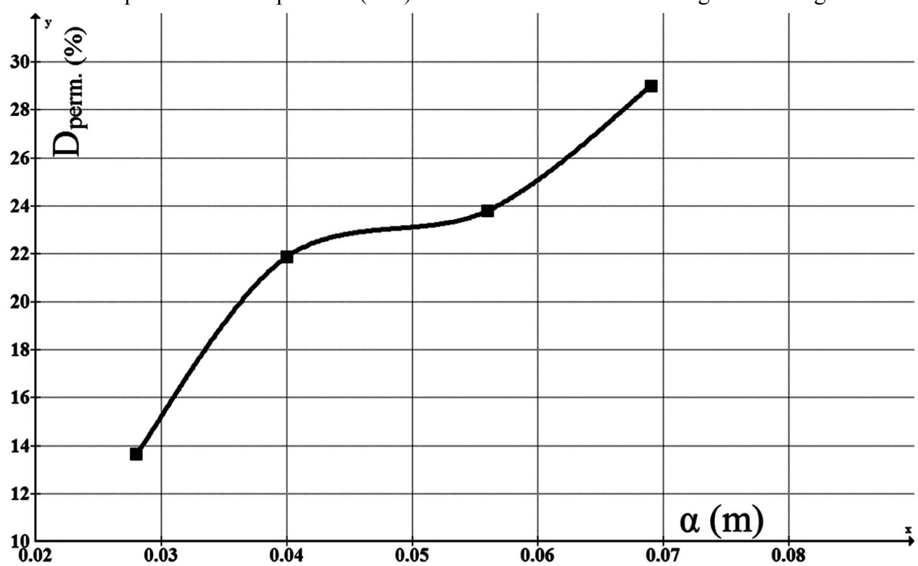

Fig. (6). Variation of the permanent caustic shape deformation per cent ($D_{perm.}\%$) versus crack length.

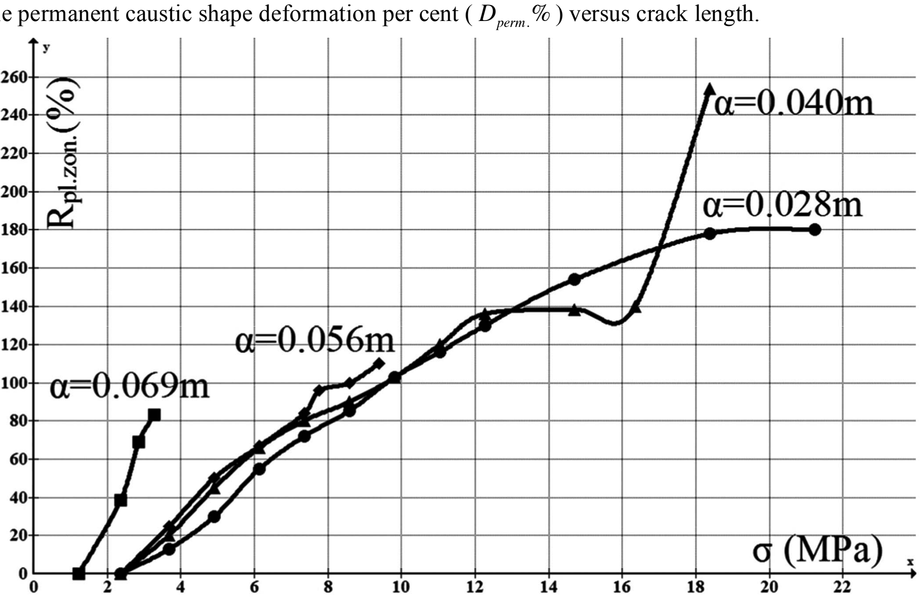

Fig. (7). Variation of the plastic zone size per cent ($R_{pl.zon.}\%$) in front of the crack tip versus stresses for various edge crack lengths.

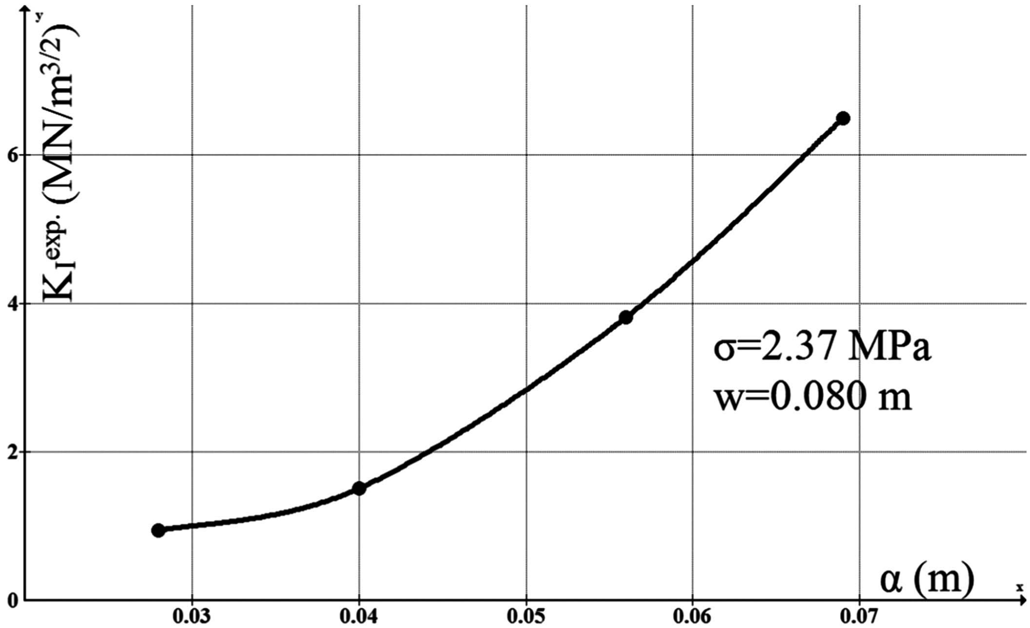

Fig. (8). Variation of the experimental stress intensity factor $K_I^{\exp.}$ versus crack length for stress $\sigma = 2.37 MPa$ and specimen width $w = 0.080m$.

Fig. (**9**) illustrates the variation of the experimental stress intensity factor $K_I^{\exp.}$ versus the stresses for crack length $\alpha = 0.040m$ and specimen width $w = 0.080m$. The stress intensity factor $K_I^{\exp.}$ was calculated by the relation (7). From this curve a nearly linear variation can be observed for high stresses.

Fig. (**10**) illustrates the variation of the experimental stress intensity correction factor f versus the ratio of crack length and specimen width (α / w) for a stress $\sigma = 2.37 MPa$.

The stress intensity correction factor f was calculated by the relation:

$$f = \frac{K_I^{\exp.}}{\sigma \sqrt{\pi \alpha}} \tag{10}$$

From this curve a nearly linear variation can be observed for high ratios (α / w). While, for small ratios a non-linear variation can be observed because a triaxiality stress state was created.

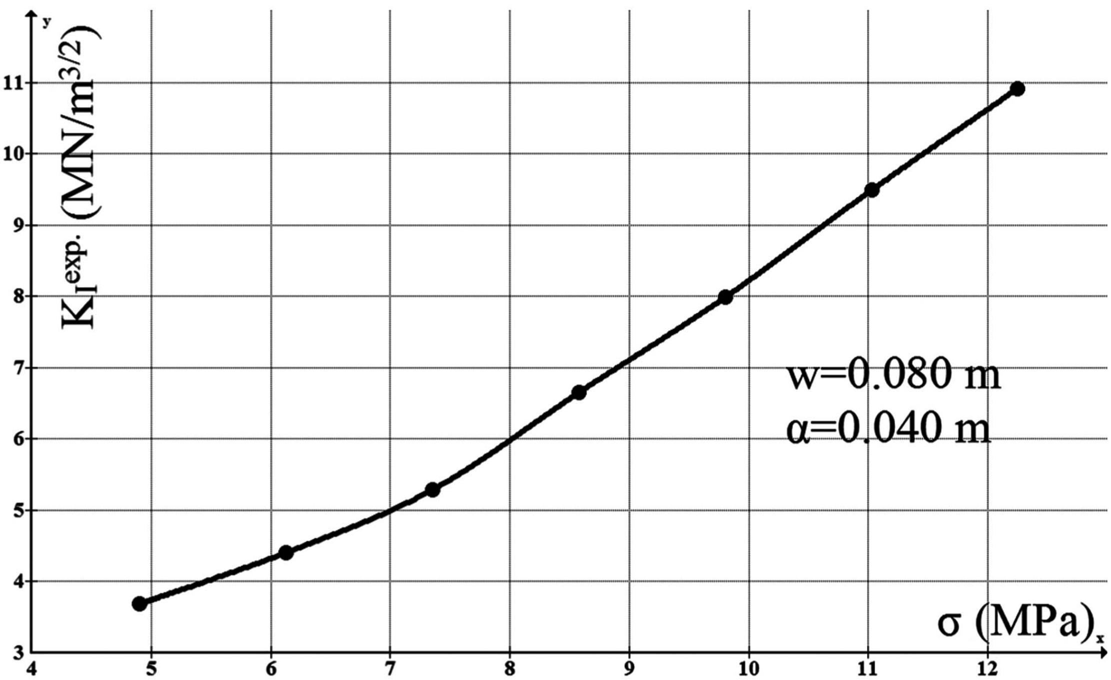

Fig. (9). Variation of the experimental stress intensity factor $K_I^{\exp.}$ versus the stresses for crack length $\alpha = 0.040m$ and specimen width $w = 0.080m$.

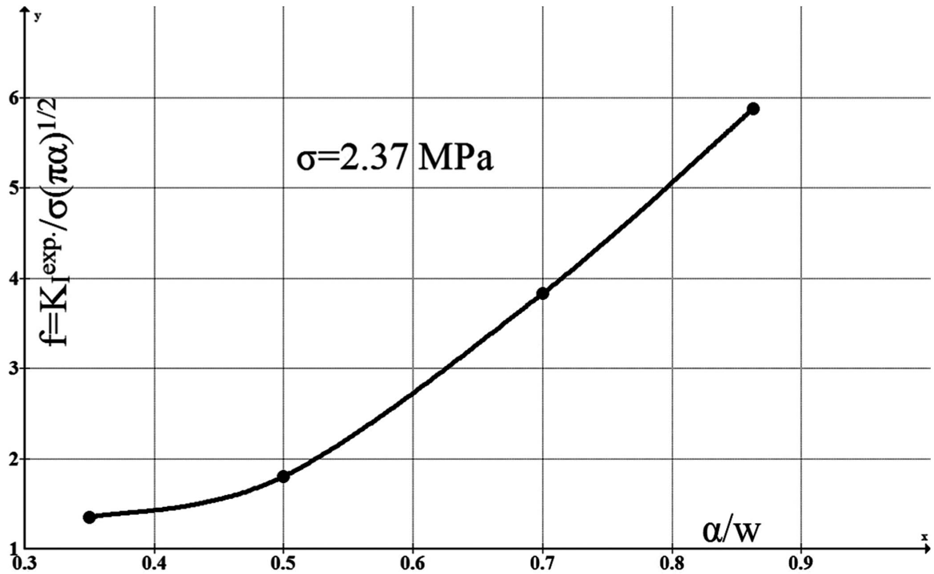

Fig. (10). Variation of the experimental stress intensity correction factor f versus the ratio of crack length and specimen width for stress $\sigma = 2.37 MPa$.

CONCLUSIONS

The aim of this work is to study the dependence of the caustic shape on the plastic zone and to show that the optical method of caustics can be used to determine the extension of the plastic zone ahead of the crack tip, on a ductile plate loaded in mode I. From this experimental study it is possible to conclude that the shape of caustics was deformed by crack length, stresses and plastic zone at crack tip. The plastic zone size depends on caustics diameters and mainly on the longitudinal diameter. The plastic zone variation was calculated by the variation of the caustic longitudinal diameter. This plastic zone variation depended on the state of stresses, the crack length and the materials. The stress intensity factor was calculated from the transverse diameter of the caustic. The stress intensity variation was linear for high values of stresses and crack lengths, while it was non-linear for small stresses and crack lengths because of the triaxiality at crack tip. The experimental stress intensity correction factor was calculated for various crack lengths. This experimental study shows that the caustic optical method can be used to give a non destructive calculation of the plasticity state of a loaded cracked ductile plate.

REFERENCES

[1] P. Manogg, Anwendung der Schattenoptik zur Untersuchung des Zerreissvorgangs von Platten. Dissertation 4/64, Universitaet Freiburg, 1964.

[2] P.S. Theocaris, “Local yielding around a crack-tip in plexiglas”, *J. Appl. Mech. ASME,* vol. 37, pp. 409-415, 1970.

[3] G.A. Papadopoulos, “The Experimental Method of Caustics and the Det.-Criterion of Fracture”, G.A. Papadopoulos ed., *Fracture Mechanics,* Springer-Verlag, London, 1993.

[4] V. Spitas, G.A. Papadopoulos, C. Spitas, and T. Costopoulos, “Experimental investigation of load sharing in multiple gear tooth contact using the stress-optical method of caustics”. *Strain*, vol. 47, pp. e227-e233, 2011.

[5] B.G. Badalouka and G.A. Papadopoulos, “Range of applicability of the method of caustics around holes”. *Strain*, vol. 42, pp. 283-290, 2006.

[6] D.J. Unger, “Perfectly plastic caustics for the opening mode of fracture”. *Theor. Appl. Fract. Mech.,* vol. 44, pp. 82-94, 2005.

[7] S. Hedans, O. Pop, V. Valle and M. Cottron, “FE and experimental investigation with shadow optical method for measuring plastic zone in a ductile cracked plate. *Strain,* vol. 47, pp. e142-e147, 2011.

Analysis of a Human Mandible with Added Temporomandibular Joints

Chinmay Swain, *Department of Mechanical Engineering, Raajdhani Engineering College, Bhubaneswar, chinmayswain1972@gmail.com*

Subhasis Sarkar, *Department of Mechanical Engineering, NM Institute of Engineering & Technology, Bhubaneswar, subhasissarkar14@yahoo.co.in*

Suraj Kumar Patel, *Department of Mechanical Engineering, Aryan Institute of Engineering & Technology, Bhubaneswar, surajpatel26@gmail.com*

Swarup Sahoo, *Department of Civil Engineering, Capital Engineering College, Bhubaneswar, swarupsahoo26@outlook.com*

Abstract: Mathematical modelling of human mandible and its temporomandibular joints (TMJs) is one of the most important steps for developing a powerful forecasting tool to analyse the stress/strain behaviour of a human masticatory system under occlusal loads.

In this work the structural behaviour of a mandible with articular discs, undergoing a unilateral occlusion, is numerically analysed by means of both Finite Element Method (FEM) and Boundary Element Method (BEM). The mandible is considered as completely edentulous and its anisotropic and non-homogeneous bone material behaviour is modelled. The material behaviour of the articular discs was assumed to be either elastic or hyper-elastic. The loads applied to the mandible are related to the active muscle groups during a unilateral occlusion. The results of FEM and BEM analyses are presented mainly in terms of stress distribution on the mandible and on the articular discs. Due to the uncertainty in the determination of the biological parameters, a sensitivity analysis is provided, which demonstrates the impact of the variation of articular disc stiffness and TMJ friction coefficient on the mandible stress peaks and on the occlusal loads (for a given intensity of muscle loads). Moreover a comparison between the effectiveness of the BEM and FEM numerical approaches on this kind of problem is provided.

Keywords: FEM, BEM, human mandible, temporomandibular joint.

INTRODUCTION

Mathematical modelling of a whole mandible, with the addition of temporomandibular joints (TMJ), certainly provides a powerful tool for the evaluation of stress-strain distribution related to the human masticatory system. A reliable analysis tool allows to understand the behaviour of a mandible with its TMJ, under both physiological and pathological conditions.

The initial studies strongly simplified the geometry of the joint surfaces, either by restricting it to a two-dimensional analysis in the sagittal plane [1, 2], or by limiting their analysis only to a part of the whole mandible [3, 4], or, even if the whole mandible was considered, by modelling the discs with just an elastic or hyper-elastic material behaviour [5]. Some of the previously mentioned limits have been overcome by recent work that accurately analyses the articular disc stresses, considering its visco-elastic [6] or porohyperelastic behaviour [7-10].

In continuation of a consolidated research activity developed by the authors [5, 11, 12], this paper describes the structural behaviour of a mandible with its TMJs, under unilateral mastication loading, as analysed by the Finite Element Method (FEM) and by the Boundary Element Method (BEM), in order to compare the two numerical approaches.

The considered mandible is completely edentulous and the articular discs are alternatively modelled as elastic or hyper-elastic.

In the first part of the paper a CAD reconstruction method is shown for modelling an A-class surface model of mandible and TMJs, starting from CT or MR scan. This kind of CAD model is very useful both in FEM and in BEM simulations because of volume/surface modelling accuracy.

The comparison between FEM and BEM approaches allows to evaluate which is more appropriate in terms of accuracy, run time and pre-processing time.

The FEM method has the advantage of high versatility, while, BEM allows a more direct coupling with CAD applications starting from mandible computerized tomography (CT) scan. In addition, BEM is best suited to accurately reproduce high surface stress gradients that generally are a modelling issue in bone-implant contact simulations.

The mandible is connected to the skull by the TMJs, the articulating surfaces of which are highly incongruent and partially with opposite convexity, which provide the mandible with a large degree of mobility (usually of roto-translatory type). A cartilaginous articular disc is interposed between upper condylar and infratemporal cavity surfaces; by increasing the contact area between articulating surfaces, the articular disc reduces contact pressure and, consequently, the risk of degeneration of joint tissues and the occurrence of para-functional disorders (e.g. bruxism).

The mastication loads are the resultant of the distributed pressures on the tooth surfaces due to contact with food during biting and chewing. The evaluation of the loads applied on TMJ, during mastication, represents one of the critical points of the practical dental clinics. The degenerative modifications of condyles, articular capsule and interposed soft tissues are often related to the pathological presence of high stresses. The complexity of mandibular geometry, the uncertainties in determination of bone material properties [13, 14] and the three-dimensional nature of the masticatory kinematics make this a pioneering problem for dentists and biomechanical engineers.

The clinical objective of this work is to provide a sensitivity analysis for the reaction loads in the articular discs and peak stresses in the mandible against the variation of articular disc stiffness and TMJ friction coefficient (there is uncertainty in assessing the effective values for such biological parameters). Such sensitivity analyses may be useful to dentists in order to assess the importance of retrieving accurate and patient specific values for the mechanical and biological parameters involved. Consistently, the results of FEM and BEM analyses are presented mainly in terms of stress distribution on the mandible and resultant loads on the articular discs.

The large amount of planned simulations prevents the adoption of a more complex TMJ model, as done in [6-10], that would require a huge computational effort; on the other hand, the stress distribution in the disc would be much influenced by the visco-elastic or porohyperelastic disc behaviour only when considering an enduring pressure on the disc (e.g. in case of prolonged clenching [6]), whereas in our case we considered a quasi-static application of the mastication load with no allowance for the time parameter. Moreover, when the disc is treated as porohyperelastic material, relevant approximations must be considered since the literature does not offer reliable material parameters for the human TMJ (properties of dog discs are generally used [8]).

The fibrocartilaginous layer that covers the articulating surfaces of bones is not included in our model but in [15] it has been reported that it only causes slight to moderate stress reductions in the disc.

Moreover, in this study, the disc anisotropic structure has been approximated as isotropic because it was mainly subjected to compression loading and consequently the resulting differences would be negligible [6].

GEOMETRIC MANDIBLE MODELLING

CAD (Computer Aided Design) modelling of the mandible and its TMJs has been carried out by a 3D approximated model consisting of triangular surfaces (only useful to 3D visualization).

The original model has been taken from a medical database in VRML (Virtual Reality Meta-Language) format; the triangulated surfaces of the model have been used for approximating the mandible geometry.

The VRML File was first translated in IGES (Initial Graphics Exchange Specification) format (following an articulated procedure described below) in order to avoid information loss during the translation procedure. The obtained IGES file is made up of more than three million triangles and has been loaded by the Advanced Surface Modeller of CATIA® Software (by IBM-Dassault-Systems): this operation allows to create a CAD model made of A-Class surfaces that are easy to mesh and to analyze by CAE (Computer Aided Engineering) software.

The main problems in A-class surface modelling come from translation information loss: in VRML *vs* IGES translation several triangles are lost, several surfaces change their normal vector orientation and several edges between triangles become unconnected. These problems have to be solved in order to create a CAD model that can be easily used to create a surface or volumetric mesh for respectively BEM and FEM analyses.

The following hypotheses were postulated to simplify the modelling operation:

1. The mandible was considered symmetric with respect to the sagittal plane.
2. The front mandible part was modelled as an extruded surface, having a “geometric spine”.
3. The geometric spine intersects the geometric centres of transverse sections of the mandible IGES model.
4. Condyles were created by free-surface-modelling technique.

The model translation and creation were carried out as follows:

1. The lower part of the mandible was divided into eight sections using seven planes orthogonal to the geometric spine. The spine was obtained as follows:
   a. one plane (LPl - Lower Plane) that intersects the lower part of the mandible (the chin) was identified;
   b. on this plane (LPl) several points (obtained by intersection of the triangle edges with LPl plane) have been identified (LPt - Lower points);
   c. these points have been used to create a Cubic Spline Curve that intersects the mandible surfaces and follows the lower-mandible profile;
   d. several planes (OPl - Orthogonal Planes) have been created (approximately orthogonal to the main mandible profile) and several points (Opt - Orthogonal points) are identified through the intersections of those planes with triangle edges;
   e. for each plane (OPl) one point Pp, whose Cartesian coordinates are the mean values of coordinates of section points (Opt), has been pointed out;
   f. the spine is defined as a Cubic Spline Curve passing through the Points Pp. After that, this spine was divided into eight identical parts by seven points (NP-Nodal points).
2. Seven new planes were created so that each plane is orthogonal to the spine and passes through one Nodal Point. Each of these planes intersects about 40/50

triangles (belonging to the original IGES model) by generating a closed line-strip (loop).

3. The CAD-modeller has chosen two series of nine points (First point on the sagittal plane, Last point on the Closing plane and seven points on each of the seven OPl) to design two Poly-Hermite Curves (PHC) that represent the bounds between the inner part and the outer part of the mandible.
4. The PHC intersect (and divide) each closed Line-strip in two open poly-lines (the inner one and the outer one).
5. Poly-lines' points have been interpolated using a "Constrained Curve" (CC) whose interpolation points, weights and tangents can be controlled by the modeller. Those curves represent the generating profiles for sections surfaces. They show a C2 continuity (useful to create A-class surfaces).
6. CC characteristics are the following:
   a. they belong to the Opl;
   b. Inner and Outer CC have C2 continuity properties;
   c. CC are orthogonal to the spine and to the PHC.

These characteristics are needed to use the CC as "generating curves" in CATIA Advanced Surface Modeller to create surfaces by the command "Crv-crv along spine". The created surface is a modified Parametric Cubic surface in which:

- the CC can be used as generating curves;
- the PHC can be used like Limits (bound) Curves;
- the spine can be used like Spine Curve;
- the torsion vectors for each section of the surface are always equal to zero.

This command for surface creation uses an algorithm to minimize the local curvature on the whole surface; the whole surface becomes a parametric-variational surface with an "associated History" (each modification of generating parameters causes a controlled modification of the whole surface). These kinds of surfaces are very powerful to create complex geometry using a B-Rep Modelling approach.

Steps N. 1 to 6 allow creating the lower part of the mandible. Another modelling approach has been used to create the rear part of the mandible and the condyles.

1. The rear part of the mandible has been created using a "Crv-crv along spine" surface through the last profile of the lower part of the mandible and one point opportunely chosen under the "coronoid process" (one curve degenerates in one point so creating a multi-tangent Triangular Parametric Patch). The creation has been repeated for the inner and for the outer part of the rear mandible.
2. The same approach has been used to define condyle surfaces.
3. All surfaces have been merged into a single one in order to check the continuity and the presence of holes.
4. Obtained surface-model has been exported in IGES format for CAE analyses (Fig. **1**).

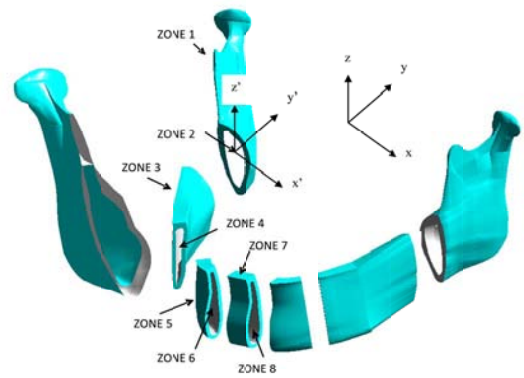

Fig. (1). Mandible exploded view with highlights of the zones characterized by different stiffness (cancellous and cortical parts) and material direction.

GEOMETRIC MODELLING OF THE TEMPORO-MANDIBULAR JOINT (TMJ)

The articular discs allow the relative movements within the TMJ, reducing the stress level on the mandible during the masticatory phase. The disc is primarily constituted of cartilage and is kept in position by means of the retrodiscal tissue and by the constraints imposed by the condyle and the glenoid fossa. The geometrical reconstruction of the disc was made with reference to literature data, even if, in order to improve the accuracy of results, it would be better to reconstruct the numerical model by using the patient's Magnetic Resonance.

Considering that the articular disc is positioned between the condyle (Fig. **2**) and the infra-temporal cavity and that it is overlapped with the former, it was possible to start its reconstruction from the condyle CAD model that was imported in IGES format using the CATIA® utility IGECAT®.

Once the disc surface was created in contact with the infra-temporal cavity (the disc is nearly completely in contact with both the infra-temporal cavity and the front and upper parts of the condyle), the other four side surfaces embedding the volume of the joint disc and not in contact with other parts of the TMJ were modelled as planar for simplicity.

The first modelling step was the creation of the geometry of the articular disc using its main sections as obtained by literature references [1, 3] in order to identify several points and tangents useful to model the surfaces; these points were interpolated by a "constrained curve" (a Poly-Hermite Curve was used in order to obtain the main profiles of surfaces and to enforce the C2 continuity). In this way the main longitudinal and transverse sections were modelled (Figs. **3**, **4**) in order to create a section frame to support (through interpolation) the TMJ external surfaces..

The longitudinal curves are created in such a way to be orthogonal to the transverse ones and intersect them in extreme points. This requirement must be satisfied to generate the surface by using the powerful CATIA® feature "crv-crv along spine". The median longitudinal curve has been used as a spine for surface modelling. For those surfaces, the curvature optimization algorithm was also used.

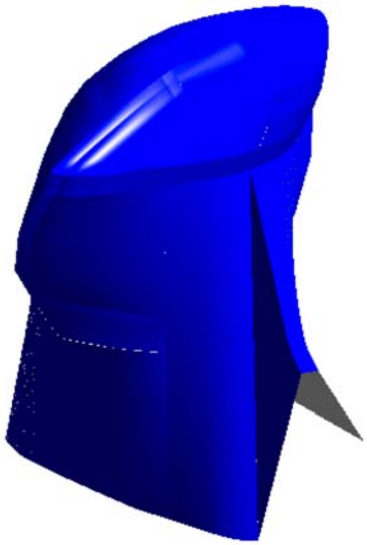

Fig. (2). Condyle CAD model.

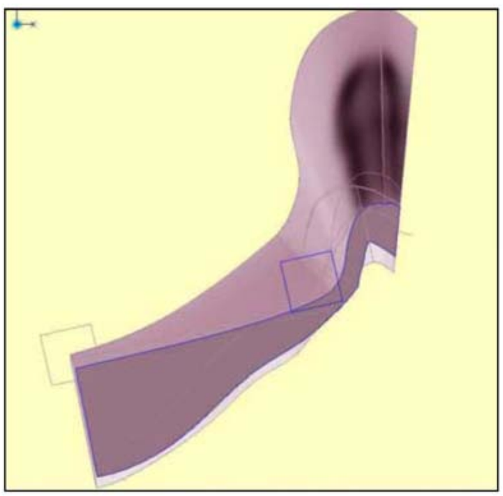

Fig. (3). Longitudinal section of articular disc.

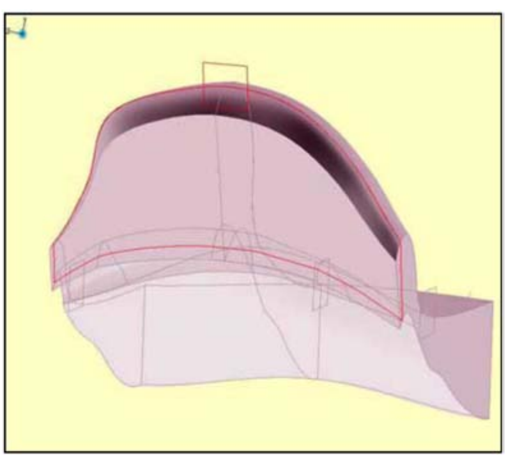

Fig. (4). Transverse section of articular disc.

Finally, the three remaining "free" surfaces were modelled as Flat patches in order to simplify the model (Fig. **5**).

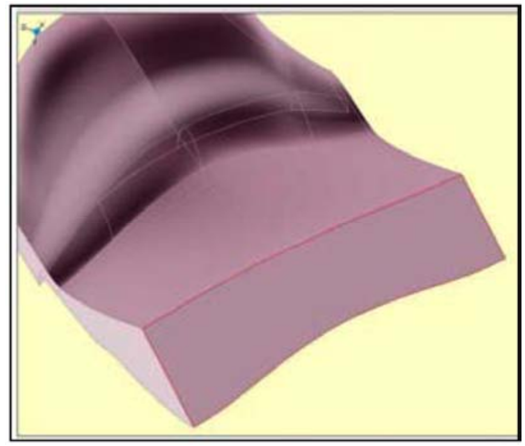

Fig. (5). Upper view of articular disc with highlight of flat surfaces.

The whole surfaces' group was checked and used to create a closed volume for generating the 3D solid-model using the Solid modelling command of CATIA® (Figs. **6**, **7**).

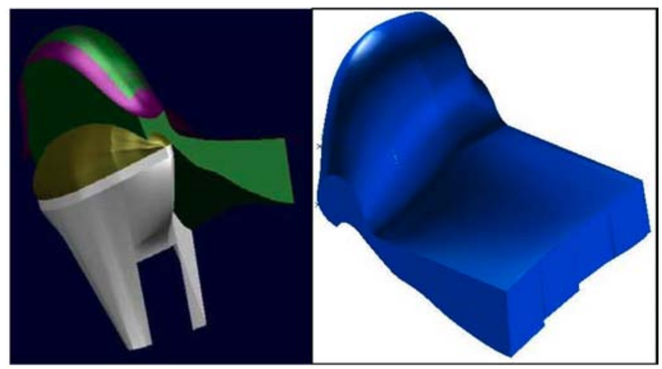

Fig. (6). Solid model of the disc interposed between infra-temporal cavity and condyle.

The so modelled TMJ is perfectly connected with the infra-temporal cavity and with the front-upper part of the condyle.

The created solid was exported to the pre-processing software in order to be analyzed using BEM and FEM techniques.

PROBLEM DESCRIPTION

Human mandible Finite Element (FE) and Boundary Element (BE) models have been developed in order to investigate the functional loads at the TMJs and the mandible stress distribution caused by occlusal loads, with a varying position of the unilateral occlusion point.

The mandible model (Fig. **1**) takes into account the non homogeneity and the anisotropy of the bone material [5]. The mandible model is divided in internal zones, with cancellous bone properties and external zones with cortical bone properties (Fig. **1**). The mandible is further divided into fourteen sections, characterized by varying stiffness properties (the stiffness increases from the posterior to the anterior part of the mandible). In each of the considered zones the material has been modelled as transversally isotropic, with specified material directions and elastic compliances (Table **1**). It should be pointed out that the highest stiffness value is in the axial direction (y', that

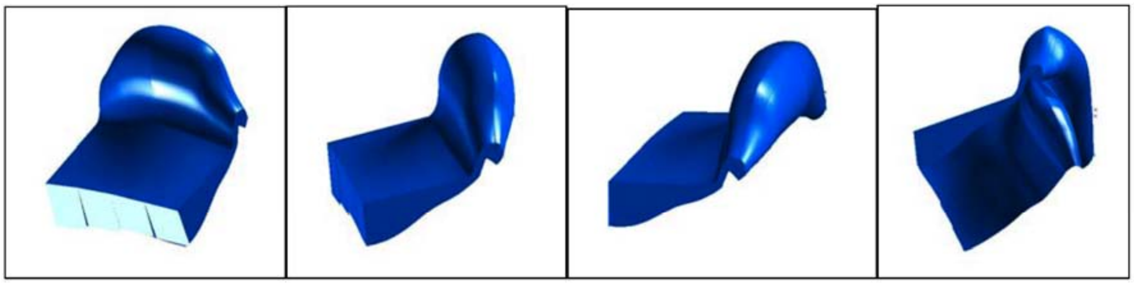

Fig. (7). Articular disc views.

is normal to the generic transversal section plane), followed by section coplanar (x', z') directions. This hypothesis was formulated in accordance with the theory of bone re-modelling, which states that the bone orients its tissues and its general framework so as to achieve the maximum stiffness with the minimum weight. The axial direction is the one requiring larger stiffness so as to resist the stresses caused in the mandible by the mastication process which produces mainly bending loads [14].

In one of the proposed models, the disc is able to slide among the joint surfaces of condyle and infratemporal cavity, being kept in its position by contact loads; a variable friction coefficient is hypothesised, simulating the range of clinical conditions going from a well lubricated (by the synovial liquid) joint, with a friction coefficient equal to nearly 0 [8], to a pathological non lubricated joint, with friction coefficient higher than 0.3; moreover the contribution of the retrodiscal tissue attached to the articular disc is neglected due to its high compliance. In a closed jaw position the articular disc upper surface assumes a shape corresponding to that of the infratemporal cavity whereas the articular disc bottom surface overlaps the upper condylar surface.

The articular disc material behaviour is here approximated as linear elastic or hyper-elastic. In the former case, the disc elasticity modulus was assumed constant and equal to 60 MPa (from the literature this value can vary from 6 to 100 MPa) and the Poisson's coefficient is equal to 0.40.

In the articular disc mathematical reconstruction, the transition zone between the fibrous part of the upper lateral pterygoid muscle and the articular disc is also taken into account (this explains the strong thickness in the disc rear zone) [3].

The six main muscle groups (Fig. **8**), activated in the occlusal masticatory phase are: deep and superficial masseter (DM and SM), medial and lateral pterygoid (MP and LP), and temporalis muscle, divided into anterior and posterior portions (AT and PT). The intensity and the direction of the resultant load of each muscle are generally obtained by experimental measurements, in particular by means of electromyography combined with measurement of muscular section; their values are taken from [5] and reported in Table **2**.

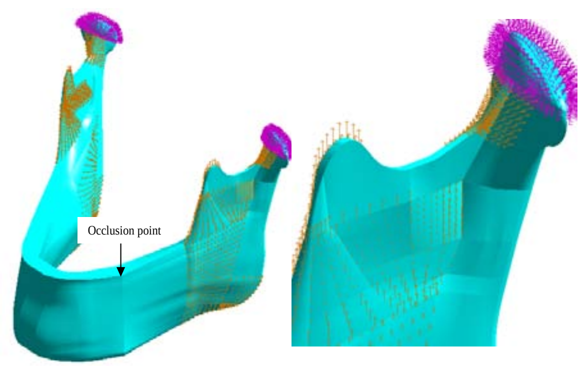

Fig. (8). BEM boundary conditions applied to the mandible model: springs on the condyle surface along the normal direction, surface tractions in the insertion area of each muscle and nodal constraint in the z-axis direction at the occlusion point.

Table 1. Mandible Material Properties and Material Axis Orientations (z=z') (Zones from 9 to 14 are Symmetric with Respect to Zones from 1 to 6)

Zone	1	2	3	4	5	6	7	8
$\theta_{xx'}$ [degrees]	28	28	28	28	59	59	90	90
$E_{x'}$ [MPa]	1.00E+04	2.42E+02	1.22E+04	2.78E+02	1.36E+04	3.46E+02	1.35E+04	2.94E+02
$E_{z'}$ [MPa]	1.00E+04	2.42E+02	1.93E+04	8.35E+02	2.40E+04	1.04E+03	2.04E+04	8.83E+02
$E_{y'}$ [MPa]	1.68E+04	7.27E+02	1.22E+04	2.78E+02	1.36E+04	3.46E+02	1.35E+04	2.94E+02
$G_{x'z'}$ [MPa]	3.72E+03	1.61E+02	4.37E+03	1.89E+02	4.80E+03	2.08E+02	4.60E+03	1.99E+02
$G_{x'y'}$ [MPa]	4.09E+03	5.37E+01	4.54E+03	1.04E+02	5.06E+03	1.29E+02	5.02E+03	1.09E+02
$G_{y'z'}$ [MPa]	4.09E+03	5.37E+01	4.37E+03	1.89E+02	4.80E+03	2.08E+02	4.60E+03	1.99E+02
$\nu_{x'z'}$	3.45E-01	3.45E-01	2.36E-01	2.36E-01	2.36E-01	2.36E-01	2.36E-01	2.36E-01
$\nu_{x'y'}$	2.36E-01	2.36E-01	3.45E-01	3.45E-01	3.45E-01	3.45E-01	3.45E-01	3.45E-01
$\nu_{z'y'}$	2.36E-01	2.36E-01	2.36E-01	2.36E-01	2.36E-01	2.36E-01	2.36E-01	2.36E-01

Table 2. Magnitude and Direction of the Mandible Muscle Loads on the Left (L _ _) and Right (R_ _) Side (PT=Posterior Temporalis; AT=Anterior Temporalis; DM=Deep Masseter; SM=Superficial Masseter; MP=Medial Pterygoid; LP=Lateral Pterygoid)

Muscle	Components of the Unit Force Vector			Muscle Force Magnitude [N]	Muscle Insertion Area [mm^2]
	x	y	z		
LPT	0.10	-0.76	0.64	11.0	363
LAT	0.07	0.34	0.94	27.9	363
LDM	-0.27	-0.18	0.94	27.3	470
LSM	-0.27	0.15	0.95	20.2	1098
LMP	-0.32	0.03	0.94	17.1	1199
LLP	0.25	-0.94	-0.25	7.4	123
RPT	-0.10	-0.76	0.64	20.2	363
RAT	-0.07	-0.34	0.94	21.9	363
RDM	0.27	-0.18	0.94	13.5	470
RSM	0.27	0.15	0.95	9.8	1098
RMP	0.32	0.03	0.94	16.1	1199
RLP	-0.25	-0.94	-0.25	7.4	123

Intensity and direction of the muscular actions were considered as constant during the occlusion even if, in reality, muscle activation varies in relation to the occlusion point: the reduction of the muscle activation level when the occlusion point get closer to the condyles (that act as pivots in the final phase of the masticatory process) is related to the corresponding decrease in the occlusion load momentum. Moreover it would be better to provide an estimation of masticatory loads by patient-specific analysis [16].

The bite force location was modelled by imposing a constraint along a direction orthogonal to the occlusal plane in correspondence of the considered occlusion point (Fig. **8**).

The occlusion point considered is the premolar.

A simplified model with just the mandible (no TMJ), hinged in correspondence of the condyles is also analysed in order to simplify the comparison between FEM and BEM results: one condyle node (the one on the top) is constrained in x, y and z directions, while the occlusion point node is constrained along the z direction.

BOUNDARY ELEMENT MODEL (BEM)

The muscular actions are modelled as surface tractions, distributed in correspondence of the insertion areas of each muscle.

The boundary mesh, generated using the commercial code BEASY®, is made of 4.200 elements: the polynomial order is reduced quadratic (the central element node is missing) with respect to the functional variables (displacements and tractions) and quadratic for geometry interpolation.

In a first simplified model there is no explicit modelling of the articular disc; it is replaced by springs applied to the condylar surfaces in the normal direction and uniformly distributed on the anterior superior part of the condyles (Fig. **8**). The spring stiffness is assumed to be consistent with the adopted articular disc Young modulus (E = 60 MPa). The correctness of the chosen spring stiffness is confirmed by the good correspondence between the mandible stress results obtained by the aforementioned simplification and by explicitly modelling the articular disc.

In a second more refined BEM model, the TMJs are complete with the fibro-cartilaginous disc, interposed between condyle and infra-temporal cavity. The superior and inferior disc surfaces are respectively connected to the rigidly clamped infratemporal cavity and to the upper condylar surface by contact elements.

FINITE ELEMENT MODEL

The commercial software used is Ansys®. Muscle loads are distributed throughout the nodes located in the insertion areas of each muscle. The TMJ model includes the fibro-cartilaginous disc interposed between the condyle and the infratemporal cavity. The muscular loads have been modelled as forces applied on the superficial nodes where the muscular bundles are attached; their values have been obtained by dividing the components of the resultant of each muscular load by the number of involved nodes.

Tetrahedral Mesh

The volume mesh is implemented by 82.720 10-node tetrahedral elements, where 55.102 elements belong to the mandible and 21.288 elements belong to the articular disc (Fig. **9**).

The superior and inferior disc surfaces are respectively connected to the surfaces of the infratemporal cavity (rigid and fully clamped) and to the superior condylar surface by contact elements: in particular, 3.074 TARGET and 3.256 CONTACT elements are introduced.

Hexahedral Mesh

The mandible and related discs are modelled by hexahedral 8-node elements (Fig. **10**): this type of mesh

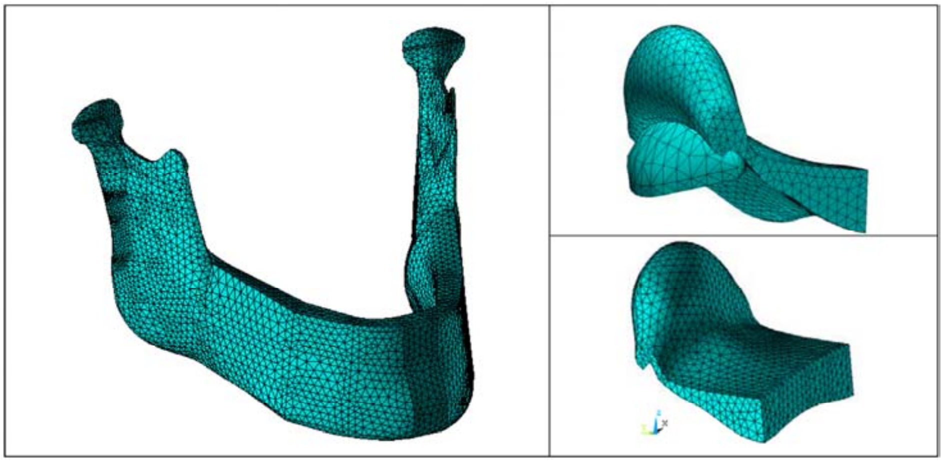

Fig. (9). FEM mesh of the whole mandible and of articular disc.

involves a time consuming pre-processing phase but allows a faster solution; moreover, it can be used with the CAD-modelling approach explained previously: as a matter of fact, the division of the mandible in CAD-sections allows to easily create an ordered mesh and to use brick elements.

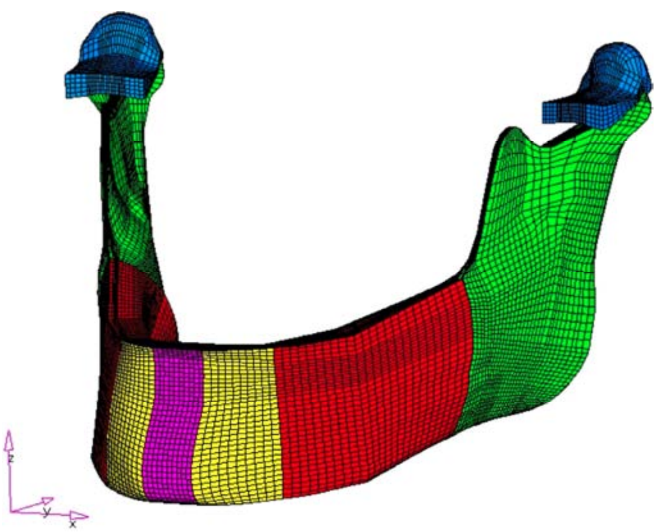

Fig. (10). Finite Element hexahedral mesh of the mandible with TMJ.

The Finite Element (FEM) mandible mesh, including the articular discs, is composed by 121.476 nodes and 109.616 elements; in particular, 101.756 elements are needed to model the entire mandible and 4.460 elements to model the articular discs. The remaining 3.400 elements are of contact type, interposed between disc and condyles and between disc and infratemporal cavity.

With reference to Fig. (**10**), the global reference system is indicated as xyz, whereas the local material reference system is indicated x'y'z' (z' ≡ z and y' is normal to the generic mandible transversal section).

The disc material is considered as linear elastic or hyper-elastic. In the latter case the well known formulation of Mooney-Rivlin for the equation of the deformation energy has been considered [2]:

$$W = \sum_{i+j=1}^{N} c_{ij}(I_1 - 3)^i (I_2 - 3)^j + \sum_{k=1}^{N} \frac{1}{d_k}(J-1)^{2k} \qquad (1)$$

where W is the strain energy potential, I_1 and I_2 are the first and the second deviatoric strain invariants, J is the determinant of the elastic deformation gradient, c_{ij} are material constants characterizing the deviatoric deformation of the material and d_k are material constants characterizing the hydrostatics part of the deformation. In case of small nominal deformations (less than 6% as it is hypothesized in the case of the disc), N can be set equal to 1, so that, in the hypothesis of hyper-elastic incompressible material, eq. (1) becomes:

$$W = c_{10}(I_1 - 3) + c_{01}(I_2 - 3). \qquad (2)$$

In this work, according to [2], it has been assumed that c_{10} = 27.91 MPa and c_{01} = -20.81 MPa.

FEM AND BEM RESULTS

FEM Tetrahedral Mesh

A first simple case is to be used for a reciprocal validation of FEM and BEM results and it refers to the mandible modelled as hinged on condyles and characterized by a premolar occlusion. Fig. (**11**) shows an excellent agreement between FEM and BEM results.

In the second considered case, the mandible is modelled together with TMJs and the occlusion is on the premolar. The interface between the mandibular condyle and the inferior surface of the disc, and between the superior surface of the disc and the temporal bone, are modelled with contact elements ("GAP" type). It follows that the analysis is non linear and this entails a larger computational burden but, on the other hand, gives the opportunity to analyze the stress distribution induced in the disc during unilateral mastication. A different accuracy in TMJ modelling does not significantly impact on the mandible stress distribution far from the surfaces in contact with the TMJ, as shown in Fig. (**12**).

The FEM reaction loads acting on the condyles are equal to Fz =-43.1 N for the ipsilateral condyle, Fz =-53 N for the controlateral condyle and Fz=-43 N for the premolar constraint.

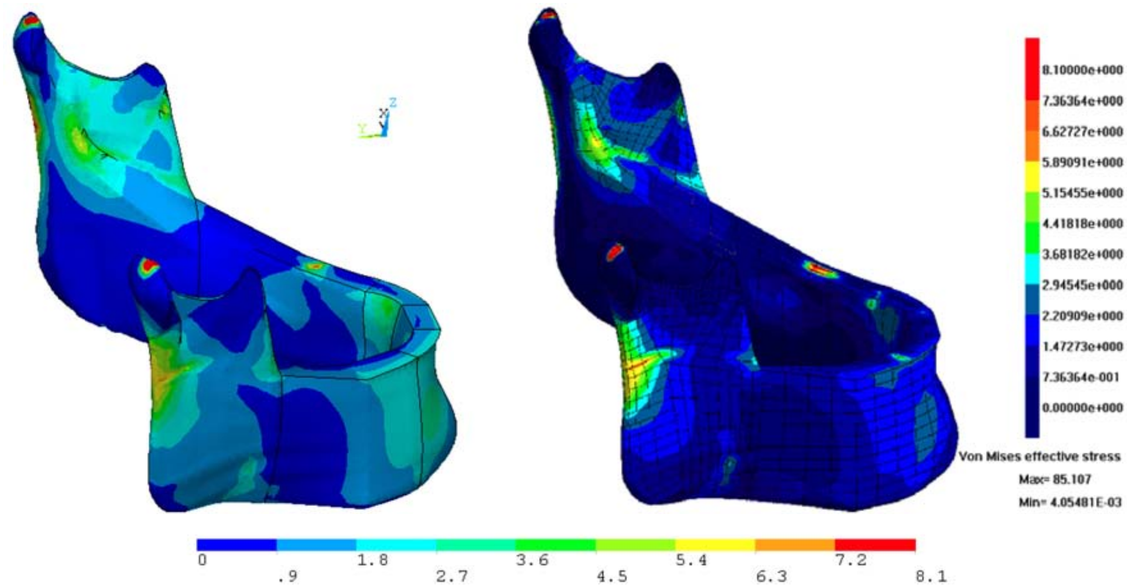

Fig. (11). Von Mises equivalent stress [MPa], obtained by FEM (left) and BEM (right) approaches.

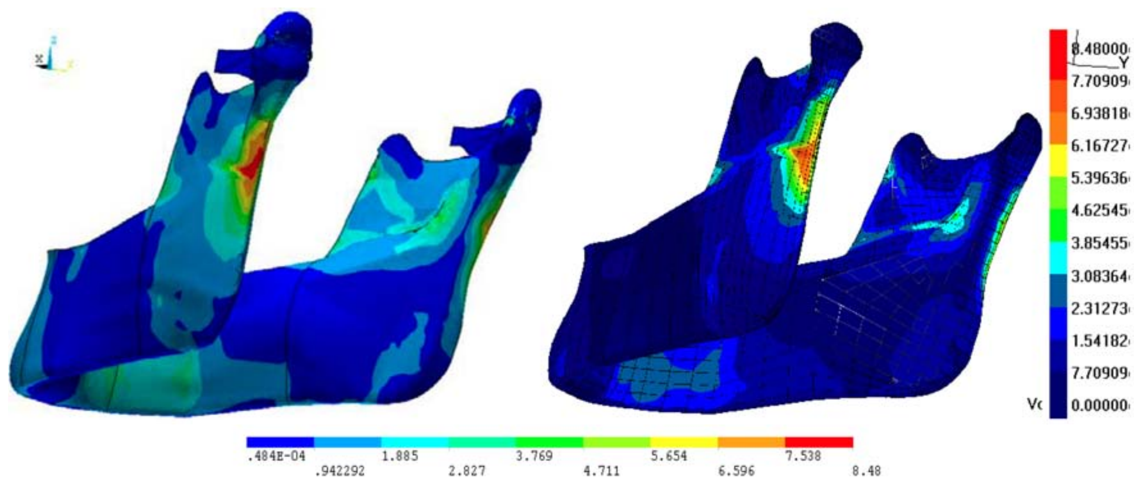

Fig. (12), Von Mises stresses (MPa) for the FEM model of the mandible complete with the TMJs (left) and for the BEM mandible characterized by springs on the condyles to simulate the articular disc (right). The occlusion point is on the premolar.

TMJ

BEM - With No Explicit Modelling of Articular Disc

Fig. (**13**) shows the condylar displacements obtained by a BEM elastic-static analysis.

The functional loads on TMJ resulting from BEM analysis are shown in Fig. (**14**), in which the disc is approximated by a uniform distribution of springs and the occlusion point is on the premolar: the contra-lateral condyle is subjected to a higher load than the ipsi-lateral one, as found in [17].

BEM with Explicit Modelling of Articular Discs

In order to speed up the calculations and limit the memory requirements, it is necessary to avoid a non-linear analysis involving the whole mandible and, consequently, the submodelling approach is adopted as detailed in the following:

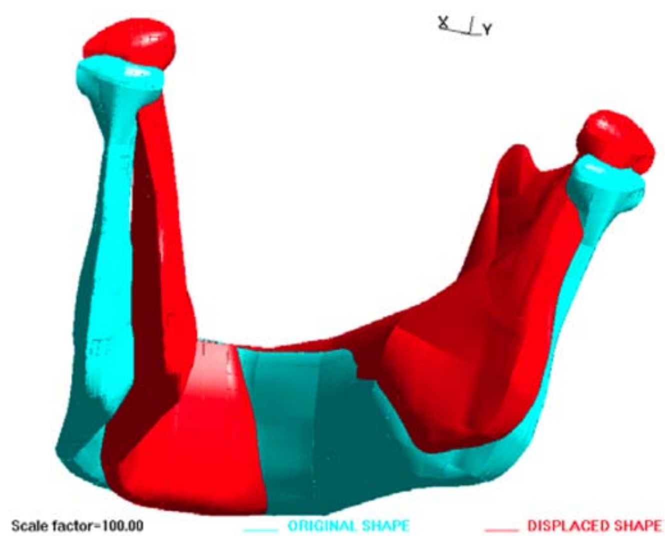

Fig. (13). Magnified deformation (scale factor 100) of the BEM mandible, with occlusion on the premolar.

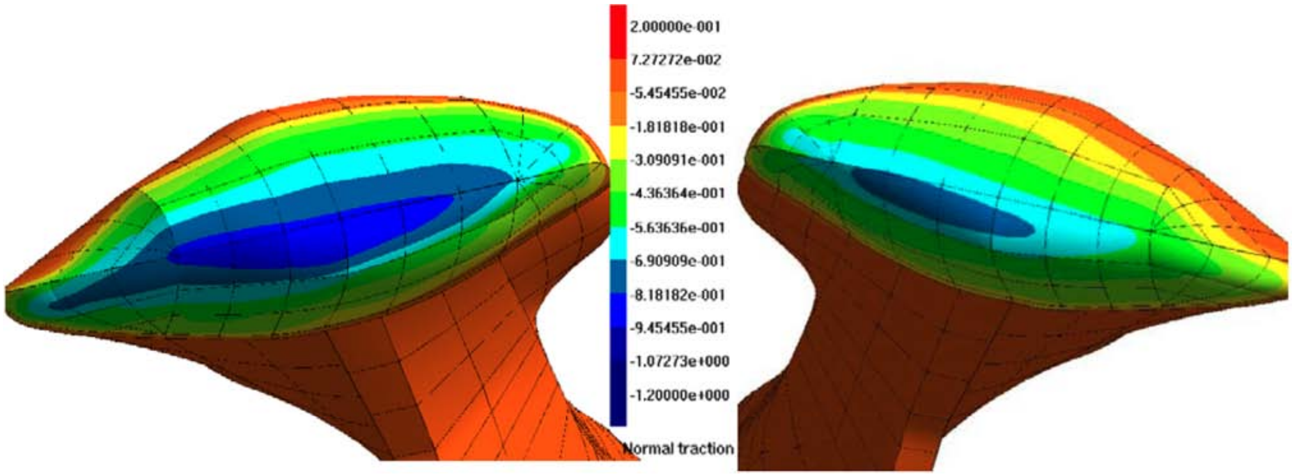

Fig. (14). Normal tractions (MPa) in contra-lateral (sx) and ipsi-lateral condyles (dx), with occlusal position on the premolar.

1. A linear elastic analysis of the whole mandible is performed: the (nonlinear) modelling of condyle and articular disc contact is skipped whereas a physical continuity between them is imposed; moreover the disc interaction with the infratemporal cavity is modelled by a uniform distribution of normal constraints (Fig. **15**). The mandible is discretized by 5390 "reduced quadratic" (the central element node is lacking) elements that are quadrilateral for the most part. Such an approximation completely alters the local stress distributions at disc-condyle and disc-infratemporal cavity interfaces, nevertheless its effects certainly extinguish at the base of the mandibular jaw, where the sub-models cut is operated (Fig. **16**). The correspondence between the stress distributions on the sub-models (Fig. **16**) and on the corresponding parts of the overall model (Fig. **15**), (clearly far from the discs) confirm the correctness of this approach.
2. The previous analysis on the global model provides the displacements to be applied as sub-model boundary conditions on the cutting surfaces (Fig. **16**).
3. Then, a non linear analysis is performed on the sub-model, by applying the GAP elements at the disc-condyle interface and using a node to node contact algorithm. The adopted mesh consists of 2.067 reduced quadratic elements (the geometric interpolation is always made by quadratic elements).

The disc Poisson coefficient and Young modulus are respectively ν=0.4 and E=60 MPa. The articular disc results obtained in terms of Von Mises stresses are presented in Figs. (**17**, **18**) in case of frictionless contact between discs and condyles and are qualitatively consistent with corresponding results from literature [3] (a rigorous comparison is prevented because in [3] the disc loading process is different and the finite deformation theory is adopted).

FEM (Hexahedral Mesh) with Explicit Modelling of Articular Disc

Numerous FEM simulations are performed in order to assess the mandible stress sensitivity against variation of disc Young modulus, against the articular disc friction coefficient and against elastic or hyper-elastic disc material properties.

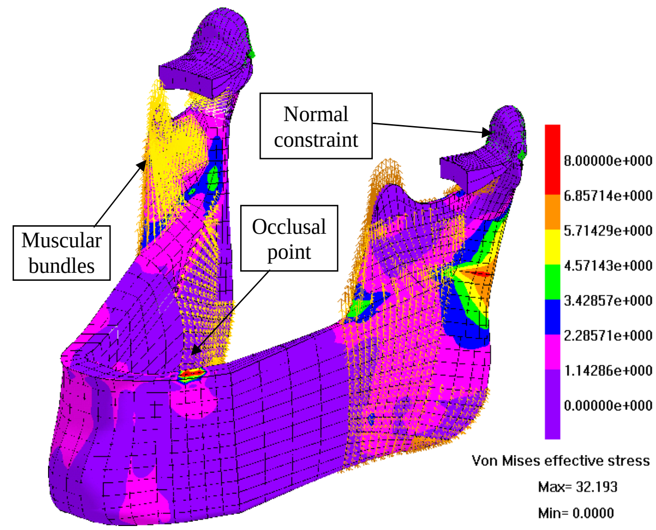

Fig. (15). Stress state and boundary conditions on the whole mandible.

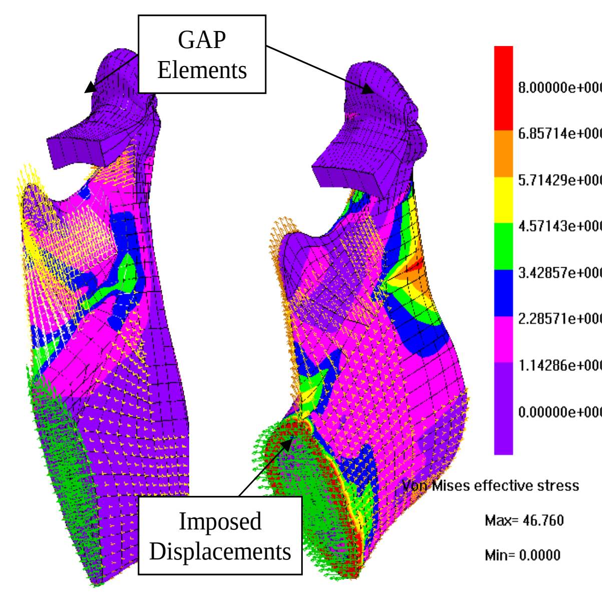

Fig. (16). Sub-models of contra-lateral (sx) and ipsi-lateral (dx) mandibular branches.

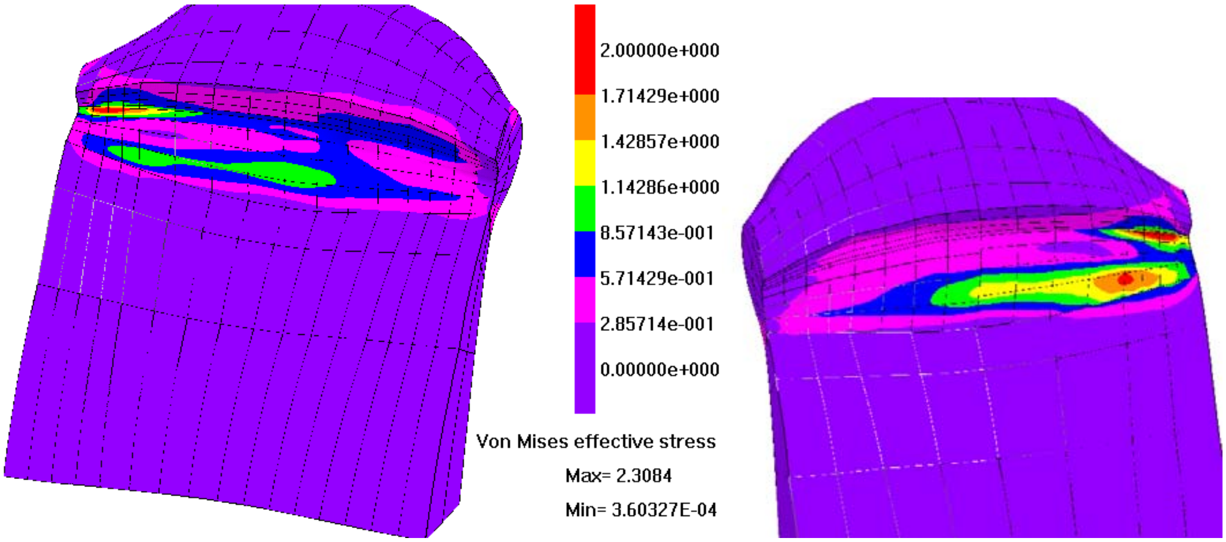

Fig. (17). BEM Von Mises equivalent stresses [MPa] on the ipsi- (dx) and contra-lateral (sx) inferior articular disc surface, with occlusion on the premolar.

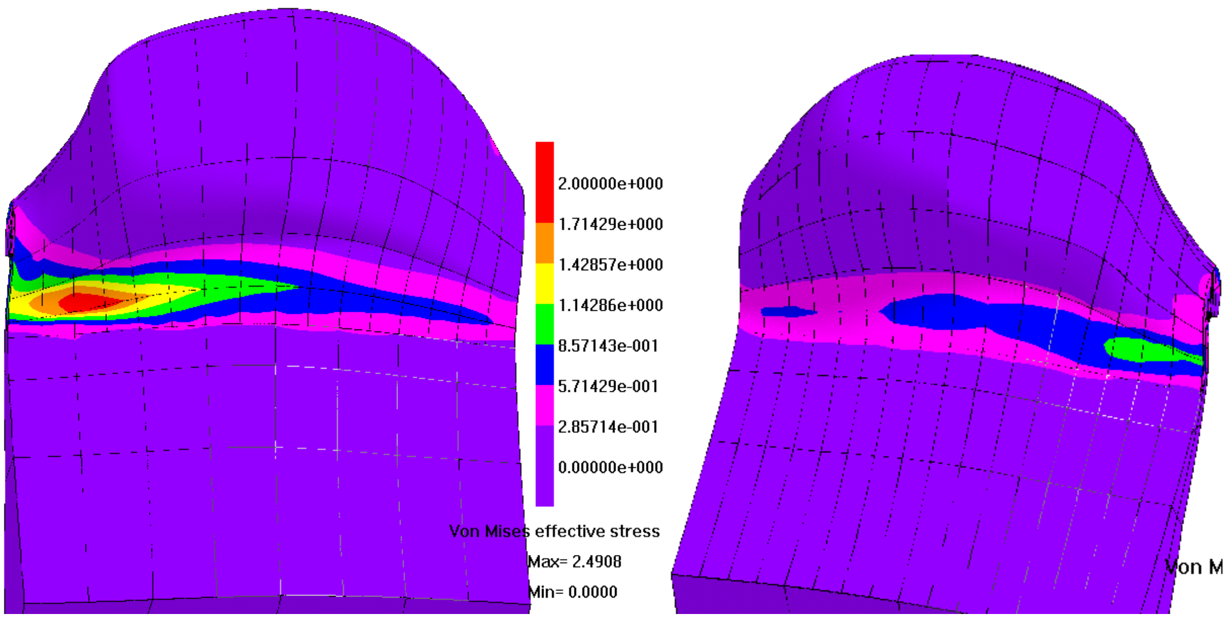

Fig. (18). BEM Von Mises equivalent stresses on the ipsi- (dx) and contra-lateral (sx) superior articular disc surface, with occlusion on the premolar.

The FEM simulations, which involved the use of a 2800 GHz Xeon processor and 2 GB RAM, assuming linear elastic material behaviour and frictionless contact, took about 45 minutes, whereas in presence of friction and hyper-elastic material, run times increased to approximately 60 minutes, also depending on the chosen value of friction coefficient (varying from 0.1 to 0.9).

The simulation without friction and with linear elastic material, gave results consistent with those obtained by BEM.

The obtained results, in terms of Von Mises stresses, considering a non null friction between discs and condyles (μ=0.3), with Poisson coefficient and Young modulus for the discs respectively equal to ν= 0.4 and E=60 MPa and with occlusion on the premolar, are represented in Figs. (**19**, **20**).

Actually a rigorous comparison between BEM and FEM disc results is prevented as there is a slight difference in the mandible boundary conditions: in case of FEM analysis, sub-modelling is not used, and consequently the overall model boundary conditions at the TMJ were represented by a more realistic contact type, allowing disc slippage; on the other hand, in the BEM global analysis, normal constraints were distributed on the upper disc surface and the continuity was assumed between the disc and the condyle; only with the submodelling, the same TMJ contact boundary conditions are implemented in both BEM and FEM approaches.

From a comparative analysis between cases with and without friction it is possible to state that in the former case higher and differently localized stress peaks are obtained on the disc. As a consequence, a clinical consideration can be forwarded: the lack of joint lubrication (caused for example

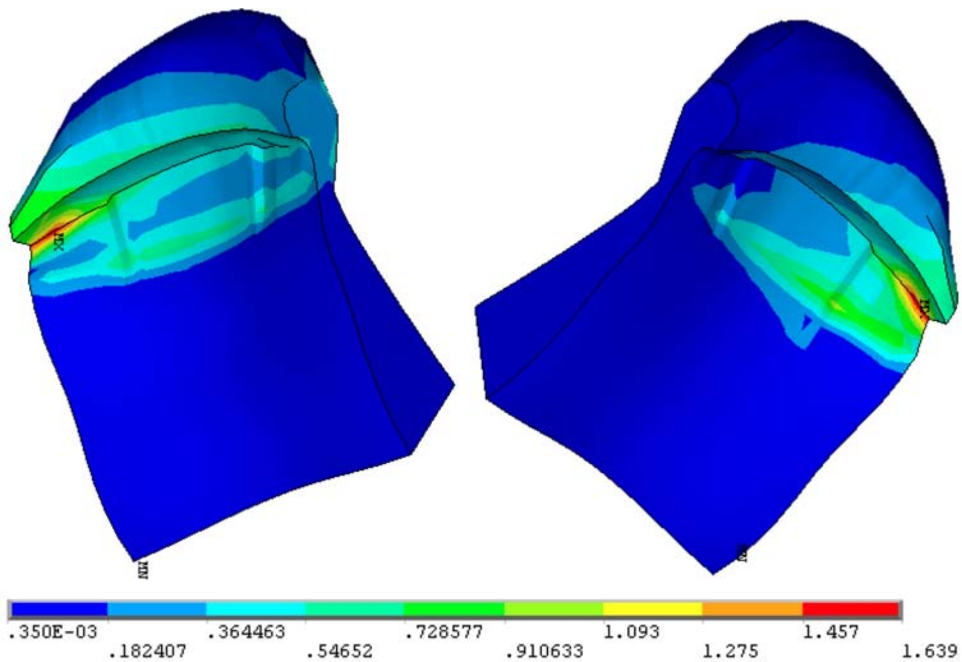

Fig. (19). Von Mises equivalent stresses on the ipsi- (dx) and contra-lateral (sx) inferior surface of articular discs, obtained *via* FEM in case of elastic disc (E = 60 MPa) and friction coefficient equal to μ = 0.3.

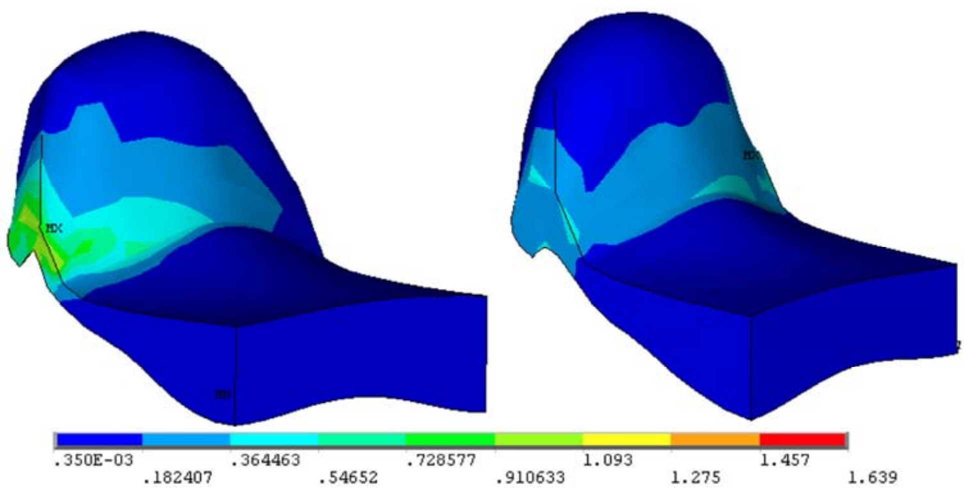

Fig. (20). Von Mises equivalent stresses on the ipsi- (dx) and contra-lateral (sx) superior surface of articular discs, obtained *via* FEM in case of elastic disc (E = 60 MPa) and friction coefficient equal to μ = 0.3.

by a reduction in synovial fluid) causes more severe operating conditions for the articulation and generates greater risk of tissue degeneration.

The consistency of the obtained results is demonstrated by a satisfactory qualitative agreement with literature data [3] as well as by qualitative agreement between FEM and BEM results.

FEM Sensitivity Analysis

A parametric study is done by determining the maximum Von Mises stress in the disc and in the mandible with a varying value of disc Young modulus (E) from 6 to 60 MPa (Table **3**): the disc works better at distributing the stress more evenly when the lower value of E is used and this is consistent with what reported in [18].

The resultant loads on condyles and occlusal point are practically not affected by the aforementioned variations.

Moreover, the disc is assumed as either elastic or hyper-elastic, with or without friction, but in all cases the stress distribution on the mandible (Fig. **21**) is nearly insensitive to the aforementioned variations.

In the following Figs. (**22**, **23**), ipsi- and contra-lateral disc results are shown.

The FEM numerical investigations gave rise to the following points:

- The overall loads on the tooth and on the articular discs do not change appreciably with changes of the disc material behaviour and with the friction value; in case of premolar occlusion, the contra-lateral disc is more loaded than the ipsi-lateral one;

Table 3. Maximum Von Mises Stresses with Varying Disc Mechanical Properties

		σ_{max} [MPa]
Elastic material disc E = 6 MPa Frictionless	Mandible bone	8.5
	Contra-lateral disc	1.5
	Ipsi-lateral disc	1.4
Elastic material disc E = 30 MPa Frictionless	Mandible bone	8.3
	Contra-lateral disc	1. 7
	Ipsi-lateral disc	1.6
Elastic material disc E = 60 MPa Frictionless	Mandible bone	8.2
	Contra-lateral disc	1.9
	Ipsi-lateral disc	1.9
Elastic material disc E = 60 MPa Friction (μ=0.3)	Mandible bone	7.3
	Contra-lateral disc	1.6
	Ipsi-lateral disc	1.6
Hyper-elastic material disc Frictionless	Mandible bone	8.3
	Contra-lateral disc	1.7
	Ipsi-lateral disc	1.3
Hyper-elastic material disc Friction (μ=0.3)	Mandible bone	7.5
	Contra-lateral disc	1.1
	Ipsi-lateral disc	1.1

- The maximum mandibular bone peak stress is reached in correspondence of the lowest disc Young modulus (E = 6 MPa) as shown in Fig. (**24**).
- With regard to the condylar discs, the maximum stress is influenced by the assumed value of the Young modulus in a non negligible way (Figs. **25**, **26**), whereas the influence of friction coefficient variation on the peak stresses in the mandible bone and in the discs is shown in Figs. (**27-29**); a varying position of such peaks is also observed.

CONCLUSIONS

Based on the performed analyses the following conclusions can be made:

- a full hexahedral FE mesh can significantly reduce the computational burden in non-linear analysis, if compared to the case of a full tetrahedral FE mesh; on the other hand, there is an increase in the time needed for model preparation. The only way to create a regular hexahedral mesh is to preliminary develop a rational CAD model with ordered sections as has been achieved by the authors.
- in case of investigation of mandible models obtained from CT scan, a FEM model with tetrahedral elements is a better alternative for the mandible finite element model development when an automatic procedure has to be implemented;
- the provided sensitivity analysis can be very useful due to the uncertainty associated to the characterization of the friction coefficient and stiffness values of the articular disc.

Even if it is very time consuming in the solution phase, the BEM enables more accuracy and pre-processing flexibility (than FEM), especially during the interfacing with CAD and CAE applications for the reconstruction process of the mandible numerical model. In any case, the availability of more and more powerful and general purpose automatic FE pre-processors tends to reduce this gap and undoubtedly facilitates the creation of an integrated environment, which starting from the patient CT scan automatically leads to the mathematical reconstruction of the numerical model and subsequent analysis, allowing engineers and medical teams to concentrate on result analysis. BEM analysis is more efficient and stable when a CAD-model made by A-Class surfaces is prepared (as authors have done).

The good agreement between the results (e.g. Von Mises stresses) coming from two different numerical methods

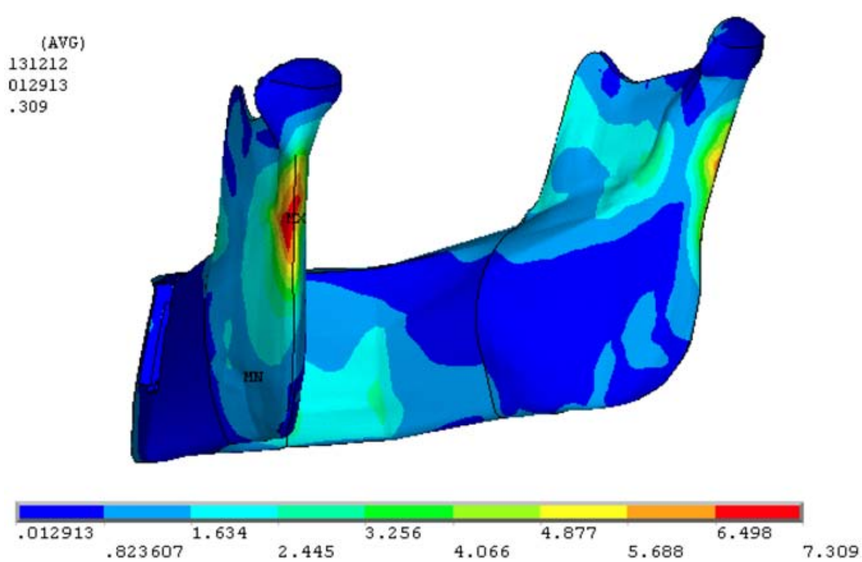

Fig. (21). Von Mises stresses (MPa) - elastic material discs (E = 60 MPa) - presence of friction (μ = 0.3).

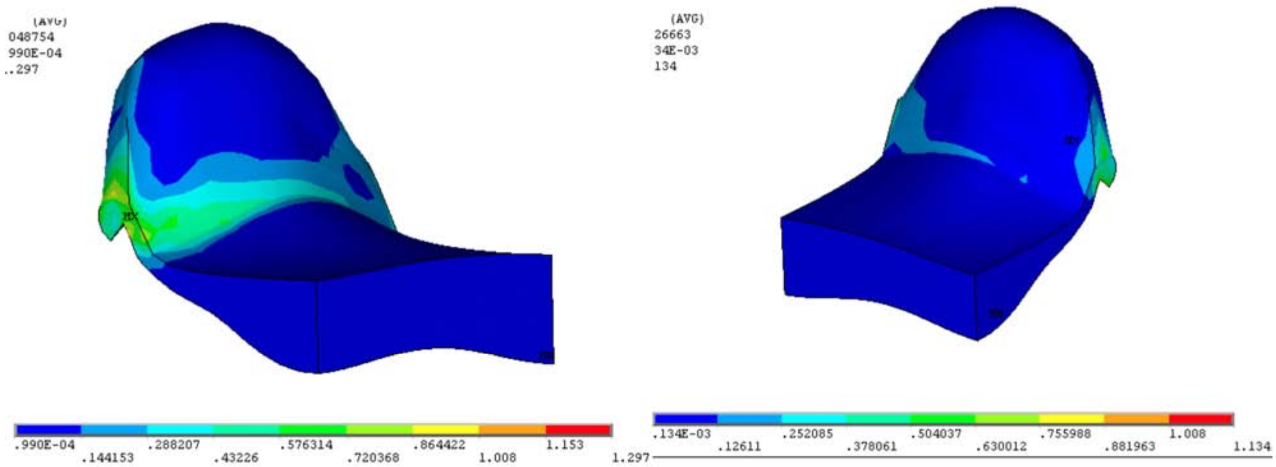

Fig. (22). Von Mises equivalent stresses (MPa) on the superior surface of the ipsi-lateral disc in case of hyper-elastic material: frictionless contact (sx) and non null friction with $\mu = 0.3$ (dx).

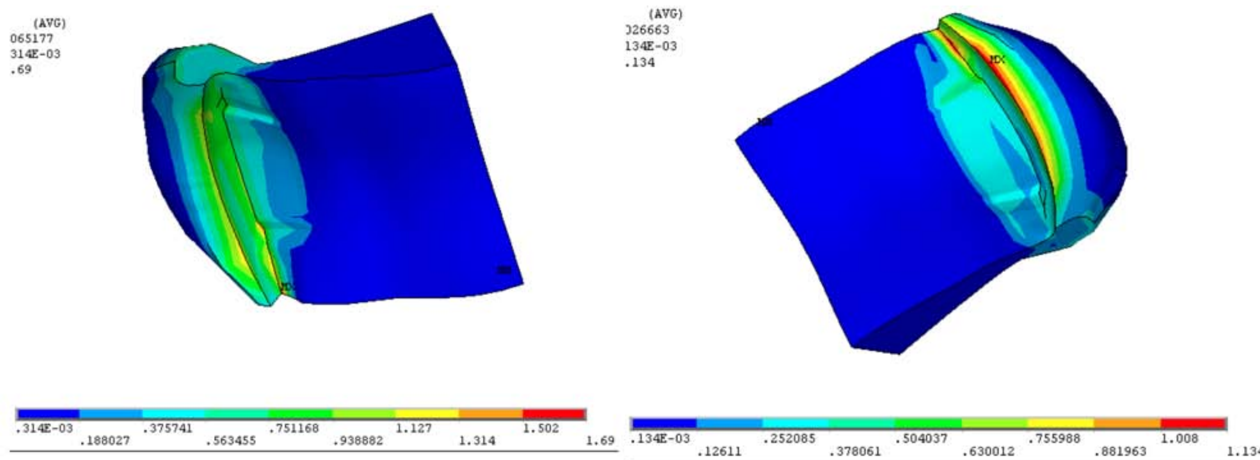

Fig. (23). Von Mises equivalent stresses (MPa) on the inferior surface of the contra-lateral disc in case of hyper-elastic material: frictionless contact (sx) and non null friction with $\mu = 0.3$ (dx).

(FEM-BEM), shifts the critical point of such kind of analysis to the correct evaluation of the boundary conditions and therefore to the availability of realistic and patient specific biological data (e.g. bone density and related stiffness) [19-25] and the intensity and direction of the loads exerted by muscle groups involved, for example, during the mastication phase.

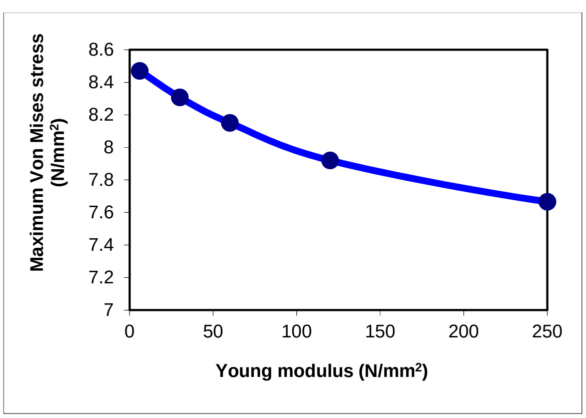

Fig. (24). Von Mises maximum stress in the mandible bone, versus disc Young modulus (linear elastic material).

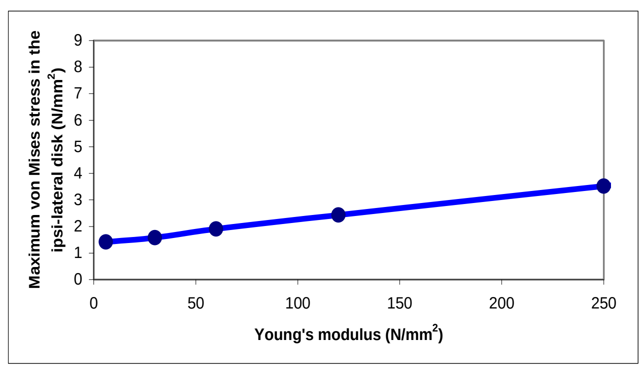

Fig. (25). Von Mises maximum stress in the ipsi-lateral disc, versus disc Young modulus (linear elastic material).

Both from a qualitative and a quantitative point of view, the authors' results are coherent with both the physical and the medical aspects of the examined problem.

Different approaches to the computer simulation of the structural behaviour of the mandible have been showed, highlighting the respective advantages and limits. In the opinion of the authors, both approaches represent an efficient and effective engineering tool for the dentist.

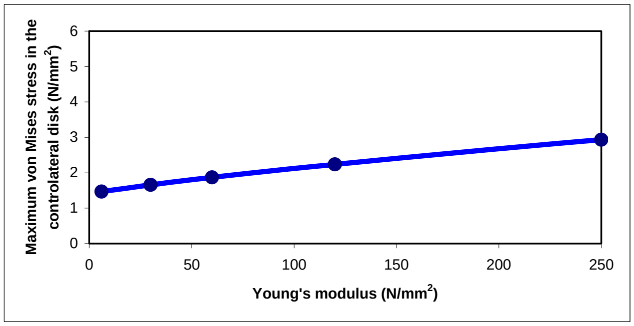

Fig. (26). Von Mises maximum stress in the contra-lateral disc, versus disc Young modulus (linear elastic material).

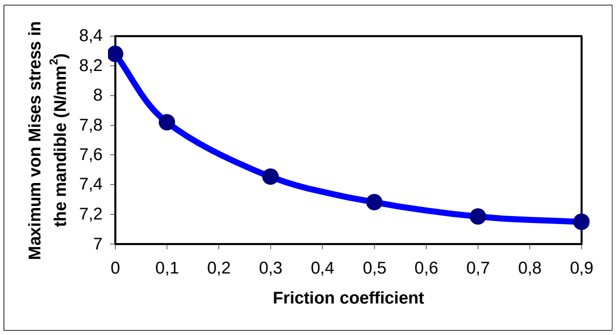

Fig. (27). Von Mises maximum stress in the mandible bone, versus disc friction coefficient (hyper-elastic material discs).

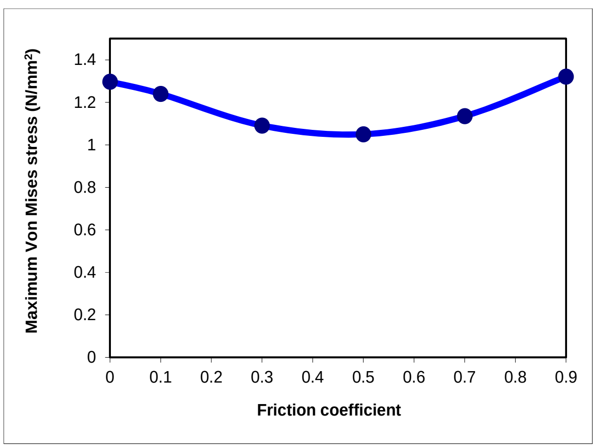

Fig. (28). Von Mises maximum stress in the ipsi-lateral disc, versus disc friction coefficient (hyper-elastic material discs).

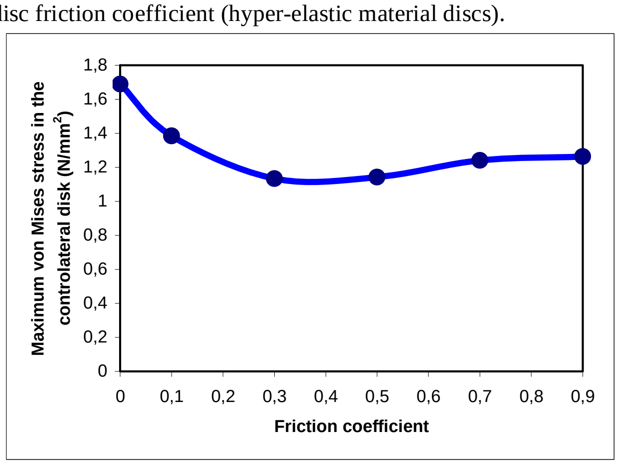

Fig. (29). Von Mises maximum stress in the contra-lateral disc, versus friction coefficient (hyper-elastic material discs).

REFERENCES

[1] J. Chen, and L. Xu, “A Finite element analysis of the human temporomandibular joint”, *Journal of Biomechanics Engineering*, vol. 116, pp. 401-407, 1994.

[2] J. Chen, U. Akyuz, L. Xu, and R. M. V. Pidaparti, “Stress analysis of the human temporomandibular joint”, *Medical Engineering and Physics*, vol. 20, pp. 565-572, 1998.

[3] M. Beek, J. H. Koolstra, L. J. van Ruijven, and T. M. G. J. van Eijden, “Three-dimensional finite element analysis of the human temporomandibular joint disc”, *Journal of Biomechanics Engineering*, vol. 33, pp. 307-316, 2000.

[4] R. del Pozo, E. Tanaka, M. Tanaka, M. Kato, T. Iwabe, M. Hirose, and K. Tanne, “Influence of Friction at Articular Surfaces of the Temporomandibular Joint on Stresses in the Articular Disc: A Theoretical Approach with the Finite Element Method”, *Angle Orthodontist*, vol. 73, no. 3, pp. 319-327, 2003.

[5] E. Armentani, F. Caputo, and R. Citarella, FEM sensitivity analyses on the stress levels in a human mandible with a varying ATM modelling complexity, *The Open Mechanical Engineering Journal*, vol. 4, pp. 8-15, 2010.

[6] M. Hirose, E. Tanaka, M. Tanaka, R. Fujita, Y. Kuroda, E. Yamano, T. M. G. J. van Eijden, and K. Tanne, “Three-dimensional finite-element model of the human temporomandibular joint disc during prolonged clenching”, *European Journal of Oral Sciences*, vol. 114, pp. 441-448, 2006.

[7] A. Pérez Del Palomar, and M. Doblaré, “Anterior displacement of the TMJ disc: Repositioning of the disc using a mitek system. A 3D finite element study”, *Journal of Biomechanical Engineering*, vol. 128, no. 5, pp. 663-673, 2006.

[8] B. Pérez Del Palomar, and M. Doblare, “Finite element analysis of the temporomandibular joint during lateral excursions of the mandible”, *Journal of Biomechanics*, vol. 39, pp. 2153-2163, 2006.

[9] Pérez Del Palomar, and M. Doblaré, “The effect of collagen reinforcement in the behaviour of the temporomandibular joint disc”, *Journal of Biomechanics*, vol. 39, pp. 1075-1085, 2006.

[10] Pérez Del Palomar, and M. Doblaré, “An accurate simulation model of anteriorly displaced TMJ discs with and without reduction”, *Medical Engineering and Physics*, vol. 29, pp. 216-226, 2007.

[11] G. Sammartino, G. Marenzi, R. Citarella, R. Ciccarelli, and H. L. Wang, “Analysis of the occlusal stress transmitted to the inferior alveolar nerve by an Osseo integrated threaded fixture”, *Journal of Periodontology*, vol. 79, no. 9, pp. 1735-1744, 2008.

[12] R. Citarella, E. Armentani, F. Caputo, and M. Lepore, “Stress Analysis of an Endosseus Dental Implant by BEM and FEM”, *The Open Mechanical Engineering Journal*, vol. 6, p. 100, 2012.

[13] F. V. Antunes, C. Pereira, and M. C. Gaspar, Experimental Evaluation of Physical Properties of Bone Structures, *Applied Mechanics and Materials*, vol. 5-6, pp. 71-76, 2006.

[14] J. M. Reina, J. M. García-Aznar, J. Domínguez, and M. Doblaré, Numerical estimation of bone density and elastic constants distribution in a human mandible, *Journal of Biomechanics*, vol. 40, no. 4, pp. 828-836, 2007.

[15] Hu. K, Qiguo. R, Fang. J, and Mao. J. J, “Effects of Condylar Fibro-cartilage on the Biomechanical Loading of the Human Temporomandibular joint ina three-Dimensional, Non Linear Finite Element model, *Medical Engineering & Physics*, 25, pp.107-113, 2003.

[16] M. Koseki, N. Inou, and K. Maki, “Estimation of masticatory forces for patient-specific stress analysis of the human mandible”, *Modelling in Medicine and Biology*, vol. 6, pp. 491-500, 2005.

[17] M. G. Faulkner, D. C. Hatcher, and A. Hay, “A Three-Dimensional Investigation of Temporomandibular Joint Loading”, *Journal of Biomechanics*, vol. 20, 1987, pp. 997-1002.

[18] J. W. Devocht, V. K. Goel, D. L. Zeitler, and D. Lew, A Study of the Control of Disc Movement Within the Temporomandibular

Joint Using the Finite Element Technique, *Journal of Oral and Maxillofacial Surgery*, vol. 54, pp. 1431-1437, 1996.

[19] R. S. Hobson, “A pilot study of mineralization distribution in the cortical bone of the human mandible”, *Archives of Oral Biology*, vol. 43, pp. 633-639, 1998.

[20] J. Y. Rho, L. Kuhn-Spearing, and P. Zioupos, “Mechanical properties and the hierarchical structure of bone”, *Medical Engineering and Physics*, vol. 20, pp. 92-102, 1998.

[21] P. Homolkaa, A. Beer, W. Birkfellner, A. Gahleitner, R. Nowotny, and H. Bergmann, “Local calibrated bone mineral density in the mandible presented using a colour coding scheme”, *Medical Engineering and Physics*, vol. 23, no. 9, pp. 673-677, 2001.

[22] M. Soncini, R. Rodiguez, R. Pietrabissa, V. Quaglini, S. Rizzo, and D. Zaffe, “Experimental procedure for the evaluation of the mechanical properties of the bone surrounding dental implants”, *Biomaterials*, vol. 23, pp. 9-17, 2002.

[23] K. Maki, A. J. Miller, T. Okano, and Y. Shibasaki, “A three-dimensional quantitative computed tomographic study of changes in distribution of bone mineralization in the developing human mandible”, *Archives of Oral biology*, vol. 46, pp. 667-678, 2001.

[24] Verna, B. Melsen, F. Melsen, “Differences in static cortical bone remodeling parameters in human mandible and iliac crest”, *Bone*, vol. 25, no. 5, pp. 577-583, 1999.

[25] E. Tanaka, M. S. Detamore, K. Tanimoto, and N. Kawai, “Lubrication of the Temporomandibular Joint”, *Annals of Biomedical Engineering*, vol. 36, no. 1, pp. 14-29, 2008.

Analysis of Stress in an Endosseus Dental Implant

Bidyuta Ranjan Rout, *Department of Mechanical Engineering, Aryan Institute of Engineering & Technology, Bhubaneswar, bidyutaranjan1@gmail.com*

Sidharth Pradhan, *Department of Mechanical Engineering, Capital Engineering College, Bhubaneswar, sidharthpradhan265@gmail.com*

Monalika Mohanty, *Department of Civil Engineering, Raajdhani Engineering College, Bhubaneswar, monalika_m256@gmail.com*

Suchampa Bagchi, *Department of Civil Engineering, NM Institute of Engineering & Technology, Bhubaneswar, suchampabagchi@yahoo.co.in*

Abstract: In this work the Boundary Element Method (BEM) and the Finite Element Method (FEM) have been used for an elastic-static analysis of both a Branemark dental implant and a generic conic threaded implant, modelled either in the complete mandible or in a mandibular segment, under axial and lateral loading conditions. Two different hypotheses are considered with reference to degree of osteo-integration between the implant and the mandibular bone: perfect and partial osteointegration. The BEM analysis takes advantage of the submodelling technique, applied on the region surrounding the implant. Such region is extracted from the overall mandible and the boundary conditions for such submodel are obtained from the stress analysis realised on the complete mandible.

The obtained results provide the localisation of the most stressed areas at the bone-implant interface and at the mandibular canal (containing the alveolar nerve) which represent the most critical areas during mastication.

This methodology, enriched with the tools necessary for the numerical mandible reconstruction, is useful to realise sensitivity analysis of the stress field against a variation of the localisation, inclination and typology of the considered implant, in order to assess the optimal implant conditions for each patient under treatment.

Due to the high flexibility in the pre- and post-processing phase and accuracy in reproducing superficial stress gradients, BEM is more efficient than FEM in facing this kind of problem, especially when a linear elastic constitutive material law is adopted.

Keywords: Alveolar nerve, BEM, dental implant, FEM, human mandible, mandibular canal, submodelling technique.

INTRODUCTION

Dental implantology practice is still highly dependent on empirical factors related to the morphological and biological characteristics of the individual patient. This results in considerable inconveniences both to the operator, who is often obliged to choose solutions on short notice without any feedback from the implant design point of view, and to the patient, who sometimes undergoes unsuccessful attempts.

Unfortunately, the extent of involved biological, morphological and mechanical parameters makes a reliable generalization of these applications difficult, if not impossible.

The level of stresses and deformations in that part of the mandible bone surrounding the implant is critical for the implant stability [1]. In case of full osteointegration it is important for long term life and stability, whereas in case of partial osteointegration it is important in order to ensure an optimal transition towards a correct development of a full osteointegration.

On the other hand, implant placement can cause an insult to the nervous structure and lead to transitory or irreversible alterations of inferior nerve functionality [2]. Paraesthesia and disaesthesia following implant loading, due to compression on the nerve, have been reported [3]. To prevent this complication, a correct assessment of the mandibular canal position and a suitable choice of size and positioning of implant is needed [4, 5]. Studies have suggested the favourable positioning of a fixture with respect to adjacent natural teeth or, in more complex rehabilitations, the distance between fixtures to get an optimal distribution of occlusal forces and the best aesthetical result [6].

Several authors have also treated the problem of stress and strain assessment at the bone implant interface in order to scientifically address implantologist related decisions, in terms of implant positioning, inclination and sizes (diameter, length, profile...) [7-11].

In this work, elastic-static analyses are developed with specific reference to a Branemark implant and to a generic conic threaded implant undergoing axial and lateral forces [12, 13], using the finite element method (FEM) and the boundary element method (BEM).

The obtained results revealed the localisation of the most stressed areas at the bone-implant interface and at the mandibular canal (containing the alveolar nerve). These are the most critical bone parts during mastication.

Moving from continuity conditions at the implant-bone interface to slightly more complex numerical models, namely with contact elements that simulate the clinical condition of partial rather than full osteointegration, substantial differences in bone structural behaviour become evident.

There is limited evidence with regards to the proper distance from implant to mandibular canal to assure the nerve integrity and physiological activity. This distance should be determined based not only on the evaluation of clinical data (retrospective study), but also on biomechanical analyses. A numerical mandibular model was therefore created to simulate a mandibular segment containing a couple of implants, so that the mechanical stresses on the mandibular canal induced by the occlusal load could be assessed.

The commercial codes used for FEM and BEM analyses are respectively ANSYS® and BEASY.

The accuracy of mandible stress distribution is enhanced by a realistic modelling of temporomandibular joints (one of the most critical areas after dental interventions) [14, 15], thus obtaining a higher precision in the boundary condition definition.

The resulting accuracy is evaluated by cross-comparisons between the two numerical methods (FEM and BEM) and with data available from literature.

One further objective of this work is to study the methodological problem concerning the selection of optimal numerical methods (between FEM and BEM) for this type of application.

PROBLEM DESCRIPTION AND NUMERICAL MODELS

In this work the implant is inserted in a mandibular segment or in the whole mandible; in the latter case the temporo-mandibular joints are effectively modelled. The orthotropic properties of cortical and spongy bone are implemented in the model.

The forces exerted by the muscle bundles are evaluated by electromyography combined with the knowledge of muscle bundle sections and are applied in the areas of insertion of mandible muscles [14].

A partial or complete osteointegration is assumed at the bone-implant interface in order to consider different clinical conditions.

The bone material properties are calculated starting from data available from literature [14-17]. The value of bone-implant interface friction coefficient μ=0.42 is taken from reference [18].

The elastic-static analyses are performed with reference to a Branemark implant [19-21] or to a conic threaded implant [8], modelled as inserted in a mandible segment (Figs. **1a**, **b**) or in the overall mandible (Figs. **2a**, **b**) and subject to axial or lateral occlusion forces, arising from mastication.

The geometry of a Branemark implant made of titanium, with the modulus of elasticity equal to E_i=120 GPa and Poisson coefficient ν_i=0.4, is shown in Fig. (**1a**). The thread of the implant body was not represented in its continuous helical characteristics but as axial-symmetric independent rings. On the contrary the modelling of the conic threaded implant, with a diameter d= 4.5 mm and a length l=11 mm, included the thread helix of the screw (Fig. **1b**).

FEM and BEM Local Analysis with Branemark Implant

In a first approximation, useful to provide a benchmark between the two FEM and BEM methodologies and to compare results of both with literature data [19-21], the

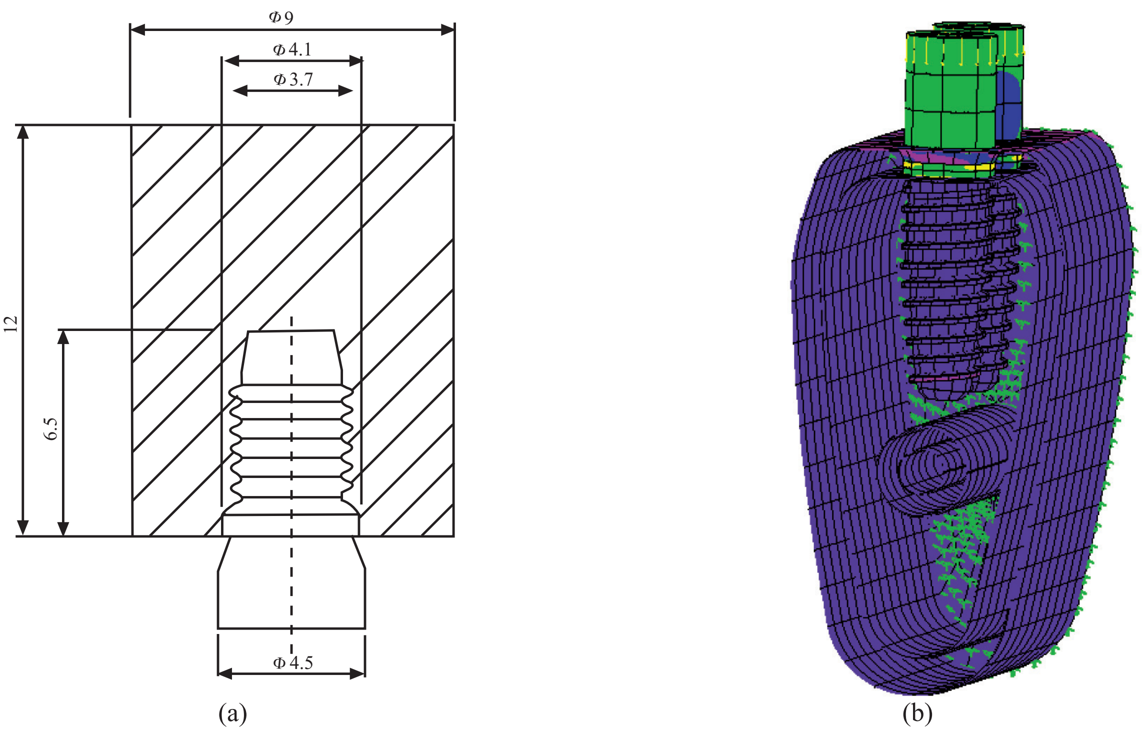

(a) (b)

Fig. (1). Geometry of the Branemark implant (**a**) and of a conic threaded implant (**b**).

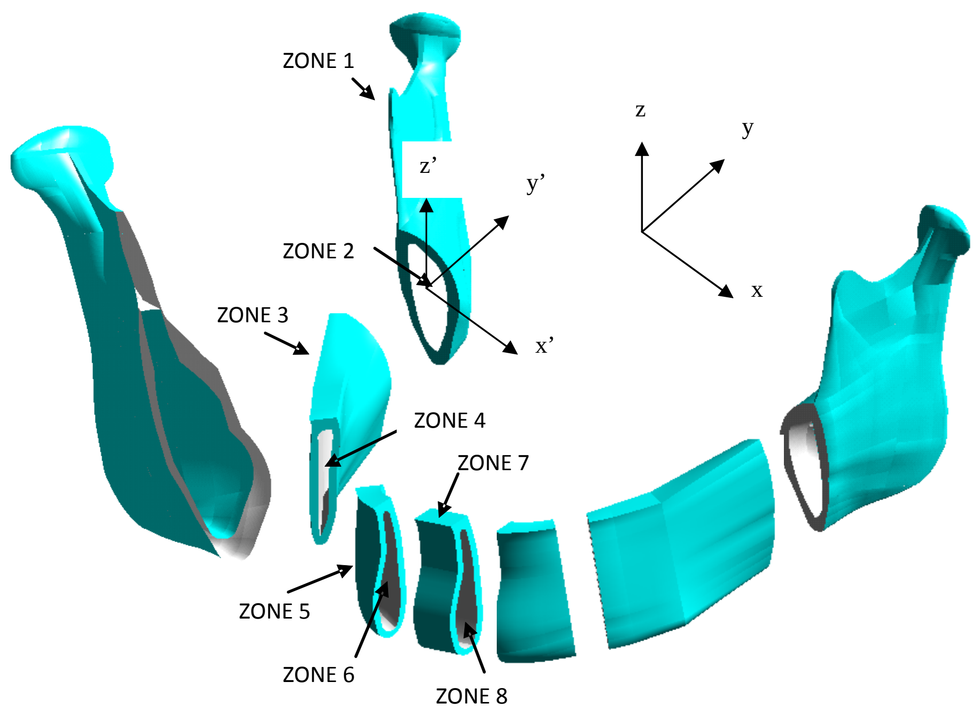

Fig. (2a). Mandible exploded view with highlight of the different modelled zones: the local reference system (x'y'z' is built with z'//z and y' oriented along the normal to the section plane considered).

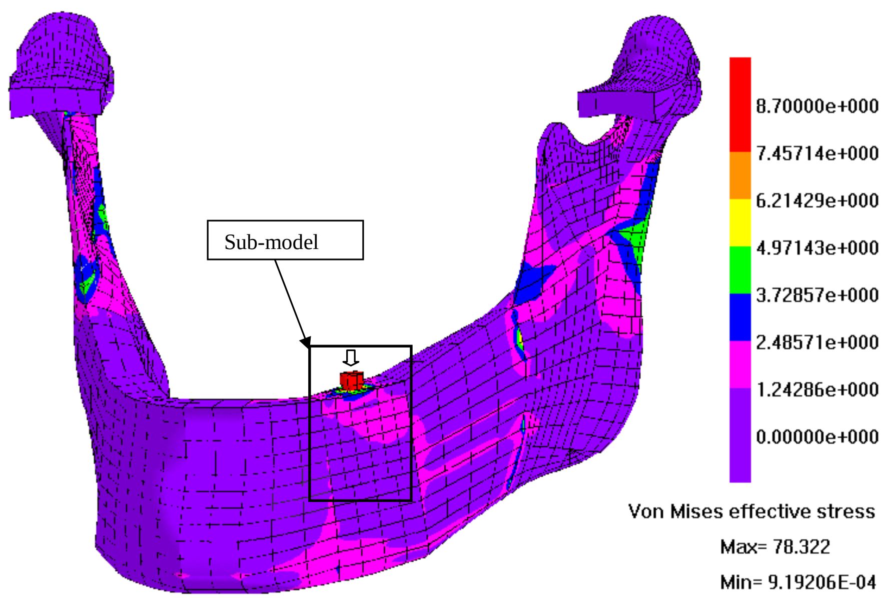

Fig. (2b). Mandible BEM numerical model (the considered submodel is also highlighted) with Von Mises stress (MPa) distribution.

implant is inserted in a mandibular segment that is clamped on the lateral surfaces, without allowance for the overall mandible and related boundary conditions (Fig. **3**). Two loading conditions are considered: an axial resultant load, equal to 100 N, applied on the abutment by means of a uniform pressure distribution and a lateral resultant load, equal to 75 N, applied by a uniform distribution of internal forces along the abutment axis (Fig. **3**).

When considering the vertical load condition, the problem is modelled as axial-symmetric, with isotropic mechanical properties for the bone (E_o=16 GPa and ν_o=0.3).

The FEM and BEM axial-symmetric models, undergoing vertical load, are discretized by 1370 elements (SOLID 82, eight-node axial-symmetric) and 86 quadratic elements (Fig. **3**).

When modelling the lack of osteo-integration at the interface between implant and bone, unidirectional contact elements (of GAP type) are introduced in both FEM and BEM approaches. Such GAP elements also allow the modelling of friction conditions between the surfaces in contact.

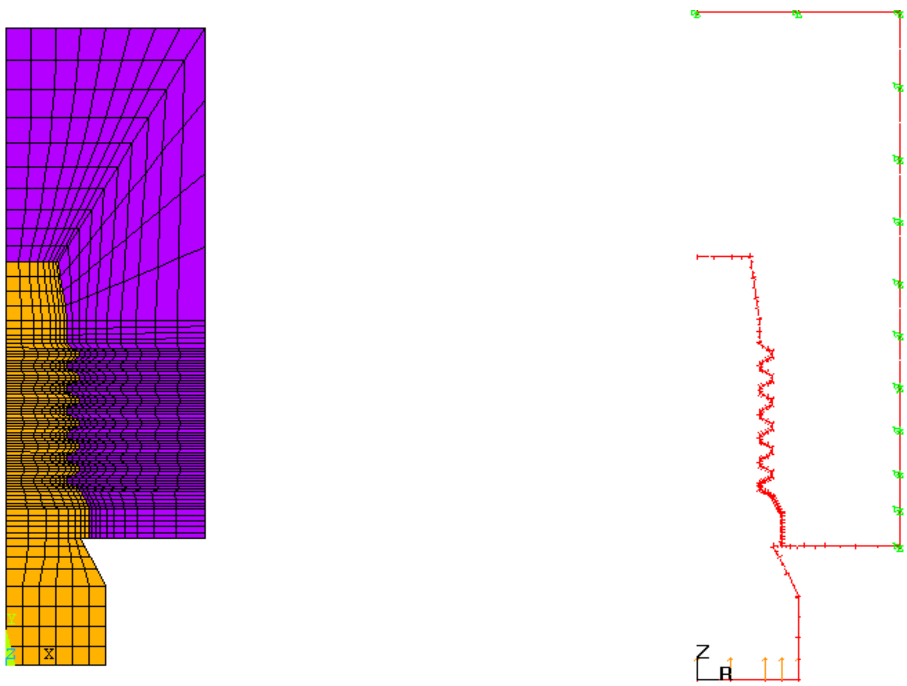

Fig. (3). FEM (left) and BEM (right) axial-symmetric numerical models.

After some tests with the axial-symmetric simplification, 3D FE and BE models are realised, consisting of 24660 brick finite elements (SOLID 95 with 20 nodes) and 1000 boundary elements with different interpolation orders (linear, quadratic and "reduced quadratic").

BEM Local Analysis with Conic Threaded Implant and Mandibular Canal

The mandibular segment was modelled, in a linear elastic analysis, with a mesh of about 3370 linear elements, with the fixture connected to a prosthesis abutment on which the axial load was applied (Fig. **4**).

The average density and dimensional values of each examined anatomical structure were taken from [8] and reproduced in this simulated model. Both the cortical and the cancellous bones were modelled as transversely isotropic. The elastic behaviour of the transversely isotropic bone can be fully characterized by 5 elastic modules whose values are listed in Table **1**, whereas the orientation of the material axes are listed in Table **2** (see also Fig. **2a**).

The trigeminal nerve was modelled as isotropic with Young modulus E=1.3 MPa and Poisson ratio ν=0.4. The metallic implant parts were clearly modelled as isotropic with E=120000 MPa, and ν=0.3.

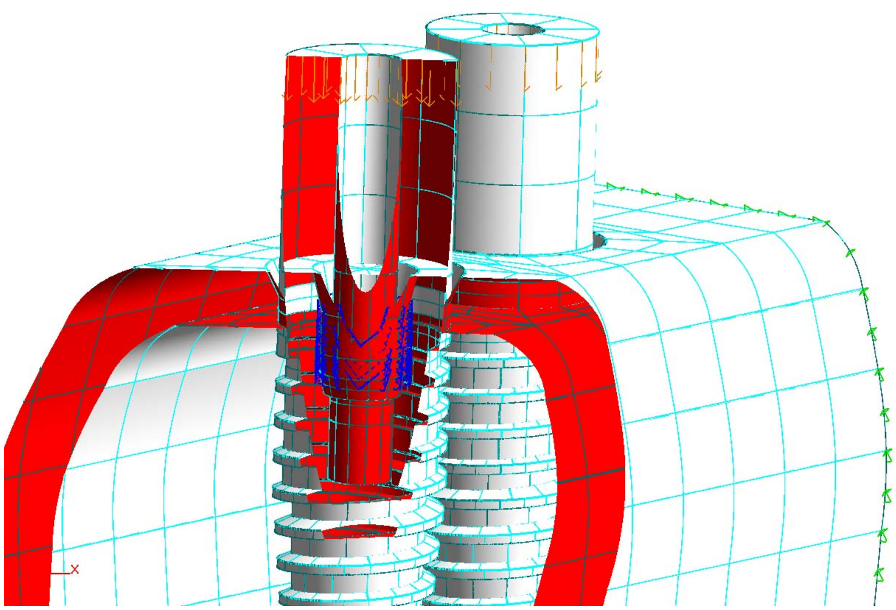

Fig. (4). BEM numerical model of the mandibular segment and implants with highlight of the axial applied load, mesh and abutment geometry.

Table 1. Material Properties Under Transversal Isotropic Material Behaviour (*x'z'* is the Isotropic Plane)

	Average Density Bone		
	Canal	**Spongy Bone**	**Cortical Bone**
$E_{x'}$ (MPa)	2.03E+03	7.19E+02	1.22E+04
$E_{y'}$ (MPa)	3.20E+03	1.14E+03	1.93E+04
$G_{x'y'}$ (MPa)	7.24E+02	2.55E+02	4.37E+03
$\nu_{y'x'}$	0.364	0.368	0.366
$\nu_{x'z'}$	0.341	0.342	0.345

Table 2. Orientation of the Material Reference System x'y'z' in the Global Reference System xyz (z//z')

Area	1	2	3	4	5	6	7	8
$q_{x'x}$ (degree)	-28	-28	-28	-28	-59	-59	-90	-90

To calculate the pressure on the nerve, a nonlinear BEM contact analysis was performed, with a null clearance imposed between the nerve and the surrounding canal structures (this is the worst case because generally a minimum clearance is available between the nerve and the canal).

The applied load was equal to 300 N along the implant axis, corresponding to 150 N on each implant (Fig. **4**); all the simulations considered a canal that is orthogonal to the implant axis.

The pressure distribution induced on the underlying nervous structure, was evaluated considering a distance of d=1.0 mm from the fixture to the mandibular canal.

BEM Analysis on the Overall Mandible and Submodelling

In order to reduce the computational time and memory requirements, when considering the whole mandible, the submodelling technique is adopted: the mandible part surrounding the implant has been extracted from the overall model and the displacements, calculated from the global analysis on the whole mandible (Fig. **2b**), have been applied on the cutting surfaces (Fig. **5**).

When considering the whole mandible model, including temporo-mandibular joints [14, 15], the real implant is replaced by a non threaded cylinder with the same external size (Fig. **6**), in order to reduce the computational burden. The effects of such approximations on the cutting surfaces are negligible. Traction and displacements continuity conditions are imposed between cylindrical surface and implant bone.

ANALYSIS RESULTS

FEM and BEM Local Analyses (Isotropic Bone Properties with No Allowance for the Whole Mandible)

With reference to the axial load case, Von Mises stress distributions in the bone undergoing axial masticatory load are shown in Fig. (**7**), and are calculated by means of BEM and FEM codes respectively. The fillet radius is equal to 0.15 mm immediately under the first thread and 0.3 mm further down (Fig. **7**).

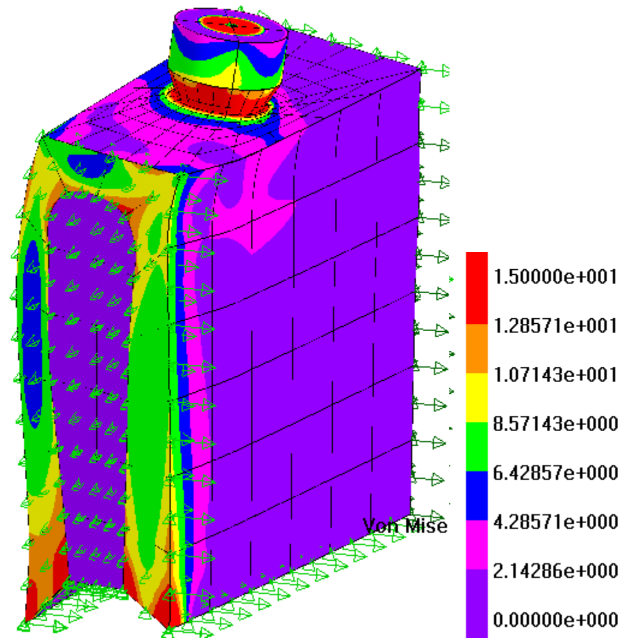

Fig. (5). Submodel with imposed displacement boundary conditions and contour plot of Von Mises stresses (MPa).

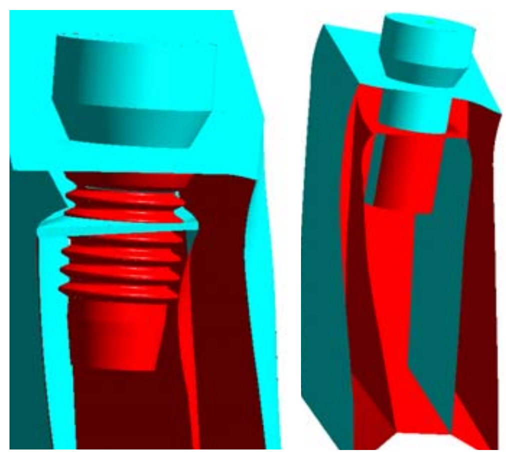

Fig. (6). Branemark implant embedded in the submodel (left) and related approximate shape when considering the global analysis on the overall model (right).

With the introduction of bone-implant interface contact elements, and disregarding friction, the distribution of BEM and FEM Von Mises equivalent stresses varies significantly with a strong increase in the maximum values (Fig. **8**).

The analysis with friction between implant and bone is carried out with a friction coefficient μ=0.42. The BEM and FEM analysis results are shown in Fig. (**9**), with lower stress peaks in comparison to the previous frictionless case.

The axial load case, with bone-implant interface continuity, is also developed with a 3D modelling approach in order to make a cross comparison with the results obtained by axial-symmetric modelling. The BEM and FEM Von Mises stress distributions are shown in Fig. (**10a**, **b**)

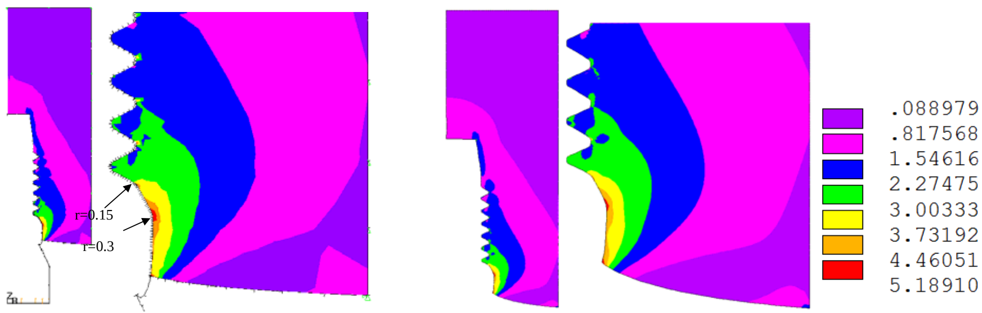

Fig. (7). BEM (left) and FEM (right) Von Mises equivalent stress (MPa) with close-up of the most stressed area.

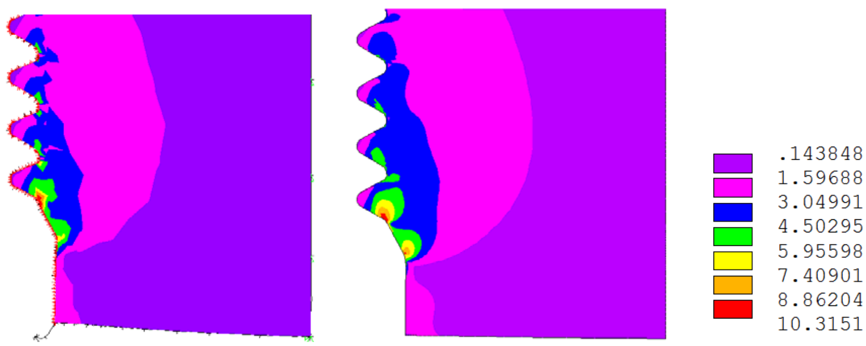

Fig. (8). BEM (left) and FEM (right) Von Mises equivalent stress (MPa) with contact elements at the bone-implant interface.

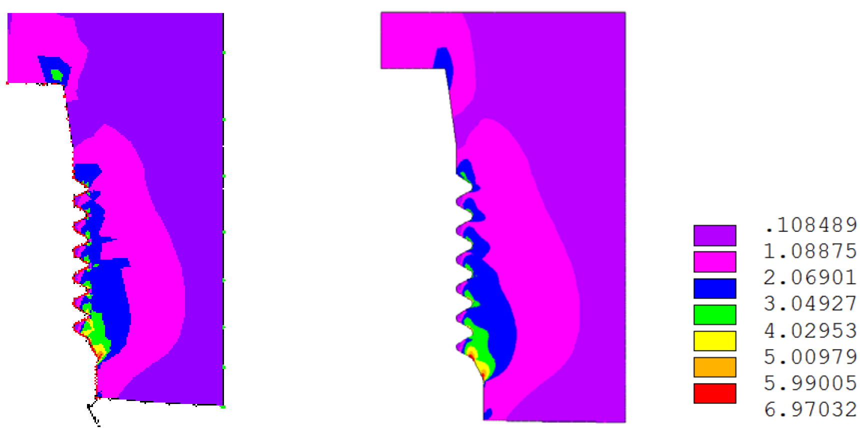

Fig. (9). BEM (left) and FEM (right) Von Mises equivalent stresses (MPa) with contact elements at the bone-implant interface, in case of friction with coefficient $\mu = 0.42$.

respectively and correspond to those shown in Fig. (**7**). The lateral load case is then considered (Fig. **11**) and in this case the three-dimensional approach is mandatory.

The satisfactory correspondence between FEM and BEM bone stress distribution is apparent from the previous figures and it is clear that these results are also in good agreement with those available from literature [19-21].

BEM Local Analysis with Conic Threaded Implant and Mandibular Canal

In Fig. (**12a-d**), the BEM contour plot shows the pressure on the nervous structure for a varying distance between the fixtures in case of axial load.

These results showed the sensitivity of nerve pressure against variations of distance between implants, considering

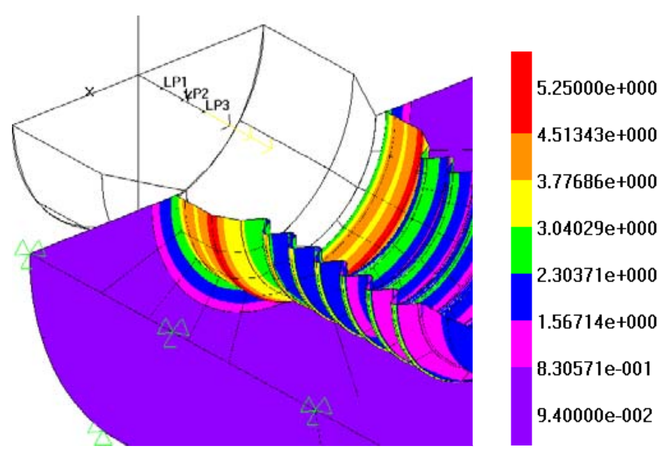

Fig. (10a). Von Mises stresses in the bone (MPa), under axial load, by BEM three-dimensional modelling.

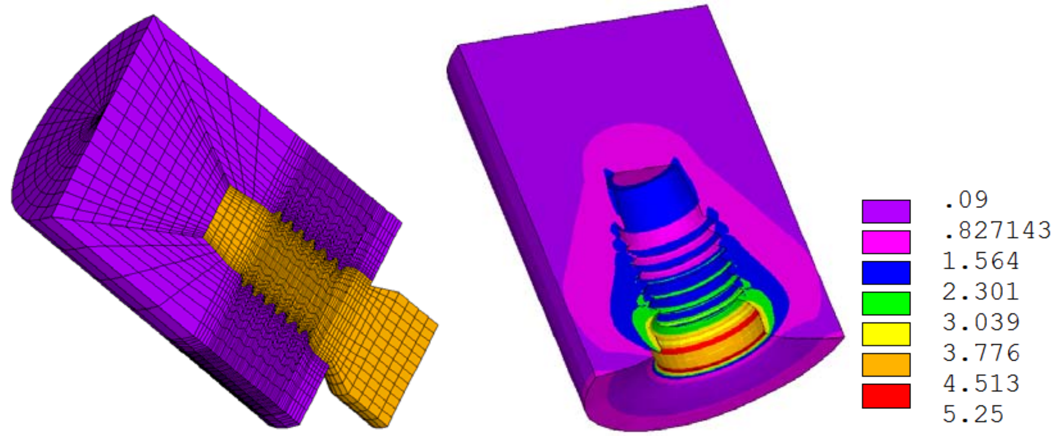

Fig. (10b). Von Mises stresses in the bone (MPa), under axial load, by FEM three-dimensional modelling.

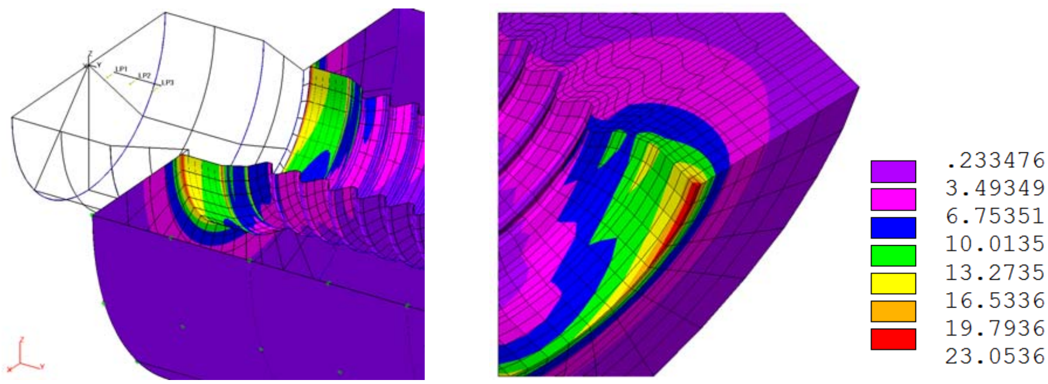

Fig. (11). BEM (left) and FEM (right) Von Mises equivalent stress (MPa) under lateral load.

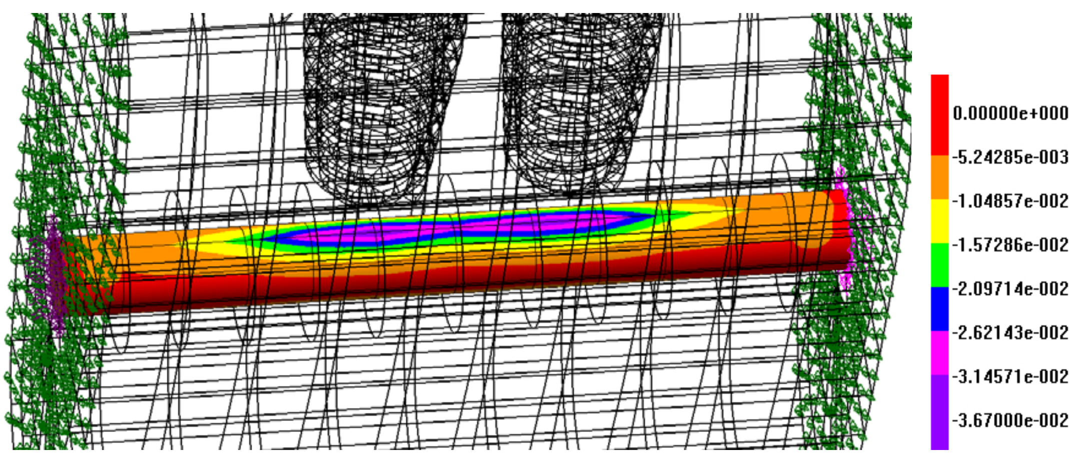

Fig. (12a). Pressure (MPa) on the inferior alveolar nerve, with a distance between implants equal to 5 mm.

a distance between implant bottom and canal (upper part) equal to 1 mm. As expected, the nerve pressure increased as implant distance decreased.

BEM Analysis on the Overall Mandible and Related Submodelling

Linear elastic BEM analyses for both the mandible model and submodel were developed using a mixed mesh of linear and quadratic elements. The former with 5534 elements and the latter with 1905 elements.

The coincidence between the resultant reaction force (equal to nearly 100 N), provided by the constraints in the z direction applied on the abutment (Fig. **2b**) and calculated in both the global analysis and in the local submodel analysis, represents a first verification of the accuracy of the submodelling technique.

A further confirmation is provided by the comparison between the Von Mises stresses on the submodel boundaries as calculated from the global analysis and from the submodel analysis. Their agreement, far from the threaded part is evident from Fig. (**13**).

Particularly significant is the stress concentration at the implant-bone interface, due to the implant specific geometrical profile and loading conditions. It is observed that, with reference to the cortical bone, Fig. (**14**), the most loaded part is the collar surrounding the implant. In fact, in

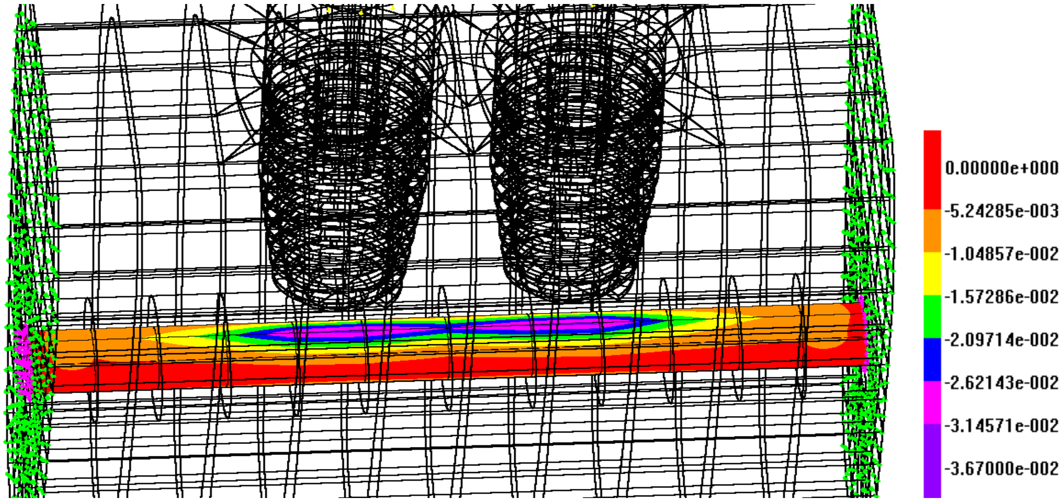

Fig. (12b). Pressure (MPa) on the inferior alveolar nerve, with a distance between implants equal to 5.5 mm.

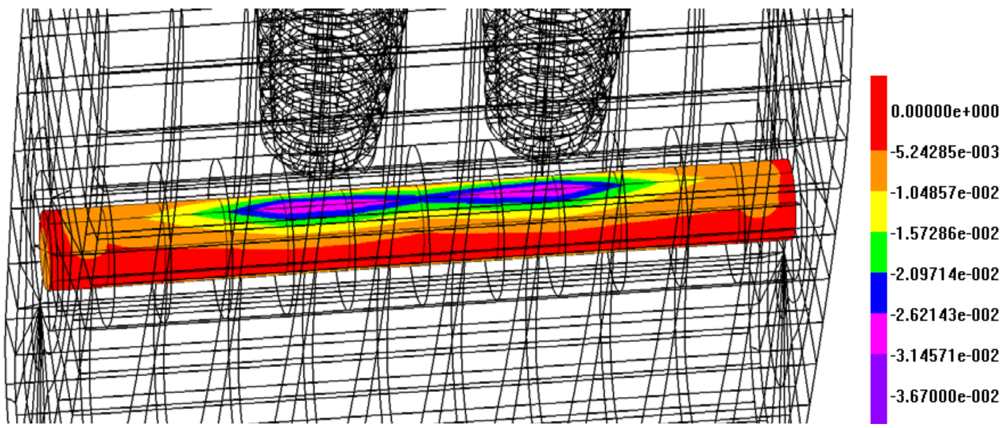

Fig. (12c). Pressure (MPa) on the inferior alveolar nerve, with a distance between implants equal to 6 mm.

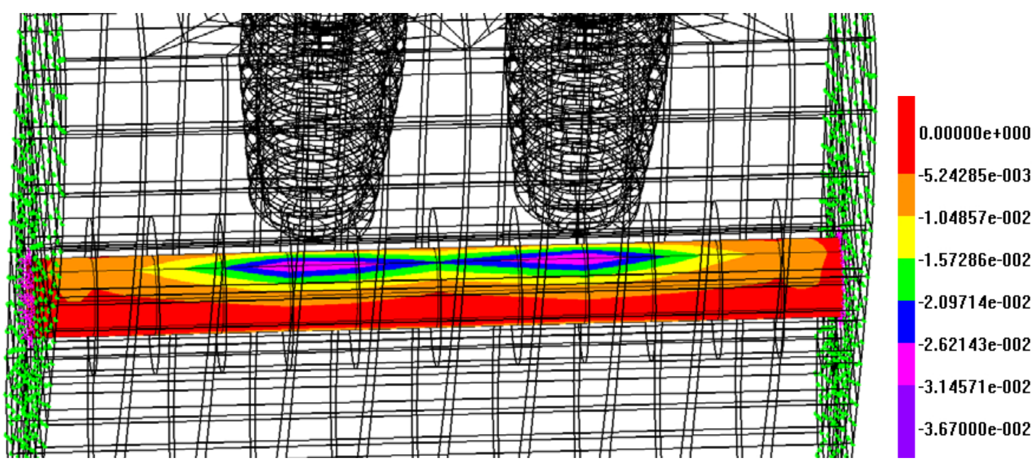

Fig. (12d). Pressure (MPa) on the inferior alveolar nerve, with a distance between implants equal to 6.5 mm.

the event of complete osteointegration, this is the part that absorbs most of the chewing forces, as a consequence of a higher stiffness compared to the cancellous bone (Fig. **15**).

CONCLUSIONS

The analysis performed highlighted BEM and FEM peculiarities when tackling this kind of problem. In addition to defining the main design features of an endosseous dental implant of the type considered, with sufficient accuracy, this work intends to reveal how the BEM approach can be advantageous when an implant shape optimization (depending on the patient's specific mandibular morphology) is attempted. In particular, the parametric analysis reveals the typical BEM preprocessing flexibility which allows quick geometric changes and re-meshing, that would be more difficult to achieve by using FEM.

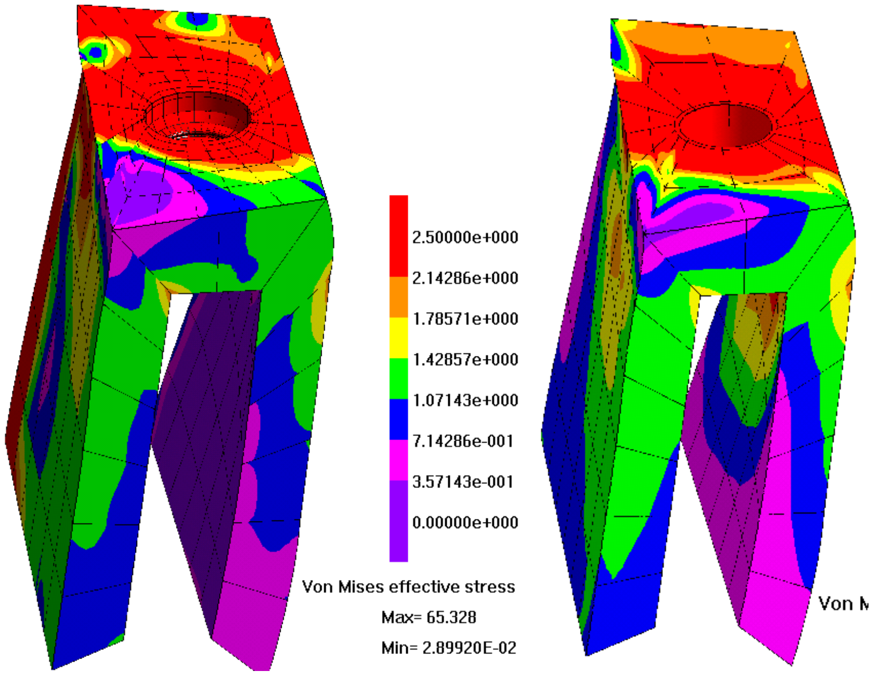

Fig. (13). Sub-model (left) and overall model (right) Von Mises stresses (MPa) in the cortical part.

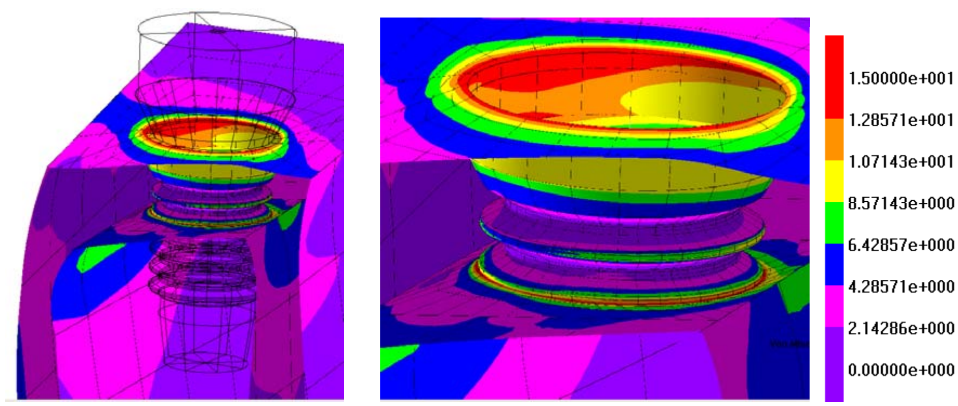

Fig. (14). Von Mises stresses (MPa) in the submodel cortical part and cortical collar magnification.

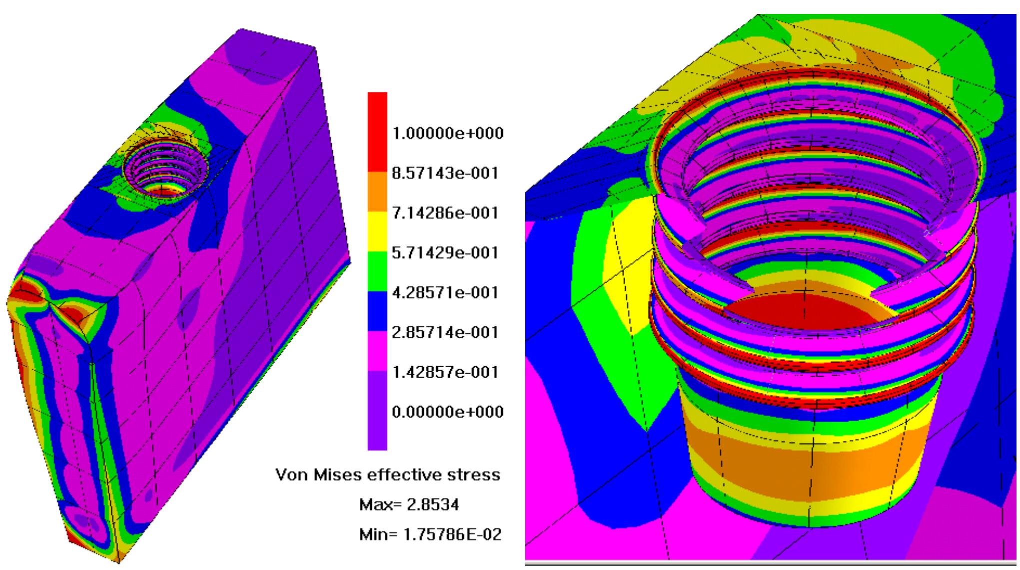

Fig. (15). Von Mises stresses (MPa) in the sub-model spongy part and close-up to the threaded part.

Finally, working with 3D models, the mesh refinement in the neighbouring areas where high stress gradients are expected is much more flexible when using BEM, rather than FEM also because it is possible to use discontinuous elements.

Future perspectives of this kind of simulation will require to cope with mechano-biological aspects [22]. Shape and elasticity of bone change over time (bone remodelling) and consequently the equations have to be related to the rate of change of bone geometry (internal shape and porosity) with time, depending on a mechanical stimulus (such as strain energy density or damage).

REFERENCES

[1] E. Kitamura, R. Stegaroiu, S. Nomura, O. Miyakawa, "Biomechanical aspects of marginal bone resorption around osteointegrated implants: considerations based on a three –dimensional finite element analysis", *Clinical Oral Implants Research*, vol. 15, no. 4, pp. 401-412, 2004.

[2] D. Wismeijer, M.A.J. van Waas, W.K. Vermeeren, "Patient's perception of sensory disturbances of the mental nerve before and after implant surgery: a prospective study of 110 patients", *British Journal of Oral and Maxillofacial Surgery*, vol. 35, pp. 254-259, 1997.

[3] D.S. Levitt, "Apicoectomy of an endosseous implant to relieve paresthesia: a case report", *Implant Dentistry*, vol. 12, no. 3, pp. 202-205, 2003.

[4] G. Greenstein, D. Tarnow, "The mental foramen and nerve: Clinical and anatomical factors related to dental implant placement: a literature review", *Journal of Periodontology*, vol. 20, pp. 1933-1943, 2006.

[5] G. Santler, H. Karcher, C. Ruda, "Indications and limitations of three-dimensional models in cranio-maxillofacial surgery", *Journal of Cranio-Maxillofacial Surgery*, vol. 26, pp. 11-16, 1998.

[6] J.C. Kois, "Predictable single tooth peri-implant aesthetics: five diagnostic keys", *Compendium of Continuing Education in Dentistry,* vol. 22, pp. 199-206, 2001.

[7] B. Bono, A. Cirello. D. Geraci, A. Pasta, A. Cassaro, "FEM model achievement for dental implant characterization", *European Journal of Implant Prosthodontics*, vol. 2, pp. 75-85, 2005.

[8] G. Sammartino, G. Marenzi, R. Citarella, R. Ciccarelli, H.-L. Wang, "Analysis of the occlusal stress transmitted to the inferior alveolar nerve by an osseointegrated threaded implant", *Journal of Periodontology*, vol. 79, no. 9, pp. 1735-1744, 2008.

[9] M. Cehreli, J. Duyck, M. De Cooman, R. Puers, I. Naert, "Implant design and interface force transfer", *Clinical Oral Implants Research*, vol. 15, no. 2, pp. 249-257, 2004.

[10] P. Franciosa, M. Martorelli, "Stress-based performance comparison of dental implants by finite element analysis", *International Journal on Interactive Design and Manufacturing*, vol. 6, No. 2, 2012, pp. 123-129.

[11] P. Ausiello, P. Franciosa, M. Martorelli, D.C. Watts, "Effects of thread features in osseo-integrated titanium implants using a statistics-based finite element method", *Dental Materials*, vol. 28, no. 8, 2012, pp. 919-927.

[12] C.H. Gibbs, P.E. Mahan, H.C. Lundeen, "Occlusal forces during chewing and swallowing as measured by sound transmission", *Journal of Prosthetic Dentistry*, vol. 46, pp. 443-449, 1982.

[13] J.H. Koolstra, T.M. van Eijden, W.A. Weijs, M. Naeije, "A three dimensional mathematical model of the human masticatory system predicting maximum possible bite forces", *Journal of Biomechanics*, vol. 21, pp. 573-576, 1988.

[14] E. Armentani, F. Caputo, R. Citarella, "FEM sensitivity analyses on the stress levels in a human mandible with a varying ATM modelling complexity", *The Open Mechanical Engineering Journal*, vol. 4, pp. 8-15, 2010.

[15] R. Citarella, E. Armentani, F. Caputo, A. Naddeo, "FEM and BEM analysis of a human mandible with added temporomandibular joints", *The Open Mechanical Engineering Journal*, vol. 6, pp. 100-114, 2012.

[16] F.V. Antunes, C. Pereira, M.C. Gaspar, "Experimental Evaluation of Physical Properties of Bone Structures", *Applied Mechanics and Materials*, vol. 5 - 6, pp. 71-76, 2006.

[17] J.M. Reina, J.M. García-Aznar, J. Domínguez, M. Doblaré, "Numerical estimation of bone density and elastic constants distribution in a human mandible", *Journal of Biomechanics*, vol. 40, no. 4, pp. 828-836, 2007.

[18] A. Shirazi-Adl, M. Dammak, G. Paiement, "Experimental determination of friction characteristics at the trabecular bone/porous-coated metal interface in cementless implants", *Journal of Biomedical Materials Research.*, vol. 27, pp. 167-175, 1993.

[19] S. E. Clift, J. Fisher, C. J. Watson, "Finite element stress and strain analysis of the bone surrounding a dental implant: effect of variations in bone modulus", *Proceedings of the Institution of Mechanical Engineers*, vol. 206, pp. 233-241, 1992.

[20] D. Siegele, U. Soltesz, H. Scheicher, "Dental implants inserts – A possibility to improve the stress distribution in the jaw", *Fraunhofer – Institute fur Werkstoffmechanik*, Freiburg, F.R.G., 1985.

[21] D. Siegele, U. Soltész, "Numerical investigations of the influence of implant shape on stress distribution in the jaw bone", *The International Journal of Oral & Maxillofacial Implants*, vol. 4, no. 4, pp. 333-340, 1989.

[22] M. Doblarè, J.M. Garcia, M.J. Gomez, "Modeling bone tissue fracture and healing: a review", *Engineering Fracture Mechanics*, vol. 71, pp. 1809-1840, 2004.

Residual Stress Analysis of AA2024-T3 Friction Stir Welding

Nirmal Charan Mallik, *Department of Mechanical Engineering, Aryan Institute of Engineering & Technology, Bhubaneswar, nirmal_m26@gmail.coma*

Priyabrata Jena, *Department of Mechanical Engineering, Capital Engineering College, Bhubaneswar, priyabratajena456@yahoo.co.in*

Kalpana Mallick, *Department of Mechanical Engineering, Raajdhani Engineering College, Bhubaneswar, kalpanam11@outlook.com*

Abstract: Friction Stir Welding (FSW) is an innovative solid-state joining process, which is gaining a great deal of attention in several applicative sectors. The opportune definition of process parameters, i.e. minimizing residual stresses, is crucial to improve joint reliability in terms of static and dynamic performance. Longitudinal residual stresses, induced by FSW in AA2024-T3 butt joints, have been inferred by means of a recently developed technique, namely the contour method. Two approaches to stress measurement have been adopted; the former is based on the assumption of uniform material properties, the latter takes into account microstructural effects and material properties variations in the welding zones. The influence of process parameters, namely rotating and welding speeds, on stress distribution is also discussed.

Keywords: AA2024-T3, friction stir welding, contour method, residual stress, material properties.

1. INTRODUCTION

Medium to high strength aluminum alloys, such as 2xxx, 6xxx, and 7xxx series, are currently considered of great interest in the transport industries. In particular, the precipitation hardenable AA2024 (Al-Cu) alloy is gaining considerable attention for the realization of barrier beams or fuselage panels. In this context, remarkable research effort is focused on the application of the Friction Stir Welding (FSW) process, as a suitable alternative to fusion welding processes. Indeed, the poor dendritic microstructure and the high porosity in the weld zone, induced using conventional techniques, strongly reduce the mechanical behavior of the assembly. Furthermore, the reduction of production costs and weight and the increase of strength and damage tolerance with respect to riveted lap joints make FSW a very attractive process to the aerospace industry.

FSW is a solid-state welding process, developed and patented by The Welding Institute (TWI) of Cambridge in 1991. Following the early successful applications in aluminum welding, FSW has been applied to other engineering materials, such as copper, steel, titanium, and metal matrix composites. During the process a non-consumable rotating tool, constituted by a shoulder and a pin, is plunged between the adjoining edges of the parts to be welded and moved along the desired weld line. The combined rotation and translation of the tool locally increase the work piece temperature, due to heat generated by frictional effects and plastic deformation. The induced softening allows the processing material to flow around the pin, from the front (leading edge) to the rear (trailing edge) according to complex patterns, resulting in a solid state weld [1]. Temperature increase and high strain rate deformation lead to the formation of micro-structurally different zones: the nugget or stir zone (NZ) in the center of the weld, surrounded by the thermo-mechanical affected zone (TMAZ) and the heat affected zone (HAZ). Nowadays, a deeper understanding of static strength as well as of fatigue behavior of FSWed assemblies is highly desired for a wider implementation of the technique in safety-critical components. It is commonly accepted that the aforementioned properties mainly rely on residual stresses, microstructure, and microhardness. Even if FSW residual stresses are generally lower if compared to conventional welding processes, an accurate knowledge of their distributions is crucial to numerically investigate buckling behavior [3-5] as well as crack growth and fatigue response [6-13] of welded assemblies. In this sense some results have already been presented in the inherent literature, regarding, for instance, AA5083 [14-16], AA6082 [6,17,18], AA2195 [13], AA2219 [19], and AA2024 [8-12,17,18,20,21] FSW. In more details, Peel *et al.* investigated the influence of the welding speed on microstructural, microhardness and residual stress on 3 mm thick AA5083 FSWed butt joints. The stress distribution was inferred by means of synchrotron X-rays, evidencing a tensile status in both the longitudinal and transverse direction. Moreover an increase of the tensile peak was found increasing the welding speed [14]. FSW process was simulated using a fully thermo-mechanical model in [15], declaring good agreement with available results [14]. The influence of dynamical recrystallization effects on residual stress distribution was also suggested. Synchrotron X-ray radiation was employed by Lombard *et al.* in [16] to analyze 6 mm thick FSWed plate. The typical residual stresses M-shaped profile was detected, confirming also the dominant role of the welding speed on the tensile peak. Three different aluminum alloys (5754-H111, 2024-T3, and 6082-T6) were joined using FSW in [17]. Residual stress measurements were carried on using the slitting (crack compliance) method. Two different inverse methods, namely the linear elastic fracture mechanics (LEFM) and finite element (FE) methods, were implemented, providing similar results. Reported data highlighted the correlation between the stress profile and the microstructural changes in the processing material. The hole drilling technique was applied in [18] to measure through the thickness residual stress in four aluminum alloys, namely AA1050-O, AA2024-T4, AA6082-T6, and AA7075-T6, welded according to three different processing conditions. Compressive stresses were found on joint surface in correspondence of the advancing side, replaced by tensile stress inside the joint. An experimental residual stress analysis on 12 mm thick AA2219-T6 plates, butt joined by FSW, was carried on by Xu *et al*. using the hole-drilling strain-gauge method [19]. Different stress profiles were detected at the top and bottom surfaces, following, respectively, a M-shape and a V-shape. Moreover, an increase of the tensile peak was highlighted in defected joints.

As far as AA2024 FSW is regarded, several studies have been focused on the analysis of residual stresses, using numerical and experimental approaches. Two process settings, defined as hot and cold weld, were used by Deplus *et al*. to weld 2 mm thick AA2024-T3 plates in the butt joint configuration [17]. Longitudinal stresses were measured using the slitting method, evidencing a more severe residual status assuming cold weld parameters. The adopted method, however, did not allow for the detection of stress variations through the thickness. The same technique was used by Milan *et al*. to investigate longitudinal and transverse residual stresses in 3.2 mm thick AA2024-T3 plates [20]. A higher tensile residual stress was measured on the advancing side of the weld and related to the larger heat input, resulting from the higher relative speed between the tool and the material. Sutton *et al*. measured longitudinal, transverse and normal stresses distributions in 7 mm thick AA2024 plates in the T3 condition [21], by means of neutron diffraction (ND). The longitudinal stress was found to be the largest tensile component. The analysis was performed assuming one processing condition; the influence of process parameters was not investigated. Despite the relevant data and intriguing conclusions reported in the cited papers, it should be noted that most of the cited works explored very few, if not unique, combinations of process parameters. Moreover, residual stresses were measured in selected locations of the joined plates or considering average values due to intrinsic limits of the employed techniques.

In this paper results provided by an experimental investigation on longitudinal residual stresses in 4 mm thick AA2024-T3 FSWed butt joints are reported and discussed. The contour method has been applied to map the stresses acting on a section normal to the weld line. The aim of the work is to investigate the influence of process parameters, namely rotating and welding speed, on stress distribution, considering also the influence of microstructural changes on the computed stress field. Two stress maps have been inferred for each test, assuming, respectively, constant material properties and properties variations in the different welding zones (NZ, TMAZ, HAZ). The extension of each zone has been defined by means of a numerical-experimental approach, following experimentally calibrated criteria based on temperature, dynamic viscosity, and grain size values. Local material properties have been quantified using ultrasonic analysis and then employed for stress calculation. The paper is structured as follows: in Section 2 details regarding material, manufacturing process, and analysis procedures are reported, while in Section 3 results are exposed and discussed. Finally, Section 4 deals with relevant findings of the work.

2. MATERIALS AND METHODS

2.1. Material and Welding Process

In the present investigation, AA2024-T3 aluminum rolled plates (100 mm x 30 mm x 4 mm) were joined by FSW. The nominal composition (wt%) of the base material is as follows: 3.8-4.9 Cu, 1.2-1.8 Mg, 0.3-0.9 Mn, 0.5 Si, 0.5 Fe, 0.25 Zn, 0.15 Ti, 0.1 Cr, balance Al. The considered material has been subjected to a solution heat treatment, followed by cold working and natural ageing. Welds have been executed normally to the rolling direction on a MCX 600 ECO machining center. The process set up is shown in Fig. (**1**).

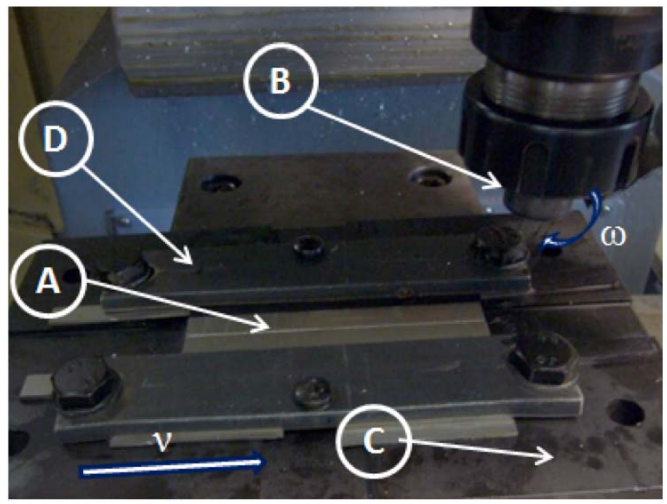

Fig. (1). Friction stir welding process set up (**A**: plates in reference pocket, **B**: tool and tool-holder, **C**: Inclined base plane imposing the tilt angle, **D**: clamping system).

A full factorial design of experiments has been adopted, assuming respectively five and three levels for the rotating speed ω (800, 1000, 1200, 1400, 1600 rpm) and feed rate ν (35, 70, 140 mm/min). Tilt angle and pin penetration have been defined as 2° and 0.2 mm, following literature indications. An AISI1040 quenched steel tool (56 HRC) consisted of a 20 mm diameter shoulder with a conical unthreaded pin has been employed. Pin dimensions are: height 3.80 mm, major diameter 6.20 mm, and cone angle 30°. Preliminary visual inspections and microscopic observations of the joint section showed the presence of internal defects, such as tunnel defect and kissing bonds at rotating speeds lower than 1400 rpm, significantly reducing the process window. Taking into account that defect analysis is not the main focus of the present investigation, detailed information are not herein reported. Omitted data, analysis, and related discussions can be found in [22].

2.2. Welding Zones Identification and Characterization

In this paragraph, numerical and experimental methods used to individuate the different welding zones (NZ, TMAZ, HAZ) and to evaluate the related properties are reported. As far as AA2024-T3 FSW is concerned, it is relevant to notice that extension, microstructure and mechanical properties of each zone are significantly affected by dynamic recrystallization, dissolution, coarsening, and re-precipitation phenomena, whose kinetics are strongly influenced by thermal effects coupled to plastic deformations [23]. Conventional optical metallographic procedures allows for a clear detection of NZ as well as of TMAZ. Indeed, the former is interested by continuous dynamic recrystallization phenomena, resulting in an evident grain refinement with respect to the parent material. In the latter a variable amount of grain distortion, without significant size changes, is generally observed [2,10,20,22]. HAZ boundaries are quite difficult to observe using the aforementioned techniques, since no relevant modifications of grain size and shape are induced. However, the temperature field experienced by the processing material during the welding strongly affects precipitates distribution and properties, influencing the microhardness (HV) distribution. As a consequence, the peculiar HV trend in the HAZ, allows one to indirectly evaluate the HAZ extension [23]. Experimental data have been used to calibrate some criteria, based on temperature, dynamic viscosity, and grain size considerations, implemented in a CFD process model, presented and validated in [22,24], providing an automatic definition of welding zones boundaries.

Taking into account what aforementioned, NZ boundaries have been defined, for each processing conditions, in correspondence of the (numerically computed) onset of recrystallization and grain size change [24]. A criterion based on dynamic viscosity calculation, as reported in [25,26], has been adopted to define TMAZ extension, assuming a reference value of 4E6 Pa·s in correspondence of the separation between TMAZ and HAZ [22]. In Fig. (**2**) a comparison between the numerically computed and experimentally observed NZ and TMAZ has been reported, showing also a contour of the grain size distribution in the NZ. An indirect definition of HAZ - BM boundaries has been adopted, considering, as generally accepted, that no relevant phenomena take place in the considered material below a threshold temperature [23], herein defined as 250°C considering microhardness results presented in [22].

Regarding material characterization, it is relevant to emphasize that the method employed for residual stress evaluation requires elastic properties only. The local elastic modulus has been evaluated by ultrasonic time of flight (TOF) measurements. The used device was a PANAMETRICS 5058PR high voltage pulser-receiver, working in a pulse-echo mode. A V544 ultrasonic probe, generating 10 MHz longitudinal waves, has been used. Other parameters have been defined by trial and error as follows: 100 Ω damping, 200 V pulse height, 30 dB attenuation, and 0.1 MHz HP filter. Time of flight measurements have been performed in correspondence of the NZ, TMAZ and HAZ on both sides of the weld. The local elastic modulus has been then inferred according to the following equation:

$$V_l = \sqrt{\frac{E(1-\nu)}{\rho(1+\nu)(1-2\nu)}} \tag{1}$$

being V_l the ultrasonic longitudinal speed, ρ the density and ν the Poisson ratio. Three measurements have been performed in correspondence of each zone, assuming the average value for the subsequent analysis.

2.3. Residual Stress Measurement

2.3.1. The Contour Method

The contour method (CM) is a relaxation method allowing one to evaluate the stress distribution on a specimen section [27]. From a theoretical point of view, the contour method is a derivation of the Bueckner's elastic superposition principle, which states that: "if a cracked body subject to external loading or prescribed displacements at the boundary has forces applied to the crack surfaces to close the crack together, these forces must be equivalent to the stress distribution in an uncracked body of the same geometry subject to the same external loading" [28]. In other words stresses to be applied on a specimen section in order to deform the surface to its initial undeformed shape are equivalent to the residual stresses acting on the same section before the cut. Theoretically, all of the three stress components acting on the cut surface can be derived, however, evident limitations in in-plane displacements measurement reduce the effective applicability of CM to normal stresses [27]. The most intriguing capability of the

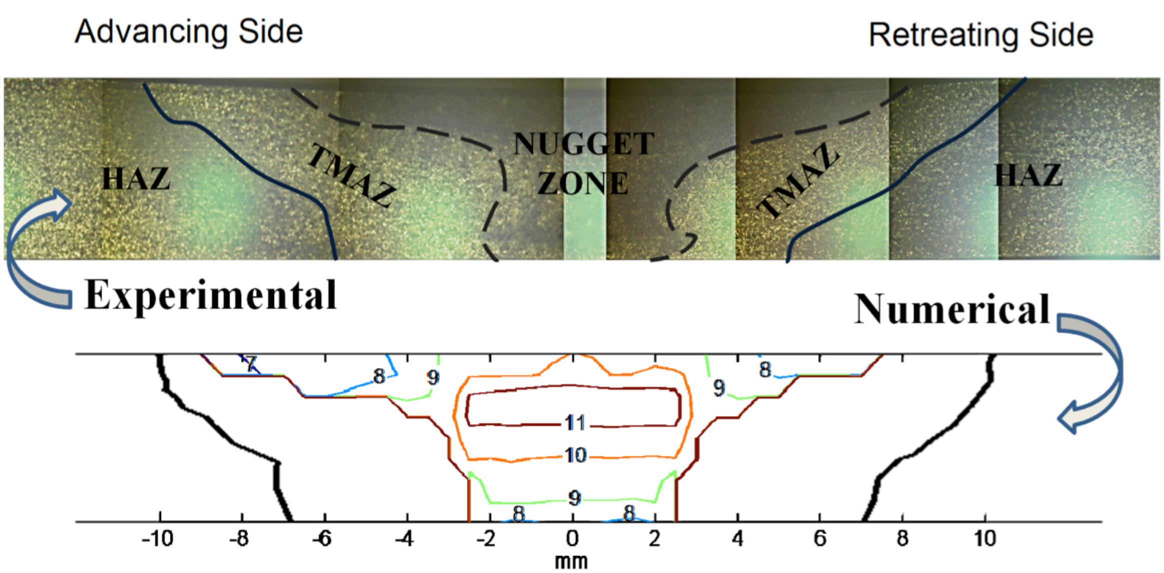

Fig. (2). Experimental and numerical NZ and TMAZ (Test 15). Numbers on contour lines indicated the grain size in µm.

method, if compared to other destructive techniques, is that a complete residual stresses mapping can be achieved, following a relatively simple and cheap procedure. Moreover, the experimental steps can be realized using devices and machines currently available in most industrial as well as academic research laboratories. For these reasons, CM has been widely applied in several contexts, including FSW. Woo *et al*. in [29] discussed some results provided by an experimental investigation on friction stir processing of AZ31B magnesium alloy. ND and CM were applied for residual stress evaluation providing similar stress distributions. An application of CM to analyse the effect of shot peening and laser shock peening on AA2195 and AA7075 friction stir welds was detailed in [30], highlighting a remarkable through the thickness variation of the longitudinal stress. ND and CM were employed by Prime *et al.* to investigate longitudinal residual stresses in AA7050-T7451 and AA2024-T351 friction stir butt joints [31]. Good agreement was found in stress mapping, evidencing also an M-shaped longitudinal stress profile. More recently, Richter-Trummer implemented the CM to analyse the effect of clamping forces in FSW of 3.18 mm thick AA2198-T851 plates [32]. It was found that higher clamping forces lead to more uniform residual stress distribution through the thickness.

2.3.2. Sample Cut

The application of the contour method is based on four consecutive steps: specimen cut, relaxed surface acquisition, data reduction, and stress computation. Specimen sectioning is a crucial step, since it potentially affects the shape of the relaxed surface and, as a consequence, the reliability of the inferred normal stress. The cutting process should respect some prerequisites to avoid or at least reduce measurement errors. The cut should be flat and of high surface finishing, the cut width should be constant and very small and the specimens should be rigidly clamped on both sides. Additionally, the just cut (and relaxed) surfaces should not be re-machined by the cutting tool. The cutting technology more suitable to accomplish this step is the wire electro discharge machining (WEDM). In the present investigation, FSWed specimens have been sectioned in correspondence of the mid-length and orthogonally to the weld line. The WEDM process has been performed by means of a MITSUBISHI FA-20 machine, using a copper 0.25 mm diameter wire in a deionized water bath. Skim-cut parameters have been used to minimize effects on pre-existing stresses.

2.3.3. Contour Measurement

After sectioning, residual stresses are free to relax, leading to a three dimensional displacement of the cut surfaces. Two approaches to contour measurement are generally applied, based, respectively, on contact (tactile) or non-contact (optical) techniques. Optical devices are nominally less accurate than tactile machines, such as Coordinates Measuring Machines (CMM), however, the improvement of the acquisition rate and the enlargement of the dataset virtually result in accuracy comparable with tactile systems [33].

In the present analysis, out of plane displacements of the sectioned surfaces have been recorded by means of a CMM (DEA IMAGE GLOBAL CLIMA), in a moisture and temperature controlled room. The resolution of the used CMM is 0.1 μm. The machine has been equipped with a contact probe constituted by a 30 mm height steel stylus and a 3 mm diameter ruby tip. The machine-probe system has been calibrated before each acquisition, to properly compensate stylus deflection. A 0.5 mm x 0.5 mm measurement grid has been programmed in a reference coordinate system associated with the sample, resulting into about 1100 data points for each surface. Taking into account the reduced extension of the cut surface, a hen-peck acquisition mode has been adopted to improve measurement accuracy without excessive penalization of the acquisition time. As aforementioned, the contour method allows for the evaluation of normal stress only: shear stress should be compensated by averaging the opposite displaced contours [27]. To accomplish this prerequisite, cut surfaces on both halves of each specimen have been measured.

2.3.4. Data Reduction

This step is relevant for the effectiveness of the whole procedure, since stress computation magnifies measurement errors. What is more, an analytical description of the displaced surface is highly desirable, considering that it allows one to define the FE mesh independently of the measurement grid. Intuitively, nodal displacements can be easily derived if a mathematical representation of the relaxed surface is available. Experimental data have been imported in the MATLAB environment and then averaged and fit to an unique smoothing surface, significantly improving the quality of the regression with respect to the polynomial surface fitting adopted by the same authors in [34]. Finally, nodal displacements from the base plane have been inferred and exported for FE calculations. In Fig. (**3a**, **b**) the smoothing surface approximating experimental data and the nodal displacements are shown.

2.3.5. Stress Computation

Longitudinal residual stresses distribution has been computed by means of an elastic FE model of the cut sample. The digitalized out of plane displacements have been used, with reversed sign, as input nodal boundary conditions, assuming an initial block shaped geometry. This procedure, commonly adopted for the application of the contour method, is less labor intensive with respect to the creation of the deformed model and the successive forcing of the relaxed surface to a flat status [27-34]. Additional constraints have been imposed on a node on the surface opposed to the displaced section to prevent rigid body motion. The commercial software ANSYS has been used to solve the linear elastic boundary value problem. In Fig. (**3c**) a computed deformed shape of the half specimen has been depicted. Two stress maps have been inferred for each processing condition. In the first case (LRS1 in what follows) no variation of elastic properties of the processed material is considered, assuming the parent material properties for all the welding zones. In the second set of simulations (LRS2), thermal and mechanical effects in the different welding zones have been considered assigning the ultrasonically detected Young modulus to each zone. As a first approximation, the same set of displacements has been used in both cases.

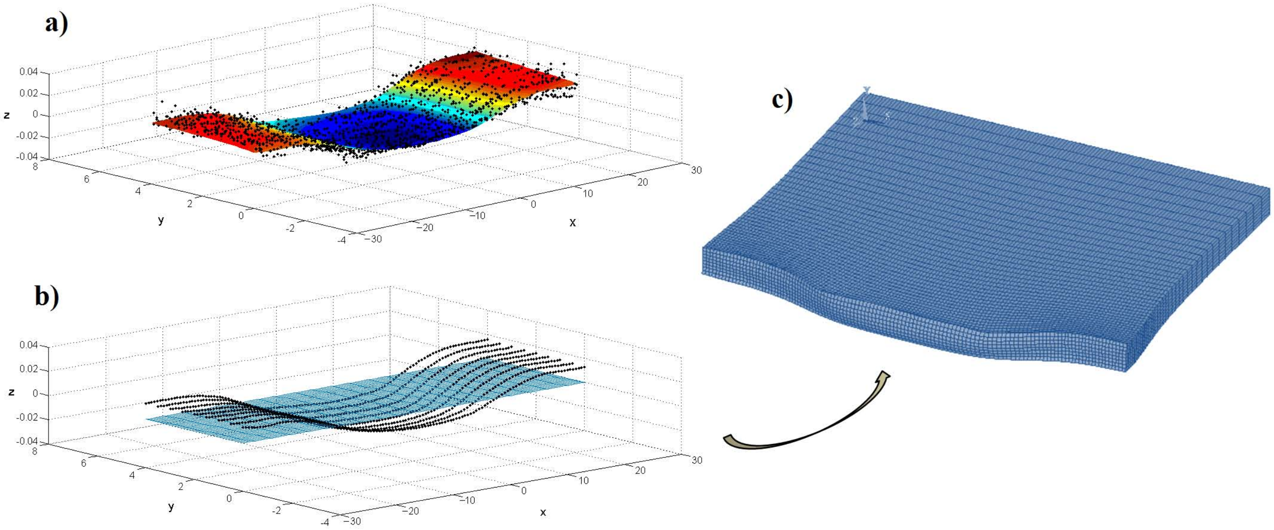

Fig. (3). Experimental points and smoothing surface (**a**); base plane and nodal displacements (**b**); deformed shape (Test 12) due to stress relaxation after the cut (**c**).

3. RESULTS AND DISCUSSION

3.1. Material Characterization and Influence of Properties Variations on Stress Computing

As aforementioned, during FSW material heating and stirring induce several microstructural phenomena, significantly affecting the final material properties. The base material welded in the present investigation showed the typical rolling microstructure, characterized by elongated grains, whit mean grain size equal to 59.18 μm. A remarkable grain refinement has been found in the NZ of all samples, ranging the recrystallized grain size between 8.43 and 11.13 μmin the central point, respectively in Test 3 and Test 13 [22,24]. No significant grain size variation has been observed in HAZ and TMAZ with respect to the parent material. Ultrasonic measurements showed that, as relatively to the grain size, no significant TOF (and consequently elastic modulus) variations are induced in the HAZ and TMAZ with respect to the base material (see Fig. **4**), whose Young modulus resulted equal to 73.3 GPa. Slight major, but still not elevated, deviations have been found at the weld line (in correspondence of the NZ) of all samples, being the maximum increase equal to 3.4 GPa (4.6% with respect to the parent material modulus) in Test 10. The positive variation of Young modulus has been related to the grain refinement in the NZ due to continuous dynamic recrystallization. Differently from what already declared relatively to microhardness [22], no evident correlation was found between the Young modulus and process parameters. This aspect can be related to variation of shape and extension of the NZ, as well as the grain size distribution, with process parameters. Considering that ultrasonically measured properties are averaged through the thickness and that at lower ω the recrystallized zone do not reach the weld root, an increase of the TOF and a reduction of the derived elastic modulus are expected.

In Fig. (**5a-d**) some results concerning the influence of properties variations on the inferred stress field have been depicted. In particular, Fig. (**5a**, **b**) show (in vertical sequence) the LRS distribution computed using uniform material properties, variable material properties, the absolute (Δ_{LRS} = LRS2-LRS1) and the percentage difference (Δ_{LRS}/LRS2)·100 relatively to opposite process conditions (Test 1: minimum ω and ν; Test 15: maximum ω and ν). A minimum threshold (± 2 MPa) has been adopted for the computation of the LRS percentage difference to avoid calculations in (practically) stress free zone, resulting in the conditioning of the overall evaluation. In Fig. (**5c**) a summary graph from all test cases, showing the maximum Δ_{LRS} and the absolute maximum tensile LRS, has been reported.

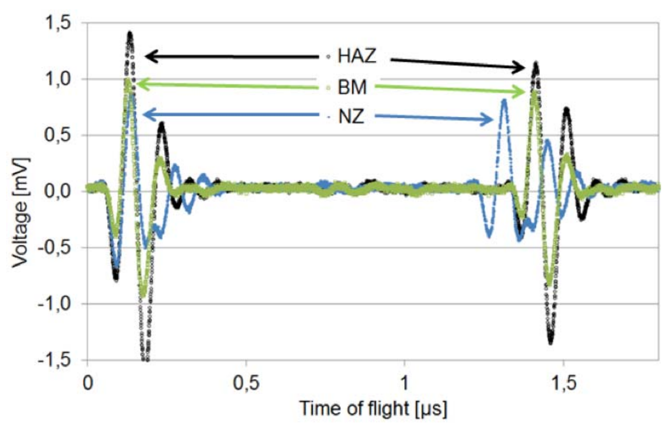

Fig. (4). Ultrasonic signal in the BM, HAZ and NZ (Test 15).

As can be seen, the LRS1 and LRS2 distributions overlap without significant (qualitative as well as quantitative) deviations. Indeed, the maximum stress difference (in absolute value) ranged between about 1 and 4 MPa in all cases, apart Test 3 (7 MPa) and Test 12 (5 Mpa). It should be also noted that the higher differences have been found in correspondence of relatively more stressed zone, resulting in few percentage points of maximum deviations between results provided by the two procedures. The above comparison justifies the widely used assumption of uniform material properties in residual stress evaluation following the contour method [28, 30-34], avoiding deeper metallographic and mechanical characterization of the processed material.

However, even focusing on the residual stress field induced by FSW process, it should be noted that the above statement can not be generalized and extended, without further verifications, to more specific cases, i.e. for instance hybrid aluminum-copper, aluminum-steel, or aluminum-titanium FSW. Indeed, obtained outcomes indicate that the maximum difference in LRS corresponds to the maximum Young modulus increase (Test 3), implicitly suggesting the need for a preliminary materials characterization for the effective application of the method to hybrid welding processes. What is more, in this case, the equilibrium condition of force and moments acting on the cut section could not be enforced by the equilibrium of displacements and rotations, imposing the implementation of iterative procedures to define the base plane position.

The LRS distribution, as provided by the contour method in Test 6, is shown in Fig. (**5d**), magnifying the sample thickness for clarity. The depicted stress field is qualitatively representative of LRS maps computed in the whole measurement campaign and evidences a tensile residual stress status in correspondence of the weld line. Two different tensile peaks have been found, localized at a distance from the weld center approximately equal to the shoulder radius into the advancing (AS) and retreating (RS) sides. The largest tensile stress, equal to 145MPa, has been detected in the AS below the top surface, in agreement with other reports [14,18,19], whereas the tensile peak in the RS resulted equal to about 125MPa (85% of the absolute maximum). The typical M-shaped profile has been observed, as already detected by other researchers, testing AA2024 and other aluminum alloys by means of several measurement techniques [11-14,16,17,20,31,32]. The observed asymmetry in the LRS distribution with respect to the weld line can be easily explained considering the different relative (processing material - tool) velocity moving from the AS to the RS. Moreover, line plots (on the right in the same subfigure) of LRS highlight some through the thickness stress variations in correspondence of the tensile peak (AS). As can be seen compressive stresses have been found also in correspondence of the top and bottom surfaces of the welded sample, changing to tensile at a distance from the external surface of about 0.5 mm. A relatively less severe stress profile has been computed at the center of the weld line. The tensile stress in the central region is balanced by compressive residual stresses moving towards the base material, reaching the minimum values about 20 mm away from the weld line and then slowly approaching (in absolute terms) lower values.

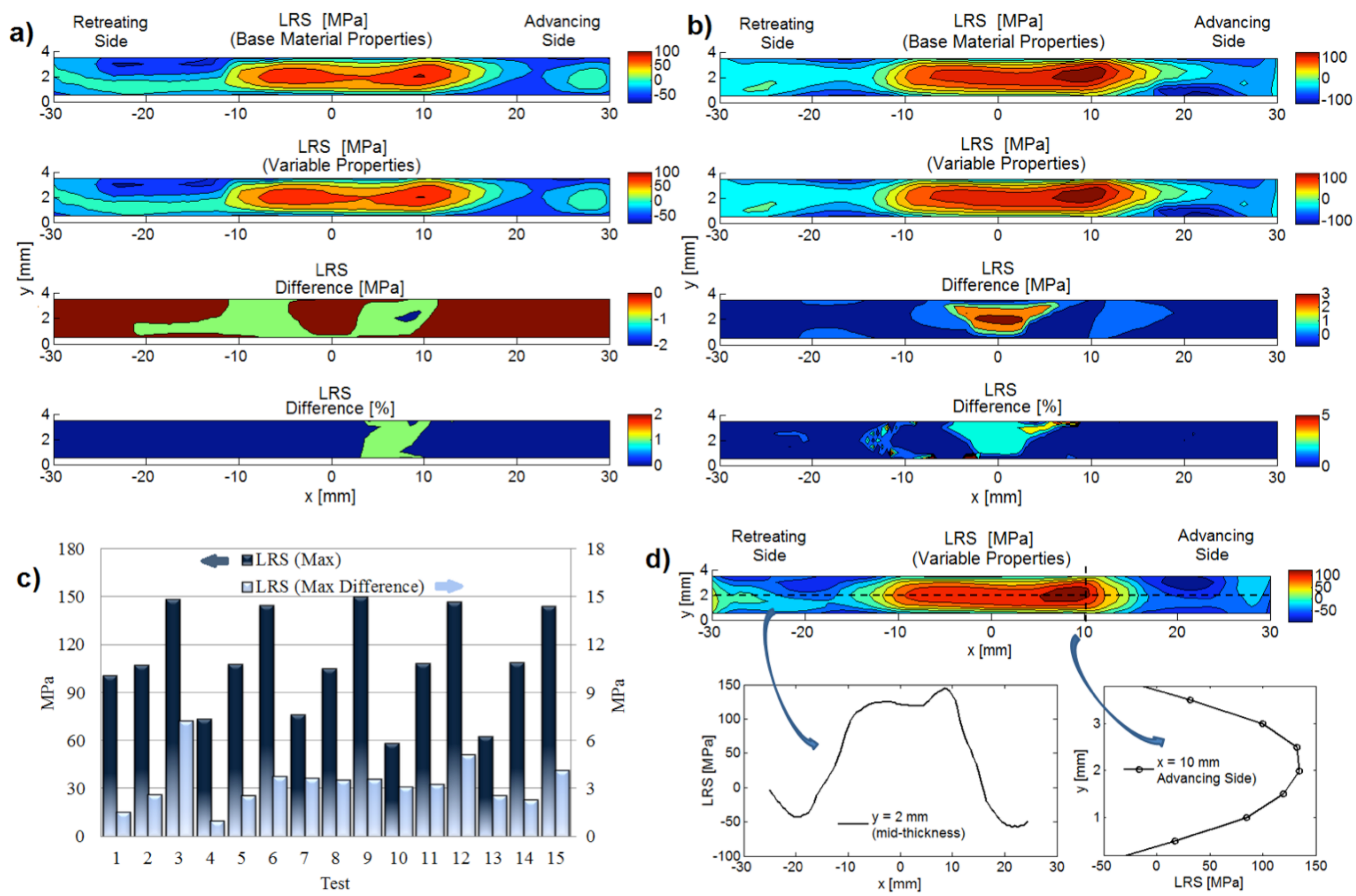

Fig. (5). Longitudinal residual stresses results, as provided by the contour method, assuming uniform material properties and variable material properties (absolute and percentage stress difference are also shown), in correspondence of the two limit test case **a**) Test 1 (ω = 800 rpm - ν = 35 mm/min, defected joint); and **b**) Test 15(ω = 1600 rpm - ν = 140 mm/min, sound joint). **c**) Bar plot of LRS results from all test cases; **d**) LRS distributions and profiles at the mid-thickness and across the thickness in the advancing side in Test 6 (ω = 1000 rpm - ν = 140 mm/min).

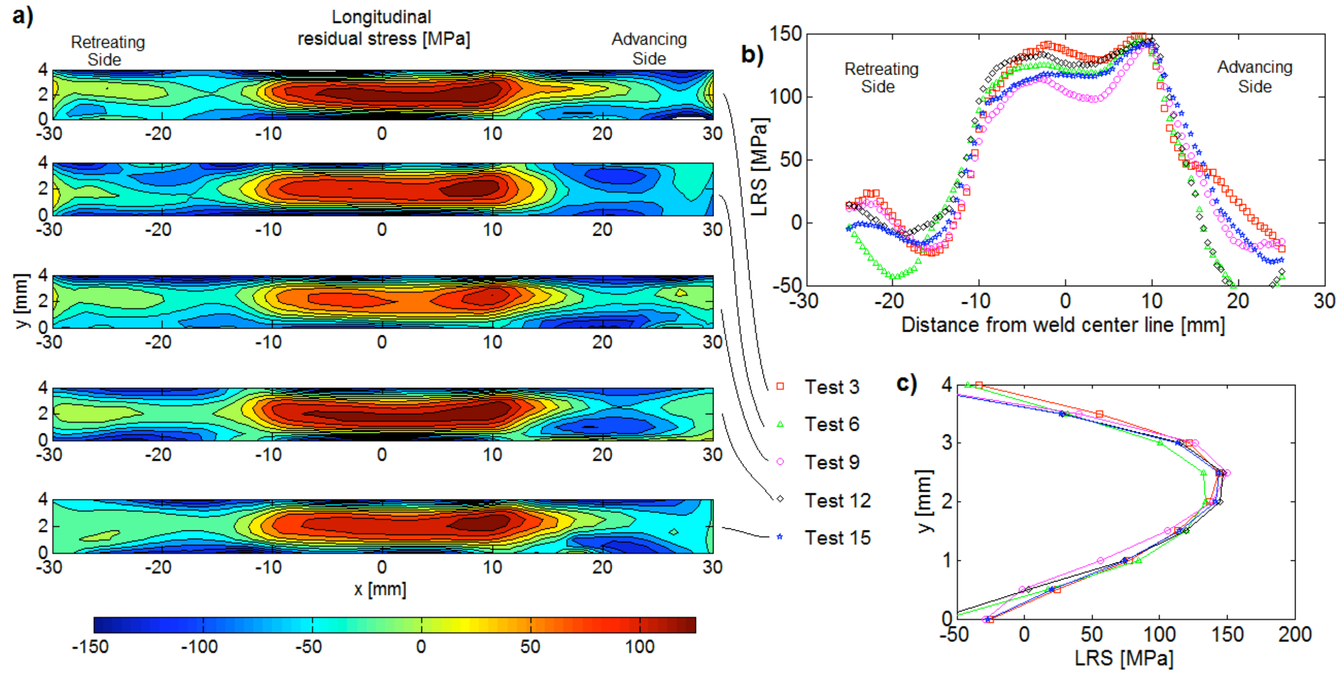

Fig. (6). Influence of rotational speed ω on LRS: **a**) stress distribution on the transverse section; **b**) LRS profiles at the mid-thickness; **c**) LRS profiles across the thickness in the advancing side (ν = 140 mm/min in all test cases).

3.2. Influence of Process Parameters on LRS

Figs. (**6**, **7**) graphically outline the influence of process parameters ω and ν on LRS. Again, the reported distributions and profiles fairly agree with results presented in the herein cited bibliography, evidencing two peaks in the tensile stressed zone and the presence of compression on both sides of the weld line. Furthermore, a stress reduction is observed at the center of the section (x = 0), preserving, in all the examined cases, the positive sign. The absolute maximum is always localized in the AS at a distance from the weld line approximately equal to the shoulder radius, i.e. at higher relative velocity and shear strain rate. The value of the tensile peak in the RS lied in a range whose lower limit was about the 80% of the peak value in the advancing side. In particular, the gap between tensile peaks appears more evident at lower ω, i.e. when the difference in material - tool relative motion between the AS and the RS is higher.

Obtained outcomes, in terms of stress profiles and tensile peaks, suggest a key role played by ν. As depicted in Fig. (**6b**, **c**), a fair superimposition of stress profiles can be observed varying ω in the considered range and assuming ν as fixed. On the other hand, the increase of ν induces relatively more severe residual stress status, as highlighted also in Fig. (**7a-c**). The predominant role of ν can be justified keeping in mind that it directly establishes the thermal cycle in terms of heating and cooling rates. Indeed, for a fixed value of ω, similar temperature peaks are experienced by the processing material despite consistent ν variations [22]. The increase of ν reduces the time available for the diffusion of the heat dissipated in the material away from the weld line. As a consequence, higher temperature gradients are induced and higher stresses on cooling should be expected. Inferred distributions evidenced also the influence of the presence of welding defects on LRS. In defected joints, at lower ν (Tests 1, 4, and 7), a remarkable increase of the tensile stress peak with respect to sound joints processed using the same ν (Tests 10 and 13) has been detected, in agreement with other reports [19]. This effect vanishes at higher ν.

The influence of ν on the tensile peak has been also tested by means of simple regression analysis. In particular linear and logarithmic regressions have been performed considering the whole dataset (A) and reducing the dataset to sound joints (B). A remarkable correlation coefficient R^2 has been obtained in all conditions, as summarized in Table **1**.

On the other hand, a very low correlation coefficient has been found repeating the procedure assuming ω as independent variable. It should be remarked, however, that the reduced extension of the dataset, in particular in Case B, did not allow for a rigorous statistical analysis, therefore the aforementioned considerations should be considered as indicative of the key role played by ν. It is worth also noting that the relatively better correlation adopting a logarithmic regression indicates the probable approaching of a tensile peak limit as ω increases, in agreement with the temperature peak trend described in [22].

CONCLUSIONS

The longitudinal residual stress distribution in AA2024-T3 friction stir welded butt joints has been investigated by means of the contour method. Two approaches to stress computation have been adopted, assuming, respectively, uniform and variable material properties. Taking into account what above reported, the following conclusions can be highlighted:

i. an increase of the Young modulus is induced by the grain refinement in the NZ, however, no evident correlation with process parameters has been observed. Negligible elastic modulus variations have

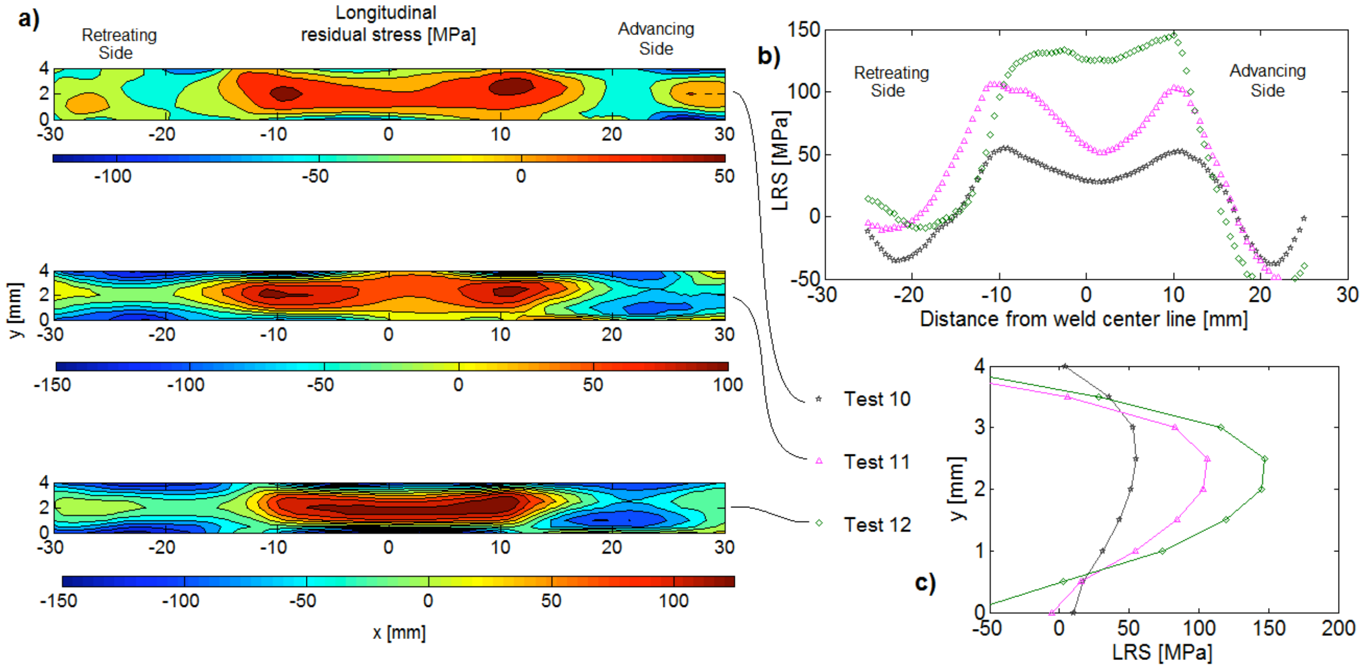

Fig. (7). Influence of welding speed v on LRS: **a**) stress distribution on the transverse section; **b**) LRS profiles at the mid-thickness; **c**) LRS profiles across the thickness in the advancing side (ω = 1400 rpm in all test cases).

been found in the HAZ and TMAZ with respect to the parent material;

ii. a detailed mapping of longitudinal residual stresses has been achieved by means of the used procedure, providing suitable material to validate computational simulative models of the process and to be included in static as well as dynamic analysis of welded assemblies;

iii. the assumption of uniform material properties appears acceptable in the investigated case, but not generalizable. Further development of the method are needed in order to investigate more complex cases, such as hybrid FSW;

iv. an asymmetric longitudinal residual stress distribution has been found for all processing conditions, characterized by a tensile stress in correspondence of the weld line, balanced by compressive residual stresses moving toward the base material. Two tensile peaks, describing the typical M shaped stress profile, have been measured in the tensile region, being the minor peak (in the RS) at least the 80% of the absolute maximum (in the AS);

v. the welding speed resulted the dominant process parameter relatively to process induced longitudinal residual stresses, since it directly affects heating and cooling cycles. The increase of v reduces the time available for heat diffusion away from the weld line, inducing higher temperature gradients and higher stresses on cooling. A minor influence of the rotating speed has been observed.

Table 1. Regression Analysis Results

Dataset	Regression Type	Equation	R^2
A	linear	0.672 v + 54.64	0.90
	logarithmic	52.34 ln(v) - 112.77	0.92
B	linear	0.771 v + 41.93	0.93
	logarithmic	61.44 ln(v) - 156.15	0.99

REFERENCES

[1] H.N.B. Schmidt, T.L. Dickerson, and J.H. Hattel, “Material flow in butt friction stir welds in AA2024-T3”, *Acta Mater.*, vol. 54, pp. 1199-1209, February 2006.

[2] M.A. Sutton, B. Yang, A.P. Reynolds, and R. Taylor, “Microstructural studies of friction stir welds in 2024-T3 aluminum”, *Mater. Sci. Eng. A Struct.*, vol. 323, pp. 160-166, January 2002.

[3] J.W. Yoon, G.H. Bray, R.A.F. Valente, and T.E.R. Childs, “Buckling analysis for an integrally stiffened panel structure with a friction stir weld”, *Thin Wall. Struct.*, vol. 47, pp. 1608-1622, December 2009.

[4] R.M.F. Paulo, P. Carlone, R.A.F. Valente, F. Teixeira-Dias, and G.S. Palazzo, “Integrated design and numerical simulation of stiffened panels including friction stir welding effects”, *Key. Eng. Mater.*, vol. 554-557, pp. 2237-2242, April 2013

[5] R.M.F. Paulo, F. Teixeira-Dias, and R.A.F. Valente, “Numerical simulation of aluminium stiffened panels subjected to axial compression: Sensitivity analyses to initial geometrical imperfections and material properties”, *Thin Wall Struct.*, vol. 62, pp. 65-74, January 2013.

[6] P.M.G.P. Moreira, A.M.P. de Jesus, A.S. Ribeiro, and P.M.S.T. de Castro, “Fatigue crack growth in friction stir welds of 6082-T6 and 6061-T6 aluminium alloys: A comparison”, *Theor. Appl. Fract. Mech.*, vol. 50, pp. 81-91, October 2008.

[7] P.M.G.P. Moreira, F.M.F. de Oliveira, and P.M.S.T. de Castro, "Fatigue behaviour of notched specimens of friction stir welded aluminium alloy 6063-T6", *J. Mater. Process. Technol.*, vol. 207, pp. 283-292, October 2008.

[8] G. Bussu and and P.E. Irving, "The role of residual stress and heat affected zone properties on fatigue crack propagation in friction stir welded 2024-T351 aluminium joints", *Int. J. Fatigue*, vol. 25, pp. 77-88, January 2003.

[9] R. Citarella, P. Carlone, M. Lepore, and G.S. Palazzo, "A FEM-DBEM investigation of the influence of process parameters on crack growth in aluminum friction stir welded butt joints", *Key. Eng. Mater.*, vol. 554-557, pp. 2118-2126, April 2013.

[10] A. Ali, X. An, C.A. Rodopoulos, M. W. Brown, P. O'Hara, A. Levers, and S. Gardiner, "The effect of controlled shot peening on the fatigue behavior of 2024-T3 aluminium friction stir welds", *Int. J. Fatigue*, vol. 29, pp.1531-1545, August 2007.

[11] A.F. Golestaneh, Aidy Ali, and M. Zadeh, "Modelling the fatigue crack growth in friction stir welded joint of 2024-T351 Al alloy", *Mater. Des.*, vol. 30, pp. 2928-2937, September 2009.

[12] L. Fratini, S. Pasta, and A.P. Reynolds, "Fatigue crack growth in 2024-T351 friction stir welded joints: Longitudinal residual stress and microstructural effects", *Int. J. Fatigue*, vol. 31, pp. 495-500, March 2009.

[13] O. Hatamleh, "A comprehensive investigation on the effects of laser and shot peening on fatigue crack growth in friction stir welded AA 2195 joints", *Int. J. Fatigue*, vol. 31, pp. 974-988, May 2009.

[14] M. Peel, A. Steuwer, M. Preuss, and P.J. Withers, "Microstructure, mechanical properties and residual stresses as a function of welding speed in aluminium AA5083 friction stir welds", *Acta Mater.*, vol. 51, pp. 4791-4801, September 2003.

[15] M. Grujicic, G. Arakere, H.V. Yalavarthy, T. He, C.-F. Yen, and B.A. Cheeseman, "Modeling of AA5083 material-microstructure evolution during butt friction-stir welding", *J. Mater. Eng. Perform.*, vol. 19, pp.672-684, July 2010.

[16] H. Lombard, D.G. Hattingh, A. Steuwer, and M.N. James, "Effect of process parameters on the residual stresses in AA5083-H321 friction stir welds", *Mater. Sci. Eng. A Struct.*, vol. 501, pp. 119-124, February 2009.

[17] K. Deplus, A. Simar, W. Van Haver, and B. de Meester, "Residual stresses in aluminium alloy friction stir welds", *Int. J. Adv. Manuf. Technol.*, vol. 56, pp. 493-504, September 2011.

[18] L. Fratini, and B. Zuccarello, "An analysis of through-thickness residual stresses in aluminium FSW butt joints", *Int. J. Mach. Tool. Manuf.*, vol. 46, pp. 611-619, May 2006.

[19] W. Xu, J. Liu, and H. Zhu, "Analysis of residual stresses in thick aluminum friction stir welded butt joints", *Mater. Des*., vol. 32, pp. 2000-2005, April 2011.

[20] M.T. Milan, W.W. Bose Filho, J.R. Tarpani, A.M.S. Malafaia, C.P.O. Silva, B.C. Pellizer, and L.E. Pereira, "Residual stress evaluation of AA2024-T3 friction stir welded joints", *J. Mater. Eng. Perform.*, vol. 16, pp. 86-92, February 2007.

[21] M.A. Sutton, A.P. Reynolds, D.-Q. Wang, and C.R. Hubbard, "A study of residual stresses and microstructure in 2024-T3 Aluminum friction stir butt welds", *J. Eng. Mater.-T.ASME*, vol. 124, pp. 215-221, April 2002.

[22] P. Carlone and G.S. Palazzo, "Influence of process parameters on microstructure and mechanical properties in AA2024-T3 friction stir welding", *Metallogr. Microstruct. Anal.*, DOI 10.1007/s13632-013-0078-4, 2013.

[23] C. Genevois, D. Fabrègue, A. Deschamps, and W.J. Poole, "On the coupling between precipitation and plastic deformation in relation with friction stir welding of AA2024 T3 aluminium alloy", *Mater. Sci. Eng. A Struct.*, vol. 441, pp. 39-48, December 2006.

[24] P. Carlone and G.S. Palazzo, "A numerical and experimental analysis of microstructural aspects in AA2024-T3 friction stir welding", *Key. Eng. Mater.*, vol. 554-557, pp. 1022-1030, April 2013.

[25] H. Atharifar, D. Lin, and R. Kovacevic, "Numerical and experimental investigations on the loads carried by the tool during friction stir welding", *J. Mater. Eng. Perform.*, vol. 18, pp. 339-350, June 2009.

[26] R. Nandan, G.G. Roy, and T. Debroy, "Numerical Simulation of Three-Dimensional Heat Transfer and Plastic Flow During Friction Stir Welding", *Metall. Mater. Trans. A*, vol. 37, pp. 1247-1259, April 2006.

[27] M.B. Prime, "Cross-sectional mapping of residual stresses by measuring the surface contour after a cut", *J. Eng. Mater.-T.ASME*, vol. 123, pp.162-168, April 2001.

[28] H.F Bueckner., "The propagation of cracks and the energy of elastic deformations", *Trans. A.S.M.E.*, vol. 80, pp. 1225-1230, August 1958.

[29] W. Woo, H. Choo, M.B. Prime, Z. Feng, and B. Clausen, "Microstructure, texture and residual stress in a friction-stir-processed AZ31B magnesium alloy", *Acta Mater.*, vol. 56, pp. 1701-1711, May 2008.

[30] O. Hatamleh and A. DeWald, "An investigation of the peening effects on the residual stresses in friction stir welded 2195 and 7075 aluminum alloy joints", *J. Mater. Process. Technol.*, vol. 209, pp. 4822-4829, June 2009.

[31] M.B. Prime, T. Gnäupel-Herold, J.A. Baumann, R.J. Lederich, D.M. Bowden, and R.J. Sebring, "Residual stress measurements in a thick, dissimilar aluminum alloy friction stir weld", *Acta Mater.*, vol. 54, pp. 4013-4021, September 2006.

[32] V. Richter-Trummer, E. Suzano, M. Beltrão, A. Roos, J.F. dos Santos, and P.M.S.T. de Castro, Influence of the FSW clamping force on the final distortion and residual stress field, *Mater. Sci. Eng. A Struct.*, vol. 538, pp. 81- 88, March 2012.

[33] M.B. Prime, R. J. Sebring, J. M. Edwards, D. J. Hughes, and P. J. Webster, "Laser surface-contouring and spline data-smoothing for residual stress measurement", *Exp. Mech.*, vol. 44, pp.176-184, April2004.

[34] P. Carlone and G.S. Palazzo, "Experimental analysis of the influence of the process parameters on residual stress in AA2024-T3 friction stir welds", *Key. Eng. Mater.*, vol. 504-506, pp. 753-758, February 2012.

Heave Compensation Control for Benthic Coring Drill

Babita Meher, *Department of Mechanical Engineering, Aryan Institute of Engineering & Technology, Bhubaneswar, baitamh784@gmail.com*

Debi Prasad Singh, *Department of Mechanical Engineering, Raajdhani Engineering College, Bhubaneswar, deboprasad_1159@gmail.com*

Kankan Mandal, *Department of Civil Engineering, Capital Engineering College, Bhubaneswar, kankanmandal2@outlook.com*

Subhasis Sarkar, *Department of Mechanical Engineering, NM Institute of Engineering & Technology, Bhubaneswar, subhasissarkar14@yahoo.co.in*

Abstract: Severe environment in deep ocean affects operating reliability and security of coring drill. Adopting heave motion signal measured by accelerometer to confirm heave compensation of coring drill, the compensation control method is proposed using disturbance observer to restrain the disturbance. Then, the disturbance observer is designed. The heave motion simulation for coring drill is done with this control method, and the results show that the heave motion compensation control of coring drill using disturbance observer avoids the disturbance with high tracking quality, and provides high reliability and security to coring drill operating.

Keywords: Coring drill, disturbance observe, heave motion, hydraulic system, path tracking, winch.

INTRODUCTION

With the development of resource exploration in deep sea, the working depth for resource exploration equipment is deeper, and the working environment is more abominable [1, 2]. The power and control signal for benthic coring drill is acquired by umbilical cable. Under the effects of surge, wave and flow in deep sea, horizon and vertical movements are produced. The heave motion in vertical makes the loads in umbilical cable increase, which would destroy the umbilical cable making coring drill dropped, and reduce the working reliability and security of benthic coring drill. In order to avoid the effects on abominable environment, active heave compensation control is studied widely. According to ship movement and cylinder displacement, Hu [3] proposes the compensation control method to heave motion with crown block compensation device; Yang [4] adopts a novel approximate feedback linearization approach to realize the heave motion compensation of a spatial 6-DOF hydraulic parallel manipulator; Kord [5] uses linear control technology to compensate the ship heave motion; Johansen [6] establishes the heave compensation system for crane on ship using synchronous control to wave; considering the loads generated by abominable environment, Skaare and Egeland [7] design the complex controller of force and displacement. Benthic coring drill is draw by winch under the inhibition of weight and space. However, the study on active compensation control using winch is very little [8].

In the paper, the active heave motion compensation control using winch is carried on. Using ship heave motion displacement measured by accelerometer to calculate the heave compensation value of benthic coring drill, combining disturbance observe to restrain the disturbance of sever environment, the active heave compensation control system is put forward, which improves heave motion tracking precision of the drill, and ensures the working reliability and security.

COMPOSITION OF HEAVE MOTION SYSTEM FOR BENTHIC CORING DRILL

The heave motion compensation system using winch is shown in Fig. (**1**). The effects of environment on coring drill are acquired through ship heave motion measured by accelerometer. The controller calculates the heave motion compensatory value according to the moving signal of a ship. Combing disturbance observer to control proportional directional valve, the heave motion track of winch is realized. When the accelerometer detects the ship sinkage under ocean disturbance load, the controller calculates the compensation value and makes proportion direction valve work on the underside. A part of high pressure oil flows into the brake cylinder, which makes the brake open. Other high pressure oil flows into the hydraulic motor. The hydraulic motor makes the winch running in counter-clockwise, and the umbilical cable is taken back. When the accelerometer detects the ship raise under ocean disturbance load, the controller calculates the compensation value and makes proportion direction valve work on the upside. A part of high pressure oil flows into the brake cylinder, which makes the brake open. Other high pressure oil flows into the hydraulic motor. The hydraulic motor makes the winch run in clockwise, and the umbilical cable is released.

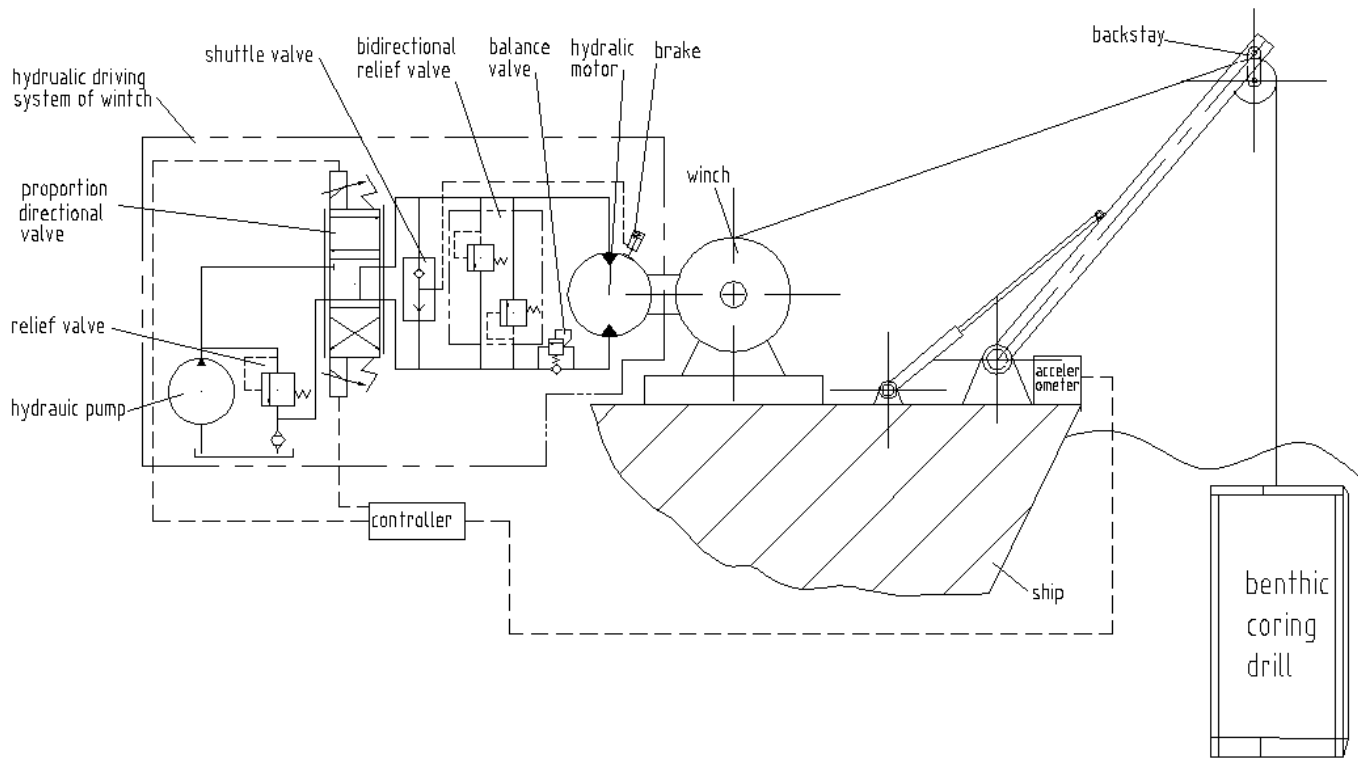

Fig. (1). Heave motion compensation system scheme of coring drill.

Neglecting the elastic deforming of umbilical cable, the relation of winch movement, coring drill movement and ship movement is written as follows:

$$W(t) = S(t) + D(t) \ldots \tag{1}$$

where, $W(t)$ is moving displacement of winch; $S(t)$ is moving displacement of ship; $D(t)$ is moving displacement of benthic coring drill.

To ensure working reliability and security of benthic coring drill, the moving displacement of coring drill must be very small, $D(t) \approx 0$. Then, the compensation control of coring drill movement is transformed to reverse movement tracking of winch moving displacement $W(t)$ and ship moving displacement $S(t)$. Therefore, the reverse moving track can be realized through proportion directional valve control winch moving, which ensures the compensation control of coring drill movement.

MATHEMATICAL MODEL OF HEAVE COMPENSATION SYSTEM FOR BENTHIC CORING DRILL

Moving Equation of Winch

The dynamic character of coring drill drawing through hydraulic winch is affected by loads. The load is composed by inertia force, viscosity force and disturbance force by wave. The torque equation of hydraulic winch is as follows:

$$J_{dr}\ddot{\theta} + B_{dr}\dot{\theta} + F_t(\theta,\dot{\theta},t)R_{dr} = (p_i - p_o)D_m \ldots \tag{2}$$

where, θ is the revolving angle for roller of hydraulic winch, rad; J_{dr} is equivalent revolve inertia, $kg \cdot m^2$; B_{dr} is the viscosity coefficient, $N \cdot s \cdot rad^{-1}$; R_{dr} is the diameter of roller, m; p_i is the inlet pressure of hydraulic motor for winch, Pa; p_o is the outlet pressure of hydraulic motor for winch, pa; D_m is equivalent displacement considering gear ratio, $D_m = V_m i$, V_m is the displacement of driving motor for hydraulic winch, $m^3 \cdot rad^{-1}$, i is the gear ratio of planet retard for hydraulic winch; R_{dy} is the diameter of roller for hydraulic winch, m; $F_t(\theta,\dot{\theta},t)$ is the equivalent load on umbilical cable, N;

$$F_t(\theta,\dot{\theta},t) = m_{rd}g - \rho_w g V_{rd} + f(\theta,\dot{\theta},t) \ldots \tag{3}$$

where, m_{rd} is the mass of coring drill, kg; ρ_w is the density of seawater, $kg \cdot m^{-3}$; g is the acceleration of gravity, $kg \cdot m \cdot s^{-2}$; V_{rd} is the volume of coring drill, m^3; $f(\theta,\dot{\theta},t)$ is the disturbance load of sever environment in deep sea, N.

Mathematical Model of Hydraulic System for Coring Drill Heave Motion Control

Suppose the connection pipe of proportion directional valve and driving motor is disposed symmetry, the pressure in the working chambers is the same, the inside and outside leakage of hydraulic motor is laminar flow, treating bulk modulus of hydraulic oil as constant and ignoring the pressure loss in connecting pipe, the flow into and out of the hydraulic motor are written as follows:

$$\begin{cases} q_i = D_m \dot{\theta} + C_{im}(p_i - p_o) + C_{em} p_i + \frac{V_1}{\beta_e} \dot{p}_1 \\ q_o = D_m \dot{\theta} + C_{im}(p_i - p_o) - C_{em} p_o - \frac{V_2}{\beta_e} \dot{p}_o \end{cases} \cdots \quad (4)$$

where, q_i is the flow into hydraulic motor, $m^3 \cdot s^{-1}$; q_o is the flow out of hydraulic motor, $m^3 \cdot s^{-1}$; θ is revolving angle for roller of hydraulic winch, rad; C_{im} is inside leakage coefficient of hydraulic motor, $m^3 \cdot s^{-1} \cdot Pa^{-1}$; C_{em} is outside leakage coefficient of hydraulic motor, $m^3 \cdot s^{-1} \cdot Pa^{-1}$; V_1 is the inlet chamber of hydraulic motor, m^3; V_2 is the outlet chamber of hydraulic chamber, m^3; β_e is the bulk modulus of hydraulic oil, Pa.

Neglecting the dynamic effects of the pipe between proportion valve and hydraulic motor, the flow through the proportion valve is equivalent to the flow out of the motor. The flow through proportion valve can be written as follows by orifice flow formula.

$$q_i = c_d \psi x_{pv} \sqrt{\frac{2}{\rho} \Delta p_1}\ ,\ \Delta p_1 = \begin{cases} p_s - p_i; x_{pv} > 0 \\ p_i - p_T; x_{pv} < 0 \end{cases} \cdots \quad (5)$$

$$q_o = c_d \psi x_{pv} \sqrt{\frac{2}{\rho} \Delta p_2}\ ,\ \Delta p_2 = \begin{cases} p_s - p_i; x_{pv} < 0 \\ p_i - p_T; x_{pv} > 0 \end{cases} \cdots \quad (6)$$

where, c_d is flow coefficient ; ψ is Proportional valve port area gradient, m; x_{pv} is the spool displacement of proportional valve, m; ρ is the density of oil, $Kg \cdot m^{-3}$; p_i is the pressure in inlet chamber of hydraulic motor, Pa; p_o is the pressure in outlet chamber of hydraulic motor, Pa; p_s is the system pressure, Pa; p_T is the pressure of return oil, Pa.

Through control compensation, the relation between input of proportional directional valve and spool displacement can be written as follows using one order inertial.

$$\dot{x}_{pv} = -\frac{1}{T_{pv}} x_{pv} + \frac{k_{pv}}{T_{pv}} u \ldots \quad (7)$$

where, x_{pv} is the spool displacement of proportion directional valve, m; T_{pv} is constant coefficient of time for proportion valve, s; k_{pv} is the gain of proportional valve, m.

Linearization Model of Heave Compensation System for Benthic Coring Drill

Proportional directional valve is zero four sides spool valve, four throttles are disposed symmetry. Having a linearization of throttle flow on spool displacement $x_{pv} = 0$, we can get

$$\begin{cases} q_i = K_q x_{pv} - K_p p_i \\ q_o = K_q x_{pv} + K_p p_o \end{cases} \cdots \quad (8)$$

where, K_q is the flow gain of throttle for proportion valve, $m^2 \cdot s^{-1}$; K_p is the gain between flow and pressure, $m^3 \cdot s^{-1} \cdot Pa^{-1}$.

The transform function of heave motion for benthic coring drill is written as follows through the Laplace transformation to Eq.(2), Eq.(4), Eq.(7) and Eq.(8).

$$\theta(s) = \frac{\frac{k_{pv} k_q D_m}{1 + T_{pv} s} U(s) - (k_{ce} + \frac{V_e}{2\beta_e} s) R_{dr} F_t(s)}{\frac{J_{dr} V_e}{2\beta_e} s^3 + (\frac{B_{dr} V_e}{2\beta_e} + k_{ce} J_{dr}) s^2 + (k_{ce} B_{dr} + D_m^2) s} \cdots \quad (9)$$

where, $U(s)$ is the system control input of heave motion compensation, $F_t(s)$ is the disturbance load.

The viscosity coefficient B_{dr} is very small. Neglecting the volume difference of inlet and outlet chamber in hydraulic motor, the dynamic equation of heave motion for benthic drill can be simplified as follows:

$$\begin{cases} \theta(s) = G_u(s) U(s) + G_d(s) F_t(s) \\ G_u(s) = \frac{k_{pv} k_q}{D_m (1 + T_{pv} s)} \cdot \frac{\omega_n^2}{s(s^2 + 2\xi \omega_n s + \omega^2)} \\ G_d(s) = -(\frac{k_{ce}}{D_m^2} + \frac{V_e}{2\beta_e D_m^2} s) \cdot \frac{\omega_n^2}{s(s^2 + 2\xi \omega_n s + \omega^2)} \end{cases} \cdots \quad (10)$$

where, k_{pv} is the gain of proportion valve; K_q is the flow gain of throttle for proportion valve; D_m is equivalent displacement considering gear ratio; T_{pv} is constant coefficient of time for proportion valve,

$$s\ ; \omega_n = \sqrt{\frac{2\beta_e D_m^2}{J_{dr} V_e}}$$

is the hydraulic natural frequency, V_e is the equivalent volume of inlet chamber for motor;

$$\xi = \frac{k_{ce}}{D_m} \sqrt{\frac{\beta_e J_{dr}}{2V_e}}$$

is the hydraulic damping ratio, and $k_{ce} = k_p + C_{im} + \frac{C_{em}}{2}$ is the total gain of flow.

DESIGN OF DISTURBANCE OBSERVER FOR BENTHIC CORING DRILL HEAVE MOTION SYSTEM

According to the disturbance observer design method used by Velardocchia [9] and Traverso [10], the control block diagram of benthic coring drill with disturbance observer is designed as shown in Fig. (**2**). In the figure, r is the reference input, θ is the revolve angel of roller, d is the equivalent disturbance load on umbilical cable, n is the measured noise. The disturbance observe is in range of double point line, $G_n(s)$ is the nominal model, $G_u(s)$ is control object, $\hat{d}$ is the estimate value of equivalent disturbance load, $Q(S)$ is the low pass filter. Disturbances observer uses the inverse of nominal model $G_n^{-1}(s)$ to estimate u. The estimate value $\hat{d}$ of equivalent disturbance load is acquired by the difference in the value of $\hat{u}$ and u_1. The controller inhibits the disturbance according to the feedback estimate value $\hat{d}$ of equivalent disturbance load. However, the accurate control object model $G_u(s)$ cannot be acquired, making the estimate value $\hat{d}$ hardly acquired. The design method of disturbance observe proposed by Kempf [11, 12] makes the design simplified to choose the nominal model $G_n(s)$ and the design of a low pass filter $Q(s)$.

Nominal Model of Control Object

According to Eq.(9), $G_u(s)$ can be transformed as follows

$$G_u(s)=\frac{k_e}{s(1+T_{pv}s)}\cdot\frac{\omega_n^2}{s^2+2\xi\omega_n s+\omega^2} \quad \cdots \tag{11}$$

where, $k_e=\frac{k_q k_{pv}}{D_m}$, equivalent coefficient; k_{pv} is the gain of proportion valve; K_q is the flow gain of throttle for proportion valve; D_m is the equivalent displacement considering gear ratio; T_{pv} is constant coefficient of time for proportion valve, s; ω_n is the hydraulic natural frequency; V_e is the equivalent volume of inlet chamber for motor; ξ is the hydraulic damping ratio.

By Eq. (11), control object $G_u(s)$ can be obtained by integration, control object, inertia and two order vibration link in series. In practice, $\frac{V_e}{\beta_e}<<D_m^2$ and the hydraulic damper is relatively small making hydraulic natural frequency ω_n of two second concussion link very large, the gain characteristics in the low frequency range is very straight and the phase lag is small. Ignoring dynamic characteristics in high frequency of this link, the simplified nominal model is written as Eq. (12) shown.

$$G_u(s)=\frac{k_e}{s(1+T_{pv}s)} \quad \cdots \tag{12}$$

where, k_e is the equivalent coefficient; T_{pv} is constant coefficient of time for proportion valve.

Design of Low Pass Filter

In Fig. (**2**), the function between system output θ and input parameters u, d and n can be written as Eq.(13).

$$\begin{cases} G_{U\theta}=\dfrac{G_u(s)G_n(s)}{G_n(s)+Q(s)[G_u(s)-G_n(s)]} \\ G_{D\theta}=\dfrac{G_u(s)G_n(s)[1-Q(s)]}{G_n(s)+Q(s)[G_u(s)-G_n(s)]} \\ G_{N\theta}=\dfrac{G_u(s)Q(s)}{G_n(s)+Q(s)[G_u(s)-G_n(s)]} \end{cases} \quad \cdots \tag{13}$$

Suppose the bandwidth of low pass filter is f_q, when $f\le f_q$, $Q(s)\approx 1$, $G_{D\theta}(s)\approx 0$, $G_{U\theta}(s)\approx G_n(s)$, $G_{N\theta}(s)\approx 0$. This shows that in the bandwidth of low pass filter $Q(s)$, the disturbance observer makes system output equal to output through the nominal model having a strong inhibitory effect on the interference. In the design disturbance observer, $Q(s)G_n^{-1}(s)$ must be regular. According to the design method of Lee [13], $Q(s)$ is designed as follow:

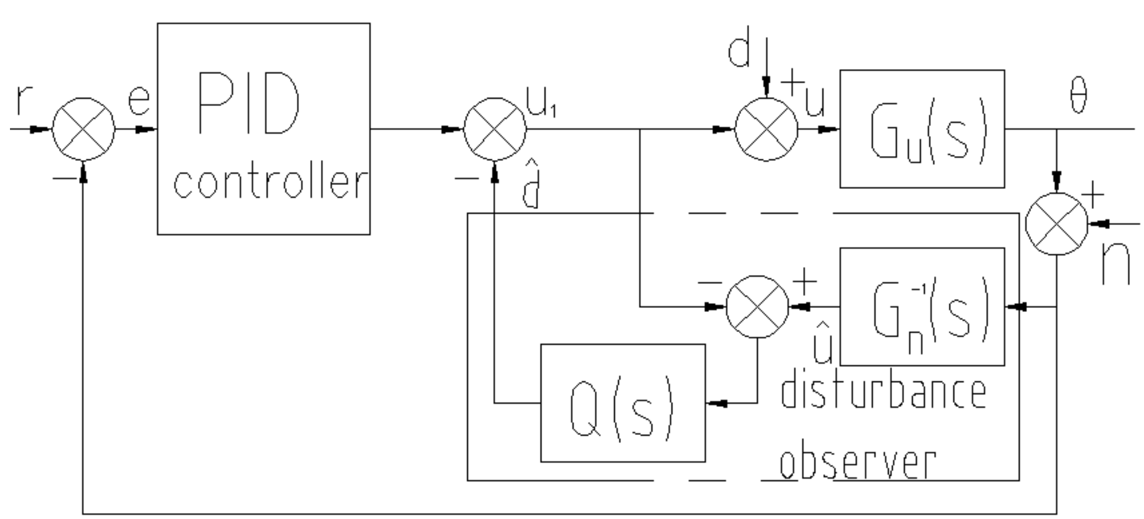

Fig. (2). Control block diagram of coring drill heave motion with disturbance observer.

$$Q(s)=\frac{\sum_{k=0}^{M}\alpha_k(\tau s)^k}{(\tau s+1)^N} \dots \tag{14}$$

where, $\alpha_k=\dfrac{N!}{(N-k)!k!}$ is the coefficient; N is the order of denominator ; M is the order of numerator.

The control object $G_u(s)$ can be described by perturbation of nominal model $G_n(s)$ as Eq. (15) shows.

$$G_u(s)=G_n(s)(1+\Delta(s)) \dots \tag{15}$$

where, $\Delta(s)$ is the perturbation of nominal model to actual control object. Therefore, the necessary and sufficient robust stable condition for $Q(s)$ is $\|Q(s)\Delta(s)\|_\infty \le 1$.

By Eq. (11) ~ (14), the low pass filter $Q(s)$ is written as follows:

$$Q(s)=\frac{3\tau s+1}{s^3+3\tau s^2+3\tau s+1} \dots \tag{16}$$

In Eq. (16), the value of τ decides the bandwidth of $Q(s)$, which should consider the ability of disturbance inhibition and the sensitivity of measured noise to choose.

SIMULATION ANALYSIS OF HEAVE MOTION CONTROL FOR BENTHIC CORING DRILL

The dead zone of proportional controller in the test can be eliminated by voltage compensation through soft control. Therefore, the effect of dead zone to system response can be ignored. According to Eq. (2) ~ Eq. (16), the simulation model of heave motion control is built as Fig. (**3**). The value of main parameters is given in Table **1**.

The heave motion control curve in the model is decided by ship heave motion. In the forth sea trial condition, the heave motion control curve $W(t)$ and the disturbance load $f(\theta,\dot{\theta},t)$ can be written as follows:

$$\begin{cases} W(t)=1.3\sin(0.84t) \\ f(\theta,\dot{\theta},t)=2000\sin(0.84t) \end{cases} \dots \tag{17}$$

Using this model, the simulations with and without disturbance observer are carried on. The heave motion curve of benthic drill without disturbance observer is shown in Fig. (**4**), and the curve with disturbance observer is shown in Fig. (**5**). The observer of disturbance load using disturbance observer is shown as Fig. (**6**).

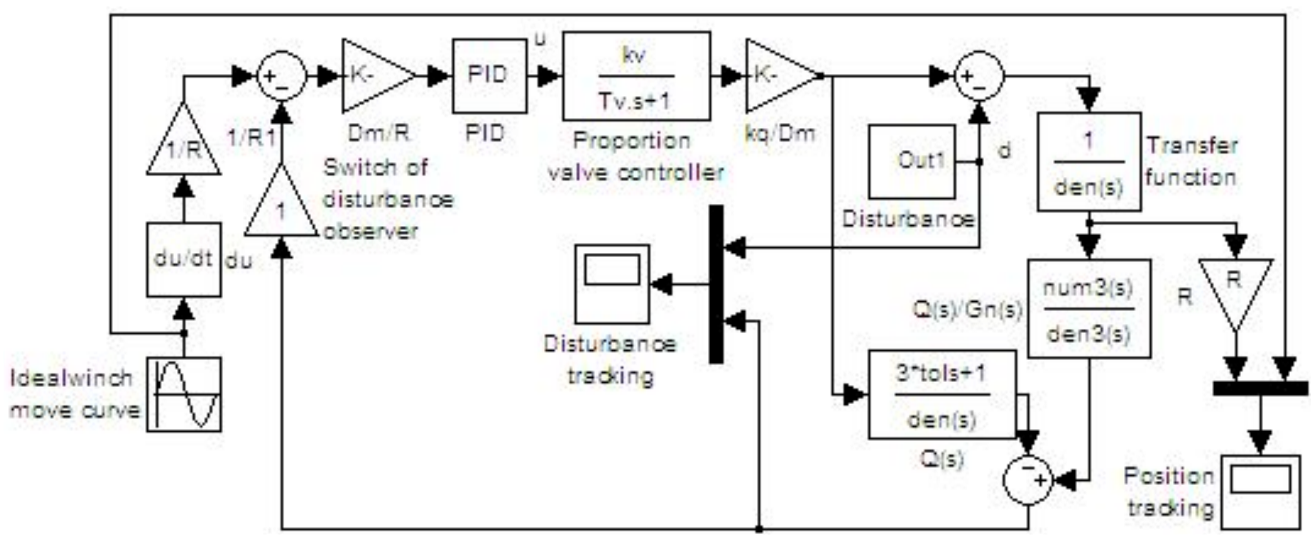

Fig. (3). Simulation model of heave motion control for coring drill.

Table 1. Parameters of Heave Motion Control Model for Coring Drill

Parameters	Value	Parameters	Value
$K_q / m^2 \cdot s^{-1}$	0.467	$D_m / m^3 \cdot rad^{-1}$	1.43×10^{-3}
T_{pv} / s	0.06	β_e / Pa	1.7×10^{9}
m_{rd} / kg	8000	k_{pv} / m	1.25×10^{-5}
R_{dr} /m	1	$k_{ce} / m^3 \cdot s^{-1} \cdot Pa^{-1}$	6.48×10^{-12}
$J_{dr} / kg \cdot m^2$	1028	V_e / m^3	4×10^{-3}

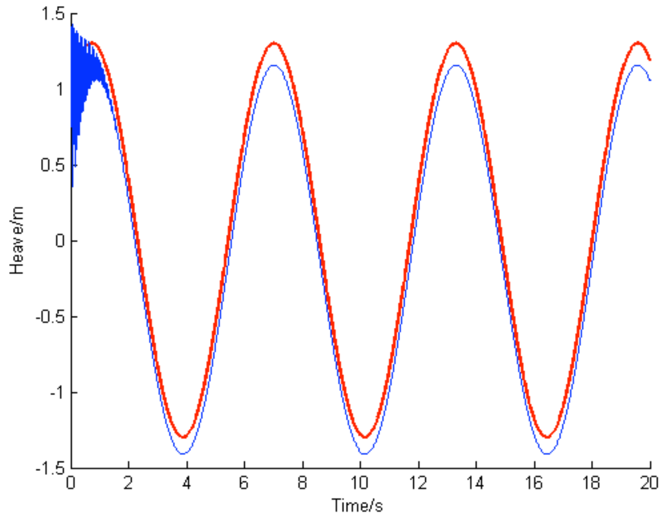

Fig. (4). Drill moving curve without disturbance observer.

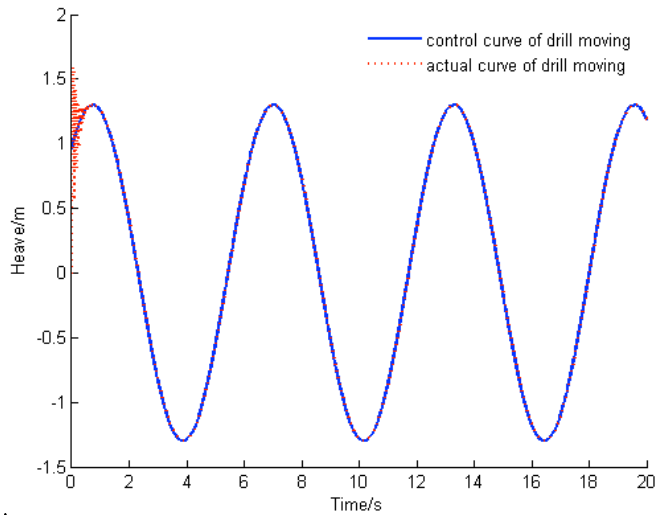

.

Fig. (5). Drill moving curve with disturbance observer.

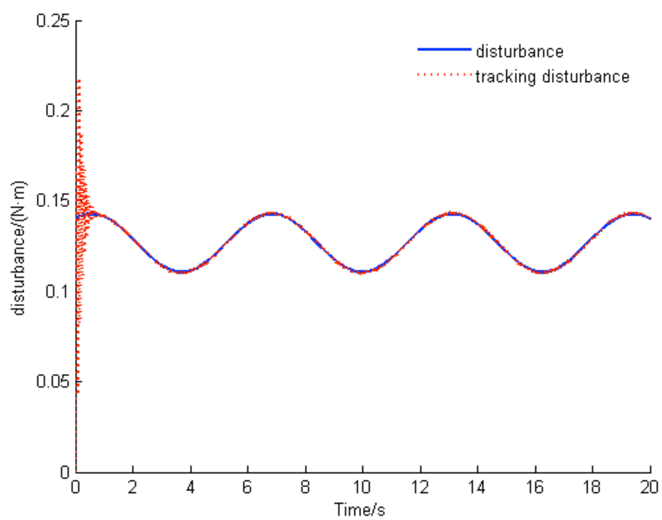

Fig. (6). Observed disturbance curve.

The figures show that the compensation system without disturbance observes works in steady status after 1.513s. However, the compensation systems with disturbance observe works in steady status after 1.29s, and the tracing disturbance load achieves steady status in 0.822s. The responses of the compensation system with disturbance observe is quicker than the compensation system without disturbance observes.

The figures also show that the maximum relative error of disturbance load between the acquirement of disturbance observe and the actual value is 11.9% after reaching the steady-state, which realize the good tracking precision of disturbance load. The minimum relative error of heave motion displacement acquired without disturbance observe to ideal moving displacement is 15.1%, and the maximum relative error of heave motion displacement acquired with disturbance observe to ideal moving displacement is only 6.5%. Therefore, the control with disturbance observe improves the heave motion tracking accuracy of benthic coring drill, and also avoid disturbance of environment load to benthic drill control.

CONCLUSION

Using accelerometer measure ship heave motion to decide heave motion compensation value of benthic coring drill, the heave motion compensation control model using disturbance observe is designed. Using this model, the maximum relative disturbance load error is 11.9% and the maximum relative displacement tacking error is 6.5%. The control with disturbance observe makes heave motion control of benthic drill have a high tracking precision and disturbance inhibition, which can avoid the disturbance of environment load to benthic drill control and ensure the working reliability and security of the drill.

CONFLICT OF INTEREST

The authors confirm that this article content has no conflict of interest.

REFERENCES

[1] K. D. Do, and J. Pan, “Nonlinear control of an active heave compensation system”, *Ocean Engineering*, vol. 35, pp. 558-571, April, 2008.

[2] W. L. Yang, Z. Y. Zhang, and A. Q. Zhang, “Study on active heave compensation system for underwater vehicle”, *The Ocean Engineering*, Vol. 25, pp. 68-73, March, 2007.

[3] Q. Hu, S. J. Liu, and H. Zheng, “Design and implementation of model test installation of heave compensation system of deep-sea mining”, *Journal of Central South University of Technology*, Vol. 18, pp. 642-649, November, 2011.

[4] C. Yang, S. Zheng, O. O. Peter, Q. Huang, and J. Han, "Approximate Feedback Linearization Control for Spatial 6-DOF

Hydraulic Parallel Manipulator", *The Open Mechanical Engineering Journal*, vol. 5, pp. 117-123, February, 2011.

[5] U. A. Korde, “Active heave compensation on drill-ships in irregular waves”, *Ocean Engineering*, Vol. 25, pp. 541-561, July, 1998.

[6] T. A. Johansen, T. I. Fossen, S. I. Sagatun, and F. G. Nielsen, “Wave synchronizing crane control during water entry in offshore moonpool operations-experimental result”, *IEEE Journal of Oceanic Engineering*, Vol. 28, pp. 720-728, October, 2003.

[7] B. Skaare, and O. Egeland O, “Parallel force/position crane control in marine operation “, *IEEE Journal of Oceanic Engineering*, Vol. 31, pp. 599-613, July, 2006.

[8] W. X. Wang, Y.M. Gong, X. H. Lai, X. J. Yu, and Z. H. Huang, “Technical analysis on offshore drilling draw works heave compensation system”, *Oil Field Equipment*, Vol. 12, PP. 18-21, December, 2010.

[9] M. Velardocchia, and A. Vigliani, "Control systems integration for enhanced vehicle dynamics", *The Open Mechanical Engineering Journal*, vol. 7, pp. 58-69, September, 2013.

[10] A. Traverso, R. Bertone, and A. F. Massardo, "Transient Modelling of a Rotary-Kiln Pyrolyser", *The Open Mechanical Engineering Journal*, vol. 1, pp. 1-13, August, 2007.

[11] C. J. Kempf, and S. Kobayashi, “Disturbance observer and feed forward design for a high-speed-direct-drive positioning table”, *IEEE Transaction on Control System and Technology*, Vol. 7, pp. 513-526, September, 1999.

[12] S. Zhou, Y. T. Li, G. Meng, and H. Ding, “Active vibration isolation with switching control method based on disturbance observer”, *Journal of vibration and shock*, Vol. 25, pp. 121-123, June, 2006.

[13] H. S. Lee, Robust digital tracking controller for high speed high-accuracy positioning systems. California, Berkeley, 1994.

PLOTTING

Citicon Engineers has now come up with this new township to give ownership of the land to aspiring and potential buyers.However, most of the buyers are sceptical about the authenticity of land they purchase;

INDEPENDENT HOUSES

A way of living that is kinder to the planet. Citicon Engineers belief has inspire to create a lush,tropical villa community where nature and innovation walk hand in hand. Where the gift of solar energy...

APARTMENT

Citicon Engineers focuses on building aesthetically and structurally remarkable projects. A full service landholding development company that offers the best commercial properties and residential properties .